Numerical Methods and Advanced Simulation in Biomechanics and Biological Processes

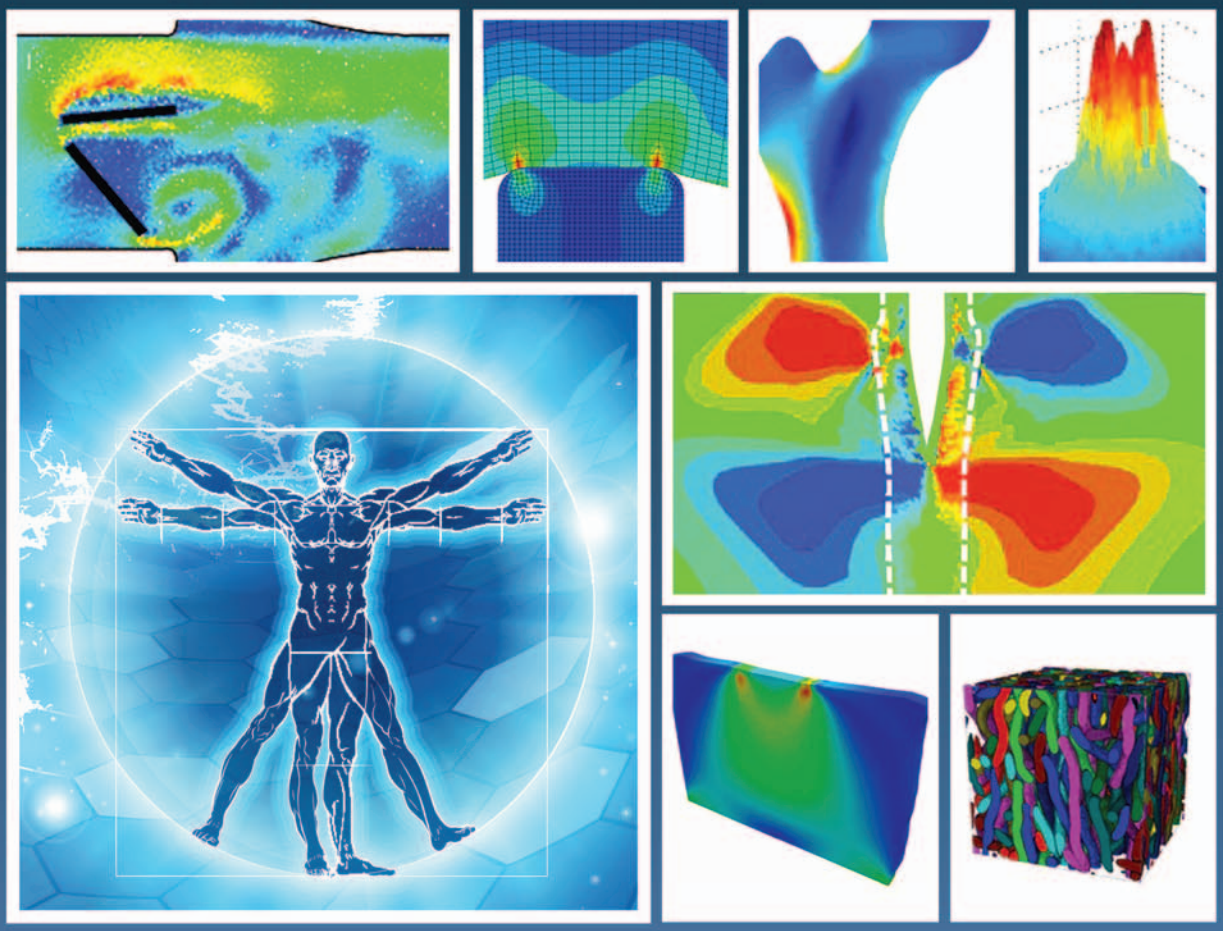

Edited by
Miguel Cerrolaza, Sandra J. Shefelbine
and Diego Garzón-Alvarado

Numerical Methods and Advanced Simulation in Biomechanics and Biological Processes

This book belongs to

Central Library

BADJI Mokhtar-ANNABA UNIVERSITY

Copyright Elsevier 2024

This page intentionally left blank

This book belongs to Central Library BADJI Mokhtar-ANNABA UNIVERSITY

Copyright Elsevier 2024

Numerical Methods and Advanced Simulation in Biomechanics and Biological Processes

Edited by

Miguel Cerrolaza, Sandra J. Shefelbine and Diego Garzón-Alvarado

ELSEVIER

ACADEMIC PRESS
An imprint of Elsevier

This book belongs to Central Library BADJI Mokhtar-ANNABA UNIVERSITY

Copyright Elsevier 2024

Academic Press is an imprint of Elsevier
125 London Wall, London EC2Y 5AS, United Kingdom
525 B Street, Suite 1800, San Diego, CA 92101-4495, United States
50 Hampshire Street, 5th Floor, Cambridge, MA 02139, United States
The Boulevard, Langford Lane, Kidlington, Oxford OX5 1GB, United Kingdom

Copyright © 2018 Elsevier Ltd. All rights reserved.

No part of this publication may be reproduced or transmitted in any form or by any means, electronic or mechanical, including photocopying, recording, or any information storage and retrieval system, without permission in writing from the publisher. Details on how to seek permission, further information about the Publisher's permissions policies and our arrangements with organizations such as the Copyright Clearance Center and the Copyright Licensing Agency, can be found at our website: www.elsevier.com/permissions.

This book and the individual contributions contained in it are protected under copyright by the Publisher (other than as may be noted herein).

Notices
Knowledge and best practice in this field are constantly changing. As new research and experience broaden our understanding, changes in research methods, professional practices, or medical treatment may become necessary.

Practitioners and researchers must always rely on their own experience and knowledge in evaluating and using any information, methods, compounds, or experiments described herein. In using such information or methods they should be mindful of their own safety and the safety of others, including parties for whom they have a professional responsibility.

To the fullest extent of the law, neither the Publisher nor the authors, contributors, or editors, assume any liability for any injury and/or damage to persons or property as a matter of products liability, negligence or otherwise, or from any use or operation of any methods, products, instructions, or ideas contained in the material herein.

Library of Congress Cataloging-in-Publication Data
A catalog record for this book is available from the Library of Congress

British Library Cataloguing-in-Publication Data
A catalogue record for this book is available from the British Library

ISBN: 978-0-12-811718-7

For information on all Academic Press publications visit our website at https://www.elsevier.com/books-and-journals

ELSEVIER
Book Aid International
Working together to grow libraries in developing countries
www.elsevier.com • www.bookaid.org

Publisher: Mara E. Conner
Acquisition Editor: Fiona Geraghty
Editorial Project Manager: Jennifer Pierce
Production Project Manager: Mohanapriyan Rajendran
Designer: Victoria Pearson

Typeset by TNQ Books and Journals

This book belongs to Central Library BADJI Mokhtar-ANNABA UNIVERSITY
Copyright Elsevier 2024

Contents

List of Contributors xiii
Foreword xv
Preface xvii

Part I
Finite Element Methods

1. Discontinuous Finite Element Model of Hydrogels: Predicting Stiffness of Nanofibers

X. Gao, E. Sozumert, V. Silberschmidt

1.1 Introduction 3
1.1.1 Background 3
1.1.2 Experimental Measurements 3
1.1.3 Inverse Parameter Estimation 4
1.2 Multiscale Modeling 4
1.2.1 Continuous Modeling Approaches 5
1.2.2 Discontinuous-Based Modeling 5
1.2.3 Fiber Cross-Links 9
1.2.4 Generation of a Computational Model 10
1.3 A Case Study: Prediction of Axial Modulus of Nanofibers in Bacterial Cellulose Hydrogel 11
1.3.1 Microstructure of Bacterial Cellulose Hydrogel 11
1.3.2 Correlation of Microstructure Behavior and Global Response 12
1.3.3 Generation of Discontinuous Finite Element Model 13
1.3.4 Representative Volume Element 14
1.4 Summary and Conclusions 14
References 14

2. Modeling the Influence of Mechanics on Biological Growth

E. Comellas, A. Carriero, M. Giorgi, A. Pereira, S.J. Shefelbine

2.1 Introduction 17
2.2 Initial State 18
2.3 Mechanical Stimuli 19
2.4 Mechanobiological Algorithm 20
2.5 Examples of Mechanobiological Growth Simulations 25
2.5.1 Hypertrophic Muscle Growth 26
2.5.2 Joint Morphogenesis 28
2.5.3 Bone Deformities in the Proximal Femur in Cerebral Palsy 30
2.5.4 Adaptation of Murine Cortical Bone 31
2.6 Conclusions 32
References 32

3. Finite Element Modeling and Simulation of the Multiphysic Behavior of Articular Cartilage

M.H. Doweidar, M. Doblaré

3.1 Introduction 37
3.2 Numerical Modeling 38
3.2.1 Model Formulation 39
3.2.2 Numerical Implementation 45
3.3 Validation and Experimental Examples 45
3.3.1 Model Validation 45
3.3.2 Boundary Conditions 45
3.3.3 Initial Conditions 48
3.3.4 Free Swelling 48
3.3.5 Sample Subjected to Loading 50
3.4 Discussion and Conclusions 51
Acknowledgments 52
References 52

This book belongs to Central Library BADJI Mokhtar-ANNABA UNIVERSITY
Copyright Elsevier 2024

4. Image-Driven Constitutive Modeling for FE-Based Simulation of Soft Tissue Biomechanics

D.M. Pierce, T. Ricken, C.P. Neu

4.1 Introduction 55
4.1.1 Hallmarks of Soft Tissues 55
4.1.2 Finite Element Modeling of Soft Tissues 55
4.1.3 Need for Imaging Data to Drive Models 56
4.2 Building Blocks of a Multiphase Continuum Model 56
4.2.1 Multiphase Framework 56
4.2.2 Biphasic, Fiber-Reinforced Example for Soft Tissues 61
4.3 Image-Based Data Acquisition 63
4.3.1 Morphology and Geometry 64
4.3.2 Diffusion 64
4.3.3 Mapping Strain and Material Properties 65
4.4 Image-Driven Constitutive Models: Cartilage as a Representative System 65
4.4.1 Biphasic Cartilage Model 66
4.4.2 Integration of Computational Modeling and Experimental Data 69
4.4.3 Tissue Complexity Captured via Model Complexity 71
4.4.4 Model Tradeoffs and Considerations 71
4.5 Discussion and Future Directions 72
Acknowledgments 72
References 72

5. Finite Element Modeling of Turing Pattern Formation: An Application to Appearance and Location of Dentinal Tubules

J. Nino-Barrera, J.A. Guerrero, G. Nino, M. Cerrolaza, E.B. de las Casas, A.M. Ramírez Martínez, D.A. Garzón-Alvarado

5.1 Introduction 77
5.2 The Reaction–Diffusion Systems: Modeling and Solving 79
5.2.1 Reaction–Diffusion Equation 79
5.2.2 Biological Models: Brief Discussion on the Reactive Term 79
5.2.3 Conditions for Turing Instability 80
5.2.4 Finite Element Method 85
5.3 Case of Study 1: Morphogenesis of the Dentinal Tubules 87
5.3.1 Modeling Biochemical Factors Involved in Odontoblasts Differentiation 88
5.3.2 Numerical Implementation 88
5.3.3 Results 88
5.4 Case of Study 2: Role of DLX3 in the Heterogeneous Location of the Dentinal Tubules 89
5.4.1 Discussion of Results 90
References 92
Further Reading 94

6. A Discontinuous Galerkin Model for the Simulation of Chemotaxis Processes: Application to Stem Cell Injection After a Myocardial Infarction

F.J. Vermolen, L.Y.D. Crapts, J.K. Ryan

6.1 Introduction 95
6.2 Background on Stem Cell Therapy and the Numerical Method 97
6.3 The Mathematical Model 97
6.4 Numerical Method 99
6.4.1 The One-Dimensional Implementation 99
6.4.2 Extension to Two Spatial Dimensions 106
6.5 Numerical Results 110
6.5.1 One-Dimensional Results 110
6.5.2 Two-Dimensional Results 112
6.6 Discussion and Conclusions 113
6.6.1 The Snail Trail Model 113
6.6.2 The Numerical Method 113
References 114
Further Reading 115

Part II
Boundary Integral Methods

7. On the Use of Boundary Integral Methods in Bioelectromagnetics

D. Poljak

7.1 Introduction 119
7.2 Governing Equations of Theoretical Dosimetry 120
7.2.1 Exposure to Low-Frequency Fields 120
7.2.2 Exposure to High-Frequency Fields 120

This book belongs to Central Library BADJI Mokhtar-ANNABA UNIVERSITY
Copyright Elsevier 2024

7.3 Human Head Exposed to Video Display Unit Electrostatic Field 121
7.3.1 Boundary Element Solution 122
7.3.2 Computational Examples 123
7.4 Pregnant Woman/Fetus Exposure to Low-Frequency Fields 125
7.4.1 Boundary Element Solution 128
7.4.2 Computational Examples 128
7.5 Exposure to High-Frequency Electromagnetic Radiation: The Human Eye Exposed to Plane Wave 130
7.5.1 Boundary Element Solution 132
7.5.2 Finite Element Solution of Bioheat Transfer Equation 133
7.5.3 Computational Examples 134
7.6 Exposure to High-Frequency Electromagnetic Radiation: The Human Brain Exposed to Plane Wave 136
7.6.1 Dosimetry 137
7.6.2 Computational Examples 138
7.7 Exposure to High-Frequency Electromagnetic Radiation: Whole Body Exposed to Plane Wave 141
7.7.1 Tensor Volume Integral Equation—Solution via Method of Moments 141
7.8 Conclusion 142
References 142

8. BEM in Biomechanics: Modeling Advances and Limitations

M. Perrella, S. Gerbino, R. Citarella

Nomenclature 145
8.1 Introduction 145
8.2 Boundary Element Method 149
8.2.1 Applications in Fracture 150
8.2.2 Boundary Element Procedure for Elastostatic Problems 151
8.3 Dual Boundary Element Method 153
8.3.1 Crack Modeling 154
8.3.2 Modeling Strategy 155
8.3.3 Discontinuous Elements 156
8.4 Boundary Element Modeling in Biomedical Engineering Applications 156
8.4.1 Finite Element Model and Boundary Element Model Meshing Issues 156
8.4.2 Modeling Issues in Biomedical Engineering Applications 158
8.5 Comparison of Stress Results by Boundary Element Method and Finite Element Method in a Bone–Implant Application 163
8.6 Concluding Remarks 163
References 165

Part III
Discrete and Particle Methods

9. A Particle Finite Element–Based Framework for Differentiation Paths of Stem Cells to Myocytes and Adipocytes: Hybrid Cell–Based and Finite Element Modeling

F.J. Vermolen, S.D. Harrevelt, A. Gefen, D. Weihs

9.1 Introduction 171
9.2 The Mathematical Framework 173
9.2.1 A Ternary Cell System 173
9.3 Numerical Method 179
9.3.1 The Finite Element Method for the Partial Differential Equations 179
9.3.2 The ZZ-Gradient Recovery Method 180
9.3.3 Cell Maturation and Migration 181
9.4 Simulations and Discussion 182
9.5 Conclusions 184
References 184
Further Reading 185

10. Numerical Simulation of Bone Cutting: Hybrid SPH–FE Approach

S. Li, A. Zahedi, V. Silberschmidt

10.1 Introduction 187
10.2 Model Challenges and Requirement 188
10.3 Smoothed Particle Hydrodynamic Approach 189
10.4 Model Formulation and Implementation 191
10.4.1 Model Geometry 191
10.4.2 Sensitivity Analysis 191
10.4.3 Contact Formulation 192
10.4.4 Material Properties 193

This book belongs to Central Library BADJI Mokhtar-ANNABA UNIVERSITY
Copyright Elsevier 2024

10.5 Model Results and Analysis 194
10.5.1 Force—Displacement Characterization 194
10.5.2 Anisotropy of Deformation Process 195
10.5.3 Effect of Progressive Damage 196
10.5.4 Anisotropic Toughening Mechanisms 197
10.6 Discussion 199
References 200

11. Smoothed Particle Hydrodynamics Method and Its Applications to Cardiovascular Flow Modeling

S. Shahriari, L. Kadem

11.1 Introduction 203
11.2 Mathematical Formulation 204
11.2.1 Smoothed Particle Hydrodynamics Formulation 204
11.3 Navier—Stokes Equations 207
11.4 Conservation of Mass 207
11.5 Conservation of Momentum 207
11.6 Numerical Features 209
11.6.1 Particle Movement and XSPH Variant 209
11.6.2 Numerical Time Integration 209
11.6.3 Variable Time Step 210
11.6.4 Search of the Neighboring Particles—Linked List Method 210
11.7 Implementation of Boundary Conditions in Smoothed Particle Hydrodynamics: Rigid, Periodic, and Inflow/Outflow Boundary Conditions 210
11.7.1 Rigid Boundary Conditions 210
11.7.2 Periodic Boundary Conditions 212
11.7.3 Inflow/Outflow Boundary Conditions 212
11.8 Applications of Smoothed Particle Hydrodynamics to Unsteady Cardiovascular Flows 213
11.8.1 Benchmark Case for Smoothed Particle Hydrodynamics Simulation of Unsteady Flows 213
11.9 Determination of the Wall Shear Stress Using Smoothed Particle Hydrodynamics 216
11.10 Shear Loading History Downstream of a Bileafet Mechanical Heart Valve Evaluated Using Smoothed Particle Hydrodynamics 217
11.11 Conclusion and Future Developments 217
References 218

Part IV
Agent-Based Methods

12. Agent-Based Lattice Models of Multicellular Systems: Numerical Methods, Implementation, and Applications

D. Drasdo, A. Buttenschön, P. Van Liedekerke

12.1 Introduction 223
12.2 Lattice-Based Models: Types and Resolution 224
12.3 Cellular Automaton With One Cell per Lattice Site (Type B) 224
12.3.1 Choice of the Lattice 224
12.3.2 Lattice-Based Growth Models 225
12.3.3 Definition of Time 227
12.3.4 Cell Movement and Multiplicity of States 228
12.3.5 Growth and Division 229
12.3.6 Influence of Lattice Symmetry on Growth Figures 230
12.3.7 Energy-Dependent Moves 231
12.3.8 Conclusion: Pros and Cons of Type B Lattice Growth Models 231
12.3.9 Cellular Automaton With Many Cells per Lattice Site (Type A) and Lattice Gas Cellular Automaton 231
12.3.10 Conclusion: Pros and Cons 232
12.4 Lattice Gas Cellular Automaton Models 233
12.5 Lattice Models With Many Lattice Sites per Cell (Type C; Cellular Potts Models) 233
12.5.1 Concept of Energy Functional 233
12.5.2 Cell Growth and Division 234

This book belongs to Central Library BADJI Mokhtar-ANNABA UNIVERSITY
Copyright Elsevier 2024

12.5.3 Choice of Lattice 234
12.5.4 Simulation of Dynamics 234
12.5.5 Directed Active Cell Movement 235
12.5.6 Conclusion: Pros and Cons 235
12.6 Short Conclusion 235
Acknowledgments 236
References 236

13. Multiscale Agent-Based Computer Models in Skeletal Tissue Regeneration

S. Checa

13.1 Introduction 239
13.2 Components of Agent-Based Models and Their Application to Skeletal Regeneration 239
13.2.1 Cells as Agents 240
13.2.2 The Environment 240
13.2.3 The "Rules" 240
13.3 Considering Processes at the Different Length and Time Scales 241
13.3.1 Simulations at the Cellular Level 241
13.3.2 Emergent Behavior at the Tissue Scale 241
13.3.3 Cellular Activity Driven by Intracellular Processes 242
13.4 Discussion 242
Acknowledgments 243
References 243

14. Off-Lattice Agent-Based Models for Cell and Tumor Growth: Numerical Methods, Implementation, and Applications

P. Van Liedekerke, A. Buttenschön, D. Drasdo

14.1 Introduction 245
14.2 Center-Based Models 245
14.2.1 Equation of Motion 246
14.2.2 Cell Interaction Forces 247
14.2.3 Cell Migration and Chemotaxis 248
14.2.4 Cell Growth, Division, and Death 250
14.2.5 Measures for Deformation, Stress, and Pressure 251
14.2.6 Extensions and Solutions 252
14.2.7 Implementation 252
14.2.8 Conclusion 254
14.3 Deformable Cell Models 254
14.3.1 Equation of Motion 255
14.3.2 Internal Forces Between Nodes 255
14.3.3 Adhesion and Repulsion Forces 258
14.3.4 Cell Migration and Chemotaxis 259
14.3.5 Cell Growth, Division, and Death 259
14.3.6 Measures for Deformation, Stress, and Pressure 259
14.3.7 Implementation 261
14.3.8 Conclusion 261
14.4 Hybrid Modeling 261
14.5 Conclusion 263
Acknowledgments 263
References 263

15. Agent-Based Numerical Methods for 3D Bioprinting in Tissue Engineering

T.J. Sego, N.I. Moldovan, A. Tovar

15.1 State of the Art in 3D Bioprinting 269
15.1.1 Scaffold-Based Methods 269
15.1.2 Scaffold-Free Methods 269
15.2 Models in 3D Bioprinting 270
15.2.1 Lattice Boltzmann Methods 270
15.2.2 Cellular Particle Dynamic Methods 270
15.2.3 Kinetic Monte Carlo Methods 271
15.3 Agent-Based Models in Scaffold-Free 3D Bioprinting 271
15.3.1 Abstract Description of an Agent 271
15.3.2 From Cells Come Biological Patterns: Scales and Emergence 272
15.3.3 Generalized Cellular Potts Model 272
15.4 Applications 276
15.4.1 Cell Sorting 276
15.4.2 Spheroid Fusion 277
15.4.3 Diffusion 277
15.4.4 Chemotaxis 278
15.4.5 Hypoxia 278
15.5 Discussion and Outlook 279
References 280

This book belongs to Central Library BADJI Mokhtar-ANNABA UNIVERSITY
Copyright Elsevier 2024

16. Coupled Finite Element–Agent-Based Models for the Simulation of Vascular Growth and Remodeling

D. Nolan, C. Lally

16.1 Introduction 283
16.2 Methods in the Literature 284
16.2.1 Paradigms for Agent-Based Models of Vascular Tissue 284
16.3 Schemes and Algorithms for the Implementation of Coupled Finite Element–Agent-Based Models 286
16.3.1 Agent-Based Models 286
16.3.2 Finite Element Models 290
16.3.3 Coupling Agent-Based and Finite Element Domains 293
16.4 Future Perspectives 298
References 298

Part V
Meshless and Meshfree Methods

17. The Mechanologic Bone Tissue Remodeling Analysis: A Comparison Between Mesh-Depending and Meshless Methods

M. Peyroteo, J. Belinha, L. Dinis, R. Natal Jorge

17.1 Introduction 303
17.2 Numerical Methods 304
17.2.1 The Finite Element Method 305
17.2.2 Meshless Methods 305
17.3 Discrete Equation System 309
17.4 Mechanologic Model 311
17.4.1 Phenomenological Law 311
17.4.2 Remodeling Criterion 313
17.4.3 Remodeling Procedure 313
17.4.4 Interpretation of the Results 315
17.5 2D Bone Patch Analysis 315
17.5.1 Initial Conditions 315
17.5.2 Results and Discussion 316
17.6 2D Femoral Analysis 317
17.6.1 Initial Conditions 317
17.6.2 Results and Discussion 319
17.6.3 Conclusions 320
Acknowledgments 321
References 321

18. Strong- and Weak-Form Meshless Methods in Computational Biomechanics

G.C. Bourantas, G.R. Joldes, A. Wittek, K. Miller

18.1 Introduction 325
18.2 Meshless Interpolation Schemes 326
18.2.1 Modified Moving Least Squares 326
18.2.2 Discretization Corrected Particle Strength Exchange 328
18.3 Weighted Residual Method 330
18.3.1 Collocation Method 331
18.3.2 Galerkin Method 331
18.4 Strong-Form Meshless Methods 331
18.4.1 Blood Flow in Aorta 331
18.4.2 Tumor Ablation Simulation 332
18.5 Weak-Form Meshless Methods 334
18.5.1 Numerical Examples 334
18.5.2 Brain Deformation 334
18.5.3 Whole-Body Image Registration 336
18.6 Conclusions 337
Acknowledgments 338
References 338

19. The Finite Volume Particle Method: Toward a Meshless Technique for Biomedical Fluid Dynamics

N. Quinlan, L. Lobovský

19.1 Introduction 341
19.2 The Finite Volume Particle Method 342
19.2.1 Smoothed Particle Hydrodynamics and the Finite Volume Particle Method 342
19.2.2 Finite Volume Particle Method as a Finite Volume Method 344
19.2.3 Computation of Interparticle Area 344
19.2.4 Extensions of the Basic Method 346
19.3 Inlet and Outlet Boundary Conditions in Finite Volume Particle Method 346
19.4 Validation for Flow Coupled with Rigid Body Motion 347
19.5 Application to Simplified Mechanical Heart Valve 349
19.5.1 Control of Particle Distribution Near Moving Bodies 349

This book belongs to Central Library BADJI Mokhtar-ANNABA UNIVERSITY Copyright Elsevier 2024

19.5.2 Mechanical Heart Valve 350
19.6 Conclusions 352
Acknowledgments 352
References 353

Part VI
Lattice Boltzmann Methods

20. Multicomponent Lattice Boltzmann Models for Biological Applications

A. Montessori, I. Halliday, M. Lauricella, S.V. Lishchuk, G. Pontrelli, T.J. Spencer, S. Succi

20.1 Introduction 357
20.2 The Lattice Boltzmann Equation 358
20.3 The Pseudopotential Approach for Multiphase and Multicomponent Flows 358
20.3.1 Discretization of the Non-ideal Forcing Term on Higher-Order Lattices 359
20.3.2 Nonideal Equations of State in Pseudopotentials Approach 360
20.3.3 Pseudopotential Approach for Interacting Multicomponent Fluids 360
20.4 Biofluidic Applications 361
20.4.1 Droplet Dynamics With Applications to Biomicrofluidics 361
20.5 Modified Color-Gradient Method 363
20.5.1 Two Immiscible Fluids 363
20.5.2 Many Mutually Immiscible Fluids 365
20.6 Modeling Membranes as Fluid—Fluid Interfaces 366
20.7 Fluid-Filled Vesicles in a Shear Flow 368
20.8 Conclusions 368
Acknowledgments 369
References 369

21. Lattice Boltzmann Models of Highly Viscous Fluids and Multicellular Self-Assembly

A. Cristea, A. Neagu

21.1 Viscous Fluids and the Lattice Boltzmann Method 371
21.2 Numerical Schemes for Reducing Velocities at Interfaces 375
21.2.1 Finite Difference Schemes 376
21.2.2 Flux Limiter Schemes 377
21.2.3 Total Variation Diminishing Schemes 378
21.2.4 Surface Tension in the Force Term 379
21.2.5 Corrections on the Force Term 382
21.3 Simulations of Multicellular Self-Assembly in Bioprinted Tissue Constructs 384
21.4 Conclusions 386
References 387

22. The Lattice Boltzmann Modeling: Solving Complex Flows Including Biological Cells

Z. Hashemi

22.1 Introduction 391
22.2 Lattice Boltzmann Method 392
22.2.1 General Concepts 392
22.2.2 Mathematical Formulation 393
22.2.3 Numerical Implementation 394
22.2.4 Boundary Conditions 395
22.3 Immersed Boundary Method 396
22.3.1 General Concepts 396
22.3.2 Mathematical Formulation 397
22.3.3 Numerical Implementation 398
22.3.4 Immersed Boundary—Lattice Boltzmann Method 399
22.4 Membrane Mechanics 399
22.4.1 General Concepts 399
22.4.2 Membrane Discretization 400
22.4.3 Constitutive Law 401
22.4.4 Finite Element Method 402
22.4.5 Volume Correction 403
22.5 Solution Algorithm 404
22.6 Application of the Combined Method to Suspended Biological Cells 404
22.6.1 A Spherical Capsule in Simple Shear Flow 404
22.6.2 Red Blood Cell in Simple Shear Flow 406
22.6.3 Red Blood Cell in a Pressure-Driven Capillary Flow 408

This book belongs to Central Library BADJI Mokhtar-ANNABA UNIVERSITY
Copyright Elsevier 2024

22.7 Limitations of the Combined Method 409
22.7.1 Lattice Boltzmann Method 409
22.7.2 Immersed Boundary Method 410
22.7.3 Finite Element Method 411
22.8 Discussion 411
References 411

23. Lattice Boltzmann Methods for Bioengineering Applications

D.V. Papavassiliou, N.H. Pham, O.E. Kadri, R.S. Voronov

23.1 Introduction 415
23.2 Lattice Boltzmann Method Algorithm 416
23.2.1 Flow Simulation 416
23.2.2 Two-Phase Flow 418
23.2.3 Parallelization Approach 418
23.2.4 Mass and Heat Transport With Lagrangian Particle Tracking 420
23.3 Application I—Universal Stress Distribution and Correlating Flow Forces to Single Cell Biology in Engineered Bone Scaffold Cultures 422
23.4 Application II—Drug and Agonist Transport Within Thrombi In Vivo 424
23.5 Discussion and Conclusions 425
Acknowledgments 426
References 426

Index 431

This book belongs to Central Library BADJI Mokhtar-ANNABA UNIVERSITY

Copyright Elsevier 2024

List of Contributors

J. Belinha, Faculty of Engineering of the University of Porto (FEUP), Porto, Portugal

G.C. Bourantas, The University of Western Australia, Perth, WA, Australia

A. Buttenschön, University of Alberta, Edmonton, AB, Canada

A. Carriero, City College, New York City, NY, United States

M. Cerrolaza, Universidad Politécnica de Cataluña, Barcelona, España

S. Checa, Charité – Universitätsmedizin Berlin, Berlin, Germany

R. Citarella, University of Salerno, Fisciano, Italy

E. Comellas, University of Erlangen-Nürnberg, Erlangen, Germany

L.Y.D. Crapts, Delft University of Technology, Delft, The Netherlands

A. Cristea, Romanian Academy-Timisoara Division, Timisoara, Romania

E.B. de las Casas, Universidade Federal de Minas Gerais, Belo Horizonte, Brazil

L. Dinis, Faculty of Engineering of the University of Porto (FEUP), Porto, Portugal

M. Doblaré, The University of Zaragoza, Zaragoza, Spain; The Biomedical Research Networking Center in Bioengineering, Biomaterials and Nanomedicine (CIBER-BBN), Zaragoza, Spain

M.H. Doweidar, The University of Zaragoza, Zaragoza, Spain; The Biomedical Research Networking Center in Bioengineering, Biomaterials and Nanomedicine (CIBER-BBN), Zaragoza, Spain

D. Drasdo, INRIA Paris & Sorbonne Universités UPMC Univ Paris 6, Paris, France

X. Gao, Loughborough University, Loughborough, United Kingdom

D.A. Garzón-Alvarado, Universidad Nacional de Colombia, Bogota, Colombia

A. Gefen, Tel Aviv University, Tel Aviv, Israel

S. Gerbino, University of Molise, Campobasso, Italy

M. Giorgi, University of Sheffield, Sheffield, United Kingdom

J.A. Guerrero, Universidad Nacional de Colombia, Bogota, Colombia; Universidade Federal de Minas Gerais, Belo Horizonte, Brazil

I. Halliday, Sheffield Hallam University, United Kingdom

S.D. Harrevelt, Delft University of Technology, Delft, The Netherlands

Z. Hashemi, Islamic Azad University, Bushehr, Iran

G.R. Joldes, The University of Western Australia, Perth, WA, Australia; Murdoch University, Perth, WA, Australia

L. Kadem, Concordia University, Montreal, QC, Canada

O.E. Kadri, University Heights Newark, Newark, NJ, United States

C. Lally, Trinity College Dublin, Dublin, Ireland

M. Lauricella, Istituto per le Applicazioni del Calcolo - CNR, Roma, Italy

S. Li, Loughborough University, Loughborough, United Kingdom

S.V. Lishchuk, Sheffield Hallam University, United Kingdom

L. Lobovský, University of West Bohemia, Plzeň, Czech Republic

K. Miller, The University of Western Australia, Perth, WA, Australia; Cardiff University, Cardiff, United Kingdom

N.I. Moldovan, Indiana University-Purdue University Indianapolis, Indianapolis, IN, United States

A. Montessori, University of Rome "Roma Tre", Rome, Italy

R. Natal Jorge, Faculty of Engineering of the University of Porto (FEUP), Porto, Portugal

A. Neagu, Victor Babes University of Medicine and Pharmacy Timisoara, Timisoara, Romania; University of Missouri, Columbia, MO, United States

This book belongs to Central Library BADJI Mokhtar-ANNABA UNIVERSITY

Copyright Elsevier 2024

C.P. Neu, University of Colorado Boulder, Boulder, CO, United States

J. Nino-Barrera, Universidad Nacional de Colombia, Bogota, Colombia

G. Nino, The George Washington University School of Medicine and Health Sciences, Washington, DC, United States

D. Nolan, Trinity College Dublin, Dublin, Ireland

D.V. Papavassiliou, The University of Oklahoma, Norman, OK, United States

A. Pereira, Imperial College, London, United Kingdom

M. Perrella, University of Salerno, Fisciano, Italy

M. Peyroteo, Institute of Mechanical Engineering and Industrial Management (INEGI), Porto, Portugal

N.H. Pham, The University of Oklahoma, Norman, OK, United States

D.M. Pierce, University of Connecticut, Storrs, CT, United States

D. Poljak, University of Split, Split, Croatia

G. Pontrelli, Istituto per le Applicazioni del Calcolo - CNR, Roma, Italy

N. Quinlan, NUI Galway, Galway, Ireland

A.M. Ramírez Martínez, Universidad Central de Colombia, Bogota, Colombia

T. Ricken, TU Dortmund University, Dortmund, Germany

J.K. Ryan, University of East Anglia, Norwich, United Kingdom

T.J. Sego, Indiana University-Purdue University Indianapolis, Indianapolis, IN, United States

S. Shahriari, Concordia University, Montreal, QC, Canada

S.J. Shefelbine, Northeastern University, Boston, MA, United States

V. Silberschmidt, Loughborough University, Loughborough, United Kingdom

E. Sozumert, Loughborough University, Loughborough, United Kingdom

T.J. Spencer, Sheffield Hallam University, United Kingdom

S. Succi, Istituto per le Applicazioni del Calcolo - CNR, Roma, Italy; Harvard University, Cambridge, MA, United States

A. Tovar, Indiana University-Purdue University Indianapolis, Indianapolis, IN, United States

P. Van Liedekerke, INRIA Paris & Sorbonne Universités UPMC Univ Paris 6, Paris, France

F.J. Vermolen, Delft University of Technology, Delft, The Netherlands

R.S. Voronov, University Heights Newark, Newark, NJ, United States

D. Weihs, Technion—Israel Institute of Technology, Haifa, Israel

A. Wittek, The University of Western Australia, Perth, WA, Australia

A. Zahedi, De Montfort University, Leicester, United Kingdom

This book belongs to Central Library BADJI Mokhtar-ANNABA UNIVERSITY

Copyright Elsevier 2024

Foreword

The field of biomechanics has a long history. In the 17th century, Galileo wrote in his *Discourse on Two New Sciences* about the structural demands on bones and the necessity for these biological structures to assume certain geometries in animals of different sizes. He used conceptual mechanical models to argue his point. In the 17th century, Borelli also used mathematical models in studies of animal movement and blood flow. Since that time many biomechanical models have been developed for many different living things on the molecular, cellular, tissue, and organ levels. Models help us to organize, formulate, and understand our observations and to predict how living things may respond in different circumstances. A general characteristic of biomechanical models is that they are valid over a short time interval, so that the basic geometry and chemical composition does not change appreciably. This modeling characteristic begins to vanish when we look at mechanobiological models in which the physical forces cause biological changes that alter geometry and/or composition.

The field of mechanobiology was established as a result of the insights and predictive abilities of mathematical models. Julius Wolff, the 19th century German surgeon, and his contemporaries believed that bones were not only elegantly formed to support in vivo forces but that alterations in those forces would lead to biological processes that would remodel the morphology of the bones. He believed that those remodeling processes would follow mathematical laws, which were in his time yet to be formulated. Since the 1980s, substantial progress has been made in establishing those mathematical rules and further advances have been made in modeling the adaptation of skeletal development, growth, remodeling, regeneration, and aging. The insights and predictive abilities of these mathematical models and similar models developed for cardiovascular, muscular, nervous, and connective tissues gave rise to a surge in experimental studies of the influence of imposed forces on the biology of cells, tissues, and organs. The influence of physical forces on cell biology, gene expression, and molecular pathways is now a focus in many laboratories.

One of the most intriguing and influential scientific books of the early 20th century is the beautifully written *On Growth and Form* by D'Arcy Thompson. Admirers of the book are struck by the elegant mathematical arguments reflecting Thompson's belief that physical forces are fundamental influences on the growth and morphogenesis of living things. Thompson's message, no matter how compelling, lay sterile for many years because there was no clear argument linking physical influences to the modern chemical, molecular biology research explosion and knowledge that soon followed. Finally, however, because of relatively new research in the area of mechanobiology, the knowledge gap between physical and biochemical influences on ontogeny and phylogeny has begun to narrow.

We can now look back at the many examples presented in *On Growth and Form* and begin to hypothesize about the mechanobiological processes involved. To formulate and test those hypotheses and others that may interest us, we would probably want to create mathematical models. The assumptions used in the models and the model predictions would need to be challenged by experiments on the molecular, cellular, and organ levels. This entire field of modeling and experimentation is referred to as multiscale mechanobiology, which has a tremendous potential to develop a deeper understanding of both ontogeny and phylogeny.

Therefore, it seems that mathematical modeling is fundamental to understanding biological processes. Biomechanical models are really just mechanobiological models that represent a short time interval in which the morphology and composition do not change appreciably. The chapters in *Numerical Methods and Advanced Simulation in Biomechanics and Biological Processes* provide excellent modern examples and advice on how to formulate and explore mathematical models in biology. As you read these chapters, you may think of Lord Kelvin's view that "I can never satisfy myself until I can make a mechanical model of a thing. If I can make a mechanical model, I can understand it. As long as I cannot make a mechanical model all the way through I cannot understand…".

Dennis Carter, PhD
Stanford University

This book belongs to Central Library BADJI Mokhtar-ANNABA UNIVERSITY
Copyright Elsevier 2024

This page intentionally left blank

This book belongs to Central Library BADJI Mokhtar-ANNABA UNIVERSITY

Copyright Elsevier 2024

Preface

Biological systems are complex. Numerical methods and computational simulations of biological systems allow us to probe, measure, and better understand biological processes. The accuracy and reliability of the solution lies not only in the mathematical formulation but also in the type of numerical method used to generate the system of equations that governs the problem. In this sense, the researcher must carefully analyze the problem to be modeled before choosing the right numerical method. Domain methods are useful in certain type of problems, whereas boundary methods or discrete methods could be more appropriate in other problems. The aim of this book is to give an overview of the different numerical methods available in modeling biomechanics and biological processes. We highlight their advantages, discuss their limitations, and provide example applications.

The use of numerical simulations and computational modeling in biomechanics allows us to understand mechanical environments that are often immeasurable and inaccessible, such as stresses, strains, and fluid flow profiles in living organisms. The mechanical environment of in vivo systems can provide information about the state of health, predict the onset of disease, or assess the outcome of treatments. Living systems contain complex material properties, time-varying mechanical loads, and complicated structural shapes. In addition, cells are able to translate biophysical signals into biological processes, a phenomenon called mechanobiology. This allows living systems to adapt to their mechanical environment. Using modeling we can understand the mechanical environment of living systems to develop more accurate diagnoses and design effective therapies.

Researchers and modelers test different biological scenarios using conservation laws, constitutive relationships, and an appropriate numerical method to have an in silico biological laboratory. Biological models address the complex challenges in understanding the behavior of biological systems and human diseases often from a multidisciplinary point of view. Numerical solution of biological models can develop new hypotheses, suggest experiments, interpret, provide a sensitivity analyses, generate new knowledge, and suggest new questions. Biological models help to push the boundaries of numerical methods with complex mechanical properties, multiscale structures, and multiphysics phenomena.

The book is aimed at academic researchers, postgraduate students, research and technology development professionals in industry, and all those interested in going further and deeper in these fascinating fields of computational simulations in biomechanics and biological processes. We demonstrate a wide range of numerical simulation techniques across broad disciplinary realms, spanning biology, mechanics, and medicine. The audience for this book is wide, because many specialists worldwide are related to or are dealing with many fields that require complex simulation and numerical methods in biomechanics and biological processes, and selective at the same time, because of a very specialized audience.

The book is organized into six parts, each one devoted to a type of numerical method. Thus, **Part I** contains chapters that use the finite element method for the numerical simulation of both physical and biological phenomena. A wide range of applications covering stiffness of nanofibers, biological growth, articular cartilage behavior, soft tissue biomechanics, turing patterns, and chemotaxis processes are discussed. **Part II** covers boundary integral methods, such as the boundary element method, modeling bioelectromagnetics, and bone-implant coupling, among others. **Part III** deals with particle and discrete methods, discussing differentiation paths of stem cells, bone-cutting models, and cardiovascular flow, whereas **Part IV** groups chapters in agent-based methods for simulating a wide variety of interesting problems, such as multicellular systems, skeletal regeneration, tumor growth, tissue bioprinting, and vascular growth. **Part V** is devoted to meshless/meshfree methods. Applications in tissue remodeling and biomedical fluids, including discussion on strong and weak forms are described. Finally, **Part VI** collects chapters in lattice Boltzmann methods mainly oriented toward fluid dynamics. These chapters cover multicomponent models, multicellular self-assembly, biological complex flows, and bone scaffold cultures.

We extend our thanks to all the authors who accepted our invitation to contribute to this book. All of the contributing authors are international experts in their fields and are pushing the boundaries in computational modeling in biomechanics and biological processes. The expertise, knowledge, and enthusiasm that authors convey in their chapters are highly

This book belongs to Central Library BADJI Mokhtar-ANNABA UNIVERSITY

Copyright Elsevier 2024

appreciated. We also want to acknowledge all those who with their effort and dedication contributed to the publication and production of this book.

The future is very promising in the progress of numerical methods and its vast field of applications. For example, hybrid and multiscale methods are emerging and contributing to the solution of problems that before seemed quite complicated to solve. We are excited to see what new generations bring to us, both new researchers and new numerical methods applied in biomechanics and biological processes. We anticipate spectacular results and believe that our capacity for wonder is far from exhausted.

The Editors
M. Cerrolaza
S. Shefelbine
D. Garzón-Alvarado
Barcelona, Boston, Bogotá

This book belongs to Central Library BADJI Mokhtar-ANNABA UNIVERSITY
Copyright Elsevier 2024

Part I

Finite Element Methods

This book belongs to Central Library BADJI Mokhtar-ANNABA UNIVERSITY

Copyright Elsevier 2024

This page intentionally left blank

This book belongs to Central Library BADJI Mokhtar-ANNABA UNIVERSITY

Copyright Elsevier 2024

Chapter 1

Discontinuous Finite Element Model of Hydrogels: Predicting Stiffness of Nanofibers

X. Gao*, E. Sozumert* and V. Silberschmidt
Loughborough University, Loughborough, United Kingdom

1.1 INTRODUCTION

1.1.1 Background

In recent years, because of rapidly increasing demands for clinic applications, a number of biomaterials were developed and successfully used in implants. For biomedical applications, the priority is to understand overall properties of candidate biomaterials, i.e., their structural features and biological and mechanical properties. The structural features at various length scales are usually regarded as an important determinant for materials' characteristics. Because biomaterials are employed in human-body environments, their biological properties are one of the key issues for their qualification as appropriate candidates. Because of the complex loading environment in vivo, mechanical behavior of implanted materials under relevant conditions is important for assessment and identification of their effectiveness in a human body.

The area of hydrogels has rapidly developed and attracted growing interest because many hydrogels demonstrate a high level of biocompatibility, suggesting a good host response of implants to a body environment. In addition, they usually consist of randomly distributed long fibers with a high content of water, thus mimicking a structure of real human tissues and providing a good microenvironment for adhesion, growth, migration, and differentiation of cells (Shi et al., 2016). As a result, many potential biomedical applications of hydrogels have been proposed.

Many studies have identified the importance of mechanical behavior of hydrogels, especially under physiological loading conditions. Most studies focus on behavior at a macroscopic level because macromechanical behavior can be used directly to compare a load-bearing capacity of various candidates with required performance and assess risks of failure. However, micromechanical behavior is of equal importance because mechanical signals (response) of hydrogels at the level of their nanofibers might influence local behavior and activities of tissues and cell. Thus, mechanical properties of nanofibers that act as a main load-bearing component in hydrogels should be investigated.

1.1.2 Experimental Measurements

To date, several techniques have been used intensively for mechanical characterization of fibers, such as tensile and bending (Tan and Lim, 2006; Tan et al., 2005). Atomic force microscopy (AFM)—based tests, such as nanotension and nanobending, were used alongside other custom-made nanotesting systems. Nanotension allows testing of a nanofiber until its failure (Haque and Saif, 2003). Owing to extremely small dimensions of nanofibers, one of the challenges in such tests is a griping method because conventional grips are ineffective (Haque and Saif, 2003); epoxy glue is widely employed to

* Equal contribution.

Numerical Methods and Advanced Simulation in Biomechanics and Biological Processes. https://doi.org/10.1016/B978-0-12-811718-7.00001-0
Copyright © 2018 Elsevier Ltd. All rights reserved.

This book belongs to Central Library BADJI Mokhtar-ANNABA UNIVERSITY
Copyright Elsevier 2024

fix a nanofiber (Hang et al., 2011). Another challenge is to avoid misalignment between a fiber axis and a loading direction (Haque and Saif, 2003). Like in macroscopic tensile tests, elastic properties of nanofiber are calculated from uniaxial force−displacement relations; therefore, the reliability of the obtained properties depends on the accuracy of the force and displacement measurements. A more applicable AFM-based testing scheme—a three-point bending nanotest—was developed as an alternative to nanotension (Guhados et al., 2005), with more convenient procedures for sample preparation, a griping method and localization. Additionally, tested specimens could be randomly placed on a microplatform with parallel grooves (Iwamoto et al., 2009).

AFM-based nanotests provide a means of direct measurement of mechanical moduli of nanofibers. Unfortunately, these schemes are rather expensive because an in situ system of AFM suitable for the use with SEM is required; in addition, they are time-consuming because of challenges in sample preparation and manipulating the AFM system. Another issue is that to use SEM to locate nanofibers, they should be conductive; thus, gold coating is necessary to make nanofibers conductive so that fibers cannot be fully hydrated. Consequently, the results obtained with the AFM-based nanotesting techniques might deviate from real stiffness of hydrogel nanofibers. The hydrated state affects physical properties of nanofibers; hence, current AFM-based nanotesting might not be suitable for measurement of mechanical properties of nanofibers in hydrogels.

Raman spectroscopy has also been widely used in characterization of polymers in recent years. This method can provide information on alignment arrangement of nanofibers in the network (details can be found in (Tanpichai et al, 2012)) as well as the Young's modulus based on negative correlation of Raman band shifts and global strain induced by uniform stress. Raman spectroscopy provides a convenient method avoiding a need to prepare single-fiber specimens. Still, this procedure is time-consuming because it requires a large number of measurements for one specimen at a single strain state. Besides, its implementation for hydrogels with high water content presents additional challenges. Consequently, current schemes of Raman spectroscopy might not support measurement of axial modulus of nanofibers in hydrogels.

1.1.3 Inverse Parameter Estimation

Generally, mechanical behavior of a material depends on its material properties and structural arrangement. For hydrogels, nanofibers act as the main load-bearing component determining its deformational behavior because of high fluidity of interstitial matrix of water (potential application are not limited to pure hydrostatic compression). In addition, fibrous microstructure (volume fraction, orientation distribution, intersection type) should be accounted in assessments of structural effects on mechanical behavior. Numerical models used for the analysis of mechanical behavior of fibrous materials should reflect two main features: (1) fiber properties and (2) their arrangement in a real material. An inverse scheme is employed to predict either constituent's properties or its structural arrangement by calibrating modeling results with experimental ones. Such approaches are widely used in mechanical engineering and generally called *inverse parameter estimation*. Based on this idea, a numerical modeling method is suggested here to predict stiffness of nanofiber in hydrogels.

1.2 MULTISCALE MODELING

Finite element (FE) analysis that incorporates microstructures of fibrous materials is a powerful tool to simulate the complicated deformation and damage mechanisms of hydrogels. Multiscale modeling approaches, on the other hand, allow simulations of macroscale mechanical responses of fibrous or other types of complex materials by upscaling their microscale responses. Currently, inverse parameter estimation methods in multiscale FE models are feasible to predict mechanical properties of nanofibers, saving experimental time and cost, and providing an understanding of microstructural changes under loading and environmental conditions. Generation of a numerical model representing real microstructure is the first step before starting any estimation of material parameters. FE models of fibrous networks can be classified based on a type of representative units—continuous or discontinuous. There is also a difference in dimensionality of used models, with some researchers proposing two-dimensional (2D) schemes with controlled material and geometry properties for fibrous networks. In fact, real fibrous materials demonstrate rather complex microstructure, including fibers with in-plane or out-of-plane directions, fiber curvature, 3D fibers. Before choosing any complicated modeling approach, it is crucial to define its features and constraints. For instance, in the case of a thin-layer fibrous network loaded in in-plane tension, the effect of fiber friction on its mechanical response is rather small and, thus, a 3D model, such as in Altendorf and Jeulin (2011), Kulachenko and Uesaka (2012), Gaiselmann et al. (2012), and Dirrenberger et al. (2014), would be unnecessary and 2D schemes, such as in Sabuncuoglu et al. (2013) and Raina and Linder (2014), would be sufficient. On the other hand, for a reasonably thick fibrous network in compression through-thickness loading, fiber-to-fiber interactions (i.e., bonds, contacts, and cross-links) ought to be incorporated into a numerical model, as they are essential in a load transfer in

This book belongs to Central Library BADJI Mokhtar-ANNABA UNIVERSITY
Copyright Elsevier 2024

the material. In the next subsection, numerical models (particularly discontinuous ones) of fibrous materials available in the literature are discussed and compared.

1.2.1 Continuous Modeling Approaches

In continuous models of fibrous networks, the fibers are not individually modeled as they are in a discontinuous model, in which fibers are placed individually using various techniques. In some studies (Raina and Linder, 2014; Ridruejo et al., 2012), continuous models based on various constitutive descriptions have been proposed to capture macroscopic features of deformational behavior of fibrous networks. Rubberlike materials are generally regarded as analogues of fibrous networks in biomaterials, nonwovens, or other engineered structures. This analogy is based on the idea that randomly oriented fibers with cross-links in networks are similar to microscopic polymer chains. Available polymer chain−based models consider large numbers of randomly oriented chains, affecting mechanical responses to various loading conditions (Arruda and Boyce, 1993). An example of such study is Demirci et al. (2011), based on an algorithm, taking orientation distributions of fiber into account to calculate anisotropic effective (macroscopic) material properties of polymeric fibrous materials. This algorithm essentially employed a well-known rule of mixture and Halpin−Tsai equations to compute elastic and shear moduli in principal directions of the network.

1.2.2 Discontinuous-Based Modeling

In discontinuous schemes, individual fibers are modeled directly in discontinuous, or discrete, FE models of fibrous networks. In this case, properties of fibers and their orientation distributions functions are introduced to the models.

1.2.2.1 Lattice Models

A fibrous network can be presented as a system of discrete units, i.e., rheological elements (springs) (Ostoja-Starzewski, 2002). These units could be in a form of triangle, square, or hexagonal shapes, and the fiber system is known as a *lattice network system*. This modeling technique can be applied to various materials such as metals, composites, biomaterials, and paper; sample lattice systems are shown in Fig. 1.1 together with an SEM image of paper microstructure. A model of lattice structure consists mainly of beam or truss elements in 2D or 3D. Lattice systems are not unique and, to construct a lattice structure at microscale, various lattice geometries can be utilized. Some lattice systems contain a symmetric distribution of lattices such as in Beex et al. (2014a), Mueller and Kochmann (2004), Liu et al. (2010), whereas some others can present

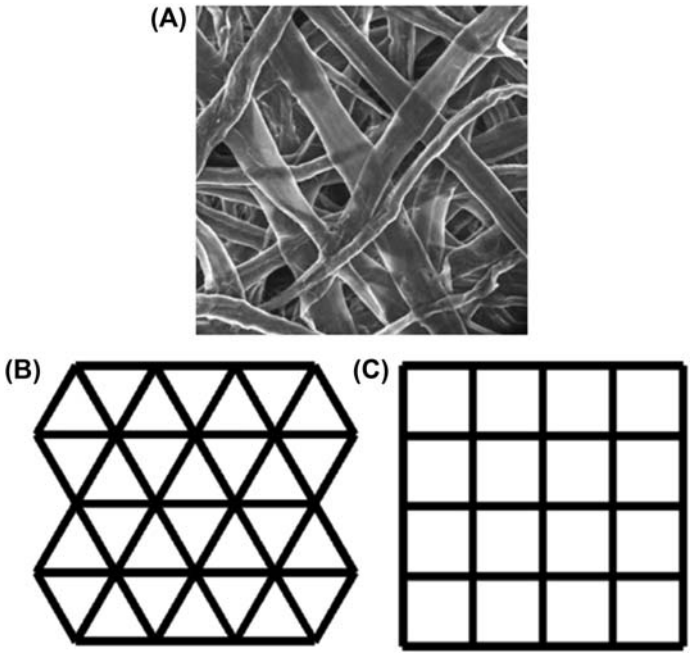

FIGURE 1.1 (A) SEM image of fibers on paper surface; (B) triangular lattice structure; (C) square lattice structure (Liu et al., 2010).

This book belongs to Central Library BADJI Mokhtar-ANNABA UNIVERSITY Copyright Elsevier 2024

disordered lattice structures (Ostoja-Starzewski, 2002). Microscale changes with deformation or loading, such as fiber reorientation, fiber failure, and bond failure, which are precursors for failure in macroscale, can be successfully modeled with lattice models (Beex et al., 2014b).

In each lattice system, material properties of beams or trusses are obtained by measuring (where feasible) actual fiber properties and a volume density of fibers. It is essential to keep in mind that a lattice segment (a beam or a truss) does not represent an actual individual fiber. An element stiffness matrix and a material's stiffness matrix in each lattice segment are assigned effective properties, based on a number of presented fibers by each element. They can then be calculated in unit cells of a lattice network, i.e., triangular, square, hexagonal lattice units; some sample calculations can be found in Ostoja-Starzewski (2002), Liu et al. (2010), and Beex et al. (2014b). The global stiffness matrix describing the complete lattice system is a sum of these element stiffness matrices within the framework of the FE method.

Considering advantages and deficiencies of this modeling approach, the lattice models with periodic structures (see Fig. 1.1A and B) are relatively easy to construct in comparison with other discrete models presenting more adequate microstructures. A lattice segment length is one of controlling parameters. Its experimental measured magnitudes can be used directly in a model; on the other hand, a number of real fiber-to-fiber intersections per unit area cannot be achieved in such a scheme. Similarly, the effect of experimentally observed orientation distribution of fibers cannot be introduced in lattice models (or with additional special efforts).

1.2.2.2 Embedded Fiber Models

An alternative framework—a so-called *embedded fiber approach* (Fig. 1.2)—was proposed to study relationship between microscopic and macroscopic behaviors of fibrous materials. This approach aims to homogenize fibrous networks into a continuous surrounding matrix by introducing fully coupled fiber-to-matrix interactions (Jin and Stanciulescu, 2015). An algorithm to construct a network using this modeling method approach can be summarized as follows:

1. Define a boundary of the matrix in 2D and assign a fiber diameter in the matrix.
2. Calculate coordinates of a random starting point inside the boundary.
3. Using the random starting point and a random angle in $(-\pi, \pi)$, generate the first fiber segment with a certain length.
4. Generate the second fiber segment with a relative angle of Θ in $(-\Theta_{max}, \Theta_{max})$. This process is repeated until the max segment number is reached or any portion of the last fiber segment is outside the chosen boundary.
5. Repeat steps (1)−(4) until a predefined volume fraction of fibers is achieved.
6. Calculate intersection points of fiber segments and form cross-links.

This modeling approach enables to control the segment length and the fiber orientation distribution as well as the volume fraction of fiber. However, it requires user-defined FE formulation and its respective subroutine should run on an

FIGURE 1.2 Fibrous network embedded in matrix (Picu, 2011).

This book belongs to Central Library BADJI Mokhtar-ANNABA UNIVERSITY
Copyright Elsevier 2024

FE solver. It is only available for 2D problems and does not allow simulating a through-thickness mechanical response of a fibrous network, as fiber-to-fiber contact interactions are not specified. Besides, there is no intersection between fibers initially contacting each other.

1.2.2.3 Fiber-Deposition Models

A model based on fiber deposition was proposed by Persson and Isaksson (2014) to simulate rapid deformation and fracture of fibrous materials such as paper, nonwoven felts, and polyester textiles. The model idealizes fiber cross sections such as circular or square. It allows forces, fiber displacements, and deformations in all three directions. The underlying idea to generate such a network is to assume that each fiber consists of a set of fiber segments and each segment is represented by a particle with 6 degrees of freedom: three rotations and three displacements, shown in Fig. 1.3. Initially, each fiber is presented by two particles and when two fibers intersect at a point, a new particle is placed at the intersection point for each fiber. To form a physical bond, a linear spring with constant stiffness is inserted between the particles at the intersections.

This model can simulate deformation behavior of the initial contact points using linear spring elements. In real fibrous networks, when a material is extended or compressed, some fibers are not bonded anymore and new contacts can appear because of their displacements and rotations. This behavior was not explained in this particle-based fiber-deposition model. More complex models based on this method were mentioned in Ekman et al. (2012) and Redenbach and Vecchio (2011). Fibers are deposited onto a flat surface and, as the surface was covered with fibers, the deposited fibers start to bend to conform to other fibers. Meanwhile, a smoothing algorithm is applied for contacting fibers to minimize their mutual penetration. However, to achieve this for low tolerances of fiber penetration, highly dense meshes around the contact points are essential (Redenbach and Vecchio, 2011).

This model can accommodate complex fiber-to-fiber contact mechanisms such as jump to contact, compression or tension on the contact, and separation. Still, fiber-to-fiber contact points need fine meshes resulting in higher numbers of finite elements. Deformation of fibrous networks at micro- and mesoscale can be simulated relatively easily with this approach. However, generation of a large model for macroscale simulations is a highly time-demanding process because it includes high numbers of particles and springs. This method does not enable control of fiber segment lengths because fibers are deposited in a vertical direction.

1.2.2.4 Alternative Modeling Approaches

Various methods to generate 3D complex microstructures of fibrous networks with 3D fibers were applied to various media. Micro−computed tomography (micro-CT)−based methods are used, for instance, to extract a volumetric geometry from material's micro-CT data (Ekman et al., 2012; Redenbach and Vecchio, 2011; El Said et al., 2016; Huang et al., 2013, 2015). Unfortunately, these methods do not enable any parametric numerical investigations of fibrous materials because

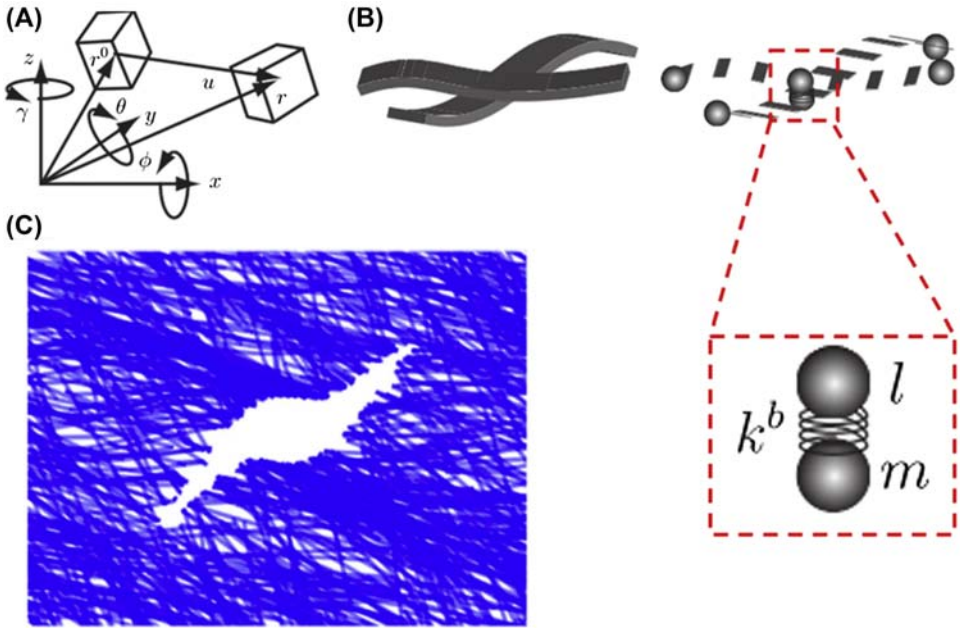

FIGURE 1.3 (A) Particle with 6 degrees of freedom at initial and deformed configurations; (B) two fibers represented by particles and linear spring; (C) model of fibrous network generated with fiber-deposition approach (Persson and Isaksson, 2014).

This book belongs to Central Library BADJI Mokhtar-ANNABA UNIVERSITY Copyright Elsevier 2024

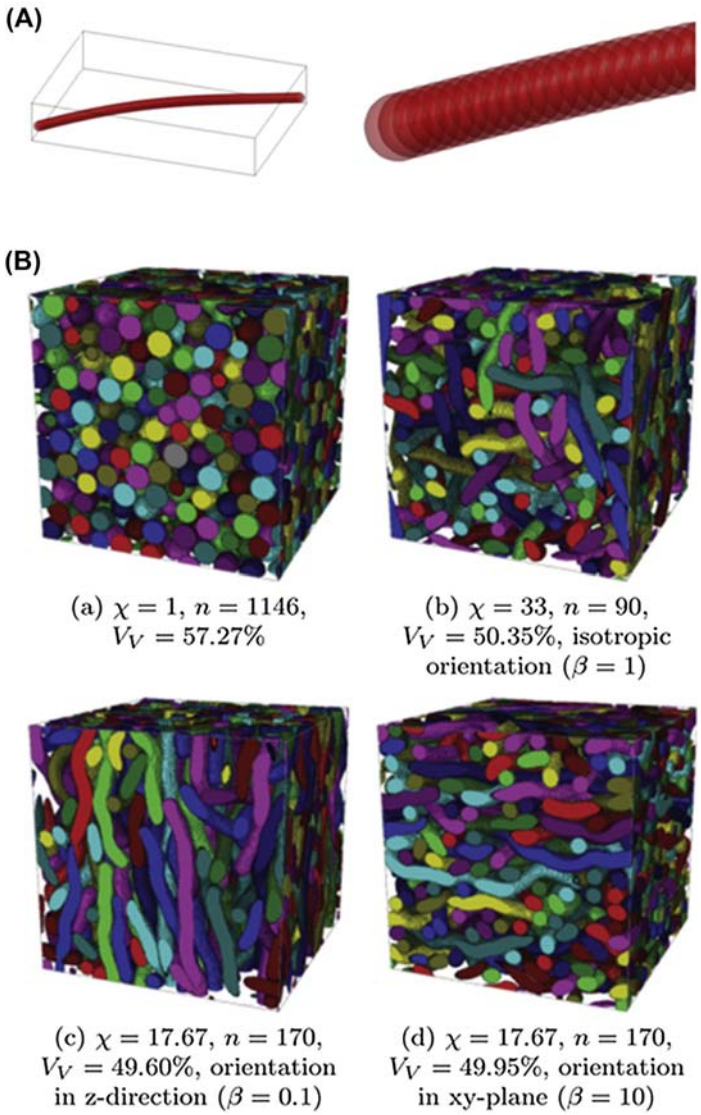

FIGURE 1.4 (A) Fiber model generated with random-walk algorithm (Chapelle et al., 2015); (B) realizations of fiber packing systems with various modeling parameters (Altendorf and Jeulin, 2011).

they are only capable of modeling performance of the scanned network. As a result, contributions of each material or geometry parameter to the overall mechanical response cannot be separated in such methods.

Karayiannis and Laso introduced a Monte Carlo−based scheme to generate dense random packings of freely jointed chains of hard spheres, with a solid volume fraction close to 60% (Karayiannis and Laso, 2008). Fibrous networks can be achieved by employing 2D random walks and a multivariate form of von Mises−Fisher distribution, assuring fiber bending and limited changes in orientation distribution. A force-biased algorithm can generate an irregular close packing of chains of hard spheres up to a packing fraction of 65%; however, orientation and diameter distributions of these chains limit higher packing densities (Mościński et al., 1989). Altendorf and Jeulin created soft-core fibrous systems by means of random walks of chains of spheres controlled by the multivariate von Mises−Fisher distribution, with fiber overlaps (Altendorf and Jeulin, 2011), and minimized these overlaps with a force-biased algorithm discussed in Mościński et al. (1989). Fibers are modeled as a chain of overlapping spheres within a defined fiber domain (Fig. 1.4A).

A computational model proposed by Altendorf and Jeulin (2011) can generate 3D networks with high volume fractions of fibers (Fig. 1.4B); it controls parameters of their in-plane and out-of-plane orientation distributions. Despite the fact that it is a rather complex model incorporating many features of fibers and a network, it was tested only for small window sizes at microscale; no fiber-to-fiber interaction, such as cross-links or fused contact points, was defined. The model was used to simulate characteristics of a flow through such a fibrous medium.

This book belongs to Central Library BADJI Mokhtar-ANNABA UNIVERSITY
Copyright Elsevier 2024

TABLE 1.1 Comparison of Various Numerical Modeling Approaches for Fibrous Materials

	Control on Fiber ODF	Large Models	Uniform Distribution on Fiber Intersections	Computational Cost	Control of Segment Length	Control of Fiber Intersections	Fiber-to-Fiber Interactions
Lattice systems	−	+	+	++	+	+	−
Embedded fiber approach	+	+	−	+++	+	+	−
Fiber deposition	+	−	−	+++	−	+	+
mCT-based models	−	−	−	++++	−	−	−
3D random walk	+	−	−	++++	−	−	−
2D fiber deposition	+	+	+	++	+	+	−

mCT, micro−computed tomography; *ODF,* orientation distribution function.
+, existing feature; −, no feature. In "Computational cost," the number of plus signs is related to a computational cost of a numerical scheme.

Summarizing the above discussion, Table 1.1 presents features of various numerical modeling approaches employed for fibrous materials; these features include control of the orientation distribution function for fibers. The last method in the table, in contrast to others, was not discussed and is explained in detail in the following sections before being employed in our case study.

1.2.3 Fiber Cross-Links

The nature of cross-links is related directly with a mechanical response of a network (Picu, 2011) because the number of degrees of freedom at the intersection is based on the joint type. There are four main types of joints (see Fig. 1.5):

1. A *pin joint* represents a contact of fibers involving only friction during deformation; hence, the pin joint transmits no moment.
2. A *flexible cross-link* is a joint without full constraints at fiber intersections and links having their own constitutive behavior (e.g., some actin-binding proteins acting as cross-links to reinforce the network).

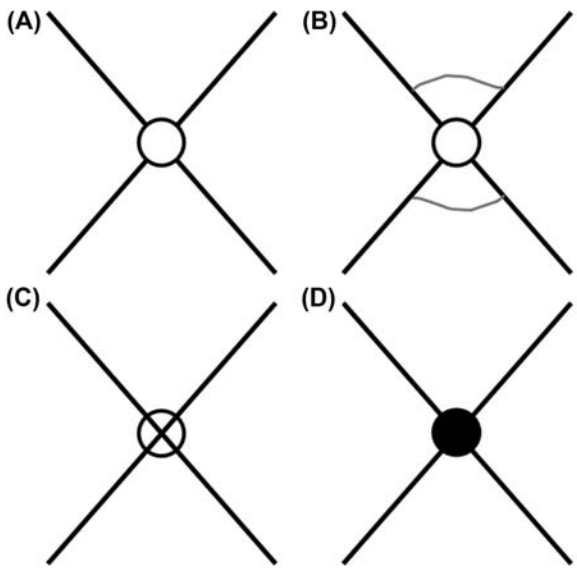

FIGURE 1.5 Four types of cross-linking in fibrous network: (A) pin joint; (B) flexible cross-link; (C) rotating joint; (D) wielded joint. *Modified after Picu, R., 2011. Mechanics of random fiber networks—a review. Soft Matter 7 (15), 6768−6785.*

This book belongs to Central Library BADJI Mokhtar-ANNABA UNIVERSITY Copyright Elsevier 2024

3. A *rotating joint* describes the behavior of bending of two fibers at the joint caused by applied force; in addition, rotating of each fiber-segment is allowed at the rotating joint.
4. A *welded joint* corresponds to the case of fully constrained intersection, with the angles between each fiber-segment remaining constant in the process of deformation.

1.2.4 Generation of a Computational Model

Capabilities of a discontinuous fibrous model rely on its extent of adequate introduction of geometry of a real material. Hence, it is crucial to generate the model geometry based on real fiber distribution employing some scientific method. Main steps of an effective method for determining fiber distribution are

- characterizing the geometric features of fiber distribution;
- developing a statistical description for the fiber distribution;
- deriving the key geometric relationships for the fiber distribution;
- developing an algorithm to implement the model geometry based on statistics of the fiber distribution and geometric relationships.

This process can be enhanced by obtaining high-quality SEM images of fibrous structure at various length scales by simplifying characterization of fiber distribution. Unlike AFM mapping, an outer fibrous network can be observed in background of SEM images, thus complicating measurement of some important geometric features, such as intersection density and porosity ratio. It was suggested (D'Amore et al., 2010) to separate and remove the outer fibrous network from the background by increasing the contrast of images to recognize the top layer of fibers.

Some image analysis software allows characterization of orientation, length, and diameter of fibers, whereas most of them depend on human operator-based analysis with its well-known deficiency—objectivity, potentially affecting the obtained results. Therefore, an automated algorithm is desirable to overcome this limitation. In the work of D'Amore et al. (2010), an image analysis algorithm based on gray intensity was developed. To increase the tracking accuracy, original images were divided into a series of subdomains with their length equal to 10 average fiber diameters; the same technique was also implemented in Demirci et al. (2012). The fiber intersections were found uniformly distributed over the network. Hence, the first step of algorithm to generate the model geometry was to reproduce random intersections controlled by their density; then, positions of generated intersections were modified based on orientation distribution of fibers; finally, some isolated fibers were removed in case of singularities (D'Amore et al., 2010).

Based on the fiber orientation distribution and positions of intersections, individual fibers were generated and placed within the model boundaries. In most fibrous hydrogels, fibers demonstrate some curliness rather than being straight lines. To account for curvature, for instance, a walk algorithm was introduced by Carleton et al. (2015) based on the idea to divide fibers into several connected straight segments. The angle between each two connected segments (thus, related to the curvature) is within a certain range measured experimentally; thus, the extent of curvature can be controlled by the range of these angles.

1.2.4.1 Representative Volume Element

The geometry of a heterogeneous model should be based of real microstructure of the material. To allow comparability, the model should also have boundary conditions similar to those of the whole specimen. So, for practical reasons, the model size usually is the same as of the whole specimen. Hydrogels are composed of nanofibers with various diameters that are, generally, of the order of hundreds of nanometers, with fibers interacting with each other by entanglements or friction at intersections. Hence, even in a small volume of 1 mm $\times$ 1 mm $\times$ 1 mm, hundreds of millions fiber segments and intersections are required to reflect the real material. Considering that each intersection has 3 degrees of freedom (in 2D), the computational cost becomes prohibitive.

Generally, if the microstructure is periodic at a certain length scale, a repeating volume has the same mechanical response as the whole specimen because each periodic element has the same volume-averaged properties. In the case of fibrous hydrogels, randomness of fibers results in variation of properties at various length scales; thus, it is theoretically nearly impossible to find a periodic volume (PV). The idea of homogenization approximation assumes that the effect of random microstructure on the global response decreases with an increase in sample size. Therefore, when the model size is large enough, the sample is capable of representing the behavior of the whole specimen because the effect of randomness of fibers is considered negligible. This allows a compromise between the computational cost (dictated by model size) and precision of expected results.

This book belongs to Central Library BADJI Mokhtar-ANNABA UNIVERSITY
Copyright Elsevier 2024

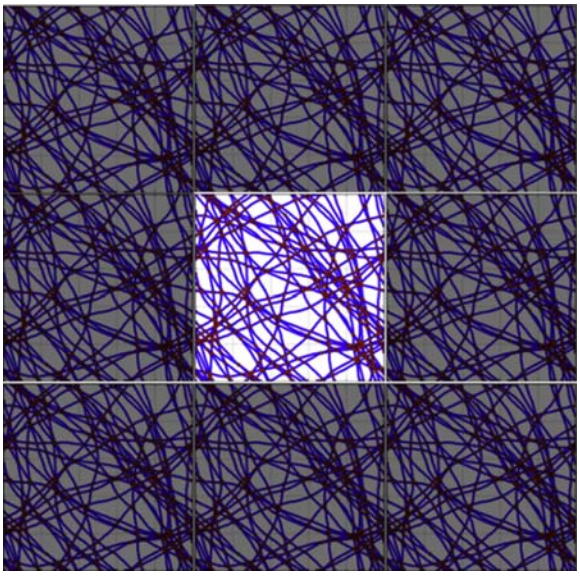

FIGURE 1.6 Illustration of presumed periodic volume in fibrous materials. *Modified from Carleton, J.B., et al., 2015. Geometric characterization and simulation of planar layered elastomeric fibrous biomaterials. Acta Biomaterialia 12, 93–101.*

One of the feasible approaches to solve this problem is to use a representative volume element (RVE). It is based on the idea that RVE is the smallest volume to represent a response of the whole because, for volumes larger than RVE, representative properties are the same as RVEs. In other words, the properties of large volumes become size independent. Therefore, to save computational cost, the effective way to identify the size of RVE is to increase the volume size until the properties of interest are size independent.

An example can be found in a 2D random triangulation model developed by D'Amore et al. (2010). The network behavior is sensitive to model size at small length scale up to 200 μm^2; then the sensitivity decreased dramatically with the model size increased to 500 μm^2. It is worth noticing that there is no obvious point separating size-dependent and size-independent regimes. In 3D modeling, Liu et al. (2013, 2014) and Lu et al. (2013) reported that the effective mechanical properties decreased with the increased model size, and when the model size reached a normalized length parameter of 1.5, the properties became insensitive to the model size, implying that this model size was sufficient to represent the effective properties of the whole specimen.

1.2.4.2 Periodic Boundary Conditions

In some homogeneous materials, such as metals, atoms are arranged regularly, so a PV (some studies call it *unit cell*) can be used to approximate the global behavior. Normally, a PV cannot be detected in fibrous biomaterials because of randomness of fibers, whereas a presumed PV can be developed in a model by applying periodic boundary conditions (PBCs). It is assumed that a heterogeneous material could be regarded as the assembly of PVs (Fig. 1.6). The benefit to use the PBCs is its capacity to create a PV to represent the whole specimen; thus, to verify whether the presumed PV can describe a real microstructure is essential. Hence, the foremost step is to generate fibers based on a real distribution of fibers. Because RVE could be used to identify the smallest model size that can represent the global response, some studies applied PBCs in the process to generate RVE to understand micromechanics of fibrous materials (Liu et al., 2013).

1.3 A CASE STUDY: PREDICTION OF AXIAL MODULUS OF NANOFIBERS IN BACTERIAL CELLULOSE HYDROGEL

1.3.1 Microstructure of Bacterial Cellulose Hydrogel

A good understanding of hydrogels' microstructure would assist a decision on an appropriate technique to generate a discontinuous FE model. Bacterial cellulose (BC) hydrogel (Fig. 1.7A) is a product of primary metabolism of a certain type

This book belongs to Central Library BADJI Mokhtar-ANNABA UNIVERSITY Copyright Elsevier 2024

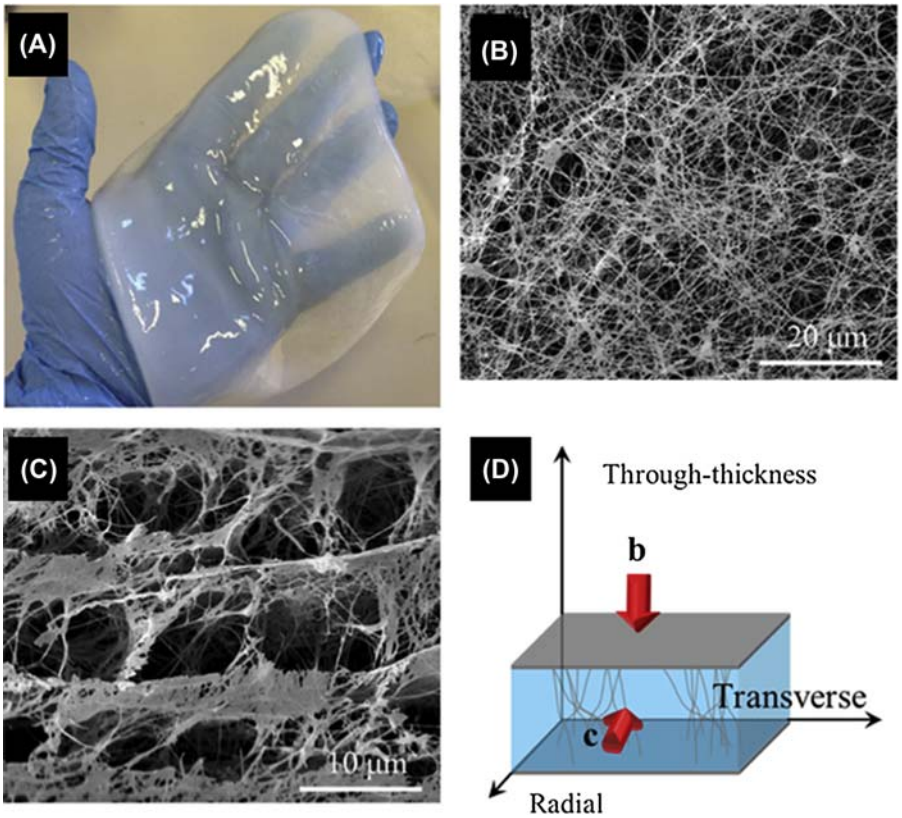

FIGURE 1.7 (A) Bacterial cellulose hydrogel with a random distribution of fibers (B) in a plane of a fibrous layer and a multilayer structure (C) with some weak links along a through-thickness direction. (D) Schematic diagram of radial, transverse, and through-thickness directions (Gao et al., 2016a).

of bacteria. Under static culturing conditions, nutrition and oxygen can be considered uniformly distributed in a culturing media, so that bacteria could choose any direction to grow and produce BC nanofiber with a diameter of ~100 nm, as a result, forming a random fiber distribution in the plane of a fibrous layer (radial-transverse plane in Fig. 1.7B). Because of the supply of oxygen, bacteria live and grow on the air—liquid interface rather than within a nutrient solution; as a result, they form a multilayer structure with some weak links along a through-thickness direction (Fig. 1.7C), allowing for hydrogel to hold a large content of water. With regard to the life cycle of bacteria, each BC nanofiber is produced by an individual, and producing nanofiber is a continuous process; thus, resultant BC nanofibers are long. BC nanofibers are composed of carbon, oxygen, and hydrogen with the formula of $(C_6H_{10}O_5)_n$ and BC nanofibers have only few branches.

1.3.2 Correlation of Microstructure Behavior and Global Response

BC hydrogel shows an extremely complex microstructure that necessitates a 3D model to represent it. For inverse parameter estimation, hundreds of models with random microstructures should be developed, and for each model, several trials with various predefined parameters are necessary to provide a database for calibrating the model results with experimental data. Therefore, considering the related computation demands, maximal simplification of model geometries becomes a significant objective. A simplified 3D model could be a sandwich with two fibrous layers and one layer of cross-links (Fig. 1.7D). In a case of in-plane tension, fibrous layers are in parallel and carry most of the load, with the effect of cross-links being negligible. So, behavior of a single fibrous layer can be used to represent the global response of the BC hydrogel in this case.

Because of microstructural changes caused by stretching, the BC hydrogel demonstrated nonlinear viscous (Gao et al., 2016a,b,c,d) and inelastic (Gao et al., 2015) behaviors. To minimize the viscous effect, the global elastic response of a deformed fibrous network is assumed to be observed at instantaneous unloading, corresponding to behavior of a single fibrous layer at a certain strain level with a certain microstructural distribution (e.g., fiber orientation distribution, fiber fraction, intersection density) (Fig. 1.8). Then, the scheme of inverse parameter estimation is used to calibrate modeling results with experimental data.

This book belongs to Central Library BADJI Mokhtar-ANNABA UNIVERSITY
Copyright Elsevier 2024

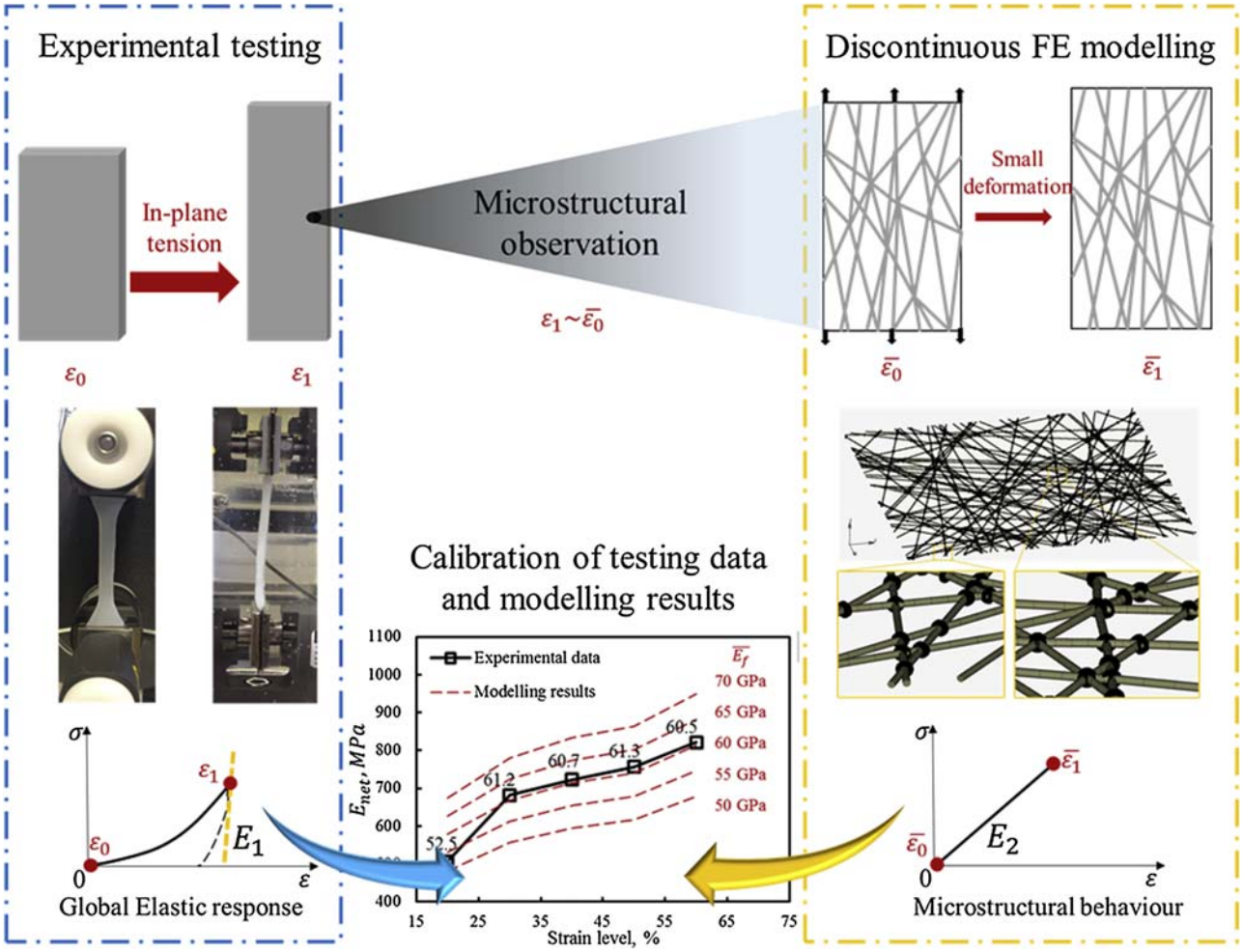

FIGURE 1.8 A general procedure of inverse parameter estimation; microstructural behavior during the instantaneous unloading is related to the global elastic response for the in-plane tension regime. Based on the microstructure of deformed experimental samples, a discontinuous finite element model is developed. An optimized value of fiber's stiffness can be predicted by calibrating modeling results obtained with various levels of fiber stiffness with experimental data.

1.3.3 Generation of Discontinuous Finite Element Model

The whole procedure of this case study, including experimental procedure, model generation, RVE, data analysis and calibration, can be found in Gao et al. (2017). Here, the focus is on selection of the most suitable technique to generate the discontinuous FE modeling approach.

1.3.3.1 Network Structure

In its natural state, the BC fibrous network is a long-fiber system. In the process of stretching in in-plane tension, long fibers were divided by a series of fiber-segments by entanglement; as a result, a deformed BC fibrous network became a short-fiber system. Hence, fiber-deposition and random-walk models are not suitable for this case. Fiber reorientation is a basic deformation mechanism for hydrogels, dominating material stiffening with increasing strain (Gao et al., 2015); hence, controlling fiber-orientation distribution is a priority, so that embedded fiber model is most suitable in this case.

The long BC nanofibers are curved; the respective demand of computational cost should be considered because more elements are required to present curvature with more segments. Still, in the in-plane tension regime, the following deformation mechanisms were observed: (1) entanglements were formed at positions where fibers interweaved and (2) curl fibers were straightened by stretching of local entanglements (Gao et al., 2015). Hence, in a deformed fibrous layer, straight fibers are a more reasonable approximation than accounting for curvature.

This book belongs to Central Library BADJI Mokhtar-ANNABA UNIVERSITY Copyright Elsevier 2024

1.3.3.2 Fiber Cross-Links

For the long-fiber system with fibers without branches contacting each other, such as BC hydrogel in its natural state, pin joints dominate behavior at intersections. During the fermentation process in synthesis of the BC hydrogel, fibers are naturally interwoven; thus, it is assumed that some entanglements are easily formed in the process of stretching. Consequently, the rotating joint is involved in the mechanical response of a stretched BC network.

1.3.4 Representative Volume Element

Considering the dimensions of BC nanofibers, the use of RVE is essential to reduce computational efforts. An effective way to assess suitability of a specific model as RVE is by testing its extent of representativeness; in other words, properties of interest should be model size independent. For most studies, model-size convergence would be the most appropriate approach. In practical terms this means increasing the model size until the properties of interest stop changing.

Representativeness of the RVE means that its mechanical behavior is repeatable; one effective way to verify this is to compare responses of different RVEs with the same size but different realizations of their random microstructure. As already mentioned, a PV element does not exist for most fibrous biomaterial; therefore, in a real material, a volume unit of a certain size has a unique microstructure, resulting in unique (local) mechanical behavior. Apparently, behavior of the whole specimen is the result of contributions of all the elements. Hence, the effective properties are considered equal to volume-averaged properties. One way to obtain such properties is to measure them for a series of RVEs and then calculate the average value. It is known that the averaged properties tend to converge when the amount of numerical samples is large enough, assessed by the trends of a relative error of mean value (REMV) and a relative standard deviation (RSD) (Liu et al., 2013). The convergence of REMV and RSD demonstrates that the averaged properties of these RVEs represent the effective properties of the whole specimen.

The FE method treats a continuous material as the assembly of connected finite elements with certain numbers of degrees of freedom; in fact, real materials are composed by infinite element with infinite degrees of freedom. Hence, the meshing process in the FE method theoretically increases constraints for elements, increasing material stiffness. Therefore, the results from the FE method are mesh size dependent; the magnitude of stiffness reduces with an increasing number of degrees of freedom (reducing mesh size) and, concurrently, increasing computational cost. Therefore, mesh-convergence analysis is usually used to compromise the mesh size dependence and computational cost. Empirically, when the changes in interest quantities are not more than 5%, the mesh size is fine enough, considering mesh size independent.

1.4 SUMMARY AND CONCLUSIONS

In this chapter, challenges related to three main experimental techniques (nanoscale tensile test, three-point bending, and Raman spectroscopy) in identifying material properties of nanofibers were used as motivation for employing numerical computations as an alternative approach. Various modeling techniques accounting for microstructure of fibrous materials were reviewed. The suggested approach, employing computational models, was based on inverse parameter identification, where the realistic material parameters were sought by comparing experimental and computational results. The chapter discusses appropriateness of various modeling schemes for this, focusing on their main features, advantages, and deficiencies. This was followed by a case study, presenting a typical challenge of modeling a BC hydrogel—a network of nanofibers. Ways to determine a RVE for such a material were discussed together with a method of assessing the modulus of elasticity of constituent nanofibers. The strength of inverse parameter estimation with computational models was proven. The readers can select their modeling techniques based on discussion of the models presented in this chapter.

REFERENCES

Altendorf, H., Jeulin, D., 2011. Random-walk-based stochastic modeling of three-dimensional fiber systems. Physical Review E 83 (4), 041804.

Arruda, E.M., Boyce, M.C., 1993. A three-dimensional constitutive model for the large stretch behavior of rubber elastic materials. Journal of the Mechanics and Physics of Solids 41 (2), 389−412.

Beex, L., Peerlings, R., Geers, M., 2014a. A multiscale quasicontinuum method for lattice models with bond failure and fiber sliding. Computer Methods in Applied Mechanics and Engineering 269, 108−122.

Beex, L., Peerlings, R., Geers, M., 2014b. A multiscale quasicontinuum method for dissipative lattice models and discrete networks. Journal of the Mechanics and Physics of Solids 64, 154−169.

This book belongs to Central Library BADJI Mokhtar-ANNABA UNIVERSITY

Copyright Elsevier 2024

Carleton, J.B., et al., 2015. Geometric characterization and simulation of planar layered elastomeric fibrous biomaterials. Acta Biomaterialia 12, 93–101.
Chapelle, L., et al., 2015. Generation of non-overlapping fiber architecture. In: 20th International Conference on Composite Materials.
D'Amore, A., et al., 2010. Characterization of the complete fiber network topology of planar fibrous tissues and scaffolds. Biomaterials 31 (20), 5345–5354.
Demirci, E., et al., 2011. Finite element modelling of thermally bonded bicomponent fibre nonwovens: tensile behaviour. Computational Materials Science 50 (4), 1286–1291.
Demirci, E., et al., 2012. Computation of mechanical anisotropy in thermally bonded bicomponent fibre nonwovens. Computational Materials Science 52 (1), 157–163.
Dirrenberger, J., Forest, S., Jeulin, D., 2014. Towards gigantic RVE sizes for 3D stochastic fibrous networks. International Journal of Solids and Structures 51 (2), 359–376.
Ekman, A., et al., 2012. The number of contacts in random fibre networks. Nordic Pulp and Paper Research Journal 27 (2), 270.
El Said, B., et al., 2016. Multi-scale modelling of strongly heterogeneous 3D composite structures using spatial Voronoi tessellation. Journal of the Mechanics and Physics of Solids 88, 50–71.
Gaiselmann, G., et al., 2012. Stochastic 3D modeling of fiber-based materials. Computational Materials Science 59, 75–86.
Gao, X., et al., 2015. Inelastic behaviour of bacterial cellulose hydrogel: in aqua cyclic tests. Polymer Testing 44, 82–92.
Gao, X., et al., 2016a. Through-thickness stress relaxation in bacterial cellulose hydrogel. Journal of the Mechanical Behavior of Biomedical Materials 59, 90–98.
Gao, X., et al., 2016b. Time-dependent rheological behaviour of bacterial cellulose hydrogel. Materials Science and Engineering: C 58, 153–159.
Gao, X., et al., 2016c. Effect of microstructure on anomalous strain-rate-dependent behaviour of bacterial cellulose hydrogel. Materials Science and Engineering: C 62, 130–136.
Gao, X., et al., 2016d. Fracture behaviour of bacterial cellulose hydrogel: microstructural effect. Procedia Structural Integrity 2, 1237–1243.
Gao, X., et al., 2017. Assessing stiffness of nanofibres in bacterial cellulose hydrogels: numerical-experimental framework. Materials Science and Engineering: C 77, 9–18.
Guhados, G., Wan, W., Hutter, J.L., 2005. Measurement of the elastic modulus of single bacterial cellulose fibers using atomic force microscopy. Langmuir 21 (14), 6642–6646.
Hang, F., et al., 2011. In situ tensile testing of nanofibers by combining atomic force microscopy and scanning electron microscopy. Nanotechnology 22 (36), 365708.
Haque, M., Saif, M., 2003. A review of MEMS-based microscale and nanoscale tensile and bending testing. Experimental Mechanics 43 (3), 248–255.
Huang, X., et al., 2013. A simple fracture energy prediction method for fiber network based on its morphological features extracted by X-ray tomography. Materials Science and Engineering: A 585, 297–303.
Huang, X., et al., 2015. Morphology and transport properties of fibrous porous media. Powder Technology 283, 618–626.
Iwamoto, S., et al., 2009. Elastic modulus of single cellulose microfibrils from tunicate measured by atomic force microscopy. Biomacromolecules 10 (9), 2571–2576.
Jin, T., Stanciulescu, I., 2015. Numerical simulation of fibrous biomaterials with randomly distributed fiber network structure. Biomechanics and Modeling in Mechanobiology 1–14.
Karayiannis, N.C., Laso, M., 2008. Monte carlo scheme for generation and relaxation of dense and nearly jammed random structures of freely jointed hard-sphere chains. Macromolecules 41 (4), 1537–1551.
Kulachenko, A., Uesaka, T., 2012. Direct simulations of fiber network deformation and failure. Mechanics of Materials 51, 1–14.
Liu, Q., et al., 2013. Finite element analysis on tensile behaviour of 3D random fibrous materials: model description and meso-level approach. Materials Science and Engineering: A 587, 36–45.
Liu, Q., et al., 2014. Experimental and FEM analysis of the compressive behavior of 3D random fibrous materials with bonded networks. Journal of Materials Science 49 (3), 1386–1398.
Liu, J., Chen, Z., Li, K., 2010. A 2-D lattice model for simulating the failure of paper. Theoretical and Applied Fracture Mechanics 54 (1), 1–10.
Lu, Z., et al., 2013. Experiment and modeling on the compressive behaviors for porous silicon nitride ceramics. Materials Science and Engineering: A 559, 201–209.
Mościński, J., et al., 1989. The force-biased algorithm for the irregular close packing of equal hard spheres. Molecular Simulation 3 (4), 201–212.
Mueller, D.H., Kochmann, M., 2004. Numerical modeling of thermobonded nonwovens. International Nonwovens Journal 13 (1), 56–62.
Ostoja-Starzewski, M., 2002. Lattice models in micromechanics. Applied Mechanics Reviews 55 (1), 35–60.
Persson, J., Isaksson, P., 2014. A mechanical particle model for analyzing rapid deformations and fracture in 3D fiber materials with ability to handle length effects. International Journal of Solids and Structures 51 (11), 2244–2251.
Picu, R., 2011. Mechanics of random fiber networks—a review. Soft Matter 7 (15), 6768–6785.
Raina, A., Linder, C., 2014. A homogenization approach for nonwoven materials based on fiber undulations and reorientation. Journal of the Mechanics and Physics of Solids 65, 12–34.
Redenbach, C., Vecchio, I., 2011. Statistical analysis and stochastic modelling of fibre composites. Composites Science and Technology 71 (2), 107–112.
Ridruejo, A., González, C., LLorca, J., 2012. A constitutive model for the in-plane mechanical behavior of nonwoven fabrics. International Journal of Solids and Structures 49 (17), 2215–2229.

This book belongs to Central Library BADJI Mokhtar-ANNABA UNIVERSITY Copyright Elsevier 2024

Sabuncuoglu, B., Acar, M., Silberschmidt, V.V., 2013. Parametric code for generation of finite-element model of nonwovens accounting for orientation distribution of fibres. International Journal for Numerical Methods in Engineering 94 (5), 441−453.

Shi, Z., et al., 2016. Electroconductive natural polymer-based hydrogels. Biomaterials.

Tan, E., et al., 2005. Tensile test of a single nanofiber using an atomic force microscope tip. Applied Physics Letters 86 (7), 073115.

Tan, E., Lim, C., 2006. Mechanical characterization of nanofibers−a review. Composites Science and Technology 66 (9), 1102−1111.

Tanpichai, S., et al., 2012. Effective Young's modulus of bacterial and microfibrillated cellulose fibrils in fibrous networks. Biomacromolecules 13 (5), 1340−1349.

This book belongs to Central Library BADJI Mokhtar-ANNABA UNIVERSITY

Copyright Elsevier 2024

Chapter 2

Modeling the Influence of Mechanics on Biological Growth

E. Comellas[1], A. Carriero[2], M. Giorgi[3], A. Pereira[4] and S.J. Shefelbine[5]

[1]University of Erlangen-Nürnberg, Erlangen, Germany; [2]City College, New York City, NY, United States; [3]University of Sheffield, Sheffield, United Kingdom; [4]Imperial College, London, United Kingdom; [5]Northeastern University, Boston, MA, United States

2.1 INTRODUCTION

Growth is a fundamental feature of every living system both during initial development and in mature adaptation. The effect of mechanical stimuli on growth is called *mechanobiological growth*. Here we examine the use of finite element (FE) modeling in determining the effects of mechanical forces on growth. The role of mechanical forces in biological growth has been simulated using FE analysis in many different tissues, such as joint development (Giorgi et al., 2014, 2015); bone growth (Carriero et al., 2011; Shefelbine and Carter, 2004a; Shefelbine et al., 2002; Yadav et al., 2016; Castro-Abril et al., 2016; Guevara et al., 2015; Villemure et al., 2002); muscle adaptation (Zöllner et al., 2015); axon growth (Holland et al., 2015); embryonic development of the heart (Ramasubramanian et al., 2008; Shi et al., 2014), brain (Garcia et al., 2017), and eye (Oltean et al., 2016); cardiac remodeling (Sáez et al., 2014; Rausch et al., 2011; Kerckhoffs, 2012) and angiogenesis (Edgar et al., 2015); plant root growth (Krupinski et al., 2016); and tumor growth (Wijeratne et al., 2016; Dong et al., 2016). These models can help to identify the mechanical stimuli that may be involved in mechanobiological signaling by exploring the effects of different stimuli on growth patterns (Giorgi et al., 2014; Sáez et al., 2014; Pereira et al., 2015). Computational models of mechanobiological growth can also help to determine possible causes of disease states (Sáez et al., 2014; Rausch et al., 2011) or pathologic growth (Giorgi et al., 2015; Carriero et al., 2011; Villemure et al., 2002).

Regardless of the tissue of interest, computational models of mechanobiological growth share the following features:

1. *Assumption of an initial state*. This includes the initial geometry, material properties, and stress state. Some models assume a no stress state (Ramasubramanian and Taber, 2008), whereas others may assume some initial prestress based on physiological states, such as the pressure in blood vessels (Sáez et al., 2014).
2. *Mechanical stimuli*. The mechanical stimuli are the mechanical signals that trigger a change in growth. The stimuli may be *external* forces or pressures, such as the skeletal joint loads during bone growth (Giorgi et al., 2014; Carriero et al., 2011; Yadav et al., 2016) or cardiac pressure in the vessels (Sáez et al., 2014) or *internal* stresses caused by differential growth (Shi et al., 2014; Wijeratne et al., 2016; Henderson et al., 2007).
3. *Mechanobiological algorithm*. The mechanobiological algorithm mathematically links the mechanical stimulus to a mathematical representation of growth. This is commonly accomplished by splitting the deformation gradient tensor $\mathbf{F}$ into an elastic component ($\mathbf{F}^e$) and a growth component ($\mathbf{F}^g$). Standard FE modeling is used to determine the elastic component of the deformation, and a mechanobiological algorithm is used to determine the growth component, which is often a function of the elastic component.
4. *Simulating biological effects*. Growth is typically implemented as an isotropic or anisotropic deformation. Either the elements or the boundary of the elements are expanded and the model is remeshed if necessary.

In this chapter we will discuss each of these components in more detail with examples of how they have been implemented in previous research.

Numerical Methods and Advanced Simulation in Biomechanics and Biological Processes. https://doi.org/10.1016/B978-0-12-811718-7.00002-2
Copyright © 2018 Elsevier Ltd. All rights reserved.

This book belongs to Central Library BADJI Mokhtar-ANNABA UNIVERSITY

Copyright Elsevier 2024

2.2 INITIAL STATE

The initial state of the tissue includes the geometry, material properties, and loading conditions. For many models of mechanobiological growth, the geometry is idealized to a generic shape such as a cylinder for a blood vessel (Sáez et al., 2014), a sphere for a tumor (Wijeratne et al., 2016), or an idealized bone morphology (Carriero et al., 2011; Shefelbine and Carter, 2004a). Sometimes surrounding tissues are included in the model, particularly if these tissues may affect the growth. For example, the stroma around a growing tumor (Wijeratne et al., 2016) or the joint capsule around a growing joint (Giorgi et al., 2014) affects the stresses in the growing tissue, but does not contribute to the growth directly. Generic and idealized geometries are useful to develop mechanobiological algorithms and explore the influence of certain stimuli or factors on mechanobiological growth in a hypothetical context. Because the geometry is not "real," it is difficult to validate the predicted geometric changes due to growth. However, generic models can readily be used in parametric studies to examine sensitivity of growth to different factors and explore generalized phenomena.

It is critical to assess how initial geometry and surrounding tissues alter the mechanical environment of the growing tissue. Studies have shown that modeling a realistic (magnetic resonance imaging (MRI) based) growth plate of the proximal femur alters the stress patterns and growth predictions compared with an idealized generic growth plate (Yadav et al., 2016). It is critical therefore to maintain geometric integrity when shape influences the mechanobiological stimuli of interest. Many models obtain initial geometries from 3D scans, such as computed tomography (CT), MRIs, or optical coherence tomography (used particularly for small prenatal tissues (Ramasubramanian et al., 2008)). The geometry is identified in the scan and becomes a surface or a volume of the FE model typically using an imaging software intermediary, such as commercial software MIMICS (Materialise, Belgium) or Amira (FEI, Oregon), or open source software such as VTK (Kitware, NY). The imaging software is used to identify the tissues of interest through segmentation, thresholding, and masks. Many image analysis programs output a surface mesh (e.g., STL or IGES formats), which can be brought into standard FE programs and meshed. Some imaging software can output FE meshes directly, typically using tetrahedral meshes that preserve surface smoothness. Maintaining geometric verity is important when the geometry affects the mechanobiological stimuli of interest and when the model is validated with images of "real" growth. The use of both geometrically accurate models for overall mechanical loading and idealized models for particular regions of interest in growth is a computationally efficient way to ensure the appropriate stress state is computed in a geometry that is easy to manipulate (Ramasubramanian et al., 2008; Sáez et al., 2014).

The material properties of the tissues are typically taken from values in the literature or measured directly from the tissues. Many biological materials have directionally organized structural proteins, which result in anisotropic material properties in the tissue. For example, the elasticity of arterial tissue is modeled using an isotropic contribution for elastin and an anisotropic contribution for collagen, reflecting the organization of collagen around the artery (Sáez et al., 2014). Anisotropic material properties are particularly important in cases where asymmetric growth may occur because of differences in material properties in different directions and where underlying structure of the matrix is anisotropic. Material anisotropy does not necessarily mean growth will be anisotropic; in most models the material properties are defined separately from the growth properties.

The loading conditions encompass boundary constraints and the magnitude and direction of loading, which are time varying in living organisms. In most biomechanical models of tissues, obtaining accurate (or at least representative) loading conditions is a major challenge. As with geometry, there are two options: (1) idealize the loading conditions or (2) measure the loading conditions to resemble realistic loads as closely as possible. Idealized loading conditions make it possible to isolate the effects of direction and magnitude. For example, in modeling the developing proximal femur, loads of unit magnitude were used so that the influence of the direction of the load on growth could be identified (Shefelbine and Carter, 2004b). In models where direction may not play an important role, such as pressurized arteries, average physiological pressure may be sufficient (Sáez et al., 2014). Many models of growth use quasistatic loading conditions, which means a single stress state represents the time-varying stresses in the tissue. To capture the variability of loading, multiple quasistatic states can be used such as multiple instances during a gait cycle in lower limb loading (Carriero et al., 2011; Yadav et al., 2016) or dynamic loading conditions can be used exploiting explicit dynamic analysis methods of the FE solver (Giorgi et al., 2015). The choice of generic loads versus realistic loads and quasistatic loads versus dynamic loads depends on the research question and the available data on the loading state. For example, musculoskeletal models of human gait provide realistic muscle and joint loading conditions on the femur, so realistic loading conditions are possible in FE models of growth in the femur (Carriero et al., 2011; Yadav et al., 2016). However, prenatal joint kinematics and kinetics is not accessible, so generic loading conditions were chosen for FE models of joint morphogenesis (Giorgi et al., 2014, 2015). If the mechanical stimuli of interest is the peak stress (or strain), then a quasistatic model at the peak load

This book belongs to Central Library BADJI Mokhtar-ANNABA UNIVERSITY
Copyright Elsevier 2024

would efficiently model the stresses of interest. However, if the time-averaged stress is of interest, then dynamic loading conditions may be more appropriate (Pereira et al., 2015; Giorgi et al., 2015).

Many models incorporate a state of prestress into the model, which becomes the baseline from which other stresses are measured. In tissues that are normally naturally stressed, such as blood vessels (Sáez et al., 2014), this prestress is critical for accurate assessment of a "baseline" state.

2.3 MECHANICAL STIMULI

All mechanobiological growth models assume a mechanical stimulus (Ξ) is involved in modulating growth. Most models are phenomenological and simply state this stimulus causes growth without exploring the molecular-level transduction of the physical signal into biological mediators of the response (growth proteins, etc.). Recent studies have begun to combine reaction-diffusion equations to link mechanical signals with biochemical synthesis, such as the combination of oxygen concentration and pressure in tumor growth (Wijeratne et al., 2016) and the importance of Rho-of-plant protein and stress in location of root growth in plants (Krupinski et al., 2016). However, for most mechanobiological growth, we still do not know the exact mechanical signal nor the transduction pathways involved at the molecular level.

For soft tissues it is common to assume *stress* is the mechanical signal that stimulates growth or adaptation. It has been postulated that each tissue has a target stress and changes in stress drive the morphogenic process (Ramasubramanian and Taber, 2008). Various generalized growth phenomena such as bending, curving, and invagination have been explored using a homeostatic stress-free configuration as the driver for morphogenesis (Ramasubramanian and Taber, 2008). Stress has been used as the mechanical cue driving prenatal cardiac and brain growth (Ramasubramanian et al., 2008; Shi et al., 2014; Oltean et al., 2016), adaptation to hypertension (Rausch et al., 2011), cartilage growth during joint morphogenesis (Giorgi et al., 2014, 2015), and tumor growth (Wijeratne et al., 2016). *Strain* is often used as the driver in muscle growth and adaptation (Taber, 1998), such as in cardiac growth (Kerckhoffs, 2012; Kerckhoffs et al., 2012) and skeletal muscle lengthening (Zöllner et al., 2015, 2012).

For growth of hard tissues (bones) different stimuli are used for the different biological growth processes in bone. Bone growth occurs longitudinally through endochondral ossification and circumferentially through intramembranous ossification. In endochondral ossification, cartilage in the growth plate hypertrophies and is mineralized. Typically, mechanobiological stimuli in the cartilage growth plate is stress based, with cyclic hydrostatic stress inhibiting growth and cyclic octahedral shear stress promoting growth (Shefelbine and Carter, 2004a; Yadav et al., 2016; Villemure et al., 2002; Carter and Wong, 1988a). For intramembranous ossification, bone forms directly on bone and is thought to be mediated by the osteocytes. Unlike soft tissues where stress in the matrix is likely similar to stress of the cells, the stress in the bone matrix is higher than the stress felt by the osteocytes due to the difference in material properties. Therefore, it is unlikely that stress is the direct mechanical cue directing osteocytes to initiate the osteogenic signaling pathways. The strain of the matrix and the cell are the same, but strain as a stimulus does not capture the importance of loading rate on intramembranous ossification (Mosley and Lanyon, 1998; Rubin and Lanyon, 1984). Mechanobiological models have proposed that fluid flow in the lacuna-canalicular network of bone may be the mechanical signal in intramembranous ossification during intramembranous bone formation (Price et al., 2011; Knothe Tate et al., 2000; Cowin et al., 1995). Fluid flow induced by external stresses creates fluid shear stress on the cells (Weinbaum et al., 1994) that lies within the osteogenic range (Klein-Nulend et al., 1995). FE models have shown that fluid flow predicts the load rate and rest insertion-dependent osteogenic behavior of bone (Pereira and Shefelbine, 2014) and predicts region of bone formation more accurately than strain energy density (Pereira et al., 2015).

The mechanical stimuli (Ξ as stress, strain, fluid flow, or other combination of mechanical cues) may be generated by external loads such as blood pressure, fluid pressure or joint loading, or by internal loads, namely, the stresses or strains induced by differential growth rates of tissues. Most mechanobiological growth models examine the influence of external loads on growth because, often, there is a physiological basis for the loading or a pathologic state that alters the loading. However, in rapidly growing tissues, such as during prenatal growth, the stresses and strains from differential growth can be sufficient to alter growth patterns. Models have used internal loads to explain ossification of cranial sutures (Henderson et al., 2004), cranial healing in infants (Henderson et al., 2005; Fong et al., 2003), limb morphogenesis (Henderson and Carter, 2002), and formation of the perichondrium and bone collar (Henderson et al., 2007), all of which occur during periods of rapid growth.

This book belongs to Central Library BADJI Mokhtar-ANNABA UNIVERSITY
Copyright Elsevier 2024

2.4 MECHANOBIOLOGICAL ALGORITHM

Growth is typically modeled by the multiplicative decomposition of the deformation gradient $\mathbf{F}$ into an elastic component $\mathbf{F}^e$ and a growth component $\mathbf{F}^g$ (Rodriguez et al., 1994),

$$\mathbf{F} = \frac{\mathrm{d}\mathbf{x}}{\mathrm{d}\mathbf{X}} = \mathbf{F}^e \cdot \mathbf{F}^g. \tag{2.1}$$

The deformation gradient maps an infinitesimal material point $\mathrm{d}\mathbf{X}$ from the reference configuration to an infinitesimal spatial point $\mathrm{d}\mathbf{x}$ in the current configuration at any given time t. Then, the multiplicative decomposition is interpreted as a mapping from the reference configuration to the current configuration through an intermediate growth configuration, as illustrated in Fig. 2.1. The growth component $\mathbf{F}^g$ defines the irreversible deformation due to growth (Jones and Chapman, 2012). The intermediate configuration attained is not a physical state actually experienced by the tissue, it is an *incompatible* configuration. The current configuration is then reached through the elastic component $\mathbf{F}^e$, which defines the mechanical response of the tissue. This is often considered to be purely elastic or hyperelastic (Chagnon et al., 2015) and, therefore, reversible in nature. The incompatibility of the intermediate configuration makes the definition of evolution equations for $\mathbf{F}^g$ difficult because they cannot be described through direct experimental observations. Nonetheless, different expressions have been used for $\mathbf{F}^g$ to successfully model growth, which we will review next. We will focus first on *how* the tissue grows (the directionality of the deformation) and then discuss *where and why* it grows (the nonuniformity and driving mechanisms that promote or inhibit this deformation).

The simplest form of growth is volumetric growth, in which the tissue grows uniformly in all directions. Then, the growth tensor is of the type

$$\mathbf{F}^g = \vartheta \mathbf{1}, \tag{2.2}$$

where $\mathbf{1}$ is the second-order identity tensor and ϑ is the growth multiplier, a stretchlike variable. For $\vartheta = 1$, the growth tensor is equal to the identity tensor and the deformation gradient is reduced to its elastic component, $\mathbf{F} = \mathbf{F}^e$. Hence, no growth is observed in the tissue. Values of ϑ above 1 indicate growth, whereas values below 1 indicate resorption or atrophy in the tissue. As is the case with stretch, the growth multiplier cannot take a negative value. The evolution of the growth multiplier will be defined in terms of the mechanobiological factors driving the growth phenomenon.

Isotropic volumetric growth has been successfully used to model a wide range of growing tissues, including developmental folding in the brain (Budday et al., 2014b), necrosis in cardiac tissues (Bellomo et al., 2012), and fruit growth (Böl and Bolea Albero, 2014). Yet, assuming isotropic growth is a gross oversimplification in most applications. In general, growth will not be isotropic but, rather, have a certain directionality. Anisotropic volumetric growth models have been used to simulate a vascular tumor growth (Xue et al., 2016) and ductal carcinoma (Ciarletta et al., 2012), among many other growing tissues. In these models, the growth rates are different for each principal spatial direction.

Note the conceptual difference between anisotropic and inhomogeneous growth. Isotropic volumetric models can result in inhomogeneous deformations if the growing tissue is constrained by physical or metabolic factors. A same tissue will

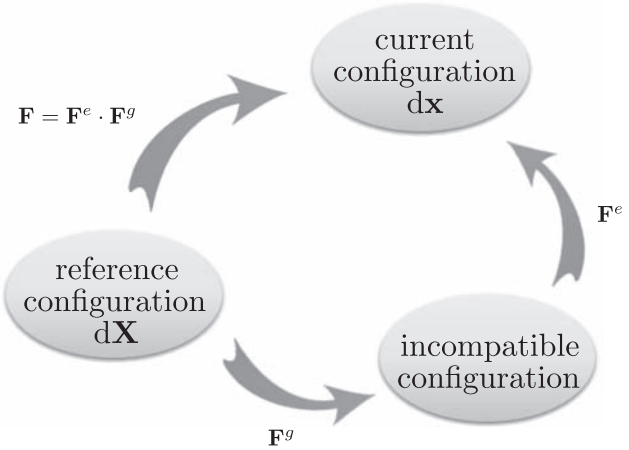

FIGURE 2.1 Schematic representation of the multiplicative decomposition of the deformation gradient $\mathbf{F}$ used to model growth in a continuum framework.

This book belongs to Central Library BADJI Mokhtar-ANNABA UNIVERSITY
Copyright Elsevier 2024

FIGURE 2.2 Under normal homogeneous growth conditions, isotropic volumetric growth results in equal growth in all directions (left). However, external constraints, such as the plastic six-pack ring in which the turtle in the right image was caught (Minnesota Department of Natural Resources, 2017), may result in inhomogeneous growth, even for isotropic growth models.

grow at different rates in zones with different concentrations of the driving mechanisms stimulating growth. It might not even grow at all if there is an external physical obstacle that does not allow the tissue to expand into a certain space (see Fig. 2.2).

In contrast, anisotropic growth seeks to capture the directionality of growth, that is, the fact that growth in a certain direction is fundamentally driven by different mechanobiological factors than in another direction of the same tissue. For example, in cardiac tissue, ventricular dilation is believed to be strain driven whereas wall thickening is thought to be stress driven (Göktepe et al., 2010). Tissue histology has also an important role in defining anisotropic growth. Muscle adaptation is either defined along the muscle fiber direction through the addition and removal of sarcomeres (Zöllner et al., 2015) or perpendicular to the fiber direction by hypertrophy of fibers, as seen in pathologies such as cardiac hypertrophy (Rausch et al., 2011). Brain tissue growth is often associated with axonal growth in the direction of the axon shaft (Holland et al., 2015; García-Grajales et al., 2016). Arteries may grow in the longitudinal direction or in the transverse (radial) direction, depending on the pathological condition under study (Lee et al., 2016; Sáez et al., 2014). Tissue growth may also occur exclusively along a certain plane, usually associated with a particular biological structure. For example, transversally isotropic growth has been used to explore the skin wrinkling observed in wet fingers (Sáez and Zöllner, 2017), whereas growing skin has been modeled with an anisotropic area growth (Buganza Tepole et al., 2016).

Overall, these different anisotropic models can be described by the same generic growth tensor

$$\mathbf{F}^g = 1 + (\vartheta_a - 1)\mathbf{N}_a \otimes \mathbf{N}_a + (\vartheta_b - 1)\mathbf{N}_b \otimes \mathbf{N}_b + (\vartheta_c - 1)\mathbf{N}_c \otimes \mathbf{N}_c, \tag{2.3}$$

where $\mathbf{N}_{(\bullet)}$ is the unit vector associated with the structural direction $(\bullet)$ in the reference configuration and $\vartheta_{(\bullet)}$ is its corresponding growth multiplier. Assuming the growth multiplier is exactly the same in all three directions {a, b, c} of the structural basis chosen, we recover the isotropic volumetric growth defined in Eq. (2.2). Isotropic in-plane or area growth with $\vartheta_a = \vartheta_b = \vartheta$ and $\vartheta_c = 1$ is then defined by the growth tensor

$$\mathbf{F}^g = \mathbf{1} + (\vartheta - 1)(\mathbf{N}_a \otimes \mathbf{N}_a + \mathbf{N}_b \otimes \mathbf{N}_b). \tag{2.4}$$

Finally, if growth occurs exclusively along a preferred direction, then $\vartheta_a = \vartheta$ and $\vartheta_b = \vartheta_c = 1$, resulting in

$$\mathbf{F}^g = \mathbf{1} + (\vartheta - 1)\mathbf{N}_a \otimes \mathbf{N}_a. \tag{2.5}$$

The advantage of using such a generic growth tensor is that it allows for a whole range of combinations of the possible growth directions within a single simple definition (see Fig. 2.3). For example, anisotropic in-plane or area growth is given by $\vartheta_a \neq \vartheta_b$ and $\vartheta_c = 1$, while transversally isotropic volumetric growth corresponds to $\vartheta_a = \vartheta_b \neq \vartheta_c$.

The structural nature of the growth tensor $\mathbf{F}^g$ is directly related to the directionality of the grown tissue. In an artery, we would associate the given structural directions a, b, and c with the radial r, circumferential θ, and longitudinal z directions described by a cylindrical coordinate system. Then, an increase in the wall thickness of the artery would correspond to $\vartheta_r = \vartheta$ and $\vartheta_\theta = \vartheta_z = 1$ (see bottom image in Fig. 2.3), whereas the longitudinal growth of the artery would be given by $\vartheta_z = \vartheta$ and $\vartheta_r = \vartheta_\theta = 1$. Another possibility would be to assume transversally isotropic growth in the plane of the artery wall, which corresponds to $\vartheta_\theta = \vartheta_z = \vartheta$ and $\vartheta_r = 1$ (see second image from the bottom in Fig. 2.3).

We must now describe the mechanobiological mechanisms driving the growth process in each of these directions, which are contained in the corresponding growth multipliers $\vartheta_{(\cdot)}$ and their evolution. Precisely, one of the most challenging aspects of modeling growth is determining the appropriate mechanobiological formulation that mathematically links the mechanical stimuli (Ξ) with biological growth ($\mathbf{F}^g$). Different evolution equations for ϑ have been proposed to define the

This book belongs to Central Library BADJI Mokhtar-ANNABA UNIVERSITY Copyright Elsevier 2024

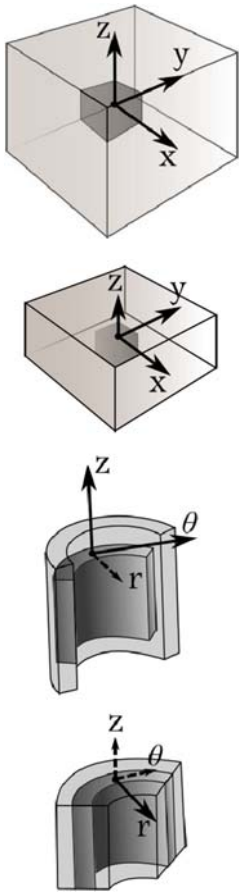

Isotropic volumetric growth
$$\mathbf{F}^g = \vartheta\,\mathbf{1}$$

Transversally isotropic volumetric growth
$$\mathbf{F}^g = \mathbf{1} + (\vartheta_{\mathrm{xy}} - 1)\ (\mathbf{N}_{\mathrm{x}} \otimes \mathbf{N}_{\mathrm{x}} + \mathbf{N}_{\mathrm{y}} \otimes \mathbf{N}_{\mathrm{y}}) + (\vartheta_{\mathrm{z}} - 1)\ \mathbf{N}_{\mathrm{z}} \otimes \mathbf{N}_{\mathrm{z}}$$

Isotropic area growth
$$\mathbf{F}^g = \mathbf{1} + (\vartheta - 1)\ (\mathbf{N}_\theta \otimes \mathbf{N}_\theta + \mathbf{N}_{\mathrm{z}} \otimes \mathbf{N}_{\mathrm{z}})$$

Uni-directional growth
$$\mathbf{F}^g = \mathbf{1} + (\vartheta - 1)\ \mathbf{N}_{\mathrm{r}} \otimes \mathbf{N}_{\mathrm{r}}$$

FIGURE 2.3 Conceptual examples of different types of growth related to the structural nature of the growth tensor $\mathbf{F}^g$. The continuous axes in the figures indicate the amount and direction of growth.

growth rate, typically based on experimental and clinical observations. The evolution of the growth multiplier can be generally reduced to the product of two functions,

$$\dot{\vartheta} = \kappa(\vartheta)\phi(\Xi), \tag{2.6}$$

where $\kappa(\vartheta)$ is a limiting function and $\phi(\Xi)$ is the actual growth criterion, dependent on the chosen driving mechanism or growth stimulus, Ξ.

The simplest and most commonly used growth stimulus function is

$$\phi(\Xi) = \left\langle \Xi - \Xi^0 \right\rangle, \tag{2.7}$$

where the Macaulay brackets $\langle\rangle$ indicate the Heaviside step function and Ξ^0 is the critical threshold above which growth will occur (see Fig. 2.4). Establishing a critical threshold allows accounting for the homeostatic equilibrium zone where the tissue neither undergoes growth nor resorption, albeit having low values of the growth stimulus Ξ. This equilibrium zone may, for example, account for the biological state in which new cells are produced only to replace those that die, so mass and volume remain constant and there is no effective growth (Bellomo et al., 2012).

A wide range of variables has been used as the mechanical growth stimulus, which can be loosely classified into either purely mechanical cues or biochemically motivated cues. Mechanical stimuli include several forms of stress (Göktepe et al., 2010; Rausch et al., 2011; Bellomo et al., 2012; Liu et al., 2014) and strain (Buganza Tepole et al., 2011; Zöllner et al., 2012; Kerckhoffs, 2012; Budday et al., 2014b) induced by the loading on the tissue, whereas biochemical stimuli are modeled through varying concentrations of nutrients, hormones, growth factors, or other quantifiable biological factors known to promote growth in the tissue (Kuhl, 2014). Constant values of the growth stimulus function have been used, e.g., to model the purely morphogenetic growth in a developing brain (Budday et al., 2014a; Holland et al., 2015), to

This book belongs to Central Library BADJI Mokhtar-ANNABA UNIVERSITY
Copyright Elsevier 2024

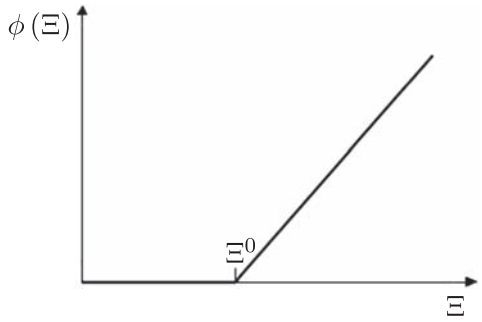

FIGURE 2.4 A simple growth criterion commonly used is $\phi(\Xi) = \langle \Xi - \Xi^0 \rangle$, where the critical threshold Ξ^0 establishes the growth stimulus value Ξ above which growth will occur. The no-growth zone below the threshold can be a representation of the tissue's homeostatic equilibrium zone.

reproduce skin wrinkling due to water exposure (Sáez and Zöllner, 2017), or to study the role of differential growth in the folding pattern of bilayered mucosa (Moulton and Goriely, 2011; Xie et al., 2014).

The limiting function $\kappa(\vartheta)$ in Eq. (2.6) is a growth modulator, i.e., it avoids an unbounded growth of the tissue by establishing upper and lower boundaries beyond which no growth will occur, regardless of the present growth stimulus. This is necessary to ensure an uncontrolled cancerlike growth does not take place, as well as to avoid the complete disappearance of a tissue undergoing resorption. In general, functions of the type

$$\kappa^+(\vartheta) = \kappa_0^+ \left(\frac{\vartheta^+_{max} - \vartheta}{\vartheta^+_{max} - \vartheta^+_0}\right)^{\gamma^+} \quad \text{and} \quad \kappa^-(\vartheta) = \kappa_0^- \left(\frac{\vartheta - \vartheta^-_{max}}{\vartheta^-_0 - \vartheta^-_{max}}\right)^{\gamma^-}, \tag{2.8}$$

are used for growth and resorption, respectively (Lubarda and Hoger, 2002). Here, ϑ_0^+ and ϑ^+_{max} represent the minimum and maximum stretch values for which growth may occur. Then, the limiting growth function $\kappa^+(\vartheta)$ is defined for the interval $\vartheta_0^+ \leq \vartheta \leq \vartheta^+_{max}$ of the growth multiplier. For other values of the growth multiplier there will be no tissue growth since $\kappa^+(\vartheta) = 0$. The effect of these two values is illustrated in Fig. 2.5. In an analogous manner, ϑ_0^- and ϑ^-_{max} represent the minimum and maximum stretch values for which resorption may occur. Typically, $\vartheta_0 = 1$ is taken for both functions (Himpel et al., 2005; Göktepe et al., 2010; Buganza Tepole et al., 2011; Zöllner et al., 2012; Saez, 2016) because this lower threshold plays an analogous role to Ξ^0 in the growth stimulus function. However, one might want to introduce $\vartheta_0 > 1$ in cases in which a growth stimulus function with no lower threshold has been used, e.g., for a constant $\phi(\Xi) = \Xi$. Also, it might be more convenient to define this threshold in terms of the effect (growth multiplier, ϑ) rather than the cause (growth stimulus, Ξ).

The parameters κ_0^+ and κ_0^- in Eq. (2.8) control the growth and resorption rate, whereas γ^+ and γ^- allow adjusting the nonlinearity of the growth and resorption processes. Fig. 2.6 illustrates the effect of these two parameters for growth processes. Experimental information to adequately calibrate these material parameters is not easily available. Hence, these parameters are typically chosen in a relatively arbitrary manner based on informed assumptions. However, sensitivity

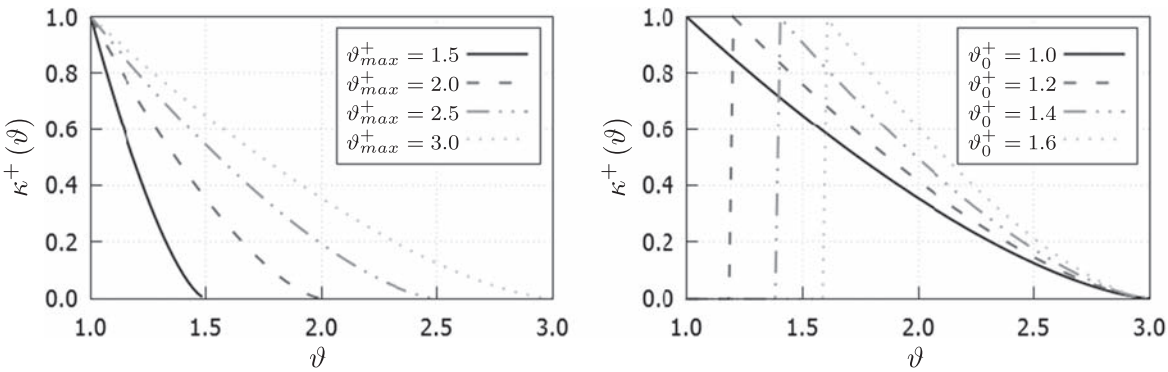

FIGURE 2.5 The growth modulator $\kappa^+(\vartheta)$ (Eq. 2.8) is plotted against the growth multiplier ϑ for varying values of ϑ^+_{max} at a fixed $\vartheta_0^+ = 1.0$ (left) and for varying values of ϑ_0^+ at a fixed $\vartheta^+_{max} = 3.0$ (right). The fixed values $\kappa_0^+ = 1.0$ and $\gamma^+ = 1.5$ have been considered in both plots. The parameter ϑ^+_{max} establishes the cut-off value of the growth multiplier above which no growth will occur, whereas ϑ_0^+ is the minimum value of the growth multiplier required for growth to take place.

This book belongs to Central Library BADJI Mokhtar-ANNABA UNIVERSITY Copyright Elsevier 2024

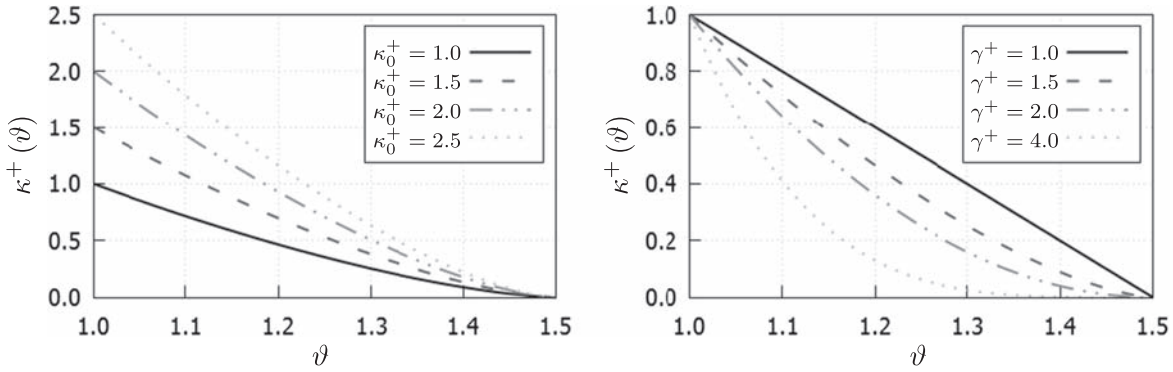

FIGURE 2.6 The growth modulator $\kappa^+(\vartheta)$ (Eq. 2.8) is plotted against the growth multiplier ϑ for varying values of κ_0^+ at a fixed $\gamma^+ = 1.5$ (left) and varying values of γ^+ at a fixed $\kappa_0^+ = 1.0$ (right). The fixed values $\vartheta_{max}^+ = 1.5$ and $\vartheta_0^+ = 1.0$ have been considered in both plots. The amount of growth increases with increasing values of κ_0^+, whereas the nonlinearity of the growth process increases with increasing values of γ^+.

analyses demonstrate that $\kappa_0^\pm$ and $\gamma^\pm$ influence the growth/resorption rate and the shape of the curve, but not the final state of biological equilibrium (Buganza Tepole et al., 2011).

A temporal function is also often used (Ambrosi and Mollica, 2002; Papastavrou et al., 2013; Holland et al., 2013) instead of Eq. (2.8) to control unbounded exponential growth or resorption,

$$\kappa(t) = \frac{1}{\tau_0}(\vartheta_{max} - \vartheta_0)\exp[-t/\tau_0]. \tag{2.9}$$

Here, again, ϑ_0 is the initial growth value, usually defined as $\vartheta_0 = 1$, and ϑ_{max} establishes the maximum growth value, above which no more growth occurs. Note that a time variable t is introduced, which may be directly associated to ϑ through the loading speed in the tissue or, instead, may be used as an independent variable to adjust the growth rate and shape of the curve, as illustrated in Fig. 2.7. The parameter τ_0 characterizes the velocity of the growth function.

Alternative approaches include not limiting growth at all, that is, $\kappa(\vartheta) = 1$ (Budday et al., 2014a; Holland et al., 2015), or limiting growth through the introduction of an additional variable ξ in the function $\kappa(\vartheta, \xi)$. The latter is conceptually different from the limiting functions described above in that they introduce a new field with a concrete biological basis to define *how* and *when* the growth criterion $\phi(\Xi)$ is limited. The variable ξ can be a specific physical variable such as the temperature T. Then, the function $\kappa(\vartheta, T)$ represents the amount of energy supplied by the biochemical sources in the tissue that can be transformed into growth (Ambrosi et al., 2017). It can also be a more abstract field such as the "biological availability" θ in the tissue, which represents the amount of growth the tissue's metabolism can sustain with the available nutrients (Bellomo et al., 2011). Note that nutrients here refer to the complete set of internal elements (proteins, enzymes, growth factors, etc.) necessary for growth to take place. The additional variable can be easily introduced as a static field with a spatial inhomogeneous distribution or with a given predefined evolution. However, coupling this variable to a diffusion model allows enriching the growth model by incorporating the driving forces for the distribution of biochemical

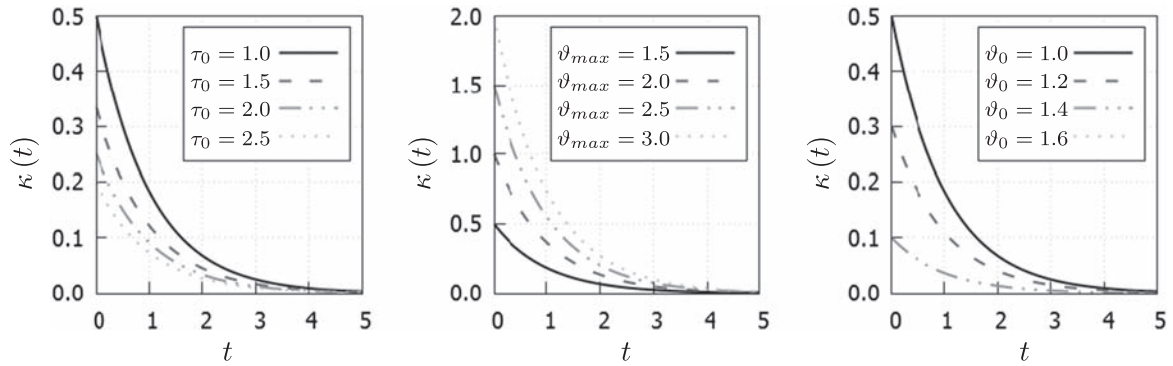

FIGURE 2.7 The temporal growth function $\kappa(t)$ (Eq. 2.9) is plotted against time t for a varying values of τ_0 (left), ϑ_{max} (center), and ϑ_0 (right). The fixed values considered are $\tau_0 = 1.0$, $\vartheta_{\max}$=1.5, and $\vartheta_0 = 1.0$. Using this type of limiting function requires the explicit integration of time.

This book belongs to Central Library BADJI Mokhtar-ANNABA UNIVERSITY
Copyright Elsevier 2024

growth drivers in the tissue, e.g., to study the influence of nutrient diffusion and chemical signaling in a growing tumor (Ambrosi and Mollica, 2002; Ciarletta et al., 2012; Ramírez-Torres et al., 2015).

In specific applications, researchers have proposed expressions for the evolution of growth that do not exactly fit the representative function described in Eq. (2.6). These distinct functions are usually motivated by specific mechanobiological observations or particular growth phenomena in a tissue. For example, neuron growth evolution has been defined in terms of the polymerization and depolymerization rates of, on the one hand, the microtubules in the axoplasm, and on the other hand, the F-actin in the cortical membrane (García-Grajales et al., 2016). A different example is the use of finite plasticity theory to model fluidlike growth in which barely no residual stresses exist, even when the growing tissue is constrained by boundary conditions. Prominent representatives of this case are tumors where the characteristic macromechanical growth behavior can be explained based on cellular arguments (Böl and Bolea Albero, 2014).

We have focused on the continuum modeling of growth through the decomposition of the deformation gradient tensor, often referred to as kinematic growth models; however, there exist alternative approaches. The most popular uses constrained mixture theory (Lubarda and Hoger, 2002; Ateshian, 2007; Ateshian and Humphrey, 2012; Cyron and Humphrey, 2016; Lee et al., 2016) to explicitly model the separate contribution of the different constituents in the tissue. The tissue is no longer seen as a homogenized solid continuum; instead, it is represented by a sum of structurally significant constituents. Mass increments from the different constituents deposited at different times form a constrained mixture such that they undergo the same elastic deformation over time in each volume element. It is assumed that most constituents undergo a continuous turnover (i.e., production and/or degradation rates are defined for each constituent) and that a preferred homeostatic biomechanical state in the tissue is sought. Then, growth is due to a positive net production rate in the turnover of constituents.

The constrained mixture approach will involve potentially large numbers of equations and, hence, both its computational cost and implementation effort are much higher than for kinematic growth models. Yet, it can easily account for certain mechanobiological processes that kinematic growth models cannot incorporate in a direct manner, such as the interaction between the solid and fluid phases of the tissue. For example, many growth processes are known to involve a variation in proteoglycan content resulting in changes in the osmotic pressure of the interstitial fluid on the solid matrix, which plays an important role in the evolution of the tissue response. Hybrid approaches (Eriksson et al., 2014; Cyron et al., 2016) have been proposed in an attempt to exploit the computational simplicity of kinematic theories while retaining the biologically motivated micromechanical foundation of constrained mixture theories.

Alternatively, continuum growth models have been developed that do not fall within these two classic approaches, usually tailored to a particular application. For example, the modeling of pathological collagen turnover in aortic tissue has been used to study the growth of an abdominal aortic aneurysm (Martufi and Gasser, 2012) and a multiscale treatment has been introduced to model mechanotransduction in cancer growth (Ciarletta et al., 2013).

2.5 EXAMPLES OF MECHANOBIOLOGICAL GROWTH SIMULATIONS

In this section we present four examples of mechanobiological growth simulations and their implementation:

1. muscle growth due to fiber hypertrophy, adapted from (Bellomo et al., 2014);
2. joint morphogenesis (Giorgi et al., 2014);
3. development of bone deformities in the proximal femur in cerebral palsy (Carriero et al., 2011);
4. adaptation of murine cortical bone to applied loading (Pereira et al., 2015).

Except the first example, which is described here more exhaustively, these models have been presented elsewhere in full detail. Here we focus on the implementation of growth into a FE algorithm. The examples were chosen to demonstrate a range of geometry, material properties, loading conditions, mechanical stimulus, and growth parameters (see Table 2.1).

The flowchart in Fig. 2.8 illustrates how the mechanobiological growth algorithm fits within the FE analysis framework. Here, the standard FE method used will depend on the problem under study and is closely related to the constitutive models selected to reproduce the mechanical behavior of the tissues involved. Hard tissues such as bone often behave in a linear elastic manner and can be studied using the classic displacement-based formulation. Soft tissues, on the other hand, have high water content and are known to behave in a highly nonlinear and quasiincompressible manner. Then, the hyperelastic models used cannot uniquely determine stress from strains and require mixed displacement-pressure or poroelastic formulations. These overcome numerical problems associated with incompressibility such as an ill-conditioned stiffness matrix, volumetric locking, and inaccuracies of the solution. The scheme presented can be easily implemented in both total Lagrangian and updated Lagrangian frameworks. For the former, the constitutive models and FE equations should be defined in the reference configuration, whereas the latter would require that all variables are referred to the

This book belongs to Central Library BADJI Mokhtar-ANNABA UNIVERSITY Copyright Elsevier 2024

TABLE 2.1 Summary of the Mechanobiological Growth Examples Presented in This Chapter

	Geometry and loading	Growth modulator $\kappa(\vartheta)$	Growth stimulus Ξ	Growth function $\phi(\Xi)$	Growth direction
	- Generic geometry - Generic loading conditions - Non-linear elastic material properties, quasi-incompressibility	ϑ, growth multiplier, and θ, biological availability	$\mathrm{Tr}(\boldsymbol{\sigma})$, trace of the Cauchy stress tensor (in compression)	$\phi = k\left(\mathrm{Tr}(\boldsymbol{\sigma}) - \sigma^*_{eq}\right)$ above σ^*_{eq} threshold, with an upper limit $\hat{\vartheta}_{max}$	isotropic in transversal area
	- Generic geometry - Generic loading conditions - Linear elastic material properties	C_d, chondrocyte density	$\sigma_{h,ave}$, dynamic hydrostatic stress	$\phi = C_d\left(k - \sigma_{h,ave}\right)$	volumetrically isotropic
	- Generic geometry - Specific loading conditions from gait analysis - Linear elastic material properties, which are updated	–	$\sigma_{h,max}$, maximum hydrostatic stress, and $\sigma_{s,max}$, maximum octahedral shear stress	$\phi = k + \sigma_{h,max} + a\sigma_{s,max}$	longitudinal in direction of deformation
	- Specific geometry - Specific loading conditions - Poroelastic material properties	–	V_{max}, peak fluid velocity	V_{max} threshold, integrated in time and averaged over space: $\bar{\phi}(n) = \frac{1}{2}\left(\phi(n) + \frac{\int_\Omega w(r)\phi(r)d\Omega}{\int_\Omega w(r)d\Omega}\right)$	in direction of surface normal

current configuration. In any case, the evolution of the growth multiplier and constitutive equations must be consistent with the chosen framework.

2.5.1 Hypertrophic Muscle Growth

Athletes involved in strength and powersports build their muscular strength through exercise-induced muscle growth, which involves the enlargement of the cross-sectional area of their muscles. In a process termed muscle hypertrophy, the fibers in musculoskeletal tissue are known to increase their transversal section without appreciable changes in length. The enlargement of the contractile elements in the muscle is accompanied by the expansion of the extracellular matrix to support growth. Many factors mediate this hypertrophic process (Schoenfeld, 2010), but muscular growth is mainly associated with damage repair and inflammation in the muscle, with the damage directly depending on the stress state induced in the tissue through exercise. In addition, the metabolic effect derived from the inflammation in the muscular fibers is also associated with growth. Given the complexity of this phenomenon, a simplified approach has been considered. We modeled the effect of the compressive stress state in the muscular tissue (Bellomo et al., 2014; Comellas, 2016) on hypertrophic growth.

Geometry: A generic geometry of a human biceps was obtained from BodyParts3D (Mitsuhashi et al., 2009) and meshed using 5481 quadratic tetrahedral elements. The biceps is about 20 cm in length and has a central mean diameter of approximately 3 cm.

Material properties: In the sake of simplicity, the whole model was assumed to be of a single homogeneous and isotropic material. However, this is clearly an oversimplification because muscular tissue is composed of highly directional fibers and the extremes of biceps, where the muscle is inserted to the bone, are mostly composed of ligament tissue. Owing to the high water content present in soft biological tissue, a quasiincompressible neo-Hookean model was considered ($E = 60$ kPa, $\nu = 0.5$ (Gennisson et al., 2010; Chung et al., 2016)), which requires the use of mixed displacement-pressure formulation.

Loading conditions: We used generic loading conditions to represent the tensile loading in the longitudinal direction of the biceps. We imposed an instantaneous uniform longitudinal extension of the whole muscle, which results in a transversal contraction of the muscular tissue inducing, thus, compressive stresses in the transversal plane of the biceps. This is the initial state from which growth takes place; we fixed the muscle in the loaded position and allowed for growth to occur over 34 time steps.

This book belongs to Central Library BADJI Mokhtar-ANNABA UNIVERSITY
Copyright Elsevier 2024

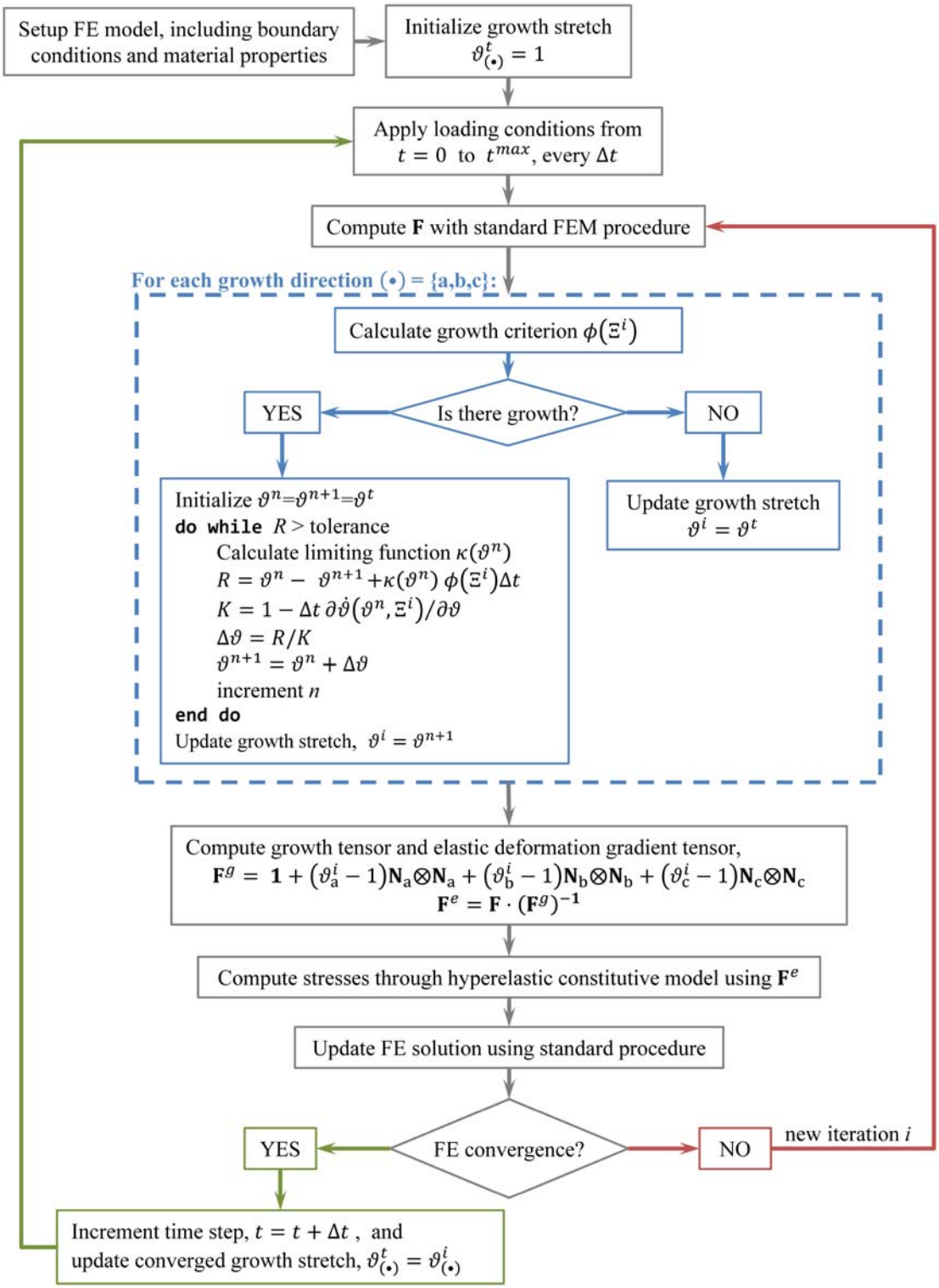

FIGURE 2.8 Algorithm describing a possible numerical implementation of the general growth algorithm in a standard finite element (FE) code.

This book belongs to Central Library BADJI Mokhtar-ANNABA UNIVERSITY Copyright Elsevier 2024

Mechanical stimuli: We define the growth criterion in the plane transversal to the muscle fibers as

$$\phi(\mathrm{Tr}(\boldsymbol{\sigma})) = \begin{cases} \dot{\vartheta}_{max} & \text{if } \mathrm{Tr}(\boldsymbol{\sigma}) > \sigma^*_{eq} \text{ and } k\left(\mathrm{Tr}(\boldsymbol{\sigma}) - \sigma^*_{eq}\right) \geq \dot{\vartheta}_{max}, \\ k\left(\mathrm{Tr}(\boldsymbol{\sigma}) - \sigma^*_{eq}\right) & \text{if } \mathrm{Tr}(\boldsymbol{\sigma}) > \sigma^*_{eq} \text{ and } k\left(\mathrm{Tr}(\boldsymbol{\sigma}) - \sigma^*_{eq}\right) < \dot{\vartheta}_{max}, \\ 0 & \text{if } \sigma^*_{eq} > \mathrm{Tr}(\boldsymbol{\sigma}). \end{cases} \tag{2.10}$$

Here, σ^*_{eq} is the compressive value beyond which growth begins. For smaller values, the homeostatic equilibrium is maintained, i.e., new cells are solely generated to replace those that die (see Fig. 2.9). The constant k determines the speed of the growth rate and $\dot{\vartheta}_{max}$ is the mechanical growth limit defined in terms of the maximum rate of mass production T_{max} through $\dot{\vartheta}_{max} = T_{max}/(2\vartheta^2)$.

Mechanobiological algorithm: To simulate hypertrophic muscle growth, isotropic area growth in the transversal plane of the biceps was considered such that $\vartheta_a = \vartheta_b = \vartheta$ in the transversal plane and $\vartheta_c = 1$ in the longitudinal direction of the biceps. Then, the growth tensor is as in Eq. (2.4). Growth was limited in a small patch of tissue, with the aim of roughly reproducing the effects of ischemia, namely, how the restriction in blood supply (and, therefore, a shortage of oxygen and glucose needed for cellular metabolism) results in impaired growth and, ultimately, may lead to necrosis. The limiting variable considered, in addition to the growth multiplier ϑ, was the biological availability θ, such that the limiting function is

$$\kappa(\vartheta, \theta) = \begin{cases} 1 & \text{if } \phi \leq \dot{\theta}/(2\vartheta^2), \\ \dfrac{\dot{\theta}/(2\vartheta^2)}{\phi} & \text{if } \phi > \dot{\theta}/(2\vartheta^2). \end{cases} \tag{2.11}$$

The variable θ represents the mass production the metabolism can sustain with the available nutrients (oxygen, glucose, etc.) at a given time and is defined as $\theta = N_i - J^g$, where $J^g = \det(\mathbf{F}^g)$ and N_i are the nutrients stored in the tissue described in terms of allowed mass increment. For example, a value of $N_i = 1.1$ indicates that the nutrients available in the system can generate an increase of mass in the tissue of 10% with respect to its original mass. The nutrient function has been defined as an initial reserve R_i and a value increasing over time with slope A_i. In this example, $R_i = 0.3$ and $A_i = 0.01$ for a randomly selected patch of elements, such that there is not enough biological availability to sustain growth, even if the mechanical stimulus exists. The rest of elements in the model are given full biological availability.

Implementation: We implemented the algorithm described in Fig. 2.8 in the in-house FE code PLCd (PLCd research group, n.d.), which uses a mixed displacement-pressure formulation in a total Lagrangian finite strain framework. The results obtained are shown in Figs. 2.10 and 2.11.

2.5.2 Joint Morphogenesis

The formation of a skeletal joint is a highly regulated process, which is controlled by a host of biochemical factors (morphogeneic proteins, growth factors, Hox genes). In addition, mechanical factors impose stresses and strains on the developing tissue as muscles start to contract, articulating the joint. Studies have shown that immobilization of the joint results in altered joint morphology, demonstrating the importance of mechanical loads in the morphogenic process. We modeled the influence of mechanical loads on joint morphogenesis using mechanobiological simulations (Giorgi et al., 2014).

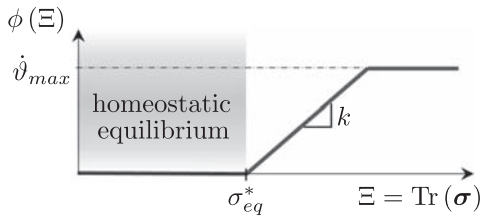

Parameter	Value
σ^*_{eq}	1 kPa
k	$2 \cdot 10^{-6}$
T_{max}	0.1

FIGURE 2.9 Growth criterion $\phi(\Xi) = (\mathrm{Tr}(\boldsymbol{\sigma}))$ used to compute the growth multiplier in the hypertrophic muscle growth example (left). The mechanical growth stimulus is the trace of the Cauchy stress tensor, considered positive in compression. Material properties considered for the growth model (right), where the maximum rate of mass production T_{max} is used to compute $\dot{\vartheta}_{max} = T_{max}/(2\vartheta^2)$.

This book belongs to Central Library BADJI Mokhtar-ANNABA UNIVERSITY
Copyright Elsevier 2024

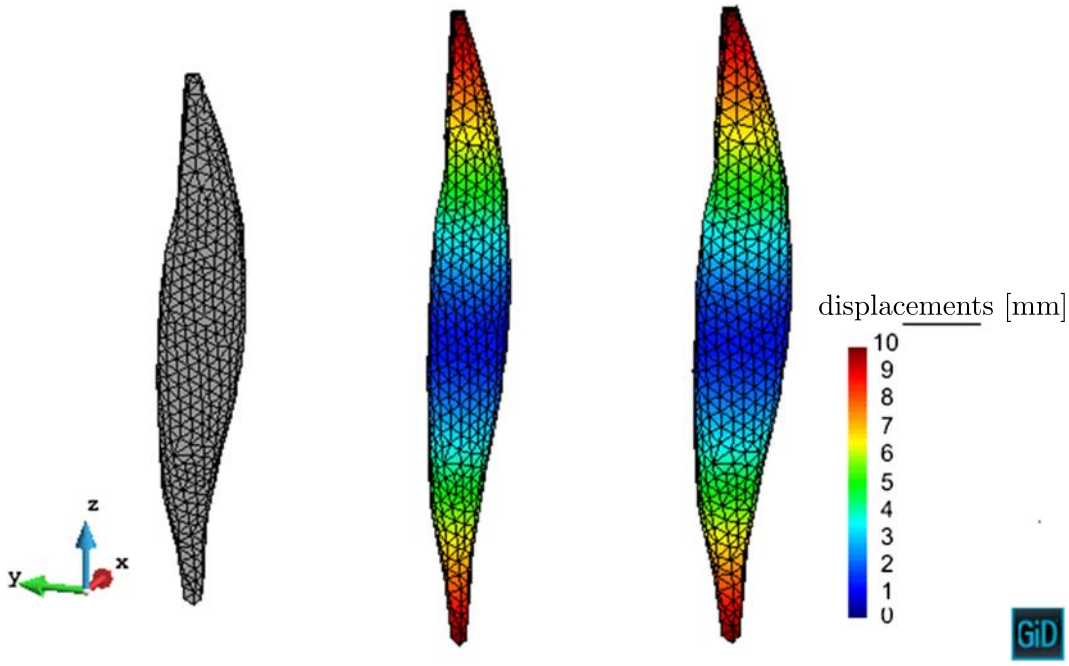

FIGURE 2.10 Original meshed biceps model (left). Displacements immediately after uniform longitudinal extension (center). This is the initial state for growth: imposed displacements induce stresses that will be the stimulus for growth, but $\vartheta = 1$ at this state and no growth has taken place yet. Displacements after growth without restrictions (right). We observe in the final state that the biceps has grown only in the transversal direction (the growth multiplier is $\vartheta = 1.07$, see Fig. 2.11). Vertical displacements have not changed, indicating no growth in the vertical directions.

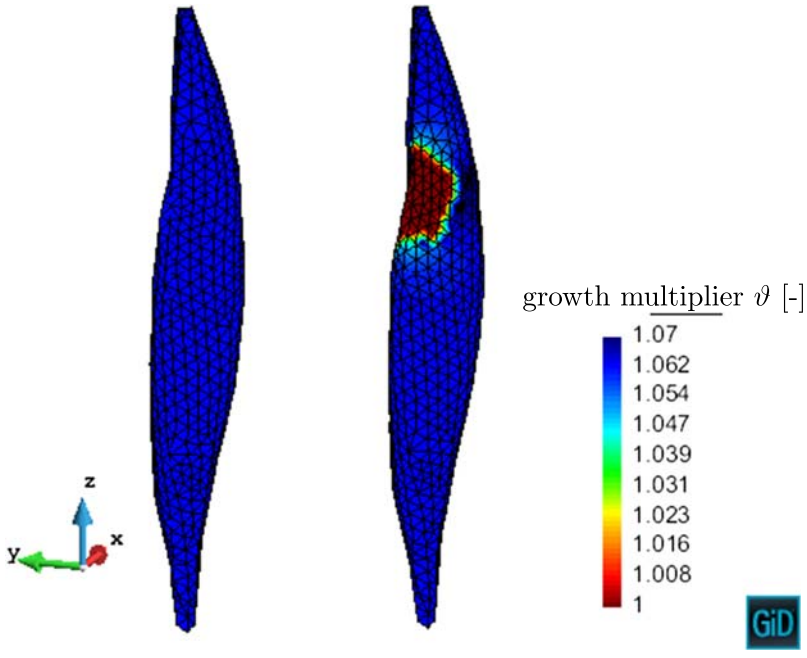

FIGURE 2.11 Growth multiplier ϑ in the transversal plane for the unrestricted growth case (left) and for the case in which a patch of tissue was assigned restricted biological availability (right). We observe that the affected patch of tissue has not grown at all (zone shown in red (gray in print versions)).

Geometry: We used a generic geometry to represent a diarthrodial synovial joint. The joint was surrounded by a synovial capsule, which reduced the contact stresses at the surface of the joint.

Material properties: Cartilage was modeled as homogeneous and linear elastic ($E = 1.1$ MPa, $\nu = 0.49$), a large assumption given the high water content of cartilage. However, under dynamic loading conditions, it was assumed that

This book belongs to Central Library BADJI Mokhtar-ANNABA UNIVERSITY Copyright Elsevier 2024

linear elastic and short timescale poroelastic results were similar (Carter and Beaupre, 1999). The joint was surrounded by a synovial capsule (E = 0.287 kPa, $\nu = 0.4$).

Loading conditions: Because loading conditions of a joint in utero are difficult to quantify, we used generic loading conditions. We represented flexion of a diarthrodial joint as asymmetric loading in four separate steps at 0, 45, 90, and 120 degrees. In each step a 10 μm displacement was given at the proximal end while the distal end remained fixed.

Mechanical stimuli: We assumed that static hydrostatic stress inhibited growth and cyclic hydrostatic stress promoted growth. The mechanobiological contribution to growth, ϕ_m is given by:

$$\phi = \begin{cases} \sigma_{h,ave}, & \text{when loading is static} \\ -\sigma_{h,ave}, & \text{when loading is dynamic} \end{cases} \tag{2.12}$$

When hydrostatic stress σ_h is dynamic and compressive (i.e., negative in sign), the mechanobiological contribution to growth is positive. Because loads were all applied as quasistatic, we defined which loads were static and which were dynamic directly in the algorithm implementation.

Mechanobiological algorithm: Growth was isotropic and limited by the chondrocyte density (C_d).

$$\kappa(\vartheta) = C_d = a - b\zeta + c\zeta^2 - c\zeta^3, \tag{2.13}$$

where chondrocyte density C_d is given by a function of the distance ζ along the proximal/distal axis, $f(\zeta)$, determined from experimental values of cell densities (Germiller and Goldstein, 1997). The growth stimulus was the sum of a constant biological factor $\phi_b = k$ and a mechanobiological factor ϕ_m,

$$\phi = C_d(k - \sigma_{h,ave}). \tag{2.14}$$

The constant k was chosen such that the biological contribution of growth was 75%−80% of the total growth. The mechanobiological factor was the hydrostatic stress in each element averaged across all loading instances.

Implementation: Loads were applied, stresses determined, growth calculated, and the model was grown using thermal expansion capabilities of the solver (temperature was proportional to growth). The model was then remeshed (in the grown position) and the position of the joints reestablished before being loaded again. Therefore, the mesh had no residual growth-related stresses. ABAQUS (Dassault Systems, Rhode Island) was used for solving FE models, Matlab (Mathworks, Natick, MA) calculated growth for each element, and Python was used to communicate between Matlab and ABAQUS.

2.5.3 Bone Deformities in the Proximal Femur in Cerebral Palsy

Cerebral palsy is caused by brain trauma at birth and results in skeletal muscle dysfunction. Although the primary cause is neurological, multiple bone deformities occur because of the altered mechanical loads imposed on the bones in affected gait. We modeled the effect of altered loads on proximal femoral bone growth (Carriero et al., 2011).

Geometry: The geometry of the proximal femur was obtained directly from the musculoskeletal model used to determine the loading. This was a scaled model of an adult and, therefore, did not have the morphology (neck-shaft angle and anteversion angle) of a child. Subsequent studies used the exact geometry of a child from MR images and demonstrated the limitation of the adult-generic geometry. The mesh in this model was hexahedral (instead of tetrahedral) to preserve an ordered orthonormal coordinate system in the elements.

Material properties: All material properties were modeled as linear elastic and isotropic. A cartilage growth plate was inserted in the approximate position of a growth plate of a 10-year-old child. The model consisted of cortical bone (E = 20 GPa), trabecular bone (head and neck of femur, E = 600 MPa), a marrow cavity (E = 1 MPa), and growth plate cartilage (E = 5 MPa, $\nu = 0.49$). Proximal and distal to the growth plate cartilage, a transition zone with linearly increasing modulus represented newly mineralized bone.

Loading conditions: Specific loading conditions were obtained from gait analysis of three children with cerebral palsy and one unaffected child. Musculoskeletal models (Simm, MusculoGraphics, Inc.) were used to determine the joint loads and muscle contractions for each specific gait. The entire gait cycle was represented by the joint loads and muscle contractions of four specific load cases, determined by: the maximum muscle activity in normal gait (10 of a normalized gait cycle), the first and second peak of the ground reaction force (30% and 45%), and the start of the swing phase of gait (70%). Each load case was applied as a quasistatic load. Subsequent work used nine load cases to represent a gait cycle (Yadav et al., 2016).

This book belongs to Central Library BADJI Mokhtar-ANNABA UNIVERSITY
Copyright Elsevier 2024

Mechanical stimulus: The stimulus for bone growth and ossification was based on the osteogenic index (Wong and Carter, 1990). Peak cyclic octahedral shear stress promoted growth and ossification; peak cyclic hydrostatic compressive stress inhibited growth and ossification.

$$\phi_m = \sigma_{h,max} + a\sigma_{s,max}, \tag{2.15}$$

where $\sigma_{h,max}$ is the maximum hydrostatic stress, $\sigma_{s,max}$ is the maximum octahedral shear stress over a loading cycle, and a is a proportionality constant weighting the relative contributions of the stresses (previous studies have used $a = 0.5$ (Carter and Wong, 1988b)). A compressive hydrostatic stress (i.e., negative) decreases the mechanobiological contribution to growth and thereby decreases the rate of ossification and maintains cartilage.

Mechanobiological algorithm: Growth of cartilage in the growth plate was orthonormal and occurred only in the longitudinal direction. The amount of growth was the sum of a constant biological growth, k, and the mechanobiological growth, ϕ_m.

$$\phi = k + \sigma_{h,max} + a\sigma_{s,max}, \tag{2.16}$$

where k was chosen such that the mechanobiological contribution to growth was approximately 25% of the total growth. The direction of growth was determined by the average deformation direction over one load cycle. This deformation direction was implemented into elemental coordinate systems for each element in the growth region (one layer of elements in the growth plate), and growth was limited to the longitudinal direction for each element deformation assigned coordinate system.

Implementation: Stresses and deformations of the growth plate were determined in ABAQUS; amount and direction of growth were determined in Matlab; growth was implemented using orthonormal thermal expansion of the elements in ABAQUS with growth defining the temperature. Because the model simulated growth and ossification, material properties of the grown elements were updated to represent newly mineralized bone. The grown model became the new mesh for the next iteration, so no residual growth stresses occurred. The model was not remeshed, so growth was limited to the number of elements in the growth plate.

2.5.4 Adaptation of Murine Cortical Bone

Animal models of bone adaptation to mechanical loading provide controlled environments for establishing necessary conditions for adaptation. The murine tibial loading model applies axial compression across the tibia with the flexed ankle and the knee held in loading cups. We use mechanobiological models of periosteal bone growth to predict regions of bone formation in this model (Pereira et al., 2015).

Geometry: The mouse tibial geometry was obtained directly from a micro-CT scan of the tibia and meshed with a tetrahedral mesh.

Material properties: Material properties were linear elastic at the proximal and distal ends and poroelastic in the shaft where adaptation was simulated (Pereira et al., 2015). We used poroelastic properties because fluid flow was considered a stimulus for periosteal bone adaptation. The fibular growth plate, which affected tibial stresses, was modeled as poroelastic cartilage. We used membranes (a layer of elements on the surface) with no stiffness and a relatively high permeability to allow limited fluid flow out of the periosteal surface. These membranes provided boundary conditions between free-flow and no-flow boundary conditions.

Loading conditions: The loading conditions were obtained directly from the experimental model, with placement of the loads determined from imaging the joint (Poulet et al., 2011) as it was loaded. Load was applied as a dynamic load with the same load rate, magnitude, and hold as experiments.

Mechanical stimulus: We used peak fluid velocity (V_{max}) as the stimulus for adaptation. We used a threshold algorithm such that when the V_{max} was greater than a threshold V_A, bone apposition occurred. Λ was the dimensionless quantity representing bone formation in every n node at every t time:

$$\Lambda(n,t) = \begin{cases} 1, & \text{when } V_{max} > V_A \\ 0 & \text{otherwise} \end{cases} \tag{2.17}$$

The growth rate was calculated as the integral of Λ over time in which the peak fluid velocity was over the threshold (i.e., the stimulus was high if the velocity was over the threshold for a long time),

$$\phi(n) = C\int_t \Lambda(n,t)dt, \tag{2.18}$$

This book belongs to Central Library BADJI Mokhtar-ANNABA UNIVERSITY
Copyright Elsevier 2024

where C is a proportionality constant. The stimulus for each node influenced the nodes around it with a linear decay. The weighting of the stimulus of surrounding nodes was given by

$$w(R) = \frac{R - r}{R}, \tag{2.19}$$

where R was 150 μm, given by physical limits of nutrient perfusion and osteocyte action reach in bone. The average stimulus at each node was given by

$$\overline{\phi}(n) = \frac{1}{2}\left(\phi(n) + \frac{\int_\Omega w(r)\phi(r)d\Omega}{\int_\Omega w(r)d\Omega}\right), \tag{2.20}$$

with Ω as a spherical region of integration, centered in n. The spatial variations of peak fluid velocity within the bone during a loading cycle resulted in variable amounts of growth on the surface of the tibia within one iteration.

Mechanobiological algorithm: The amount of growth was determined by the mechanobiological stimulus averaged over time and space, $\overline{\phi}(n)$. The growth direction was defined as the surface normal at each node. Growth was obtained by displacing nodes along the surface normal by an amount determined by the stimulus. The volume was remeshed at the start of each iteration to preserve mesh quality.

Implementation: Fluid flow was determined in ABAQUS; the mechanobiological stimulus was determined from the FE output in Matlab; and Python was used to communicate between ABAQUS and Matlab and iteratively run the simulation.

2.6 CONCLUSIONS

Adaptation processes in living tissues are extremely complex, and the fundamental aspects of the underlying mechanisms involved are not completely understood yet. These are leading topics of research in the biomechanics and biomedical engineering communities, who strive to identify the factors that drive and regulate adaptation processes such as growth. Mechanical stimuli have been known to play a key role in many growth processes, and their effect is called *mechanobiological growth*. Computational biomechanics, and FE analyses in particular, provide a useful tool to study the factors influencing mechanobiological growth.

In this chapter we have discussed the common features of mechanobiological growth models in a computational FE framework. We have reviewed different assumptions typically made in modeling the initial state of the tissue under study and the mechanical stimuli usually considered to drive the mechanobiological growth in these models. Then, we have described a generic mechanobiological algorithm based on the multiplicative decomposition of the deformation gradient. Here, we have discussed how the tissue grows (isotropic vs. anisotropic growth) and where and why it grows (driving and limiting factors in the evolution of growth). Finally, we have presented four examples of mechanobiological growth simulations and their implementation in FE codes.

REFERENCES

Ambrosi, D., Mollica, F., 2002. On the mechanics of a growing tumor. International Journal of Engineering Science 40 (12), 1297−1316.

Ambrosi, D., Beloussov, L.V., Ciarletta, P., 2017. Mechanobiology and morphogenesis in living matter: a survey. Meccanica 1−17.

Ateshian, G.A., 2007. On the theory of reactive mixtures for modeling biological growth. Biomechanics and Modeling in Mechanobiology 6 (6), 423−445.

Ateshian, G.A., Humphrey, J.D., 2012. Continuum mixture models of biological growth and remodeling: past successes and future opportunities. Annual Review of Biomedical Engineering 14, 97−111.

Bellomo, F.J., Oller, S., Armero, F., Nallim, L.G., 2011. A general constitutive model for vascular tissue considering stress driven growth and biological availability. Computer Modeling in Engineering and Sciences 80 (1), 1−21.

Bellomo, F.J., Armero, F., Nallim, L.G., Oller, S., 2012. A constitutive model for tissue adaptation: necrosis and stress driven growth. Mechanics Research Communications 42 (0), 51−59.

Bellomo, F.J., Comellas, E., Nallim, L.G., Oller, S., 2014. Numerical simulation of the directioned growth and remodelling of soft biological tissues generated by mechanical stimuli (in Spanish). In: Bertolino, G., Cantero, M., Storti, M., Teruel, F. (Eds.), Mecánica Computacional Vol. XXXIII. Number 41. Computational Modeling in Bioengineering Applications (A). Asociación Argentina de Mecánica Computacional, pp. 2667−2676.

Böl, M., Bolea Albero, A., 2014. On a new model for inhomogeneous volume growth of elastic bodies. Journal of the Mechanical Behavior of Biomedical Materials 29, 582−593.

Budday, S., Raybaud, C., Kuhl, E., 2014a. A mechanical model predicts morphological abnormalities in the developing human brain. Scientific Reports 4 (September), 5644.

This book belongs to Central Library BADJI Mokhtar-ANNABA UNIVERSITY Copyright Elsevier 2024

Budday, S., Steinmann, P., Kuhl, E., 2014b. The role of mechanics during brain development. Journal of the Mechanics and Physics of Solids 72 (October), 75−92.

Buganza Tepole, A., Ploch, C.J., Wong, J., Gosain, A.K., Kuhl, E., 2011. Growing skin: a computational model for skin expansion in reconstructive surgery. Journal of the Mechanics and Physics of Solids 59 (10), 2177−2190.

Buganza Tepole, A., Gart, M., Purnell, C.A., Gosain, A.K., Kuhl, E., 2016. The incompatibility of living systems: characterizing growth-induced incompatibilities in expanded skin. Annals of Biomedical Engineering 44 (5), 1734−1752.

Carriero, A., Jonkers, I., Shefelbine, S.J., 2011. Mechanobiological prediction of proximal femoral deformities in children with cerebral palsy. Computer Methods in Biomechanics and Biomedical Engineering 14 (3), 253−262.

Carter, D.R., Beaupre, G.S., 1999. Linear elastic and poroelastic models of cartilage can produce comparable stress results: a comment on Tanck et al. (J Biomech 32:153-161, 1999). Journal of Biomechanics 32 (11), 1255−1257.

Carter, D.R., Wong, M., 1988a. Mechanical stresses and endochondral ossification in the chondroepiphysis. Journal of Orthopaedic Research 6 (1), 148−154.

Carter, D.R., Wong, M., 1988b. The role of mechanical loading histories in the development of diarthrodial joints. Journal of Orthopaedic Research 6 (6), 804−816.

Castro-Abril, H.A., Gutiérrez, M.L., Garzón-Alvarado, D.A., 2016. Proximal femoral growth plate mechanical behavior: comparison between different developmental stages. Computers in Biology and Medicine 76, 192−201.

Chagnon, G., Rebouah, M., Favier, D., 2015. Hyperelastic energy densities for soft biological tissues: a review. Journal of Elasticity 120 (2), 129−160.

Chung, W.-H., Min, D.-K., Hwang, H.-J., Lim, J.-K., Park, J.-H., Kim, H.-S., 2016. In vivo stiffness measurement and in silico stiffness prediction of biceps brachii muscle using an isometric contraction exercise. Journal of Mechanical Science and Technology 30 (6), 2881−2889.

Ciarletta, P., Ambrosi, D., Maugin, G., 2012. Mass transport in morphogenetic processes: a second gradient theory for volumetric growth and material remodeling. Journal of the Mechanics and Physics of Solids 60 (3), 432−450.

Ciarletta, P., Ambrosi, D., Maugin, G.A., Preziosi, L., 2013. Mechano-transduction in tumour growth modelling. The European Physical Journal E 36 (3), 23.

Comellas, E., 2016. Advisors: S. Oller and F.J.Bellomo Ph. D. dissertation: Numerical Modelling of the Growth and Remodelling Phenomena in Biological Tissues (Ph.D. thesis). Universitat Politècnica de Catalunya.

Cowin, S.C., Weinbaum, S., Zeng, Y., 1995. A case for bone canaliculi as the anatomical site of strain generated potentials. Journal of Biomechanics 28 (11), 1281−1297.

Cyron, C.J., Humphrey, J.D., 2016. Growth and remodeling of load-bearing biological soft tissues. Meccanica 52 (3), 1−20.

Cyron, C.J., Aydin, R.C., Humphrey, J.D., 2016. A homogenized constrained mixture (and mechanical analog) model for growth and remodeling of soft tissue. Biomechanics and Modeling in Mechanobiology 15 (6), 1−15.

Dong, S., Yan, Y., Tang, L., Meng, J., Jiang, Y., 2016. Simulation of 3D tumor cell growth using nonlinear finite element method. Computer Methods in Biomechanics and Biomedical Engineering 19 (8), 807−818.

Edgar, L.T., Maas, S.A., Guilkey, J.E., Weiss, J.A., 2015. A coupled model of neovessel growth and matrix mechanics describes and predicts angiogenesis in vitro. Biomechanics and Modeling in Mechanobiology 14 (4), 767−782.

Eriksson, T.S.E., Watton, P.N., Luo, X.Y., Ventikos, Y., 2014. Modelling volumetric growth in a thick walled fibre reinforced artery. Journal of the Mechanics and Physics of Solids 73, 134−150.

Fong, K.D., Warren, S.M., Loboa, E.G., Henderson, J.H., Fang, T.D., Cowan, C.M., Carter, D.R., Longaker, M.T., 2003. Mechanical strain affects dura mater biological processes: implications for immature calvarial healing. Plastic and Reconstructive Surgery 112 (5), 1312−1327.

Garcia, K.E., Okamoto, R.J., Bayly, P.V., Taber, L.A., 2017. Contraction and stress-dependent growth shape the forebrain of the early chicken embryo. Journal of the Mechanical Behavior of Biomedical Materials 65, 383−397.

García-Grajales, J.A., Jérusalem, A., Goriely, A., 2016. Continuum mechanical modeling of axonal growth. Computer Methods in Applied Mechanics and Engineering 314, 147−163.

Gennisson, J.L., Deffieux, T., Macé, E., Montaldo, G., Fink, M., Tanter, M., 2010. Viscoelastic and anisotropic mechanical properties of in vivo muscle tissue assessed by supersonic shear imaging. Ultrasound in Medicine and Biology 36 (5), 789−801.

Germiller, J.A., Goldstein, S.A., 1997. Structure and function of embryonic growth plate in the absence of functioning skeletal muscle. Journal of Orthopaedic Research 15 (3), 362−370.

Giorgi, M., Carriero, A., Shefelbine, S.J., Nowlan, N.C., 2014. Mechanobiological simulations of prenatal joint morphogenesis. Journal of Biomechanics 47 (5), 989−995.

Giorgi, M., Carriero, A., Shefelbine, S.J., Nowlan, N.C., 2015. Effects of normal and abnormal loading conditions on morphogenesis of the prenatal hip joint: application to hip dysplasia. Journal of Biomechanics 48 (12), 3390−3397.

Göktepe, S., Abilez, O.J., Kuhl, E., 2010. A generic approach towards finite growth with examples of athlete's heart, cardiac dilation, and cardiac wall thickening. Journal of the Mechanics and Physics of Solids 58 (10), 1661−1680.

Guevara, J.M., Moncayo, M.A., Vaca-González, J.J., Gutiérrez, M.L., Barrera, L.A., Garzón-Alvarado, D.A., 2015. Growth plate stress distribution implications during bone development: a simple framework computational approach. Computer Methods and Programs in Biomedicine 118 (1), 59−68.

Henderson, J.H., Carter, D.R., 2002. Mechanical induction in limb morphogenesis: the role of growth-generated strains and pressures. Bone 31 (6), 645−653.

This book belongs to Central Library BADJI Mokhtar-ANNABA UNIVERSITY Copyright Elsevier 2024

Henderson, J.H., Longaker, M.T., Carter, D.R., 2004. Sutural bone deposition rate and strain magnitude during cranial development. Bone 34 (2), 271–280.

Henderson, J.H., Nacamuli, R.P., Zhao, B., Longaker, M.T., Carter, D.R., 2005. Age-dependent residual tensile strains are present in the dura mater of rats. Journal of the Royal Society Interface 2 (3), 159–167.

Henderson, J.H., De La Fuente, L., Romero, D., Colnot, C.I., Huang, S., Carter, D.R., Helms, J.A., 2007. Rapid growth of cartilage rudiments may generate perichondrial structures by mechanical induction. Biomechanics and Modeling in Mechanobiology 6 (1–2), 127–137.

Himpel, G., Kuhl, E., Menzel, A., Steinmann, P., 2005. Computational modelling of isotropic multiplicative growth. Computer Modeling in Engineering and Sciences 8 (2), 119–134.

Holland, M.A., Kosmata, T., Goriely, A., Kuhl, E., 2013. On the mechanics of thin films and growing surfaces. Mathematics and Mechanics of Solids 18 (6), 561–575.

Holland, M.A., Miller, K.E., Kuhl, E., 2015. Emerging brain morphologies from axonal elongation. Annals of Biomedical Engineering 43 (7), 1640–1653.

Jones, G.W., Chapman, S.J., 2012. Modeling growth in biological materials. SIAM Review 54 (1), 52–118.

Kerckhoffs, R.C.P., 2012. Computational modeling of cardiac growth in the post-natal rat with a strain-based growth law. Journal of Biomechanics 45 (5), 865–871.

Kerckhoffs, R.C.P., Omens, J.H., McCulloch, A.D., 2012. A single strain-based growth law predicts concentric and eccentric cardiac growth during pressure and volume overload. Mechanics Research Communications 42, 40–50.

Klein-Nulend, J., van der Plas, A., Semeins, C.M., Ajubi, N., Frangos, J.A., Nijweide, P.J., Burger, E.H., 1995. Sensitivity of osteocytes to biomechanical stress in vitro. The FASEB Journal: Official Publication of the Federation of American Societies for Experimental Biology 9 (5), 441–445.

Krupinski, P., Bozorg, B., Larsson, A., Pietra, S., Grebe, M., Jönsson, H., 2016. A model analysis of mechanisms for radial microtubular patterns at root hair initiation sites. Frontiers in Plant Science 7 (October), 1–12.

Kuhl, E., 2014. Growing matter: a review of growth in living systems. Journal of the Mechanical Behavior of Biomedical Materials 29, 529–543.

Lee, L., Kassab, G., Guccione, J., 2016. Mathematical modeling of cardiac growth and remodeling. Wiley Interdisciplinary Reviews: Systems Biology and Medicine 8 (3), 211–226.

Liu, Y., Zhang, H., Zheng, Y., Zhang, S., Chen, B., 2014. A nonlinear finite element model for the stress analysis of soft solids with a growing mass. International Journal of Solids and Structures 51 (17), 2964–2978.

Lubarda, V.A., Hoger, A., 2002. On the mechanics of solids with a growing mass. International Journal of Solids and Structures 39 (18), 4627–4664.

Martufi, G., Gasser, T.C., 2012. Turnover of fibrillar collagen in soft biological tissue with application to the expansion of abdominal aortic aneurysms. Journal of the Royal Society Interface 9 (77), 3366–3377.

Minnesota Department of Natural Resources, 2017. Adopt-a-River Program: Peanut's Story.

Mitsuhashi, N., Fujieda, K., Tamura, T., Kawamoto, S., Takagi, T., Okubo, K., 2009. BodyParts3D: 3D structure database for anatomical concepts. Nucleic Acids Research 37, D782–D785.

Mosley, J.R., Lanyon, L.E., 1998. Strain rate as a controlling influence on adaptive modeling in response to dynamic loading of the ulna in growing male rats. Bone 23 (4), 313–318.

Moulton, D.E., Goriely, A., 2011. Possible role of differential growth in airway wall remodeling in asthma. Journal of Applied Physiology 110 (4), 1003–1012.

Oltean, A., Huang, J., Beebe, D.C., Taber, L.A., 2016. Tissue growth constrained by extracellular matrix drives invagination during optic cup morphogenesis. Biomechanics and Modeling in Mechanobiology 15 (6), 1–17.

Papastavrou, A., Steinmann, P., Kuhl, E., 2013. On the mechanics of continua with boundary energies and growing surfaces. Journal of the Mechanics and Physics of Solids 61 (6), 1446–1463.

Pereira, A.F., Shefelbine, S.J., 2014. The influence of load repetition in bone mechanotransduction using poroelastic finite-element models: the impact of permeability. Biomechanics and Modeling in Mechanobiology 13 (1), 215–225.

Pereira, A.F., Javaheri, B., Pitsillides, A.A., Shefelbine, S.J., 2015. Predicting cortical bone adaptation to axial loading in the mouse tibia. Journal of The Royal Society Interface 12 (110).

PLCd Research Group (n.d.), PLCd: Non-Linear Thermo-Mechanic Finite Element Code for Research-Oriented Applications, free Access Code Developed at CIMNE. Available at: http://www.cimne.com/PLCd.

Poulet, B., Hamilton, R.W., Shefelbine, S., Pitsillides, A.A., 2011. Characterizing a novel and adjustable noninvasive murine joint loading model. Arthritis and Rheumatism 63 (1), 137–147.

Price, C., Zhou, X., Li, W., Wang, L., 2011. Real-time measurement of solute transport within the lacunar-canalicular system of mechanically loaded bone: direct evidence for load-induced fluid flow. Journal of Bone and Mineral Research 26 (2), 277–285.

Ramasubramanian, A., Taber, L.A., 2008. Computational modeling of morphogenesis regulated by mechanical feedback. Biomechanics and Modeling in Mechanobiology 7 (2), 77–91.

Ramasubramanian, A., Nerurkar, N.L., Achtien, K.H., Filas, B.A., Voronov, D.A., Taber, L.A., 2008. On modeling morphogenesis of the looping heart following mechanical perturbations. Journal of Biomechanical Engineering 130 (6), 061018.

Ramírez-Torres, A., Rodríguez-Ramos, R., Merodio, J., Bravo-Castillero, J., Guinovart-Díaz, R., Alfonso, J.C.L., 2015. Action of body forces in tumor growth. International Journal of Engineering Science 89, 18–34.

Rausch, M.K., Dam, A., Göktepe, S., Abilez, O.J., Kuhl, E., 2011. Computational modeling of growth: systemic and pulmonary hypertension in the heart. Biomechanics and Modeling in Mechanobiology 10 (6), 799–811.

This book belongs to Central Library BADJI Mokhtar-ANNABA UNIVERSITY

Copyright Elsevier 2024

Rodriguez, E.K., Hoger, A., McCulloch, A.D., 1994. Stress-dependent finite growth in soft elastic tissues. Journal of Biomechanics 27 (4), 455−467.

Rubin, C.T., Lanyon, L.E., 1984. Regulation of bone formation by applied dynamic loads. The Journal of Bone and Joint Surgery. American Volume 66 (3), 397−402.

Saez, P., 2016. On the theories and numerics of continuum models for adaptation processes in biological tissues. Archives of Computational Methods in Engineering 23 (2), 301−322.

Sáez, P., Zöllner, A.M., April 2017. Mechanics reveals the biological trigger in wrinkly fingers. Annals of Biomedical Engineering 45 (4), 1039−1047.

Sáez, P., Peña, E., Martínez, M.A., Kuhl, E., 2014. Computational modeling of hypertensive growth in the human carotid artery. Computational Mechanics 53 (6), 1183−1196.

Schoenfeld, B.J., 2010. The mechanisms of muscle hypertrophy and their application to resistance training. Journal of Strength and Conditioning Research/National Strength and Conditioning Association 24 (10), 2857−2872.

Shefelbine, S.J., Carter, D.R., 2004a. Mechanobiological predictions of femoral anteversion in cerebral palsy. Annals of Biomedical Engineering 32 (2), 297−305.

Shefelbine, S.J., Carter, D.R., 2004b. Mechanobiological predictions of growth front morphology in developmental hip dysplasia. Journal of Orthopaedic Research 22 (2), 346−352.

Shefelbine, S.J., Tardieu, C., Carter, D.R., 2002. Development of the femoral bicondylar angle in hominid bipedalism. Bone 30 (5), 765−770.

Shi, Y., Yao, J., Young, J.M., Fee, J.A., Perucchio, R., Taber, L.A., August 2014. Bending and twisting the embryonic heart: a computational model for c-looping based on realistic geometry. Frontiers in Physiology 5, 297.

Taber, L.A., 1998. Biomechanical growth laws for muscle tissue. Journal of Theoretical Biology 193 (2), 201−213.

Knothe Tate, M.L., Steck, R., Forwood, M.R., Niederer, P., 2000. In vivo demonstration of load-induced fluid flow in the rat tibia and its potential implications for processes associated with functional adaptation. The Journal of Experimental Biology 203 (Pt 18), 2737−2745.

Villemure, I., Aubin, C.E., Dansereau, J., Labelle, H., 2002. Simulation of progressive deformities in adolescent idiopathic scoliosis using a biomechanical model integrating vertebral growth modulation. Journal of Biomechanical Engineering 124 (6), 784−790.

Weinbaum, S., Cowin, S.C., Zeng, Y., 1994. A model for the excitation of osteocytes by mechanical loading-induced bone fluid shear stresses. Journal of Biomechanics 27 (3), 339−360.

Wijeratne, P.A., Vavourakis, V., Hipwell, J.H., Voutouri, C., Papageorgis, P., Stylianopoulos, T., Evans, A., Hawkes, D.J., 2016. Multiscale modelling of solid tumour growth: the effect of collagen micromechanics. Biomechanics and Modeling in Mechanobiology 15 (5), 1079−1090.

Wong, M., Carter, D.R., 1990. A theoretical model of endochondral ossification and bone architectural construction in long bone ontogeny. Anatomy and Embryology 181 (6), 523−532.

Xie, W.H., Li, B., Cao, Y.P., Feng, X.Q., 2014. Effects of internal pressure and surface tension on the growth-induced wrinkling of mucosae. Journal of the Mechanical Behavior of Biomedical Materials 29, 594−601.

Xue, S.L., Li, B., Feng, X.Q., Gao, H., 2016. Biochemomechanical poroelastic theory of avascular tumor growth. Journal of the Mechanics and Physics of Solids 94, 409−432.

Yadav, P., Shefelbine, S.J., Gutierrez-Farewik, E.M., 2016. Effect of growth plate geometry and growth direction on prediction of proximal femoral morphology. Journal of Biomechanics 49 (9), 1613−1619.

Zöllner, A.M., Abilez, O.J., Böl, M., Kuhl, E., 2012. Stretching skeletal muscle: chronic muscle lengthening through sarcomerogenesis. PLoS One 7 (10), e45661.

Zöllner, A.M., Pok, J.M., McWalter, E.J., Gold, G.E., Kuhl, E., 2015. On high heels and short muscles: a multiscale model for sarcomere loss in the gastrocnemius muscle. Journal of Theoretical Biology 365, 301−310.

This book belongs to Central Library BADJI Mokhtar-ANNABA UNIVERSITY

Copyright Elsevier 2024

This page intentionally left blank

This book belongs to Central Library BADJI Mokhtar-ANNABA UNIVERSITY

Copyright Elsevier 2024

Chapter 3

Finite Element Modeling and Simulation of the Multiphysic Behavior of Articular Cartilage

M.H. Doweidar and M. Doblaré

The University of Zaragoza, Zaragoza, Spain; The Biomedical Research Networking Center in Bioengineering, Biomaterials and Nanomedicine (CIBER-BBN), Zaragoza, Spain

3.1 INTRODUCTION

Computational simulations of tissues and organs in tissue engineering bring together different sciences, using knowledge of engineering, anatomy, physics, and mechanics among others with the aim of getting a better understanding of the influence of the many factors affecting the particular biomedical problem in hands. The finite element method (FEM) is a widely used technique to mimic different organs and biostructures, such as skeletal muscle tissue, bone, cartilage, and tendons (Hayes and Mockros, 1971; Hughes, 2000; Taylor et al., 2002; Viceconti et al., 2004; Anderson et al., 2008; Kiapour et al., 2014; Manzano et al., 2014a,b; Bayod et al., 2012). These constitutive models can reproduce the behavioral patterns observed in soft tissues, such as the nonlinear response (Mow and Guo, 2002; Teng et al., 2012), the anisotropy given by the preferential arrangement of collagen fibers (Driessen et al., 2003; Gasser et al., 2006), and particularly, in the case of articular cartilage, proteoglycans (PGs) and ions distribution inside and outside the tissue that generate an electrical potential difference (Fig. 3.1) (Sun et al., 2004; Manzano et al., 2016a,b, 2015a,b).

Articular cartilage is a complex material (see Fig. 3.1) where specific mechanoelectrochemical phenomena act together to regulate tissue behavior. Its structure and heterogeneous constituents result in a highly anisotropic material that does not

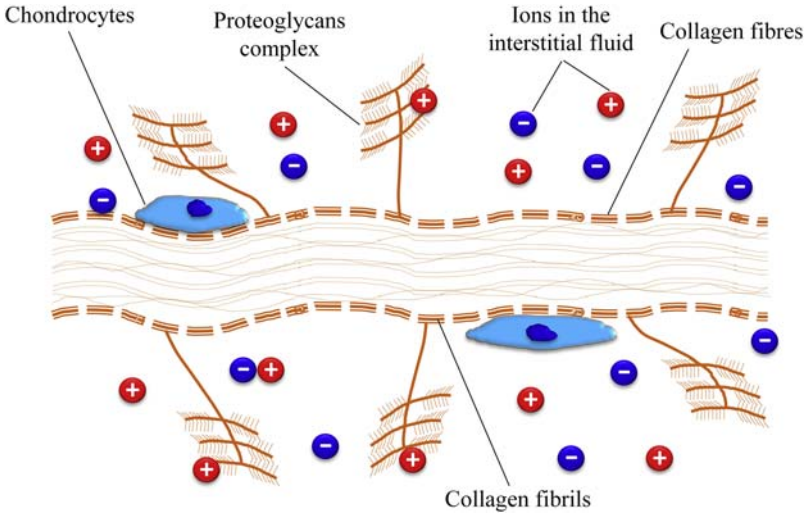

FIGURE 3.1 Main components of the articular cartilage microstructure (chondrocytes, proteoglycans complex, collagen fibers, and ions dissolved in the interstitial fluid).

Numerical Methods and Advanced Simulation in Biomechanics and Biological Processes. https://doi.org/10.1016/B978-0-12-811718-7.00003-4
Copyright © 2018 Elsevier Ltd. All rights reserved.

This book belongs to Central Library BADJI Mokhtar-ANNABA UNIVERSITY

Copyright Elsevier 2024

present nerves or vessels, thus its maintenance is mainly due to convection−diffusion processes (Mansour, 2003; Pearle et al., 2005; Sophia Fox et al., 2009).

Extensive efforts have been developed to predict in vivo cartilage behavior and address on its application to clinical diagnosis and prognosis (Teng et al., 2012; Driessen et al., 2003; Sun et al., 2004; Pearle et al., 2005; Sophia Fox et al., 2009). Earlier models considered only a group of known phenomena depending on the particular aspects of interest (Li et al., 1999a; Korhonen et al., 2013; Besier et al., 2005; Smith et al., 2016). These models consider a group of known phenomenon depending on the particular aspects of interest (Li et al., 1999a; Besier et al., 2005; Smith et al., 2016). For instance, the first studies of cartilage mechanics based on the theory of linear elasticity were not able to predict the time-dependent response of the tissue (Hayes and Mockros, 1971). Viscoelastic monophasic models were then introduced to describe the time-dependent stress−strain relation of the tissue without explicit consideration of the interstitial fluid flow (Hayes and Mockros, 1971). The most commonly used theory for biological tissues is the quasilinear viscoelastic theory (Lai et al., 1991; Li et al., 1999b; Soulhat et al., 1999) where the biphasic and fibril-reinforced models were introduced which brought out some initial success in predicting the time-dependent mechanical response of the tissue. In most articular cartilage models, convective terms associated to the relative movement of fixed charges attached to PGs are neglected because of the complexity of the resulting formulation. However, it is well known that convective−diffusive processes are essential in cartilage modeling. Similarly, these events are significantly affected in cartilage diseases, resulting its alterations as potential biomarkers to quantify the progression of the disease. Thus, this is an interesting point to include in such models to extend its predictive capability. In this line, unlike ligaments, tendons, muscle, and other soft tissues, there is no general agreement about the main phenomena to be considered in cartilage modeling (Huey et al., 2012). Thus, the criterion to select a specific model is based on the research question to study.

Recent knowledge on fundamental structural aspects of cartilage behavior has shown the necessity to offer a unified view incorporating wide interpretations of cartilage physicochemical and swelling properties, mechanical behavior, and electromechanical effects (Mow and Guo, 2002; Wilson et al., 2007). However, only some attempts have been made to take the mentioned complexities of the tissue into account in a single model (Carter and Wong, 2003; Hosoda et al., 2009; Korhonen et al., 2013).

Furthermore, most cartilage computational models are limited to one- or two-dimensional geometries (Wu and Herzog, 2002; Carter and Wong, 2003; Kaasschieter et al., 2003). Because such models are consuming less time and resources, this is useful for studying simple mechanical cartilage behavior when considering isotropic tissue. However, this simplification limits its use, being necessary to consider anisotropies and inhomogeneities of the tissue, not only along the thickness but also in the radial direction. Therefore, three-dimensional (3D) models with an optimized formulation are required to get a more accurate representation of important involved phenomena in physiological and pathological articular cartilage behaviors.

Regarding the inclusion of ionic phases, only triphasic models can consider this aspect. This inclusion allows studying the contribution of ion charges and ion repulsion to compressive, tensile, electrokinetic, and transport behaviors of the cartilage. This is crucial in diseases such as osteoarthritis or for evaluating the functionality of new engineered cartilage constructs (Goldring and Goldring, 2010; Egloff et al., 2012; Manzano et al., 2014b, 2015b). However, most of the existent triphasic models neglect the PG repulsion phenomena that take place as a result of the negative charges attached to these proteins and its effects in swelling and shrinking (Gu et al., 1993; Kaasschieter et al., 2003; Sun et al., 2004).

The main goal of this chapter is to study the behavior of articular cartilage through computational simulation by using the triphasic theory for charged and hydrated soft tissues. The model aims to incorporate the main biological phenomena experimentally observed to be essential in the cartilage behavior in a 3D environment. With this aim, a 3D computational model has been proposed and implemented within a user code. The proposed model considers the porosity of the extracellular matrix (ECM), ionic diffusivity, electrochemical potentials, and mechanical ECM properties, as well as PG repulsion phenomenon that occurs when fixed charges attached to glycosaminoglycans (GAGs) approximate each other generating electric repulsion that induces tissue electrochemical response as well as the anisotropic properties of the tissue.

3.2 NUMERICAL MODELING

The mathematical model developed is based on the so-called triphasic mechanoelectrochemical theory (Lai et al., 1991). This theory considers a charged hydrated soft tissue as a mixture of a porous-permeable charged solid phase (ECM, collagen fibers, and PGs), a fluid phase (water), and ionic phase with two monovalent species (Na^+ and Cl^-). It is assumed that the different phases interact simultaneously at each point and are considered intrinsically incompressible. The fundamental balance equations for the solid matrix (mass, momenta, and charge density), the fluid (interstitial fluid), cations, and anions are all considered. Fluxes of fluid and ions depend on fluid pressure and ion concentration, respectively, thus driving to a full coupled and highly nonlinear set of differential equations.

This book belongs to Central Library BADJI Mokhtar-ANNABA UNIVERSITY
Copyright Elsevier 2024

3.2.1 Model Formulation

The following equations are the basis of the mathematical model to determine the four basic unknowns of triphasic theory ($\mathbf{u}^s$, the displacement of the solid matrix; ε^w, the modified chemical potential of water; and ε^+ and ε^-, the modified chemical potential for cations and anions, respectively (Sun et al., 1999)):

- *balance of the mixture momentum*

$$\nabla \cdot \boldsymbol{\sigma} = 0, \tag{3.1}$$

- *balance of the mixture mass*

$$\nabla \cdot \mathbf{v}^s + \nabla \cdot \mathbf{J}^w = 0, \tag{3.2}$$

- *balance for each ion charge*

$$\frac{\partial(\phi^w c^+)}{\partial t} + \nabla \cdot \mathbf{J}^+ + \nabla \cdot (\phi^w c^+ \mathbf{v}^s) = 0, \tag{3.3}$$

$$\frac{\partial(\phi^w c^-)}{\partial t} + \nabla \cdot \mathbf{J}^- + \nabla \cdot (\phi^w c^- \mathbf{v}^s) = 0 \tag{3.4}$$

where $\boldsymbol{\sigma}$ is the tensor of the total mixture stress, which is the summation of the stress tensors of the fluid, chemical, and solid phases.

$$\boldsymbol{\sigma} = \boldsymbol{\sigma}^f + \boldsymbol{\sigma}^c + \boldsymbol{\sigma}^s.$$

Hence, $\boldsymbol{\sigma}$ can be can be expressed as

$$\boldsymbol{\sigma} = -p\mathbf{I} + \lambda_s \theta \mathbf{I} + 2\mu_s \boldsymbol{\varepsilon}, \tag{3.5}$$

where p is the fluid pressure, $\theta = div\ \mathbf{u^s}$ is the solid matrix dilatation related to the infinitesimal strain tensor of the solid matrix, λ_s and μ_s are the Lamé constants of the solid matrix (a linear elastic isotropic material has been here used for the sake of simplicity), $\boldsymbol{\varepsilon} = \frac{1}{2}(\nabla \cdot \mathbf{u^s} + \nabla^{\mathbf{T}} \cdot \mathbf{u^s}))$ is the solid matrix deformation, and $\mathbf{I}$ is the identity tensor.

In Eqs. (3.2)–(3.4), $\mathbf{v}^s = \frac{\partial \mathbf{u}^s}{\partial t}$ is the velocity of the solid matrix, and $\partial/\partial t$ is the temporal derivative. c^+ and c^- are cation and anion concentrations, respectively, ϕ^w represents the cartilage porosity. $(\phi^w c^+ \mathbf{v}^s)$ and $(\phi^w c^- \mathbf{v}^s)$ are the convective terms associated to ion-matrix coupling, which are neglected in the most cartilage models in the literature (Wu and Herzog, 2002; Kaasschieter et al., 2003). These last terms are essential for capturing the coupled movement of the ions attached to collagen fibers through the GAG chains. The water flux, $\mathbf{J}^w$; cation flux, $\mathbf{J}^+$; and the anion flux $\mathbf{J}^-$ can be expressed as a combination of the electrochemical potentials as (Sun et al., 1999)

$$\mathbf{J}^w = -\frac{RT\phi^w}{\alpha}\left(\nabla \varepsilon^w + \frac{c^+}{\varepsilon^+}\nabla \varepsilon^+ + \frac{c^-}{\varepsilon^-}\nabla \varepsilon^-\right), \tag{3.6}$$

$$\mathbf{J}^+ = -\frac{RT\phi^w c^+}{\alpha}\nabla \varepsilon^w - \left[\frac{\phi^w c^+ D^+}{\varepsilon^+} + \frac{RT\phi^w (c^+)^2}{\alpha \varepsilon^+}\right]\nabla \varepsilon^+ - \frac{RT\phi^w c^+ c^-}{\alpha \varepsilon^+}\nabla \varepsilon^-, \tag{3.7}$$

$$\mathbf{J}^- = -\frac{RT\phi^w c^-}{\alpha}\nabla \varepsilon^w - \left[\frac{\phi^w c^- D^-}{\varepsilon^-} + \frac{RT\phi^w (c^-)^2}{\alpha \varepsilon^-}\right]\nabla \varepsilon^- - \frac{RT\phi^w c^+ c^-}{\alpha \varepsilon^+}\nabla \varepsilon^+, \tag{3.8}$$

where α is the drag coefficient between the solid and the water phases, D^+ and D^- are the ion diffusivities, and ϕ^w the porosity of the tissue. Note that the combination of the porosity and the drag coefficient of the material gives rise to the permeability of the tissue, $k = \frac{\phi^w}{\alpha}$ (Sun et al., 1999).

ε^w, ε^+, and ε^- can be written in terms of the basic variables of the problem as (Sun et al., 2004)

$$\varepsilon^w = \frac{P}{RT} - \phi(c^+ + c^-) + \frac{B_w}{R\,T}\theta, \tag{3.9}$$

This book belongs to Central Library BADJI Mokhtar-ANNABA UNIVERSITY
Copyright Elsevier 2024

$$\varepsilon^{+} = \gamma^{+} c^{+} exp\left(\frac{F_c \psi}{R\,T}\right), \tag{3.10}$$

$$\varepsilon^{-} = \gamma^{-} c^{-} exp\left(-\frac{F_c \psi}{R\,T}\right), \tag{3.11}$$

where F_c is the Faraday constant, ψ is the electrical potential, B_w is the fluid−solid coupling coefficient, ϕ is the osmotic coefficient, γ^{+} and γ^{-} are the activity coefficients of anion and cation, respectively, R is the universal gas constant, and T is the absolute temperature.

The cation concentrations, c^{+} and c^{-}, can be expressed in terms of modified electrochemical potentials and fixed charged density as follows (Sun et al., 1999):

$$c^{+} = \frac{1}{2}\left(c^{F} + \sqrt{\left(c_0^{F}\right)^2 + \frac{4\varepsilon^{+}\varepsilon^{-}}{\gamma^{+}\gamma^{-}}}\right), \tag{3.12}$$

$$c^{-} = \frac{1}{2}\left(-c^{F} + \sqrt{\left(c_0^{F}\right)^2 + \frac{4\varepsilon^{+}\varepsilon^{-}}{\gamma^{+}\gamma^{-}}}\right), \tag{3.13}$$

where c_0^F is the initial fixed charge density (FCD), the amount of charges that are attached to collagen fibers within the GAGs (Fig. 3.2).

Note that, the intrafibrillar water within collagen fibers can be considered as bound water and consequently part of the solid phase. Because of the intrinsic incompressibility, for infinitesimal strains, ϕ^{w} can be expressed as

$$\phi^{w} = 1 - \frac{\phi_0^{s}}{1+\theta}, \tag{3.14}$$

where ϕ_0^s is the solid volume fraction at a physicochemical reference configuration (selected as the initial state). The second part of this equation, $\frac{\phi_0^s}{1+\theta}$, corresponds to the solid volume fraction of the tissue, ϕ^s, at any time along the deformation process.

Considering the electroneutrality condition between cations and anions, the following relation is considered (Sun et al., 1999):

$$c^{+} = c^{-} + c^{F}, \tag{3.15}$$

where c^F is the FCD. According to experimental observations, increasing the volumetric deformation of the sample (e.g., tissue free swelling) is followed by a reduction in the fixed charge due to the water intake and consequently ion

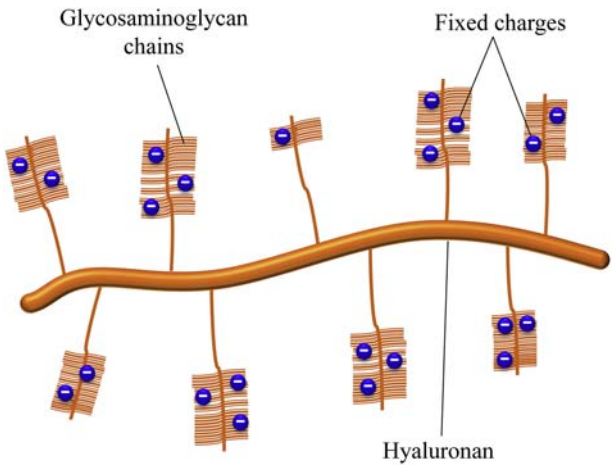

FIGURE 3.2 Proteoglycan macromolecule aggregation with charged-glycosaminoglycan chains attached to a hyaluronic chain.

This book belongs to Central Library BADJI Mokhtar-ANNABA UNIVERSITY
Copyright Elsevier 2024

concentration and fixed charges reduction. Similarly, the opposite phenomenon also occurs when the volumetric deformation decreases (e.g., the tissue shrinks). Under these considerations (Sun et al., 1999),

$$c^F = \frac{c_0^F}{1+\dfrac{\theta}{\phi_0^w}}, \tag{3.16}$$

where c_0^F and ϕ_0^w is the initial water content in the tissue at reference state.

3.2.1.1 System of Differential Equation

Substituting the constitutive Eqs. (3.5) and (3.9)–(3.11) as well as the flux Eqs. (3.6)–(3.8) into the governing Eqs. (3.1)–(3.4), we can get the following system of differential equations:

$$\nabla\cdot(\lambda_s\theta\mathbf{I}+2\mu_s\varepsilon)-\nabla\left(RT\varepsilon^w+RT\phi c^k-B_w\theta\right) = 0, \tag{3.17}$$

$$\nabla\cdot\mathbf{v}^s-\nabla\cdot\frac{RT}{\alpha}\left[\phi^w\nabla\varepsilon^w+\frac{\phi^w c^+}{\varepsilon^+}\nabla\varepsilon^+ +\frac{\phi^w c^-}{\varepsilon^-}\nabla\varepsilon^-\right] = 0, \tag{3.18}$$

$$\begin{aligned}\nabla\cdot\left[-\frac{RT}{\alpha}\phi^w c^F\nabla\varepsilon^w\right]-\nabla\cdot\left[\frac{\phi^w c^+D^+}{\varepsilon^+}+\frac{RT}{\alpha}\frac{\phi^w(c^+)^2}{\varepsilon^+}-\frac{RT}{\alpha}\frac{\phi^w c^+c^-}{\varepsilon^+}\right]\nabla\varepsilon^+\\ +\nabla\cdot\left[\frac{\phi^w c^-D^-}{\varepsilon^-}+\frac{RT}{\alpha}\frac{\phi^w(c^-)^2}{\varepsilon^-}-\frac{RT}{\alpha}\frac{\phi^w c^+c^-}{\varepsilon^+}\right]\nabla\varepsilon^- = 0,\end{aligned} \tag{3.19}$$

$$\begin{aligned}\frac{\partial(\phi^w c^k)}{\partial t}-\nabla\cdot\left[-\frac{RT}{\alpha}\phi^w c^k\nabla\varepsilon^w\right]-\nabla\cdot\left[\frac{\phi^w c^+D^+}{\varepsilon^+}+\frac{RT}{\alpha}\frac{\phi^w(c^+)^2}{\varepsilon^+}-\frac{RT}{\alpha}\frac{\phi^w c^+c^-}{\varepsilon^+}\right]\nabla\varepsilon^+\\ -\nabla\cdot\left[\frac{\phi^w c^-D^-}{\varepsilon^-}+\frac{RT}{\alpha}\frac{\phi^w(c^-)^2}{\varepsilon^-}-\frac{RT}{\alpha}\frac{\phi^w c^+c^-}{\varepsilon^+}\right]\nabla\varepsilon^- +\nabla\cdot(\phi^w c^k\mathbf{v}^s) = 0,\end{aligned} \tag{3.20}$$

where $c^k = c^+ + c^-$.

3.2.1.2 Weak Formulation

A finite element formulation has been used to obtain the solution of the governing Eqs. (3.17)–(3.20). The primary unknowns of the model [$\mathbf{u}$, ε^w, ε^+, ε^-] are interpolated from nodal values through shape functions (Sun et al., 1999). The time derivatives are approximated with the Crank–Nicolson method (Crank and Nicolson, 1947) that yields an implicit approximation to the solution of the initial value problem $y' = f(x, y)$ with $y(x_0) = y_0$ at x for a given time step h. To obtain the fully coupled nonlinear system of equations describing the discretized model, the weak formulation of the governing equations is established as follows:

$$\int \nabla\delta_{\mathbf{u}}\cdot\boldsymbol{\sigma}\, dV = \int_\Gamma \delta_{\mathbf{u}}\boldsymbol{\sigma}^*\mathbf{n}\, d\Gamma, \tag{3.21}$$

$$\int \nabla\delta_{\varepsilon^w}\cdot\mathbf{v}^s dV + \int \nabla\delta_{\varepsilon^w}\cdot\mathbf{J}^w dV = -\int_\Gamma \delta_{\varepsilon^w}\mathbf{J}^{w*}\mathbf{n}\, d\Gamma, \tag{3.22}$$

$$\int \nabla\delta_{\varepsilon^+}\cdot\mathbf{J}^+ dV - \int_\Omega \nabla\delta_{\varepsilon^+}\cdot\mathbf{J}^- dV = \int_\Gamma \delta_{\varepsilon^+}\left(\mathbf{J}^{-^*}-\mathbf{J}^{+^*}\right)\mathbf{n}\, d\Gamma, \tag{3.23}$$

$$\int \delta_{\varepsilon^-}\frac{\partial(\phi^w c^k)}{\partial t}dV + \int \nabla\delta_{\varepsilon^-}\cdot\mathbf{J}^+ dV + \int \nabla\delta_{\varepsilon^-}\cdot\mathbf{J}^- dV + \int \nabla\delta_{\varepsilon^-}\cdot\left(\phi^w c^k\mathbf{v}^s\right) dV = -\int_\Gamma \delta_{\varepsilon^-}\left(\mathbf{J}^{+^*}+\mathbf{J}^{-^*}\right)\mathbf{n}\, d\Gamma, \tag{3.24}$$

where $\mathbf{n}$ is the unit normal vector to the boundary and $\delta_{\mathbf{u}}$, δ_{ε^w}, δ_{ε^+}, and δ_{ε^-} are the so-called test functions satisfying a set of mathematical requirements associated with continuity and integrability (Hughes, 1987). Trilinear 8-noded hexahedral elements with $2\times2\times2$ Gaussian integration points were used. The superscript * indicates the quantities in the bathing solution.

This book belongs to Central Library BADJI Mokhtar-ANNABA UNIVERSITY
Copyright Elsevier 2024

3.2.1.3 Temporal Discretization

For the temporal discretization of the governing Eqs. (3.17)–(3.20), the partition $\bigcup_{n=1}^{n_{\text{step}}-1}[t_n,\ t_{n+1}]$ of the time interval of interest T is considered. The subinterval $[t_n, t_{n+1}]$ with $\Delta t = t_{n+1} - t_n \geq 0$ denotes a typical time increment. It is assumed that the primary unknowns and all derived and required quantities are known at time t_n. The generalized trapezoidal method is applied (Crank and Nicolson, 1947), with $\alpha\ \varepsilon\ (0,1]$, such that $t_{n+\alpha} = t_n + \alpha\Delta t$. The following scheme is used for the temporal discretization of primary variables (ε^{w} is shown here, while ε^{+} and ε^{-} and $\mathbf{u}$ have the same discretization):

$$\varepsilon^{w}_{n+1} = \varepsilon^{w}_{n} + \Delta t\ \dot{\varepsilon}^{w}_{n+\alpha}, \tag{3.25}$$

$$\dot{\varepsilon}^{w}_{n+\alpha} = \dot{\varepsilon}^{w}_{n}(1-\alpha) + \dot{\varepsilon}^{w}_{n+1}\alpha, \tag{3.26}$$

where ε^{w}_{n+1}, $\dot{\varepsilon}^{w}_{n+\alpha}$, and $\dot{\varepsilon}^{w}_{n+1}$ are approximations of $\varepsilon^{w}(t_{n+1})$, $\left(\frac{\partial\varepsilon^{w}}{\partial t}\right)(t_{n+\alpha})$, and $\left(\frac{\partial\varepsilon^{w}}{\partial t}\right)(t_{n+1})$, respectively. From a practical standpoint, $\widetilde{\varepsilon}^{w}_{n+1}$ is introduced as a predictor value of ε^{w}_{n+1}, which only depends on magnitudes at time t_n:

$$\widetilde{\varepsilon}^{w}_{n+1} = \varepsilon^{w}_{n} + (1-\alpha)\Delta t\cdot\dot{\varepsilon}^{w}_{n}, \tag{3.27}$$

where $\dot{\varepsilon}^{w}_{n+1}$ can be calculated by

$$\dot{\varepsilon}^{w}_{n+1} = \frac{\varepsilon^{w}_{n+1} - \widetilde{\varepsilon}^{w}_{n+1}}{\alpha\Delta t}. \tag{3.28}$$

Substitution of Eqs. (3.27) and (3.28) in the weak form of the problem yields a semidiscrete set of equations that are discretized in time.

3.2.1.4 Spatial Discretization

The semidiscretized system (after time discretization) is the discretized in space using the FEM. The domain Ω is discretized into n_{el} elements Ω^e, such that $\Omega = \bigcup_{e=1}^{n_{\text{el}}}\Omega^e$. The primary unknown fields are interpolated within a generic element Ω^e in terms of the nodal values through shape functions as follows:

$$\begin{aligned}
\varepsilon^{w^h}\big|_{\Omega^e} &= \mathbf{N}_{\varepsilon^w}\boldsymbol{\varepsilon}^{w^e},\\
\varepsilon^{+^h}\big|_{\Omega^e} &= \mathbf{N}_{\varepsilon^+}\boldsymbol{\varepsilon}^{+^e},\\
\varepsilon^{-^h}\big|_{\Omega^e} &= \mathbf{N}_{\varepsilon^-}\boldsymbol{\varepsilon}^{-^e},\\
\mathbf{u}^{h}\big|_{\Omega^e} &= \mathbf{N}_{\mathbf{u}}\mathbf{u}^{e},
\end{aligned} \tag{3.29}$$

where $\boldsymbol{\varepsilon}^{w^e}, \boldsymbol{\varepsilon}^{+^e}, \boldsymbol{\varepsilon}^{-^e}$, and $\mathbf{u}^e$ are the vectors of nodal values of the primary unknowns at element e and $\mathbf{N}_{\varepsilon^w}$, $\mathbf{N}_{\varepsilon^+}$, $\mathbf{N}_{\varepsilon^-}$, and $\mathbf{N}_{\mathbf{u}}$ are matrices of element shape functions defined as

$$\begin{aligned}
\mathbf{N}_{\varepsilon^w} &= \left[N^1_{\varepsilon^w}, \ldots, N^{n_{en}}_{\varepsilon^w}\right],\\
\mathbf{N}_{\varepsilon^+} &= \left[N^1_{\varepsilon^+}, \ldots, N^{n_{en}}_{\varepsilon^+}\right],\\
\mathbf{N}_{\varepsilon^-} &= \left[N^1_{\varepsilon^-}, \ldots, N^{n_{en}}_{\varepsilon^-}\right],
\end{aligned} \tag{3.30}$$

$$\mathbf{N}_{\mathbf{u}} = \begin{bmatrix} N^1_u & 0 & 0\\ 0 & N^1_u & 0\\ 0 & 0 & N^1_u \end{bmatrix} \ldots \begin{bmatrix} N^{n_{en}}_u & 0 & 0\\ 0 & N^{n_{en}}_u & 0\\ 0 & 0 & N^{n_{en}}_u \end{bmatrix},$$

This book belongs to Central Library BADJI Mokhtar-ANNABA UNIVERSITY

Copyright Elsevier 2024

where N_u^i is the shape function associated with element node i and n_{en} is the number of element nodes. Following a Bubnov−Galerkin scheme, the same shape functions are also employed to interpolate the test functions:

$$\begin{aligned}
\delta\varepsilon^{w^h}\big|_{\Omega^e} &= \mathbf{N}_{\varepsilon^w}\delta\varepsilon^{w^e},\\
\delta\varepsilon^{+^h}\big|_{\Omega^e} &= \mathbf{N}_{\varepsilon^+}\delta\varepsilon^{+^e},\\
\delta\varepsilon^{-^h}\big|_{\Omega^e} &= \mathbf{N}_{\varepsilon^-}\delta\varepsilon^{-^e},\\
\delta\mathbf{u}^h\big|_{\Omega^e} &= \mathbf{N}_{\mathbf{u}}\delta\mathbf{u}^e.
\end{aligned} \tag{3.31}$$

Similarly, the discretization of the associated gradients of the test functions and the primary unknowns take the following form:

$$\begin{aligned}
\nabla\varepsilon^{w^h}\big|_{\Omega^e} &= \nabla\cdot\mathbf{N}_{\varepsilon^w}\boldsymbol{\varepsilon}^{w^e} \xrightarrow{yields} \nabla\delta\varepsilon_h\big|_{\Omega^e} = \nabla\cdot\mathbf{N}_{\varepsilon^w}\delta\boldsymbol{\varepsilon}^{w^e},\\
\nabla\varepsilon^{+^h}\big|_{\Omega^e} &= \nabla\cdot\mathbf{N}_{\varepsilon^+}\boldsymbol{\varepsilon}^{+^e} \xrightarrow{yields} \nabla\delta\varepsilon_h^+\big|_{\Omega^e} = \nabla\cdot\mathbf{N}_{\varepsilon^+}\delta\boldsymbol{\varepsilon}^{+^e},\\
\nabla\varepsilon^{-^h}\big|_{\Omega^e} &= \nabla\cdot\mathbf{N}_{\varepsilon^-}\boldsymbol{\varepsilon}^{-^e} \xrightarrow{yields} \nabla\delta\varepsilon_h^-\big|_{\Omega^e} = \nabla\cdot\mathbf{N}_{\varepsilon^-}\delta\boldsymbol{\varepsilon}^{-^e}.
\end{aligned} \tag{3.32}$$

The strains are then obtained as

$$\varepsilon^h\big|_{\Omega^e} = \mathbf{B}_{\mathbf{u}}\mathbf{u}^e, \tag{3.33}$$

where $\mathbf{B}_{\mathbf{u}}$ is a matrix of shape function derivatives:

$$\mathbf{B}_{\mathbf{u}} = \mathbf{H}\mathbf{N}_{\mathbf{u}}, \tag{3.34}$$

$$\mathbf{H} = \begin{bmatrix} \frac{\partial}{\partial x} & 0 & 0\\ 0 & \frac{\partial}{\partial y} & 0\\ 0 & 0 & \frac{\partial}{\partial z}\\ \frac{1}{2}\frac{\partial}{\partial y} & \frac{1}{2}\frac{\partial}{\partial x} & 0\\ \frac{1}{2}\frac{\partial}{\partial y} & 0 & \frac{1}{2}\frac{\partial}{\partial y}\\ 0 & \frac{1}{2}\frac{\partial}{\partial z} & \frac{1}{2}\frac{\partial}{\partial y} \end{bmatrix}. \tag{3.35}$$

Substituting Eqs. (3.29), (3.31), and (3.34) into the semidiscrete system and choosing appropriate arbitrary coefficients $\delta\boldsymbol{\varepsilon}^{w^e}$, $\delta\boldsymbol{\varepsilon}^{+^e}$, $\delta\boldsymbol{\varepsilon}^{-^e}$, and $\delta\mathbf{u}^e$ of the test functions, a set of nonlinear algebraic equations sufficient to determine the nodal values of the primary unknowns is obtained that can be written as:

$$\mathbf{F}^{\text{int}} = \left(\mathbb{Z}_{n+1}, \frac{\mathbb{Z}_{n+1} - \widetilde{\mathbb{Z}}_{n+1}}{\alpha\Delta t}\right) = \mathbf{F}^{ext}(\mathbb{Z}_{n+1}), \tag{3.36}$$

where $\mathbb{Z}_{n+1}$ and $\widetilde{\mathbb{Z}}_{n+1}$ are the global vectors of the nodal values of the primary unknown fields at time t_{n+1} and the corresponding predictor value, respectively. These vectors can be written as

$$\mathbb{Z}_{n+1} = \mathcal{R}_{e=1}^{n_{\text{en}}}\mathbf{d}_{n+1}^e, \tag{3.37}$$

$$\widetilde{\mathbb{Z}}_{n+1} = \mathcal{R}_{e=1}^{n_{\text{en}}}\widetilde{\mathbf{d}}_{n+1}^e, \tag{3.38}$$

This book belongs to Central Library BADJI Mokhtar-ANNABA UNIVERSITY
Copyright Elsevier 2024

where $\mathcal{R}$ denotes the standard finite element assembly operator. $\mathbf{d}^e_{n+1}$ and $\widetilde{\mathbf{d}}^e_{n+1}$ are defined as

$$\mathbf{d}^e_{n+1} = \left[\boldsymbol{\varepsilon}^{w^e}_{n+1}, \boldsymbol{\varepsilon}^{+^e}_{n+1}, \boldsymbol{\varepsilon}^{-^e}_{n+1}, \mathbf{u}^e_{n+1}\right]^{\mathrm{T}}, \tag{3.39}$$

$$\widetilde{\mathbf{d}}^e_{n+1} = \left[\widetilde{\boldsymbol{\varepsilon}}^{w^e}_{n+1}, \widetilde{\boldsymbol{\varepsilon}}^{+^e}_{n+1}, \widetilde{\boldsymbol{\varepsilon}}^{-^e}_{n+1}, \widetilde{\mathbf{u}}^e_{n+1}\right]^{\mathrm{T}}. \tag{3.40}$$

The internal and external global force vectors represented by $\mathbf{F}^{int}$ and $\mathbf{F}^{ext}$ come from the assembly of element contributions:

$$F^{int}_{n+1} = \mathscr{R}^{n_{en}}_{e=1}\mathbf{f}^{int,e}_{n+1}, \tag{3.41}$$

$$F^{ext}_{n+1} = \mathscr{R}^{n_{en}}_{e=1}\mathbf{f}^{ext,e}_{n+1}, \tag{3.42}$$

where

$$\mathbf{f}^{int,e}_{n+1} = \left[\mathbf{f}^{int,e}_{\varepsilon^w,n+1}; \mathbf{f}^{int,e}_{\varepsilon^+,n+1}; \mathbf{f}^{int,e}_{\varepsilon^-,n+1}; \mathbf{f}^{int,e}_{u,n+1}\right]^T, \tag{3.43}$$

$$\mathbf{f}^{ext,e}_{n+1} = \left[\mathbf{f}^{ext,e}_{\varepsilon^w,n+1}; \mathbf{f}^{ext,e}_{\varepsilon^+,n+1}; \mathbf{f}^{ext,e}_{\varepsilon^-,n+1}; \mathbf{f}^{ext,e}_{u,n+1}\right]^T. \tag{3.44}$$

The element contributions to the internal force can be written as

$$\begin{aligned}
\mathbf{f}^{int,e}_{\varepsilon^w,n+1} &= \int \boldsymbol{\nabla}\cdot\mathbf{N}^T_{\boldsymbol{\varepsilon}^w}\left[\frac{\mathbf{u}^h_{n+1} - \widetilde{\mathbf{u}}^h_{n+1}}{\alpha\Delta t} + \frac{RT}{\alpha}\,\phi^w\boldsymbol{\nabla}\varepsilon^{w^h} + \frac{RT}{\alpha}\,\phi^w\frac{c^+}{\varepsilon^{+^h}}\boldsymbol{\nabla}\varepsilon^{+^h} + \frac{RT}{\alpha}\,\phi^w\frac{c^-}{\varepsilon^{-^h}}\boldsymbol{\nabla}\varepsilon^{-^h}\right]_{n+1} dV,\\
\mathbf{f}^{int,e}_{\varepsilon^+,n+1} &= \int_\Omega \boldsymbol{\nabla}\cdot\mathbf{N}^T_{\varepsilon^+}\left[-\frac{RT}{\alpha}\,\phi^w c^F\boldsymbol{\nabla}\cdot\mathbf{N}_{\boldsymbol{\varepsilon}^w}\varepsilon^w - \left(\frac{\phi^w c^+ D^+}{\varepsilon^{+^h}} + \frac{RT}{\alpha}\,\phi^w\frac{(c^+)^2}{\varepsilon^{+^h}} - \frac{RT}{\alpha}\,\phi^w\frac{c^+c^-}{\varepsilon^{+^h}}\right)\boldsymbol{\nabla}\varepsilon^{+^h}\right.\\
&\quad\left. + \left(\frac{\phi^w c^- D^-}{\varepsilon^{-^h}} + \frac{RT}{\alpha}\,\phi^w\frac{(c^-)^2}{\varepsilon^{-^h}} - \frac{RT}{\alpha}\,\phi^w\frac{c^+c^-}{\varepsilon^{-^h}}\right)\boldsymbol{\nabla}\varepsilon^{+^h}\right]_{n+1} dV,\\
\mathbf{f}^{int,e}_{\varepsilon^-,n+1} &= \int_\Omega \boldsymbol{\nabla}\cdot\mathbf{N}^T_{\boldsymbol{\varepsilon}^-}\left[-\frac{RT}{\alpha}\,\phi^w c^F\boldsymbol{\nabla}\cdot\mathbf{N}_{\boldsymbol{\varepsilon}^w}\varepsilon^w + \frac{\phi^w c^+ D^+}{\varepsilon^{+^h}} + \frac{RT}{\alpha}\,\phi^w\frac{(c^+)^2}{\varepsilon^{+^h}} + \frac{RT}{\alpha}\,\phi^w\frac{c^+c^-}{\varepsilon^{+^h}}\right)\boldsymbol{\nabla}\varepsilon^{+^h}\right.\\
&\quad\left. + \frac{\phi^w c^- D^-}{\varepsilon^{-^h}} + \frac{RT}{\alpha}\,\phi^w\frac{(c^-)^2}{\varepsilon^{-^h}} + \frac{RT}{\alpha}\,\phi^w\frac{c^+c^-}{\varepsilon^{-^h}}\right)\boldsymbol{\nabla}\varepsilon^{-^h}\right]_{n+1} dV\\
&\quad + \int \boldsymbol{\nabla}\cdot\mathbf{N}^T_{\boldsymbol{\varepsilon}^-}\left.\phi^w c^{k^h}\frac{\mathbf{u}^h_{n+1} - \widetilde{\mathbf{u}}^h_{n+1}}{\alpha\Delta t}\right) dV + \int \mathbf{N}^T_{\boldsymbol{\varepsilon}^-}\left.\phi^w\frac{c^{k^h}_{n+1} - \widetilde{c}^{k^h}_{n+1}}{\alpha\Delta t}\right) dV,\\
\mathbf{f}^{int,e}_{u,\,n+1} &= \int \mathbf{B}^T_{\mathbf{u}}[\mathbf{D}_{elas}\mathbf{H}\mathbf{u}^h - RT\varepsilon^{w^h}\mathbf{I} + RT\phi c^{k^h}\mathbf{I} - B_w\mathbf{H}\mathbf{u}^h]_{n+1} dV,
\end{aligned} \tag{3.45}$$

where $\mathbf{D}_{elas}$ is the elastic constitutive matrix:

$$\mathbf{D}_{elas} = \xi\begin{bmatrix}
1-\nu & \nu & \nu & & & \\
\nu & 1-\nu & \nu & & \widetilde{0} & \\
\nu & \nu & 1-\nu & & & \\
 & & & \frac{1-2\nu}{2} & 0 & 0\\
 & \widetilde{0} & & 0 & \frac{1-2\nu}{2} & 0\\
 & & & 0 & 0 & \frac{1-2\nu}{2}
\end{bmatrix}, \tag{3.46}$$

with $\xi = \frac{E}{(1+\nu)(1-2\nu)}$.

This book belongs to Central Library BADJI Mokhtar-ANNABA UNIVERSITY

Copyright Elsevier 2024

In the case of the external force vector, the element contributions have the following expressions:

$$\begin{aligned}
\mathbf{f}^{ext,e}_{\mathbf{u},n+1} &= \int \mathbf{N}^T_{\mathbf{u}} \boldsymbol{\sigma}^{*^h}_{n+1}\, dV, \\
\mathbf{f}^{ext,e}_{\varepsilon^w,n+1} &= -\int \mathbf{N}^T_{\varepsilon^{w^h}} \mathbf{J}^{w^{*^h}}_{n+1}\, dV, \\
\mathbf{f}^{ext,e}_{\varepsilon^+,n+1} &= \int \mathbf{N}^T_{\varepsilon^+} \left(\mathbf{J}^{+^{*^h}}_{n+1} - \mathbf{J}^{-^{*^h}}_{n+1}\right) dV, \\
\mathbf{f}^{ext,e}_{\varepsilon^-,n+1} &= -\int \mathbf{N}^T_{\varepsilon^+} \left(\mathbf{J}^{+^{*^h}}_{n+1} + \mathbf{J}^{-^{*^h}}_{n+1}\right) dV.
\end{aligned} \tag{3.47}$$

3.2.2 Numerical Implementation

The model presented above has been implemented within the commercial FE software ABAQUS through the user-defined subroutine UEL. Initially, the cartilage sample is in equilibrium with the external bath (initial equilibrium). Therefore, the initial volumetric dilatation is equal to zero and initial values for ion concentrations correspond to those measured in the initial state of the external solution. After modifying the external solution, electrochemical potentials between the bath and the tissue ($\nabla\varepsilon^w$, $\nabla\varepsilon^+$ and $\nabla\varepsilon^-$) are created, generating a new ion distribution within the cartilage. Fluxes of water and ions tend to enter and leave the tissue, respectively, to recover the equilibrium state and, as result, the tissue swells in the absence of external loads. Specific values for displacement and ion concentrations are calculated in every node and updated via a Lagrangian formulation (in terms of the initial coordinates). The volumetric deformation at each finite element node is also computed. The full analysis presented in this work corresponds to a total time analysis (t_f) of 3600 s coincident with usual experimental periods in cartilage free swelling assays (Lai et al., 1991). The implementation scheme of the 3D mechanoelectrochemical model is shown in Fig. 3.3.

3.3 VALIDATION AND EXPERIMENTAL EXAMPLES

3.3.1 Model Validation

To validate the present 3D mechanoelectrochemical computational model of cartilage, we will reproduce the results obtained by Sun et al. (1999) in one dimension (1D) for cartilage.

The mesh of both models has 50 linear elements in depth. To accurately reproduce the 1D case of Sun et al., we consider a diameter of four orders of magnitude smaller than the height of the sample ($\phi_{\text{sample}} \ll h_{\text{sample}}$), with only one element per row and a total of 50 elements. The selected average mesh size was 0.01 mm. Similar to Sun et al. (1999), the displacements in x and y axis are constrained ($u_x = u_y = 0$). All parameters used in this example are collected in Table 3.1.

The present simplified 3D model accurately reproduced the deformation evolution obtained by the 1D model of Sun et al. (1999), who found a maximum steady-state deformation of 0.0135 mm height at 1000 s (Fig. 3.4).

The gradient of cations was also monitored after 100 s of free swelling, and again the model reproduces the results reported by the 1D model Sun et al., where a progressive decrease of cation concentration toward the upper surface of the sample is produced (from 273 mol/m^3 at $x = 0$ mm height to 255 mol/m^3 at $x = 0.5$ mm height) (Fig. 3.5).

3.3.2 Boundary Conditions

The lateral sides as well as the lower surface of the sample are impermeable and confined ($u_x = u_y = 0$ and $u_x = u_y = u_z = 0$) (Figs. 3.6 and 3.7). Therefore, zero flux is considered for ions and water through these surfaces $\left(J^w_{x,y} = J^+_{x,y} = J^-_{x,y} = 0 \text{ and } J^w_z = J^+_z = J^-_z = 0\right)$. The electrochemical potential of water and ions in the external bath, $\varepsilon^w = \varepsilon^{w^*}$; $\varepsilon^+ = \varepsilon^{+^*}$; $\varepsilon^- = \varepsilon^{-^*}$. $\varepsilon^{w^*}, \varepsilon^{+^*}$ and ε^{-^*} are kept constant through the process.

This book belongs to Central Library BADJI Mokhtar-ANNABA UNIVERSITY
Copyright Elsevier 2024

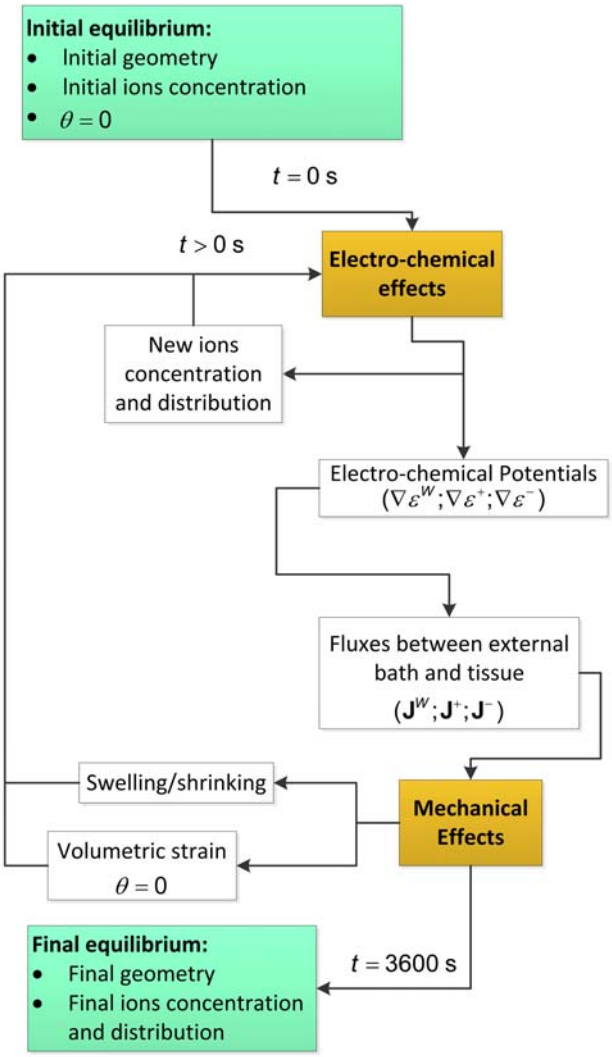

FIGURE 3.3 Schematic diagram of the computational process.

TABLE 3.1 The Parameters of the Simplified 3D Model of Cartilage

Description	Symbol	Value	References
Initial thickness of the sample	h_{sample}	0.5 mm	Sun et al. (1999)
Initial diameter of the sample	ϕ_{sample}	0.0005 mm	–
Number of mesh elements	NELEM	50	Sun et al. (1999)
Number of mesh nodes	NNODES	204	–
Young's modulus	E	$3.85 \cdot 10^5$ Pa	Sun et al. (2004)
Poisson coefficient	ν	0.28	Sun et al. (2004)
Drag coefficient between the solid and the water phase	α	$7 \cdot 10^{14}$ N s/m^4	Sun et al. (1999)
Diffusivity of the cations	D^+	$5 \cdot 10^{-10}$ m/s	Sun et al. (1999)
Diffusivity of the anions	D^-	$8 \cdot 10^{-10}$ m/s	Sun et al. (1999)

Continued

This book belongs to Central Library BADJI Mokhtar-ANNABA UNIVERSITY
Copyright Elsevier 2024

TABLE 3.1 The Parameters of the Simplified 3D Model of Cartilage—cont'd

Description	Symbol	Value	References
Initial fixed charge density	c_0^F	0.2 mEq/mL	Sun et al. (1999)
Activity coefficient of cations	γ^+	1.0	Sun et al. (1999)
Activity coefficient of anions	γ^-	1.0	Sun et al. (1999)
Gas constant	R	8.314 J/mol K	Sun et al. (1999)
Absolute temperature	T	298K	Sun et al. (1999)
Osmotic coefficient	ϕ	1.0	Sun et al. (2004)
Initial amount of water in the tissue	ϕ_0^w	0.75	Sun et al. (1999)

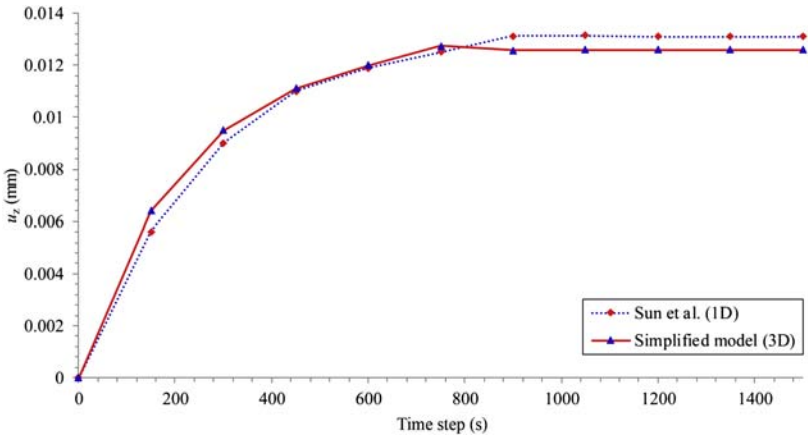

FIGURE 3.4 Comparison of the upper surface displacement in the free swelling test of the 1D model of Sun et al. (1999) and the present simplified 3D model after 1500 s of swelling.

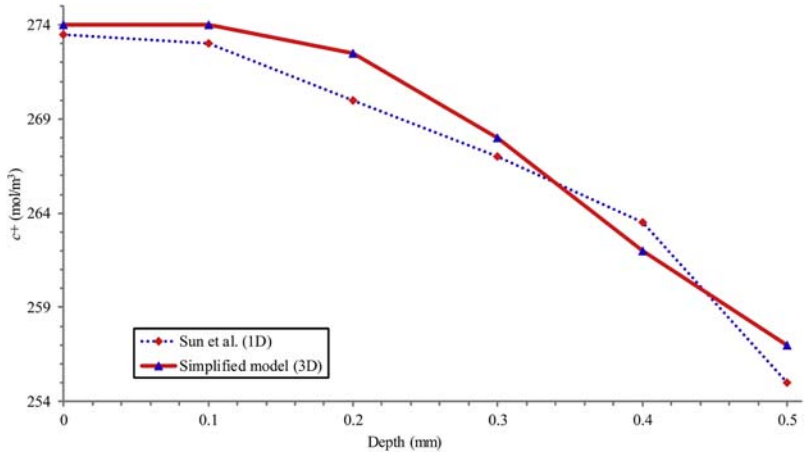

FIGURE 3.5 Comparison of cation concentration distribution in the free swelling test of the 1D model of Sun et al. (1999) and the present simplified 3D model after 100 s of swelling.

This book belongs to Central Library BADJI Mokhtar-ANNABA UNIVERSITY Copyright Elsevier 2024

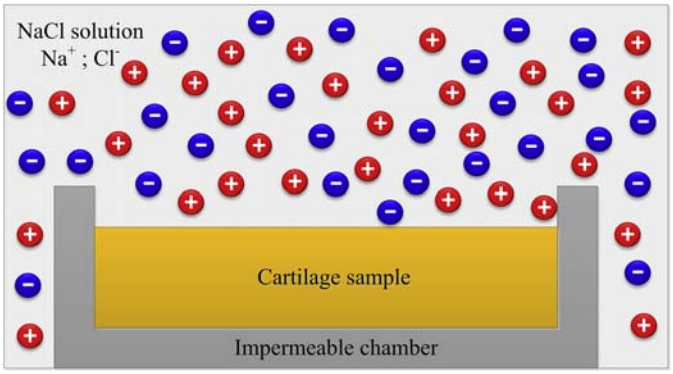

FIGURE 3.6 A sample of a cartilage of 0.5 mm thickness and 1.5 mm diameter is immersed in a NaCl solution with an initial concentration of 0.15 M. The sample is confined in an impermeable chamber.

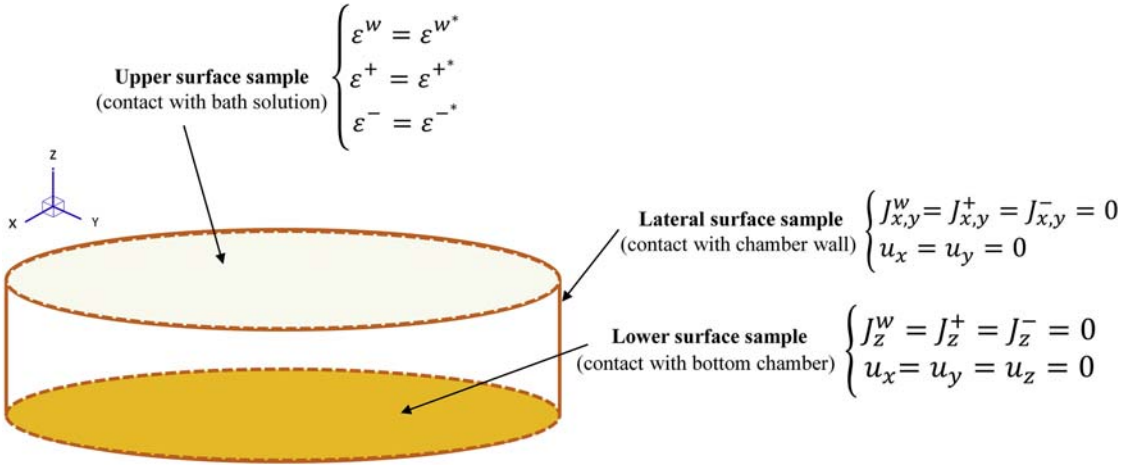

FIGURE 3.7 Boundary conditions of the cartilage sample applied in the computational simulations.

3.3.3 Initial Conditions

Initially, it is considered that the sample is in equilibrium with the external bath solution with a concentration $c_0^* = 0.15$ M of monovalent ions (Na^+ and Cl^-). At $t = 0$ s, the concentration of the external solution is decreased to 0.125 M. This reduction yields to a new equilibrium state. The initial modified chemical potential of the water $\varepsilon_0^{w^*}$ and the electrochemical potential for cations and ions, $\varepsilon_0^{+^*}$ and $\varepsilon_0^{-^*}$, inside the tissue are $\varepsilon_0^{w} = \varepsilon_0^{w^*}$; $\varepsilon_0^{+} = \varepsilon_0^{+^*}$; $\varepsilon_0^{-} = \varepsilon_0^{-^*}$. Choosing this free swollen state as the reference configuration (initial equilibrium), the initial displacement is measured from this reference state; therefore, $\mathbf{u} = 0$.

3.3.4 Free Swelling

The experiment described by Sun et al. (1999) is reproduced considering a sample diameter of 1.5 mm and the 3D confined environment reported experimentally by Frijns et al. (1997). The physiological properties of cartilage later presented in Sun et al. (2004) are considered here (Table 3.2).

Fluxes of water, cations, and anions during the process were computed, monitored, and analyzed. Furthermore, displacements of the free healthy cartilage surface are simulated.

Displacement (u_z), water (J^w), cation (J^+), and anion (J^-) fluxes are simulated during 3600 s. Simulation results were divided into five phases corresponding to the main phenomenon known experimentally (Brown and Byers, 1989). A description of the status of each phase is as follows:

Phase I (initial equilibrium): In this period, the external solution is diluted to 0.125 M of NaCl that generates an imbalance between the inner medium and outer medium of the sample. At time 0 the sample remains equilibrated with the 0.15 M of NaCl. 3D computational results did not show any deformation (Fig. 3.8). Fluxes of water (Fig. 3.9) and ions (Figs. 3.10 and 3.11) are minimum.

This book belongs to Central Library BADJI Mokhtar-ANNABA UNIVERSITY
Copyright Elsevier 2024

TABLE 3.2 3D Free Swelling Model for Healthy Cartilage Parameters

Description	Symbol	Value	References
Initial thickness of the sample	h_{sample}	0.5 mm	Sun et al. (1999)
Initial diameter of the sample	ϕ_{sample}	1.5 mm	Sun et al. (1999)
Number of mesh elements	NELEM	760	Sun et al. (1999)
Number of mesh nodes	NNODES	1026	–
Young's modulus	E	$3.85 \cdot 10^5$ Pa	Sun et al. (2004)
Poisson coefficient	ν	0.28	Sun et al. (2004)
Drag coefficient between the solid and the water phase	α	$7 \cdot 10^{14}$ N s/m^4	Sun et al. (1999)
Diffusivity of the cations	D^+	$5 \cdot 10^{-10}$ m/s	Sun et al. (1999)
Diffusivity of the anions	D^-	$8 \cdot 10^{-10}$ m/s	Sun et al. (1999)
Initial fixed charge density	c_0^F	0.2 mEq/mL	Sun et al. (1999)
Activity coefficient of cations	γ^+	0.86	Maroudas et al. (1988)
Activity coefficient of anions	γ^-	0.85	Maroudas et al. (1988)
Gas constant	R	8.314 J/mol K	Sun et al. (1999)
Absolute temperature	T	298K	Sun et al. (1999)
Osmotic coefficient	ϕ	0.8	Maroudas et al. (1988)
Initial amount of water in the tissue	ϕ_0^w	0.75	Sun et al. (1999)

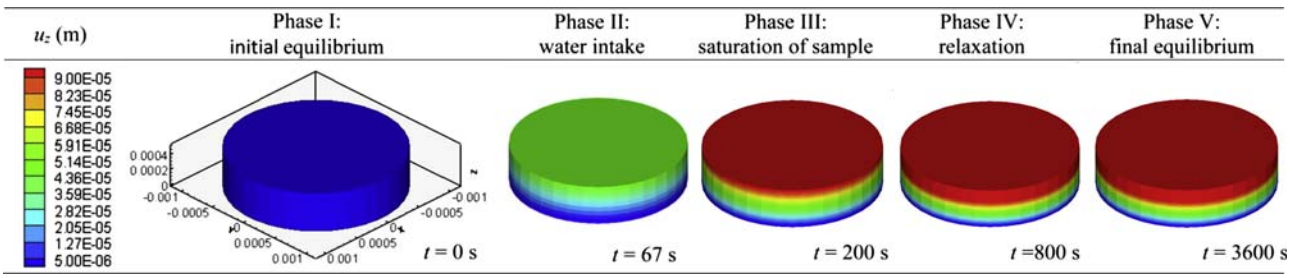

FIGURE 3.8 z-displacement (u_z) obtained with the 3D computational model during five phases of swelling in the cartilage sample.

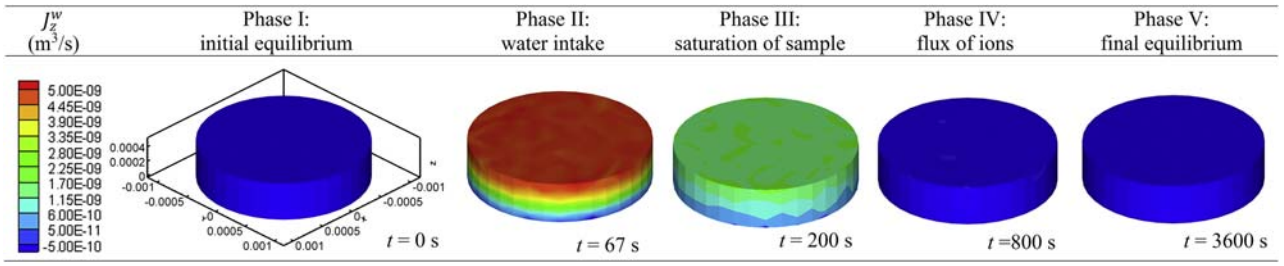

FIGURE 3.9 Water (J^w) flux obtained with the presented 3D computational model during five phases of swelling in the cartilage sample.

This book belongs to Central Library BADJI Mokhtar-ANNABA UNIVERSITY

Copyright Elsevier 2024

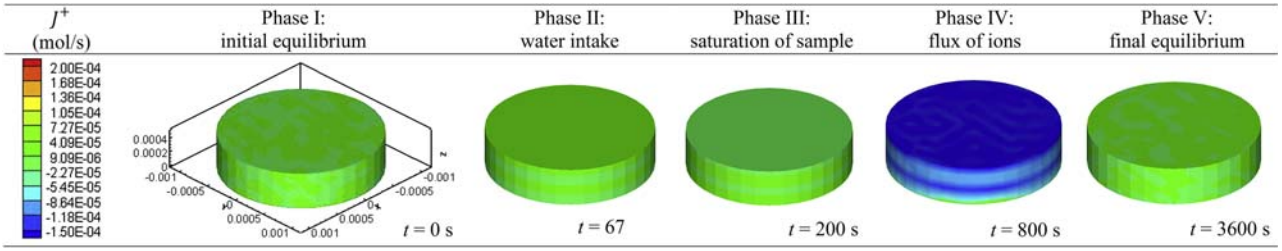

FIGURE 3.10 Cation (J^+) flux obtained with the presented 3D computational model during five phases of swelling in the cartilage sample.

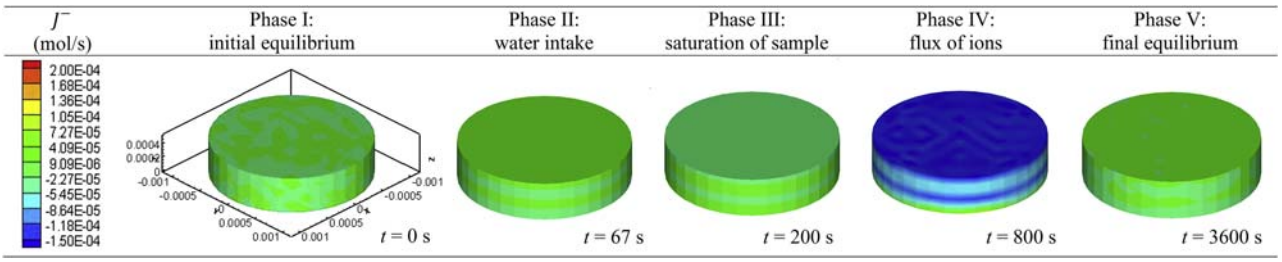

FIGURE 3.11 Anion (J^-) flux obtained with the presented 3D computational model during five phases of swelling in the cartilage sample.

Phase II: This phase represents a sudden deformation of the cartilage (Fig. 3.8) because of the considerable water intake ($5.0 \cdot 10^{-9}$ m^3/s) (Fig. 3.9). At this period, outgoing ion fluxes would be expected; nevertheless, these are clearly overwhelmed by the intake water flux (Figs. 3.10 and 3.11), which leads to subsequent substrate swelling during the next phase.

Phase III: During this phase, high displacement of the upper surface of the sample (Fig. 3.8) is observed at 200 s. This is due to the previous and continuous water flux intake during this stage (Fig. 3.9), when the maximum water content within the sample is reached. Consistently, cation flux (Fig. 3.10) and ions flux (Fig. 3.11) keep on the basal level.

Phase IV: After 800 s of simulation, the substrate deformation is maintained (Fig. 3.8); water flux is considerably reduced (Fig. 3.9) while internal and external solutions recover the equilibrium state, which enables the visualization of the previously impeded ion outflow (Fig. 3.10 and 3.11).

Phase V (final equilibrium): Finally, this phase represents the complete restoration of electrochemical equilibrium between the external and internal solution. The cartilage sample does not show any further deformation (Fig. 3.8), in agreement with no external load applied on the sample and the lack of Na and Cl ions gradient. Consistently, water (Fig. 3.9) and ion fluxes (Figs. 3.10 and 3.11) are null at this stage.

3.3.5 Sample Subjected to Loading

Compression loads relating to normal weight people (BMI $= 22.262 \mp 1.172$ kg/m^2) are applied on top of the sample. The applied pressure is that corresponding to the maximum pressure observed after 0.44 s of the human gait cycle. The experimental data are extracted from Travascio et al. (2014). Note that, for this study, they developed specific measurements in a total of 10 male subjects aged between 18 and 35 years who are volunteers. Prior to experiments, anthropometric and body measurements were collected and recorded. Accurate quantification of cation fluxes and distributions within the samples have been performed. Besides, monitoring of tissue changes during the loading processes was also carried out (Fig. 3.12).

Under normal weight (BMI $= 22.262$ kg/m^2), the model displays a maximum surface displacement of $-1.83 \cdot 10^{-4}$ m (Fig. 3.12) after 0.44 s of simulated time. This reduction in tissue deformation results in a lower outgoing water flux from the cartilage sample. A maximum value of water outflow is registered in the upper surface of the sample, $J^{\mathrm{w}} = 1.41 \cdot 10^{-8}$ m^3/s. A similar trend to that of water outflow is observed for cation fluxes. Cartilage samples show a maximum cation flux of $8.39 \cdot 10^{-4}$ mol/s in the upper surface. This flux is reduced to $6.26 \cdot 10^{-4}$ mol/s in the bottom surface. The results obtained for anion fluxes show high similarities with cation fluxes. Anions show the maximum value at the upper surface, $J^- = 7.46 \cdot 10^{-4}$ mol/s, whereas the minimum is located at the bottom surface, $J^- = 2.57 \cdot 10^{-4}$ mol/s.

This book belongs to Central Library BADJI Mokhtar-ANNABA UNIVERSITY
Copyright Elsevier 2024

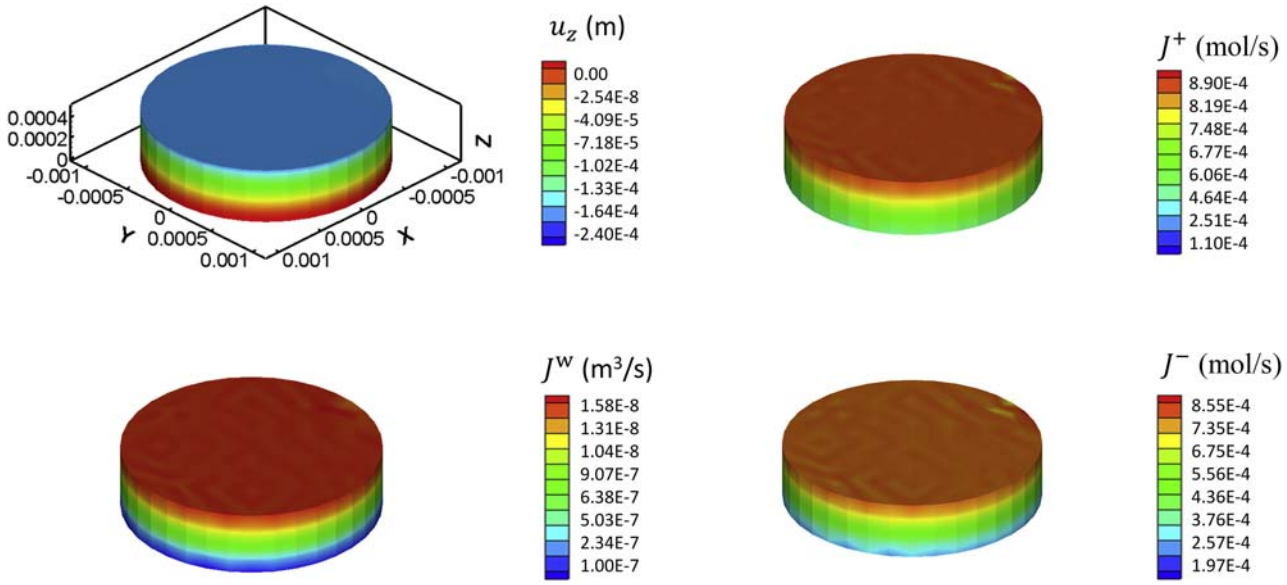

FIGURE 3.12 z-displacement (u_z), water (J^w), cation (J^+), and anion (J^-) fluxes obtained after 0.44 s of simulated human gait cycle for people with BMI = 22.262 kg/m^2.

3.4 DISCUSSION AND CONCLUSIONS

Experimental models have tried to highlight the specific relation between cartilage composition, structure, and behavior. However, the cost associated with this kind of research and the number of animals required for experiments have encouraged the emergence of computational simulations of articular tissue. In this work, a 3D mechanoelectrochemical cartilage behavior model is presented. The model incorporates important biological and physical aspects of articular cartilage such as PG repulsion due to attached negative charges, diffusive−convective phenomena, and the combined mechanoelectrochemical events that occur in cartilage tissue. It has been employed to study the cartilage free swelling as well as cartilages subjected to loading. We analyzed and quantified the effect of FCD, the porosity of the ECM, ionic diffusivity, electrochemical potentials, and mechanical ECM properties in the behavior of the cartilage tissue. The presented model has been validated by comparing the results with the 1D simulation and the experimental results of Sun et al. (1999). Despite the promising use of the model, it does have some limitations, such as including the anisotropic properties to analyze the influence of heterogeneity in tissue behavior.

Because swelling is a key process in cartilage tissue (Eisenberg and Grodzinsky, 1985; Carter and Wong, 2003; Nagel and Kelly, 2013), this event was carefully analyzed within the 3D framework. After the external solution concentration change, initial equilibrium was broken and an incoming flux of water into the sample arises to rebalance both solutions. The quick water intake results in sharp swelling of the sample. During this stage, water flux hides the comparatively low outgoing ion fluxes. However, during the later stage, this last flow becomes clear, as water current decreases.

Because of its 3D consideration, the model is sensitive to radial boundary conditions as occurs experimentally. Specifically, in the 3D model, the initial swelling delay is induced not only for values of FCD lower than 0.05 mEq/ml, as Sun et al. (1999) mentioned, but also for values of 0.11 mEq/mL. The increased sensitivity of our model is perhaps due to the inclusion of 3D boundary conditions. Furthermore, it is noted that a minimal shrinking and an associated delay in the net response are induced when including small FCDs.

The present model can be considered as a pioneer 3D computational model for simulating cartilage behavior. It could be a valuable tool for analyzing the effects of several cartilage pathologies, taking mechanoelectrochemical tissue behavior into consideration. Because of the complexity of in-vivo experimental measurements of cartilage behavior in normal loading conditions. This model presents a predictive tool to study physiological and pathological processes such as the swelling process in immobilized persons or cartilage tissue behavior in people with obesity. This, together with the capacity of the model to display the results in clinically interpretable 3D images, makes it a remarkable novel tool for the diagnosis, monitoring, and evaluation of cartilage therapies.

This book belongs to Central Library BADJI Mokhtar-ANNABA UNIVERSITY Copyright Elsevier 2024

ACKNOWLEDGMENTS

The authors gratefully acknowledge the financial support from the Spanish Ministry of Economy and Competitiveness (MINECO MAT2016-76039-C4-4-R, AEI/FEDER, UE), the Government of Aragon (DGA), and the Biomedical Research Networking Center in Bioengineering, Biomaterials and Nanomedicine (CIBER-BBN). CIBER-BBN is financed by the Instituto de Salud Carlos III with assistance from the European Regional Development Fund.

REFERENCES

Anderson, A.E., Ellis, B.J., Maas, S.A., Peters, C.L., Weiss, J.A., 2008. Validation of finite element predictions of cartilage contact pressure in the human hip joint. Journal of Biomechanical Engineering-Transactions of the Asme 130.

Bayod, J., Becerro-de-Bengoa-Vallejo, R., Losa-Iglesias, M.E., Doblare, M., 2012. Mechanical stress redistribution in the calcaneus after autologous bone harvesting. Journal of Biomechanics 45, 1219−1226.

Besier, T.F., Gold, G.E., Beaupre, G.S., Delp, S.L., 2005. A modeling framework to estimate patellofemoral joint cartilage stress in vivo. Medicine and Science in Sports and Exercise 37, 1924−1930.

Brown, R.A., Byers, P.D., 1989. Swelling of cartilage and expansion of the collagen network. Calcified Tissue International 45, 260−261.

Carter, D.R., Wong, M., 2003. Modelling cartilage mechanobiology. Philosophical Transactions of the Royal Society of London Series B-Biological Sciences 358, 1461−1471.

Crank, J., Nicolson, P., 1947. A practical method for numerical evaluation of solutions of partial differential equations of the heat-conduction type. Proceedings of the Cambridge Philosophical Society 43, 50−67.

Driessen, N.J.B., Peters, G.W.M., Huyghe, J.M., Bouten, C.V.C., Baaijens, F.P.T., 2003. Remodelling of continuously distributed collagen fibres in soft connective tissues. Journal of Biomechanics 36, 1151−1158.

Egloff, C., Hugle, T., Valderrabano, V., 2012. Biomechanics and pathomechanisms of osteoarthritis. Swiss Medical Weekly 142, 14.

Eisenberg, S.R., Grodzinsky, A.J., 1985. Swelling of articular-cartilage and other connective tissues − electromechanochemical forces. Journal of Orthopaedic Research 3, 148−159.

Frijns, A.J.H., Huyghe, J.M., Janssen, J.D., 1997. A validation of the quadriphasic mixture theory for intervertebral disc tissue. International Journal of Engineering Science 35, 1419−1429.

Gasser, T.C., Ogden, R.W., Holzapfel, G.A., 2006. Hyperelastic modelling of arterial layers with distributed collagen fibre orientations. Journal of the Royal Society Interface 3, 15−35.

Goldring, M.B., Goldring, S.R., 2010. Articular cartilage and subchondral bone in the pathogenesis of osteoarthritis. Skeletal Biology and Medicine 1192, 230−237.

Gu, W.Y., Lai, W.M., Mow, V.C., 1993. Transport of fluid and ions through a porous-permeable charged-hydrated tissue, and streaming potential data on normal bovine articular-cartilage. Journal of Biomechanics 26, 709−723.

Hayes, W.C., Mockros, L.F., 1971. Viscoelastic properties of human articular cartilage. Journal of Applied Physiology 31, 562−568.

Hosoda, N., Sakai, N., Sawae, Y., Murakami, T., 2009. Finite element analysis of articular cartilage model considering the configuration and biphasic property of the tissue. In: 13th International Conference on Biomedical Engineering, vols. 1−3, 23, pp. 1883−1887.

Huey, D.J., Hu, J.C., Athanasiou, K.A., 2012. Unlike bone, cartilage regeneration remains elusive. Science 338, 917−921.

Hughes, T.J.R., 1987. The Finite Element Method: Linear Static and Dynamic Finite Element Analysis. Prentice-Hall, United States of America, Englewood Cliffs, NJ.

Hughes, T.J.R., 2000. The Finite Element Method: Linear Static and Dynamic Finite Element Analysis. Dover Publications, Mineola, NY.

Kaasschieter, E.F., Frijns, A.J.H., Huyghe, J.M., 2003. Mixed finite element modelling of cartilaginous tissues. Mathematics and Computers in Simulation 61, 549−560.

Kiapour, A.M., Kaul, V., Kiapour, A., Quatman, C.E., Wordeman, S.C., Hewett, T.E., Demetropoulos, C.K., Goel, V.K., 2014. The effect of ligament modeling technique on knee joint kinematics: a finite element study. Applied Mathematics 4, 91−97.

Korhonen, R.K., Julkunen, P., Li, L., van Donkelaar, C.C., 2013. Computational models of articular cartilage. Computational and Mathematical Methods in Medicine 2013, 254507, 2 p.

Lai, W.M., Hou, J.S., Mow, V.C., 1991. A triphasic theory for the swelling and deformation behaviors of articular cartilage. Journal of Biomechanical Engineering-Transactions of the Asme 113, 245−258.

Li, G., Gil, J., Kanamori, A., Woo, S.L., 1999a. A validated three-dimensional computational model of a human knee joint. Journal of Biomechanical Engineering-Transactions of the Asme 121, 657−662.

Li, L.P., Soulhat, J., Buschmann, M.D., Shirazi-Adl, A., 1999b. Nonlinear analysis of cartilage in unconfined ramp compression using a fibril reinforced poroelastic model. Clinical Biomechanics 14, 673−682.

Mansour, J.M., 2003. Biomechanics of cartilage. In: Oatis, C.A. (Ed.), Kinesiology: The Mechanics and Pathomechanics of Human Movement. Lippincott Williams & Wilkins, Baltimore.

Manzano, S., Gaffney, E.A., Doblare, M., Doweidar, A.H., 2014a. Cartilage dysfunction in ALS patients as side effect of motion loss: 3D mechano-electrochemical computational model. Biomed Research International 2014, 179070, 13 p.

Manzano, S., Poveda-Reyes, S., Ferrer, G.G., Ochoa, I., Doweidar, M.H., 2014b. Computational analysis of cartilage implants based on an interpenetrated polymer network for tissue repairing. Computer Methods and Programs in Biomedicine 116, 249−259.

This book belongs to Central Library BADJI Mokhtar-ANNABA UNIVERSITY

Copyright Elsevier 2024

Manzano, S., Doblare, M., Doweidar, M.H., 2015a. Parameter-dependent behavior of articular cartilage: 3D mechano-electrochemical computational model. Computer Methods and Programs in Biomedicine 122, 491–502.

Manzano, S., Manzano, R., Doblare, M., Doweidar, M.H., 2015b. Altered swelling and ion fluxes in articular cartilage as a biomarker in osteoarthritis and joint immobilization: a computational analysis. Journal of the Royal Society Interface 12.

Manzano, S., Armengol, M., Price, A.J., Hulley, P.A., Gill, H.S., Doblare, M., Doweidar, M.H., 2016a. Inhomogeneous response of articular cartilage: a three-dimensional multiphasic heterogeneous study. PLoS One 11.

Manzano, S., Doblaré, M., Doweidar, M.H., 2016b. Altered mechano-electrochemical behavior of articular cartilage in populations with obesity. Applied Sciences 6.

Maroudas, A., Weinberg, P.D., Parker, K.H., Winlove, C.P., 1988. The distributions and diffusivities of small ions in chondroitin sulphate, hyaluronate and some proteoglycan solutions. Biophysical Chemistry 32, 257–270.

Mow, V., Guo, X.E., 2002. Mechano-electrochemical properties of articular cartilage: their inhomogeneities and anisotropies. Annual Review of Biomedical Engineering 4, 175–209.

Nagel, T., Kelly, D.J., 2013. Altering the swelling pressures within in vitro engineered cartilage is predicted to modulate the configuration of the collagen network and hence improve tissue mechanical properties. Journal of the Mechanical Behavior of Biomedical Materials 22, 22–29.

Pearle, A.D., Warren, R.F., Rodeo, S.A., 2005. Basic science of articular cartilage and osteoarthritis. Clinics in Sports Medicine 24, 1–12.

Smith, D.W., Gardiner, B.S., Davidson, J.B., Grodzinsky, A.J., 2016. Computational model for the analysis of cartilage and cartilage tissue constructs. Journal of Tissue Engineering and Regenerative Medicine 10, 334–347.

Sophia Fox, A.J., Bedi, A., Rodeo, S.A., 2009. The basic science of articular cartilage: structure, composition, and function. Sports Health 1, 461–468.

Soulhat, J., Buschmann, M.D., Shirazi-Adl, A., 1999. A fibril-network-reinforced biphasic model of cartilage in unconfined compression. Journal of Biomechanical Engineering-Transactions of the Asme 121, 340–347.

Sun, D.N., Gu, W.Y., Guo, X.E., Lai, W.M., Mow, V.C., 1999. A mixed finite element formulation of triphasic mechano-electrochemical theory for charged, hydrated biological soft tissues. International Journal for Numerical Methods in Engineering 45, 1375–1402.

Sun, D.D., Guo, X.E., Likhitpanichkul, M., Lai, W.M., Mow, V.C., 2004. The influence of the fixed negative charges on mechanical and electrical behaviors of articular cartilage under unconfined compression. Journal of Biomechanical Engineering-Transactions of the Asme 126, 6–16.

Taylor, M., Cotton, J., Zioupos, P., 2002. Finite element simulation of the fatigue behaviour of cancellous bone. Meccanica 37, 419–429.

Teng, Z.Z., Trabelsi, O., Ochoa, I., He, J., Gillard, J.H., Doblare, M., 2012. Anisotropic material behaviours of soft tissues in human trachea: an experimental study. Journal of Biomechanics 45, 1717–1723.

Travascio, F., Eltoukhy, M., Cami, S., Asfour, S., 2014. Altered mechano-chemical environment in hip articular cartilage: effect of obesity. Biomechanics and Modeling in Mechanobiology 13, 945–959.

Viceconti, M., Davinelli, M., Taddei, F., Cappello, A., 2004. Automatic generation of accurate subject-specific bone finite element models to be used in clinical studies. Journal of Biomechanics 37, 1597–1605.

Wilson, W., Huyghe, J.M., van Donkelaar, C.C., 2007. Depth-dependent compressive equilibrium properties of articular cartilage explained by its composition. Biomechanics and Modeling in Mechanobiology 6, 43–53.

Wu, J.Z., Herzog, W., 2002. Simulating the swelling and deformation behaviour in soft tissues using a convective thermal analogy. BioMedical Engineering Online 1, 8.

This book belongs to Central Library BADJI Mokhtar-ANNABA UNIVERSITY

Copyright Elsevier 2024

This page intentionally left blank

This book belongs to Central Library BADJI Mokhtar-ANNABA UNIVERSITY

Copyright Elsevier 2024

Chapter 4

Image-Driven Constitutive Modeling for FE-Based Simulation of Soft Tissue Biomechanics

D.M. Pierce[1], T. Ricken[2] and C.P. Neu[3]

[1]University of Connecticut, Storrs, CT, United States; [2]TU Dortmund University, Dortmund, Germany; [3]University of Colorado Boulder, Boulder, CO, United States

4.1 INTRODUCTION AND MOTIVATION

4.1.1 Hallmarks of Soft Tissues

Structural complexity and hierarchy are hallmarks of natural biological tissues. The remarkable characteristics of biological materials include their multiconstituent, hierarchical, and heterogeneous structure. The mechanical response of such materials relies on physical phenomena occurring at multiple length-scales, from the molecular scale all the way up to tissue and organ scales. In fact, soft tissues derive their properties from complex interactions among their microstructural components and arise as a kind of "emergent behavior" from the underlying constituents.

Load-bearing tissues of the body, including the articular cartilage covering the bony ends of our joints, exhibit exquisite structural (zonal) complexity and hierarchical elements that transfer tissue-level forces directly to cellular (chondrocyte) substructures. When damage or disease occurs in tissues, the complex organization that constitutive biomolecules form to support cell function is often lost. Moreover, tissue biomechanics and chondrocyte mechanobiology and gene expression are altered in the pathophysiology of osteoarthritis (OA), a degenerative disease and common orthopedic problem, afflicting nearly 20% of the US population.

Articular cartilage has features representative of many soft tissues and thus lends itself toward use as a model system for controlled computational and experimental studies. Cartilage in the adult or mature form is generally considered avascular and aneural. The tissue is thin, with a high (width to depth) aspect ratio. The primary mechanical functions are load transfer and low friction/wear, such that articulation of joints is possible for many decades of life (Neu et al., 2008). The tissue's simplicity on first glance is deceptive, especially considering the complex arrangement of structural elements and biomolecules that define cartilage. The tissue is known to exhibit a strong structural gradient through its thickness, with collagen fiber orientation, concentrations of collagens, proteoglycans and other small molecules, cell subpopulations and morphologies, and material stiffness, all varying from the articular surface to the underlying subchondral bone. Cartilage shares many features of the structural heterogeneity observed in related soft tissues and thus serves as an ideal model system for the development of computational and experimental approaches, with significant disease relevance.

4.1.2 Finite Element Modeling of Soft Tissues

Medical imaging may be used to estimate tissue morphology, microstructure, and even strains, but estimating and predicting intratissue stresses, e.g., in joints, requires computational modeling. Despite the extreme complexity of the mechanisms underlying the function of soft tissues, computational modeling can bring together biological and medical data with physics and engineering to generate new knowledge, e.g., to understand biological mechanisms, to predict disease onset or progression, or to measure therapeutic benefits. Finite element (FE) simulations of fibrous soft tissues

Numerical Methods and Advanced Simulation in Biomechanics and Biological Processes. https://doi.org/10.1016/B978-0-12-811718-7.00004-6
Copyright © 2018 Elsevier Ltd. All rights reserved.

This book belongs to Central Library BADJI Mokhtar-ANNABA UNIVERSITY

Copyright Elsevier 2024

(e.g., cartilage) are an increasingly valuable tool in biomechanical analyses. Given the complexity of soft tissues, we suggest that 3D large-strain, multiscale, and multiphase material models, implemented in FEs, present the best opportunity to establish a generally applicable mathematical framework for studying questions in soft tissue mechanics.

There are three general approaches to quantify complex material behaviors with material modeling: (1) theoretically, based on detailed microstructural information; (2) experimentally, based directly on experimentally generated data; and (3) by trial and error, based on testing formulations for their ability to fit data (Humphrey, 2008). As in many areas of applied mechanics, phenomenological formulations based on years of experience, and possibly motivated by limited microstructural data, continue to pervade biomechanics (Humphrey, 2008). This approach has been successful in matching many global tissue responses using simulations (e.g., arteries Weisbecker et al., 2012; Pierce et al., 2015, myocardium Göktepe et al., 2011, cornea Coudrillier et al., 2012, and cartilage Ateshian et al., 2009) and even extended to include phenomenological measures of fiber−matrix interactions (e.g., tendon Guerin and Elliott, 2005, muscle Gao et al., 2008, and planar soft tissues Fan and Sacks, 2014). Regarding soft tissues, including cartilage, the theory of porous media (TPM) provides a particularly relevant approach because these tissues comprise of a large fraction of water (Bowen, 1982; Ehlers, 1993; de Boer, 2000; Pence, 2012).

4.1.3 Need for Imaging Data to Drive Models

Recent advances in medical imaging modalities make previously unavailable biological and structural data available for the study of complex biological tissues and tissue replacements. Critical to these experimental advancements is the incorporation of advanced mathematical and computational models for simulating and characterizing tissue response and deformation, e.g., in image processing and data analysis. Conversely, data generated from such medical imaging modalities also directly impact many fields in mechanics, e.g., inspiring new constitutive formulations and calibrating computational models of biological tissues. Combinations of these elements are also important in the pursuit of a more complete biological characterization of cellular function, including mechanosensing and mechanotransduction. Medical and morphological imaging-based experimental characterization, multiscale and multiphase computational modeling, and potential synergies among these fundamental ingredients are therefore potentially transformational when applied to the study of biological tissues in health and disease, and engineered tissue replacements.

We focused our discussion of experimental techniques toward imaging methods capable of providing numerous noninvasive and nondestructive measures of structural/microstructural integrity, i.e., without altering the material or removing it from a native environment and without causing or propagating damage. Imaging modalities, including magnetic resonance imaging (MRI), are able to provide measures of morphology and shape defining the geometry of a tissue or material. However, modern developments in imaging, based on conventional methods, now also provide numerous additional and critical measures defining mechanical parameters that may directly motivate and support developments in continuum modeling, including diffusion, material properties, and strain.

4.2 BUILDING BLOCKS OF A MULTIPHASE CONTINUUM MODEL

In light of the complex fluid, ion, and solid interactions, which occur in many soft tissues during deformation, the most successful constitutive modeling approaches for 3D FE modeling build on some variation of multiphase continuum modeling. Constitutive models describing multiphase materials are generally based on the mixture theory (Whitaker, 1977; Hassanizadeh and Gray, 1979a,b, 1980; Mow et al., 1989; Lai et al., 1991), the theory of poromechanics (Abousleiman et al., 1996; Chen and Detournay, 1998; Coussy, 2004), or the TPM (Bowen, 1980, 1982; Ehlers, 1989, 1993; de Boer, 2000). As a representative example, we focus here on a continuum description of a multiconstituent material using the macroscopic TPM.

4.2.1 Multiphase Framework

The basics of the TPM include the mixture theory, the concept of volume fractions in connection with the saturation condition, the kinematics, the balance equations, and evaluation of the entropy inequality in view of the derivation of restrictions for constitutive relations (Drumheller, 1978; Bowen, 1980, 1982; Ehlers, 1989, 2002; de Boer, 1996, 2000; Bluhm, 2002). This theory facilitates the description of a variety of materials characterized by a solid matrix filled with one or more mobile fluid or gas phases.

Because of different material properties, individual motion of the constituents and the high number of interactions among them, describing the material behavior directly via an FE discretization becomes highly complex. In the case of

This book belongs to Central Library BADJI Mokhtar-ANNABA UNIVERSITY
Copyright Elsevier 2024

locally homogeneous and statistically regular composition of the constituents, however, the material can be modeled using mixture theory in connection with the concept of volume fractions. In this concept a "smeared" substitute continuum results with reduced densities for the constituents. One proceeds, therefore, from the microlevel to a macrolevel, whereby one averages the microquantities and substitutes macroquantities. Mechanical analyses are thus performed on the macroscale, avoiding complications connected with the microscale.

In the following sections, we present the basic concepts of the TPM required to develop constitutive models.

4.2.1.1 Concept of Volume Fractions

In the framework of TPM we consider a porous material composed of k individual constituents. We assume that the constituents are homogeneously distributed over the control space. In connection with the macroscopic description, we assume that each individual partial constituent occupies the whole control space separately and simultaneously. We define all geometric and physical quantities of the individual phases, such as motion, deformation, or stress, within the total control space. Thus we interpret those quantities as statistically averaged values of the real quantities. We locally define the volume fractions as the ratio of the partial volume to the total volume. Constituents are identifiable at a point in the control volume, and we represent microlevel actions on the macrolevel (de Boer, 1996).

Here we formulate the volume fraction concept with respect to both the reference and current configurations. We define the control space by corresponding configurations of the solid phase. In the reference configuration (time $t = t_0$) we consider the control space $\mathcal{B}_{0S}$ with the surface $\partial\mathcal{B}_{0S}$ and in the current configuration (time t) we consider the control space $\mathcal{B}_S$ with the surface $\partial\mathcal{B}_S$. The surface of the solid phase builds a material surface for the solid constituent, whereas the surface is of a nonmaterial type in the case of the mobile liquid and gas phases.

Now, in the reference configuration for constituent φ^α, we postulate the existence of the volume fraction as

$$n_{0\alpha}^\alpha = n_{0\alpha}^\alpha(\mathbf{X}_\alpha, t = t_0), \tag{4.1}$$

at a material point X_α at the position $\mathbf{X}_\alpha$. Therefore we define the partial volume V_0^α of φ^α as

$$V_0^\alpha = \int_{\mathcal{B}_{0S}} n_{0\alpha}^\alpha \mathrm{d}V_{0\alpha} = \int_{\mathcal{B}_{0S}} \mathrm{d}V_{0\alpha}^\alpha, \tag{4.2}$$

where

$$\mathrm{d}V_{0\alpha}^\alpha = n_{0\alpha}^\alpha \mathrm{d}V_{0\alpha}. \tag{4.3}$$

The quantities $\mathrm{d}V_{0\alpha}$ and $\mathrm{d}V_{0\alpha}^\alpha$ in Eqs. (4.2) and (4.3) represent the real and partial volume elements, respectively, in the reference configuration. Considering Eqs. (4.1) and (4.2), the volume of the control space is

$$V_0 = \int_{\mathcal{B}_{0S}} \mathrm{d}V_{0\alpha} = \sum_{\alpha=1}^{k} V_0^\alpha = \int_{\mathcal{B}_{0S}} \sum_{\alpha=1}^{k} \mathrm{d}V_0^\alpha = \int_{\mathcal{B}_{0S}} \sum_{\alpha=1}^{k} n_{0\alpha}^\alpha \mathrm{d}V_{0\alpha}. \tag{4.4}$$

From this it follows that the volume fractions in the reference configuration must satisfy the local statement

$$\sum_{\alpha=1}^{k} n_{0\alpha}^\alpha = 1, \tag{4.5}$$

at every point in the control space $\mathcal{B}_{0S}$. In the TPM this constraint is the saturation condition in the reference configuration. Moreover, analogous to Eq. (4.1), we postulate the volume fraction

$$n^\alpha = n^\alpha(\mathbf{x}, t), \tag{4.6}$$

for constituent φ^α at the position $\mathbf{x}$ at time t with regard to the current configuration. We define the partial control volume by

$$V^\alpha = \int_{\mathcal{B}_S} n^\alpha \mathrm{d}v, \tag{4.7}$$

in the control space, wherein $\mathrm{d}v = \mathrm{d}v(\mathbf{x}, t)$ represents the volume element in the current configuration. In the current configuration the partial volume elements are

$$\mathrm{d}v^\alpha = n^\alpha \mathrm{d}v. \tag{4.8}$$

This book belongs to Central Library BADJI Mokhtar-ANNABA UNIVERSITY
Copyright Elsevier 2024

We assign total volume of the control space $\mathcal{B}_S$ with the surface $\partial\mathcal{B}_S$ analogous to Eq. (4.4) with

$$V = \int_{\mathcal{B}_S} \mathrm{d}v = \sum_{\alpha=1}^{k} V^{\alpha} = \int_{\mathcal{B}_S} \sum_{\alpha=1}^{k} \mathrm{d}v^{\alpha} = \int_{\mathcal{B}_S} \sum_{\alpha=1}^{k} n^{\alpha} \mathrm{d}v, \tag{4.9}$$

where once again, the saturation condition

$$\sum_{\alpha=1}^{k} n^{\alpha} = 1, \tag{4.10}$$

must be satisfied for the sum of the volume fractions in the current configuration. Considering the concept of volume fractions in mixture theory, it is necessary to introduce effective densities. As a result, we obtain a relationship among the quantities in the balance equations of mixture theory, the volume fractions, and the saturation condition in Eq. (4.5) or (4.10). We describe the total mass of all k constituents of the multiphase body in the reference configuration (with respect to $\mathcal{B}_{0S}$) as

$$M_0 = \sum_{\alpha=1}^{k} M_0^{\alpha} = \int_{\mathcal{B}_{0S}} \sum_{\alpha=1}^{k} \rho_{0\alpha}^{\alpha} \mathrm{d}V_{0\alpha}, \tag{4.11}$$

and in the current configuration (with respect to $\mathcal{B}_S$) as

$$M = \sum_{\alpha=1}^{k} M^{\alpha} = \int_{\mathcal{B}_S} \sum_{\alpha=1}^{k} \rho^{\alpha} \mathrm{d}v. \tag{4.12}$$

In Eqs. (4.11) and (4.12) the quantities

$$\rho_{0\alpha}^{\alpha} = \rho_{0\alpha}^{\alpha}(\mathbf{X}_{\alpha}, t = t_0), \tag{4.13}$$

and

$$\rho^{\alpha} = \rho^{\alpha}(\mathbf{x}, t), \tag{4.14}$$

denote the partial densities in the reference configuration at position $\mathbf{X}_{\alpha}$ and in the current configuration at position $\mathbf{x}$, respectively. We define the real densities in the reference configuration as

$$\rho_{0\alpha}^{\alpha\mathrm{R}} = \rho_{0\alpha}^{\alpha\mathrm{R}}(\mathbf{X}_{\alpha}, t = t_0), \tag{4.15}$$

relating to the partial volume element $\mathrm{d}V_{0\alpha}^{\alpha}$ and for the current configuration as

$$\rho^{\alpha\mathrm{R}} = \rho^{\alpha\mathrm{R}}(\mathbf{x}, t), \tag{4.16}$$

relating to the partial volume element $\mathrm{d}v$. With Eqs. (4.15) and (4.16), we describe the partial mass of the constituent φ^{α} in the reference configuration as

$$M_0^{\alpha} = \int_{\mathcal{B}_{0S}} \rho_{0\alpha}^{\alpha} \mathrm{d}V_{0\alpha} = \int_{\mathcal{B}_{0S}} \rho_{0\alpha}^{\alpha\mathrm{R}} \mathrm{d}V_{0\alpha}^{\alpha}, \tag{4.17}$$

and in the current configuration as

$$M^{\alpha} = \int_{\mathcal{B}_S} \rho^{\alpha} \mathrm{d}v = \int_{\mathcal{B}_S} \rho^{\alpha\mathrm{R}} \mathrm{d}v^{\alpha}. \tag{4.18}$$

When comparing Eqs. (4.17) and (4.18) with Eqs. (4.11) and (4.12), respectively, and with regard to Eqs. (4.3) and (4.8), we describe the relationship between the partial densities and the real densities in the reference configuration as

$$\rho_{0\alpha}^{\alpha} = n_{0\alpha}^{\alpha} \rho_{0\alpha}^{\alpha\mathrm{R}}, \tag{4.19}$$

and in the current configuration as

$$\rho^{\alpha} = n^{\alpha} \rho^{\alpha\mathrm{R}}. \tag{4.20}$$

Physically, the real densities represent the true densities of the k constituents φ^{α} on the macrolevel.

This book belongs to Central Library BADJI Mokhtar-ANNABA UNIVERSITY
Copyright Elsevier 2024

4.2.1.2 Kinematics

We treat the saturated multiphase solid as an immiscible mixture of all constituents φ^α with particles X_α, thereby assuming that the partial bodies exist with a homogeneous distribution of the constituents over the control space. Invoking superposition of the continua, at any time t, each spatial point $\mathbf{x}$ of the current configuration must simultaneously be occupied by material points X_α of all k constituents φ^α. We assign each constituent its own independent motion function

$$\mathbf{x} = \boldsymbol{\chi}_\alpha(\mathbf{X}_\alpha, t), \quad \mathbf{x} \in \mathcal{B}_S, \tag{4.21}$$

and we postulate the motion function $\boldsymbol{\chi}_\alpha$ to be unique and continuous (Holzapfel, 2000). Using the Lagrangian description of motion, i.e., Eq. (4.21), we define the velocity and acceleration of the material points X_α as

$$\mathbf{x}'_\alpha = \frac{\partial \boldsymbol{\chi}_\alpha(\mathbf{X}_\alpha, t)}{\partial t}, \quad \mathbf{x}''_\alpha = \frac{\partial^2 \boldsymbol{\chi}_\alpha(\mathbf{X}_\alpha, t)}{\partial t^2}, \tag{4.22}$$

respectively. Inverting the Lagrangian motion function Eq. (4.21) yields the Eulerian description of motion

$$\mathbf{X}_\alpha = \boldsymbol{\chi}_\alpha^{-1}(\mathbf{x}, t). \tag{4.23}$$

With Eq. (4.23), we obtain Eulerian descriptions of the velocity and acceleration fields as

$$\mathbf{x}'_\alpha = \mathbf{x}'_\alpha(\mathbf{x}, t) = \mathbf{x}'_\alpha\left[\boldsymbol{\chi}_\alpha^{-1}(\mathbf{x}, t), t\right], \quad \mathbf{x}''_\alpha = \mathbf{x}''_\alpha(\mathbf{x}, t) = \mathbf{x}''_\alpha\left[\boldsymbol{\chi}_\alpha^{-1}(\mathbf{x}, t), t\right], \tag{4.24}$$

respectively.

Starting from the Lagrangian motion function of each constituent Eq. (4.21) we define $\mathbf{F}_\alpha$, the deformation gradient of the constituent φ^α, as

$$\mathbf{F}_\alpha = \frac{\partial \boldsymbol{\chi}_\alpha(\mathbf{X}_\alpha, t)}{\partial \mathbf{X}_\alpha} = \frac{\partial \mathbf{x}}{\partial \mathbf{X}_\alpha} = \mathrm{Grad}_\alpha \boldsymbol{\chi}_\alpha. \tag{4.25}$$

Additionally, the Eulerian description of the motion Eq. (4.23) implies that $\mathbf{F}_\alpha$ is nonsingular, and with a nonzero Jacobian J_α as

$$J_\alpha = \det \mathbf{F}_\alpha. \tag{4.26}$$

We give the inverse of the deformation gradient $\mathbf{F}_\alpha$ as

$$\mathbf{F}_\alpha^{-1} = \frac{\partial \boldsymbol{\chi}_\alpha^{-1}(\mathbf{x}, t)}{\partial \mathbf{x}} = \frac{\partial \mathbf{X}_\alpha}{\partial \mathbf{x}} = \mathrm{grad}\, \mathbf{X}_\alpha. \tag{4.27}$$

Considering Eqs. $(4.22)_1$ and $(4.24)_1$, we define the material and spatial velocity gradients as

$$(\mathbf{F}_\alpha)'_\alpha = \frac{\partial \mathbf{x}'_\alpha}{\partial \mathbf{X}_\alpha} = \mathrm{Grad}_\alpha \mathbf{x}'_\alpha, \quad \mathbf{l}_\alpha = \left(\mathrm{Grad}_\alpha \mathbf{x}'_\alpha\right)\mathbf{F}_\alpha^{-1} = \mathrm{grad}\, \mathbf{x}'_\alpha, \tag{4.28}$$

respectively. Additive decomposition of the spatial velocity gradient $\mathbf{l}_\alpha$ as

$$\mathbf{l}_\alpha = \mathbf{d}_\alpha + \mathbf{w}_\alpha, \tag{4.29}$$

yields the symmetric rate of deformation tensor $\mathbf{d}_\alpha$ and the skew-symmetric spin (rate of rotation) tensor $\mathbf{w}_\alpha$ of $\mathbf{l}_\alpha$ with

$$\mathbf{d}_\alpha = \frac{1}{2}\left(\mathbf{l}_\alpha + \mathbf{l}_\alpha^{\mathrm{T}}\right), \quad \mathbf{w}_\alpha = \frac{1}{2}\left(\mathbf{l}_\alpha - \mathbf{l}_\alpha^{\mathrm{T}}\right). \tag{4.30}$$

In general, the individual constituents k undergo different motions, and we must therefore consider different material time derivatives. For scalar fields depending on $\mathbf{x}$ and t, we define the material time derivatives as

$$(\cdot)'_\alpha = \frac{\partial(\cdot)}{\partial t} + [\mathrm{grad}(\cdot)]\cdot \mathbf{x}'_\alpha, \tag{4.31}$$

with $\mathrm{grad}(\cdot) = \partial(\cdot)/\partial \mathbf{x}$. A review of the kinematics of porous media can be found in de Boer (2000).

4.2.1.3 Balance Equations

In the TPM, we establish balance equations—balance of mass, balance of linear momentum, balance of angular momentum, and balance of energy—for each constituent φ^α analogous to the classical (one constituent) continua and for

This book belongs to Central Library BADJI Mokhtar-ANNABA UNIVERSITY
Copyright Elsevier 2024

the whole mixture. Additionally, we must account for interaction effects (supply terms) (von Terzaghi, 1943). We introduce interaction effects into the balance equations such that the summation of the balance equations of all k constituents results in the balance equation of a one-component material when superimposed, i.e., the sum of the interaction effects must equal zero. This condition results from the third metaphysical principle of Truesdell (1984).

The balance of mass for constituent φ^α in the local form reads

$$(\rho^\alpha)'_\alpha + \rho^\alpha \operatorname{div} \mathbf{x}'_\alpha = \widehat{\rho}^\alpha, \tag{4.32}$$

where the mass supply $\widehat{\rho}^\alpha$ results from the mass exchange between constituent φ^α and the remaining $(k-1)$ constituents simultaneously present at point $\mathbf{x}$ at time t. We represent the total balance of mass for the mixture as (Truesdell, 1984)

$$\sum_{\alpha=1}^{k}\left[(\rho^\alpha)'_\alpha + \rho^\alpha \operatorname{div} \mathbf{x}'_\alpha\right] = \sum_{\alpha=1}^{k}\widehat{\rho}^\alpha \overset{!}{=} 0. \tag{4.33}$$

Excluding mass exchanges between the constituents φ^α, we obtain

$$\rho^\alpha = \rho^\alpha_{0\alpha}(\det \mathbf{F}_\alpha)^{-1}. \tag{4.34}$$

The balance of linear momentum for constituent φ^α in the local form reads

$$\operatorname{div}\boldsymbol{\sigma}^\alpha + \rho^\alpha\left(\mathbf{b}^\alpha - \mathbf{x}''_\alpha\right) = \widehat{\rho}^\alpha \mathbf{x}'_\alpha - \widehat{\mathbf{p}}^\alpha, \tag{4.35}$$

where $\boldsymbol{\sigma}^\alpha$ is the partial Cauchy stress tensor, $\mathbf{b}^\alpha$ is the body force per unit mass and $\widehat{\mathbf{p}}^\alpha$ describes the interaction forces between constituent φ^α and the remaining $(k-1)$ constituents simultaneously present at point $\mathbf{x}$ at time t. The sum of Eq. (4.35) over all k constituents yields the total local balance of linear momentum for the mixture as

$$\sum_{\alpha=1}^{k}\left[\operatorname{div}\boldsymbol{\sigma}^\alpha + \rho^\alpha\left(\mathbf{b}^\alpha - \mathbf{x}''_\alpha\right)\right] = \sum_{\alpha=1}^{k}\left[\widehat{\rho}^\alpha \mathbf{x}'_\alpha - \widehat{\mathbf{p}}^\alpha\right]. \tag{4.36}$$

Following the third metaphysical principle of Truesdell, we must fulfill the condition

$$\sum_{\alpha=1}^{k}\widehat{\mathbf{p}}^\alpha \overset{!}{=} 0. \tag{4.37}$$

Assuming nonpolar partial bodies, the balance of angular momentum at a fixed point 0 for constituent φ^α in the local form reads

$$\mathbf{x} \times \left[\operatorname{div}\boldsymbol{\sigma}^\alpha + \rho^\alpha\left(\mathbf{b}^\alpha - \mathbf{x}''_\alpha\right) + \widehat{\mathbf{p}}^\alpha - \widehat{\rho}^\alpha \mathbf{x}'_\alpha\right] + \boldsymbol{\varepsilon}\colon (\boldsymbol{\sigma}^\alpha)^{\mathrm{T}} = \mathbf{0}, \tag{4.38}$$

where $\boldsymbol{\varepsilon}$ is the third order permutation tensor (cf. Holzapfel, 2000). Given the local balance of linear momentum Eq. (4.35), the local balance of angular momentum Eq. (4.38) simplifies to

$$\boldsymbol{\varepsilon}\colon (\boldsymbol{\sigma}^\alpha)^{\mathrm{T}} = \mathbf{0}, \tag{4.39}$$

which we have fulfilled if the partial Cauchy stress tensor is symmetric, i.e.,

$$\boldsymbol{\sigma}^\alpha = (\boldsymbol{\sigma}^\alpha)^{\mathrm{T}}, \tag{4.40}$$

for all k constituents.

To describe thermomechanical effects, e.g., phase transitions in multiphase solids, one must include additional equations for the balance of energy, as they couple thermal fields (temperature, heat flux and internal heat supply) with mechanical fields (motion, velocity, acceleration, deformation, and velocity of deformation). In the case of a one-component material, the balance of energy states that the sum of material time derivatives of the internal and kinetic energies equals the sum of the rates of both mechanical work and mechanical heat. We can also apply this statement to multiphase materials in the context of the TPM to obtain equations for the local balance of energy governing each constituent φ^α, as well as the total mixture. Because most models for soft tissues assume isothermal conditions, either under in vivo conditions or thermally controlled laboratory conditions, these equations are out of the current scope; for more information see, e.g., (de Boer, 2000; Ehlers, 2002). One can find detailed discussions about the balance equations in the TPM in Bowen (1980, 1982), Ehlers (1989), and de Boer (1996, 2000).

This book belongs to Central Library BADJI Mokhtar-ANNABA UNIVERSITY
Copyright Elsevier 2024

4.2.1.4 Entropy Inequality and Constitutive Formulation

To develop thermodynamically consistent constitutive models, we must account for the entropy inequality of the total body (de Boer, 1996, 2000; Ehlers, 2002). Using the balance equations (Section 4.2.1.4), we describe the local entropy inequality for the total body under quasistatic, isothermal conditions with mass exchanges as

$$\sum_{\alpha=1}^{k}\left\{-\rho^{\alpha}(\Psi^{\alpha})'_{\alpha}-\widehat{\rho}^{\alpha}\left(\Psi^{\alpha}-\frac{1}{2}\mathbf{x}'_{\alpha}\cdot\mathbf{x}'_{\alpha}\right)+\boldsymbol{\sigma}^{\alpha}:\mathbf{d}_{\alpha}-\widehat{\mathbf{p}}^{\alpha}\cdot\mathbf{x}'_{\alpha}\right\}\geq 0, \tag{4.41}$$

where Ψ^{α} is the Helmholtz free-energy function for constituent φ^{α}. The arguments and form of the Helmholtz free-energy functions for each constituent form the foundation of modern continuum constitutive modeling in the context of the TPM. This form of the entropy inequality Eq. (4.41) is sufficient and convenient for obtaining restrictions on subsequent constitutive modeling.

4.2.2 Biphasic, Fiber-Reinforced Example for Soft Tissues

To illustrate the basic framework of the TPM, we detail a general approach to modeling soft tissues as fiber-reinforced, biphasic materials.

4.2.2.1 Assumptions

First, we assume that the soft tissue consists of two phases: a porous matrix solid rich in collagen φ^{S} saturated by an interstitial fluid φ^{F}; hence $\varphi=\varphi^{\mathrm{S}}+\varphi^{\mathrm{F}}$. Second, we assume that both phases are individually incompressible, i.e., $(\rho^{\mathrm{SR}})'_{\mathrm{S}}=0$ and $(\rho^{\mathrm{FR}})'_{\mathrm{F}}=0$. This idealization is valid for most biological tissues because the volume change of the real material is negligible in contrast to the pore deformation (Humphrey, 2002). Our third assumption is that we can neglect mass exchanges between the solid and the fluid constituents (immiscibility). Finally, we assume that dynamic effects are negligible (quasistatic), so we restrict both phases to exclude inertial terms, i.e., $\mathbf{x}''_{\mathrm{S}}=\mathbf{0}$ and $\mathbf{x}''_{\mathrm{F}}=\mathbf{0}$.

4.2.2.2 Volume Fractions

We represent the microscopic structure of the tissue with a homogeneous distribution of the constituents over a representative elementary volume in such a way that we describe the distribution of the constituents by an average volume fraction n^{α}. The volume fractions n^{α} relate the volume elements $\mathrm{d}v^{\alpha}$ of the individual constituents φ^{α} to the bulk volume element $\mathrm{d}v$ with

$$n^{\alpha}(\mathbf{x},t)=\frac{\mathrm{d}v^{\alpha}}{\mathrm{d}v},\quad \sum_{\alpha=1}^{k}n^{\alpha}(\mathbf{x},t)=\sum_{\alpha=1}^{k}\frac{\rho^{\alpha}}{\rho^{\alpha\mathrm{R}}}=1,\quad \alpha\in\{\mathrm{S},\mathrm{F}\}, \tag{4.42}$$

where $\mathbf{x}$ is the position vector of the spatial point x, t is the time, and S and F denote the solid and fluid, respectively. The volume fractions n^{α} in Eq. $(4.42)_1$ satisfy the saturation condition Eq. $(4.42)_2$ for k constituents φ^{α}. From Eq. (4.42) we develop a homogenized model with superimposed continua, see Fig. 4.1.

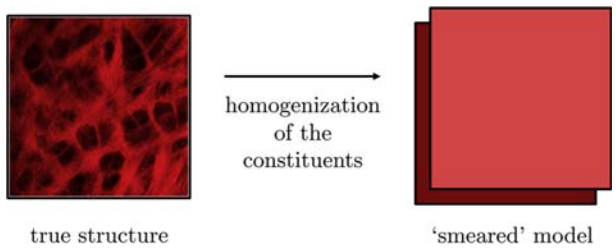

FIGURE 4.1 Schematic representation of the true structure of a soft tissue and the corresponding statistically isotropic homogenization in the context of the theory of porous media. *Adapted from Pierce, D.M., 2013. Constitutive Modeling of Articular Cartilage [Habilitation (Venia Legendi) Thesis in Experimental and Computational Biomechanics]. Graz University of Technology, Austria.*

This book belongs to Central Library BADJI Mokhtar-ANNABA UNIVERSITY Copyright Elsevier 2024

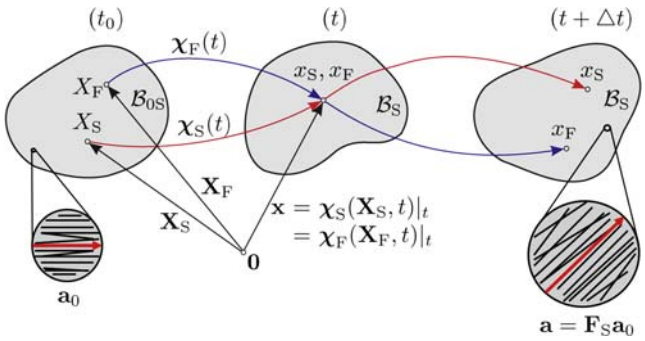

FIGURE 4.2 Schematic illustration of the motions of solid and fluid particles within a soft tissue modeled as a fluid saturated, fiber-reinforced porous solid in the context of the theory of porous media (Pierce, 2013).

4.2.2.3 Kinematics

We treat the saturated porous solid as an immiscible mixture of constituents φ^α, $\alpha \in \{S, F\}$, with particles X_α, where at any time t each spatial point x_S of the current solid placement is simultaneously occupied by fluid particles x_F. These particles proceed from different reference positions $\mathbf{X}_\alpha$ at time $t = t_0$, so we assign each constituent its own independent motion function. Fig. 4.2 schematically illustrates the motions of solid and fluid particles within cartilage tissue modeled as a fluid-saturated, fiber-reinforced porous solid in the context of the TPM.

In Fig. 4.2 the (reference) direction vector $\mathbf{a}_0$, with $|\mathbf{a}_0| = 1$ characterizes the local direction of principal collagen fiber reinforcement. We obtain the current direction of principal collagen fiber reinforcement by the push forward of $\mathbf{a}_0$ as $\mathbf{a} = \mathbf{F}_S\mathbf{a}_0$. In connection with $\mathbf{a}_0$, the pseudoinvariant $I_4 = \mathbf{C}_S{:}\mathbf{a}_0 \otimes \mathbf{a}_0 = \mathbf{a}_0 \cdot \mathbf{C}_S\mathbf{a}_0 = \mathbf{F}_S\mathbf{a}_0 \cdot \mathbf{F}_S\mathbf{a}_0 = \mathbf{a} \cdot \mathbf{a}$ often arises in the context of constitutive modeling of fiber-reinforced materials, with $\mathbf{M}_0 = \mathbf{a}_0 \otimes \mathbf{a}_0$ a corresponding Lagrangian structural tensor and with $\mathbf{M} = \mathbf{a} \otimes \mathbf{a}$ as its Eulerian counterpart. Note that I_4 has a clear physical interpretation as it is the square of the stretch of the collagen fiber network in the direction $\mathbf{a}$ (Holzapfel, 2000). During deformation $\mathbf{F}_\alpha$ is restricted to $\det \mathbf{F}_\alpha > 0$. Furthermore, we define the Jacobian J_α following Eq. (4.26), where $\mathbf{F}_\alpha$ is the deformation gradient of the constituent φ^α following Eq. (4.27).

To use a material objective measure of the fluid velocity with respect to the solid velocity, we introduce the seepage velocity $\mathbf{w}_{FS}$ which describes the difference in velocity between the fluid phase $\mathbf{x}'_F$ and the solid phase $\mathbf{x}'_S$ as

$$\mathbf{w}_{FS} = \mathbf{x}'_F - \mathbf{x}'_S. \tag{4.43}$$

In connection with the fluid volume fraction, this leads to the definition of the filtration velocity $n^F\mathbf{w}_{FS}$.

4.2.2.4 Entropy Inequality and Constitutive Formulation

Based on our four assumptions (Section 4.2.2.1), we generate a quasistatic, two-phase model with individually incompressible phases under isothermal conditions and without mass exchanges. Under these assumptions, we simplify the entropy inequality Eq. (4.41) as

$$\sum_{\alpha}^{S,F} \left\{ -\rho^\alpha (\Psi^\alpha)'_\alpha + \boldsymbol{\sigma}^\alpha : \mathbf{d}_\alpha - \widehat{\mathbf{p}}^\alpha \cdot \mathbf{x}'_\alpha \right\} \geq 0, \tag{4.44}$$

where $\widehat{\mathbf{p}}^\alpha$ describes the interaction forces of the constituents φ^α, which are restricted to $\widehat{\mathbf{p}}^S + \widehat{\mathbf{p}}^F = \mathbf{0}$.

We postulate the arguments for the Helmholtz free-energy functions as $\Psi^S = \Psi^S(\mathbf{C}_S, \mathbf{a}_0 \otimes \mathbf{a}_0)$ and $\Psi^F = \Psi^F(-)$, where $\mathbf{C}_S = \mathbf{F}_S^T\mathbf{F}_S$ is the right Cauchy–Green tensor. As is usual in incompressible fluid mechanics, and for simplicity, we assume that the Helmholtz free energy of the fluid phase does not depend on the deformation gradient $\mathbf{F}_F$ when viscous properties are negligible (based on dimensional arguments) (see, e.g., Hassanizadeh and Gray, 1990; Markert, 2007). Thus, Ψ^F does not depend on any process variable.

Considering the arguments of the Helmholtz free-energy functions, the material time derivatives of these functions follow as

$$(\Psi^S)'_S = 2\mathbf{F}_S \frac{\partial \Psi^S(\mathbf{C}_S, \mathbf{a}_0 \otimes \mathbf{a}_0)}{\partial \mathbf{C}_S} \mathbf{F}_S^T, \quad (\Psi^F)'_F = 0, \tag{4.45}$$

This book belongs to Central Library BADJI Mokhtar-ANNABA UNIVERSITY
Copyright Elsevier 2024

for the solid and fluid phases, respectively.

In the case of a biphasic model with two material incompressible constituents, a macroscopic volumetric deformation only occurs through a change in the volume fraction. To account for the saturation constraint, we constrain the material time derivative of the saturation condition Eq. $(4.42)_2$ following the motion of the solid phase as

$$(n^{\mathrm{S}})'_{\mathrm{S}} + (n^{\mathrm{F}})'_{\mathrm{S}} = 0. \tag{4.46}$$

Using this constraint, the balance of mass Eq. (4.33) and the definition of the seepage velocity Eq. (4.43), we introduce an additional unknown Lagrange multiplier p to evaluate the entropy inequality of the mixture (Ricken and Bluhm, 2010), which leads to an alternative form of the entropy inequality

$$\mathbf{d}_{\mathrm{S}} : \left\{\boldsymbol{\sigma}^{\mathrm{S}} + n^{\mathrm{S}} p \mathbf{I} - 2\rho^{\mathrm{S}} \mathbf{F}_{\mathrm{S}} \frac{\partial \Psi^{\mathrm{S}}(\mathbf{C}_{\mathrm{S}}, \mathbf{a}_0 \otimes \mathbf{a}_0)}{\partial \mathbf{C}_{\mathrm{S}}} \mathbf{F}_{\mathrm{S}}^{\mathrm{T}}\right\} + \mathbf{d}_{\mathrm{F}} : \{\boldsymbol{\sigma}^{\mathrm{F}} + n^{\mathrm{F}} p \mathbf{I}\} - \mathbf{w}_{\mathrm{FS}} \cdot \left\{\widehat{\mathbf{p}}^{\mathrm{F}} - p \,\mathrm{grad} n^{\mathrm{F}}\right\} \geq 0, \tag{4.47}$$

where we interpret p as the interstitial fluid pressure.

The first two terms on the left-hand side of Eq. (4.47) are energy conserving and yield the thermodynamic restrictions

$$\boldsymbol{\sigma}^{\mathrm{S}} = -n^{\mathrm{S}} p \mathbf{I} + 2\rho^{\mathrm{S}} \mathbf{F}_{\mathrm{S}} \frac{\partial \Psi^{\mathrm{S}}(\mathbf{C}_{\mathrm{S}}, \mathbf{a}_0 \otimes \mathbf{a}_0)}{\partial \mathbf{C}_{\mathrm{S}}} \mathbf{F}_{\mathrm{S}}^{\mathrm{T}}, \tag{4.48a}$$

$$\boldsymbol{\sigma}^{\mathrm{F}} = -n^{\mathrm{F}} p \mathbf{I}, \tag{4.48b}$$

for the solid and fluid partial Cauchy stresses, respectively, and with the total Cauchy stress equal to the sum of the partial Cauchy stresses. The third term of Eq. (4.47) is energy dissipating, given explicitly as

$$-\mathbf{w}_{\mathrm{FS}} \cdot \left\{\widehat{\mathbf{p}}^{\mathrm{F}} - p \,\mathrm{grad} n^{\mathrm{F}}\right\} \geq 0, \tag{4.49}$$

which we satisfy with the common ansatz

$$\widehat{\mathbf{p}}^{\mathrm{F}} = p \,\mathrm{grad} n^{\mathrm{F}} - \mathbf{R}_{\mathrm{F}} \mathbf{w}_{\mathrm{FS}}, \tag{4.50}$$

where $\mathbf{R}_{\mathrm{F}}$ denotes a positive definite material parameter tensor representing the (possibly anisotropic) intrinsic hydraulic resistance of the porous solid matrix (Ricken and Bluhm, 2010; Pierce et al., 2013b).

In writing the constitutive relations for the partial Cauchy solid stress tensor, it is common to define the effective solid Cauchy stress tensor $\boldsymbol{\sigma}_{\mathrm{E}}^{\mathrm{S}}$ as

$$\boldsymbol{\sigma}_{\mathrm{E}}^{\mathrm{S}} = 2\rho^{\mathrm{S}} \mathbf{F}_{\mathrm{S}} \frac{\partial \Psi^{\mathrm{S}}(\mathbf{C}_{\mathrm{S}}, \mathbf{a}_0 \otimes \mathbf{a}_0)}{\partial \mathbf{C}_{\mathrm{S}}} \mathbf{F}_{\mathrm{S}}^{\mathrm{T}}, \tag{4.51}$$

cf. Eq. (4.48a) (e.g., Bishop, 1959; Skempton, 1960).

In the biphasic model presented here, we characterize the mechanical response of the solid constituent φ^{S} by the specification of the Helmholtz free-energy function for the solid $\Psi^{\mathrm{S}}(\mathbf{C}_{\mathrm{S}}, \mathbf{a}_0 \otimes \mathbf{a}_0)$, which we propose to include, e.g., effects of the collagen fibers and the proteoglycan aggregates, as well as compaction of the complete porous solid. We cannot, however, directly incorporate effects from the ionic phases and interactions of the charged groups leading to osmotic pressure/swelling. Their explicit inclusion requires additional phases in total mixture body, as well as additional constitutive relations.

The biphasic model, in the context of the TPM, naturally leads to a numerical solution of the coupled solid−fluid behavior in the framework of an FE formulation. Therein, we elegantly and efficiently capture the relevant physical properties stemming from the porous microstructure.

4.3 IMAGE-BASED DATA ACQUISITION

Data acquisition using imaging methods provides a means to capture characteristics of a biological system noninvasively, i.e., without interfering or destroying mechanical processes during measurements. Constitutive modeling often requires input data to drive model formulation, calibration of key variables, e.g., material properties, and for independent validation of the modeling framework using, e.g., specific boundary conditions. To address these needs, data acquisition by various imaging modalities is ideal. In the case of OA and articular cartilage, common imaging modalities include MRI (Peterfy et al., 2004; Stehling et al., 2010) (noted as perhaps the most versatile method, capable of capturing multiple physical phenomena Neu, 2014), ultrasound (Iagnocco et al., 2012), and radiography (Kellgren and Lawrence, 1957). Medical

This book belongs to Central Library BADJI Mokhtar-ANNABA UNIVERSITY
Copyright Elsevier 2024

imaging allows typically for an assessment of tissue-scale (i.e., millimeter to micrometer) properties in a broad range of natural and engineered tissues. Images depict structure and morphology information in multiple spatial dimensions. Extended image modalities, including MRI, can provide additional functional information on physiology, such as tissue motion (Chan and Neu, 2012), flow (Muir et al., 2014), diffusion (Burstein et al., 1993), and metabolism (Haris et al., 2014). Effective assessment of changing physiology through the lifetime of organisms, including damage or disease (Setton et al., 1994, 1999), may require the full range of available measures from imaging modalities. As a consequence, imaging biomarkers of changing physiology, including variations in shape, deformation, strain, stress, or material properties may represent promising metrics.

4.3.1 Morphology and Geometry

Imaging depicts spatial positions of materials and important object features in two and three dimensions. As such, imaging is a natural starting point for importing morphology and geometry of numerous body tissues and, in individual people, laying the most basic groundwork for subject-specific analyses. Numerous examples illustrate importing radiography or computed tomography data representing bone for analyses of complex structures such as the wrist (Crisco et al., 1999; Wolfe et al., 2000), hip (Thevenot et al., 2014), and other joint and tissue systems (Roos et al., 2005; Papaioannou et al., 2008). Likewise, structural alterations in tissues such as ligament (Choo et al., 2014) or the osteochondral interface (Bae et al., 2010) may represent advancing states of disease or may guide surgical planning (H et al., 2013).

For soft tissues, MRI is generally a preferred choice because of the ability to visualize structures with excellent spatial resolution (approaching 50 μm or better on dedicated research magnets) and contrast in image intensity to clearly distinguish differences between adjacent tissues. A common fast spin echo acquisition of the knee joint can visualize bright cartilage against decreased image intensity of subchondral bone and meniscus, facilitating tissue segmentation and other analyses. Structural measures often include volume and thickness (Le Graverand et al., 2009; C et al., 2010; Mosher et al., 2010; B et al., 1990; Graichen et al., 2003; Favre et al., 2013) or contact area (Shin et al., 2011; Wan et al., 2006; Hinterwimmer et al., 2005).

Ultrasound provides an alternative approach for analyses of soft tissues, including musculoskeletal, abdominal, and related tissues (Goergen et al., 2011; Liisberg et al., 2017). However, for deep structures of the knee (Eşen et al., 2013) and hip (Iagnocco et al., 2012) (e.g., cartilage), ultrasound assessments are often less effective due to loss of signal or inability to directly measure signal from these tissues.

4.3.2 Diffusion

Diffusion tensor MRI (DT-MRI) can measure quantities describing the microstructures of soft tissues (e.g., the collagen fiber orientations) due to the influence of this network on the fluid transport properties of the tissue. For example, the diffusional properties of articular cartilage are principally controlled by two components: (1) a homogenous ground substance of proteoglycan−water gel that gives a baseline isotropic diffusivity and (2) a highly anisotropic collagenous fiber network that overlays the baseline (Filidoro et al., 2005). Thus, the diffusion of interstitial fluid within cartilage, as visualized, by DT-MRI, is principally influenced by the general orientation of the (largely type II) collagen fibers (Filidoro et al., 2005; Meder et al., 2006; Abdullah et al., 2007; de Visser et al., 2008a,b).

DT-MRI can currently provide 3D spatially resolved principal fiber directions at micron scale lengths if performed ex vivo. In an example study, DT-MRI at 9.4 T and a voxel resolution of 39 × 78 μm in-plane and 1500 μm out-of-plane resolved the principal fiber orientation, as determined by the eigenvector associated with the first principal eigenvalue of each diffusion tensor and verified by corresponding SEM data (Filidoro et al., 2005). In our work, ex vivo DT-MRI measurements at 17.6 T and a voxel resolution of 50 × 100 μm in-plane and 800 μm out-of-plane yielded similar results (Pierce et al., 2010).

It is important to consider that DT-MRI does not assess soft tissues directly. Rather, it utilizes the fact that diffusion of water molecules within soft tissues differs from that in free solution. DT-MRI provides quantitative information about the degree and direction of water diffusion within individual units of volume within the MR image, and by inference, about the microstructure of the soft tissue (Feldman et al., 2010). For DT-MRI, eigenvectors and eigenvalues are calculated from tensor representations in specified regions of interest. A formal treatment of the method requires definition of $\mathbf{D}$ as one such tensor, where the unique solution to the eigenproblem $\mathbf{D}\widehat{\mathbf{n}}_i = \Lambda_i \widehat{\mathbf{n}}_i,\ i = 1, 2, 3$, no summation, leads to the eigenbasis $\widehat{\mathbf{n}}_i$, with corresponding eigenvalues Λ_i. For further analyses, the apparent diffusion coefficient (ADC)

$$\mathrm{ADC} = \overline{\Lambda} = 1/3\ \mathrm{tr}\mathbf{D}, \tag{4.52}$$

and the fractional anisotropy (FA)

This book belongs to Central Library BADJI Mokhtar-ANNABA UNIVERSITY
Copyright Elsevier 2024

$$\mathrm{FA} = \sqrt{\frac{2}{3}\frac{\left(\Lambda_1 - \overline{\Lambda}\right)^2 + \left(\Lambda_2 - \overline{\Lambda}\right)^2 + \left(\Lambda_3 - \overline{\Lambda}\right)^2}{\Lambda_1^2 + \Lambda_2^2 + \Lambda_3^2}}, \tag{4.53}$$

are often calculated for each voxel. In this context, ADC quantifies the average diffusivity in the measurement voxel, whereas FA describes the relative degree of anisotropy. More specific interpretations of these measures depend on the particular soft tissue, e.g., cerebral white matter (Feldman et al., 2010; Alexander et al., 2011) or cartilage (Pierce et al., 2010; Lilledahl et al., 2011; Raya et al., 2011, 2013).

4.3.3 Mapping Strain and Material Properties

The demands of constitutive modeling often require determination of material properties and verification of strain distributions within materials, as boundary conditions or as a means of validation. In light of these demands, simple measures of morphology and geometry (e.g., surface shape and volume) are insufficient to determine intratissue mechanical behavior, which is often complex for heterogeneous soft tissues and engineered materials.

Elastography methods for MRI and ultrasound enable classification of material properties and stress under specified loading conditions (e.g., Muthupillai et al., 1995). Elastography often includes external introduction of high-frequency vibration or stimulation, and material properties are then determined using material models and inverse methods (Hardy et al., 2005; Lopez et al., 2007, 2008; Tervonen et al., 1993). Unfortunately, conventional elastography is not well developed in cartilage (Lopez et al., 2007) and related musculoskeletal systems, where constraints in tissue location, stiffness, and available stimulation methods limit utility, especially in applications in vivo.

Measurement of deformation and strain has emerged as an established means of tissue assessment (Butz et al., 2011), especially utilizing MRI methods (Neu, 2014). For tissues, including cartilage, numerous techniques based on pattern matching of tissue tagging (Neu et al., 2005a,b,c; Axel and Dougherty, 1989; Mosher and Smith, 1990; Zerhouni et al., 1988) or phase contrast analyses (Chan and Neu, 2012; Neu and Walton, 2008) provide deformation with minimal experimental error. Important to phase-contrast measurements, in particular displacements under applied loading by MRI (dual MRI), is the synergy of external mechanical loading with appropriate MRI postprocessing algorithms (Chan and Neu, 2012). Strain can be measured with high spatiotemporal resolution, approaching 100 μm pixel dimensions with a temporal resolution <3 ms and with minimal error (on the order of 0.001). Finite (i.e., large) deformation is also possible at relatively low frequency to mimic a walking cadence with loading near or exceeding body weight (Neu and Walton, 2008; Chan and Neu, 2012; Chan et al., 2016). Strain mapping in systems with complex morphology and geometry, such as the knee joint is also established (Griebel et al., 2013; Neu et al., 2009; Chan et al., 2009), including recent experiments demonstrating in vivo capabilities (see Fig. 4.3). These advancements highlight the possibility to track changes due to disease, damage, and repair through time and following treatment in human populations.

4.4 IMAGE-DRIVEN CONSTITUTIVE MODELS: CARTILAGE AS A REPRESENTATIVE SYSTEM

Articular cartilage comprises, by percentage wet weight, heterogeneously distributed fluid and electrolytes (68%−85%), collagen fibers (15%−25%), proteoglycans (5%−10%), and chondrocytes (<4%). The heterogeneous solid phase

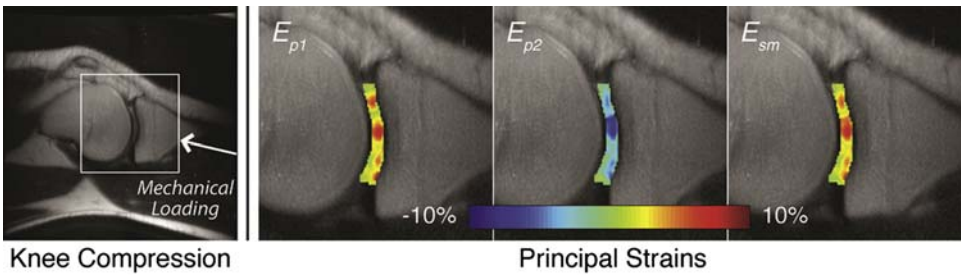

FIGURE 4.3 In vivo strains within the cartilage of human subjects can be computed using magnetic resonance imaging. During compressive loading to the foot, as one example loading mode, principal strains or other quantities can be computed through precise timing of the loading device and imaging acquisition actions. The ability to compute mechanical quantities such as strain within humans enables future studies aimed at development and validation of computation models in vivo. *Adapted from Chan, D.D., Cai, L., Butz, K.D., Trippel, S.B., Nauman, E.A., Neu, C.P., 2016. In vivo articular cartilage deformation: noninvasive quantification of intratissue strain during joint contact in the human knee. Scientific Reports 6, 19220.*

This book belongs to Central Library BADJI Mokhtar-ANNABA UNIVERSITY Copyright Elsevier 2024

constitutes a proteoglycan gel and a fiber network of predominantly type II collagen, both of which contribute to mechanical stiffness and permeation of the fluid phase. The collagen fibers exhibit a high level of structural organization usually consisting of three subtissue zones starting from the surface to the subchondral bone (Mow et al., 2005).

We have established continuum models for cartilage and, corresponding 3D nonlinear FE implementations, designed to incorporate structural data on the sample- or patient-specific collagen fiber networks (e.g., Pierce et al., 2009, 2010, 2013a,b, 2016; Lilledahl et al., 2011). We implement our material formulations in 3D large-strain FEs. To demonstrate, we simulate mechanical indentation tests and investigate the following hypotheses: in Eq. (4.1), the through-thickness structural arrangement of collagen adjusts fluid permeation to maintain fluid pressure (Federico and Herzog, 2008); in Eq. (4.2), the heterogeneity of mechanical properties through the cartilage thickness acts to maintain fluid pressure at the articular surface (Krishnan et al., 2003). To determine the effects of the collagen fiber network and through-thickness tissue heterogeneity (of tissue constituents) independently, we selectively simplify our model by removing either the fiber network or the tissue heterogeneity, or both.

4.4.1 Biphasic Cartilage Model

Our constitutive model is based on four main assumptions (cf. Section 4.2.2.1). First, we assume that the cartilage tissue consists of two phases: a porous solid matrix saturated by a pore fluid. This assumption implies that under physiologic loading conditions the magnitude of the swelling strain due to Donnan osmotic pressure is relatively small in comparison to the tissue strains, so that we are justified in approximating the physiological response using a biphasic model (Soltz and Ateshian, 2000). Second, we assume that both phases are individually incompressible (Jurvelin et al., 1997; Bachrach et al., 1998; Soltz and Ateshian, 1998; Wong et al., 2000; Humphrey, 2002; Park et al., 2003; Huang et al., 2005). Our third assumption is that mass exchanges between the solid and the fluid constituents can be neglected (immiscibility). Finally, we assume that dynamic effects are negligible (quasistatic) so we exclude inertial terms.

We describe cartilage as a biphasic continuum $\varphi = \varphi^{\mathrm{S}} + \varphi^{\mathrm{F}}$, which consists of a porous solid phase φ^{S} saturated with the fluid phase φ^{F}, the latter representing the interstitial water. The solid phase represents an incompressible tissue with an isotropic and statistically regular pore distribution and with an imbedded reinforcing collagen fiber network. We represent the microscopic tissue structure with a statistical distribution of the constituents over a representative elementary volume by their average volume fractions n^{α}, $\alpha \in \{\mathrm{S}, \mathrm{F}\}$. The volume fractions n^{α} refer the volume elements $\mathrm{d}v^{\alpha}$ of the individual constituents φ^{α} to the bulk volume element $\mathrm{d}v$ following Eq. (4.42). We further partition the solid volume increment $\mathrm{d}v^{\mathrm{S}}$ into the volume fraction of fiber network ν relative to total solid and that of isotropic matrix $(1-\nu)$. See Fig. 4.4 for a schematic representation of the constitutive modeling approach, illustrating the true cartilage structure, its representation using volume fractions, and the corresponding homogenization within the TPM.

4.4.1.1 Fluid and Elastic Solid Contributions to the Stress

Following Eqs. (4.48a), (4.48b), and (4.51) we propose the constitutive relation for the total Cauchy stress tensor as

$$\boldsymbol{\sigma} = -p\,\mathbf{I} + 2\rho^{\mathrm{S}}\mathbf{F}_{\mathrm{S}}\frac{\partial \Psi^{\mathrm{S}}}{\partial \mathbf{C}_{\mathrm{S}}}\mathbf{F}_{\mathrm{S}}^{\mathrm{T}} = -p\,\mathbf{I} + \boldsymbol{\sigma}_{\mathrm{E}}^{\mathrm{S}}. \tag{4.54}$$

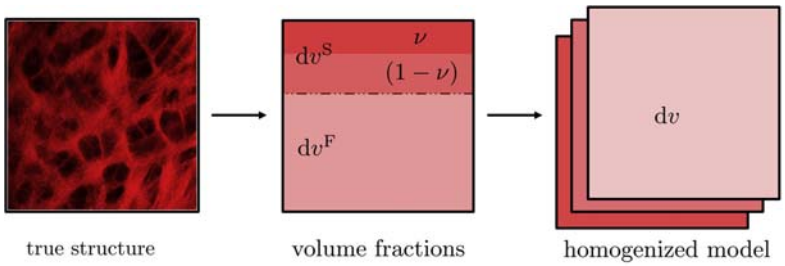

FIGURE 4.4 Schematic representation of the true cartilage structure (multiphoton microscopy image), its representation using volume fractions, and the corresponding homogenization within the theory of porous media. *Adapted from Pierce, D.M., Unterberger, M.J., Trobin, W., Ricken, T., Holzapfel, G.A., 2016. A microstructurally based continuum model of cartilage viscoelasticity and permeability incorporating statistical fiber orientation. Biomechanics and Modeling in Mechanobiology 15, 229–244.*

This book belongs to Central Library BADJI Mokhtar-ANNABA UNIVERSITY
Copyright Elsevier 2024

We use an additive decomposition of the superimposed solid Helmholtz free-energy function Ψ^{S} into an isotropic matrix part $\Psi^{\mathrm{S}}_{\mathrm{IM}}$, and a transversely isotropic fiber network part $\Psi^{\mathrm{S}}_{\mathrm{FN}}$ as

$$\Psi^{\mathrm{S}} = (1-\nu)\Psi^{\mathrm{S}}_{\mathrm{IM}}(J_{\mathrm{S}}, I_1) + \nu\Psi^{\mathrm{S}}_{\mathrm{FN}}(\mathbf{C}_{\mathrm{S}}), \tag{4.55}$$

where ν is the volume fraction of the collagen fiber network to the total solid, $J_{\mathrm{S}} = \det \mathbf{F}_{\mathrm{S}}$ is the Jacobian, and $I_1 = \mathrm{tr}\mathbf{C}_{\mathrm{S}}$ is the first invariant of $\mathbf{C}_{\mathrm{S}}$.

In the case of volumetric compression, we introduce a compaction point defining the state where no further compression is possible, i.e., all transportable fluid is pressed out of the tissue (Wilson et al., 2007; Federico and Grillo, 2012). We capture the response of the isotropic (largely) proteoglycan solid matrix, including compaction effects, as (Simo and Pister, 1984; Bluhm, 2002; Pierce et al., 2013a,b)

$$\Psi^{\mathrm{S}}_{\mathrm{IM}}(J_{\mathrm{S}}, I_1) = \frac{1}{\rho^{\mathrm{S}}_{0\mathrm{S}}}\left[U(J_{\mathrm{S}}) + \frac{1}{2}\mu^{\mathrm{S}}(I_1 - 3)\right], \tag{4.56}$$

where

$$U(J_{\mathrm{S}}) = \chi^{\mathrm{S}}_{\mathrm{cp}}\left[\frac{1}{2}(\log J_{\mathrm{S}})^2 + \zeta^{\mathrm{S}}\right] - \mu^{\mathrm{S}}\log J_{\mathrm{S}}, \tag{4.57}$$

and where we use the abbreviations

$$\begin{aligned}
\chi^{\mathrm{S}}_{\mathrm{cp}} &= \lambda^{\mathrm{S}}\left[1 + J^{\mathrm{S}}_{\mathrm{cp}}\left(1 + \frac{\left(J^{\mathrm{S}}_{\mathrm{cp}}\right)^2}{1 - J^{\mathrm{S}}_{\mathrm{cp}}}\right)\right]^{-1}, \\
\zeta^{\mathrm{S}} &= J^{\mathrm{S}}_{\mathrm{cp}}\log J_{\mathrm{S}} + \frac{1 - J^{\mathrm{S}}_{\mathrm{cp}}}{J^{\mathrm{S}}_{\mathrm{cp}} - 2}\left[\log\frac{J^{\mathrm{S}}_{\mathrm{cp}} - J_{\mathrm{S}}}{J_{\mathrm{S}}\left(J^{\mathrm{S}}_{\mathrm{cp}} - 1\right) - J^{\mathrm{S}}_{\mathrm{cp}}} - \log\left(1 - J^{\mathrm{S}}_{\mathrm{cp}}\right)\right].
\end{aligned} \tag{4.58}$$

In Eqs. (4.56)–(4.58) μ^{S} is Lamé's second parameter, λ^{S} is Lamé's first parameter (a non-physical, (positive) penalty parameter used to enforce incompressibility (cf. Pence, 2012), and $n^{\mathrm{S}}_{0\mathrm{S}} \le J^{\mathrm{S}}_{\mathrm{cp}} \le 1$ defines the point of compaction for the tissue, where $n^{\mathrm{S}}_{0\mathrm{S}}$ is the solid volume fraction in the reference configuration.

To capture the anisotropic and nonlinear response of the dispersed collagen fiber network, we assume that a distribution of fibers is embedded in this isotropic matrix such that each fiber deforms with the matrix. Let $\rho(\mathbf{M})$ be the angular density of fibers (the ODF) so that (Miehe et al., 2004; Lei and Szeri, 2006)

$$\frac{1}{4\pi}\int_{\Omega}\rho(\mathbf{a}_0)\mathrm{d}\Omega = 1, \tag{4.59}$$

where $\Omega = \mathbf{a}_0 \in \mathbb{R}^3 : |\mathbf{a}_0| = 1$ is the unit sphere.

For a single fiber of reference angular orientation $\mathbf{a}_0$ the fourth pseudoinvariant I_4 is the square of the stretch of this fiber in the direction $\mathbf{a} = \mathbf{F}_{\mathrm{S}}\mathbf{a}_0$, i.e., $I_4(\mathbf{a}_0) = \lambda^2(\mathbf{a}_0) = \mathbf{a}_0 \cdot \mathbf{C}_{\mathrm{S}}\mathbf{a}_0$. We define the strain energy of a single collagen fiber as (Holzapfel et al., 2000; Pierce et al., 2016)

$$w(I_4) = \frac{k_1}{2k_2}\left\{\exp\left[k_2(I_4 - 1)^2\right] - 1\right\}\mathcal{H}(I_4 - 1), \tag{4.60}$$

where $k_1 > 0$ is a material parameter, $k_2 > 0$ is a dimensionless parameter, and $\mathcal{H}$ is a Heaviside step function evaluated at $(I_4 - 1)$, i.e., the collagen fibers only engage under $\lambda > 1$ (Sun et al., 2002).

Assuming that all of the collagen fibers have the same mechanical response, i.e., the same form for $w(I_4)$, we calculate the total strain energy function (over all orientations) as

$$\Psi_{\mathrm{FN}}(\mathbf{C}, \mathbf{a}_0) = \frac{1}{\rho^{\mathrm{S}}_{0\mathrm{S}}}\int_{\Omega}\rho(\mathbf{a}_0)w(I_4)\,\mathrm{d}\Omega. \tag{4.61}$$

This book belongs to Central Library BADJI Mokhtar-ANNABA UNIVERSITY
Copyright Elsevier 2024

4.4.1.2 Viscoelasticity of the Solid Constituents

We calculate the viscous contribution to the total stress state in the Lagrangian configuration using the second Piola–Kirchhoff effective stress tensor $\mathbf{S}_{\mathrm{E}}^{\mathrm{S}} = J_{\mathrm{S}}\mathbf{F}_{\mathrm{S}}^{-1}\boldsymbol{\sigma}_{\mathrm{E}}^{\mathrm{S}}\mathbf{F}_{\mathrm{S}}^{-\mathrm{T}}$. For clarity in what follows we drop the superscript S and the subscript E and denote the second Piola–Kirchhoff effective stress tensor of the solid by $\mathbf{S}$. We specify $\mathbf{S}$ by summing the matrix, fiber network, and viscoelastic contributions as

$$\mathbf{S} = \sum_{\gamma=\mathrm{IM,FN}} \left(\mathbf{S}_{\gamma} + \mathbf{Q}_{\gamma}\right), \tag{4.62}$$

where $\mathbf{S}_{\mathrm{IM}} = 2\rho_{0\mathrm{S}}^{\mathrm{S}}\partial\Psi_{\mathrm{IM}}/\partial\mathbf{C}_{\mathrm{S}}$ is the matrix and $\mathbf{S}_{\mathrm{FN}} = 2\rho_{0\mathrm{S}}^{\mathrm{S}}\partial\Psi_{\mathrm{FN}}/\partial\mathbf{C}_{\mathrm{S}}$ is the fiber network contribution to the second Piola–Kirchhoff effective stress $\mathbf{S}$, respectively, and $\mathbf{Q}_{\gamma}$ represent the viscoelastic contributions where we assume $\gamma \in \{\mathrm{IM, FN}\}$ time-dependent processes.

We consider a partition of the closed time interval $t \in [0^{+}, T]$ and focus attention on a typical time subinterval $[t_n, t_{n+1}]$, with $\Delta t = t_{n+1} - t_n$ characterizing the associated time increment (cf. Herrmann and Peterson, 1968; Taylor et al., 1970; Simo, 1987; Holzapfel, 1996). All relevant kinematic quantities at times t_n and t_{n+1} are known and the stress $\mathbf{S}_n$ at time t_n is specified uniquely via the associated constitutive equation. We compute the second Piola–Kirchhoff stress tensor $\mathbf{S}_{n+1}$ at time t_{n+1} (the algorithmic stress tensor generalized from Eq. 4.62) as

$$\mathbf{S}_{n+1} = \sum_{\gamma=\mathrm{IM,FN}} \left(\mathbf{S}_{\gamma,n+1} + \mathbf{Q}_{\gamma,n+1}\right). \tag{4.63}$$

The stress contributions $\mathbf{S}_{\mathrm{IM},n+1}$ and $\mathbf{S}_{\mathrm{FN},n+1}$ describe the total elastic response computed from the given strain measures at t_{n+1}. The terms $\mathbf{Q}_{\gamma,n+1}$ in Eq. (4.63) represent the nonequilibrium stresses at time t_{n+1}. We use a second-order accurate recurrence update formula for the nonequilibrium stresses as

$$\mathbf{Q}_{\gamma,n+1} = \beta_{\gamma}\exp(-\Delta t/2\tau_{\gamma})\mathbf{S}_{\gamma,n+1} + \mathcal{H}_{\gamma,n}, \tag{4.64}$$

with

$$\mathcal{H}_{\gamma,n} = \exp(-\Delta t/2\tau_{\gamma})\left[\exp(-\Delta t/2\tau_{\gamma})\mathbf{Q}_{\gamma,n} - \beta_{\gamma}\mathbf{S}_{\gamma,n}\right], \tag{4.65}$$

where β_{γ} is a dimensionless strain-energy factor controlling the magnitude of the viscous response and τ_{γ} is the associated relaxation time. We determine the algorithmic history term $\mathcal{H}_{\gamma,n}$, $\gamma \in \{\mathrm{IM, FN}\}$, at time t_n, from the known stresses $\mathbf{Q}_{\gamma}$ and $\mathbf{S}_{\gamma}$ at t_n (for numerical purposes we assumed $\mathbf{Q}_{\gamma}^{0^{+}} = \mathbf{O}$) (Holzapfel, 1996; Holzapfel and Gasser, 2001). At thermodynamical equilibrium, only the elastic response remains, i.e., $\mathbf{Q}_{\gamma} = \mathbf{O}$.

4.4.1.3 Corresponding Permeability

The presence of collagen fibers restricts the permeation of interstitial fluid within cartilage, leading to a correspondingly higher diffusivity in directions parallel to local fiber orientations. Considering the collagen fibers, we determine the filtration velocity $n^{\mathrm{F}}\mathbf{w}_{\mathrm{FS}}$ as (cf. Pierce et al., 2013a,b).

$$n^{\mathrm{F}}\mathbf{w}_{\mathrm{FS}} = \mathbf{K}_{\mathrm{F}}(-\operatorname{grad} p + \rho^{\mathrm{FR}}\,\mathbf{b}), \tag{4.66}$$

where $\mathbf{K}_{\mathrm{F}}$ is a positive definite material parameter tensor representing the intrinsic permeability of the cartilage solid matrix and $\mathbf{b}$ is the body force per unit mass. We propose $\mathbf{K}_{\mathrm{F}}$ as (Ricken and Bluhm, 2010; Pierce et al., 2013b, 2016)

$$\begin{aligned} \mathbf{K}_{\mathrm{F}} &= k_{0\mathrm{S}}\left(\frac{n^{\mathrm{F}}}{1-n_{0\mathrm{S}}^{\mathrm{S}}}\right)^{m}\mathbf{H}, \\ \mathbf{H} &= \frac{1}{4\pi}\int_{\Omega}\frac{\rho(\mathbf{a}_0)}{I_4(\mathbf{a})}\mathbf{a}\otimes\mathbf{a}\,\mathrm{d}\Omega, \end{aligned} \tag{4.67}$$

where $\mathbf{H}$ is a spatial structure tensor defined by the integration of $\rho(\mathbf{a}_0)$ over all normalized, spatial fiber orientations $\widehat{\mathbf{a}} = \lambda^{-1}\mathbf{F}_{\mathrm{S}}\mathbf{a}_0$ (with $\lambda = |\mathbf{a}|$), $k_{0\mathrm{S}}$ [m^4/Ns] is the initial Darcy permeability, and m is a dimensionless parameter controlling the general isotropic deformation dependence of the permeability (cf. Eipper, 1998). Inclusion of the volume fraction n^{F} relates to the change of permeability caused by the change of pore space, where $n_{0\mathrm{S}}^{\mathrm{S}}$ denotes the reference solid volume fraction. Here we used $\mathbf{H}$, via $\rho(\mathbf{a}_0)$, to define the range of permeabilities resulting from ideal alignment of collagen fibers to an isotropic distribution of the collagen fibers.

This book belongs to Central Library BADJI Mokhtar-ANNABA UNIVERSITY
Copyright Elsevier 2024

4.4.2 Integration of Computational Modeling and Experimental Data

4.4.2.1 Diffusion Tensor Magnetic Resonance Imaging Experiment

We use DT-MRI data generated in our previous work (Pierce et al., 2010), which we briefly outline here for completeness. Previously we harvested the left patella of a healthy 27-year-old male within 24 h from death and stored it in physiologic solution for 36 h at 4°C. We cut a cuboid sample patellar cartilage measuring $\sim 2.8 \times 2.8 \times 2.6$ mm and another ~ 1 mm in bone thickness. We performed MRI experiments with a 17.6 T scanner (UltraStabilized magnet system, Brucker BioSpin, Rheinstetten, Germany). We immersed the sample in physiologic solution at $17 - 19$°C and imaged for ~ 140 min through the cartilage thickness, diagonal to the square footprint. One can find more details on the MRI experiments and protocols in (Pierce et al., 2010; Raya et al., 2011, 2013).

4.4.2.2 Implementation of Diffusion Tensor Magnetic Resonance Imaging Data

Fig. 4.5A depicts the first principal eigenvalues of the tensor field, the rectangular gray area is the articular cartilage layer, and the noisy black area directly right is the subchondral bone (Pierce et al., 2010). The cartilage–bone sample is surrounded by phosphate-buffered saline (solid white) and is enclosed in a cylindrical container (solid black border).

Based on this data we infer the sample-specific geometric boundaries as well as the fiber distribution within the cartilage. Following our previous work (Pierce et al., 2010): we first locate the geometric boundaries as subvoxel-accurate zero crossings of the second spatial derivative (Laplacian of Gaussian filter), then we use the voxel grid from the DT-MRI experiment as structured mesh. Along the boundaries of the cartilage region, we use a semiautomatic process to transition from the structured voxel grid to the natural cartilage boundary while maintaining good element aspect ratios. Finally, we extruded the resulting 2D mesh to generate a 3D mesh of 20-node brick elements, representing the volume of the imaged DT-MRI slice.

By construction there is a one-to-one mapping from diffusion tensors to elements within the "inner" regions. This one-to-one mapping breaks down along the boundary. For every element in these "outer" regions of the mesh, we perform a weighted interpolation of the element's four nearest diffusion tensors using a Log-Euclidean framework (Arsigny et al., 2006; Pierce et al., 2010).

The element-wise tensor data naturally maps to the model's ODF for the fiber network. We first convert the diffusion probability density function Eq. (4.59) to spherical coordinates (r, θ, ϕ), then marginalize out the radius r (Pierce et al., 2016). An analytical form of the required ODF results as

$$\rho(\mathbf{a}_0, \mathbf{D}) = \frac{\sin\theta}{\left|\mathbf{D}\right|^{1/2} \left(\mathbf{a}_0^{\mathrm{T}} \mathbf{D}^{-1} \mathbf{a}_0\right)^{3/2}}, \tag{4.68}$$

where $(\mathbf{a}_0) = (\cos\theta\sin\phi, \sin\theta\sin\phi, \cos\phi)^{\mathrm{T}}$ and $\mathbf{D}$ is the symmetric, positive-definite diffusion tensor for a specific element.

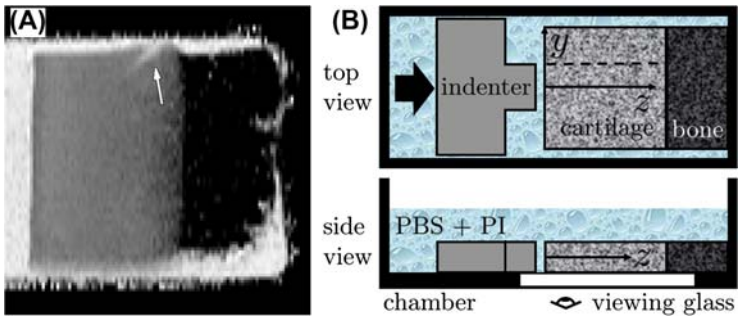

FIGURE 4.5 (A) Grayscale representation of the first principal eigenvalues of the diffusion tensor magnetic resonance imaging data, a small fissure close to the cartilage-bone transition is indicated by the *white arrow* (Pierce et al., 2010). Principal diffusion in PBS is represented using white voxels, whereas regions with negligible PBS content are represented as black voxels. Intermediate values span the range from black to white; (B) schematic diagram of a near 2D indentation test replicating the intratissue deformation that occurs during 3D indentation with a plane-ended cylindrical indenter, where PBS + PI indicates phosphate-buffered saline plus protease inhibitors. *Adapted from Bae, W.C., Lewis, C.W., Levenston, M.E., Sah, R.L., 2006. Indentation testing of human articular cartilage: effects of probe tip geometry and indentation depth on intra-tissue strain. Journal of Biomechanics 39, 1039–1047; Pierce, D.M., Unterberger, M.J., Trobin, W., Ricken, T., Holzapfel, G.A., 2016. A microstructurally based continuum model of cartilage viscoelasticity and permeability incorporating statistical fiber orientation. Biomechanics and Modeling in Mechanobiology 15, 229–244.*

This book belongs to Central Library BADJI Mokhtar-ANNABA UNIVERSITY Copyright Elsevier 2024

TABLE 4.1 Material, Compositional, and Structural Parameters Required to Approximate the Response of Cartilage and Corresponding Units.

Material Parameter			Unit
Fluid real density	ρ^{FR}	9.9×10^2	kg/m^3
Solid real density	ρ^{SR}	1.5×10^3	kg/m^3
Solid shear modulus	μ^S	2.3×10^5	N/m^2
Fiber-stored strain energy	k_1, k_2	4.3×10^5, 40	N/m^2,–
Matrix viscosity	β_{IM}, τ_{IM}	1.0, 1	–,s
Fiber viscosity	β_{FN}, τ_{FN}	2.2, 100	–,s
Compositional Parameter			**Unit**
Initial solid volume fraction	$n^S_{0S}(z^*)$	$0.15 + 0.15(z^*)$	–
Fiber volume fraction to solid	$\nu(z^*)$	$0.43(z^*)^2 - 0.60(z^*) + 0.85$	–
Tissue compaction point	$J^S_{cp}(z^*)$	$0.36 + 0.11(z^*)$	–
Initial Darcy permeability	$k_{0S}(z^*)$	$1 \times 10^{-15} - 0.9 \times 10^{-15}(z^*)$	m^4/Ns
k_{0S} deformation dependence	$m(z^*)$	$3.0 + 5.0(z^*)$	–
Structural Parameter			**Unit**
Diffusion tensor	**D**	DT-MRI	–

The parameter $z^* \in [0, 1]$ is the normalized tissue thickness, from the articular surface to the subchondral bone (Pierce et al., 2016).
DT-MRI, Diffusion tensor magnetic resonance imaging.

4.4.2.3 Material, Compositional, and Structural Parameters

Table 4.1 summarizes the required material, compositional, and structural parameters—values used to approximate the response of the cartilage through the tissue thickness—and corresponding units (cf. Pierce et al., 2013a,b, 2016). Material parameters are intrinsic to the properties of the tissue constituents. Compositional parameters refer to the local distribution of constituents within the tissue. We determine the structural parameter **D** required for the ODF $\rho(\mathbf{a}_0, \mathbf{D})$ directly from sample-specific DT-MRI data (cf. Section 4.4.2.2).

4.4.2.4 Finite Element Simulations

Following (Pierce et al., 2016), we performed "near" 2D indentation tests to study the intratissue interstitial fluid pressure and maximum shear stress resulting in the cartilage sample due to indentation with a plane-ended, 1-mm diameter cylindrical indenter (cf. Pierce et al., 2013a). An indentation test using a rectangular prismatic tip compressing a rectangular sample, with a constrained side to prevent out-of-plane motion, will exhibit the main features of intratissue deformation under 3D indentation using a plane-ended cylinder (Bae et al., 2006), cf. Fig. 4.5B.

We fix all displacements for nodes at the subchondral bone interface and set the corresponding fluid flux across this surface to zero. We apply symmetry boundary conditions to both cross-sectional surfaces of the tissue, one side representing the imaging plane of the experiment in Fig. 4.5B and the other resulting from the relative thickness of the FE model. At the surface contacting the impermeable indenter (the left surface in Fig. 4.5A) we prescribe the axial displacement to cause 1% global tissue strain in 150 s and set the corresponding fluid flux across this surface to zero. We specify all remaining nodes in contact with the physiological solution as freely moving and draining.

To study the effects of the collagen fiber network and through-the-thickness tissue heterogeneity (of mechanical properties) independently, we complete simulations of the indentation experiment using four models—Model 1: patient-specific collagen fiber network (defined using the measured DT-MRI, Section 4.4.2.1), heterogeneous compositional parameters (defined using the normalized tissue thickness z^*, Table 4.1); Model 2: patient-specific collagen fiber network, homogeneous compositional parameters; Model 3: no collagen fiber network, heterogeneous compositional parameters;

This book belongs to Central Library BADJI Mokhtar-ANNABA UNIVERSITY
Copyright Elsevier 2024

and Model 4: no collagen fiber network, homogeneous compositional parameters (Pierce et al., 2013a, 2016). Models with heterogeneous compositional parameters use the through-the-thickness parameters (cf. Table 4.1) while homogeneous models use constant mean parameters.

Each simulation employed 1938 20-node hexahedral, Taylor-Hood elements. We completed all simulations in the FE program ParFEAP (University of California at Berkeley, USA) using a total Lagrangian formulation and the included Newton−Raphson algorithm.

4.4.3 Tissue Complexity Captured via Model Complexity

Fig. 4.6 depicts simulation results for the indentation experiment with an impermeable, plane-ended cylinder of diameter 1 mm compressing the cartilage sample to 1% global strain in 150 s.

Reviewing quantitative values in the simulation results, the maximum interstitial fluid pressure at the indentation surface is 11.0 kPa for Model 1 (maximum among models); 10.1 kPa for Model 2 (a drop of −8.18% relative to Model 1); 4.10 kPa for Model 3 (−62.7%); and 3.46 kPa for Model 4 (−68.5%). Reviewing the maximum shear stress similarly, the maximum intratissue value is 8.64 kPa for Model 2 (maximum among models); 8.41 kPa for Model 1 (a drop of −2.66% relative to Model 2); 2.78 kPa for Model 3: (−67.8%); and 3.68 kPa for Model 4 (−57.4%).

4.4.4 Model Tradeoffs and Considerations

Overall, Model 1 retains the highest interstitial fluid pressure among the four models, and the fluid pressure is concentrated in the superficial zone and particularly the articular surface. Not surprisingly, the fluid pressure is higher directly underneath the edge of the indenter versus underneath its center. The result for Model 1, in the context of the full results, demonstrates that both the fiber network and the tissue's heterogeneity modulate the fluid pressure distribution to maintain fluid pressure beneath the contact surface and thus enhance load support and surface frictional properties.

We study the maximum shear stress in the solid because destructive effects are known to be associated with shear stress in particular (Smith et al., 2000, 2004; Wang et al., 2010a,b; Zhu et al., 2010; Bader et al., 2011). The maximum shear stress distributions through the tissue thickness for both Models 3 and 4 are significantly lower relative to Models 1 and 2, which are similar. This is likely due to the fact that we apply the same fixed global strain to all models, although the relative stiffness of the materials differs due to the differences in the collagen networks. Hence, it will take larger forces to compress Models 1 and 2 versus Models 3 and 4, thus leading to higher stresses. The solid extra stress results between fiber network-reinforced and unreinforced models should be viewed with caution.

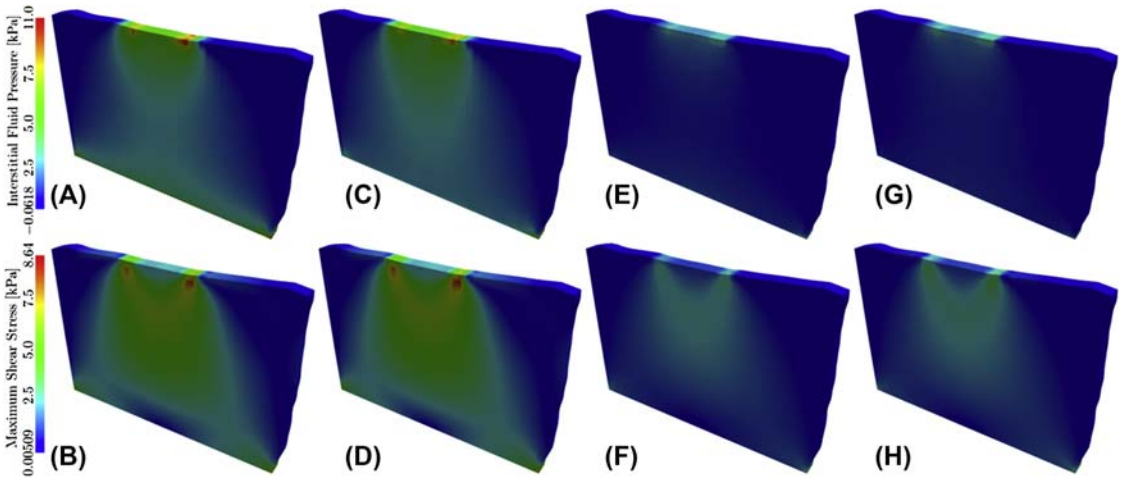

FIGURE 4.6 Both the collagen network and the tissue heterogeneity dramatically affect fluid pressure and shear stress within the tissue. Simulation results for indention to 1% strain in 150 s. Row 1: interstitial fluid pressure; Row 2: maximum shear stress. Column 1: material model with patient-specific collagen fiber network and heterogeneous material parameters; Column 2: model with patient-specific collagen fiber network but with homogeneous material parameters; Column 3: model without collagen fiber network and with heterogeneous material parameters; Column 4: model without collagen fiber network but with homogeneous material parameter. *Adapted from Pierce, D.M., Unterberger, M.J., Trobin, W., Ricken, T., Holzapfel, G.A., 2016. A microstructurally based continuum model of cartilage viscoelasticity and permeability incorporating statistical fiber orientation. Biomechanics and Modeling in Mechanobiology 15, 229−244.*

This book belongs to Central Library BADJI Mokhtar-ANNABA UNIVERSITY Copyright Elsevier 2024

Overall, the results of this study support both hypotheses. For the tissue sample investigated, the through-the-thickness heterogeneities of both the collagen fiber network and of the material parameters serve to influence the interstitial fluid pressure distribution and maintain fluid pressure near the cartilage surface. More specifically, our results demonstrate that the fiber network dramatically increases interstitial fluid pressure and focuses it near the surface. This is important because increased fluid pressure at the articular surface reduces the coefficient of friction of the interface thus improving motion and reducing wear (Ateshian et al., 1998). Furthermore, heterogeneity in the material parameters increases fluid pressure in the tissue. Heterogeneity in the orientation of the fiber network through the thickness of the cartilage appears to have a larger effect than heterogeneity of the material parameters on this cartilage sample's advantageous distribution of interstitial fluid pressure in response to mechanical loading.

4.5 DISCUSSION AND FUTURE DIRECTIONS

Advances in computational methods and imaging techniques, and their interactions, promote new strategies to probe complex biological systems. Traditional methods to characterize the bulk properties of tissues or engineered materials are rapidly being augmented or replaced by novel multiscale techniques for mechanical characterization and visualization, and microstructural and component-wise imaging. One challenge for the development of new imaging methods is to provide sufficient spatial and temporal resolution to enable the description of small (e.g., subcellular) structures at dynamic rates to capture a broad range of physiologic actions over multiple scales. Simultaneously, computational modeling across length-scales (molecular, cellular, tissue, organ, and organism levels) enables quantifying physics (e.g., stress) that cannot be measured using experimental techniques alone.

By combining imaging and computational modeling, we may unlock many barriers required to conduct multidisciplinary research, e.g., computationally driven mechanistic understanding of experimental findings, and experiments and visualizations that support calibration or validation of computational models.

As a representative example we detailed a 3D finite strain constitutive model capable of simultaneously addressing both solid (reinforcement) and fluid (permeability) dependence of the intratissue mechanical response on the patient-specific collagen fiber network. While demonstrated for articular cartilage, the framework is suitable for numerous biological tissues. We represented fiber reinforcement as a heterogeneous, dispersed network, where the fluid permeability is intimately dependent on this network and on a fixed intrafibrillar water portion. This approach, in which the model parameters are physically motivated, implements image-based morphological data in a computational setting.

ACKNOWLEDGMENTS

We thank José Raya and Christian Glaser from the NYU Langone Medical Center for the use of the diffusion tensor magnetic resonance imaging data and Magnus B. Lilledahl from the Norwegian University of Science and Technology for the use of the multiphoton microscopy image in Figs. 4.1 and 4.4 (left).

REFERENCES

Abdullah, O.M., Othman, S.F., Zhou, X.J., Magin, R.L., 2007. Diffusion tensor imaging as an early marker for osteoarthritis. In: Proc. Intl. Soc. Magn. Reson. Med., vol. 15, p. 814.

Abousleiman, Y., Cheng, A.H.D., Jiang, C., Roegiers, J.C., 1996. Poroviscoelastic analysis of borehole and cylinder problems. Acta Mechanica 109 (1–4), 199–219.

Alexander, A.L., Hurley, S.A., Samsonov, A.A., Adluru, N., Hosseinbor, A.P., Mossahebi, P., et al., 2011. Characterization of cerebral white matter properties using quantitative magnetic resonance imaging stains. Brain Connectivity 6, 423–446.

Arsigny, V., Fillard, P., Pennec, X., Ayache, N., 2006. Geometric means in a novel vector space structure on symmetric positive-definite matrices. SIAM Journal on Matrix Analysis and Applications 29, 328–347.

Ateshian, G.A., Wang, H., Lai, W.M., 1998. The role of interstitial fluid pressurization and surface porosities on the boundary friction of articular cartilage. Journal of Tribology-Transactions of the Asme 120, 241–251.

Ateshian, G.A., Rajan, V., Chahine, N.O., Canal, C.E., Hung, C.T., 2009. Modeling the matrix of articular cartilage using a continuous fiber angular distribution predicts many observed phenomena. Journal of Biomechanical Engineering 131, 61003.

Axel, L., Dougherty, L., 1989. MR imaging of motion with spatial modulation of magnetization. Radiology 171, 841–845.

Bachrach, N.M., Mow, V.C., Guilak, F., 1998. Incompressibility of the solid matrix of articular cartilage under high hydrostatic pressures. Journal of Biomechanics 31, 445–451.

Bader, D.L., Salter, D.M., Chowdhury, T.T., 2011. Biomechanical influence of cartilage homeostasis in health and disease. Arthritis 16, 979032. PMC3196252.

This book belongs to Central Library BADJI Mokhtar-ANNABA UNIVERSITY Copyright Elsevier 2024

Bae, W.C., Lewis, C.W., Levenston, M.E., Sah, R.L., 2006. Indentation testing of human articular cartilage: effects of probe tip geometry and indentation depth on intra-tissue strain. Journal of Biomechanics 39, 1039−1047.

Bae, W.C., Dwek, J.R., Znamirowski, R., Statum, S.M., Hermida, J.C., D'Lima, D.D., et al., 2010. Ultrashort echo time MR imaging of osteochondral junction of the knee at 3T: identification of anatomic structures contributing to signal intensity. Radiology 254, 837−845.

Bishop, A.W., 1959. The principle of effective stress. Teknisk Ukeblad 39, 859−863.

Bluhm, J., 2002. Modelling of saturated thermo-elastic porous solids with different phase temperatures. In: Ehlers, W., Bluhm, J. (Eds.), Porous Media: Theory, Experiments and Numerical Applications. Springer-Verlag, Berlin, Heidelberg, New York, pp. 87−120.

de Boer, R., 1996. Highlights in the historical development of the porous media theory - toward a consistent macroscopic theory. Applied Mechanics Reviews 4, 201−262.

de Boer, R., 2000. Theory of porous media. In: Highlights in the Historical Development and Current State. Springer-Verlag, Heidelberg.

Bowen, R.M., 1980. Incompressible pourous media models by use of theory of mixtures. International Journal of Engineering Science 18, 1129−1148.

Bowen, R.M., 1982. Compressible porous media models by use of the theory of mixtures. International Journal of Engineering Science 20, 697−735.

Burstein, D., Gray, M.L., Hartman, A.L., Gipe, R., Foy, B.D., 1993. Diffusion of small solutes in cartilage as measured by nuclear magnetic resonance (NMR) spectroscopy and imaging. Journal of Orthopaedic Research 11, 465−478.

Butz, K.D., Chan, D.D., Nauman, E.A., Neu, C.P., 2011. Stress distributions and material properties determined in articular cartilage from MRI-based finite strains. Journal of Biomechanics 44 (15), 2667−2672.

Chan, D.D., Neu, C.P., 2012. Transient and microscale deformations and strains measured under exogenous loading by noninvasive magnetic resonance. PLoS One 7, e33463.

Chan, D.D., Neu, C.P., Hull, M.L., 2009. In situ deformation of cartilage in cyclically loaded tibiofemoral joints by displacement-encoded MRI. Osteoarthritis Cartilage 17, 1461−1468.

Chan, D.D., Cai, L., Butz, K.D., Trippel, S.B., Nauman, E.A., Neu, C.P., 2016. In vivo articular cartilage deformation: noninvasive quantification of intratissue strain during joint contact in the human knee. Scientific Reports 6, 19220.

Chen, A.H.D., Detournay, E., 1998. On singular integral equations and fundamental solutions of poroelasticity. International Journal of Solids and Structures 35 (34/35), 4521−4555.

Choo, H.J., Lee, S.J., Kim, D.W., Jeong, H.W., Gwak, H., 2014. Multibanded anterior talofibular ligaments in normal ankles and sprained ankles using 3D isotropic proton densityweighted fast spin-echo MRI sequence. American Journal of Roentgenology 202, W87−W94.

Coudrillier, B., Tian, J., Alexander, S., Myers, K.M., Quigley, H.A., Nguyen, T.D., 2012. Biomechanics of the human posterior sclera: age- and glaucoma-related changes measured using inflation testing. Investigative Ophthalmology and Visual Science 53, 1714−1728.

Coussy, O., 2004. Poromechanics. John Wiley & Sons, Chichester.

Crisco, J.J., McGovern, R.D., Wolfe, S.W., 1999. Noninvasive technique for measuring in vivo three-dimensional carpal bone kinematics. Journal of Orthopaedic Research 17, 96−100.

de Visser, S.K., Crawford, R.W., Pope, J.M., 2008a. Structural adaptations in compressed articular cartilage measured by diffusion tensor imaging. Osteoarthritis Cartilage 16, 83−89.

de Visser, S.K., Bowden, J.C., Wentrup-Bryne, E., Rintoul, L., Bostrom, T., Pope, J.M., et al., 2008b. Anisotropy of collagen fibre alignment in bovine cartilage: comparison of polarised light microscopy and spatially resolved diffusion-tensor measurements. Osteoarthritis Cartilage 16, 689−697.

Drumheller, D.S., 1978. The theoretical treatment of a porous solid using a mixture theory. International Journal of Solids and Structures 14, 441−456.

Ehlers, W., 1989. Poröse Medien - ein kontinuumsmechanisches Modell auf der Basis der Mischungstheorie. Universität GH Essen. Forschungsbericht aus dem Fachbereich Bauwesen 47.

Ehlers, W., 1993. Constitutive equations for granular materials in geomechanical context. In: Hutter, K. (Ed.), Continuum Mechanics in Environmental Sciences and Geophysics. Springer-Verlag, Wien, pp. 313−402. CISM Courses and Lectures no. 337.

Ehlers, W., 2002. Foundations of multiphasic and porous materials. In: Ehlers, W., Bluhm, J. (Eds.), Porous Media: Theory, Experiments and Numerical Applications. Springer-Verlag, Berlin, pp. 3−86.

Eipper, G., 1998. Theorie und Numerik finiter elastischer Deformationen in fluidgesättigten porösen Festkörpern. Universität Stuttgart. Bericht Nr. II-1 aus dem Institut für Mechanik (Bauwesen).

Eşen, S., Akarırmak, Ü., Aydın, F.Y., Ünalan, H., 2013. Clinical evaluation during the acute exacerbation of knee osteoarthritis: the impact of diagnostic ultrasonography. Rheumatology International 33, 711−717.

Fan, R., Sacks, M.S., 2014. Simulation of planar soft tissues using a structural constitutive model: finite element implementation and validation. Journal of Biomechanics 47, 2043−2054.

Favre, J., Scanlan, S.F., Erhart-Hledik, J.C., Blazek, K., Andriacchi, T.P., 2013. Patterns of femoral cartilage thickness are different in asymptomatic and osteoarthritic knees and can be used to detect disease-related differences between samples. Journal of Biomechanical Engineering 135, 101002−101010.

Federico, S., Grillo, A., 2012. Elasticity and permeability of porous fibre reinforced materials under large deformations. Mechanics of Materials 44, 58−71.

Federico, S., Herzog, W., 2008. On the anisotropy and inhomogeneity of permeability in articular cartilage. Biomechanics and Modeling in Mechanobiology 7, 367−378.

Feldman, H.M., Yeatman, J.D., Lee, E.S., Barde, L.H.F., Gaman-Bean, S., 2010. Diffusion tensor imaging: a review for pediatric researchers and clinicians. Journal of Developmental and Behavioral Pediatrics 31, 346−356.

Filidoro, L., Dietrich, O., Weber, J., Rauch, E., Oether, T., Wick, M., et al., 2005. High-resolution diffusion tensor imaging of human patellar cartilage: feasibility and preliminary findings. Magnetic Resonance in Medicine 53, 993−998.

This book belongs to Central Library BADJI Mokhtar-ANNABA UNIVERSITY Copyright Elsevier 2024

Gao, Y., Waas, A.M., Faulkner, J.A., Kostrominova, T.Y., Wineman, A.S., 2008. Micromechanical modeling of the epimysium of the skeletal muscles. Journal of Biomechanics 41, 1–10.

Goergen, C.J., Azuma, J., Barr, K.N., Magdefessel, L., Kallop, D.Y., Gogineni, A., et al., 2011. Influences of aortic motion and curvature on vessel expansion in murine experimental aneurysms. Arteriosclerosis, Thrombosis, and Vascular Biology 31, 270–279.

Göktepe, S., Acharya, S.N.S., Wong, J., Kuhl, E., 2011. Computational modeling of passive myocardium. International Journal for Numerical Methods in Biomedical Engineering 27, 1–12.

Graichen, H., Jakob, J., von Eisenhart-Rothe, R., Englmeier, K.H., Reiser, M., Eckstein, F., 2003. Validation of cartilage volume and thickness measurements in the human shoulder with quantitative magnetic resonance imaging. Osteoarthritis Cartilage 11, 475–482.

Griebel, A.J., Trippel, S.B., Neu, C.P., 2013. Noninvasive dualMRI-based strains vary by depth and region in human osteoarthritic articular cartilage. Osteoarthritis Cartilage 21, 394–400.

Guerin, H.A.L., Elliott, D.M., 2005. The role of fiber-matrix interactions in a nonlinear fiber-reinforced strain energy model of tendon. Journal of Biomedical Engineering 127, 345–350.

Hardy, P.A., Ridler, A.C., Chiarot, C.B., Plewes, D.B., Henkelman, R.M., 2005. Imaging articular cartilage under compressioncartilage elastography. Magnetic Resonance in Medicine 53, 1065–1073.

Haris, M., Singh, A., Cai, K., Kogan, F., McGarvey, J., DeBrosse, C., et al., 2014. A technique for in vivo mapping of myocardial creatine kinase metabolism. Nature Medicine 20, 209–214.

Hassanizadeh, S.M., Gray, W.G., 1979a. General conservation equations for multi-phase systems: 1. Averaging procedure. Advances in Water Resources 2, 131–144.

Hassanizadeh, S.M., Gray, W.G., 1979b. General conservation equations for multi-phase systems: 2. Mass, momenta, energy, and entropy equations. Advances in Water Resources 2, 191–208.

Hassanizadeh, S.M., Gray, W.G., 1980. General conservation equations for multi-phase systems: 3. Constitutive theory for porous media flow. Advances in Water Resources 3, 25–40.

Hassanizadeh, S.M., Gray, W.G., 1990. Mechanics and thermodynamics of multiphase flow in porous media including interphase boundaries. Advances in Water Resources 13, 169–186.

Herrmann, L.R., Peterson, F.E., 1968. A numerical procedure for viscoelastic stress analysis. In: Proceedings 7th Meeting of ICRPG Mechanical Behavior Working Group, Orlando.

Hinterwimmer, S., Gotthardt, M., von Eisenhart-Rothe, R., Sauerland, S., Siebert, M., Vogl, T., et al., 2005. In vivo contact areas of the knee in patients with patellar subluxation. Journal of Biomechanics 38, 2095–2101.

Holzapfel, G.A., 1996. On large strain viscoelasticity: continuum formulation and finite element applications to elastomeric structures. International Journal for Numerical Methods in Engineering 39, 3903–3926.

Holzapfel, G.A., 2000. Nonlinear solid mechanics. In: A Continuum Approach for Engineering. John Wiley & Sons, Chichester.

Holzapfel, G.A., Gasser, T.C., 2001. A viscoelastic model for fiber-reinforced composites at finite strains: continuum basis, computational aspects and applications. Computer Methods in Applied Mechanics and Engineering 190, 4379–4403.

Holzapfel, G.A., Gasser, T.C., Ogden, R.W., 2000. A new constitutive framework for arterial wall mechanics and a comparative study of material models. Journal of Elasticity 61, 1–48.

Huang, C.Y., Stankiewicz, A., Ateshian, G.A., Mow, V.C., 2005. Anisotropy, inhomogeneity, and tension-compression nonlinearity of human glenohumeral cartilage in finite deformation. Journal of Biomechanics 38, 799–809.

Humphrey, J.D., 2002. Cardiovascular solid mechanics. In: Cells, Tissues, and Organs. Springer-Verlag, New York.

Humphrey, J.D., 2008. Biological soft tissues. In: Sharpe, W.N.J. (Ed.), Springer Handbook of Experimental Solid Mechanics. Springer Science+-Business Media, LCC, New York, pp. 169–185.

Iagnocco, A., Filippucci, E., Riente, L., Meenagh, G., Sedie, A.D., Sakellariu, G., et al., 2012. Ultrasound imaging for the rheumatologist XLI. Sonographic assessment of the hip in OA patients. Clinical and Experimental Rheumatology 30, 652–657.

Jurvelin, J.S., Buschmann, M.D., Hunziker, E.B., 1997. Optical and mechanical determination of Poisson's ratio of adult bovine humeral articular cartilage. Journal of Biomechanics 30, 235–241.

Kellgren, J.H., Lawrence, J.S., 1957. Radiological assessment of osteo-arthrosis. Annals of the Rheumatic Diseases 16, 494–502.

Krishnan, R., Park, S., Echstein, F., Ateshian, G.A., 2003. Inhomogeneous cartilage properties enhance superficial interstitial fluid support and frictional properties, but do not provide a homogeneous state of stress. Journal of Biomechanical Engineering 125, 569–577.

Lai, W.M., Hou, J.S., Mow, V.C., 1991. A triphasic theory for the swelling and deformation behaviours of articular cartilage. Journal of Biomechanical Engineering 113, 245–258.

Le Graverand, M.P.H., Buck, R.J., Wyman, B.T., Vignon, E., Mazzuca, S.A., Brandt, K.D., et al., 2009. Change in regional cartilage morphology and joint space width in osteoarthritis participants versus healthy controls: a multicentre study using 3.0 Tesla MRI and Lyon–Schuss radiography. Annals of the Rheumatic Diseases 69, 155–162.

Lei, F., Szeri, A.Z., 2006. The influence of fibril organization on the mechanical behaviour of articular cartilage. Proceedings of the Royal Society of London – Series A 462, 3301–3322.

Liisberg, M., Diederichsen, A.C., Lindholt, J.S., 2017. Abdominal ultrasound-scanning versus non-contrast computed tomography as screening method for abdominal aortic aneurysm – a validation study from the randomized DANCAVAS study. BMC Medical Imaging 17, 14.

Lilledahl, M.B., Pierce, D.M., Ricken, T., Holzapfel, G.A., de Lange Davies, C., 2011. Structural analysis of articular cartilage using multiphoton microscopy: input for biomechanical modeling. IEEE Transactions on Medical Imaging 30, 1625–1648.

This book belongs to Central Library BADJI Mokhtar-ANNABA UNIVERSITY

Copyright Elsevier 2024

Lopez, O., Amrami, K.K., Manduca, A., Rossman, P.J., Ehman, R.L., 2007. Developments in dynamic MR elastography for in vitro biomechanical assessment of hyaline cartilage under high-frequency cyclical shear. Journal of Musculoskeletal and Neuronal Interactions 25, 310–320.

Lopez, O., Amrami, K.K., Manduca, A., Ehman, R.L., 2008. Characterization of the dynamic shear properties of hyaline cartilage using high-frequency dynamic MR elastography. Magnetic Resonance in Medicine 59, 356–364.

B, E.M., B, K.D., A, M., 1990. MRI demonstration of hypertrophic articular cartilage repair in osteoarthritis. Skeletal Radiology 19, 335–339.

Markert, B., 2007. A constitutive approach to 3-D nonlinear fluid flow through finite deformable porous continua. Transport in Porous Media 70, 427–450.

Meder, R., de Visser, S.K., Bowden, J.C., Bostrom, T., Pope, J.M., 2006. Diffusion tensor imaging of articular cartilage as a measure of tissue microstructure. Osteoarthritis Cartilage 14, 875–881.

Miehe, C., Göktepe, S., Lulei, F., 2004. A micro-macro approach to rubber-like materials – Part I: the non-affine micro-sphere model of rubber elasticity. Journal of the Mechanics and Physics of Solids 52, 2617–2660.

Mosher, T.J., Smith, M.B., 1990. A DANTE tagging sequence for the evaluation of translational sample motion. Magnetic Resonance in Medicine 15, 334–339.

Mosher, T.J., Liu, Y., Torok, C.M., 2010. Functional cartilage MRI T2 mapping: evaluating the effect of age and training on knee cartilage response to running. Osteoarthritis Cartilage 18, 358–364.

Mow, V.C., Gibbs, M.C., Lai, W.M., Zhu, W.B., Athanasiou, K.A., 1989. Biphasic indentation of articular cartilage-II. A numerical algorithm and an experimental study. Journal of Biomechanics 22, 853–861.

Mow, V.C., Gu, W.Y., Chen, F.H., 2005. Structure and function of articular cartilage and meniscus. In: Mow, V.C., Huiskes, R. (Eds.), Basic Orthopaedic Biomechanics & Mechano-biology, third ed. Lippincott Williams & Wilkins, Philadelphia, pp. 181–258.

Muir, E.R., Watts, L.T., Tiwari, Y.V., Bresnen, A., Duong, T.Q., 2014. Quantitative cerebral blood flow measurements using MRI. Methods in Molecular Biology 1135, 205–211.

Muthupillai, R., Lomas, D.J., Rossman, P.J., Greenleaf, J.F., Manduca, A., Ehman, R.L., 1995. Magnetic resonance elastography by direct visualization of propagating acoustic strain waves. Science 269, 1854–1857.

Neu, C.P., 2014. Functional imaging in OA: role of imaging in the evaluation of tissue biomechanics. Osteoarthritis Cartilage 22, 1349–1359.

Neu, C.P., Walton, J.H., 2008. Displacement encoding for the measurement of cartilage deformation. Magnetic Resonance Imaging 59, 149–155.

Neu, C.P., Hull, M.L., Walton, J.H., 2005a. Heterogeneous three-dimensional strain fields during unconfined cyclic compression in bovine articular cartilage explants. Journal of Orthopaedic Research 23, 1390–1398.

Neu, C.P., Hull, M.L., Walton, J.H., 2005b. Error optimization of a three-dimensional magnetic resonance imaging tagging-based cartilage deformation technique. Magnetic Resonance Imaging 54, 1290–1294.

Neu, C.P., Hull, M.L., Walton, J.H., Buonocore, M.H., 2005c. MRI-based technique for determining nonuniform deformations throughout the volume of articular cartilage explants. Magnetic Resonance Imaging 53, 321–328.

Neu, C.P., Komvopoulos, K., Reddi, A.H., 2008. The interface of functional biotribology and regenerative medicine in synovial joints. Tissue Engineering. Part B, Reviews 14, 235–247.

Neu, C.P., Arastu, H.F., Curtiss, S., Reddi, A.H., 2009. Characterization of engineered tissue construct mechanical function by magnetic resonance imaging. Journal of Tissue Engineering and Regenerative Medicine 3, 477–485.

Papaioannou, G., Nianios, G., Mitrogiannis, C., Fyhrie, D., Tashman, S., Yang, K.H., 2008. Patient-specific knee joint finite element model validation with high-accuracy kinematics from biplane dynamic Roentgen stereogrammetric analysis. Journal of Biomechanics 41, 2633–2638.

Park, S., Krishnan, R., Nicoll, S.B., Ateshian, G.A., 2003. Cartilage interstitial fluid load support in unconfined compression. Journal of Biomechanics 36, 1785–1796.

Pence, T.J., 2012. On the formulation of boundary value problems with the incompressible constituents constraint in finite deformation poroelasticity. Mathematical Methods in the Applied Sciences 35, 1756–1783.

Peterfy, C.G., Guermazi, A., Zaim, S., Tirman, P.F.J., Miaux, Y., White, D., et al., 2004. Whole-organ magnetic resonance imaging score (WORMS) of the knee in osteoarthritis. Osteoarthritis Cartilage 12, 177–190.

Pierce, D.M., 2013. Constitutive Modeling of Articular Cartilage [Habilitation (Venia Legendi) Thesis in Experimental and Computational Biomechanics]. Graz University of Technology, Austria.

Pierce, D.M., Trobin, W., Trattnig, S., Bischof, H., Holzapfel, G.A., 2009. A phenomenological approach toward patient-specific computational modeling of articular cartilage including collagen fiber tracking. Journal of Biomechanical Engineering 131, 091006.

Pierce, D.M., Trobin, W., Raya, J.G., Trattnig, S., Bischof, H., Glaser, C., et al., 2010. DT-MRI based computation of collagen fiber deformation in human articular cartilage: a feasibility study. Annals of Biomedical Engineering 38, 2447–2463.

Pierce, D.M., Ricken, T., Holzapfel, G.A., 2013a. Modeling sample/patient-specific structural and diffusional response of cartilage using DT-MRI. International Journal for Numerical Methods in Biomedical Engineering 29, 807–821.

Pierce, D.M., Ricken, T., Holzapfel, G.A., 2013b. A hyperelastic biphasic fiber-reinforced model of articular cartilage considering distributed collagen fiber orientations: continuum basis, computational aspects and applications. Computer Methods in Biomechanics and Biomedical Engineering 16, 1344–1361.

Pierce, D.M., Maier, F.S., Weisbecker, H., Viertler, C., Verbrugghe, P., Famaey, N., et al., 2015. Human thoracic and abdominal aortic aneurysmal tissues: damage experiments, statistical analysis and constitutive modeling. Journal of the Mechanical Behavior of Biomedical Material 41, 92–107.

Pierce, D.M., Unterberger, M.J., Trobin, W., Ricken, T., Holzapfel, G.A., 2016. A microstructurally based continuum model of cartilage viscoelasticity and permeability incorporating statistical fiber orientation. Biomechanics and Modeling in Mechanobiology 15, 229–244.

H, C.R., A, A.E., W, J.A., 2013. Subject-specific analysis of joint contact mechanics: application to the study of osteoarthritis and surgical planning. Journal of Biomechanical Engineering 135, 021003–021026.

This book belongs to Central Library BADJI Mokhtar-ANNABA UNIVERSITY Copyright Elsevier 2024

Raya, J.G., Melkus, G., Adam-Neumair, S., Dietrich, O., Mützel, E., Kahr, B., et al., 2011. Change of diffusion tensor imaging parameters in articular cartilage with progressive proteoglycan extraction. Investigative Radiology 46, 401−409.

Raya, J.G., Melkus, G., Adam-Neumair, S., Dietrich, O., Mützel, E., Reiser, M.F., et al., 2013. Diffusion-tensor imaging of human articular cartilage specimens with early signs of cartilage damage. Radiology 266, 831−841.

Ricken, T., Bluhm, J., 2010. Remodeling and growth of living tissue: a multiphase theory. Archive of Applied Mechanics 80, 453−465.

Roos, P.J., Neu, C.P., Hull, M.L., Howell, S.M., 2005. A new tibial coordinate system improves the precision of anteriorposterior knee laxity measurements: a cadaveric study using Roentgen stereophotogrammetric analysis. Journal of Orthopaedic Research 23, 327−333.

C, S., RD, S., H, M., H, M., W, W., S, A.M., et al., 2010. Effects of exercise intervention on knee morphology in middle-aged women: a longitudinal analysis using magnetic resonance imaging. Cells Tissues Organs 192, 64−72.

Setton, L.A., Mow, V.C., Mller, F.J., Pita, J.C., Howell, D.S., 1994. Mechanical properties of canine articular cartilage are significantly altered following transection of the anterior cruciate ligament. Journal of Orthopaedic Research 12, 451−463.

Setton, L.A., Elliott, D.M., Mow, V.C., 1999. Altered mechanics of cartilage with osteoarthritis: human osteoarthritis and an experimental model of joint degeneration. Osteoarthritis Cartilage 7, 2−14.

Shin, C.S., Souza, R.B., Kumar, D., Link, T.M., Wyman, B.T., Majumdar, S., 2011. In vivo tibiofemoral cartilage-to-cartilage contact area of females with medial osteoarthritis under acute loading using MRI. Journal of Musculoskeletal and Neuronal Interactions 34, 1405−1413.

Simo, J.C., 1987. On a fully three-dimensional finite-strain viscoelastic damage model: formulation and computational aspects. Computer Methods in Applied Mechanics and Engineering 60, 153−173.

Simo, J.C., Pister, K.S., 1984. Remarks on rate constitutive equations for finite deformation problems: computational implications. Computer Methods in Applied Mechanics and Engineering 46, 201−215.

Skempton, A.W., 1960. Terzaghi's discovery of effective stress. In: Bjerrum, L., Casagrande, A., Peck, R.B., Skempton, A.W. (Eds.), From Theory to Practice in Soil Mechanics. John Wiley, New York, London, pp. 42−53.

Smith, R.L., Trindade, M.C.D., Ikenoue, T., Mohtai, M., Das, P., Carter, D.R., et al., 2000. Effects of shear stress on articular chondrocyte metabolism. Biorheology 37, 95−107.

Smith, R.L., Carter, D.R., Schurman, D.J., 2004. Pressure and shear differentially alter human articular chondrocyte metabolism: a review. Clinical Orthopaedics and Related Research (Suppl. 427), S89−S95.

Soltz, M.A., Ateshian, G.A., 1998. Experimental verification and theoretical prediction of cartilage interstitial fluid pressurization at an impermeable contact interface in confined compression. Journal of Biomechanics 31, 927−934.

Soltz, M.A., Ateshian, G.A., 2000. A conewise linear elasticity mixture model for the analysis of tension-compression nonlineartiy in articular cartilage. Journal of Biomechanical Engineering 122, 576−586.

Stehling, C., Lane, N.E., Nevitt, M.C., Lynch, J., McCulloch, C.E., Link, T.M., 2010. Subjects with higher physical activity levels have more severe focal knee lesions diagnosed with 3T MRI: analysis of a non-symptomatic cohort of the osteoarthritis initiative. Osteoarthritis Cartilage 18, 776−786.

Sun, Y.L., Luo, Z.P., Fertala, A., An, K.A., 2002. Direct quantification of the flexibility of type I collagen monomer. Biochemical and Biophysical Research Communications 295, 382−386.

Taylor, R.L., Pister, K.S., Goudreau, G.L., 1970. Thermomechanical analysis of viscoelastic solids. International Journal for Numerical Methods in Engineering 2, 45−59.

Tervonen, O., Dietz, M.J., Carmichael, S.W., Ehman, R.L., 1993. MR imaging of knee hyaline cartilage: evaluation of two- and three-dimensional sequences. Journal of Musculoskeletal and Neuronal Interactions 3, 663−668.

von Terzaghi, K., 1943. Theoretical Soil Mechanics. John Wiley and Sons, New York.

Thevenot, J., Koivumäki, J., Kuhn, V., Eckstein, F., Jämsä, T., 2014. A novel methodology for generating 3D finite element models of the hip from 2D radiographs. Journal of Biomechanics 47, 438−444.

Truesdell, C., 1984. Rational Thermodynamics, second ed. Springer, Berlin - Heidelberg - New York.

Wan, L., de Asla, R.J., Rubash, H.E., Li, G., 2006. Determination of in-vivo articular cartilage contact areas of human talocrural joint under weightbearing conditions. Osteoarthritis Cartilage 14, 1294−1301.

Wang, P., Zhu, F., Lee, N.H., Konstantopoulos, K., 2010a. Shear-induced interleukin-6 synthesis in chondrocytes: roles of E prostanoid (EP) 2 and EP3 in cAMP/protein kinase A- and PI3-K/Akt-dependent NF-kappaB activation. Journal of Biological Chemistry 285, 24793−24804.

Wang, P., Zhu, F., Konstantopoulos, K., 2010b. Prostaglandin E2 induces interleukin-6 expression in human chondrocytes via cAMP/protein kinase A- and phosphatidylinositol 3-kinase-dependent NF-kappaB activation. American Journal of Physiology - Cell Physiology 298, 1445−1456.

Weisbecker, H., Pierce, D.M., Regitnig, P., Holzapfel, G.A., 2012. Layer-specific damage experiments and modeling of human thoracic and abdominal aortas with non-atherosclerotic intimal thickening. Journal of the Mechanical Behavior of Biomedical Materials 12, 93−106.

Whitaker, S., 1977. Simultaneous Heat, Mass, and Momentum Transfer in Porous Media: A Theory of Drying, vol. 13, pp. 119−203.

Wilson, W., Huyghe, J.M., van Donkelaar, C.C., 2007. Depth-dependent compressive equilibrium properties of articular cartilage explained by its composition. Biomechanics and Modeling in Mechanobiology 6 (1−2), 43−53.

Wolfe, S.W., Neu, C.P., Crisco, J.J., 2000. In vivo scaphoid, lunate, and capitate kinematics in flexion and in extension. The Journal of Hand Surgery 25, 860−869.

Wong, M., Ponticiello, M., Kovanen, V., Jurvelin, J.S., 2000. Volumetric changes of articular cartilage during stress relaxation in unconfined compression. Journal of Biomechanics 33, 1049−1054.

Zerhouni, E.A., Parish, D.M., Rogers, W.J., Yang, A., Shapiro, E.P., 1988. Human heart: tagging with MR imaging−a method for noninvasive assessment of myocardial motion. Radiology 169, 59−63.

Zhu, F., Wang, P., Lee, N.H., Goldring, M.B., Konstantopoulos, K., 2010. Prolonged application of high fluid shear to chondrocytes recapitulates gene expression profiles associated with osteoarthritis. PLoS One 5, E15174.

This book belongs to Central Library BADJI Mokhtar-ANNABA UNIVERSITY

Copyright Elsevier 2024

Chapter 5

Finite Element Modeling of Turing Pattern Formation: An Application to Appearance and Location of Dentinal Tubules

J. Nino-Barrera[1], J.A. Guerrero[1,4], G. Nino[2], M. Cerrolaza[3], E.B. de las Casas[4], A.M. Ramírez Martínez[5] and D.A. Garzón-Alvarado[1]

[1]Universidad Nacional de Colombia, Bogota, Colombia; [2]The George Washington University School of Medicine and Health Sciences, Washington, DC, United States; [3]Universidad Politécnica de Cataluña, Barcelona, España; [4]Universidade Federal de Minas Gerais, Belo Horizonte, Brazil; [5]Universidad Central de Colombia, Bogota, Colombia

5.1 INTRODUCTION

Mathematical models are used to predict, simulate, and study complex biological phenomena such as the fracture healing process (Jiang-Jun et al., 2014), growth (Garzon-Alvarado et al., 2014; Farzaneh et al., 2015), and joint formation (Cardiff et al., 2014), among others. These models, which are governed by the conservation laws and are accompanied by constitutive laws (Anguelova et al., 2007), allow prediction of migration, cell proliferation, and differentiation, among other biological phenomena. In some cases, the mathematical models are solved by analytic formalism for geometric situations with high simplification, which can limit its scope in real situation. Therefore, the numerical solution is preferred and will be the central topic of this chapter.

From the mathematical point of view of development biology, there are two basic model categories in each stage: (1) models that predict the concentration evolution of biochemical and molecular species and (2) models that determine the cell location, migration, and differentiation in the development tissue. In the chemical patterns modelers use reaction−diffusion equations, and if the diffusion is dominant, a uniform steady state can be obtained. On the other hand, if the reaction term is dominant, the model solution can generate complex patterns. The prediction of those patterns is an important field of mathematics called dynamical systems, and it defines the space parameters that produce different distributions. Finally, in the cellular movement category, the mathematical models represent the formation of spatial patterns by changes in cellular density in response to specific chemical substances and aggregation or repulsion between the cells (Vanegas et al., 2009; Vanegas-Acosta and Garzón-Alvarado, 2014).

Reaction−diffusion equations with a reactive dominant term were studied by Alain Turing in the early 1950s. Turing attributed the pattern formation in the nature to chemical interactions and studied the biological model solutions described by reaction−diffusion equations (Turing, 1952). He found three possible types of instabilities: (1) oscillatory over time and uniform in space, (2) stationary in time and periodic in space, and (3) oscillatory in space and time. Turing instability corresponds to a type b instability and is generated when a chemical reaction−diffusion system evolves into heterogeneous spatial patterns from a uniform stationary state in response to small perturbations.

The solution of these reaction−diffusion systems can be carried out by different numerical methods, such as finite difference method (FDM) (Plazl and Lakner, 2010), finite elements (Garzon-Alvarado et al., 2009), and discontinuous finite elements (Ghosh et al., 2009), among others. The FDM has been widely used (Plazl and Lakner, 2010) despite its limitation for the solution in irregular domains. In cases where the domain geometry is complex, a mapping is required that

Numerical Methods and Advanced Simulation in Biomechanics and Biological Processes. https://doi.org/10.1016/B978-0-12-811718-7.00005-8
Copyright © 2018 Elsevier Ltd. All rights reserved.

This book belongs to Central Library BADJI Mokhtar-ANNABA UNIVERSITY

Copyright Elsevier 2024

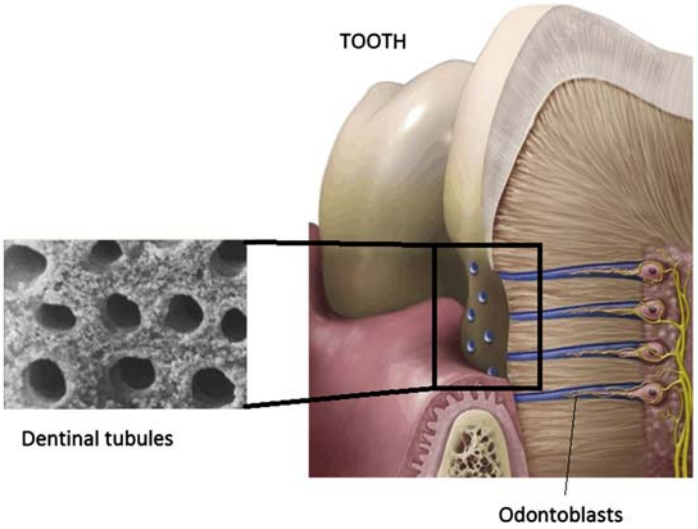

FIGURE 5.1 Odontoblast pattern. *Taken from Decker Keenan, 2017. Root Canal Dentinal Tubules. W Walnut St, Rogers Dentist AR. http://www.deckerdental.org/dental-health/sensitive-teeth/.*

can increase the method complexity in comparison with, for example, the finite element method (FEM). The FEM is widely used in engineering (Nino-Barrera et al., 2013) and in sciences (Garzon-Alvarado et al., 2009) and allows to solve differential equations in highly irregular domains. On the other hand, the discontinuous Galerkin finite element method (DGFEM) is used in multiphysics problems. The DGFEM has advantages, including easy parallelization and good behavior in highly connective problems (Ghosh et al., 2009; Long et al., 2016). In this chapter we model a reaction–diffusion process and solved by FEM of dentinal tubules morphogenesis. In the dentinal formation, we can see a well-organized pattern of the odontoblast resembling a Turing pattern formation (Fig. 5.1).

Dental morphogenesis is a complex process involving genetic (Lesot et al., 2001; Mina and Kollar, 1987; Ruch et al., 1995; Thesleff, 1995a,b), biochemical (Aberg et al., 1997; Kettunen et al., 2000; Kettunen and Thesleff, 1998; Thesleff and Mikkola, 2002; Thesleff et al., 1995a,b, 1996), mechanical (Mammoto et al., 2011), and cellular factors (Ruch et al., 1995; Arana-Chavez and Massa, 2004; Lisi et al., 2003; Mitsiadis and Graf, 2009). Tooth structure formation is guided by genetic factors, which depend on the type of species and ethnicity of a particular individual, delimiting its shape, size, and position (Ferrario et al., 1999). Additionally, some studies emphasize that hormonal biochemical signaling, both local and systemic, affects the tooth formation and alters its normal structure (Kumasaka et al., 2010). In conjunction with biochemical and genetic factors, mechanical loads influence cell behavior, modifying tooth morphology and function (Kumasaka et al., 2010). As a result, different tissues are developed during morphogenesis: enamel, cementum, and dentine (Nanci, 2008; Bartold and Narayanan, 1998).

The differentiation of odontoblasts from the papilla is a highly organized process that entails well-established patterns of location and shape (Lesot et al., 2001; Ruch et al., 1995; Arana-Chavez and Massa, 2004; Lisi et al., 2003) (Fig. 5.1). The geometric arrangement of the differentiation of these cells suggests a pattern that establishes mean distances between the functional odontoblasts to form the tubules in the future (Carda and Peydro, 2006; Linde, 2009). The odontoblast moves to the inside of the papilla and leaves behind a cytoplasmic prolongation that shapes dentin tubule formation generated by mineralization of its surrounding matrix (Arana-Chavez and Massa, 2004; Nanci, 2008).

The mechanism of morphogenesis and differentiation of the odontoblast is an ongoing research topic (Tziafas et al., 2010). Recently, hypotheses have been suggested to explain the geometric pattern of the sites where osteoblast differentiation occurs under the influence of biochemical factors. For example, Ruch et al. (1995), Lisi et al. (2003), and Schmitt and Ruch (2000) have postulated that only the preodontoblasts that have fulfilled a certain number of cell cycles become postmitotic and are competent to differentiate into functional odontoblasts. Considering the above, the spatial distribution of growth factors on the basement membrane, specifically bone morphogenetic proteins BMP2 and BMP4, would likely determine the possible sites of differentiation of the competent preodontoblasts. On the other hand, Mitsiadis and Graf (2009) have stated that the differentiation of dental cells is induced by different chemical signals. This chemical influence may induce cells to differentiate into a specialized cell type at a specific site or it may only support survival and proliferation with the specific site of differentiation being chosen stochastically (Mitsiadis and Graf, 2009). The exact mechanism of molecular signaling and the biological events that precede the differentiation of the mesenchymal cell into

This book belongs to Central Library BADJI Mokhtar-ANNABA UNIVERSITY Copyright Elsevier 2024

odontoblasts are still a subject of constant scientific discussion (Plikus et al., 2005). Therefore, in this chapter, we explore a mathematical model (reaction–diffusion equations) to investigate the appearance, location, and morphology of the odontoblasts and the dentinal tubules. The model proposed is solved by FEM.

5.2 THE REACTION–DIFFUSION SYSTEMS: MODELING AND SOLVING

5.2.1 Reaction–Diffusion Equation

It can be assumed that a set of molecules is on a tissue (geometric domain). Molecules could produce cell proliferation, differentiation, or death. So, the description of the concentration of those molecules is important to evaluate their interaction, formation, and degradation in each time step and their effect on the surrounding cells. We will start the deduction with the Fick's law to describe the movement of each molecule.

The Fick's Law establishes that the movement of species $u(\mathbf{x},t)$ indicates the changes in concentration from points of higher concentration to points of lower concentration (Garzón-Alvarado, 2007; Vanegas-Acosta and Garzón-Alvarado, 2014). The law is expressed as follows:

$$\mathbf{J}(\mathbf{x},t) = -D\nabla u(\mathbf{x},t) \tag{5.1}$$

where $\mathbf{J}$ is the diffusive flux vector and D is the diffusion coefficient. An additional reactive function $f(u,\mathbf{x},t)$ is required to analyze the reaction between two or more species and represents the change in the $u(\mathbf{x},t)$ concentration due to interaction effects such as production, proliferation, and consumption. Because of the conservation principle, the total flow of mass through the surface S of the volume V plus the amount of mass transformed inside the volume by the reactive term should be equal to the rate of change of the amount of mass contained in V. It can be seen below:

$$\frac{\partial}{\partial t}\int_V u(\mathbf{x},t)dV = -\int_S (\mathbf{J}\cdot\mathbf{n})dS + \int_V f dV \tag{5.2}$$

where $\mathbf{n}$ is the normal vector to the surface S. With the purpose to leave all terms of the equation in the same domain (the volume), the divergence theorem is applied to the diffusive term and Eqs. (5.1) and (5.2) are combined. The result, in differential form, is as follows:

$$\frac{\partial u(\mathbf{x},t)}{\partial t} = \nabla\cdot(D\nabla u(\mathbf{x},t)) + f(u,\mathbf{x},t) \tag{5.3}$$

where $\nabla\cdot(D\nabla u(\mathbf{x},t))$ is the diffusion term and $f(u,\mathbf{x},t)$ is the reactive term.

5.2.2 Biological Models: Brief Discussion on the Reactive Term

The zebra skin pigmentation (Ball, 2015) and the ossification patterns formation (Garzon-Alvarado, 2014), among others, have been modeled with reaction–diffusion equations. Among the most prominent models are the Schnakenberg, glycolysis, and chemotaxis models. These models have their high concordance with a lot of biological and, in general, natural phenomena as a fundamental characteristic.

5.2.2.1 Schnakenberg Model

The Schnakenberg model is known as one of the simplest and most used reaction–diffusion models in morphogenesis. This explains the behavior of chemical activator in the presence of chemical inhibitor. These reaction–diffusion equations represent a theoretical approach to a generic chemical interaction between two species. Let us suppose that u is the activator and v is the inhibitor substance. The reaction term for the activator substance is described as a constant production (a), a linear consumption, and the production of the activator in presence of the inhibitor (a nonlinear kinetic reaction). The reaction term for the inhibitor substance is described as a constant production (b) and a nonlinear kinetic reaction for the consumption of the activator in the presence of the inhibitor.

In its dimensionless form, the model is described by the following equations (Garzón-Alvarado, 2007; Vanegas-Acosta and Garzón-Alvarado, 2014):

$$\frac{\partial u}{\partial t} = \gamma\left(a - u + u^2 v\right) + \nabla^2 u \tag{5.4a}$$

This book belongs to Central Library BADJI Mokhtar-ANNABA UNIVERSITY Copyright Elsevier 2024

$$\frac{\partial v}{\partial t} = \gamma\left(b - u^2 v\right) + \nabla^2 v \tag{5.4b}$$

5.2.2.2 Glycolysis Model

This model describes the glucose molecule synthesis that provides energy to a cell. In the model, u is the glucose concentration and v is the pyruvate (component that surges due to the glucose reaction sequences). The diffusion of two substances is regulated by the diffusion coefficients D_u and D_v. In the reaction term for the glucose concentration, δ represents a constant production, k is the linear consumption coefficient, and the last term is the nonlinear consumption. On the other hand, in the reaction term for the pyruvate, k is the linear production coefficient, the quadratic term is the nonlinear activation, and the last one is the linear consumption.

In its dimensionless form, the model is described by the following equations (Garzón-Alvarado, 2007; Vanegas-Acosta and Garzón-Alvarado, 2014):

$$\frac{\partial u}{\partial t} = D_u \nabla^2 u + \delta - ku - u^2 v \tag{5.5a}$$

$$\frac{\partial v}{\partial t} = D_v \nabla^2 v + ku + uv^2 - v \tag{5.5b}$$

5.2.2.3 Chemotaxis Model

The chemotaxis model is based in the existence of a chemoattractant. This substance is an external chemical stimulus that promotes cell migration directed toward the gradient of concentration or agglomeration. The cell density and the concentration of chemoattractant are expressed by u and v, respectively. D_u and D_v are the diffusion coefficients, $f(u,v)$ and $g(u,v)$ are terms that take into account the production and degradation, and α is known as chemotaxis sensibility.

In its dimensionless form, the model is described by the following equations (Garzón-Alvarado, 2007; Vanegas-Acosta and Garzón-Alvarado, 2014; Painter, 1997):

$$\frac{\partial u}{\partial t} = \nabla \cdot (D_u \nabla_u - \alpha u \nabla v) + f(u, v) \tag{5.6a}$$

$$\frac{\partial v}{\partial t} = D_v \nabla^2 v + g(u, v) \tag{5.6b}$$

5.2.3 Conditions for Turing Instability

Reaction−diffusion equations can present highly regular patterns and are used, among others, in the modeling of molecular patterns in the bone development (Garzon-Alvarado, 2014) and in the formation of the skin pigmentation of some fishes (Kondo and Miura, 2010).

It is important to take into account that there are three possibilities in the reaction−diffusion equation behavior under homogeneous Neumann condition:

1. When the diffusive term is dominant: the species concentration reaches a constant single value in the time and the space (stationary).
2. When the reactive term is dominant, it's possible to obtain a Turing instability. This instability could represent, for example, the pigmentation on the skin of the tiger. At birth, the tigers do not have any pigmentation; as they grow, its skin is pigmented until it reaches a definitive pattern of stripes distribution. In this way, the stationary state is reached but with spatial instabilities (value differences in the domain).
3. When there is a temporal and spatial instability simultaneously, for example, in this case, the tiger would change its stripes over time; that means, the stripes are formed in the adult age but those change constantly, along the time, transforming into others (obviously, this type of tiger does not exist! That would be more like a chameleon).

Therefore, it is fundamental to describe the necessary conditions for the Turing pattern formation. It was mentioned that those kinds of patterns depend of the relationship between diffusive term parameters and those of the reactive term.

This book belongs to Central Library BADJI Mokhtar-ANNABA UNIVERSITY
Copyright Elsevier 2024

In the reaction−diffusion system defined by the set of Eq. (5.4), u and v are the chemical species (activator and inhibitor, respectively) and $f(u,v) = (a - u + u^2v)$ and $g(u,v) = (b - u^2v)$ are the reaction terms. In addition, γ is a dimensionless value and a and b are constant parameters of the model. Homogeneous Neumann conditions have been imposed and the initial conditions are small perturbations around the homogeneous steady state of each reactive terms, namely, $f(u_s, v_s) = 0$ and $g(u_s, v_s) = 0$.

5.2.3.1 Conditions for Instability by Diffusion

The conditions for instability could give us information about the presence (or not) of the Turing patterns. This section will define those conditions. Therefore, without the diffusive term, u and v must satisfy:

$$\begin{aligned} \frac{\partial u}{\partial t} &= \gamma\left(a - u + u^2 v\right) \\ \frac{\partial v}{\partial t} &= \gamma\left(b - u^2 v\right) \end{aligned} \tag{5.7}$$

where, for small perturbations (ξ and η) around the steady state, we have $(u,v) = (u_s + \xi,\ v_s + \eta)$, then Eq. (5.7) can be linearized as

$$\begin{pmatrix} \frac{\partial u}{\partial t} \\ \frac{\partial v}{\partial t} \end{pmatrix} = \underbrace{\begin{pmatrix} \frac{\partial \xi}{\partial t} \\ \frac{\partial \eta}{\partial t} \end{pmatrix}}_{\frac{\partial \boldsymbol{\varphi}^t}{\partial t}} = \gamma \underbrace{\begin{pmatrix} f_u & f_v \\ g_u & g_v \end{pmatrix}}_{\mathbf{A}} \underbrace{\begin{pmatrix} \xi \\ \eta \end{pmatrix}}_{\boldsymbol{\varphi}^t} \tag{5.8}$$

where $f_u = 2uv - 1$, $f_v = u^2$, $g_u = -2uv$, and $g_v = -u^2$. It should be noted that $f(u,v)$ and $g(u,v)$ in the previous equation will be evaluated in the steady state given by $f(u_s, v_s) = 0$ and $g(u_s, v_s) = 0$. So, we have $(u_s, v_s) = \left(a + b, \frac{b}{(a+b)^2}\right)$.

Therefore, a solution for Eq. (5.8) can be written in the form:

$$\boldsymbol{\varphi}^t(\mathbf{t}) \cong \boldsymbol{a} e^{\lambda_t t} \tag{5.9}$$

where $\boldsymbol{\varphi}^t(\mathbf{t}) = \begin{bmatrix} \xi \\ \eta \end{bmatrix}$, $\boldsymbol{a}$ is a vector that contains information about the initial conditions and λ_t is the temporal eigenvector. Substituting Eq. (5.9) into Eq. (5.8):

$$(\mathbf{A} - \lambda_t \boldsymbol{I})\boldsymbol{a} = 0 \tag{5.10}$$

where $\boldsymbol{I}$ is the identity matrix. Therefore, $\det(\mathbf{A} - \lambda_t \boldsymbol{I}) = 0$ is a condition to get a nontrivial solution, thus yielding the following characteristic equation:

$$\lambda_t^2 - (f_u + g_v)\lambda_t + (f_u g_v - f_v g_u) = 0 \tag{5.11}$$

Therefore, the solution of Eq. (5.11) is as shown below:

$$\lambda_t = \frac{(f_u + g_v)\sqrt{(f_u + g_v)^2 - 4(f_u g_v - f_v g_u)}}{2} \tag{5.12}$$

If the system should be temporally stable, its eigenvalues, λ_t, should be negative, so:

$$tr(\mathbf{A}) = f_u + g_v < 0 \tag{5.13a}$$

$$\mathrm{Det}(\mathbf{A}) = f_u g_v - f_v g_u > 0 \tag{5.13b}$$

Now, introducing the diffusive term, it is possible to obtain a linearized equation from the reaction−diffusion system that is given by

$$\frac{\partial \boldsymbol{\Psi}}{\partial t} = \gamma \mathbf{A}\boldsymbol{\Psi} + \mathbf{D}\nabla^2 \boldsymbol{\Psi} \tag{5.14}$$

This book belongs to Central Library BADJI Mokhtar-ANNABA UNIVERSITY
Copyright Elsevier 2024

with $\mathbf{D} = diag(1, d)$. Expanding the spatial−temporal solution it will have $\mathbf{\Psi}(\mathbf{x},t) = \boldsymbol{\varphi}^t(\mathbf{t})\ \boldsymbol{\varphi}^x(\mathbf{x})$ where $\boldsymbol{\varphi}^t(\mathbf{t})$ is the temporal solution already found and $\boldsymbol{\varphi}^x(\mathbf{x})$ is the spatial solution. Thus, the solution obtained is

$$\Psi(\mathbf{x}, t) = \sum_k \mathbf{c_k} e^{\lambda t} \varphi_k(\mathbf{x}) \tag{5.15}$$

where k is the wave number of the spatial pattern (eigenvalue), $\mathbf{c_k}$ is the vector of Fourier coefficients, and $\varphi_k(\mathbf{x})$ is the eigenfunction of the Laplacian (with $(n \bullet \nabla)\varphi = 0$) given by

$$\nabla^2 \varphi_k + k^2 \varphi_k = 0 \tag{5.16}$$

Substituting Eq. (5.15) into Eq. (5.14) yields

$$\left(\lambda \boldsymbol{I} - \gamma \boldsymbol{A} + \mathbf{D}k^2\right)\mathbf{c_k} = 0 \tag{5.17}$$

where $\mathbf{0}$ is a null vector and $\boldsymbol{I}$ is the identity matrix. As in the case of the differential equation without diffusion, the vector of Fourier coefficients must be nontrivial, so the following condition should be met:

$$\det\left(\lambda \boldsymbol{I} - \gamma \boldsymbol{A} + \mathbf{D}k^2\right) = \mathbf{0} \tag{5.18}$$

The dispersion relation or characteristic Eq. (5.17), is obtained:

$$\lambda^2 + b\left(k^2\right)\lambda + c\left(k^2\right) = 0, \text{ con} \tag{5.19a}$$

$$b\left(k^2\right) = k^2(1 + d) - \gamma(f_u + g_v) \tag{5.19b}$$

$$c\left(k^2\right) = dk^4 - \gamma(df_u + g_v)k^2 + \gamma^2(f_u g_v - f_v g_u) \tag{5.19c}$$

Therefore, for Turing instability to occur, the roots of Eq. (5.19a) must satisfy $\mathscr{R}e\ \lambda(k^2) > 0$ for any k^2. To have a driven instability, the exponential coefficient must be positive. According to Routh−Hurwitz conditions, the real part of the eigenvalue is required to be positive $b(k^2) > 0$ and $c(k^2) < 0$ or vice versa. From the condition in Eq. (5.13a) it can be concluded that $b(k^2) > 0$ for any k^2, then it is required that $c(k^2) < 0$. In Eq. (5.19c) it can be observed that $d > 0$ and in Eq. (5.13b) it is known that $f_u g_v - f_v g_u > 0$. Thus, it must be satisfied that $df_u + g_v > 0$, which is a necessary, but not sufficient, condition. The additional relationship is found by minimizing $c(k^2)$ where $c_{min}(k^2) < 0$; the equation for this is $\frac{dc\left(k^2\right)}{dk^2} = 2dk^2 - \gamma(df_u + g_v) = 0$, yielding:

$$k^2 = \frac{\gamma(df_u + g_v)}{2d} \tag{5.20}$$

Substituting Eq. (5.20) in Eq. (5.19c) yields:

$$c_{min}\left(k^2\right) = -\frac{(df_u + g_v)^2}{4d} + (f_u g_v - f_v g_u) < 0 \tag{5.21}$$

Thus, Turing instability is obtained when the following inequalities are satisfied:

$$f_u g_v - f_v g_u > 0 \tag{5.22a}$$

$$f_u + g_v < 0 \tag{5.22b}$$

$$df_u + g_v > 0 \tag{5.22c}$$

$$(df_u + g_v)^2 > 4d(f_u g_v - f_v g_u) \tag{5.22d}$$

5.2.3.2 Definition of the Wave Number

Starting from Eq. (5.21), spatial instability will not be present if, in the limit case, the term $c_{min}(k^2) = -\frac{(d_c f_u + g_v)^2}{4d_c} + (f_u g_v - f_v g_u) = 0$, for which the critical diffusion coefficient, d_c, above which Turing instability will result. Then, the critical value is given by

$$f_u d_c^2 + 2(2f_v g_u - f_u g_v)d_c + g_v^2 = 0 \tag{5.23}$$

This book belongs to Central Library BADJI Mokhtar-ANNABA UNIVERSITY
Copyright Elsevier 2024

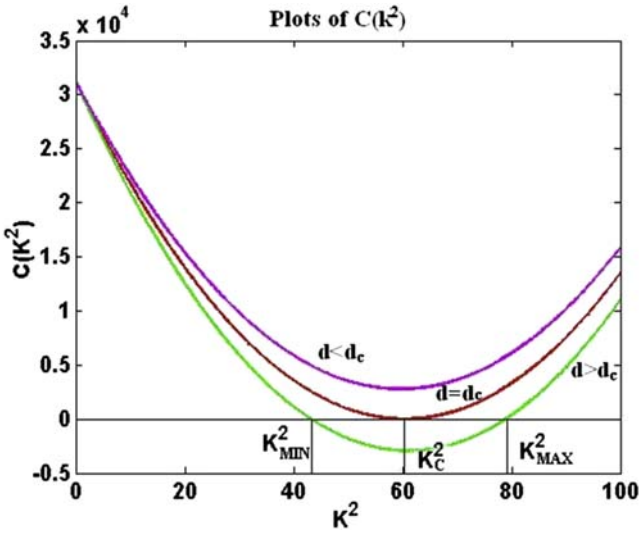

FIGURE 5.2 Diagram for $c(k^2)$. The curves have been drawn for the Schnakenberg reaction model with $a = 0.1$, $b = 0.9$, and $\gamma = 176.72$. Using Eq. (5.21) results in $d_c = 8.5676$ and replacing this value in $c(k^2)$, Eq. (5.19c), the red (dark gray in print versions) curve is obtained. The magenta (gray in print versions) curve is obtained with $d = 0.8$ and the green (light gray in print versions) curve is obtained for $d = 9.1676$. In the graph, $K^2_{min} = 43.1469$ and $K^2_{max} = 78.9525$.

On the other hand, with $c(k^2) = 0$, it is possible to obtain the value k^2 for which a range of wave numbers is present as long as $d > d_c$, as shown in Fig. 5.2.

As seen in Fig. 5.2, if $d > d_c$ is satisfied at the cutting point of $c(k^2)$ with the axis k^2, two important points are obtained, K^2_{min} and K^2_{max}. These points define wave numbers and are given by

$$K^2_{min} = \frac{\gamma(df_u + g_v) - \sqrt[2]{(\gamma(df_u + g_v))^2 - 4d\gamma^2(f_u g_v - f_v g_u)}}{2d} \tag{5.24a}$$

$$K^2_{min} = \frac{\gamma(df_u + g_v) + \sqrt[2]{(\gamma(df_u + g_v))^2 - 4d\gamma^2(f_u g_v - f_v g_u)}}{2d} \tag{5.24b}$$

This interval $\left(K^2_{min}, K^2_{max}\right)$ defines the wave numbers of the reaction−diffusion system solution in a Turing space. To define the behavior of the instability, the domain where the solution is obtained must be defined (in this case, a rectangle will be used).

5.2.3.3 Eigen Functions of a Rectangle

Consider a rectangle with L_x and L_y sides, so the eigenfunctions for Eq. (5.16) are given by

$$\varphi_k = \varphi_{L_x,L_y} = \cos\left(\frac{m\pi x}{L_x}\right)\cos\left(\frac{n\pi y}{L_y}\right) \tag{5.25}$$

whose eigenvalues are of the form:

$$k^2 = \pi^2 \left.\frac{m^2}{L_x^2} + \frac{n^2}{L_y^2}\right) \tag{5.26}$$

When $t \to \infty$, the solution of the linearized system Eq. (5.12) is of the form:

$$\Psi(\mathbf{x}, t) = \sum_{m,n \in I} \mathbf{c}_{m,n} e^{\lambda t} \cos\left(\frac{m\pi x}{L_x}\right)\cos\left(\frac{n\pi y}{L_y}\right) \tag{5.27}$$

This book belongs to Central Library BADJI Mokhtar-ANNABA UNIVERSITY
Copyright Elsevier 2024

where

$$I = \left\{ (m,n) \in Z^2 \middle| K_{min}^2 < \pi^2 \left(\frac{m^2}{L_x^2} + \frac{n^2}{L_y^2} \right) < K_{max}^2 \right\} \tag{5.28}$$

For example, in the case shown in Fig. 5.2, with $a = 0.1$, $b = 0.9$, $\gamma = 176.72$, and $d = 9.1676$, the results are $K_{min}^2 = 43.1469$ and $K_{max}^2 = 78.9525$. Therefore, in a unit square ($L_x = L_y = 1.0$), the interval is given by $4.3717 < m^2 + n^2 < 7.9996$. Thus, we can find two integers m^2 and n^2 that meet the proposed interval are chosen. In this case, the values are $m = 2$ and $n = 1$ or vice versa. In other words, $m = 2$ and $n = 1$ are in the possible wave number for the interval $4.3717 < 2^2 + 1^2 < 7.9996$. Following a similar analysis, Table 5.1 contains the wave numbers and the values for d and γ, for the constant values of a and b mentioned before.

Therefore, it is possible to see different examples of wave numbers of the Turing pattern. In Fig. 5.3 the steady state is shown, in time, of variable u. In this figure, we can see the solution of Eq. (5.4) with the parameters given in Table 5.1. This solution develops a Turing pattern with "spots" distribution that can recall the location of the dentinal tubules (Fig. 5.1). As it can be seen, the patterns obtained are stable in time but unstable in space.

The wave number indicates the number of half sine waves in each of the x and y directions. In Fig. 5.4, an explanation for a number wave (4,2) is made, where 4 half waves in x direction and 2 half waves in y direction are observed.

TABLE 5.1 Modes of Vibration (m,n) for Different Values of d and γ

Mode (m,n)	d	γ
(1,0)	10.0000	29.0000
(1,1)	11.5776	70.6000
(2,0)	10.0000	114.0000
(2,1)	9.1676	176.7200
(2,2)	8.6676	230.8200
(3,0)	8.6176	265.2200
(3,1)	8.6676	329.2000
(3,2)	8.8676	379.2100
(3,3)	8.6076	535.0900
(4,0)	8.6676	435.9900
(4,1)	8.5876	492.2800
(4,2)	8.7176	625.3500
(4,3)	8.6676	666.8200
(4,4)	8.6076	909.6600

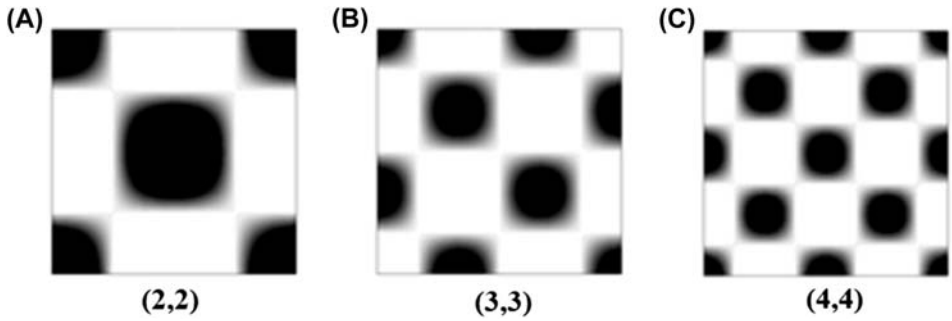

FIGURE 5.3 Turing patterns at steady state for different wave numbers. (A) (2,2); (B) (3,3); (C) (4,4). The values of γ and d were taken from Table 5.1. White color means high concentrations, whereas black color means low concentrations. The figure was made for the u concentration of Eq. (5.8).

This book belongs to Central Library BADJI Mokhtar-ANNABA UNIVERSITY
Copyright Elsevier 2024

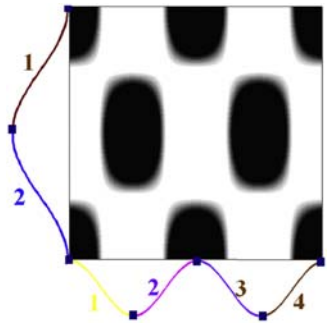

FIGURE 5.4 Correspondence of the wave number and the Turing pattern for a value (4,2) with the respective values of γ and d given in Table 5.1.

5.2.4 Finite Element Method

Eq. (5.4) can be written as shown below, where a differentiation equation that depends of one of the morphogenes is added. These equations have the same structure of the Schnakenberg equations seen previously:

$$\frac{\partial S_N}{\partial t} - C\left(\alpha_1 - \mu S_N + \gamma_0 S_N^2 S_B\right) - D_N \nabla^2 S_N = 0 \tag{5.29a}$$

$$\frac{\partial S_B}{\partial t} - C\left(\alpha_2 - \gamma_0 S_N^2 S_B\right) - D_B \nabla^2 S_B = 0 \tag{5.29b}$$

$$\frac{\partial c_O}{\partial t} - \eta \frac{S_B^n}{S_B^n + S_T^n} \cdot \frac{T_a^r}{T_a^r + t^r} = 0 \tag{5.29c}$$

To solve this system of Eq. (5.29) a finite element mesh based on bilinear quadrilateral elements was used. Because of nonlinear terms included in the model, the Newton−Raphson method was used to solve the problem of time evolution of the N and B molecules that interact to develop Turing patterns. Additionally, it is possible to establish a differentiation equation dependent of a particular molecule in Eq. (5.29c). In this case, the dependence of the second molecule was used. Using weighted residuals, the system of Eq. (5.29) becomes

$$\begin{aligned}
&\int_\Omega w_1 \left(\frac{\partial S_N}{\partial t} - C\left(\alpha_1 - \mu S_N + \gamma_0 S_N^2 S_B\right) - D_N \nabla^2 S_N\right) d\Omega = 0 \\
&\int_\Omega w_2 \left(\frac{\partial S_B}{\partial t} - C\left(\alpha_2 - \gamma_0 S_N^2 S_B\right) - D_B \nabla^2 S_B\right) d\Omega = 0 \\
&\int_\Omega w_3 \left(\frac{\partial c_O}{\partial t} - \eta \frac{S_B^n}{S_B^n + S_T^n} \cdot \frac{T_a^r}{T_a^r + t^r}\right) d\Omega = 0
\end{aligned} \tag{5.30}$$

where Ω represents the problem domain, which is limited at the boundary Γ, while w_1, w_2, and w_3 are the weighting functions. Using Green's theorem and weakening the system of Eq. (5.30), the residue of the problem is given by

$$\begin{aligned}
r_N &= \int_\Omega w_1 \frac{\partial S_N}{\partial t} d\Omega - \int_\Omega w_1 C \alpha_1 d\Omega + \int_\Omega w_1 C \mu S_N d\Omega - \int_\Omega w_1 C \gamma_0 S_N^2 S_B d\Omega + \int_\Omega D_N \nabla w_1 \nabla S_N d\Omega - \int_\Gamma w_1 D_N (\nabla S_N \cdot \mathbf{n}) d\Gamma = 0 \\
r_B &= \int_\Omega w_2 \frac{\partial S_B}{\partial t} d\Omega - \int_\Omega w_2 C \alpha_2 d\Omega + \int_\Omega w_2 C \gamma_0 S_N^2 S_B d\Omega + \int_\Omega D_B \nabla w_2 \nabla S_B d\Omega - \int_\Gamma w_2 D_B (\nabla S_B \cdot \mathbf{n}) d\Gamma = 0 \\
r_{C_0} &= \int_\Omega w_3 \left(\frac{dc_O}{dt} - \eta \frac{S_B^n}{S_B^n + S_T^n} \cdot \frac{T_a^r}{T_a^r + t^r}\right) d\Omega = 0
\end{aligned} \tag{5.31}$$

This book belongs to Central Library BADJI Mokhtar-ANNABA UNIVERSITY
Copyright Elsevier 2024

Assigning null flow conditions at the boundary, terms related to the boundary in Eq. (5.31) are canceled and the residue is expressed as

$$
\begin{aligned}
r_N &= \int_\Omega w_1 \frac{\partial S_N}{\partial t} d\Omega - \int_\Omega w_1 C\alpha_1 d\Omega + \int_\Omega w_1 C\mu S_N d\Omega - \int_\Omega w_1 C\gamma_0 S_N^2 S_B d\Omega + \int_\Omega D_N \nabla w_1 \nabla S_N d\Omega = 0 \\
r_B &= \int_\Omega w_2 \frac{\partial S_B}{\partial t} d\Omega - \int_\Omega w_2 C\alpha_2 d\Omega + \int_\Omega w_2 C\gamma_0 S_N^2 S_B d\Omega + \int_\Omega D_B \nabla w_2 \nabla S_B d\Omega = 0 \\
r_{C_0} &= \int_\Omega w_3 \left(\frac{dc_O}{dt} - \eta \frac{S_B^n}{S_B^n + S_T^n} \cdot \frac{T_a^r}{T_a^r + t^r} \right) d\Omega = 0
\end{aligned}
\tag{5.32}
$$

The discretization is based on shape functions written as a linear combination of orthogonal functions, as shown below:

$$
\begin{aligned}
S_N^e &= \mathbf{N}_N \mathbf{S}_N \\
S_B^e &= \mathbf{N}_B \mathbf{S}_B \\
c_O^e &= \mathbf{N}_O \mathbf{c}_O
\end{aligned}
\tag{5.33}
$$

where $\mathbf{N}_B$, $\mathbf{N}_N$, and $\mathbf{N}_O$ represent the shape functions for the space used for discretization, and $\mathbf{S}_N$ and $\mathbf{S}_B$ are the values of S_N and S_N at the nodal points, while superscript e indicates the variable discretization. The Bubnov−Galerkin formulation was used, indicating that the functions w take the same form of the approximation functions $\mathbf{N}$.

Replacing Eq. (5.32) into Eq. (5.33), the discrete form of the residual vector is obtained, where r_N^e, r_B^e, and r_O^e are the residue vectors for each equation and $\nabla\mathbf{N}$ is the gradient vector of the approximation functions.

$$
\begin{aligned}
\underline{r_N^e} &= \int_\Omega \mathbf{N}^T \frac{\partial S_N^e}{\partial t} d\Omega - \int_\Omega \mathbf{N}^T C\gamma_0 \alpha_1 d\Omega + \int_\Omega \mathbf{N}^T C\gamma_0 \mu S_N^e d\Omega - \int_\Omega \mathbf{N}^T C\gamma_0 \left(S_N^e\right)^2 S_B^e d\Omega + \int_\Omega D_N \nabla\mathbf{N}^T \nabla S_N^e d\Omega \\
\underline{r_B^e} &= \int_\Omega \mathbf{N}^T \frac{\partial S_B^e}{\partial t} d\Omega - \int_\Omega \mathbf{N}^T C\gamma_0 \alpha_2 d\Omega + \mathbf{N}^T + \int_\Omega w_2 C\gamma_0 \left(S_N^e\right)^2 S_B^e d\Omega + \int_\Omega D_B \nabla\mathbf{N}^T \nabla S_B^e d\Omega \\
\underline{r_O^e} &= \int_\Omega \mathbf{N}^T \left(\frac{\partial c_O}{\partial t} - \eta \frac{S_B^n}{S_B^n + S_T^n} \cdot \frac{T_a^r}{T_a^r + t^r} \right) d\Omega
\end{aligned}
\tag{5.34}
$$

Using the time discretization based on the Crank−Nicolson equation, Eq. (5.34) becomes

$$
\begin{aligned}
\underline{r_N^e} &= \int_\Omega \mathbf{N}^T \frac{\widetilde{S}_N^e - S_N^e}{\Delta t} d\Omega + \alpha \left(\int_\Omega D_N \nabla\mathbf{N}^T \nabla \widetilde{S}_N^e d\Omega - \int_\Omega \mathbf{N}^T C\gamma_0 \alpha_1 d\Omega + \int_\Omega \mathbf{N}^T C\gamma_0 \mu \widetilde{S}_N^e d\Omega - \int_\Omega \mathbf{N}^T C\gamma_0 \left(\widetilde{S}_N^e\right)^2 \widetilde{S}_B^e d\Omega \right)^{t+\Delta t} \\
&\quad + (1-\alpha) \left(\int_\Omega D_N \nabla\mathbf{N}^T \nabla S_N^e d\Omega - \int_\Omega \mathbf{N}^T C\gamma_0 \alpha_1 d\Omega + \int_\Omega \mathbf{N}^T C\gamma_0 \mu S_N^e d\Omega - \int_\Omega \mathbf{N}^T C\gamma_0 \left(S_N^e\right)^2 S_B^e d\Omega \right)^t \\
\underline{r_B^e} &= \int_\Omega \mathbf{N}^T \frac{\widetilde{S}_B^e - S_B^e}{\Delta t} d\Omega + \alpha \left(\int_\Omega D_B \nabla\mathbf{N}^T \nabla \widetilde{S}_B^e d\Omega - \int_\Omega \mathbf{N}^T C\gamma_0 \alpha_2 d\Omega + \int_\Omega w_2 C\gamma_0 \left(\widetilde{S}_N^e\right)^2 \widetilde{S}_B^e d\Omega \right)^{t+\Delta t} \\
&\quad + (1-\alpha) \left(\int_\Omega D_B \nabla\mathbf{N}^T \nabla S_B^e d\Omega - \int_\Omega \mathbf{N}^T C\gamma_0 \alpha_2 d\Omega + \int_\Omega w_2 C\gamma_0 \left(S_N^e\right)^2 S_B^e d\Omega \right)^t \\
\underline{r_o^e} &= \int_\Omega \mathbf{N}^T \frac{\widetilde{c}_O - c_O}{\Delta t} d\Omega - \left(\int_\Omega \mathbf{N}^T \eta \frac{S_B^n}{S_B^n + S_T^n} \cdot \frac{T_a^r}{T_a^r + t^r} d\Omega \right)^t
\end{aligned}
\tag{5.35}
$$

where $\widetilde{S}_N^e$ and $\widetilde{S}_B^e$ are the nodal values of S_N^e and S_B^e evaluated at time $t + \Delta t$ and α represents a characteristic parameter of the integration method.

This book belongs to Central Library BADJI Mokhtar-ANNABA UNIVERSITY

Copyright Elsevier 2024

The terms of the tangential stiffness matrix are determined using Eq. (5.35):

$$
\begin{aligned}
\frac{\partial \underline{r_N^e}}{\partial \underline{\widetilde{\mathbf{S}}_N}} &= \frac{1}{\Delta t}\int_\Omega \mathbf{N}^T\mathbf{N}d\Omega + \alpha\left(\int_\Omega D_N\nabla\mathbf{N}^T\nabla\mathbf{N}d\Omega + \int_\Omega C\mu\gamma_0\mathbf{N}^T\mathbf{N}d\Omega - \int_\Omega \mathbf{N}^T\mathbf{N}C\gamma_0 2\left(\widetilde{S}_N^e\right)\widetilde{S}_B^e d\Omega\right)\\
\frac{\partial \underline{r_N^e}}{\partial \underline{\widetilde{\mathbf{S}}_B}} &= -\alpha\int_\Omega \mathbf{N}^T\mathbf{N}C\gamma_0\left(\widetilde{S}_N^e\right)^2 d\Omega\\
\frac{\partial \underline{r_B^e}}{\partial \underline{\widetilde{\mathbf{S}}_N}} &= \alpha\int_\Omega \mathbf{N}^T\mathbf{N}C\gamma_0 2\left(\widetilde{S}_N^e\right)\widetilde{S}_B^e d\Omega\\
\frac{\partial \underline{r_B^e}}{\partial \underline{\widetilde{\mathbf{S}}_B}} &= \frac{1}{\Delta t}\int_\Omega \mathbf{N}^T\mathbf{N}d\Omega + \alpha\left(\int_\Omega D_B\nabla\mathbf{N}^T\nabla\mathbf{N}d\Omega + \int_\Omega \mathbf{N}^T\mathbf{N}C\gamma_0\left(\widetilde{S}_N^e\right)^2 d\Omega\right)\\
\frac{\partial \underline{r_O^e}}{\partial \underline{\widetilde{\mathbf{c}}_O}} &= \frac{1}{\Delta t}\int_\Omega \mathbf{N}^T\mathbf{N}d\Omega
\end{aligned}
\tag{5.36}
$$

The nodal values $\boldsymbol{S_N}$ and $\boldsymbol{S_B}$ at time $t+\Delta t$ can be approximated by the Newton−Raphson iterative algorithm, as described in Eq. (5.36), where $\Delta\boldsymbol{S_N^e}$ and $\Delta\boldsymbol{S_B^e}$ represent the difference of the nodal values between two consecutive iterations.

$$
\begin{bmatrix}
\frac{\partial \underline{r_N^e}}{\partial \underline{\widetilde{\mathbf{S}}_N}} & \frac{\partial \underline{r_N^e}}{\partial \underline{\widetilde{\mathbf{S}}_B}}\\
\frac{\partial \underline{r_B^e}}{\partial \underline{\widetilde{\mathbf{S}}_N}} & \frac{\partial \underline{r_B^e}}{\partial \underline{\widetilde{\mathbf{S}}_B}}
\end{bmatrix}
\begin{bmatrix}
\Delta\mathbf{S_N^e}\\
\Delta\mathbf{S_B^e}
\end{bmatrix}
= -\begin{bmatrix}
\underline{r_N^e}\\
\underline{r_B^e}
\end{bmatrix}
\tag{5.37}
$$

These equations will be applied to the solution of the dentinal tubules formation, which will be described below.

5.3 CASE OF STUDY 1: MORPHOGENESIS OF THE DENTINAL TUBULES

The solution of reaction−diffusion equation systems mentioned above allows to represent the dentinal tubules formation as shown in Fig. 5.1. In that figure we can see a regular pattern for the odontoblast location (and tubule formation). This pattern is very similar to those obtained from Turing pattern formation. We are seeking the best model that could reproduce the appearance and location of these dentinal tubules. To evaluate it, based on the work of Niño-Barrera and Garzon-Alvarado (2012), the location of the dentinal tubules is on the odontoblast differentiation places. For this purpose, reaction−diffusion equations are used with parameters that guarantee that the system is in the Turing space. Briefly, two biochemical agents operate in a tissue: one promotes cell growth and operates at short range, and the second one inhibits growth and operates at long range. In the case of dentinal tubule formation, the model is based on the effect of two morphogenetic proteins interacting sequentially with epithelial and mesenchymal tissues to create geometric patterns of odontoblast differentiation.

During embryological processes of cell differentiation, BMPs are regulated by antagonistic molecules, including Noggin (Plikus et al., 2005; Zhu et al., 2006; Walsh et al., 2010). Noggin has been reported to be a specific inhibitor of BMP activity in mesenchymal cells (Zhu et al., 2006; Walsh et al., 2010). Noggin regulates the response of undifferentiated cells to BMPs through a negative feedback mechanism (Fig. 5.5) that maintains the cells in an undifferentiated state, thus controlling the rate of cell growth (Zhu et al., 2006). The suggested mechanism of inhibition is based on the binding of Noggin to BMPs, which prevents them from interacting with cell surface receptors (Walsh et al., 2010). Because of the feedback process, the BMPs in turn induce the mesenchymal cells to express Noggin (Zhu et al., 2006). Once the process of cell differentiation and proliferation is activated, the production of Noggin is reduced (Zhu et al., 2006). In addition, DLX3 is always present in the process. Actually DLX3 has a constant concentration on the domain, but if it presents differences in concentration in a closed space, the location and appearance of the odontoblasts and dentinal tubules could be abnormal.

This book belongs to Central Library BADJI Mokhtar-ANNABA UNIVERSITY
Copyright Elsevier 2024

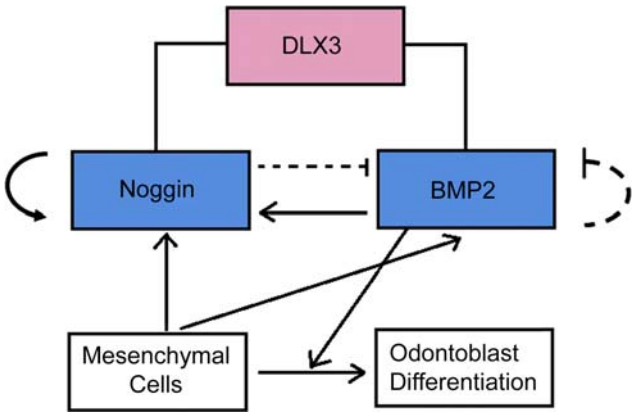

FIGURE 5.5 Control system of the molecular process. BMP2, differentiation factor of mesenchymal cell into odontoblasts; Noggin, regulatory factor of the differentiation that self-activates. The relationship of the molecular signals produced by the ectomesenchymal tissue and the basement membrane is shown. *Solid lines* mean activation, *dotted lines* inhibition, *continuous curved lines* self-activation, and *dotted curved lines* self-inhibition.

5.3.1 Modeling Biochemical Factors Involved in Odontoblasts Differentiation

BMP2 is expressed throughout the entire process of dental differentiation and plays a role as an antagonist of Noggin (Yang et al., 2012; Zhu et al., 2006). There is a competition process observed between these two proteins that correspond to the type activator−inhibitor or activator−substrate. This regulation follows a strongly coupled loop and is represented by reaction−diffusion equations, which parameters are in the Turing space leading to a stable pattern in time and unstable in space, like the patterns of differentiation of odontoblasts from mesenchymal cells. Therefore, the aim of this section is to present a biochemical mathematical model that simulates the dentinal tubules pattern formation from the differentiation of the odontoblasts. This mathematical model will simulate spatial distribution patterns that are repeatable under different types of initial conditions, similar to the high repeatability of the odontoblast differentiation process.

5.3.2 Numerical Implementation

The computational simulation is carried out in an iterative incremental scheme to solve the evolution of both the concentration of molecular factors and the appearance of odontoblasts. The mesenchymal tissue is assumed as a structural matrix with an initial concentration of mesenchymal cells of $4(10^6)$ cell/mm^3. The initial concentrations of Noggin and BMP2 are randomly distributed in the mesenchymal tissue, with a 10% perturbation on the steady-state concentration given by $\left(S_N^*, S_B^*\right) = (0.1, 0.09)[\mathrm{ng}/\mathrm{mm}^3]$. The selection of random initial conditions around the steady state is similar to the event of molecular expression by the mesenchymal cells in the zone of odontoblast differentiation. The flow condition for each molecular factor at the boundary is assumed to be zero. To obtain the distribution pattern of cell differentiation to odontoblasts, numerical tests were performed in a two-dimensional 11 μm—side quadrilateral—element mesh. The size of the mesh was 10,201 nodes and 2500 elements, while time increment was $\Delta t = 0.1423$ s, and values were obtained after the convergence study.

5.3.3 Results

It is observed that the concentration of the molecular factors in the ectomesenchyme and the action of the diffusive process allow the formation of a stable pattern in the time that is replicated in the whole domain. From the reaction−diffusion mechanism, the change in Noggin and BMP2 concentrations at each time instant are computed, as shown in Fig. 5.6A and B.

The concentrations of Noggin (S_N) and BMP2 (S_B) into mesenchymal tissue evolve according to their diffusivity, their interaction, and their expression by the mesenchymal cells. Therefore, both Noggin and BMP2 are concentrated in high amounts in specific areas, allowing the cellular differentiation similar to what happened in the biological process (Aberg et al., 1997; Zhu et al., 2006). It is important to see that in areas with the highest Noggin concentration, no cell differentiation occurs, whereas in areas with a greater presence of BMP2, differentiation takes place.

According to the results, a chemical feedback between the two reactant molecular factors (activator−substrate) may be the major cause for regular patterns, as observed in odontoblast differentiation and dentin tubule formation (Nino-Barrera

This book belongs to Central Library BADJI Mokhtar-ANNABA UNIVERSITY
Copyright Elsevier 2024

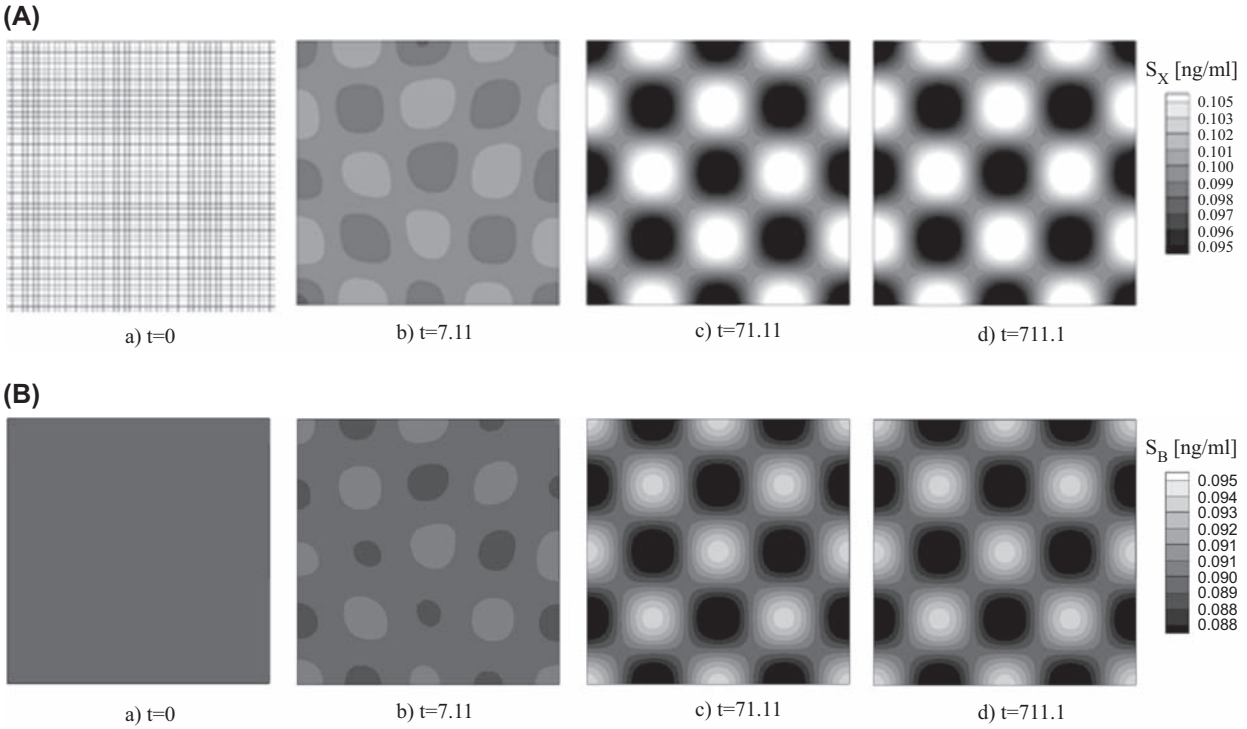

FIGURE 5.6 (A) Patterns of Noggin distribution in mesenchymal tissue. (B) Patterns of BMP2 distribution in mesenchymal tissue.

and Garzon-Alvarado, 2012). These patterns are highly stable and repeatable among different individuals and species, showing clearly defined areas of differentiation for the correct future tubule formation. However, these results have been obtained with a mathematical model based on assumptions and simplifications. In addition, like any other physical system, the biological system modeled is subjected to various disturbances that can change the pattern established by the proposed model. It is evident that the Noggin−BMP2 relation is not the only governing factor that controls the entire process of differentiation (Ruch et al., 1995; Thesleff, 1995b; Lisi et al., 2003), but the existence of an activator−substrate mechanism ensures high stability for the development of this biological process. Finally, despite all the limitations and simplifications, the proposed mathematical model reproduces the patterns of formation of the dentinal tubule from cell differentiation into odontoblasts (Fig. 5.7).

5.4 CASE OF STUDY 2: ROLE OF DLX3 IN THE HETEROGENEOUS LOCATION OF THE DENTINAL TUBULES

Tricho−dento−osseous syndrome (TDOS) is a pathology caused by a DLX3 gene mutation (Price et al., 1998a,b), resulting in a disruption in the odontoblast palisade and alterations in the dentin and dentinal tubules (Choi et al., 2010). In addition, the functional role of DLX3 via DSPP during normal conditions is regulated by a positive loop between DLX3 and BMP2 (Viale-Bouroncle et al., 2012). Specifically, when there is an alteration in DLX3 expression, the loop between BMP2 and Noggin is modified (Fig. 5.5), leading to complex heterogeneous domains with different parameters in the Turing space. Thus, the location of the odontoblasts will not be evenly distributed and the tubules will have a heterogeneous and disordered formation.

This heterogeneity can be seen in the reaction−diffusion equation parameters in Eq. (5.29), that is, the parameters will not be constant as in the first case; these will depend on the DLX3 amount that is present in the tissue. In other words,

$$\begin{aligned} \gamma_0 &= \gamma_0(C_D(\mathbf{x})) \\ d &= \frac{D_N}{D_B} = d(C_D(\mathbf{x})) \end{aligned} \tag{5.38}$$

This book belongs to Central Library BADJI Mokhtar-ANNABA UNIVERSITY
Copyright Elsevier 2024

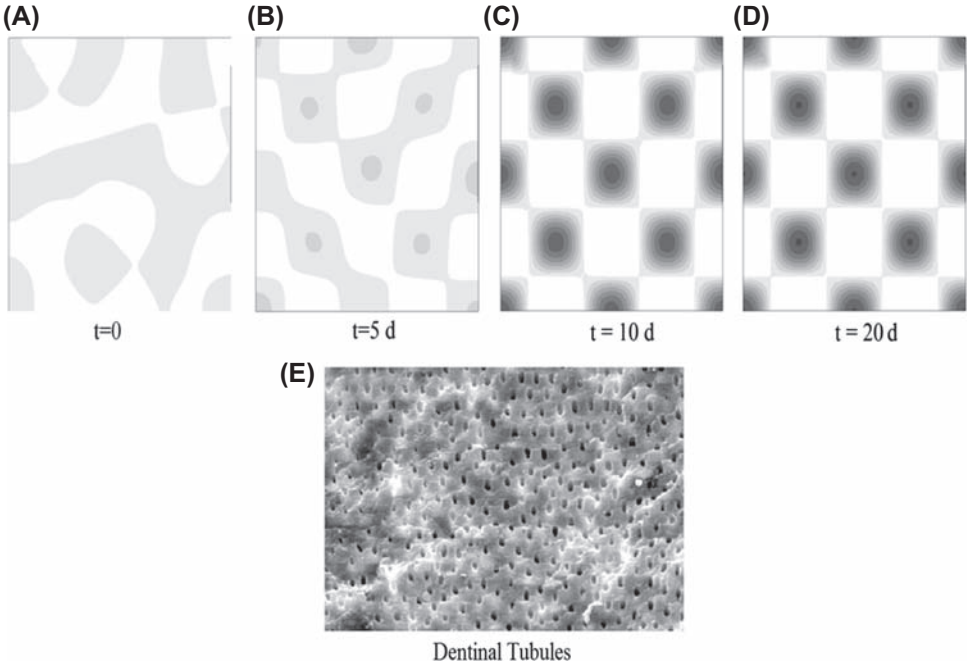

FIGURE 5.7 (A−D) Geometric location where cell differentiation takes place. Black areas represent cell differentiation; white areas stand for mesenchymal cells. Note that the presence of BMP determines the locations where mesenchymal cells differentiate into odontoblasts. (E) Scanning electron microscopy of exposed dentinal tubules. *Taken from Nino-Barrera, J.L., Garzon-Alvarado, D.A., 2012. Does the geometric location of odontoblast differentiation and dentinal tubules depend on a reaction-diffusion system between BMP2 and Noggin? A mathematical model. Journal of Endodontics 38 (12), 1635−1638.*

Eq. (5.38) indicates that the DLX3 concentration given by $C_D(\mathbf{x})$ could be different in each part of the domain. In the example 1, we had a constant (in other words, $C_D(\mathbf{x}) = C_D$), then we have the same parameter in every point of the domain. Here, we will have different parameters (for γ_0 and d) in each subdomain (see Fig. 5.8).

In this section, the computational model of the reaction−diffusion system presented explains the interaction between DLX3, BMP2, and Noggin. The purpose of this model is to show the irregular patterns of location of the dentinal tubules when DLX3 gene mutation is present, as in the TDOS. To observe the independence of the location of the subdomains in the formation of Turing patterns, several numerical tests were performed. The domain is divided into two subdomains, with a different DLX3 concentration in each one, which draws to have different parameters for the reaction−diffusion equation in the same domain; that means heterogeneity of space parameters is presented. The corresponding parameters are taken according to the specific wave number given in Table 5.1.

Even with the same initial conditions, each temporal steady-state path is different. Then, different spatial patterns are observed in time $t = 0.1$ and $t = 0.4$, but in $t = 0.7$ the same kind of pattern is obtained (Fig. 5.8). The difference is in the 90-degree rotation, as expected if the initial conditions do not affect the steady-state results. In Fig. 5.8 the two-domain division, where the parameters are different, is observed, which leads to have nonperiodic Turing patterns.

Special attention to the solution shown in Fig. 5.9 is given. In this case, a combination of dots and lines without symmetry is observed. This would suggest that there is a heterogeneous distribution of odontoblasts and dentinal tubules.

5.4.1 Discussion of Results

Various biological processes can be systematized and analyzed using mathematical and computational techniques (Nino-Barrera et al., 2013; Garzon-Alvarado, 2014; Cardenas Sandoval et al., 2012; Garzon-Alvarado et al., 2014). Thus, mathematics applied to biology enables us to understand and quantify physiological and pathological phenomena in the light of the universal laws of physics, biology, and biochemistry. Here, a specific feature of the pathology, such as the shape and heterogeneous location of the dentinal tubules, was analyzed.

Genetic diseases, such as TDOS, are characterized by failure in the expression of the proteins encoded by a given gene, in this case the DLX3 (Duverger et al., 2008). The family of DLX genes encodes growth factors that allow proper morphogenesis in early stages of development (Takechi et al., 2013). In the odontoblast differentiation, mutation of DLX3 has been reported to modify the formation of the dentinal tubules by altering the differentiation of odontoblasts

This book belongs to Central Library BADJI Mokhtar-ANNABA UNIVERSITY
Copyright Elsevier 2024

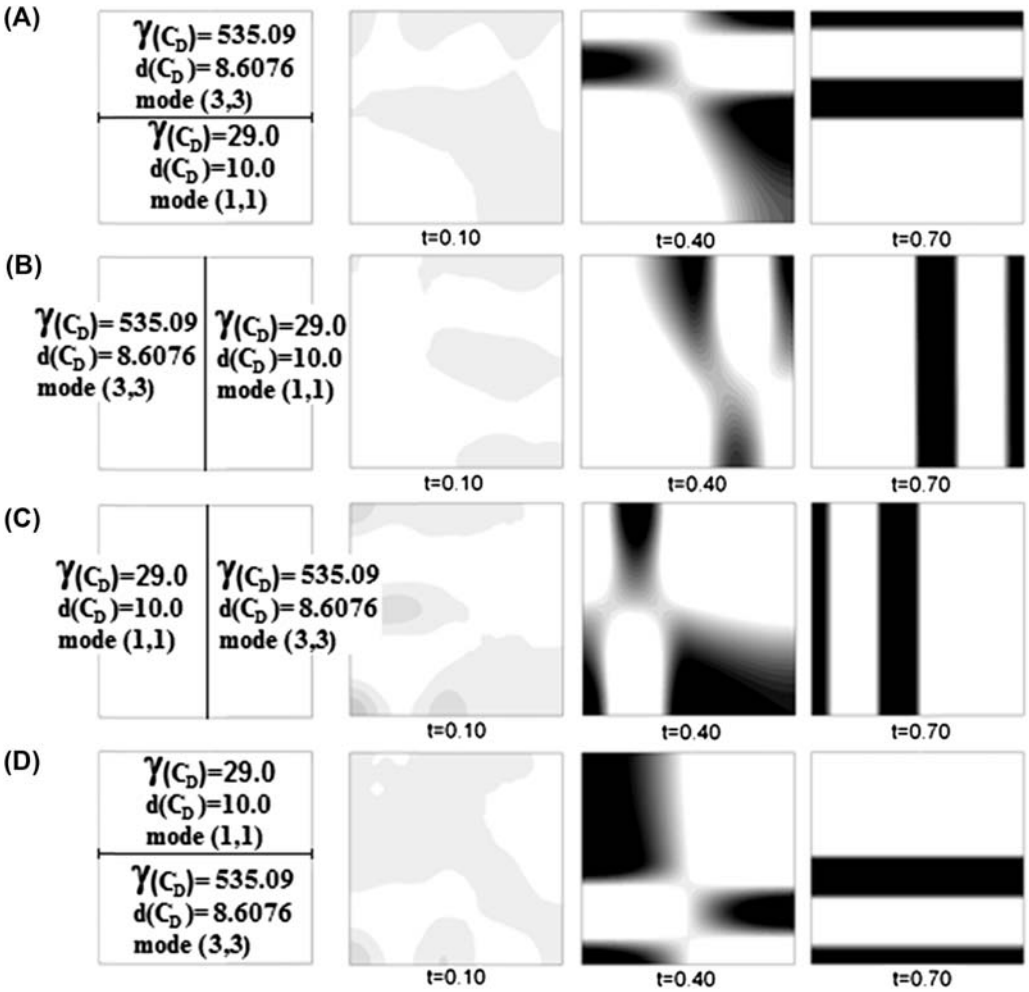

FIGURE 5.8 Numerical examples for a heterogeneous domain. The distribution of subdomains, given in this figure, are represented in (A−D). In (D), time is shown during the transient simulation to reach the steady state at $t = 0.7$.

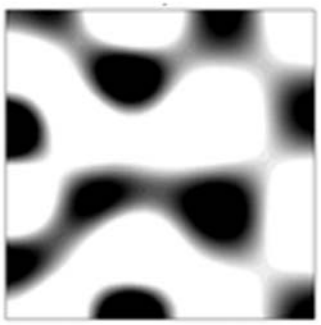

FIGURE 5.9 Turing patterns at steady state for two heterogeneous media with different wave numbers. Black color means low concentration and white color means high concentration. This figure shows the BMP concentration for Eq. (5.8).

(Duverger et al., 2012). This alteration weakens the dentin and turns it susceptible to breakage and decay, which can lead to pulp necrosis and makes it prone to a periapical abscess (Choi et al., 2010). In this finite element analysis, it was shown that the distribution of DLX3 can influence the location of the dentinal tubules. When the distribution is constant, the parameters of the reaction−diffusion system are homogeneously distributed. With nonuniform distribution of DLX3, the parameters are heterogeneously distributed. Then, the present numerical analysis theoretically represents the disordered location of the dentinal tubules in tooth affected by TDOS.

This book belongs to Central Library BADJI Mokhtar-ANNABA UNIVERSITY Copyright Elsevier 2024

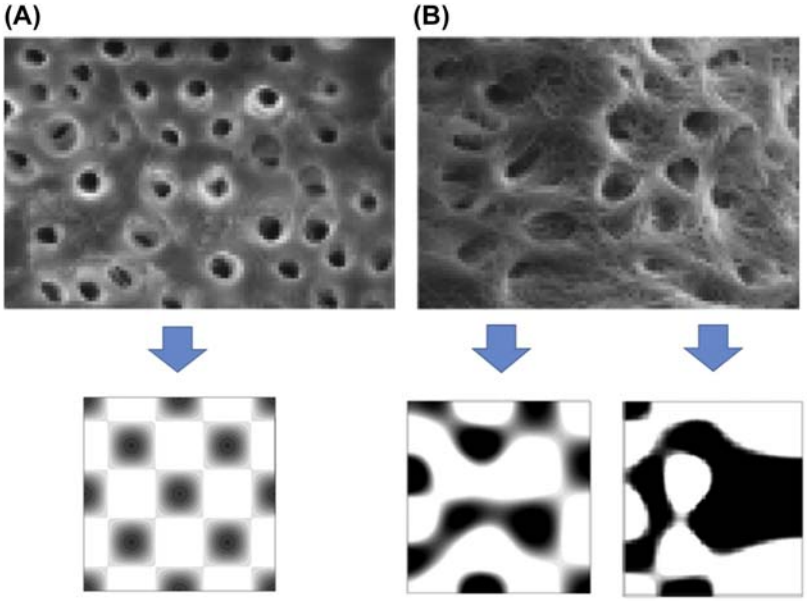

FIGURE 5.10 (A) Comparison of the histological picture of normal dentin tubules and the mathematical model of its geometrical location with normal distribution of DLX3. (B) Comparison of the histological picture of dentin tubules and the mathematical model of its geometrical location with nonuniform distribution of DLX3. *Images taken from Nino-Barrera, J.L., Garzon-Alvarado, D.A., 2012. Does the geometric location of odontoblast differentiation and dentinal tubules depend on a reaction-diffusion system between BMP2 and Noggin? A mathematical model. Journal of Endodontics 38 (12), 1635−1638; Duverger, O., Zah, A., Isaac, J., Sun, H.W., Bartels, A.K., Lian, J.B., Berdal, A., Hwang, J., Morasso, M.I., 2012. Neural crest deletion of Dlx3 leads to major dentin defects through down-regulation of Dspp. The Journal of Biological Chemistry 287 (15), 12230−12240.*

Despite the similarity observed between the simulation results and histological sections (Fig. 5.10), it is a mathematical model that has several simplifications. As previously mentioned, it is evident that the Noggin−BMP2−DLX 3 relationship is not the only interaction in the differentiation process. Other factors that are involved in the process are the BMP4(3), DPP (Bègue-Kirn et al., 1998), and BMP7 (Aberg et al., 1997). Additionally, mechanical forces can alter the course of development and differentiation. Genetics may also have an important influence not quantified in this mathematical model. Even with all considerations and simplifications, the mathematical model proposed is suitable to reproduce the morphological and geometric abnormality that occurs in the dentinal tubules as a result of TDOS.

REFERENCES

Aberg, T., Wozney, J., Thesleff, I., 1997. Expression patterns of bone morphogenetic proteins (Bmps) in the developing mouse tooth suggest roles in morphogenesis and cell differentiation. Developmental Dynamics: An Official Publication of the American Association of Anatomists 210 (4), 383−396.

Anguelova, M., Cedersund, G., Johansson, M., Franzen, C.J., Wennberg, B., 2007. Conservation laws and unidentifiability of rate expressions in biochemical models. IET Systems Biology 1, 230−237.

Arana-Chavez, V.E., Massa, L.F., 2004. Odontoblasts: the cells forming and maintaining dentine. The International Journal of Biochemistry and Cell Biology 36 (8), 1367−1373.

Ball, P., 2015. Forging patterns and making waves from biology to geology: a commentary on Turing (1952) 'The chemical basis of morphogenesis'. Philosophical Transactions of the Royal Society of London. Series B, Biological Sciences 370.

Bartold, P.M., Narayanan, A.S., 1998. Biology of the Periodontal Connective Tissues. Quintessence Publishing, Chicago.

Bègue-Kirn, C., Krebsbach, P.H., Bartlett, J.D., Butler, W.T., 1998. Dentin sialoprotein, dentin phosphoprotein, enamelysin and ameloblastin: tooth-specific molecules that are distinctively expressed during murine dental differentiation. European Journal of Oral Sciences 106 (5), 963−970.

Carda, C., Peydro, A., 2006. Ultrastructural patterns of human dentinal tubules, odontoblasts processes and nerve fibres. Tissue and Cell 38 (2), 141−150.

Cardiff, P., Karac, A., FitzPatrick, D., Ivankovic, A., 2014. Development of a hip joint model for finite volume simulations. Journal of Biomechanical Engineering 136, 011006.

Cardenas Sandoval, R.P., Garzon-Alvarado, D.A., Ramirez Martinez, A.M., 2012. A mathematical model of the process of ligament repair: effect of cold therapy and mechanical stress. Journal of Theoretical Biology 302, 53−61.

Choi, S.J., Song, I.S., Feng, J.Q., Gao, T., Haruyama, N., Gautam, P., Robey, P.G., Hart, T.C., 2010. Mutant DLX 3 disrupts odontoblast polarization and dentin formation. Developmental Biology 344 (2), 682−692.

This book belongs to Central Library BADJI Mokhtar-ANNABA UNIVERSITY Copyright Elsevier 2024

Duverger, O., Lee, D., Hassan, M.Q., Chen, S.X., Jaisser, F., Lian, J.B., Morasso, M.I., 2008. Molecular consequences of a frameshifted DLX3 mutant leading to Tricho-Dento-Osseous syndrome. The Journal of Biological Chemistry 283 (29), 20198–20208.

Duverger, O., Zah, A., Isaac, J., Sun, H.W., Bartels, A.K., Lian, J.B., Berdal, A., Hwang, J., Morasso, M.I., 2012. Neural crest deletion of Dlx3 leads to major dentin defects through down-regulation of Dspp. The Journal of Biological Chemistry 287 (15), 12230–12240.

Farzaneh, S., Paseta, O., Gomez-Benito, M.J., 2015. Multi-scale finite element model of growth plate damage during the development of slipped capital femoral epiphysis. Biomechanics and Modeling in Mechanobiology 14, 371–385.

Ferrario, V.F., Sforza, C., Colombo, A., Carvajal, R., Duncan, V., Palomino, H., 1999. Dental arch size in healthy human permanent dentitions: ethnic differences as assessed by discriminant analysis. The International Journal of Adult Orthodontics and Orthognathic Surgery 14 (2), 153–162.

Garzón-Alvarado, D.A., 2007. Simulación de procesos de reacción-difusión: aplicación a la morfogénesis del tejido óseo (Ph.D. thesis), Zaragoza, España.

Garzon-Alvarado, D.A., Garcia-Aznar, J.M., Doblare, M., 2009. Appearance and location of secondary ossification centres may be explained by a reaction-diffusion mechanism. Computers and Biology and Medicine 39 (6), 554–561.

Garzon-Alvarado, D.A., 2014. A biochemical strategy for simulation of endochondral and intramembranous ossification. Computer Methods in Biomechanics and Biomedical Engineering 17 (11), 1237–1247.

Garzon-Alvarado, D.A., Gutierrez, M.L., Calixto, L.F., 2014. A computational model of clavicle bone formation: a mechano-biochemical hypothesis. Bone 61, 132–137.

Ghosh, P., Sen, S., Riaz, S.S., Ray, D.S., 2009. Galerkin analysis of light-induced patterns in the chlorine dioxide-iodine-malonic acid reaction-diffusion system. Physical Review. E, Statistical, Nonlinear, and Soft Matter Physics 79, 056216.

Jiang-Jun, Z., Min, Z., Ya-Bo, Y., Wei, L., Ren-Fa, L., Zhi-yu, Z., Rong-Jian, C., Wei-Tao, Y., Cheng-Fei, D., 2014. Finite element analysis of a bone healing model: 1-year follow-up after internal fixation surgery for femoral fracture. Pakistan Journal of Medical Sciences 30, 343–347.

Kettunen, P., Thesleff, I., 1998. Expression and function of FGFs-4, -8, and -9 suggest functional redundancy and repetitive use as epithelial signals during tooth morphogenesis. Developmental Dynamics 211 (3), 256–268.

Kettunen, P., Laurikkala, J., Itaranta, P., Vainio, S., Itoh, N., Thesleff, I., 2000. Associations of FGF-3 and FGF-10 with signaling networks regulating tooth morphogenesis. Developmental Dynamics 219 (3), 322–332.

Kondo, S., Miura, T., 2010. Reaction-diffusion model as a framework for understanding biological pattern formation. Science 329, 1616–1620.

Kumasaka, S., Shimozuma, M., Kawamoto, T., Mishima, K., Tokuyama, R., Kamiya, Y., Davaadorj, P., Saito, I., Satomura, K., 2010. Possible involvement of melatonin in tooth development: expression of melatonin 1a receptor in human and mouse tooth germs. Histochemistry and Cell Biology 133 (5), 577–584.

Lesot, H., Lisi, S., Peterkova, R., Peterka, M., Mitolo, V., Ruch, J.V., 2001. Epigenetic signals during odontoblast differentiation. Advances in Dental Research 15, 8–13.

Linde, A., 2009. Dentin mineralization and the role of odontoblasts in calcium transport. Connective Tissue Research 33 (1–3), 163–170.

Lisi, S., Peterkova, R., Peterka, M., Vonesch, J.L., Ruch, J.V., Lesot, H., 2003. Tooth morphogenesis and pattern of odontoblast differentiation. Connective Tissue Research 44 (Suppl. 1), 167–170.

Long, F., Li, F., Intes, X., Kotha, S.P., 2016. Radiative transfer equation modeling by streamline diffusion modified continuous Galerkin method. Journal of Biomedic Optics 21, 36003.

Mammoto, T., Mammoto, A., Torisawa, Y.S., Tat, T., Gibbs, A., Derda, R., Mannix, R., de Bruijn, M., Yung, C.W., Huh, D., Ingber, D.E., 2011. Mechanochemical control of mesenchymal condensation and embryonic tooth organ formation. Developmental Cell 21 (4), 758–769.

Mina, M., Kollar, E.J., 1987. The induction of odontogenesis in non-dental mesenchyme combined with early murine mandibular arch epithelium. Archives of Oral Biology 32 (2), 123–127.

Mitsiadis, T.A., Graf, D., 2009. Cell fate determination during tooth development and regeneration. Birth Defects Research Part C: Embryo Today 87 (3), 199–211.

Nanci, A., 2008. Oral Histology, seventh ed. Elsevier Inc.

Nino-Barrera, J.L., Garzon-Alvarado, D.A., 2012. Does the geometric location of odontoblast differentiation and dentinal tubules depend on a reaction-diffusion system between BMP2 and Noggin? A mathematical model. Journal of Endodontics 38 (12), 1635–1638.

Nino-Barrera, J.L., Gutierrez, M.L., Garzon-Alvarado, D.A., 2013. A theoretical model of dentinogenesis: dentin and dentinal tubule formation. Computer Methods and Programs in Biomedicine 112 (1), 219–227.

Painter, K., 1997. Chemotaxis as a Mechanism for Morphogenesis (Ph.D. thesis). Oxford University, United Kingdom.

Plazl, I., Lakner, M., 2010. Modeling and finite difference numerical analysis of reaction-diffusion dynamics in a microreactor. Acta Chimica Slovenica 57, 100–109.

Plikus, M.V., Zeichner-David, M., Mayer, J.A., Reyna, J., Bringas, P., Thewissen, J.G., Snead, M.L., Chai, Y., Chuong, C.M., 2005. Morphoregulation of teeth: modulating the number, size, shape and differentiation by tuning Bmp activity. Evolution and Development 7 (5), 440–457.

Price, J.A., Bowden, D.W., Wright, J.T., Pettenati, M.J., Hart, T.C., 1998a. Identification of a mutation in DLX3 associated with tricho-dento-osseous (TDO) syndrome. Human Molecular Genetics 7 (3), 563–569.

Price, J.A., Wright, J.T., Kula, K., Bowden, D.W., Hart, T.C., 1998b. A common DLX3 gene mutation is responsible for tricho-dento-osseous syndrome in Virginia and North Carolina families. Journal of Medical Genetics 35 (10), 825–828.

Ruch, J.V., Lesot, H., Begue-Kirn, C., 1995. Odontoblast differentiation. International Journal of Developmental Biology 39 (1), 51–68.

Schmitt, R., Ruch, J.V., 2000. In vitro synchronization of embryonic mouse incisor preodontoblasts and preameloblasts: repercussions on terminal differentiation. Eurpean Journal of Oral Sciences 108 (4), 311–319.

Takechi, M., Adachi, N., Hirai, T., Kuratani, S., Kuraku, S., 2013. The Dlx genes as clues to vertebrate genomics and craniofacial evolution. Seminars in Cell and Developmental Biology 24 (2), 110–118.

This book belongs to Central Library BADJI Mokhtar-ANNABA UNIVERSITY Copyright Elsevier 2024

Thesleff, I., 1995a. Homeobox genes and growth factors in regulation of craniofacial and tooth morphogenesis. Acta Odontologica Scandinavica 53 (3), 129–134.

Thesleff, I., 1995b. Tooth morphogenesis. Advances in Dental Research 9 (3 Suppl.), 12.

Thesleff, I., Mikkola, M., 2002. The role of growth factors in tooth development. International Review of Cytology 217, 93–135.

Thesleff, I., Vaahtokari, A., Vainio, S., Jowett, A., 1996. Molecular mechanisms of cell and tissue interactions during early tooth development. The Anatomical Record 245 (2), 151–161.

Turing, A., 1952. The chemical basis of morphogenesis. Philosophical Transactions of the Royal Society of London. Series B, Biological Sciences 237, 37–72.

Tziafas, D., Kodonas, K., 2010. Differentiation potential of dental papilla, dental pulp, and apical papilla progenitor cells. Journal of Endodontics 36 (5), 781–789.

Vanegas, J., Landinez, N., Garzón, D., 2009. Análisis de la inestabilidad de turing en modelos biológicos. Dyna 158, 123–134.

Vanegas-Acosta, J., Garzón-Alvarado, D., 2014. Biological modelling and computational implementation using the finite elements method. Computational and Applied Mathematics 33, 621–640.

Viale-Bouroncle, S., Felthaus, O., Schmalz, G., Brockhoff, G., Reichert, T.E., Morsczeck, C., 2012. The transcription factor DLX3 regulates the osteogenic differentiation of human dental follicle precursor cells. Stem Cells and Development 21 (11), 1936–1947.

Walsh, D.W., Godson, C., Brazil, D.P., Martin, F., 2010. Extracellular BMP-antagonist regulation in development and disease: tied up in knots. Trends in Cell Biology 20 (5), 244–256.

Yang, W., Harris, M.A., Cui, Y., Mishina, Y., Harris, S.E., Gluhak-Heinrich, J., 2012. Bmp2 is required for odontoblast differentiation and pulp vasculogenesis. Journal of Dental Research 91 (1), 58–64.

Zhu, W., Kim, J., Cheng, C., Rawlins, B.A., Boachie-Adjei, O., Crystal, R.G., Hidaka, C., 2006. Noggin regulation of bone morphogenetic protein (BMP) 2/7 heterodimer activity in vitro. Bone 39 (1), 61–71.

FURTHER READING

Garzon-Alvarado, D.A., Gonzalez, A., Gutierrez, M.L., 2013. Growth of the flat bones of the membranous neurocranium: a computational model. Computer Methods and Programs in Biomedicine 112 (3), 655–664.

This book belongs to Central Library BADJI Mokhtar-ANNABA UNIVERSITY

Copyright Elsevier 2024

Chapter 6

A Discontinuous Galerkin Model for the Simulation of Chemotaxis Processes: Application to Stem Cell Injection After a Myocardial Infarction

Discontinuous Galerkin Methods

F.J. Vermolen[1], L.Y.D. Crapts[1] and J.K. Ryan[2]
[1]Delft University of Technology, Delft, The Netherlands; [2]University of East Anglia, Norwich, United Kingdom

6.1 INTRODUCTION

In many biological processes, cells migrate in the direction to the gradient of a concentration. This process is commonly referred to as chemotaxis or haptotaxis in fluidic or solid environments, respectively. Chemotaxis of cells occurs not only in many important biological processes, such as wound healing, but also in tumor growth and metastasis. Healing processes typically involve the repair of tissues and, to this end, it is necessary that certain cells migrate and regenerate the appropriate tissues such as bone or skin. Cells secrete signaling agents by which either cells of the same or different phenotypes are attracted toward them so that certain biological processes such as the repair of extracellular matrix can occur. Furthermore, the immune response system operates on the basis of chemotactic migration of white blood cells toward pathogens as a result of biotic lactates that are effectively transported away from pathogens as a result of the acidification of the environment. In various treatments, it is aimed at trying to make certain cells migrate to desired locations. In this chapter, we consider the application of stem cell therapy to improve the structure and efficacy of the heart muscle, where stem cells activate migration of endothelial cells to damaged regions of the heart. An experimental study on stem cell migration induced by chemokines was presented in, among many other studies, Baek et al. (2011).

Myocardial infarctions have been a very common cause of death in the industrialized countries for many decades. The cause of a myocardial infarction (heart attack) gradually develops as a result of the increasing blockage of the coronal artery of the heart. This gradual blockage is referred to as atherosclerosis, see Shimamoto (1969) for an early experimental study. Once the coronal artery is blocked, then the flow of blood stops and herewith the transport of oxygen ceases, and then sudden death of heart tissue sets in. This is the myocardial infarction (heart attack). After a myocardial infarction, the mechanical structure of the heart tissue changes as a result of fibrosis (stiffening as a result of the development of fibrous tissue). An experimental reference regarding the temporal evolution of mechanical properties (in particular stiffening) of the scar tissue that develops after a myocardial infarction is given in Fomovsky and Holmes (2010), where they also observed that the collagen orientation tends to be more isotropically aligned in rats than in other animals such as pigs and goats. The dead part of the heart muscle no longer contracts and has become stiffer and thereby the pumping mechanism is inhibited, whereas the parts of the heart that are still viable are working harder. This causes rhythmic disorder and eventually heart failure and hence possibly sudden death of the patient.

Heart cells (cardiocytes) were thought to be irreplaceable (see for instance Olivetti et al., 1991); however, the more recent insights point at a "self-healing" capacity of the heart (see for instance Kajstura et al., 2008). Here it can be seen that

Numerical Methods and Advanced Simulation in Biomechanics and Biological Processes. https://doi.org/10.1016/B978-0-12-811718-7.00006-X
Copyright © 2018 Elsevier Ltd. All rights reserved.

This book belongs to Central Library BADJI Mokhtar-ANNABA UNIVERSITY
Copyright Elsevier 2024

this is really a change of paradigm as the last author supervised both studies. It is possible to influence the mechanical properties of the heart by preventing fibrosis as much as possible. This is done by the injection of stem cells onto the heart surface; this is also known as *stem cell therapy*, which seems to be a very promising therapy after myocardial infarctions (see for instance Przybyt and Harmsen, 2013). The idea is that the stem cells secrete vascular endothelial growth factors (VEGF or TG-β), which activate the proliferation and migration of endothelial cells. These cells form the backbone of small blood vessels, which improves the blood transport to the damaged regions of the heart. Another important side effect is that they reduce the stiffness of the damaged regions of the heart so that the pumping efficacy and capacity increase without requiring too much force from the cardiocytes.

In this manuscript, we consider the process of angiogenesis in the heart, which is the formation and extension of the capillary network over the damaged regions of the heart. The migration of endothelial cells toward the damaged regions of the heart proceeds as a result of chemo- and haptotaxis. To model angiogenesis, several classes of models exist: cell-based formalisms on the small scales, in which cells are tracked on an individual basis, and continuum-based models, where cell densities in terms of number of cells per unit of volume or area are considered rather than individual cells. The small-scale models generally have a stochastic nature for cell proliferation and death, as well as for cell migration in terms of stochastic differential equations. Some cell-scale models are lattice based, that is, cells are allowed to occupy predefined regions of a lattice and migrate on minimization of a functional of (virtual) energy. These models fall within the class of cellular automata formalisms, which are very popular in modeling angiogenesis (van Oers et al., 2014). Recently a semicontinuous cell-based model has been developed for angiogenesis where cells have a certain predefined or evolving geometry (Bookholt et al., 2016).

Currently, we, however, consider angiogenesis on the continuum scale on the basis of a system of partial differential equations. To approximate the solution of partial differential equations, finite element techniques offer a large amount of freedom with respect to geometry and sudden changes of coefficients, see for instance the books Atkinson and Han (2009) and Brenner and Scott (2008). The present chapter deals with a Keller−Segel type (Byrne and Chaplain, 1995, for instance) of formalism for the migration of endothelial cells. This model is characterized by the strong dominance of the convective (first-order) term in the reaction transport equations. Furthermore, the gradient of a chemical signal, which is approximated by a numerical solution to a partial differential equation as well, has to be determined. This poses several numerical challenges because standard Galerkin methods generally need very high grid resolutions to deal with convection-dominated problems. Despite the enormous popularity of SUPG (streamline upwind Petrov−Galerkin) methods because of their ease of implementation and reliability, one has sought useful and reliable alternatives that are able to maintain a high quality of the numerical solution in terms of an accurate approximation in regions with large gradients, preferably at low computational cost and where monotonicity of the solution is preserved. As an alternative, several studies report of the application of the algebraic flux correction method to handle hyperbolic partial differential equations in a finite element setting, see for instance the study by Moller (2013). If it comes to hyperbolic equations, or equations with a high degree of hyperbolicity, then finite volume methods are very popular because slope or flux limiting procedures are relatively straightforward to implement. We refer to Leveque (2002) as a standard work in this area.

To this end, discontinuous Galerkin (DG) methods have been developed to deal with hyperbolic (convection) problems with large gradients. These methods have been combined with flux and slope limiters that enable a computationally cheap treatment of the convective terms in case of convection-dominated problems. DG methods have been developed and analyzed in many studies and for various applications with elliptic, parabolic, and predominantly hyperbolic partial differential equations. For some classical references, we cite the work by Cockburn (1997), Hesthaven and Warburton (2008), and Paillere (1996). The application and construction of limiters and filtering to remove highly oscillatory parts of the numerical solution can be found in the studies by Qiu and Shu (2005) and Mirzaee et al (2014). Particular applications of the DG method have been studied in Hesthaven and Warburton (2008). We finally remark that chemotaxis processes were modeled using DG methods by Epshteyn and Kurgonov (2008), Epshteyn and Izmirlioglu (2009), and Epshteyn (2009, 2012). The key messages of the current manuscript are as follows:

- The application of the DG method to a chemotactic snail trail model is described.
- One- and two-dimensional methods are presented on quadrilateral meshes.
- A large order of accuracy is obtained using the DG method under the use of Runge−Kutta time integration methods.

The present chapter starts with the introduction of the mathematical model and continues with the presentation of the numerical method based on a combination of slope limiting and a DG method. Subsequently, some results have been shown in terms of simulations and we end up with some discussion and conclusions. For more mathematical details, regarding exact solution representations for simple cases in which the construction is based on the method of characteristics, the interested reader is referred to Crapts (2012).

This book belongs to Central Library BADJI Mokhtar-ANNABA UNIVERSITY Copyright Elsevier 2024

6.2 BACKGROUND ON STEM CELL THERAPY AND THE NUMERICAL METHOD

A myocardial infarction is the regional death of myocardiocytes, which are responsible for the periodic contraction of the heart muscle. The death of myocardiocytes results in a self-reparative mechanism, in which the damaged heart tissue is replaced with a fibrotic scar, which is produced by fibroblasts and myofibroblasts (see Talman and Ruskoaho, 2016). In principle this mechanism avoids rupture of the heart ventricular walls; however, a setback is that the local mechanical stiffness in the damaged parts is higher than in the undamaged regions of the heart. The increase in local stiffness of the scarred region, which hardly contributes to the contraction mechanism, frustrates the contraction mechanism of the cardiocytes that are located at other positions of the heart. This process can play a pivotal role in the development of dangerous heart rhythm disorders and sudden death of the patient (see Lazzerini et al., 2006, for instance). To transform the fibrosis-effected scar to a less stiff tissue, stem cells are injected near fibrosis-effected regions of the heart. In this stem cell therapy, the stem cells will adhere onto the fibrotic regions of the heart (see Przybyt and Harmsen, 2013). The stem cells secrete chemokines, which make the endothelial cells (note that the endothelial cells are the backbone of blood vessels (arteries)), migrate toward the fibrosis-effected region, and reestablish a capillary network in this scar-effected region of the heart muscle. This migration toward the gradient of the concentration is referred to chemotaxis or haptotaxis. This transformation makes the region less stiff and thereby the efficiency of the contraction mechanism will increase, which also leads to a mechanically less demanding environment of the cardiocytes (see Wingstrand et al., 2016). This process can thereby prevent premature death of the patient, as well as increase the patient's quality of life.

Because the migration of endothelial cells is largely determined by movement according to the gradient of the concentration of the chemokine (chemotaxis), it is necessary to determine the gradient of the chemokine. To this extent, we use order reduction, as in mixed finite element schemes, to solve for both the gradient of the concentration and the concentration itself for the chemokine. The snail trail mechanism is dealt with analogously. This approach circumvents the need of using complicated gradient reconstruction schemes, such as the ZZ-patch-based scheme. Furthermore, the migration component from chemotaxis may be much larger than the component induced by random walk. This makes the reaction transport rather hyperbolic, for which DG methods are known to be very suitable. In particular, if the solution is characterized by large spatial variations (e.g., large gradients), then DG methods are very attractive and a good alternative to standard Galerkin methods, or SUPG methods, which introduce significant numerical diffusion in the upstream direction. We also note that conservation laws that are largely hyperbolic require the conservation of signals (such as mass) to a large degree, and from this it follows that accurate discretization methods are required in terms of spatial discretization and time integration. Finite volume methods are conservative but suffer from relatively poor accuracy if classical lower-order versions are applied. In this light, DG methods can be considered as "higher-order" finite volume methods. This makes the DG methods combined with Runge−Kutta time integration methods accurate candidates. We also note that the DG methods unfortunately are characterized by large CPU times per time step.

6.3 THE MATHEMATICAL MODEL

We model angiogenesis by a *tip-sprout* system of (hyperbolic and parabolic) partial differential equations that was originally formulated by Byrne and Chaplain (1995). In this manuscript, we simplify the surface of the heart by considering a square domain of computation. We consider a domain of computation Ω with boundary $\partial\Omega$, that is fixed in time. Presently, we use an open nonempty square domain:

$$\Omega = \left\{(x,y)\in\mathbb{R}^2 : |x| < 1, |y| < 1\right\}.$$

Furthermore, the damaged domain is given by $\Omega_\delta \subset \Omega$:

$$\Omega_\delta = \left\{(x,y)\in\mathbb{R}^2 : |x| < \delta, |y| < \delta\right\}, \quad 0 < \delta < 1.$$

We assume that at $t = 0$ (t denoting time), stem cells are injected homogeneously over the damaged region. Let $m = m(t, \mathbf{x})$ denote the stem cell density at time t and location $\mathbf{x}$, then at $t = 0$, we have

$$m(0,\mathbf{x}) = \begin{cases} m_0, & \mathbf{x}\in\Omega_w, \\ 0, & \mathbf{x}\in\Omega\setminus\Omega_w. \end{cases} \tag{6.1}$$

The natural decay of the stem cells as a result of cell death and due to migration away from the heart is modeled by

$$\frac{\partial m}{\partial t} = -\beta_1 m, \tag{6.2}$$

This book belongs to Central Library BADJI Mokhtar-ANNABA UNIVERSITY
Copyright Elsevier 2024

where $\beta_1 \geq 0$ is a stem cell decay rate coefficient whose dimension is the reciprocal time. The secretion and diffusion of the chemoattractant (TG-β) by the stem cells is modeled by

$$\frac{\partial c}{\partial t} - D_1 \Delta c + \lambda c = \alpha m, \quad (t, \mathbf{x}) \in \mathbb{R}^+ \times \Omega. \tag{6.3}$$

Here $D_1 > 0$ represents the diffusion coefficient of the chemoattractant over the domain (being the heart surface), $\lambda \geq 0$ and $\alpha \geq 0$, respectively, represent the natural decay rate and the regeneration rate by the stem cells. We note that Δ represents the two-dimensional Laplacian. As the initial condition, we assume that the concentration of chemoattractants is zero and that there is no flux over the boundary of the domain, that is

$$c(0, \mathbf{x}) = 0, \quad \text{in } \Omega, \quad D_1 \frac{\partial c}{\partial n} = 0, \quad \text{on } t > 0, \quad \mathbf{x} \in \partial\Omega.$$

In the current model, we distinguish between capillary tips and sprouts. The tips are the leading edges of the sprouts. The tips, which are constituted by the leading endothelial cells, are subject to chemotaxis, random walk (diffusion), bifurcation on both existing sprouts and the tips, as well as tip−sprout anastomosis (merging). Let the tip density and sprout density, respectively, be denoted by u and ρ, both being functions of time and space. This gives the following equation:

$$\frac{\partial u}{\partial t} + \chi_1 \nabla \cdot (u \nabla c) - D_2 \Delta u = \alpha_0 \rho c + \alpha_1 H(c - \widehat{c}) u c - \beta_2 u \rho, \quad (t, \mathbf{x}) \in \mathbb{R}^+ \times \Omega. \tag{6.4}$$

The first, second, and third terms of the left-hand side of the above equation, respectively, represent the accumulation, chemotaxis, and random walk (diffusion) of the tips. The right-hand side contains bifurcation and hence arising of tips on sprouts, bifurcation at tips (hence on the leading ends), and anastomosis (merging of tips to tips or sprouts), respectively. Further $\chi_1 \geq 0$, $D_2 > 0$, α_0, $\alpha_1 \geq 0$, and $\beta_2 \geq 0$, respectively, represent the chemotactic coefficient, diffusion coefficient, sprout bifurcation rate constant, tip bifurcation rate constant, and the anastomosis rate coefficient. It is assumed that tip bifurcation only takes place if the concentration of chemoattractant exceeds a threshold value $\hat{c} \geq 0$. The function $H(.)$ represents the Heaviside function. Initially it is assumed that the number of capillary tips is zero. Furthermore, no flux is assumed over the boundary of the domain of computation, and this results in

$$u(0, \mathbf{x}) = 0, \quad \text{in } \Omega, \quad D_2 \frac{\partial u}{\partial n} - \chi_1 u \frac{\partial c}{\partial n} = 0, \quad \text{on } t > 0, \quad \mathbf{x} \in \partial\Omega.$$

The sprouts are assumed to follow the tips. They consist of *stalking* endothelial cells. One can interpret their migration as a *snail trail* in combination with random walk and hence any position in space is occupied by a sprout once was occupied by a tip cell. In the work by Byrne and Chaplain (1995), a one-dimensional case was considered. Because we consider migration of tips predominantly toward the center of the region, we extend the one-dimensional case considered to the migration of sprouts toward the center by

$$\frac{\partial \rho}{\partial t} - D_3 \Delta \rho - (D_2 \nabla u + \chi_1 u \nabla c) \cdot \frac{\mathbf{x}}{\|\mathbf{x}\|_2} + \gamma(\rho - \rho_{\text{eq}}) = 0, \quad (t, \mathbf{x}) \in \mathbb{R}^+ \times \Omega. \tag{6.5}$$

This equation is supplemented with a Dirichlet boundary condition, which reads as

$$\rho(t, \mathbf{x}) = \rho_{\text{eq}}, \quad \text{on } t > 0, \quad \mathbf{x} \in \partial\Omega. \tag{6.6}$$

As an initial condition for the sprout density ρ, we use

$$\rho(0, \mathbf{x}) = \begin{cases} 0, & \mathbf{x} \in \Omega_w, \\ \rho_{\text{eq}}, & \mathbf{x} \in \Omega \setminus \Omega_w. \end{cases} \tag{6.7}$$

We realize that this model is not the only partial differential equation-based model for angiogenesis. Maggelakis (2003, 2004) formulated an angiogenesis where hypoxia (shortage of oxygen) was included. In her model, however, tip anastomosis and branching was neglected. Furthermore, Pettet et al. (1996) considered an alternative model that incorporates tip branching and anastomosis. Their model was not based on a *snail trail* mechanism. In the next section, we describe the numerical method based on a DG method.

This book belongs to Central Library BADJI Mokhtar-ANNABA UNIVERSITY
Copyright Elsevier 2024

6.4 NUMERICAL METHOD

The standard finite element method exhibits oscillations if the contribution of chemotaxis is large with respect to the diffusive part. To this extent, an SUPG method can be used for the suppression of oscillations. The disadvantage of the SUPG method, however, is the smearing behavior of the numerical solution, in which the large gradients are approximated by gradients that are too small. Therefore, we choose to use a DG method to solve the problem. To maintain monotonicity, the DG method can be extended with a slope limiter. Although the DG method has been explained in several manuscripts, such as Cockburn (1997) and Hesthaven and Warburton (2008), we outline the method applied to the current model. Furthermore, because the two-dimensional implementation is based on the extension of the one-dimensional implementation, we start with the explanation of the one-dimensional implementation.

6.4.1 The One-Dimensional Implementation

As in other classical discretization methods, the domain of computation is divided into elements, which reduce to line segments as elements in the one-dimensional implementation. We denote the elements by $e_j = [x_{j-1/2}, x_{j+1/2}]$. Like in the standard finite element, the differential equations are multiplied by a test function and integrated by parts to obtain a weak formulation. However, unlike in the finite-element method where one integrates over the entire domain of computation, we integrate over the element e_j. We treat the three partial differential equations in three separate subsections.

6.4.1.1 The Diffusion–Reaction Equation

Before, we write the weak formulation, we split the differential equation into a system where only first-order derivatives with respect to spatial coordinates occur, to obtain the auxiliary formulation

$$\begin{aligned} &\frac{\partial c}{\partial t} + D_1 \frac{\partial q}{\partial x} + \lambda c = \alpha m, \quad \text{for } (t,x) \in \mathbb{R}^+ \times (0,1), \\ &q + \frac{\partial c}{\partial x} = 0, \quad \text{for } (t,x) \in \mathbb{R}^+ \times (0,1). \end{aligned} \tag{6.8}$$

Here q represents the flux over element boundaries, which we describe later. Note that the initial and boundary conditions are given by $c(0, x) = 0$ and $q(t, 0) = q(t, 1) = 0$. Multiplying both equations by a test function ϕ_j, and integrating by parts over the element e_j, gives the following weak form over e_j:

$$\begin{aligned} &\int_{e_j} \left(\phi_j \frac{\partial c}{\partial t} - D_1 \frac{d\phi_j}{dx} q + \lambda \phi_j c \right) dx + \left[D_1 \phi_j q \right]_{x_{j-1/2}}^{x_{j+1/2}} = \int_{e_j} \alpha \phi_j m dx, \quad \text{for } t > 0, \\ &\int_{e_j} \left(\phi_j q - \frac{d\phi_j}{dx} c \right) dx + \left[c \phi_j \right]_{x_{j-1/2}}^{x_{j+1/2}} = 0, \quad \text{for } t > 0. \end{aligned} \tag{6.9}$$

For the test function on e_j, we use Legendre polynomials up to order k, given by

$$P_n(x) = \frac{1}{2^n n!} \frac{d^n}{dx^n} \left(x^2 - 1 \right)^n, \tag{6.10}$$

and for convenience we scale the interval e_j to the reference interval $[-1, 1]$. Let x_j be the midpoint of e_j and let $\Delta x_j = x_{j+1/2} - x_{j-1/2}$, we define $r = \frac{2(x - x_j)}{\Delta x_j}$, then each integral over e_j is represented by

$$\int_{e_j} f(x) dx = \frac{\Delta x_j}{2} \int_{-1}^{1} f\left(x_j + \frac{\Delta x_j r}{2} \right) dr. \tag{6.11}$$

The above relation is used with the orthogonality of the Legendre functions, for which we have

$$\int_{-1}^{1} P_n(x) P_m(x) dx = \frac{2}{2m+1} \delta_{n,m}, \tag{6.12}$$

This book belongs to Central Library BADJI Mokhtar-ANNABA UNIVERSITY
Copyright Elsevier 2024

where $\delta_{n,m}$ represents the Kronecker Delta. On element e_j, we choose as a test function

$$\phi_j^m(x) = P_m\left(\frac{2(x-x_j)}{\Delta x_j}\right),$$

and, on e_j, the solution is approximated by

$$c(t,x) = c_h(t,x) = \sum_{\ell=0}^{k} c_l(t)\phi_j^\ell(x) = \sum_{\ell=0}^{k} c_\ell(t)P_\ell\left(\frac{2(x-x_j)}{\Delta x_j}\right), \quad \text{and } q(t,x) = q_h(t,x) = \sum_{\ell=0}^{k} q_\ell(t)P_\ell\left(\frac{2(x-x_j)}{\Delta x_j}\right).$$

It is clear from the initial condition for $c(t, x)$ that $c_\ell(0) = 0$. Furthermore, we obtain

$$\sum_{\ell=0}^{k} c_\ell'(t)\int_{e_j}\phi_j^m\phi_j^\ell dx - \sum_{\ell=0}^{k} D_1 q_\ell(t)\int_{e_j}\frac{d\phi_j^m}{dx}\phi_j^\ell dx + \sum_{\ell=0}^{k} c_\ell(t)\int_{e_j}\lambda\phi_j^m\phi_j^\ell dx + \left[D_1\phi_j^m q_h(t,x)\right]_{x_{j-1/2}}^{x_{j+1/2}} = \int_{e_j}\alpha\phi_j^m m dx, \quad \text{for } t>0,$$

$$\sum_{\ell=0}^{k} q_\ell(t)\int_{e_j}\phi_j^m\phi_j^\ell dx - \sum_{\ell=0}^{k} c_\ell(t)\int_{e_j}\frac{d\phi_j^m}{dx}\phi_j^\ell dx + \left[c_h(t,x)\phi_j^m\right]_{x_{j-1/2}}^{x_{j+1/2}} = 0, \quad \text{for } t>0. \tag{6.13}$$

The above system of equations contains several integrals that need to be computed. Furthermore, the boundary terms need to be defined as they are multivalued. First, we define the matrices containing the integral terms. Then, we introduce the element matrices over element e_j

$$M_{m\ell}^j = \int_{e_j}\phi_j^m(x)\phi_j^\ell(x)dx = \frac{\Delta x_j}{2}\int_{-1}^{1}P_m(r)P_\ell(r)dr = \frac{\Delta x}{2m+1}\delta_{m,\ell}, \tag{6.14}$$

and

$$S_{m\ell}^j = -\int_{e_j}\phi_j^m(x)\frac{d\phi_j^\ell}{dx}(x)dx = -\int_{-1}^{1}P_m(r)P_\ell'(r)dr. \tag{6.15}$$

For the case that $k = 3$ (four polynomials), which we consider in this chapter, we obtain

$$M^j = \Delta x\cdot\begin{pmatrix} 1 & 0 & 0 & 0 \\ 0 & \frac{1}{3} & 0 & 0 \\ 0 & 0 & \frac{1}{5} & 0 \\ 0 & 0 & 0 & \frac{1}{7} \end{pmatrix}, \quad \text{and } S^j = \begin{pmatrix} 0 & 0 & 0 & 0 \\ 2 & 0 & 0 & 0 \\ 0 & 2 & 0 & 0 \\ 2 & 0 & 2 & 0 \end{pmatrix}.$$

The boundary terms are determined using central fluxes, by

$$\begin{aligned}\left[D_1\phi_j^m q_h(t,x)\right]_{x_{j-1/2}}^{x_{j+1/2}} &= \frac{D_1}{2}\sum_{\ell=0}^{k}\left(q_j^\ell(t)\phi_j^\ell\left(x_{j+1/2}\right) + q_{j+1}^\ell(t)\phi_{j+1}^\ell\left(x_{j+1/2}\right)\right)\phi_j^m\left(x_{j+1/2}\right) \\ &\quad - \frac{D_1}{2}\sum_{\ell=0}^{k}\left(q_j^\ell(t)\phi_j^\ell\left(x_{j-1/2}\right) + q_{j-1}^\ell(t)\phi_{j-1}^\ell\left(x_{j-1/2}\right)\right)\phi_j^m\left(x_{j-1/2}\right).\end{aligned} \tag{6.16}$$

The same holds for

$$\begin{aligned}\left[\phi_j^m c_h(t,x)\right]_{x_{j-1/2}}^{x_{j+1/2}} &= \frac{1}{2}\sum_{\ell=0}^{k}\left(c_j^\ell(t)\phi_j^\ell\left(x_{j+1/2}\right) + c_{j+1}^\ell(t)\phi_{j+1}^\ell\left(x_{j+1/2}\right)\right)\phi_j^m\left(x_{j+1/2}\right) \\ &\quad - \frac{1}{2}\sum_{\ell=0}^{k}\left(c_j^\ell(t)\phi_j^\ell\left(x_{j-1/2}\right) + c_{j-1}^\ell(t)\phi_{j-1}^\ell\left(x_{j-1/2}\right)\right)\phi_j^m\left(x_{j-1/2}\right).\end{aligned} \tag{6.17}$$

This book belongs to Central Library BADJI Mokhtar-ANNABA UNIVERSITY
Copyright Elsevier 2024

Note that D_1 is constant. As an alternative, one may use an upwind flux. In the above relations, we use $\phi_j^\ell(x_{j+1/2}) = P_\ell(1) = 1$ and $\phi_j^\ell(x_{j-1/2}) = P_\ell(-1) = (-1)^\ell$ to get the resulting discretization matrices, to obtain

$$\left[\phi_j^m c_h(t,x)\right]_{x_{j-1/2}}^{x_{j+1/2}} = A\mathbf{c}_{j-1} - B\mathbf{c}_{j-1} + C\mathbf{c}_{j+1}, \tag{6.18}$$

where

$$\begin{cases} A = \dfrac{1}{2}\begin{pmatrix} 1 & 1 & 1 & 1 \\ 1 & 1 & 1 & 1 \\ 1 & 1 & 1 & 1 \\ 1 & 1 & 1 & 1 \end{pmatrix} - \dfrac{1}{2}\begin{pmatrix} 1 & -1 & 1 & -1 \\ -1 & 1 & -1 & 1 \\ 1 & -1 & 1 & -1 \\ 1 & -1 & 1 & -1 \end{pmatrix}, \\ B = \dfrac{1}{2}\begin{pmatrix} 1 & 1 & 1 & 1 \\ -1 & -1 & -1 & -1 \\ 1 & 1 & 1 & 1 \\ -1 & -1 & -1 & -1 \end{pmatrix}, \quad C = \dfrac{1}{2}\begin{pmatrix} 1 & -1 & 1 & -1 \\ 1 & -1 & 1 & -1 \\ 1 & -1 & 1 & -1 \\ 1 & -1 & 1 & -1 \end{pmatrix}. \end{cases}$$

Furthermore, we use the convention

$$\mathbf{c}_j(t) = \left[c_j^0(t)\ldots c_j^k(t)\right]^T, \quad \text{and } \mathbf{q}_j(t) = \left[q_j^0(t)\ldots q_j^k(t)\right]^T,$$

which are the vectors with degrees of freedom on element e_j. The procedure is similar for the q-term. The right-hand side is given by

$$\int_{e_j} \alpha\phi_j^m m dx = \alpha\frac{\Delta x_j}{2}\int_{-1}^{1} m\left(t, x_j + \frac{\Delta x_j r}{2}\right)P_m(r)dr = \alpha\frac{\Delta x_j}{2}m(t,x_j)\int_{-1}^{1} P_m(r)dr. \tag{6.19}$$

Here we used that $m(t, x)$ is constant over the element e_j. This implies that

$$f_j(t) = \frac{\Delta x_j}{2}\alpha m(t,x_j)\begin{pmatrix} 2 \\ 0 \\ 0 \\ 0 \end{pmatrix}.$$

Now we have all the ingredients to set up the following system of ordinary differential equations to be integrated over time:

$$\begin{aligned} M\frac{d\mathbf{c}_j(t)}{dt} &= D_1(A-S)\mathbf{q}_j - D_1 B\mathbf{q}_{j+1} - \lambda M\mathbf{c}_j + \mathbf{f}_j, \\ M\mathbf{q}_j &= (A-S)\mathbf{c}_j - B\mathbf{c}_{j-1} + C\mathbf{c}_{j+1}. \end{aligned} \tag{6.20}$$

The above system is integrated using a third-order total variation diminishing (TVD) Runge−Kutta method Gottlieb and Shu (1998). For a semidiscrete scheme, given by

$$\frac{du}{dt} = L(u),$$

This book belongs to Central Library BADJI Mokhtar-ANNABA UNIVERSITY
Copyright Elsevier 2024

this gives

$$
\begin{aligned}
u^{(1)} &= u^n + \Delta t L(u^n),\\
u^{(2)} &= \frac{3}{4}u^n + \frac{1}{4}u^{(1)} + \frac{1}{4}\Delta t L\big(u^{(1)}\big),\\
u^{n+1} &= \frac{1}{3}u^n + \frac{2}{3}u^{(2)} + \frac{2}{3}\Delta t L\big(u^{(2)}\big).
\end{aligned}
\tag{6.21}
$$

The discretization in space using DG has the advantage that it is able to handle complicated geometries and arbitrary triangulations. Using a TVD scheme, such as RK3-TVD, has the advantage that it can compute approximations, which are either smooth or have weak shocks and other discontinuities, without any further modification. Hence, discontinuities may become smeared in future time steps; however, eventually, they will not become oscillatory. If, however, the discontinuities are too strong, then oscillations and even nonlinear instability can occur. To avoid both these nuisances, a slope limiter, such as the minmod limiter, can be applied.

6.4.1.2 The Tips Equation

Subsequently, we deal with the one-dimensional chemotaxis−diffusion−reaction equation, given by

$$
\frac{\partial u}{\partial t} + \chi_1 \frac{\partial}{\partial x}(uq) - D_2 \frac{\partial w}{\partial x} = uF(c,\rho) + \alpha_0 \rho c,
\tag{6.22}
$$

where two of the reactive terms have been simplified to a single function $F(c, \rho)$. Further, $q + \frac{\partial c}{\partial x} = 0$ and

$$
w + \frac{\partial u}{\partial x} = 0.
$$

Multiplication of the equations by test function ϕ_j and integrating (by parts) over element e_j gives

$$
\begin{aligned}
&\int_{e_j} \phi_j \frac{\partial u}{\partial t} dx + \int_{e_j} \chi_1 uq \frac{d\phi_j}{dx} dx - \int_{e_j} D_2 w \frac{d\phi_j}{dx} dx - \big[\chi_1 uq\phi_j\big]_{x_{j-\frac{1}{2}}}^{x_{j+\frac{1}{2}}} + \big[D_2 w\phi_j\big]_{x_{j-\frac{1}{2}}}^{x_{j+\frac{1}{2}}} = \int_{e_j} \big(\phi_j uF(c,\rho) + \alpha_0 \rho c\big) dx,\\
&\int_{e_j} w\phi_j dx - \int_{e_j} u \frac{d\phi_j}{dx} dx - \big[\phi_j u\big]_{x_{j-\frac{1}{2}}}^{x_{j+\frac{1}{2}}} = 0.
\end{aligned}
\tag{6.23}
$$

Subsequently, as in the previous subsection, we write the solution u in terms of the basis functions, that is, as

$$
u(t,x) \approx u_h(t,x) = \sum_{\ell=0}^{k} u_j^{\ell}(t)\phi_j^{\ell}(x), \quad w(t,x) \approx w_h(t,x) = \sum_{\ell=0}^{k} w_j^{\ell}(t)\phi_j^{\ell}(x),
$$

over element e_j and we set $\phi_j = \phi_j^m$, for $m = 0,\ldots,k$, to obtain

$$
\begin{aligned}
&\sum_{\ell=0}^{k} \frac{du_j^{\ell}(t)}{dt} \int_{e_j} \phi_j^m \phi_j^{\ell} dx + \sum_{\ell=0}^{k} u_j^{\ell}(t) \int_{e_j} \chi q \phi_j^{\ell} \frac{d\phi_j^m}{dx} dx - \sum_{\ell=0}^{k} w_j^{\ell}(t) \int_{e_j} D_2 \frac{d\phi_j^m}{dx} \phi_j^{\ell} dx - \Big[\chi (qu)^* \phi_j^m\Big]_{x_{j-\frac{1}{2}}}^{x_{j+\frac{1}{2}}}\\
&+ \Big[D_2 w^* \phi_j^m\Big]_{x_{j-\frac{1}{2}}}^{x_{j+\frac{1}{2}}} = \sum_{\ell=0}^{k} u_j^{\ell}(t) \int_{e_j} \phi_j^m \phi_j^{\ell} F(c,\rho) dx + \int_{e_j} \alpha_0 \rho c dx,\\
&\sum_{\ell=0}^{k} w_j^{\ell}(t) \int_{e_j} \phi_j^m \phi_j^{\ell} dx - \sum_{\ell=0}^{k} u_j^{\ell}(t) \int_{e_j} \frac{d\phi_j^m}{dx} \phi_j^{\ell} dx + \sum_{\ell=0}^{k} u_j^{\ell}(t) \Big[\phi_j^m \phi_j^{\ell}\Big]_{x_{j-\frac{1}{2}}}^{x_{j+\frac{1}{2}}} = 0.
\end{aligned}
\tag{6.24}
$$

This book belongs to Central Library BADJI Mokhtar-ANNABA UNIVERSITY
Copyright Elsevier 2024

All terms in the above equations are dealt with analogously to the treatment in the previous subsection. Except for the boundary terms, which are treated using the local Lax−Friedrich flux (which is a central flux with an additional stabilization term), this gives

$$\begin{aligned}
\left[w^*\phi_j^m\right]_{x_{j-\frac{1}{2}}}^{x_{j+\frac{1}{2}}} &= \frac{1}{2}\sum_{\ell=0}^{k}\left(w_j^\ell(t)\phi_j^\ell\left(x_{j+\frac{1}{2}}\right) + w_{j+1}^\ell(t)\phi_{j+1}^\ell\left(x_{j+\frac{1}{2}}\right)\right)\phi_j^m\left(x_{j+\frac{1}{2}}\right)\\
&\quad -\frac{1}{2}\sum_{\ell=0}^{k}\left(w_j^\ell(t)\phi_j^\ell\left(x_{j-\frac{1}{2}}\right) + w_{j-1}^\ell(t)\phi_{j-1}^\ell\left(x_{j-\frac{1}{2}}\right)\right)\phi_j^m\left(x_{j-\frac{1}{2}}\right),\\
\left[(uq)^*\phi_j^m\right]_{x_{j-\frac{1}{2}}}^{x_{j+\frac{1}{2}}} &= \frac{1}{2}\sum_{\ell=0}^{k}\left(u_j^\ell(t)\phi_j^\ell\left(x_{j+\frac{1}{2}}\right) + u_{j+1}^\ell(t)\phi_{j+1}^\ell\left(x_{j+\frac{1}{2}}\right)\right)q\left(t,x_{j+\frac{1}{2}}\right)\phi_j^m\left(x_{j+\frac{1}{2}}\right)\\
&\quad -\frac{1}{2}\sum_{\ell=0}^{k}\left(u_j^\ell(t)\phi_j^\ell\left(x_{j-\frac{1}{2}}\right) + u_{j-1}^\ell(t)\phi_{j-1}^\ell\left(x_{j-\frac{1}{2}}\right)\right)q\left(t,x_{j-\frac{1}{2}}\right)\phi_j^m\left(x_{j-\frac{1}{2}}\right) - \left[\frac{z}{2}[[u]]\right]_{x_{j-\frac{1}{2}}}^{x_{j+\frac{1}{2}}},\\
\left[u^*\phi_j^m\right]_{x_{j-\frac{1}{2}}}^{x_{j+\frac{1}{2}}} &= \frac{1}{2}\sum_{\ell=0}^{k}\left(u_j^\ell(t)\phi_j^\ell\left(x_{j+\frac{1}{2}}\right) + u_{j+1}^\ell(t)\phi_{j+1}^\ell\left(x_{j+\frac{1}{2}}\right)\right)\phi_j^m\left(x_{j+\frac{1}{2}}\right)\\
&\quad -\frac{1}{2}\sum_{\ell=0}^{k}\left(u_j^\ell(t)\phi_j^\ell\left(x_{j-\frac{1}{2}}\right) + u_{j-1}^\ell(t)\phi_{j-1}^\ell\left(x_{j-\frac{1}{2}}\right)\right)\phi_j^m\left(x_{j-\frac{1}{2}}\right),
\end{aligned} \tag{6.25}$$

where

$$\begin{aligned}
\left[\left[u\left(t,x_{j+\frac{1}{2}}\right)\right]\right] &= u_j\left(t,x_{j+\frac{1}{2}}\right) - u_{j+1}\left(t,x_{j+\frac{1}{2}}\right),\\
\left[\left[u\left(t,x_{j-\frac{1}{2}}\right)\right]\right] &= u_j\left(t,x_{j-\frac{1}{2}}\right) - u_{j-1}\left(t,x_{j-\frac{1}{2}}\right),\\
z\left(x_{j-\frac{1}{2}}\right) &= \max\left\{\left|q_j\left(t,x_{j-\frac{1}{2}}\right)\phi_j^m\left(x_{j-\frac{1}{2}}\right)\right|, \left|q_{j-1}\left(t,x_{j-\frac{1}{2}}\right)\phi_{j-1}^m\left(x_{j-\frac{1}{2}}\right)\right|\right\},\\
z\left(x_{j+\frac{1}{2}}\right) &= \max\left\{\left|q_j\left(t,x_{j+\frac{1}{2}}\right)\phi_j^m\left(x_{j+\frac{1}{2}}\right)\right|, \left|q_{j+1}\left(t,x_{j+\frac{1}{2}}\right)\phi_{j+1}^m\left(x_{j+\frac{1}{2}}\right)\right|\right\}.
\end{aligned} \tag{6.26}$$

Substituting $r = \frac{2(x-x_j)}{\Delta x_j}$, and using the Legendre polynomials with Gauss−Legendre quadrature, we introduce

$$\begin{aligned}
V_{1j,ml} &= \sum_{i=1}^{6}\chi q\left(t,x_j+\frac{\Delta x_j}{2}r_i\right)P_l(r_i)\frac{dP_m(r)}{dt}w_i,\\
V_{2j,ml} &= \sum_{i=1}^{6}\frac{\Delta x_j}{2}P_l(r_i)P_m(r_i)F\quad c\left(t,x_j+\frac{\Delta x_j}{2}r_i\right),\rho\left(t,x_j+\frac{\Delta x_j}{2}r_i\right)\Bigg)w_i,\\
V_{3j,m} &= \sum_{i=1}^{6}\frac{\Delta x_j}{2}\alpha_0\rho\left(t,x_j+\frac{\Delta x_j}{2}r_i\right)c\left(t,x_j+\frac{\Delta x_j}{2}r_i\right)P_m(r_i)w_i,\\
\left[\chi(uq)^*\phi_j^m\right]_{x_{j-\frac{1}{2}}}^{x_{j+\frac{1}{2}}} &= (C\mathbf{u}_{j+1}+A_1\mathbf{u}_j)\sum_{\ell=0}^{k}q_j^\ell P_\ell(1) - (A_2\mathbf{u}_j+B\mathbf{u}_{j-1})\sum_{\ell=0}^{k}q_j^\ell P_\ell(-1).
\end{aligned} \tag{6.27}$$

This book belongs to Central Library BADJI Mokhtar-ANNABA UNIVERSITY

Copyright Elsevier 2024

TABLE 6.1 Six Points and Their Weights for the Gauss–Legendre Quadrature

Points	Weights
±0.23861918	0.46791393
±0.66120939	0.36076157
±0.93246951	0.17132449

Here we used the Gauss–Legendre points from Table 6.1.

The numerical approximation for the coefficients using DG for the one-dimensional form can be developed now. Therewith, we get

$$M\frac{d\mathbf{u}_j}{dt} = D_2(A-S)\mathbf{w}_j + \mathbf{q}_j - D_2B\mathbf{w}_{j-1} + D_2C\mathbf{w}_{j+1} + (V_{1j}+V_{2j})\mathbf{u}_j + V_{3j}$$

$$-\chi \quad (C\mathbf{u}_{j+1} + A_1\mathbf{u}_j)\sum_{\ell=0}^{k} q_j^{\ell}(t)P_{\ell}(1) - (A_2\mathbf{u}_j + B\mathbf{u}_{j-1})\sum_{\ell=0}^{k} q_j^{\ell}(t)P_{\ell}(-1)\Bigg), \tag{6.28}$$

$$M\mathbf{w}_j = (A-S)\mathbf{u}_j - B\mathbf{u}_{j-1} + C\mathbf{u}_{j+1}.$$

The above system is, as in the previous section, also integrated over time using the third-order TVD Runge–Kutta method.

6.4.1.3 The Vessel Density

The vessel equation is rewritten using $q = -\frac{\partial c}{\partial x}$, $w = -\frac{\partial u}{\partial x}$ to obtain

$$\begin{aligned} &\frac{\partial \rho}{\partial t} + D_3\frac{\partial v}{\partial x} + \mu_1 w - \chi_1 uq + \gamma\left(\rho - \rho_{\text{eq}}\right) = 0, \\ &v + \frac{\partial \rho}{\partial x} = 0. \end{aligned} \tag{6.29}$$

The above equation is subject to initial and boundary conditions

$$\rho(0,x) = \begin{cases} 0, & x \in \Omega_w, \\ \rho_{\text{eq}}, & x \in \Omega \setminus \Omega_w, \end{cases} \tag{6.30}$$

$$v(t,0) = 0, \quad \rho(t,1) = \rho_{\text{eq}}.$$

The numerical solution is determined by

$$\rho(t,x) \approx \rho_h(t,x) = \sum_{\ell=0}^{k} \rho_j^{\ell}(t)\phi_j^{\ell}(x),$$

and

$$v(t,x) \approx v_h(t,x) = \sum_{\ell=0}^{k} v_j^{\ell}(t)\phi_j^{\ell}(x).$$

This book belongs to Central Library BADJI Mokhtar-ANNABA UNIVERSITY

Copyright Elsevier 2024

Using the orthogonal structure of the Legendre polynomials, we determine the initial coefficients in the numerical solution by

$$\rho_j^m(0) = \frac{2m+1}{2}\int_{-1}^{1}\rho\left(0, x_j + \frac{\Delta x}{2}r\right)P_m(r)dr \approx \frac{2m+1}{2}\sum_{i=1}^{6}\rho\left(0, x_j + \frac{\Delta x}{2}r_i\right)P_m(r_i)w_i. \tag{6.31}$$

To determine the weak formulation, we multiply the equations by ϕ_j and integrate over the element e_j. Integration by parts gives

$$\begin{aligned}
&\int_{e_j}\left(\frac{\partial\rho}{\partial t}\phi_j - D_3 v\frac{d\phi_j}{dx} + \mu_1 w\phi_j - \chi_1 uq\phi_j + \gamma\left(\rho - \rho_{\mathrm{eq}}\right)\phi_j\right)dx + \left[D_3 v\phi_j\right]_{x_{j-\frac{1}{2}}}^{x_{j+\frac{1}{2}}} = 0,\\
&\int_{e_j}\left(v\phi_j - \rho\frac{d\phi_j}{dx}\right)dx + \left[\rho\phi_j\right]_{x_{j-\frac{1}{2}}}^{x_{j+\frac{1}{2}}} = 0.
\end{aligned} \tag{6.32}$$

Substitution of $\rho(t,x) \approx \rho_h(t,x) = \sum_{\ell=0}^{k}\rho_j^l(t)\phi_j^\ell(x)$ and $v(t,x) \approx v_h(t,x) = \sum_{\ell=0}^{k}v_j^\ell(t)\phi_j^\ell(x)$ and $\phi_j = \phi_j^m$ gives the following Galerkin equations:

$$\begin{aligned}
&\sum_{\ell=0}^{k}\frac{d\rho_j^\ell(t)}{dt}\int_{e_j}\phi_j^m\phi_j^\ell dx - D_3\sum_{\ell=0}^{k}v_j^\ell(t)\int_{e_j}\frac{d\phi_j^m}{dx}\phi_j^\ell dx + \left[D_3 v^*\phi_j^m\right]_{x_{j-\frac{1}{2}}}^{x_{j+\frac{1}{2}}} + \gamma\sum_{l=0}^{k}\rho_j^l(t)\int_{e_j}\phi_j^m\phi_j^l dx = \int_{e_j}\left(\chi_1 uq - \mu_1 w + \gamma\rho_{\mathrm{eq}}\right)\phi_j^m dx,\\
&\sum_{\ell=0}^{k}u_j^\ell(t)\int_{e_j}\phi_j^m\phi_j^\ell dx - \sum_{\ell=0}^{k}\rho_j^\ell(t)\int_{e_j}\frac{\partial\phi_j^m}{dx}\phi_j^\ell dx + \left[\rho^*\phi_j^m\right]_{x_{j-\frac{1}{2}}}^{x_{j+\frac{1}{2}}} = 0.
\end{aligned} \tag{6.33}$$

Here we use the central fluxes

$$\begin{aligned}
\left[v^*\phi_j^m\right]_{x_{j-\frac{1}{2}}}^{x_{j+\frac{1}{2}}} &= \frac{1}{2}\quad\sum_{\ell=0}^{k}u_j^\ell(t)\phi_j^\ell\left(x_{j+\frac{1}{2}}\right) + u_{j+1}^\ell(t)\phi_{j+1}^\ell\left(x_{j+\frac{1}{2}}\right)\Bigg)\phi_j^m\left(x_{j+\frac{1}{2}}\right)\\
&\quad -\frac{1}{2}\quad\sum_{\ell=0}^{k}u_j^\ell(t)\phi_j^\ell\left(x_{j-\frac{1}{2}}\right) + u_{j-1}^\ell(t)\phi_{j-1}^\ell\left(x_{j-\frac{1}{2}}\right)\Bigg)\phi_j^m\left(x_{j-\frac{1}{2}}\right),\\
\left[\rho^*\phi_j^m\right]_{x_{j-\frac{1}{2}}}^{x_{j+\frac{1}{2}}} &= \frac{1}{2}\quad\sum_{\ell=0}^{k}\rho_j^\ell(t)\phi_j^\ell\left(x_{j+\frac{1}{2}}\right) + \rho_{j+1}^\ell(t)\phi_{j+1}^\ell\left(x_{j+\frac{1}{2}}\right)\Bigg)\phi_j^m\left(x_{j+\frac{1}{2}}\right)\\
&\quad -\frac{1}{2}\quad\sum_{\ell=0}^{k}\rho_j^\ell(t)\phi_j^\ell\left(x_{j-\frac{1}{2}}\right) + \rho_{j-1}^\ell(t)\phi_{j-1}^\ell\left(x_{j-\frac{1}{2}}\right)\Bigg)\phi_j^m\left(x_{j-\frac{1}{2}}\right).
\end{aligned} \tag{6.34}$$

Substituting $r = \frac{2(x-x_j)}{\Delta x_j}$, using Legendre polynomials and using Gauss−Legendre quadrature, we arrive at

$$\begin{aligned}
\mathbf{g}_{1j,m} &= \frac{\Delta x_j}{2}\int_{-1}^{1}\gamma\rho_{\mathrm{eq}}P_m(r)dr \Rightarrow \mathbf{g}_{1j} = \frac{\Delta x_j}{2}\gamma\rho_{\mathrm{eq}}\left[2\quad 0\quad 0\quad 0\right]^T,\\
\mathbf{g}_{2j,m} &= \mu_1\frac{\Delta x_j}{2}\sum_{i=1}^{6}w\left(t, x_j + \frac{\Delta x_j}{2}r_i\right)P_m(r_i)w_i,\\
\mathbf{g}_{3j,m} &= \chi_1\frac{\Delta x_j}{2}\sum_{i=1}^{6}u\left(t, x_j + \frac{\Delta x_j}{2}r_i\right)q\left(t, x_j + \frac{\Delta x_j}{2}r_i\right)P_m(r_i)w_i.
\end{aligned} \tag{6.35}$$

This book belongs to Central Library BADJI Mokhtar-ANNABA UNIVERSITY
Copyright Elsevier 2024

Here j represents the element number. Further four Legendre polynomials are used, hence up to third order, and the weights from Table 6.1 are used, such that

$$\mathbf{g}_j = \mathbf{g}_{1j} + \mathbf{g}_{2j} - \mathbf{g}_{3j}, \tag{6.36}$$

which is substituted to get the system of ordinary differential equations that is integrated over time. The system reads as

$$\begin{aligned} M\frac{d\rho_j}{dt} &= D_3(A-S)\mathbf{u}_j - D_3B\mathbf{u}_{j-1} + D_3C\mathbf{u}_{j+1} - \gamma M\rho_j + \mathbf{g}_j, \\ M\mathbf{u}_j &= (A-S)\rho_j - B\rho_{j-1} + C\rho_{j+1}. \end{aligned} \tag{6.37}$$

The above system is also integrated using the third-order TVD Runge−Kutta time integration scheme.

6.4.2 Extension to Two Spatial Dimensions

We extended the formalism and method to circular symmetry so that the problem remains quasi one-dimensional with respect to space. We refer to the MSc thesis written by Crapts for the results. In this section, the genuine 2D case for rectangular geometry is presented. This gives the freedom to deal with various geometries of the damage. The rectangular domain has been partitioned into rectangular elements, where we use N and M elements in the x and y directions. The elements are denoted by e_{ij}, with dimensions $\Delta x \Delta y$, and Legendre polynomials up to order k per coordinate direction are used as basis functions on each element. This implies that per element we have $(k+1)\times(k+1)$ polynomials and unknowns. Let P_j be the jth order Legendre polynomial, then for each element the following set of basis functions is used:

$$\mathbb{P}^k = \{P_pP_q : (p,q) \in \{0,\ldots,k\} \times \{0,\ldots,k\}\}. \tag{6.38}$$

To solve the equations by the 2D DG method, we will start reducing the order of spatial derivatives to one again as in the 1D case.

6.4.2.1 The Concentration Equation

The equation for the 2D concentration is rewritten by

$$\begin{aligned} &\frac{\partial c}{\partial t} + D_1\nabla\cdot\mathbf{q} + \lambda c = \alpha m, \\ &\mathbf{q} + \nabla c = 0. \end{aligned} \tag{6.39}$$

The solution vector $\mathbf{q}$ is written as $\mathbf{q} = [q_1\ q_2]^T$ is terms of its components. First the weak form is derived by multiplication by a test function ϕ_{ij}, integration over element e_{ij}, and subsequent integration by parts. One arrives at

$$\begin{aligned} &\int_{e_{ij}} \phi_{ij}\frac{\partial c}{\partial t} - D_1\mathbf{q}\cdot\nabla\phi_{ij} + \lambda\phi_{ij}c\,d\Omega + \int_{\partial e_{ij}} D_1\phi_{ij}\mathbf{q}\cdot n\,d\Gamma = \int_{e_{ij}} \alpha\phi_{ij}m\,d\Omega, \\ &\int_{e_{ij}} \phi_{ij}q_1 - c\frac{\partial\phi_{ij}}{\partial x}d\Omega + \int_{\partial e_{ij}} c\phi_{ij}n_1\,d\Gamma = 0, \\ &\int_{e_{ij}} \phi_{ij}q_2 - c\frac{\partial\phi_{ij}}{\partial y}d\Omega + \int_{\partial e_{ij}} c\phi_{ij}n_2\,d\Gamma = 0, \end{aligned} \tag{6.40}$$

where n_1 and n_2, respectively, denote the x and y components of the outward pointing unit normal vector. Note that we wrote the weak form per component. The test function is written as $\phi_{ij}(x,y) = \phi_i^{(m_x)}(x)\phi_j^{(m_y)}(y)$ and the solution is approximated by

$$c(t,x,y) \approx c_h(t,x,y) = \sum_{\ell_x=0}^{k}\sum_{\ell_y=0}^{k} c_{ij}^{(\ell_x,\ell_y)}(t)\phi_i^{(\ell_x)}(x)\phi_i^{(\ell_y)}(y).$$

This book belongs to Central Library BADJI Mokhtar-ANNABA UNIVERSITY
Copyright Elsevier 2024

From the initial condition, we have $c_{ij}^{(\ell_x,\ell_y)} = 0$. Substitution of the test function and numerical solution gives the following Galerkin equations over element e_{ij}:

$$\begin{aligned}
&\sum_{\ell_x=0}^{k}\sum_{\ell_y=0}^{k}\frac{dc_{ij}^{(\ell_x,\ell_y)}}{dt}\int_{e_{ij}}\phi_i^{(\ell_x)}\phi_j^{(\ell_y)}\phi_i^{(m_x)}\phi_i^{(m_y)}d\Omega + D_1\sum_{\ell_x=0}^{k}\sum_{\ell_y=0}^{k}q_{1_{ij}}^{(\ell_x,\ell_y)}\int_{e_{ij}}\phi_i^{(\ell_x)}\phi_j^{(\ell_y)}\frac{d\phi_i^{(m_x)}}{dx}\phi_i^{(m_y)}d\Omega \\
&\quad + D_1\sum_{\ell_x=0}^{k}\sum_{\ell_y=0}^{k}q_{2_{ij}}^{(\ell_x,\ell_y)}\int_{e_{ij}}\phi_i^{(l_x)}\phi_j^{(l_y)}\phi_i^{(m_x)}\frac{d\phi_i^{(m_y)}}{dy}d\Omega + \sum_{\ell_x=0}^{k}\sum_{\ell_y=0}^{k}\lambda c_{ij}^{(\ell_x,\ell_y)}\int_{e_{ij}}\phi_i^{(\ell_x)}\phi_j^{(\ell_y)}\phi_i^{(m_x)}\phi_i^{(m_y)}d\Omega \\
&\quad - \int_{\partial e_{ij}} D_1\left(q_1^* n_x + q_2^* n_y\right)\phi_i^{(m_x)}\phi_j^{(m_y)}d\Gamma = \alpha\int_{e_{ij}} m(t,x,y)\phi_i^{(m_x)}\phi_j^{(m_y)}d\Omega, \\
&\sum_{\ell_x=0}^{k}\sum_{\ell_y=0}^{k}q_{1_{ij}}^{(\ell_x,\ell_y)}\int_{e_{ij}}\phi_i^{(\ell_x)}\phi_j^{(\ell_y)}\phi_i^{(m_x)}\phi_i^{(m_y)}d\Omega \\
&\quad - \sum_{\ell_x=0}^{k}\sum_{\ell_y=0}^{k}c_{ij}^{(\ell_x,\ell_y)}\int_{e_{ij}}\phi_i^{(\ell_x)}\phi_j^{(\ell_y)}\frac{d\phi_i^{(m_x)}}{dx}\phi_i^{(m_y)}d\Omega + \int_{\partial e_{ij}} c^* n_x\phi_i^{(m_x)}\phi_j^{(m_y)}d\Gamma = 0, \\
&\sum_{\ell_x=0}^{k}\sum_{\ell_y=0}^{k}q_{2_{ij}}^{(\ell_x,\ell_y)}\int_{e_{ij}}\phi_i^{(\ell_x)}\phi_j^{(\ell_y)}\phi_i^{(m_x)}\phi_i^{(m_y)}d\Omega \\
&\quad - \sum_{\ell_x=0}^{k}\sum_{\ell_y=0}^{k}c_{ij}^{(\ell_x,\ell_y)}\int_{e_{ij}}\phi_i^{(\ell_x)}\phi_j^{(\ell_y)}\phi_i^{(m_x)}\frac{d\phi_j^{(m_y)}}{dy}d\Omega + \int_{\partial e_{ij}} c^* n_y\phi_i^{(m_x)}\phi_j^{(m_y)}d\Gamma = 0, \\
&(m_x, m_y)\in\{0,\ldots,l\}\times\{0,\ldots,k\}.
\end{aligned} \tag{6.41}$$

Here we use the central flux in the both the x and y directions. For the test functions, we use Legendre polynomials and we use the dimensionless coordinates $r = \frac{2(x-x_i)}{\Delta x}$ and $s = \frac{2(y-y_i)}{\Delta y}$ and transformed functions $\phi_i^{(\ell_x)}\left(x_i + \frac{\Delta x}{2}r\right) = P_{\ell_x}(r)$ and $\phi_j^{(\ell_y)}\left(y_j + \frac{\Delta y}{2}s\right) = P_{\ell_y}(s)$. Substitution, integration, and using the orthogonality relations give

$$\begin{aligned}
M_{m\ell} &= \frac{\Delta x}{2}\frac{\Delta y}{2}\int_{-1}^{1}\int_{-1}^{1}P_{\ell_x}P_{\ell_y}P_{m_x}P_{m_y}drds = \frac{\Delta x\Delta y}{(2\ell_x+1)(2\ell_y+1)}\delta_{m_x,\ell_x}\delta_{m_y,\ell_y}, \\
S_{\mathbf{x},m\ell} &= \frac{\Delta y}{2}\int_{-1}^{1}\int_{-1}^{1}P_{\ell_x}P_{\ell_y}\frac{dP_{m_x}}{dr}P_{m_y}drds = \frac{\Delta y}{2\ell_y+1}\delta_{m_y,\ell_y}\int_{-1}^{1}P_{\ell_x}\frac{dP_{m_x}}{dr}dr, \\
S_{\mathbf{y},m\ell} &= \frac{\Delta x}{2}\int_{-1}^{1}\int_{-1}^{1}P_{\ell_x}P_{\ell_y}P_{m_x}\frac{dP_{m_y}}{ds}drds = \frac{\Delta y}{2\ell_y+1}\delta_{m_y,\ell_y}\int_{-1}^{1}P_{\ell_x}\frac{dP_{m_x}}{ds}ds
\end{aligned} \tag{6.42}$$

This book belongs to Central Library BADJI Mokhtar-ANNABA UNIVERSITY
Copyright Elsevier 2024

Because we use $k = 2$, we get

$$S_{\mathbf{x}} = \begin{pmatrix} 0 & 0 & 0 & 0 & 0 & 0 & 0 & 0 & 0 \\ 2 & 0 & 2 & 0 & 0 & 2 & 0 & 0 & 0 \\ 0 & 0 & 0 & 0 & 0 & 0 & 0 & 0 & 0 \\ 2 & 0 & 2 & 0 & 0 & 2 & 0 & 0 & 0 \\ 0 & 2 & 0 & 2 & 0 & 0 & 0 & 2 & 0 \\ 0 & 0 & 0 & 0 & 0 & 0 & 0 & 0 & 0 \\ 0 & 2 & 0 & 2 & 0 & 0 & 0 & 2 & 0 \\ 2 & 0 & 2 & 0 & 0 & 2 & 0 & 0 & 0 \\ 0 & 2 & 0 & 2 & 0 & 0 & 0 & 2 & 0 \end{pmatrix}, \quad S_{\mathbf{y}} = \begin{pmatrix} 0 & 0 & 0 & 0 & 0 & 0 & 0 & 0 & 0 \\ 0 & 0 & 0 & 0 & 0 & 0 & 0 & 0 & 0 \\ 2 & 2 & 0 & 0 & 2 & 0 & 0 & 0 & 0 \\ 2 & 2 & 0 & 0 & 2 & 0 & 0 & 0 & 0 \\ 0 & 0 & 0 & 0 & 0 & 0 & 0 & 0 & 0 \\ 0 & 0 & 2 & 2 & 0 & 0 & 2 & 0 & 0 \\ 2 & 2 & 0 & 0 & 2 & 0 & 0 & 2 & 0 \\ 0 & 0 & 2 & 2 & 0 & 0 & 2 & 0 & 0 \\ 0 & 2 & 2 & 2 & 0 & 0 & 2 & 0 & 0 \end{pmatrix} \tag{6.43}$$

The right-hand side becomes

$$\mathbf{f}_{ij} = \frac{\Delta x}{2}\frac{\Delta y}{2}\alpha m(t, x_i, y_j)\cdot[40\ldots0]^T. \tag{6.44}$$

Subsequently, we consider the flux terms. As an example, we write out the "c-term":

$$\int_{\partial e_{ij}} c^* n_x \phi_i^{(m_x)} \phi_i^{(m_y)} d\Gamma = \frac{\Delta y}{2(2l_y+1)} \sum_{\ell_x=0}^{k} \sum_{\ell_y=0}^{k} \left\{ c_{ij}^{(\ell_x,\ell_y)} + (-1)^{\ell_x} c_{i+1,j}^{(\ell_x,\ell_y)} - (-1)^{\ell_x}(-1)^{m_x} c_{ij}^{(\ell_x,\ell_y)} - (-1)^{m_x} c_{i-1,j}^{(\ell_x,\ell_y)} \right\}. \tag{6.45}$$

Analogously to the 1D case, we can assemble all the equations into a matrix-vector format. The resulting system of ordinary differential equations is integrated over time using the third-order TVD Runge−Kutta integration method. More details have been given in Crapts (2012).

6.4.2.2 The Tips Equation

Reducing the order of the spatial derivatives using $\mathbf{w} = -\nabla u$ gives

$$\begin{aligned} \frac{\partial u}{\partial t} + \chi_1 \nabla\cdot(u\mathbf{q}) - D_2 \nabla\cdot\mathbf{w} &= uF(c,\rho) + \alpha_0 \rho c, \\ \mathbf{w} + \nabla u &= 0. \end{aligned} \tag{6.46}$$

The weak form has been derived several before, and, also for the 1D case of the equation, this has already been presented in this manuscript. Therefore, we omit the weak form here. The most important issue is the way the flux equation as an integration over the boundary of an element is treated. This gives the coupling between adjacent elements. The hyperbolic nature as a result of the chemotaxis term necessitates us to use a central flux with an additional stabilization term, so that we get

$$\begin{aligned} \int_{\partial e_{ij}} u^* q_1 \phi_i^{(m_x)} \phi_j^{(m_y)} n_x d\Gamma &= \int_{y_{j-\frac{1}{2}}}^{y_{j+\frac{1}{2}}} \left[u^* q_1 \phi_i^{(m_x)} \phi_j^{(m_y)} \right]_{x_{i-\frac{1}{2}}}^{x_{i+\frac{1}{2}}} d\Gamma \\ &= \int_{y_{j-\frac{1}{2}}}^{y_{j+\frac{1}{2}}} u\left(t, x_{i+\frac{1}{2}}, y\right) q_1\left(t, x_{i+\frac{1}{2}}, y\right) \phi_i^{(m_x)}\left(x_{i+\frac{1}{2}}\right) \phi_j^{(m_y)}(y) - u\left(t, x_{i-\frac{1}{2}}, y\right) q_1\left(t, x_{i-\frac{1}{2}}, y\right) \phi_i^{(m_x)}\left(x_{i-\frac{1}{2}}\right) \phi_j^{(m_y)}(y) \\ &\quad - \frac{z_x\left(x_{i+\frac{1}{2}}\right)}{2} \left[\left[u\left(t, x_{i+\frac{1}{2}}, y_j\right)\right]\right] \phi_j^{(m_y)}(y) - \frac{z_x\left(x_{i-\frac{1}{2}}\right)}{2} \left[\left[u\left(t, x_{i-\frac{1}{2}}, y_j\right)\right]\right] \phi_j^{(m_y)}(y) dy, \end{aligned} \tag{6.47}$$

where the integrals are expressed by means of the Gauss−Legendre quadrature and

$$\begin{aligned} z_x\left(x_{i+\frac{1}{2}}\right) &= \max\left\{ \left| \mathbf{q}_{1,ij}\left(t, x_{i+\frac{1}{2}}, y_j\right) \phi_i^{(m_x)}\left(x_{i+\frac{1}{2}}\right) \right|, \left| \mathbf{q}_{1,i+1,j}\left(t, x_{i+\frac{1}{2}}, y_j\right) \phi_{i+1}^{(m_x)}\left(x_{i+\frac{1}{2}}\right) \right| \right\}, \\ z_x\left(x_{i-\frac{1}{2}}\right) &= \max\left\{ \left| \mathbf{q}_{1,ij}\left(t, x_{i-\frac{1}{2}}, y_j\right) \phi_i^{(m_x)}\left(x_{i-\frac{1}{2}}\right) \right|, \left| \mathbf{q}_{1,i-1,j}\left(t, x_{i-\frac{1}{2}}, y_j\right) \phi_{i-1}^{(m_x)}\left(x_{i-\frac{1}{2}}\right) \right| \right\}. \end{aligned} \tag{6.48}$$

This book belongs to Central Library BADJI Mokhtar-ANNABA UNIVERSITY
Copyright Elsevier 2024

For the jumps over the element faces, we have

$$\begin{aligned}\left[\left[n\left(t,x_{i-\frac{1}{2}},y\right)\right]\right] &= n_{ij}\left(t,x_{i-\frac{1}{2}},y\right)-n_{i-1,j}\left(t,x_{i-\frac{1}{2}},y\right),\\ \left[\left[n\left(t,x_{i+\frac{1}{2}},y\right)\right]\right] &= n_{i+1,j}\left(t,x_{i+\frac{1}{2}},y\right)-n_{i,j}\left(t,x_{i+\frac{1}{2}},y\right).\end{aligned} \tag{6.49}$$

The y direction is treated analogously. The discretization matrices V_1, V_2, and V_3 are determined similarly to the 1D case. Here Gauss−Legendre quadrature is used per direction. The finally resulting system of ordinary differential equations is integrated over time using the third-order TVD Runge−Kutta method.

6.4.2.3 The Vessels Equation

Reduction of the order of spatial derivatives and using $\mathbf{v}=-\nabla p$ gives

$$\begin{aligned}&\frac{\partial\rho}{\partial t}+D_3\nabla\cdot\mathbf{v}+(\mu_1\mathbf{w}-\chi_2 u\mathbf{q})\cdot\frac{\mathbf{x}}{\|\mathbf{x}\|}+\gamma\left(\rho-\rho_{\mathrm{eq}}\right) = 0,\\ &\mathbf{v}+\nabla\rho = 0.\end{aligned} \tag{6.50}$$

The weak form simply follows from multiplication by a test function and subsequent integration by parts. Because this equation differs in the 2D case from the 1D case, we give the weak form

$$\begin{aligned}&\int_{e_{ij}}\phi_{ij}\frac{\partial\rho}{\partial t}-D_3\mathbf{v}\cdot\nabla\phi_{ij}+\gamma\phi_{ij}\left(\rho-\rho_{\mathrm{eq}}\right)+\phi_{ij}(\mu_1\mathbf{w}-\chi_2 u\mathbf{q})\cdot\frac{\mathbf{x}}{\|\mathbf{x}\|}d\Omega+\int_{\partial e_{ij}}D_3\phi_{ij}\mathbf{v}\cdot\mathbf{n}d\Gamma = 0,\\ &\int_{e_{ij}}\phi_{ij}v_1-\rho\frac{\partial\phi_{ij}}{\partial x}d\Omega+\int_{\partial e_{ij}}\phi_{ij}\rho n_x d\Gamma = 0,\\ &\int_{e_{ij}}\phi_{ij}v_2-\rho\frac{\partial\phi_{ij}}{\partial y}d\Omega+\int_{\partial e_{ij}}\phi_{ij}\rho n_y d\Gamma = 0.\end{aligned} \tag{6.51}$$

Most of the terms in the above equations are handled using the procedures that we outlined in the earlier subsections. However, for completeness, we present the term with ρ_{eq} and with the snail trail term, that is

$$\begin{aligned}\mathbf{g}_{1ij,m} &= \frac{\Delta x\Delta y}{4}\int_{-1}^{1}\int_{-1}^{1}\gamma\rho_{\mathrm{eq}}P_{m_x}P_{m_y}drds\Rightarrow\mathbf{g}_{1ij} = \frac{\Delta x\Delta y}{4}\gamma\rho_{\mathrm{eq}}\cdot[40\ldots0]^T,\\ \mathbf{g}_{2ij,m} &= \mu_1\frac{\Delta x\Delta y}{4}\sum_{r=1}^{6}\sum_{s=1}^{6}w_r w_s P_{m_x}(x_r)P_{m_y}(y_r)\mathbf{w}(\mathbf{x}_{rs})\cdot\frac{\mathbf{x}_{rs}}{\|\mathbf{x}_{rs}\|},\\ \mathbf{g}_{3ij,m} &= \chi_2\frac{\Delta x\Delta y}{4}\sum_{r=1}^{6}\sum_{s=1}^{6}w_r w_s P_{m_x}(x_r)P_{m_y}(y_r)u(\mathbf{x}_{rs})\mathbf{q}(\mathbf{x}_{rs})\cdot\frac{\mathbf{x}_{rs}}{\|\mathbf{x}_{rs}\|}.\end{aligned} \tag{6.52}$$

Here Gauss−Legendre quadrature has been applied and w_r and w_s are the weights from Table 6.1. Furthermore, the integration points are given by $\mathbf{x}_{rs}=[x_r\ y_s]^T$ where x_r and y_s, respectively, are the weight points in Gauss−Legendre quadrature from Table 6.1. From this, a system of ordinary differential equations is constructed and integrated over time using a third-order TVD Runge−Kutta scheme. The time integration is schematized in Algorithm 6.1.

This algorithm is based on the third-order Runge−Kutta time integration scheme applied on the ordinary differential equations that result after discretizing using the DG equation. The above algorithm entails the one-dimensional case. The two-dimensional case is dealt with analogously, where additional functions are introduced for the vertical coordinate direction.

This book belongs to Central Library BADJI Mokhtar-ANNABA UNIVERSITY
Copyright Elsevier 2024

ALGORITHM 6.1 Time Integration Algorithm

```
Determine Initial Solution
n = 0; t = 0
while t < t_end do
  for j = 1 to N do
    Compute c_j^(1) using c^n, q^n, u^n, w^n, ρ^n, v^n
    Compute q_j^(1) using c_j^(1)
    Compute u_j^(1) using c^n, q^n, u^n, w^n, ρ^n, v^n
    Compute w_j^(1) using u_j^(1)
    Compute ρ_j^(1) using c^n, q^n, u^n, w^n, ρ^n, v^n
    Compute v_j^(1) using ρ_j^(1)
    Compute c_j^(2) using c^n, q^n, u^n, w^n, ρ^n, v^n, c_j^(1), q_j^(1), u_j^(1), w_j^(1), ρ_j^(1), v_j^(1)
    Compute q_j^(2) using c_j^(2)
    Compute u_j^(2) using c^n, q^n, u^n, w^n, ρ^n, v^n, c_j^(1), q_j^(1), u_j^(1), w_j^(1), ρ_j^(1), v_j^(1)
    Compute w_j^(2) using u_j^(2)
    Compute ρ_j^(2) using c^n, q^n, u^n, w^n, ρ^n, v^n, c_j^(1), q_j^(1), u_j^(1), w_j^(1), ρ_j^(1), v_j^(1)
    Compute v_j^(2) using ρ_j^(2)
    Compute c_j^(n+1) using c^n, q^n, u^n, w^n, ρ^n, v^n, c_j^(2), q_j^(2), u_j^(2), w_j^(2), ρ_j^(2), v_j^(2)
    Compute q_j^(n+1) using c_j^(n+1)
    Compute u_j^(n+1) using c^n, q^n, u^n, w^n, ρ^n, v^n, c_j^(2), q_j^(2), u_j^(2), w_j^(2), ρ_j^(2), v_j^(2)
    Compute w_j^(n+1) using u_j^(n+1)
    Compute ρ_j^(n+1) using c^n, q^n, u^n, w^n, ρ^n, v^n, c_j^(2), q_j^(2), u_j^(2), w_j^(2), ρ_j^(2), v_j^(2)
    Compute v_j^(n+1) using ρ_j^(n+1)
  end for
  n ← n + 1
  t ← t + dt
end while
```

6.5 NUMERICAL RESULTS

We present the results after solving Eqs. (6.3)–(6.5). We use the data from Table 6.2.

We consider a hypothetical region that has been effected by fibrosis, where stem cells have been injected. The model assumes that (some of the) stem cells adhere to the fibrotic heart tissue and takes into account a gradual loss over time due to detachment or cellular death. The stem cells secrete chemokines that trigger the endothelial cells to migrate toward the center of the fibrosis inflicted region. This establishes the blood vessel network. First we present some of the one-dimensional results, aiming at illustrating the solutions from the DG method. Subsequently, we present some two-dimensional results.

6.5.1 One-Dimensional Results

In Fig. 6.1, it can be seen that the solution exhibits discontinuities on the element boundaries, which is characteristic for the DG method. At the initial stages, the tip density increases on the boundary of the damage (being located at around $x = 0.1$). Subsequently, the tip density increases as a result of cell proliferation until it reaches a maximum over time. Then the tip density gradually decreases down to zero as time proceeds because the vessel network is gradually forming closed loops, which means that there are no tips anymore. During the same interval, the tips are closing and the vessel density continues to increase so that the damaged part of the heart gets sufficient amounts of oxygen and endothelial cells, which will make the heart tissue less stiff. Next to these results, the error as a function of the grid resolution is plotted in Fig. 6.2. We did this

This book belongs to Central Library BADJI Mokhtar-ANNABA UNIVERSITY
Copyright Elsevier 2024

TABLE 6.2 Input Data in the Simulations

Quantity	Value	Unit
D_1	1	mm^2/s
D_2	0.001	mm^2/s
D_3	0.01	mm^2/s
λ	1	1/s
α	3	$1/(mm^3\ s)$
α_0	50	$1/(mm^3\ mol\ s)$
α_1	10	$1/(mm^3\ mol\ s)$
β_1	0.5	1/s
β_2	50	mm^3/s
χ_1	0.4	$mm^5/(s\ mol)$
χ_2	0.4	$mm^5/(s\ mol)$
γ	0.25	$mm^5/(s\ mol)$
$\hat{c}$	0.2	mol
ρ_{eq}	0.001	$1/mm^3$
m_0	2	–

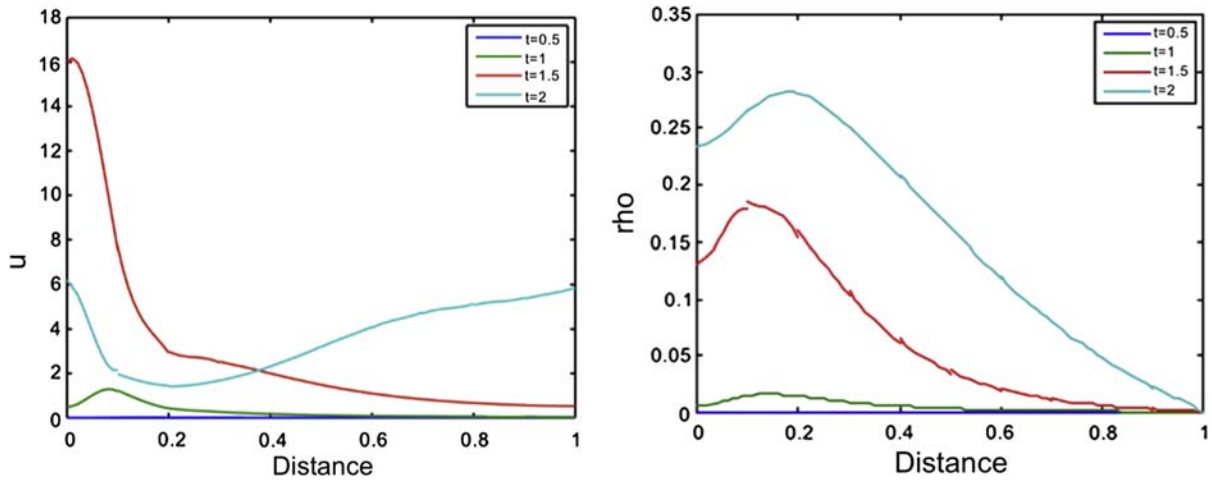

FIGURE 6.1 Top: The tip density u as a function of the distance from the center of the damaged area at various times. Bottom: The vessel density ρ as a function of the distance from the center of the damaged area at various times. The solution was computed using 10 elements and using a DG method with third-order Legendre polynomials $k = 3$ and a time step $\Delta t = 10^{-4}$.

for the advection problem for which we know the exact solution. We determined the order of the method using the L_2-norm, given by

$$\|u_h - u\|^2_{L^2(\Omega)} = \int_\Omega (u_h - u)^2 d\Omega, \tag{6.53}$$

where u_h and u, respectively, represent the DG and exact solution. To compute the norm, Gauss−Legendre quadrature has been used. From the slope in the graph of Fig. 6.2, it follows that $P = 3.9096$, which is only slightly smaller than 4, which is the maximal order of accuracy, given the combination of the time integration and polynomial order of the basis functions.

This book belongs to Central Library BADJI Mokhtar-ANNABA UNIVERSITY Copyright Elsevier 2024

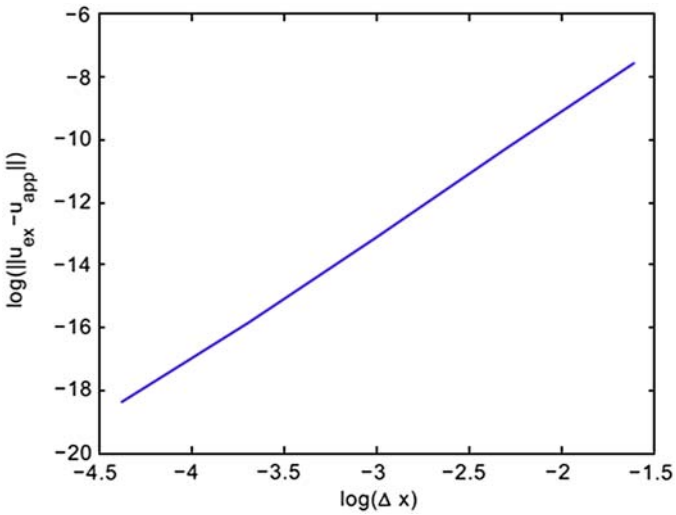

FIGURE 6.2 The error as a function of the element size.

6.5.2 Two-Dimensional Results

Again, we consider the numerical approximation of the solution of Eqs. (6.3)−(6.5) and we use the input data from Table 6.2. For the two-dimensional results, we consider a wound of rectangular geometry. Fig. 6.3 for the tip density shows some interesting minima/maxima. These minima are related to the fact that the wound has a rectangular shape and that the length over which transport from the external boundary takes place changes over the wound edge. Furthermore, after a short time the maxima in the capillary tip density are from the center of the wound to the points of the boundary of the wound on the x- and y-axes. The minima on the wound edge are located on the $y = \pm x$ rays. We see the same phenomenon for the vessel density in Fig. 6.3. From the simulations of Section 6.4.1, we know that the vessel density starts to increase on the boundary of the wound beacuse that is the first location where the attractant vessels and the tips meet. For a rectangular wound this means that the attractant meets vessels and tips at the corner points after meeting of the attractant with the vessels and tips at the other points of the boundary. This occurs due to the fact that the distance from the center to a corner is longer than any other distance from the center to a point on the boundary of the wound. This means that the vessel density on the corner points has increased less than at other points on the boundary after the short time $t = 0.5$. This gives the four minima for the vessel density that are shown in Fig. 6.3. Note that these simulations are done after a relative short

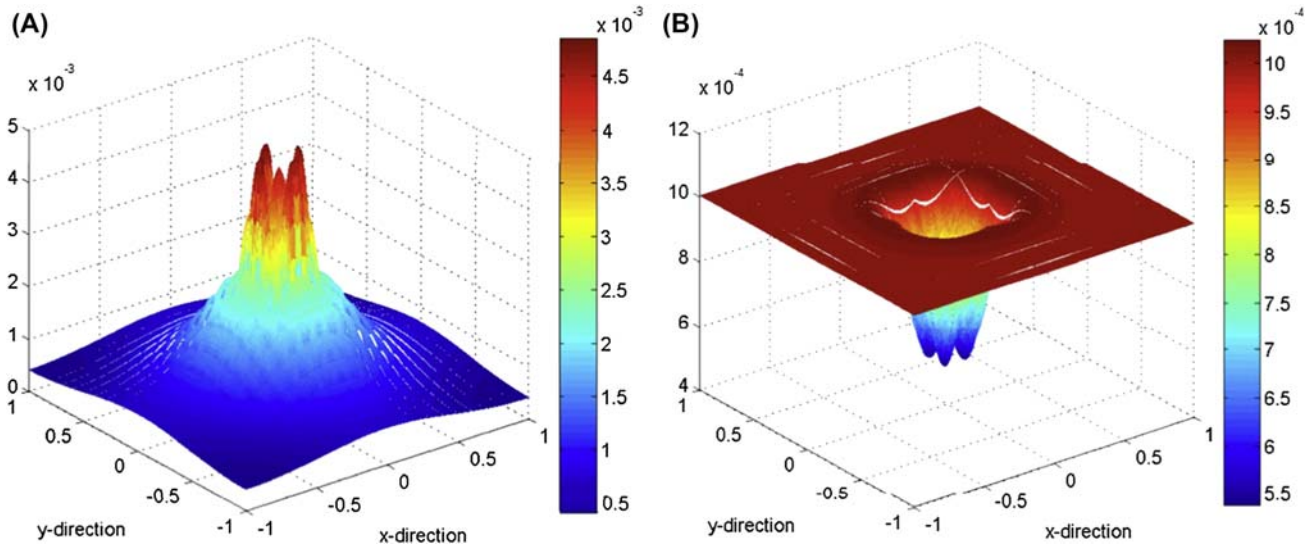

FIGURE 6.3 Three-dimensional snapshot of the tip and vessel density at time $t = 0.5$ with a time step of $\Delta t = 0.0001$.

This book belongs to Central Library BADJI Mokhtar-ANNABA UNIVERSITY
Copyright Elsevier 2024

time $t = 0.5$ so the biological process has just started. Furthermore, we have only used approximations up to order $k = 2$. Because this a relative low order, we have some big discontinuities between the different solutions on the boundaries of the elements. To get better approximations, we should use at least Legendre polynomials up to order $k = 3$.

Certainly, the cost of the method could be improved. At each time we needed to determine the nine coefficients per element (there are 100 elements) corresponding to the nine combinations of polynomials. We needed to do this for all six equations (the concentration TG-β, the capillary tip density, the vessel density, and the three equations caused by the splitting of the diffusion terms). Because we used RK3-TVD for the time integration, we did this calculation three times per time step. Using a time step of $\Delta t = 0.0001$ we did this for all 5000 times to come at $t = 0.5$, which is the time of the simulations plotted in the figures above. In the present computer implementation, one iteration takes approximately 83 s. Therefore, all the 5000 time steps take together approximately 4.83 days. Because this is still just a very short time, we see that it is very expensive. This could be improved by implementing this code in parallel.

6.6 DISCUSSION AND CONCLUSIONS

6.6.1 The Snail Trail Model

First, as mentioned in the model section, the sprouts are assumed to follow the tips. We extended the one-dimensional case in Byrne and Chaplain (1995) to two dimensions where the migration of tips is directed toward the center of the domain of computation, that is, the center of the damaged region. In the present case, this is a reasonable approximation given the symmetry and the damaged region being located around the origin of the domain of computation. However, for more generic cases, the model needs to be revised. In Spill et al. (2015), this issue was treated recently. Because the sprouts follow the location of the tips, the extension of the snail trail is determined by the migration rate of the tips at this location. This needs to be averaged over a representative elementary volume to derive the resulting partial differential equation. Their final result is that the sprout snail trail contribution given by the 1-norm of the flux of tips, that is

$$\frac{\partial \rho}{\partial t} - D_3 \Delta \rho - \left\| D_2 \frac{\partial u}{\partial n} - \chi_1 u \frac{\partial c}{\partial n} \right\|_1 + \gamma\left(\rho - \rho_{\mathrm{eq}}\right) = 0, \quad (t, \mathbf{x}) \in \mathbb{R}^+ \times \Omega, \tag{6.54}$$

or

$$\frac{\partial \rho}{\partial t} - D_3 \Delta \rho - D_2 \left\| \frac{\partial u}{\partial n} \right\|_1 + \chi_1 \left\| u \frac{\partial c}{\partial n} \right\|_1 + \gamma\left(\rho - \rho_{\mathrm{eq}}\right) = 0, \quad (t, \mathbf{x}) \in \mathbb{R}^+ \times \Omega, \tag{6.55}$$

using different assumptions regarding the transition rate between stalk and tip cells. The above 1-norm is taken over the spatial coordinates.

6.6.2 The Numerical Method

To construct a numerical method, which is applicable to the model from Section 6.3 in this chapter, we have to consider different aspects. First, the method should be able to handle complicated geometries because wounds can have any possible shape. Both the finite element method and the DG method are eligible. Because the DG method is more expensive, we first applied the finite element method. This method gave some good results. Secondly, the method should be able to handle hyperbolic or convection-dominated problems. Because if it turns out that the chemotaxis term has more influence than has been assumed, the degree of hyperbolicity of the problem will increase. In the finite element method, the convection term has been made larger by assigning a higher value for the chemotaxis constant χ_1. Unfortunately, we had to conclude from the results that the finite element method was not suitable, unless an ultrahigh grid resolution was used, whereas the DG method was more suitable. Because the DG method meets both requirements, we wanted to implement this method for the two-dimensional model. First we applied the DG method to a relative simple advection equation in one dimension with different kinds of boundary conditions. There, we have introduced a limiter to prevent the appearance of wiggles. In this manuscript, we first described the DG method applied to the one-dimensional model. This is done to present the method and to show some advantages regarding accuracy of this method in comparison to the finite element method. Subsequently, we used it to construct the approximations to the two-dimensional model. The DG method was found to be a very complex and expensive method. Therefore, we were only able to approximate situations with a two-dimensional circular wound (using polar coordinates, see Crapts, 2012) and situations with a rectangular-shaped wound using rectangular elements.

The DG method is relatively expensive due to several facts. First, the DG method has many degrees of freedom which makes the method very expensive. Think of N, the number of elements and $p + 1$ the number of basis functions per

This book belongs to Central Library BADJI Mokhtar-ANNABA UNIVERSITY
Copyright Elsevier 2024

element. The higher the order of the Legendre Polynomials, the more accurate the approximation is; however, also the more the degrees of freedom, the more expensive the method. Secondly, we used the so-called local DG method, which is an extension of the DG method with Runga−Kutta time integration for purely hyperbolic or convection-diffusion systems. This results into the high-order accuracy and easy handling of complicated geometries. Basically, it means splitting the diffusion term such that we obtain a second equation for each equation of our model. The more equations to solve, the more expensive the method becomes. Finally, we use the central flux, which uses a stencil of five elements, instead of an upwind or downwind flux, which uses a stencil of only three elements. We do this because the central flux is the only one that gives good results. The disadvantage is again that it is more expensive. However, we note that the DG method can achieve a given error tolerance faster than a low-order method. In addition, the flux can be improved by performing suitable stability analysis for this equation.

Our DG method can handle the complicated geometries and the relative high degree of hyperbolicity of the model. The only problem is that the method is very expensive; hence the question whether the DG method is suitable to use for application is quite legitimate. The long computation times make the method unattractive at the moment. Hence the method could be improved by implementing in parallel or suitable use of graphics processing unit (GPU) computers.

In the framework of a literary study, we tried to improve the finite element approximations for the convection dominated problem, in only one dimension. At that moment only basic SUPG method was implemented and it did not improve the simulations. Because we only implemented some basic SUPG, we cannot exclude SUPG as one of the options to improve the approximations. Therefore, for further research, the option to improve the approximations using the finite element with SUPG should be reconsidered.

We performed some simulations using the DG method for our model with a square-shaped wound. Because of limited computational resources, we were only able to perform the simulations to time $t = 0.5$, when the biological process has just begun. In these simulations we already see some differences with respect to the simulations for a circular wound. To draw more and better conclusions about the healing of a square wound, the simulation should run for a longer time. Furthermore, we have only used Legendre polynomials up to order 2. To get a better approximation, we need at least an approximation that uses Legendre polynomials up to order 3. To be able to say more about the healing of a rectangularly shaped wound, the simulation should run for a rectangular wound because we have only done it for a square wound. The same Matlab code can be used for this. While determining the approximations to the solution of the equations in the model, in one and two dimensions, using the DG method, we did not use a limiter of any kind. It was not necessary because no wiggles appeared. However, it is worth investigating whether a limiter may improve the approximation. Note that the use of a limiter would add additional expense.

We also remark that this is, as far as we know, the first simulation study on stem cell treatment in the framework of postcardiac infarction treatment. At this stage, experimental validation is beyond the scope of the manuscript. This manuscript should be considered as a feasibility study where it is illustrated that the DG method can be applied to the modeling of this class of biomedical phenomena.

REFERENCES

Atkinson, K., Han, W., 2009. Theoretical Numerical Analysis, third ed. Springer, Dordrecht, Heidelberg, London, New York.

Baek, S.J., Kang, S.K., Ra, J.C., 2011. In vitro migration capacity of human adipose tissue-derived mesenchymal stem cells reflects their expression of receptors for chemokines and growth factors. Experimental and Molecular Medicine 43, 596−603.

Bookholt, F.D., Monsuur, H.N., Gibbs, S., Vermolen, F.J., 2016. Mathematical modelling of angiogenesis using continuous cell-based models. Biomechanics and Modelling in Mechanobiology 15 (6), 1577−1600.

Brenner, S.C., Scott, L.R., 2008. The Mathematical Theory of Finite Element Methods, third ed. Springer.

Byrne, H.M., Chaplain, M.A.J., 1995. Explicit Solutions of a Simplified Model of Capillary Sprout Growth During Tumor Angiogenesis. School of Mathematical Sciences, University of Bath, Claverton Down, Bath BA2 7AY, UK.

Cockburn, B., 1997. An introduction to the discontinuous Galerkin method for convection-dominated problems. In: Quarteroni, A. (Ed.), Advanced Numerical Approximation of Nonlinear Hyperbolic Equations (Lecture Notes in Mathematics).

Crapts, L.Y.D., 2012. Modelling an Angiogenesis Treatment After a Myocardial Infarction. M.Sc. thesis at the Delft Institute of Applied Mathematics. Delft University of Technology, The Netherlands. Downloadable at: http://repository.tudelft.nl.

Epshteyn, Y., Izmirlioglu, A., 2009. Fully discrete analysis of a discontinuous finite element method for the Keller-Segel chemotaxis model. Journal of Scientific Computing 40, 211−256.

Epshteyn, Y., Kurgonov, A., 2008. New interior penalty discontinuous Galerkin methods for the Keller-Segel chemotaxis model. SIAM Journal on Numerical Analysis 47, 386−408.

Epshteyn, Y., 2009. Discontinuous Galerkin methods for the chemotaxis and haptotaxis models. Journal of Computational and Applied Mathematics 244 (1), 168−181.

This book belongs to Central Library BADJI Mokhtar-ANNABA UNIVERSITY

Copyright Elsevier 2024

Epshteyn, Y., 2012. Upwind-difference potentials method for Patlak-Keller-Segel chemotaxis model. Journal of Scientific Computing 53, 689−713.

Fomovsky, G.M., Holmes, J.W., 2010. Evolution of scar structure, mechanics, and ventricular function after myocardial infarction in the rat. Americal Journal of Physiology. Heart and Circulation Physiology 298 (1), H221−H228.

Gottlieb, S., Shu, C.-W., 1998. Total variation diminishing Runge-Kutta schemes. Mathematics of Computation 67, 73−85.

Hesthaven, J.S., Warburton, T., 2008. Nodal Discontinuous Galerkin Methods. Springer, New York.

Kajstura, J., Hosoda, T., Bearzi, C., Rota, M., Maestroni, S., Urbanek, K., Leri, A., Anversa, P., 2008. The human heart: a self-renewing organ. Clinical and Translational Science 1 (1), 80−86.

Lazzerini, P.E., Capecchi, P.L., Guideri, F., Acampa, M., Galeazzi, M., Laghi Pasini, F., 2006. Connective tissue diseases and cardiac rhythm disorders: an overview. Autoimmunity Reviews 5 (5), 306−313.

Leveque, R.J., 2002. Finite Methods for Hyperbolic Problems. Cambridge Texts in Applied Mathematics, sixth ed. Cambridge University Press, New York.

Maggelakis, S.A., 2003. A mathematical model of tissue replacement during epidermal wound healing. Applied Mathematical Modelling 27, 189−196.

Maggelakis, S.A., 2004. Modeling the role of angiogenesis in epidermal wound healing. Discrete and Continuous Dynamical Systems − Series B 4 (1), 267−273.

Mirzaee, H., Ryan, J.K., Kirby, R.M., 2014. Smoothness-increasing accuracy-conserving (SIAC) filters for discontinuous Galerkin solutions: application to structured tetrahedral meshes. Journal of Scientific Computing 58, 690−704.

Moller, M., 2013. Algebraic flux correction for nonconforming finite element discretizations of scalar transport. Computing 95 (5), 425−448.

Oers, R.F.M., Rens, E.G., LaValley, D.J., Reinhart−King, C.A., Merks, R.M.H., 2014. Mechanical cell−matrix feedback explains pairwise and collective endothelial cell behavior in vitro. PLoS Computational Biology 10 (3), e1003774.

Olivetti, G., Melissari, M., Capasso, J.M., Anversa, P., 1991. Cardiomyopathy of the aging human heart. Myocyte loss and reactive cellular hypertrophy. Circulation Research 68 (6), 1560−1568.

Paillere, H., 1996. Multidimensional upwind residual distribution schemes for the convection-diffusion equation. International Journal for Numerical Methods in Fluids 23 (9), 923−936.

Pettet, G.J., Byrne, H.M., McElwain, J., Norbury, J., 1996. A model of wound-healing angiogenesis in soft tissue. Mathematical Biosciences 136 (1), 35−63.

Przybyt, E., Harmsen, M.C., 2013. Mesenchymal stem cells: promising for myocardial regeneration? Current Stem Cell Research and Therapy 8 (4), 270−277.

Qiu, J., Shu, C.-W., 2005. Runge−Kutta discontinuous Galerkin method using Weno limiters. SIAM Journal of Scientific Computing 26 (3), 907−929.

Shimamoto, T., 1969. Experimental study on atherosclerosis − an attempt at its prevention and treatment. Acta Pathologica Japanonica 19 (1), 15−43.

Spill, F., Guerrero, P., Alarcon, T., Maini, P.K., Byrne, H.M., 2015. Mesoscopic and continuum modelling of angiogenesis. Journal of Mathematical Biology 70 (3), 485−532.

Talman, V., Ruskoaho, H., 2016. Cardiac fibrosis in myocardial infarction − from repair and remodelling to regeneration. Cell and Tissue Research 365 (3), 563−581.

Wingstrand, V.L., Larsen, C.G., Jensen, D.H., Bork, K., Sebbesen, L., Balle, J., von Buchwald, C., 2016. Mesenchymal stem cell therapy for the treatment of vocal fold scarring: a systematic review of preclinical studies. PLoS One 11 (9), e0162349.

FURTHER READING

Flegg, J.A., Byrne, H.M., McElwain, D.L.S., 2010. Mathematical model of hyperbaric oxygen therapy applied to chronic diabetic wounds. Bulletin of Mathematical Biology 72, 1867−1891.

This book belongs to Central Library BADJI Mokhtar-ANNABA UNIVERSITY Copyright Elsevier 2024

This page intentionally left blank

This book belongs to Central Library BADJI Mokhtar-ANNABA UNIVERSITY

Copyright Elsevier 2024

Part II

Boundary Integral Methods

This book belongs to Central Library BADJI Mokhtar-ANNABA UNIVERSITY

Copyright Elsevier 2024

This page intentionally left blank

This book belongs to Central Library BADJI Mokhtar-ANNABA UNIVERSITY

Copyright Elsevier 2024

Chapter 7

On the Use of Boundary Integral Methods in Bioelectromagnetics

D. Poljak
University of Split, Split, Croatia

7.1 INTRODUCTION

The tremendous growth of various power and communication installation in modern society has initiated a continuous public concern regarding possible adverse health effects due to exposure to electromagnetic fields generated from these sources.

In last few decades the problem has been widely researched and a comprehensive view to the subject is available in many review papers, such as Hand (2008) and Poljak (2011). However, the human body is a rather complex structure to analyze as measurement of induced currents and fields in the body in realistic scenarios are not possible in vivo. Consequently, measurements of relevant electromagnetic quantities are carried out on laboratory animals or on phantoms having some electrical parameters corresponding to humans (Nagasawa et al., 2005; Koyanagi et al., 2001; Ito and Kawai, 2004). However, it is extremely difficult to extrapolate findings arising from experiments on phantoms and/or animal studies. Therefore, several theoretical dosimetry procedures for the assessment of human exposure to nonionizing radiation, pertaining to the use of highly sophisticated numerical methods (Nielsen et al., 1996; Gonzalez et al., 2007; Singh et al., 2006), are of great importance in the analysis of bioelectromagnetic phenomena.

In general, computational models used in bioelectromagnetics are often divided into two groups:

- Realistic human body (or some of its parts, organs, etc.) models with relatively high resolution (sophisticated discretization schemes)—mostly based on magnetic resonance imaging (MRI) (Hand, 2008; Nagaoka et al., 2008; Kos et al., 2010; Togashi et al., 2006; Hirata et al., 2000; Hirata, 2005; Hand et al., 2010). These models usually require rather high computational cost.
- Simplified models, computationally much less expensive, (Hand, 2008; Poljak, 2011; Nagasawa et al., 2005; Koyanagi et al., 2001; Ito and Kawai, 2004; Kawai et al., 2003) fail to ensure accurate results in many realistic scenarios.

This chapter aims to review some boundary integral equation techniques used in certain bioelectromagnetic applications pertaining to the low-frequency (LF) and high-frequency (HF) exposures.

Computational examples presented throughout this work are related to the human head exposed to electrostatic field from video display unit (VDU), pregnant woman/fetus exposed to high-voltage (HV) extremely low-frequency (ELF) electric fields generated by overhead power lines (Gonzalez et al., 2008; Peratta et al., 2010), the human eye exposed to plane wave (Hirata, 2005; Dodig et al., 2012), the brain exposed to plane wave (Cvetkovic and Poljak, 2015; Cvetković et al., 2016), and the whole body exposed to GSM base station antenna radiation (Poljak et al., 2016). The electrostatic and LF analysis is based on the calculation of induced currents and electric fields obtained by solving the corresponding Laplace equation type via boundary element method (BEM) (Gonzalez et al., 2008; Peratta et al., 2010), whereas the HF exposure analysis is based on the assessment of specific absorption rate (SAR) distribution and the corresponding BEM solution of vector Helmholtz equation (Dodig et al., 2012), method of moments (MoM) solution of the coupled surface integral equations (SIEs) (Cvetkovic and Poljak, 2015; Cvetković et al., 2016), and MoM solution of the volume tensor integral equation (Poljak et al., 2016).

Numerical Methods and Advanced Simulation in Biomechanics and Biological Processes. https://doi.org/10.1016/B978-0-12-811718-7.00007-1
Copyright © 2018 Elsevier Ltd. All rights reserved.

This book belongs to Central Library BADJI Mokhtar-ANNABA UNIVERSITY
Copyright Elsevier 2024

In particular, boundary integral equation methods, such as BEM or MoM, are considered to be promising efficient approaches for static and ELF dosimetry. As documented in ICNIRP (1998) and ICNIRP (2010) the stair-casing error (Laakso and Hirata, 2012) is significant not only for the current density but also for the internal electric field, i.e., 99th percentile value of *E*-field is suggested. However, such a measure is not quite appropriate for localized exposures. Therefore, BEM-oriented approach seems rather important aiming to verify conventional finite difference−based approaches.

7.2 GOVERNING EQUATIONS OF THEORETICAL DOSIMETRY

Regarding operating frequency, the electromagnetic radiation is classified as nonionizing or ionizing. Nonionizing fields are then split into two main categories: low frequencies (up to about 30 kHz) and high frequencies (from 30 kHz to 300 GHz).

While LF fields may cause excitation of sensory, nerve, and muscle cells, HF fields, because of the resonance effect (the body dimensions are comparable to the external field wavelength), are absorbed by the body, and the related tissue heating effects become dominant.

In the case of LF exposures the thermal effects are practically negligible, and possible nonthermal effects are related to the cellular level.

Note that according to ICNIRP (1998) guidelines the current density was a principal parameter for the estimation of LF exposure effects, while the ICNIRP (2010) guidelines propose the induced electric field instead of the induced current density. However, there is a substantial amount of the numerical results for the current density in the relevant literature; therefore, for the comparison purpose, this work pertains to the assessment of current density, as well.

On the contrary, the aims and scopes of HF dosimetry are related to thermal effects, i.e., one deals with the magnitude and distribution of the fields induced in the body. The corresponding dosimetric quantity for HF internal fields is the SAR.

Computational models are necessary to analyze various exposure scenarios and thereby establish appropriate safety guidelines and exposure limits for human beings ICNIRP (1998). Because of the high mathematical complexity of the problem, many researchers in early days of dosimetry investigated simple models such as plane slab, cylinders, homogeneous and layered spheres, and prolate spheroids (Poljak, 2003).

As a matter of fact, sophisticated simulation tools based on realistic numerical modeling are necessary for an accurate prediction of the electromagnetic energy absorbed by the human body (Gonzalez et al., 2008; Peratta et al., 2010). A number of anatomically based computational models comprising of cubical cells are related to the application of the finite difference time domain methods. The finite element method (FEM), BEM, and MoM are generally used to a somewhat lesser extent (Poljak et al., 2016).

7.2.1 Exposure to Low-Frequency Fields

The internal current density is generated because of an external electric or magnetic field, respectively. The current density J induced in the body due to electric fields is axial in nature and is given by the following constitutive equation (differential form of Ohm's law):

$$J = \sigma E \tag{7.1}$$

where σ is tissue conductivity while E is the corresponding internal electrical field.

The internal current density generated by the magnetic field has circular character and is given by Poljak (2003):

$$J = \sigma \pi r f B \tag{7.2}$$

where B is the corresponding magnetic induction normal to the human body, f is the operating frequency, and r is the radius of the loop.

7.2.2 Exposure to High-Frequency Fields

The basic quantity in HF dosimetry, SAR, is defined as the rate of energy W absorbed by, or dissipated in the unit body mass:

$$\mathrm{SAR} = \frac{dP}{dm} = \frac{d}{dm}\frac{dW}{dt} = C\frac{dT}{dt} \tag{7.3}$$

where C is the specific heat capacity of tissue, T is the temperature, and t denotes time.

This book belongs to Central Library BADJI Mokhtar-ANNABA UNIVERSITY
Copyright Elsevier 2024

In addition, SAR is proportional to the square of the internal electric field:

$$\mathrm{SAR} = \frac{dP}{dm} = \frac{dP}{\rho dV} = \frac{\sigma}{2\rho}|E|^2 = \frac{\sigma}{\rho}|E_{\mathrm{rms}}|^2 \tag{7.4}$$

where E and E_{rms} is the peak and root mean square value of the electric field, respectively, ρ is the tissue density and σ is the tissue conductivity.

The distribution of SAR inside the body appreciably depends on the incident field parameters, the characteristics of the exposed body, ground effects, and reflector effects. The maximal values of the whole-body SAR occur when the electric field is oriented parallel to the long body axis.

Provided the SAR distribution in a tissue is determined, the related temperature increase is obtained from the solution of the steady-state Pennes bioheat equation (Cvetković et al., 2016):

$$\nabla\cdot(k\nabla T) + \rho_b c_b w(T_a - T) + Q_m + \rho\cdot\mathrm{SAR} = 0 \tag{7.5}$$

where k stands for the heat conduction, ρ_b is the blood mass density, c_b is the specific heat capacity of blood, w is the blood perfusion rate, T_a is the arterial temperature, Q_m is the tissue-dependent heat source due to metabolic processes, and term $\rho\cdot\mathrm{SAR}$ represents the volumetric heat source due to an external electromagnetic field.

7.3 HUMAN HEAD EXPOSED TO VIDEO DISPLAY UNIT ELECTROSTATIC FIELD

VDUs based on cathode ray tube (CRT) are sources of many types of radiation, e.g., X-ray radiation, ultraviolet radiation, infrared radiation, and electromagnetic radiation. On one hand, the radiation levels, such as levels of X-ray radiation, optical radiation, and HF (∼MHz) and LF (∼kHz) electromagnetic fields stay well below exposure limits (ICNIRP, 1994; IEEE, 1997); however, electrostatic fields and LF fields might be associated with some skin diseases, suppression of melatonin, or induction of phosphenes in the eyes, despite of the fact that there is no strong evidence of adverse health effects from domestic levels of ELF electromagnetic fields (ICNIRP, 1994; IEEE, 1997).

The present section reviews some aspects of human exposure to electrostatic fields, as high-intensity trostatic fields have been detected from several types of VDUs and possibly associated with skin rashes (Nielsen et al., 1996; ARPNSA, 2003). In addition, the main concern related to the exposure to these fields is linked with particle transport and deposition (Nielsen and Schneider, 1998).

This section deals with three-dimensional, anatomically based model of the human head exposed to electrostatic field from VDU via BEM contrary to the usual approach featuring the use of the finite difference method (Nagasawa et al., 2005). The results obtained by BEM are compared with the results computed via FEM. The formulation is based on the Laplace equation for scalar potential (Gonzalez et al., 2007; Poljak et al., 2014). The results are obtained for different face geometries.

Neglecting the charge density in the space between the head and the display, a 3D electrostatic field between a VDU and the head is given by Laplace equation for scalar potential φ (Gonzalez et al., 2007; Poljak et al., 2014):

$$\nabla^2\varphi = 0 \tag{7.6}$$

with the associated boundary conditions:

$$\varphi = \varphi_s \text{ on the display,} \tag{7.7}$$

$$\varphi = \varphi_h \text{ on the head,} \tag{7.8}$$

$$\nabla\varphi\cdot\vec{n} = 0 \text{ on the far field boundaries.} \tag{7.9}$$

As depicted in Fig. 7.1, the Dirichlet boundary conditions Eqs. (7.7) and (7.8) are specified on the face and display, respectively, whereas Neumann conditions Eq. (7.9) are imposed on the rest of the outer boundary.

The head is assumed to be perfectly conductor, thus representing an equipotential surface potential φ_h.

The parameters l_s, d_s, φ_s, and φ_h represent the distance between display and nose tip, the size of display (diagonal display size given in inches), the electrostatic potential on the display, and the electrostatic potential on the head, respectively. The electric potential on a CRT monitor is taken to be between 1 and 15 kV. In this work the potential of the display is assumed to be relatively rather high (15 kV)—the worst-case scenario. The conditions for human in front of display are defined as follows: $l_s = 40$ cm, $d_s = 17$ in., $\varphi_s = 15$ kV, and $\varphi_h = 0$ kV. The monitor is 4:3 format type, i.e.,

This book belongs to Central Library BADJI Mokhtar-ANNABA UNIVERSITY
Copyright Elsevier 2024

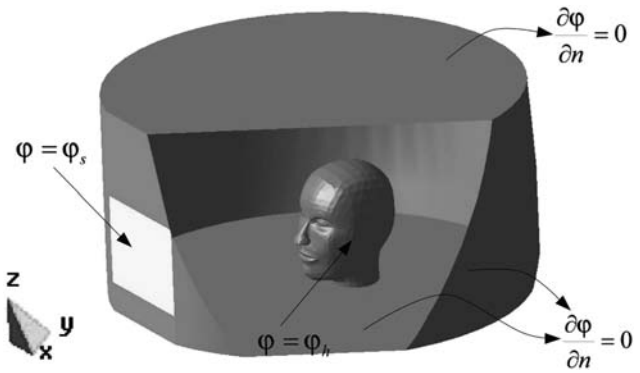

FIGURE 7.1 Geometry and associated boundary conditions for the head in front of a video display unit.

the width of the screen is 34.3 cm (13.6 in.) and height is 25.7 cm (10.2 in.). The radius of the computational domain is around 0.5 m, while the height of around 0.6 m, i.e., the head dimensions are 21 cm × 16.5 cm (NASA, 1995).

The eyebrows potential is assumed to be the same potential as for the face. Other parameters, such as temperature, humidity, and conductivity of the screen glass surface, are simply neglected, and the air humidity is considered to be very low (dry air).

Fig. 7.2 shows two types of faces to be analyzed.

Note that the meshing has been carried out with GiD (CIMNE).

7.3.1 Boundary Element Solution

The boundary integral representation of Eq. (7.5) is given as follows (Poljak et al., 2014):

$$c_i\varphi_i = \int_\Gamma \Psi \frac{\partial\varphi}{\partial n} d\Gamma - \int_\Gamma \varphi \frac{\partial\Psi}{\partial n} d\Gamma \tag{7.10}$$

where ψ is the fundamental solution Laplace equation:

$$\psi = \frac{1}{4\pi R} \tag{7.11}$$

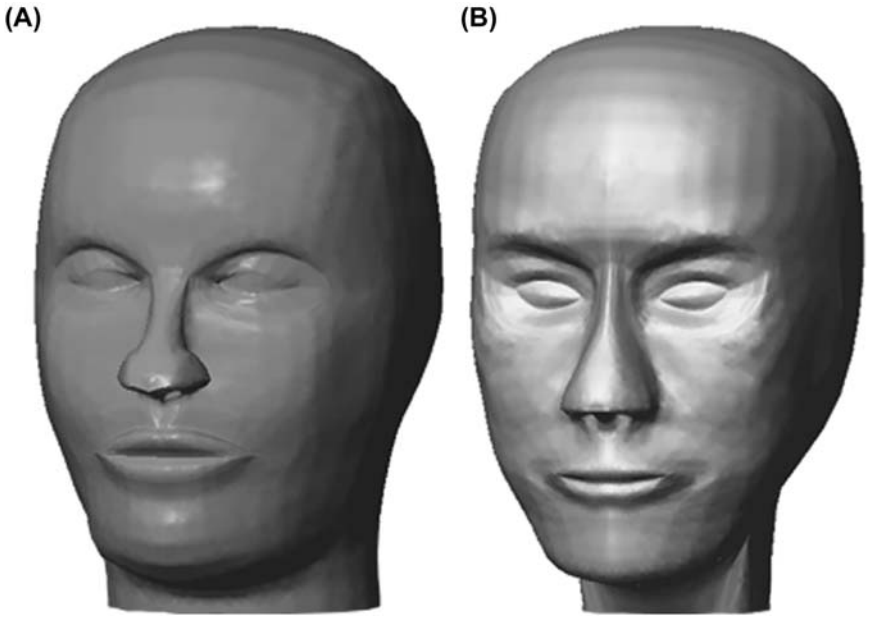

FIGURE 7.2 Head models of (A) person 1 and (B) person 2.

This book belongs to Central Library BADJI Mokhtar-ANNABA UNIVERSITY
Copyright Elsevier 2024

where $R = \left|\vec{r} - \vec{r}'\right|$ is the distance between the source point i and field point in Γ, and

$$c_i = \begin{cases} 1, & i \in \Omega \\ 1/2, & i \in \Gamma(\text{smooth boundary}) \end{cases} \tag{7.12}$$

The details of the finite element solution can be found elsewhere, e.g., in Cavka et al. (2011).

7.3.2 Computational Examples

The numerical results are obtained for both head types shown in Fig. 7.2.

Both BEM and FEM meshes are generated by using the general preprocessor and geometry modeler GiD (CIMNE). For person 1 the BEM mesh consists of 4558 constant triangle elements and 4558 nodes, whereas FEM mesh consists of 80,771 linear tetrahedral elements (20,184 nodes).

Fig. 7.3 shows the electrostatic field distribution over the face of person 1 for FEM and BEM solutions, respectively.

Maximal field values are obtained in the close vicinity of the nose, whereas significant field values are calculated on the lips, chin, and forehead. Some "hot spots" appear on the nose ($\approx$1960 V/m for the FEM model, and $\approx$1760 V/m for the BEM model).

Figs. 7.4–7.6 show E_x, E_y, and E_z components of the electrostatic field induced on the face, both computed via BEM and FEM solutions.

It can be noticed that E_y is the highest field component as the screen is located 40 cm away from the face in y direction. Highest values of E_y are located on the nose, lips, chin, and forehead, whereas the highest values of E_z component are located on the bottom of the nose, around nostrils.

For the case of person 2 BEM mesh consists of 6066 constant triangle elements (6066 nodes), whereas FEM mesh contains 104,082 linear tetrahedral elements (26,659 nodes). Fig. 7.7 shows the electrostatic field E[V/cm] on the face of the person 2 obtained by FEM and BEM methods, respectively.

Higher field levels are found on the nose (maximal), lips, chin, forehead, and eyebrows. Eyes and neighboring regions are not so exposed (around 300–400 V/cm) compared with the nose (maximal value around 2100 V/cm).

Comparing the results obtained for person 1 and person 2, appreciable differences in field values are noticed on certain parts of the face, such as nose, caused due to the different shape of the face, particularly the shape of the nose.

Fig. 7.8 shows the field computed via BEM versus distance l_s between nose tip and screen.

The closer the face to the screen, the greater is the field on the nose. In addition, the field values in the eyes area are less, i.e., the peaky shape of the nose in a certain sense protect the eyes. At distance $l_s = 10$ cm the field in the nose tip is approximately 3600 and 980 V/cm in the eye, whereas at $l_s = 50$ cm the field on the nose tip is $E = 1230$ V/cm and 350 V/cm in the eye, respectively.

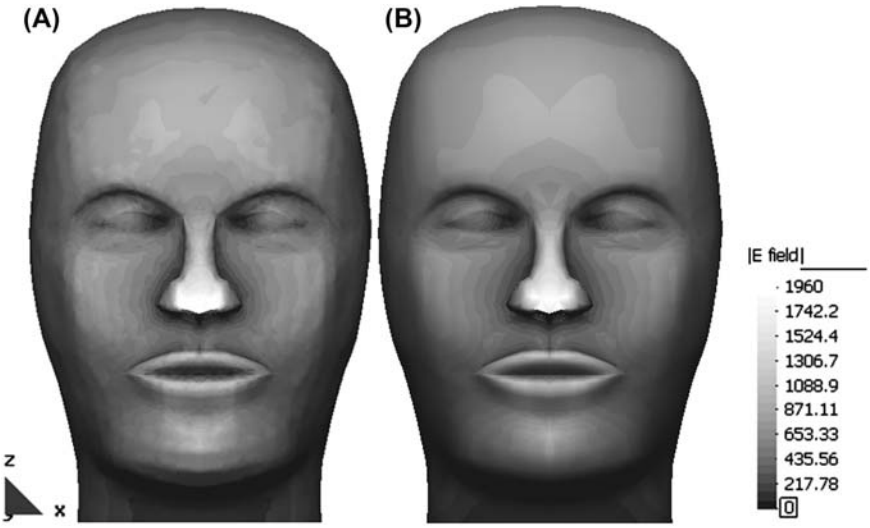

FIGURE 7.3 Electrostatic field on the face of the person 1. (A) Finite element method solution; (B) boundary element method solution.

This book belongs to Central Library BADJI Mokhtar-ANNABA UNIVERSITY
Copyright Elsevier 2024

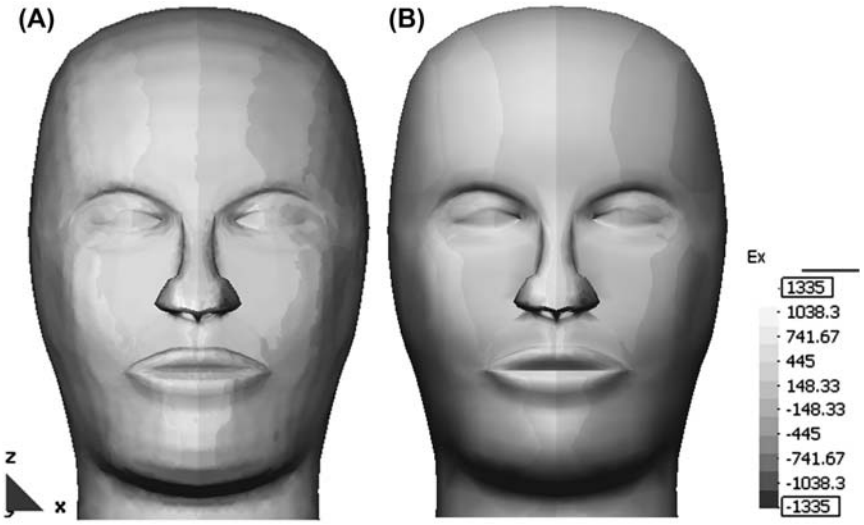

FIGURE 7.4 E_x [V/cm] component. (A) Finite element method solution; (B) boundary element method solution.

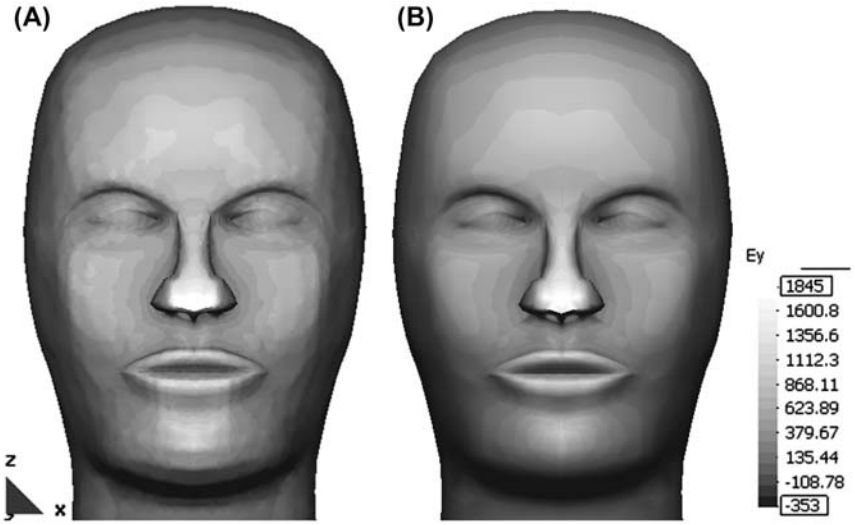

FIGURE 7.5 E_y [V/cm] component. (A) Finite element method solution; (B) boundary element method solution.

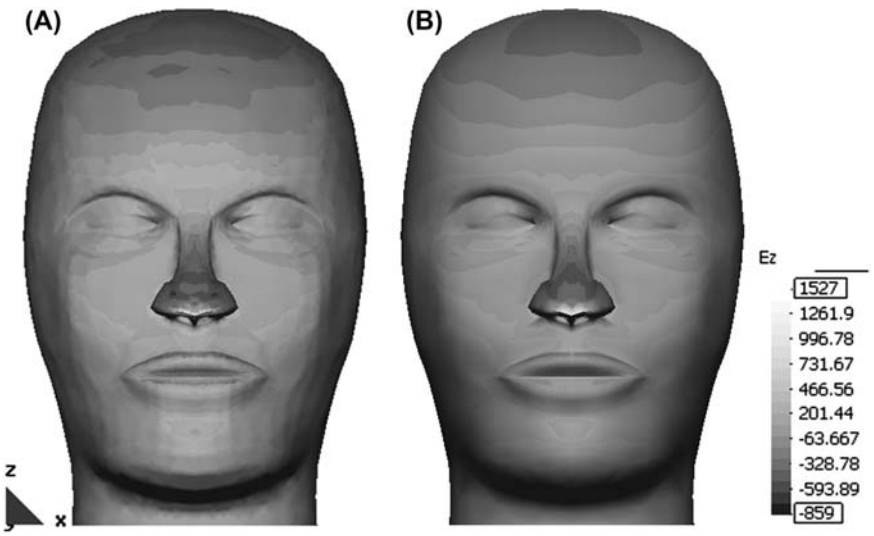

FIGURE 7.6 E_z [V/cm] component of the field. (A) Finite element method solution; (B) boundary element method solution.

This book belongs to Central Library BADJI Mokhtar-ANNABA UNIVERSITY Copyright Elsevier 2024

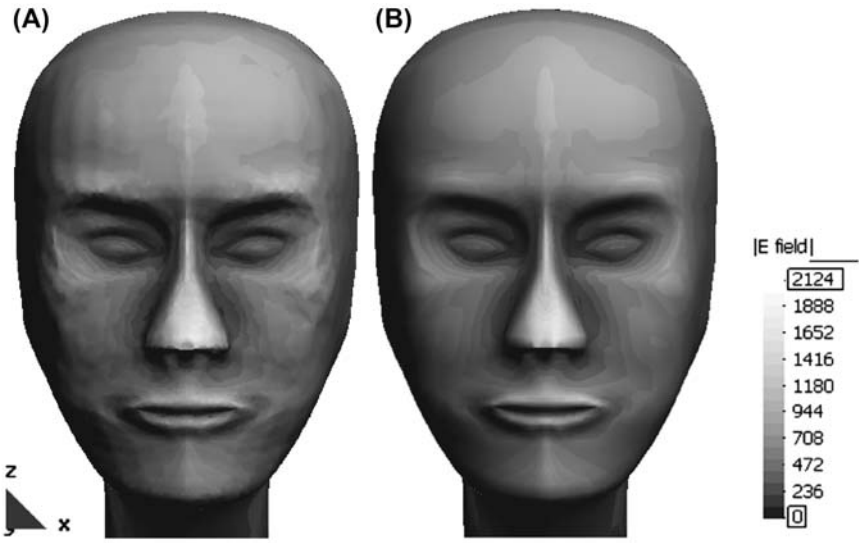

FIGURE 7.7 Electrostatic field on the face of the person 2. (A) Finite element method solution; (B) boundary element method solution.

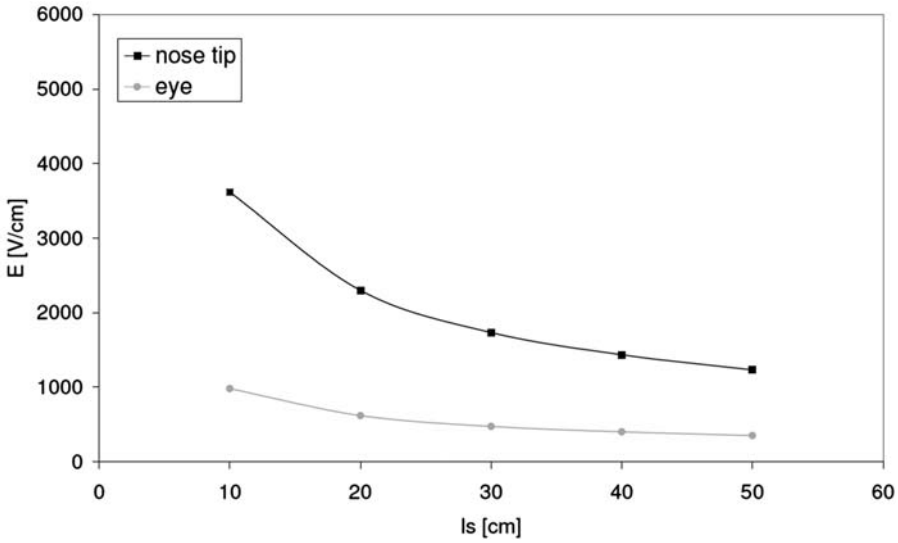

FIGURE 7.8 Electrostatic field on the nose tip and eyes versus distance between display and head for 17 in display size.

Fig. 7.9 shows the field computed via BEM versus the display size d_s with the 40 cm distance between screen and nose tip. The results are also obtained via BEM. Note that the electrostatic field is almost linearly dependent on the display size.

The field increase is slow and, for example, the nose tip increases approximately 19% by increasing the display size from 14 to 19 in. at 40 cm display—face distance.

Generally, BEM solution requires much less computational time compared with FEM, which is discussed in detail in Cavka et al. (2011). The implementation of BEM was proved to be more suitable for the given problem in terms of accuracy, efficiency, and stability (Poljak et al., 2014).

7.4 PREGNANT WOMAN/FETUS EXPOSURE TO LOW-FREQUENCY FIELDS

The section deals with pregnant woman and fetus exposed to ELF electric field by means of BEM approach. Various physical and geometrical properties of corresponding tissues are taken from medical data available in relevant literature. For the case of LF exposures realistic, anatomically based model of pregnant woman/fetus uses a quasistatic approximation based on the Laplace equation formulation and a solution via three dimensional multidomain BEM. The model accounts for variations in geometry, body mass, fat, and overall chemical composition in the female body.

This book belongs to Central Library BADJI Mokhtar-ANNABA UNIVERSITY Copyright Elsevier 2024

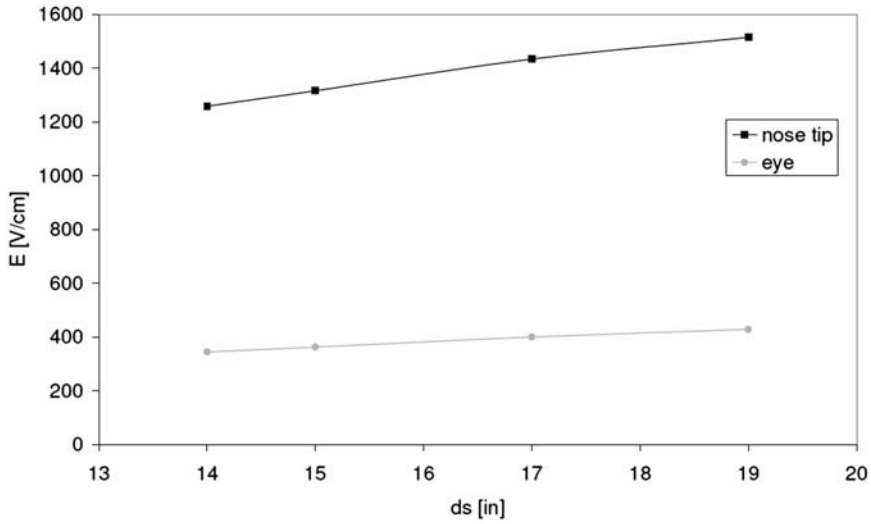

FIGURE 7.9 Electrostatic field in the nose tip and eyes versus display size for 40 cm distance between display and head.

At LF exposures, human tissues and organs are good conductors with tissues conductivity σ varying from 0.2 to 0.5 S/m, while the relative permittivity is assumed to be around 100.

Through the fetal period (from 8th to 40th gestational week), the growth, development, and maturation of the already formed structures occur. Pregnancy stages studied in this model are 8th, 13th, 26th, and 38th gestational weeks (Poljak et al., 2014).

For the maternal abdomen, the decomposition into subdomains is based on the different properties of the tissues, as depicted in Fig. 7.10A. The amniotic fluid (AF) has the highest conductivity, which also varies through the periods of gestation. Kidney, muscle bone cortical, bladder, spleen, and skin have conductivity very close to 0.1 S/m, whereas the ovary and cartilage conductivity is around 0.2 S/m. Therefore, all these tissues can be grouped into one subdomain—maternal tissue. Furthermore, the uterus conductivity is 0.23 S/m (similar to the conductivity of the maternal tissue) while the placenta is assumed to have the same conductivity as the blood and considered as part of the maternal tissue subdomain. Consequently, the maternal abdomen is divided into three subdomains: maternal tissue, AF, contained within the uterus, and fetus, as shown in Fig. 7.10B.

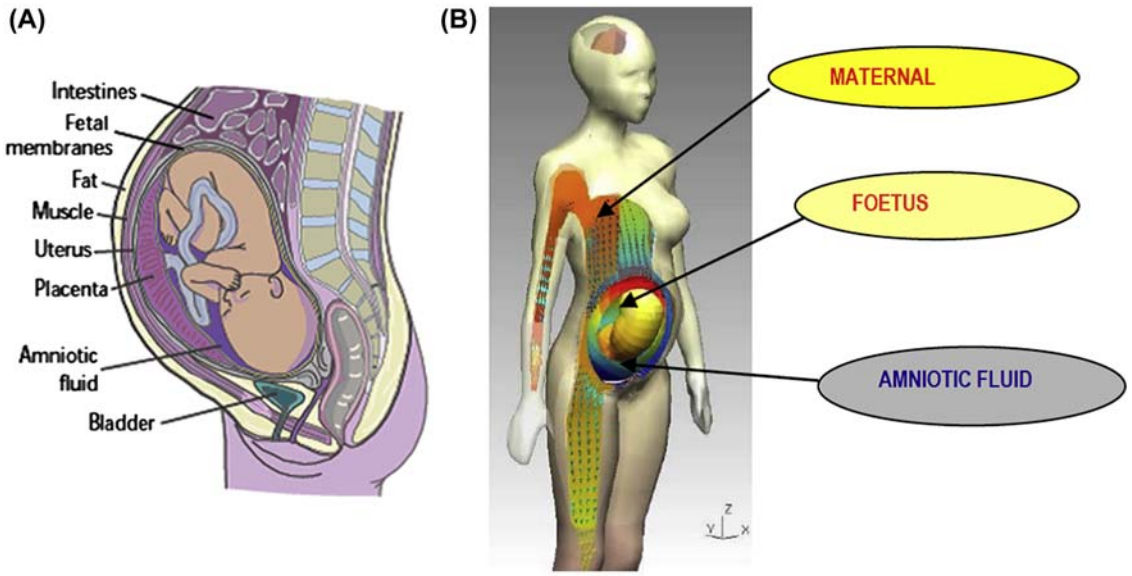

FIGURE 7.10 A view to the calculation domain. (A) Different tissues; (B) division of maternal abdomen into equivalent subdomains.

This book belongs to Central Library BADJI Mokhtar-ANNABA UNIVERSITY
Copyright Elsevier 2024

The fetal length change is greatest in the second trimester, whereas fetal weight variation is greatest in the final weeks of development. Therefore, the fetus is free to move inside the maternal abdomen, mostly until the 24th week. Since then, the movement is more constrained. Fig. 7.11 shows a general 3D view of 1.7 m tall at 26th week of pregnancy (fetus in the cephalic position).

Both cephalic and breech position of the fetus are taken into account within this model.

At LFs, adopting the quasistatic approximation, the body dimensions become electrically short, i.e., negligible when compared with the external field wavelength.

Furthermore, constant values of σ and ε are assumed within a subdomain and the static approximation for the ELF exposure model can be formulated via the Laplace equation:

$$\nabla[(\sigma + j\omega\varepsilon)\nabla\varphi] = 0 \tag{7.13}$$

where φ is the scalar electric potential, while ε and σ stand for the medium permittivity and conductivity, respectively, and $\omega = 2\pi f$ is the operating frequency.

The internal current density is expressed via the scalar potential through the following constitutive equation:

$$\overrightarrow{J} = -\sigma\nabla\varphi \tag{7.14}$$

To solve the Laplace Eq. (7.13) the corresponding air−body interface conditions have to be specified.

In addition to interface conditions (Gonzalez et al., 2008; Peratta et al., 2010), certain boundary conditions have to be specified:

$$\varphi = \overline{\phi} \text{ on } \Gamma 1 \text{ and } \frac{\partial\varphi}{\partial x_j} n_j = \frac{\partial\overline{\phi}}{\partial n_j} \text{ on } \Gamma 2 \tag{7.15}$$

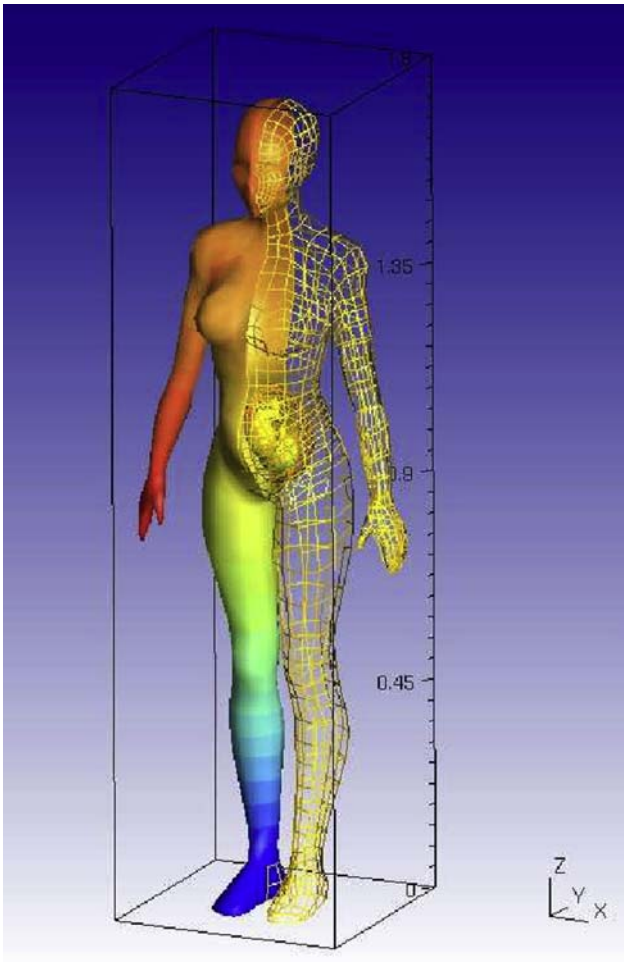

FIGURE 7.11 A 3D view of the model at 26th week of pregnancy (cephalic presentation).

This book belongs to Central Library BADJI Mokhtar-ANNABA UNIVERSITY
Copyright Elsevier 2024

The computational domain is regarded as piecewise homogeneous and is decomposed into an assembly of N homogeneous subdomains Γ_k ($k = 1, m$), where Γ_1 and Γ_2 form the domain boundary.

Utilizing the Green's theorem, the following integral representation for a subdomain yields (Poljak et al., 2014):

$$c(\xi)\varphi(\xi) + \int_{\Gamma_k} \varphi \frac{\partial \varphi^*}{\partial n} d\Gamma = \int_{\Gamma_k} \frac{\partial \varphi}{\partial n} \varphi^* d\Gamma \tag{7.16}$$

where ϕ^* is the 3D fundamental solution of Laplace equation,$\partial\varphi^*/\partial n$ is the derivative in normal direction to the boundary, and $c(\xi)$ is the geometrically dependent free term accounting for the Cauchy-type singularity of the integral on the left-hand side.

7.4.1 Boundary Element Solution

Discretizing Eq. (7.16) with N_k elements leads to an integral expression:

$$c_i\varphi_i + \sum_{j=1}^{N_k} \int_{\Gamma_{k,j}} \varphi \frac{\partial \varphi^*}{\partial n} d\Gamma = \sum_{j=1}^{N_k} \int_{\Gamma_{k,j}} \frac{\partial \varphi}{\partial n} \varphi^* d\Gamma \tag{7.17}$$

where i stands for the source point and $\Gamma_{k,j}$, represents the jth boundary element of Γ_k.

The actual implementation is based on the isoparametric approach with quadratic interpolation functions defined for triangular elements.

More mathematical details on the actual BEM procedure can be found elsewhere, i.e., in Poljak (2007).

The sparse and highly banded resulting system of equations is one of the main advantages of the domain decomposition technique, in addition to its capabilities in dealing with piecewise homogeneous material properties.

The electric field over a flat ground plane is assumed to be vertical and uniform near the ground level; the human body is located between the parallel circular plate electrodes, in the middle of the lower one. A calculation domain with the associated boundary conditions is shown in Fig. 7.12.

The lower plate electrode represents the ground zero potential, whereas the upper plate electrode is at the potential of a HV power line. Three different conductivity scenarios, as shown in Table 7.1, are used in this work (Gonzalez et al., 2008).

The multidomain BEM (Poljak, 2007) has been applied to solve the Laplace equation and determine internal currents, potentials, and electric fields.

7.4.2 Computational Examples

Fig. 7.13 shows a lateral view of the sliced pregnant woman model at 8th, 13th, 26th, and 38th gestational weeks. The direction of the electric field in the maternal tissues is assigned with black arrows and the isolines represent the related scalar potential.

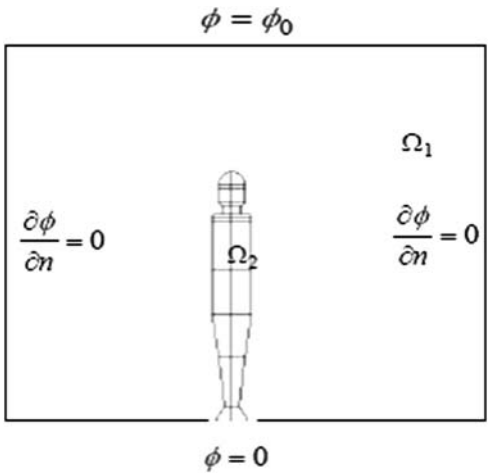

FIGURE 7.12 The calculation domain with the associated boundary conditions.

This book belongs to Central Library BADJI Mokhtar-ANNABA UNIVERSITY
Copyright Elsevier 2024

TABLE 7.1 Conductivity Scenarios

Scenario	Conductivity [S/m]	Week 8	Week 13	Week 26	Week 38
1	σ_f	0.23	0.23	0.23	0.23
	σ_{AF}	1.28	1.28	1.27	1.10
	σ_m	0.20	0.20	0.20	0.20
2	σ_f	0.996	0.996	0.574	0.574
	σ_{AF}	1.70	1.70	1.64	1.64
	σ_m	0.52	0.52	0.52	0.52
3	σ_f	0.732	0.732	0.396	0.396
	σ_{AF}	1.70	1.70	1.64	1.64
	σ_m	0.17	0.17	0.17	0.17

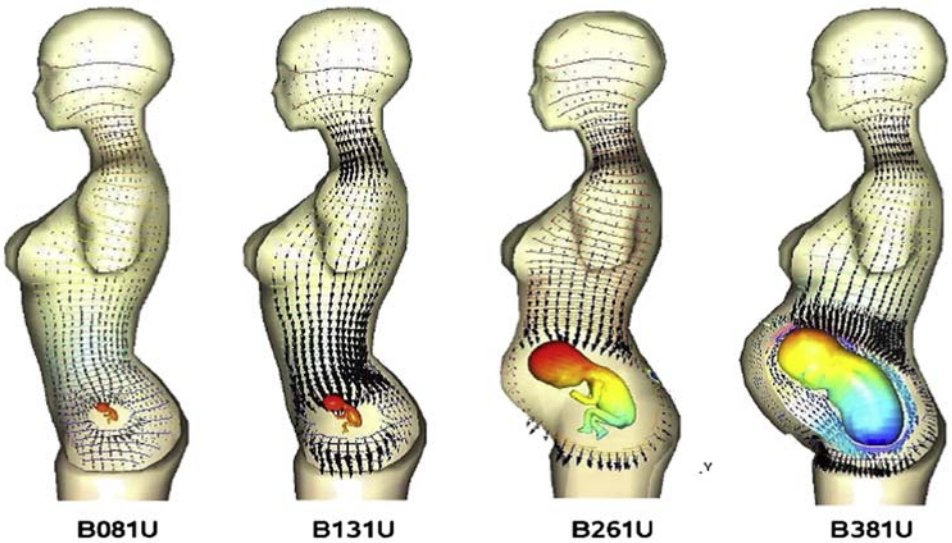

FIGURE 7.13 Lateral view of the pregnant woman at 8th, 13th, 26th, and 38th gestational weeks (breech presentation).

Fig. 7.14 shows a view to the sliced model of the pregnant woman/fetus with the electric field/scalar potential lines for the fetus in cephalic and breach presentation, respectively.

Observing the results presented in Figs. 7.13 and 7.14 it is visible that the uterus, because of its higher conductivity comparing to the maternal tissue, focuses the field lines.

The maximal value of current density is induced at the eighth gestational week and decreases progressively as the fetus develops due to following reasons. First, both the fetus and AF conductivity decrease with age. Second, as the fetus grows, the extremities drawn in toward the center of the chest and head tucked down to the chest. Thus, the fetus surface is getting smoother and the cross-sectional area becomes more regular.

Fig. 7.15 show the mean, maximum, and minimum values of current density calculated in the fetus at different weeks of pregnancy.

The induced current density decreases with age because of the increasing uniformity of the fetus model, i.e., the smoother the geometry, the less fluctuations in the results are expected. The maximum value of current density in the fetus occurs during the eighth gestation week for all conductivity scenarios.

Another body part with high current density is in the mother's brain and neck. Maximum value of internal current density in the brain decreases from 0.43 to 0.41 mA/m^2 from week 8 to week 38. As expected, this value is not sensitive to the different conductivity scenarios related to pregnancy.

This book belongs to Central Library BADJI Mokhtar-ANNABA UNIVERSITY Copyright Elsevier 2024

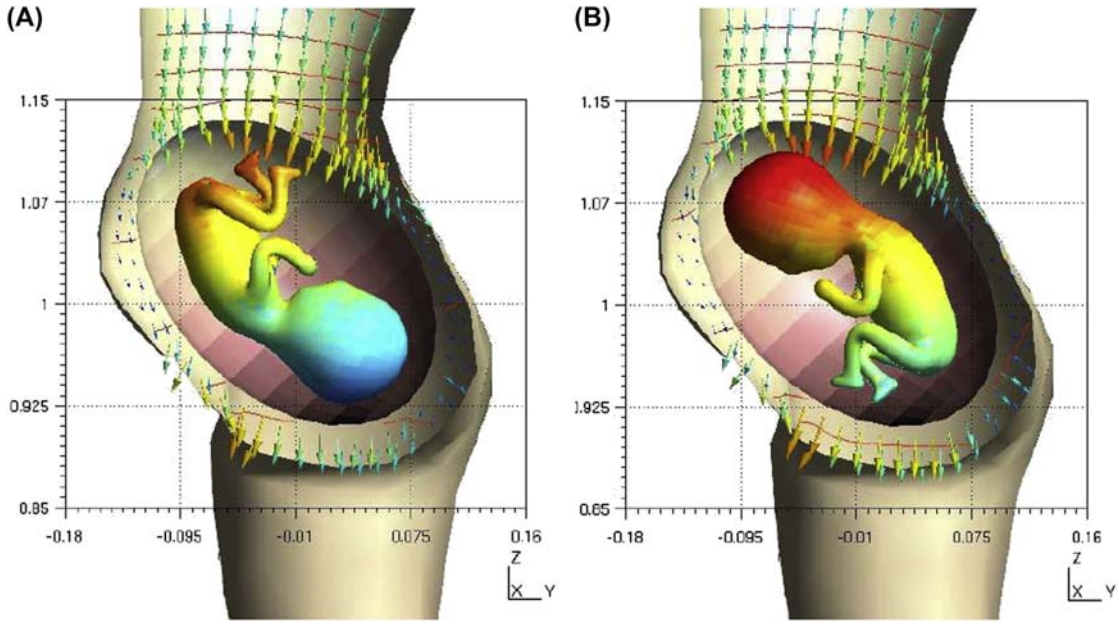

FIGURE 7.14 Lateral view of the pregnant woman at 26th gestational week. (A) Fetus in the cephalic presentation; (B) fetus in the breach presentation.

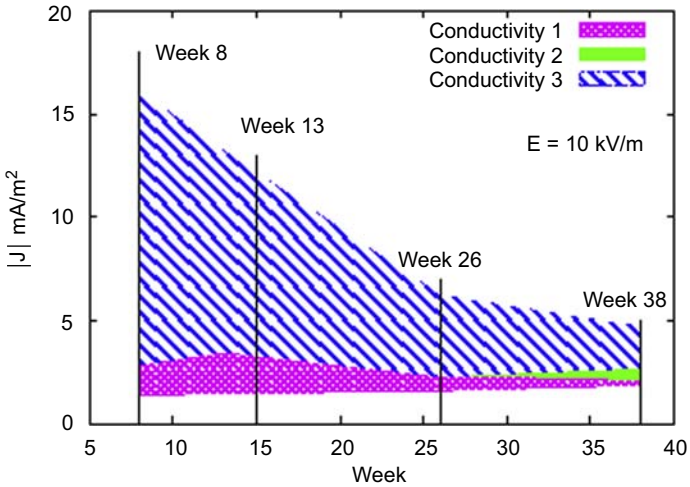

FIGURE 7.15 Mean current density in the fetus during the pregnancy for different conductivity scenarios.

Furthermore, in all conductivity scenarios the current density in breech configuration is higher than in the cephalic. This effect becomes less evident in the final pregnancy stage (38th week). In particular, for a given exposure, the maximum value of the current density induced in the fetus is during the eighth gestational week. In particular, the maximum current density obtained in the fetus for an incident external field $E = 10$ kV/m is 7.4 mA/m^2, whereas the maximum value recommended for public exposure by ICNRP (2010) is 2 mA/m^2.

7.5 EXPOSURE TO HIGH-FREQUENCY ELECTROMAGNETIC RADIATION: THE HUMAN EYE EXPOSED TO PLANE WAVE

This section deals with the human eye exposure to a plane wave. As the eye exposed to plane wave represents an exterior field problem (unbounded electromagnetic scattering problem) the hybrid BEM/FEM with edge elements (Poljak et al., 2014) is used to calculate corresponding internal fields.

This book belongs to Central Library BADJI Mokhtar-ANNABA UNIVERSITY
Copyright Elsevier 2024

Furthermore, in the frequency range from 1 to 2 GHz, the absorbed electromagnetic energy is concentrated in the lens area of an eye, whereas at frequencies between 2 and 6 GHz, the highest concentrations of the energy are in the vitreous body.

The use of imaging techniques, such as MRI, UBM, and CT, provides data on the eye geometry is available (Singh et al., 2006; Ishikawa and Schuman, 2004; Navarro, 2009). In this section 27 mm schematic eye is used as shown in the Fig. 7.16. The corneal surface is represented as follows (Navarro, 2009):

$$x_{\text{cor}}(y,z) = \frac{c_y y^2 + c_z z^2}{1 - \sqrt{1 - (1+Q_y)c_y^2 y^2 - (1+Q_z)c_z^2 z^2}} \tag{7.18}$$

where x_{cor} is the distance along the optical axis, Q_y and Q_z are conic constants, and $c_y = 1/R_y$, $c_z = 1/R_z$. R_y and R_z are orthogonal corneal curvatures.

Similar to Ishikawa and Schuman (2004), $R_y = R_z = 7.83$ mm is used, whereas the conic constant is $Q_y = Q_z = -0.66$ mm. The geometrical shape of the lens is calculated according to Diaz et al. (2007):

$$\eta(x,y,z) = 1.371 + n_1(\cos n_2 x - 1) + n_3 \sin n_4 x + n_5\left(y^2 + z^2\right) \tag{7.19}$$

where parameters n_1, n_2, n_3, n_4, and n_5 are age dependent and can be calculated as follows:

$$\begin{aligned} n_1 &= 0.0394 - 0.000355 \times \text{age} \\ n_2 &= 1.238 - 0.00561 \times \text{age} \\ n_3 &= 0.1092 - 0.00077 \times \text{age} \\ n_4 &= 0.79 - 0.00312 \times \text{age} \\ n_5 &= -0.0023 + 1.32 \times 10^{-5} \times \text{age} \end{aligned} \tag{7.20}$$

where parameter *age* is given in years, and Eq. (7.19) is solved numerically for $\mu(x, y, z) = 1.371$ to obtain the outer shape of the lens.

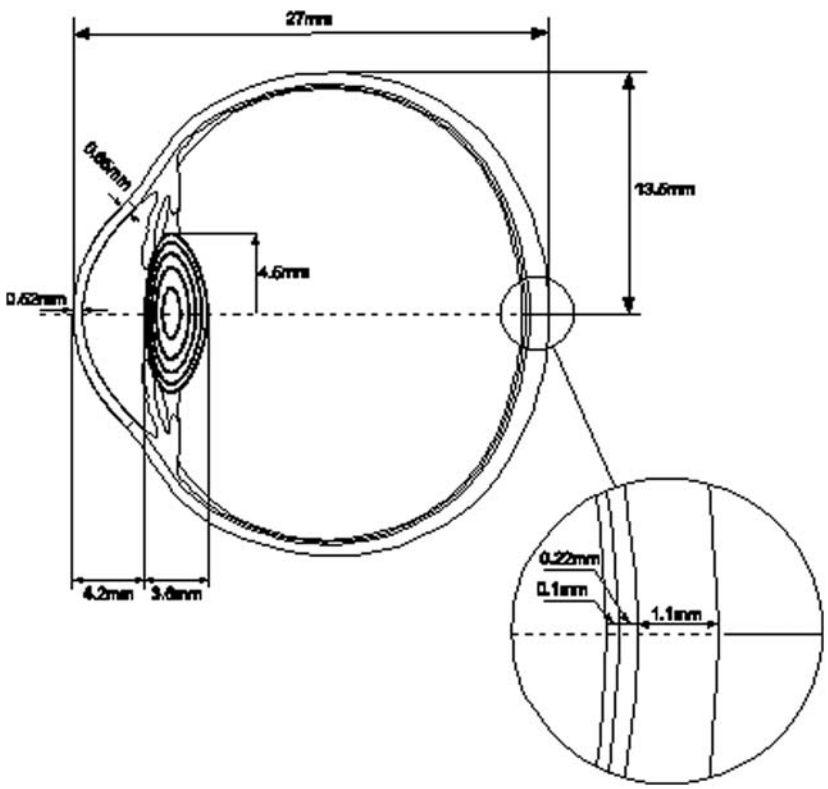

FIGURE 7.16 The 27-mm eye model. *Dashed line* represents the optical axis of an eye.

This book belongs to Central Library BADJI Mokhtar-ANNABA UNIVERSITY
Copyright Elsevier 2024

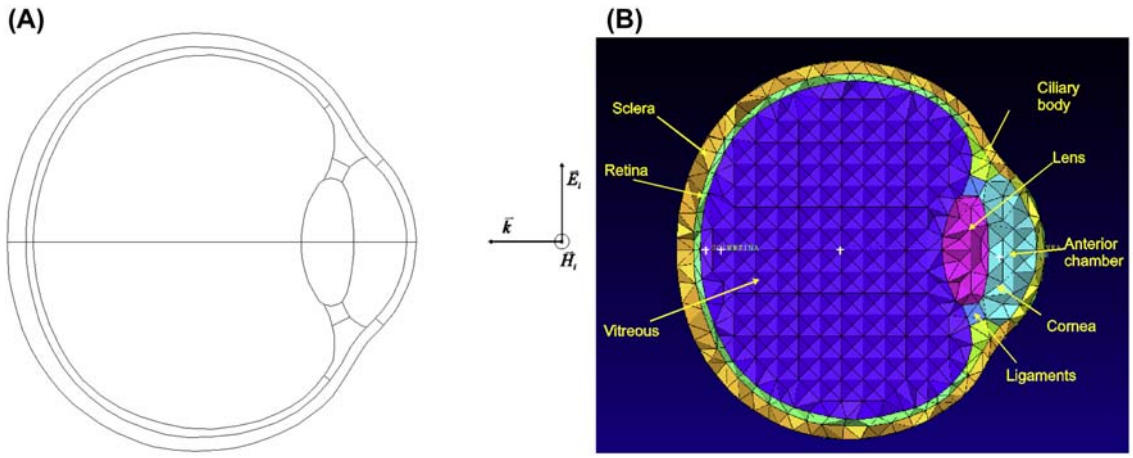

FIGURE 7.17 (A) Model of the eye exposed to plane wave (B) Meshing detail, an eye is modeled with 36,027 tetrahedral elements.

Plane wave incident on the corneal region of eye is treated as unbounded scattering problem as shown in Fig. 7.17A. According to Stratton−Chu formulation, the external time-harmonic electric is represented by means of the following boundary integral equation (Poljak et al., 2014):

$$\alpha\vec{E} = \vec{E}_{i'} + \oint_{\partial V'} \vec{n}' \times \left(\nabla' \times \vec{E}\right) G dS' + \oint_{\partial V'} \left[\left(\vec{n}' \times \vec{E}\right) \times \nabla' G + \left(\vec{n}' \cdot \vec{E}\right) G\right] dS' \tag{7.21}$$

where $\vec{n}'$ is an outer normal to surface $\partial V'$ bounding the volume V and α is the solid angle subtended at an observation point.

Furthermore, G represents the fundamental solution of the Helmholtz equation:

$$\nabla^2 G + k^2 G = -\delta \tag{7.22}$$

By substituting expressions

$$\nabla' \times \vec{E} = -j\omega\mu\vec{H} = k_B\vec{H} \tag{7.23}$$

$$\vec{n}' \cdot \vec{E} = -\frac{1}{\sigma + j\omega\varepsilon}\nabla \cdot \left(\vec{n} \times \vec{H}\right) = \frac{1}{k_A}\nabla \cdot \left(\vec{n} \times \vec{H}\right) \tag{7.24}$$

into Eq. (7.21) it follows:

$$\alpha\vec{E} = \vec{E}_i + \oint_{\partial V'} \vec{n}' \times k_B\vec{H} G dS' + \oint_{\partial V'} \left[\left(\vec{n}' \times \vec{E}\right) \times \nabla' G - \frac{1}{k_A}\nabla \cdot \left(\vec{n}' \times \vec{H}\right) G\right] dS' \tag{7.25}$$

The set of governing equations for the interior of the eye containing inhomogeneous regions can be derived starting from the time-harmonic Maxwell's equation:

$$\nabla \times \vec{E} = -j\omega\mu\vec{H} = k_B\vec{H} \tag{7.26}$$

Dividing Eq. (7.26) by k_B and taking the curl operator, one obtains

$$\nabla \times \left(\frac{1}{k_B}\nabla \times \vec{E}\right) = \nabla \times \vec{H} = (\sigma + j\omega\varepsilon)\vec{E} = k_A\vec{E} \tag{7.27}$$

Note that generation of hot spots generation inside the brain is also discussed elsewhere, e.g., in Poljak et al. (2014) and Nedelec (1980).

7.5.1 Boundary Element Solution

Applying the weighted residual approach to Eq. (7.27) and introducing the vector test functions $\vec{W}_i$ the following integral representation is obtained:

$$\int_{V'} \left[\nabla \times \left(\frac{1}{k_B}\nabla \times \vec{E}\right) - k_A\vec{E}\right] \cdot \vec{W}_i dV' = 0 \tag{7.28}$$

This book belongs to Central Library BADJI Mokhtar-ANNABA UNIVERSITY
Copyright Elsevier 2024

Taking the standard vector identity valid for any two vectors: $\vec{a}, \vec{b}$, i.e., $\nabla\cdot\left(\vec{a}\times\vec{b}\right) = \vec{b}\cdot\nabla\times\vec{a} - \vec{a}\cdot\nabla\times\vec{b}$, Eq. (7.28) becomes

$$\int_{V'}\left[\frac{1}{k_B}\left(\nabla\times\vec{W}_i\right)\cdot\left(\nabla\times\vec{E}\right) - k_A\vec{W}_i\cdot\vec{E}\right]dV' = \oint_{\partial V'} d\vec{S}'\cdot\vec{W}_i\times\vec{H} \tag{7.29}$$

Utilizing the Galerkin−Bubnov procedure, i.e., the weight functions $\vec{W}_i$ are equal to interpolation functions, i.e.,

$$\vec{E} = \sum_j \vec{W}_j\delta_j e_j \tag{7.30}$$

$$\vec{H} = \sum_j \vec{W}_j\delta_j h_j \tag{7.31}$$

where e_j, h_j are the unknown coefficients associated with each edge of the model.

The coefficient $\delta_j = \pm 1$ and it is equal to 1 if the local edge direction coincides with chosen global edge direction, otherwise it is -1.

Vector base shape function $\vec{W}_k$ is given by Liu et al. (2009):

$$\vec{W}_k = f_i\nabla f_j - f_j\nabla f_i \tag{7.32}$$

where f_i, f_j are regular first-order barycentric shape functions.

Inserting Eqs. (7.30) and (7.31) into (7.25) yields the system of equations related to edges at bounding surface of the problem:

$$[A_b]\{e_b\} = \{e_I\} + [B_b]\{h_b\} \tag{7.33}$$

where e_b, h_b are unknown coefficients associated with boundary surface of the scattering problem, e_I are known coefficients calculated from the incident field, and elements of dense matrices $[A_b]$, $[B_b]$ can be evaluated from Eq. (7.25).

Furthermore, from Eq. (7.29) the following matrix equation is obtained:

$$[A_f]\{e\} = [B_f]\{h_b\} \tag{7.34}$$

where $\{e\}$ is the vector of unknown coefficients associated with every edge in the model.

As Eq. (7.25) is expressed in terms of tangential components of $\vec{E}$ and $\vec{H}$ and in the right-hand side of Eq. (7.29), tangential components of $\vec{H}$ appear, and Eqs. (7.33) and (7.34) are then combined into a single matrix whose solution yields the set of unknown coefficients $\{e\}$ and consequently the electric field $\vec{E}$.

Once the electric field $\vec{E}$ is determined, SAR is computed as follows:

$$\mathrm{SAR} = \frac{\sigma}{2\rho}\vec{E}\cdot\vec{E}^* = \frac{\sigma}{2\rho}\left|\vec{E}\right|^2 \tag{7.35}$$

where σ is conductivity, ρ is mass density, and $\vec{E}^*$ is the complex conjugate of the electric field $\vec{E}$. Applying the standard weighted residual approach to Eq. (7.35)

$$\int_{V'}\left[\mathrm{SAR} - \frac{\sigma}{2\rho}\left|\vec{E}\right|^2\right]\cdot f_i dV' = 0 \tag{7.36}$$

the global matrix equation is obtained.

Solving the global matrix equation provides the value of SAR at each node of the computational domain.

7.5.2 Finite Element Solution of Bioheat Transfer Equation

The temperature rise in a tissue caused by exposure to external HF fields is obtained by solving the bioheat transfer equation:

$$\nabla\cdot(k\nabla T) + \rho_b c_b w(T_a - T) + Q_m + \rho\cdot\mathrm{SAR} = 0 \tag{7.37}$$

by means of FEM.

The integral formulation of (Eq. 7.37) convenient for the implementation of FEM is (Poljak et al., 2017)

$$\int_{V'}[k\nabla f_j\cdot\nabla T + \rho_b c_b w\cdot T\cdot f_j]dV' = \int_{V'}(\rho_b c_b w\cdot T_a + Q_m + \rho\cdot\mathrm{SAR})\cdot f_j dV' + \oint_{\partial V'} kf_j\nabla T\cdot d\vec{S} \tag{7.38}$$

This book belongs to Central Library BADJI Mokhtar-ANNABA UNIVERSITY
Copyright Elsevier 2024

The appropriate boundary condition at the interface between skin and air is

$$q = H(T_s - T_a) \tag{7.39}$$

where q is the heat flux density:

$$q = -\lambda \frac{\partial T}{\partial n} \tag{7.40}$$

while H, T_s, and T_a denote, respectively, the convection coefficient, the temperature of the skin, and the temperature of the air.

The standard finite element discretization of Helmholtz equation yields the following matrix equation:

$$[K]\{T\} = \{M\} + \{P\} \tag{7.41}$$

where $[K]$ is the finite element matrix given by

$$K_{ji} = \int_{\Omega_e} \nabla f_j(\lambda \nabla f_i) d\Omega_e + \int_{\Omega_e} W_b C_{pb} f_j f_i d\Omega_e \tag{7.42}$$

while $\{M\}$ denotes the flux vector:

$$M_j = \int_{\Gamma_e} \lambda \frac{\partial T}{\partial n} f_j d\Omega_e \tag{7.43}$$

and $\{P\}$ stands for the source vector:

$$P_j = \int_{\Omega_e} (W_b C_{pb} T_a + Q_m + \rho \cdot \mathrm{SAR}) \cdot f_j d\Omega_e \tag{7.44}$$

More details can be found elsewhere, e.g., in Poljak et al. (2017).

7.5.3 Computational Examples

Figs. 7.18 and 7.19 show the numerical results obtained via the hybrid BEM/FEM procedure for the electric field induced in the eye because of the incident plane wave with power density of 10 W/m^2.

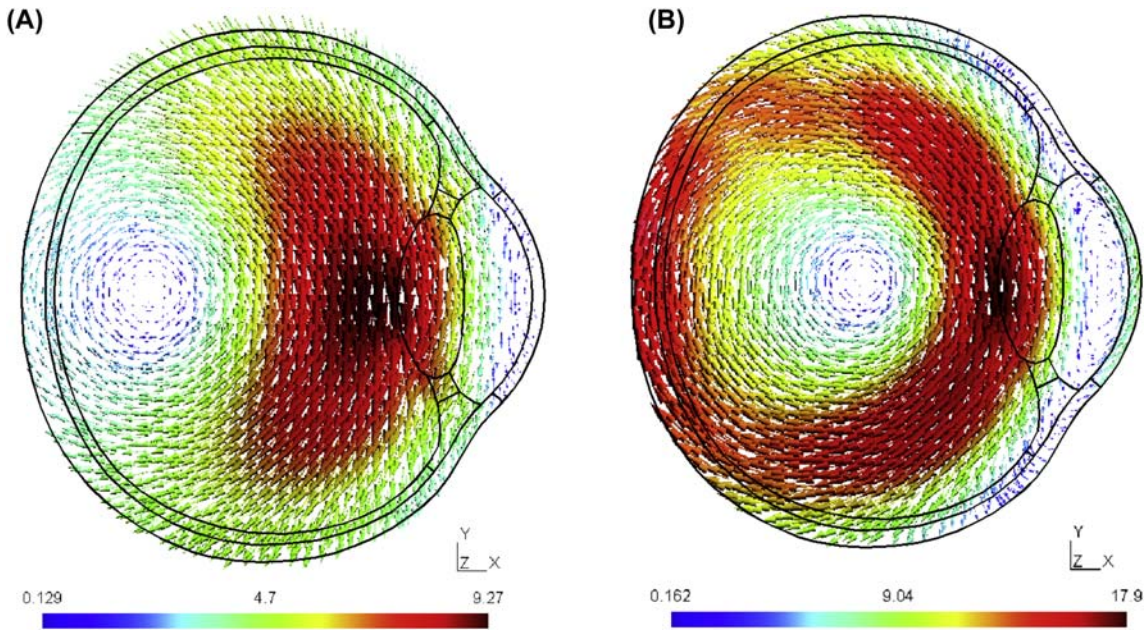

FIGURE 7.18 Vector plot of electric field in xy plane inside an eye induced by plane wave of power density 10 W/m^2 at frequencies (A) 1 GHz (B) 2 GHz.

This book belongs to Central Library BADJI Mokhtar-ANNABA UNIVERSITY
Copyright Elsevier 2024

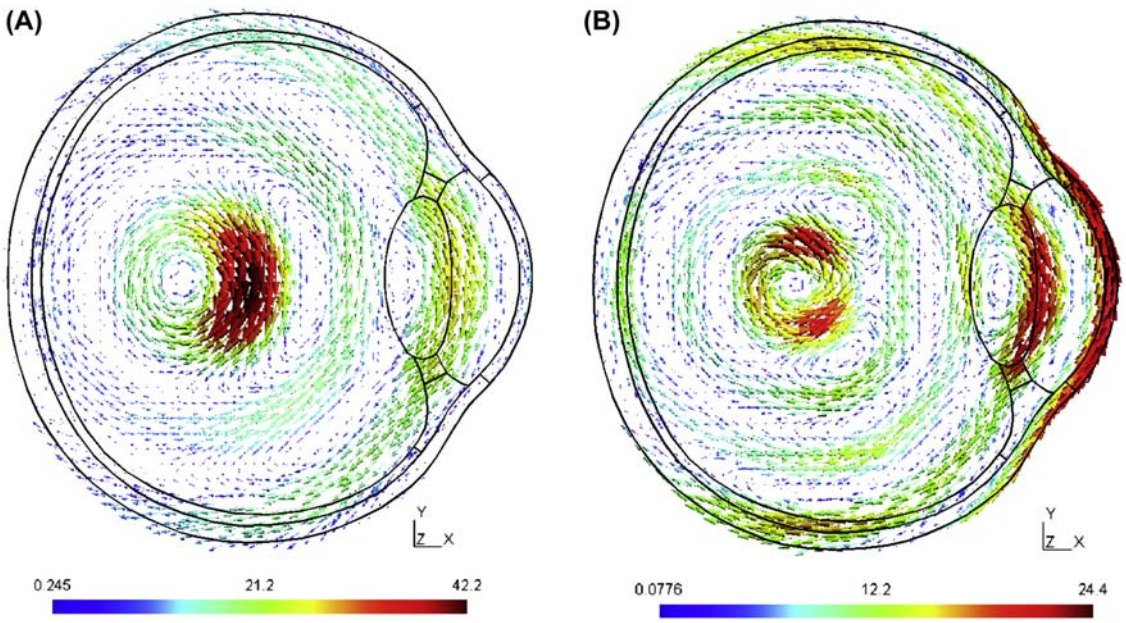

FIGURE 7.19 Vector plot of electric field in xy plane inside an eye induced by plane wave with power density 10 W/m^2 at frequencies (A) 4 GHz (B) 6 GHz.

The corresponding SAR results are shown in Figs. 7.20 and 7.21. The results for SAR averaged over the whole eye are given in Table 7.2. The results shown in Fig. 7.21 are in a satisfactory agreement with the results available in Hirata (2005).

It can be seen that the hot spot formation occurs below the frequencies of 6 GHz. At higher frequencies the region where the electromagnetic energy is concentrated is the surface of an eye. In addition, the whole eye averaged SAR values stay below exposure limits proposed by ICNIRP (1998).

In addition to handle the electromagnetic scattering from the human eye an unbounded problem, the hybrid approach provides the successful treatment of tissue inhomogeneities. In addition, because of the singularities arising from the SIE formulation, an adaptive contour integration technique is used (Dodig et al., 2012). This technique is accurate, fast, and immune to the proximity of the observation point.

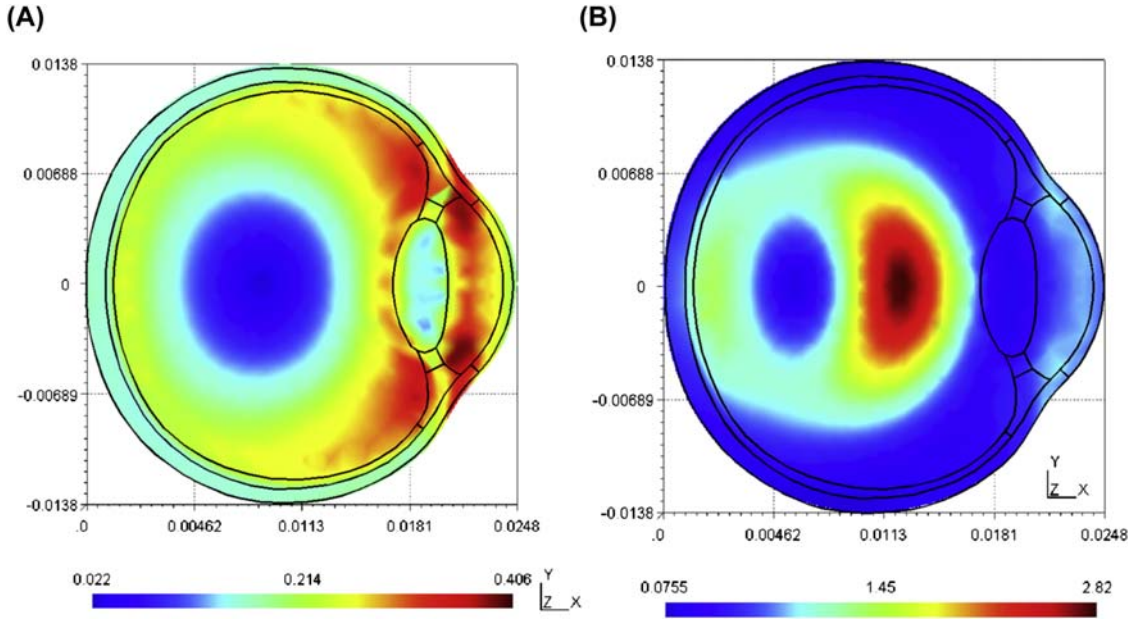

FIGURE 7.20 Computed specific absorption rate in the eye induced by plane wave of power density 10 W/m^2 at frequency (A) 1 GHz (B) 2 GHz.

This book belongs to Central Library BADJI Mokhtar-ANNABA UNIVERSITY Copyright Elsevier 2024

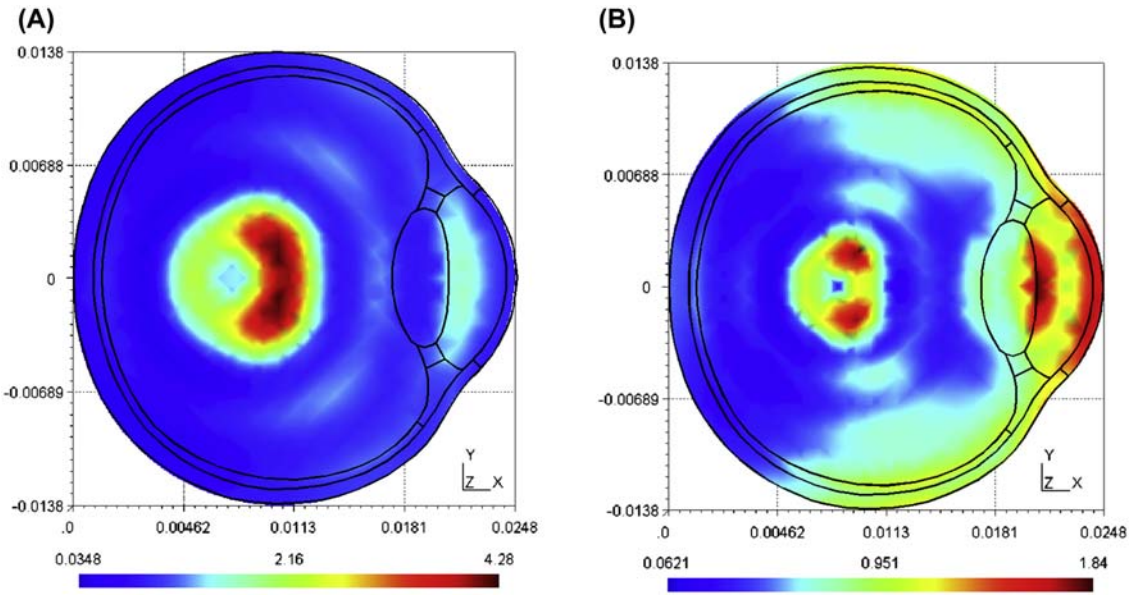

FIGURE 7.21 Computed specific absorption rate in the eye induced by plane wave of power density 10 W/m^2 at frequency (A) 4 GHz (B) 6 GHz.

TABLE 7.2 Whole Eye Averaged Specific Absorption Rate (SAR) at Frequencies of 1 GHz, 2 GHz, 4 GHz, and 6 GHz

Frequency [GHz]	SAR [W/kg]
1	0.3352
2	0.6189
4	1.2617
6	1.0689

7.6 EXPOSURE TO HIGH-FREQUENCY ELECTROMAGNETIC RADIATION: THE HUMAN BRAIN EXPOSED TO PLANE WAVE

The homogeneous lossy dielectric model of the human brain exposed to HF radiation is based on the SIE approach (Cvetkovic and Poljak, 2015; Cvetković et al., 2016). The formulation can be readily derived from the equivalence theorem and by using the appropriate interface conditions for the electric and/or magnetic field, as depicted in Fig. 7.22.

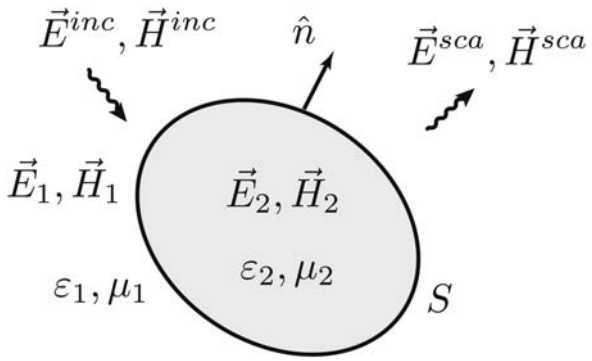

FIGURE 7.22 The brain represented by a lossy homogeneous dielectric.

This book belongs to Central Library BADJI Mokhtar-ANNABA UNIVERSITY
Copyright Elsevier 2024

The lossy homogeneous object representing the brain is illuminated by the incident electromagnetic field ($\vec{E}^{\text{inc}}$; $\vec{H}^{\text{inc}}$).

7.6.1 Dosimetry

Using the equivalence theorem, two problems are formulated, in terms of the equivalent electric and magnetic current densities $\vec{J}$ and $\vec{M}$ existing at the surface S, one for the region 1 (exterior to dielectric) and other for the region 2 (inside the dielectric) (Cvetkovic and Poljak, 2015; Cvetković et al., 2016).

The boundary conditions at the surface S are satisfied by introducing equivalent surface currents $\vec{J}_2 = -\vec{J}_1$ and $\vec{M}_2 = -\vec{M}_1$.

Taking the same procedure for the interior equivalent problem yields the other homogeneous domain introducing the equivalent surface currents $\vec{J}_1$ and $\vec{M}_1$.

Performing some mathematical manipulations, the following set of integral equations is obtained (Cvetkovic and Poljak, 2015; Cvetković et al., 2016):

$$j\omega\mu_n \iint_S \vec{J}\left(\vec{r}'\right) G_n\left(\vec{r}, \vec{r}'\right) dS' - \frac{j}{\omega\varepsilon_n} \iint_S \nabla'_S \cdot \vec{J}\left(\vec{r}\right) \nabla G_n\left(\vec{r}, \vec{r}'\right) dS' + \iint_S \vec{M}\left(\vec{r}\right) \times \nabla' G_n\left(\vec{r}, \vec{r}'\right) dS' = \begin{cases} \vec{E}^{\text{inc}}, & n = 1 \\ 0, & n = 2 \end{cases} \tag{7.45}$$

where the Green's function for the homogeneous medium is given by

$$G_n\left(\vec{r}, \vec{r}'\right) = \frac{e^{-jk_n R}}{4\pi R}; \quad R = \left|\vec{r} - \vec{r}'\right| \tag{7.46}$$

and R is the distance from the source to observation point, respectively, while k_n is the wave number of a medium n ($n = 1;\ 2$).

The set of the coupled SIEs Eq. (7.45) is solved by means of the MoM.

The brain model is assembled by using a freely available Google SketchUp rendering of the human brain as shown in Fig. 7.23A. A view to the triangular brain model mesh is shown in Fig. 7.23B.

The set of integral Eq. (7.2) is solved by MoM (reported elsewhere, e.g., in Cvetkovic and Poljak, 2015; Cvetković et al., 2016; Poljak et al., 2017).

As a first step, the equivalent electric and magnetic currents $\vec{J}$ and $\vec{M}$ in Eq. (7.45) are expressed by means of a linear combination of basis functions $\vec{f}_n$ and $\vec{g}_n$, respectively.

$$\vec{J}\left(\vec{r}\right) = \sum_{n=1}^{N} J_n \vec{f}_n\left(\vec{r}\right) \tag{7.47}$$

$$\vec{M}\left(\vec{r}\right) = \sum_{n=1}^{N} M_n \vec{g}_n\left(\vec{r}\right) \tag{7.48}$$

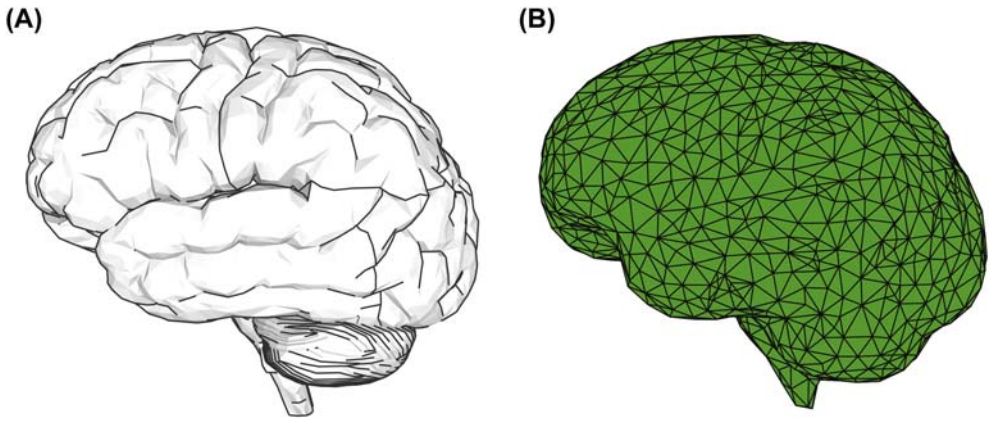

FIGURE 7.23 The human brain model for surface integral equation formulation. (A) Detailed 3D model from Google SketchUp. (B) Final model discretized using the triangular elements imported into MATLAB.

This book belongs to Central Library BADJI Mokhtar-ANNABA UNIVERSITY Copyright Elsevier 2024

where J_n and M_n are unknown coefficients, while N is the total number of triangular elements.

Applying the weighted residual approach, i.e., multiplying the integral Eq. (7.45) by the set of a test functions $\vec{f}_m$ and integrating over the surface S, performing some mathematical manipulations, it follows:

$$
\begin{aligned}
& j\omega\mu_i \sum_{n=1}^{N} J_n \iint_S \vec{f}_m\left(\vec{r}\right)\cdot \iint_{S'} \vec{f}_n\left(\vec{r}'\right) G_i dS' dS + \frac{j}{\omega\varepsilon_i}\sum_{n=1}^{N} J_n \iint_S \nabla_S \cdot \vec{f}_m\left(\vec{r}\right) \iint_{S'} \nabla'_S \cdot \vec{f}_n\left(\vec{r}'\right) G_i dS' dS \\
& \pm \sum_{n=1}^{N} M_n \iint_S \vec{f}_m\left(\vec{r}'\right)\cdot\left[\hat{n}\times \vec{g}_n\left(\vec{r}'\right)\right] dS + \sum_{n=1}^{N} M_n \iint_S \vec{f}_m\left(\vec{r}'\right)\cdot \iint_{S'} \vec{g}_n\left(\vec{r}'\right)\times \nabla' G_i dS' dS \\
& = \begin{cases} \iint_S \vec{f}_m\left(\vec{r}'\right)\cdot \vec{E}^{\text{inc}}\, dS, & i = 1 \\ 0, & i = 2 \end{cases}
\end{aligned}
\tag{7.49}
$$

where subscript i denotes the index of the medium. The details of the numerical solution procedure could be found elsewhere, e.g., in Poljak et al. (2017).

7.6.2 Computational Examples

Computational examples are related to the brain illuminated by a plane wave at $f = 900$ MHz and 1800 MHz, respectively. The brain surface is discretized using 696 triangular elements and 1044 edge elements while the corresponding brain parameters can be found in Poljak et al. (2017).

The power density of the incident plane wave is $P = 5$ mW/cm^2 (oriented perpendicular to the right side of the brain—positive x coordinate).

Figs. 7.24–7.27 show the SAR distribution and related temperature rise in the brain at $f = 900$ MHz and $f = 1800$ MHz for the case of horizontal and vertical polarization, respectively.

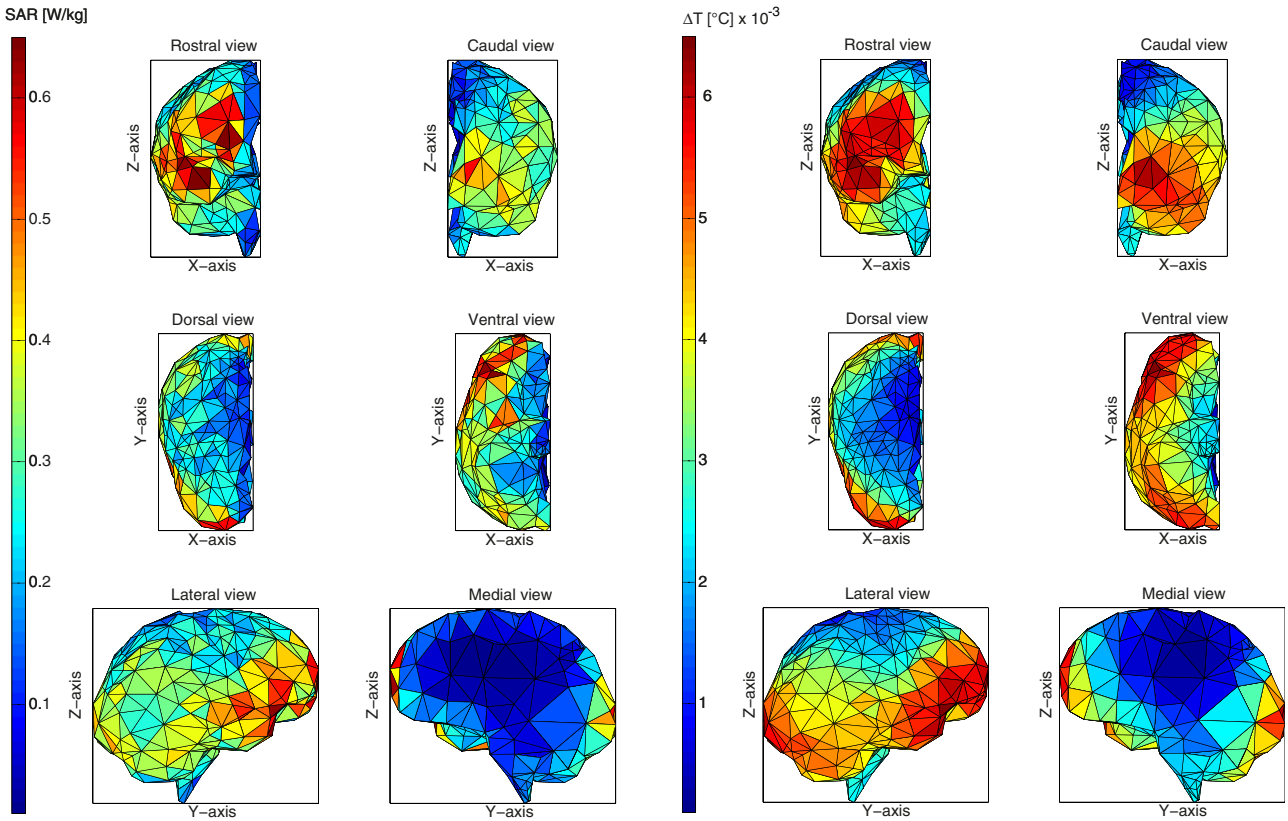

FIGURE 7.24 Specific absorption rate (SAR) distribution and temperature increase at $f = 900$ MHz—horizontal polarization.

This book belongs to Central Library BADJI Mokhtar-ANNABA UNIVERSITY
Copyright Elsevier 2024

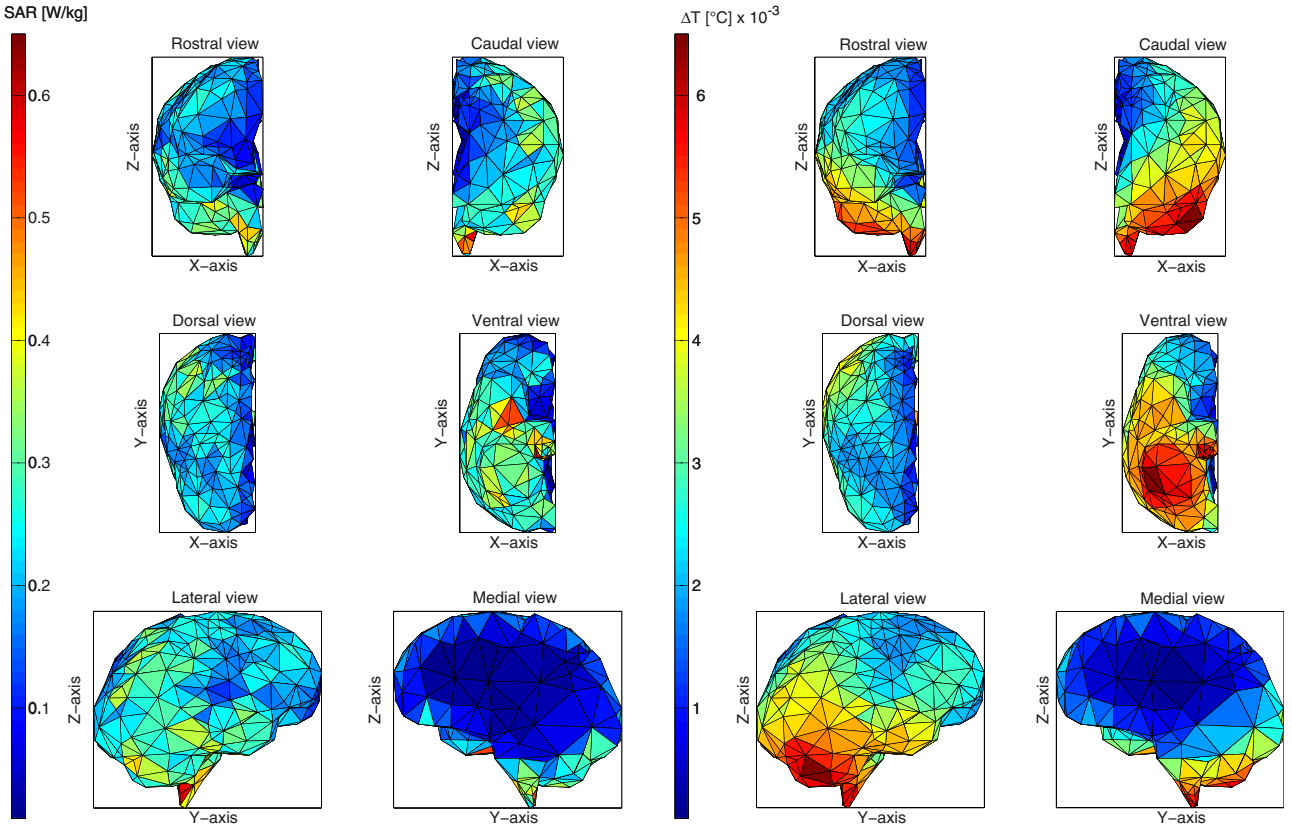

FIGURE 7.25 Specific absorption rate (SAR) distribution and temperature increase at $f = 900$ MHz—vertical polarization.

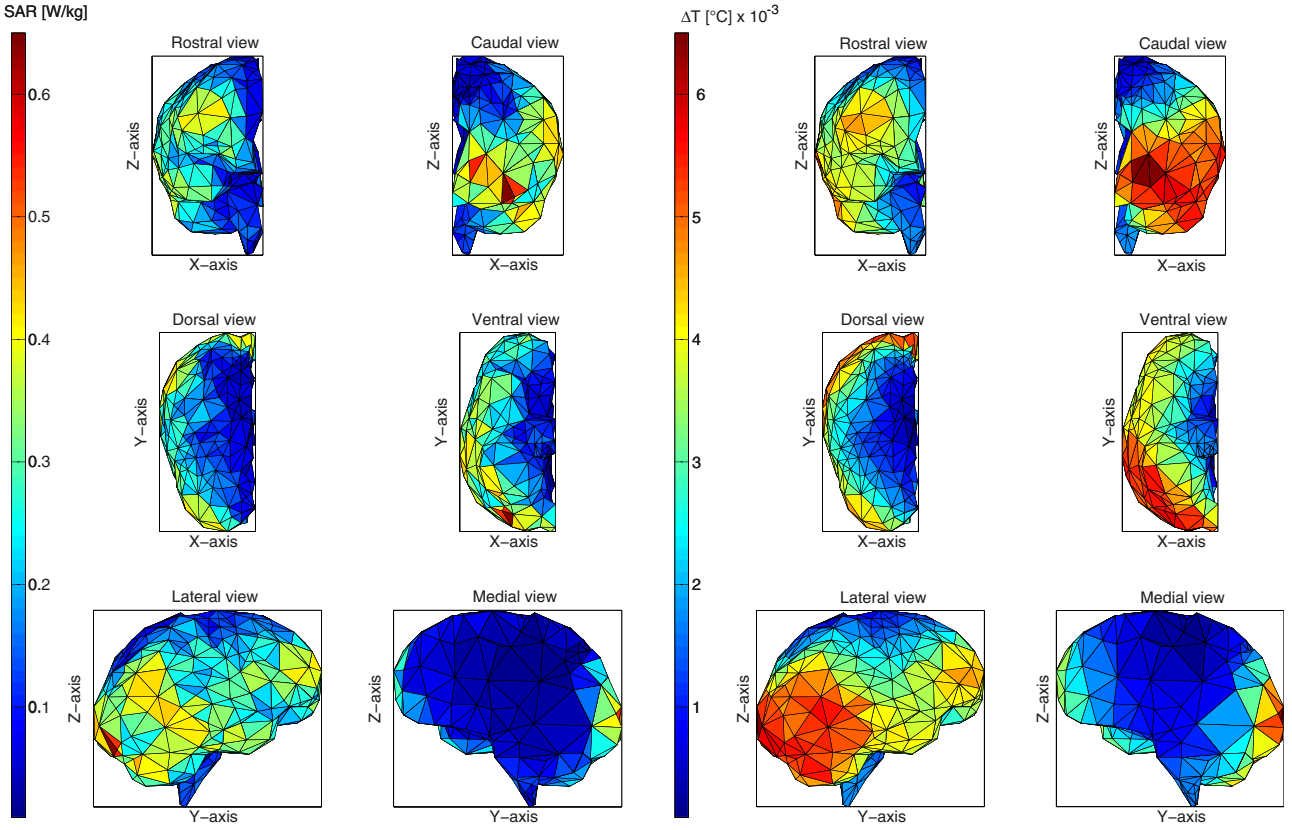

FIGURE 7.26 Specific absorption rate (SAR) distribution and temperature increase at $f = 1800$ MHz—horizontal polarization.

This book belongs to Central Library BADJI Mokhtar-ANNABA UNIVERSITY

Copyright Elsevier 2024

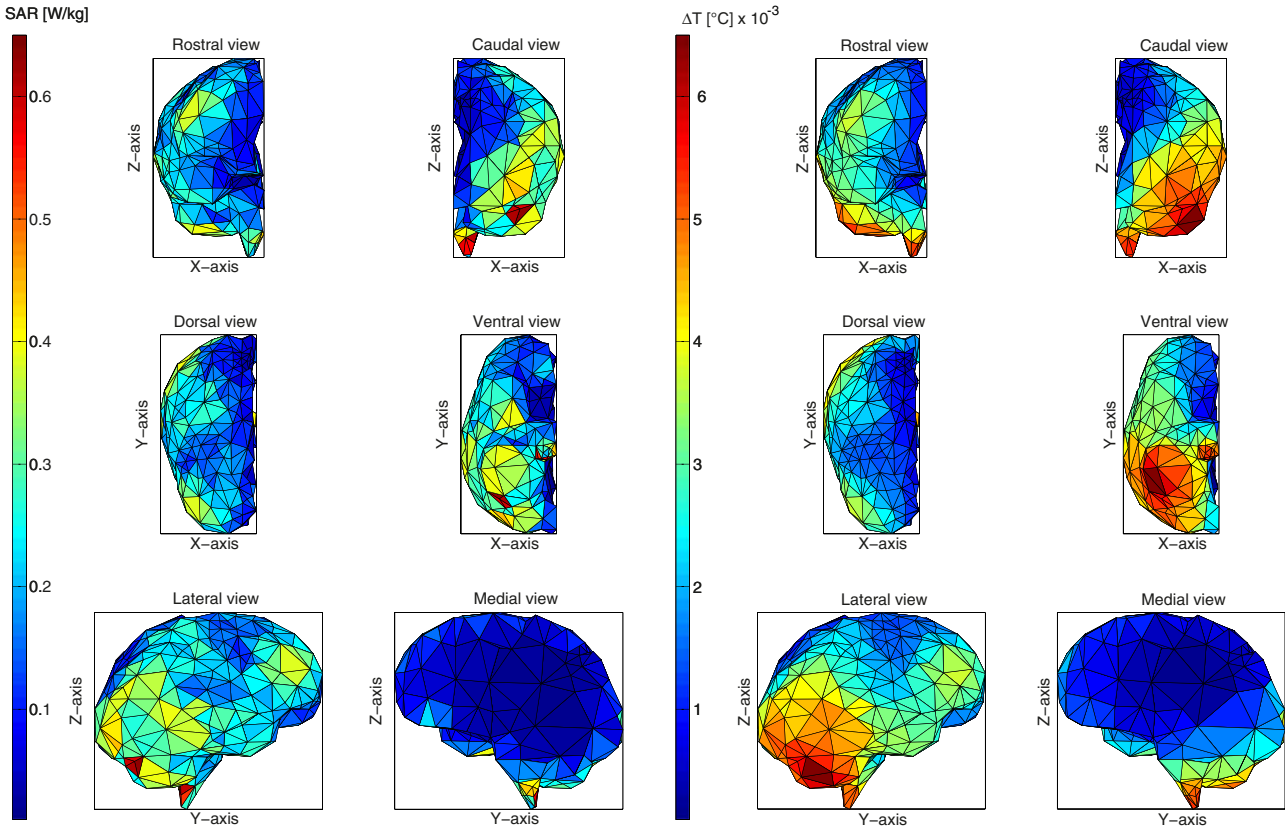

FIGURE 7.27 Specific absorption rate (SAR) distribution and temperature increase at $f = 1800$ MHz—vertical polarization.

The obtained peak and average SAR values for both polarization types and for $f = 900$ MHz and $f = 1800$ MHz are given in Table 7.3.

The obtained peak SAR values in the brain do not exceed the ICNIRP limits (1998) for localized SAR in the head averaged per 10 g of tissue (10 W/kg for the occupational exposure).

However, the exposure limit for the general public exposure limit (2 W/kg localized in the head and trunk) has been exceeded at $f = 1800$ MHz for both polarizations.

The whole brain averaged SAR at $f = 900$ MHz is 0.17 W/kg, which stays below the ICNIRP exposure limits for localized SAR in the head of 2 W/kg averaged per 10 g of tissue (Nielsen et al., 1996). The maximal temperature rise in the brain is found to be less than 0.01°C in this scenario.

TABLE 7.3 The Peak and Average Specific Absorption Rate (SAR) Values for Different Exposure Scenarios

	H		V	
	900 MHz	1800 MHz	900 MHz	1800 MHz
SAR_{max} [W/Kg]	0.856486	4.390451	0.866016	2.678407
SAR_{avg} [W/Kg]	0.174457	0.411736	0.158206	0.348032

H, horizontal polarization; *V*, vertical polarization.

This book belongs to Central Library BADJI Mokhtar-ANNABA UNIVERSITY

Copyright Elsevier 2024

7.7 EXPOSURE TO HIGH-FREQUENCY ELECTROMAGNETIC RADIATION: WHOLE BODY EXPOSED TO PLANE WAVE

7.7.1 Tensor Volume Integral Equation—Solution via Method of Moments

The whole body exposure to HF radiation can be analyzed via tensor integral equation (Poljak et al., 2016). The electric field induced inside the body exposed to the plane wave incident field E^i is governed by the tensor volume integral equation and is given by (Poljak et al., 2016)

$$\left[1+\frac{\tau(\vec{r})}{3j\varpi\varepsilon_0}\right]\vec{E}(\vec{r})-PV\int_v \tau(\vec{r})\vec{E}(\vec{r})\cdot\underline{G}((\vec{r},\vec{r}')dv') = \vec{E}^i(\vec{r}) \tag{7.50}$$

where PV stands for principal value and $\tau(\vec{r}) = \sigma + j\varpi[\varepsilon(\vec{r}) - \varepsilon_0]$.

Integral Eq. (7.50) is treated via MoM by discretizing the body into N subvolumes V_m by assuming E and τ to be constant within each cell. If $\vec{r}_m$ is the center of the mth cell, requiring that each scalar component of Eq. (7.50) be satisfied at $\vec{r}_m$, it follows

$$\left[1+\frac{\tau(\vec{r})}{3j\varpi\varepsilon_0}\right]E_{x_p}(\mathbf{r}_m)-\sum_{q=1}^{3}\left[\sum_{q=1}^{3}\tau(\vec{r})PV\int_{V_m}G_{x_px_q}(\vec{r}_m,\vec{r}')dv'\right]E_{x_q}(\vec{r}_n) = E_{x_p}(\vec{r}_m) \tag{7.51}$$

where $G_{x_px_q}$ is the tensor Green's function:

$$G_{x_px_q}\left(\vec{r},\vec{r}'\right) = -j\varpi\mu_0\left[\delta_{pq}+\frac{1}{k_0^2}\frac{\partial^2}{\partial x_p\partial x_q}\right]G_0\left(\vec{r},\vec{r}'\right), \quad p,q = 1,2,3 \tag{7.52}$$

where m, $n = 1, 2, \ldots, N$, p, $q = 1, 2, 3$.

The computational example is related to the whole body exposure to UMTS base station antenna system at $f = 2.14$ GHz mounted on roof at the height $h = 15$ m.

Fig. 7.28 shows a single-layered 3D model of an adult torso with a height of 1.7 m assembled from 62 cubic cells. The human body is located approximately 24 m from the radio base station antenna. The measured value of the electric field

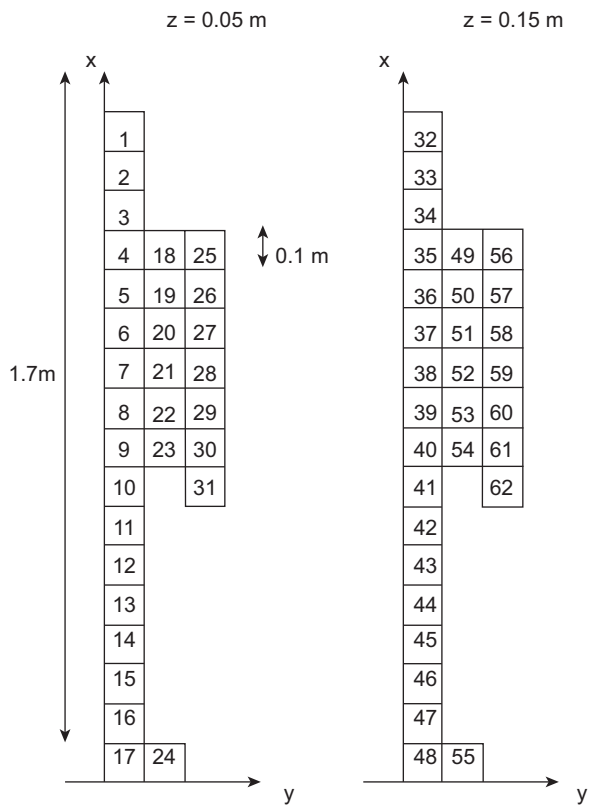

FIGURE 7.28 A view to the half of the body model assembled from 62 cells.

This book belongs to Central Library BADJI Mokhtar-ANNABA UNIVERSITY
Copyright Elsevier 2024

illuminating the body is 14.87 V/m. The human body parameters are $\varepsilon_r = 53.11$ and $\sigma = 1.54$ S/m, i.e., it follows $\tau = 1.54 + j\,6.1978$.

The maximum value of SAR is 0.31 mW/kg, in the region of the waist, whereas the calculated value of the whole-body average SAR is 82.4701 μW/kg, which stays far below the ICNIRP exposure limit. Local SAR in any cube is also below the exposure limits proposed by relevant international guidelines. Therefore the corresponding heating effects are negligible.

7.8 CONCLUSION

The chapter deals with various applications of boundary integral methods in bioelectromagnetics, featuring the human exposure to electrostatic, LF, and HF fields, respectively. The use of certain BEM, hybrid BEM/FEM, and MoM procedures is presented. The boundary integral methods are shown to provide an efficient treatment of exterior field problems, avoiding the application of absorbing boundary conditions. Furthermore, the use of FEM within the hybrid BEM/FEM scheme enables one to efficiently treat inhomogeneous domains, such as the human eye. Finally, the exact geometrical representation of the problem boundary via isoparametric elements avoids stair-casing errors occurring when rectilinear meshes and voxels are used.

Future work will deal with nonhomogeneous model of the entire human head rather than with particular organs, such as the eye or the brain. Furthermore, coupled deterministic−stochastic models will be developed to account for the uncertainties in the input data set pertaining to the geometry and electrical properties of the organs, respectively.

REFERENCES

Australian Radiation Protection and Nuclear Safety Agency, 2003. Radiation Emission From Video Display Terminals. Australian Radiation Protection and Nuclear Safety Agency.

Cavka, D., Poljak, D., Peratta, A., 2011. Comparison between finite and boundary element methods for analysis of electrostatic field around human head generated by video display units. Journal of Communications Software and Systems 7, 22−28.

Cvetkovic, M., Poljak, D., 2015. Electromagnetic-thermal dosimetry comparison of the homogeneous adult and child brain models based on the SIE approach. Journal of Electromagnetic Waves and Applications 29 (17), 2365−2379.

Cvetković, M., Poljak, D., Hirata, A., 2016. The electromagnetic-thermal dosimetry for the homogeneous human brain model. Engineering Analysis with Boundary Elements 63, 61−73.

Diaz, J.A., Pizzaro, C., Arasa, J., 2007. Single dispersive gradient-index profile for the aging human lens. Optical Society of America 25 (1), 250−261.

Dodig, D., Poljak, D., Peratta, A., 2012. Hybrid BEM/FEM edge element computation of the thermal rise in the 3D model of the human eye induced by high frequency EM waves. In: 2012 International Conference on Software, Telecommunications and Computer Networks.

Gonzalez, C., Peratta, A., Poljak, D., 2007. Boundary element modelling of the realistic human body exposed to extremely-low-frequency (ELF) electric fields: computational and geometrical aspects. IEEE Trans on Electromagnetic Compatibility 49, 153−162.

Gonzalez, C., Peratta, A., Poljak, D., 2008. Electromagnetic modelling of foetus and pregnant woman exposed to extremely low frequency electromagnetic fields. In: Skerget, L. (Ed.), Boundary Elements and Other Mesh Re-duction Methods XXX, Transactions on Modelling and Simulation, first ed., vol. 47. WIT Press, pp. 85−94. Book Advanced Computational Techniques.

Hand, J.W., 2008. Modeling the interaction of electromagnetic fields (10 MHz−10 GHz) with the human body: methods and applications. Physics in Medicine and Biology 53 (16), 243−286.

Hand, J.W., Li, Y., Hajnal, J.V., 2010. Numerical study of RF exposure and the resulting temperature rise in the foetus during a magnetic resonance procedure. Physics in Medicine and Biology 55 (8), 913−930.

Hirata, A., 2005. Temperature increase in human eyes due to near-field and far-field exposures at 900 MHz, 1.5 GHz, and 1.9 GHz. IEEE Transactions on Electromagnetic Compatibility 47 (1), 68−76.

Hirata, A., Matsuyama, S., Shiozawa, T., 2000. Temperature rises in the human eye exposed to EM waves in the frequency range 0.6−6 GHz. IEEE Transactions on Electromagnetic Compatibility 42 (4), 386−393.

Institute of Electrical and Electronics Engineers, 1997. Biological and health effects of electric and magnetic fields from video display terminals. IEEE Engineering in Medicine and Biology Magazine 16 (3), 87−92.

International Center for Numerical methods in Engineering (CIMNE), Barcelona, Spain, GID resources [Online]. Available from: http://gid.cimne.upc.es.

International Commission on Non-Ionizing Radiation Protection (ICNIRP) and International labour organization, 1994. Visual Display Units: Radiation Protection Guidelines. International Labour Office, Geneva.

International Commission on Non-Ionizing Radiation Protection, 1998. Guidelines for limiting exposure to time-varying electric, magnetic and electromagnetic fields (up to 300 GHZ). Health Physics 74 (4), 494−522.

International Commission on Non-Ionizing Radiation Protection, 2010. Guidelines for limiting exposure to time-varying electric and magnetic fields (1 HZ−100 kHZ). Health Physics 99 (6), 818−836.

Ishikawa, H., Schuman, J.S., 2004. Anterior segment imaging: ultrasound biomicroscopy. Opthalmology Clinics of North America 17, 7−20.

This book belongs to Central Library BADJI Mokhtar-ANNABA UNIVERSITY Copyright Elsevier 2024

Ito, K., Kawai, H., 2004. Phantoms for evaluation of interactions between antennas and human body. In: International Symposium on Electromagnetic Theory − URSI EMT-S 2004, Pisa, Italy, vol. 2, pp. 1104−1106.

Kawai, H., Koyanagi, Y., Ogawa, K., Sato, K., Ito, K., 2003. A study on the evaluation of the electromagnetic exposure in the human fetus model at 150 MHz. In: Antennas and Propagation Society International Symposium, vol. 3, pp. 1087−1090.

Kos, B., Zupanic, A., Valic, B., Kotnik, T., Gajsek, P., 2010. Exposure of mother and fetus to electromagnetic fields. In: 6th International Workshop on Biological Effects of Electromagnetic Fields, Bodrum, Turkey, pp. 1−5.

Koyanagi, Y., Kawai, K., Ogawa, K., Yoshimura, H., Ito, K., 2001. Estimation of the radiation and SAR characteristics of the NHA at 150 MHz by use of the cylindroid whole body phantom. In: International Symposium on Antennas and Propagation, Boston, USA, vol. 3, pp. 78−81.

Laakso, I., Hirata, A., 2012. Reducing the staircasing error in computational dosimetry of low-frequency electromagnetic fields. Physics in Medicine and Biology 57 (4), 25−34.

Liu, L., Nikolova, N.K., Sangary, N.T., 2009. Evaluation of the specific absorption rate and the temperature rise in the human eyes with account for resonance. IEEE T-MTT 57 (12), 3450−3460.

Nagaoka, T., Saito, K., Takahashi, M., Ito, K., Watanabe, S., 2008. Estimating specific absorption rates in pregnant women by using models at 12-, 20- and 26-weeks' gestation for plane wave exposures. In: International Symposium on Electromagnetic Compatibility − EMC Europe, Hamburg, Germany, pp. 1−4.

Nagasawa, K., Kawai, H., Takahashi, M., Saito, K., Ito, K., Ueda, T., Saito, M., Ito, H., Osada, H., Koyanagi, Y., Ogawa, K., 2005. Experimental evaluation of the EM exposure in the simple abdomen solid phantom. In: Proceedings of ISAP2005, Seul, Korea, pp. 881−884.

NASA, 1995. Man-Systems Integration Standards: Anthropometry and Biomechanics (Washington).

Navarro, R., 2009. The optical design of the human eye. Journal of Optometry 2 (1), 3−18.

Nedelec, J.C., 1980. Mixed finite element in R^3. Numerische Mathematik 35, 315−341.

Nielsen, N.F., Michelsen, J., Michalsen, J.A., Schneider, T., 1996. Numerical calculation of electrostatic field surrounding a human head in visual display environments. Journal of Electrostatic 36, 209−223.

Nielsen, N.F., Schneider, T., 1998. Particle deposition onto a human head: influence of electrostatic and wind fields. Bioelectromagnetics 19, 246−258.

Peratta, C., Peratta, A., Poljak, D., 2010. BEM modelling of high voltage electric field applied to a 3D pregnant woman model. Journal of Communications and Software Systems 6 (1), 31−38.

Poljak, D., 2003. Human Exposure to Electromagnetic Fields. WIT Press, Southampton-Boston.

Poljak, D., 2007. Advanced Modeling in Computational Electromagnetic Compatibility. John Wiley & Sons, Inc., New Jersey.

Poljak, D., 2011. Electromagnetic fields: environmental exposure. In: Nriagu, J.O. (Ed.), Encyclopedia of Environmental Health, vol. 2. Elsevier, Burlington, pp. 259−268.

Poljak, D., Cvetković, M., Dodig, H., Peratta, A., 2017. Electromagnetic-thermal analysis for human exposure to high frequency (HF) radiation. International Journal of Design and Nature and Ecodynamics 12 (1), 55−67.

Poljak, D., Cvetkovic, M., Peratta, A., Peratta, C., Dodig, H., Hirata, A., 2016. On some integral equation approaches in electromagnetic dosimetry. Ghent Belgium. In: BioEM 2016.

Poljak, D., Čavka, D., Dodig, H., Peratta, C., Peratta, A., 2014. On the use of boundary element analysis in bioelectromagnetics. Engineering Analysis with Boundary Elements, (Special Issue on Bioelectromagnetics) 49, 2−14.

Singh, K.D., Longan, N.S., Gilmartin, B., 2006. Three dimensional modeling of the human eye based on magnetic resonance imaging. Investigative Opthamology and Visual Science 47, 2272−2279.

Togashi, T., Nagaoka, T., Saito, K., Takahashi, M., Ito, K., Watanabe, S., Ueda, T., Saito, M., Ito, H., Osada, H., 2006. Development of Japanese 7-month pregnant woman model and evaluation of SAR generated by mobile radio terminals. In: 1st European Conference on Antennas and Propagation − EuCAP 2006, Nice, Italy, pp. 1−4.

This book belongs to Central Library BADJI Mokhtar-ANNABA UNIVERSITY

Copyright Elsevier 2024

This page intentionally left blank

This book belongs to Central Library BADJI Mokhtar-ANNABA UNIVERSITY

Copyright Elsevier 2024

Chapter 8

BEM in Biomechanics: Modeling Advances and Limitations

M. Perrella[1], S. Gerbino[2] and R. Citarella[1]
[1]University of Salerno, Fisciano, Italy; [2]University of Molise, Campobasso, Italy

NOMENCLATURE

BEM boundary element method
BIE boundary integral equation
B-rep boundary representation
CAD computer-aided design
CAE computer-aided engineering
CT computed tomography
DBEM dual boundary element method
DBIE displacement boundary integral equation
FDM finite difference method
FDTD finite-difference time-domain
FEM finite element method
HIFU high-intensity focused ultrasound
LBIE local boundary integral equation
MRI magnetic resonance imaging
RE reverse engineering
SIF stress intensity factor

8.1 INTRODUCTION

Design problems in bioengineering areas are becoming increasingly complex and multidisciplinary so that, to limit costs, it is essential to use numerical simulation instead of more expensive experimental tests. Generally, engineering problems are described by physics laws, which are mathematically represented by differential equations with partial derivatives. In several problems, it is possible to find an alternative and equivalent mathematical representation in terms of integral equations. Nowadays, with the considerable improvements obtained in the last years in numerical modeling and with availability of more powerful computers, numerical techniques based, in particular, on boundary integral equations can be used in simulations of several engineering applications. Widely used methods to solve boundary integral equations are boundary element method (BEM) and finite element method (FEM).

FEM is commonly used as a general analysis tool but BEM, even if less versatile, nowadays is surely a valid alternative to FEM, also in the bioengineering field. The BEM is nowadays widely applied in simulation of biological problems. Common alternative to BEM are the finite difference method (FDM), meshless method (MM) and the FEM.

The FDM allows to create a mesh on a component with a complex geometry but at the expense of very large computational effort. Although the meshes for this method are of an easy structure if applying a fixed grid, it can be cumbersome to build a detailed complex component geometry and the desired variety of subcomponent models within such a fixed grid.

Numerical Methods and Advanced Simulation in Biomechanics and Biological Processes. https://doi.org/10.1016/B978-0-12-811718-7.00008-3
Copyright © 2018 Elsevier Ltd. All rights reserved.

This book belongs to Central Library BADJI Mokhtar-ANNABA UNIVERSITY
Copyright Elsevier 2024

FEM is the most used simulation technique, working on a large amount of data, because the whole domain must be discretized in finite elements. FEM generates large, but sparse, matrices with some nonzero bands, and the equations can be solved iteratively using for example Gauss−Seidel iteration. This means that both memory and CPU requirements can be lower than with BEM, which in turn generates relatively small, but full, matrices. However, the mesh generation for the FEM is much more complicated and less flexible.

Although FEM is a well-known and robust numerical method, when applied to problems dealing with phase changes, it suffers from global remeshing when new born surfaces or material phases appear. To this end, MMs have gained significant interest because no background cells are required for the numerical evaluation of the involved integrals (Sellountos and Sequeira, 2008; Sellountos and Polyzos, 2008).

A theoretical description of BEM can be retrieved in many books (see, e.g., Aliabadi, 2002; Banerjee, 1994; Becker, 1992) where basic formulations are reported together with corresponding fundamental solutions. The peculiarities listed below are believed to support the applicability of BEM as a framework for biomechanics simulations:

1. Multidomain capability (Citarella et al., 2012a) that allows handling the change of material properties in a simplified manner considering the homogeneity by region. Clearly, such domain capability is also available with FEM (see for instance Armentani et al., 2010; Ausiello et al., 2012; Franciosa and Martorelli, 2012).
2. Being a boundary method, the numerical discretization is conducted at reduced spatial dimension.
3. Displacements and tractions at the boundaries can be calculated simultaneously and with the same accuracy.
4. High accuracy in modeling complex three-dimensional contact problems between two deformable bodies (see, e.g., Citarella et al., 2012b; Leahy and Becker, 1999; Sammartino et al., 2008, 2013).
5. Accurate discretization of the boundary conditions at the interface and a natural representation of unbounded regions without truncation of the computational domain.
6. The dimensional reduction, in combination with fast computational algorithms, results in efficient simulation of large-scale problems.
7. Being based on Green's function representations, the BEM is devoid of numerical dispersion and dissipation effects.

In the following, applications of BEM to different areas of biomechanics will be sequentially introduced, following a thematic partitioning. Complex simulations, like for **bone healing**, can be carried out successfully based on BEM that turns out to be an attractive tool for external shape remodeling. Fracture healing is initiated and strictly regulated by growth factors and mechanical environment around the callus site, whereas the strain/stress fields represent the main mechanical stimuli affecting cell differentiation and ossification pathway. BEM can represent an attractive alternative to the more familiar FD and FE methods when having to assess the strain/stress environment at appropriate callus locations.

Remodeling problems affecting bone behavior have been widely studied using BEM to improve the capabilities of bone healing simulation techniques. In the following, some of the specific advantages when using BEM for bone healing simulation are listed:

1. The need to modify the geometry as a function of time (surface remodeling refers to the resorption or deposition of bone material on the external surface of the bone.) favors the use of BEM because, unlike FEM, the adapting process leads to the mesh nodes repositioning without modifying the connectivity or defining additional elements (e.g., remeshing is no longer needed to update callus size and shape). This will be applicable provided that the geometry is uniform and distortions are not so big as to result in a significant size alteration. This peculiarity of the method reduces considerably the computational cost.
2. Kernels for time-dependent analysis of diffusion and particles migration problems are available (e.g., in Qiu et al., 1995; Zerroukat et al., 1998).

On the other hand, the BEM usage involves a calculation complexity when working with nonhomogeneous (e.g., white/gray matter inhomogeneity) and anisotropic materials. The external bone remodeling models generally assume that the level of damage and the strain energy near the periosteum and endosteum completely control the process. Martínez et al. (2006) used BEM to evaluate the displacements and tractions field and modify the geometry according to the remodeling law.

Sfantos and Aliabadi (2007) proposed an alternative boundary element (BE) formulation to simulate three-dimensional wear in artificial hip joints. A parametric study of the wear evolution was carried out, including different update periods for the worn geometry of the acetabular cup, different loading angles, different femoral head sizes, and different materials combinations, all under the same variable loading conditions based on the hip activity. Gonzalez et al. (2009) highlighted the capability of BEM to characterize the tissue phenotypes during a progressive healing process; the pore pressure was included as a part of the stimuli function and incorporated into a poroelastic axisymmetric boundary element callus model, using the

This book belongs to Central Library BADJI Mokhtar-ANNABA UNIVERSITY
Copyright Elsevier 2024

axisymmetric fundamental solutions for steady-state poroelastic problems in a linear-elastic, isotropic, and nonhomogeneous media (Biot consolidation theory). In Duarte et al. (2011) the tissue differentiation model proposed by Claes and Heigele was numerically implemented using a poroelastic BE framework to characterize fracture healing, leading to a new poroelastic correlation between mechanical conditions and local tissue formation. Martínez and Cerrolaza (2006) presented a BEM model to analyze the external bone remodeling process, with a focus on the damage evolution along such process. The load history and the damage accumulation at the microstructure level were allowed by a stimulus function, defined to control the bone formation and influenced by the strain energy density and a damage variable. Such a damage process ends up with the crack formation and growing on the bone surfaces.

The dynamics of the mesenchymal cells is usually described by complicated and nonlinear systems of partial differential equations that correlate all the types of cells that take part in the bone healing process (Sellountos et al., 2012). Such boundary value problem is solved through a meshless local boundary integral equation (LBIE) method. In Grivas et al. (2013) the LBIE methodology of Sellountos et al. (2012) is properly modified to model cell proliferation during bone healing via a diffusive process. Then LBIE method is employed to derive cell predictions in bone healing by considering a 2D model of fractured bone.

BEM and surface bone adaptation theory are employed in Sadegh et al. (1993) to investigate the microstructural remodeling of bone at the bone−implant interface. Various cases are considered, and for each of them the bone in growth is determined as a function of the geometry and the applied load.

BEM is widely applied in dentistry and more specifically when considering **implantology problems** (Citarella et al., 2012b; Sammartino et al., 2008, 2013). An efficient solution of the inverse geometric problem for **cavity detection** (e.g., in a cross section of a cortical bone) using a point load superposition technique in the elastostatics BEM is presented in Ojeda et al. (2008). A superposition of point load clusters technique is used, in combination with genetic algorithms, to simulate the presence of cavities. This technique offers relevant advantages in reducing run times for the elastostatics field solution because no boundary rediscretization is necessary throughout the inverse problem solution process.

The occlusal stresses transmitted to the inferior alveolar nerve by a single (Sammartino et al., 2008) or multiple osseointegrated threaded implants (Sammartino et al., 2013), undergoing mastication typical occlusal loads, are calculated by a BEM implementation. A sensitivity analysis is provided against varying bone density (Sammartino et al., 2008), levels of implant osseointegration (Sammartino et al., 2013), and fixture-canal distances (Sammartino et al., 2008, 2013). Allowance for nonlinear contact between nerve and canal is included in all the analyses. Moreover, in Sammartino et al. (2013), performances of two- and three-abutment configurations are compared.

In Citarella et al. (2012a), some of the authors provide an assessment on effectiveness of the BEM and FEM numerical approaches when analyzing the structural behavior of a mandible with articular disks, undergoing a unilateral occlusion. The mandible is considered as completely edentulous and its anisotropic and nonhomogeneous bone material behavior are modeled. The material behavior of the articular disks is assumed to be either elastic or hyperelastic. The following conclusions are provided about the FEM versus BEM comparison, when the aim is to develop a procedure that, starting from the patient computed tomography (CT) scan, automatically leads to the mathematical reconstruction of the numerical model and subsequent analysis:

1. A full hexahedral FE mesh can significantly reduce the computational burden in nonlinear analysis, if compared to the case of a full tetrahedral FE mesh or to a BE mesh; on the other hand, there is an increase in the time needed for model preparation. The only way to create a regular hexahedral mesh is to preliminarily develop a rational computer-aided design (CAD) model with ordered sections.
2. In case of investigation of mandible models obtained from CT scan, a FEM model with tetrahedral elements is mandatory when an automatic procedure has to be implemented, whereas BEM can enable an automatic meshing without compromises on accuracy (as imposed by the usage of tetrahedral elements with FEM);
3. Even if time-consuming in the solution phase, BEM enables more accuracy and preprocessing flexibility than FEM (even if the growing availability of powerful and general purpose automatic FE preprocessors tends to reduce this gap), especially during the model exchange between CAD and computer-aided engineering (CAE) applications for the reconstruction process of the mandible numerical model. BEM analysis can take advantage from a highly accurate CAD surface description of the model and discontinuous elements that speed up the meshing process.

In Citarella et al. (2012b) some of the authors provided an assessment on effectiveness of the BEM and FEM numerical approaches when analyzing the stress state of a Brånemark dental implant and a generic conic threaded implant, undergoing typical mastication loads. Perfect and partial osteointegration between the implant and the mandibular bone were considered. The BEM analysis leverages on the submodeling technique (a subregion surrounding the implant is extracted from the overall BEM mandible model to allow a local mesh refinement) to accurately assess the most stressed areas at the

This book belongs to Central Library BADJI Mokhtar-ANNABA UNIVERSITY Copyright Elsevier 2024

bone−implant interface and at the mandibular canal, representing the most critical areas during mastication. The following conclusions are provided about the FEM versus BEM comparison:

1. Due to the high flexibility in the pre- and postprocessing phases and accuracy in reproducing superficial stress gradients, BEM is more efficient than FEM in facing this kind of problem, especially when a linear elastic constitutive material law is adopted.
2. The BEM approach can be advantageous when an implant shape optimization is attempted because of the typical BEM preprocessing flexibility, which allows quick geometric changes and remeshing, which would be more difficult to achieve by using FEM.
3. Working with 3D models, the mesh refinement in the neighboring areas where high stress gradients are expected is much more flexible when using BEM, rather than FEM for the possibility to use discontinuous elements.

A BEM model for acoustic responses in individual **ear canals** is presented in Lee and Ahn (2014). The variability of the BEM model due to the uncertain acoustic boundary conditions and measurement locations is predicted using the eigenvector dimension reduction method. To enhance the simulation model performance, the acoustic boundary conditions of the BEM model are updated using a statistical calibration approach that maximizes the likelihood function value between the calculated probability density functions of the simulation model and the measurement data.

High-intensity focused ultrasound (HIFU) is a medical procedure that uses high-amplitude ultrasound to heat and ablate a localized region of tissue. For HIFU therapies of, e.g., liver cancer, one of the main challenges is the accurate focusing of the acoustic field inside a rib cage. This requires the accurate modeling of acoustic scattering at rib cages. BEM turns out to be an effective approach for such problems because only the boundaries of the ribs have to be discretized, differently from volumetric approaches that need to model the entire volume around the rib cage. As a matter of fact, in BEM, the exterior scattering problem is reformulated into an integral equation on the surface of the object. The Helmholtz system that describes the wave propagation in the exterior domain can be reformulated into a boundary integral equation, thanks to the availability of a fundamental solution. Thus, instead of solving for a volumetric pressure field, the model is solved for a surface potential that, once defined on the scattering surface, uniquely determines the scattered field at any point in the exterior domain. Allowance for both reflecting and absorbing boundary conditions on the ribs can be provided together with efficient modeling of scattering of the acoustic field by arbitrary 3D rib topologies. Difficulties arise when trying to allow for effects due to nonlinear propagation in tissue by BEM.

The efficiency of BEM in the high-frequency range necessary for transcostal HIFU applications can be gained using a combination of fast algorithms, as presented in Van't Wout et al. (2015), where a Galerkin-discretized Burton−Miller formulation is used in combination with preconditioning and matrix compression techniques.

To undertake a **virtual reality simulation of surgery**, a real-time deformable and cuttable model of the tissue is required. In brain surgery, it is reasonable to treat a crack as a small gap rather than a perfect crack with infinite stress at the crack tip. When cutting starts, a gap can be introduced where, in addition to new surface elements created in the new cut surfaces, the geometries of a few existing surface elements around the cut must also be modified. BEM, with its peculiarity of surface-only modeling, has considerable potential for virtual reality surgery simulation that requires real-time deformations and surface remeshing during cutting.

Current surgical simulators simplify the analysis by assuming a linear elastic behavior and utilizing a small deformation theory, thus allowing the use of the superposition principle. However, to provide a more realistic haptic feel and more accurate deformations of human organs, more complex nonlinear formulations that also incorporate large deformations and prestresses have to be considered. Meier et al. (2005) identified BEM as being potentially one of the most promising routes to real-time deformable models for surgical simulation.

A BEM approach to simulate the three basic actions of prodding, pinching, and cutting deformable objects is presented in Wang et al. (2007). This work explores whether the BE method offers a potentially more scalable alternative to the FE method to create an effective neurosurgical simulation framework, useful to provide haptic and visual feedback when specific actions are applied to deformable objects.

In Kim et al. (2010) a multiscale model to simulate deformation in the microscopic environment of an articular cartilage explant is set up by using an axisymmetric elastic BEM for domains with internal interfaces. The BEM approach is integrated into an efficient inverse optimization algorithm, leveraging on its efficiency and geometric simplicity. An inverse BEM computational model is so made available, providing the capability to determine the mechanical properties of the pericellular matrix in situ. This study assumes small strain and isotropy because of the adopted axisymmetric BEM formulation and, as such, it was limited to analysis of midzone data at small levels of macroscopic strain for chondrons near the central axis of the explant.

This book belongs to Central Library BADJI Mokhtar-ANNABA UNIVERSITY Copyright Elsevier 2024

Ooi et al. (2007) proposed a BEM **bioheat transfer model** of the human eye, with an iterative approach to treat the nonlinear heat radiation term. BEM was able to calculate the normal heat flux more accurately than FEM on the corneal surface. In Ooi et al. (2009) a 3D BE model of the human eye was developed to investigate the thermal effects of eye tumor on the ocular temperature distribution. The human eye was modeled as a multidomain, including the tumor, with varying thermal properties.

To analyze the influence of strut structure on **hemodynamic characteristics**, considering also the blood flow fields, shear stresses on a vessel wall, and pressures on the struts, a BEM approach was set up in Peng (2014), with the objective to avoid the formation of low shear stress areas and to improve the stent stability.

BEM has been used extensively to study the dynamics of a single vesicle suspended in Stokes flow. A new method for the evolution of inextensible vesicles immersed in a Stokesian fluid is presented in Veerapaneni et al. (2009). A boundary integral formulation is adopted for the fluid that results in a set of nonlinear integrodifferential equations for the vesicle dynamics.

Modeling **human skin deformation** has many applications in the fields of human biomechanics and computer graphics. A physics-based approach to model human skin deformation using BEM was presented in Tang (2010).

8.2 BOUNDARY ELEMENT METHOD

BEM principles come from mathematical formulations introduced by Fredholm (1903) and Mikhlin (1957) in potential theory, by Betti (1872), Somigliana (1885), and Kupradze (1963) in elasticity theory, but only with the consistent contribute of Lachat and Watson (1976) it has become a real numerical technique. As a matter of fact, they developed an isoparametric formulation very similar to those used in FEM and showed that BEM can be used to solve problems with complex geometry. Typical spatial discretization of integral equation formulations is based on Galerkin or collocation projection schemes using polynomial bases—also referred as BEM.

The main reason of interest in BEM is surely the reduction of the problem dimensions: in two-dimensional problems only the line of the domain boundary has to be discretized (Fig. 8.1), whereas in three-dimensional problems only the

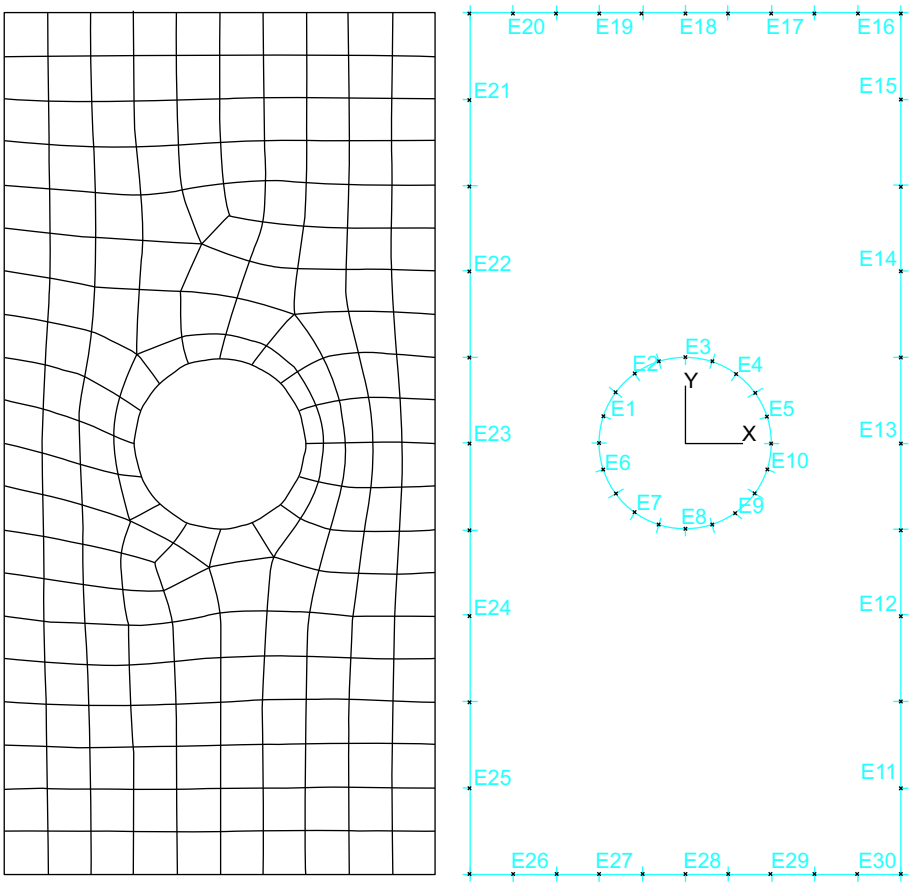

FIGURE 8.1 Comparison between finite element method and boundary element method discretizations.

This book belongs to Central Library BADJI Mokhtar-ANNABA UNIVERSITY
Copyright Elsevier 2024

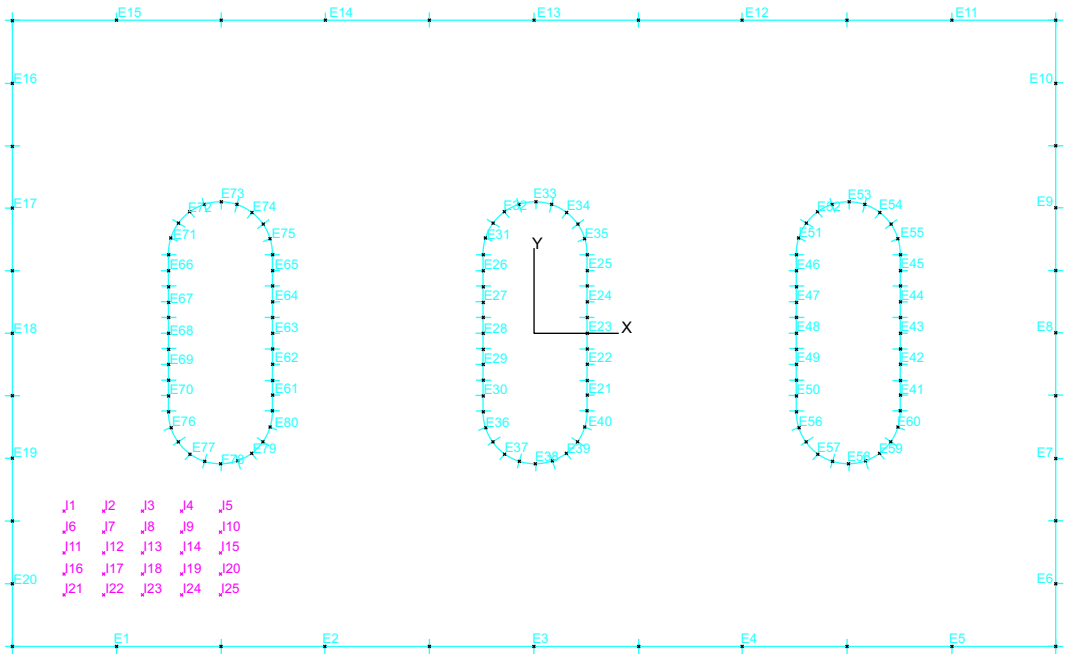

FIGURE 8.2 Highlight of internal points distribution where to monitor the stress state at inside the domain if requested.

external surfaces of the model have to be discretized. So, BEM formulation leads to a significant reduction of the preprocessing effort avoiding the need to generate interior nodes and element data. Moreover, the unknown variables such as displacements and stresses are just approximated on the domain boundary, thus resulting in a smaller system of equations than that obtained using FEM. In addition, BEM allow a high level of integration with CAD systems and can efficiently solve problems with geometrically complex boundaries.

The BEM coefficient matrix is full and not symmetric so that, using direct solvers, run times turn out to be proportional to the third power of the number of degrees of freedom (dof) and consequently prohibitive for simulation of complex structures, where the availability of an iterative solver becomes a prerequisite to effectively get a solution. Another important feature is that BEM provides the primary solution in terms of displacements and tractions at the boundary. Then, the solution at internal points (Fig. 8.2) is calculated if needed during the postprocessing phase, after the solution of unknown variables at the boundary and with reduced computational effort.

It should be remarked that FEM, unlike BEM, is supported by a larger number of commercial software, but, in the last years, FEM−BEM interface routines have been made available enabling the use of combined approaches acting simultaneously on the same problem and leveraging on the best prerogatives of the two methods (Fischer et al., 2000; Sikora et al., 2004).

8.2.1 Applications in Fracture

One of the most important application field for BEM in biomechanics is the simulation of crack propagation in bones, both for single and multiple cracks. The BEM capability to follow crack propagation through a limited remesh area, without any user intervention, is surely the feature that makes it an excellent numerical tool for Fracture Mechanics simulations. During each step of propagation, BEM perform a remesh simply adding new elements near the crack tip, with no alterations to the mesh made before, but for the surroundings of break through points in cases of three-dimensional crack problems (Fig. 8.3).

Linear elastic fracture mechanics can be used to describe the behavior of cracks (e.g., in bones). The fundamental postulate of linear elastic fracture mechanics is that the crack behavior is solely determined by stress intensity factors (SIFs), which are related to the applied load and to the geometry of the cracked structure. The process of crack propagation has to be simulated by incremental numerical analysis, and, for each propagation step, a stress analysis has to be performed to calculate SIFs. Then, according to one or more criterions, based on SIFs values, the new crack front is predicted and the simulation goes on.

This book belongs to Central Library BADJI Mokhtar-ANNABA UNIVERSITY
Copyright Elsevier 2024

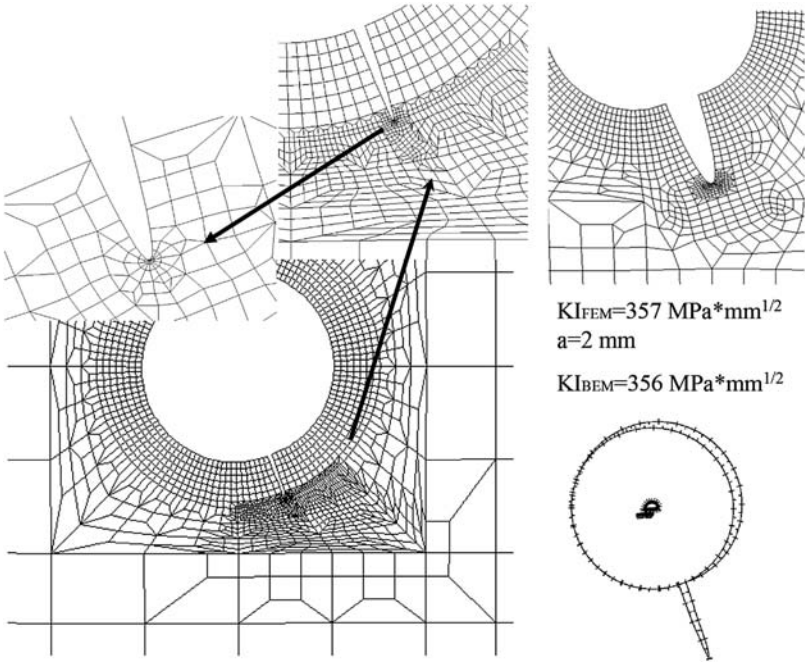

FIGURE 8.3 Crack modeling by boundary element method and finite element method with related comparison of computed stress intensity factor.

Generally, because of the complex shape and the continuously varying crack front, in engineering structures, numerical methods have to be used for the calculation of SIFs. In fracture mechanics applications, several in-depth studies have been made through FEM, but with the intrinsic complexity related to the need of a continuous volume remeshing to follow the crack evolution (Kim et al., 2006; Ota et al., 1999).

Another method that is well established in fracture mechanics applications is BEM. This method, when based only on the displacement boundary integral equation (DBIE), has been successfully applied to several linear elastic problems in domains containing a symmetric crack in an overall symmetric problem, where just one edge need to be modeled. Differently, the solution cannot be achieved by a single region analysis: indeed, because of the geometric coincidence of the crack boundaries, a singular system of algebraic equations results. The equation for a collocation point located on a crack boundary turns out to be coincident with that corresponding to a collocation point located on the opposite surface and with the same coordinates, causing an ill-posed system of equations. Such situation arises because the same integral equation is used with the same integration path starting from two coincident points.

Different techniques were introduced to overcome this difficulty, e.g., the subregion method. It works introducing artificial boundaries inside the body, to connect crack tips to the external boundary, so the whole domain is divided into two subregions without cracks. However, during the crack propagation, these added boundaries have to be redefined at each step and, because of the fact that there is not a unique way to create such boundaries, it is difficult to implement an automatic procedure during the crack growth. Moreover, this method leads to a larger system of algebraic equations.

8.2.2 Boundary Element Procedure for Elastostatic Problems

In this method, the fundamental differential equations pointwise defined in the volume are transformed into integral equations defined on body surface. They are integrated on a boundary that is divided into elements. Enforcing the boundary conditions, a system of linear algebraic equations is obtained, and for a well-posed problem a unique solution is available. The BEM procedure applied to elastostatic problems consists of the following steps:

- derive Navier equations and substitute strain−displacement relation in Hooke's law and in differential equation to equilibrium;
- obtain a fundamental solution to the governing differential equations; the Kelvin fundamental solution provides displacements and tractions for an infinite body loaded with a point force and is a function of the distance between the load application point (collocation point) and every other point of the domain (field point);

This book belongs to Central Library BADJI Mokhtar-ANNABA UNIVERSITY Copyright Elsevier 2024

- use the Betti's reciprocity theorem establishing that if two different stress states (a) and (b) satisfy equilibrium, then work made by force of system (a) on the displacement system related to (b) is equal to the work made by force system (b) on the displacement system related to (a); this can be mathematically traduced as

$$\sum_P F_P^{(a)} u_p^{(b)} = \sum_P F_P^{(b)} u_p^{(a)} \tag{8.1}$$

  where P is any point on which a force F is applied; if external forces are limited to the surface, then it is possible to write:

$$\int_S t_i^{(a)} u_i^{(b)} dS = \int_S t_i^{(b)} u_i^{(a)} dS \tag{8.2}$$

  where $i = 1, 2, 3$ (corresponding to the Cartesian coordinates x, y, z) and the traction vector is defined as $t_i = \sigma_{ij} n_j$, being n_j the outward normal to the surface; the result is an integral equation defined on the boundary and relating the displacements and tractions;
- divide the surface in segments or elements, and for each of them, use a shape function, which can be linear, quadratic, or even higher order, to describe geometry and variables; numerical integration is performed using the numerical method of Gauss quadrature, whereas special outlines are recalled to integrate singular or quasisingular terms, when field points and collocation points are very close to each other or coincident (this is due to the fact that fundamental solution includes singular terms when r approaches zero);
- calculate integrals on the whole surface summing up those evaluated on each element;
- build the solution matrix, doing again the integration process with all collocation points that cover all the surface, to obtain the resulting system of linear equations:

$$[\mathbf{A}][\mathbf{u}] = [\mathbf{B}][\mathbf{t}] \tag{8.3}$$

- apply the boundary conditions and reorganize the linear equation putting all unknown variable on the left side and the known variables on the right side, obtaining:

$$[\mathbf{A}^*][\mathbf{x}] = [\mathbf{B}^*][\mathbf{y}] = [\mathbf{C}] \tag{8.4}$$

  where the unknown vector [**x**] includes a mix of unknown displacements and tractions, whereas [**y**] contains all known values of tractions and displacements; [**C**] is the vector of known coefficients;
- solve the whole system of linear equations with a direct method because the matrix of the final system is full and not symmetric;
- calculation of extra information (stress, strain, strain energy, and SIF values) from computed displacements and tractions on the boundary; in addition, displacements and tractions at internal points can be easily calculated from values on the boundary.

The DBIE, when there are no body forces, is as follows:

$$u_i(X') = \int_S U_{ij}(X', x) t_j(x) dS - \int_S T_{ij}(X', x) u_j(x) dS \tag{8.5}$$

This equation is named Somigliana identity for displacements, and T_{ij} (X', x) and U_{ij} (X', x) represent the Kelvin fundamental solutions of traction and displacement at the field point x on boundary S, respectively (Fig. 8.4).

This equation comes directly from the Betti's reciprocal work theorem and is valid for every source point X′ inside the domain V. The displacement integral equation can be written as

$$C_{ij}(x') u_j(x') + \int_S T_{ij}(x', x) u_j(x) dS = \int_{S_\varepsilon} U_{ij}(x', x) t_j(x) dS \tag{8.6}$$

where the free term is calculated as

$$C_{ij}(x') = \delta_{ij}(x') + \alpha_{ij}(x') \tag{8.7}$$

with the Kronecker delta

$$\delta_{ij} = \begin{cases} 0 & i \neq j \\ 1 & i = j \end{cases} \tag{8.8}$$

This book belongs to Central Library BADJI Mokhtar-ANNABA UNIVERSITY
Copyright Elsevier 2024

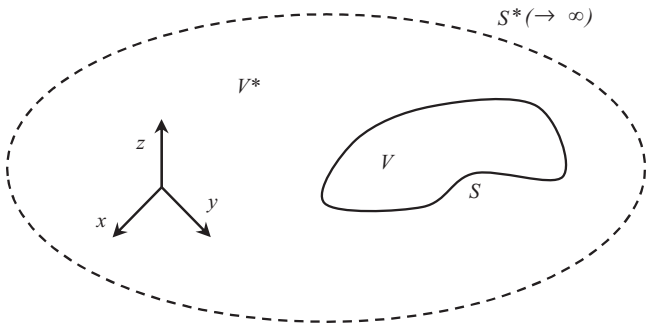

FIGURE 8.4 Kelvin infinite domain embedding the physical domain to be analyzed.

Stresses at points inside the domain can be obtained differentiating, with respect to the source point X', the displacements in Somigliana identity as

$$u_{i,k}(X') = \int_S U_{ij,k}(X',x)t_j(x)dS - \int_S T_{ij,k}(X',x)u_j(x)dS \tag{8.9}$$

where $U_{ij,\,k}$ and $T_{ij,\,k}$ are derived from Kelvin fundamental solutions.

Somigliana identity for stresses can be obtained by replacing the equation above in Hooke's law:

$$\sigma_{ij} = \lambda\delta_{ij}\varepsilon_{kk} + 2\mu\varepsilon_{ij} \tag{8.10}$$

where $\lambda = 2\nu\mu/(1-2\nu)$ is Lamè constant and $\mu = E/2(1+\nu)$ is the tangential elasticity modulus, ν is Poisson's ratio, and δ_{ij} is Kronecker delta. With such substitution, it results:

$$\sigma_{ij}(X') = \int_S D_{kij}(X',x)t_k(x)dS - \int_S S_{kij}(X',x)u_k(x)dS \tag{8.11}$$

where D_{kij} and S_{kij} are obtained from $U_{ij,\,k}$ and $T_{ij,\,k}$, using Hooke's law. In a way similar to the displacements, Somigliana identity can be used to obtain an integral equation of stresses on the boundary. This new equation is jointly used with the displacement equation in the dual boundary element method (DBEM), adopted in problems related to crack modeling.

8.3 DUAL BOUNDARY ELEMENT METHOD

MMs, such as the LBIE method (Sellountos and Sequeira, 2008) and the Meshless local Petrov−Galerkin method (Atluri and Shen, 2002), have been effectively used for the solution of engineering fracture mechanics problems, but in this work we will emphasize the possibilities offered by an effective and efficient methodology for the fatigue crack growth under linear elastic fracture mechanics assumption: the DBEM (Portela and Aliabadi, 1992; Portela, 1993). Such an approach is, e.g., adopted in Gámez et al. (2010) where the evaluation of fatigue crack growth in human cortical bone is presented. The solution is based on the development and application of a computational algorithm to obtain stresses and displacements on the boundary and the crack-tip SIF for (cracked) components undergoing fatigue or static load.

The mathematical foundation of BEM is the BIE method. It has been shown that the solutions of these boundary value problems can be found in terms of single-layer and double-layer potentials, i.e., in the form of an integral of the product of the unknown densities and the kernel functions, known as the fundamental solutions. This representation allows to reduce a boundary value problem to the systems of weakly singular, singular, and hypersingular BIEs, which can be subsequently solved by the BEM (Aliabadi, 2002).

However, as previously said, application of the DBIE-based BEM to crack problems results in a singular system matrix, because of the coincident crack surfaces, and therefore it is limited to problems with symmetry, which avoid the use of one of the coincident boundaries. The most common approach to overcome this difficulty, which has been successfully used in classical elasticity, is known as the DBEM and it consists in simultaneous use of the both types of the BIEs on the crack surfaces.

Portela firstly introduced DBEM (Portela and Aliabadi, 1992; Portela, 1993; Gámez et al., 2010): the method incorporates both displacement and traction boundary integral equations in a unique general formulation. Using this formulation, crack problems can be solved in a single-region analysis, using both the displacement and the traction equations for collocation on the two coincident crack fronts. Therefore, the integration paths are still the same, as in

This book belongs to Central Library BADJI Mokhtar-ANNABA UNIVERSITY Copyright Elsevier 2024

BEM, but the integral equations are different when collocating on the two crack edges. The J-integral technique, based on a path-independent integral, can be adopted to calculate SIFs. In particular, for mixed mode problems the J-path evaluation is based on the decomposition of the elastic field into its respective symmetric and antisymmetric mode components (Rigby and Aliabadi, 1993, 1998).

8.3.1 Crack Modeling

Physical cracks have to be described in DBEM as discontinuity, and this situation introduces some mathematical issues in standard application of integral displacement and traction boundary equations.

In the absence of body forces, Somigliana identity for displacement for an inner point X' is:

$$u_i(X') = \int_{S^*+S_c^++S_c^-} U_{ij}(X',x)t_j(x)dS - \int_{S^*+S_c^++S_c^-} T_{ij}(X',x)u_j(x)dS \tag{8.12}$$

where S_c^+ and S_c^- represent, respectively, upper and lower crack surfaces, and S^* represents the other part of the boundary, as shown in Fig. 8.5.

T_{ij} (X', x) and U_{ij} (X', x) represent, respectively, Kelvin fundamental solutions for stresses and displacements in a field point x on the boundary S. Stresses and displacements on upper and lower crack faces are related:

$$U_{ij}(X',x^+) = +U_{ij}(X',x^-) \tag{8.13}$$

$$T_{ij}(X',x^+) = -T_{ij}(X',x^-) \tag{8.14}$$

In stresses T_{ij} there is a change of sign, because normal direction is opposite on the two crack surface.

Letting the faces be coincident, the equation becomes

$$u_i(X') = \int_{S^*} U_{ij}(X',x)t_j(x)dS - \int_{S^*} T_{ij}(X',x)u_j(x)dS + \int_{S_c} U_{ij}(X',x)\sum t_j dS - \int_{S_c} T_{ij}(X',x)\Delta u_j dS \tag{8.15}$$

where

$$\Delta u_j = u_j(x^+) - u_j(x^-) \;\; and \;\; \sum t_j = t_j(x^+) + t_j(x^-)$$

If the crack is not loaded or if the crack is loaded with stresses equal in magnitude but opposite in direction, then $\sum t_j = 0$. Following the usual BEM procedure, X' tends to x^+ on crack boundary S_c^+; therefore the equation for a non-loaded crack becomes

$$C_{ij}(x^+)u_j(x^+) + C_{ij}(x^-)u_j(x^-) = \int_{S^*} U_{ij}(x^+,x)t_j(x)dS - \int_{S^*} T_{ij}(x^+,x)u_j(x)dS + \int_{S_c}^{-} T_{ij}(x^+,x)\Delta u_j(x)dS \tag{8.16}$$

where the symbol $\int^-$ indicates the Cauchy principal value integral and the term C_{ij} (x^-) u_j (x^-) is due to the coincidence of the collocation point x^+ with the other collocation point x^- on the opposite crack surface S_c^-. If the same operation is made on the collocation point x^-, it will result the same equation. Then the final equation system has couples of coincident equations, where the collocation point is on a crack surface, obtaining in this way a system of equations where the number of independent equations is lower than the number of unknown variables.

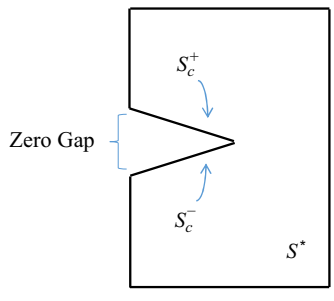

FIGURE 8.5 Domain with crack.

This book belongs to Central Library BADJI Mokhtar-ANNABA UNIVERSITY
Copyright Elsevier 2024

In a way similar to integral displacement equation, stress integral equation can be written on collocation points on the crack surface x^- as:

$$\frac{1}{2}\sigma_{ij}(x^-) + \frac{1}{2}\sigma_{ij}(x^+) = \int_S^{-} D_{kij}(x^-, x)t_k(x)dS - \int_S^{-} S_{kij}(x^-, x)u_k(x)dS \tag{8.17}$$

where the symbol $\int^{-}$ indicates the Hadamard principal value integral.

Multiplying the equation above by the normal outward vector $n_i\,(x^-)$ and taking note that $n_i\,(x^-) = -n_i\,(x^+)$, boundary stress equation on crack surface can be written as follows:

$$\frac{1}{2}t_j(x^-) - \frac{1}{2}t_j(x^+) = n_i(x^-)\int_S^{-} D_{kij}(x^-, x)t_k(x)dS - n_i(x^-)\int_S^{-} S_{kij}(x^-, x)u_k(x)dS \tag{8.18}$$

Fundamental solutions have the following properties:

$$D_{kij}(x, x^+) = +D_{kij}(x, x^-) \;\; and \;\; S_{kij}(x, x^+) = -S_{kij}(x, x^-)$$

Thus the equations, after some mathematical developments, become

$$\int_S^{-} S_{kij}(x^-, x)u_k(x)dS = \int_{S_c^+}^{-} S_{kij}(x^-, x)\Delta u_k(x)dS + \int_{S^*} S_{kij}(x^-, x)u_k(x)dS \tag{8.19}$$

$$\int_S^{-} D_{kij}(x^-, x)t_k(x)dS = \int_{S_c^-}^{-} D_{kij}(x^-, x)\left[t_k^-(x) + t_k^+(x)\right]dS + \int_{S^*} D_{kij}(x^-, x)t_k(x)dS \tag{8.20}$$

and then

$$\begin{aligned}\frac{1}{2}t_j(x^-) - \frac{1}{2}t_j(x^+) = {} & -n_i(x^-)\int_{S_c^-}^{-} S_{kij}(x^-, x)\Delta u_k(x)dS - n_i(x^-)\int_{S^*} S_{kij}(x^-, x)u_k(x)dS + n_i(x^-)\int_{S^*} D_{kij}(x^-, x)t_k(x)dS \\ & + n_i^-(x)n_i(x^-)\int_{S_c^-}^{-} D_{kij}(x^-, x)\left[t_k^-(x) + t_k^+(x)\right]dS\end{aligned} \tag{8.21}$$

Assuming the hypothesis of stresses equilibrium is valid, i.e., $t_k\,(x^-) = -t_k\,(x^+)$, then the equation above can be written on crack surfaces as

$$t_j(x^-) + n_i(x^-)\int_{S_c^-}^{-} S_{kij}(x^-, x)\Delta u_k(x)dS + n_i(x^-)\int_{S^*}^{-} S_{kij}(x^-, x)u_k(x)dS = n_i(x^-)\int_{S^*} D_{kij}(x^-, x)t_k(x)dS \tag{8.22}$$

This equation, unlike to the integral displacement equation, can be used to analyze the domain with the presence of cracks. The solution will be obtained in terms of displacement discontinuity on crack surfaces.

8.3.2 Modeling Strategy

To guarantee the existence of the principal value integrals obtained in the derivation of dual boundary equations, some restrictions on the discretization must be satisfied. The discontinuous element satisfies the need of smoothness of the geometry at the collocation points, allowing to model discontinuous traction fields as well. The general modeling strategy can be summarized as shown below:

1. traction equation (**T**) is applied on one of the two crack front;
2. displacement equation (**D**) is applied on the other crack front and on the rest of the body boundary.

This simple strategy is robust and allows the DBEM to be used for every crack problem without difficulties (see Fig. 8.6).

This book belongs to Central Library BADJI Mokhtar-ANNABA UNIVERSITY
Copyright Elsevier 2024

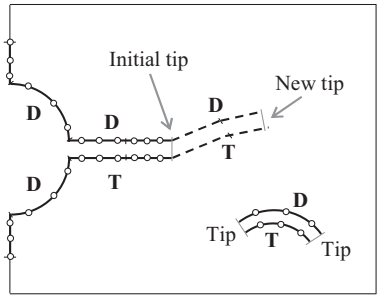

FIGURE 8.6 Dual boundary element method modeling strategy.

8.3.3 Discontinuous Elements

To apply DBEM, discontinuous and semidiscontinuous elements must be used to cope with continuity conditions inherent the use of the traction equation. For two-dimensional problems, several types of elements are used: the most important are the linear and quadratic elements, with respectively two or three nodes; all these types of element can be discontinuous or semidiscontinuous as shown in Fig. 8.7.

For three-dimensional problems, quadrilateral and triangular elements are used, with a varying number of nodes depending on the adopted interpolation order. All these types of element can be discontinuous or semidiscontinuous. Fig. 8.8 displays the discontinuous and semidiscontinuous quadrilateral eight-node elements are shown.

8.4 BOUNDARY ELEMENT MODELING IN BIOMEDICAL ENGINEERING APPLICATIONS

In biomedical engineering problems, the geometrical models have complex shapes and some reconstruction techniques adopted for the model description rely on the approximated representation based on polygons (also called tessellated, faceted, or triangular models), but they do not directly offer a ready-to-use surface from which to generate the computational mesh. In the following, the authors explore and discuss some issues related to meshing process with reference to boundary models in biomedical engineering applications also in comparison with FEM. The description is intended to address possible solutions to meshing problems very common in bio-CAD modeling.

8.4.1 Finite Element Model and Boundary Element Model Meshing Issues

In terms of meshing issues, an advantage of BEM over FEM is that the boundary discretization is easier to generate as it directly interfaces with the widely adopted B-rep topology representation of CAD models. B-rep stands for boundary representation, which is the most common topology description of a solid CAD model through the boundary faces of the model. The underlying topological relationships are also used for the surface model representation.

Generally speaking, the mesh quality is widely recognized as a key factor to assure the convergence of the numerical solution and its stability. Mesh quality concerns the characteristics of a mesh that permit a particular numerical partial derivative equation simulation to be efficiently performed, with fidelity to the underlying physics, and with the accuracy required for the problem (Knupp, 2007). It affects the accuracy of the solution and the calculation speed. By high-quality mesh models, the solver converges to the correct solution while minimizing run times. The mesh must also consist of valid shape elements with appropriate spatial distribution, and this can be reached by an appropriate use of different grid quality

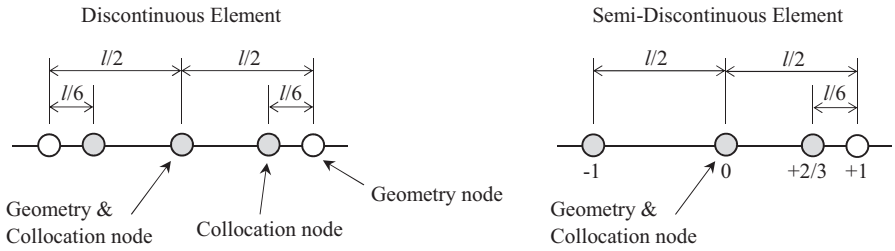

FIGURE 8.7 Bidimensional discontinuous or semidiscontinuous elements.

This book belongs to Central Library BADJI Mokhtar-ANNABA UNIVERSITY
Copyright Elsevier 2024

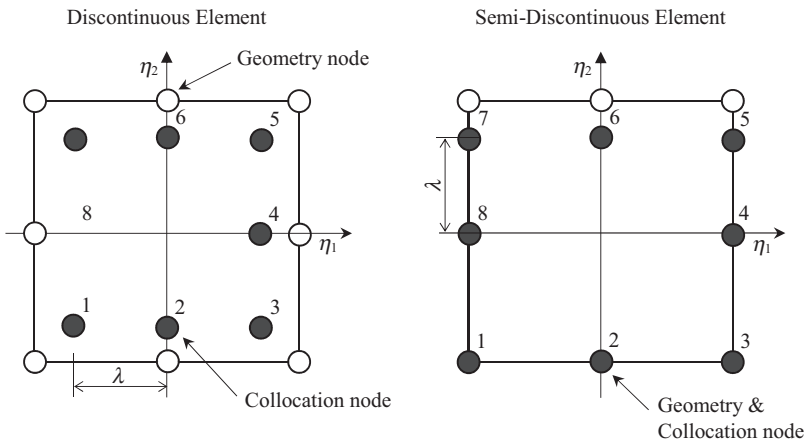

FIGURE 8.8 Three-dimensional discontinuous or semidiscontinuous elements.

metrics (Thornburg, 2012). Reported studies are related to computational fluid dynamics analysis, but the stated problems are common to other fields of analysis, wherever the numerical calculation makes use of a domain discretization.

In some cases, a very poor mesh can make the computational solver unstable (it may affect the condition number of the matrix system, making it ill conditioned). Therefore, the importance of generating high-quality mesh can never be overemphasized. Despite the automatic or semiautomatic mesh generation technique, a good mesh must properly follow well the CAD model, that is the topology of the geometry, but it is also strictly related to the nature of the physics to be solved.

Aspect ratio, warpage, orthogonality, and shearing are some factors that can affect the mesh quality. Mesh quality can be improved by choosing the appropriate topology, which controls the distortion of the elements, and using smoothing algorithms to evenly distribute elements. Topology will also determine how key features of the domain will be captured and how this characteristic will affect other regions of the mesh.

Already in the early 1990s, experiments made in Zhou et al. (1993) on both FEM and BEM models also suggested to refine mesh, aimed to improving the accuracy of the numerical solution, by adding nodes, and then elements, mainly in high curvatures areas (so that elements follow more closely the actual geometry of the domain involved) and where a higher stress/strain gradient is expected: newly introduced nodes must be located on the interpolated boundary surface if the underlying CAD surface does not exist.

Moreover, although the FEM mesh quality should be globally high all over the analyzed domain, the limited number of elements located on the boundary, on which BEM focuses the calculation, makes the mesh quality of such elements a key factor to limit the computational effort and get accurate results. This solution, performed on original boundary integral equations, is also used to run the integral analysis within the interior domain points. Thus, BEM users should take more care to mesh quality than that required for FEM studies. FEM solvers, in fact, working with a large number of elements, are able to mitigate the detrimental effects of the low-quality mesh of few elements, by averaging their response with that of several neighboring elements of higher quality. In BEM, instead, the mitigation effect is related to only few neighboring elements, so the propagation effect of the response of a low-quality element is more evident. The key aspects in generating a boundary mesh for a contact problem in a biomechanical application are reported in Perrella et al. (2015).

In Clerc et al. (2002), for an electro- and magnetoencephalography problem, authors concluded that the only significant disadvantage of FEM is the necessity of creating the 3D solid mesh, which can be much more difficult than creating the surface mesh, in case of presence of several small features. They also stated that for both methods the precision improves with the number of elements but with a higher rate when considering BEM.

Several studies that could be successfully applied in biomedical engineering problems, exploiting simultaneously advantages offered by both FEM and BEM were also documented. For example, in Elleithy (2008) a coupled FEM−BEM study is proposed for elastoplastic problems with adaptive FEM and BEM subdomains. BEM is used in regions where elastic material behavior occurs, whereas FEM is used for local plastic material behavior, all in a global adaptive procedure while calculation goes on. In this way, the global computational effort is reduced as most of the domain is only meshed on the boundary. See also the fast simulation with BEM of the human gait motion described in Tang and Hui (2011).

As previously said, BEM works on boundary elements over which the solution is approximated using interpolation functions: with high interpolation order, one issue is the computation time. For electrocardiographic imaging (ECGI)

This book belongs to Central Library BADJI Mokhtar-ANNABA UNIVERSITY Copyright Elsevier 2024

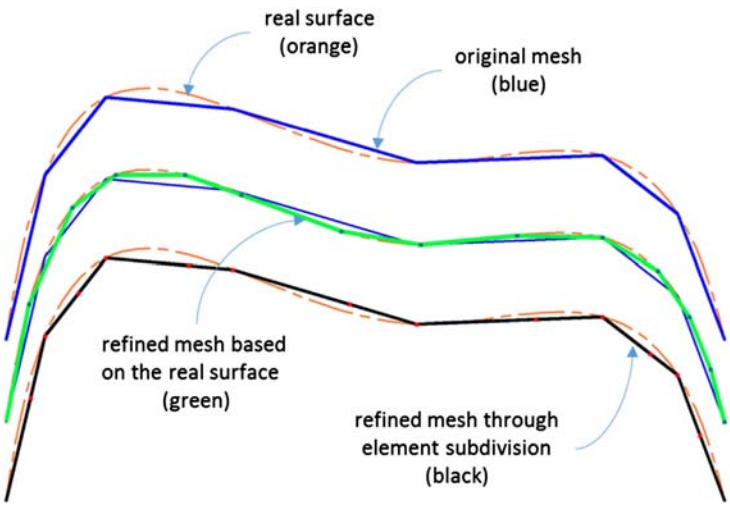

FIGURE 8.9 Refining mesh without and with underlying surface.

reconstruction problems, a study of linear interpolation (LI) versus quadratic interpolation (QI) is documented in Ghosh and Rudy (2005): QI requires about twice the computation time of LI for the same number of boundary nodes. However, QI significantly improves the accuracy and resolution.

Mesh refinement with h-adaptive and p-adaptive methods in BEM is documented in Kita and Kamiya (2001). P-adaptive mesh refinement method seems to be more promising because it does not require a local remeshing, which sometimes can be difficult to perform in an automatic way (and with the guarantee to generate a good mesh quality) in areas with high curvature and small features; therefore the mesh remains the same and only the polynomial order of the interpolating functions increases. This is useful especially for 3D tessellated biomodels created from medical images, as described later on in this chapter, where no original CAD surface exists. If the underlying surface geometry is available, the remeshing task is easier (the added nodes always belong to the surface) than in case of lack of the mathematical characterization of the surface. In the latter case, the simplest way to refine a mesh is to generate new elements by a subdivision of existing elements (Fig. 8.9). A very common alternative technique comes from the discrete differential geometry field and consists in adding new elements on the inferred surface, based on the local discrete curvature defined by neighboring elements (Mesmoudi et al., 2012).

The meshing process in BEM studies can take advantages from the use of discontinuous elements with no (or few) interelement nodes (Parreira, 1998). This technique simplifies the mesh generation and makes easier to improve the mesh quality as few constraints occur, but the number of degrees of freedom increases and much computational effort is required. A nonconforming mesh is common in coupled FEM−BEM studies (Gonzalez et al., 2007), and it is also used in FEM when meshing issues come out when trying to generate a regular mesh (with shared nodes between adjacent elements) or to easily manage large-scale simulations. A gluing method is required to enforce interdomain continuity, when using a nonconforming mesh (Tian and Yagawa, 2007).

8.4.2 Modeling Issues in Biomedical Engineering Applications

Much of the above discussions about mesh design can be usefully recalled for BEM simulation studies involving 3D biomedical engineering models with complex free-form shapes. In BEM analysis, in fact, the user attention is only focused on the boundary mesh and this represents a simplification when working on very complex, although quite smooth, shapes.

The CAD representation of anatomical parts is often used for its ability to show detailed features, and as a reference model for subsequent computational analysis with mesh-based approaches. The availability, if any, of the boundary representation (B-rep model) of the body being analyzed offers more possibilities when running meshing algorithms based on the underlying surface.

If the aim of the study is not only the visualization of the model but also the computer simulation of its behavior under certain conditions, more graphical elaborations are necessary. In this context, image-based bio-CAD modeling is drawing more and more attention for the possibility to model and simulate body structures and tissues starting from a set of 2D image data collected by CT or magnetic resonance imaging (MRI) techniques widely used in diagnostic medicine (Sun et al., 2005).

This book belongs to Central Library BADJI Mokhtar-ANNABA UNIVERSITY Copyright Elsevier 2024

A quick tessellated representation of the surfaces can be used as is for diagnostic purposes, but to make the mesh suitable for FEM or BEM studies the application of denoising and smoothing/fairing algorithms is necessary (Bernardini et al., 1999). Smoothing/fairing a tessellated surface is the process of slightly modifying the shape to improve the distribution of curvature across it. It is usually required to remove wrinkles and local spikes, very common in reconstructed biomedical models, or also to attenuate the staircase characteristics of the voxel-based reconstruction, as discussed later on.

Several modeling issues are related to models of anatomical structures generated from a stack of 2D images, such as CT/MRI imaging techniques. In this wide field, a very common technique is the *contour-based approach* that, for each 2D image, generates the contour of the body through the segmentation process based on the grayscale value of each pixel determined solely by tissue density. Regions with almost homogeneous intensity values (in Hounsfield unit, HU) typically represent anatomical structures; local strong variations correspond to tissue boundaries. The threshold range used to detect the right tissue boundary plays an important role to differentiate between adjacent tissues and some automated methods were proposed to make a quick and accurate segmentation (Huang et al., 2010). In some cases, the manual local editing of the segmentation is still needed.

A more complex, but highly efficient, alternative to the contour-based approach is represented by the *voxel-based approach* where 2D slices of images are represented by a 3D array of volume elements (voxels) starting from the pixels of each image. Voxel dimensions depends on pixel dimension and slice distance; higher image resolution and smaller slice distance permit to reconstruct very small structures but the amount of data to manage can be computationally very expensive. The initial discrete model representation is entirely made of hexahedra. To avoid the staircase issues of such a model, algorithms such as marching cubes are then adopted to create the 3D topologically consistent triangular model of constant-density tessellated surfaces (Young et al., 2008). Mesh relaxing methods (Fig. 8.10 displays an example generated in Simpleware ScanIP software by Synopsys, Mountain View, USA) or a local mesh refinement process, starting from the almost uniform triangular mesh, can also be applied. Missing data in the segmentation process (due to the assigned threshold range) can cause imprecise reconstruction and requires special attention and dedicated algorithms as proposed in Huang et al. (2010).

Regarding the contour-based approach, the set of created contours (polygonal curves) are directly used to build up the 3D representation of the tissue's skin. In some cases, for simple geometries the CAD loft (skinning) operation through 2D curves can be sufficient to reconstruct the CAD surface or solid model of the part. Manual operations by a skilled user are often required for the presence of branches, multiple loops, and small features.

More often, the wide set of 2D contours described by points, representing a large point cloud, are used to generate a faceted model of the whole point data set through a triangulation method. This process is common in Reverse Engineering (RE) software, such as Geomagic Studio by 3D System and PolyWorks by InnovMetric or open systems such as MeshLab by Visual Computing Lab of the ISTI-CNR (www.meshlab.net; Cignoni et al., 2008). Additional computer operations are then usually necessary to get a clean, closed, and smooth representation of the body.

To clarify this process, a faceted model of a human edentulous mandible generated by CT imaging is shown in Fig. 8.11. The decimated model consists of 46,572 triangular elements. The detailed view in Fig. 8.11B shows the quality level (low for computational analyses) of the original mesh and the improved mesh (Fig. 8.11C) by adopting remeshing and smoothing algorithms. The generated new mesh, with 46,924 almost equilateral triangles, fits well the original mesh as shown in Fig. 8.11D. This mesh is ready for the conversion in a computational mesh for a BEM analysis, while it requires additional work for meshing the interior volume useful for a FEM analysis. Fig. 8.12 shows the comparison of a triangular boundary mesh (suitable for BEM) and a tetrahedral volume mesh (suitable for FEM), generated starting from the previous surface mesh.

In the latter case, the advancing front method (Frey et al., 1996) can be adopted to generate the volumetric mesh by progressively adding mesh elements moving from the boundary elements toward the interior domain.

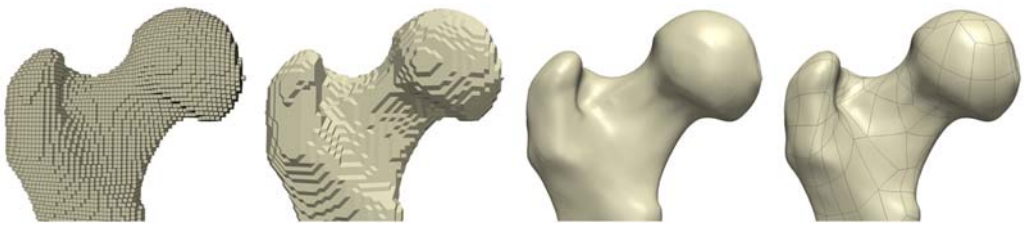

FIGURE 8.10 Reconstruction from computed tomography with (from left to right) the voxel-based model, the coarsely triangulated model, the smoothly refined model, and the final patch-fitted surface model. *Courtesy of Simpleware by Synopsys, Mountain View, USA.*

This book belongs to Central Library BADJI Mokhtar-ANNABA UNIVERSITY Copyright Elsevier 2024

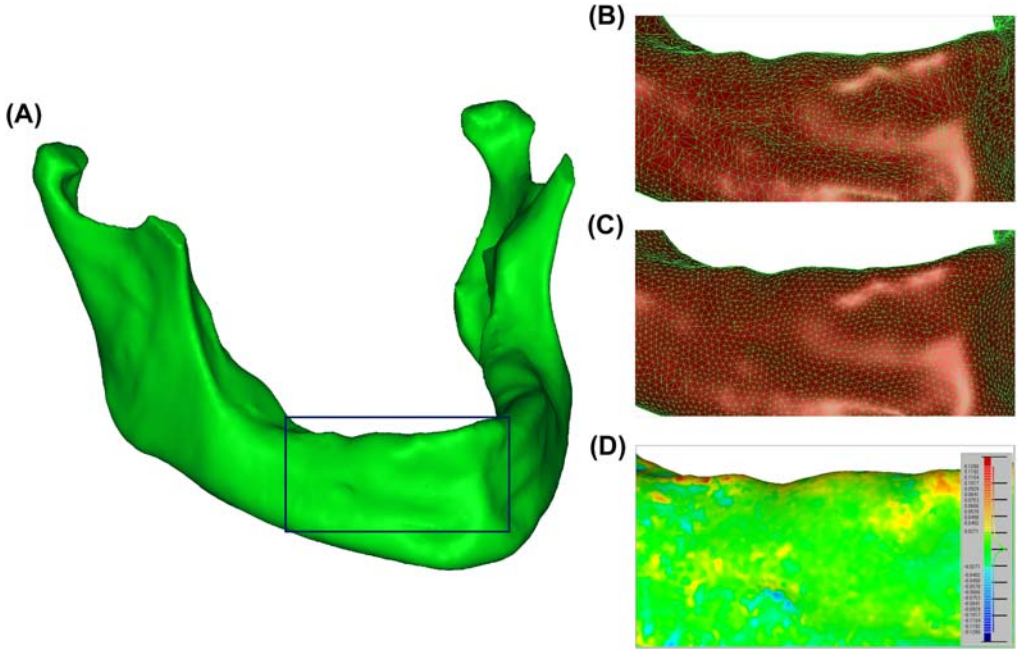

FIGURE 8.11 Improving surface mesh: tessellated model of the human edentulous mandible (A); detail of the original mesh from CT (B); detail of the remeshed and smoothed model (C); deviations (D).

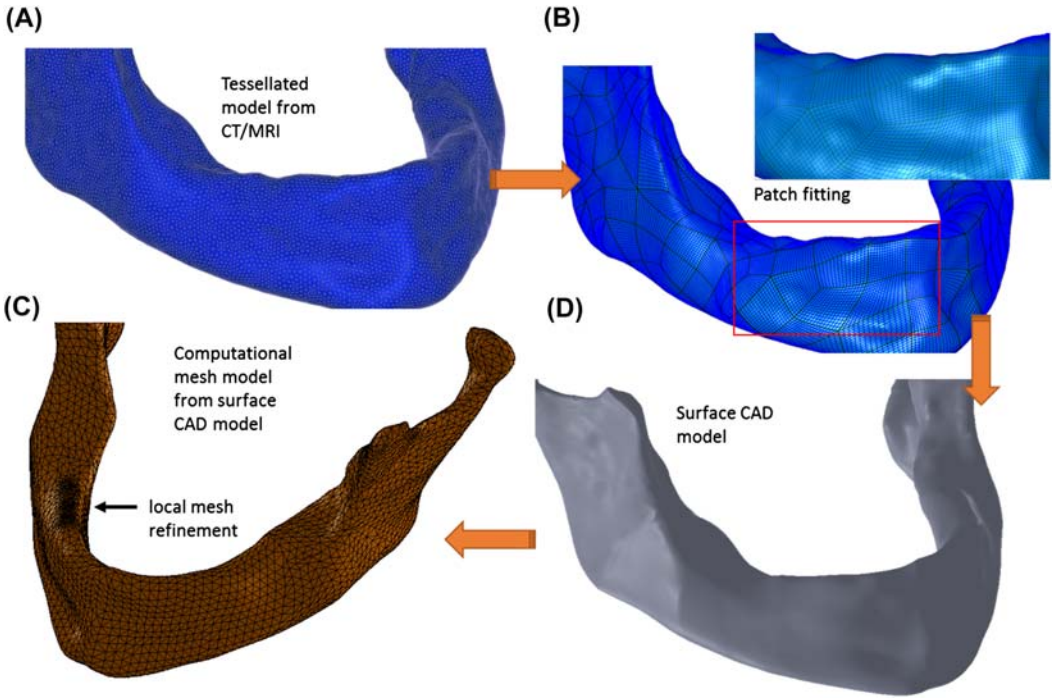

FIGURE 8.12 Pathway to computer-aided design (CAD) surface-based computational mesh model. The creation of the local mesh control is easier in the preprocessing environment.

RE software offers useful tools for fitting surface patches, usually with B-spline or non uniform rational basis-splines (NURBS) formulation, on a tessellated model so as to generate a smooth (surface or solid) CAD model (Bernardini et al., 1999). See also Fig. 8.10 for an example of a surface model with fitted patches over the faceted model. Patches can be merged to represent larger portions of surfaces. Smaller patches can better fit local high curvature geometry, but the file size

This book belongs to Central Library BADJI Mokhtar-ANNABA UNIVERSITY Copyright Elsevier 2024

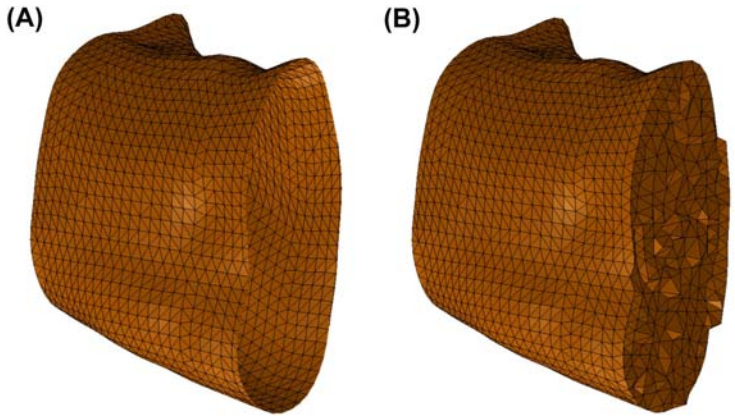

FIGURE 8.13 (A) Surface mesh and (B) tetrahedral volume mesh (generated starting from the surface mesh on the left).

usually increases. Often, the model from which a computational mesh is generated in dedicated environments (CAE preprocessors) offers several tools for a better control of the local mesh, where needed, based on the underlying CAD surfaces. Following the above steps, Fig. 8.13 shows a common pathway to generate a computational mesh from CT/MRI images: after creating the 3D tessellated geometry from a set of 2D contours, surface patches are fit and then sewed to form a CAD surface model (or solid, if all the surfaces together define a topologically closed model). That model is then used to create the computational mesh according to the boundary conditions to be applied (constraints and loads) and the physics to analyze. The availability of the underlying surface permits to edit and control the mesh, properly adapted to the local curvature of the geometry; on the other hand, this is not easy to guarantee if the mathematical representation of the surface is missing.

Before running the computational analysis with this type of models, much attention must be focused on the normal vector of each element. In BEM modeling, elements must be properly oriented and normal to define the relative position of the internal volume then making this aspect crucial in CAD−CAE data exchange. Useful free tools for creating, editing, and checking surface and volumetric mesh are, among others, the CGAL library (www.cgal.org) and Iso2Mesh, a Matlab-based mesh generation and processing toolbox (iso2mesh.sourceforge.net; Fang and Boas, 2009). In the field of biomedical imaging, common commercial solutions are offered by Mimics (Materialise, 2016), Simpleware (Synopsys, 2016) and Amira (FEI, 2016). This software also offers options to fit surface patches on the polygonal models and export them to any CAD-based environment, along with the possibility to directly work on imported CAD models to tailor the reconstructed geometry.

An optimization problem involving the adaptation of the boundary, described as β-spline surfaces, is reported in Annicchiarico et al. (2007). The β-spline formulation it used for its flexibility and relative simplicity to modeling geometry that can be easily modified and locally controlled, by few parameters, to be adapted to the remodeling action of the bone. Some authors proposed the isogeometric approach by using directly the NURBS formulation of the CAD surfaces for BEM analysis purposes (Taus, 2015). A similar research, relying on the representation model of the boundary surface with Bezier triangular patches, is proposed in Zieniuk and Szerszen (2013). These researches demonstrate the great potential of BEM over other numerical methods when working directly on the smooth CAD representations without requiring an explicit mesh domain.

To obtain a better controlled mesh, users can also create a CAD model from the intersection curves of the polygonal model with a set of cross-planes (Odesanya et al., 1993). Different configurations can be considered for the cutting planes (parallel, nonparallel, unorganized) following the topology of the model and able to capture some specific features. The set of obtained curves can be used to create the 3D model by using common CAD surface tools or specific surface fitting algorithms (Amini et al., 2013; Li et al., 2015).

In the following, an example of surface reconstruction in a CAD environment, related to the mandible model already shown in Fig. 8.11A, is described. The polygonal model is subdivided in five regions with specific cross-sectioning set of planes following the topology of the model (Fig. 8.14) and adopting a constant degree of NURBS curves for each region. In this way, no distortion of the loft surfaces (that can influence the subsequent meshing phase) is introduced. An example of highly distorted lofting operation is shown in Fig. 8.15. Blending operation is then used to connect regions. The automatic procedure was implemented in Rhinoceros V4 environment in VBS language; the user can set the number of cross-sectional planes and check the accuracy of the intersecting cross-sectional curves, as well as of the loft surface, with

This book belongs to Central Library BADJI Mokhtar-ANNABA UNIVERSITY Copyright Elsevier 2024

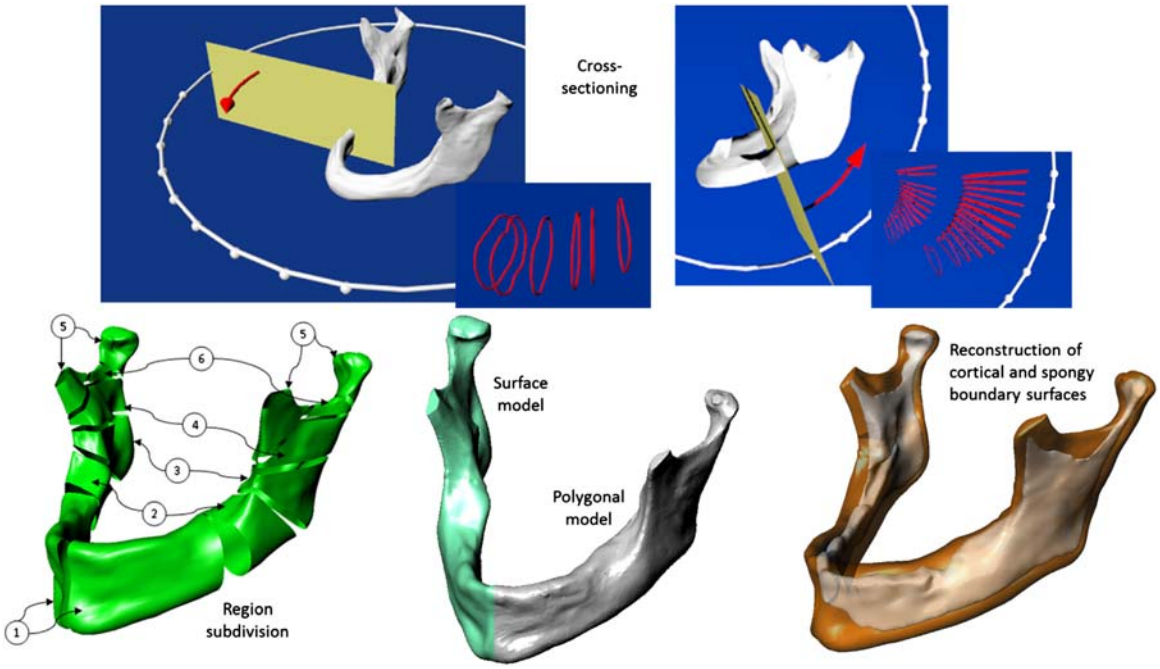

FIGURE 8.14 Cross-sectioning and surface reconstruction of the mandible polygonal model.

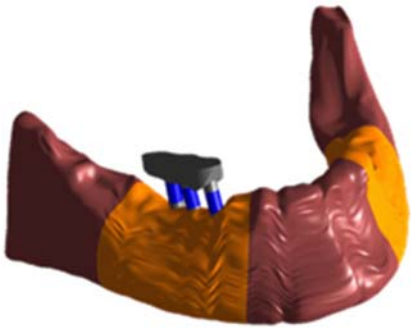

FIGURE 8.15 Example of distorted lofting operation through cross-sectional *curves*. Surface relaxing algorithms are necessary before meshing the model.

respect to the underlying polygonal model. The procedure can be applied to both external (cortical bone) and internal (spongy bone) boundary of the mandible. Anyway, this approach can only be used in an automatic way on quite simple geometries. More user control is required to set the best position of cross-sectional planes in case of mandible with teeth, or in presence of hole for missing tooth.

Perrella et al. (2015) analyzed in FEM and BEM environments the problem of partial osteointegration between the implant and the mandibular bone, under isotropic and orthotropic bone material assumptions. A nonlinear contact with friction was modeled to allow for interaction between implant and bone. The authors focused the attention on the correct surface modeling of the implant threads finalized to the creation of a proper mesh in FEM (COMSOL Multiphysics, 2017) and, in particular, in BEM (BEASY, 2014) environments.

Generally speaking, when dealing with 3D geometrical models to be transferred from a CAx environment to another, via neutral exchange format (such as IGES and STEP), it is necessary to tackle translation issues, resorting to healing tools to repair the models. Best practices leverage on the proper setting of the translation parameters and of the model accuracy, defined in each software to control the translation process. Moreover, common set of entities that systems are able to handle have to be selected. This process not always ends up successfully as reported in Perrella et al. (2015). The translated "multiedge" surface patches (with more than four edges) were not effectively meshed by the adopted BEM code (Fig. 8.16), so that a CAD editing effort was needed to arrange all surfaces in three- or four-edge patches and then mesh

This book belongs to Central Library BADJI Mokhtar-ANNABA UNIVERSITY Copyright Elsevier 2024

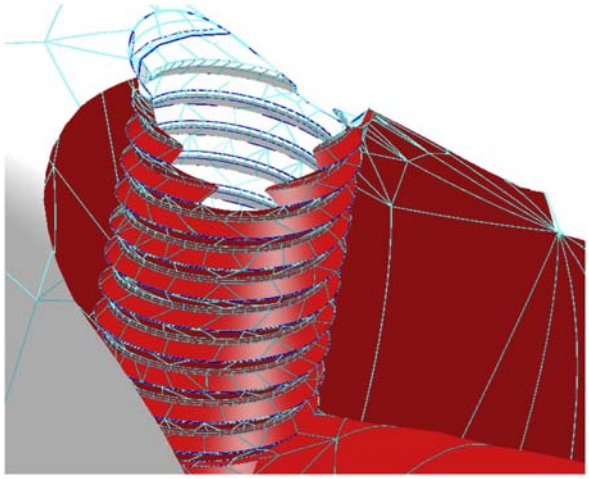

FIGURE 8.16 Example of bad mesh generation due to the multiedge patches coming from the computer-aided design model.

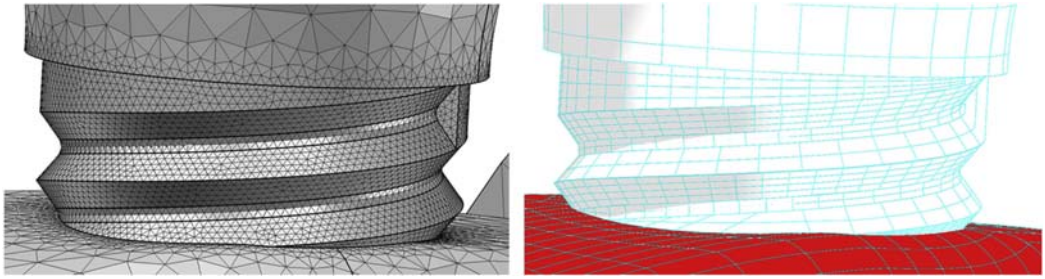

FIGURE 8.17 Detail of the mesh density on finite element method and boundary element method models in Perrella et al. (2015).

them with boundary elements. Such problem with the meshing algorithm is a consequence of the underlying mathematical definition of the curves/surfaces that provide the mesh "support."

In terms of accuracy enabled by a well-structured boundary mesh, in Fig. 8.17, the reader can note that relatively few elements on the implant's threads in BEM can reproduce the same stress gradient of the very dense mesh necessary with FEM, especially considering a nonlinear contact problem. Such very refined FEM mesh, needed on the boundary to properly tackle contact problems, produces also a huge number of elements in the interior domain of the FEM model.

A mixed linear-quadratic mesh BEM model of 39.000 dof was adopted (quadratic elements along the threads for the inclined load condition), about 19 times lesser than the linear mesh FEM model, with about 730.000 dof. A relatively longer mesh improvement study for FEM model was required to reach the reported results.

8.5 COMPARISON OF STRESS RESULTS BY BOUNDARY ELEMENT METHOD AND FINITE ELEMENT METHOD IN A BONE–IMPLANT APPLICATION

With reference to the models depicted in Fig. 8.17, it is interesting to highlight the satisfactory matching between FEM and BEM stress results, so as to provide the reader with an insight into the relative mesh refinement required by the two methods to get comparable accuracy. In particular, contour plots of the pressure on the thread are shown, as taken from Perrella et al. (2015), under different hypotheses related to material properties, loading conditions, and interface friction coefficients (Figs. 8.18 and 8.19).

Again a satisfactory matching between FEM and BEM results is described in Citarella et al. (2012a), where a FEM and a BEM mesh of comparable accuracy are shown (Fig. 8.20).

8.6 CONCLUDING REMARKS

In this chapter, a description of BEM applications in biomechanics is provided, with a focus on advantages and limitations of BEM versus other numerical methods such as FEM, FDM and MMs.

This book belongs to Central Library BADJI Mokhtar-ANNABA UNIVERSITY Copyright Elsevier 2024

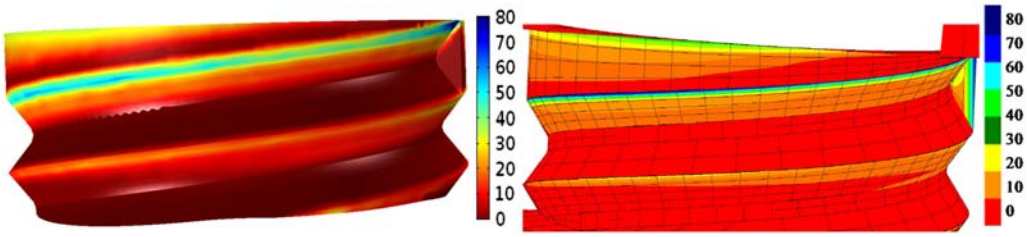

FIGURE 8.18 Contour plot of normal tractions (MPa) for finite element method (left) and boundary element method (right) models on the implant/cortical bone interface—with friction allowance, axial loading, and isotropic bone properties.

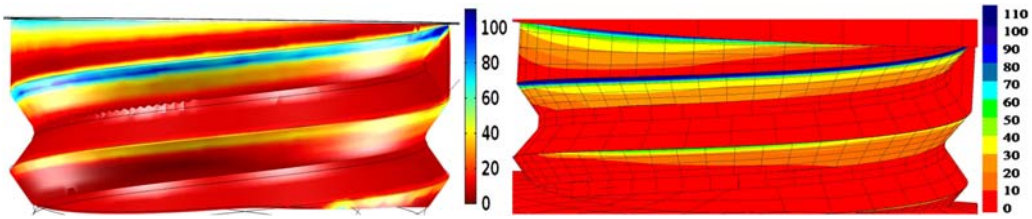

FIGURE 8.19 Contour plot of normal tractions (MPa) for finite element method (left) and boundary element method (right) models on the implant/cortical bone interface—with friction allowance, axial loading, and transversely isotropic bone properties.

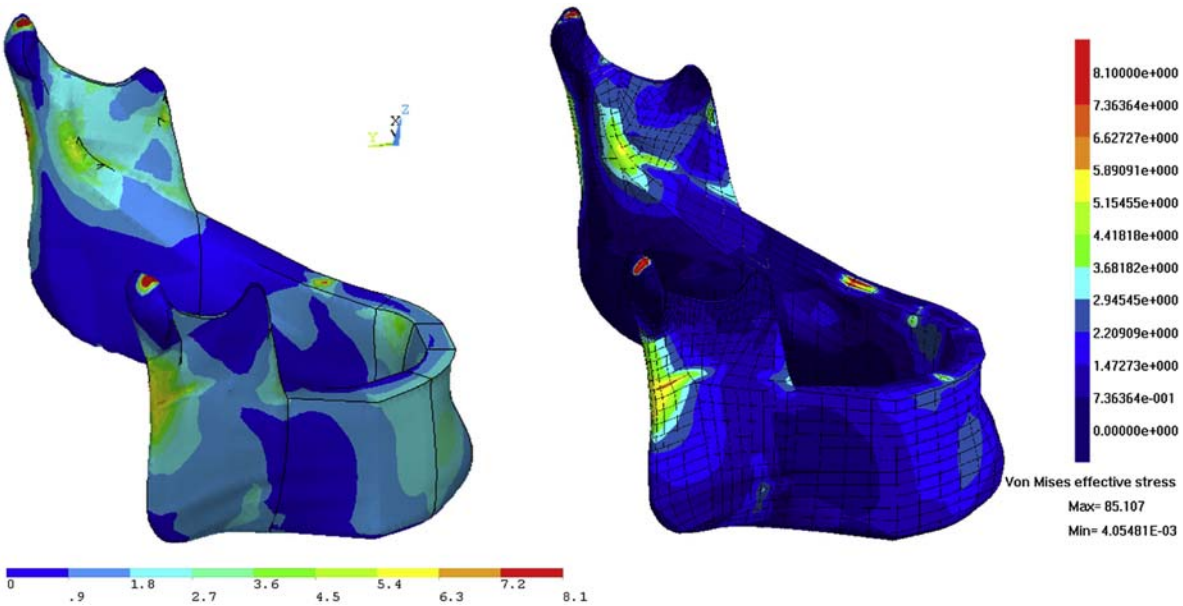

FIGURE 8.20 Finite element method (FEM) mesh (A) and von Mises equivalent stresses (MPa), obtained by FEM (B) and boundary element method (C) approaches.

In particular, BEM approach turns out to be advantageous in biomechanical problems involving fracture mechanics and contact modeling because of its preprocessing flexibility to tackle sharp geometric changes and complex remeshing. This is the reason for a particular emphasis in this chapter to the DBEM formulation that turns out to be one of the most efficient approaches to tackle fracture problems (e.g., in bones). A comparison among BEM and other numerical approaches is described in terms of relative accuracy and pre-/postprocessing efforts.

As BEM works on the domain boundary, special attention must be drawn to the mathematical reconstruction of bio-CAD models to facilitate the meshing process and reduce the geometrical imperfections generated during the CAD to CAE translation phase.

BEM is best suited to reproduce accurately high surface stress gradients that generally are modeling issues (e.g., in bone−implant contact simulations). Working with 3D models, the mesh refinement in the neighboring areas where high

This book belongs to Central Library BADJI Mokhtar-ANNABA UNIVERSITY Copyright Elsevier 2024

stress gradients are expected is much facilitated when using BEM, also because it is possible to use discontinuous elements and circumvent the constraints of a continuous mesh.

BEM is certainly more accurate for linear analysis but, on the other hand, less versatile in some areas such as those of highly nonlinear material behavior.

For complex shapes, such as those generated in biomedicine from CT/MRI techniques, the possibility to limit the meshing process only to the boundary may be decisive to circumvent several critical meshing issues inherent to the FEM approach, which also requires to discretize the interior domain. As a matter of fact, for analyses where the remeshing is a critical step, the advantage of BEM versus FEM is more evident, e.g., in case of optimization problems and fracture problems.

The peculiarities of BEM facilitate the formulation of new methods relying directly on the full CAD mathematical formulation of the solid model (with B-spline, NURBS, β-spline, and other similar descriptions). This approach seems to be very promising for biomechanical problems that involve complex shapes that can be fully reconstructed with surface patches, following the common approach in the RE field. An open issue related to this methodology is the need to properly convert the topological model from the CAD environment to the BEM-based system, which often requires healing tools to repair the imported geometry. The typology of generated surface patches is critical to get optimized meshes by automatic remeshing with BEM software.

REFERENCES

Aliabadi, M.H., 2002. The boundary element method. In: Applications in Solids and Structures, vol. 2. John Wiley & Sons Ltd., Chichester.

Amini, O., Boissonnat, J.D., Memari, P., 2013. Geometric tomography with topological guarantees. Discrete and Computational Geometry 50, 821−856.

Annicchiarico, W., Martinez, G., Cerrolaza, M., 2007. Boundary elements and b-spline surface modeling for medical applications. Applied Mathematical Modelling 31, 194−208.

Armentani, E., Caputo, F., Citarella, R., 2010. FEM sensitivity analyses on the stress levels in a human mandible with a varying ATM modelling complexity. The Open Mechanical Engineering Journal 4, 8−15.

Atluri, S.N., Shen, S., 2002. The Meshless Local Petrov-Garlekin (MLPG). Tech. Science Press.

Ausiello, P., Franciosa, P., Martorelli, M., Watts, D.C., 2012. Effects of thread features in osseo-integrated titanium implants using a statistics-based finite element method. Dental Materials 28 (8), 919−927.

Banerjee, P.K., 1994. The Boundary Element Methods in Engineering. McGraw-Hill, New York.

BEASY Ltd., 2014. BEASY V10r16, Documentation. www.beasy.com.

Becker, A.A., 1992. The Boundary Element Method in Engineering. McGraw-Hill, London.

Bernardini, F., Bajaj, C.L., Chen, J., Schikore, D.R., 1999. Automatic reconstruction of 3D CAD models from digital scans. International Journal of Computational Geometry and Applications 9, 327−369.

Betti, E., 1872. Teoria della elasticità. Nuovo Cimento 2, 6−10.

Cignoni, P., Callieri, M., Corsini, M., Dellepiane, M., Ganovelli, F., Ranzuglia, G., 2008. MeshLab: an open-source mesh processing tool. In: Scarano, V., De Chiara, R., Erra, U. (Eds.), Eurographics Italian Chapter Conference. The Eurographics Association, Italy, pp. 129−136.

Citarella, R., Armentani, E., Caputo, F., Naddeo, A., 2012a. FEM and BEM analysis of a human mandible with added temporomandibular joints. The Open Mechanical Engineering Journal 6, 100−114.

Citarella, R., Armentani, E., Caputo, F., Lepore, M., 2012b. Stress analysis of an endosseus dental implant by BEM and FEM. The Open Mechanical Engineering Journal 6, 115−124.

Clerc, M., Dervieux, A., Faugeras, O., Keriven, R., Kybic, J., Papadopoulo, T., 2002. Comparison of BEM and FEM methods for the E/MEG problem. In: Proceedings of BIOMAG Conference.

COMSOL Inc., 2017. COMSOL Multiphysics Modeling Software. www.comsol.com.

Duarte, V., González, Y., Cerrolaza, M., 2011. Boundary element simulation of bone tissue. International Journal of Biomedical Engineering and Technology 5, 211−228.

Elleithy, W., 2008. Analysis of problems in elasto-plasticity via an adaptive FEM−BEM coupling method. Computer Methods in Applied Mechanics and Engineering 197, 3687−3701.

Fang, Q., Boas, D.A., 2009. Tetrahedral mesh generation from volumetric binary and gray-scale images. In: International Symposium on Biomedical Imaging, Boston, MA.

FEI Company, 2016. Amira. www.fei.com/software/amira-for-life-sciences/.

Fischer, G., Tilg, B., Modre, R., et al., 2000. A bidomain model based BEM-FEM coupling formulation for anisotropic cardiac tissue. Annals of Biomedical Engineering 28, 1229−1243.

Franciosa, P., Martorelli, M., 2012. Stress-based performance comparison of dental implants by finite element analysis. International Journal of Interactive Design and Manufacturing 6, 123−129.

Fredholm, I., 1903. Sur une classe d'equations fonctionelles. Acta Mathematica 27, 365−390.

Frey, P.J., Borouchaki, H., George, P.L., 1996. Delaunay tetrahedralization using an advancing-front approach. In: 5th International Meshing Roundtable, IMRT'96. Sandia National Laboratories, pp. 31−46.

This book belongs to Central Library BADJI Mokhtar-ANNABA UNIVERSITY Copyright Elsevier 2024

Gámez, B., Divo, E., Kassab, A.J., Cerrolaza, M., 2010. Evaluation of fatigue crack growing in cortical bone using the BEM. International Journal of Healthcare Technology and Management 11 (3), 202–221.

Ghosh, S., Rudy, Y., 2005. Accuracy of quadratic versus linear interpolation in noninvasive electrocardiographic imaging (ECGI). Annals of Biomedical Engineering 33 (9), 1187–1201.

Gonzalez, J.A., Park, K.C., Felippa, C.A., 2007. FEM and BEM coupling in elastostatics using localized lagrange multipliers. International Journal for Numerical Methods in Engineering 69 (10), 2058–2074.

Gonzalez, Y., Cerrolaza, M., Gonzalez, C., 2009. Poroelastic analysis of bone tissue differentiation by using the boundary element method. Engineering Analysis with Boundary Elements 33, 731–740.

Grivas, K.N., Vavva, M.G., Sellountos, E.J., Polyzos, D., Fotiadis, D.I., 2013. A meshless local boundary integral equation (LBIE) method for cell proliferation predictions in bone healing. Conference Proceeding IEEE Engineering in Medicine and Biology Society 2013, 2676–2679. http://dx.doi.org/10.1109/EMBC.2013.6610091.

Huang, C.-Y., Luo, L.-J., Lee, P.-Y., Lai, J.-Y., Wang, W.-T., Lin, S.-C., 2010. Efficient segmentation algorithm for 3D bone models construction on medical images. Journal of Medical and Biological Engineering 31 (6), 375–386.

Kim, B., Moon, B., Park, J., 2006. Biomechanical finite element analysis of bone cemented hip crack initiation according to stem design. Journal of Mechanical Science and Technology 20 (12), 2168–2177.

Kim, E., Guilak, F., Haider, M.A., 2010. An axisymmetric boundary element model for determination of articular cartilage pericellular matrix properties in situ via inverse analysis of chondron deformation. Journal of Biomechanical Engineering 132 (3), 031011.

Kita, E., Kamiya, N., 2001. Error estimation and adaptive mesh refinement in boundary element method, an overview. Engineering Analysis with Boundary Elements 25 (7), 479–495.

Knupp, P.M., 2007. Remarks on mesh quality. In: 45th AIAA Aerospace Sciences Meeting and Exhibit, Reno, NV.

Kupradze, V.D., 1963. Dynamical problems in elasticity. In: Sneddon, I.N., Hills, R. (Eds.), Progress in Solid Mechanics, vol. III. North-Holland.

Lachat, J.C., Watson, J.O., 1976. Effective numerical treatment of boundary integral equations: a formulation for three-dimensional elastostatics. International Journal for Numerical Methods in Engineering 10, 991–1005.

Leahy, J.G., Becker, A.A., 1999. A quadratic boundary element formulation for three-dimensional contact problems with friction. The Journal of Strain Analysis for Engineering Design 34, 235–251.

Lee, D., Ahn, T.S., 2014. A boundary element model for acoustic responses in the ear canal and its statistical validation and updating. Journal of Mechanical Science and Technology 28 (4), 1203–1217.

Li, Y., Chen, W., Cai, Y., Nasri, A., Zheng, J., 2015. Surface skinning using periodic T-spline in semi-NURBS form. Journal of Computational and Applied Mathematics 273, 116–131.

Martínez, G., García Aznar, J.M., Doblaré, M., Cerrolaza, M., 2006. External bone remodeling through boundary elements and damage mechanics. Mathematics and Computers in Simulation 73, 183–199.

Martínez, G., Cerrolaza, M., 2006. A bone adaptation integrated approach using BEM. Engineering Analysis with Boundary Elements 30 (2), 107–115.

Materialise, N.V., 2016. Mimics. www.materialise.com/en/medical/software/mimics.

Meier, U., Lopez, O., Monserrat, C., Juan, M.C., Alcaniz, M., 2005. Real-time deformable models for surgery simulation: a survey. Computer Methods and Programs in Biomedicine 77 (3), 183–197.

Mesmoudi, M.M., De Floriani, L., Magillo, P., 2012. Discrete curvature estimation methods for triangulated surfaces. In: Applications of Discrete Geometry and Mathematical Morphology, vol. 7346 Of the Series Lecture Notes in Computer Science, pp. 28–42.

Mikhlin, S.G., 1957. Integral Equation. Pergamon Press, London.

Odesanya, O.S., Waggenspack Jr., W.N., Thompson, D.E., 1993. Construction of biological surface models from cross sections. IEEE Transactions on Biomedical Engineering 40 (4), 329–334.

Ojeda, D., Divo, E., Kassab, A., Cerrolaza, M., 2008. Cavity detection in biomechanics by an inverse evolutionary point load BEM technique. Inverse Problems in Science and Engineering 16 (8), 981–993.

Ooi, E.H., Ang, W.T., Ng, E.Y.K., 2007. Bioheat transfer in the human eye: a boundary element approach. Engineering Analysis with Boundary Elements 31 (6), 494–500.

Ooi, E.H., Ang, W.T., Ng, E.Y.K., 2009. A boundary element model for investigating the effects of eye tumor on the temperature distribution inside the human eye. Computers in Biology and Medicine 39 (8), 667–677.

Ota, T., Yamamoto, I., Morita, R., 1999. Fracture simulation of the femoral bone using the finite-element method: how a fracture initiates and proceeds. Journal of Bone and Mineral Metabolism 17 (2), 108–112.

Parreira, P., 1998. On the accuracy of continuous and discontinuous boundary elements. Engineering Analysis 5 (4), 205–211.

Peng, H., 2014. Influence of strut structure on hemodynamic characteristics by the boundary element method. WIT Transactions on Modelling and Simulation 56, 471–477.

Perrella, M., Franciosa, P., Gerbino, S., 2015. FEM and BEM stress analysis of mandibular bone surrounding a dental implant. The Open Mechanical Engineering Journal 9, 282–292.

Portela, A., 1993. Dual Boundary Element Analysis of Crack Growth. WIT Press, Southampton.

Portela, A., Aliabadi, M.H., 1992. The dual boundary element method: effective implementation for crack problems. International Journal for Numerical Methods in Engineering 33, 1269–1287.

Qiu, Z.H., Wrobel, L.C., Power, H., 1995. Boundary element approach to mass and charge transport in electrochemical cells. Engineering Analysis with Boundary Elements 15, 299–312.

This book belongs to Central Library BADJI Mokhtar-ANNABA UNIVERSITY

Copyright Elsevier 2024

Rigby, R.H., Aliabadi, M.H., 1993. Mixed-mode J-integral method for analysis of 3D fracture problems using BEM. Engineering Analysis with Boundary Elements 11, 239–256.

Rigby, R.H., Aliabadi, M.H., 1998. Decomposition of the mixed-mode J-integral – revisited. International Journal of Solids and Structures 35 (17), 2073–2099.

Sadegh, A.M., Luo, G.M., Cowin, S.C., 1993. Bone in growth: an application of the boundary element method to bone remodelling at the implant interface. Journal of Biomechanics 26, 167–182.

Sammartino, G., Marenzi, G., Citarella, R., Ciccarelli, R., Wang, H.-L., 2008. Analysis of the occlusal stress transmitted to the inferior alveolar nerve by an osseointegrated threaded fixture. Journal of Periodontology 79 (9), 1735–1744.

Sammartino, G., Wang, H.-L., Citarella, R., Lepore, M., Marenzi, G., 2013. Analysis of occlusal stresses transmitted to the inferior alveolar nerve by multiple threaded implants. Journal of Periodontology 84 (11), 1655–1661.

Sellountos, E.J., Polyzos, D., 2008. A meshless local boundary integral equation method for solving transient elastodynamic problems. Computational Mechanics 35, 265–276.

Sellountos, E.J., Sequeira, A., 2008. An advanced meshless LBIE/RBF method for solving two-dimensional incompressible fluid flows. Computational Mechanics 41 (5), 617–631.

Sellountos, E.J., Polyzos, D., Atluri, S.N., 2012. A new and simple meshless LBIE-RBF numerical scheme in linear elasticity. Computer Modeling in Engineering and Sciences 89 (6), 513–551.

Sfantos, G.K., Aliabadi, M.H., 2007. Total hip arthroplasty wear simulation using the boundary element method. Journal of Biomechanics 40, 378–389.

Sikora, J., Arridge, S.R., Bayford, R.H., Horesh, L., 2004. The application of hybrid BEM/FEM methods to solve electrical impedance tomography's forward problem for the human head. In: CEBI'04-XII Int Conf Electrical Bio-impedance Joint with EIT-v Electrical Impedance Tomography, pp. 621–624.

Somigliana, C., 1885. Sopra l'equilibrio di un corpo elastico isotropo. Nuovo Cimento 3, 17–20.

Sun, W., Starly, B., Nam, J., Darling, A., 2005. Bio-CAD modeling and its applications in computer-aided tissue engineering. Computer-Aided Design 37 (11), 1097–1114.

Synopsys Inc., 2016. Simpleware. www.simpleware.com.

Tang, Y.M., 2010. Modeling skin deformation using boundary element method. Computer-Aided Design and Applications 7 (1), 101–108.

Tang, Y.M., Hui, K.C., 2011. Human foot modeling towards footwear design. Computer-Aided Design 43, 1841–1848.

Taus, M.F., 2015. Isogeometric Analysis for Boundary Integral Equations (Ph.D. dissertation). The University of Texas at Austin.

Thornburg, H.J., 2012. Overview of the PETTT Workshop on Mesh Quality/Resolution, Practice, Current Research, and Future Directions. AIAA paper no. 2012–0606.

Tian, R., Yagawa, G., 2007. Non-matching mesh gluing by meshless interpolation – an alternative to lagrange multipliers. International Journal for Numerical Methods in Engineering 71 (4), 473–503.

Van't Wout, E., Gélat, P., Betcke, T., Arridge, S., 2015. A fast boundary element method for the scattering analysis of high-intensity focused ultrasound. Journal of the Acoustical Society of America 138 (5), 2726–2737.

Veerapaneni, S.K., Gueyffier, D., Zorin, D., Biros, G., 2009. A boundary integral method for simulating the dynamics of inextensible vesicles suspended in a viscous fluid in 2D. Journal of Computational Physics 228 (7), 2334–2353.

Wang, P., Becker, A.A., Jones, I.A., Glover, A.T., Benford, S.D., Greenhalgh, C.M., Vloeberghs, M., 2007. Virtual reality simulation of surgery with haptic feedback based on the boundary element method. Computers and Structures 85 (7–8), 331–339.

Young, P.G., Beresford-West, T.B.H., Coward, S.R.L., Notarberardino, B., Walker, B., Abdul-Aziz, A., 2008. An efficient approach to converting three-dimensional image data into highly accurate computational models. Philosophical Transactions of the Royal Society A 366, 3155–3173.

Zerroukat, M., Power, H., Wrobel, L.C., 1998. Heat and solute diffusion with a moving interface: a boundary element approach. International Journal of Heat and Mass Transfer 41 (16), 2429–2436.

Zhou, H., Peters, M., van Oosterom, A., 1993. On Mesh Refinement and Accuracy of Numerical Solutions. IEEE Engineering in Medicine and Biology Society, San Diego, CA, pp. 1476–1477.

Zieniuk, E., Szerszen, K., 2013. Triangular Bézier surface patches in modeling shape of boundary geometry for potential problems in 3D. Engineering with Computers 29 (4), 517–527.

This book belongs to Central Library BADJI Mokhtar-ANNABA UNIVERSITY

Copyright Elsevier 2024

This page intentionally left blank

This book belongs to Central Library BADJI Mokhtar-ANNABA UNIVERSITY

Copyright Elsevier 2024

Part III

Discrete and Particle Methods

This book belongs to Central Library BADJI Mokhtar-ANNABA UNIVERSITY

Copyright Elsevier 2024

This page intentionally left blank

This book belongs to Central Library BADJI Mokhtar-ANNABA UNIVERSITY

Copyright Elsevier 2024

Chapter 9

A Particle Finite Element–Based Framework for Differentiation Paths of Stem Cells to Myocytes and Adipocytes: Hybrid Cell–Based and Finite Element Modeling

F.J. Vermolen[1], S.D. Harrevelt[1], A. Gefen[2] and D. Weihs[3]

[1]Delft University of Technology, Delft, The Netherlands; [2]Tel Aviv University, Tel Aviv, Israel; [3]Technion–Israel Institute of Technology, Haifa, Israel

9.1 INTRODUCTION

Differentiation of mesenchymal stem cells is an important (sub)process in many biological and medical phenomena related to tissue maintenance, regeneration, healing, and tissue repair, or to development of pathologies such as cancer and tissue atrophies. See Wu et al. (2007) for a study where cell differentiation of mesenchymal stem cells enhances wound healing. To prevent or treat certain diseases, or to enhance the health of individuals, various treatment procedures aim at revising the differentiation paths of (stem) cells, see Sell (2004) and Yan and Liu (2016) for applications in the framework of cancer. Because cell differentiation merely represents a specialization of cells to perform a certain biological task, the differentiation process of a cell depends largely not only on its environment but also on genetic programming and also age or a disease, when relevant. See for instance Guilak et al. (2010) for a presentation of stem cell fate by interactions with its environment and Stolzing et al. (2007) for more information about the influence of age on the differentiation of bone marrow–derived mesenchymal stem cells. It is well known that stimuli for cell differentiation that originate from the environment (locally or globally) can have varying natures, such as mechanical or chemical. A common treatment of patients involving stem cells, primarily in the field called regenerative medicine, is therefore aimed at influencing the differentiation pathways by modifying the mechanics and/or biochemical nature of the cell environment, see Gimble et al. (2007) for instance.

Considering biomedical processes such as wound healing, contractures as a result of large damage, formation of hypertrophic scars, initiation, and progression of cancer have been modeled in various studies. One may distinguish between various kinds of mathematical models on different scales, such as tissue scale, or cell colony-scale or even (sub)cellular scales. In this work, we will limit ourselves to the cell colony scale, where individual cells are considered in interaction with their environment through which they migrate and where they change their phenotypes. Some of the early cell-scale models have been developed by Drasdo and Höhme (2005) and Groh and Louis (2010). The experimental work by Reinhart-King et al. (2008) indicated that cells on a substrate communicate with each other through mechanical pulling forces that are exerted on the substrate if the forces exceed a certain threshold. Based on this observation, later different colony-scale models were constructed by Rey and Garcia-Aznar (2013) and Mousavi et al. (2013). Bookholt et al. (2016), Vermolen et al. (2015), Vermolen and Gefen (2015) and Vermolen (2015) extended the models to applications in contraction in burns and to model the early stages of cancer. The work of Bookholt et al. (2016) is, as far as we know, the

Numerical Methods and Advanced Simulation in Biomechanics and Biological Processes. https://doi.org/10.1016/B978-0-12-811718-7.00009-5
Copyright © 2018 Elsevier Ltd. All rights reserved.

This book belongs to Central Library BADJI Mokhtar-ANNABA UNIVERSITY

Copyright Elsevier 2024

first to apply the cell-based formalism to modeling angiogenesis. Angiogenesis was classically modeled by cellular automata or in particular cellular Potts models for example by Van Oers et al. (2014), where cell differentiation was only addressed in few of those works. Vermolen and Gefen (2015) model cell differentiation from fibroblasts to myofibroblast through entirely stochastic principles, where it is assumed that the probability of cell differentiation satisfies an exponential distribution, which is a special case of a Poisson process.

Differentiation phenomena have been modeled in biological context using different approaches. Most of the classical models treat cells at a continuum scale, in terms of population densities, cells per unit of volume (or area), using partial differential equations (PDEs). These PDEs generally contain terms for, if applicable, cell migration (by random walk, chemotaxis, haptotaxis, or tensotaxis), cell proliferation and death, and cell differentiation. In most classical models, cell differentiation is modeled by the inclusion of a reaction-like term, implying immediate, yet in many cases, incomplete differentiation. Recently, Prokharau et al. (2012, 2014) formulated a mathematical framework where the differentiation of each cell takes place over nonzero, finite intervals of time. The model is based on solving PDEs with a specified maturation space parameter. In that formalism, cells are hypothesized to achieve only one phenotype (fate) to minimize the dimensionality of the maturation space. The stem cells are then divided into several "groups" representing the various phenotypes that the stem cells may differentiate to.

In this chapter, we modify the formalism of Prokharau et al. (2012, 2014) where we treat the cells as discrete objects, that is, we take a cell-based modeling approach. The formalism to be developed is, as far as we know, original. We will illustrate potential applications of the model to differentiation processes that are relevant to tissue disuse, e.g., after a spinal cord injury (see Fig. 9.1 for an illustration); similar effects may occur with aging or with a sedentary lifestyle. First, we present the mathematical framework for the differentiation of mesenchymal stem cells to two different phenotypes and, subsequently, we extend the framework to a generic number of phenotypes a cell can differentiate to. Then, we show computations that illustrate the formation of skeletal muscle and fat tissues and the muscle/fat tissue balance. Finally, we will discuss the current framework. We note that the chapter has been written to meet the scope of the book, which is being descriptive in the numerical methodology, rather than digressing about the model results and implications. The present model falls within the class of hybrid models, where cells are treated as identities, and concentration as well as mechanical quantities are treated as field parameters that follow from the solving PDEs. Summarized, the key points of the current chapter are the following:

- We describe a hybrid method on cellular scale where cells are treated as individual objects and where the solution of PDEs (concentrations and mechanical balance) is approximated by the finite element method.
- The formalism is applied to cell differentiation where stem cells interacting with muscle and fat cells are considered.
- The numerical method contains both deterministic and stochastic processes.

Furthermore, we only provide the most important references that were used in this study in the present chapter. If the reader is interested in a more in-depth explanation on various modeling approaches, including full continuum-scale models, we refer to our reviews in Weihs et al. (2016) and Vermolen (2015).

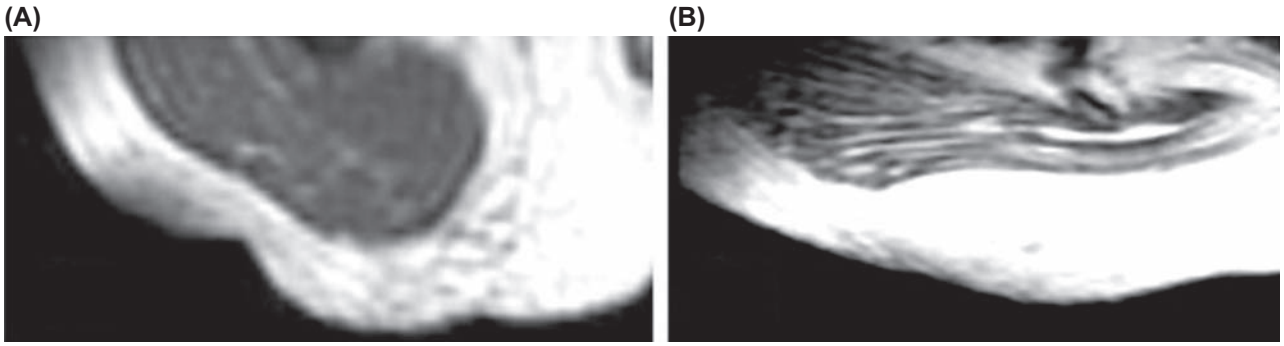

FIGURE 9.1 The influence of disuse on muscle/fat contents in humans can be demonstrated by means of magnetic resonance imaging: (A) healthy gluteus muscle (dark) and surrounding subcutaneous fat tissue in the buttocks (white). A relatively small, normal mass of intramuscular adipose tissue can be observed within the muscle tissue. (B) Gluteus muscle (dark) showing severe fat infiltration (white straps) intramuscularly, and an increased thickness of subcutaneous fat at the same anatomical site, in an individual within a year after a spinal cord injury (SCI). The intramuscular fat in both individuals contains mesenchymal stem cells, but apparently, the differentiation fate of these cells was biased toward the adipocyte phenotype in the SCI case, where the mechanical stimuli influencing stem cell differentiation where altered to the static regime due to the disuse.

This book belongs to Central Library BADJI Mokhtar-ANNABA UNIVERSITY Copyright Elsevier 2024

9.2 THE MATHEMATICAL FRAMEWORK

First, we present the model as we apply it to the differentiation of mesenchymal stem cells to two different phenotypes and, subsequently, we show its extension to any number of phenotypes.

9.2.1 A Ternary Cell System

We illustrate the effect of use (e.g., physical exercise) or disuse (e.g., a sedentary lifestyle) on the composition of the tissue by considering stem cells that have the ability to differentiate to either myocytes or adipocytes; those are, respectively, muscle and fat cells. The myocytes are cells that gradually acquire the ability to contract, being the contractile components of skeletal muscles. The adipocytes are cells that build up triglyceride depots in the form of lipid droplets (LDs), used for storage of energy. These LDs increase in size during the differentiation to adipocytes, causing the adipocytes to grow substantially in volume as adipogenesis progresses in a process called hypertrophy. At the macroscopic scale, the outcome would be increased fat tissue mass, which can lead to obesity. The interested reader is referred to Shoham et al. (2014) and Gefen and Benayahu (2015). In a physiological environment, adipose-derived stem cells, myocytes, and adipocytes exist in adjacent populations. For example, skeletal muscles contain intramuscular fat (fat depots within the muscles) that provide readily available energy supply to muscles. The intramuscular fat in turn contains mesenchymal stem cells that are potentially able to either build or repair the surrounding muscle tissue mass. The tissue is supplemented by mesenchymal stem cell differentiation into myoblasts and further into myocytes, or, alternatively, these cells are able to gradually differentiate into adipocytes, which will eventually increase the fat tissue mass, intramuscularly or extramuscularly. Differentiation pathways of adipose-derived stem cells (into either myocytes or adipocytes) are determined by genetics, age, and presence of a disease and, importantly, by the influence of the environment, including the mechanical and chemical environment, and by biomolecular signaling from surrounding cells.

9.2.1.1 Differentiation Model

The modeling presented here takes into account that stem cells gradually acquire the phenotype they are differentiating to. The mathematical formalism for the differentiation process is based on the following assumptions:

Assumption 1: Complete cell differentiation is irreversible: a stem cell that has *fully* differentiated to a certain phenotype, cannot dedifferentiate. That is, dedifferentiation is only possible if the differentiation process has not yet completed and the cell did not acquire the complete set of biological features of the phenotype.
Assumption 2: A stem cell is able to gradually adopt the properties of *only one* phenotype.

From the second assumption, it follows that if a cell's chemicomechanical environment dictates that it differentiates toward another phenotype, then it will first dedifferentiate and subsequently differentiate toward the other phenotype. These two assumptions were also used in the model of Prokharau et al. (2012, 2014), where both assumptions gave important implications on the boundary conditions in the *maturation* space (well posedness). Furthermore, Assumption 2 reduced the dimensionality of the maturation space in the model of Prokharau et al. (2012, 2014). As we model cells individually, let us consider a population of n_c (t) cells, where t denotes time and the number of cells may vary with time as a result of cell proliferation, cell death, or applied treatments (e.g., injection or local delivery of stem cells). Let $j \in \{1,\ldots, n_c\}$ be the index of a viable cell. For each cell, we introduce the maturation parameter $a_j \in [0, 1]$ such that it represents the extent by which a cell j has adopted the properties of a certain phenotype given by $e_j \in \{1, 2\}$. The functional behavior of a_j over time represents the evolutionary differentiation path of cell j. If $a_j \in (0, 1)$ then cell j is a stem cell (possibly attaining the properties of either phenotype), and if $a_j = 1$ then cell j has fully differentiated to either phenotype, whereas $a_j = 0$ represents the situation where cell j is still fully undifferentiated (that is, at the stem cell state). Further, $e_j = 1$ and $e_j = 2$, respectively, correspond to the phenotype myocyte and adipocyte.

Hence, at this stage, we consider the possibility that stem cells can differentiate to either myocytes or adipocytes and we use the following convention for the pair a_j and e_j; this is summarized in

$$(a_j(t), e_j(t)) : \begin{cases} = (1,1), & \text{myocyte (M)}, \\ \in (0,1) \times \{1\}, & \text{tending to myocyte}, \\ = 0 \times \{1,2\}, & \text{undifferentiated stemcell (S)}, \\ \in (0,1) \times \{2\}, & \text{tending to adipocye}, \\ = (1,2), & \text{adipocyte (A)}. \end{cases} \tag{9.1}$$

This book belongs to Central Library BADJI Mokhtar-ANNABA UNIVERSITY
Copyright Elsevier 2024

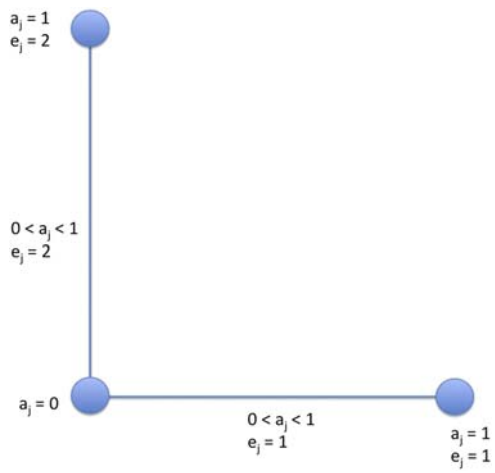

FIGURE 9.2 A schematic of the differentiation pathway that is represented via the $a-$parameter.

The situation is schematically depicted in Fig. 9.2. The adipocyte and myocyte phenotypes are represented by (A) and (M), respectively. Let $U = U\left(t, \mathbf{x}, \underline{\psi}, a\right)$ be the differentiation rate of cell j, which depends on time, spatial location $\mathbf{x}$, and p stimuli $\underline{\psi} = \left[\psi_1, \ldots, \psi_p\right]^T$; the gradual transition of stem cells is modeled by

$$\frac{da_j}{dt} = U\left(t, \mathbf{x}(t), \underline{\psi}(t), a_j(t)\right), \quad a_j(0) = a_j^0. \tag{9.2}$$

Here we also take into account the spatial migration ability of the cell. We assume that cells gradually lose their ability to migrate as they differentiate, so that a mesenchymal stem cell is fully mobile, but once it has started differentiating, say to a preadipocyte, this ability decreases and is completely lost when reaching full maturation. Indeed, mature adipocytes are not mobile, and neither are fully differentiated myocytes; therefore, for example, for muscle cells, the migration ability is lost in the transition from myoblasts to myocytes.

9.2.1.2 Chemical Signals

In this application, the differentiation rate depends on two chemical stimuli and on a mechanical stimulus. The chemical stimuli are signaling molecules (e.g., cytokines) that are secreted by already differentiated adipocytes and myocytes and to a lesser extent by stem cells that are in the process of adopting the properties of these phenotypes. This assumption is motivated by the observed adjustment of the cells to the behavior and phenotype of their nearest neighbors (see, for instance, Shoham et al., 2014; Or-Tzadikario et al., 2010). The distribution of the signaling molecules c_M and c_A over the domain Ω, bounded by $\partial\Omega$, that are released by myocytes and adipocytes, respectively, is, for $k \in \{M, A\}$, modeled by linear diffusion:

$$\begin{aligned}
&\frac{\partial c_k}{\partial t} + \nabla \cdot (\mathbf{v}_m c_k) - D_k \Delta c_k = \sum_{j=1}^{n_c(t)} \sum_{i=1}^{L} \gamma_k^i(a_j, e_j)\delta(\mathbf{x} - \mathbf{x}_j(t))\Delta A_j^i(t) + S_k(t, \mathbf{x}), \\
&c_k(0, \mathbf{x}) = 0, \quad \mathbf{x} \in \overline{\Omega}, \\
&D_k \frac{\partial c_k}{\partial \mathbf{n}} + \kappa c_k = 0, \quad \mathbf{x} \in \partial\Omega.
\end{aligned} \tag{9.3}$$

The second term on the left-hand side in the above equation represents passive convection as a result of the movement of the mesh over the domain, including the extracellular matrix and the cells. The mesh velocity is given by $\mathbf{v}_m$, and this velocity results from the displacements of the nodes caused by the time evolution of the forces that are applied by the cells. In other words, we have $\mathbf{v}_m = \frac{d}{dt}\mathbf{u}(t, \mathbf{x}(t))$, where the total (or material) derivate of the displacements is used. The third term on the left-hand side in the above PDE accounts for linear diffusion of the cytokine. The first term on the right-hand side contains the Dirac Delta function and accounts for the production of the cytokine by the individual cells depending on

This book belongs to Central Library BADJI Mokhtar-ANNABA UNIVERSITY
Copyright Elsevier 2024

their differentiation state. It involves a summation over all cells, as well as over the boundary segments of the cells. The second term in the right-hand side defines any other addition of the cytokine as a result of applied treatments and therapies. The boundary condition reflects the fact that the boundary of the domain cannot be taken infinitely far away and that the outflow on the boundary is balanced by the flow into the tissue away from the domain of computation. Both cytokine concentrations, released by either (pre)adipocytes or myoblasts, which are modeled as premyocytes, and myocytes, act as chemical stimuli for the differentiation path of the stem cells. The amount of cytokines that is injected by each stem cell depends on its maturation. In this study, we use a linear relationship where we normalize with respect to the total area of the cell boundary curve:

$$\gamma_k^j(a_j, e_j) = \frac{\gamma_k^0 \, a_j}{\sum_{i=1}^{L} \Delta \, A_j^i} \, \delta_{k,e_j}, \tag{9.4}$$

where $\delta_{k,\ ej}$ represents the Kronecker Delta, j is the cell number, and the summation over indexes i is carried out over the boundary segments of cell j. We realize that any relationship can be used here as long as the amount of production increases for the particular phenotype as a moves away from zero. From the concentration of myokine or adipokine, the chemical stimulus is determined by the use of the average concentration that is experienced by the nodal points on the boundary of the cell. For cell i, this concentration is calculated by

$$c_k^i(t) = \frac{1}{L} \sum_{j=1}^{L} c_k\left(t, \mathbf{x}_j^i\right), \quad k \in \{M, A\}. \tag{9.5}$$

9.2.1.3 Differentiation Rate and Stimuli

Next, we treat the function for the differentiation rate. To this extent, we use

$$u = u\left(t, \mathbf{x}, \underline{\psi}, a\right) = \frac{1}{2}\left(u_c(\psi_1, \psi_2) + u_m(\psi_3)\right), \tag{9.6}$$

where u_c and u_m, respectively, represent the chemical and mechanical contributions to the stimulus. For the chemical stimulus, we set

$$\psi_1 = c_M, \quad \psi_2 = c_A. \tag{9.7}$$

We use the following assumption for the function u_c:

Assumption 3: Consider cell j, then

1. If $e_j = 1$ (cell j is acquiring myocyte properties), then

$$u_c : \begin{cases} < 0, & c_M < c_A, \\ = 0, & c_M = c_A, \\ > 0, & c_M > c_A; \end{cases}$$

2. If $e_j = 2$ (cell j is acquiring adipocyte properties), then

$$u_c : \begin{cases} < 0, & c_A < c_M, \\ = 0, & c_M = c_A, \\ > 0, & c_A > c_M; \end{cases}$$

Consider ψ_3, u_m (ψ_3), and let $\widetilde{\psi} \in \mathbb{R}$, then the mechanical stimulus is treated analogously, using the following assumption.

This book belongs to Central Library BADJI Mokhtar-ANNABA UNIVERSITY
Copyright Elsevier 2024

Assumption 4: Consider cell j, then

1. If $e_j = 1$ (cell j is acquiring myocyte properties), then

$$u_m: \begin{cases} < 0, & \psi_3 < \widetilde{\psi} \\ = 0, & \psi_3 = \widetilde{\psi}, \\ > 0, & \psi_3 > \widetilde{\psi}; \end{cases}$$

2. If $e_j = 2$ (cell j is acquiring adipocyte properties), then

$$u_m: \begin{cases} < 0, & \psi_3 > \widetilde{\psi} \\ = 0, & \psi_3 = \widetilde{\psi} \\ > 0, & \psi_3 < \widetilde{\psi}; \end{cases}$$

From these assumptions, the following proposition is proved:

Proposition 1: Let Assumptions 3 and 4 be valid, then

$$(-1)^{e_j-1} u_c \cdot (c_M - c_A) \geq 0, \quad \text{and } (-1)^{e_j-1} u_m \cdot \left(\psi_3 - \widetilde{\psi}\right) \geq 0. \tag{9.8}$$

Proof: We prove the first inequality on the left. Let $e_j = 1$, then, according to Assumption 3, $c_M < c_A$ implies $u_c < 0$, and hence $u_c\,(c_M - c_A) > 0$ and hence $(-1)^{e_j-1} u_c \cdot (c_M - c_A) > 0$. Further, if $c_M > c_A$, then from Assumption 3, we have $u_c > 0$ and hence again this yields $u_c\,(c_M - c_A) > 0$ and $(-1)^{e_j-1} u_c \cdot (c_M - c_A) > 0$. Case 2, where $e_j = 2$, is treated analogously. Further, $c_M = c_A$ implies $(-1)^{e_j-1} u_c \cdot (c_M - c_A) = 0$ directly. The second inequality is proved similarly. □

To have a chemical component for the maturation speed that satisfies the above assumption, we set

$$u_c(\psi_1, \psi_2; e_j) = \overline{u}(\psi_1 - \psi_2; e_j) = (-1)^{e_j-1}\, U_M \tanh\left(\frac{c_M - c_A}{\xi}\right) = (-1)^{e_j-1}\, U_M \tanh\left(\frac{\psi_1 - \psi_2}{\xi}\right), \tag{9.9}$$

where U_M, $\xi > 0$, respectively, represent the maximal differentiation speed and the slope of the transition between the two cell phenotypes. It is immediately clear that the above relation immediately satisfies the prerequisites of Proposition 1. The mechanical stimulus, ψ_3, is used analogously as follows:

$$u_m(\psi_3; e_j) = (-1)^{e_j-1}\, U_M \tanh\left(\frac{\psi_3 - \widetilde{\psi}}{\eta}\right), \quad U_M \geq 0, \tag{9.10}$$

where $\widetilde{\psi}$ and η, respectively, represent the point of transition that the mechanical stimulus changes its phenotypical direction and the slope of the transition between the two cell phenotypes. The octahedral shear strain (also known as the engineering shear strain on an octahedral plane, where the octahedral plane is a plane that is oriented equally with respect to the principal axes), ϕ, is computed from

$$\phi = \frac{1}{3}\sqrt{(\varepsilon_1 - \varepsilon_2)^2 + (\varepsilon_1 - \varepsilon_3)^2 + (\varepsilon_2 - \varepsilon_3)^2}, \tag{9.11}$$

where ε_l represent the principle strains (eigenvalues of the strain tensor). The mechanical stimulus is based on the history path of the octahedral shear strain a cell is exposed to. Because the variations in ϕ over time is of importance rather than the octahedral shear strain at a specific time instant, we use the following integral expression

$$\psi_3(t, \mathbf{x}_j(t)) = \int_{(t-\tau)_+}^{t} w(s) \left(\frac{d\phi}{ds}(s, \mathbf{x}_j(s))\right)^2 ds. \tag{9.12}$$

Here τ represents the length of the time interval that has an impact on the differentiation behavior at certain time t. The nonnegative function $w\,(s)$ has been added as a weight function to account for larger influences at the latest times before time t. We use the following kernel for $w\,(s)$:

$$w(s) = e^{s-t}. \tag{9.13}$$

This book belongs to Central Library BADJI Mokhtar-ANNABA UNIVERSITY
Copyright Elsevier 2024

Because we only want the transformation to muscle cells (myocytes) to occur if the cellularly experienced octahedral strain is subject to a sufficiently high frequency, we apply a high-pass filter on ϕ to suppress the influence of low frequency components.

9.2.1.4 The Cell Geometry and Its Evolution

The cells are modeled with evolving geometry where the myocytes are modeled as ellipses with a large eccentricity (aspect ratio), and in contrast the adipocytes are modeled as circles that expand as they mature. To this end, we describe the 2D case; the 3D case is treated analogously. The cell boundary is divided into nodal points $j \in \{1,\ldots, N\}$. Note that for the 2D case the number of nodal points is equal to the number of elements on the cell boundary. Let the axes of the elliptical geometry be given by $L(t)$ and $W(t)$, then we have for cell i

$$x_j^i(t) = L^i(t)\cos\left(\frac{2\pi j}{N}\right), \quad y_j^i(t) = W^i(t)\sin\left(\frac{2\pi j}{N}\right). \tag{9.14}$$

From this relation, it is clear that the outward unit normal vector is given by

$$\mathbf{n}_j^i(t) = \left[\frac{x_j^i(t)}{L^i(t)}, \frac{y_j^i(t)}{W^i(t)}\right]^T. \tag{9.15}$$

Because the cell is allowed to migrate to different directions, its orientation changes over time, and to this extent, rotation of the cell is incorporated by the rotation matrix given by

$$R(\theta_i) = \begin{pmatrix} \cos(\theta_i) & -\sin(\theta_i) \\ \sin(\theta_i) & \cos(\theta_i) \end{pmatrix}, \tag{9.16}$$

where θ_i is the angle of cell i with respect to the x-axis. The above rotation matrix is applied via left multiplication by the coordinates of the cell boundary. Note that in the present model only elliptic cell shapes are allowed. The normal vector will be used for the determination of the force vector on each boundary segment. Next we consider the geometrical evolution of the cells. We assume that the cell dimensions are entirely determined by the degree of maturation and the phenotype they are differentiating to. Consider cell i, then we have

$$\begin{cases} L^i(a_j(t), e_j(t)) = L_0 + (L_M - L_0)a_j(t)\delta_{1,e_j(t)} + (L_A - L_0)a_j(t)\delta_{2,e_j(t)}, \\ W^i(a_j(t), e_j(t)) = W_0 + (W_M - W_0)a_j(t)\delta_{1,e_j(t)} + (W_A - W_0)a_j(t)\delta_{2,e_j(t)}, \end{cases} \tag{9.17}$$

where δ_{ij} denotes the Kronecker Delta. This function takes into account that different end shapes of adipocytes and myocytes. Note that $L_A = W_A$ to keep the end morphology of adipocytes circular. Further, $L_0 = W_0$ is the radius of the circular stem cells.

9.2.1.5 Mechanical Approach

For the computation of the octahedral shear strain, the mechanical balance is solved. To this extent, we use the Navier–Cauchy formulation to solve

$$\nabla \cdot \underline{\underline{\sigma}} + \mathbf{F}_M + \mathbf{F}_G = 0, \tag{9.18}$$

in Ω with a spring boundary condition

$$\underline{\underline{\sigma}} \cdot \mathbf{n} + K\mathbf{u} = 0, \tag{9.19}$$

on $\partial\Omega$. Here K represents a spring force on the boundary of the domain exerted by the surrounding tissue. Further, the oscillatory pulling (contraction) forces that are exerted by the myoblasts and myocytes are embedded within $\mathbf{F}_M$ and the forces exerted by the expanding adipocytes and myocytes are incorporated in the $\mathbf{F}_G$ term. For the two-dimensional setting where all cells are living *on* a substrate, this force does not exist and hence $\mathbf{F}_G = 0$. In a three-dimensional setting, the last-mentioned force should be incorporated. We also incorporate the expansion force in the 2D setting for the sake completeness of the algorithm. The myoblast force is decomposed into the separate contributions of all individual cells;

$$\mathbf{F}_M(t, \mathbf{x}, \overline{a}(t)) = \sum_{j=1}^{n_c(t)} \mathbf{F}_j^M(t, \mathbf{x}, a_j(t)), \tag{9.20}$$

This book belongs to Central Library BADJI Mokhtar-ANNABA UNIVERSITY Copyright Elsevier 2024

where $\overline{a}(t) = \left[a_1(t), \ldots, a_{n_c(t)}(t)\right]^T$ represents the vector containing the maturation parameters of the viable cells. For the computation of the contraction force that is acted by cell j, we decompose surface of the cells into line segments of length $\Delta\Gamma$ with inward normal $\mathbf{n}$ (note that this vector is *outward* with respect to the domain of computation). Each of these line segment is treated as a point source exerting a force toward $\mathbf{n}$ directed *into* the cell. Therewith, at point $\mathbf{x}'$ on the cell boundary, the actual force becomes

$$\Delta\mathbf{F}_j^M(t, \mathbf{x}, a_j(t)) = P(t, a_j)\mathbf{n}\delta(\mathbf{x} - \mathbf{x}')\Delta\Gamma. \tag{9.21}$$

Subsequently, summing over all contributions on the boundary of cell j gives

$$\mathbf{F}_j^M(t, \mathbf{x}, a_j(t)) \approx \sum_{m=1}^{N} P(t, a_j)\mathbf{n}_m\delta(\mathbf{x} - \mathbf{x}_m)\Delta\Gamma, \tag{9.22}$$

where N represents the number of line segments on the cell boundary in the polygonal approximation of the cell. Further, $\mathbf{x}_m$ represents the midpoint of line segment m with unit normal vector $\mathbf{n}_m$ and length $\Delta\Gamma$. All these quantities correspond to cell j. Taking a limit $\Delta\Gamma \to 0^+$ (e.g., $N \to \infty$), gives

$$\mathbf{F}_j^M(t, \mathbf{x}, a_j(t)) = \int_{\partial\Omega_j} P(t, a_j)\mathbf{n}(\mathbf{x}\prime)\delta(\mathbf{x} - \mathbf{x}')d\Gamma', \tag{9.23}$$

where $d\Gamma'$ represents a line element and note that one has to integrate over $\mathbf{x}'$, which is in any case located on the cell boundary. Further, the quantity P should be considered as a force per unit length over the cell boundary. This force is used to quantify the force exerted by cell j on its extracellular tissue. An alternative formulation is to consider this force as a boundary condition on the region outside the cell. The boundary condition treatment will require adaptation of the computational grid at all times as the cell moves or expands. This grid adaptation will make the computations more expensive and, therefore, an alternative approach has been chosen in the present work. Because the diameters of the cells are much smaller than the domain of computation, and note that the boundary of the cell is divided into a sequence of point sources in the development of the chemical signal, we think that our treatment is reasonable and, as far as we know, the current treatment is original. We further note that the current treatment is applicable to any shape of cells. However, in the current study, we will barely use circular cross sections of the cells. The extension of the current formalism to three dimensions is straightforward as it is given by

$$\mathbf{F}_j^M(t, \mathbf{x}, a_j(t)) = \int_{\partial\Omega_j} P(t, a_j)\mathbf{n}(\mathbf{x}')\delta(\mathbf{x} - \mathbf{x}')dS', \tag{9.24}$$

where dS' represents a line element and note that one has to integrate over $\mathbf{x}'$, which is in any case located on the cell boundary. Furthermore, the quantity P should be considered as a force per unit area over the cell boundary in a three-dimensional case. In a fully analytic framework, one could use shifted radial Green's functions from elasticity for each cell to treat the cells really as point sources. This last-mentioned approach is omitted in the present study, but it will be applied in future analyses for the reason of its ease to use and its ultracheap computations. In the present work, we want to study the effects of the contraction and expansion of the tissue in relation with its surroundings as well. We model the activity of the subject by imposing a periodical time pattern on the forcing. For instance one can use

$$P(t, a, e) = \begin{cases} \widehat{P}(a)\cdot\cos(\omega t), & \text{if } e = 1, \\ 0, & \text{if } e = 2. \end{cases} \tag{9.25}$$

Here we use an increasing function for $\widehat{P}(a)$, as an example we take

$$\widehat{P}(a) = P_0 a. \tag{9.26}$$

Next we consider the pushing forces of the adipocytes and myocytes as a result of their growth. This issue is more important in 3D than 2D, nevertheless for the sake of generality we carry out the same discussion in 2D. We postulate that these forces are proportional to the time derivative of the cell area in 2D and to the time derivative of the cell volume in 3D. These forces are steady as long as the adipocytes do not change size. However, as they grow, the steady force that they exert on the extracellular tissue will change. We use a similar relation as earlier:

$$\mathbf{F}_j^G(t, \mathbf{x}, a_j(t)) = \int_{\partial\Omega_j} Q\mathbf{n}(\mathbf{x}')\delta(\mathbf{x} - \mathbf{x}')d\Gamma', \tag{9.27}$$

This book belongs to Central Library BADJI Mokhtar-ANNABA UNIVERSITY
Copyright Elsevier 2024

where Q represents the force per unit length exerted by the adipocytes on the extracellular structure, which only becomes active if the adipocyte is growing in area (in 2D) or in volume (in 3D)

$$Q = k\frac{dA}{dt} = \pi\left(L\frac{dW}{dt} + W\frac{dL}{dt}\right), \tag{9.28}$$

for the 2D case with an ellipse with axes L and W. Further, k is a nonnegative constant of proportionality. Note that this force is negative if the cell is shrinking.

9.2.1.6 Cell Migration

Mesenchymal stem cells are known to possess the property of *active* cell motility, whereas myocytes and adipocytes are immobile and only move if contact forces are applied to them or if they are subject to mechanical drag, also known as *passive migration*. In this work, we assume that *active* cell migration is determined by *chemotaxis* and random walk. Hence cell-based migration is modeled by

$$d\mathbf{x}_j(t) = \sigma d\mathbf{W}(t) + \mathbf{v}_p(t, \mathbf{x}_j(t))dt + 4\big(\mu_M a_j(1-a_j)\delta_{1,e_j(t)}\nabla c_M(t, \mathbf{x}_j(t)) + \mu_A a_j(1-a_j)\delta_{2,e_j(t)}\nabla c_A(t, \mathbf{x}_j(t))\big)dt. \tag{9.29}$$

The terms in the right-hand side determine the various migration modes. The first term denotes migration by random walk represents a measure of cell motility due to random walk. The σ parameter is related to cell diffusivity by $\sigma = \sqrt{2D}$, and $\mathbf{W}$ (t) is a vector Wiener process. The second term represents migration as a result of intercellular contact forces, see Vermolen and Gefen, and as a result of passive movement due to mechanical drag. The third term represents the contribution to migration as a result of chemotaxis where cells tend to migrate toward the gradient of a chemical. The term containing μ_M is active whenever $e_j(t) = 1$. It mimics the sensitivity of the cells with respect to the gradient of myocyte-secreted cytokines. The same, but now with respect to differentiation to the adipocyte phenotype, is exhibited in the μ_A-containing term.

9.3 NUMERICAL METHOD

We use a finite element method for the solution of the PDEs, such as the mechanical balance and all the chemical quantities. To obtain the mechanical signal on a cell, a postprocessing step of the finite element approximation is carried out. The Euler–Maruyama method is used to solve the stochastic differential equations. For completeness, we will describe the method in somewhat more detail.

9.3.1 The Finite Element Method for the Partial Differential Equations

We use the method that was proposed by Madzvamuse et al. (2003). The domain of computation is divided into a triangular mesh in 2D and into a tetrahedral mesh in 3D. Linear elements are used in all cases. The approach is based on the Galerkin finite element method where a weak form of the problem is constructed for all the PDEs. The solution, being the displacement or chemical quantities, is expressed as a linear combination of the unknowns at the mesh points. The development of the weak form is straightforward for the mechanical balance. For the chemical quantities, which we denote by c $(t, \mathbf{x})$ for reasons of illustration, we use the displacement of the mesh as a result of the mechanical forces that are exerted by the cells. Because the pulling and pushing forces by the cells imply the presence of a displacement field, which follows from the mechanical balance, the derivative of the displacement on each mesh point, which gives the mesh velocity, is computed by $\mathbf{v}(t, \mathbf{x}) = \frac{d}{dt}\mathbf{u}(t, \mathbf{x}(t))$, where u denotes the displacement on position $\mathbf{x}$ in the reference frame, and d/dt stands for the total time derivative (being the material derivative now). Then we have

$$\frac{\partial\phi}{\partial t} + \nabla\cdot\mathbf{J} = f(t, \mathbf{x}, \phi), \tag{9.30}$$

subject to initial and boundary conditions. Then to include the mesh velocity, the dynamics of the movement of the coordinates is incorporated in the above equation by the *passive* convection term $\nabla\cdot(\mathbf{v}\phi)$

$$\frac{\partial\phi}{\partial t} + \nabla\cdot(\mathbf{v}\phi) + \nabla\cdot\mathbf{J} = f(t, \mathbf{x}, \phi). \tag{9.31}$$

The product rule and the total derivative (material derivative) for ϕ gives

$$\frac{d\phi}{dt} + \phi(\nabla\cdot v) + \nabla\cdot\mathbf{J} = f(t, \mathbf{x}, \phi). \tag{9.32}$$

This book belongs to Central Library BADJI Mokhtar-ANNABA UNIVERSITY Copyright Elsevier 2024

Using Galerkin's finite element method, we multiply the PDE by a test function $\varphi \in H^1(\Omega)$, which depends on time as a result of the temporal evolution of the mesh, for which Dziuk and Elliott (2013) proved

$$\frac{d}{dt}\varphi(t;\mathbf{x}(t)) = 0,$$

for Lagrangian basis functions, and we realize that

$$\frac{d}{dt}[\phi\varphi] = \frac{\partial}{\partial t}[\phi\varphi] + \nabla\cdot[\mathbf{v}\phi\varphi] - \phi\varphi(\nabla\cdot v).$$

Integration by parts and using the above equation gives

$$\int_{\Omega_t}\left(\frac{\partial(\phi\varphi)}{\partial t} + \nabla\cdot[\phi\varphi\mathbf{v}] + \varphi\nabla\cdot\mathbf{J}\right)d\Omega = \int_{\Omega_t}\varphi f d\Omega. \tag{9.33}$$

Subsequently, Gauss' theorem is applied on the second term and the third term is integrated by parts to get

$$\int_{\Omega_t}\left(\frac{\partial(\phi\varphi)}{\partial t} - \nabla\varphi\cdot\mathbf{J}\right)d\Omega + \int_{\partial\Omega_t}\varphi(J\cdot\mathbf{n} - \phi\mathbf{v}\cdot\mathbf{n})d\Gamma = \int_{\Omega_t}\varphi f d\Omega. \tag{9.34}$$

Finally we apply Reynold's transport theorem to get

$$\frac{d}{dt}\int_{\Omega_t}\phi\varphi d\Omega - \int_{\Omega_t}\nabla\varphi\cdot\mathbf{J}d\Omega + \int_{\partial\Omega_t}\varphi J\cdot\mathbf{n}d\Gamma = \int_{\Omega_t}\varphi f d\Omega. \tag{9.35}$$

The above boundary integral is further elaborated based on the boundary conditions. The numerical approximations are written in terms of linear combinations of basis functions with time-dependent weights. The backward Euler method is used to integrate the resulting system of ordinary differential equations over time. An IMEX method is used in the case of nonlinear equations.

9.3.2 The ZZ-Gradient Recovery Method

We need to determine the strain to get the octahedral shear strain as well as the strain energy density including its gradient. Furthermore, we need to determine the gradient of chemokines for the haptotaxis part of the cellular migration. This requires the determination of spatial derivatives of the displacement, which follows from the mechanical balance equation. Because we obtain the displacement field as a finite element approximation on the basis of piecewise linear basis functions, the error is of order $O(h^2)$, where h represents a measure for the elements. However, determining the gradient could lead to a decreased order, and furthermore, because we need to project the result on the positions (the centers) of the cells by the use of interpolation, the accuracy of the solution on the cellular positions could be further worsened. To prevent this to happen, we use the so-called ZZ-patch recovery method by Zienkiewicz and Zhu (1992a,b). For completeness we explain the main principles of the method. Suppose that we need to determine the derivative of a quantity u, say $\varepsilon = \frac{\partial u}{\partial x}$, then on each element the ε_h can be determined from the finite element solution. In this way, using linear elements, the variable ε_h is constant over each element. The idea is that we determine ε on the mesh points. Consider a mesh point, say $\mathbf{x}_k$, then we use a *patch* around $\mathbf{x}_k$, that consist of all the elements that contain mesh point $\mathbf{x}_k$ as a vertex. In each element of the patch, we determine ε_h. Then we want to determine a smoothed version of ε_h, which we call $\varepsilon^* = P\mathbf{a}$, then we determine ε^* such that

$$\text{Find } \varepsilon^* \text{ such that } \quad F(\varepsilon^*) \le F(\varepsilon), \quad \text{for all } \varepsilon, \quad \text{where } F(\varepsilon) = \sum_{j=1}^{N}\left(\varepsilon_h(\mathbf{x}_j) - \varepsilon_j^*\right)^2,$$

where $P = [1\ x\ y]$ for linear elements in 2D and N denotes the number of sampling points. In the case of linear elements, we use one sampling point per element; hence, in this case N is equal to the number of elements in the patch of mesh point $\mathbf{x}_k$. In the case of linear elements, one takes the midpoint of all elements that contain a certain shared vertex. In the above equation, one determines the vector $\mathbf{a}$. This least-squares problem gives the following system of linear equations for $\mathbf{a}$:

$$\sum_{j=1}^{N} P^T(\mathbf{x}_j)P(\mathbf{x}_j)\mathbf{a} = \sum_{j=1}^{N} P^T(\mathbf{x}_j)\varepsilon_h(\mathbf{x}_j)$$

The procedure is repeated for each vertex of the mesh and therewith a superconverging approximation for ε is obtained. This allows an accurate determination of the strain energy density as well of the octahedral shear strain. The procedure

This book belongs to Central Library BADJI Mokhtar-ANNABA UNIVERSITY
Copyright Elsevier 2024

along with its mathematical analysis are outlined in Zienkiewicz and Zhu (1992a,b). An alternative promising method could be the application of filtering techniques that were constructed and analyzed in Mirzaee et al. (2014).

9.3.3 Cell Maturation and Migration

First we update the cell maturation by use of the forward Euler's method, which reads as

$$a_j^{p+1} = a_j^p + \Delta t U\left(t^p, \widetilde{\mathbf{x}}_j^p, \underline{\psi}(t^p), a_j^p\right), \tag{9.36}$$

for cell j, time t^p and on the p-th time step. From this equation, the differentiation axis is also determined. If a_j reaches one, then the new phenotype is adopted. The equations for the chemical concentrations are solved using an IMEX method where all nonlinear terms are evaluated at the previous time step, whereas the linear parts are incorporated at the new time step. The maturity of the cell and the differentiation axis are used from the new time step. To integrate the equations for cell migration over time, we divide the time into discrete time steps and use the Euler—Maruyama method to approximate the solution. Consider cell j, then

$$\begin{aligned}\widetilde{\mathbf{x}}_j^{p+1} &= \widetilde{\mathbf{x}}_j^p + \mathbf{v}\left(t^p, \widetilde{\mathbf{x}}_j^p\right)\Delta t + \sqrt{2D}\Delta\mathbf{W} + \left(\mathbf{u}\left(t^{p+1}, \widetilde{\mathbf{x}}_j^f(t^{p+1})\right) - \mathbf{u}\left(t^p, \widetilde{\mathbf{x}}_j^f\left(t^p\right)\right)\right) + \\ &4\left(\mu_M a_j^{p+1}\left(1 - a_j^{p+1}\right)\delta_{1,e_j(t^{p+1})}\nabla c_M\left(t^p, \widetilde{\mathbf{x}}_j^p\right) + \mu_A a_j^{p+1}\left(1 - a_j^{p+1}\right)\delta_{2,e_j(t^{p+1})}\nabla c_A\left(t, \widetilde{\mathbf{x}}_j^p\right)\right)\Delta t.\end{aligned} \tag{9.37}$$

where $\mathbf{v}$ denotes the velocity as a result of mechanical impingement determined by the gradient of the strain energy density. See Vermolen and Gefen (2012) for more details regarding this contribution. The gradient is determined by the use of the earlier ZZ-patch reconstruction method. Furthermore, the vectorial stochastic variable $\Delta\mathbf{W}$ (t^p) contains a vector with two or three realizations from a normal distribution as follows:

$$\Delta\mathbf{W} = [\Delta W_x \quad \Delta W_y \quad \Delta W_z]^T, \tag{9.38}$$

for the two-dimensional case, where ΔW_x, ΔW_y, and $\Delta W_z \sim \mathcal{N}(0, \Delta t)$ are three independent realizations from the normal distribution with zero mean and variance Δt. Furthermore, mechanical drag has been taken into account by the displacement vector over a time step Δt, see the third term between brackets in the above equation. Note that the displacements are obtained by mapping the solution of the displacement from mechanical equilibrium to the position of the centers of the cells. Because we use linear basis functions on the triangular finite element mesh, we use linear interpolation based on the finite element basis functions. The time stepping was chosen such that cells do not migrate more than one-fourth of their diameter. This warrants a sufficiently small time step such that numerical stability is obtained.

For clarity, we add a schematic of the algorithm that we used: Algorithm 9.1 Time-integration algorithm.

ALGORITHM 9.1 Time-Integration Algorithm

```
Initialise
n = 0; t = 0
while t < t_end do
    Compute Cellular Forces
    Compute Mechanical Displacements
    Update Mesh
    Compute Strain Energy Density
    Compute Concentration of Chemokines
    Map Solutions onto Cellular Positions
    Update Cell Maturations
    Update Cell Positions
    n ← n + 1
    t ← t + dt
end while
```

This book belongs to Central Library BADJI Mokhtar-ANNABA UNIVERSITY
Copyright Elsevier 2024

9.4 SIMULATIONS AND DISCUSSION

In this section, we show some examples of results that can be computed using the model. For all parametric choices, we refer to the thesis of Harrevelt (2015). The focus of the present chapter is on the numerical method, and thus the biological aspects are emphasized less. Because the strain is needed at the cellular positions, we use the ZZ-gradient recovery method that was described in the previous section. Fig. 9.3 shows the approximation of the gradient, using a direct gradient computation and using the ZZ-approach. It can be seen that the direct approach causes a discontinuous gradient pattern, which is not useful for the computation of the mechanical stimulus. The ZZ-recovery method gives a continuous gradient pattern as a result of the smoothening by incorporation of a patch of elements to approximate the gradient. Because the migrating cells may be located in several elements, this is an important improvement.

Subsequently, we show the results of two simulations in Fig. 9.4 to show what the model is capable of in terms of biological application. In the case of continuous exposure to cyclic mechanical force, the cells tend to differentiate to myocytes, whereas if cells are not exposed to any cyclic forces, then the stem cells tend to differentiate toward adipocytes. Although the parameters taken are mostly hypothetical, it can be seen that the model can be used to simulate both extreme cases. The input parameters have been given in Harrevelt (2015).

We note that the model qualitatively predicts well the concurrent differentiation to various phenotypes. The signals for differentiation are both chemical and mechanical, where in the latter case one has to use the gradient of a precomputed solution. Because the solutions of the mechanical force balance are continuous up to the second partial derivatives with respect to position, one should be able to use the derivatives of the solution. When computing the first-order derivatives of

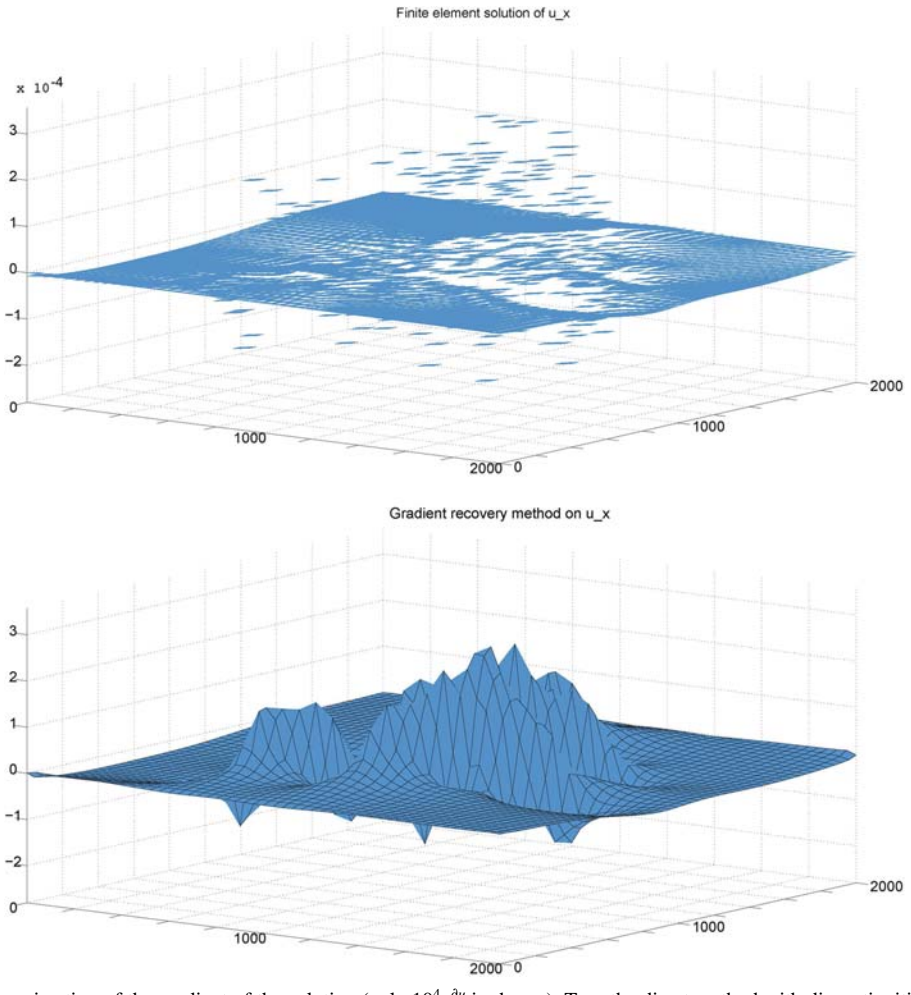

FIGURE 9.3 The approximation of the gradient of the solution (only $10^4 \frac{\partial u}{\partial x}$ is shown). Top: the direct method with discontinuities of the gradient over the element faces; bottom: the ZZ-approach with a continuous representation of the gradient.

This book belongs to Central Library BADJI Mokhtar-ANNABA UNIVERSITY
Copyright Elsevier 2024

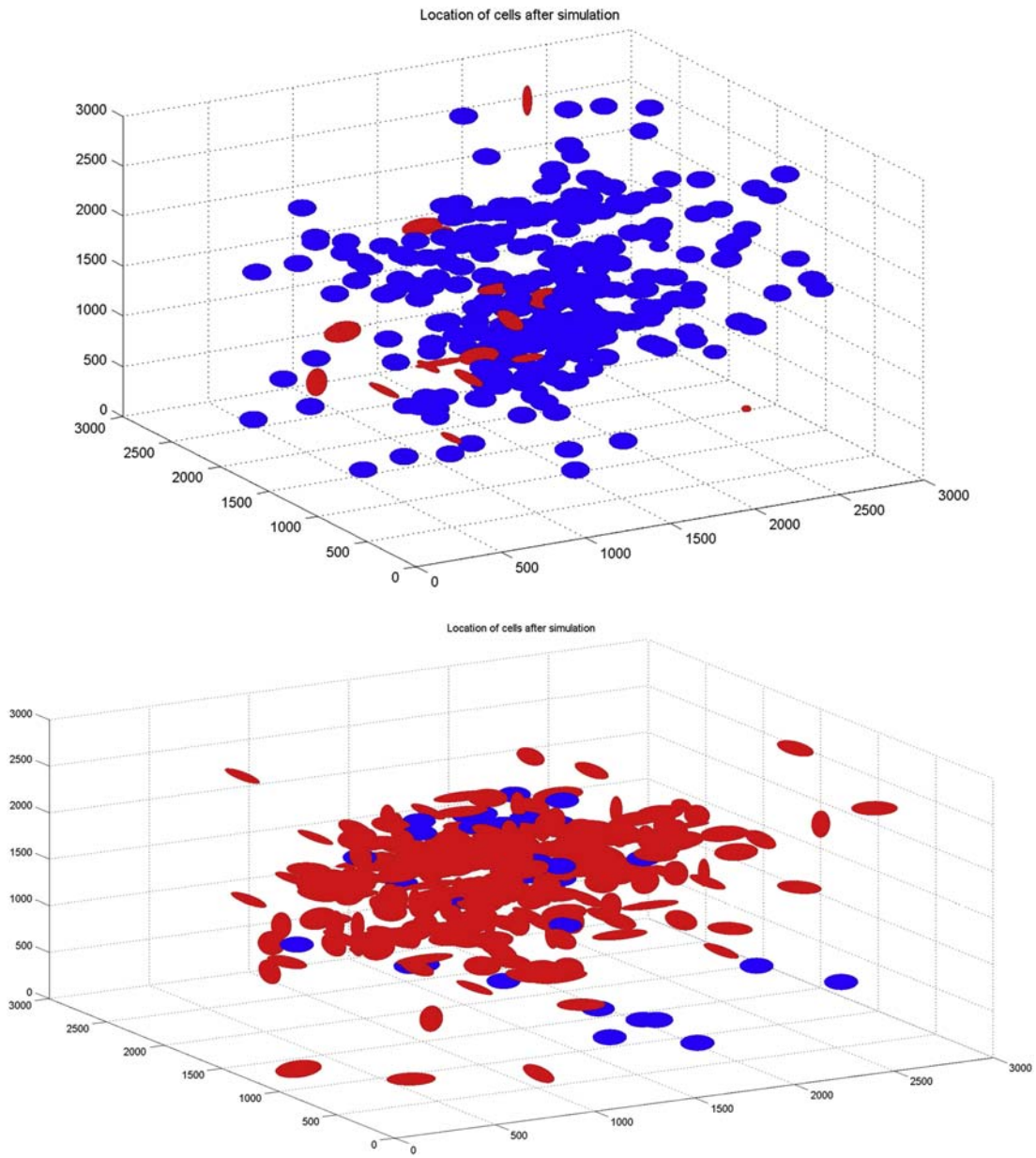

FIGURE 9.4 Myocytes and adipocytes after a period of exposure to noncyclic and cyclic loading on the top and bottom, respectively. The spherical blue (black in print versions) cells represent the (pre)adipocytes; the red (gray in print versions), more elongated, cells represent the muscle cells. Top: preferential differentiation to adipocytes; bottom: preferential differentiation to myocytes.

a finite element solution obtained with linear triangles, the gradient is discontinuous if a direct method is used, since over an element e with set of vertices $\mathbb{E}$, one obtains

$$\frac{\partial u}{\partial x} = \frac{\partial}{\partial x}\sum_{p\in\mathbb{E}} u_p\phi_p(x,y) = \sum_{p\in\mathbb{E}} u_p\frac{\partial\phi_p}{\partial x}, \tag{9.39}$$

where ϕ_p and u_p, respectively, represent the basis function of node p and (the approximation of) the solution on node p. This gives a discontinuity of the gradient over the element boundaries. An alternative is to use a weighed approach by considering the weak derivative. Then, one computes the gradient on the nodal points and one get a more smoothed representation of the solution. However, a disadvantage is that one still loses one order of accuracy, that is if the accuracy of the solution is $O(h^{p+1})$, then the accuracy possibly becomes $O(h^p)$. To prevent this loss of accuracy, one can use the

This book belongs to Central Library BADJI Mokhtar-ANNABA UNIVERSITY Copyright Elsevier 2024

ZZ-patch gradient recovery method. In Zienkiewicz and Zhu (1992a,b), it is shown that the method does preserve accuracy. As an alternative, one can also use one of the filtering approaches that even increase accuracy, see Mirzaee et al. (2014) as an example. This is what we want to explore for this class of problems in the future. Both cell-based and continuum-scale models will likely benefit from this approach.

9.5 CONCLUSIONS

A numerical method for a cell-based model for cell migration and differentiation has been presented. The hybrid method resides on a combination of a moving mesh finite element method and a particle method and its interaction. The formalism can be used to model cell differentiation to various phenotypes at the same time. The signals can both be chemical and mechanical, where mechanical signals require the use of the gradient of the solution. The gradient of the solution is determined by the use of the ZZ-gradient recovery method. The method is generic and can be used for various applications involving cell differentiation. The currently presented formalism along with its numerical method can be generalized easily to applications with different cell phenotypes, if characteristics such as shape, strength, secretion rates, and migration speeds are known. For instance it is possible to treat fracture healing, which involves fibroblasts, osteoblasts, and chondrocytes analogously to what has been done in the present manuscript.

REFERENCES

Bookholt, F.D., Monsuur, H.N., Gibbs, S., Vermolen, F.J., 2016. Mathematical modelling of angiogenesis using continuous cell-based models. Biomechanics and Modelling in Mechanobiology 15 (6), 1577–1600.

Drasdo, D., Höhme, S., 2005. A single–cell–based model of tumor growth in vitro: monolayers and spheroids. Physical Biology 2 (3), 133–147.

Dziuk, G., Elliott, C.M., 2013. Finite element methods for surface PDEs. Acta Numerica 22, 289–296.

Gefen, A., Benayahu, D., 2015. The mechanobiology of obesity and related diseases. In: Studies in Mechanobiology, Tissue Engineering and Biomaterials, vol. 16. Springer–Verlag, Berlin Heidelberg.

Gimble, J.M., Katz, A.J., Bunnell, B.A., 2007. Adipose-derived stem cells for regenerative medicine. Circulation Research 100, 1249–1260.

Groh, A., Louis, A.K., 2010. Stochastic modeling of biased cell migration and collagen matrix modification. Journal of Mathematical Biology 61, 617–647.

Guilak, F., Cohen, D.M., Estes, B.T., Gimble, J.M., Liedtke, W., Chen, C.S., 2010. Control of stem cell fate by physical interactions with the extracellular matrix. Cell Stem Cell 5 (1), 17–26.

Harrevelt, S.D., 2015. Simulating the Differentiation of Stem Cells Using a 2D and 3D Mathematical Model (M.Sc.-thesis at the Delft Institute of Applied Mathematics). Delft University of Technology, The Netherlands. Downloadable at: http://repository.tudelft.nl.

Madzvamuse, A., Wathen, A., Maini, P.K., 2003. A moving grid finite element method applied to a biological pattern generator. Journal of Computational Physics 190, 478–500.

Mirzaee, H., Ryan, J.K., KIrby, R.M., 2014. Smoothness-increasing accuracy-conserving (SIAC) filters for discontinuous galerking solutions: application to structured tetrahedral meshes. Journal of Scientific Computing 58, 690–704.

Mousavi, S.J., Doweidar, M.H., Doblare, M., 2013. Modeling of cell migration: a mechano-chemo-electrotaxis approach. Journal of Theoretical Biology 329, 64–73.

Or-Tzadikario, S., Sopher, R., Gefen, A., 2010. Quantitative monitoring of lipid accumulation over time in cultured adipocytes as function of culture conditions: towards controlled adipose tissue engineering. Tissue Engineering (Part C) 16, 1167–1181.

Prokharau, P.A., Vermolen, F.J., Garcia–Aznar, J.M., 2012. Model for direct bone apposition on pre-existing surfaces, during peri-implant osseointegration. Journal of Theoretical Biology 304, 131–142.

Prokharau, P.A., Vermolen, F.J., Garcia–Aznar, J.M., 2014. A mathematical model for cell differentiation, as an evolutionary and regulated process. Computer Methods in Biomechanics and Biomedical Engineering 17 (10), 1051–1070.

Reinhart–King, C.A., Dembo, M., Hammer, D.A., 2008. Cell–cell mechanical communication through compliant substrates. Biophysics Journal 95, 6044–6051.

Rey, R., Garcia–Aznar, J.M., 2013. A phenomenological approach to modelling collective cell movement in 2D. Biomechanics and Modelling in Mechanobiology 12 (6), 1089–1100.

Sell, S., 2004. Stem cell origin of cancer and differentiation therapy. Critical Reviews in Oncology/Hematology 51 (1), 1–28.

Shoham, N., Girshovitz, P., Katzengold, R., Shaked, N.T., Benayahu, D., Gefen, A., 2014. Adipocyte stiffness increases with accumulation of lipid droplets. Biophysics Journal 106 (6), 1421–1431.

Stolzing, A., Jones, E., McGonagle, D., Scutt, A., 2007. Age-related changes in human bone marrow-derived mesenchymal stem cells: consequences for cell therapies. Mechanisms of Aging and Development 129 (3), 163–173.

Van Oers, R.F.M., Rens, E.G., LaValley, D.J., Reinhart–King, C.A., Merks, R.M.H., 2014. Mechanical cell–matrix feedback explains pairwise and collective endothelial cell behavior in vitro. PLoS Computational Biology 10 (3), e1003774.

Vermolen, F.J., Gefen, A., 2012. A semi-stochastic cell-based formalism to model the dynamics of migration of cells in colonies. Biomechanics and Modeling in Mechanobiology 11 (1–2), 183–195.

This book belongs to Central Library BADJI Mokhtar-ANNABA UNIVERSITY Copyright Elsevier 2024

Vermolen, F.J., 2015. Particle methods to solve modelling problems in wound healing and tumor growth. Computational Particle Mechanics 2 (4), 381–399.

Vermolen, F.J., Gefen, A., 2015. Semi-stochastic cell-level computational modelling of cellular forces: application to contractures in burns. Biomechanics and Modeling in Mechanobiology 14 (6), 1181–1195.

Vermolen, F.J., Van der Meijden, R.P., Van Es, M., Gefen, A., Weihs, D., 2015. Towards a mathematical formalism for semi—stochastic cell—level computational modelling of tumor initiation. Annals of Biomedicine 43 (7), 1680–1694.

Weihs, D., Gefen, A., Vermolen, F.J., 2016. Review on experiment-based two- and three dimensional models for wound healing. Interface Focus 6, 20160038.

Wu, Y., Chen, L., Scott, P.G., Tredget, E.E., 2007. Mesenchymal stem cells enhance wound healing through differentiation and angiogenesis. Stem Cells 25, 2648–2659.

Yan, M., Liu, Q., 2016. Differentiation therapy: a promising strategy for cancer treatment. Chinese Journal of Cancer 35 (1), 3.

Zienkiewicz, O.C., Zhu, J.Z., 1992a. The superconvergent patch recovery and a posteriori error estimates. Part 1: the recovery technique. International Journal for Numerical Methods in Engineering 33 (7), 1331–1364.

Zienkiewicz, O.C., Zhu, J.Z., 1992b. The superconvergent patch recovery and a posteriori error estimates. Part 2: error estimates and adaptivity. International Journal for Numerical Methods in Engineering 33 (7), 1365–1382.

FURTHER READING

Byrne, H.M., Drasdo, D., 2009. Individual—based and continuum models of growing cell populations: a comparison. Journal of Mathematical Biology 58, 657–687.

Levy, A., Enzer, S., Shoham, N., Zaretsky, U., Gefen, A., 2012. Large, but not small sustained tensile strains stimulate adipogenesis in culture. Annals of Biomedical Engineering 40, 1052–1060.

Shoham, N., Gottlieb, R., Shaharabani-Yosef, O., Zaretsky, U., Benayahy, D., Gefen, A., 2012. Static mechanical stretching accelerates lipid production by adipocytes by activating the MEK signaling pathway. American Journal of Physiology and Cell Physiology 302, C429–C441.

This book belongs to Central Library BADJI Mokhtar-ANNABA UNIVERSITY Copyright Elsevier 2024

This page intentionally left blank

This book belongs to Central Library BADJI Mokhtar-ANNABA UNIVERSITY

Copyright Elsevier 2024

Chapter 10

Numerical Simulation of Bone Cutting: Hybrid SPH–FE Approach

S. Li[1], A. Zahedi[2] and V. Silberschmidt[1]
[1]Loughborough University, Loughborough, United Kingdom; [2]De Montfort University, Leicester, United Kingdom

10.1 INTRODUCTION

Cutting into bone tissue is an intrinsic part of many clinical procedures, such as orthopedic surgery. The success of such surgery depends largely on precision of the operation and the extent of damage it causes to the surrounding tissue. An excessive force generated by a surgical cutting tool can lead to the formation of microcracks and fractures in the adjacent area of cortical bone tissue (Ebacher et al., 2012; Launey et al., 2010a,b). Temperature raises close the cutting region due to friction between cutting tool and bone can cause thermal necrosis (Currey, 2010), leading ultimately to permanent damage, which can, in turn, delay postoperative recovery (Wazen et al., 2013) or induce other clinical complications such as loosening of an implant interface (Marco et al., 2015). Therefore, it is necessary to understand mechanical behavior of a bone tissue in the vicinity of the tool–bone interaction zone to develop new surgical instruments and techniques, to minimize damage caused to the surrounding bone tissues. As well known, bone' anisotropy and its intrinsic hierarchical microstructure alter stress and strain distributions around the cutting region. With an onset of damage, both extrinsic and intrinsic fracture toughening mechanisms act at various length scales either as crack barriers to deflect cracks or as protective structures, increasing an amount of energy needed to extend the crack by undergoing large plastic deformation.

Earlier experimental studies of bone cutting (Alam et al., 2010; Aro et al., 1981; Jacobs et al., 1974; Wang et al., 2014; Yu et al., 2014) focused on parameters derived from the field of machining; factors such as cutting forces and speed, depth of cut, chip morphology, and surface finish were the primary concerns of the studies. Information about the remaining uncut bone region was rather limited. Despite a continuing research interest in bone cutting, it still remains a challenging field of study, which cannot be easily analyzed due to variations in material (bone) property, (cutting) tool geometry, and experimental conditions (Marco et al., 2015). Inadequate access to relevant bone samples and ethical concerns over conducting in vivo experiments further restrict our understanding of mechanics of bone cutting through the experimental route. On the other hand, numerical simulations provide an alternative solution, once validated, offering comprehensive information on field variables that otherwise would be very difficult to measure. From the modeling perspective, a recent review done by Marco et al. (2015) highlighted the latest development in computational modeling of bone cutting. There are only a handful of finite element models in the literature addressing issues associated with bone cutting. The effects of depth of cut and cutting speed (Alam et al., 2009, 2010), materials anisotropy (Li et al., 2014; Santiuste et al., 2014), damage and fracture (Kasiri et al., 2010; Sugita et al., 2009), and microstructure (Hage and Hamade, 2013) were often evaluated independently. Although it is well known that a constitutive model of bone tissue is crucial for the accuracy of finite element model of bone cutting, there is still no adequate model that can fully describe the material's anisotropy and the damage behavior of cortical bone under conditions of cutting tool penetration. A comprehensive understanding of anisotropic deformation and damage mechanisms involved in the tool–bone interaction process is required for the development of an accurate model of bone cutting.

This lack of sophisticated models in the literature can be partially ascribed to nontrivial material properties of cortical bone and numerical difficulties of simulation of the penetration process due to the large deformations and element distortion. From a modeling point of view, mechanical behavior of a cortical bone is highly anisotropic, with higher values

Numerical Methods and Advanced Simulation in Biomechanics and Biological Processes. https://doi.org/10.1016/B978-0-12-811718-7.00010-1
Copyright © 2018 Elsevier Ltd. All rights reserved.

This book belongs to Central Library BADJI Mokhtar-ANNABA UNIVERSITY
Copyright Elsevier 2024

of the Young's modulus, yield, ultimate stresses, and fracture toughness reported for bone's main axis (parallel to the osteons) and lower for the transverse direction (perpendicular to the osteons) (Novitskaya et al., 2011). Its mechanical behavior also varies markedly across anatomic quadrants (Abdel-Wahab et al., 2011) as a result of a random heterogeneous arrangement of its microstructural constituents (Li et al., 2013a) and an ongoing remodeling process. Being a natural composite material (mainly consisting of mineralized nanoparticles and collagen fibers), its deformation behavior combines brittle and ductile features. The inelastic deformation region spans 0.27%–2.5%, depending on loading conditions and material orientation (Mercer et al., 2006), while failure can start at a strain of 0.4%, as reported in Budyn and Hoc (2006). At the microscopic level, preferentially aligned microstructural constituents and variations of their material properties activate distinct deformation and toughening mechanisms according to the applied load and its orientation, causing anisotropy in both its mechanical behavior and fracture resistance (Li et al., 2013b).

To the authors' knowledge, there is no experimental data available in the literature about deformation, damage, and fracture processes in the vicinity of the tool–bone interaction zone during the cutting process, while numerical models do not account for material anisotropy or the effect of damage mechanisms. In addition, a conventional finite element scheme faces numerical challenges related to large deformation and highly localized distortion in the process zone.

In this chapter, a new smoothed particle hydrodynamic (SPH) model incorporating anisotropic mechanical properties and damage mechanisms is developed to provide an insight into the development of deformation and damage in the vicinity of the tool–bone interaction zone.

10.2 MODEL CHALLENGES AND REQUIREMENT

Modeling of large deformations induced by cutting processes has always been a challenging subject. Numerical difficulties arise when severe deformation and generation of new surfaces become a dominant feature of the cutting region. Typical mesh-based elements in this region are prone to errors due to large mesh distortion and convergence problems associated with topological changes. High contact stress and stress gradients at the cutting interface mean that simulation often breaks down before analysis is complete because of the convergence issue associated with topological changes. Several finite element approaches such as Lagrangian and Eulerian formulations, as well as unzipping, remeshing, and element-deletion techniques, were employed individually or in various combinations to tackle such numerical challenges (Movahhedy et al., 2000; Barge et al., 2005). The advantages and limitations of each type of cutting simulation are discussed below.

In contrast to the Lagrangian formulation, in which a mesh is fixed to the material geometry and moves with the deformed material, the Eulerian approach describes the material's deformation within a spatially fixed mesh domain, with material flowing through mesh elements depending on deformation kinematics. The Eulerian method is more computationally expensive than its Lagrangian counterpart, because the deformation history of the material modeled cannot be tracked (Khoei et al., 2007). Having the advantage of no mesh distortion, the Eulerian formulation is able to handle extreme deformations without using small time steps. However, having mesh independence with respect to the flowing material, it is difficult to apply boundary conditions to the Eulerian material. Instead, a coupling between the Eulerian and Lagrangian formulations is needed to model solid mechanics problems such as the cutting process. In general, there are two ways to apply this coupling to address the mesh distortion associated with large deformations.

The coupled Eulerian–Lagrangian method employs both Eulerian (usually the internal section) and Lagrangian (external free surface) domains, linked to each other through Eulerian–Lagrangian interaction/contact. Material separation and chip morphology are generally not the primary investigation targets due to the definition of the Lagrangian boundaries. Therefore, the method is suitable for simulating steady-state cutting processes where chip geometry can be predetermined through experiment (Haglund, 2001).

The arbitrary Lagrangian–Eulerian (ALE) approach combines the advantages of both Eulerian and Lagrangian schemes and was introduced mainly to handle large distortions within Lagrangian mesh domains. Mesh distortion is controlled by adaptively remapping an internal mesh framework while maintaining its original topology. This technique has been used in studies (Donea et al., 2004) to simulate the cutting process of ductile materials, in which damage and fracture phenomena are not generally the primary concern. The success of the ALE approach in modeling cutting processes is somewhat limited due to its Lagrangian formulation, restricting topological changes of the domain. Therefore, it is not possible to simulate chip separation or generation of free surfaces (e.g., in cutting modeling) without using another surface separation criterion (Pantalé et al., 2004) such as element unzipping (node release) or element deletion/removal.

Another Lagrangian-based technique, remeshing, tackles element distortion by transferring field variables from the previous distorted mesh onto a newly formed, undeformed mesh. Although the change of mesh topology is permitted in

This book belongs to Central Library BADJI Mokhtar-ANNABA UNIVERSITY
Copyright Elsevier 2024

remeshing, it is limited by the accumulated error during the transformation process whereby the stress field from the previous time step is neglected (Ambati et al., 2012). Other techniques such as element deletion/removal and unzipping (or node release) are used in certain scenarios such as modeling cutting processes of ductile materials, where element removal only activates a small fraction of elements, or modeling crack propagation due to tensile load, with new surfaces separated from each other. However, when simulating the cutting of brittle materials, excessive element deletion could cause numerical instability as a result of losing contact definition or unbalanced mass/energy equilibrium arising from excessive material removal. Using the unzipping or node-releasing technique in a predominantly compressive process, i.e., cutting, could lead to an inappropriate definition of the contact interaction between cutting tool and workpiece, or contact penetration. Hence, it is necessary to develop a new modeling approach capable to solve the element distortion problem without compromising the accuracy of simulation.

10.3 SMOOTHED PARTICLE HYDRODYNAMIC APPROACH

SPH, first proposed by Gingold and Monaghan (Ebacher et al., 2012), is part of a large family of mesh-free methods used to model discrete deformation processes (Zahedi et al., 2013a; Heinstein and Segalman, 1997; Limido et al., 2007; Zahedi et al., 2012). The use of the Lagrangian scheme and particle-based elements avoids mesh tangling and element distortion while keeping a track of history-dependent variables (Zahedi et al., 2013b). Chip formation and material separation process, which involve the generation of free surfaces, can be resolved without defining specific boundary conditions or criteria.

The interpretation of the relationship between particles uses kernel estimation (based on the Monte Carlo method) to represent processes of hydrodynamics or continuum mechanics derived from the equations of motion, where the properties of particles can be calculated (Ebacher et al., 2012). The concept of integral representation of a function $f(x)$ in the SPH method starts from the following equation:

$$f(x) = \int_{\Omega} f(x')W(x - x', h)dx' \tag{10.1}$$

where $f(x')$ is the scalar function of the position vector x, Ω is the volume of the integration domain that contains x, h is the smoothing length defining the influence area of the smoothing W, and $W(x - x', h)$ is the smoothing kernel function.

Particles within a predefined radius, smoothing length (h), have a weighted power of influence on the central particle. Interactions are defined by the kernel function through a gradient depending on a relative distance between two particles (Fig. 10.1). Each integration point in SPH has more than one neighboring element that is interchangeable during each interpolation of the field variables. Specifically, the kernel appears as a bell-shaped function with a smooth and continuous first (and usually second) derivative. The particles are sorted at least once in every cycle to define current neighboring particles. When this kernel is used, the contribution is assumed to be zero when the distance from the particle is greater than 2 h. Still, many particles have to contribute to the calculation for the sampling to be adequate, which leads to increased computational effort.

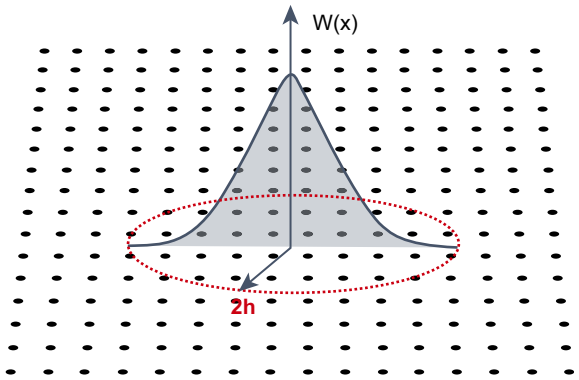

FIGURE 10.1 Interpolation of gradient influence of neighboring particles through kernel function $W(r, h)$ within circle of 2h (Rodriguez-Paz and Bonet, 2005).

This book belongs to Central Library BADJI Mokhtar-ANNABA UNIVERSITY Copyright Elsevier 2024

Because $W(x - x', h)$ is not a Dirac delta function (a distribution function that is zero everywhere expect at zero), the integral representation in Eq. (10.2) is only an approximation. Thus, an angle bracket $\langle\rangle$ is used for a kernel approximation and presented as follows:

$$\langle f(x)\rangle = \int_{\Omega} f(x')W(x - x', h)dx'. \tag{10.2}$$

The smoothing function W should satisfy a number of conditions. The normalization condition is the first, according to:

$$\int_{\Omega} W(x - x', h)dx' = 1. \tag{10.3}$$

The second condition is a delta function property that is observed when the smoothing length approaches zero:

$$\lim_{h \to 0} W(x - x', h) = \delta(x - x'), \tag{10.4}$$

and the final one is the compact condition:

$$W(x - x', h) = 0 \text{ when } |x - x'| > kh, \tag{10.5}$$

where k is a constant value linked to the smoothing function at a point at x and defines the effective (nonzero) area of the smoothing function called the *support domain* of that point (see Fig. 10.1). In this chapter, k was fixed at 2. By using this compact condition, integration over the entire problem domain was localized as integration over the support domain of the smoothing function.

A cubic spline, which has good properties of regularity as the interpolation polynomial, was used as a smoothing function as follows:

$$W(x - x', h) = \frac{1}{h^D}\delta\left(\frac{|x - x'|}{h}\right), \tag{10.6}$$

with

$$\delta(\mathrm{y}) = \mathrm{T} \times \begin{cases} 1 - \frac{3}{2}\mathrm{y}^2 + \frac{3}{4}\mathrm{y}^3 & \text{for } 0 < \mathrm{y} \leq 1 \\ \frac{1}{4}(2 - \mathrm{y})^3 & \text{for } 1 < \mathrm{y} \leq 2\,, \\ 0 & \text{for } \mathrm{y} > 2 \end{cases} \tag{10.7}$$

where T is a constant parameter that depends on the space dimension as follows:

$$\mathrm{T} = \begin{cases} \frac{2}{3} & \text{for 1 dimension;} \\ \frac{10}{7\pi} & \text{for 2 dimensions;} \\ \frac{1}{\pi} & \text{for 3 dimensions.} \end{cases} \tag{10.8}$$

The SPH computational framework is available in Abaqus/Explicit (v.6.11) and this was used in this chapter. Physical quantities and their derivatives at any integration points were calculated based on a kernel discretization method, according to a wish to represent the particles as a continuum, rather than individual points in space. This is important for overcoming problems with highly distorted of elements in the cutting zone with its extremely high strains and strain gradients, typical for continuum formulations. The kernel approximation provides stability and has a smoothing effect on physical filed equations in the limit as the particle separation approaches zero. The smoothing length at the beginning of the analysis was chosen to be 2.2 times the characteristic length. Therefore, around 30 particles were considered for each element to balance computational efficiency and accuracy (the maximum number of allowed particles associated with one element is set at 140 by default). The smoothing length was constant during the analysis. Thus, the average number of particles per element could either decrease or increase during the analysis depending on the average behavior in the model—expansion or compression.

This book belongs to Central Library BADJI Mokhtar-ANNABA UNIVERSITY
Copyright Elsevier 2024

In this chapter, a new 3D finite element modeling approach, encompassing both continuum FE and SPH elements, is developed in ABAQUS (Dassault Systèmes, 2011). The SPH elements were implemented directly along the cutting path to analyze large deformations that cannot be computed accurately using conventional continuum elements, while conventional elements were employed in other parts to diminish the computational cost and enhance the accuracy at small deformations.

10.4 MODEL FORMULATION AND IMPLEMENTATION

10.4.1 Model Geometry

The hybrid SPH + FE models were configured in accordance with the experimental setup, with a sharp cutting tool used to penetrate cortical bone. A 3D specimen with dimension 6 mm × 3 mm × 3 mm (length × width × thickness) was used in the current study with the assumption of a plane strain condition throughout the thickness (see Fig. 10.2A). For comparison of the experimental data and the simulation results, the same cutting tool geometry, measured with a 3D scanning optical microscope (OGP Smartscope Flash 200), was used. The cutting tool tip radius was 4 μm with the wedge angle and vertical edge height 18 degrees and 0.7 mm, respectively (see Fig. 10.2B). For computational efficiency, a thickness of 0.02 mm was modeled with symmetric boundary conditions applied to the x–y plane as shown in Fig. 10.2A. The cortical specimen was fully constrained at the bottom surface and constrained in the y–z plane at the two lateral edges. The FE domain was meshed with eight-node brick elements with reduced integration (C3D8R) with a single-bias mesh transition, and PC3D particle elements with one integration point per element were used in the middle section of the specimen with a width of 0.4 mm (Fig. 10.2B). Tied constraints were applied at the interface between the continuum C3D8R and PC3D particle elements.

10.4.2 Sensitivity Analysis

Prior to the main simulation, model reliability tests were conducted to evaluate the sensitivity of the model to changes in mesh size and geometric features. Geometric analysis was conducted to evaluate the effect of the SPH section's size on the overall stress and strain distributions and continuity of transition between continuum elements and particle elements. Two sizes of the SPH section were modeled, and the results indicated that variation due to the different size SPH sections remained insignificant (Fig. 10.3A). Mesh sensitivity studies were completed for three mesh sizes, 2, 4, and 10 μm, and a mesh size of 4 μm was chosen for both computational efficiency and accuracy.

To ensure that the simulation results were within the same confined quasistatic conditions as the experiments, verification tests with various loading velocities were conducted. The ratios of kinetic energy and the total internal energy are compared in Fig. 10.3B to evaluate the effect of loading speed on the overall kinetic energy of the model. The results, shown in Fig. 10.3B, demonstrate that the overall kinetic energy does not constitute a significant part (less than 5%) of the entire internal energy of the model when the speed is below 10 m/s. Hence, the loading speed of 1 m/s was chosen throughout the simulation.

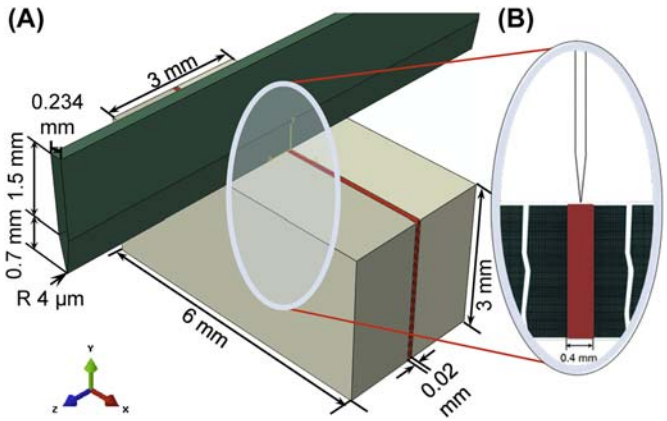

FIGURE 10.2 (A) Simulation of penetration of cortical bone using the hybrid (smoothed particle hydrodynamics (SPH) + finite element (FE)) model (gray area represents the shape of the experimental specimen, red is the SPH + FE model); (B) x–y plane of FE model (with SPH domain represented in red (gray in print versions) color mesh).

This book belongs to Central Library BADJI Mokhtar-ANNABA UNIVERSITY
Copyright Elsevier 2024

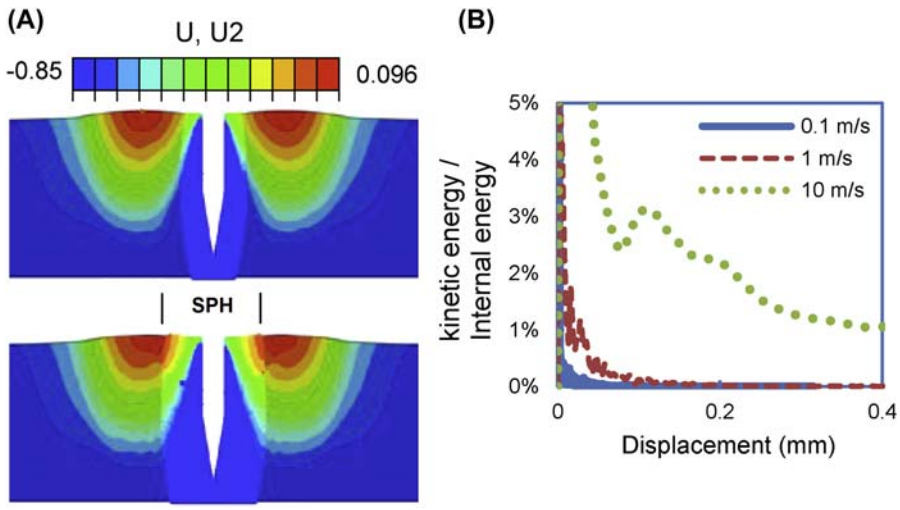

FIGURE 10.3 (A) Contour plots of vertical displacement for two models with particle sections of different size indicating no significant variation due to geometric change; (B) comparison of evolution of energy ratios (kinetic energy/internal energy) with penetration depth for various loading rates. *SPH*, smoothed particle hydrodynamics.

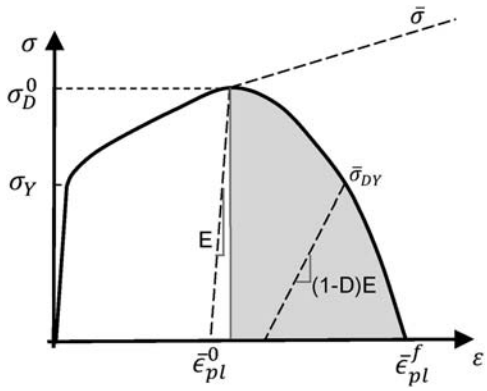

FIGURE 10.4 Stress−strain response of elastoplastic material with progressive damage initiation and evolution (σ_{DY} and $\bar{\varepsilon}_{pl}$ are equivalent yield stress and equivalent plastic strain at onset of damage initiation, while $\bar{\varepsilon}_{pl}^f$ is equivalent plastic strain at failure).

10.4.3 Contact Formulation

A master−slave contact algorithm with a traditional Coulomb friction law was applied to the interaction of the cutting tool and SPH particles. In the Coulomb friction law the critical shear stress is defined as $\tau = \mu p$, where μ is the coefficient of friction and p is the contact pressure between the surfaces. In this chapter $\mu = 0.3$ is used to represent a simple model of frictional behavior along the workpiece−tool interface, following previous results (Shi and Liu, 2004).

SPH particles and FE elements were coupled by a master−slave algorithm with a tie contact at the boundaries between the domains with continuum and particle elements. The interface node accepts forces from both the neighboring nodes and the attached finite element domain. The particle node is assumed to be in contact with the finite element mesh when the equations of motion cause the edge of the circular particle to cross over the master surface. In this algorithm, the nodes of both domains have the same displacement and there is no relative movement between them. This is convenient, since, from experience of using the SPH method, the size (smoothing length) of the SPH particle should be approximately half that of a Lagrange cell to give the same accuracy. Therefore, particles behave as spheres with radii equal to the radius of a sphere inscribed in a small cube associated with the particle volume. In the contact domain, the same number of elements was implemented. Because PC3D elements do not have faces or edges, an element-based surface cannot be defined using these elements. Consequently, the constrained node-based surfaces were defined as particles for stable computation without distortion.

This book belongs to Central Library BADJI Mokhtar-ANNABA UNIVERSITY
Copyright Elsevier 2024

10.4.4 Material Properties

The cutting tool used in the experiment was made of tungsten carbide and analytically modeled as a rigid body to maximize computational efficiency. The bovine cortical bone tissue was modeled as a macroscopically homogenized material with transversely isotropic elastoplastic properties (see Table 10.1) employing the Hill's anisotropic yield criterion and progressive material degradation. The material properties used in the models were obtained predominantly from experimental results of the research group at Loughborough University (Abdel-Wahab et al., 2011; Li et al., 2013b,c). The anisotropic Hill's yield behavior is described by the von Mises stress potential:

$$f(\sigma) = \sqrt{F(\sigma_{22}-\sigma_{33})^2 + G(\sigma_{33}-\sigma_{11})^2 + H(\sigma_{11}-\sigma_{22})^2 + 2L\sigma_{23}^2 + 2M\sigma_{31}^2 + 2N\sigma_{12}^2} \tag{10.9}$$

where σ_{ij} are components of the stresses tensor, subscripts 1, 2, and 3 represent the three perpendicular bone axes: longitudinal (parallel to the main axis of the femur), radial, and circumferential, respectively (see Fig. 10.2). The material anisotropic constants F, G, H, L, M, and N are parameters to be computed from the experimental data, determined by normal yield stresses:

$$\begin{cases} F = \dfrac{(\sigma^0)^2}{2}\left[\dfrac{1}{(\sigma_{22}^y)^2} + \dfrac{1}{(\sigma_{33}^y)^2} - \dfrac{1}{(\sigma_{11}^y)^2}\right] \\ G = \dfrac{(\sigma^0)^2}{2}\left[\dfrac{1}{(\sigma_{33}^y)^2} + \dfrac{1}{(\sigma_{11}^y)^2} - \dfrac{1}{(\sigma_{22}^y)^2}\right] \\ H = \dfrac{(\sigma^0)^2}{2}\left[\dfrac{1}{(\sigma_{11}^y)^2} + \dfrac{1}{(\sigma_{22}^y)^2} - \dfrac{1}{(\sigma_{33}^y)^2}\right] \end{cases} \tag{10.10}$$

and shear yield stresses:

$$L = \frac{3}{2}\left(\frac{\tau^0}{\tau_{23}^y}\right)^2, \quad M = \frac{3}{2}\left(\frac{\tau^0}{\tau_{13}^y}\right)^2, \quad N = \frac{3}{2}\left(\frac{\tau^0}{\tau_{12}^y}\right)^2 \tag{10.11}$$

where σ^0 and τ^0 are reference yield stresses. The Hill's constants were calculated based on the literature, shown in Table 10.2 (Reilly and Burstein, 1975). Plastic strain hardening was defined as isotropic, using previous experimental data (Table 10.3; Abdel-Wahab et al., 2011; Li et al., 2013c). Criteria for progressive damage were chosen based on experimental observation (Mercer et al., 2006). Damage initiation introduced in the current study was based on a strain-driven criterion commonly seen for hard biological tissue (Nalla et al., 2003), defining the onset of damage when a fracture strain

TABLE 10.1 List of Material Properties Used in Simulations

	References	Anterior	Posterior	Medial	Lateral
Density (kg/m^3)	Martin and Boardman, (1993)	2	2	2	2
E_{11} (GPa)	Li et al. (2013c)	23.2	19.3	21.1	15.1
E_{22}, E_{33} (GPa)	Li et al. (2013c)	13.2	9.9	14.7	11.2
ν_{12}, ν_{13}	Pithioux et al. (2002)	0.27	0.27	0.27	0.27
ν_{23}	Pithioux et al. (2002)	0.39	0.39	0.39	0.39
G_{12}, G_{13} (GPa)	van den Broek (1918)	6.1	6.1	6.1	6.1
G_{23} (GPa)	van den Broek (1918)	4.7	3.6	5.3	4
ε_{y11} (%)	Li et al. (2013c)	1	1	1	1
ε_{f11}, ε_{f22} (%)	Li et al. (2013c)	2	2	2	2
J_{IC11} (N/m)	Li et al. (2013b)	1653	1534	1868	2664
J_{IC22} (N/m)	Li et al. (2013b)	4087	3029	4765	4296

This book belongs to Central Library BADJI Mokhtar-ANNABA UNIVERSITY
Copyright Elsevier 2024

TABLE 10.2 Hill's Parameters for Cortical Bone Calculated Using Experimental Data

F	*G*	*H*	*L*	*M*	*N*
2.8	0.5	0.5	3	6	6

Data from Reilly, D., Burstein, A., 1975. The elastic and ultimate properties of compact bone tissue. Journal of Biomechanics.

TABLE 10.3 Postyield Stress–Strain Relationships for Different Cortices

	Flow Stress (MPa)			
Flow Strain (%)	Anterior	Posterior	Medial	Lateral
0.00	215.9	178.1	203	167
0.08	226.73	188.9	213.83	178
0.23	237.29	199.5	224.39	188
0.47	244.67	206.9	231.77	195
0.72	252.51	214.7	239.61	203
0.98	258.25	220.5	245.35	209
1.23	263.75	226.0	250.85	215
1.47	269.49	231.7	256.59	220
1.72	275.16	237.4	262.26	226

of 2% is reached (Li et al., 2013c). On damage initiation, the damage evolution process was described by employing an energy-based approach. The evolution criterion defines progressive degradation of the material in two forms: the decrease in the yield stress σ_{DY} and the degradation of the effective material stiffness $(1 - D)E$ (see Fig. 10.4). Based on the continuum damage mechanics theory, the criterion assumes that material damage increases gradually up to its complete failure, when the energy dissipated at the onset of damage is equal to a critical energy release per unit area. A summary of material properties used in the numerical models is given in Tables 10.1–10.3.

10.5 MODEL RESULTS AND ANALYSIS

10.5.1 Force–Displacement Characterization

To fully understand the damage and fracture behavior of the cortical bone tissue in the vicinity of the cutting tip, eight hybrid FE models (SPH + FE) simulated the penetration of cortical bone in two directions (perpendicular: L-C and L-R planes; and parallel: C-L and C-R planes, to osteons; where L, C, and R represent longitudinal, circumference, and radial directions, respectively) and four anatomical cortices (anterior, media, posterior, and lateral). Five experimental tests were made for each cutting direction, and the results of the models are compared against the experimental data in Fig. 10.5. The specific force (per unit width) and displacement (i.e., penetration depth D) obtained from the simulation demonstrate good agreement with the experimental data (Fig. 10.5) for all the cutting directions and cortices. The developed models were able to realize the linear increment of the force–displacement curves, adequately supporting the experimental observation both in terms of the initial slope and the peak cutting force both for directions and cortices.

Among the various cortices, cutting through the medial cortex resulted in the highest average force, while the posterior cortex required the lowest cutting force. This disparity in the level of maximum force across anatomical cortices of the bovine femur indicates the influence of mechanical properties, which are, in turn, affected by the underpinning microstructural changes along the bone's circumference. Although statistical analysis of the experimental data using Tukey

This book belongs to Central Library BADJI Mokhtar-ANNABA UNIVERSITY
Copyright Elsevier 2024

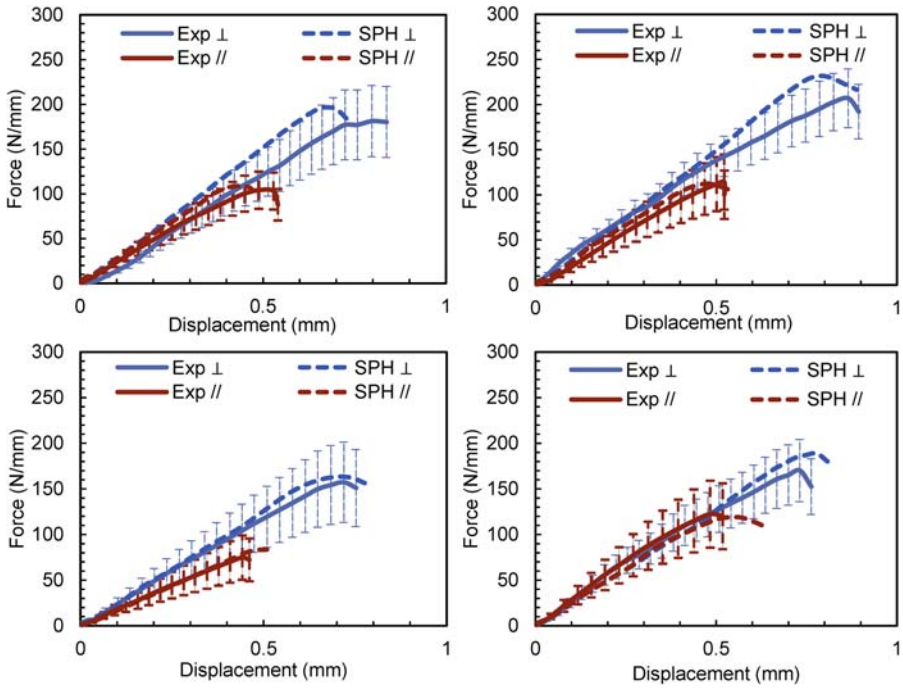

FIGURE 10.5 Comparison of force (per unit width) and displacement diagrams between experimental data (*solid line*) and simulation results (*dotted line*) for cutting perpendicular (⊥) and parallel (//) to osteons across four cortices: anterior (top left), medial (top right), posterior (bottom left) and lateral (bottom right). *SPH*, smoothed particle hydrodynamics.

honest significant difference tests ($\alpha = 0.05$) reveals a statistical difference ($P = .03$) between the posterior and lateral cortices for cutting parallel to the osteons, no significance was found for all other cortices, meaning an unstable correlation between the variation of microstructures (Li et al., 2013c) and postyield material behavior due to a mixture, but diluted effects of material stiffness, toughness, and localized damage mechanisms.

10.5.2 Anisotropy of Deformation Process

The obtained results show significant anisotropic behavior for cutting in different directions and considerable variation across anatomic cortices. In general, cutting forces are higher when cutting perpendicular to osteons (L-C and L-R) and lower when cutting parallel to osteons (C-L and C-R). The ratios of forces for these two directions ranged from 1.43 to 2.15 in the experimental tests. This lower cutting resistance could be attributed to the distinct microstructure-dependent deformation and damage mechanisms observed in our experiments (see Fig. 10.10). By incorporating the orientation-dependent material formulation, damage initiation, and evolution criteria, the models developed captured this anisotropic character of the deformation and failure processes. The simulation results demonstrated in Figs. 10.6–10.8 reveal the detailed character of localized stresses and strains caused by material anisotropy around the cutting tip (similar deformation contours were observed cutting perpendicular and parallel to osteons; hence, only one direction is shown). The evolution of the deformation process in the cortical bone escalated as the cutting tool penetrated into the depth of the specimen. Deformation was initiated in a relatively small region localized around the cutting tip, with a high concentration of stresses (Figs. 10.6A, 10.7A and 10.8A). As penetration continued, deformation accumulated and the material in front of the cutting tip underwent increased plastic deformation (Figs. 10.6B, 10.7B and 10.8B). Formation of a large shear band can also be observed in front of the cutting blade due to the combined effect of the rake angle and material's anisotropy (Fig. 10.8C–E). This deformation pattern continued expanding around the cutting edges until a saturation state was reached, at which point the cutting force attained its maximum value. After that point, plastic deformation and damage mechanisms became increasingly dominant, with deformation starting to accumulate toward the upper free edge with more damage in the vicinity of the cutting region (Figs. 10.6D, 10.7D, and 10.8D). Finally, material softening, as a result of plastic deformation and degradation of material stiffness (Figs. 10.6–10.8), led to complete failure of the surrounding structure and the reduction of the cutting force.

This book belongs to Central Library BADJI Mokhtar-ANNABA UNIVERSITY Copyright Elsevier 2024

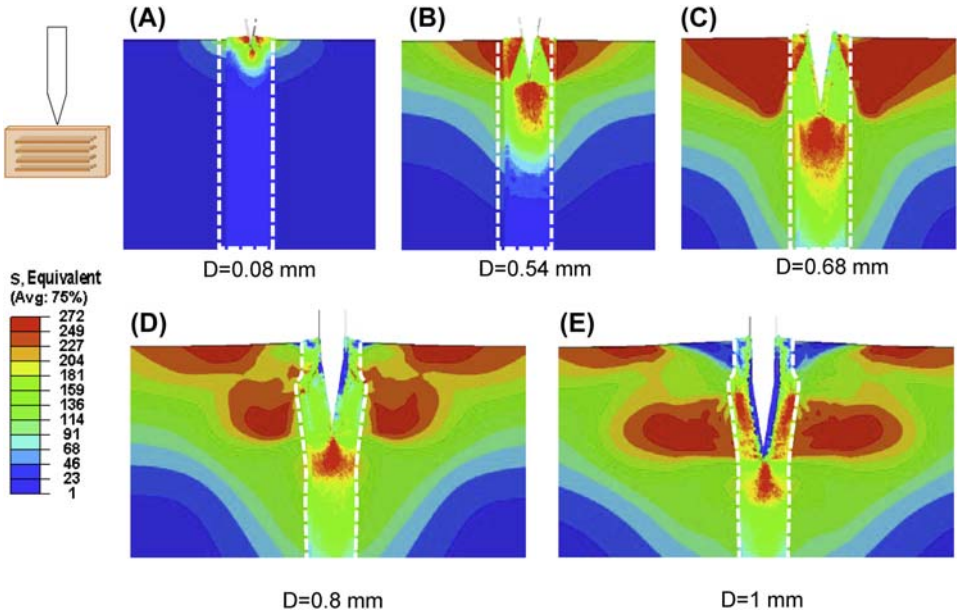

FIGURE 10.6 Distribution of equivalent stress (in MPa) for various levels of penetration depth D = 0.08 mm (A), 0.54 mm (B), 0.68 mm (C), 0.8 mm (D), and 1 mm (E) (the *white box* represents the smoothed particle hydrodynamic domain).

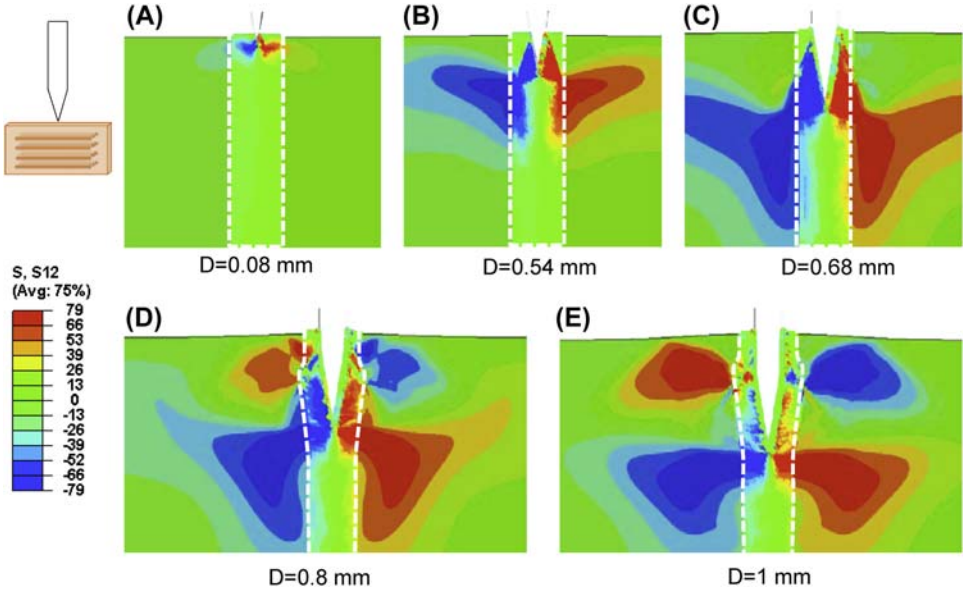

FIGURE 10.7 Distribution of shear stress component (σ_{12}; in MPa) at various penetration stages: D = 0.0>8 mm (A), 0.54 mm (B), 0.68 mm (C), 0.8 mm (D), and 1 mm (E) (the *white box* represents the smoothed particle hydrodynamic domain).

10.5.3 Effect of Progressive Damage

It is important to know that incorporating the continuum damage theory into the current modeling scheme is necessary to simulate large deformation and damage processes of quasibrittle or low-ductility materials, such as cortical bone tissue (Atkins, 2009). Neglecting such behavior may lead to inadequate or erroneous solutions. The effect, with and without the progressive damage model, is illustrated in Fig. 10.9. Comparing the specific force−displacement curves, the model without the damage criterion showed an unrealistic continuous growth of the cutting force (indicated by the dotted line in Fig. 10.9); when the damage criterion was considered, after a peak, the cutting force degraded progressively with displacement in a way similar to that observed in the experiment.

This book belongs to Central Library BADJI Mokhtar-ANNABA UNIVERSITY
Copyright Elsevier 2024

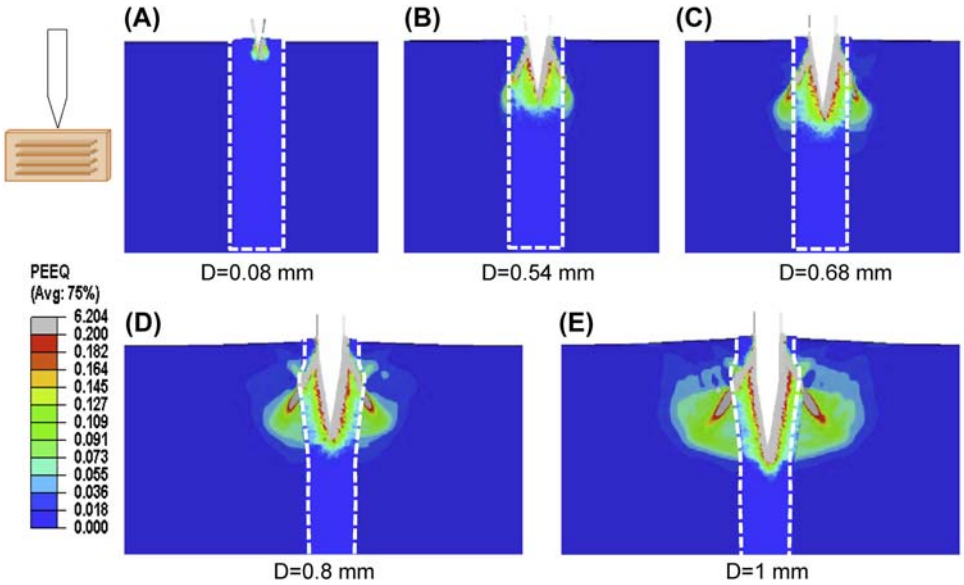

FIGURE 10.8 Distribution of equivalent plastic strain at various penetration stages, D = 0.08 mm (A), 0.54 mm (B), 0.68 mm (C), 0.8 mm (D), and 1 mm (E) (the *white box* represents the smoothed particle hydrodynamic domain).

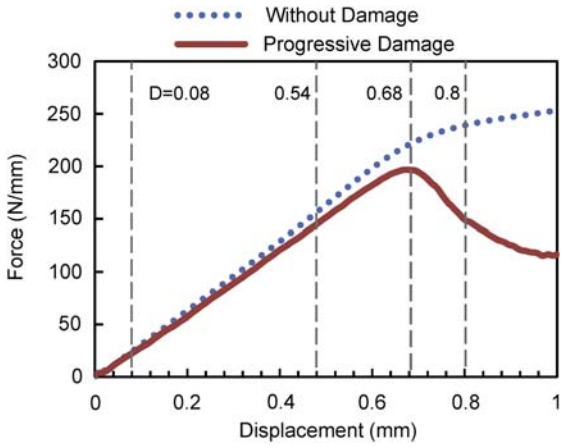

FIGURE 10.9 Effect of cutting force (per unit width) with penetration depth (D) in cases with and without accounting for damage (*vertical dash lines* represent penetration at various stages).

10.5.4 Anisotropic Toughening Mechanisms

The experiments revealed different microstructure-related toughening mechanisms for varying cutting directions. Generally, for cutting along the longitudinal axis (C-L direction), damage was well ahead of the cutting tip and caused mainly by splitting and separation. As a result, uncracked ligament bridging (Launey et al., 2010a) was the dominant toughening mechanism during the process of osteon splitting, rupture, and interface failure (Fig. 10.10A). Similarly, for cutting in the radial direction (C-R), the bridging effect was still present due to the splitting of osteons or fibers/fibrils. However, the microstructural constituents had a more profound effect on the direction of crack propagation compared with the previous case. As a result of the material's heterogeneity, cracks were deflected toward, and arrested at, cavities, such as Haversian canals (Fig. 10.10B). In contrast to the previous two cases, cutting perpendicular to the osteons (L-C and L-R) required higher energy to propagate through the region because of its higher fracture toughness. Cracks were therefore more likely to be deflected transversely to the cutting direction, as a result of the material's porosity and heterogeneity (Fig. 10.10C and D). Among the four anatomic cortices, two types of damage mechanisms were observed in the experiments: a brittle damage pattern involving fragmentation and material peeling off was found predominantly in the plexiform bone region (Fig. 10.10C) and a diffuse ductile damage pattern was associated with the large deformation of the osteonal structure (Fig. 10.10D).

This book belongs to Central Library BADJI Mokhtar-ANNABA UNIVERSITY Copyright Elsevier 2024

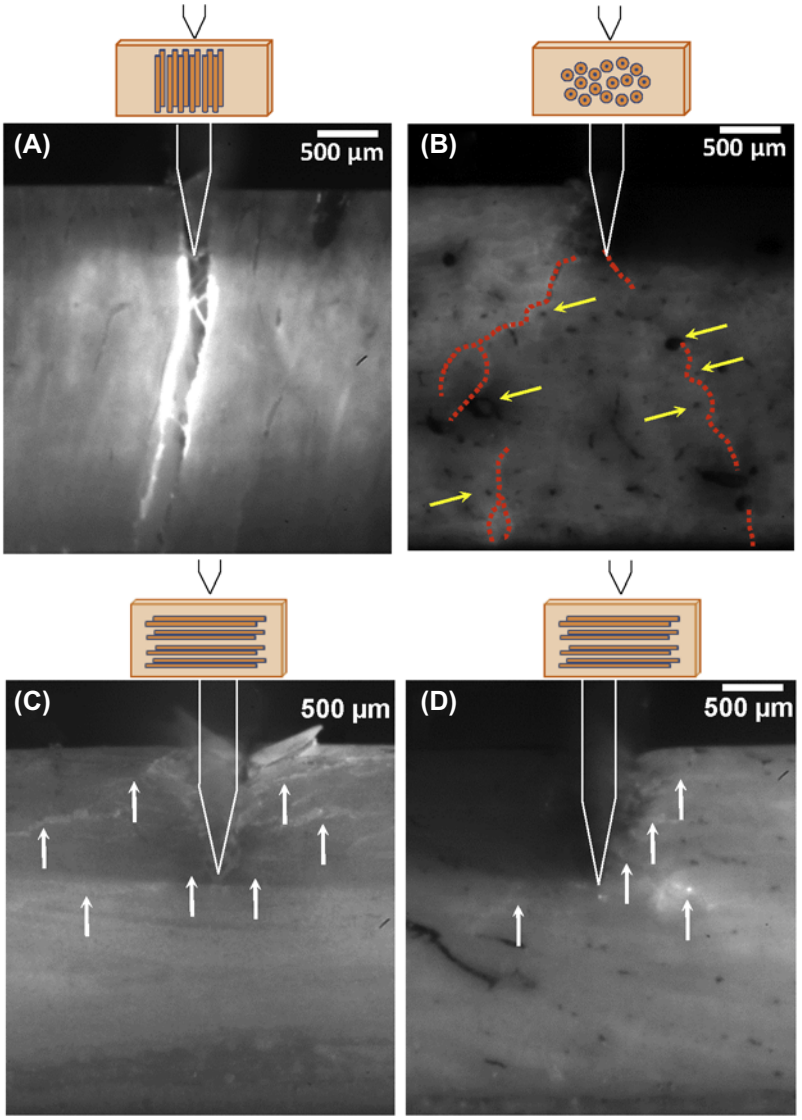

FIGURE 10.10 High-speed camera images capturing distinct damage processes during cutting parallel to osteon direction: (A) C-L direction; (B) C-R direction; and perpendicular to osteon direction: (C) L-C direction with brittle damage pattern predominantly observed at plexiform bone region; (D) L-R direction diffused ductile damage pattern associated with large deformation of osteonal structure (*white lines* designate the profile of the razor blade, *red (gray in print versions) dotted lines* indicate crack paths and *yellow (gray in print versions) arrows* point at the positions of osteons, whereas *white arrows* point at the positions of cracks).

The anisotropic fracture toughening mechanisms in the experimental tests, described above, were not modeled explicitly because of computational cost. Instead, orientation-dependent fracture toughness, i.e., strain energy release rate, was used to simulate anisotropic damage and fracture. The model successfully captures dissimilar damage and fracture processes observed in the experiments (see Fig. 10.11). A comparison of the simulation results and images taken with a high-speed camera and optical microscopy of damage induced by cutting in both parallel and perpendicular directions are shown in Fig. 10.11. At the maximum cutting force, the level of damage, presented by a damage scalar index SDEG in the simulation (Fig. 10.11), was much higher for cutting parallel to the osteons (Fig. 10.11B) than perpendicular to them (Fig. 10.11A). Lower fracture resistance for the C-L and C-R directions facilitated damage propagation in front of the cutting tip as observed in both simulations and experiments (Fig. 10.11B, E and F), whereas higher fracture toughness in L-C and L-R directions led to lateral damage (Fig. 10.11A–C). Consequently, the higher cutting force was the result of low material degradation and higher fracture toughness when cutting perpendicular to osteons (Fig. 10.11).

This book belongs to Central Library BADJI Mokhtar-ANNABA UNIVERSITY
Copyright Elsevier 2024

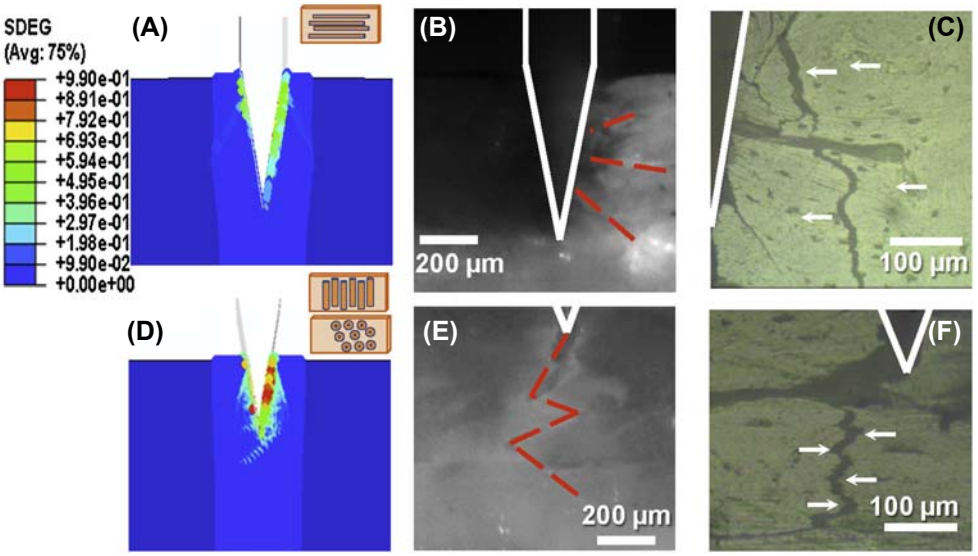

FIGURE 10.11 Comparison of simulation results (A, D) with images taken with high-speed camera (B, E) and optical microscopy (C, F) of damage induced by cutting in various directions: (A, B, C) perpendicular to bone axis, where lateral damage propagation is observed; and (D, E, F) parallel to bone axis, with damage in front of the cutting tip (*white lines* designate the profile of the razor blade, *red (gray in print versions) dotted lines* indicate crack lines and *arrows* point at crack paths).

As well as capturing qualitatively the distinct damage patterns, the current model is able to evaluate quantitatively the damage evolution processes for two cutting directions. Normalized energy dissipation, based on calculating the ratio of energy dissipation in damage (ALLDMD in Abaqus) and plastic deformation (ALLPD), as shown in Fig. 10.12, was used for this. Apparently, the processes of cutting along the two directions had some similar features in terms of their energy dissipation ratio. At the beginning, the energy ratio was similar for the two directions, followed by a sudden decrease and plateau, then a rapid growth stage where the energy dissipation as a result of damage outgrew that due to plastic deformation. The difference, however, between cutting for two directions is that the process happened earlier when cutting parallel to osteons. The overall damage ratio when cutting parallel was higher than when cutting perpendicular to osteons. As a result, considerably lower cutting forces were needed when cutting parallel to osteons because of the wider spread of material degradation.

10.6 DISCUSSION

A numerical simulation of bone cutting using a hybrid SPH + FE approach was developed to simulate large deformations and damage processes in the cortical bone tissue induced by penetration. In this chapter, the results are validated against,

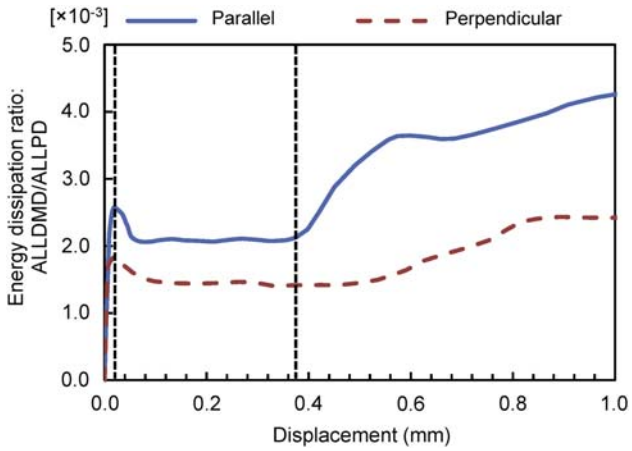

FIGURE 10.12 Effect of the energy evolution (energy ratio between damage (ALLDMD) and plastic deformation (ALLPD) against penetration depth for two cutting directions).

This book belongs to Central Library BADJI Mokhtar-ANNABA UNIVERSITY Copyright Elsevier 2024

and agree well with, our experimental findings. The challenge of modeling the processes of large deformation and damage of the quasibrittle material was resolved naturally by implementing SPH particle elements in the vicinity of the cutting region. Orientation-dependent material behavior and the effect of the damage mechanism were addressed using anisotropic material properties alongside the progressive damage criteria. The model successfully captured the nonuniformity and anisotropy of the deformation and damage processes in cortical bone during cutting in various directions and cortices. The anisotropic damage criteria employed in the current models were able to reproduce the distinct orientation-dependent damage patterns observed in our experimental tests and the literature (Sugita et al., 2009). However, the microstructure-related toughening mechanisms observed in the experiments such as uncracked ligament bridging, crack deflection due to microstructural heterogeneity, and orientation were not accounted for because the microstructural constituents were not introduced directly into the homogenized model. Characterization of deformation behavior linked to the local microstructure would certainly assist to understand further the main mechanisms. However, a microstructural modeling approach in the current case would be computationally impractical and well beyond the scope of this study and, therefore, is not discussed here.

In summary, cutting forces depend largely on the orientation of the underlying microstructure. Higher forces were measured in cutting perpendicular to osteons, with considerably lower ones observed for penetration parallel to osteons. The results clearly demonstrate the necessity of incorporating anisotropic material behavior and progressive damage mechanisms into the modeling scheme to characterize the mechanical behavior of the cortical bone tissue for various loading conditions and orientations. The results of the model provide a useful insight into the deformation behavior of, and damage mechanisms in, anisotropic material under such loading conditions. The model provides a powerful analytical tool for further studies that can improve the accuracy of orthopedic surgical procedures and optimize surgical cutting tools.

REFERENCES

Abdel-Wahab, A.A., Alam, K., Silberschmidt, V.V., 2011. Analysis of anisotropic viscoelastoplastic properties of cortical bone tissues. Journal of the Mechanical Behavior of Biomedical Materials 4, 807−820. http://dx.doi.org/10.1016/j.jmbbm.2010.10.001.

Alam, K., Mitrofanov, A.V., Silberschmidt, V.V., 2010. Thermal analysis of orthogonal cutting of cortical bone using finite element simulations. International Journal of Experimental and Computational Biomechanics 1, 236. http://dx.doi.org/10.1504/IJECB.2010.035259.

Alam, K., Mitrofanov, A.V., Bäker, M., Silberschmidt, V.V., 2009. Stresses in ultrasonically assisted bone cutting. Journal of Physics: Conference Series 12014. http://dx.doi.org/10.1088/1742-6596/181/1/012014.

Ambati, R., Pan, X., Yuan, H., Zhang, X., 2012. Application of material point methods for cutting process simulations. Computational Materials Science 102−110. http://dx.doi.org/10.1016/j.commatsci.2011.06.018.

Aro, H., Kallioniemi, H., Aho, A.J., Kellokumpu-Lehtinen, P., 1981. Ultrasonic device in bone cutting. A histological and scanning electron microscopical study. WWW Document Acta Orthopaedica Scandinavica. http://www.tandfonline.com/doi/abs/10.3109/17453678108991750.

Atkins, A.G., 2009. The Science and Engineering of Cutting the Mechanics and Processes of Separating, Scratching and Puncturing Biomaterials, Metals and Non-metals. Butterworth-Heinemann/Elsevier.

Barge, M., Hamdi, H., Rech, J., Bergheau, J.M., 2005. Numerical modelling of orthogonal cutting: influence of numerical parameters. Journal of Materials Processing Technology 164−165, 1148−1153.

Budyn, E., Hoc, T., 2006. Multi-scale modeling of human cortical bone: aging and failure studies. MRS Online Proceedings Library 975. http://dx.doi.org/10.1557/PROC-975-0975-DD02-06.

Currey, J.D., 2010. Mechanical properties and adaptations of some less familiar bony tissues. Journal of the Mechanical Behavior of Biomedical Materials 3, 357−372.

Dassault Systèmes, 2011. Abaqus v6.11 Documentation − Abaqus Analysis User's Manual.

Donea, J., Huerta, A., Ponthot, J.-P., Rodríguez-Ferran, A., Donea, J., Huerta, A., Ponthot, J.-P., Rodríguez-Ferran, A., 2004. Arbitrary Lagrangian-Eulerian methods. In: Encyclopedia of Computational Mechanics. John Wiley & Sons, Ltd., Chichester, UK, pp. 413−433 doi:10.1002/0470091355.ecm009.

Ebacher, V., Guy, P., Oxland, T.R., Wang, R., 2012. Sub-lamellar microcracking and roles of canaliculi in human cortical bone. Acta Biomaterialia 8, 1093−1100. http://dx.doi.org/10.1016/j.actbio.2011.11.013.

Hage, I.S., Hamade, R.F., 2013. Micro-FEM orthogonal cutting model for bone using microscope images enhanced via artificial intelligence. Procedia CIRP 385−390. http://dx.doi.org/10.1016/j.procir.2013.06.121.

Haglund, A., 2001. On Friction Modeling in Orthogonal Machining: An Arbitrary Lagrangian-Eulerian Finite Element Model. Library and Archives Canada (Bibliotheque et Archives Canada).

Heinstein, M., Segalman, D., 1997. Simulation of Orthogonal Cutting with Smooth Particle Hydrodynamics. Sandia National Laboratories.

Jacobs, C.H., Pope, M.H., Berry, J.T., Hoaglund, F., 1974. A study of the bone machining process—orthogonal cutting. Journal of Biomechanics 7, 131−136. http://dx.doi.org/10.1016/0021-9290(74)90051-7.

Kasiri, S., Reilly, G., Taylor, D., 2010. Wedge indentation fracture of cortical bone: experimental data and predictions. Journal of Biomechanical Engineering 132.

This book belongs to Central Library BADJI Mokhtar-ANNABA UNIVERSITY Copyright Elsevier 2024

Khoei, A.R., Anahid, M., Shahim, K., 2007. An extended arbitrary Lagrangian – Eulerian finite element method for large deformation of solid mechanics. Finite Elements in Analysis and Design 98, 1–37. http://dx.doi.org/10.1016/j.finel.2007.12.005.

Launey, M.E., Buehler, M.J., Ritchie, R.O., 2010a. On the mechanistic origins of toughness in bone. Annual Review of Materials Research. http://dx.doi.org/10.1146/annurev-matsci-070909-104427.

Launey, M.E., Chen, P.Y., McKittrick, J., Ritchie, R.O., 2010b. Mechanistic aspects of the fracture toughness of elk antler bone. Acta Biomaterialia 6, 1505–1514. http://dx.doi.org/10.1016/j.actbio.2009.11.026.

Li, S., Abdel-Wahab, A., Demirci, E., 2013a. Fracture process in cortical bone X-FEM analysis of microstructured models. International Journal of Fracture 184, 43–55.

Li, S., Abdel-Wahab, A., Silberschmidt, V.V., 2013b. Analysis of fracture processes in cortical bone tissue. Engineering Fracture Mechanics 110, 448–458.

Li, S., Demirci, E., Silberschmidt, V.V., 2013c. Variability and anisotropy of mechanical behavior of cortical bone in tension and compression. Journal of the Mechanical Behavior of Biomedical Materials 21, 109–120.

Li, S., Abdel-Wahab, A., Demirci, E., Silberschmidt, V.V., 2014. Penetration of cutting tool into cortical bone: experimental and numerical investigation of anisotropic mechanical behaviour. Journal of Biomechanics 47, 1117–1126.

Limido, J., Espinosa, C., Salau, M., Lacome, J.L., 2007. Article in press SPH method applied to high speed cutting modelling. International Journal of Mechanical Sciences 49, 898–908.

Marco, M., Rodríguez-Millán, M., Santiuste, C., Giner, E., Miguélez, M.H., 2015. A review on recent advances in numerical modelling of bone cutting. Journal of the Mechanical Behavior of Biomedical Materials 44, 179–201. http://dx.doi.org/10.1016/j.jmbbm.2014.12.006.

Martin, R., Boardman, D., 1993. The effects of collagen fiber orientation, porosity, density, and mineralization on bovine cortical bone bending properties. Journal of Biomechanics 26, 1047–1054.

Mercer, C., He, M., Wang, R., Evans, A., 2006. Mechanisms governing the inelastic deformation of cortical bone and application to trabecular bone. Acta Biomaterialia 2, 59–68.

Movahhedy, M., Gadala, M.S., Altintas, Y., 2000. Simulation of the orthogonal metal cutting process using an arbitrary Lagrangian–Eulerian finite-element method. Journal of Materials Processing Technology 103 (2), 267–275.

Nalla, R., Kinney, J., Ritchie, R., 2003. Mechanistic fracture criteria for the failure of human cortical bone. Nature Materials 2, 164–168.

Novitskaya, E., Chen, P.Y., Lee, S., Castro-Ceseña, A., Hirata, G., Lubarda, V.A., McKittrick, J., 2011. Anisotropy in the compressive mechanical properties of bovine cortical bone and the mineral and protein constituents. Acta Biomaterialia 7, 3170–3177. http://dx.doi.org/10.1016/j.actbio.2011.04.025.

Pantalé, O., Bacaria, J., Dalverny, O., 2004. 2D and 3D numerical models of metal cutting with damage effects. Computer Methods in Applied Mechanics and Engineering 193 (39–41), 4383–4399.

Pithioux, M., Lasaygues, P., Chabrand, P., 2002. An alternative ultrasonic method for measuring the elastic properties of cortical bone. Journal of Biomechanics 35 (7), 961–968.

Reilly, D., Burstein, A., 1975. The elastic and ultimate properties of compact bone tissue. Journal of Biomechanics 8 (6), 393–396.

Rodriguez-Paz, M., Bonet, J., 2005. A corrected smooth particle hydrodynamics formulation of the shallow-water equations. Computers and Structures 83 (17–18), 1396–1410.

Santiuste, C., Rodríguez-Millán, M., Giner, E., 2014. The influence of anisotropy in numerical modeling of orthogonal cutting of cortical bone. Composite Structures 116, 423–431.

Shi, J., Liu, C.R., 2004. The influence of material models on finite element simulation of machining. Journal of Manufacturing Science and Engineering 126, 849. http://dx.doi.org/10.1115/1.1813473.

Sugita, N., Osa, T., Aoki, R., Mitsuishi, M., 2009. A new cutting method for bone based on its crack propagation characteristics. CIRP Annals – Manufacturing Technology 58, 113–118. http://dx.doi.org/10.1016/j.cirp.2009.03.057.

van den Broek, J.A., 1918. The effects of cold-working on the elastic properties of steel. Carnegie Scholarship Memorial Iron and Steel Institute 9, 125–169.

Wang, Y., Cao, M., Zhao, X., Zhu, G., McClean, C., Zhao, Y., Fan, Y., 2014. Experimental investigations and finite element simulation of cutting heat in vibrational and conventional drilling of cortical bone. Medical Engineering and Physics 36, 1408–1415. http://dx.doi.org/10.1016/j.medengphy.2014.04.007.

Wazen, R.M., Currey, J.A., Guo, H., Brunski, J.B., Helms, J.A., Nanci, A., 2013. Micromotion-induced strain fields influence early stages of repair at bone – implant interfaces. Acta Biomaterialia 9, 6663–6674. http://dx.doi.org/10.1016/j.actbio.2013.01.014.

Yu, K., Iwata, S., Ohnishi, K., Usuda, S., Nakagawa, T., Kawana, H., 2014. Modeling and experimentation of drilling vibration for implant cutting force presenting system. International Workshop on Advanced Motion Control 711–716. http://dx.doi.org/10.1109/AMC.2014.6823368.

Zahedi, S.A., Li, S., Roy, A., Babitsky, V., Silberschmidt, V.V., 2012. Application of smooth-particle hydrodynamics in metal machining. Journal of Physics Conference Series 382, 12017. http://dx.doi.org/10.1088/1742-6596/382/1/012017.

Zahedi, S.A., Demiral, M., Roy, A., Silberschmidt, V.V., 2013a. FE/SPH modelling of orthogonal micro-machining of f.c.c. single crystal. Computational Materials Science 104–109. http://dx.doi.org/10.1016/j.commatsci.2013.05.022.

Zahedi, S.A., Roy, A., Silberschmidt, V.V., 2013b. Modeling of micro-machining single-crystal f.c.c. Metals. Procedia CIRP 346–350. http://dx.doi.org/10.1016/j.procir.2013.06.114.

This book belongs to Central Library BADJI Mokhtar-ANNABA UNIVERSITY Copyright Elsevier 2024

This page intentionally left blank

This book belongs to Central Library BADJI Mokhtar-ANNABA UNIVERSITY

Copyright Elsevier 2024

Chapter 11

Smoothed Particle Hydrodynamics Method and Its Applications to Cardiovascular Flow Modeling

S. Shahriari and L. Kadem
Concordia University, Montreal, QC, Canada

11.1 INTRODUCTION

Smoothed particle hydrodynamics (SPH) is a fully Lagrangian mesh-free particle method suitable for computational modeling of continuum physical systems such as fluids. The main concept behind SPH is to approximate the numerical solutions of physical partial differential equations through the use of a large enough number of fluid particles mimicking a continuum domain (Gingold and Monaghan, 1977). The decomposed computational domain does not need to hold the connectivity among the particles with a computational mesh. Each particle carries its physical properties such as mass, pressure, and velocity that are obtained using constitutive relations and interpolation with its computational neighboring particles (Vignjevic and Campbell, 2009). Table 11.1 shows the main advantages and disadvantages of SPH compared with mesh-based methods.

SPH was originally developed to model compressible flows in astrophysics and not to address incompressible fluid problems. It was developed independently by Lucy and Gingold and Monaghan in 1977 to simulate the formation of binary star systems, hardly achievable at that time using mesh-based methods. The primary model, although it did not exactly conserve linear and angular momentum, led to promising results in the simulation of the complex behavior of celestial bodies (Fig. 11.1).

The move from astrophysics problems to terrestrial problems involving incompressible fluids was initiated by a specific interest in archeology and how a tsunami may have destroyed the Minoan civilization in Crete (Monaghan, 2015; Monaghan and Kos, 1999). Since then, SPH has been used to simulate a large panel of physical problems including shock wave problems (Monaghan and Gingold, 1983), solitary and breaking waves, shallow water and dam breakdown (Monaghan and Kos, 1999; Monaghan, 1994), industrial die-casting processes (Cleary et al., 2002), multiphase flows (Monaghan and Kocharyan, 1995; Richie and Thomas, 2001; Hu and Adams, 2006), flow through porous media (Zhu et al., 1999), viscoelastic flows (Ellero et al., 2002), and interacting and interfacial fluid flows (Colagrossi and Landrini, 2003; Monaghan et al., 1999). Most of the SPH simulations of internal incompressible flows were performed at low Reynolds numbers (Morris et al., 1997; Sigalotti et al., 2003).

SPH has also been applied to simulate the elastic dynamical behavior of solids with large deformation and the development of fractures in solid mechanics (Libersky and Petschek, 1991; Wingate and Stellingwerf, 1994; Benz and Asphaug, 1995; Randles and Libersky, 1996; Bonet and Kulasegaram, 2000; Gray et al., 2001).

SPH appears to be a promising tool for simulating cardiovascular flows as well. The pulsatile nature of these types of flows with highly deformable boundaries makes it challenging to develop well-adapted algorithms and their implementation. SPH has been proven to be capable of modeling FSI without increasing the complexity of the algorithm (Qin et al., 2010; Farahani et al., 2008) and to be suitable for modeling unsteady and oscillating flows (Shahriari et al., 2013). SPH has been applied to simulate the deformation of red blood cells (RBC) in low Reynolds number flows using both RBC

Numerical Methods and Advanced Simulation in Biomechanics and Biological Processes. https://doi.org/10.1016/B978-0-12-811718-7.00011-3
Copyright © 2018 Elsevier Ltd. All rights reserved.

This book belongs to Central Library BADJI Mokhtar-ANNABA UNIVERSITY
Copyright Elsevier 2024

TABLE 11.1 Main Advantages and Disadvantages of Smoothed Particle Hydrodynamics (SPH) Compared to Mesh-Based Methods

Advantages	Disadvantages
The SPH simulation domain does not need to be bounded and no computation time is spent on empty space as in mesh-based methods (of importance for simulation of hydraulic flows).	Computation time is spent updating the neighbor list for each particle in the domain.
There is no need in SPH to remesh or refine the domain. SPH is not subject to mesh-related problems such as mesh distortion.	The resolution is fixed at the beginning of the simulations by setting the number of particles.
Extracting time history of fluid particles is straightforward and natural. This is of importance for investigating blood particle damage, blood particle residence time, and finite-time Lyapunov exponent fields.	
Extending simulations to 3D and including more complex physics is relatively easy in SPH and does not lead to an increase in the complexity of the code.	

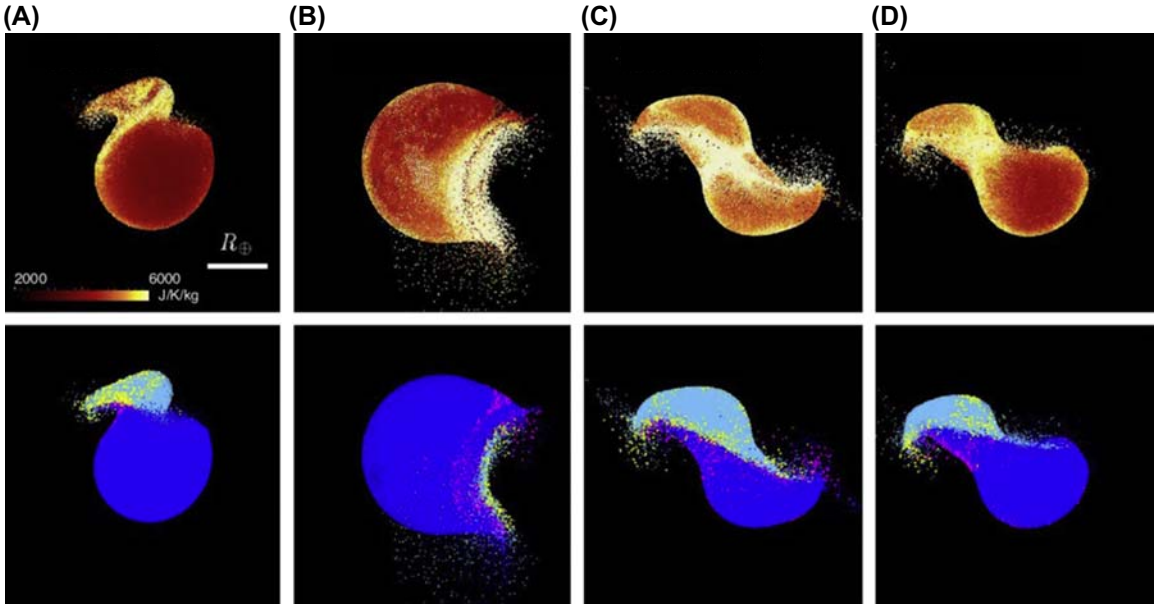

FIGURE 11.1 Initial state of the moon-forming disk as simulated by smoothed particle hydrodynamics (Nakajima and Stevenson, 2014). (A) Standard; (B) Fast-spinning Earth; (C) Sub-Earths; (D) Intermediate.

and plasma as particles (Tanaka and Takano, 2005) and showed interesting applications in virtual interactive surgery training (Müller et al., 2004) purposes and prediction of arterial wall rupture (Tanaka and Takano, 2005) at higher Reynolds numbers. The pioneering works of Shahriari et al. (2013), Sinnott et al. (2006), and Shahriari et al. (2012a,b) helped to examine SPH method capabilities and challenges for the simulation of realistic cardiovascular flows. Sinnott et al. (2006) showed the first results of simulations in a real carotid bifurcation and Shahriari et al. (2013) presented the first applications of the method in simulating left ventricle flows and turbulence downstream of a bileaflet mechanical heart valve (Shahriari et al., 2012a,b).

11.2 MATHEMATICAL FORMULATION

11.2.1 Smoothed Particle Hydrodynamics Formulation

In SPH, a continuum domain is discretized by a set of particles, instead of using a grid. Each particle has its own macroscopic physical properties (density, velocity, pressure) that are statistically interpolated using the properties of all its

This book belongs to Central Library BADJI Mokhtar-ANNABA UNIVERSITY
Copyright Elsevier 2024

neighboring particles. In this case, the value of any physical property A at position $\boldsymbol{r}$ in the domain can be obtained using the concept of an integral interpolant (Monaghan, 1992)

$$A(\boldsymbol{r}) = \int A(\boldsymbol{r}')W(\boldsymbol{r}-\boldsymbol{r}',h)d\boldsymbol{r}' \tag{11.1}$$

where h is called the smoothing length, which determines the size of the neighbor domain and $W(\boldsymbol{r}-\boldsymbol{r}', h)$ is a weighting function or so-called interpolating kernel, which is a symmetric function.

If the physical property A is only known at specific discrete points, then this integral is approximated using a summation operator that can be applied numerically as (Monaghan, 1992)

$$A(\boldsymbol{r}) = \sum_b m_b \frac{A_b}{\rho_b} W(\boldsymbol{r}-\boldsymbol{r_b},h) \tag{11.2}$$

where A_b represents each physical property at particle "b" with mass m_b, density ρ_b, and position $\boldsymbol{r_b}$ within the neighboring domain of a particle located at position $\boldsymbol{r}$. As a consequence, $\frac{m_b}{\rho_b}$ represents the volume associated with particle "b." Note that although the term "particle" is used in SPH literature, one has to consider "b" as an interpolation point rather than as a true mass element. The above equation represents the basic formulation of the SPH method. The concept of SPH interpolation is shown in Fig. 11.2.

Formulation Eq. (11.2) can then be used to derive the gradient and the Laplacian of the smoothed quantity A, assuming the smoothing kernel function is first- and second-order differentiable:

$$\nabla A(\boldsymbol{r}) = \sum_b m_b \frac{A_b}{\rho_b} \nabla W(\boldsymbol{r}-\boldsymbol{r_b},h) \tag{11.3}$$

and a higher order formulation as

$$\nabla A(\boldsymbol{r}) = \rho \sum_b m_b \left(\frac{A_b}{\rho_b^2} + \frac{A}{\rho^2}\right) \nabla W(\boldsymbol{r}-\boldsymbol{r_b},h). \tag{11.4}$$

The Laplacian can be obtained as

$$\nabla^2 A(\boldsymbol{r}) = \sum_b m_b \frac{A_b}{\rho_b} \nabla^2 W(\boldsymbol{r}-\boldsymbol{r_b},h). \tag{11.5}$$

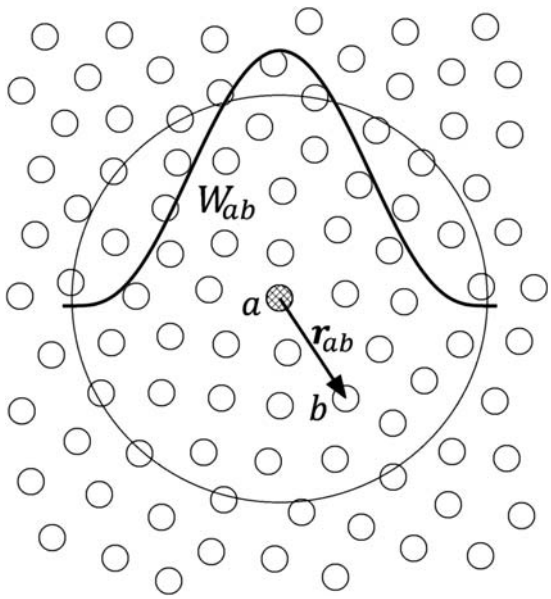

FIGURE 11.2 The main concept behind smoothed particle hydrodynamics interpolation: Kernel function, supporting domain, and neighboring particles.

This book belongs to Central Library BADJI Mokhtar-ANNABA UNIVERSITY Copyright Elsevier 2024

11.2.1.1 Interpolating Kernel Function

The interpolating kernel, or weighting function, is one of the most important factors in the SPH formulation. A kernel function defines the interpolation form and determines the influence dimension of the neighboring domain (h). The kernel function must satisfy the following properties: (1) be positive; (2) have compact support, i.e., has a zero value except inside the finite domain defined by twice the smoothing length ($2h$); and (3) being normalized and treated as a Dirac delta function when the smoothing length (h) tends to zero (Liu and Liu, 2003).

Several forms of kernels can be used ranging from polynomial to Gaussian forms. One of the kernels used in SPH is the Gaussian kernel. However, it does not have compact support and is computationally expensive because it requires the evaluation of expensive exponential functions. The most commonly used kernel function is in the form of a cubic spline. It has, when compared with higher order splines, less computational cost, but shows lower stability. The standard form of the cubic spline kernel is (Morris et al., 1997)

$$W_{ab} = \frac{C}{h^D}\begin{cases} 1-\frac{3}{2}q^2+\frac{3}{4}q^3 & 0 \le q < 1 \\ \frac{(2-q)^3}{4} & 1 \le q < 2 \\ 0 & 2 \le q \end{cases} \tag{11.6}$$

where $q = \boldsymbol{r}_{ab} / h$, and D is the number of dimensions in the problem: 1 for unidimensional, 2 for bidimensional or 3 for three-dimensional. The constant (C) is a scaling factor that is a function of the number of dimensions in the problem. This constant has to ensure that the aforementioned properties of the kernel function are satisfied.

$$C = \begin{cases} \text{for } D = 1: & \frac{2}{3} \\ \text{for } D = 2: & \frac{10}{7\pi} \\ \text{for } D = 3: & \frac{1}{\pi} \end{cases}$$

The supporting size of this kernel is $2h$.

Other kernel functions, such as the fourth-order, quartic, spline kernel, can also be used. This kernel can be written for 2D simulations as (Violeau and Issa, 2007)

$$W_{ab} = \frac{96}{1199\pi h^2}\begin{cases} \left(\frac{5}{2}-q\right)^4 - 5\left(\frac{3}{2}-q\right)^4 + 10\left(\frac{1}{2}-q\right)^4 & 0 \le q < 0.5 \\ \left(\frac{5}{2}-q\right)^4 - 5\left(\frac{3}{2}-q\right)^4 & 0.5 \le q < 1.5 \\ \left(\frac{5}{2}-q\right)^4 & 1.5 \le q < 2.5 \\ 0 & 2.5 \le q \end{cases} \tag{11.7}$$

Comparing with a cubic kernel, this kind of kernel has a supporting size of $2.5h$ and its influence domain is wider, which leads to a higher computational time, but higher stability.

Variable smoothing length. Under some specific flow conditions, such as in the presence of large deformations or compression, the use of a constant smoothing length during the calculations may lead to significant drawbacks. Large deformations may lead to a significantly large spacing between the particles, leading to a reduction in the interaction between the particles by having fewer particles within the supporting size of the kernel. In contrast, compression phenomena may lead to an increase in the number of particles in the supporting size of the kernel that can significantly increase the computational cost. For such problems, the use of a variable smoothing length is recommended:

$$h = h_0\left(\frac{\rho_0}{\rho}\right)^{\frac{1}{n}}$$

This book belongs to Central Library BADJI Mokhtar-ANNABA UNIVERSITY
Copyright Elsevier 2024

where h and ρ are the current smoothing length and density, whereas h_0 and ρ_0 are the initial smoothing length and density. The value of n (=1, 2, or 3) is the number of dimensions in the problem (Benz and Asphaug, 1995). Note that another approach can also be used, taking into account conservation of mass: $\frac{dh}{dt} = \frac{1}{n}\, h\, \nabla \cdot \overrightarrow{V}$, where V is velocity.

11.3 NAVIER–STOKES EQUATIONS

Using Eq. (11.2) and its derivatives, fluid dynamic equations can be transformed to a discretized form under the SPH formulation.

Classical SPH formulates the governing equations of incompressible fluid flows as weakly compressible flows. The Navier–Stokes equations in the Lagrangian form are written as

$$\frac{d\rho}{dt} + \nabla \cdot V = 0 \tag{11.8}$$

$$\rho \frac{dV}{dt} = f_{body} - \nabla P + \mu \nabla^2 V \tag{11.9}$$

where t stands for time, ρ is the fluid density, V is the velocity vector, f_{body} represents body forces per unit volume acting on the fluid, P is the thermodynamic pressure, and μ is the dynamic viscosity.

11.4 CONSERVATION OF MASS

In SPH, conservation of mass leads to the calculation of the particle density at its local position ($\boldsymbol{r}_a$). Two formulations can be used:

The first SPH formulation for conservation of mass can be derived directly from the summation interpolant, Eq. (11.2), as

$$\rho_a = \sum_b m_b W_{ab} \tag{11.10}$$

where $\rho_a = \rho(\boldsymbol{r}_a)$ and $W_{ab} = W(\boldsymbol{r}_a - \boldsymbol{r}_b, h)$.

The second formulation leads to the time derivative form of conservation of mass (Monaghan, 1992):

$$\frac{d\rho_a}{dt} = \sum_b m_b (\boldsymbol{V}_a - \boldsymbol{V}_b) \cdot \boldsymbol{\nabla}_a W_{ab} \tag{11.11}$$

where $\nabla_a W_{ab}$ is the gradient of the kernel function with respect to the coordinates of particle "a." Eq. (11.11) is more appropriate for liquids and links the rate of density change to the relative velocity of the particles within the support domain (Morris et al., 1997; Monaghan, 1992). It also creates an even distribution of weight ensuring stability in density calculations based on the interaction between the velocity and the pressure changes and reduces the computation time.

11.5 CONSERVATION OF MOMENTUM

The SPH formulation of conservation of momentum requires the development of specific formulations for both the pressure gradient and the viscous terms. In the literature, different forms for both terms have been suggested (Monaghan, 1992, 2006; Cleary, 1998).

The conventional form for the pressure gradient is the symmetric form as it satisfies the conservation of linear and angular momentum (Monaghan, 1992):

$$\frac{\boldsymbol{\nabla} P}{\rho} = \frac{P}{\rho^\sigma} \boldsymbol{\nabla}\left(\frac{1}{\rho^{1-\sigma}}\right) + \frac{1}{\rho^{2-\sigma}} \boldsymbol{\nabla}\left(\frac{P}{\rho^{\sigma-1}}\right) \tag{11.12}$$

and then

$$\left(\frac{\boldsymbol{\nabla} P}{\rho}\right)_a = \sum_b m_b \left(\frac{P_b}{\rho_a^{2-\sigma}\rho_b^\sigma} - \frac{P_a}{\rho_a^\sigma \rho_b^{2-\sigma}}\right) \boldsymbol{\nabla}_a W_{ab}. \tag{11.13}$$

This book belongs to Central Library BADJI Mokhtar-ANNABA UNIVERSITY
Copyright Elsevier 2024

This form is symmetric for all values of the parameter σ. The most prevalent type of the symmetric form is the one for $\sigma = 2$:

$$\left(\frac{\nabla P}{\rho}\right)_a = \sum_b m_b \left(\frac{P_b}{\rho_b^2} + \frac{P_a}{\rho_a^2}\right) \nabla_a W_{ab}. \tag{11.14}$$

An alternative symmetric formulation for the pressure gradient is

$$\left(\frac{\nabla P}{\rho}\right)_a = \sum_b m_b \left(\frac{P_a + P_b}{\rho_a \rho_b}\right) \nabla_a W_{ab}. \tag{11.15}$$

This form is variationally consistent and can provide slightly superior results compared with the conventional pressure gradient term (Colagrossi and Landrini, 2003; Vila, 1999).

SPH simulations do not handle liquid flows as strictly incompressible but approximate them instead as slightly compressible. It is performed by introducing an artificial equation of state relating density to pressure. In this case, the continuity equation is only used to evolve the density over time. The use of a quasiincompressible equation of state, instead of an actual equation of state, allows for a reduction in the computational cost. In the SPH literature, a stiff equation of state is often used to simulate water flows (Monaghan, 1994):

$$P = P_0 \left(\left(\frac{\rho}{\rho_0}\right)^{\gamma} - 1 \right) \tag{11.16}$$

where P_0 is the pressure at the reference density of ρ_0 and γ is the specific heat ratio. This equation has, however, been introduced for modeling free surface flows and is sensitive to density fluctuations. This makes it less appropriate for simulating internal flows or more complex cardiovascular flows. In this case, the following equation of state can be used instead (Morris et al., 1997):

$$P = c^2 \rho \tag{11.17}$$

where c is the speed of sound. As in terrestrial applications of fluid mechanics, the speed of sound is large compared with the bulk velocity of the fluid, an artificial speed of sound should be employed to avoid very small computational time steps while keeping density fluctuations within an acceptable range (1%−3%, to maintain incompressible flow behavior). A value of 0.1 or less is suggested as a rough estimate for the Mach number to specify the artificial speed of sound (Morris et al., 1997; Monaghan, 1994).

For the viscous term, the most commonly used form is similar to the von Neumann−Richtmyer viscosity in mesh-based methods. In SPH, it was presented as a combination of shear and bulk viscosity when particles are approaching each other. In this approach, the viscous force per unit mass of a fluid particle is modeled as

$$\left(\frac{\mu}{\rho}\nabla^2 \boldsymbol{V}\right)_a = \sum_b m_b \frac{\alpha \overline{c}_{ab} \mu_{ab}}{\overline{\rho}_{ab}} \nabla_a W_{ab}. \tag{11.18}$$

With the addition of the following term (Ellero et al., 2002)

$$-\sum_b m_b \frac{\beta \mu_{ab}^2}{\overline{\rho}_{ab}} \nabla_a W_{ab}, \tag{11.19}$$

where μ_{ab} is defined as,

$$\mu_{ab} = \frac{h \boldsymbol{V}_{ab} \cdot \boldsymbol{r}_{ab}}{r^2 + \eta^2}, \tag{11.20}$$

where $\overline{c}_{ab} = (c_a + c_b)/2$ is the average artificial speed of sound, $\overline{\rho}_{ab} = (\rho_a + \rho_b)/2$ is the average density, $\boldsymbol{V}_{ab} = \boldsymbol{V}_a - \boldsymbol{V}_b$, and $\boldsymbol{r}_{ab} = \boldsymbol{r}_a - \boldsymbol{r}_b$. The order of α is around 1 and $\beta = 2\alpha$. The η^2 is a small term to avoid a singularity ($\eta^2 = 0.01h^2$).

Artificial viscosity should be applied only when a compression is happening (particles are approaching each other). Using this approach to model the real viscosity leads to spurious viscosity in areas away from the compression region. To eliminate this unphysical effect, several types of artificial viscosities have been introduced. The most common one is to multiply Eq. (11.19) by (Balsara, 1995; Morris and Monaghan, 1997)

This book belongs to Central Library BADJI Mokhtar-ANNABA UNIVERSITY
Copyright Elsevier 2024

$$\bar{f}_{ab} = \frac{f(a) + f(b)}{2} \tag{11.21}$$

where

$$f(a) = \frac{\left|(\boldsymbol{\nabla}\cdot\boldsymbol{V})_a\right|}{\left|(\boldsymbol{\nabla}\cdot\boldsymbol{V})_a\right| + \left|(\boldsymbol{\nabla}\times\boldsymbol{V})_a\right| + 0.0001c/h}. \tag{11.22}$$

This limits unphysical effects only to the region of compression. Although this approach is used in the literature, it is not recommended to simulate cardiovascular flows because the viscous force results in unrealistic viscous effects.

A standard form to model the real viscous force, presented in its original form in (Monaghan, 1994; Violeau and Issa, 2007), is

$$\left(\frac{\mu}{\rho}\nabla^2\boldsymbol{V}\right)_a = \sum_b m_b \frac{16}{\rho_a\rho_b}\frac{\mu_a\mu_b}{(\mu_a+\mu_b)}\frac{\boldsymbol{V}_{ab}\cdot\boldsymbol{r}_{ab}}{\boldsymbol{r}_{ab}^2}\boldsymbol{\nabla}_a W_{ab}. \tag{11.23}$$

This form was developed to simulate free surface flows and has been widely used to model other types of flows. It should be noted, however, that Cleary (1998) proposed and successfully applied a calibration coefficient for Eq. (11.23) based on a series of numerical tests. The proposed coefficient, however, still needs to be generalized for different kernel functions.

Another formulation used to model the viscous term, at very low Reynolds number, is obtained by combining standard SPH and finite difference approximations of the first derivative (Morris and Monaghan, 1997):

$$\left(\frac{\mu}{\rho}\nabla^2\boldsymbol{V}\right)_a = \sum_b m_b \frac{(\mu_a+\mu_b)\boldsymbol{r}_{ab}\cdot\boldsymbol{\nabla}_a W_{ab}}{\rho_a\rho_b\,\boldsymbol{r}_{ab}^2}\boldsymbol{V}_{ab}. \tag{11.24}$$

This formulation leads to conservation of linear momentum, while angular momentum is approximately conserved. In addition to being computationally efficient, it is also less influenced by computational errors for cases dealing with a low number of particles (Morris and Monaghan, 1997).

Shahriari et al. (2013) showed that Eq. (11.24) provides better results for simulating unsteady flows and is not dependent on the type of the kernel function used.

11.6 NUMERICAL FEATURES

11.6.1 Particle Movement and XSPH Variant

In SPH, fluid particles move in a Lagrangian frame of reference, based on

$$\frac{d\boldsymbol{r}_a}{dt} = \boldsymbol{V}_a. \tag{11.25}$$

The new position of particles is derived by time integration of the velocity at each instant. In SPH literature, a variant, referred to as XSPH, is proposed to smooth SPH particle movements (Monaghan, 1992) as

$$\frac{d\boldsymbol{r}_a}{dt} = \boldsymbol{V}_a + \varepsilon\sum_b m_b \frac{(\boldsymbol{V}_b - \boldsymbol{V}_a)}{(\rho_a+\rho_b)/2}W_{ab} \tag{11.26}$$

where ε is a constant between 0 and 1.

Shahriari et al. (2013) showed that the XSPH variant can lead to undesirable particle disorders in high velocity gradient flow regions, specifically when the particle resolution is not high enough.

11.6.2 Numerical Time Integration

In general, the flow is simulated, in SPH, by advancing the particles through time using a global fixed time step Δt and by integrating the accelerations numerically. Several integration schemes can be used including the implicit Euler scheme, the Verlet scheme, or the leapfrog scheme. However, a more appropriate scheme is a second-order accurate time integration scheme such as a predictor-corrector algorithm (Monaghan et al., 1999). For a first-order differential equation in the general form

This book belongs to Central Library BADJI Mokhtar-ANNABA UNIVERSITY Copyright Elsevier 2024

$$\frac{dy}{dt} = f \tag{11.27}$$

the predictor part consists of an explicit half time step integration,

$$y^{n+\frac{1}{2}} = y^n + \frac{\Delta t}{2} f^n, \tag{11.28}$$

followed by a corrector part to correct the approximated properties in the previous part as

$$y^{n+\frac{1}{2}} = y^n + \frac{\Delta t}{2} f^{n+\frac{1}{2}}. \tag{11.29}$$

Finally, the properties at the new time step are calculated based on the values obtained at predictor and corrector steps as

$$y^{n+1} = 2y^{n+\frac{1}{2}} - y^n. \tag{11.30}$$

At each step, pressure is calculated using the equation of state.

11.6.3 Variable Time Step

The time step in SPH is usually determined based on the Courant–Friedrichs–Lewy condition, external force, and viscous diffusion terms (Morris et al., 1997; Monaghan, 1992)

$$\Delta t \leq min\left\{0.25\frac{h}{c}, 0.25\sqrt{\frac{h}{max|\boldsymbol{f}_a|}}, 0.125\frac{h^2}{\nu}\right\} \tag{11.31}$$

where $|\boldsymbol{f}_a|$ is the force magnitude per unit of mass of a particle. This inequality states that the maximum speed of numerical propagation cannot exceed the maximum speed of physical propagation. A variable time step is used according to Eq. (11.31) to obtain a good compromise between computational efficiency and stability.

11.6.4 Search of the Neighboring Particles—Linked List Method

In contrast to mesh-based methods where the neighboring nodes for each node are clearly defined, in Lagrangian particle methods, the neighboring particles for each particle are changing with time and need to be found at each time step.

The simplest way to find the neighboring particles, "*b*," of the particle under consideration, "*a*," within the kernel supporting size is to calculate the distance of all particles in the domain from particle "*a*" and compare it with the kernel supporting size. This direct search approach is particularly inefficient and time consuming (order N^2), where N is the number of particles in the domain. A more efficient approach uses a linked list method or a bucket sort algorithm (Dominguez et al., 2010). In this method, an imaginary Cartesian network of cells, with dimension corresponding to the kernel supporting size (h), is constructed on the domain (Fig. 11.3). After updating the particle positions at each time step, it is possible to determine how many and which particles are positioned in a specific cell in the domain. Therefore, only particles in the same cell as the particle of interest, "*a*," and in its neighboring cells are considered (in 2D simulations, 9 cells). Applying this method reduces the computational time from N^2 to $N\,logN$. This method is not applicable when a variable influence length is used.

11.7 IMPLEMENTATION OF BOUNDARY CONDITIONS IN SMOOTHED PARTICLE HYDRODYNAMICS: RIGID, PERIODIC, AND INFLOW/OUTFLOW BOUNDARY CONDITIONS

11.7.1 Rigid Boundary Conditions

The implementation of wall boundary conditions in SPH requires special attention because the particles near the wall boundary do not have enough neighbors in their domain (the kernel is truncated). This leads to an inappropriate computation of density and pressure. Furthermore, simply setting the velocity of the particles on stationary walls to zero cannot entirely prevent fluid particles from penetrating rigid walls.

This book belongs to Central Library BADJI Mokhtar-ANNABA UNIVERSITY
Copyright Elsevier 2024

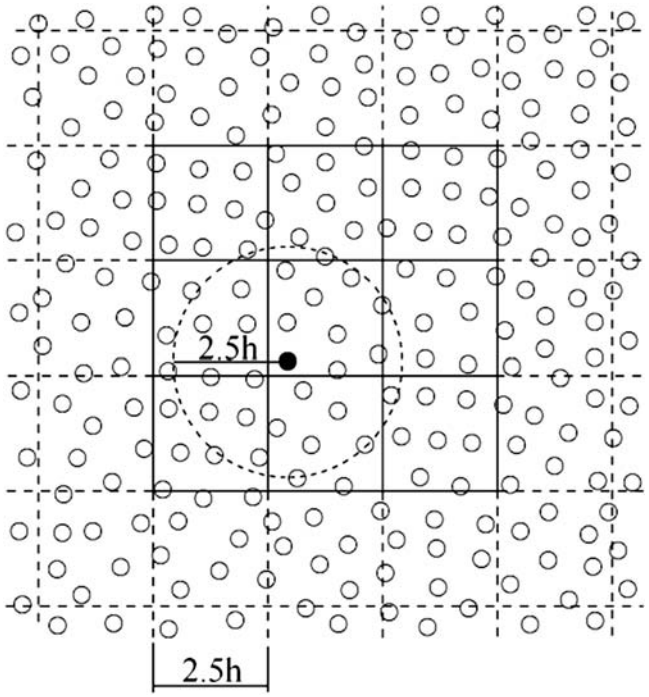

FIGURE 11.3 Imaginary cells used to search the neighboring particles of a given particle using the linked list method. The dimension of the cells is based on the selected interpolating function (for a quartic spline kernel, it is 2.5*h*).

Lennard-Jones force. One suggested method makes use of the Lennard-Jones force on the fluid particles approaching the wall (Fig. 11.4) (Monaghan, 1994)

$$f(\boldsymbol{r}) = D\left(\left(\frac{r_0}{r}\right)^{12} + \left(\frac{r_0}{r}\right)^{6}\right)\frac{\boldsymbol{r}}{r^2} \tag{11.32}$$

where r_0 is the initial particle spacing and D is a coefficient dependent on the physical characteristics of the problem.

Mirror particles. An alternative method is to use mirror particles that are created by reflecting particles approaching the walls (reflection with respect to the wall boundary). These mirror particles have the same density and pressure as their reference fluid particles, but a velocity vector with an opposite direction (Cummins and Rudman, 1999). Another approach is to consider some fixed particles outside the wall boundaries with an extrapolated velocity to satisfy the no-slip condition on the wall (Morris and Monaghan, 1997; Takeda et al., 1994). In this case, an artificial velocity is allocated to each particle based on

$$\boldsymbol{V}_{ab} = \beta \boldsymbol{V}_a \tag{11.33}$$

such that

$$\beta = min\left(\beta_{max}, 1 + \frac{d_b}{d_a}\right) \tag{11.34}$$

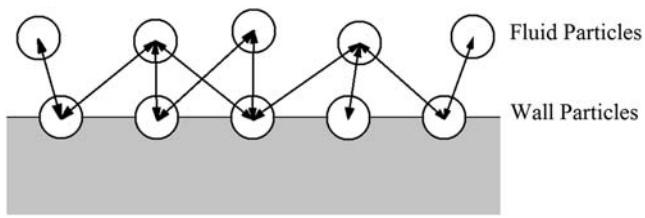

FIGURE 11.4 Attraction and repulsion between the wall and the fluid particles.

This book belongs to Central Library BADJI Mokhtar-ANNABA UNIVERSITY Copyright Elsevier 2024

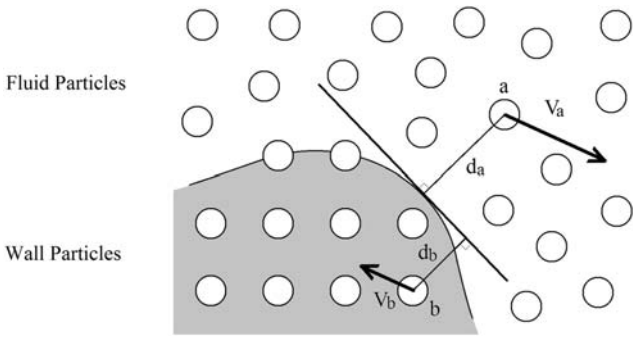

FIGURE 11.5 No-slip boundary condition implemented by fixed boundary particles with an artificial velocity.

where $\boldsymbol{V}_{ab}$ is the relative velocity between fluid particle "*a*" and the imagined fixed particle "*b*" located outside the wall boundary (Fig. 11.5). In Eq. (11.34), d_b is the distance of particle "*b*" normal to the tangent line at the wall curvature. β_{max} is a parameter set to 1.5 (Morris and Monaghan, 1997).

Imaginary particles. Rigid wall boundary conditions can also be handled by placing a set of a finite number of particles exactly on the wall boundaries (located at the same distance as the initial fluid particles) and some layers of fixed imaginary, or dummy, particles constructed outside the boundaries parallel to the walls (Violeau and Issa, 2007; Koshizuka et al., 1998; Shao and Gotoh, 2004). The wall and imaginary particles have zero velocity. Implementation of this idea is presented in Fig. 11.6.

11.7.2 Periodic Boundary Conditions

A periodic boundary condition is used to model a large physical domain by simulating only a part of it. A schematic of this technique is depicted in Fig. 11.7. The periodic boundary condition is implemented by forcing the particles near a boundary, an outlet for example, to interact with the ones near the opposite boundary, an inlet for example. To satisfy conservation of mass within the region of interest, the particles exiting the domain are forced to enter the opposite inflow boundary while keeping the same physical properties.

11.7.3 Inflow/Outflow Boundary Conditions

The cardiovascular system is characterized by complex geometries that require a specific treatment. For example, modeling the flow in a left ventricle requires the implementation of inflow and outflow boundary conditions in SPH. One can use a periodic boundary condition; however, in cardiovascular flow simulations, the inflow is usually imposed by having a uniform arrangement of the particles, whereas this is not necessary the case at the outlet. To overcome this, Shahriari et al. (2012b) introduced a simple and effective approach that consists of defining imaginary numerical injection and ejection boundaries with a length greater than the supporting size of the interpolating kernel (Fig. 11.8).

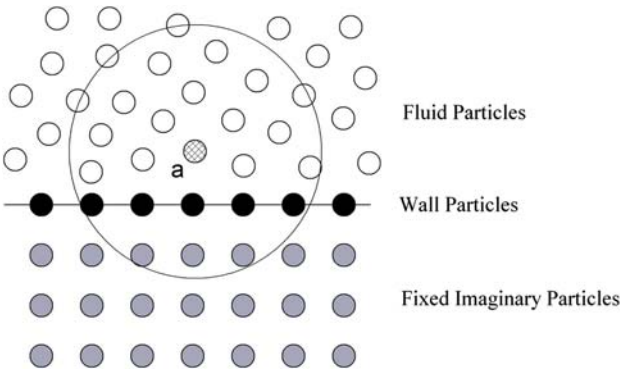

FIGURE 11.6 Wall particles and three layers of imaginary particles.

This book belongs to Central Library BADJI Mokhtar-ANNABA UNIVERSITY
Copyright Elsevier 2024

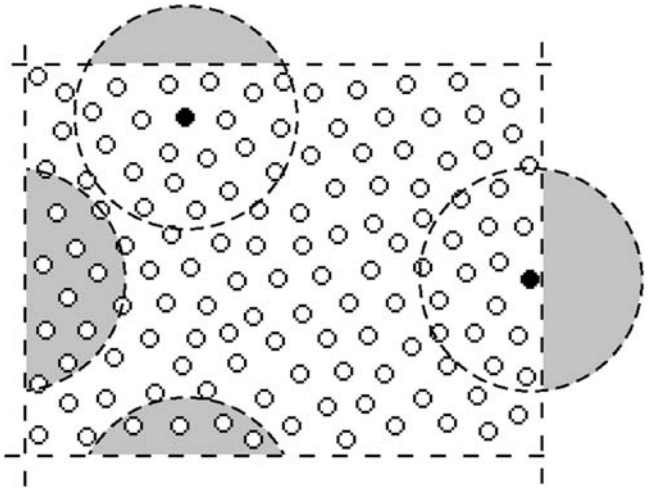

FIGURE 11.7 Periodic boundary condition implementation using smoothed particle hydrodynamics.

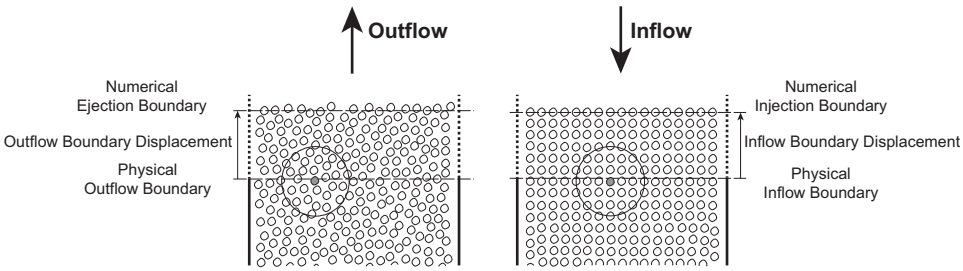

FIGURE 11.8 Implementation of inflow/outflow boundary conditions in smoothed particle hydrodynamics.

11.8 APPLICATIONS OF SMOOTHED PARTICLE HYDRODYNAMICS TO UNSTEADY CARDIOVASCULAR FLOWS

In the SPH literature, only a limited number of studies have simulated unsteady incompressible flows including dam breaking, shallow water, and wave flumes (Gomez-Gesteira et al., 2010). Studies also investigated the transient start-up of internal steady flows due to constant driving forces at low Reynolds numbers, typically compressible flows with $Re \leq 55$ (Takeda et al., 1994), incompressible flows with $Re \leq 1$ (Morris et al., 1997; Sigalotti et al., 2003), and viscoelastic flows with $Re \leq 2.5$ (Ellero et al., 2002). An SPH simulation of complex unsteady flows like those existing in the cardiovascular system is very limited and requires the introduction of specific validation as described in the following section.

11.8.1 Benchmark Case for Smoothed Particle Hydrodynamics Simulation of Unsteady Flows

Internal flow subject to an oscillating pressure gradient (Womersley type flow). Cardiovascular flows are characterized by their unsteady and pulsatile nature. A good simple benchmark for validating SPH codes will be an oscillating pressure gradient driving a flow between two plates. The axial oscillating pressure gradient can be expressed as

$$\frac{dP}{dx} = -A\,cos(\omega t) \tag{11.35}$$

This book belongs to Central Library BADJI Mokhtar-ANNABA UNIVERSITY
Copyright Elsevier 2024

where A is the amplitude of the imposed pressure gradient, ω is the oscillation frequency, and t is time. The analytical solution for the velocity field can be written as

$$u(y,t) = \frac{A}{\omega\rho\gamma}\{[sinh\ \varphi_1(y)\cdot sin\ \varphi_2(y) + sinh\ \varphi_2(y)\cdot sin\ \varphi_1(y)]cos(\omega t) + [\gamma - cosh\ \varphi_1(y)\cdot cos\ \varphi_2(y) - cosh\ \varphi_2(y)\cdot cos\ \varphi_1(y)]sin(\omega t)\} \tag{11.36}$$

where

$$\varphi_1(y) = \frac{W_o}{\sqrt{2}}\left(1+\frac{2y}{d}\right); \varphi_2(y) = \frac{W_o}{\sqrt{2}}\left(1-\frac{2y}{d}\right); \gamma = cosh\left(\sqrt{2}\,W_o\right) + cos\left(\sqrt{2}\,W_o\right) \text{ and } W_o = \frac{d}{2}\sqrt{\frac{\omega}{\upsilon}}.$$

where d is the distance between the two plates and W_o is called the Womersley number representing the ratio of oscillating inertial effects to viscous effects. Figs. 11.9 and 11.10 show the comparison between SPH simulations and the analytical solution for two different W_o numbers of 1 and 10.

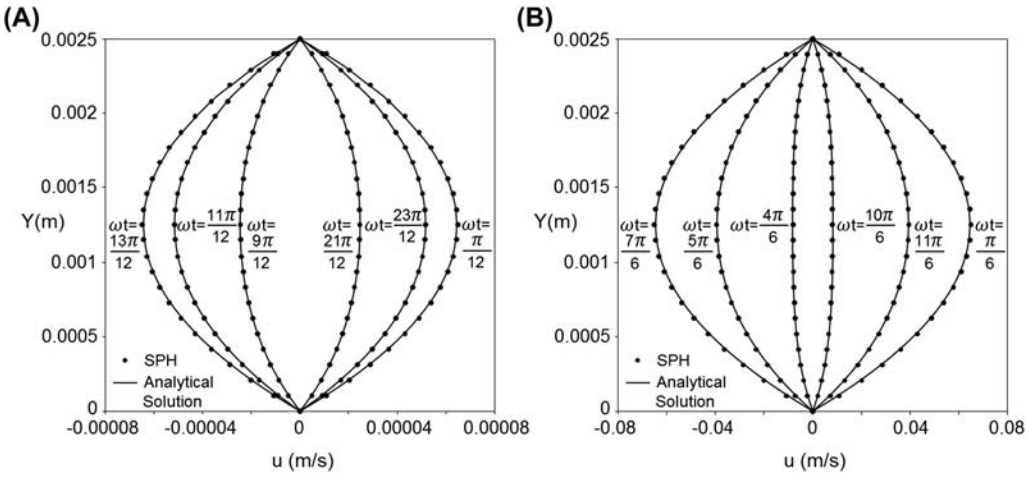

FIGURE 11.9 Comparison between analytical and smoothed particle hydrodynamics (SPH) simulations of an oscillating flow between two plates for $W_o = 1$ and (A) $A = 0.09$ N/m^3 and (B) $A = 90$ N/m^3 (Shahriari et al., 2013).

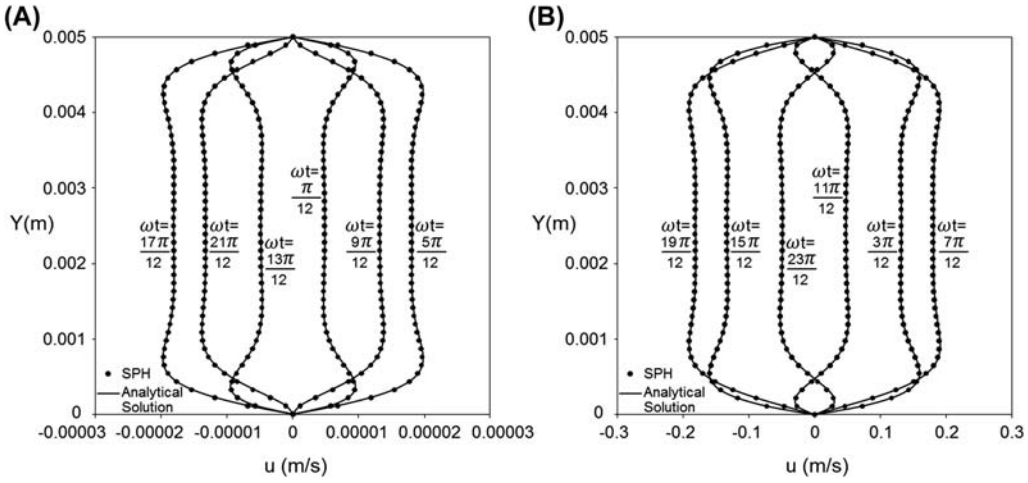

FIGURE 11.10 Comparison between analytical and smoothed particle hydrodynamics (SPH) simulations of an oscillating flow between two plates for $W_o = 10$ and (A) $A = 0.3$ N/m^3 and (B) $A = 3000$ N/m^3 (Shahriari et al., 2013).

This book belongs to Central Library BADJI Mokhtar-ANNABA UNIVERSITY Copyright Elsevier 2024

Flow above an oscillating plate (Stokes' second problem). Here a stationary fluid above a plate is moved by oscillating the plate at different frequencies. This case introduces a phase lag between the different layers of the fluid above the plate. For a plate oscillating at a velocity of $U_o(t) = U_{o,m}\ cos(\omega t)$, where $U_{o,m}$ is the amplitude of the oscillations and ω is the angular frequency, the analytical solution can be written as

$$u(y,t) \ = \ U_{o,m} exp(-\eta) cos(\omega t - \eta) \tag{11.37}$$

with $\eta \ = \ y\sqrt{\frac{\omega}{2v}}$.

Figs. 11.11 and 11.12 show the comparison between SPH simulations and the analytical solution for $\omega = \pi$ rad/s and $\omega = 10\pi$ rad/s. The results demonstrate that SPH was capable of capturing the oscillating boundary layer for this benchmark case.

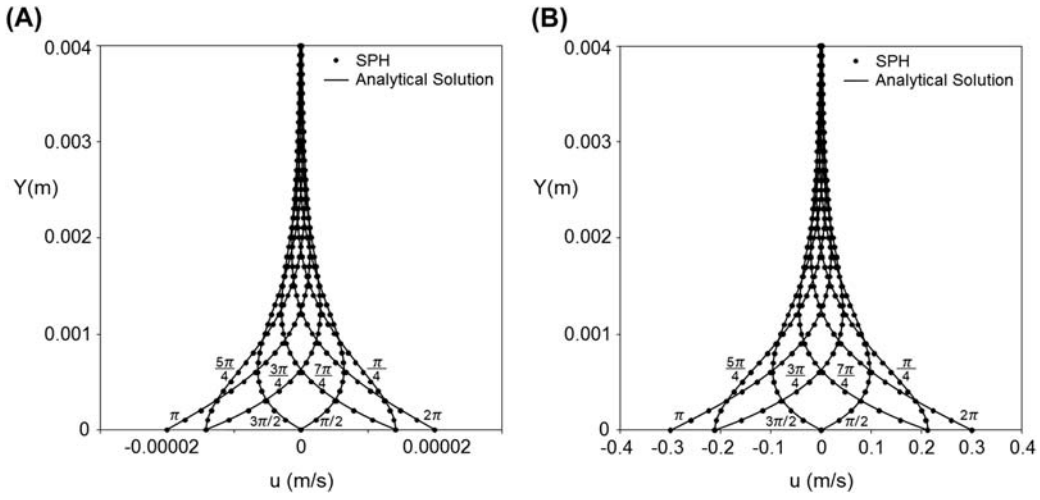

FIGURE 11.11 Comparison between analytical and smoothed particle hydrodynamics (SPH) simulations of flow above an oscillating plate for $\omega = \pi$ rad/s and (A) $U_{o,m} = 2\ 10^{-5}$ m/s and (B) $U_{o,m} = 0.3$ m/s (Shahriari et al., 2013).

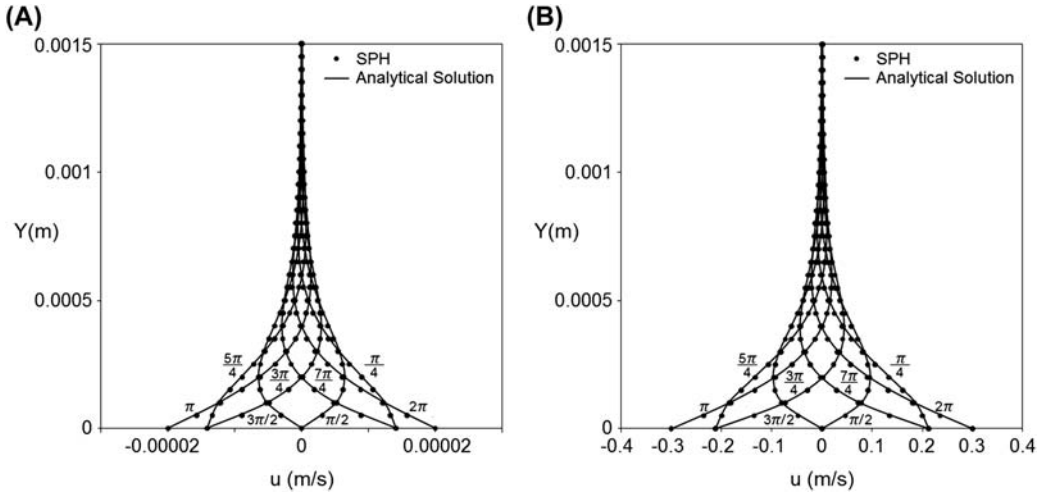

FIGURE 11.12 Comparison between analytical and smoothed particle hydrodynamics (SPH) simulations of flow above an oscillating plate for $\omega = 10$ rad/s and (A) $U_{o,m} = 2\ 10^{-5}$ m/s and (B) $U_{o,m} = 0.3$ m/s (Shahriari et al., 2013).

This book belongs to Central Library BADJI Mokhtar-ANNABA UNIVERSITY Copyright Elsevier 2024

11.9 DETERMINATION OF THE WALL SHEAR STRESS USING SMOOTHED PARTICLE HYDRODYNAMICS

Wall shear stress (WSS) is a key parameter in cardiovascular flows because of its direct relationship to the development of cardiovascular disease and atherosclerosis in general. The determination of the WSS using SPH is not straightforward because the kernel is truncated close to the wall, meaning particles close to the wall do not have enough neighbors (Fig. 11.13).

To account for this, Shahriari et al. (2013) introduced a formulation for the WSS as

$$\langle \tau_w \rangle_{a \in wall} = -\frac{\mu}{\rho_a} \sum_b m_b C_\xi (V_{t,b} - V_{t,a}) \frac{\partial W(r_a - r_b, h)}{\partial x_n} \tag{11.38}$$

where $\langle \tau_w \rangle$ represents the SPH approximation of the WSS, x_n is the local coordinate normal to the wall, V_t is the tangential local velocity with respect to the wall, and C_ξ is a correction factor compensating for the truncation of the kernel close to the wall. The correction factor C_ξ is calculated based on the area (or volume for 3D simulations) covered by the kernel function divided by the area of the continuum domain represented by the particles in a truncated kernel. The values of C_ξ for different kernel functions and smoothing lengths are displayed on Fig. 11.14. Comparisons between the SPH

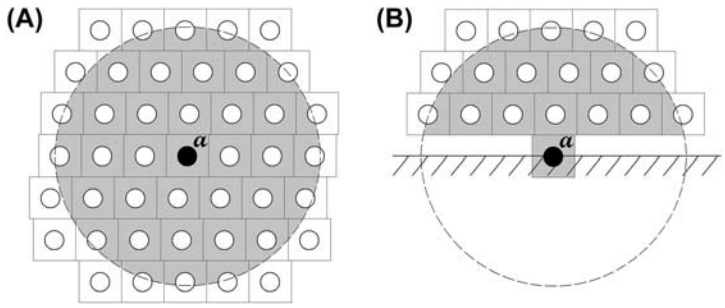

FIGURE 11.13 (A) A particle in the fluid domain with a nontruncated kernel; and (B) a particle on the wall with a truncated kernel (Shahriari et al., 2013).

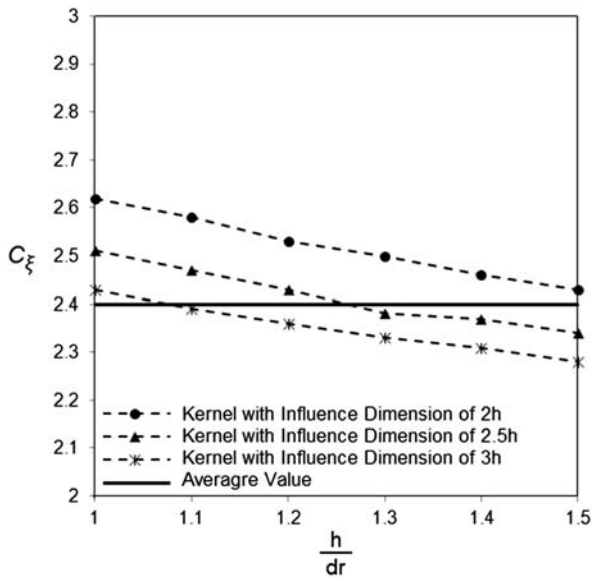

FIGURE 11.14 Values for the correction coefficient C_ξ as a function of different kernel functions and smoothing lengths (Shahriari et al., 2013).

This book belongs to Central Library BADJI Mokhtar-ANNABA UNIVERSITY
Copyright Elsevier 2024

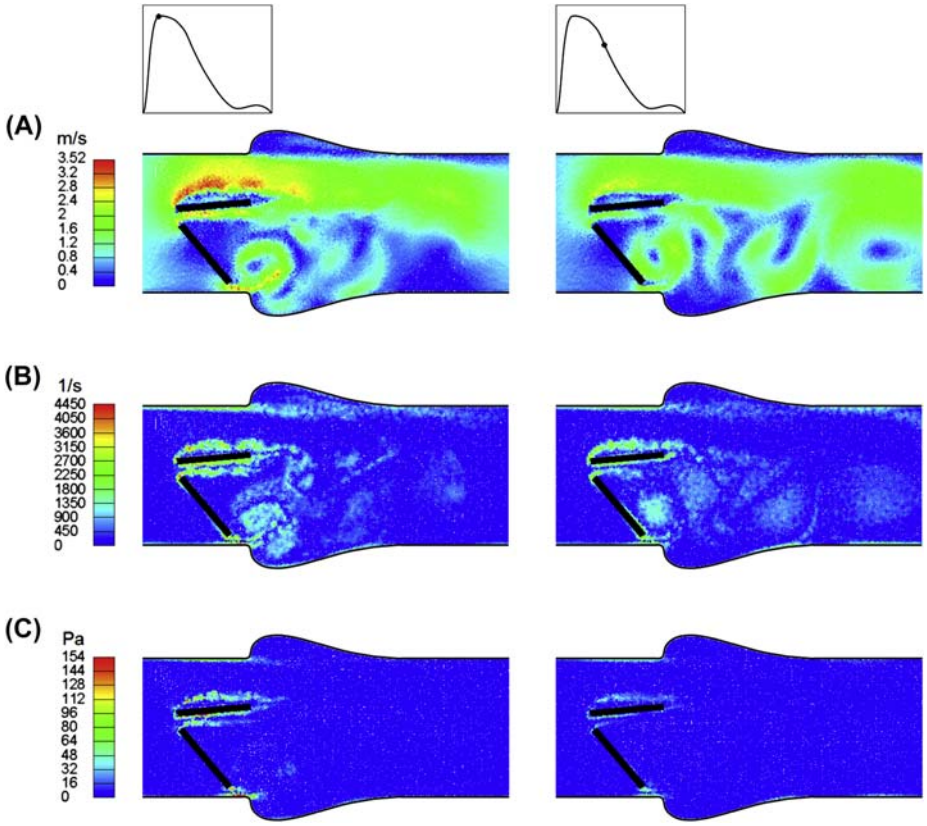

FIGURE 11.15 Two-dimensional (A) velocity magnitude, (B) vorticity, and (C) turbulent shear stresses at the peak of the systolic phase corresponding to the flow through a normal (left) and dysfunctional (right) bileaflet mechanical heart valve (Shahriari et al., 2012a).

approximation of the WSS and the analytical prediction for Womersley flows and Stokes' second problem can be found in Shahriari et al. (2013).

11.10 SHEAR LOADING HISTORY DOWNSTREAM OF A BILEAFET MECHANICAL HEART VALVE EVALUATED USING SMOOTHED PARTICLE HYDRODYNAMICS

Aortic valve replacement has been shown to be a viable solution in patients with severe symptomatic aortic stenosis. The stenotic aortic valve is most often replaced by a prosthetic valve: biological or mechanical. Bileaflet mechanical heart valves (BMHVs) are known to surpass biological valves in terms of durability. However, they are associated with postsurgical complications, such as thrombus formation, that can lead to a dysfunctional BMHV dysfunction. Thrombus formation is directly related to shear loading accumulation and damage of blood components (mainly platelets). SPH's fully Lagrangian nature makes it a very promising tool for a direct and more accurate evaluation of shear stress accumulation on blood components downstream of BMHVs or induced by implanted medical devices. Fig. 11.15 shows the 2D velocity magnitude, vorticity, and turbulent shear stresses at the peak of the systolic phase corresponding to the flow through a normal and dysfunctional BMHV (Shahriari et al., 2012a).

Fig. 11.16 displays the corresponding accumulative shear stress and the statistical distribution of accumulative shear stress loading for a normally functioning BMHV and valves with different severities of dysfunctions.

11.11 CONCLUSION AND FUTURE DEVELOPMENTS

The purely Lagrangian nature of the SPH method makes it an ideal candidate for simulating cardiovascular flows. Furthermore, the ability to run SPH codes on GPUs allows for targeting more complex 3D simulations under normal and pathological conditions. However, several future developments are still required for SPH to compete with established mesh-based methods. The most important one will likely be a thorough quantitative validation of SPH results against

This book belongs to Central Library BADJI Mokhtar-ANNABA UNIVERSITY Copyright Elsevier 2024

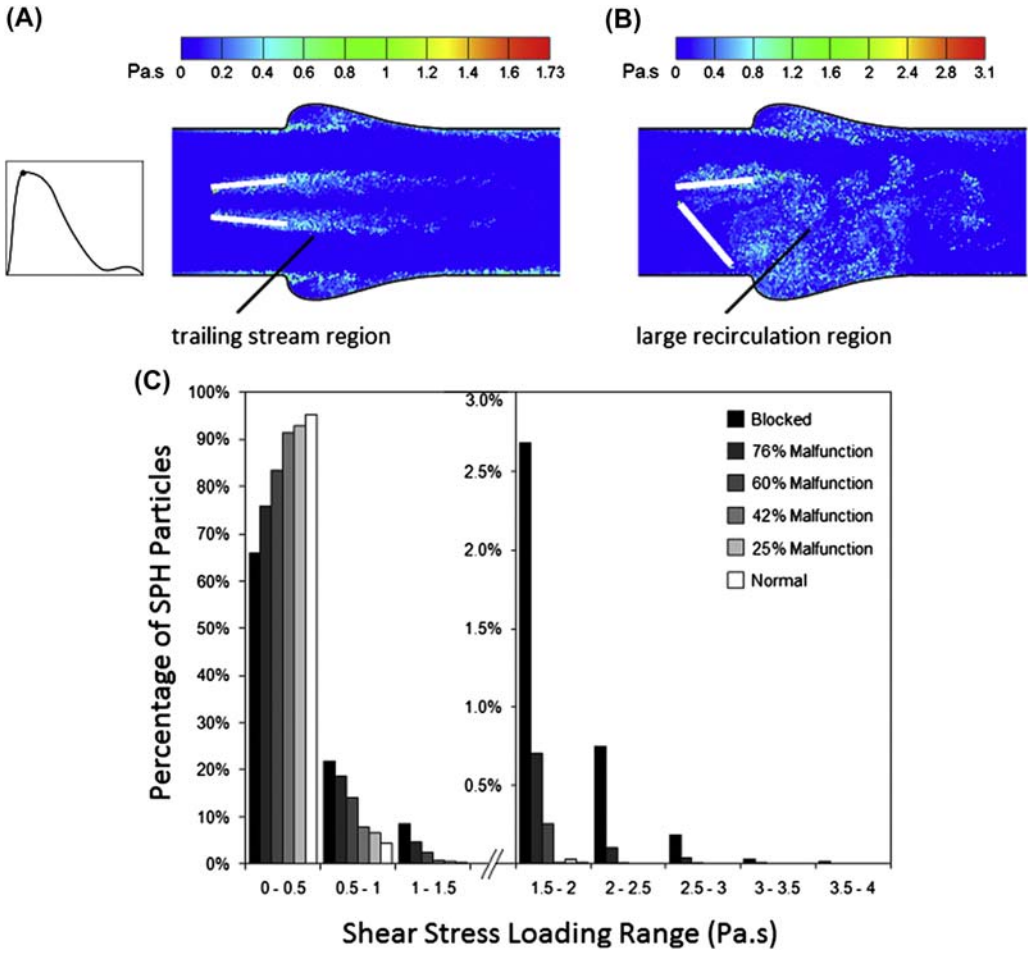

FIGURE 11.16 Two-dimensional accumulation of viscous shear stress through (A) a normal bileaflet mechanical heart valve (BMHV) and (B) a dysfunctional BMHV. (C) Statistical distribution of particle accumulative shear stress loading until 0.3 s of the cardiac cycle for different severities of BMHV dysfunctions (Shahriari et al., 2012a). *SPH*, smoothed particle hydrodynamics.

experimental measurements. This is of primary importance because SPH is still considered "a promising but immature method" (Violeau and Rogers, 2016). Other developments include the use of SPH for the validation of new Doppler ultrasound algorithms such as high-speed echo-particle image velocimetry. Finally, the potential of SPH in terms of extracting Lagrangian structures and finite-time Lyapunov fields has to be further investigated.

REFERENCES

Balsara, D.S., 1995. Von Neumann stability analysis of smoothed particle hydrodynamics-suggestions for optimal algorithms. Journal of Computational Physics 121, 357–372.

Benz, W., Asphaug, E., 1995. Simulations of brittle solids using smoothed particle hydrodynamics. Computer Physics Communications 87, 253–265.

Bonet, J., Kulasegaram, S., 2000. Correction and stabilization of smooth particle hydrodynamics methods with applications in metal forming simulations. International Journal for Numerical Methods in Engineering 47, 1189–1214.

Cleary, P.W., Ha, J., Alguine, V., Nguyen, T., 2002. Flow modeling in casting processes. Applied Mathematical Modelling 26, 171–190.

Cleary, P.W., 1998. Modelling confined multi-material heat and mass flows using SPH. Applied Mathematical Modelling 22, 981–993.

Colagrossi, A., Landrini, M., 2003. Numerical simulation of interfacial flume by smoothed particle hydrodynamics. Journal of Computational Physics 191, 448–475.

Cummins, S.J., Rudman, M., 1999. An SPH projection method. Journal of Computational Physics 152, 584–607.

Dominguez, J.M., Crespo, A.J.C., Gómez-Gesteira, M., Marongiu, J.C., 2010. Neighbour lists in smoothed particle hydrodynamics. International Journal for Numerical Methods in Fluids. http://dx.doi.org/10.1002/fld.2481.

Ellero, M., Kroger, M., Hess, S., 2002. Viscoelastic flows studied by smoothed particle hydrodynamics. Journal of Non-Newtonian Fluid Mechanics 105, 35–51.

This book belongs to Central Library BADJI Mokhtar-ANNABA UNIVERSITY Copyright Elsevier 2024

Farahani, M.H., Amanifard, N., Pouryoussefi, G., 2008. Numerical simulation of a pulsatory flow moving through flexible walls using smoothed particle hydrodynamics. In: Proceedings of the World Congress on Engineering, vol. 2.

Gingold, R.A., Monaghan, J.J., 1977. Smoothed particle hydrodynamics: theory and application to non-spherical stars. Monthly Notices of the Royal Astronomical Society 181 (3), 375–389.

Gomez-Gesteira, M., Rogers, B.D., Violeau, D., Grassa, J.M., Crespo, A.J.C., 2010. Foreword: SPH for free-surface flows. Journal of Hydraulic Research 48 (Extra Issue), 3–5.

Gray, J.P., Monaghan, J.J., Swift, R.P., 2001. SPH elastic dynamics. Computer Methods in Applied Mechanics and Engineering 190, 6641–6662.

Hu, X.Y., Adams, N.A., 2006. A multi-phase SPH method for macroscopic and mesoscopic flows. Journal of Computational Physics 213, 844–861.

Koshizuka, S., Nobe, A., Oka, Y., 1998. Numerical analysis of breaking waves using the moving particle semi-implicit method. International Journal for Numerical Methods in Fluids 26, 751–769.

Libersky, L., Petschek, A.G., 1991. Smooth particle hydrodynamics with strength of materials. Advances in the free Lagrange method. Lecture Notes in Physics 395, 248–257.

Liu, G.R., Liu, M.B., 2003. Smoothed Particle Hydrodynamics: a Meshfree Particle Method. World Scientific Publishing Co. Pte. Ltd., New Jersey, USA.

Monaghan, J.J., Gingold, R.A., 1983. Shock simulation by the particle method SPH. Journal of Computational Physics 52 (2), 374–389.

Monaghan, J.J., Kocharyan, A., 1995. SPH simulation of multi-phase flow. Computer Physics Communications 87, 225–235.

Monaghan, J.J., Kos, A., 1999. Solitary waves on a Cretan beach. Journal of Waterway, Port, Coastal, and Ocean Engineering 125 (3), 145–155.

Monaghan, J.J., Cas, R.F., Kos, A., Hallworth, M., 1999. Gravity currents descending a ramp in a stratified tank. Journal of Fluid Mechanics 379, 39–69.

Monaghan, J.J., 1992. Smoothed particle hydrodynamics. Annual Review of Astronomy and Astrophysics 30 (1), 543–574.

Monaghan, J.J., 1994. Simulating free surface flows with SPH. Journal of Computational Physics 110 (2), 399–406.

Monaghan, J.J., 2006. Smoothed particle hydrodynamic simulations of shear flow. Monthly Notices of the Royal Astronomical Society 365, 199–213.

Monaghan, J.J., 2015. A Brief History of SPH in Hydraulics. https://www.iahr.org/uploadedfiles/userfiles/files/brief%20history(1).pdf.

Morris, J.P., Monaghan, J.J., 1997. A switch to reduce SPH viscosity. Journal of Computational Physics 136, 41–50.

Morris, J.P., Fox, P.J., Zhu, Y., 1997. Modeling low Reynolds number incompressible flows using SPH. Journal of Computational Physics 136, 214–226.

Müller, M., Schirm, S., Teschner, M., 2004. Interactive blood simulation for virtual surgery based on smoothed particle hydrodynamics. Technology and Health Care 12 (1), 25–31.

Nakajima, M., Stevenson, D.J., 2014. Investigation of the initial state of the moon-forming disk: bridging SPH simulations and hydrostatic models. Icarus 233, 259–267.

Qin, J., Pang, W.M., Nguyen, B.P., Ni, D., Chui, C.K., August 2010. Particle-based simulation of blood flow and vessel wall interactions in virtual surgery. In: Proceedings of the 2010 Symposium on Information and Communication Technology. ACM, pp. 128–133.

Randles, P.W., Libersky, L., 1996. Smoothed particle hydrodynamics some recent improvements and applications. Computer Methods in Applied Mechanics and Engineering 139, 375–408.

Richie, B.W., Thomas, P.A., 2001. Multiphase smoothed-particle hydrodynamics. Monthly Notices of the Royal Astronomical Society 323, 743–756.

Shahriari, S., Maleki, H., Hassan, I., Kadem, L., 2012a. Evaluation of shear stress accumulation on blood components in normal and dysfunctional bileaflet mechanical heart valves using smoothed particle hydrodynamics. Journal of Biomechanics 45 (15), 2637–2644.

Shahriari, S., Kadem, L., Rogers, B.D., Hassan, I., 2012b. Smoothed particle hydrodynamics method applied to pulsatile flow inside a rigid two-dimensional model of left heart cavity. International Journal for Numerical Methods in Biomedical Engineering 28 (11), 1121–1143.

Shahriari, S., Hassan, I.G., Kadem, L., 2013. Modeling unsteady flow characteristics using smoothed particle hydrodynamics. Applied Mathematical Modelling 37 (3), 1431–1450.

Shao, S., Gotoh, H., 2004. Simulating coupled motion of progressive wave and floating curtain wall by SPH-LES model. Coastal Engineering Journal 46, 171–202.

Sigalotti, L.D.G., Klapp, J., Sira, E., Melean, Y., Hasmy, A., 2003. SPH simulations of time-dependent Poiseuille flow at low Reynolds numbers. Journal of Computational Physics 191, 622–638.

Sinnott, M., Cleary, P.W., Prakash, M., December 2006. An investigation of pulsatile blood flow in a bifurcation artery using a grid-free method. In: Proc. Fifth International Conference on CFD in the Process Industries.

Takeda, H., Miyama, S.M., Sekiya, M., 1994. Numerical simulation of viscous flow by smoothed particle hydrodynamics. Progress of Theoretical Physics 92, 939–960.

Tanaka, N., Takano, T., 2005. Microscopic-scale simulation of blood flow using SPH method. International Journal of Computational Methods 2 (04), 555–568.

Vignjevic, R., Campbell, J., 2009. Review of development of the smooth particle hydrodynamics (SPH) method. In: Predictive Modeling of Dynamic Processes. Springer, US, pp. 367–396.

Vila, J.P., 1999. On particle weighted methods and smooth particle hydrodynamics. Mathematical Models and Methods in Applied Sciences 9 (2), 161–209.

Violeau, D., Issa, R., 2007. Numerical modeling of complex turbulent free-surface flows with the SPH method: an overview. International Journal for Numerical Methods in Fluids 53, 277–304.

Violeau, D., Rogers, B.D., 2016. Smoothed particle hydrodynamics (SPH) for free-surface flows: past, present and future. Journal of Hydraulic Research 54 (1), 1–26.

Wingate, C.A., Stellingwerf, R., 1994. SPHINX Users Manual, LAUR 932476. Los Alamos National Lab., Los Alamos, NM, p. 87545.

Zhu, Y., Fox, P.J., Morris, J.P., 1999. A pore-scale numerical model for flow through porous media. International Journal for Numerical and Analytical Methods in Geomechanics 23, 881–904.

This book belongs to Central Library BADJI Mokhtar-ANNABA UNIVERSITY Copyright Elsevier 2024

This page intentionally left blank

This book belongs to Central Library BADJI Mokhtar-ANNABA UNIVERSITY

Copyright Elsevier 2024

Part IV

Agent-Based Methods

This book belongs to Central Library BADJI Mokhtar-ANNABA UNIVERSITY

Copyright Elsevier 2024

This page intentionally left blank

This book belongs to Central Library BADJI Mokhtar-ANNABA UNIVERSITY

Copyright Elsevier 2024

Chapter 12

Agent-Based Lattice Models of Multicellular Systems: Numerical Methods, Implementation, and Applications

D. Drasdo[1], A. Buttenschön[2] and P. Van Liedekerke[1]
[1]INRIA Paris & Sorbonne Universités UPMC Univ Paris 6, Paris, France; [2]University of Alberta, Edmonton, AB, Canada

12.1 INTRODUCTION

Over the past decades, biomedical sciences have created plenty of challenges and endowed several new subjects for the biomechanics and mechanobiology modeling community. Modeling biological phenomena is a nontrivial task due to their complexity and the various scales involved. Agent-based models (ABMs)—also called individual-based models (IBMs)—for cellular systems are a class of computer models that aim to simulate multicellular dynamics, identifying the behavior of every individual cell and capturing natural spatial in homogeneities and variability between cells. In recent years, numerous ABMs have been developed to mimic multicellular organization processes. More recently, ABMs are used to understand the interplay of single-cell and multicellular mechanics. The nature of ABM is well suited to include the variability observed in biological cells as each cell can be represented as an individual unit. This variability can be established on the level of physical and biomechanical properties (such as Young's Modulus, cell size) as well as on the level of genes, gene expression, RNA or protein concentrations, that impact on biochemical reactions of intracellular molecular pathways.

Our focus here is on spatial−temporal models. "Space-free" ABMs have been considered and are reported elsewhere (Roeder and Loeffler, 2002). Spatial ABMs can roughly been distinguished by those operating on space-fixed lattices (e.g., Deutsch and Dormann, 2004; Alber et al., 2003; Van Liedekerke et al., 2015 and refs. therein) and those operating without a lattice ("lattice free," "off lattice"; e.g., Drasdo et al., 2007; Van Liedekerke et al., 2015 and refs. therein). Among lattice models, a first subcategory are the cellular automata (CA) with either one lattice site that may be occupied by many cells (e.g., Radszuweit et al., 2009; Dormann and Deutsch, 2002; Deutsch and Dormann, 2004), allowing modeling of large cell population sizes, or one lattice site occupied by at most one cell (e.g., Kansal et al., 2000a; Alarcón et al., 2003; Drasdo, 2005; Jagiella et al., 2016). A second subcategory are cellular Potts models (CPMs), where many lattice sites may be occupied by one biological cell allowing to model arbitrary cell shapes (e.g., Graner and Glazier, 1992; Savill and Hogeweg, 1996; Marée and Hogeweg, 2001; Merks and Glazier, 2005; Alber et al., 2007; Lushnikov et al., 2008; Scianna and Preziosi 2012). Among lattice-free models that will be discussed in the next chapter, one can roughly distinguish between center-based models (CBMs) and deformable cell models (DCMs). In the CBMs, the interaction of cells is described by pairwise forces or energy functions defined between cell centers, while cell shape is not resolved precisely. Deformable cell models describe forces at a subcellular detail and permit a representation of complex cell shapes.

The choice of a particular ABM with regard to the envisaged problem depends on the observations in the experiment and the features that the model type is able to address. Simulations of some experiments may require a detailed cell shape, whereas in others only the cell numbers or a statistical representation of shape counts. Biological processes are inherently

Numerical Methods and Advanced Simulation in Biomechanics and Biological Processes. https://doi.org/10.1016/B978-0-12-811718-7.00012-5
Copyright © 2018 Elsevier Ltd. All rights reserved.

This book belongs to Central Library BADJI Mokhtar-ANNABA UNIVERSITY
Copyright Elsevier 2024

stochastic, and ABMs can cope well with this stochasticity. For example, cell division, death, and migration usually have probabilistic components. On molecular scales, well-established stochastic frameworks exist based on principles of statistical physics. Such a well-established framework does not exist for ABMs, but still a number of the principles developed for the description of processes at the molecular scale can be applied—sometimes based on formal or conceptual analogies—in ABM dynamics.

Finally, we note that next to the capability of representing a biological system, the model choice may also be influenced by the available software and computational feasibility.

This chapter focuses on lattice-based models only, whereas lattice-free (or off-lattice) models will be explained in Chapter 14. The chapter is organized as follows. In Section 12.2 we classify the different lattice models by their spatial resolution and some characteristics. Then we explain the different types in more detail.

12.2 LATTICE-BASED MODELS: TYPES AND RESOLUTION

Lattice-based models have in common that space is subdivided into space-fixed discrete compartments, and movement of cells is possible only in discrete steps by shifts of the cell position from one to another space compartment. In d dimensional space, the compartments are d dimensional, most times convex, and objects are separated by $d-1$ dimensional manifolds. In $d=2$ the compartments are areas bounded by lines. The intersecting lines form a $2d$ lattice. Common lattices based on the bounds of space compartments are the square lattice, the hexagonal lattice, or the Voronoi tessellation that, as a generalization of the former two regular lattice types, square and hexagonal lattices, can be irregular. This will be described below in detail.

Lattice-based models of multicellular systems are distinguished by whether they record only the cell positions or both cell positions and cell speed (e.g., Van Liedekerke et al., 2015). In the literature, they are often referred to as "cellular automaton models." Models where only the positions are recorded may further be subdivided into three classes depending on their spatial resolution.

The same lattice site (or lattice compartment; see below for a more precise description) may either be occupied by many ($N>1$) cells (Type A), or by exactly one cell (Type B), or several lattice sites (or lattice compartments) may simultaneously be associated with the same cell (Type C).

A further model type recording besides the spatial position also the speed is called lattice gas cellular automaton (LGCA) model and here defined as Type D. Different from Types A, B, and C, the Type D models explicitly record cell speed.

For didactic reasons, we first discuss model Type B, then model Types A, C, and D in subsequent subsections.

12.3 CELLULAR AUTOMATON WITH ONE CELL PER LATTICE SITE (TYPE B)

To model a multicellular tissue organization process on the lattice, the type of lattice has to be chosen and the processes to be considered have to be defined. Typical processes that are taken into account are growth, division, movement, and death of cells (Fig. 12.1). Below it is explained how these processes may be realized within a Type B lattice model.

12.3.1 Choice of the Lattice

In the CA Type B approach, cells can neither be compressed nor deformed. On regular lattices such as the square or (in two dimensions) a hexagonal lattice, each lattice compartment has the same size, hence cell size is constant. On a regular lattice, only rigid body movements in a few discrete directions are possible, which are a priori the same at each lattice site. On an irregular, unstructured lattice, cell size of a moving cell is only conserved on average, and the local direction of movement is in general different from lattice site to lattice site. An unstructured lattice can be constructed in such a way that the size distribution of the space compartment can be controlled (see Box 12.1 and Fig. 12.2 for an example in two dimensions). These construction rules can be easily generalized to $d>2$ dimensions. A square and a hexagonal lattice emerge as special cases of unstructured lattices.

The algorithm in Box 12.1 has been proposed by Drasdo (2005), Block et al. (2007), and Radszuweit et al. (2009) based on a lattice size l of the construction square lattice to ensure that cell sizes only slightly vary around l^d (d being the spatial dimension). A Voronoi tessellation has been published in Kansal et al. (2000b) for brain tumor simulations, where the compartment sizes were largely varied depending on the distance of the space point from the tumor center. Such an approach has to be taken with caution as space homogeneity is violated.

It is also noteworthy that the number of cell neighbors found in a Voronoi tessellation corresponds to the value found in epithelial tissues (Honda, 1978, 1983).

This book belongs to Central Library BADJI Mokhtar-ANNABA UNIVERSITY
Copyright Elsevier 2024

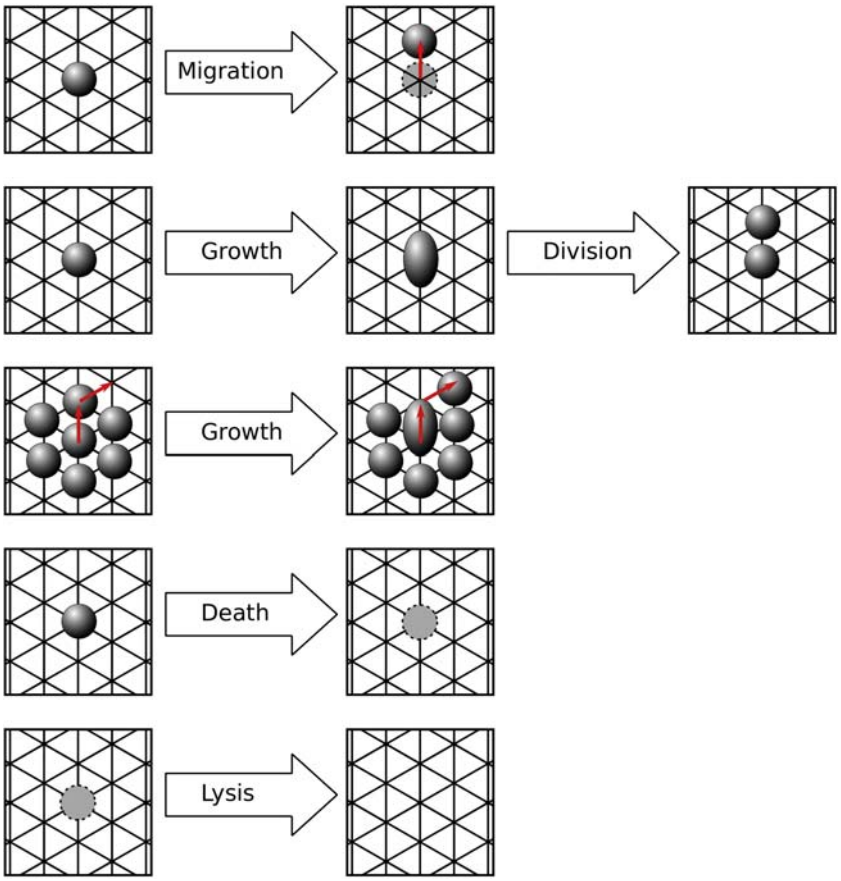

FIGURE 12.1 Typical rules for lattice models of Type B on a hexagonal lattice (Jagiella et al., 2016). Migration is realized on a lattice by a hopping process; growth is often merged with division, but here separated. Growth can also occur to cells inside a cluster by pushing surrounding cells away. The body of a cell after its death is usually removed by phagocytosis, but this may take some time, which is why cell death and lysis of the body may be distinguished as separated processes.

BOX 12.1 Construction Rules of the Irregular Lattice

An unstructured lattice can be generated as follows (Block et al., 2007; Van Liedekerke et al., 2015) (compare Fig. 12.2):

1. First a square lattice is generated with one point in each square. These points are named construction points. (Note: if this point is precisely in the center of the square then the emerging lattice is again a perfect square lattice.)
2. Use the Voronoi rule to construct a Voronoi diagram: assign each point in space to its closest construction point. Points with equal distance to two construction points form a border between those Voronoi cells that are associated with the two construction points. These borders between neighboring point sets define the Voronoi diagram (or Voronoi tessellation).
3. Link nearest neighbor construction points by lines. (Note: A Voronoi border forms the perpendicular bisection the lines connecting the two construction points that are separated by this Voronoi border.) The lines define the dual graph of the Voronoi tessellation, named Delaunay triangulation.

12.3.2 Lattice-Based Growth Models

Eden (1961) suggested a model to a vascular tumor growth on a square lattice where each lattice point can at most be occupied by one individual cell. This assumption takes into account the excluded volume effect: each cell occupies a particular volume in space. The choice of the spatial compartment being equal to the average size of a biological cell is natural and since then often taken (e.g., Düchting and Vogelsaenger, 1985; Anderson et al., 2006; Lee et al., 2006; Radszuweit et al., 2009; Enderling and Hahnfeldt, 2011; Alfonso et al., 2014). Different versions of the Eden model have

This book belongs to Central Library BADJI Mokhtar-ANNABA UNIVERSITY Copyright Elsevier 2024

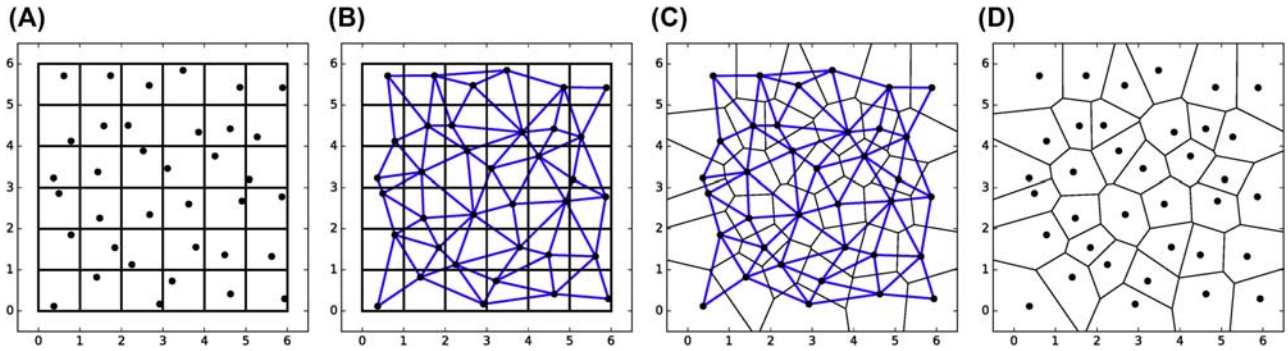

FIGURE 12.2 Construction of an unstructured lattice (Block et al., 2007; Van Liedekerke et al., 2015). From left to right: (A) a square lattice with a single construction point (*solid black*), whose coordinates are chosen from a uniform distribution; (B) the nearest neighbors are connected generating a Delaunay triangulation [blue (light gray in print versions)]; (C) the Voronoi tessellation is calculated from the Delaunay triangulation (the average number of neighbors in a Delaunay triangulation in an infinite two-dimensional plane is proven to be 6); (D) the final Voronoi tessellation with the center points used for construction. The Delaunay triangulation becomes a regular square lattice if the construction points are placed precisely into the center of each square in step (A). A hexagonal lattice is shown in Fig. 12.1. Here each lattice site has exactly six nearest neighbor sites.

been suggested. They are distinguished by the way cell divisions are performed (see e.g., Krug and Spohn, 1991 and refs. therein, Drasdo and Hohme, 2003 and refs. therein). In each of these versions, in the published literature referred to as version A, B, C of the Eden model (not to be confused with the enumeration of Types A−D of lattice models used in this chapter), cell division can only take place onto an unoccupied lattice site adjacent to an occupied lattice site. Usually only lattice sites in the horizontal or vertical direction are considered as adjacent, whereas lattices sites situated diagonally are not considered. However, diagonal directions may be taken into account.

- In version A of the Eden model, a free site in the neighborhood of all occupied lattice sites is randomly chosen with equal probability of being occupied.
- In Eden's original model (named as version B), all possible paths from occupied to adjacent-free lattice sites are determined, i.e., each occupied site is linked with each of its adjacent-free sites. Then one of the distinct paths is chosen at random with equal probability.
- In version C, first an occupied lattice site with at least one free neighbor site is randomly chosen and then one of its free neighbor sites is randomly occupied, both random variables being selected according to a uniform distribution.

A number of modifications and generalizations of the Eden model have been proposed. In the William and Bjerkness (1972) model for tumor growth a pair of neighbor sites, one being occupied and one being free, has a probability of α to become both occupied and of β to become both unoccupied in the next instant of time. For $\alpha/\beta > 1$ an existing cluster grows. From computer simulations, Williams and Bjerkness originally believed that their simulations showed a fractal surface structure, but this interpretation has been disproved analytically by Mollison (1972). The surface structure was self-affine, hence not fractal, which means smooth on large spatial scales. In the Richardson model (Richardson, 1973) each free site adjacent to an occupied site becomes occupied with probability P (independent for each free site). For $P = 1$ the growth process is completely deterministic (in that each free lattice site is occupied with probability 1), for $P \to 0$ combined with an appropriate rescaling of time the Eden model is recovered. Large Eden clusters contain growth sites only in a thin surface layer that occupies a negligible fraction of the cluster volume in the limit $N \to \infty$. This implies that the clusters attain a compact shape as they become larger (e.g., Richardson, 1973; Krug and Spohn, 1991).

Batchelor and Henry (1991) have looked at the cluster symmetry in the Eden model and a noise-reduced variant. This corresponds to the F-family models by Richardson (1973). They assigned a counter M to each cell and increased it by one each time the cell was selected. After having selected a cell m times, it was divided according to the rules of the standard Eden model.

Another version of the model, conceptually similar to the version by Richardson with $P = 1$, is that each surface cell attempts to divide with probability one at the same moment in time. However, if two surface cells share the same free neighbor lattice site as their only free neighbor lattice site, only one of the two surface cells is able to divide. The cell that divides is usually chosen at random with uniform probability. However, from a biological point of view this can hardly be justified because once a cell enters the cell cycle, which is the case once the cell passed the restriction point, it is committed to divide.

There are later cell cycle check points though, but there is no indication that a cell would not divide as another cell just occupies the free space next to it before.

This book belongs to Central Library BADJI Mokhtar-ANNABA UNIVERSITY Copyright Elsevier 2024

12.3.3 Definition of Time

Each of these models contains stochastic elements hence define a stochastic growth process. The definition of the variable "time" in these processes is sometimes not obvious and has also partially been erroneous. A reasonable reference time scale is the duration of the cell cycle. If the cell cycle duration were strictly regulated and the cell cycle length exactly the same for each cell, the time should be advanced by one cell cycle time duration after each cell in the system that is capable of division has divided i.e., $t \rightarrow t + \Delta t$ with $\Delta t = \tau$ (τ being the cell cycle time). However, notice that this can generate conflicts as only one cell is able to divide in case two or more cells compete for the same empty lattice site. Moreover, in reality the cell cycle duration is not precisely the same for all cells but is peaked, resembling an Erlang distribution (Gomes et al., 2011).

In the different versions A, B, C of the Eden model, either a free lattice site next to an occupied lattice site or an occupied lattice site next to a free lattice site is chosen randomly for division. Defining time here has to be done with caution. In Bunde and Havlin (2012) after each cell division the time is either advanced by $\Delta t/P$, P being the number of surface lattice sites (called growth sites) prior to division, or by a constant Δt after each division. In the latter case, $t \sim N$, so the variable time has no relation to true "physical" time. However, with the first definition of time $\Delta t/P$, small differences in the population size $N(t)$ between the different versions of the Eden models occur reflecting the small differences in their update rules. Other time definitions have been proposed in Drasdo (2005) and Block et al. (2007). One time definition was to choose an individual waiting time from a waiting time distribution for each cell right after division and note the event times in a sorted list that is executed event by event. If right at the event of a cell division, the division was inhibited because no free neighbor lattice site was available (anymore) and the cell was removed from the list. The cycle time distribution that corresponds closest to the versions of the Eden model is the waiting time distribution generated by a Poisson process between two successive division events:

$$f(\tau) = \lambda e^{-\lambda\tau}. \tag{12.1}$$

However, as the cell cycle time distribution found experimentally is peaked resembling an Erlang distribution, not an exponential, it does not correspond to the assumption that the cell cycle time duration should be distributed as the time span between two successive events in a Poisson process. A peaked waiting time distribution can be generated by introducing $m - 1$ intermediate states, whereby the transition from $m' \rightarrow m' + 1,\ m' \leq m,\ m = 1, 2, \ldots$ follows a Poisson process. The emerging cell cycle distribution is an Erlang distribution:

$$f(\tau) = \frac{\lambda_m (\lambda_m \tau)^{m-1}}{(m-1)!}\, e^{-\lambda_m \tau}, \tag{12.2}$$

where $\lambda_m = m/\tau_e$ is the transition rate between subsequent states, τ the cell cycle time, and m the total number of states. This yields $\langle\tau\rangle = \tau_e$, τ_e the expected cycle time duration. Note that for $m = 1$ (no intermediate state) the original exponentially distributed waiting time emerges again.

The Erlang distribution mimics well the experimentally observed cell cycle distribution (Jagiella, 2012).

The algorithm choosing the cell cycle time for each cell individually describes a process that can be represented as a master equation. The advantage of formulating the master equation and then solving it numerically is that this gives a well-defined framework, which can easily be extended to include growth, division, movement of cells by "hopping" or cell death, or other processes. The master equation for the change of the multivariate probability to find the multicellular systems in a certain system state Z with time t reads:

$$\frac{\partial p(Z,t)}{\partial t} = \sum_{Z'} W(Z' \rightarrow Z) p(Z',t) - W(Z \rightarrow Z') p(Z,t). \tag{12.3}$$

Here the first term denotes all transition from neighbor states Z' into the "current" state Z and the second term denotes all transitions from the current state Z into any accessible neighbor state Z'. Standard ways of solving the master equation are either by a fixed time-step algorithm choosing the time step Δt so small that only a single event is likely to occur within $[t \ldots, t + \Delta t]$ (Box 12.2), or by the Gillespie algorithm (often also called kinetic Monte Carlo) (Bortz et al., 1975; Gillespie, 1977).

The advantage of choosing a fixed time step is that the scheme can easily be matched to numerical schemes solving, e.g., partial differential equations with a fixed time step. This is useful, for instance, when growth processes are coupled to molecular processes, which typically require the simultaneous solving of reaction diffusion equations (Jagiella et al., 2016).

This book belongs to Central Library BADJI Mokhtar-ANNABA UNIVERSITY
Copyright Elsevier 2024

BOX 12.2 Numerical Simulation of the Master Equation With Fixed Time Step

Fixed time-step algorithm:

- Calculate the total rate with which the current state of each cell can be left:

$$W_Z = \sum_{Z'} W(Z \to Z') \tag{12.4}$$

  Note, however, that for cells, the counting of the target states may be different (see Section 12.3.4 for details).
- Calculate the time step from the condition that the time step needs to be much smaller than 1 ($\ll \tau$ if Δt is considered with units) during the entire simulation:

$$\Delta t \ll \alpha \left[\sum_{Z'} W(Z \to Z') \right]_{\max}^{-1} = \alpha / W_Z^{\max} \tag{12.5}$$

  with $\alpha \ll 1$ (usually, $\alpha = 0.01$ is sufficient, $\alpha = 0.001$ recommended). As the time step is fixed, the biggest value for $\sum_{Z'} W(Z \to Z') = W_Z^{\max}$ has to be estimated a priori. It is strongly recommended to monitor that the upper condition is never violated as a violation would distort the temporal dynamics. If the time interval is chosen large such that in reality during it more than one event may occur, then the kinetics becomes incorrect.
- Until a certain stopping condition is met, execute the following steps:
  - Calculate the actual W_Z.
  - Throw a uniformly distributed random number $\xi \in [0,1)$.
  - If $\xi > W_Z \Delta t$, $t \to t + \Delta t$.
  - If $\xi \leq W_Z \Delta t$, change $Z \to Z'$ and *update* $t \to t + \Delta t$. The choice of the new state Z' can be done as in Box 12.4.

BOX 12.3 Event-Based Numerical Simulation of the Master Equation: Gillespie Algorithm

Event-driven algorithm, variable time step:

- Calculate the total rate with which the current state can be left:

$$W_z = \sum_{Z'} W(Z \to Z')$$

  $W(Z \to Z')$ again denotes the rate of a transition from Z to Z'.
- Then, choose the time step until the next event according to

$$\Delta t = -1 / W_z \log(1 - \xi) = -1 \Big/ \left(\sum_{Z'} W(Z \to Z') \right) \log(1 - \xi), \tag{12.6}$$

  where $\xi \in [0, 1)$ is a uniformly distributed random variable. Then choose the new state as in Box 12.4 and continue with the first step.

In the Gillespie algorithm a variable time step is calculated after which a state change of the multicellular configuration occurs with probability 1. Hence, it is an event-based algorithm, where the period until the next event is calculated (Box 12.3).

12.3.4 Cell Movement and Multiplicity of States

Different from chemical particles, movement of cells is experimentally observed to not depend on the precise amount of free space available in the neighborhood as long as the space is sufficient for the cells to squeeze through. Cell migration is active, not controlled by collisions with molecules as it is for molecules or colloidal particles in solution. Some cells such as embryonic cells can even move within aggregates of other cells (Mombach et al., 1993).

Translated into the lattice model, the hopping of cells should not depend on the number of free neighbor sites as long as at least one free neighbor site exists. However, it is important to notice that fine calibration of the model requires data from the experimental system that should be considered.

To understand the consequences of the difference between particle and cell movement if more than one free neighbor lattice site is available, consider the following case (Fig. 12.3). Either a particle or a cell is located on a 2D square lattice with lattice spacing l at position (x, y) with the left neighbor at $(x - l, y)$ occupied by another particle (or cell), the other three neighbor sites on the lattice, $(x + l, y)$, $(x, y - l)$, and $(x, y + l)$ being unoccupied. Let the hopping rate in the $+x$ direction be denoted by $\lambda^{+,0}$, in the $+y$ direction by $\lambda^{0,+}$, and the $-y$ direction by $\lambda^{0,-}$ (for the superscripts of λ^{xy}, $x, y \in \{+, -\}$). In the case of a particle A (e.g., a molecule), the total rate with which the particle could leave its site is $\lambda^{-,0} + \lambda^{0,+} + \lambda^{0,-} = \lambda_\Sigma$. Hence this rate would be larger than, for example, a particle that has only one single free neighbor site as long as not two of

This book belongs to Central Library BADJI Mokhtar-ANNABA UNIVERSITY
Copyright Elsevier 2024

BOX 12.4 Choice of New State

- Calculate the rate with which state Z can be left:

$$W_z = \sum_{Z'} W(Z \rightarrow Z').$$

- Calculate ξW_Z where $\xi \in [0, 1)$ is a uniformly distributed random number. The summands in the equation for W_Z refer to the different processes that would lead from Z to Z' and may be enumerated one by one by an integer $N_{Z'} = 1, 2, \ldots, n_{Z'}$ with $n_{Z'}$ the total number of state changes taken into account as target states. The variable has been introduced to separate it from the variable Z' that characterizes (quantifies) all accessible states. From the possible transitions leading from $Z \rightarrow Z'$ now choose that process k, for which

$$\sum_{Z';N_{Z'}=1}^{n_k} W(Z \rightarrow Z') \leq \xi W_Z < \sum_{Z';N_{Z'}=1}^{n_{k+1}} W(Z \rightarrow Z'). \quad (12.7)$$

Notice: the algorithm can be pictured as a linear arrangement of open boxes, each box representing the rate of one possible process, where the size of each box orifice is proportional to the rate it represents. The upper algorithm can be viewed as throwing a ball that falls with probability one into one of these boxes, whereby the individual probability to fall into a particular box is proportional to its relative size (weight), i.e., the size of its orifice divided by the sum of the size of all orifices.

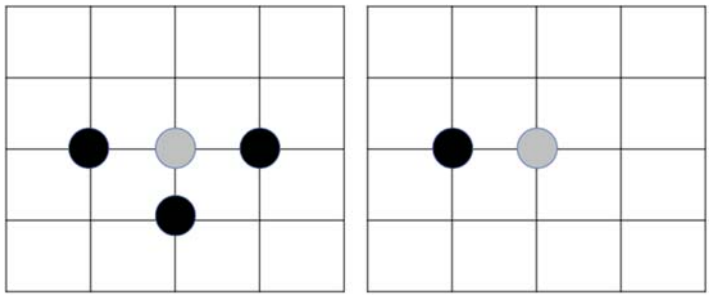

FIGURE 12.3 Two exemplary configurations of cells on a two-dimensional lattice. *Filled circles* denote occupied lattice sites. In the left configuration, only one free lattice exists to which the gray cell could move, whereas in the right configuration, three free lattice sites are accessible. For both configurations the chance that the gray cell moves should be the same as a cell can actively sense its neighborhood. For particles, the rate of hopping for the gray particle in the left configuration should be smaller than in the right configuration. (See text for further details where x direction refers to horizontal direction, y direction to vertical direction.)

the three rates were zero. In case of an actively migrating cell, the cell can sense its environment and make active decisions, even in case of only one free neighbor site could choose to move right away to that one. For the above example, in case $\lambda^{-,0} = \lambda^{0,+} = \lambda^{0,-} := \lambda$ the rate of movement would be λ. However, in case of different rates, the solution is difficult and not unique. One option is to randomly choose only one of the three directions for the list of possible moves that could change the multicellular system state, the $+x$ direction with rate $\lambda^{0,+}/\lambda_\Sigma$, the $+y$ direction with rate $\lambda^{0,+}/\lambda_\Sigma$, and finally the $-y$ direction with rate $\lambda^{0,-}/\lambda_\Sigma$. Then the process that has been chosen is added to the list of possible moves. In this case the sum is over $\widetilde{Z}(Z')$ states assuming that the rate at which a cell changes its state by a hop, a progress in the cell cycle, a division, or death process is independent of the number of accessible states as long as at least one state is accessible, that is, one free adjacent lattice site.

12.3.5 Growth and Division

The magnitude of the expansion speed of dense one-cell-thick monolayers is incompatible with the assumption that only those cells at the monolayer border (i.e., next to free lattice sites) grow and divide (Hoehme and Drasdo, 2005). Furthermore, in monolayers both glucose and oxygen are abundant, suggesting that the expansion speed of the monolayer may be controlled by physical forces (Hoehme and Drasdo, 2005; Drasdo, 2005; Block et al., 2007). Observation of cells in the interior of monolayers leads to the conclusion that growing and dividing cells can exert forces on neighboring cells pushing them aside to generate free space for its division (Brú et al., 1998). In Type B cellular automaton this can be taken

This book belongs to Central Library BADJI Mokhtar-ANNABA UNIVERSITY Copyright Elsevier 2024

into account by defining a certain length ΔL over which a cell is able to push neighbor cells away (Drasdo, 2005; Kansal et al., 2000b; Block et al., 2007). This would generate a constant proliferating rim thickness and comply with the observations in growing monolayers and multicellular spheroids. A cell can only divide if at least one lattice site within radius ΔL is free. To make space for the daughter cells, a line is drawn linking the cell's site to the closest free lattice site and all intersecting neighbors are shifted one position toward the free lattice site. Next, one daughter cell is placed at the site of the mother cell and the other one is placed at the lattice site that was freed by the shifting procedure. This procedure ensures that the daughter cells of the same mother cell are neighbors directly after division. Instead of using a fixed length ΔL, one may also use an upper bound for the number of neighbor cells a dividing cell can push aside. The algorithm mimics that a dividing cell exerts forces on its environment, leading to a rearrangement of cells in its neighborhood such that the total energy needed to push the neighbor cells away is minimal. Using the shifting procedure in a Type B cellular automaton, the growth kinetics of one-cell-thick monolayers can be reproduced.

Most models used ΔL as a threshold parameter with cells having the same chance of dividing if their distance to the next free lattice site does not exceed ΔL (Drasdo, 2005; Kansal et al., 2000b; Block et al., 2007), but direct comparison with experimental data on multicellular spheroids suggests that the probability of division depends on the distance of the cell to the spheroid border leading to slightly different dynamics, namely to a division rate $\propto e^{-\Delta L/L_{\text{ref}}}$, with L_{ref} being a reference length (Jagiella et al., 2016).

Growth and division can also be separated by first allowing a cell to occupy two (or more) adjacent lattice sites simultaneously without considering the cell as having divided (the cell growth) and later divide the cell into two daughter cells (Fig. 12.1; Jagiella et al., 2016).

Recent tendencies consider intracellular processes and environmental distributions in deciding on cell cycle progression (e.g., Jagiella et al., 2016 and refs. therein). In this case cell cycle progression may depend on additional conditions; hence the processes appear more complex.

12.3.6 Influence of Lattice Symmetry on Growth Figures

The advantage of an unstructured lattice is that the emerging growth figures do not reflect the lattice symmetry even in the presence of noise reduction (see Fig. 12.4).

In case of noise reduction for example, if $m \gg 1$, the rate of movement $\lambda = 0$, and $\Delta L = 1$, the emerging growth pattern reflects the lattice symmetry (Drasdo, 2005; Block et al., 2007). As these are absent in unstructured lattices, quantities sensitive to lattice artifacts can be studied by Type B lattice models on unstructured lattices. Examples are the surface scaling properties of growing monolayers that require simulation of many realizations of the stochastic growth process (Block et al., 2007). In that reference, the authors could show that interpretations of surface scaling properties in experiments of growing monolayers must have been erroneous in that the growth dynamics has been classified by the wrong universality class (Brú et al., 2003). The universality class predicted by the simulations could later be validated by a

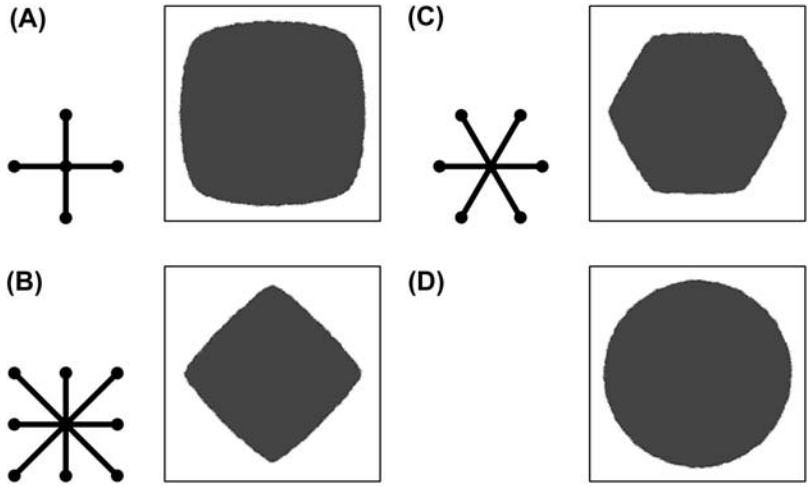

FIGURE 12.4 Simulation results of growth simulations for $m = 60$, $\Delta L = l$, and $\varphi = 0$ (Block et al., 2007). Each simulation started with one cell in the middle of the lattice. On (A) a regular lattices (square lattice with nearest neighbors along the coordinate axes), (B) a square lattice with Moore neighborhood, or (C) a hexagonal lattice, the growth pattern reflects the lattice symmetry, which is not the case on (D) an unstructured lattice.

This book belongs to Central Library BADJI Mokhtar-ANNABA UNIVERSITY Copyright Elsevier 2024

BOX 12.5 Numerical Lattice Model Simulation

- Choose a lattice. A preferable choice is an unstructured lattice to avoid lattice effects.
- Initialize the initial conditions: number and positions of cells.
- Initialize the model parameters.
- If a fixed time-step algorithm is used: Determine the time step size Δt according to Box 12.2 and perform the iterations as explained in that box.
- If otherwise the event-driven Gillespie algorithm is used, pursue the steps as in Box 12.3.

novel set of experiments (Huergo et al., 2011, 2012). This indicates that, despite their simplicity, the Type B lattice growth model simulations can provide valid predictions.

However, large variations in cell cycle time duration, hopping rate (by $\lambda \gg 1/\tau$) or $\Delta L \gg l$ reduce or even eliminate lattice effects (Drasdo, 2005; for ΔL, see also Yates and Baker, 2013).

12.3.7 Energy-Dependent Moves

Both growing and migrating cells may be able to exert forces on a neighbor cell, which can be implemented in the same way as division (Block et al., 2007). Cell—cell or cell—extracellular matrix interactions can be included in the transition rate for each move (hop, growth, or division step), which then becomes $\propto e^{-\Delta E/F_T}$ where ΔE denotes the total energy of change for a particular cell move, F_T a reference energy, which was proposed to represent the membrane fluctuation energy as a formal equivalent to $k_B T$ in fluids (k_B: Boltzmann constant, T: temperature) (Beysens et al., 2000). If for example, cell—matrix contacts have to be released, the energy necessary to push a row of $\Delta L/l$ (l the lattice size) cells should be $\propto \Delta L$, which may be taken as physical explanation of the above reported division rate $\propto e^{-\Delta L/L_{\text{ref}}}$ in multicellular spheroids (Jagiella et al., 2016).

The key steps of a lattice growth model Type B simulations are summarized in Box 12.5.

By systematic simulations it was possible to infer the asymptotic (i.e., large-scale) growth speed $v(\phi, \Delta L, \tau, m)$ of a growing population with hopping rate ϕ and shift radius ΔL (Radszuweit et al., 2009). In the limit of large population sizes and sufficiently large hopping rates ϕ, the long-time dynamics can be related to the Fisher—KPP equation (Drasdo, 2005; Byrne and Drasdo, 2009). Insofar, simulations with this model can be used to guide development of continuum models.

12.3.8 Conclusion: Pros and Cons of Type B Lattice Growth Models

Pros of Type B cellular automaton models are that each cell is represented individually; the precise cell position is resolved in time and space, movement, and division; and death of cells can be represented. As their requirements in terms of simulation time are modest, simulations are fast; the limitations are rather due to large memory requirement than due to simulation time. Because of the short simulation times, simulated parameter sensitivity analyses are feasible. Weak points are that the cell size and shape are fixed and a lattice property, the existence of the lattice spacing as a lower length scale, and that the stochastics plays a key role in the simulation dynamics of the processes, which are all simulated by jump-type processes. The physics is represented by rules that are hoped to cover the physical processes correctly, which can be a significant shortcoming compared to models that implement physical laws directly.

Evaluations on the computation times are done with regard to a standard PC.

12.3.9 Cellular Automaton With Many Cells per Lattice Site (Type A) and Lattice Gas Cellular Automaton

In Type A lattice growth models and LGCA models, many cells ($N_{\max} > 1$) can occupy the same lattice site. Hence, each lattice site represents a spatial compartment much larger than the size of an individual cell. Type A lattice growth models are otherwise very similar to Type B lattice growth models and will be described first. Birth and migration processes in Type A lattice growth models can occur within each compartment and between neighboring compartments. Again processes such as migration, growth, and division can be modeled by a master equation, similarly to Type B lattice models. The master equation is a classical multivariate (or also called chemical) master equation for the probability $p(\underline{X}, t)$ to find the multicellular system in a certain state represented by the state vector $\underline{X} = (\underline{x}_1, \underline{x}_2, \ldots, \underline{x}_i, \ldots)$, where i denotes the lattice compartment (a vector of vectors). In case cells can exist only in one state, $\underline{x}_i$ denotes the number of cells in lattice

This book belongs to Central Library BADJI Mokhtar-ANNABA UNIVERSITY
Copyright Elsevier 2024

BOX 12.6 Differences Between Type A and Type B Numerical Simulations

- Choice of the lattice. A preferable choice is an unstructured lattice to avoid lattice effects. The lattice compartment size in general determines the number of cells that maximally fit into the same compartment. The lattice spacing should be $b > a \approx V^{1/3}$ where V denotes the cell volume (Radszuweit et al., 2009). Accordingly, the maximum number of cells fitting in a compartment is b^3/V.
- Instead of tracking each individual cell, now within each compartment sets of cells with identical parameters can be built to define the state vector mimicking the state in each lattice compartment i as described in the text. This way the simulations are significantly accelerated but cells are not tracked individually anymore.
- In the absence of hopping, division of a cell in compartment i would first fill this compartment and only deposit one of the daughter cells in a neighbor compartment if compartment i is full.
- The proliferation depth ΔL can be directly used to determine the size of the lattice compartment. If b is chosen to be $b = 0.863\Delta L + l$ (Jagiella et al., 2016; Jagiella, 2012), then the result of the growth simulations corresponds to those of the Type B model (Van Liedekerke et al., 2015). Also φ and m translate directly from Type B to Type A lattice models.

compartment i and would just be a scalar. However, cells may exist in different states (also different cell types may have to be taken account) requiring an additional classifier for cells of different type or state in each lattice compartment i. For this reason each component of $\underline{X}$ is generally a vector itself. For example, for spatial compartment i, $\underline{x}_i = (x_{i,1}, x_{i,2}, \ldots, x_{i,j}, \ldots)$, where $x_{i,j}$ denotes the number of cells in a state j within spatial compartment i (note: we could equally well have described the system state again by a general variable Z, we here specify Z in analogy to the chemical master equation (Gardiner, 1994)). For example, if different cells in spatial compartment i are in the same state $j = m'$ in the cell cycle (m' was the variable we used above to enumerate intermediate states in the cell cycle), then $x_{i,1}$ would denote the cells in i with $j = m' = 1$, $x_{i,j}$ with $m' = j$ and $x_{i,m}$ with $j = m' = m$. In higher dimensions, i may be replaced by $\underline{i} = (i_1, i_2, \ldots, i_d)$ to simplify enumerating the lattice compartments along the different coordinate directions. (Note that, in principle, one could enumerate each individual cell in a certain lattice compartment by choosing the number of j components at each lattice compartment equal to the number of cells in that compartment. However, this is computationally more costly than tracking all cells with the same state in that compartment.)

We briefly describe the differences between modeling with Type A and Type B cellular automaton models in Box 12.6.

Population sizes of about $N = 10^9 - 10^{10}$ cells as those found in xenografts are not amenable to Type B lattice growth models on standard PCs but may pose no problem to Type A lattice growth models (Radszuweit et al., 2009). However, growth, division, and death of tumor cells in vivo are largely controlled by the availability of oxygen, glucose, and growth factors. Hence, the spatial profiles of these molecules have to be equally coarse grained. Preliminary attempts at developing numerical schemes for this indicated that for high concentrations of molecules outside the tumor, coarse graining schemes yielding to the same growth and death of tumor cell populations can be found while for small concentrations of molecules growth and death of the tumor cells deviated strongly. As a result, the growth dynamics in the coarse grain Type A lattice growth models can deviate significantly from the growth dynamics of the Type B lattice growth models where each single cell is represented. These deviations may occur because at high consumption rates, caused by a large number of cells in a compartment, the approximation schemes fail (Jagiella, 2012).

A way to deal with this problem is to construct a hybrid lattice, where the cell population is represented at high resolution by a Type B cellular automaton at locations where strong gradients may occur (e.g., at tumor surfaces), and otherwise consider the coarse grained Type A lattice growth model (Van Liedekerke et al., 2015). To maximize the resolution where necessary and coarse grain where no accuracy is needed, ideally the hybrid model would perform automated switches of the resolution depending on some criterion.

12.3.10 Conclusion: Pros and Cons

Because of the coarse lattice, centimeter simulations are feasible, and the low computing time permits simulated parameter sensitivity analyses. The precise positions of the cell cannot be tracked anymore and cell shape is not represented hence spatial direct cell–cell neighborhood cannot be defined. The lattice spacing is the lower length scale. Again all processes, migration, division death, and pushing, are mimicked by jump-type processes. The physics such as mechanical pushing

This book belongs to Central Library BADJI Mokhtar-ANNABA UNIVERSITY
Copyright Elsevier 2024

needs to be implemented by rules, which promotes overlooking effects compared with approaches that implement the physical laws directly.

12.4 LATTICE GAS CELLULAR AUTOMATON MODELS

LGCA models have a further explicit dynamical variable, the cell speed. LGCA models include velocity channels, i.e., particles are characterized by their position and velocity. Both are discrete. Frisch, Hasslacher, and Pomeau demonstrated in 1986 that by defining a set of rules for the interaction (in their case collision) and propagation of particles on a regular lattice with discrete time steps and a small set of velocities, one can generate dynamics that, on large scale, reproduce the behavior of the incompressible Navier−Stokes equation (Frisch et al., 1986; Rothman and Zaleski, 2004; Rivet and Boon, 2005). A simple intuitive derivation can be found in Gershenfeld (1999). In the simulations of fluids, the velocity channels represented particle collisions. Deutsch and coworkers extended the framework to model growth and migration of cells in multicellular environments (Dormann and Deutsch, 2002; Deutsch and Dormann, 2004; Bottger et al., 2012; Tektonidis et al., 2011).

An excellent article introducing LGCA is the one by Hatzikirou and Deutsch in Hoekstra et al. (2010), which is why we do not describe it here in detail. Advantages and disadvantages are similar as in Type A lattice models and are discussed in (Van Liedekerke et al., 2015).

12.5 LATTICE MODELS WITH MANY LATTICE SITES PER CELL (TYPE C; CELLULAR POTTS MODELS)

The CPM is an energy-based, lattice-based modeling method for cell-based modeling. It uses an energy functional generalized from the Potts model, originally derived for a ferromagnet, to evaluate a multicellular state.

In a CPM, one cell occupies many lattice sites. Different from the CA models discussed before, the CPM provides an explicit model of cell shape, which has made the CPM a popular tool to model morphogenic processes such as cell sorting (Graner and Glazier, 1992; Glazier and Graner, 1993), cancer and tumor growth (Turner and Sherratt, 2002; Rubenstein and Kaufman, 2008; Shirinifard et al., 2009; Boghaert et al., 2014; Szabó and Merks, 2013; Li and Lowengrub, 2014; Gao et al., 2013; Rubenstein and Kaufman, 2008; Shirinifard et al., 2009; Boghaert et al., 2014; Szabó and Merks, 2013; Li and Lowengrub, 2014; Gao et al., 2013), and angiogenesis (Merks and Glazier, 2006; Merks et al., 2008; Palm and Merks, 2013; Boas and Merks, 2014; Bauer et al., 2007, 2009; Daub and Merks, 2013; van Oers et al., 2014).

12.5.1 Concept of Energy Functional

In the CPM, cells are positioned on a 2D or 3D lattice. Each lattice site $\underline{x}$ is assigned an identifier $\sigma \in \mathbb{N}^0$. Sites with the same identifier $\sigma > 0$ belong to the same cell, and all remaining lattice sites, with $\sigma = 0$, belong to the extracellular medium.

The assignment of lattice sites to cells and extracellular medium are controlled by an effective energy functional on the lattice. The minimal standard effective energy functional of the CPM consists of three terms:

$$E = \sum_{(\underline{x},\underline{x}')} J\left(\sigma(\underline{x}), \sigma(\underline{x}')\right)\left(1 - \delta\left(\sigma(\underline{x}), \sigma(\underline{x}')\right)\right) + \lambda_S \sum_{\sigma} \left(S_0(\sigma) - S(\sigma)\right)^2 + \lambda_V \sum_{\sigma} \left(V_0(\sigma) - V(\sigma)\right)^2 \tag{12.8}$$

The first term represents both cell−cell adhesion and cell−ECM adhesion that is computed for all sets of neighboring lattice sites $(\underline{x}, \underline{x}')$ where $J\left(\sigma(\underline{x}), \sigma(\underline{x}')\right)$ represents the energy cost of an interface between lattice sites belonging to two different cells. Because only interfaces at the cell membrane are associated with an energy costs, the Kronecker delta ($\delta(x, y) = \{1, x = y; 0, x \neq y\}$) is used such that the contact energy becomes zero for $\sigma(\underline{x}) = \sigma(\underline{x}')$. The second term denotes a surface constraint with actual surface S, target surface S_0, and penalty parameter λ_S, and the third term denotes a volume constraint, with cell volume $V(\sigma)$ and target volume $V_0(\sigma)$, and penalty parameter λ_V. In 2D simulations the volume is replaced with the area and the surface by the circumference.

The magnitudes of shape constraints are not invariant with respect to the fineness of the lattice. This can be addressed by introducing relative shape constraint (Scianna and Preziosi, 2013; van Oers et al., 2014; Albert and Schwarz, 2014).

The penalty parameters λ_S and λ_V can be viewed as Lagrangian parameters, which permit to add constraints and may be related to physical quantities. For example, the Lagrangian parameter λ_V for the volume constraint can be related to

This book belongs to Central Library BADJI Mokhtar-ANNABA UNIVERSITY
Copyright Elsevier 2024

the material properties of the cell. If the cell is approximated by a homogeneous isotropic elastic object, one would expect

$$\lambda_V = K_V = E/(3(1-2\nu)), \tag{12.9}$$

with E being the Young modulus, ν the Poisson ratio, and K_V the bulk modulus of the cell. Then if we consider the movement of an incompressible moving cell, i.e., a cell with a Poisson's ratio of $\nu = 0.5$, then λ_V is infinitely large.

12.5.2 Cell Growth and Division

Cell growth may be modeled by increasing the target volume V_0 with increasing simulation steps. Once the target volume has increased by a factor of two, and the ratio of the actual volume and target volume $\Theta = V/V_0$ overcomes a critical threshold, then the cell splits into two daughter cells (Leoncini, 2010). It can be shown that the dependency of the growth kinetics on the model parameters is the same for the CPM as for lattice growth Type A and B models (Van Liedekerke et al., 2015). The target surface area can even be set to zero, in which case the optimal surface is a sphere. Fundamentally, if $S_0 \leq (4\pi)^{1/3}(3V_0)^{2/3}$ the surface and volume terms favor the shape of a sphere for an isolated cell.

12.5.3 Choice of Lattice

Almost all CPMs are implemented on a square lattice, which can show lattice symmetry effects (Graner and Glazier, 1992; Glazier and Graner, 1993). The CPM can equally be implemented on a Voronoi lattice (Van Liedekerke et al., 2015), where lattice effects can be avoided but bookkeeping is more difficult.

12.5.4 Simulation of Dynamics

In principle the dynamics could again be modeled by a multivariate master equation, mimicking the time development for the probability to find the multicellular system in a particular multicellular state. However, the neighbor states of a give state are so numerous that this way is usually not pursued.

Instead, cell migration, cell growth, and cell shape changes are modeled using a Markov chain Monte Carlo method using the algorithm in Box 12.7. The underlying conceptual idea originating from statistical mechanics is that the energy functional ("Hamiltonian" in statistical mechanics) characterizes the equilibrium of the system and hence permits calculation of the equilibrium probability distribution. The master equation should then be constructed such that its stationary probability $p^*(Z)$ (for which $\partial p(Z,t)/\partial t = 0$ in the master Eq. 12.3) corresponds to the equilibrium probability distribution. To better control the aforementioned case, one usually requires detailed balance: $W(Z' \to Z)p^*(Z') = W(Z \to Z')p^*(Z)$. This is for example the case for the Metropolis algorithm (Box 12.7). However, note that this conceptual analogy to statistical mechanics is not obvious as growth and division represent a permanent perturbation of the system so that equilibrium is not reached. Insofar one assumes that these perturbations are rare enough such that the system tries to reach (a transient) equilibrium before the next growth or division happens.

BOX 12.7 Metropolis Algorithm-Based Simulation Algorithm for Cellular Potts Model

- Choice of the lattice. A preferable choice is an unstructured lattice to avoid lattice effects.
- Determine parameters.
- Iterate now using the Metropolis algorithm:
  - Choose a certain lattice site and change its identifier σ to one of its neighbor sites (this is called a "flip" or "move"). The neighbor site from which the identifier is taken over is chosen randomly with uniform probability.
  - Calculate the energy change that this flip (move) would generate:

$$\Delta E = E(\text{after flip}) - E(\text{before flip}).$$

  - Decide whether the flip (move) is accepted using the Metropolis algorithm. If $\Delta E \leq 0$, accept the flip (move). If $\Delta E > 0$, choose a uniformly distributed random number $\xi \in [0,3)$; if $\xi < e^{-\Delta E/F_T}$, accept the flip (move), otherwise reject the move. F_T denotes an effective fluctuation energy controlling cell motility.
  - Once every site has been considered once, $t \to t + \Delta t$.
  - Continue this iteration until a certain stop criterion is met.

This book belongs to Central Library BADJI Mokhtar-ANNABA UNIVERSITY
Copyright Elsevier 2024

Here, the CPM iteratively attempts to change the state of a randomly chosen lattice site $\underline{x}$ to that of a randomly chosen neighboring lattice site $\underline{x}'$. To determine whether such a move attempt is successful, the change in effective energy (ΔE) between the two configurations is evaluated using the Metropolis algorithm (Box 12.7).

Model parameters and nonenergy-driven processes such as cell division can be updated between time steps.

12.5.5 Directed Active Cell Movement

The effective energy only includes static cell properties such as size and neighbors as long as no cell growth and division occurs. Cell growth and division lead to pushing effects as in Type A and Type B lattice growth models. To include directed cell movement, such as chemotaxis, extra terms may be added to the energy change ΔE. The most common mechanism to include chemotaxis (Savill and Hogeweg, 1996), for example, is

$$\Delta E_{\text{chemotactic}} = -\chi\left(c\left(\underline{x}'\right) - c\left(\underline{x}\right)\right), \tag{12.10}$$

where χ denotes the chemotactic sensitivity and $c(\underline{x})$ is the concentration at position $\underline{x}$. In Swat et al. (2014), external forces have been defined for any external potential. For a more in depth discussion, including more advanced topics, we refer to the recent book (Scianna and Preziosi, 2013).

12.5.6 Conclusion: Pros and Cons

The CPM has been established as a standard simulation method used frequently for modeling biological phenomena. It is straightforward to implement and computationally inexpensive in 2D and quasi-3D. It is therefore possible to perform large-scale parameter sweeps and carry out sensitivity analyses with CPM-based models (Boas et al., 2015; Palm and Merks, 2015). Furthermore, several open-source projects that implement CPM-based models are now available (Swat et al., 2012; Mirams et al., 2013; Starruβ et al., 2014), making it even easier to implement and simulate models using the CPM and to build on existing models so that reimplementation work can largely be avoided.

However, there are some major disadvantages to the CPM. First, although the CPM performs well in 2D and quasi-3D, real 3D simulations take long and are therefore uncommon. Second, because the CPM minimizes the effective energy, cell behavior is highly linked to cell motility. Cell motility on the other hand links to material parameters of the cell. For example, an incompressible cell, that is, a cell with a Poisson's ratio of $\nu = 0.5$ and hence λ_V is infinitely large, would not move. This is because there is usually no distinction between the main cell body and filopodia.

In summary, clear advantages are that each cell is represented individually; precise cell position is resolved; cell size and shape are statistically represented (if cell fragments are permitted to dissociate from the cell body) or directly represented (if dissociation moves are inhibited); movement, growth, division, and death of cells can be represented; and high cell densities can straightforwardly be handled. The CPM provides a flexible modeling framework, which is used and has been extended by numerous authors. On the other hand, large-scale simulations are due to computation time not always feasible, at most around 10^6 cells can be simulated in reasonable time on standard PCs. This makes parameter sensitivity analysis challenging. Moreover, some of the parameters cannot be associated directly with physically known quantities. The physics is partially directly represented (e.g., mechanics, adhesion), but partially unphysical couplings of migration and physical properties can occur. Because of the lattice, there is a lower length scale, but if sufficiently many lattice sites are associated with the same cell, this is less inhibiting than in lattice growth models of Type A and B. All dynamics processes (migration, division, death, pushing) are modeled by a jump-type stochastic process. As a given multicellular configuration has usually a very large number of possible neighbor configurations, too large to be completely listed, the dynamics is by Monte Carlo sampling, which can lead to unnatural distortions of the time scale.

12.6 SHORT CONCLUSION

In this section we addressed lattice-based ABMs to mimic organization processes in multicellular systems. One agent is usually identified with one biological cell. We distinguished between four types of lattice-based models depending on the spatial resolution they represent and depending on whether they track only the position of the cell or also its velocity. Advantages of lattice-based models are that in general they are more easily to implement, and their simulation times are shorter than for their lattice-free agent-based analogues at the same resolution. The disadvantage of lattice-based models is the existence of a lower length scale (migration or division over distances that are smaller than the lattice spacing are not possible) and that they are largely rule based (Types A, B, D). Moreover, the simulation of the multicellular dynamics is intrinsically stochastic, which makes it difficult to model tissue organization processes for which stochastic contributions

This book belongs to Central Library BADJI Mokhtar-ANNABA UNIVERSITY Copyright Elsevier 2024

may be negligible. Different from lattice-based models, the physical interactions in lattice-free models can usually be directly implemented (see next chapter and Van Liedekerke et al., 2015). Given the complexity in implementation of lattice-free ABMs, lattice-based models may be used to study qualitative phenomena potentially by verification simulations with lattice-free models. Because of their shorter simulation times, they may be well suited for simulated parameter sensitivity analyses that require a huge number of simulations.

ACKNOWLEDGMENTS

D.D. gratefully acknowledges funding by ANR INVADE, ANR PHYSCANCER, and BMBF Cancersys/Lungsys. P.V.L. acknowledges funding by ANR PHYSCANCER, ANR INVADE, and EU NOTOX. A.B. acknowledges funding by Alberta Innovates, MITACS Canada, and hospitality at INRIA during his stay at INRIA from December 2015 to May 2016.

REFERENCES

Alarcón, T., Byrne, H.M., Maini, P.K., 2003. A cellular automaton model for tumour growth in inhomogeneous environment. Journal of Theoretical Biology 225 (2), 257−274.

Alber, M.S., Kiskowski, M.A., Glazier, J.A., Jiang, Y., 2003. On cellular automaton approaches to modeling biological cells. In: Mathematical Systems Theory In Biology, Communications, Computation, and Finance. Inst Math & Its Appl, vol. 134.

Alber, M., Chen, N., Lushnikov, P.M., Newman, S.A., 2007. Continuous macroscopic limit of a discrete stochastic model for interaction of living cells. Physical Review Letters 99 (16).

Albert, P.J., Schwarz, U.S., 2014. Dynamics of cell shape and forces on micropatterned substrates predicted by a Cellular Potts Model. Biophysical Journal 106 (11), 2340−2352.

Alfonso, J.C.L., Jagiella, N., Nunez, L., Herrero, M.A., Drasdo, D., January 2014. Estimating dose painting effects in radiotherapy: a mathematical model. Plos One 9, e89380.

Anderson, A.R.A., Weaver, A.M., Cummings, P.T., Quaranta, V., 2006. Tumor Morphology and Phenotypic Evolution Driven by Selective Pressure from the Microenvironment.

Batchelor, M., Henry, B., July 1991. Limits to Eden growth in two and three dimensions. Physics Letters A 157, 229−236.

Bauer, A.L., Jackson, T.L., Jiang, Y., May 2007. A cell-based model exhibiting branching and anastomosis during tumor-induced angiogenesis. Biophysical Journal 92, 3105−3121.

Bauer, A.L., Jackson, T.L., Jiang, Y., July 2009. Topography of extracellular matrix mediates vascular morphogenesis and migration speeds in angiogenesis. Plos Computational Biology 5, e1000445.

Beysens, D.A., Forgacs, G., Glazier, J.A., 2000. Cell sorting is analogous to phase ordering in fluids. Proceedings of the National Academy of Sciences of the United States of America 97, 9467−9471.

Block, M., Schöll, E., Drasdo, D., 2007. Classifying the expansion kinetics and critical surface dynamics of growing cell populations. Physical Review Letters 99 (24).

Boas, S.E.M., Merks, R.M.H., 2014. Synergy of cellcell repulsion and vacuolation in a computational model of lumen formation. Journal of The Royal Society Interface 11 (92), 20131049.

Boas, S.E.M., Jimenez, M.I.N., Merks, R.M.H., Blom, J.G., 2015. A global sensitivity analysis approach for morphogenesis models. arXiv Preprint 1−29.

Boghaert, E., Radisky, D.C., Nelson, C.M., December 2014. Lattice-based model of ductal carcinoma in situ suggests rules for breast cancer progression to an invasive state. Plos Computational Biology 10, e1003997.

Bortz, A., Kalos, M., Lebowitz, J., January 1975. A new algorithm for Monte Carlo simulation of Ising spin systems. Journal of Computational Physics 17, 10−18.

Bottger, K., Hatzikirou, H., Chauviere, A., Deutsch, A., January 2012. Investigation of the migration/proliferation dichotomy and its impact on avascular glioma invasion. Mathematical Modelling of Natural Phenomena 7, 105−135.

Brú, A., Pastor, J., Fernaud, I., Brú, I., Melle, S., Berenguer, C., 1998. Super-rough dynamics on tumor growth. Physical Review Letters 81 (18), 4008−4011.

Brú, A., Albertos, S., Luis Subiza, J., García-Asenjo, J.L., Brú, I., 2003. The universal dynamics of tumor growth. Biophysical Journal 85 (5), 2948−2961.

Bunde, A., Havlin, S., 2012. Fractals and Disordered Systems. Springer Science & Business Media.

Byrne, H., Drasdo, D., 2009. Individual-based and continuum models of growing cell populations: a comparison. Mathematical Biology 58, 657−680.

Daub, J.T., Merks, R.M.H., March 2013. A cell-based model of extracellular-matrix-guided endothelial cell migration during angiogenesis. Bulletin of Mathematical Biology 1−23.

Deutsch, A., Dormann, S., 2004. Cellular Automaton Modeling of Biological Pattern Formation: Characterization, Applications, and Analysis (Modeling and Simulation in Science, Engineering and Technology). Birkhaeuser Verlag AG.

Dormann, S., Deutsch, A., January 2002. Modeling of self-organized avascular tumor growth with a hybrid cellular automaton. In Silico Biology 2, 393−406.

Drasdo, D., Hohme, S., June 2003. Individual-based approaches to birth and death in avascu1ar tumors. Mathematical and Computer Modelling 37, 1163−1175.

This book belongs to Central Library BADJI Mokhtar-ANNABA UNIVERSITY Copyright Elsevier 2024

Drasdo, D., Hoehme, S., Block, M., 2007. On the role of physics in the growth and pattern formation of multi-cellular systems: what can we learn from individual-cell based models. Journal of Statistical Physics 128, 287−345.

Drasdo, D., 2005. Coarse graining in simulated cell populations. Advances in Complex Systems 08 (02n03), 319−363.

Düchting, W., Vogelsaenger, T., 1985. Recent progress in modelling and simulation of three-dimensional tumor growth and treatment. Biosystems 18 (1), 79−91.

Eden, M., 1961. A two-dimensional growth process. In: Proceedings of the Fourth Berkeley Symposium on Mathematical Statistics and Probability, Volume 4: Contributions to Biology and Problems of Medicine. The Regents of the University of California.

Enderling, H., Hahnfeldt, P., 2011. Cancer Stem Cells in Solid Tumors: Is 'evading Apoptosis' a Hallmark of Cancer?.

Frisch, U., Hasslacher, B., Pomeau, Y., April 1986. Lattice-gas automata for the Navier-Stokes equation. Physical Review Letters 56, 1505−1508.

Gao, X., McDonald, J.T., Hlatky, L., Enderling, H., 2013. Acute and fractionated irradiation differentially modulate glioma stem cell division kinetics. Cancer Research 73 (5), 1481−1490.

Gardiner, C.W., 1994. Handbook of Stochastic Methods for Physics, Chemistry and the Natural Sciences. Springer-Verlag.

Gershenfeld, N.A., 1999. The Nature of Mathematical Modeling. Cambridge University Press.

Gillespie, D.T., December 1977. Exact stochastic simulation of coupled chemical reactions. The Journal of Physical Chemistry 81, 2340−2361.

Glazier, J.A., Graner, F., 1993. Simulation of the differential adhesion driven rearrangement of biological cells. Physical Review E: Statistical Physics, Plasmas, Fluids, and Related Interdisciplinary Topics 47 (3), 2128−2154.

Gomes, F.L., Zhang, G., Carbonell, F., Correa, J.A., Harris, W.A., Simons, B.D., Cayouette, M., 2011. Reconstruction of rat retinal progenitor cell lineages in vitro reveals a surprising degree of stochasticity in cell fate decisions. Development 138 (2), 227−235.

Graner, F., Glazier, J.A., 1992. Simulation of biological cell sorting using a two-dimensional extended Potts model. Physical Review Letters 69, 2013−2016.

Hoehme, S., Drasdo, D., 2005. A single-cell-based model of tumor growth in vitro: monolayers and spheroids. Physical Biology 2, 133−147.

Hoekstra, A.G., Kroc, J., Sloot, P.M., 2010. Simulating Complex Systems by Cellular Automata.

Honda, H., 1978. Description of cellular patterns by Dirichlet domains: the two-dimensional case. Journal of Theoretical Biology 72 (3), 523−543.

Honda, H., January 1983. Geometrical models for cells in tissues. International Review of Cytology 81, 191−248.

Huergo, M.A.C., Pasquale, M.A., Gonzalez, P.H., Bolzan, A.E., Arvia, A.J., August 2011. Dynamics and morphology characteristics of cell colonies with radially spreading growth fronts. Physical Review E: Statistical, Nonlinear, and Soft Matter Physics 84, 021917.

Huergo, M.A.C., Pasquale, M.A., Gonzalez, P.H., Bolzan, A.E., Arvia, A.J., 2012. Growth dynamics of cancer cell colonies and their comparison with noncancerous cells. Physical Review E: Statistical, Nonlinear, and Soft Matter Physics 85 (1).

Jagiella, N., Müller, B., Muller, M., Vignon-Clementel, I.E., Drasdo, D., February 2016. Inferring growth control mechanisms in growing multi-cellular spheroids of NSCLC cells from spatial-temporal image data. PLoS Computational Biology 12, e1004412.

Jagiella, N., 2012. Parameterization of Lattice-Based Tumor Models from Data. PhD thesis.

Kansal, A., Torquato, S., Harsh IV, G., Chiocca, E., Deisboeck, T., 2000a. Cellular Automaton of Idealized Brain Tumor Growth Dynamics.

Kansal, A.R., Torquato, S., Harsh IV, G.R., Chiocca, E.A., Deisboeck, T.S., 2000b. Simulated brain tumor growth dynamics using a three-dimensional cellular automaton. Journal of Theoretical Biology 203 (4), 367−382.

Krug, J., Spohn, H., 1991. Kinetic roughening of growing surfaces. Solids far from Equilibrium 479−582.

Lee, D.-S., Rieger, H., Bartha, K., February 2006. Flow correlated percolation during vascular remodeling in growing tumors. Physical Review Letters 96, 058104.

Leoncini, E., 2010. Applied Mathematics to Biology & Medicine. PhD thesis.

Li, J.F., Lowengrub, J., November 2014. The effects of cell compressibility, motility and contact inhibition on the growth of tumor cell clusters using the Cellular Potts Model. Journal of Theoretical Biology 343, 79−91.

Lushnikov, P.M., Chen, N., Alber, M., 2008. Macroscopic dynamics of biological cells interacting via chemotaxis and direct contact. Physical Review E: Statistical, Nonlinear, and Soft Matter Physics 78 (6).

Marée, A.F., Hogeweg, P., 2001. How amoeboids self-organize into a fruiting body: multicellular coordination in *Dictyostelium discoideum*. Proceedings of the National Academy of Sciences of the United States of America 98 (7), 3879−3883.

Merks, R.M., Glazier, J.A., July 2005. A cell-centered approach to developmental biology. Physica A: Statistical Mechanics and Its Applications 352, 113−130.

Merks, R.M.H., Glazier, J.A., 2006. "Dynamic mechanisms of blood vessel growth. Nonlinearity 19 (no. 1), C1−C10.

Merks, R.M.H., Perryn, E.D., Shirinifard, A., Glazier, J.A., 2008. Contact-inhibited chemotaxis in de novo and sprouting blood-vessel growth. Plos Computational Biology 4 (9), e1000163.

Mirams, G.R., Arthurs, C.J., Bernabeu, M.O., Bordas, R., Cooper, J., Corrias, A., Davit, Y., Dunn, S.-J., Fletcher, A.G., Harvey, D.G., Marsh, M.E., Osborne, J.M., Pathmanathan, P., Pitt-Francis, J., Southern, J., Zemzemi, N., Gavaghan, D.J., January 2013. Chaste: an open source C++ library for computational physiology and biology. PLoS Computational Biology 9, e1002970.

Mollison, D., 1972. Conjecture on the spread of infection in two dimensions disproved. Nature 240 (5382), 467−468.

Mombach, J., de Almeida, R., Iglesias, J., July 1993. Mitosis and growth in biological tissues. Physical Review E: Statistical, Nonlinear, and Soft Matter Physics 48, 598−602.

van Oers, R.F.M., Rens, E.G., LaValley, D.J., Reinhart-King, C.A., Merks, R.M.H., August 2014. Mechanical cell-matrix feedback explains pairwise and collective endothelial cell behavior in vitro. PLoS Computational Biology 10, e1003774.

This book belongs to Central Library BADJI Mokhtar-ANNABA UNIVERSITY Copyright Elsevier 2024

Palm, M.M., Merks, R.M.H., 2013. Vascular networks due to dynamically arrested crystalline ordering of elongated cells. Physical Review E: Statistical, Nonlinear, and Soft Matter Physics 87 (1), 12725.

Palm, M.M., Merks, R.M.H., 2015. Large-scale parameter studies of cell-based models of tissue morphogenesis using CompuCell3D or VirtualLeaf. In: Nelson, C.M. (Ed.), Tissue Morphogenesis of Methods in Molecular Biology, vol. 1189. Springer, New York, NY, pp. 301–322.

Radszuweit, M., Block, M., Hengstler, J., Schöll, E., Drasdo, D., May 2009. Comparing the growth kinetics of cell populations in two and three dimensions. Physical Review E: Statistical, Nonlinear, and Soft Matter Physics 79, 051907.

Richardson, D., 1973. Random growth in a tessellation. In: Mathematical Proceedings of the Cambridge Philosophical Society, vol. 74. Cambridge Univ Press, pp. 515–528.

Rivet, J.-P., Boon, J.P., 2005. Lattice Gas Hydrodynamics.

Roeder, I., Loeffler, M., August 2002. A novel dynamic model of hematopoietic stem cell organization based on the concept of within-tissue plasticity. Experimental Hematology 30, 853–861.

Rothman, D.H., Zaleski, S., 2004. Lattice-Gas Cellular Automata: Simple Models of Complex Hydrodynamics.

Rubenstein, B.M., Kaufman, L.J., December 2008. The role of extracellular matrix in glioma invasion: a Cellular Potts Model approach. Biophysical Journal 95, 5661–5680.

Savill, N.J., Hogeweg, P., February 1996. Modelling morphogenesis: from single cells to crawling slugs. Journal of Theoretical Biology 184, 229–235.

Scianna, M., Preziosi, L., 2012. A Hybrid Model Describing Different Morphologies of Tumor Invasion Fronts.

Scianna, M., Preziosi, L., 2013. Cellular Potts Models: Multiscale Extensions and Biological Applications. CRC Press.

Shirinifard, A., Gens, J.S., Zaitlen, B.L., Poplawski, N.J., Swat, M., Glazier, J.A., 2009. 3D multi-cell simulation of tumor growth and angiogenesis. Plos One 4 (10), e7190.

Starruß, J., de Back, W., Brusch, L., Deutsch, A., May 2014. Morpheus: a user-friendly modeling environment for multiscale and multicellular systems biology. Bioinformatics 30, 1331–1332.

Swat, M.H., Thomas, G.L., Belmonte, J.M., Shirinifard, A., Hmeljak, D., Glazier, J.A., 2012. Multi-scale modeling of tissues using CompuCell3D. In: Asthagiri, A.R., Arkin, A.P. (Eds.), Comput. Methods Cell Biol. Academic Press, pp. 325–366.

Swat, M.H., Belmonte, J., Heiland, R.W., Zaitlen, B.L., Glazier, J.A., Shirinifard, A., 2014. Compu-Cell3D Reference Manual 3.7.3.

Szabó, A., Merks, R.M.H., 2013. Cellular Potts Modeling of tumor growth, tumor invasion and tumor evolution. Frontiers in Oncology.

Tektonidis, M., Hatzikirou, H., Chauviere, A., Simon, M., Schaller, K., Deutsch, A., 2011. Identification of intrinsic in vitro cellular mechanisms for glioma invasion. Journal of Theoretical Biology 287 (1), 131–147.

Turner, S., Sherratt, J.A., may 2002. Intercellular adhesion and cancer invasion: a discrete simulation using the extended Potts Model. Journal of Theoretical Biology 216, 85–100.

Van Liedekerke, P., Palm, M.M., Jagiella, N., Drasdo, D., November 2015. Simulating tissue mechanics with agent-based models: concepts, perspectives and some novel results. Computational Particle Mechanics 2, 401–444.

Williams, T., Bjerkness, R., 1972. Stochastic model for abnormal clone spread through epithelial basal layer. Nature Physical Science 236, 19–21.

Yates, C.A., Baker, R.E., 2013. Isotropic model for cluster growth on a regular lattice. Physical Review E: Statistical, Nonlinear, and Soft Matter Physics 88 (2).

This book belongs to Central Library BADJI Mokhtar-ANNABA UNIVERSITY

Copyright Elsevier 2024

Chapter 13

Multiscale Agent-Based Computer Models in Skeletal Tissue Regeneration

S. Checa
Charité – Universitätsmedizin Berlin, Berlin, Germany

13.1 INTRODUCTION

Skeletal tissue regeneration is a highly important and fascinating process. After an injury, in most cases, the skeleton is able to self-regenerate and reach its initial function without leaving any type of scar tissue. However, there are cases in which its regeneration capacity is delayed or impaired (e.g., large bone defects due to trauma or cancer). The treatment of these situations still remains a clinical challenge. Understanding the mechanisms behind endogenous skeletal regeneration is highly important for the development of treatment strategies for these compromised conditions.

Skeletal regeneration is a highly complex and dynamic process that occurs at many different time and length scales (Einhorn and Gerstenfeld, 2015). An array of processes at the intracellular, cellular, and tissue scales are coordinated to regain skeletal function after injury. Experimental studies can provide detailed insights into specific processes taking place during the healing cascade (e.g., expression of specific growth factors, temporal mineralization of the callus); however, they are usually focused on individual processes that take place at a single length scale. Computer models allow to integrate the processes and to investigate the contribution of each individual process to the healing outcome and the interactions of processes occurring at the different length and time scales.

Early computer models of bone healing focused on the tissue scale to investigate the dynamics of tissue formation patterns over the course of healing and how it is influenced by factors such as fracture size, fixation stability, and external loading (Isaksson et al., 2006). Over the years, these models have been progressively extended to take into account the different scales and to investigate the emergence of tissue patterns as a result of processes occurring at the lower length scales (Byrne et al., 2011). Most recent models make use of agent-based modeling approaches because they allow to simulate individual entities (e.g., cells), their heterogeneity (e.g., different cell phenotypes), their interactions (e.g., cell-cell signaling), the emergence of structures at higher length scales (e.g., tissue organization), and situations of adaptation and learning (e.g., adaptation to the environment), none of which is easy to do with other type of modeling approaches.

We describe the main components of agent-based models (ABMs) and how they can be used to investigate skeletal tissue regeneration in the following sections. We make emphasis on the multiscale nature of the process and the integration of the different scales.

13.2 COMPONENTS OF AGENT-BASED MODELS AND THEIR APPLICATION TO SKELETAL REGENERATION

ABMs are based on the simulation of the system under investigation using two main components: the agents and the environment. The behavior of these two components then evolves over the simulation time using logical statements and equations, often called "rules."

Numerical Methods and Advanced Simulation in Biomechanics and Biological Processes. https://doi.org/10.1016/B978-0-12-811718-7.00013-7
Copyright © 2018 Elsevier Ltd. All rights reserved.

This book belongs to Central Library BADJI Mokhtar-ANNABA UNIVERSITY
Copyright Elsevier 2024

13.2.1 Cells as Agents

An agent is an entity that is situated in some environment and that is capable of autonomous action in this environment (Wooldridge and Jennings, 1995). In the context of skeletal tissue regeneration, a "cells-as-agents" paradigm is usually used, where each agent represents an individual cell that performs a series of processes (e.g., migrates, proliferates, differentiates) based on the conditions of the environment (e.g., surrounding extracellular matrix (ECM)) (Checa et al., 2011; Byrne et al., 2011). A number of properties can then be assigned to each individual agent (e.g., cell phenotype, age), which allows to represent the highly heterogeneous cell population that exists during the regeneration process (Fig. 13.1). With the simulation time, the properties of each agent evolve according to the set rules (see Section 2.3).

13.2.2 The Environment

The environment is the space in which the agents reside and interact. It is usually represented as a grid in which each position represents a possible position for an agent to occupy (Fig. 13.1; Wooldridge and Jennings, 1995; Checa et al., 2011). Beside the agents, the environment contains information about the local properties in each location (e.g., the amount of a specific growth factor, the properties of the ECM). Computationally, it can be implemented using matrix notation, in which each position in the matrix represents a grid position of the environment. In this way, each matrix "element" contains all the information about the environment and the agent at that location (Fig. 13.2).

13.2.3 The "Rules"

Conditional "if-then" statements and "for" and "while" loops are often used to simulate temporal changes in the properties of the agents and the environment (Prendergast et al., 2011). These rules aim to simulate the behavior of the cells over the course of healing. Rules might result in changes in the location of the agent, its properties, and/or the properties of the surrounding ECM. They can also take into account the influence of the surrounding environment on the reaction of the cell that allows to simulate cell−cell and cell−ECM interactions, highly important in bone regeneration.

Rules are established based on experimental observations of the processes being modeled. For example, if experimentally it is known that mesenchymal stem cells differentiate into osteoblasts only under defined ranges of ECM stiffness, this can be implemented as a rule that in pseudocode could look like:

```
IF (cell_phenotype[i][j]=mesenchymal_stem_cell) AND (A<stiffness_ECM[i][j]<B) THEN
    Cell phenotype[i][j]=osteoblast
END
```

where *cell_phenotype* and *stiffness_ECM* are two matrices containing information about the location of the cells and the mechanical properties of the ECM, respectively; and *i* and *j* indicate the location within those matrices. In this rule, the environment, defined by the rigidity of the ECM, determines cell phenotype.

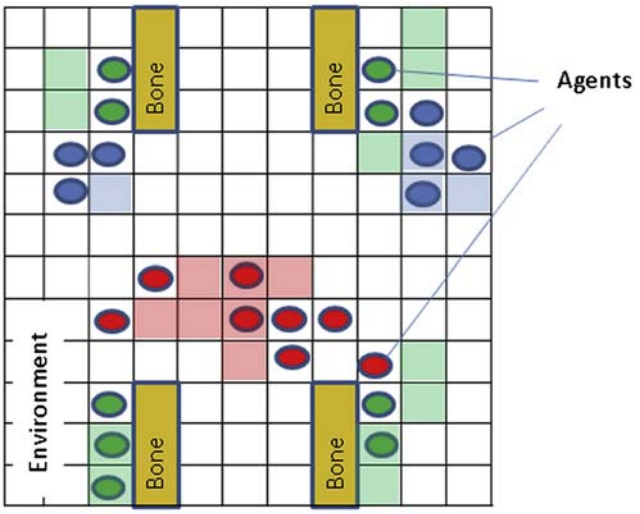

FIGURE 13.1 Schematic representation of agents, representing different cell phenotypes (e.g., osteoblasts, chondrocytes, and stem cells), in their environment, i.e., the extracellular matrix produced during bone regeneration.

This book belongs to Central Library BADJI Mokhtar-ANNABA UNIVERSITY Copyright Elsevier 2024

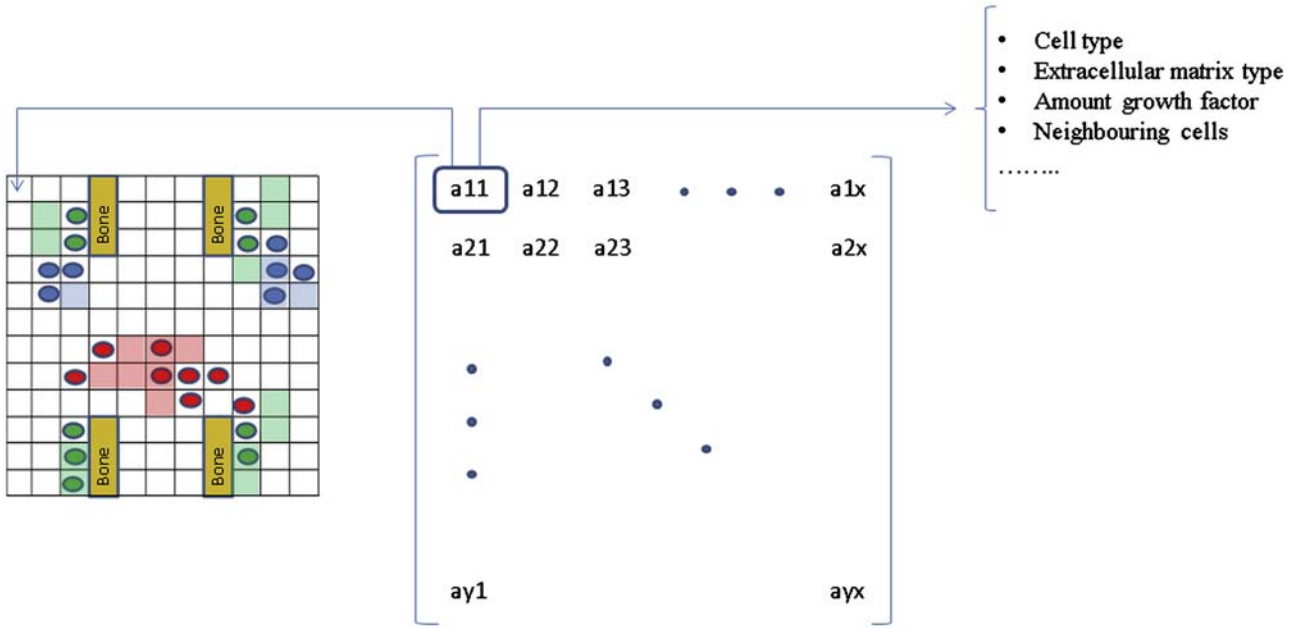

FIGURE 13.2 Matrix representation of the environment of an agent-based model. Each element matrix contains information about the properties of the environment and the agent at that location.

13.3 CONSIDERING PROCESSES AT THE DIFFERENT LENGTH AND TIME SCALES

As most biological processes, skeletal tissue regeneration occurs at many different time and length scales. The formation of new tissues over the course of skeletal regeneration is an emergent behavior from processes occurring at the cellular and subcellular levels (Einhorn and Gerstenfeld, 2015). A natural way of incorporating all these processes into an agent-based computer model is to use a cell-centered approach where agents are used to represent the individual cells and variables to describe properties and their temporal changes at the different time and length scales.

13.3.1 Simulations at the Cellular Level

The bone healing cascade initiates with the recruitment of cells from the surrounding tissues. Over time, these cells migrate, proliferate, differentiate, synthesize ECM, and secrete a myriad of factors that further influence cellular behavior. Computer models of bone regeneration aim to simulate these cellular processes and to understand interactions between them. Usually models are initiated by "seeding" specific cells at different locations within the healing region. For example, at the beginning of the bone healing process, cells are usually considered to originate from the periosteal and bone marrow side (Checa et al., 2011; Borgiani et al., 2015). To achieve this, initial cell locations are identified within the matrix configuration and the specific cell type assigned to those positions (Fig. 13.3A). Cellular migration can then be modeled as the movement of the agents to adjacent positions (Fig. 13.3B) following a set of rules. These rules can consider the directed migration of the cells due to chemotaxis (response to soluble cues), haptotaxis (response to graded adhesion to the ECM), and/or durotaxis (response to mechanical signals in the environment). In addition, different migration behaviors (e.g., migration speed) can be assigned to different cell phenotypes (e.g., stem cells, osteoblasts). Cell proliferation can be modeled through the replication of the agents, so that one agent divides into two agents occupying two different adjacent locations (Fig. 13.3C). The differentiation of the cells into a different phenotype can be implemented as a change in the type of agent at the specific location (Fig. 13.3D). This process is known to be influenced by many factors; however, most computer models have so far focused on investigating the influence of the mechanical environment on cell differentiation (Checa et al., 2011; Byrne et al., 2011; Borgiani et al., 2015; ORelly et al., 2016).

13.3.2 Emergent Behavior at the Tissue Scale

At the tissue level, different types of tissues form over the course of healing, providing the extracellular environment for the cells. In agent-based approaches, the ECM is simulated using the environment. Generally, it is assumed that cells

This book belongs to Central Library BADJI Mokhtar-ANNABA UNIVERSITY Copyright Elsevier 2024

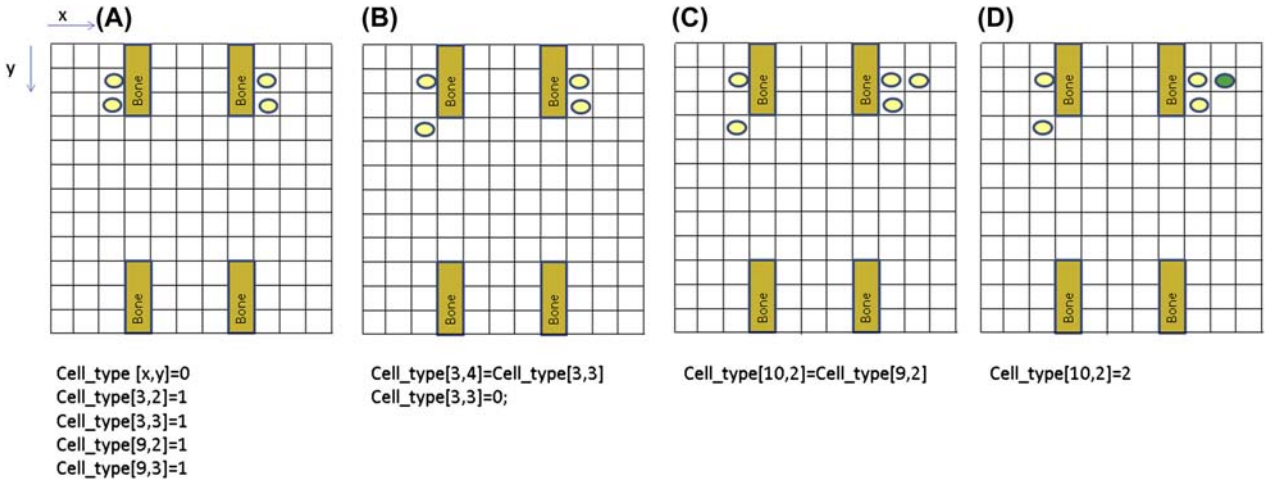

FIGURE 13.3 Schematic representation of the implementation of different cellular activities in the matrix used for the implementation of an agent-based model. (A) Cell initialization. (B) Cell migration. (C) Cell proliferation. (D) Cell differentiation.

produce ECM in their neighboring positions, following a set of rules that consider the rate of ECM production, its properties, and the location (Checa et al., 2011; Byrne et al., 2011; Borgiani et al., 2015). Therefore, the organization of the ECM is determined by the processes at the lower length scales. The properties of the ECM can then evolve over time to simulate tissue maturation or ECM resorption.

13.3.3 Cellular Activity Driven by Intracellular Processes

Ultimately, cellular activity is driven by intracellular processes. Over time, cells signal through their surface receptors based on the presence of available stimulatory ligands on the position they occupy and secrete factors that become variables of the environment. Each agent can then contain unique intracellular protein levels that control the behavior of that specific cell. The effect of the intracellular processes on the cell state can then be determined based on the levels of the receptors or the proteins. To date, almost all computer models of skeletal regeneration ignore this biological scale. Only the model of Carlier et al. (2012) includes a subcellular component to investigate lateral inhibition of endothelial cells. They used an agent-based approach to simulate blood vessel ingrowth, which they coupled to a continuum-based computer model of bone regeneration.

The following example aims to illustrate how processes at the intracellular, cellular, and tissue levels can be integrated using an agent-based approach. The model assumes that a cell can have two states (active: green or inactive: red) based on the level of an activated receptor (R_{act}). The native cell surface receptor (R_{nat}) is activated by a ligand (L). The activated receptor then promotes an intracellular pathway (P_{int}), which in turn inhibits the native cell surface receptor of the neighboring cell. The ECM is represented as a regular square grid where a gradient of ligand is present. Making use of equations, the model determines the levels of activation of the different receptors at each time point, which in turn control the cell state. Simulation of the system leads to a checkerboard pattern, where active and inactive cells alternate in space (Fig. 13.4).

13.4 DISCUSSION

In this chapter, we described how ABMs can be used to investigate the bone regeneration process at the different time and length scales (intracellular, cellular, tissue) and how the different scales can be coupled to investigate emergent behaviors.

One of the main challenges in computational modeling of biological systems, in general, is the identification of model parameters. Unfortunately, the parameters are difficult and often impossible to measure with experiments. In addition, some parameters have large variations among different experimental conditions. Parameter sensitivity studies provide a rigorous framework to test the influence of model parameters on the system behavior. In particular, in the field of skeletal regeneration, design of experiment methods have been used to identify the most important parameters in differential equation−based continuum computer models (Isaksson et al., 2008; Carlier et al., 2016). Parameter sensitivity in agent-based computer models of bone regeneration have been so far limited to single parameter analyses (Checa et al., 2011;

This book belongs to Central Library BADJI Mokhtar-ANNABA UNIVERSITY
Copyright Elsevier 2024

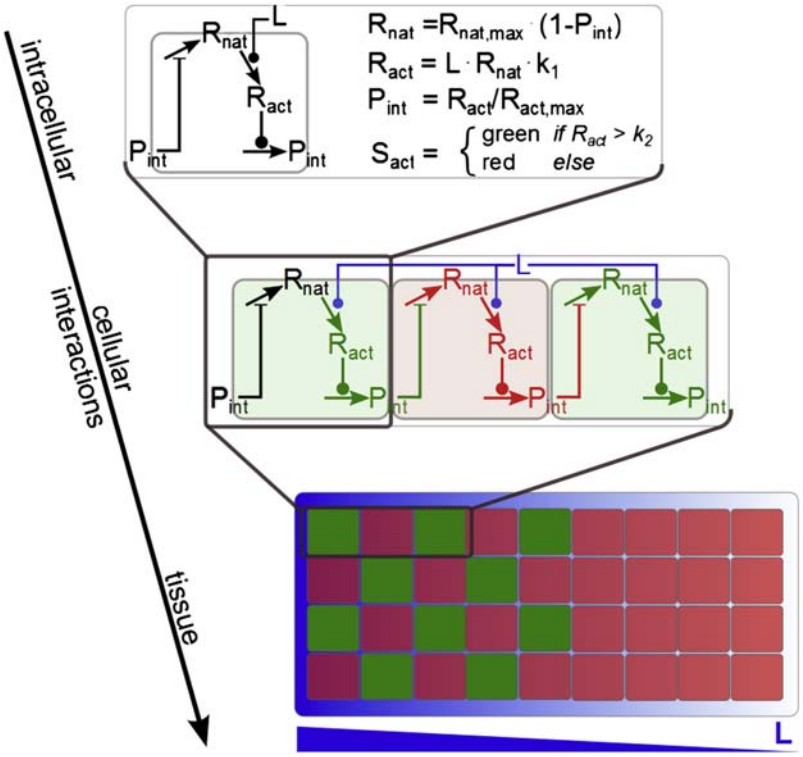

FIGURE 13.4 Multiscale agent-based model including processes at the intracellular, cellular, and tissue levels. k_1 *and* k_2, constants; L, ligand; P_{int}, intracellular pathway; R_{act}, active receptor; R_{nat}, native receptor.

Checa and Prendergast, 2009). More robust methods have been already applied to ABMs of other complex biological systems (Marino et al., 2008); their applicability to ABMs of bone healing remains to be determined.

Current trends in experimental studies are toward understanding dynamical pathways at the intracellular level and their relevance for bone regeneration (Xu et al., 2014). From a computer modeling perspective, most models have so far focused on processes taking place at the cellular and tissue scales. Future computational studies should contribute toward the understanding of interactions taking place at the intracellular level and their consequences at the cell and tissue levels.

ACKNOWLEDGMENTS

The author would like to thank Dr. Clemens Kühn for helping with preparation of Fig. 13.4. This work was supported by the German Research Foundation (CH 1123/4-1).

REFERENCES

Borgiani, E., Georg, D., Willie, B., Checa, S., 2015. Bone healing in mice: does it follow generic mechano-regulation rules? Facta Universitatis. Series: Mechanical Engineering 13, 217−227.

Byrne, D.P., Lacroix, D., Prendergast, P.J., 2011. Simulation of fracture healing in the tibia: mechanoregulation of cell activity using a lattice modeling approach. Journal of Orthopaedic Research 29, 1496−1503.

Carlier, A., Geris, L., Bentley, K., Carmeliet, G., Carmeliet, P., Van Oosterwyck, H., 2012. MOSAIC: a multiscale model of osteogenesis and sprouting angiogenesis with lateral inhibition of endothelial cells. PLoS Computational Biology 8, e1002724.

Carlier, A., Brems, H., Ashbourn, J.M.A., Nica, I., Legius, E., Geris, L., 2016. Capturing the wide variety of impaired fracture healing phenotypes in neurofibromatosis type 1 with eight key factors: a computational study. Scientific Reports 6.

Checa, S., Prendergast, P.J., 2009. A mechanobiological model for tissue differentiation that includes angiogenesis: a lattice-based modeling approach. Annals of Biomedical Engineering 37, 129−145.

Checa, S., Prendergast, P.J., Duda, G.N., 2011. Inter-species investigation of the mechano-regulation of bone healing: comparison of secondary bone healing in sheep and rat. Journal of Biomechanics 44, 1237−1245.

This book belongs to Central Library BADJI Mokhtar-ANNABA UNIVERSITY Copyright Elsevier 2024

Einhorn, T.A., Gerstenfeld, L.C., 2015. Fracture healing: mechanisms and interventions. Nature Reviews Rheumatology 11, 45–54.

Isaksson, H., Wilson, W., Van Donkelaar, C.C., Huiskes, R., Ito, K., 2006. Comparison of biophysical stimuli for mechano-regulation of tissue differentiation during fracture healing. Journal of Biomechanics 39, 1507–1516.

Isaksson, H., Van Donkelaar, C.C., Huiskes, R., Yao, J., Ito, K., 2008. Determining the most important cellular characteristics for fracture healing using design of experiments methods. Journal of Theoretical Biology 255, 26–39.

Marino, S., Hogue, I.B., Ray, C.J., Kirschner, D.E., 2008. A methodology for performing global uncertainty and sensitivity analysis in systems biology. Journal of Theoretical Biology 254, 178–196.

OReilly, A., Hankenson, K.D., Kelly, D.J., 2016. A computational model to explore the role of angiogenic impairment on endochondral ossification during fracture healing. Biomechanics and Model in Mechanobiology 15, 1279–1294.

Prendergast, P.J., Checa, S., Lacroix, D., 2011. Computational models for tissue differentiation. In: De, S., Guilak, F., Mofrad, M. (Eds.), Computational Methods in Biomechanics, 3. Springer, New York, pp. 353–372.

Wooldridge, M., Jennings, N.R., 1995. Intelligent agents – theory and practice. Knowledge Engineering Review 10, 115–152.

Xu, H., Duan, J., Ning, D., Li, J., Liu, R., Yang, R., Jiang, J.X., Shang, P., 2014. Role of Wnt signaling in fracture healing. BMB Reports 47, 666–672.

This book belongs to Central Library BADJI Mokhtar-ANNABA UNIVERSITY

Copyright Elsevier 2024

Chapter 14

Off-Lattice Agent-Based Models for Cell and Tumor Growth: Numerical Methods, Implementation, and Applications

P. Van Liedekerke[1,*], A. Buttenschön[2,*] and D. Drasdo[1,*]
[1]INRIA Paris & Sorbonne Universités UPMC Univ Paris 6, Paris, France; [2]University of Alberta, Edmonton, AB, Canada

14.1 INTRODUCTION

In lattice-free models, cells are represented by a single particle or clusters of particles, which can continuously move in space. As in lattice-based models, cells have the ability to grow, migrate, divide, and die. Among lattice-free models, one can roughly distinguish between center-based models (CBMs) and deformable cell models (DCMs). By using the term "lattice-free," we mean there is no fixed Eulerian underlying computational mesh to calculate the cells' movement. Some off-lattice models may still contain the concept of mesh in the strict sense, as a network of connected nodes (see Section 14.3). In CBMs, the interaction of cells is usually described by pairwise forces or energies functions defined between cell centers, while cell shape is not resolved precisely. DCMs consider also the intracellular forces and permit a representation of complex cell shapes.

We will focus here on force-based models, described by an equation of motion. The dynamics of a system of cells can also be mimicked using *energy-based* methods using numerical procedures, which are used also for, e.g., the CPM (see Chapter 12). The advantages of force-based models is that they have a straightforward definition of time and a more intuitive way of taking complex interactions of cells with other cells or their environment into account. In this equation of motion, there is usually a well-defined probabilistic and deterministic part. The level of stochasticity is tunable. For example, the dynamics of erythrocytes in blood plasma is described by both stochastic fluctuations and the biomechanical properties of the cells and the environment. At very small scales, stochastic events are immanent and can be quantified by principles of statistical physics. A lot of these principles are also applied in ABM dynamics (although this is not always physically or biologically justified).

This chapter starts with CBMs followed by DCMs (see Section 14.2 and 14.3, respectively). At the end, we also briefly explain some basic principles of hybrid models (Section 14.4). A conclusion with pros and cons, together with current available software, is given at the end of the sections.

14.2 CENTER-BASED MODELS

CBMs have been used with remarkable success for several decades. With cell numbers starting from few and ranging to more than 10^6 on a single processor machine, their simulation scale range is "subtissue," i.e., monolayers, small tumors, and representative tissue units. Typical application fields are tumors (Hoehme and Drasdo, 2005; Galle et al., 2006; Drasdo et al., 2007; Macklin et al., 2012), intestinal crypts and epithelial tissues (Buske et al., 2011, 2012; Dunn et al., 2013; van der Wath et al., 2013; Pin et al., 2015; van Leeuwen et al., 2007; D'Antonio et al., 2013), cell migration in

* This is author footnote.

Numerical Methods and Advanced Simulation in Biomechanics and Biological Processes. https://doi.org/10.1016/B978-0-12-811718-7.00014-9
Copyright © 2018 Elsevier Ltd. All rights reserved.

This book belongs to Central Library BADJI Mokhtar-ANNABA UNIVERSITY
Copyright Elsevier 2024

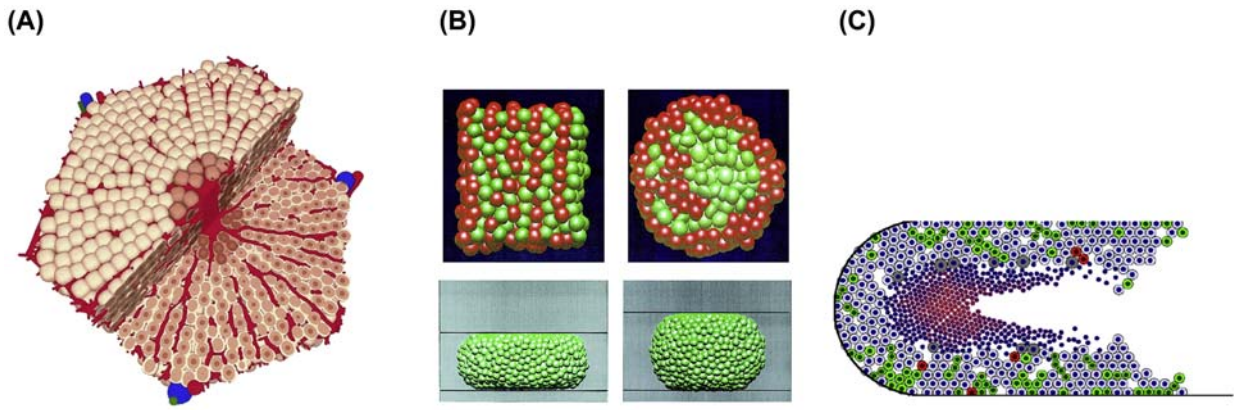

FIGURE 14.1 Achievements of simulations with center-based models. (A) Simulation snapshot of a regenerating liver lobule (the smallest functional and anatomical repetitive unit of liver) after drug-induced damage in the center of the lobule (Hoehme et al., 2010). (B) Simulation cell sorting and compression of a small spheroid using cell models with ellipsoidal shapes (Palsson and Othmer, 2000). (C) Simulation of in situ ductile carcinoma (Macklin et al., 2012).

extracellular matrix (ECM) (Zaman et al., 2005; Rangarajan and Zaman, 2008; Schluter et al., 2012), wound healing (Rey and García-Aznar, 2013; Vermolen and Gefen, 2012), tissue regeneration (Hoehme et al., 2010), and even tissue rheology (Pathmanathan et al., 2009; Basan et al., 2011). Despite the fact that the mechanical information that can be extracted from these models is rather approximate, various biomechanical aspects in these problems have been explained (see Fig. 14.1).

14.2.1 Equation of Motion

In CBMs, cells are represented by simple geometrical bodies. In formal analogy to physical particles, the assumption is that each trajectory of a cell in space can be described by an equation of motion. At first sight, this leads to Newtonian dynamics (second-order system) and the cell positions can be computed using integration algorithms typically used for molecular dynamics. In microscopic biological systems, it is supposed that inertia effects can be neglected as the Reynolds numbers are very small, meaning friction dominates the system (Odell et al., 1981). The drop of acceleration terms in the equations of motion leads to a first-order coupled system, which requires a more complex solving algorithm (see Section 14.2.7), but allows the usage of a larger time step. In the overdamped limit, the basic equation considering forces between cells and forces between cells and substrate reads for cell i

$$\mathbf{\Gamma}_i^{cs}\mathbf{v}_i + \sum_j \mathbf{\Gamma}_{ij}^{cc}(\mathbf{v}_i - \mathbf{v}_j) = \sum_j \mathbf{F}_{ij}^{int} + \mathbf{F}_i^{sub} + \mathbf{F}_i^{mig} + \mathbf{F}_i^{chem}. \tag{14.1}$$

On the left-hand side, we find the friction forces of cell with the substrate (first term) and other cells (second term). On the right-hand side, we have the forces on the cell emerging from repulsion or adhesion with other cells j and substrate, respectively $\mathbf{F}_{ij}^{\text{int}}$ and $\mathbf{F}_{ij}^{sub}$, as well as the cell migration forces $\mathbf{F}_i^{mig}$ and chemotaxis forces $\mathbf{F}_i^{chem}$. These are discussed in detail below. The friction terms involve tensors for the cell−cell friction ($\mathbf{\Gamma}_{ij}^{cc}$) and cell−substrate friction ($\mathbf{\Gamma}_i^{cs}$), which can represent ECM, capillaries or membranes.

If friction coefficients parallel and normal to the movement direction are different, the friction tensor becomes

$$\mathbf{\Gamma}_{ij} = \gamma_\perp(\mathbf{u}_{ij}\otimes\mathbf{u}_{ij}) + \gamma_{||}(\mathbf{I} - \mathbf{u}_{ij}\otimes\mathbf{u}_{ij}), \tag{14.2}$$

with $\mathbf{u}_{ij} = (\mathbf{r}_i - \mathbf{r}_j)/\|\mathbf{r}_i - \mathbf{r}_j\|$, where $\mathbf{r}_i$, $\mathbf{r}_j$ denote the position of the centers (see Fig. 14.2) of cell i and object j ($\otimes$ denotes the dyadic product, $\mathbf{I}$ is the $d \times d$ identity matrix with d the number of spatial dimensions). Note that, if object j denotes another cell, this would correspond to the superscript "cc," otherwise to the superscript "cs." Friction with ECM (s = ECM) is usually assumed to be isotropic, meaning that the cell−substrate friction matrix is diagonal. If cells move on a flat substrate, the substrate can be viewed as a sphere with infinite radius. Furthermore, $\gamma_\perp$ denotes perpendicular and $\gamma_{||}$ parallel friction. This can be seen after multiplication of the friction tensor with the cell velocity:

$$\mathbf{\Gamma}_{ij}\mathbf{v}_i = \Big(\gamma_\perp(\mathbf{u}_{ij}\otimes\mathbf{u}_{ij}) + \gamma_{||}(\mathbf{I} - \mathbf{u}_{ij}\otimes\mathbf{u}_{ij})\Big)\mathbf{v}_i = \gamma_\perp\mathbf{u}_{ij}(\mathbf{u}_{ij}\mathbf{v}_i) + \gamma_{||}(\mathbf{I}\mathbf{v}_i - \mathbf{u}_{ij}(\mathbf{u}_{ij}\mathbf{v}_i)). \tag{14.3}$$

This book belongs to Central Library BADJI Mokhtar-ANNABA UNIVERSITY
Copyright Elsevier 2024

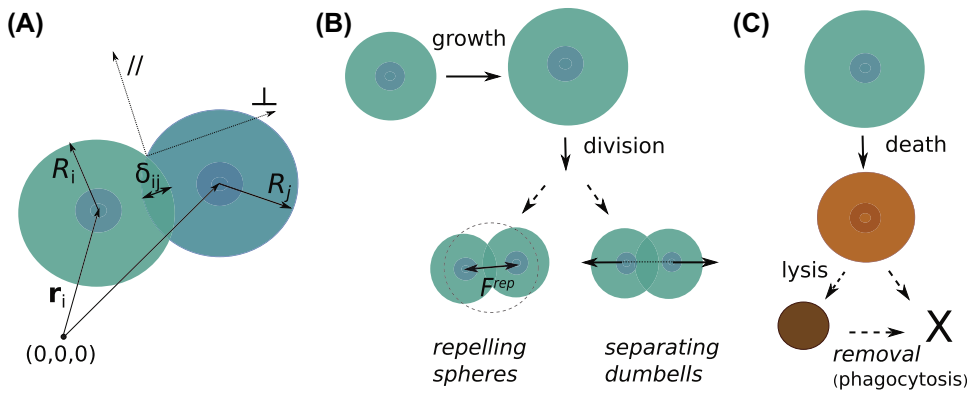

FIGURE 14.2 (A) Cartoon of center based model with cells represented as spheres, defining the basic contact variables. (B) Division of two cells in a center-based model. (C) Death and lysis.

Friction occurring in the perpendicular direction of the movement may be associated with internal friction, in particular if two cells are pushed against each other, which leads to deformation and reorganization of the cytoskeleton. Friction in the parallel direction is a description of the dissipative terms when the cell membranes slide along each other. The magnitude of the friction coefficients should be scaled with the contact area of the cell with another cell or the medium (see further).

Once all forces in Eq. (14.1) are known, we arrive at a linear problem described by a sparse symmetric matrix, which can be solved efficiently using the conjugate gradient method (see Box 14.2). Note further that the above system of equations of motion does not conserve total momentum. It basically assumes that momentum is not transferred to the substrate. This could be problematic if communication through elastic force fields between the cells mediated by the ECM would become important.

14.2.2 Cell Interaction Forces

The cells in CBM interact by pairwise potentials having a repulsive and adhesive part, which are characterized by a function of the geometrical overlap δ. A number of different approaches have been used for the interaction force, including linear springs (Drasdo and Forgacs, 2000; Drasdo and Loeffler, 2001; Meineke et al., 2001), a force derived from Lennard-Jones−like potentials (Basan et al., 2011), and a Hertz force approximating cells by isotropic homogeneous elastic bodies that are moderately deformed if pressed against each other (Galle et al., 2005; Hoehme and Drasdo, 2005). Here, we explain the latter approach and extensions based on it. Consider two spherical cells i and j, which are in each others' neighborhood (see Fig. 14.2). If the distance $d_{ij} = \|\mathbf{r}_j - \mathbf{r}_i\|$ between the cells becomes smaller than the sum of their radii, we assume a Hertzian contact force develops:

$$F_i^{rep} = 4 \Big/ 3\widehat{E}_i \sqrt{\widehat{R}_i}\,\delta_{ij}^{3/2}. \tag{14.4}$$

in which $\delta_{ij} = R_i + R_j - d_{ij}$ is the overlap between the cells and $\widehat{E}$ and $\widehat{R}$ are defined as

$$\widehat{E} = \left.\frac{1-\nu_i^2}{E_i} + \frac{1-\nu_j^2}{E_j}\right)^{-1} \text{ and } \widehat{R} = \left(\frac{1}{R_i} + \frac{1}{R_j}\right)^{-1} \tag{14.5}$$

with E_i and E_j being the Young's moduli, ν_i and ν_j the Poisson numbers, and R_i and R_j the radii of the cells i and j, respectively. Note that the radius of a cell is not constant if growth or necrosis is considered and must be recomputed from the actual volume V_i (see Section 14.2.4).

Galle et al. (2005) and Ramis-Conde et al. (2008) considered adhesion of cells to other cells or an underlying substrate by an additive term in the interaction energy, which is proportional to the Hertzian contact area, $A_{ij} = \pi\delta_{ij}\widehat{R}$ of the cells without adhesion, and the strength of the adhesion formed by bonds W. The magnitude of the adhesion force reads as follows:

$$F_i^{adh} = -\pi W \widehat{R}. \tag{14.6}$$

This book belongs to Central Library BADJI Mokhtar-ANNABA UNIVERSITY
Copyright Elsevier 2024

The total force $\mathbf{F}^{int} = \mathbf{F}^{rep} + \mathbf{F}^{adh}$ acts in the direction of the vector connection, the centers of the spheres. Note that $\mathbf{F}^{adh}$ does depend not on how much the cells actually overlap. This simplified approach, sometimes called "extended Hertz model," is convenient as it allows to express the force analytically. However, it neglects that adhesion is modifying the contact area and disregards that the force distribution within the contact area is inhomogeneous. A more realistic adhesive model taking this into account results from the Johnson−Kendal−Roberts (JKR) theory, which includes the hysteresis effect if the cells are separated from each other. JKR is an adhesion theory for solid adhesive soft spheres but can be applied realistically to cells (Chu et al., 2005). The force magnitude is computed by

$$F_i^{adh} = \frac{4\widehat{E}}{3\widehat{R}}[a(\delta_{ij})]^3 - \sqrt{8\pi\sigma\widehat{E}[a(\delta ij)]^3}. \tag{14.7}$$

The contact radius a in Eq. (14.7) must be obtained (from (Pathmanathan et al., 2009)):

$$\delta_{ij} = \frac{a^2}{\widehat{R}} - \sqrt{\frac{2\pi\sigma}{\widehat{E}}}a. \tag{14.8}$$

Compared with the JKR model, the modified Hertz model requires less computational effort because Eq. (14.8) should to be solved iteratively. However, the computational complexity of the JKR model can be reduced by nondimensionalizing Eqs. (14.7) and (14.8). The solution of the nondimensionalized JKR model can be fit to a third-order polynomial, with high accuracy. Thus, instead of the iterative method, a simple polynomial has to be computed.

A study of multicellular dynamics in monolayers reported an effect of the adhesion model choice (Drasdo et al., 2007). We note further that for high cell densities, neither JKR nor Hertz does realistically represent contact forces. This issue is further discussed in Section 14.2.6.

14.2.3 Cell Migration and Chemotaxis

The migration force $\mathbf{F}_i^{mig}$ is regarded as an active force. If no preferred migration direction of the cell is assumed, it is common to write it as a stochastic term with zero mean, which is uncorrelated at different points in time, i.e., $\left\langle \mathbf{F}_i^{mig} \right\rangle = 0$, $\left\langle \mathbf{F}_i^{mig}(t) \otimes \mathbf{F}_i^{mig}(t') \right\rangle = \mathbf{A}_i\delta(t-t')$. Here $\mathbf{A}_i$ is a $d \times d$ matrix that may be specific for each individual cell i. Using the formal analogy to colloidal particles in suspension, one obtains for the fluctuation magnitude

$$\left\langle \mathbf{F}_{||;i}^{mig}(t)\mathbf{F}_{||;i}^{mig}(t') \right\rangle = G_{||;i}\delta(t-t'), \tag{14.9}$$

$$\langle \mathbf{F}_{\perp;i}^{mig}(t)\mathbf{F}_{\perp;i}^{mig}(t') \rangle = G_{\perp;i}\delta(t-t'), \tag{14.10}$$

with $\mathbf{F}_{||;i}^{mig}(t) = (\mathbf{I} - \mathbf{u}_i \otimes \mathbf{u}_i)\mathbf{F}_i^{mig}$, $\mathbf{F}_{\perp;i}^{mig}(t) = (\mathbf{u}_i \otimes \mathbf{u}_i)\mathbf{F}_i^{mig}$. $G_{\|;i}$ and $G_{\perp;i}$ are scalars. $\mathbf{u}_i$ is the unit vector pointing into the direction of the cell movement. In colloidal particle physics, the autocorrelation amplitude of the noise is controlled by the friction coefficient and the thermal energy k_BT, k_B being the Boltzmann constant, T temperature, according to $G_{\|;i} = 4\gamma_{\|}k_BT$, $G_{\perp;i} = 2\gamma_{\perp}k_BT$. A formal analogy would lead to replacing k_BT by the membrane fluctuation strength F_T as proposed by Beysens et al. (2000). However, the mechanisms of cell movement cannot a priori be expected to follow the equipartition theorem of statistical mechanics. Cell migration is active, depending on the local matrix density and orientation; hence, we cannot claim the autocorrelation amplitude matrix $\mathbf{A}$ is properly described by the aforementioned analogy to colloidal particle movement. Instead, by measuring $\left\langle \left(\left(\mathbf{r}_i\left(t+\tau\right) - \mathbf{r}_i\left(t\right)\right) \otimes \left(\mathbf{r}_i\left(t+\tau\right) - \mathbf{r}_i\left(t\right)\right)\right) \right\rangle = 2\mathbf{D}\tau$, one can estimate the diffusion tensor $\mathbf{D}$ of the cell where again diffusion is not a consequence of collisions with smaller particles, but a parameter phenomenologically describing the cell spreading behavior. For a simple algorithm to simulate a force-based Brownian motion of a cell in an isotropic medium, see Box 14.1.

In a lot of cases, cells do have a degree of persistence in migration. Some authors describe this as a persistent random walk (PRW) model with inertia term $m_i d\mathbf{v}_i/dt$, mimicking the effect of a cell maintaining a certain direction with persistent time τ_p (Wu et al., 2014). The PRW model is actually a Langevin equation for which autocorrelation function for the cell velocity in one dimension $\langle v(t')v(0)\rangle = \frac{dD}{\tau}\exp(-t'/\tau)$ and hence the persistent time scales as $\tau_p \sim m_i/\gamma$.

This book belongs to Central Library BADJI Mokhtar-ANNABA UNIVERSITY
Copyright Elsevier 2024

BOX 14.1 Numerical Estimation of the Stochastic Force Term in the Langevin Equation

To obtain a force-based numerical representation of a Brownian motion for a particle or cell in a low Reynolds number environment in an isotropic medium, we start from the well-known relation for the square of the expectation value of the displacement vector of a Brownian particle, after a time interval Δt:

$$\left\langle \|\mathbf{r}\|^2 \right\rangle = 2dD\Delta t, \tag{14.11}$$

where D is the diffusion coefficient of the cell and d is the number of dimensions. We covert this to an equation for the force assuming overdamped motion using $\mathbf{F}^{mig} = \mathbf{v}/\gamma = \Delta\mathbf{x}/\gamma\Delta t$.

$$\left\langle \left|\left|\mathbf{F}^{mig}\right|\right|^2 \right\rangle \approx \frac{2dD\gamma^2}{\Delta t}, \tag{14.12}$$

with Δt the time step in the simulation. To get the actual force vector, at each step in the simulation, we pick a random unit vector $\boldsymbol{\eta}$ to obtain:

$$\mathbf{F}^{mig} = \sqrt{\frac{2dD\gamma^2}{\Delta t}}\boldsymbol{\eta} \tag{14.13}$$

The vector $\boldsymbol{\eta}$ must be taken with care to represent a true random direction (just normalizing three random numbers will introduce artifacts) (see, e.g., Marsaglia, 1972). Together with Stokes' formula, $\gamma = 6\pi\mu R$, we arrive at

$$\mathbf{F}^{mig} = 6\pi\mu R\sqrt{\frac{2dD}{\Delta t}}\boldsymbol{\eta} \tag{14.14}$$

where R is the cell radius and μ is the viscosity of the medium (e.g., ECM). Note that the diffusion coefficient D and the frictional resistance γ are normally related by the Einstein formula $D = k_B T/\gamma$. In violation with this, D and γ may be chosen independently in the simulation, reflecting that the diffusion coefficient regulating cell migration must be regarded as a parameter depending on the cell internal state.

The persistence as introduced above is actually an effect of inertia. Yet, it can also be modeled by introducing an extra memory term in the overdamped equations of motion. In this case, $\boldsymbol{\Gamma}_{ij}^{cx}\mathbf{v}_k$ ($x \in \{c, s\}$, $k \in \{i, j\}$) has to be replaced by $\int_{-\infty}^{\infty} \boldsymbol{\Gamma}_{ij}^{cx}(t-t')\mathbf{v}_k(t')dt'$, so that if $\boldsymbol{\Gamma}_{ij}^{cx}(t-t') = \boldsymbol{\Gamma}_{ij}^{cx}\delta(t-t')$, the basic equation of motion would be recovered (Drasdo, 2005).

A more fundamental way would be to consider the active force components explicitly that result in the preferential motion of cells. One can replace the uncorrelated noise by a force whose autocorrelation amplitude decreases over a period over which the cell has migrated a distance on the order of its diameter or even larger. Let us write $\mathbf{F}^{mig}$ as the vector $F_0^{mig}\mathbf{P}$ where F_0^{mig} is the magnitude of migration, which may depend on cell-specific and environment factors, such as the ECM fiber density. The active migration direction is defined by a polarity vector $\mathbf{P}$ for which the dynamics can be described by a Ornstein−Uhlenbeck process (Sepúlveda et al., 2013) for each cell i described by the equation:

$$\frac{d\mathbf{P}_i}{dt} = \frac{1}{\tau}(\mathbf{P}_{0,i} - \mathbf{P}_i) + \boldsymbol{\eta}_i, \tag{14.15}$$

where τ is the repolarization time, and $\mathbf{P}_{0,i}$ is the actual preferential direction of the cell. This direction may for instance depend on how the fibers are orientated in the ECM. In some models, one assumes that $\mathbf{P}$ tends to align with the actual velocity component of the cells or its neighboring cells (Szabó et al., 2006; Camley et al., 2014; Zimmermann et al., 2016).[1] The random noise component $\boldsymbol{\eta}_i$ reflects the probabilistic character of the movement and satisfies $\langle \boldsymbol{\eta}_i(t) \rangle = 0$.

Cells may have the tendency to move away from a cluster or monolayer, for example in invasive cancers or in closures of necrotic lesions. Such a "repulsive" interaction phenomenon is indeed present in many cell types on cell−cell

1. In 2D simulations, where cells are represented as discs, one can also define the polarity vector as $\mathbf{P}(\cos\alpha, \sin\alpha)$ and consider a stochastic equation for $d\alpha/dt = \Delta\alpha + \epsilon$, with $\Delta\alpha = \alpha_0 - \alpha$ defining the angular difference in direction between the actual cell velocity and current polarity, and the second last term reflecting the stochastic component, with $\langle \epsilon(t) \rangle = 0$ and $\langle \epsilon(t)\epsilon(t') \rangle = 2D_r\delta(t-t')$, D_r being the rotational diffusion coefficient.

This book belongs to Central Library BADJI Mokhtar-ANNABA UNIVERSITY
Copyright Elsevier 2024

contact and is known as contact inhibition of locomotion. In Hoehme et al. (2010), the assumption was that cells attempt to move away from cells of the same type, modeled by the additional term $\mathbf{F}_i^{CIL} = (1 - \Theta(\nabla p_i \boldsymbol{\eta}_i))\boldsymbol{\eta}_i$. Here $\Theta(x) = 1$ if $x \geq 0$, else $\Theta(x) = 0$, is the Heaviside step function, $\boldsymbol{\eta}_i$ again uncorrelated white noise. p_i is a pressure-like measure defined below (Eq. 14.20). The effect of this formula is that it inhibits all active moves that would increase cell density because the theta function becomes zero for such cases. Only active moves leading to a decrease of density can occur. Hence the expression reinforces cells to move toward empty spaces. A similar mechanism was used for simulating cells moving in epithelial layers (Camley et al., 2014; Smeets et al., 2016).

Similarly to migration behavior, chemotaxis, the effect of cells moving toward increasing concentrations of molecules, can be mimicked by a propulsion force that is proportional to a concentration gradient. Formally this is written as

$$\mathbf{F}_i^{chem} = \chi \nabla c \tag{14.16}$$

with χ being the chemotaxis coefficient, and $c(\mathbf{r}, t)$ the concentration of molecules assuming present or secreted by other cells (Hoehme et al., 2010). The concentrations are usually computed by solving reaction−diffusion equations, which may include source and sink terms at the cell positions. Some authors tried to avoid solving of these partial differential equations (PDEs) and included the effect of chemotaxis for a cell simply as distance function to neighboring cells (Boon et al., 2016).

14.2.4 Cell Growth, Division, and Death

During the cycle the volume of a mother cell roughly doubles before it splits into two daughter cells. The interphase adding up the G_1, S, and G_2 phase and mitosis phase may be described by an increase of the radius of the cell. However, several studies show that cell growth is not constant throughout the cell cycle (Neufeld and Edgar, 1998; Tzur et al., 2009; Mir et al., 2011; Kafri et al., 2013), with no consensus over a universal growth law. In a basic model assuming constant growth rate during the cell cycle, the volume V_i of cell i is updated every time step Δt as

$$V_i(t + \Delta t) = V_i(t) + \alpha_{const,i}\Delta t, \tag{14.17}$$

with $\alpha_{const,i}$ the growth rate. Alternatively, one could also assume that cell volume increases exponentially during the cell cycle:

$$V_i(t + \Delta t) = V_i(t) + V_i(t)\alpha_{\exp,i}\Delta t, \tag{14.18}$$

where we have $\alpha_{\exp,i} = \log(2)\alpha_{const,i}/V_{0,i}$.

If the cell passed a critical volume V_{crit} (doubled volume) or time point T_{div}, the cell undergoes mitosis and two new cells with volume $V_{crit,i}/2$ are created. During the *cytokinesis* process, several internal forces develop in the mother cell, involving the formation of an actin contractile ring at the cell equator (Turlier et al., 2014), which is a mechanism that cannot be fully captured by CBM but approximated in several ways.

In a first approach, the system of the two daughter cells is regarded as a rigid dumbbell with the cells gradually distancing each other (see Fig. 14.2B). Because dumbbells lack spherical symmetry, an additional equation of motion for rotation is in principle required, which maybe cumbersome to solve (Drasdo, 2005). Alternatively, this rotational motion may be regarded as striving to an energetically most favorable orientation, mimicked by an intermediate Monte Carlo dynamics using the Metropolis algorithm (Hoehme et al., 2010).

In a similar approach to division, cells entering the cell cycle are immediately represented as dumbbells, which gradually grow by increasing their distance from zero to twice the radius of the dumbbell spheres, when they separate into two spheres (Hoehme and Drasdo, 2010a; Basan et al., 2011). This algorithm has been found to generate only minor differences on timescales much larger than the cell cycle time, compared with the algorithm distinguishing between a spherical growth and a dumbbell deformation phase. A drastic simplification of the division algorithm consists of skipping the dumbbell transformation phase and placing directly two smaller daughter cells in the space originally filled by the mother cell at the end of the interphase (Schaller and Meyer-Hermann, 2005; Galle et al., 2005). This algorithm thus avoids dumbbell rotations but needs to be used with caution. When the two daughter cells are created, the Hertz interaction force will push away the two daughter cells until mechanical equilibrium is reached. If the space filled by the mother cell is small, which is often the case for cells in the interior of a cell population, the local interaction forces occurring after replacing the mother cell by two spherical daughters can adopt very large (unphysiological) values leading to unrealistic large cell displacements. This might partially be circumvented by intermediately reducing the forces between the daughter cells. Yet another problem is that cells in contact to the mother cell prior to replacing the mother cell by its daughter cells may lose contact as a consequence of the discontinuous local configuration change. For a cell at the border of a population,

This book belongs to Central Library BADJI Mokhtar-ANNABA UNIVERSITY
Copyright Elsevier 2024

this may lead to a detachment of the neighbor cell from the multicellular aggregate. Finally, note that the direction in which the cell divides may be chosen randomly, according to biological principles of the cells' environment or according to stress principles (see virial stress principle in the subsequent subsection).

During their cycle, cells take several decisions depending on certain external factors. In, e.g., contact inhibition, the cell cycle progression is controlled by the presence of other cells. Contact inhibition can be included in the model computing quantities for cell deformation, volume compression, or force and stress thresholds, each of which have proven to qualitatively predict growth limitation in tumor models (Drasdo et al., 1995; Hoehme and Drasdo, 2005; Galle et al., 2005; Schaller and Meyer-Hermann, 2005; Byrne and Drasdo, 2009; Hoehme et al., 2010; Hoehme and Drasdo, 2010a; Drasdo and Hoehme, 2012). For a cell in the interior of a multicellular aggregate, balance of forces usually leads to small distances of a cell to its neighboring cells, so a too large overlap is likely to correspond to a too large volume compression of that cell. Cells at the border can move and escape the compression, which is why border cells are not limited by this criterion. We mention, though, that the criterion that cell cycle progression can be inhibited at any time in the cycle (leaving cells in the interior of a multicellular aggregate arbitrarily long in the cell cycle) does not correspond to biological observation. Rather, a number of checkpoints are reported and generally accepted (e.g., G_1-, G_2-, M-checkpoints). Cells passing G_1-checkpoint are committed to pass the entire cell cycle.

If a cell dies, it will gradually lose its volume as a consequence of lysis and phagocytose (see Fig. 14.2C). In in vivo situations, macrophages are present to phagocytose the cell bodies, and the remains of the necrotic cell will be removed relatively quickly. This process may be modeled as a simple stochastic annihilation process with a certain waiting time T_{lys}, after which the cells is completely removed. Contrary, in in vivo experiments, there are no macrophages present and phagocytosis by neighboring cells is very slow (Jagiella et al., 2016). Here we could chose for a gradual decrease of the cell volume according to

$$V_i(t+\Delta t) = V_i(t) - V_i(t)\beta_i \Delta t, \tag{14.19}$$

with $\beta_i = 1/T_{lys}$. Depending on the situation, T_{lys} may range from several hours to several days (Cristini and Lowengrub, 2010).

14.2.5 Measures for Deformation, Stress, and Pressure

There are several possibilities to compute stresses and deformation in CBM. A straightforward quantity for deformation is the overlap function δ (see Eq. 14.4). This definition has been used in, e.g., Hoehme and Drasdo (2010a) to model contact inhibition effects in tumor spheroids. For mechanical stress, one can, using the contact forces and surface (contact) areas, calculate different pressure-related quantities (see Byrne and Drasdo, 2009; Schaller and Meyer-Hermann, 2005; Drasdo and Hoehme, 2012).

The disadvantage of these measures is that they only give a scalar measure but do not allow to calculate an entire stress tensor as in continuum theories. An estimation of a full cellular stress tensor can be obtained by introducing the concept of *virial stress*, deduced from theories in molecular dynamics to compute macroscopic stress originating from the interaction of many particles (Irving and Kirkwood, 1950). The general formulation of virial stress defines the average stress[2] in a box of particles due to contact forces $\mathbf{F}_{ij}^{int}$ with other particles by:

$$\sigma_i = \frac{1}{V}\sum_j \left(\mathbf{F}_{ij}^{int} \otimes \mathbf{r}_{ij}\right) \tag{14.20}$$

where $\mathbf{r}_{ij} = \mathbf{r}_j - \mathbf{r}_i$ and V is the *sampling* volume. In principal this volume needs to be large enough to obtain reliable averages over an ensemble of particles, yet one can still use it as an estimator for individual cell stresses, by taking the sampling volume as the volume of the cell and regarding $\mathbf{r}_{ij}$ as the vector pointing from the center of cell i to the contact plane with cell j, i.e., $\|\mathbf{r}_{ij}\| = (d_{ij} + R_i - R_j)/2$. The hydrostatic pressure p_i on a cell can now be computed by

$$p_i = \frac{1}{3}\mathrm{tr}(\sigma_i). \tag{14.21}$$

Eq. (14.20) defines a full stress tensor for the cell, which will allow extraction of more information than just a pressure. An example and the applicability of this method is given in Van Liedekerke et al. (2015). From the stress tensor, we can

2. This formula is not complete as the general formula of viral stress includes a kinetic term related to the temperature of the molecular particle system. For a system of cells, however, the latter term can be neglected and the stress corresponds to the Cauchy stress of the microscopic system (Ghysels et al., 2009).

This book belongs to Central Library BADJI Mokhtar-ANNABA UNIVERSITY Copyright Elsevier 2024

also derive the principal stress directions $\{n_1, n_2, n_3\}$ and eigenvalues $\{\sigma_1, \sigma_2, \sigma_3\}$ by diagonalization of Eq. (14.20), yielding important information on how stresses on the cells are oriented. The algorithm for diagonalization of Eq. (14.20) is trivial in 2D and not demanding in 3D, using e.g., Cardano's method.

14.2.6 Extensions and Solutions

Several extensions have been proposed to alleviate the limitations of CBM. To model more realistic cell shapes, Palsson and Othmer (2000), Palsson (2001), and Dallon and Othmer (2004) used ellipsoidal shapes with axial degrees of freedom resulting in deformability in three principal directions (Fig. 14.1). Herein the deformability was controlled by viscoelastic elements and the cell shape was adapted according to the forces that act on the cell. The ellipsoidal approach introduces anisotropy in the cells, but this comes at a price, as contact resolution between ellipsoids is expensive. In addition, artifacts can appear as the deformation depends on the relative orientation of the force vector and the fixed three principal directions. Note that anisotropy and polarity in cells can also be simulated in a rather simple fashion, by assigning a polarity vector to each cell. The vector indicates a cell has a preferential direction, polar adhesion, or biased motion (see, e.g., Hoehme et al., 2010). Explicit representation of filopodia, even if computationally costly, may become necessary, as performed in, e.g., Krinner (2010), who modeled filopodia with a CBM by lines radially stretched from the cell border in such a way that they may touch but not intersect with neighboring cells. A similar approach was proposed in Schluter et al. (2012) where the cells interact directly with individual collagen fibers, which are explicitly represented and can change direction.

A major issue in CBMs, often ignored in simulations, is that common pairwise contact forces (type Hertz, JKR, …) and contact areas become inaccurate when cells are densely packed, leading to errors and possible wrong results. The origin of this problem is that Hertz forces are defined pairwise and exclude the contributions from other interactions. They exclude any notion of cell volume, even when setting $\nu = 0.5$ in the Hertz (or JKR) force models in Eq. (14.5). Related to this point is that in a dense cell packing the Hertz contact area (or in the presence of adhesion the JKR contact area) does not represent anymore a good estimate of the contact area, as in a dense packing the contact regions of the central cell overlap with those of the neighbor cells, themselves neighbors of each other.

One general solution to this problem is the Voronoi tessellation approach, originally proposed by Honda, (1983) and Honda et al. (1984). Voronoi tessellations have been shown to produce realistic polygonal cell shapes and were considered by other authors in combination with center-based type modeling approaches (Drasdo et al., 1995; Meineke et al., 2001; Schaller and Meyer-Hermann, 2005; Kempf et al., 2010). A particular solution for the errors introduced by Hertz' law uses one of the key properties of Voronoi, namely an accurate representation cell volume. Defining a compression modulus $K_V = -V(\partial p/\partial V)$, with p and V the pressure and the volume on the polygonal cells, a volume corrected pairwise force term was proposed in Boulanger (2009). In a second approach, alleviating this problem that does not require Voronoi algorithms, the Young's modulus in Eq. (14.4) of the cells is artificially increased based on the average relative distance between neighboring cells, increasing the contact stiffness as more cells are around (Van Liedekerke et al., 2017).

14.2.7 Implementation

Simulations with CBM require a software with efficient and flexible data structure. Each cell may have a potentially high number of variables. After initializing variables and assigning initial conditions for the cells, the first step in the algorithm is to identify contacts between cells. A large part of the computational efforts will be spend in the *contact detection*, meaning that for each cell all possible contact partners have to be identified (i.e., update list of neighbors). The cost for this is usually $\mathcal{O}(N)$ up to $\mathcal{O}(N \log N)$ with $N =$ number of cells, when using proper searching algorithms such as grid search methods, bounding box sorting, or hierarchical trees (Hockney and Eastwood, 1988; Krijgsman et al., 2014). After contact detection, *contact resolution* is applied the overlap and forces are computed, which is particularly easy for spherical cells but may be nontrivial for other geometries. Once these forces are calculated, other variable such as stress and deformation can be updated. With this information, the cell can adapt its state or behavior (for example, if the cell pressure becomes too high, it may go into quiescence).

Once all forces are known, one can proceed with solving the system Eq. (14.1). In case cell−cell friction is ignored (Schaller and Meyer-Hermann, 2005; Milde et al., 2014), $\mathbf{v}_i$ is easily computed by $\mathbf{v}_i = \mathbf{F}_i/\gamma^{cs}$, where $\mathbf{F}$ is the total force on the cell and γ^{cs} denotes the cell−substrate friction coefficient. The computational effort of this is lower, but caution is needed with respect to the physical realism when one ignores these shear effects. If, on the other hand, cell−cell friction is included, one need to retrieve $\mathbf{v}_i$ by matrix solving of Eq. (14.1); for implementation details, see Box 14.2.

This book belongs to Central Library BADJI Mokhtar-ANNABA UNIVERSITY
Copyright Elsevier 2024

BOX 14.2 Conjugate Gradient in Agent-Based Models

The conjugate gradient is an iterative method to solve matrix equations, of the form $\mathbf{\Gamma v} = \mathbf{F}$, where $\mathbf{\Gamma}$ is symmetric and positive definite. The structure of the matrix is determined by the topology and the number of the cell interactions. This allows an implementation of the conjugate gradient, which does not require an explicit sparse matrix structure. Three different things have to be considered when using a conjugate gradient method: (1) the robustness of the stopping criterion, (2) the type of preconditioner, and (3) the bandwidth of the matrix $\mathbf{\Gamma}$.

Once the solution approximation is sufficiently accurate, the iteration should terminate. For this a so-called stopping condition is used. For an overview of commonly used stopping criteria, see Barrett et al. (1995). The selection of a robust stopping criteria can be challenging. This is because both the structure of the matrix $\mathbf{\Gamma}$ and the force vector $\mathbf{F}$ change between time steps. In addition, the magnitudes of the initial guess, the matrix entries, or the force vector may vary dramatically depending on the modeled situation. These restrictions disqualify many of the commonly used stopping criteria outlined in Barrett et al. (1995). In our experience a robust stopping criterion is the one proposed in Axelsson and Kaporin (2001). This criterion, however, requires an estimate of the smallest eigenvalue of the preconditioned matrix. This eigenvalue can be approximated by exploiting the relationship of the conjugate gradient with Lanczos algorithm (Meurant, 2006) and the algorithm for eigenvalues of a symmetric tridiagonal matrix outlined in Barth et al. (1967). This stopping criterion guarantees that

$$\|\mathbf{v} - \mathbf{v}_i\|_{\mathbf{\Gamma}} \leq \varepsilon \|\mathbf{v} - \mathbf{v}_0\|_{\mathbf{\Gamma}}, \tag{14.22}$$

where ε is the desired accuracy, $\mathbf{v}$ is the exact solution of the linear system, $\mathbf{v}_i$ is the ith solution approximation, and $\mathbf{v}_0$ is the initial solution guess. For an implementation of this criterion and further details, we refer to Axelsson and Kaporin (2001). The additional computational work encountered by using this criterion can be reduced by checking this criterion only every d iteration steps.

The speed of convergence of the conjugate gradient is determined by the ratio of the largest and smallest eigenvalue (Barrett et al., 1995). A preconditioner can be used to improve the speed of convergence by modifying the spectral properties of $\mathbf{\Gamma}$ (Barrett et al., 1995). The simplest preconditioner to implement is the diagonal preconditioner. However, more complicated preconditioners, such as an incomplete LU decomposition, are possible. Generally, convergence will be faster when the diagonal components of the friction matrix Γ are dominant.

Finally, the velocity vector is given by $\mathbf{v} = (v_1, \ldots, v_n)$, where v_k is the velocity vector of cell k. A naive ordering of this vector may result in a high bandwidth of matrix $\mathbf{\Gamma}$. A matrix's bandwidth impacts convergence speed of the conjugate gradient, with smaller bandwidths improving convergence (Benzi, 2002; Oliker et al., 2002). The entries of the matrix $\mathbf{\Gamma}$ represent cell interactions, which only occur when cells are in close proximity. Thus, grouping velocity vectors of cells that are in proximity of each other reduces the bandwidth of the friction matrix. Such an ordering is obtained by exploiting the information from the contact detection phase. While such an ordering is clearly better than a random ordering, it should be subject of future research to work out its detailed properties.

In the final step, the positions may be updated using a simple Eulerian integration scheme

$$\mathbf{r}_i(t + \Delta t) = \mathbf{r}_i(t) + \mathbf{v}_i(t)\Delta t \tag{14.23}$$

where $\mathbf{v}_i(t)$ is the velocity of the cell. The stability of the explicit Euler scheme is formally determined by the time step Δt.

$$\Delta t \leq C\frac{\gamma}{k} \tag{14.24}$$

where C is a prefactor, k is the stiffness of the system (e.g., Young modulus of the cells), and γ is the friction (e.g., cell−cell friction). Thus, in principle, the higher the friction, the higher one can choose the time step. Small time steps may put significant restrictions to the solvability in a mechanically stiff system when the timescale of interest is long (e.g., several days or weeks in tumor simulations), because the number of steps may become prohibitively high.

Generally, one can start with choosing a fixed time step that results in a stable simulation. Alternatively, one may also use adaptive time stepping schemes (Schaller and Meyer-Hermann, 2005). A very simple implementation of this is to define a maximum spatial step size Δr_{max}, usually taken as a fraction of the cell size. During every time step, it must be verified whether $\|\mathbf{v}_i(t)\Delta t\| < \Delta r_{max}$ holds for all cells. If this is the case then the time step Δt is kept; if not, then one has to go back to the previous step and lower the time step. On the other hand, one can also define a minimal spatial step size Δr_{min}, for which the time step is always increased if $\|\mathbf{v}_i(t)\Delta t\| < \Delta r_{min}$. This can result in a significant speedup. Note that Δr_{max} may need to be varied to the point until no further differences are observed in the simulation results.

This book belongs to Central Library BADJI Mokhtar-ANNABA UNIVERSITY Copyright Elsevier 2024

Another way to work around the time stepping problem is to modify certain physical parameters such that the simulation time can be shortened, but the dynamics remains unaffected. For example, suppose there are two timescales τ_1 and τ_2 in the system, with the first representing the characteristic mechanical relaxation of the cellular system and τ_2 the division time of the cells. The simulation is restricted by τ_2 and a large number of cell divisions are required to complete the simulation. In case it holds that $\tau_2 \gg \tau_1$, then one can shorten τ_2 artificially, such that this large separation in timescales remains valid. As such the simulation time can be decreased significantly.

To conclude this section, we shortly mention the current availability of software for CBMs. While a lot of researchers develop and maintain their own code for, several research groups have released tools for agent-based modeling in biology. For CBMs the most known are CellSys (Hoehme and Drasdo, 2010b), Chaste (Figueredo et al., 2013; Mirams et al., 2013), EPISIM (Sütterlin et al., 2013), Timothy (Cytowski and Szymanska, 2014, 2015), and Biocellion (Kang et al., 2014). All of these codes have their specific intentions and strengths. For instance, CellSys focuses on intracellular pathways and intends to address medical problems such as liver intoxication. Timothy and Biocellion intend to address large cell numbers ($>10^9$) with distributed computing. Most of the software can be linked to external libraries, such as SBML that provides ordinary differential equation models for intracellular dynamics (Hucka et al., 2003).

14.2.8 Conclusion

CBMs offer an entry level for force-based agent-based modeling. The cells are represented as simple geometrical objects, able to divide, migrate, and die. Because equations of motion are used, the cell position can be tracked continuously over time. The model can be parameterized by physically and biokinetic meaningful parameters that can, in principle, be measured. Large-scale simulations of tissues may not be feasible in an acceptable computational time, as usually at most around 10^6 cells can be simulated on a single core. Parallelization of the code can alleviate this problem, but this is a nontrivial task. On the other hand, cell shape in this model type is only represented statistically and the pairwise contact forces are generally not valid in systems with large cell density. In cellular systems where large deformations occur or cell shape is of particular importance, simulations with standard CBMs are not recommended and one needs to resort to corrections, extensions, or radically choose DCMs.

14.3 DEFORMABLE CELL MODELS

A number of authors have introduced a series of models, which can be categorized as DCMs. Force-based DCMs are able to capture the complex shapes of cells and quantify forces in great detail (Van Liedekerke et al., 2015). In the most basic model construction, the cell surface is discretized by a number of nodes (or vertices), which are connected by viscoelastic elements interacting via pairwise potential functions, thus creating a scaffolding structure with arbitrary degrees of freedom.

Significant research has been conducted for models of multicellular spheroids, invasive tumors, as well as normal development of epithelial ductal monolayers (Rejniak, 2007; Rejniak and Dillon, 2007; Dillon et al., 2008; Rejniak and Anderson, 2008; Jamali et al., 2010). Deformable models of erythrocytes are popular in blood flow simulations (Pivkin and Karniadakisa, 2008; Hosseini and Feng, 2009; Fedosov et al., 2010, 2011; Peng et al., 2013). Other topics include cell migration (Tozluolu et al., 2013; Kim et al., 2013), cell rheology (Sandersius and Newman, 2008), or even impact dynamics studying damage in cellular tissues (Van Liedekerke et al., 2010, 2011) (see Fig. 14.3 for some example

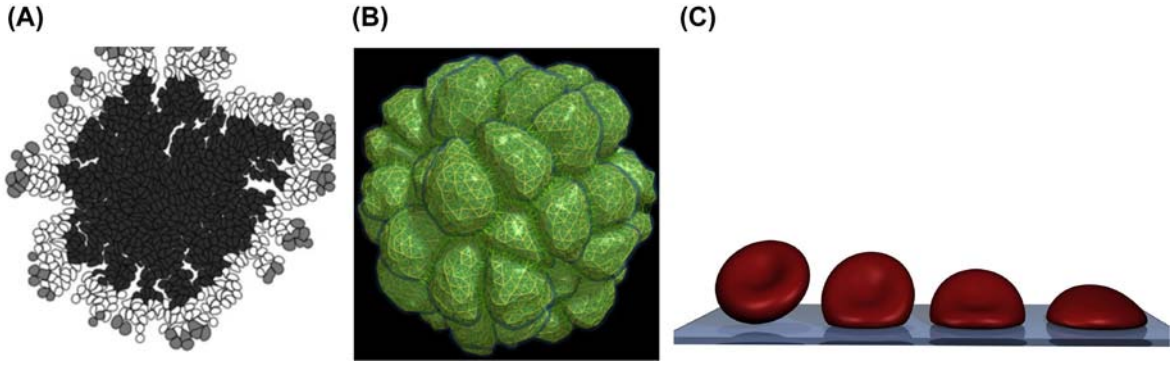

FIGURE 14.3 (A) Early work for deformable cell model (DCM) simulations of small tumors involving 2D DCM cells (Rejniak, 2007). (B) 3D DCM cells in a small cell cluster (Sandersius and Newman, 2008). (C) Simulations of cell adhesion dynamics (Odenthal et al., 2013).

This book belongs to Central Library BADJI Mokhtar-ANNABA UNIVERSITY Copyright Elsevier 2024

simulations). Because they can describe cellular mechanics at arbitrarily high detail, it could be argued that deformable cells models provide an ideal tool to investigate mechanotransduction, which is the mechanism by which cells transduce an external mechanical stimulus into an internal molecular signal.

Below, we give the basic ingredients for a DCM. We focus on a model subclass that clearly distinguishes a cell boundary for each cell. This is different from another class, called vertex models (VMs), for which the vertices form a polygonal tessellation (usually Voronoi) directly representing the common cell−cell interfaces. VMs are therefore rather suitable for tightly packed cell ensembles with negligible intercellular spaces. Most VMs represent either a cross section of an epithelial sheet, or just the apical surface of an epithelial sheet. Current VMs can handle cell growth and division, and some also incorporate rules that govern changes in connection among vertices, allowing simulation of topological changes in cell neighbor relations (e.g., T1 transitions) and alternating viscous behavior of the tissue. In VMs, one usually defines an energy function $\mathcal{U}$ that includes changes in cell area, volume, and interfacial tensions between the cells. Minimization of these energy function leads to equilibrium positions of the cells (Manning et al., 2010). Stochastic effects and fluctuations in VMs could in principle also be incorporated analogously to cellular Potts model simulations (Marmottant et al., 2009). This would involve a Metropolis algorithm, in which trial displacements are generated and accepted with a certain probability (Boltzmann factor). However, the temperature of these fluctuations, which scales the acceptance rate, is physically not sound, while in addition, timescales are not well defined. If one wants an accurate description of time-dependent phenomena, one must compute the forces on the nodes i using $\mathbf{F}_i = -\nabla_i \mathcal{U}$ and update the vertex positions by an equation of motion, i.e., $\gamma_i d\mathbf{r}_i/dt = \mathbf{F}_i$. This approach is formally very similar to the dynamics for DCM as described below, although friction between the nodes is usually not considered in VM. For an overview of VM algorithms, see Fletcher et al. (2013, 2014).

14.3.1 Equation of Motion

The network of nodes in each cell are coarse-grained viscoelastic elements that in combination, mimic the behavior of the cell. Some authors regard the cell merely as bulk assembly of interconnected nodes (Sandersius and Newman, 2008; Milde et al., 2014), whereas others do include a description of the boundary of the cell (see Fig. 14.3B). Here, we shall consider the basic building blocks of a model that represents cells as elastic shells (with cortex and plasma mechanical membrane), surrounding a homogeneous interior (cytoplasm). Although the description is not exhaustive and ignores subcellular structures such as nuclei and organelles, the same principles may be applied to include these as well.

As in CBM, the equation of motion in DCM can be read as a balance of forces and friction, and we hold the assumption that motion is overdamped. For each node i belonging to a cell, this balance reads

$$\sum_j \mathbf{\Gamma}_{ij}^{nn}(\mathbf{v}_i - \mathbf{v}_j) + \mathbf{\Gamma}_i^{ns}\mathbf{v}_i = \sum_j \mathbf{F}_{e,ij} + \sum_m \mathbf{F}_{m,i} + \sum_T \mathbf{F}_{area,i} + \mathbf{F}_{vol,i} + \mathbf{F}_{rep,i} + \mathbf{F}_{adh,i} + \mathbf{F}_{ext,i} \tag{14.25}$$

On the left-hand side, we find the friction terms, whereas on the right-hand side, all the force contributions are summed. The matrices $\mathbf{\Gamma}^{nn}$ and $\mathbf{\Gamma}^{ns}$ here represent node−node friction and node−substrate friction, respectively. The construction of these friction matrices is analogous to CBMs (see Eq. (14.2) and further).

14.3.2 Internal Forces Between Nodes

The individual elastic contributions $\mathbf{F}_e$ between the nodes can be primarily represented by Hookean spring forces. The combination with the node−node friction terms reflects the well-known Kelvin−Voigt element (KVE) representing a solid-like behavior. In the KVE the contributions from the friction element and spring element are added up and schematically positioned in *parallel* to each other (see Fig. 14.4). Let us consider the internal force $\mathbf{F}_{int}$ originating from the Kelvin−Voigt viscoelastic element between nodes i and j (for simplicity, assume $\gamma_{||} = \gamma_{\perp} = \gamma$):

$$\mathbf{F}_{int,ij} = \mathbf{F}_{e,ij} - \gamma\mathbf{v}_{ij} = -k_s(\mathbf{r}_{ij} - \mathbf{r}_{0,ij}) - \gamma\mathbf{v}_{ij} \tag{14.26}$$

where k_s is the spring stiffness and $\mathbf{r}_{0,ij}$, $\mathbf{r}_{ij}$ are the initial and actual distance vectors. The force balance equation, including external forces $\mathbf{F}_{ext}$, can be written as

$$\mathbf{F}_{ext,ij} - k_s(\mathbf{r}_{ij} - \mathbf{r}_{0,ij}) - \gamma\mathbf{v}_{ij} = 0 \tag{14.27}$$

This book belongs to Central Library BADJI Mokhtar-ANNABA UNIVERSITY
Copyright Elsevier 2024

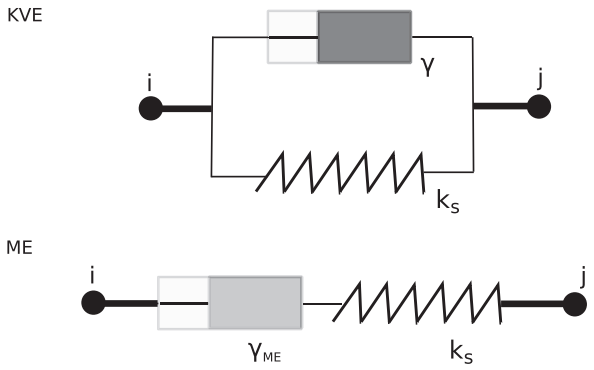

FIGURE 14.4 Schematic representation of the Kelvin–Voigt (solid) and Maxwell element (fluid).

To simulate fluid-like extension of the cortex, we can invoke the basic Maxwell element (ME). In the ME the friction element and spring element are schematically positioned in *series*. The equation of the internal force in the element $\mathbf{F}_{int}$ involves a differential and reads (we here only consider the normal direction of two nodes)

$$\frac{\dot{F}_{int,ij}}{k_s} + \frac{F_{int,ij}}{\gamma} = v_{\perp,ij} \tag{14.28}$$

with $v_{\perp,ij} = \|\mathbf{u}_{ij}(\mathbf{u}_{ij}\mathbf{v}_i)\|$. The equation contains a derivative of the force, which can be approximated by $\dot{F}_{int} = (F_{int}(t) + F_{int}(t-\Delta t))/\Delta t$. The basic equation of motion for one element thus involves the evaluation of the internal force on the previous time step:

$$F_{ext,ij} + \frac{F_{int,ij}(t-\Delta t)}{1 + k_s\Delta t/\gamma} = \frac{k\Delta t}{1 + k_s\Delta t/\gamma} v_{\perp,ij} \tag{14.29}$$

Note that this ME element can be enriched with other elements in parallel by adding frictional terms and elastic contributions. Obviously, this will change the equation of motion.

It is most convenient to represent the cell surface as a triangulated structure (see Fig. 14.5). The outer structures in a cell are the membrane and the cortical cytoskeleton. In such a triangulation, the forces as mentioned before may accurately describe the elastic resistance due to shear and expansion of the network of polymers that form the cortex. For lattices approximating sixfold symmetry (see Fig. 14.6), the linear spring constants k_{cor} can be related approximately to the cortex Young's modulus E_{cor} with thickness h_{cor} by (Boal, 2012; Van Liedekerke et al., 2010)

$$k_{cor} = \frac{2}{\sqrt{3}} E_{cor} h_{cor} \tag{14.30}$$

The plasma membrane (lipid bilayer), however, only resists to expansion of its area and little to shear forces. This can be mimicked by a force magnitude F_{area} proportional to the expansion of the surface:

$$F_{area} = k_{mem}(A - A_0)/A_0 \tag{14.31}$$

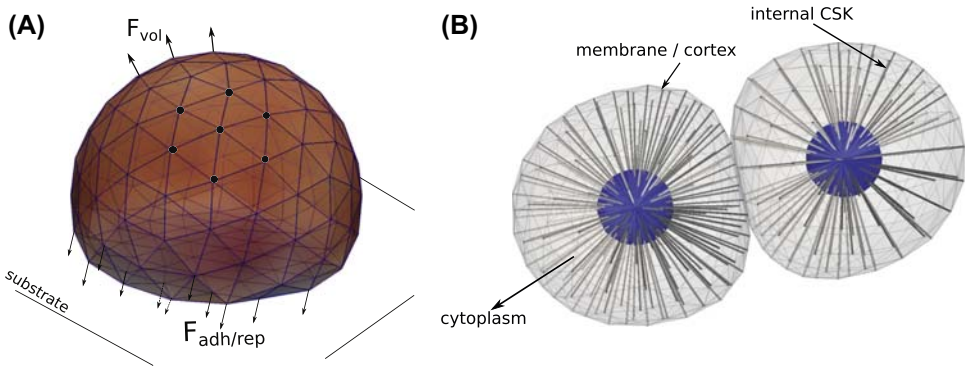

FIGURE 14.5 (A) Detail of the elements in a cell membrane triangulation. (B) Deformable cell model representation of two adhering cells, with each cell having represented a nucleus, a coarse central–oriented cytoskeleton (CSK), and a membrane/cortex.

This book belongs to Central Library BADJI Mokhtar-ANNABA UNIVERSITY Copyright Elsevier 2024

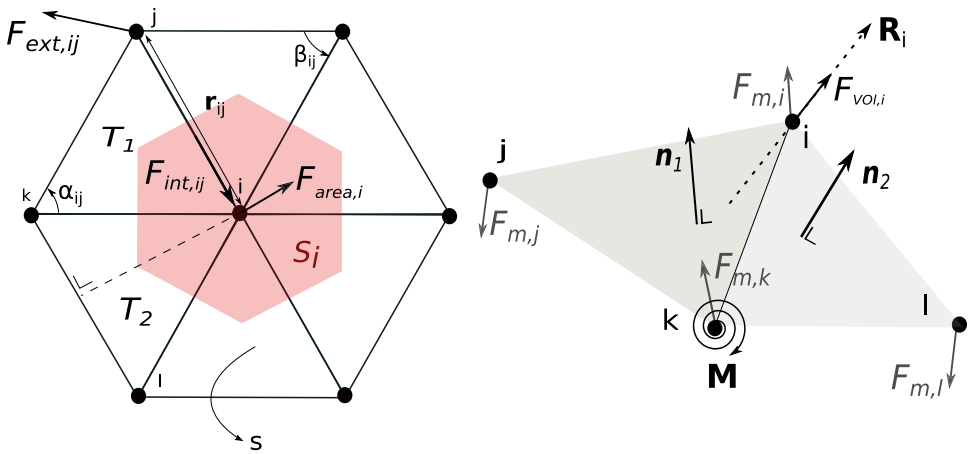

FIGURE 14.6 Detail of the elements in a cell membrane triangulation.

where A_0 and A are the initial and the current surface areas of the cell, respectively, and k_{mem} is the area compression stiffness. These can be obtained by summing all the individual triangle areas, i.e., $A = \sum_T s_T$ of the cell surface, where s is the surface area of a triangle T, see Fig. 14.6. The forces $\mathbf{F}_{area,i}$ can be applied in the plane of the triangle in the direction perpendicular to the opposite vertex edge. The membrane area compression parameter K_A measured for pure lipid bilayers is relatively high (Boal, 2012), but in case of a plasma membrane of a cell, much lower values are reported (Brugués et al., 2010). This is due to invaginations and inclusions of other molecules in a regular cell membrane. Some authors use the same formulas to add area conservation forces that are meant to avoid artifacts due to strong deformations of single triangles, similar to mesh deformations in finite element grids. Although these forces work on a local level (i.e., individual), they contribute to the mechanical behavior of the cell. The parameter k_{mem} for area conservation forces in the membrane is related to the area compression modulus K_A by

$$k_{mem} = \frac{\sqrt{3}}{4d_0} K_A \tag{14.32}$$

with d_0 the equilibrium length of triangle edge.

The bending resistance in the cortex is incorporated by the rotational resistance of the hinges determined by two adjacent triangles $T_1 = \{ijk\}$ and $T_2 = \{ijl\}$ (see Fig. 14.6). This defines a moment M around the hinge:

$$M = k_b \sin(\theta - \theta_0) \tag{14.33}$$

where k_b is the bending constant and θ is determined by the normals to the triangles $\mathbf{n}_1$, $\mathbf{n}_2$, with θ_0 being the angle of spontaneous curvature. The moment M can be transformed to an equivalent force system $F_{m,i}$ acting on each of the nodes of the triangles (Odenthal et al., 2013). To warrant conservation of momentum, it must hold that $\mathbf{F}_{m,i} + \mathbf{F}_{m,j} + \mathbf{F}_{m,k} + \mathbf{F}_{m,l} = 0$.[3] The bending stiffness of a (thin) cortex is in the same way approximated by

$$k_b = \frac{E_{cor} h^3}{12(1 - \nu^2)} \tag{14.34}$$

where ν is the Poisson ratio (=1/3 for an equilateral 2D network of linear springs). For a more a more in-depth analysis relating the spring force parameters to macroscopic constants, we refer to literature (Fedosov et al., 2010; Odenthal et al., 2013; Van Liedekerke et al., 2010; Hansen et al., 1996).

Until now, forces were assumed to behave linearly. However, many polymeric materials exhibit nonlinear elastic behavior. At a microscopic level, this nonlinearity originates from entropic effects during the stretching of large molecules. A commonly known model describing these effects is the finitely extensible nonlinear elastic (FENE) force, which behaves

3. This condition applies also to all other forces applied in the cell.

This book belongs to Central Library BADJI Mokhtar-ANNABA UNIVERSITY
Copyright Elsevier 2024

soft at low stretch but become very stiff at high stretches (similar to uncoiling a rope) and describes the microscopic force as

$$F_{e,ij} = -k_{FENE} d_{ij} \left[1 - \left(\frac{d_{ij}}{d_{max}} \right)^2 \right]^{-1}, \tag{14.35}$$

where $d_{ij} = \|\mathbf{r}_i - \mathbf{r}_j\|$ is the distance between the nodes, k_{FENE} is the stiffness, and d^{max} is the maximum distance, at which the force will diverge. The FENE force accounts for attractive forces only. To account for resistance during compression, a power law force is often used:

$$F_{e,ij} \sim \frac{1}{(d_{ij})^2}. \tag{14.36}$$

The FENE model has been used for modeling the forces in the spectrin cytoskeleton of red blood cells (Fedosov et al., 2010; Odenthal et al., 2013).

To account for the nonlinearity at a macroscopic level, Van Liedekerke et al. (2010) proposed a discretization of an incompressible neo-Hookean model, computing the force between two nodes of a triangulated network as

$$F_{e,ij} = k_{poly} \left(\lambda_{ij} - \lambda_{ij}^{-5} \right), \tag{14.37}$$

where $\lambda_{ij} = d_{ij} \big/ d_{ij}^0$ is the stretch ratio for a triangle edge. This model hence also accounts of the decrease of the thickness of the material during stretching.

The volume change of the cell depends on the applied external forces and the cell bulk compressibility K_V. In a cell, the compressibility of the cytoplasm depends on the fraction of water and the CSK structure and organelles. In addition, it may also be influenced by the permeability of the plasma membrane for water, the presence of caveolae (Sinha et al., 2011), and active responses in the cells. The volume V of the cell can be computed summing up the volumes of the individual tetrahedra that build up the cell. The forces $\mathbf{F}_{vol,i}$ on the nodes are computed by

$$\mathbf{F}_{vol,i} = -pS_i \frac{\mathbf{R}_i}{\|\mathbf{R}_i\|} \tag{14.38}$$

where p is the internal pressure calculated, as detailed in Section 14.3.5, and S_i is the Voronoi area of the central node i defined by its connecting nodes j (see Fig. 14.6). The vector $\mathbf{R}_i$ is obtained using the Laplace−Beltrami formula, which computes the local curvature at node i of the cell surface.

$$\mathbf{R}_i = \frac{1}{2S_i} \sum_j \left[\cot(\alpha_{ij}) + \cot(\beta_{ij}) \right] \mathbf{r}_{ij}, \tag{14.39}$$

with $\mathbf{r}_{ij} = \mathbf{r}_i - \mathbf{r}_j$. There are a number of simplifications in this basic model. First, we have not included explicitly internal structures of the cell such as internal cytoskeleton, nucleus, and other organelles. A very crude representation of such a CSK may be radial struts connecting the nucleus and the cortex of the cell (see Fig. 14.5). Internal structures increases the cell shear elasticity. Models without internal CSK may sometimes result in simulations exhibiting buckling instabilities of the membrane (Buenemann and Lenz, 2008). Secondly, reorganization of the cytoskeleton involving (de)polymerization was not considered. This could be realized, for instance on a coarse-grained level, by a modification of the equilibrium spring lengths. For example, applied in the growth and division of cells, the spring elements would have to be adapted to maintain certain tension cytoskeleton. For more detailed of models for active polymerization forces, see, e.g., Milde et al. (2014), Tozluolu et al. (2013), and Kim et al. (2013). Finally, coarse-grained spring networks may require remeshing. If cells are deformed too much, inaccuracies and artifacts will be introduced.

14.3.3 Adhesion and Repulsion Forces

Interactions between neighboring cells are characterized by a balance of attractive and repulsive forces. When cells approach too much, excluded volume forces $\mathbf{F}_{rep,i}$ will avoid interpenetration, whereas on separation, attractive forces avoid breaking up the contact. Interactions between cells in DCM can be included by defining interactions between the nodes belonging to difference cells, which can be regarded as a coarse graining of the molecular adhesive

This book belongs to Central Library BADJI Mokhtar-ANNABA UNIVERSITY
Copyright Elsevier 2024

bonds (e.g., cadherins). In the most simple case, one can assume permanent adhesive bonds between nodes of the cells, described by linear springs (Van Liedekerke et al., 2011). If the bonds are not static, one can define the forces as a more complex function of the distance between the nodes. Sanderus and Newman (2008) assumed a Morse potential between the nodes

$$\mathcal{U}_{ij} = \mu_0 e^{2\rho\left(1-d_{ij}^2/d_{eq,ij}^2\right)} - 2\mu_0 e^{\rho\left(1-d_{ij}^2/d_{eq,ij}^2\right)} \tag{14.40}$$

where μ_0 is the potential well depth, ρ is a scaling factor and $d_{eq,ij}$ is the equilibrium distance between nodes. The potential is repulsive for $d_{ij} < d_{eq,ij}$ and attractive for $d_{ij} > d_{eq,ij}$ which becomes very weak at high separation distances. The actual force is obtained by $F_{ij} = -\frac{\partial \mathcal{U}_{ij}}{\partial d_{ij}}$. Another approach described in Jamali et al. (2010) defines a distance $d_{adh,ij}$ and $d_{rep,ij}$ such that if $d_{ij} < d_{adh,ij}$ the force becomes attractive and if $d_{ij} < d_{rep,ij}$ the force becomes repulsive. In between these distances, the force is described by a KVE generating an elastic force $\sim d_{ij} - d_{0,ij}$ where $d_{0,ij}$ is the equilibrium distance at which the force vanishes. A hysteresis effect can also be incorporated by introducing $d_{hyst,ij} > d_{adh,ij}$ for which the contact only separates if $d_{ij} > d_{hyst,ij}$.

Interactions based on node−node potentials are easy to implement but the parameters in the force models are generally difficult to calibrate and depend on the number of nodes (discretization). In the approach detailed in Odenthal et al. (2013), the cell−cell interactions were derived from the Maugis−Dugdale continuum theory for adhesive objects, in which adhesion is fully characterized by an adhesion energy and adhesion interaction range parameter (Johnson and Greenwood, 1997). In the model, the interactions are defined on the level of the interacting triangles. The stress between two triangles belonging to different cells is computed by the overlap area of the triangles and the local curvature of the objects. This stress is then transformed to a contact force on the triangles, which is in turn distributed to the nodes, allowing to update Eq. (14.25). The model allows description of the interaction not only between two arbitrarily shaped triangulated bodies but also between a triangulated body and nontriangulated simple geometric objects as spheres and flat substrates.

14.3.4 Cell Migration and Chemotaxis

The force formulas for migration and chemotaxis as described in CBM are body forces applied to the center of mass of the cell. In principle these forces can be applied to DCM as well, simply by distributing the force component over all the nodes of the cell. Explicit filopodia can also be considered by applying directional forces to the nodes in the regions of the cell where the filopodia are formed. These forces can be regarded as attractive springs, with a certain lifetime and preferred orientation. They can attach to fixed points in space, or even to nodes that would represent ECM, hence taking into account the elastic response of the medium. Models of filopodia and protrusions in DCM are still relatively scarce. Nevertheless, in recent work (Zhu and Mogilner, 2016; Tozluolu et al., 2013; Kim et al., 2013), cell migration models at higher detail are proposed.

14.3.5 Cell Growth, Division, and Death

Cell growth in DCM is formally the same as in CBMs. However, simply imposing a volume increase in DCM will increase the pressure and mechanical tension in the membrane/cortex springs. This artificial effect must be canceled out by adapting the equilibrium length in the springs and the reference volume. Similarly, cell death and lysis can be simulated by a shrinking process and final removal of all the nodes.

Contrary to cell growth, cell division is more involved in DCM. During mitosis the cell spits up in two daughter cells that are adhering to each other. During cytokinesis, the continuous shrinking of the contractile ring, together with the separation of the mitotic spindle, slowly creates the new daughter cells. Simulating these processes in DCM generally requires a complex process of cytoskeleton modeling and remodeling. Modeling algorithms of cell division are described in, e.g., Milde et al. (2014) and Jamali et al. (2010).

14.3.6 Measures for Deformation, Stress, and Pressure

Quantities such as deformation, pressure, and stress can be computed in DCM at much greater detail than in the CBMs. Contrary to CBMs, DCM does not know the concept of virtual overlap, and hence stress and deformation are purely quantified by the relative displacement of the nodes.

This book belongs to Central Library BADJI Mokhtar-ANNABA UNIVERSITY
Copyright Elsevier 2024

For mechanical stresses, we can basically consider in our model the in-plane stresses in the cortex and internal pressure of the cell. Nonshear contributions of the elastic energy are controlled by the bulk modulus. The change of hydrostatic pressure dp and the volume change dV are related by

$$dp = -K_V \frac{dV}{V}, \tag{14.41}$$

leading to $p = p_0 - K_V \log(V/V_0)$, with $K_V = E / (3(1-2\nu))$, if E is the Young's modulus of the interior of the cell and p_0 being the hydrostatic pressure of the cell at volume V_0.

The in-plane stresses in the cortex can be obtained with the virial formula. For example, to compute the 2D stress tensor in a node i we apply

$$\sigma_i = \frac{1}{\mathcal{S}_i} \sum_j \left(\mathbf{F}_{ij}^{int} \otimes \frac{\mathbf{r}_{ij}}{2} \right) \tag{14.42}$$

where the sampling area is the Voronoi area $\mathcal{S}_i$ of the node (see Fig. 14.6). Note that in the formula we use $\mathbf{r}_{ij}/2$ instead of $\mathbf{r}_{ij}$ because the sampling area only reaches until half of the internodal connections. In Box 14.3 we use the virial stress to compute the cortical tension in a cell on isotropic expansion.

Deformation quantities in DCM can be directly inferred from the relative displacements between the nodes. If, for example, the volume of the cell decreases, this is translated in a decrease of the volume of the tetrahedra that constitute the cell (see above). Equivalent to the virial stress, the full viral left Cauchy−Green deformation tensor is given by:

$$\mathbf{b}_i = \frac{1}{\lambda_{\text{lattice}}} \sum_j \left. \frac{\mathbf{r}_{ij} \otimes \mathbf{r}_{ij}}{d_{ij}^2} \right) \tag{14.46}$$

where d_{ij} is equilibrium length of the connection between nodes i and j, and the factor λ_{lattice} depends on lattice symmetries, and the size of the neighborhood of node i. For instance, in the case of a sixfold symmetry with first-order neighbors we obtain $\lambda_{\text{lattice}} = 3$. This tensor can be used to compute strain measures such as the Eulerian strain, which for small deformations approximates the infinitesimal strain tensor. A major shortcoming of Eq. (14.46) is that it only applies in situations in which the underlying lattice has a symmetry property. This limitation can be overcome by

BOX 14.3 Compute Tension in a 2D Nodal Structure

Consider the isotropic expansion of the membrane due to an internal pressure. To know the tension in the membrane, we must compute $\sigma_{P,i} = \frac{1}{2}(\sigma_{xx,i} + \sigma_{yy,i})$. Assuming sixfold symmetry, we have six force contributions for $\sigma_{xx,i}$, with $F_{int,ij} = F_i$ and $d_{ij} = d_i$ (see Fig. 14.6):

$$\begin{aligned} \sigma_{xx,i} &= \frac{1}{\mathcal{S}_i} \left(1 + \frac{1}{4} + \frac{1}{4} + 1 + \frac{1}{4} + \frac{1}{4} \right) F_i \frac{d_i}{2} \\ &= \frac{3 F_i d_i}{2 \mathcal{S}_i}. \end{aligned} \tag{14.43}$$

Similarly, we have that $\sigma_{yy,i} = \frac{3 F_{int} d_i}{2 \mathcal{S}_i}$. The sampling Voronoi area is $\mathcal{S}_i = 2 s_i$, s_i being the triangle area. Hence, the nodal tension is

$$\sigma_{P,i} = \frac{3 F_i d_i}{4 s_i} \tag{14.44}$$

Note in the example we only considered the elastic contributions F_i from the cortex. In principle, force contributions originating from the area compressibility of the plasma membrane should also be added. Finally, one should check in the simulation that the Laplace equations holds

$$\sigma_{P,i} = \frac{p_{int}}{2R}, \tag{14.45}$$

with R the radius of the cell.

This book belongs to Central Library BADJI Mokhtar-ANNABA UNIVERSITY

Copyright Elsevier 2024

introducing an average deformation gradient at node i. For the full mathematical details and more applications we refer to Zimmermann (1999).

14.3.7 Implementation

In a software, DCMs basically will typically inherit most of the algorithms that could be originally defined for CBMs. The typical aspects of computational complexity (contact detection algorithms) in CBMs apply to deformable models as well. However, simulations are inherently computationally more expensive because they require a minimum of nodes necessary to obtain certain accuracy and avoiding artifacts. For instance, the triangulated network representing the cortex needs an appropriate number of nodes to ensure the mechanics of an elastic shell is well captured. The minimum required nodes will depend on the physical system that one envisages, but in general we recommend a minimum of 150 nodes per cell. Deformable cells models are currently implemented in following software: LBIBCell (Tanaka et al., 2015), SEM++ (Milde et al., 2014), and VirtualLeaf (VMs) (Merks et al., 2011).

14.3.8 Conclusion

The DCMs have all the advantages of CBMs, but treat cell shape and cellular forces with much greater detail (i.e., subcellular) and basically alleviate all pitfalls occurring in their simpler counterparts. The parameters are physically well defined and can be inferred from comparison of the mechanical behavior in in silico single-cell experiments, such as micropipetting, optical tweezers, and optical stretchers. Clearly, their higher complexity and extended parameter space significantly increases the number of algorithms in the code. A high number of nodes per cell combined with a required lower time step as in CBMs restrict the number of cells that can be simulated to around ~ 1000 on a single core. Nevertheless this model type will play an increasingly important role in future simulations.

14.4 HYBRID MODELING

In case one faces to model large multicellular systems or entire tissues, DCM simulations (and discrete ABMs in general) can become computationally infeasible. On way to alleviate this is to resort to continuum models. Continuum models are not concerned with individual cells and have no intrinsic scale; hence, tissue scale simulations pose no feasibility problems. They basically solve the governing mass and momentum balance PDEs for the tissue dynamics, including source terms to mimic cell growth, birth and death, cell migration, and can include reaction−diffusion PDEs to compute the concentrations of chemical substances such as oxygen, glucose, chemokines, growth factors, or cytokines. Continuum Models for tumors are often multiphase mixture descriptions encompassing a tumor cell phase, intercellular fluid phase, and ECM phase, using Darcy's law to determine the dynamics of each phase (Roose et al., 2007; Lowengrub et al., 2010; Byrne et al., 2006). The price to pay when using continuum models is the lack of representing detail, inhomogeneities, and variability that arise from the inherently discrete nature of cell−cell interactions. In recent years, however, more and more effort is put into combining strengths of continuum and discrete models. Hybrid models can bring solutions in problems where regions with a "high" and "low" information requirement can be identified. A hybrid coupling scheme for tumor growth was explored in Kim et al. (2007) who proposed a domain decomposition, whereby the active regions (proliferating cells) were represented by agents whereas the passive tissues (ECM, necrotic zone) were modeled by the finite element method discretization of a PDE governing the behavior of an elastic material. Generally, the formulation of hybrid models heavily depends on the conservation laws (mass, momentum, energy) and the key to success of the coupling is an adequate mapping between the constitutive behavior and the averaged discrete variables with respect to growth kinetics, rheology, etc. (Byrne and Drasdo, 2009; Galle et al., 2009; Murray et al., 2009; Frieboes et al., 2010; Preziosi et al., 2010; Osborne et al., 2010; Chauviere et al., 2012).

A particularly appealing approach to bridge the gaps across the scales is based on the density functional theory (Chauviere et al., 2012), which would allow calibration and validation of the cell-scale parameters and equations to be obtained directly from individual microscale measurements and formulating rigorous upscaling techniques of the continuum equations at the larger scales.

In continuum models for ECM, necrotic tissues, or fluids, the accuracy of representing the mechanics is largely determined by realism of the constitutive equation. Mesh-based methods usually do a great job in solving the equations (Rejniak, 2005; Kim et al., 2007; Zhang et al., 2007). Coarse-grained spring network models of tissue (Zhu and Mogilner, 2016), whereby the nodes or particles interact by simple atomistic or molecular potentials, may be an alternative as they are easier to implement, but often the pairwise potentials resulting in a realistic mechanical behavior are hard to find and, in

This book belongs to Central Library BADJI Mokhtar-ANNABA UNIVERSITY Copyright Elsevier 2024

addition, the topology (i.e., connectivity and definition of nearest neighbors of the nodes) significantly influences the resulting macroscopic material constants (Young's modulus, Poison's ratio). As a consequence, they must be used with caution as artifacts and errors may be introduced. Alternatively, in the last decades mesh-free methods are gaining increasingly more attention. These methods aim at solving the continuum equations using particles as computational nodes while discarding an underlying mesh. The mesh-free method called smoothed particle hydrodynamics (SPH), originally developed in astronomy and nowadays often used in fluid dynamics (Monaghan, 2012), has gained a lot of popularity. The method is particularly advantageous because it is a Lagrangian formulation and naturally deals with discontinuities, free surfaces, and multiphysics problems without the need of remeshing. In addition, because of the particle-based approach, coupling and implementation in software for discrete models such as CBM or DCM is straightforward. There are also some notable downsides: standard SPH methods can suffer from instabilities (mostly due to particle clustering), while the treatment of boundary conditions is due to the missing kernel support for boundary particles generally more complicated than for mesh-based methods. These problems may require special solutions depending on the problem one wants to tackle (Monaghan, 2000; Jiang et al., 2012; Ferrand et al., 2013).

In SPH, the starting point is that particle field variables $\mathcal{F}(\mathbf{x}_i)$ can be estimated using a convolution sum of neighboring particles j over a finite volume using a *kernel* function $W(r_{ij}, s)$.

$$\mathcal{F}(\mathbf{x}_i) \approx \sum_j \mathcal{F}(\mathbf{x}_j) W(r_{ij}, s) V_j \tag{14.47}$$

where $W(r_{ij}, s) \equiv W_{ij}$ is a bell-shaped symmetric function of the distance r_{ij} between the particles, whereby the parameter s (smoothing length) relates to the cutoff distance at which the interactions vanish. V_j is the volume associated with that particle. Applying the particle approximation to the continuum laws of momentum conservation and mass conservation leads to the standard SPH equations (Monaghan, 2012).

A rather simple hybrid modeling approach using SPH coupled to a DCM was described in Hosseini and Feng (2009), to simulate red blood cells dynamics in plasma. In this model the ECM, cell boundary, and cytoplasm are all represented by SPH particles for which a common constitutive equation is invoked. However, connected SPH particles representing the cell surface and cortical cytoskeleton experience additional pairwise elastic forces $\mathbf{F}_e$ (see Fig. 14.7). In this example the cell may be regarded as completely immersed in SPH particles and as such they are no continuum-discrete boundaries. As a consequence, the elastic forces can be simply entered as external forces in the SPH momentum equation. This coupling approach is similar to the immersed boundary method as used in Rejniak (2005). In case one wants to define an accurate boundary separating the cell and its environment, the mechanics becomes more complex (Heck et al., 2017). In the aforementioned example of Kim et al. (2007) the continuum fields are modeled by finite elements and at interface one needs to deal with the boundary conditions for displacement field and tractions. The latter are generated by the discrete system of particles (cells) and must be obtained from interpolation of the forces exerted by the discrete particles at the nearby nodes of the mesh. A naive solution for the boundary treatment in SPH would be to simply define repulsive forces

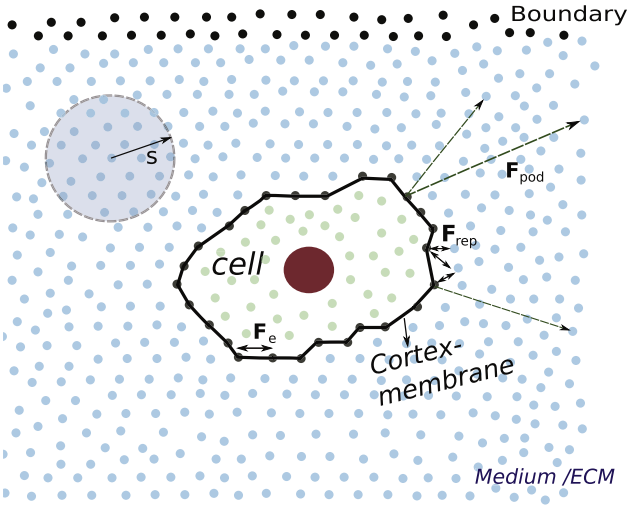

FIGURE 14.7 Schematic view of a hybrid model, using a deformable cell model for the cell and a smoothed particle hydrodynamics continuum model for the fluids. The cell can exert active migrative forces $\mathbf{F}_{pod}$ to the medium particles with reactive forces $\mathbf{F}_{rep}$ as a consequence. *ECM*, extracellular matrix.

This book belongs to Central Library BADJI Mokhtar-ANNABA UNIVERSITY
Copyright Elsevier 2024

between the SPH particles and discrete particles representing (parts of) a cell. The action−reaction mechanism will avoid interpenetration and warrant conservation of momentum. This approach, however, can lead to spurious effects due to errors made in the SPH calculations of hydrostatic pressure for particles near the boundary. A solution proposed in Ferrand et al. (2013) and Heck et al. (2017) involves a correction that is applied to the SPH formulation, based on the missing kernel area support near the boundary.

Integrating the system of SPH equations requires a second-order accurate integrator (e.g., Leapfrog) and suffers time-step restrictions due to the CFL criterion and the viscous diffusion:

$$\Delta t \sim \frac{s^2}{\mu}. \tag{14.48}$$

Especially in microscopic systems ($s \ll 1$) with high viscosity ($\mu \gg 1$), in combination with biological timescales typically being hours or days, this poses serious problems for computational feasibility. To circumvent this, Van Liedekerke et al. (2013) proposed a friction-dominated variant of SPH. The resulting equation was obtained by explicitly omitting the inertial term in the standard SPH equations. This results in a system of particle-based Stokes' equations:

$$\begin{aligned} -\sum_j \Gamma_{ij} v_{ij} &= m_i \sum_j m_j \left. \frac{p_i}{\rho_i^2} + \frac{p_j}{\rho_j^2} \right) \nabla_i W_{ij} + \mathbf{F}_{ext,i} \\ &= \sum_j \left(p_i V_i^2 + p_j V_j^2 \right) \nabla_i W_{ij} + \mathbf{F}_{ext,i}, \end{aligned} \tag{14.49}$$

with each particle having a pressure p_i and a volume $V_i = m_i/\rho_i$ assuming for simplicity that $m_i = m_j$. The pressure is calculated according to an equation of state. The friction matrix Γ_{ij} contains the shear viscosities and is obtained as

$$\Gamma_{ij} = \left(\mu_i + \mu_j \right) \frac{V_i V_j}{r_{ij}} \frac{\partial W_{ij}}{\partial r_{ij}}. \tag{14.50}$$

Eq. (14.49) is analogous to the equation of motion for the CBMs and DCMs and can be solved with a conjugate gradient algorithm to find the velocities and an explicit Euler integration scheme. The minimum time step is not restricted by the parabolic limit (Eq. 14.48) and may be several orders higher than for standard SPH.

14.5 CONCLUSION

In this chapter, we have discussed the basic components for off-lattice models. CBMs have been extensively and successfully used in the past, but more and more research is now focusing on deformable models that offer a lot more detail and information, but have a higher complexity in both physics and algorithms, and are computationally expensive in 3D. Hybrid models may present solutions to problems where both realistic scales and detail is required. One major drawback of lattice-free models compared to lattice-based models is that the former usually require more computational effort and their parallelization of algorithms is more complex to implement. On the other hand, a big plus of lattice-free models is their physical realism. However, we note that the model choice for representing a biological system will be a consideration of inherent capabilities, available software, and computational feasibility.

ACKNOWLEDGMENTS

P.V.L. acknowledges funding by ANR PHYSCANCER, ANR INVADE, and EU NOTOX. A.B. funding by Alberta Innovates, MITACS Canada, and acknowledges hospitality at INRIA during his stay at INRIA from December 2015 to May 2016. D.D. gratefully acknowledges funding by ANR INVADE, ANR PHYSCANCER, and BMBF Cancersys/Lungsys.

REFERENCES

Axelsson, O., Kaporin, I., 2001. Error norm estimation and stopping criteria in preconditioned conjugate gradient iterations. Numerical Linear Algebra with Applications 8 (4), 265−286.

Barrett, R., Berry, M., Chan, T.F., Demmel, J., Donato, J.M., Dongarra, J., Eijkhout, V., Pozo, R., Romine, C., Van der Vorst, H., 1995. Templates for the solution of linear systems: building blocks for iterative methods. Mathematics of Computation 64 (211), 1349.

Barth, W., Martin, R.S., Wilkinson, J.H., April 1967. Calculation of the eigenvalues of a symmetric tridiagonal matrix by the method of bisection. Numerische Mathematik 9, 386−393.

This book belongs to Central Library BADJI Mokhtar-ANNABA UNIVERSITY Copyright Elsevier 2024

Basan, M., Prost, J., Joanny, J.-F., Elgeti, J., April 2011. Dissipative particle dynamics simulations for biological tissues: rheology and competition. Physical Biology 8, 26014.

Benzi, M., 2002. Preconditioning techniques for large linear systems: a survey. Journal of Computational Physics 182 (2), 418–477.

Beysens, D.A., Forgacs, G., Glazier, J.A., 2000. Cell sorting is analogous to phase ordering in fluids. Proceedings of the National Academy of Sciences of the United States of America 97, 9467–9471.

Boal, D., 2012. Mechanics of the Cell, second ed. Cambridge University Press.

Boon, W.M., Koppenol, D.C., Vermolen, F.J., 2016. A Multi-Agent Cell-Based Model for Wound Contraction.

Boulanger, A.-c., August 2009. Agent-Based Model –Continuum Model in Tumor Growth. Tech. Rep., p. 2010.

Brugués, J., Maugis, B., Casademunt, J., Nassoy, P., Amblard, F., Sens, P., 2010. Dynamical organization of the cytoskeletal cortex probed by micropipette aspiration. Proceedings of the National Academy of Sciences of the United States of America 107 (35), 15415–15420.

Buenemann, M., Lenz, P., November 2008. Elastic properties and mechanical stability of chiral and filled viral capsids. Physical Review E 78, 051924.

Buske, P., Galle, J., Barker, N., Aust, G., Clevers, H., Loeffler, M., 2011. A comprehensive model of the spatio-temporal stem cell and tissue organisation in the intestinal crypt. PLoS Computational Biology 7 (1), e1001045.

Buske, P., Przybilla, J., Loeffler, M., Sachs, N., Sato, T., Clevers, H., Galle, J., 2012. On the biomechanics of stem cell niche formation in the gut modelling growing organoids. FEBS Journal 279 (18), 3475–3487.

Byrne, H., Drasdo, D., 2009. Individual-based and continuum models of growing cell populations: a comparison. Mathematical Biology 58, 657–680.

Byrne, H.M., Alarcon, T., Owen, M.R., Webb, S.D., Maini, P.K., June 2006. Modelling aspects of cancer dynamics: a review. Philosophical Transactions. Series A, Mathematical, Physical, and Engineering Sciences 364, 1563–1578.

Camley, B.A., Zhang, Y., Zhao, Y., Li, B., Ben-Jacob, E., Levine, H., Rappel, W.-J., October 2014. Polarity mechanisms such as contact inhibition of locomotion regulate persistent rotational motion of mammalian cells on micropatterns. Proceedings of the National Academy of Sciences of the United States of America 111, 14770–14775.

Chauviere, A., Hatzikirou, H., Kevrekidis, I.G., Lowengrub, J.S., Cristini, V., March 2012. Dynamic density functional theory of solid tumor growth: preliminary models. AIP Advances 2, 11210.

Chu, Y.S., Dufour, S., Thiery, J.P., Perez, E., Pincet, F., 2005. Johnson-Kendall-Roberts theory applied to living cells. Physical Review Letters 94 (2), 28102.

Cristini, V., Lowengrub, J., 2010. Multiscale Modeling of Cancer: An Integrated Experimental and Mathematical Modeling Approach. Cambridge University Press.

Cytowski, M., Szymanska, Z., September 2014. Large-scale parallel simulations of 3D cell colony dynamics. Computing in Science and Engineering 16, 86–95.

Cytowski, M., Szymanska, Z., 2015. Large scale parallel simulations of 3-d cell colony dynamics. II. Coupling with continuous description of cellular environment. Computing in Science and Engineering (99), 1–6.

D'Antonio, G., Macklin, P., Preziosi, L., February 2013. An agent-based model for elasto-plastic mechanical interactions between cells, basement membrane and extracellular matrix. Mathematical Biosciences and Engineering 10, 75–101.

Dallon, J.C., Othmer, H.G., 2004. How cellular movement determines the collective force generated by the *Dictyostelium discoideum* slug. Journal of Theoretical Biology 231, 203–222.

Dillon, R., Owen, M., et al., 2008. A single-cell-based model of multicellular growth using the immersed boundary method. AMS Contemporary Mathematics 466.

Drasdo, D., Forgacs, G., 2000. Modeling the interplay of generic and genetic mechanisms in cleavage, blastulation, and gastrulation. Developmental Dynamics 219 (2), 182–191.

Drasdo, D., Hoehme, S., 2012. Modeling the impact of granular embedding media, and pulling versus pushing cells on growing cell clones. New Journal of Physics 14 (5), 55025.

Drasdo, D., Loeffler, M., August 2001. Individual-based models to growth and folding in one-layered tissues: intestinal crypts and early development. Nonlinear Analysis: Theory, Methods and Applications 47, 245–256.

Drasdo, D., Kree, R., McCaskill, J.S., December 1995. Monte Carlo approach to tissue-cell populations. Physical Review E 52, 6635–6657.

Drasdo, D., Hoehme, S., Block, M., 2007. On the role of physics in the growth and pattern formation of multi-cellular systems: what can we learn from individual-cell based models. Journal of Statistical Physics 128, 287–345.

Drasdo, D., 2005. Coarse graining in simulated cell populations. Advances in Complex Systems 08 (02–03), 319–363.

Dunn, S.J., Näthke, I.S., Osborne, J.M., 2013. Computational models reveal a passive mechanism for cell migration in the crypt. PLoS One 8 (11).

Fedosov, D.A., Caswell, B., Karniadakis, G.E., 2010. Systematic coarse-graining of spectrin-level red blood cell models. Computer Methods in Applied Mechanics and Engineering 199 (2932), 1937–1948.

Fedosov, D.A., Caswell, B., Suresh, S., Karniadakis, G.E., January 2011. Quantifying the biophysical characteristics of Plasmodium-falciparum-parasitized red blood cells in microcirculation. Proceedings of the National Academy of Sciences of the United States of America 108, 35–39.

Ferrand, M., Laurence, D.R., Rogers, B.D., Violeau, D., Kassiotis, C., 2013. Unified semi-analytical wall boundary conditions for inviscid, laminar or turbulent flows in the meshless SPH method. International Journal for Numerical Methods in Fluids 71 (4), 446–472.

Figueredo, G.P., Joshi, T.V., Osborne, J.M., Byrne, H.M., Owen, M.R., April 2013. On-lattice agent-based simulation of populations of cells within the open-source Chaste framework. Interface Focus 3, 20120081.

Fletcher, A.G., Osborne, J.M., Maini, P.K., Gavaghan, D.J., November 2013. Implementing vertex dynamics models of cell populations in biology within a consistent computational framework. Progress in Biophysics and Molecular Biology 113, 299–326.

This book belongs to Central Library BADJI Mokhtar-ANNABA UNIVERSITY

Copyright Elsevier 2024

Fletcher, A.G., Osterfield, M., Baker, R.E., Shvartsman, S.Y., 2014. Vertex models of epithelial morphogenesis. Biophysical Journal 106 (11), 2291–2304.

Frieboes, H.B., Jin, F., Chuang, Y.-L., Wise, S.M., Lowengrub, J.S., Cristini, V., June 2010. Three-dimensional multispecies nonlinear tumor growth-II: tumor invasion and angiogenesis. Journal of Theoretical Biology 264, 1254–1278.

Galle, J., Loeffler, M., Drasdo, D., 2005. Modeling the effect of deregulated proliferation and apoptosis on the growth dynamics of epithelial cell populations in vitro. Biophysical Journal 88 (1), 62–75.

Galle, J., Aust, G., Schaller, G., Beyer, T., Drasdo, D., July 2006. Individual cell-based models of the spatial-temporal organization of multicellular systems–achievements and limitations. Cytometry. Part A: The Journal of the International Society for Analytical Cytology 69, 704–710.

Galle, J., Preziosi, L., Tosin, A., 2009. Contact inhibition of growth described using a multiphase model and an individual cell based model. Applied Mathematics Letters 22, 1483–1490.

Ghysels, P., Samaey, G., Tijskens, B., Liedekerke, P.V., Ramon, H., Roose, D., 2009. Multi-scale simulation of plant tissue deformation using a model for individual cell mechanics. Physical Biology 6 (1), 16009.

Hansen, J.C., Skalak, R., Chien, S., Hoger, A., January 1996. An elastic network model based on the structure of the red blood cell membrane skeleton. Biophysical Journal 70, 146–166.

Heck, T., Smeets, B., Vanmaercke, S., Bhattacharya, P., Odenthal, T., Ramon, H., Van Oosterwijck, H., Van Liedekerke, P., August 1, 2017. Modeling extracellular matrix viscoelasticity using non-inertial smoothed particle hydrodynamics with improved boundary treatment. Computer Methods in Applied Mechanics and Engineering 322, 515–540.

Hockney, R.W., Eastwood, J.W., 1988. Computer Simulation Using Particles. CRC Press.

Hoehme, S., Drasdo, D., 2005. A single-cell-based model of tumor growth in vitro: monolayers and spheroids. Physical Biology 2, 133–147.

Hoehme, S., Drasdo, D., 2010a. Biomechanical and nutrient controls in the growth of mammalian cell populations. Mathematical Population Studies: An International Journal of Mathematical 17 (166–187), 37–41.

Hoehme, S., Drasdo, D., 2010b. A cell-based simulation software for multicellular systems. Bioinformatics 26, 2641–2642.

Hoehme, S., Brulport, M., Bauer, A., Bedawy, E., Schormann, W., Hermes, M., Puppe, V., Gebhardt, R., Zellmer, S., Schwarz, M., Bockamp, E., Timmel, T., Hengstler, J.G., Drasdo, D., 2010. Prediction and validation of cell alignment along microvessels as order principle to restore tissue architecture in liver regeneration. Proceedings of the National Academy of Sciences of the United States of America 107 (23), 10371–10376.

Honda, H., Yamanaka, H., Dan-Sohkawa, M., March 1984. A computer simulation of geometrical configurations during cell division. Journal of Theoretical Biology 106, 423–435.

Honda, H., January 1983. Geometrical models for cells in tissues. International Review of Cytology 81, 191–248.

Hosseini, M., Feng, J.J., 2009. A particle-based model for the transport of erythrocytes in capillaries. Chemical Engineering Science 64, 4488–4497.

Hucka, M., Finney, A., Sauro, H.M., Bolouri, H., Doyle, J.C., Kitano, H., Arkin, A.P., Bornstein, B.J., Bray, D., Cornish-Bowden, A., Cuellar, A.A., Dronov, S., Gilles, E.D., Ginkel, M., Gor, V., Goryanin, I.I., Hedley, W.J., Hodgman, T.C., Hofmeyr, J.H., Hunter, P.J., Juty, N.S., Kasberger, J.L., Kremling, A., Kummer, U., Le Novère, N., Loew, L.M., Lucio, D., Mendes, P., Minch, E., Mjolsness, E.D., Nakayama, Y., Nelson, M.R., Nielsen, P.F., Sakurada, T., Schaff, J.C., Shapiro, B.E., Shimizu, T.S., Spence, H.D., Stelling, J., Takahashi, K., Tomita, M., Wagner, J., Wang, J., 2003. The systems biology markup language (SBML): a medium for representation and exchange of biochemical network models. Bioinformatics 19 (4), 524–531.

Irving, J.H., Kirkwood, J.G., June 1950. The statistical mechanical theory of transport processes. IV. The equations of hydrodynamics. The Journal of Chemical Physics 18, 817.

Jagiella, N., Müller, B., Müller, M., Vignon-Clementel, I.E., Drasdo, D., February 2016. Inferring growth control mechanisms in growing multi-cellular spheroids of NSCLC cells from spatial-temporal image data. PLoS Computational Biology 12, e1004412.

Jamali, Y., Azimi, M., Mofrad, M.R.K., 2010. A sub-cellular viscoelastic model for cell population mechanics. PLoS One 5 (8), e12097.

Jiang, T., Ouyang, J., Ren, J.-L., Yang, B.-X., Xu, X.-Y., 2012. A mixed corrected symmetric SPH (MC-SSPH) method for computational dynamic problems. Computer Physics Communications 183 (1), 50–62.

Johnson, K.L., Greenwood, J.A., 1997. An adhesion map for the contact of elastic spheres. Journal of Colloid and Interface Science 192, 326–333.

Kafri, R., Levy, J., Ginzberg, M.B., Oh, S., Lahav, G., Kirschner, M.W., 2013. Dynamics extracted from fixed cells reveal feedback linking cell growth to cell cycle. Nature 494 (7438), 480–483.

Kang, S., Kahan, S., McDermott, J., Flann, N., Shmulevich, I., November 2014. Biocellion: accelerating computer simulation of multicellular biological system models. Bioinformatics (Oxford, England) 30, 3101–3108.

Kempf, H., Bleicher, M., Meyer-Hermann, M., 2010. Spatio-temporal cell dynamics in tumour spheroid irradiation. The European Physical Journal D 60 (1), 177–193.

Kim, Y., Stolarska, M.A., Othemer, H.G., November 2007. A hybrid model for tumor spheroid growth in vitro I: theoretical development and early results. Mathematical Models and Methods in Applied Sciences 17, 1773–1798.

Kim, M.-C., Neal, D.M., Kamm, R.D., Asada, H.H., 2013. Dynamic modeling of cell migration and spreading behaviors on fibronectin coated planar substrates and micropatterned geometries. PLoS Computational Biology 9 (2), e1002926.

Krijgsman, D., Ogarko, V., Luding, S., 2014. Optimal parameters for a hierarchical grid data structure for contact detection in arbitrarily polydisperse particle systems. Computational Particle Mechanics 1 (3), 357–372.

Krinner, A., 2010. Spherical Individual Cell-Based Models: Limits and Applications (Ph.D. thesis). Inria.

Lowengrub, J.S., Frieboes, H.B., Jin, F., Chuang, Y.-L., Li, X., Macklin, P., Wise, S.M., Cristini, V., January 2010. Nonlinear modelling of cancer: bridging the gap between cells and tumours. Nonlinearity 23, R1–R9.

This book belongs to Central Library BADJI Mokhtar-ANNABA UNIVERSITY Copyright Elsevier 2024

Macklin, P., Edgerton, M.E., Thompson, A.M., Cristini, V., May 2012. Patient-calibrated agent-based modelling of ductal carcinoma in situ (DCIS): from microscopic measurements to macroscopic predictions of clinical progression. Journal of Theoretical Biology 301, 122−140.

Manning, M.L., Foty, R.A., Steinberg, M.S., Schoetz, E.-M., 2010. Coaction of intercellular adhesion and cortical tension specifies tissue surface tension. Proceedings of the National Academy of Sciences of the United States of America 107 (28).

Marmottant, P., Mgharbel, A., Käfer, J., Audren, B., Rieu, J.-P., Vial, J.-C., van der Sanden, B., Marée, A.F.M., Graner, F., Delanoë-Ayari, H., October 2009. The role of fluctuations and stress on the effective viscosity of cell aggregates. Proceedings of the National Academy of Sciences of the United States of America 106, 17271−17275.

Marsaglia, G., April 1972. Choosing a point from the surface of a sphere. The Annals of Mathematical Statistics 43, 645−646.

Meineke, F.A., Potten, C.S., Loeffler, M., August 2001. Cell migration and organization in the intestinal crypt using a lattice-free model. Cell Proliferation 34, 253−266.

Merks, R.M.H., Guravage, M., Inzé, D., Beemster, G.T.S., 2011. Virtual leaf: an open-source framework for cell-based modeling of plant tissue growth and development. Plant Physiology 155 (2), 656−666.

Meurant, G., 2006. The Lanczos and Conjugate Gradient Algorithms: From Theory to Finite Precision Computations, vol. 19. SIAM.

Milde, F., Tauriello, G., Haberkern, H., Koumoutsakos, P., May 2014. SEM++: a particle model of cellular growth, signaling and migration. Computational Particle Mechanics.

Mir, M., Wang, Z., Shen, Z., Bednarz, M., Bashir, R., Golding, I., Prasanth, S.G., Popescu, G., 2011. Optical measurement of cycle-dependent cell growth. Proceedings of the National Academy of Sciences of the United States of America.

Mirams, G.R., Arthurs, C.J., Bernabeu, M.O., Bordas, R., Cooper, J., Corrias, A., Davit, Y., Dunn, S.-J., Fletcher, A.G., Harvey, D.G., Marsh, M.E., Osborne, J.M., Pathmanathan, P., Pitt-Francis, J., Southern, J., Zemzemi, N., Gavaghan, D.J., January 2013. Chaste: an open source C++ library for computational physiology and biology. PLoS Computational Biology 9, e1002970.

Monaghan, J.J., 2000. SPH without a tensile instability. Journal of Computational Physics 159 (2), 290−311.

Monaghan, J., January 2012. Smoothed particle hydrodynamics and its diverse applications. Annual Review of Fluid Mechanics 44, 323−346.

Murray, P., Edwards, C., Tindall, M., Maini, P., September 2009. From a discrete to a continuum model of cell dynamics in one dimension. Physical Review E 80, 031912.

Neufeld, T.P., Edgar, B.A., 1998. Connections between growth and the cell cycle. Current Opinion in Cell Biology 10, 784−790.

Odell, G.M., Oster, G., Alberch, P., Burnside, B., 1981. The mechanical basis of morphogenesis. I. Epithelial folding and invagination. Developmental Biology 85 (2), 446−462.

Odenthal, T., Smeets, B., Van Liedekerke, P., Tijskens, E., Van Oosterwyck, H., Ramon, H., 2013. Analysis of initial cell spreading using mechanistic contact formulations for a deformable cell model. PLoS Computational Biology (submitted).

Oliker, L., Li, X., Husbands, P., Biswas, R., 2002. Effects of ordering strategies and programming paradigms on sparse matrix computations. SIAM Review 44 (3), 373−393.

Osborne, J.M., Walter, A., Kershaw, S.K., Mirams, G.R., Fletcher, A.G., Pathmanathan, P., Gavaghan, D., Jensen, O.E., Maini, P.K., 2010. A hybrid approach to multi-scale modelling of cancer. Philosophical Transactions of the Royal Society A 368, 5013−5028.

Palsson, E., Othmer, H.G., September 2000. A model for individual and collective cell movement in *Dictyostelium discoideum*. Proceedings of the National Academy of Sciences of the United States of America 97, 10448−10453.

Palsson, E., May 2001. A three-dimensional model of cell movement in multicellular systems. Future Generation Computer Systems 17, 835−852.

Pathmanathan, P., Cooper, J., Fletcher, A., Mirams, G., Montahan, L., Murray, P., Osborne, J., Pitt-Francis, J., Walter, A., Chapman, S.J., 2009. A computational study of discrete mechanical tissue models. Physical Biology 6 (3), 36001.

Peng, Z., Li, X., Pivkin, I.V., Dao, M., Karniadakis, G.E., Suresh, S., 2013. Lipid bilayer and cytoskeletal interactions in a red blood cell. Proceedings of the National Academy of Sciences of the United States of America 110 (33), 13356−13361.

Pin, C., Parker, A., Gunning, A.P., Ohta, Y., Johnson, I.T., Carding, S.R., Sato, T., February 2015. An individual based computational model of intestinal crypt fission and its application to predicting unrestrictive growth of the intestinal epithelium. Integrative Biology: Quantitative Biosciences from Nano to Macro 7, 213−228.

Pivkin, I.V., Karniadakisa, G.E., 2008. Accurate coarse-grained modeling of red blood cells. Physical Review Letters 101, 118105.

Preziosi, L., Ambrosi, D., Verdier, C., 2010. An elasto-visco-plastic model of cell aggregates. Journal of Theoretical Biology 262 (1), 35−47.

Ramis-Conde, I., Drasdo, D., Anderson, A.R.A., Chaplain, M.A.J., 2008. Modeling the influence of the e-cadherin-β-catenin pathway in cancer cell invasion: a multiscale approach. Biophysical Journal 95 (1), 155−165.

Rangarajan, R., Zaman, M.H., 2008. Modeling cell migration in 3D. Cell Adhesion and Migration 2 (2), 106−109.

Rejniak, K.A., Anderson, A.R.A., April 2008. A computational study of the development of epithelial acini: I. Sufficient conditions for the formation of a hollow structure. Bulletin of Mathematical Biology 70, 677−712.

Rejniak, K.A., Dillon, R.H., 2007. A single cell-based model of the ductal tumour microarchitecture. Computational and Mathematical Methods in Medicine 8 (1), 51−69.

Rejniak, K.A., July 2005. A single-cell approach in modeling the dynamics of tumor microregions. Mathematical Biosciences and Engineering: MBE 2, 643−655.

Rejniak, K.A., July 2007. An immersed boundary framework for modelling the growth of individual cells: an application to the early tumour development. Journal of Theoretical Biology 247, 186−204.

Rey, R., García-Aznar, J.M., November 2013. A phenomenological approach to modelling collective cell movement in 2D. Biomechanics and Modeling in Mechanobiology 12, 1089−1100.

This book belongs to Central Library BADJI Mokhtar-ANNABA UNIVERSITY

Copyright Elsevier 2024

Roose, T., Chapman, S.J., Maini, P.K., January 2007. Mathematical models of avascular tumor growth. SIAM Review 49, 179–208.

Sandersius, S.A., Newman, T.J., January 2008. Modeling cell rheology with the subcellular element model. Physical Biology 5, 15002.

Schaller, G., Meyer-Hermann, M., May 2005. Multicellular tumor spheroid in an off-lattice Voronoi-Delaunay cell model. Physical Review E 71, 51910.

Schluter, D., Ramis-Conde, I., Chaplain, M., September 2012. Computational modeling of single-cell migration: the leading role of extracellular matrix fibers. Biophysical Journal 103, 1141–1151.

Sepúlveda, N., Petitjean, L., Cochet, O., Grasland-Mongrain, E., Silberzan, P., Hakim, V., 2013. Collective cell motion in an epithelial sheet can be quantitatively described by a stochastic interacting particle model. PLoS Computational Biology 9 (3), e1002944.

Sinha, B., Köster, D., Ruez, R., Gonnord, P., Bastiani, M., Abankwa, D., Stan, R.V., Butler-Browne, G., Vedie, B., Johannes, L., Morone, N., Parton, R.G., Raposo, G., Sens, P., Lamaze, C., Nassoy, P., 2011. Cells respond to mechanical stress by rapid disassembly of caveolae. Cell 144 (3), 402–413.

Smeets, B., Alert, R., Pešek, J., Pagonabarraga, I., Ramon, H., Vincent, R., December 2016. Emergent structures and dynamics of cell colonies by contact inhibition of locomotion. Proceedings of the National Academy of Sciences of the United States of America 113, 14621–14626.

Sütterlin, T., Kolb, C., Dickhaus, H., Jäger, D., Grabe, N., January 2013. Bridging the scales: semantic integration of quantitative SBML in graphical multi-cellular models and simulations with EPISIM and COPASI. Bioinformatics (Oxford, England) 29, 223–229.

Szabó, B., Szöll Osi, G.J., Gönci, B., Jurányi, Z., Selmeczi, D., Vicsek, T., 2006. Phase Transition in the Collective Migration of Tissue Cells: Experiment and Model.

Tanaka, S., Sichau, D., Iber, D., 2015. LBIBCell: a cell-based simulation environment for morphogenetic problems. Bioinformatics.

Tozluolu, M., Tournier, A.L., Jenkins, R.P., Hooper, S., Bates, P.A., Sahai, E., 2013. Matrix geometry determines optimal cancer cell migration strategy and modulates response to interventions. Nature Cell Biology 15 (7), 751–762.

Turlier, H., Audoly, B., Prost, J., Joanny, J.-F., January 2014. Furrow constriction in animal cell cytokinesis. Biophysical Journal 106, 114–123.

Tzur, A., Kafri, R., LeBleu, V.S., Lahav, G., Kirschner, M.W., 2009. Cell growth and size homeostasis in proliferating animal cells. Science 325 (5937), 167–171.

van der Wath, R.C., Gardiner, B.S., Burgess, A.W., Smith, D.W., January 2013. Cell organisation in the colonic crypt: a theoretical comparison of the pedigree and niche concepts. PLoS One 8, e73204.

van Leeuwen, I.M.M., Edwards, C.M., Ilyas, M., Byrne, H.M., 2007. Towards a multiscale model of colorectal cancer. World Journal of Gastroenterology 13 (9), 1399–1407.

Van Liedekerke, P., Tijskens, E., Ramon, H., Ghysels, P., Samaey, G., Roose, D., June 2010. Particle-based model to simulate the micromechanics of biological cells. Physical Review E 81, 61906–61915.

Van Liedekerke, P., Roose, D., Ramon, H., Ghysels, P., Tijskens, E., Samaey, G., 2011. Mechanisms of Soft Cellular Tissue Bruising. A Particle Based Simulation Approach.

Van Liedekerke, P., Smeets, B., Odenthal, T., Tijskens, E., Ramon, H., 2013. Solving microscopic flow problems using Stokes equations in SPH. Computer Physics Communications 184, 1686–1696.

Van Liedekerke, P., Palm, M.M., Jagiella, N., Drasdo, D., November 2015. Simulating tissue mechanics with agent-based models: concepts, perspectives and some novel results. Computational Particle Mechanics 2, 401–444.

Van Liedekerke, P., Neistch, J., Johann, T., Alessandri, K., Nassoy, P., Drasdo, D., 2017. Quantitative hybrid modeling reveals predictable mechanical stress response of growing tumor spheroids. bioRxiv.

Vermolen, F.J., Gefen, A., January 2012. A semi-stochastic cell-based formalism to model the dynamics of migration of cells in colonies. Biomechanics and Modeling in Mechanobiology 11, 183–195.

Wu, P.-H., Giri, A., Sun, S.X., Wirtz, D., March 2014. Wu2014. Proceedings of the National Academy of Sciences of the United States of America 1318967111.

Zaman, M.H., Kamm, R.D., Matsudaira, P., Lauffenburger, D.A., August 2005. Computational model for cell migration in three-dimensional matrices. Biophysical Journal 89, 1389–1397.

Zhang, J., Daubert, C.R., Allen Foegeding, E., May 2007. A proposed strain-hardening mechanism for alginate gels. Journal of Food Engineering 80, 157–165.

Zhu, J., Mogilner, A., 2016. Comparison of cell migration mechanical strategies in three-dimensional matrices: a computational study. Interface Focus 6 (5), 20160040.

Zimmermann, J., Camley, B.A., Rappel, W.-J., Levine, H., February 2016. Contact inhibition of locomotion determines cell-cell and cell-substrate forces in tissues. Proceedings of the National Academy of Sciences of the United States of America 1522330113.

Zimmermann, J., 1999. Continuum and Atomistic Modeling of Dislocation Nucleation at Crystal Surface Ledge (Ph.D. thesis).

This book belongs to Central Library BADJI Mokhtar-ANNABA UNIVERSITY

Copyright Elsevier 2024

This page intentionally left blank

This book belongs to Central Library BADJI Mokhtar-ANNABA UNIVERSITY

Copyright Elsevier 2024

Chapter 15

Agent-Based Numerical Methods for 3D Bioprinting in Tissue Engineering

T.J. Sego, N.I. Moldovan and A. Tovar
Indiana University-Purdue University Indianapolis, Indianapolis, IN, United States

15.1 STATE OF THE ART IN 3D BIOPRINTING

In 3D bioprinting, a computerized numerical control system accurately places biomaterials and living cells with the potential to create tissue, organs, and body parts. The computerized printing system can use cell-free biopolymers, cell-seeded microcarriers (bioink), and living cell spheroids. Depending on the bioprinting material, 3D bioprinting is classified into scaffold-based and scaffold-free methods. Scaffold-based methods involve jetting, extrusion, or photopolymerization of a liquid bioink containing living cells, nutrients, and an artificial extracellular matrix (ECM) known as the scaffold (Butcher et al., 2014; de la Puente and Ludeña, 2014; Singh et al., 2016). Scaffold-free methods consist of the direct placement of living cell spheroids on a preexisting support structure in an arbitrary three-dimensional array (Pataky et al., 2012). An indirect approach to bioprinting is the fabrication of a porous structure from a cell-free biopolymer. The cell-free structure allows the introduction and proliferation of living cells shaping the desired tissue or organ. By this method, prevascularization can be employed to promote the development of the vasculature in nutrient-demanding tissue constructs (Naderi et al., 2011). In all methods, the successful implementation relies on the interaction between biomaterials and living cells, which can be predicted by numerical models described in the succeeding sections.

15.1.1 Scaffold-Based Methods

The objective in scaffold-based 3D bioprinting is to produce an artificial ECM or scaffold that mimics a natural ECM, allowing cellular proliferation, differentiation, and migration and, ultimately, supporting the survival and functioning of the living tissue. Artificial scaffolds are produced with biocompatible polymers that can be biologically degraded, absorbed, and replaced by the natural ECM produced by living cells. Biodegradable scaffolds produced from a bioabsorbable polymer have been investigated and utilized in fabrication of various tissues or organs such as skin, cornea, cartilage, bladder, and vessels (Shimizu and Matsuura, 2015).

Polymer hydrogels are the most commonly explored materials for fabricating complex 3D cellular microenvironments, as they can be tuned for ideal degradability, mechanics, and the ability to incorporate biomolecules of interest (Bajaj et al., 2014). Natural hydrogels are commonly utilized as scaffolds in tissue engineering; however, because of potential immunoreaction or infection, synthetic alternatives are preferred (Chen and Hunt, 2007). Alternatively, synthetic hydrogels offer low levels of immunoreaction or infection (Shim et al., 2011). They can also be jetted, extruded, and, in some cases, photopolymerized (Censi et al., 2011; Gudapati et al., 2016).

15.1.2 Scaffold-Free Methods

Another example of a support structure is a Cartesian needle array or kenzan in which the cell spheroids can be aggregated (Moldovan et al., 2017). These methods (scaffold-based and scaffold-free methods) can be used to construct complex biological materials with a high degree of control. This ability provides the potential to fabricate material architectures that match the ones of endogenous tissues and organs. Engineering these complex tissues requires an interdisciplinary

Numerical Methods and Advanced Simulation in Biomechanics and Biological Processes. https://doi.org/10.1016/B978-0-12-811718-7.00015-0
Copyright © 2018 Elsevier Ltd. All rights reserved.

This book belongs to Central Library BADJI Mokhtar-ANNABA UNIVERSITY
Copyright Elsevier 2024

approach, which combines material science innovations with cell biology development and growth factor chemistry by exploring the steps involved in organ development and morphogenesis.

One of the fundamental properties of cells is their propensity to self-organization. This is essential in all biological processes, from bacterial colony formation to mammalian embryology, organogenesis, and tissue repair (Neagu et al., 2005). Remarkably, although the molecular constituents are encoded in genetic information, there is no genetic "blueprint" for their assembling at any dimensional scale. Supramolecular assemblies are emergent structures basically driven by physical principles, such as energy minimization, operating under entropic constraints. For example, this explains the round shape of cell clusters, from embryos to tumors (Shirinifard et al., 2009), also called for this reason cell "spheroids." Moreover, if there are no additional barriers (such as layers of ECM), then when two such spheroids come in contact, they will fuse and collapse into a larger spheroid (Yang et al., 2012). This is possible because within the spheroids the cells perform continuous random movements similar to the Brownian motion of molecules within a lipid droplet (Mombach and Glazier, 1996). All implications of this similarity hold true for fusing spheroids, such as surface tension (Beysens et al., 2000), contact angle, and "neck" diameter (McCune et al., 2014). In addition, energy minimization obliges different cells with various adhesiveness to assume a layered distribution within the spheroids (Beysens et al., 2000). This spontaneous process called "cell sorting" is of fundamental importance in embryogenesis and beyond (Zhang et al., 2011).

These phenomena are now exploited for rational design of biosimilar constructs with tissue engineering applications (Mironov et al., 2003; Yang et al., 2012), representing the foundation of the emerging "scaffold-free" biofabrication (Mironov et al., 2009). Moreover, cell spheroid fusion, either in dual or in larger constructs, has been modeled using a variety of methods, as described in subsequent sections of this chapter.

15.2 MODELS IN 3D BIOPRINTING

To further the capabilities of tissue engineering applications, various models have been proposed to predict the dynamics of cellular aggregates. These models seek to predict morphogenetic phenomena such as proliferation (Mueller-Klieser and Sutherland, 1982), self-assembly (Jakab et al., 2008; Surapaneni et al., 1997), and cell sorting (Mombach et al., 1995; Steinberg and Takeichi, 1994), or application-specific metrics such as spheroid fusion (Shafiee et al., 2015) or viability (Freyer, 1988; Freyer and Sutherland, 1980; Haji-Karim and Carisson, 1978; Mueller-Klieser et al., 1986; Sutherland et al., 1986). Models in tissue engineering typically fall within one of three methods: lattice Boltzmann (LB) methods, cellular particle dynamics (CPD), and kinetic Monte Carlo (KMC) methods. However, other models have been proposed, including cellular automaton (CA) (Picioreanu et al., 1998) and phase-field methods (Yang et al., 2012).

15.2.1 Lattice Boltzmann Methods

On some scale, living tissue functions like a fluid. For example, the tendency of cells to sort themselves into distinct regions is comparable to the ordering of fluids (Beysens et al., 2000), and spheroid fusion has been compared to the merging of liquid drops (McCune et al., 2014). By this paradigm, the dynamics of a population of cells can be modeled according to the description of fluids in statistical mechanics. Specifically, LB methods have emerged as a discretized form of the Boltzmann equation to simulate the macroscopic dynamics of large populations of microscopic entities. These methods neglect individual cellular interactions and instead seek to efficiently model macroscopic behavior of cellular populations over extended periods of time. In LB methods, cell populations and the medium in which they are placed are described by distributions of particles with a particular velocity, which generally evolve to some equilibrium state. In this way, a system of cellular aggregates is modeled as a multiphase system, where aggregates tend to evolve according to principles such as surface tension and barycentric velocity. LB methods have been applied to provide insight into the fusion of single cell-type spheroid pairs (Cristea et al., 2011) and complex constructs (Cristea and Neagu, 2016), as well as the characteristics of multicellular populations (Krafczyk and Berrios, 1998).

15.2.2 Cellular Particle Dynamic Methods

On a smaller scale, CPD methods model cells as pointlike particles, called cellular particles (CPs), in a continuous domain, or as consisting of a collection of CPs that are modeled to obey classic descriptions of motion with the introduction of stochastic processes in some overdamped Langevin equation. The Langevin equation of a system of CPs is constructed as a system of differential equations that consists of a summation of potential energy expressions. These potential energy expressions model the influence of intercellular, environmental, and, for cells consisting of multiple CPs, intracellular

This book belongs to Central Library BADJI Mokhtar-ANNABA UNIVERSITY
Copyright Elsevier 2024

interactions. CPD methods have been applied to the modeling of aggregate fusion (Flenner et al., 2008; Kosztin et al., 2012; Shafiee et al., 2015) and cell sorting of multicellular systems (Flenner et al., 2012).

15.2.3 Kinetic Monte Carlo Methods

On a still smaller scale, KMC methods model cells as occupying points in a discretized lattice and evolving according to simple, stochastic rules. The modeling description of cellular dynamics is type specific and uniformly applied to all cells of a particular type. In this way, KMC methods most closely resemble an agent-based model (although certain aspects of LB and CPD methods accomplish the same). The rules that govern the evolution of the cellular system generally enforce a tendency of the system to some lower energy state, where events that increase the system energy still may occur, but with a decreasing probability proportional to the increase in system energy. The likelihood of events is then considered at randomly selected sites, which produces characteristics like Brownian motion (Mombach and Glazier, 1996). The dynamics of cellular activity then takes the form of the occupancy of lattice sites being traded among cells in the population, or by the medium in which they are situated, which has been successful at predicting cell sorting (Flenner et al., 2012; Graner and Glazier, 1992; Zhang et al., 2011) and fusion of aggregates (Fleming et al., 2010; Flenner et al., 2008, 2012; Jakab et al., 2008). A very popular KMC method in literature is the focus of subsequent sections of this chapter, the implementation of which is most popularly used in the software CompuCell3D (Swat et al., 2012).

15.3 AGENT-BASED MODELS IN SCAFFOLD-FREE 3D BIOPRINTING

This section introduces the basic concepts and relevance of agent-based modeling, namely the paradigm by which complex systems may be reduced to elementary, predictable components. A widely used agent-based model in the modeling of cellular dynamics is then presented, called the cellular Potts model (CPM), which is the focus of subsequent sections in this chapter.

15.3.1 Abstract Description of an Agent

It is not mere musing to propound that both a human and a block of iron are the consequences of a (practically) uncountable number of active constituents and their perpetual activities. Even if either macroscopic entity has the appearance of being stationary, at some smaller scale there are a great number of components that are very much not stationary at all. This is, of course, referring to the consistency of matter at the atomic scale, which, for most practical macroscopic modeling applications, can be represented by macroscopic descriptions.

Considering the block of iron, if subjected to some stimulus, there are many sufficiently accurate descriptions to predict how the block responds. The same is true for a whole population of blocks, whether they be colliding or joined together into some structure. But subject a human to stimuli—whether caffeine or conversation—and what will the human do? Depending on the context, the behavior of a human can be well predicted through empirical means and probabilistic descriptions: subject a human to hunger and, with a very high probability, the human will seek out and consume food. But subject a population of humans to hunger who have access to multiple sources of food, and what will the population do? And how will they go about acquiring their respective choice, given their respective level of hunger, or how they know each other, or how each source dispenses food? Introduce more humans, or more sources, or more behavioral considerations, and the scenario very quickly presents a sort of insurmountable complexity to traditional mathematical descriptions for modeling global behavior. Therefore, in the case of the human (as the sociologist or city planner would ask), how does one model the collective behavior of a population of humans? The same can be asked about cells, or about nations, or about a great many other complex systems. Except, like humans, a particular cell or nation tends to exert a particular response to a particular stimulus or to a set of stimuli.

This is all to say, although the behavior of a population of decision-making entities may be too complex to predict with mathematical precision, on some smaller scale the behavior of the individual entities is reasonably predictable. These entities are called agents, and the modeling and simulation of a population of interacting agents in an environment is called an agent-based model (Railsback and Grimm, 2011). An agent is a discrete, autonomous entity that makes decisions in response to interactions. It makes decisions according to local, rule-based behavior, which is affected by the elementary attributes of the agent. Attributes may be specific to each agent in a population, or to a subset of agent type, and each agent may modify its own attributes as part of its behavioral processes. Typically, each agent has a limited knowledge of its environments and is confined to make decisions based on local conditions, called the interaction of the agent. Agents decide according to environmental conditions (agent–environmental interactions), internal mechanisms

This book belongs to Central Library BADJI Mokhtar-ANNABA UNIVERSITY Copyright Elsevier 2024

(intraagent interactions), and neighboring agents (interagent interactions). Agents are connected through some interaction topology, whether it be by proximity in a Euclidean space or discretized lattice, or otherwise.

15.3.2 From Cells Come Biological Patterns: Scales and Emergence

The intraagent interactions of each agent can either be modeled as some set of analytic expressions, or the attributes of each agent can result from of some population of agents on a smaller scale. In the aforementioned case of a human, every agent can consist of a population of organs, or of cells, or of some other population of biological "subagents," which then constitutes the internal mechanisms of the human. Generally, the intraagent interactions of an agent on some particular scale can be the consequence of a population of agents on some smaller scale, and the global behavior of the population of agents on that particular scale can govern the behavior of a single agent on some larger scale, and so on—e pluribus unum.

Whether modeling a single population, or multiple populations at various scales, resulting macroscopic phenomena emerge from microscopic activity, broadly referred to as emergence, which is a central goal of agent-based modeling: given a population of discrete, autonomous agents, what global phenomena emerge? In the case of the block of iron, the material properties of iron emerge from a population of iron atoms. The societal constructs in which humans live emerge from a population of humans, each of which emerges from a population of cells, which emerge from populations of atoms, and so on (Deutsch et al., 2007). In biological applications, the distinction is probably less ambiguous: the terminal emergent phenomenon of a population of cells is the organism, during which various intermediary phenomena emerge.

15.3.3 Generalized Cellular Potts Model

15.3.3.1 Qualitative Description

Imagine a discretized regular domain containing a collection of integers that have aggregated by value. The integer value of each aggregate is unique so that each aggregate can be readily identified, and all of the aggregates are surrounded by another unique integer that fills the rest of the domain. Each aggregate is an agent in a medium, and the unique integers are their identification. A population of agents then exists in a medium, in which they carry out their various activities. Fig. 15.1 shows the agents (cells) and the medium.

The agents mingle and jostle each other with the characteristics of Brownian motion. On inspection of some particular agent, it is found that the agent continues to overtake some points of the domain from a neighboring agent, and surrenders others points to the neighbor, in a seemingly random manner. The agent happens to have multiple neighbors, and similar phenomena occur at its interface with each of them. Yet, despite all of the capturing, surrendering, and retaking of territory, the agent tends to maintain a particular shape, as do all of the agents of the population. In fact, some agents tend to maintain the same particular shape.

Those same similar-looking agents also appear to exert some other similar characteristics. Imagine that the agent population was initially randomly distributed and that these similar-looking agents, on meeting each other, tend to stay together; eventually, they begin to form an aggregate of similar-looking agents. Some of these agents continue to mingle within the population of other agents (who also happen to look alike); however, over time, the similar-looking agents eventually all cluster together. Occasionally one of the agents leaves the group and ventures out into the population of other agents, where it then seems more obtuse than before. Imagine that those other agents have formed a sort of perimeter around the aggregate, rather than forming their own; they must not prefer to be in contact with each other and prefer the medium even less.

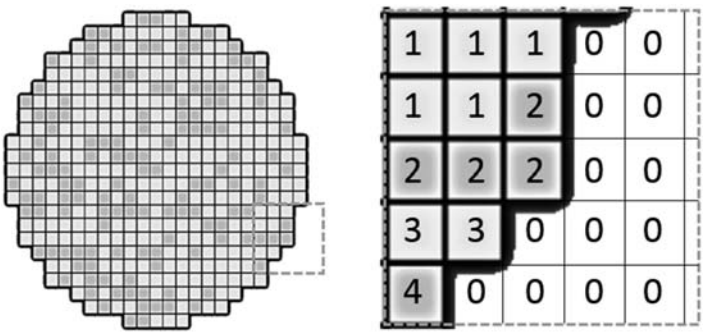

FIGURE 15.1 Discrete, two-dimensional cellular Potts model lattice. The medium is labeled with 0. The cells are labeled with unique numbers (1, 2, 3, and 4). The two different agent (cell) types are shaded light and dark gray.

This book belongs to Central Library BADJI Mokhtar-ANNABA UNIVERSITY Copyright Elsevier 2024

These are some of the emergent phenomena of a simulation produced by the generalized *CPM*, which, in its original proposal (Graner and Glazier, 1992), was intended to produce this imaginary scenario: cell sorting. In the CPM, every agent is assigned a unique *identification number*, and each is one of a set of agent types. CPM modeling characteristics are described by the agent type, and every agent of a type is assigned the same attributes such that two agents of the same type are only distinguishable by the identification number, hence the similar-looking agents with similar characteristics.

The territorial exchanges of the domain, called the *lattice*, by the agents are actually the accepted subset of randomly selected simulation events, called *copy attempts*. For each copy attempt, a lattice site is randomly selected, called the *source site*, as is one of its nearest neighbor sites, called the *target site*. The CPM considers the likelihood that the identification number at the target site becomes the identification number at the source site.

Just as the selection of the site of a copy attempt is a stochastic process, so too is its acceptance or rejection. Acceptance and rejection are dictated by a *transition rule* that expresses the probability of the occurrence of the copy attempt, which is influenced by a virtual Hamiltonian of the agent population. The transition rule dictates that if the copy attempt, at most, does not increase the Hamiltonian, then the copy attempt is accepted. If the copy attempt does increase the Hamiltonian, then the probability of occurrence decreases and continues to decrease with increasing additional virtual energy due to the copy attempt.

The Hamiltonian is a modeling description that is universally applied to the agents, but how the agents affect the Hamiltonian is contextual. Among an arbitrarily complex set of other agent-based modeling attributes, a CPM agent type is necessarily modeled with attributes that dictate how the agent type influences the Hamiltonian. The relationship between the agents and the Hamiltonian is subject of subsequent elaboration, but, for the present discussion, agents generally obey the rule of reducing the system energy, and occasionally they disobey. The CPM then models random microscopic activity such that, given the occurrence of a sufficient number of microscopic events, emergent phenomena occur because of some lower macroscopic energy state. The following sections outline the mathematical formulation of the CPM as described here, along with select applications so to demonstrate both some emergent phenomena predicted by the model as well as its usefulness.

15.3.3.2 Mathematical Formulation

Let $\mathcal{L}$ be a regular d-dimensional lattice occupied by agents of unique identification $\sigma_i \in \mathcal{J} \subset \mathbb{N}$. Let $\sigma(r,\ t) \in \mathcal{J}$ denote the identification number of the occupied site r at time t,

$$\sigma : \mathcal{L} \rightarrow \mathcal{J}, \tag{15.1}$$

where each σ_i occupies the lattice sites $\mathcal{V}^{\sigma_i} \subset \mathcal{L}$. Each σ_i has a corresponding agent type $\tau = \tau(\sigma) \in \mathcal{F}$ that defines the behavior of agent σ,

$$\tau : \mathcal{J} \rightarrow \mathcal{F}, \tag{15.2}$$

such that for some σ_i and σ_j, if $\tau(\sigma_i) = \tau(\sigma_j)$, then σ_i and σ_j are phenotypically indistinguishable.

Let $r_s \in \mathcal{L}$ denote a randomly selected lattice source site, and let $r_t \in \mathcal{N}(r_s)$ denote a randomly selected nearest neighbor target site in the neighborhood $\mathcal{N}(r_s)$ of r_s. The copy attempt $\sigma(r_t,\ t') \rightarrow \sigma(r_s,\ t)$ at time $t' > t$ occurs as a stochastic function of the system Hamiltonian $\mathcal{H}$,

$$\sigma(r_t,\ t') = \sigma(r_s,\ t) \text{ with probability } e^{-\max\{0,\ \frac{\Delta\mathcal{H}}{\mathcal{H}^*}\}}, \mathcal{H}^* > 0, \tag{15.3}$$

where $\mathcal{H}^*$ is a coefficient and $\Delta\mathcal{H}$ is the change in system Hamiltonian due to the copy attempt. This is to say, the probability that the copy attempt occurs is a Boltzmann acceptance function of the system Hamiltonian, where events that, at most, do not increase the Hamiltonian always occur. $\mathcal{H}^*$ can be thought of as a sort of system temperature, because greater $\mathcal{H}^*$ increases the probability of a copy attempt and so produces more agent motility.

15.3.3.3 Methods and Models

What, then, is a CPM agent in a biological process? Cells interact, take particular shapes, and perform particular functions, so perhaps an agent is a cell, and so do cell aggregates, organs, and organelles. One may construct a simulation that produces an agent with the phenotype of a certain cell, another with agents resembling the proteins within that cell, and then another with agents that act like a population of that cell. The mathematical framework of the CPM is ambiguous in this context (and powerfully so) in that only the tendency of the random events associated with each agent is described. That is, the agents of a CPM simulation are assigned physical meaning by their emergent attributes, which may be a product of, or contribute to, the intraagent interactions of some other agent on some other scale.

This book belongs to Central Library BADJI Mokhtar-ANNABA UNIVERSITY Copyright Elsevier 2024

The CPM has many characteristics of a traditional CA. Like the CA, the CPM consists of a lattice of states, and the states evolve according to a transition rule that considers neighboring states. However, contrarily to the CA, where the transition rule is applied globally and simultaneously, the copy attempts in the CPM occur at randomly selected lattice sites and are not simultaneously considered. For example, say some two copy attempts are to be accomplished in a simulation while modeling a volumetric constraint, and both happen to involve a particular cell. If the first copy attempt is accepted, then the volume of the cell changes, which then may affect the probability of the occurrence of the second copy attempt. And so a given set of copy attempts can only be computed independently if each attempt is sufficiently far from all other attempts, which, for a finite domain and sufficient events to produce emergence, is never the case. In this way the CPM has many of the dynamic characteristics of a CA, but is, in principle, a Monte Carlo method. More specifically, because changes in state occur in a probabilistic manner, the CPM is a KMC method and of the class of Potts models (the identification number is the Potts model spin state).

In the spirit of both CA and the general Monte Carlo method, the virtual time unit of the CPM is called a *Monte Carlo step* (MCS) and is typically demarcated as the accomplishing of a number of randomly selected copy attempts equal to the number of sites in the lattice. Therefore, similarly to the simultaneous application of a transition rule at all lattice sites in the CA, in one MCS every lattice site has equal probability of being selected once as a source site r_s and once as target site r_t in a copy attempt $\sigma(r_t, t') \rightarrow \sigma(r_s, t)$. And if T and T' denote the current and next virtual times, then T' takes the form $T' = T + |\mathcal{L}|(t' - t)$. However, it should be noted that the demarcation of an MCS with respect to the number of copy attempts is arbitrary and has no intrinsic relationship with physical time.

15.3.3.4 The Hamiltonian

In general, the Hamiltonian $\mathcal{H}$ is a summation of energy components $\mathcal{H}^i$, each of which models various emergent phenomena,

$$\mathcal{H} = \sum_i \mathcal{H}^i. \tag{15.4}$$

Hamiltonian expressions are formulated to model an agent-type attribute such that the attribute produces the minimum value of the Hamiltonian expression. Therefore if, say, an agent is to dissociate into fragments, then a corresponding Hamiltonian expression would contribute energy because of the coincident elements of the agent in the lattice. That is to say, the lowest energy state of a dissociated agent is one where no elements of the agent in the lattice are in contact.

If agent σ_i of type $\tau(\sigma_i)$ tends to occupy $v_c^{\tau(\sigma_i)}$ lattice sites, then let $\mathcal{H}^v$ be the energy contributed to the system because of deviations of $|\mathcal{V}^{\sigma_i}|$ from $v_c^{\tau(\sigma_i)}$ for all $|\mathcal{J}|$ agents:

$$\mathcal{H}^v = \sum_{i=1}^{|\mathcal{J}|} \lambda_v^{\tau(\sigma_i)} \left(|\mathcal{V}^{\sigma_i}| - v_c^{\tau(\sigma_i)}\right)^2, \ \lambda_v^{\tau(\sigma_i)} > 0, \tag{15.5}$$

where $\lambda_v^{\tau(\sigma_i)}$ is the Lagrange multiplier for the spatial occupation constraint of type $\tau(\sigma_i)$. $\mathcal{H}^v$ then contributes to the system such that copy attempts tend to maintain each σ_i at the spatial constraint $v_c^{\tau(\sigma_i)}$ of its type $\tau(\sigma_i)$.

In the same manner, if $\tau(\sigma_i)$ tends to maintain some number of boundary sites $b_c^{\tau(\sigma_i)}$, then let $\mathcal{B}^{\sigma_i} \subseteq \mathcal{V}^{\sigma_i}$ denote the set of lattice sites that form a closed boundary of $\mathcal{V}^{\sigma_i}$, and let $\mathcal{H}^b$ be the energy contributed to the system because of deviations of $|\mathcal{B}^{\sigma_i}|$ from $b_c^{\tau(\sigma_i)}$:

$$\mathcal{H}^b = \sum_{i=1}^{|\mathcal{J}|} \lambda_b^{\tau(\sigma_i)} \left(|\mathcal{B}^{\sigma_i}| - b_c^{\tau(\sigma_i)}\right)^2, \lambda_b^{\tau(\sigma_i)} > 0, \tag{15.6}$$

where $\lambda_b^{\tau(\sigma_i)}$ is the Lagrange multiplier for the boundary constraint of agent type $\tau(\sigma_i)$. When paired with $\mathcal{H}^v$, $\mathcal{H}^b$ contributes to the system such that copy attempts tend to maintain each σ_i at a particular shape. For example, for $b_c^{\tau(\sigma_i)} = 0$ and any $v_c^{\tau(\sigma_i)}$, the minimum surface area in three-dimensional space is produced by a sphere, but for very large $b_c^{\tau(\sigma_i)}$, an agent in three-dimensional space would tend to resemble a line.

For each pair of agent types τ and τ', if there is some contact energy $J(\tau, \tau')$ due to the interface between two agents, then let $\mathcal{H}^h$ describe the contact energy of all agent interfaces:

$$\mathcal{H}^h = \sum_{i=1}^{|\mathcal{L}|} \sum_{j=1}^{|\mathcal{N}(r^i)|} \left(1 - \delta_{\sigma(r^i),\sigma(r^{j,i})}\right) J\left(\tau\left(\sigma\left(r^i\right)\right), \tau\left(\sigma\left(r^{j,i}\right)\right)\right), \tag{15.7}$$

This book belongs to Central Library BADJI Mokhtar-ANNABA UNIVERSITY
Copyright Elsevier 2024

where $r^{j,i} \in \mathcal{N}(r^i)$ is the jth element of the neighborhood of the ith element $r^i \in \mathcal{L}$ and δ is the Kronecker delta. $\mathcal{H}^h$ then contributes to the system such that copy attempts tend to rearrange the agents to minimize their contact energy. The construction of $\mathcal{N}(r^i)$ can be the same as those from the CA (e.g., Neumann, Moore) or of some other formulation.

15.3.3.5 Implementation

Numerical implementation of the CPM can be accomplished in a number of ways (Swat et al., 2012), although some basic, requisite features of the formulation will always appear. Neglecting design considerations of the lattice, initial cellular configuration, and specific energy expressions (e.g., adhesion), any implementation of the CPM must maintain the elementary components of the unique identification, agent type, and, for any specific energy expression, spatial configuration of each agent. Although identification and type labels are not necessarily restricted to any class, positive integer labels are probably most advisable for efficient programming considerations such as index mapping, where identification and type labels can be used to construct complex lookup tables.

As a simple example, consider the case of modeling adhesion. Rather than allocating an array of adhesion coefficients for each simulation agent, a symmetric matrix of adhesion coefficients can be constructed, where each element in the adhesion matrix corresponds to the adhesion coefficient of a pair of agent types. When considering a copy attempt, a programming call can efficiently retrieve the relevant adhesion coefficient by using the two agent types of the attempt as the indices into the adhesion matrix. Further programming efficiencies can include maintaining the list of agent types as a one-dimensional array, where the order of each element corresponds to the agent identification number (e.g., element two is the type of agent two). This effectively eliminates the need to maintain a separate array of all identification numbers by relying on whatever structure that maintains the lattice to store information about the existence of currently present agents in the simulation. If the lattice is a multidimensional array of integers, then one can simply use the integer label at a site as an index to retrieve the agent type, which can then be used as an index into the various agent models, etc.

It should also be noted that, while calculating the total energy of the system may be useful for validation of an implementation, e.g., to demonstrate the minimization of energy (Neagu et al., 2005) or, perhaps, to formulate some convergence criterion, which is not commonly reported in literature, the only relevant information to calculating the probability of a copy attempt is the change in system energy due to its occurrence. This is particularly relevant because the copy attempt is the fundamental action of the dynamical system of a CPM simulation, which may consist of even billions of copy attempts. Considering this computational aspect, significant improvements in simulation performance may be accomplished by merely neglecting to maintain a transient history of the system energy.

The same is true for seemingly insignificant modifications such as algebraic simplifications, as well as for programming considerations such as program structure, preallocation, and parallelization (Chen et al., 2007). For an algorithm that performs the copy attempt, a mathematical expression that produces the same result with one less numerical calculation results in one less calculation per copy attempt per MCS, potentially reducing the total computational cost of a simulation by billions of calculations. While the fundamental ideas of agent-based modeling may beg the programmer to construct an object-oriented programming structure, meticulous analysis must be performed to ensure that additional communication overhead does not severely diminish computational efficiency, even to striving to reduce the time to complete an MCS on the scale of microseconds. Aforementioned attempts at parallelization of the CPM must devise an algorithm that can determine the independence of a series of copy attempts, send and receive all necessary information about the copy attempts to separate processors, and compile results from all processors, and all in less time than what would have been required to simply process them in a serial implementation. Any implementation must also account for various sizes of simulations for memory considerations, perhaps by the perpetual activity of asking, at what simulation size would this structure crash an ordinary computer?

With all these in mind, the following pseudocode presents a general implementation of one MCS for a simple simulation, using some of the aforementioned examples of index mapping and preallocation (Algorithm 15.1). In this algorithm, Δr is a previously allocated array of relative indices to a neighborhood $\mathcal{N}(r)$ of lattice site r. The function draw_a_source($\mathcal{L}$) returns a randomly selected index in $\mathcal{L}$, draw_a_target(r) returns a randomly selected site in $\mathcal{N}(r)$, and rand() returns a uniformly distributed number in [0, 1]. According to aforementioned efficiencies, the pseudocode assumes a symmetric adhesion coefficient matrix $J(\tau_1, \tau_2)$ where (τ_1, τ_2) is the index to the adhesion coefficient between types τ_1 and τ_2, as well as a one-dimensional array of agent types $\mathcal{F}$, where the identification number of an agent is the index to its type in $\mathcal{F}$. Comments are annotated in parentheses and all mathematical simplifications are neglected, for clarity.

Fig. 15.2 shows an example of the application of this algorithm on a small agent population. This particular simulation is designed to model a volumetric constraint (intraagent interactions) and intercellular adhesion (interagent interactions)

This book belongs to Central Library BADJI Mokhtar-ANNABA UNIVERSITY Copyright Elsevier 2024

ALGORITHM 15.1 (Monte Carlo Step of Copy Attempts) To Find the Resulting Lattice Configuration After One MCS, Given the Current Lattice Configuration

For copy_attempt = 1 to $|\mathcal{L}|$ (number of lattice sites)

(Get the next copy attempt site information)

$r_s =$ draw_a_source($\mathcal{L}$)

$r_t =$ draw_a_target(r_s)

$\mathcal{N}(r_t) = r_t + \Delta r$

(Get the identification and type labels)

$\sigma_s = \mathcal{L}(r_s)$

$\sigma_t = \mathcal{L}(r_t)$

$\tau_s = \mathcal{F}(\sigma_s)$

$\tau_t = \mathcal{F}(\sigma_t)$

(Calculate the energy contribution due to the volumetric constraint)

$\Delta\mathcal{H}^v = \lambda_v^{\tau_s}\left[\left(|\mathcal{V}^{\sigma_s}| + 1 - v_c^{\tau_s}\right)^2 - \left(|\mathcal{V}^{\sigma_s}| - v_c^{\tau_s}\right)^2\right]$

$\Delta\mathcal{H}^v = \Delta\mathcal{H}^v + \lambda_v^{\tau_t}\left[\left(|\mathcal{V}^{\sigma_t}| - 1 - v_c^{\tau_c}\right)^2 - \left(|\mathcal{V}^{\sigma_t}| - v_c^{\tau_c}\right)^2\right]$

(Calculate the energy contribution due to adhesion)

$\Delta\mathcal{H}^h = \sum_{r_n \in \mathcal{N}(r_t)} \left(1 - \delta_{\sigma_s, \mathcal{L}(r_n)}\right) J(\tau_s, \mathcal{F}(\mathcal{L}(r_n)))$

$\Delta\mathcal{H}^h = \Delta\mathcal{H}^h - \sum_{r_n \in \mathcal{N}(r_t)} \left(1 - \delta_{\sigma_t, \mathcal{L}(r_n)}\right) J(\tau_t, \mathcal{F}(\mathcal{L}(r_n)))$

(Calculate the probability of occurrence of the copy attempt)

$\Delta\mathcal{H} = \Delta\mathcal{H}^v + \Delta\mathcal{H}^h$

$P = \exp\left(-\max\left\{0, \frac{\Delta\mathcal{H}}{\mathcal{H}^*}\right\}\right)$

(Check for occurrence of the copy attempt and implement if accepted)

If rand() $\leq P$

$\mathcal{L}(r_t) = \mathcal{L}(r_s)$

End If

Next copy_attempt

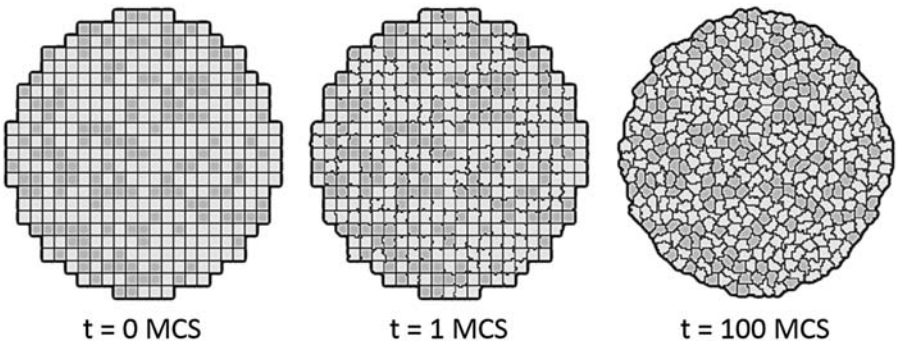

FIGURE 15.2 Two-dimensional simulation demonstrating the Monte Carlo step algorithm. The medium is depicted in white. The two different cell types are shaded light and dark gray.

and to simulate a number of copy attempts per MCS equal to the number of lattice sites $|\mathcal{L}|$. Fig. 15.2 illustrates the initial configuration, the configuration after one completed MCS, and configuration after 100 MCS.

15.4 APPLICATIONS

This section first presents two traditional applications for spheroid-based fabrication, followed by three applications of a "hybridized" CPM: cell sorting, fusion, diffusion, chemotaxis, and hypoxia.

15.4.1 Cell Sorting

In its original publication (Graner and Glazier, 1992), the CPM was presented for the application of modeling cell sorting in aggregates. From a qualitative perspective, modeling cell sorting in the CPM can be accomplished by the following

This book belongs to Central Library BADJI Mokhtar-ANNABA UNIVERSITY Copyright Elsevier 2024

thought experiment. Say an aggregate is initially populated with a random distribution of two types of cells, type 1 and type 2. If the contact energy at the interface of two cells of type 1 is greater than the energy at the interface of two cells of type 2, then what would be the distribution of the aggregate with the least system energy? The answer is a population distribution such that type 2 cells are most in contact with each other and type 1 cells are least in contact with each other. That is, type 1 cells migrate to the perimeter of the aggregate. In the CPM, agent types that are more strongly bonded are modeled as contributing less energy to the system so as to increase the probability of their maintaining an interface.

Fig. 15.3 shows results of a two-dimensional cell sorting simulation performed in CompuCell3D. In this simulation, a spheroid was initialized with a randomly distributed population of two cell types, referred to as NonCondensing and Condensing, which are less and more adhesive, respectively. By the first 20 MCS, all initiation artifacts vanished and nearby cell types collected together. Distinct regions of high- and low-adhesion cells formed by 880 MCS, as well as the completion of a monolayer of low-adhesion cells at the perimeter of the spheroid. By 10,000 MCS, cell sorting completed with a distinct core of high-adhesion cells being surrounded by a region of low-adhesion cells. Further morphological development of the spheroid would likely produce an approximately uniform thickness of the low-adhesion region, as the two cell-type regions evolve to minimize their interface.

15.4.2 Spheroid Fusion

If a domain is randomly populated with cells that contribute more energy by being in contact with the medium than with each other, given sufficient time and Brownian motion, the cells will tend to minimize the total interface of all cells with the medium: cell aggregation. Because the lowest energy state of the system has the smallest interface with the medium, the cells will tend to form a circular aggregate in two-dimensional space and a spheroid in three-dimensional space. Placing two spherical aggregates in contact, they then have the opportunity to further decrease their combined energy by further decreasing their interfaces with the medium: spheroid fusion. Fig. 15.4 demonstrates on such application, where 10 spheroids are arranged in a circle and permitted to fuse, producing a toroidal structure. Further simulation of this structure would likely produce a sorted configuration.

15.4.3 Diffusion

The CPM can be extended to modeling in a continuous domain $\mathcal{C}$, where every lattice point $r = r(X)$ has a corresponding coordinate $X \in \mathcal{C} \subset \mathbb{R}^d$ and every MCS $m = m(t)$ has a corresponding time $t \in \mathbb{R}_{\geq 0}$. For example, let $C = C(X, t)$ be the

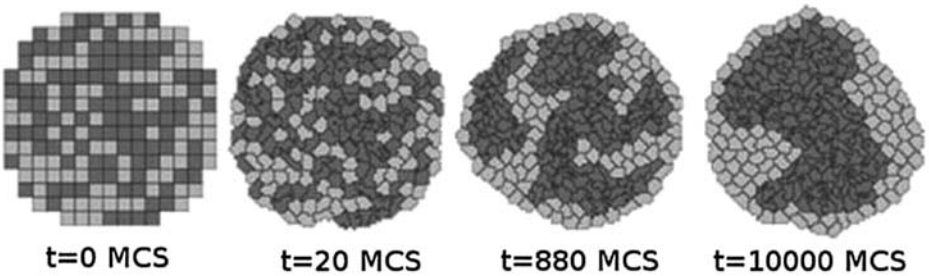

FIGURE 15.3 Snapshots of the cell-lattice configurations for the cell-sorting simulation in Listing 1. The boundary energy hierarchy drives Non-Condensing (light gray) cells to surround Condensing (dark gray) cells. The white background denotes surrounding medium (Swat et al., 2012).

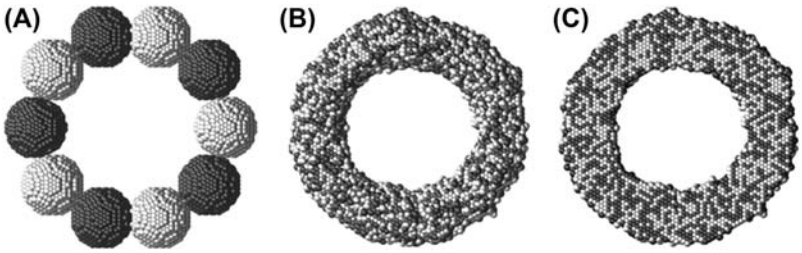

FIGURE 15.4 KMC simulation of toroidal structure formation through the fusion of 10 cell aggregates. Top view of the fusing aggregates at (A) the beginning (t = 0) and (B) the completion of fusion. (C) Cross section through the median plane of the fused toroidal structure shown in (B). Otherwise identical cells, initially located in adjacent aggregates, are colored differently to emphasize the degree of mixing during fusion (Flenner et al., 2012).

This book belongs to Central Library BADJI Mokhtar-ANNABA UNIVERSITY Copyright Elsevier 2024

concentration of a chemical species in a homogenous domain of diffusion coefficient D. If each agent is described with a chemical source rate $s = s(\tau(r, m)) \in \mathcal{S}$ (production or consumption),

$$s: \mathcal{F} \rightarrow \mathcal{S}, \tag{15.8}$$

then a corresponding source field $S = S(X, t) = s(r(X), m(t))$ can be assigned to an expression for the diffusion of C in $\mathcal{C}$

$$\dot{C} = D\partial_{ii}C + S. \tag{15.9}$$

The simultaneous updating of $\mathcal{L}$ and solutions to differential equations in $\mathcal{C}$ are readily accessible because, in numerical applications, differential equations are often discretized in a similar manner to that of the CPM and solved, whether by the finite difference method, finite element method, or otherwise. By relating the lattice of the CPM to continuous fields, the CPM can be extended to modeling the effects of discrete agents on their environment, and vice versa, such as the consumption of nutrients, cell signaling, chemotaxis, and cell state changes.

15.4.4 Chemotaxis

If an agent moves along a chemical gradient, then let $\mathcal{H}^c$ describe the energy contributed to the system because of the influence of the chemical species C on the agent:

$$\mathcal{H}^c = \sum_{i=1}^{|\mathcal{L}|} \lambda_c^{\tau(\sigma(r^i))} C\left(X\left(r^i\right)\right), \tag{15.10}$$

where $X(r^i)$ is the coordinate in $\mathcal{C}$ corresponding to r^i in $\mathcal{L}$ and $\lambda_c^{\tau(\sigma(r^i))}$ is the Lagrange multiplier for the chemotactic response of agent type $\tau(\sigma(r^i))$. Note that if $\lambda_c^\tau > 0$, type τ agents are inclined to move toward lower field values in $\mathcal{C}$, and conversely type τ agents will move toward higher field values for $\lambda_c^\tau < 0$. For $\lambda_c^\tau = 0$, type τ agents are unaffected by C.

15.4.5 Hypoxia

Additional transition rules can be applied to a CPM simulation that model the influence of field solutions in $\mathcal{C}$ on the agents in $\mathcal{L}$. Such rules may seek to model phenomena such as cell splitting, differentiation, or death. Generally speaking, transition rules of this class further capture the interactivity of CPM agents and their corresponding environmental conditions.

Fig. 15.5 demonstrates one such transition rule, which models the death of an agent due to insufficient field values in $\mathcal{C}$ (i.e., hypoxia). In this simulation, a spheroidal cross section was initiated with a population of high-adhesion, low-consumption agents.

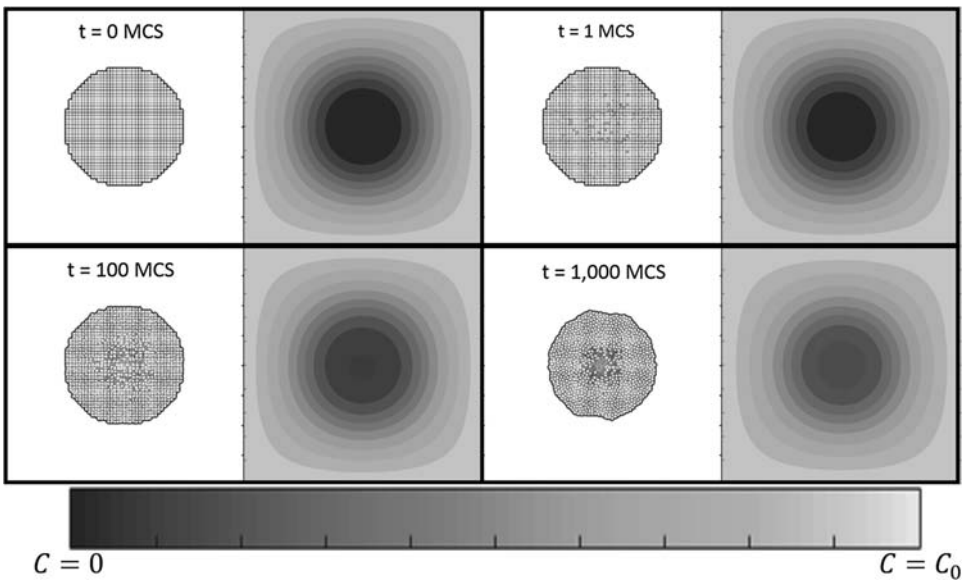

FIGURE 15.5 Hypoxic cell death in a randomly distributed cell population.

This book belongs to Central Library BADJI Mokhtar-ANNABA UNIVERSITY
Copyright Elsevier 2024

Let $\mathcal{T}^d$ be a stochastic transition rule that describes the transition of agent type τ to its dead state τ^d:

$$\tau(\sigma_i(t')) = \mathcal{T}^d(\tau(\sigma_i(t)),\ C(X^{\sigma_i})), \tag{15.11}$$

where $X^{\sigma_i} = X(\rho^j_{\sigma_i}) \in \mathcal{C}^{\sigma_i}$ for the subdomain $\mathcal{C}^{\sigma_i} \subseteq \mathcal{C}$ that corresponds to the subdomain $\rho^j_{\sigma_i} \in \mathcal{V}^{\sigma_i} \subseteq \mathcal{L}$ of agent σ_i. Agent σ_i transitions to its dead state as a function of the mean concentration C_{σ_i} in $\mathcal{C}^{\sigma_i}$:

$$C_{\sigma_i} = \frac{1}{|\mathcal{C}^{\sigma_i}|} \sum_{j=1}^{\mathcal{C}^{\sigma_i}} C\left(X\left(\rho^j_{\sigma_i}\right)\right). \tag{15.12}$$

The transition occurs with the probability

$$P(\tau(\sigma_i(t')) = \tau^d) = pe^{-\left(\frac{C_{\sigma_i}}{\gamma}\right)^2}, \tag{15.13}$$

where p and γ are coefficients. Another agent type is then introduced to the simulation, with corresponding attributes. In this example, the corresponding dead state was modeled with a 25% reduction in volumetric constraint, no consumption and no change in adhesion attributes. As cells at the core of the spheroid in Fig. 15.5 are subjected to lower concentration field values, the probability of cell death then increases. As more MCS transpire, more cells at the core die, which has been observed in experimental observations (Freyer and Sutherland, 1980; Mueller-Klieser et al., 1986; Mueller-Klieser and Sutherland, 1982).

15.5 DISCUSSION AND OUTLOOK

Comparison of different models. The process of choosing a model involves many intrinsic and extrinsic considerations. Compared with other methods, the mathematical formulation of the CPM and other KMC methods is relatively straightforward, making them more accessible for implementation. However, both LB and CPD methods are well-suited for computational parallelization, making them much more efficient for in silico experiments. This is due to that LB and CPD methods involve solving systems of discretized differential equations for each simulation step, whereas KMC methods utilize an algorithm that, as previously mentioned, performs a series of serial state changes per simulation step. Although it is possible to construct a parallel implementation of the CPM by partitioning the lattice into subdomains (Chen et al., 2007) each of which is simulated on individual cores or machines, significant effort must be put toward overcoming difficulties such as cell migration into different subdomains, minimizing communication overhead, etc. This, of course, is also subject to technical considerations such as available software and computational resources.

Computational considerations. Each method seems (at least for now) best suited for applications at particular scales. At the tissue level, where billions of cells contribute to morphology, CPD and CPM methods introduce computational requirements that are currently infeasible. In this case, the continuous distribution functions of LB methods provide a useful means to represent the activity of many cells at various locations; yet, at the cellular level, the activities of discrete, individual agents become significant. This difference in spatiotemporal resolution is apparent in the relating of physical and simulation time by comparing emergent events.

Time calibration. In simulations using each of these three methods, spheroid fusion was simulated and compared with in vitro results to determine a time correlation of the amount of time per simulation step. This calculation is performed by recording the time to accomplish fusion in vitro and then dividing that time by the number of simulation steps to accomplish fusion in silico. Those correlations were calculated as 5.184 s/MCS for an LB method simulation (Cristea and Neagu, 2016), 36 s/MCS for a CPD simulation, and 1.6×10^{-5} s/MCS for a KMC simulation (Flenner et al., 2012). Although these correlations are specific to model parameters used in each simulation, they are generally demonstrative of the scale at which each method is best applied, where KMC methods can probably be considered the most meticulous, and also the most demanding, of the three.

Capturing global/multiscale behavior. This observation presents a fundamental challenge to biological modeling: how does one predict the emergent behavior of billions of discrete agents at multiple scales, when those agents exhibit such complex behavior? True, the structure of tissue does exhibit behavior like liquid drops, except that, in this case, the drop consists not only of relatively predictable agents (e.g., a water molecule), but rather of lots of types of agents that communicate, intentionally migrate, consume, generate waste, split, change type, and die. Yet the very concept of a computer simulation allocating, simulating, and recording the behavior of a billion individual agents seems daunting, in the least. Perhaps some characterization of the CPM at the cellular level may produce analytic descriptions that can then be incorporated into CPD and LB methods, whether modeling cell migration, metabolism, or population dynamics. What can

This book belongs to Central Library BADJI Mokhtar-ANNABA UNIVERSITY
Copyright Elsevier 2024

be confidently asserted is that there is a clear need for feasible and reliable predictive capabilities at both the tissue and cellular levels to progress bioprinting technologies into medical applications.

Relevance for scaffold-free 3D bioprinting. All the methods discussed have benefited, in one way or another, the modeling needs of the emerging field of scaffold-free bioprinting, which revolves around cell spheroids biology. Their constrained size (around 20,000 cells per "building block") gives hope that, with improvements in software and computational optimizations, the capturing of even deeper aspects of their behavior and metabolism (possibly cell differentiation also) is a feasible endeavor. The rewards will be substantial in better understanding these objects of the model, in optimizing their biotechnological manipulation, and in simplifying the human−instrument interfaces (such as the operation of the Regenova bioprinting robot).

Concluding remarks. Computational modeling is the actual process of creating "virtual objects," as members of the ever-increasing realm of "virtual reality." "Virtual tissue engineering" (Sun et al., 2004) and "virtual biofabrication" (Mironov et al., 2011) are very serious candidates for citizenship in this emerging metareality, with all its advantages and challenges. Expectedly, the inhabitants of this virtual world are subjected to the same "evolutionary" constraints (i.e., validation) and selection (i.e., optimization) as the biological objects themselves. Our overview highlighted several approaches toward the creation, validation, and optimization of objects in this category, with the anticipation of an increasing number of new and (evolutionary speaking) "better fitted" examples to occur soon.

REFERENCES

Bajaj, P., Schweller, R.M., Khademhosseini, A., West, J.L., Bashir, R., 2014. 3D biofabrication strategies for tissue engineering and regenerative medicine. Annual Review of Biomedical Engineering 16, 247−276. http://dx.doi.org/10.1146/annurev-bioeng-071813-105155.

Beysens, D., Forgacs, G., Glazier, J., 2000. Cell sorting is analogous to phase ordering in fluids. Proceedings of the National Academy of Sciences 97 (17), 9467−9471.

Butcher, A.L., Offeddu, G.S., Oyen, M.L., 2014. Nanofibrous hydrogel composites as mechanically robust tissue engineering scaffolds. Trends in Biotechnology 32 (11), 564−570. http://dx.doi.org/10.1016/j.tibtech.2014.09.001.

Censi, R., Schuurman, W., Malda, J., Di Dato, G., Burgisser, P.E., Dhert, W.J.A., et al., 2011. A printable photopolymerizable thermosensitive p(HPMAm-lactate)-PEG hydrogel for tissue engineering. Advanced Functional Materials 21 (10), 1833−1842. http://dx.doi.org/10.1002/adfm.201002428.

Chen, N., Glazier, J.A., Izaguirre, J.A., Alber, M.S., 2007. A parallel implementation of the Cellular Potts Model for simulation of cell-based morphogenesis. Computer Physics Communications 176 (11−12), 670−681. http://dx.doi.org/10.1016/j.cpc.2007.03.007.

Chen, R., Hunt, J.A., 2007. Biomimetic materials processing for tissue-engineering processes. Journal of Materials Chemistry 17 (38), 3974−3979. http://dx.doi.org/10.1039/b706765h.

Cristea, A., Neagu, A., 2016. Shape changes of bioprinted tissue constructs simulated by the Lattice Boltzmann method. Computers in Biology and Medicine 70, 80−87. http://dx.doi.org/10.1016/j.compbiomed.2015.12.020.

Cristea, A., Neagu, A., Sofonea, V., 2011. Lattice Boltzmann simulations of the time evolution of living multicellular systems. Biorheology 48 (3−4), 185−197.

de la Puente, P., Ludeña, D., 2014. Cell culture in autologous fibrin scaffolds for applications in tissue engineering. Experimental Cell Research 322 (1), 1−11. http://dx.doi.org/10.1016/j.yexcr.2013.12.017.

Deutsch, A., Maini, P., Dormann, S., 2007. Cellular Automaton Modeling of Biological Pattern Formation: Characterization, Applications, and Analysis. Birkhäuser, Boston.

Fleming, P.A., Argraves, W.S., Gentile, C., Neagu, A., Forgacs, G., Drake, C.J., 2010. Fusion of uniluminal vascular spheroids: a model for assembly of blood vessels. Developmental Dynamics 239 (2), 398−406. http://dx.doi.org/10.1002/dvdy.22161.

Flenner, E., Janosi, L., Barz, B., Neagu, A., Forgacs, G., Kosztin, I., 2012. Kinetic Monte Carlo and cellular particle dynamics simulations of multicellular systems. Physical Review E 85 (3), 031907.

Flenner, E., Marga, F., Neagu, A., Kosztin, I., Forgacs, G., 2008. Relating biophysical properties across scales. Current Topics in Developmental Biology 81, 461−483.

Freyer, J.P., 1988. Role of necrosis in regulating the growth saturation of multicellular spheroids. Cancer Research 48 (9), 2432.

Freyer, J.P., Sutherland, R.M., 1980. Selective dissociation and characterization of cells from different regions of multicell tumor spheroids. Cancer Research 40 (11), 3956−3965.

Graner, F., Glazier, J.A., 1992. Simulation of biological cell sorting using a two-dimensional extended Potts model. Physical Review Letters 69 (13), 2013.

Gudapati, H., Dey, M., Ozbolat, I., 2016. A comprehensive review on droplet-based bioprinting: past, present and future. Biomaterials 102, 20−42. http://dx.doi.org/10.1016/j.biomaterials.2016.06.012.

Haji-Karim, M., Carisson, J., 1978. Proliferation and viability in cellular spheroids of human origin. Cancer Research 38 (5), 1457−1464.

Jakab, K., Norotte, C., Damon, B., Marga, F., Neagu, A., Besch-Williford, C.L., et al., 2008. Tissue engineering by self-assembly of cells printed into topologically defined structures. Tissue Engineering Part A 14 (3), 413−421.

This book belongs to Central Library BADJI Mokhtar-ANNABA UNIVERSITY

Copyright Elsevier 2024

Kosztin, I., Vunjak-Novakovic, G., Forgacs, G., 2012. Colloquium: modeling the dynamics of multicellular systems: application to tissue engineering. Reviews of Modern Physics 84 (4), 1791.

Krafczyk, M., Berrios, R., 1998. Simulating Biological Flows Using Lattice-Boltzmann Methods. Simulation con Methods Numericos, SVMNI, London.

McCune, M., Shafiee, A., Forgacs, G., Kosztin, I., 2014. Predictive modeling of post bioprinting structure formation. Soft Matter 10 (11), 1790–1800.

Mironov, V., Boland, T., Trusk, T., Forgacs, G., Markwald, R.R., 2003. Organ printing: computer-aided jet-based 3D tissue engineering. Trends in Biotechnology 21 (4), 157–161.

Mironov, V., Kasyanov, V., Markwald, R.R., 2011. Organ printing: from bioprinter to organ biofabrication line. Current Opinion in Biotechnology 22 (5), 667–673. http://dx.doi.org/10.1016/j.copbio.2011.02.006.

Mironov, V., Visconti, R.P., Kasyanov, V., Forgacs, G., Drake, C.J., Markwald, R.R., 2009. Organ printing: tissue spheroids as building blocks. Biomaterials 30 (12), 2164–2174.

Moldovan, N.I., Hibino, N., Nakayama, K., 2017. Principles of the kenzan method for robotic cell spheroid-based three-dimensional bioprinting. Tissue Engineering Part B Reviews. http://dx.doi.org/10.1089/ten.TEB.2016.0322.

Mombach, J.C., Glazier, J.A., 1996. Single cell motion in aggregates of embryonic cells. Physical Review Letters 76 (16), 3032.

Mombach, J.C., Glazier, J.A., Raphael, R.C., Zajac, M., 1995. Quantitative comparison between differential adhesion models and cell sorting in the presence and absence of fluctuations. Physical Review Letters 75 (11), 2244.

Mueller-Klieser, W., Freyer, J., Sutherland, R., 1986. Influence of glucose and oxygen supply conditions on the oxygenation of multicellular spheroids. British Journal of Cancer 53 (3), 345.

Mueller-Klieser, W., Sutherland, R., 1982. Oxygen tensions in multicell spheroids of two cell lines. British Journal of Cancer 45 (2), 256.

Naderi, H., Matin, M.M., Bahrami, A.R., 2011. Review article: critical issues in tissue engineering: biomaterials, cell sources, angiogenesis, and drug delivery systems. Journal of Biomaterials Applications. http://dx.doi.org/10.1177/0885328211408946.

Neagu, A., Jakab, K., Jamison, R., Forgacs, G., 2005. Role of physical mechanisms in biological self-organization. Physical Review Letters 95 (17), 178104.

Pataky, K., Braschler, T., Negro, A., Renaud, P., Lutolf, M.P., Brugger, J., 2012. Microdrop printing of hydrogel bioinks into 3D tissue-like geometries. Advanced Materials 24 (3), 391–396. http://dx.doi.org/10.1002/adma.201102800.

Picioreanu, C., van Loosdrecht, M.C., Heijnen, J.J., 1998. A new combined differential-discrete cellular automaton approach for biofilm modeling: application for growth in gel beads. Biotechnology and Bioengineering 57 (6), 718–731.

Railsback, S.F., Grimm, V., 2011. Agent-Based and Individual-Based Modeling: A Practical Introduction. Princeton University Press.

Shafiee, A., McCune, M., Forgacs, G., Kosztin, I., 2015. Post-deposition bioink self-assembly: a quantitative study. Biofabrication 7 (4), 045005.

Shim, J.-H., Kim, J.Y., Park, M., Park, J., Cho, D.-W., 2011. Development of a hybrid scaffold with synthetic biomaterials and hydrogel using solid freeform fabrication technology. Biofabrication 3 (3). http://dx.doi.org/10.1088/1758-5082/3/3/034102.

Shimizu, T., Matsuura, K., 2015. Myocardial Tissue Engineering. Pan Stanford Publishing.

Shirinifard, A., Gens, J.S., Zaitlen, B.L., Popławski, N.J., Swat, M., Glazier, J.A., 2009. 3D multi-cell simulation of tumor growth and angiogenesis. PLoS One 4 (10), e7190.

Singh, D., Singh, D., Han, S.S., 2016. 3D printing of scaffold for cells delivery: advances in skin tissue engineering. Polymers 8 (1). http://dx.doi.org/10.3390/polym8010019.

Steinberg, M.S., Takeichi, M., 1994. Experimental specification of cell sorting, tissue spreading, and specific spatial patterning by quantitative differences in cadherin expression. Proceedings of the National Academy of Sciences 91 (1), 206–209.

Sun, W., Darling, A., Starly, B., Nam, J., 2004. Computer-aided tissue engineering: overview, scope and challenges. Biotechnology and Applied Biochemistry 39 (1), 29–47.

Surapaneni, S., Pryor, T., Klein, M.D., Matthew, H.W., 1997. Rapid hepatocyte spheroid formation: optimization and long-term function in perfused microcapsules. ASAIO Journal 43 (5), M854.

Sutherland, R., Sordat, B., Bamat, J., Gabbert, H., Bourrat, B., Mueller-Klieser, W., 1986. Oxygenation and differentiation in multicellular spheroids of human colon carcinoma. Cancer Research 46 (10), 5320–5329.

Swat, M.H., Thomas, G.L., Belmonte, J.M., Shirinifard, A., Hmeljak, D., Glazier, J.A., 2012. Multi-scale modeling of tissues using CompuCell3D. Methods in Cell Biology 110, 325.

Yang, X., Mironov, V., Wang, Q., 2012. Modeling fusion of cellular aggregates in biofabrication using phase field theories. Journal of Theoretical Biology 303, 110–118.

Zhang, Y., Thomas, G.L., Swat, M., Shirinifard, A., Glazier, J.A., 2011. Computer simulations of cell sorting due to differential adhesion. PLoS One 6 (10), e24999.

This book belongs to Central Library BADJI Mokhtar-ANNABA UNIVERSITY

Copyright Elsevier 2024

This page intentionally left blank

This book belongs to Central Library BADJI Mokhtar-ANNABA UNIVERSITY

Copyright Elsevier 2024

Chapter 16

Coupled Finite Element–Agent-Based Models for the Simulation of Vascular Growth and Remodeling

D. Nolan and C. Lally
Trinity College Dublin, Dublin, Ireland

16.1 INTRODUCTION

The creation of computational models that can predict the multiscale response of arterial tissues provides a means to gain greater insights into complex vascular biological–biochemical–biomechanical processes. Such processes include developmental growth and remodeling, tissue maintenance, growth and response to injury as well as aging, the progression and treatment of vascular diseases, and also the design of intravascular medical devices and tissue-engineered blood vessels. With increasing technology and computational power comes the possibility of patient-specific medical devices, which are not only designed to conform to patient specific geometry but may also be optimized for the patient's specific growth and remodeling potential. One of the main advantages offered by in silico models is the possibility of replicating the variability that is observed in the general population. This can be achieved using stochastic modeling approaches, whereby variations in cell response patterns can be used to simulate the results obtained in clinical trials, for example Viceconti et al. (2016).

Until recent years, approaches to modeling the adaptive response of vessels to changes in their biomechanical environment following, for example, alterations in luminal pressure or the placement of interventional devices, such as intravascular stents, have predominantly focused on the continuum mechanics of the tissue (Fung et al., 1979; Auricchio et al., 2011; Lally and Prendergast, 2006; Keller et al., 2014; Holzapfel et al., 2005b). Tissues are living entities, however, which are constantly adapting and remodeling in response to stimuli. Continuum growth models can be developed such that they adapt the continuum biomechanics framework to predict growth and remodeling; however, a complicating factor in these models is the necessity for the mass of the system to be adaptable during such growth. Some well-known continuum growth models that have been developed to explore adaptations in response to altered blood pressure and flow include those outlined in Kuhl et al. (2007), Alford et al. (2008), Valentin and Humphrey (2009), Taber (1995, 1998), Rachev et al. (2000), and Tsamis et al. (2009).

Although the growth and adaptation response at the tissue level is critical with respect to the short-term outcome following systemic pressure changes or interventional procedures, the longer-term adaptive biological response cannot be captured by this limited approach. Where methods such as constrained mixture models (CMMs), for example, have been used to model the longer-term adaptive response of the tissue, they are typically limited to 1D or axisymmetric phenomenological models (Valentin and Humphrey, 2009; Taber, 1995) and cannot, therefore, offer spatially varying responses to complex loading patterns such as those introduced during medical device implantation (Lally et al., 2005; Zahedmanesh et al., 2010). More recently, therefore, increasing numbers of models have emerged, which aim to further explore the cell level response to biochemical and biological changes within tissues. These models can simulate numerous interacting cell groups and provide rules for their response to biochemical stimuli; however, many of these models have neglected the response to mechanical stimuli to date (Budu-Grajdeanu et al., 2008). Although a few different approaches can be used to model collective cell behavior, agent-based models (ABMs) or cellular automata (CA) offer a novel approach to the simulation of complex mechanobiological responses at the cellular level. ABMs or CAs have been used

Numerical Methods and Advanced Simulation in Biomechanics and Biological Processes. https://doi.org/10.1016/B978-0-12-811718-7.00016-2
Copyright © 2018 Elsevier Ltd. All rights reserved.

This book belongs to Central Library BADJI Mokhtar-ANNABA UNIVERSITY
Copyright Elsevier 2024

to simulate a variety of responses in the vasculature, including angiogenesis, vasculogenesis, and vascular remodeling (Bailey et al., 2007; Bentley, 2008; Checa and Prendergast, 2009; Thorne et al., 2011).

More recently this modeling approach has been further extended to coupled mechanobiological models, whereby the mechanical environment at the tissue level is determined and used to provide the driving stimuli for models at the cell level, and cell behavior, in turn, governs adaptive changes at the tissue level such as stiffness and/or structure (Nolan and Lally, 2017; Hoekstra et al., 2016; Rouillard and Holmes, 2014; Zahedmanesh and Lally, 2013). This coupled process is typically iterative in nature, such that changes at the cell level alter the mechanics of the tissue and hence the mechanical stimuli driving the cell processes. Only limited work has been done to date, however, using such coupled mechanobiological models. The aim of this chapter is to initially provide a brief overview of the approaches that have been used to date to generate mechanobiological models suitable for exploring vascular adaptions in silico. The remainder of the chapter then outlines in detail the methods used in one specific multiscale coupled mechanobiological modeling approach (Nolan and Lally, 2016, 2017), namely a finite element (FE) model coupled with an ABM, which is suitable for studying large vessel adaptations to intravascular medical device implantations.

16.2 METHODS IN THE LITERATURE

16.2.1 Paradigms for Agent-Based Models of Vascular Tissue

Many of the open questions in vascular mechanobiology can only be answered using a multiscale and multiphysics approach. Vascular growth, remodeling, and diseases are intrinsically multiscale phenomena that depend on the interactions occurring at the tissue level, cell level, and even the intracellular level (Zahedmanesh and Lally, 2013). Relevant physical systems that play a role in vascular adaptation include cell biology, biochemistry, solid mechanics, and fluid mechanics. Recent modeling strategies have incorporated multiphysics and multiscale approaches, but many different approaches can be and have been used to model or represent the growth at each of these levels and within each of these systems. The simplest approach includes models that apply constant values from other systems as boundary conditions, e.g., a constant hydrostatic pressure, in vivo measured strain (Peirce et al., 2004) or shear stress applied to a cells domain (Thorne et al., 2011). Although this is useful for initial investigations of a single scientific system, it is desirable that the systems are updated at appropriate stages. For instance, as a cell system proliferates in the lumen of a vessel, the radius of the vessel decreases, causing an increase in fluid wall shear stress, which in turn changes the behavior of cell proliferation (Bailey et al., 2007).

The COAST[1] project outlined a standardized methodology for the design of multiscience and multiscale computational simulations of complex biological systems called the complex automata (CxA) (Evans et al., 2008; Hoekstra et al., 2007, 2008). The primary recommendation from these papers is the construction of a scale separation map (SSM). The SSM firstly breaks the multiscale problem up into a list of its component systems. Next, the order of magnitude of the characteristic temporal and spatial scales of each component is determined. Each component is then plotted on a graph with the temporal scale on the *x*-axis and the spatial scale on the *y*-axis, known as the SSM (see Fig. 16.4 in Evans et al., 2008). It is common in multiscale modeling of engineering materials for a system taking place on a fast temporal and small spatial scale to be coupled to systems on a slower temporal and larger spatial scale, e.g., a fracture mechanics model of concrete coupled to a static mechanics model of a concrete beam (Ghosh and Chaudhuri, 2013). However, many biological processes operate on a small spatial scale yet have a longer temporal scale than their corresponding larger scale system to which they are coupled, e.g., the growth of vascular endothelial cells is on the micron scale and occurs over days, yet their behavior is coupled to blood fluid mechanics, which is calculated on a millimeter scale and is measured in seconds. Consequently, a small spatial scale system in such a multiscale model may need to be updated more regularly than its characteristic temporal scale might otherwise require. Detailed studies demonstrating possible optimization techniques for achieving congruency across different scales in multiphysics systems have been conducted (Hayenga et al., 2011).

The systems themselves, given that they have different spatial and temporal scales, must also be modeled using different approaches. Cellular processes are more discrete systems, where different cell groups may have behavior bounded by known thresholds but are inherently stochastic systems with considerable variability. Although biological tissues have variability at the macroscale, they are considerably more homogenous in their mechanical response and are well represented by a continuum approach in terms of biomechanics (Holzapfel et al., 2002) or CMMs can also be used to model adaptations at the continuum level (Valentin and Humphrey, 2009). In terms of modeling collective cell behavior, ABMs and CA are common approaches.

1. http://www.complex-automata.org/.

This book belongs to Central Library BADJI Mokhtar-ANNABA UNIVERSITY
Copyright Elsevier 2024

One important advantage of using agent-based or CA approaches to model cell populations is their ability to better capture the discrete nature of events occurring at the cellular level compared with continuum approaches, such as differential equations, which are more suited to bulk material behavior. In fact, although the behavior of the cells or matrix may be defined by differential equations, it is the spatial variations in cell density and cell type defined in the model that can result in highly variable responses. Although CMMs have provided insights into the mechanisms driving adaptive processes such as vascular adaptations in hypertension (Valentin and Humphrey, 2009) and cranial aneurysm development (Baek et al., 2006), they are typically limited to simplistic geometrical representations (1D, 2D, or axisymmetric) and are therefore not well suited to capturing the spatial variation in cell responses observed in processes such as in-stent restenosis.

Alternative frameworks to CMMs, which can incorporate spatial and temporal variations, include the cellular Potts model (CPM), whereby cells in the framework are defined within a regular lattice and the dynamics of the cells are described by an effective Hamiltonian, which is the sum of cell adhesion, volume, and/or surface constraint terms (Tahir et al., 2015). The CPM has been used to explore the role of smooth muscle cell migration in in-stent restenosis (Tahir et al., 2015).

The main in silico approaches to modeling the discrete behavior of cell groups involved in vascular remodeling, however, have been ABMs or CA. The phenomenological nature of ABMs or CAs allows the researcher to define the granularity of the model, provided the net system response is adequately captured. This versatility allows one to specifically focus on the research question at hand. For example, matrix metalloproteinases (MMPs) are enzymes that degrade extracellular matrix (ECM) components, such as collagen, gelatin, and elastin. They are known to play an important role in the remodeling of arterial tissue in both health and disease (Galis and Khatri, 2002). There are several subtypes of MMP, each of which preferentially degrade different subtypes of ECM components. In an ABM of vascular adaptation to hypertension, Thorne et al. (2011) introduced a detailed model of ECM degradation where MMP-1 converts collagen to gelatin, MMP-9 reduces gelatin mass, and both MMP-2 and MMP-9 reduce elastin mass, whereas, in a model of acute damage and inflammation by Zahedmanesh et al. (2014), the response of all MMPs and ECM components is lumped into a single variable.

It is important to note that both these approaches are useful. If one is interested in understanding the precise mechanisms by which ECM changes, then the detailed approach provides that information. However, for it to be meaningful, the relevant experimental data must be available with which to calibrate the rule set for the agents. Although the lumped method produces less-detailed results, this may be appropriate and adequate for the phenomena being modeled. For example, the expression of MMP-2 and MMP-9 are found to be the most significantly increased MMPs under acute vascular injury (Feldman et al., 2001). Given that they both degrade many of the same types of collagen, it may be reasonable to use a single MMP variable to model this injury (Zahedmanesh et al., 2014).

Although ABMs and CA have both been used to model adaptive processes of vascular tissue, there are a few notable differences between the two schemes. CA consist of a regular grid of cells with a predefined dimension, each in one of a finite number of states, such as on and off, and each cell of the CA has a defined set of neighboring cells (Checa and Prendergast, 2009; Checa et al., 2010; Boyle et al., 2010). In contrast, ABMs are typically lattice-free models. Agents can be initialized in random positions and new agents can be created during the simulation (Zahedmanesh and Lally, 2012). Both systems are rule based and require mathematical relations for each agent or cell to be defined as well as initial and boundary conditions to be specified.

ABMs or CAs were developed initially to model mechanobiological systems, whereby the mechanics driving the biological processes were predefined based on the theory or empirical measurements in the biological model, rather than fully coupled by using analyses at different scales. For example, Peirce et al. (2004) used an ABM to predict remodeling of microvascular networks using strains calculated in vivo to define cell behavior, although the same group later used a network flow model to calculate theoretical flow rates and pressures to inform the ABM model (Peirce et al., 2006). These models, which are biochemically focused, use a broad range of rules and the group have more recently developed a rule scoring system to assess the power and suitability of experimental data in the literature for defining such rules in similar ABM models (Thorne et al., 2011).

Although many agent based or CA models to date have overlooked or simplified the calculation of mechanical stimuli driving the vascular processes, coupling such discrete models with continuum mechanical models has enabled increased insights into mechanochemobiological processes with complex loading patterns achievable (Boyle et al., 2011; Zahedmanesh and Lally, 2012; Zahedmanesh et al., 2014; Hoekstra et al., 2016). Earlier work from our group used a coupled ABM–FE model to study both intimal hyperplasia (IH) postbypass grafting (Zahedmanesh and Lally, 2012) and stenting (Zahedmanesh et al., 2014), although a linked group investigated the role of inflammation and IH poststenting using a coupled CA–FE approach (Boyle et al., 2010, 2011). More recently the damage stimuli driving these two multiscale mechanobiological models of in-stent restenosis have been compared and contrasted using a unifying ABM–FE coupled approach (Nolan and Lally, 2016), and it is this methodology that is outlined in detail in the following sections of this chapter.

This book belongs to Central Library BADJI Mokhtar-ANNABA UNIVERSITY Copyright Elsevier 2024

16.3 SCHEMES AND ALGORITHMS FOR THE IMPLEMENTATION OF COUPLED FINITE ELEMENT–AGENT-BASED MODELS

16.3.1 Agent-Based Models

As previously outlined, ABMs are a computational tool, which can be used to simulate complex collective behaviors. Biological cells are modeled as individual agents, which exist in a spatial domain. As a simulation moves forward in time, each agent may take certain actions, such as migration or proliferation. These actions are determined by a rule set that is a function of each agent's internal state and the surrounding agents. Using these relatively simple rule sets and multiple agents, ABMs can predict the emergent complex collective behavior of a heterogeneous cell population within biological tissues. ABMs have many discrete characteristics, which make them suitable for computational modeling. Calculations are performed at fixed time steps, and the actions of an agent are usually binary (e.g., migrate/do not migrate). Information about each agent can easily be stored in arrays or else object-orientated programming concepts can be used to organize the data pertaining to an agent.

16.3.1.1 Agent-Based Model of the Artery Wall

This section will describe an ABM of the artery wall that is used for modeling in-stent restenosis and balloon angioplasty. Although there are several different cell types in the artery wall, this model considers vascular smooth muscle cells (VSMCs), which make up the bulk of the cells in the artery wall, and endothelial cells (ECs), which make up the inner surface of the artery. In this model we consider an idealized 2D quarter circumferential cross section of an artery as the spatial domain (see Fig. 16.1). This 2D model can, however, be relatively easily extended to a more realistic 3D model.

16.3.1.1.1 Agent Population, Shape, and Size

The agents for both VSMCs and ECs are idealized as circles. The density of VSMCs in a typical artery cross section can be determined from histological cross-sectional images stained with hematoxylin and eosin to show the cell nucleus. This cell density will determine the initial number of agents in the spatial domain.

There are three options available when deciding the radius R of the cell. The first is to use some type of average radius by taking measurements from images of individual VSMCs. The second is to determine the area of individual VSMCs, again from images of individual cells, and calculate the radius that will return this area. Lastly, the area fraction of VSMCs in a representative area of the artery wall can be determined. The number of red pixels in a histological image stained with Masson's trichrome[2] can be computed using image segmentation thresholding tools. Using the total number of cells and the area of the domain, the radius of a cell can be calculate such that the VSMC area fraction in maintained.

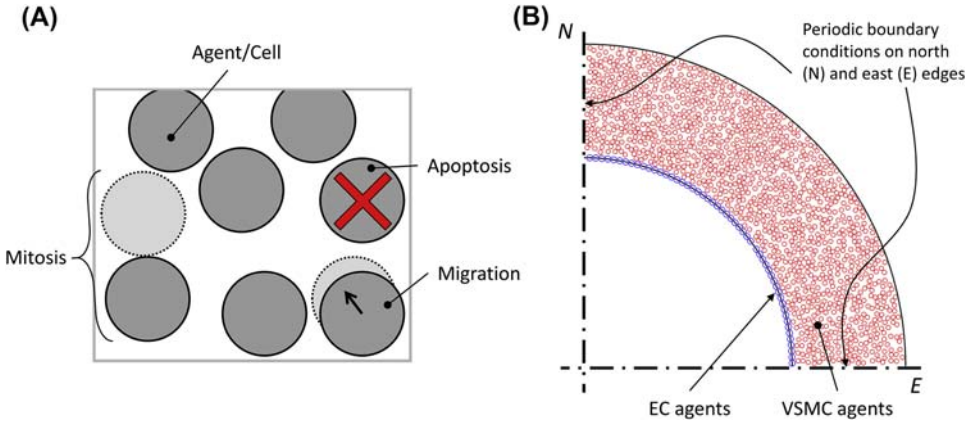

FIGURE 16.1 (A) Schematic of an agent-based model (ABM) showing the actions that an individual agent can take: migration, mitosis, and apoptosis. (B) Schematic of the initial geometry used for an ABM of the artery wall for the simulation of in-stent restenosis. *EC*, endothelial cell; *VSMC*, vascular smooth muscle cell.

2. Masson's trichrome stains smooth muscle cells red and collagen fibers blue.

This book belongs to Central Library BADJI Mokhtar-ANNABA UNIVERSITY Copyright Elsevier 2024

16.3.1.1.2 Agent Attribute Variables

In this ABM we assign three key attributes to each agent/cell. Firstly, VSMCs are known to change their behavior in response to the quality of their surrounding ECM. Therefore each agent has an attribute detailing the density (mass per cell) of ECM within its bounds. Next, MMPs are an enzyme secreted by VSMCs that degrade ECM components. Each agent has an attribute detailing the density of MMP within its bounds. Finally, VSMCs respond to mechanical forces and strains. The extent of mechanical damage has been linked with the loss of lumen area in stented vessels. Each agent has a dimensionless damage attribute that takes any value between 0 (no damage) and 1 (fully damaged). Additionally, each agent keeps track of its age and spatial position.

These attributes are largely responsible for defining the actions of the agents. They are dependent on each other and updated every time increment of the ABM simulation. Section 16.3.3 outlines the precise methodology by which these attribute variables change.

16.3.1.1.3 Seeding Agents in the Spatial Domain

Agents are seeded randomly in the spatial domain. The agent must fulfill the following criteria: the agent contained within the boundary of the spatial domain, and no two agents can overlap one another. A brute-force algorithm using these two criteria has proven to be sufficiently computationally efficient for seeding agents in a 2D scenario and its pseudocode is given in Algorithm 16.1. Whether a new agent at a point (p_x, p_y) in Cartesian space is overlapping with existing agents at points (P_x, P_y) can be determined using the following equation:

$$\sqrt{(p_x - P_x)^2 + (p_y - P_y)^2} > R \tag{16.1}$$

where agents have radius R. If Eq. (16.1) is true for all (P_x, P_y) then the new agent does not overlap with any current agents and can be added to the list of existing agents. This operation is repeated until a total number of agents, determined above by VSMC density, have been seeded.

16.3.1.1.4 Proliferation of Vascular Smooth Muscle Cell Agents

In the current model, VSMC agents may duplicate themselves provided that they meet the following three criteria: they are of a synthetic phenotype, a probabilistic decision-making algorithm has determined that the cell may duplicate, and there is sufficient space adjacent to the parent cell for a daughter cell.

VSMCs may assume either a contractile (quiescent) or synthetic (proliferative) phenotype. Only synthetic VSMCs may proliferate in this ABM. An agent's phenotype is determined by the quality of the ECM within its bounds. This is computed using a simple ECM density threshold; if the ECM density is below a critical value, it is a synthetic VSMC; otherwise it is contractile and will not proliferate.

Cells typically have a doubling time, a period after which they undergo mitosis and produce a daughter cell. However, this is not a fixed period and there is variability around the doubling time of VSMCs. A cumulative Gaussian distribution function is used to model the probability of a cell doubling P_{DT},

$$P_{DT}(t_{\text{age}}) = \frac{1}{2} \quad 1 + \text{erf}\left[\frac{t_{\text{age}} - \mu_{DT}}{\sqrt{2\sigma_{DT}^2}}\right]\Bigg) \tag{16.2}$$

ALGORITHM 16.1 Brute-Force Algorithm for Seeding Agents in a Spatial Domain for an Agent-Based Model

1. Create a new agent position in x and y coordinates p_x and p_y, respectively.
2. Is the new agent at (p_x, p_y) inside the spatial domain?
   - **a.** Yes: Continue.
   - **b.** No: Go to item 1.
3. Is overlap Equation X true for all existing agents?
   - **a.** Yes: Continue.
   - **b.** No: Go to item 1.
4. Accept the new agent and add it to the list of existing agents.

This book belongs to Central Library BADJI Mokhtar-ANNABA UNIVERSITY
Copyright Elsevier 2024

ALGORITHM 16.2 Pseudocode Outlining the Algorithm to Determine Whether There Is Sufficient Space to Form a Daughter Cell and What Possible Locations That Daughter Cell Might Form

1. Create an array of possible daughter cell center points `daughterPos`, an array of points $2R$ from the center of the parent cell spaced at an angle θ from each other.
2. Are the points in `daughterPos` within the permitted spatial domain?
   - **a.** Yes: Continue to item 3.
   - **b.** No: Remove the out-of-bounds points from `daughterPos` and continue to item 3.
3. Calculate distance between the center of the parent cell and all other cell centers.
4. Create a list of all cells within $4R$ of the center of the parent cell, `nearCell`.
   - **a.** If this is a null array, go to item 3.
5. For loop: `i = 1:length (nearCell)`
   - **a.** Calculate the distance between the members of the array `daughterPos` and the point `nearCell(i)`.
   - **b.** If any distance is less than $2R$, then the corresponding member of `daughterPos` must be eliminated because this daughter cell position overlaps an existing cell.
6. Determine the position of the parent cell with respect to stent strut(s).
7. If the parent cell center is within $3R$ of a stent strut
   - **a.** Eliminate any members of `daughterPos` less than R distance from a stent boundary.
8. Is `daughterPos` a null array?
   - **a.** Yes: Exit.
   - **b.** No: Use a random number generator to select one of the members of `daughterPos` for the new cell.
9. Add the new cell to the list of agents. Give it the attributes of the parent cell with the exception of the cell age. Give the parent and daughter cell an age of 0.

where t_{age} is the age of the cell, μ_{DT} is the mean doubling time of the cell, σ^2_{DT} is the variance of the cell doubling time, and erf( ) is the Gauss error function. This produces a sigmoid shaped curve where at small values of t there is a practically zero probability of doubling; this increases as we approach the mean value, and beyond the mean the probability of doubling is practically one. The larger the variance, the more gradual the transition between the not doubling/doubling states. At each time step in the ABM simulation, the P_{DT} for each synthetic agent is calculated based on each agent's cell age using Eq. (16.2). A random number generator produces a real number between 0 and 1 for each agent, and if this random number is less than the probability of doubling, then that agent is considered to be in a doubling state.

Finally, once a cell is in a doubling state, it must be checked whether there is sufficient space in the region around it for a daughter cell to form. Daughter cells may not overlap with existing cells or solid bodies, such as a stent strut, and will tangentially touch the parent cell. Algorithm 16.2 outlines a pseudocode of the procedure to check the surrounding space for clearance and to determine the possible locations where a daughter cell may form. Briefly, an array of potential daughter cell center point locations is created, $2R$ from the center point of the parent cell and spaced at 1 degree increments. Members of this array are eliminated if the resulting daughter cell is out-of-bounds of the spatial domain, overlaps an existing cell, or overlaps a stent strut. The remaining members of the array are legitimate locations for a daughter cell to form. A random number generator is used to pick one of these locations and the daughter cell is added to the list of agents and assigned the attributes of its parent cell. The exception being that the cell age of both parent and daughter cells is set to 0.

As a related aside, the migration of VSMCs is of secondary importance when compared with proliferation and is neglected in this model.

16.3.1.1.5 Inclusion of Endothelial Cells

In this model we have the option to include ECs as a separate population of agents. These agents have their own characteristics and may interact with VSMC agents. To simulate the healing process after stent injury, ECs may change the phenotype of a VSMC from synthetic to contractile. If the distance between a synthetic VSMC agent and an EC agent is less than a critical distance, its phenotype changes to contractile. This causes that cell to cease proliferating.

ECs line the lumen surface of the artery wall and in the ABM it may only form a monolayer on the inner edge of the 2D artery geometry. On stenting, multiple EC agents to each side of the stent strut are removed from the model. As the simulation progresses, EC agents begin to proliferate along the lumen surface. The EC agents have a doubling time after which they will produce a new cell. Unlike the proliferation of VSMC agents, EC agents undergo doubling after a fixed period and only the EC agent that is on the edge of the monolayer will double. This simulates the in vivo behavior of ECs that exist only on the

This book belongs to Central Library BADJI Mokhtar-ANNABA UNIVERSITY Copyright Elsevier 2024

ALGORITHM 16.3 Pseudocode Outlining an Algorithm for the Proliferation of Endothelial Cell (EC) Agents Along the Lumen Edge

1. There exists an array of all EC agent positions in the model, `ECpos`. The agents are sorted in an anticlockwise direction from east to north.
2. For `i=1:length (ECpos)-1`
   - **a.** Calculate the distance between `ECpos(i+1)` and `ECpos(i)`.
   - **b.** Is this distance is greater than twice the EC radius, $2R_{EC}$?
     - **i.** Yes: Calculate the angle θ_{EC} between `ECpos(i-1)` and `ECpos(i)`.
       1. For `j=1:360`
          - **a.** Compute daughter cell position, `newECposSouth`, at $\theta_{EC} + 90° + j$. Progress in an *anticlockwise* direction.
          - **b.** Does this daughter cell overlap an existing vascular smooth muscle cell (VSMC) agent?
            - **i.** Yes: `Break`.
            - **ii.** No: `Continue`.
          - **c.** Does this daughter cell overlap a stent strut?
            - **i.** Yes: `Break`.
            - **ii.** No: `Continue`.
          - **d.** Accept `newECpos` as a location of new EC agent.
       2. Calculate the distance between `newECposSouth` and `ECpos(i+1)`.
       3. Is this distance is $<4R_{EC}$ (this means that there is space for only one more EC agent) then:
          - **a.** Yes: Create a new EC agent, `newECposNorth`, that is tangential to both `newECposSouth` and `ECpos(i+1)`. End EC mitosis for all time steps. Go to item 3.
          - **b.** No: Continue.
       4. For `j=1:360`
          - **a.** Compute daughter cell position, `newECposNorth`, at $\theta_{EC} + 90° + j$. Progress in a *clockwise* direction.
          - **b.** Does this daughter cell overlap an existing VSMC agent?
            - **i.** Yes: `Break`.
            - **ii.** No: `Continue`.
          - **c.** Does this daughter cell overlap a stent strut?
            - **i.** Yes: `Break`.
            - **ii.** No: `Continue`.
          - **d.** Accept `newECposNorth` as a location of new EC agent.
     - **ii.** No: Return to item 2; `i=i+1`.
3. Add valid `newECposSouth` and `newECposNorth` agents to the list of EC agents ECpos.

lumen and will proliferate into denuded regions (Rogers et al., 1996). For every stent strut, there will be two monolayer edges where EC agents have been removed. The pseudocode outlined in Algorithm 16.3 will grow a monolayer of EC agents "on top" of the underlying VSMC agents and will not overlap any VSMC agents of solid stent struts.

16.3.1.1.6 Periodic Boundary Conditions

The quarter geometry model presented assumes that this section represents a continuous circumferential cross section of the artery. For the ABM to appropriately represent this, periodic boundary conditions must be imposed associating the east edge and the north edge of the model. For example, if an agent were to migrate past the east edge, it would then appear at the north edge, at the same radial position with respect to the center point. As there is no migration in the present model, periodic boundary conditions only need to be considered for proliferation calculations. Algorithm 16.4 outlines a pseudocode for the implementation of periodic boundary conditions in the ABM. This involves the creation of duplicates of existing VSMC agents located near the east and north edges and rotating them to their respective opposite edge. These duplicate agents act as phantom agents when computing whether a VSMC daughter cell may be created.

16.3.1.1.7 Creation of Rules for Agent-Based Models

Finally, an example is presented of how an agent rule is determined for the ABM. If a synthetic VSMC agent comes within a critical distance of an EC agent, its phenotype is changed to contractile. This simulates the effect of nitric oxide (NO), released by ECs, on synthetic VSMCs. The critical distance is determined from cell culture experimental data. An

This book belongs to Central Library BADJI Mokhtar-ANNABA UNIVERSITY Copyright Elsevier 2024

ALGORITHM 16.4 Pseudocode Outlining an Algorithm to Implement Periodic Boundary Conditions for the Calculation of Proliferation in vascular smooth muscle cells (VSMCs)

1. Is the *x*-coordinate of a VSMC agent, `VSMCposX`, is $<R$ then:
   a. Yes: The VSMC agent is near the north edge. Rotate a duplicate of this agent *clockwise* by 90°.
   b. No: Continue.
2. Is the *y*-coordinate of a VSMC agent, `VSMCposY`, is $<R$ then:
   a. Yes: The VSMC agent is near the east edge. Rotate a duplicate of this agent *anticlockwise* by 90°.
   b. No: Continue.
3. Include these duplicated agents when searching for `nearCell` in Algorithm 16.2.

experimental study by Matsusaki et al. (2011) contains data in its supplementary material on the concentration of NO in VSMCs with increasing depths below an EC layer. Extrapolating this data, at a NO concentration of 0, the depth is 60 μm. Hence the critical distance for an EC agent to change a VSMC agent's phenotype is set to 60 μm.

16.3.2 Finite Element Models

FE solid mechanics models are commonly used to simulate the behavior of arterial tissue to understand both fundamental tissue mechanics (Holzapfel et al., 2002; Nolan and McGarry, 2016) and vessel response during medical device deployment (Lally et al., 2005; Zahedmanesh and Lally, 2009). There are several constitutive laws, which can capture the nonlinear and anisotropic mechanical behaviors of arterial tissue (Fung et al., 1979; Holzapfel et al., 2000; Sun and Sacks, 2005), including models that compute tissue damage due to cyclic overloading (Balzani et al., 2012). FE models are flexible enough to simulate a range of geometries, from simple 2D models of an idealized artery under pressure (Nolan et al., 2014; Nolan and McGarry, 2016) through to complex dynamic 3D models of stent deployment in an anatomically realistic vessel (Zahedmanesh et al., 2010). In this section we will discuss the relevant fundamentals of FE analysis required to incorporate a solid mechanics system into a multiscience mechanobiological model of the arterial wall.

16.3.2.1 Geometry, Materials, and Boundary Conditions

A simplified 2D quarter model of the coronary artery is created, taking advantage of geometric symmetry (see Fig. 16.2). To enforce symmetry, the east edge can only displace in the *x* direction and the north edge in the *y* direction. Arteries consist of three concentric layers: intima, media, and adventitia. The thin innermost layer, the intima, is often regarded as being mechanically insignificant and for this reason the artery wall in the FE model is discretized into media and adventitia layers at a ratio of 1.5:1 (Holzapfel et al., 2005a). These two layers have different mechanical behavior (Holzapfel et al., 2005a); an incompressible three-term Ogden constitutive law is used to model the two layers, each with different material parameters

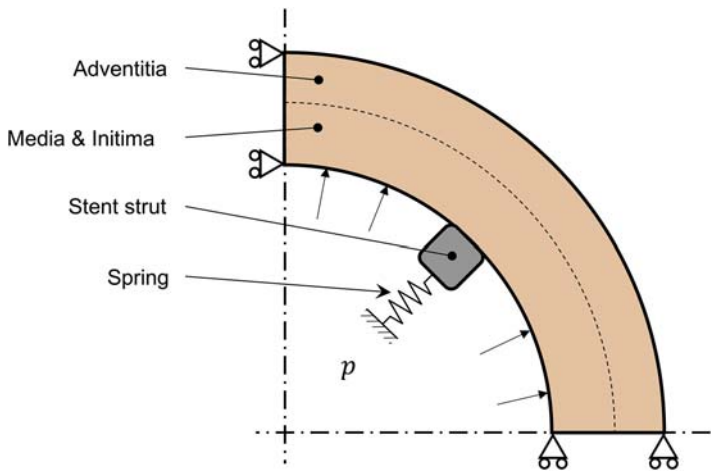

FIGURE 16.2 Schematic showing the geometry and boundary conditions used for the finite element model. The artery has an internal radius of 1.23 mm and a thickness of 0.67 mm (Holzapfel et al., 2005a). The strut is of side 170 μm with a fillet of 20 μm.

This book belongs to Central Library BADJI Mokhtar-ANNABA UNIVERSITY
Copyright Elsevier 2024

TABLE 16.1 Sequence of Boundary Conditions and Applied Loads Used for the Finite Element Simulation of Balloon Angioplasty and Stent Implantation

Simulation Step	1	2	3	4
Balloon angioplasty	*Diastole*: apply a lumen pressure of 80 mmHg (10.67 kPa)	*Systole*: increase the lumen pressure to 120 mmHg (16.00 kPa)	*Angioplasty*: remove lumen pressure and radially displace the lumen boundary to 1.4 times the radius in step 2	–
Stent implantation	*Diastole*: apply a lumen pressure of 80 mmHg (10.67 kPa)	*Systole*: increase the lumen pressure to 120 mmHg (16.00 kPa)	*Stent implantation and systole*: deploy the stent strut to 1.1 times the radius at systole	*Stent implantation and diastole*: activate the spring element on the strut and decrease the lumen pressure to 80 mmHg

(full details are given in Zahedmanesh et al., 2014). The out-of-plane behavior is simulated using plane strain elements. This setup is used to simulate balloon angioplasty and stent implantation.

Table 16.1 gives a summary of the steps used to simulate both balloon angioplasty and stent implantation and how the loads and boundary conditions change for each step. A pressure boundary condition is applied to the lumen (inner) face to simulate systolic and diastolic blood pressure. Balloon angioplasty is simulated by overexpanding the lumen to 1.4 times its radius at systole.

The stenting procedure is simulated by implanting a square-shaped rigid body into the lumen wall. The correct implementation of stent mechanics in a 2D model in this orientation is challenging; stent radial stiffness characteristics are highly dependent on its 3D structure. In mechanobiological modeling of the long-term impact of stenting, the post-deployment behavior of the stent due to cyclic loading in systole and diastole is of primary interest. To implement this in a 2D model, one must know the postdeployment radial stiffness per unit axial length of a given stent design, i.e., the radial force per unit length required to *reduce* the radius of a deployed stent by one unit. The radial stiffness per unit axial length is divided by the number of struts on the circumference to determine the response of a single strut. In the 2D model, first the strut is deployed using a displacement boundary condition to 1.1 times the radius at systole (120 mmHg pressure), while maintaining systolic pressure. Next, a spring element is activated on the body of the strut with a spring stiffness equal to the stiffness per strut of the stent. Then the lumen pressure is reduced to diastolic pressure of 80 mmHg. These are the two states outlined in simulation steps 3 and 4, respectively, in Table 16.1. The damage calculations outlined in Section 16.3.3 may be computed at either step, or an average of the two. If one wishes to calculate cyclic stress/strain due to stenting, it is the difference between states 3 and 4, respectively.

16.3.2.2 Modeling Techniques

Although the FE model presented in Section 16.3.2.1 is an idealized representation, there are some important computational techniques that should be followed to ensure its accurate and efficient solution. The model entails large deformations and contact of a rigid body into a soft incompressible material, these sources of nonlinearity must be appropriately dealt with.

16.3.2.2.1 Geometric Nonlinearity

The first issue is geometric nonlinearity; this is where there are substantial rigid body translations and/or rotations, and/or high strains (>5%) during the simulation. All these criteria are met during both the balloon angioplasty and stent implantation simulations and means that a small-strain approach is not appropriate. A geometrically nonlinear FE solver must be used to address this issue. (In Abaqus the NLGEOM option must be activated.)

16.3.2.2.2 Material Nonlinearity

The next issue is material nonlinearity; this is where the constitutive behavior of a material has a nonlinear strain–displacement and stress–strain response. The strain in an artery wall may be upward of 25%, violating the assumption that

This book belongs to Central Library BADJI Mokhtar-ANNABA UNIVERSITY Copyright Elsevier 2024

deformations are so small that changes of geometry can be neglected, and arterial tissue has a well-known nonlinear stress−strain response. This nonlinearity is addressed through the use of a hyperelastic constitutive model. Hyperelastic models are a function of the deformation gradient tensor; the fundamental measure of material deformation and the strain energy densities from which they are derived permit thermodynamically stable nonlinear stress−strain behavior. Additionally, they are insensitive to large rigid body rotations and translations making them very suitable for simulations where there is also geometric nonlinearity.

16.3.2.2.3 Enforcing Incompressibility

Arterial tissue is widely assumed to be an incompressible material, meaning that its volume does not change under any applied deformation. This is the equivalent to a linear elastic material having a Poisson's ratio of 0.5. Perfectly incompressible materials cannot be implemented in explicit FE solvers and the user must take extra care to ensure an undistorted solution is computed (Nolan et al., 2014). Implicit solvers may use a "hybrid" or "mixed formulation" elements for the accurate and efficient computation of stress in incompressible materials, where the hydrostatic pressure and the displacement are nodal solution variables. If care is not taken to correctly implement incompressibility, erroneous stresses will be calculated because of a phenomena known as volume strain locking.

16.3.2.2.4 Element Selection

The choice of element type is important not only for modeling incompressibility, but it will determine the accuracy of the solution. Fig. 16.3A shows a schematic for a linear triangular element with its integration point. This element is also known as a constant strain triangle as the single integration point means that only one stress/strain state exists within its boundary. These elements are useful because they can mesh complex geometries; however, because of the single integration point, relatively more elements must be used when modeling a heterogeneous stress field compared with quadrilateral elements. Fig. 16.3B shows a schematic of a quadrilateral element and its integration points for both full integration and reduced integration formulations. In the full integration formulation the four internal integration points permit a complex stress gradient within an element, which generally means that fewer elements are required. In problems where there is a high degree of bending the full integration elements are susceptible to a numerical problem known as shear locking, where a bending deformation is misinterpreted as a shear deformation at the integration points. To prevent this occurring, a reduced integration linear quadrilateral element may be used instead. However, reduced integration elements do not permit internal stress gradients because of their single integration point and suffer from their own numerical problem known as hourglassing.

Interestingly, reduced integration elements are often the default setting in commercial FE codes, such as Abaqus and Ansys, because they have a relatively low computational cost, the hourglassing problem can be numerically managed, and they behave well when an element is highly distorted. The novice user cannot make serious unconscious errors by using this default. In the authors' opinion, however, full integration elements should be used where appropriate. In the balloon angioplasty and stent implantation simulations, there are no bending loading modes. However, in the stent implantation simulation, there is a high gradient of stress at the site of implantation, which warrants the use of full integration elements.

Fig. 16.4 demonstrates the importance of conducting a mesh convergence study, particularly in regions with a heterogeneous stress field such as that found around the stent strut. Here, a model using a low-density mesh fails to capture the stress field behind the stent strut.

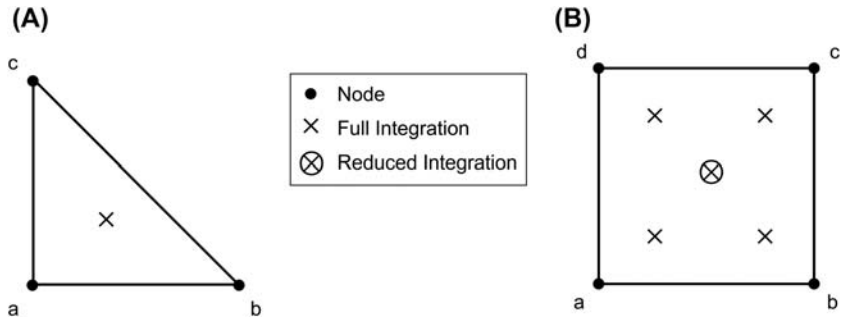

FIGURE 16.3 (A) Linear triangular element showing the nodes and integration point. (B) Linear quadrilateral element showing the integration points for a full integration and reduced integration formulation.

This book belongs to Central Library BADJI Mokhtar-ANNABA UNIVERSITY Copyright Elsevier 2024

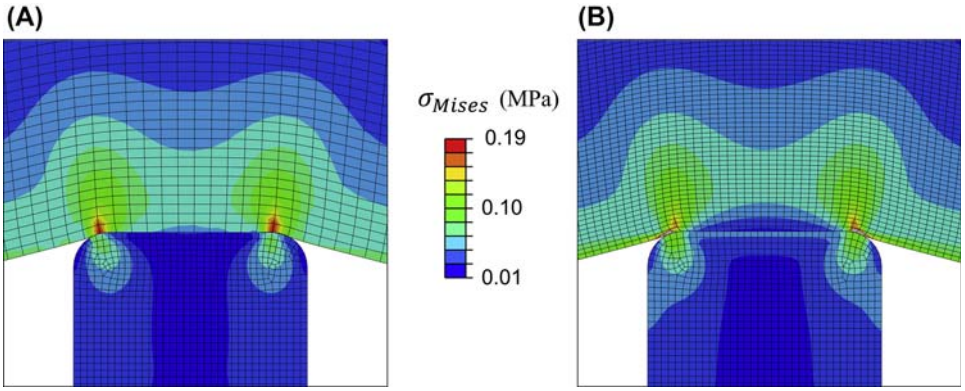

FIGURE 16.4 Contour plot of von Mises stress in the region around the implanted stent strut for (A) a low mesh density (element length ~7 μm and (B) a high mesh density (element length ~3 μm). Although the stresses are similar in locations furthest from the stent, the stress immediately behind the strut is very different for (A) and (B) demonstrating the importance of having a sufficiently dense mesh in regions of highly heterogeneous stress. Therefore, approximately 60 plane strain elements along the contact edge of the stent are required in the *undeformed* configuration.

16.3.2.2.5 Boundary Nonlinearity: Contact

The final issue is boundary nonlinearity; here this pertains to the contact between the rigid stent body and the comparably soft arterial tissue. Quadratic elements are not considered above because they do not behave well in contact. The inclusion of a midside node in these elements creates difficulties in the calculation of contact stresses. The current model uses a surface-to-surface contact algorithm. The key advantage to this method is that contact is enforced on an average basis, taking contact conditions at neighboring nodes into account. The master–slave relationship between the two contact surfaces is not strictly enforced, allowing some small degree of overclosure and avoiding the problematic issue of master nodes penetrating through the slave surface.

16.3.3 Coupling Agent-Based and Finite Element Domains

16.3.3.1 Coupled Model Overview

The previous two sections have outlined two different types of models: ABMs, which are used to simulate the collective behavior of cells, and a FE model, which simulates the mechanical behavior of arterial tissue on a continuum level. A mechanobiological model is created by coupling these two modules together. Fig. 16.5 gives a schematic that broadly outlines how the FE module and the ABM module are linked together.

The FE analysis takes place first; the user must decide what material properties and initial geometry are to be used. If simulating a stent, the depth to which the stent is deployed is critical. The stenting simulation results in the computation of a deformed geometry and von Mises stress field for each of the steps given in Table 16.1. The desired deformed geometry and stress field is passed to the ABM module. The VSMC agents are seeded on the deformed geometry and these agents are assigned a level of damage based on the stress at that location. These prescribe the initial conditions for the ABM module. The ABM simulation then proceeds and the resulting lumen loss and time to complete healing can be calculated.

The ABM–FE coupling is ideally an iterative process where updated material properties alter the mechanical stimuli sensed by the cells and hence their proliferative response (see Zahedmanesh and Lally, 2012). For simplicity in this chapter, however, this process is not iteratively coupled.

16.3.3.2 Interpreting Finite Element Model Results

When analyzing the results of a FE model, it is important to consider how these results have been calculated. In solid mechanics analyses, forces and displacements are calculated at the nodes of an element, whereas stresses and strains are computed at the Gauss/integration points within an element. This detail is important in the analysis of heterogeneous stress/strain fields, such as the region of the artery surrounding the stent strut in our 2D stent implantation analysis. Many FE postprocessing software tools interpolate the integration point data to the surrounding nodes by default. As the stress experienced by the agents is mapped directly from the spatial domain of the FE model to that of the ABM, it is important that this interpolation is compensated for if necessary. If the element size is smaller than the size of the agents, then this may not be an issue. A numerical interpolation function in 3D space, such as the interp2 in Matlab or Rbf from Scipy's interpolate package, is useful for determining the stress at the center point of an agent in 2D space.

This book belongs to Central Library BADJI Mokhtar-ANNABA UNIVERSITY Copyright Elsevier 2024

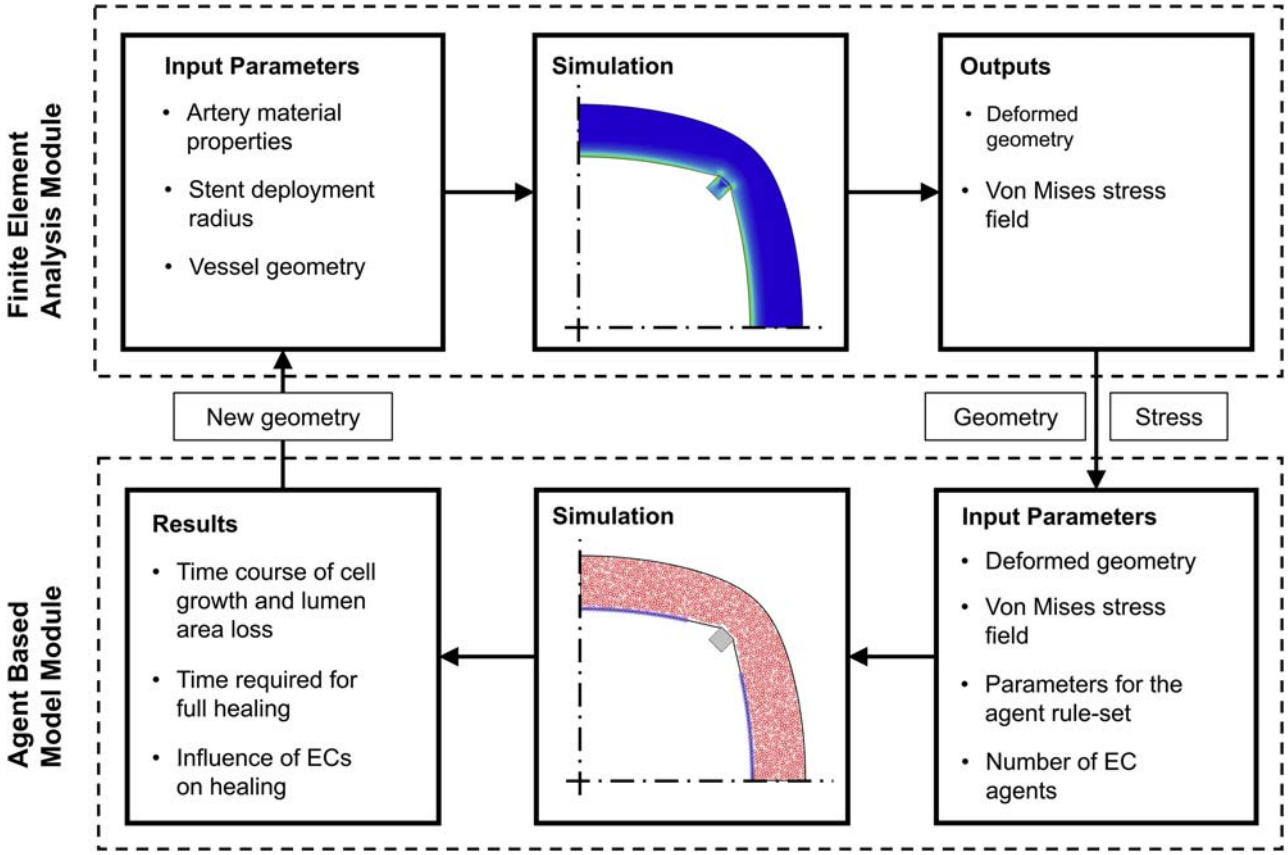

FIGURE 16.5 Flowchart schematic that outlines the coupled mechanobiological model used to simulate vascular smooth muscle cell response to mechanical damage after stent implantation. The coupled model consists of two primary modules: a finite element (FE) model that simulates the mechanical response and an agent-based model (ABM) that simulates the cell response. The models are coupled by the FE module passing the deformed geometry and von Mises stress field to the ABM model. *EC*, endothelial cell.

16.3.3.3 Mapping the Deformed Geometry

One of the key aspects of coupling the FE and ABM modules is using the deformed shape of the poststented artery as the initial geometry for the ABM. Displacements are calculated at the nodes of the mesh. A list of the nodes on the boarder of the artery (a node set) is defined in the initial configuration of the geometry of the FE model. When the FE simulation is completed, the displacement at each of the nodes in the boarder node set is exported. These node displacements are added to the initial positions of the nodes and form the boundary of the ABM model. This is simply a list of 2D coordinates that are imported into the ABM module using a text file.

The irregular deformed geometry creates difficulties for defining the boarder using simple expressions, such as the equation of a circle or a line. However, from the above, there exists a set of points on the boarder. A convex hull algorithm can be used to define a closed loop boarder, which can be used to check the validity of VSMC agents because they are seeded in Algorithm 16.1.

16.3.3.4 Stress-Driven Rule Set for Vascular Smooth Muscle Cell Agents

Stress is a complex measure of the internal forces within a body and is described using a tensor matrix with six independent components. Von Mises stress σ_{mises} is commonly used as a scalar measure to represent this complex tensor as an equivalent or effective stress in a body. It is given by the equation

$$\sigma_{\text{mises}} = \frac{1}{\sqrt{2}}\sqrt{(\sigma_{11}-\sigma_{22})^2 + (\sigma_{22}-\sigma_{33})^2 + (\sigma_{33}-\sigma_{11})^2 + 6(\sigma_{12}^2+\sigma_{23}^2+\sigma_{31}^2)} \tag{16.3}$$

This book belongs to Central Library BADJI Mokhtar-ANNABA UNIVERSITY
Copyright Elsevier 2024

where σ_{ij} are the six independent components of the stress tensor. The von Mises stress at the center point of each VSMC agent is calculated. Depending on the magnitude of the stress, the agent is then assigned a level of damage ranging from 0 to 1. This represents the degree of mechanical injury a cell has experienced. Damage D is assigned using a sigmoid of function of von Mises stress, which is based on experimental mechanical tests on coronary arteries (Holzapfel et al., 2005a; Zahedmanesh et al., 2014). This damage function is given as

$$D = \frac{\beta}{\beta + \exp[-\beta(\sigma_{\text{mises}} - \sigma_0)]} \tag{16.4}$$

where β and σ_0 are all parameters that define the shape of the sigmoid curve. Fig. 16.6A shows a plot of the sigmoid function defined by Eq. (16.4). The cell will experience approximately zero damage until it approaches 200 kPa von Mises stress, then there is a rapid increase, and by 300 kPa, a VSMC agent will experience maximum damage.

Section 16.3.1.1.2 outlines the three primary variables that control the VSMC agent behavior: damage D, MMP concentration M, and ECM density E. The evolution of each of these variables with time t is defined by a set of coupled first-order ordinary differential equations (ODEs) given as

$$\frac{dD}{dt} = -k^D_{\text{deg}} M \tag{16.5}$$

$$\frac{dM}{dt} = f(D) - k^M_{\text{deg}} M \tag{16.6}$$

$$\frac{dE}{dt} = k^E_{\text{gen}} - k^E_{\text{deg}} M \tag{16.7}$$

where k is an equation constant whose superscript indicates the ABM variable to which it applies and the subscript indicates whether it has a generative or degenerative (degrading) effect on the equation, $f(D)$ is a sigmoid function that defines the magnitude of MMP that is produced and is given by the equation

$$f(D) = \frac{\kappa_a}{1 + \kappa_b \exp(-\kappa_c D)} \tag{16.8}$$

where κ_a, κ_b, and κ_c are constants that define the shape of the function. A plot of the function defined by Eq. (16.8) is given in Fig. 16.6B; there is a gradual transition between no MMP being produced at low levels of damage and the maximum amount of MMP at high damage.

The ODEs are solved numerically using a forward Euler scheme and a time step Δt. For example, to solve for a generic variable Q, which is a function of time t,

$$Q(t) = Q(t - \Delta t) + \left[\frac{dQ^{t-\Delta t}}{dt}\right]\Delta t \tag{16.9}$$

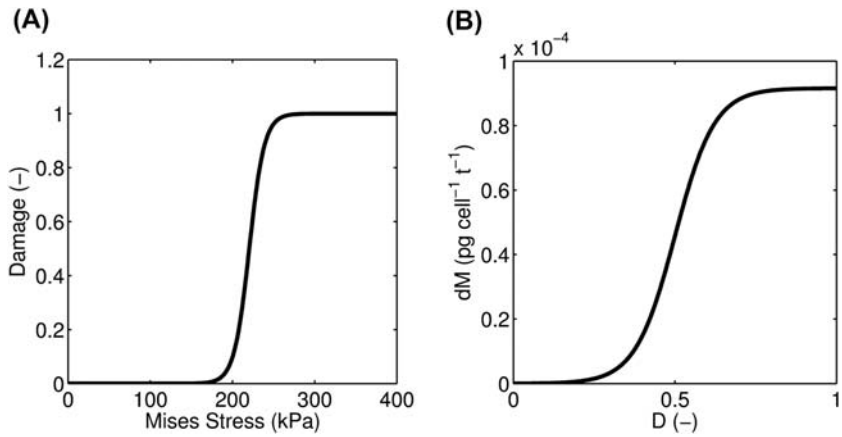

FIGURE 16.6 (A) Plot of the sigmoid function defined in Eq. (16.4) that assigns the damage to a vascular smooth muscle cell agent based on the von Mises stress at its center point ($\beta = 0.1087$, $\sigma_0 = 200$). (B) Plot of the sigmoid function defined in Eq. (16.8) that calculates the magnitude of matrix metalloproteinase that will be generated by an agent as a function of its damage level ($\kappa_a = 96.1 \times 10^{-6}$, $\kappa_b = 3468$, $\kappa_c = 16.8$).

This book belongs to Central Library BADJI Mokhtar-ANNABA UNIVERSITY
Copyright Elsevier 2024

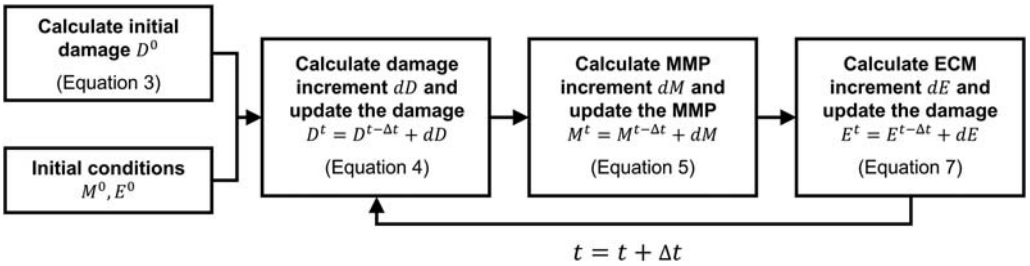

FIGURE 16.7 Flowchart outlining the solution process for the coupled ordinary differential equations that control the vascular smooth muscle cell agent variables. Initial damage conditions D_0 are calculated and initial conditions of matrix metalloproteinase (MMP) M_0 and extracellular matrix (ECM) E_0 are set. New values of damage, MMP and ECM are calculated every time step Δt.

where the ODE term in the square brackets is evaluated at time $t - \Delta t$. Additionally, to solve the first increment of the Eq. (16.9), the initial condition of the equation $Q(0) \equiv Q_0$ must be known. This is a simple, effective method for solving the coupled ODEs and is suitably accurate provided that a sufficiently small time step is used. In the present model a time step of 1 h is used. The procedure for solving the system of coupled ODEs in Eqs. (16.5)–(16.7) is outlined in Fig. 16.7. The initial condition for damage D_0 is defined by Eq. (16.4), initial MMP concentration M_0 is assumed to be 0, and the initial ECM density E_0 is 310 pg/cell.

The four k_i^j parameters in Eqs. (16.5)–(16.7) define the characteristic behavior of the coupled ODE response, and calibrating these parameters defines the response of the VSMC agents to damage. Table 16.2 lists the parameters used in Fig. 16.8 to plot the damage, MMP and ECM response for a variety of initial damage values, D_0. The damage decays with time; the larger the rate of decrease, the greater the initial damage. The MMP concentration has an initial rapid increase in response to the incidence of damage; the larger the initial damage, the higher the concentration of MMP. The MMP concentration then decreases, and the larger the damage, the longer it takes for this decrease to occur. The MMP concentration ultimately tends toward zero with time. In response to the MMP increase, the ECM concentration decreases, simulating ECM degradation. Subsequently, the ECM begins to increase and the time at which this occurs depends on the initial damage. The rate of increase is similar for all values of initial damage.

One must be careful when choosing the parameters for the ODE equations to ensure that a realistic, physical response is produced for the various sets of initial damage. As demonstrated in Fig. 16.8, the ODEs can be solved and plotted quite

TABLE 16.2 Parameters Used to Plot the Coupled Ordinary Differential Equation Given in Eqs. (16.5)–(16.7) and Plotted in Fig. 16.8

k_{deg}^D (cell/pg h)	k_{deg}^M (h^{-1})	k_{gen}^E (pg/cell h)	k_{deg}^E (h^{-1})
0.2644	0.0180	0.0288	24.60

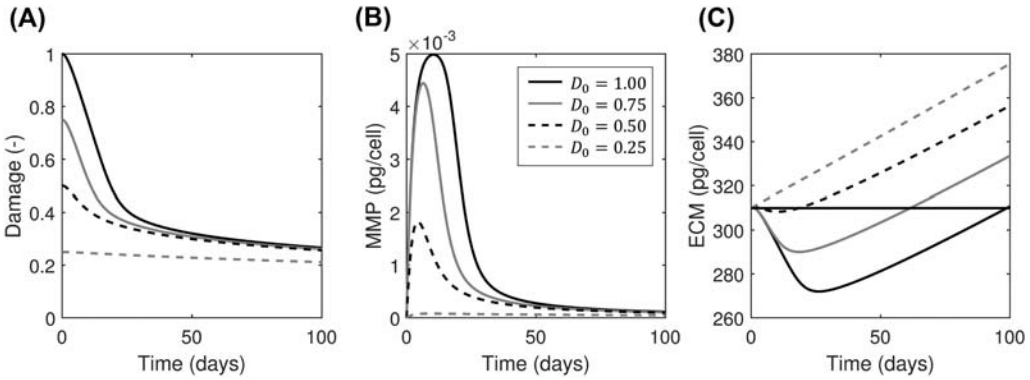

FIGURE 16.8 Plots of the three agent-based model variables with increasing time, as defined by the coupled ordinary differential equations in Eqs. (16.5)–(16.7) for a range of initial damage values D_0; (A) damage, (B) matrix metalloproteinase (MMP), (C) extracellular matrix (ECM).

This book belongs to Central Library BADJI Mokhtar-ANNABA UNIVERSITY
Copyright Elsevier 2024

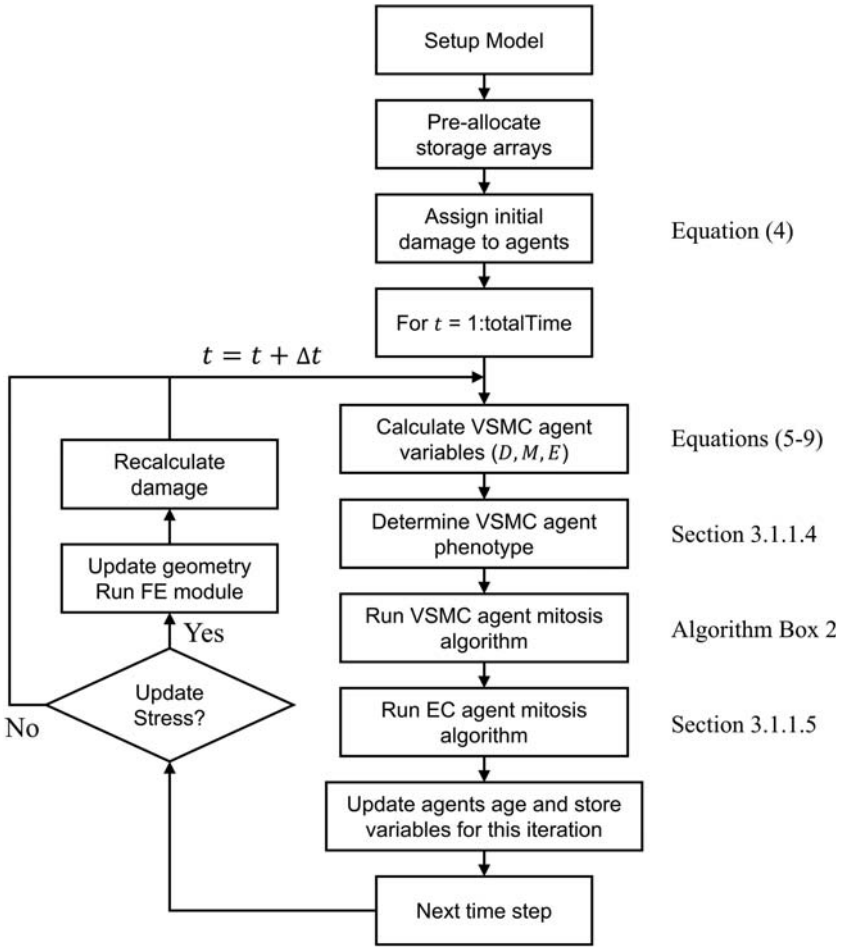

FIGURE 16.9 Flowchart outlining overall coupled finite element (FE) and agent-based model simulation environment referencing the relevant equations and algorithms. *EC*, endothelial cell; *VSMC*, vascular smooth muscle cell.

simply; there is no requirement to run an ABM simulation to gain a general understanding of how an individual agent will behave. In this scenario a VSMC agent that experiences an initial damage of 0.2 will not find its ECM dropping below the critical threshold to change its phenotype. This is not ideal and is a consequence of using a relatively simple set of ODE equations. However, it is a compromise that one may be willing to make, given that VSMCs experiencing high damage are of primary interest.

A flowchart of the complete coupled FE and ABM simulation is given in Fig. 16.9, referencing the relevant equations and algorithm boxes used for the model.

16.3.3.5 Calibration of Rule Set Through Simulation of Balloon Angioplasty

The Eqs. (16.5)–(16.7) define the damage–inflammation–recovery response of the VSMC agents; however, the constants of these equations must be determined. Although parameters such as agent size and rate of mitosis may be determined from experimental studies in a straightforward manner, it is not straightforward to determine the parameters for the ODE equations. To resolve this issue, the coupled FE–ABM described here is used to simulate a different clinical procedure: balloon angioplasty. The ODE parameters are calibrated iteratively until they reproduce clinical data. In balloon angioplasty the vessel lumen is expanded up to 1.4 times its diameter at systole. This causes mechanical damage to the artery wall and denudes it of ECs. These factors induce VSMCs to proliferate, which results in lumen area loss. The simulated lumen area loss with time is compared with clinical data of balloon injured vessels measured at fixed time points. The balloon angioplasty simulation is repeatedly performed, iteratively changing the ODE parameters, until the clinical data are reproduced.

This method is used to calibrate the VSMC agents and the same parameters are then used to simulate in-stent restenosis. Of course, there are four parameters to be calibrated, and there is only one set of experimental data with which to calibrate,

This book belongs to Central Library BADJI Mokhtar-ANNABA UNIVERSITY Copyright Elsevier 2024

which is not ideal. Additionally the balloon angioplasty simulating causes maximum damage ($D = 1$) to all the cells on the lumen. This means that there is uncertainty with regards to the response of agents subjected to lower levels of damage, which is important for in-stent restenosis simulations where damage is more heterogeneous and localized around the stent strut. This is where the lack of available experimental can limit the power of multiscale models, even with the most complex or detailed algorithms available. Ideally a models such as this would be calibrated based on experimental data where lumen area loss of vessels has been determine for a broad range of known levels of mechanical damage.

Although the damage model presented here is relatively simple, with increased available empirical data, this model can be made more numerically sophisticated and can be based on different mechanical stimuli or combinations of such stimuli such as cyclic loading and cumulative fatigue damage, cyclic strain levels, or injury (Boyle et al., 2013; Nolan and Lally, 2016; Zahedmanesh and Lally, 2012; Zahedmanesh et al., 2014).

16.4 FUTURE PERSPECTIVES

Although advancements have undoubtedly been made in recent years in multiscale and multiphysics mechanobiological models capable of elucidating the mechanisms, which drive vascular processes such as growth and remodeling, computational resources currently limit the complexity of such models. Complex, fiber-based anisotropic constitutive models are now well established for representing multilayer patient specific arteries, many including fiber remodeling capabilities in response to mechanical stimuli such as stress and strain (Creane et al., 2012). Incorporation of such adaptive models into multiscale ABM−FE coupled mechanobiological models will provide a means of better exploring the complex interplay between cell growth and matrix turnover as well as fiber alignment, particularly with respect to the load bearing collagen architecture where fiber alignment may be critical in terms of health and disease (Flamini et al., 2013). These models could provide key strategies in the development of novel intravascular device designs and optimized tissue engineered blood vessels with improved long-term outcomes.

In the future, with increasing technology and computational power comes the possibility of patient-specific medical devices, which are not only designed to conform to patient specific geometry but may also be optimized for the patient's specific growth and remodeling potential, with even the possibility of in silico clinical trials (Viceconti et al., 2016). The growth and inflammatory potential of individuals, whilst hugely variable, is something that can be ascertained using in vitro assays. Using such data could enable the development of more individualized vascular therapies and devices.

It is worth noting, however, that all models, regardless of their methodology, are merely an approximation of the physical problem they represent. The ultimate measure of a model's suitability is how well it can describe or predict what is physically reasonable and empirically or clinically observed (Valentin and Humphrey, 2009). To further develop such models and ensure their clinical relevance, therefore, requires robust experimental data to define them, and at present there is still a paucity of such data in the literature.

With increasing knowledge of cell behavior in response to mechanical stimuli and increased computational power, however, the potential of this research is vast, whereby it may ultimately be possible to develop 3D bioprinted patient-specific medical devices (Daly et al., 2016), which have been designed and developed, and even validated, using preclinical in silico predictive tools such as a coupled ABM−FE stochastic multiscale modeling framework.

REFERENCES

Alford, P.W., Humphrey, J.D., Taber, L.A., 2008. Growth and remodeling in a thick-walled artery model: effects of spatial variations in wall constituents. Biomechanics and Modeling in Mechanobiology 7, 245−262.

Auricchio, F., Conti, M., De Beule, M., De Santis, G., Verhegghe, B., 2011. Carotid artery stenting simulation: from patient-specific images to finite element analysis. Medical Engineering and Physics 33, 281−289.

Baek, S., Rajagopal, K.R., Humphrey, J.D., 2006. A theoretical model of enlarging intracranial fusiform aneurysms. Journal of Biomechanical Engineering 128, 142−149.

Bailey, A.M., Thorne, B.C., Peirce, S.M., 2007. Multi-cell agent-based simulation of the microvasculature to study the dynamics of circulating inflammatory cell trafficking. Annals of Biomedical Engineering 35, 916−936.

Balzani, D., Brinkhues, S., Holzapfel, G.A., 2012. Constitutive framework for the modeling of damage in collagenous soft tissues with application to arterial walls. Computer Methods in Applied Mechanics and Engineering 213, 139−151.

Bentley, P.J., 2008. Designing biological computers: systemic computation and sensor networks. In: Bio-inspired Computing and Communication. Springer.

Boyle, C., Lennon, A., Early, M., Kelly, D., Lally, C., Prendergast, P., 2010. Computational simulation methodologies for mechanobiological modelling: a cell-centred approach to neointima development in stents. Philosophical Transactions of the Royal Society of London A: Mathematical, Physical and Engineering Sciences 368, 2919−2935.

This book belongs to Central Library BADJI Mokhtar-ANNABA UNIVERSITY Copyright Elsevier 2024

Boyle, C.J., Lennon, A.B., Prendergast, P.J., 2011. In silico prediction of the mechanobiological response of arterial tissue: application to angioplasty and stenting. Journal of Biomechanical Engineering 133, 081001.

Boyle, C.J., Lennon, A.B., Prendergast, P.J., 2013. Application of a mechanobiological simulation technique to stents used clinically. Journal of Biomechanics 46, 918–924.

Budu-Grajdeanu, P., Schugart, R.C., Friedman, A., Valentine, C., Agarwal, A.K., Rovin, B.H., 2008. A mathematical model of venous neointimal hyperplasia formation. Theoretical Biology and Medical Modelling 5 (1).

Checa, S., Byrne, D.P., Prendergast, P.J., 2010. Predictive modelling in mechanobiology: combining algorithms for cell activities in response to physical stimuli using a lattice-modelling approach. In: Computer Methods in Mechanics. Springer.

Checa, S., Prendergast, P.J., 2009. A mechanobiological model for tissue differentiation that includes angiogenesis: a lattice-based modeling approach. Annals of Biomedical Engineering 37, 129–145.

Creane, A., Maher, E., Sultan, S., Hynes, N., Kelly, D.J., Lally, C., 2012. A remodelling metric for angular fibre distributions and its application to diseased carotid bifurcations. Biomechanics and Modeling in Mechanobiology 11, 869–882.

Daly, A.C., Cunniffe, G.M., Sathy, B.N., Jeon, O., Alsberg, E., Kelly, D.J., 2016. 3D bioprinting of developmentally inspired templates for whole bone organ engineering. Advanced Healthcare Materials 5, 2305–2449.

Evans, D.J., Lawford, P.V., Gunn, J., Walker, D., Hose, D.R., Smallwood, R.H., Chopard, B., Krafczyk, M., Bernsdorf, J., Hoekstra, A., 2008. The application of multiscale modelling to the process of development and prevention of stenosis in a stented coronary artery. Philosophical Transactions of the Royal Society of London A Mathematical Physical and Engineering Sciences 366, 3343–3360.

Feldman, L.J., Mazighi, M., Scheuble, A., Deux, J.F., De Benedetti, E., Badier-Commander, C., Brambilla, E., Henin, D., Steg, P.G., Jacob, M.P., 2001. Differential expression of matrix metalloproteinases after stent implantation and balloon angioplasty in the hypercholesterolemic rabbit. Circulation 103, 3117–3122.

Flamini, V., Kerskens, C., Simms, C., Lally, C., 2013. Fibre orientation of fresh and frozen porcine aorta determined non-invasively using diffusion tensor imaging. Medical Engineering and Physics 35, 765–776.

Fung, Y.C., Fronek, K., Patitucci, P., 1979. Pseudoelasticity of arteries and the choice of its mathematical expression. American Journal of Physiology 237, H620–H631.

Galis, Z.S., Khatri, J.J., 2002. Matrix metalloproteinases in vascular remodeling and atherogenesis: the good, the bad, and the ugly. Circulation Research 90, 251–262.

Ghosh, A., Chaudhuri, P., 2013. Computational modeling of fracture in concrete using a meshfree meso-macro-multiscale method. Computational Materials Science 69, 204–215.

Hayenga, H.N., Thorne, B.C., Peirce, S.M., Humphrey, J.D., 2011. Ensuring congruency in multiscale modeling: towards linking agent based and continuum biomechanical models of arterial adaptation. Annals of Biomedical Engineering 39, 2669–2682.

Hoekstra, A.G., Alowayyed, S., Lorenz, E., Melnikova, N., Mountrakis, L., van Rooij, B., Svitenkov, A., Závodszky, G., Zun, P., 2016. Towards the virtual artery: a multiscale model for vascular physiology at the physics–chemistry–biology interface. Philosophical Transactions of the Royal Society of London A Mathematical, Physical and Engineering Sciences 374, 20160146.

Hoekstra, A.G., Falcone, J.-L., Caiazzo, A., Chopard, B., 2008. Multi-scale modeling with cellular automata: The complex automata approach. In: International Conference on Cellular Automata. Springer, pp. 192–199.

Hoekstra, A.G., Lorenz, E., Falcone, J.L., Chopard, B., 2007. Toward a complex automata formalism for multiscale modeling. International Journal for Multiscale Computational Engineering 5, 491–502.

Holzapfel, G.A., Gasser, T.C., Ogden, R.W., 2000. A new constitutive framework for arterial wall mechanics and a comparative study of material models. Journal of Elasticity 61, 1–48.

Holzapfel, G.A., Gasser, T.C., Stadler, M., 2002. A structural model for the viscoelastic behavior of arterial walls: continuum formulation and finite element analysis. European Journal of Mechanics A-Solids 21, 441–463.

Holzapfel, G.A., Sommer, G., Gasser, C.T., Regitnig, P., 2005a. Determination of layer-specific mechanical properties of human coronary arteries with nonatherosclerotic intimal thickening and related constitutive modeling. American Journal of Physiology. Heart and Circulatory Physiology 289, H2048–H2058.

Holzapfel, G.A., Stadler, M., Gasser, T.C., 2005b. Changes in the mechanical environment of stenotic arteries during interaction with stents: computational assessment of parametric stent designs. Journal of Biomechanical Engineering 127, 166–180.

Keller, B.K., Amatruda, C.M., Hose, D.R., Gunn, J., Lawford, P.V., Dubini, G., Migliavacca, F., Narracott, A.J., 2014. Contribution of mechanical and fluid stresses to the magnitude of in-stent restenosis at the level of individual stent struts. Cardiovascular Engineering and Technology 5, 164–175.

Kuhl, E., Maas, R., Himpel, G., Menzel, A., 2007. Computational modeling of arterial wall growth. Biomechanics and Modeling in Mechanobiology 6, 321–331.

Lally, C., Dolan, F., Prendergast, P.J., 2005. Cardiovascular stent design and vessel stresses: a finite element analysis. Journal of Biomechanics 38, 1574–1581.

Lally, C., Prendergast, P., 2006. Simulation of in-stent restenosis for the design of cardiovascular stents. In: Mechanics of Biological Tissue. Springer.

Matsusaki, M., Amemori, S., Kadowaki, K., Akashi, M., 2011. Quantitative 3D analysis of nitric oxide diffusion in a 3D artery model using sensor particles. Angewandte Chemie International Edition 50, 7557–7561.

Nolan, D.R., Gower, A.L., Destrade, M., Ogden, R.W., Mcgarry, J.P., 2014. A robust anisotropic hyperelastic formulation for the modelling of soft tissue. Journal of the Mechanical Behavior of Biomedical Materials 39, 48–60.

Nolan, D.R., Lally, C., 2016. A mechanobiological framework for the prediction of in-stent restenosis; Insights into the role of load induced damage in restenotic growth. In: Hoekstra, A. (Ed.), Virtual Physiological Human 2016 Conference. University of Amsterdam, Amsterdam.

This book belongs to Central Library BADJI Mokhtar-ANNABA UNIVERSITY Copyright Elsevier 2024

Nolan, D.R., Lally, C., 2017. An investigation of damage mechanisms in mechanobiological models of in-stent restenosis. Journal of Computational Science. http://dx.doi.org/10.1016/j.jocs.2017.04.009.

Nolan, D.R., McGarry, J.P., 2016. On the compressibility of arterial tissue. Annals of Biomedical Engineering 44, 993−1007.

Peirce, S., Van Gieson, E., Skalak, T., 2004. Multicellular simulation predicts microvascular patterning. The FASEB Journal 18 (6), 731−733 express article, 10.

Peirce, S.M., Skalak, T.C., Papin, J.A., 2006. Multiscale biosystems integration: coupling intracellular network analysis with tissue-patterning simulations. IBM Journal of Research and Development 50, 601−615.

Rachev, A., Manoach, E., Berry, J., Moore Jr., J.E., 2000. A model of stress-induced geometrical remodeling of vessel segments adjacent to stents and artery/graft anastomoses. Journal of Theoretical Biology 206, 429−443.

Rogers, C., Parikh, S., Seifert, P., Edelman, E.R., 1996. Endogenous cell seeding remnant endothelium after stenting enhances vascular repair. Circulation 94, 2909−2914.

Rouillard, A.D., Holmes, J.W., 2014. Coupled agent-based and finite-element models for predicting scar structure following myocardial infarction. Progress in Biophysics and Molecular Biology 115, 235−243.

Sun, W., Sacks, M.S., 2005. Finite element implementation of a generalized fung-elastic constitutive model for planar soft tissues. Biomechanics and Modeling in Mechanobiology 4, 190−199.

Taber, L.A., 1995. Biomechanics of growth, remodeling, and morphogenesis. Applied Mechanics Reviews 48, 487−545.

Taber, L.A., 1998. A model for aortic growth based on fluid shear and fiber stresses. Journal of Biomechanical Engineering 120, 348−354.

Tahir, H., Niculescu, I., Bona-Casas, C., Merks, R.M., Hoekstra, A.G., 2015. An in silico study on the role of smooth muscle cell migration in neointimal formation after coronary stenting. Journal of the Royal Society Interface 12, 20150358.

Thorne, B.C., Hayenga, H.N., Humphrey, J.D., Peirce, S.M., 2011. Toward a multi-scale computational model of arterial adaptation in hypertension: verification of a multi-cell agent based model. Frontiers Physiology 2, 20.

Tsamis, A., Stergiopulos, N., Rachev, A., 2009. A structure-based model of arterial remodeling in response to sustained hypertension. Journal of Biomechanical Engineering 131, 101004.

Valentin, A., Humphrey, J., 2009. Evaluation of fundamental hypotheses underlying constrained mixture models of arterial growth and remodelling. Philosophical Transactions of the Royal Society of London A: Mathematical, Physical and Engineering Sciences 367, 3585−3606.

Viceconti, M., Henney, A., Morley-Fletcher, E., 2016. In silico clinical trials: how computer simulation will transform the biomedical industry. International Journal of Clinical Trials 3, 37−46.

Zahedmanesh, H., Kelly, D.J., Lally, C., 2010. Simulation of a balloon expandable stent in a realistic coronary artery-determination of the optimum modelling strategy. Journal of Biomechanics 43, 2126−2132.

Zahedmanesh, H., Lally, C., 2009. Determination of the influence of stent strut thickness using the finite element method: implications for vascular injury and in-stent restenosis. Medical and Biological Engineering and Computing 47, 385−393.

Zahedmanesh, H., Lally, C., 2012. A multiscale mechanobiological modelling framework using agent-based models and finite element analysis: application to vascular tissue engineering. Biomechanics and Modeling in Mechanobiology 11, 363−377.

Zahedmanesh, H., Lally, C., 2013. Multiscale Modeling in Vascular Disease and Tissue Engineering. Multiscale Computer Modeling in Biomechanics and Biomedical Engineering. Springer.

Zahedmanesh, H., Van Oosterwyck, H., Lally, C., 2014. A multi-scale mechanobiological model of in-stent restenosis: deciphering the role of matrix metalloproteinase and extracellular matrix changes. Computer Methods in Biomechanics and Biomedical Engineering 17, 813−828.

This book belongs to Central Library BADJI Mokhtar-ANNABA UNIVERSITY

Copyright Elsevier 2024

Part V

Meshless and Meshfree Methods

This book belongs to Central Library BADJI Mokhtar-ANNABA UNIVERSITY

Copyright Elsevier 2024

This page intentionally left blank

This book belongs to Central Library BADJI Mokhtar-ANNABA UNIVERSITY

Copyright Elsevier 2024

Chapter 17

The Mechanologic Bone Tissue Remodeling Analysis: A Comparison Between Mesh-Depending and Meshless Methods

M. Peyroteo[1], J. Belinha[2], L. Dinis[2] and R. Natal Jorge[2]

[1]Institute of Mechanical Engineering and Industrial Management (INEGI), Porto, Portugal; [2]Faculty of Engineering of the University of Porto (FEUP), Porto, Portugal

17.1 INTRODUCTION

Thanks to the growing knowledge in biomechanics, it has been proven that mechanological effects have a strong influence on many biological processes and characteristics of living tissues, such as regulation of different biological processes (homeostasis), morphological and structural adaptation, and tissue damage and repair (Doblaré and García-Aznar, 2010). Within these tissues, bone tissue has stood out by simultaneously playing important metabolic and mechanical functions. This duality of roles is indeed evidenced during the bone remodeling process. Thus, through remodeling, old bone is continuously replaced by new tissue, repairing microfractures and modifying its structure in response to stress and other biomechanical forces.

Moreover, during a remodeling cycle, the turnover of bone is managed by a sequential process performed by the bone cells, in which the activities of bone-forming osteoblasts and bone-resorbing osteoclasts are coordinated. These activities of osteoblasts and osteoclasts are controlled by a variety of hormones and cytokines, as well as by mechanical loading (Lerner, 2006). This last factor is considered a very important factor to take into account. Actually, descended cells from osteoblasts, known as osteocytes, have shown to convert mechanical stimuli into metabolic responses, organizing bone turnover under mechanical strain and immobilization (Compston, 2001; Hofbauer et al., 2004; Robling et al., 2006). Therefore, loading plays an important role. A low amount of loading leads to bone loss, because of decreased anabolic activity of osteoblasts and increased osteoclastic resorption, and high loading causes increased bone mineral density, because of the anabolic activation of osteoblasts (Lerner, 2006).

This phenomenon has been first described by the Wolff's law, stating that bone tissue progressively modifies its morphology adapting to any new external mechanical stimulus, such as the strain level or the stress level (Lotz et al., 1991). Since then, this research field has greatly evolved with the development of increasingly sophisticated theoretical and numerical models. Firstly, Carter et al. (Carter et al., 1987, 1989; Whalen et al., 1988) proposed the "self-optimization" concept focused on the functional adaptation of trabecular bone. Taking into account the influence of different load cases, Carter suggested that the mechanical stimulus was a function of the local stress state and the local apparent density. Then, taking an innovative step, Cowin et al. presented the "adaptive elasticity" model (Cowin et al., 1992; Cowin and Hegedus, 1976; Cowin and Nachlinger, 1978; Hegedus and Cowin, 1976), describing a continuum theory of bone internal remodeling defined as the sum of chemical reactions between bone matrix and the extracellular fluids. However, this model had the disadvantage of using a relatively high number of parameters. Then, based on this model, Huiskes et al. (1987) and Weinans et al. (1992) used a new approach considering the strain energy density (SED) as the mechanical stimulus for bone tissue remodeling. Following this work, Reiter et al. (1990) and Pettermann et al. (1997) proposed some modifications, introducing the effects of overstrain necrosis and the anisotropic material behavior, respectively.

Numerical Methods and Advanced Simulation in Biomechanics and Biological Processes. https://doi.org/10.1016/B978-0-12-811718-7.00017-4
Copyright © 2018 Elsevier Ltd. All rights reserved.

This book belongs to Central Library BADJI Mokhtar-ANNABA UNIVERSITY

Copyright Elsevier 2024

The remodeling algorithm conducted in this work is an adaptation of Carter's model (Carter et al., 1987). Firstly proposed by Belinha (2014) and adapted in this work, this model consists in an iterative topology optimization model for bone adaptation that seeks the minimization of the SED variable with respect to the bone apparent density. This mechanologic model is combined with mesh-depending discrete techniques, such as the finite element method (FEM), and meshless techniques, such as two distinct radial point interpolation (RPI) meshless methods.

Thus, besides this brief introduction, this chapter describes the numerical approaches used in this work, addressing the RPI meshless formulations with more detail. Additionally, it also includes a full description of the remodeling model considered in this study, as well as the phenomenological anisotropic material law used. In the end, a femur bone is submitted to three load cases and analyzed with the three numerical techniques.

17.2 NUMERICAL METHODS

Because of its complexity, the computational simulation of bone remodeling requires the use of intricate mathematical models. Thus, the equations ruling this phenomenon cannot be easily solved, symbolically or analytically, and therefore, the use of numerical methods is the ideal solution (Heckbert, 1993).

In the 1940s, the first approximation method was proposed, known as the FEM. The works of Hrennikoff (1941) and McHenry (1943) were the starting point, followed by Courant (1943), who introduced the concept of piecewise interpolation or shape functions over triangular subregions. Since then, several other studies have improved this method, contributing to make it the most popular approach to solve continuum problems in many fields, such as structural engineering, fluid dynamics, and heat or mass transfer (Zienkiewicz et al., 2013). Also, recalling the bone remodeling models mentioned previously, many were analyzed using the FEM. For instance, the "self-optimization" model of Carter, combined with the FEM, was employed to obtain the stress and strain distributions in the proximal femur according to three different typical loading cases, predicting the apparent density distribution in the actual bone (Carter et al., 1987). Later, the modified version of Reiter was used in combination with FEM to analyze the behavior of bone around implants in dental surgery and to simulate the behavior of the tibia after insertion of a knee end prosthesis (Krach et al., 1995; Reiter et al., 1994). Indeed, this led to the appearance of several successful applications of the FEM within orthopedic biomechanics, such as the prediction of the density distributions in the femoral bone before and after surgical treatment (Huiskes and Chao, 1983; Huiskes and Hollister, 1993).

However, it has been shown that the development and application of remodeling models is dependent on the numerical model used to study it because the accuracy of the remodeling algorithm is intimately dependent on the accuracy of the used numerical method (Belinha et al., 2012a). Therefore, limitations, such as the mesh-based interpolation or the difficulties that the FEM presented when analyzing numerical problems with highly irregular complex geometries, led to the creation of other alternative numerical methods, such as the meshless methods.

Within these techniques, the problem's physical domain is discretized with an unstructured nodal distribution. Regarding these methods, they can be classified in two categories. In the strong formulation category, the partial differential equations describing the phenomenon are used directly to obtain the solution, whereas the weak formulation aims to minimize the residual weight of each differential equation, given by an approximated function affected by a test function and not by the exact solution of the differential (Belinha, 2014). In this category, the first emerged meshless methods used approximation functions, such as the diffuse element method proposed by Nayroles et al. (1992) and the element-free Galerkin method proposed by Belytschko et al. (1994). However, these methods did not possess the Kronecker delta property, making it difficult to impose the essential and natural boundary conditions. Because of this fact, interpolant meshless methods were developed, such as the point interpolation method (PIM) (Liu et al., 2005). The PIM (Wang and Liu, 2002a,b) is a meshfree method developed using Galerkin weak form, in which its interpolant shape functions can have two different forms of basis functions: polynomial basis functions (Gu and Liu, 2001; Liu and Gu, 2001) or radial basis functions (RBFs) (Liu et al., 2005; Wang and Liu, 2002a,b). Thus, when RBFs are used to construct shape functions, the method is termed as the radial point interpolation method (RPIM). This method has been proved to be very stable and robust, having been successfully applied to many problems, such as 1D and 2D solid mechanics (Gu and Liu, 2001; Liu and Gu, 2001) and plate and shell structures (Liu et al., 2002). However, this method requires the use of a global background cell structure to evaluate the integration in the Galerkin weak form, calling into question the meshfree concept. Thus, other meshless methods proposing integration schemes using the nodal distribution were presented, such as the natural neighbor radial point interpolation method (NNRPIM) and the natural radial element method (Belinha et al., 2013a,b,c). The NNRPIM has been extended to many fields of computational mechanics, such as the analysis of isotropic and orthotropic plates (Dinis et al., 2008), the analysis of functionally graded material plates (Dinis et al., 2010a,b,c), the 3D shell-like approach (Belinha et al., 2016a; Dinis et al., 2010b,c, 2011a,b; Moreira et al., 2014a), the dynamic analysis of several solid mechanic problems (Dinis et al., 2009a), the analysis of large deformations (Dinis et al., 2009b), and the crack mechanics (Belinha et al., 2016b; Rossi and Wendling-Mansuy, 2007). The NNRPIM has also been extended to the field of biomechanics. The combination of this

This book belongs to Central Library BADJI Mokhtar-ANNABA UNIVERSITY Copyright Elsevier 2024

method with an SED-based remodeling algorithm allowed the study of the bone tissue remodeling process (Belinha et al., 2012a,b, 2014). This model was capable to predict efficiently the trabecular bone architecture, having been validated with clinical cases of the femur bone and the calcaneus bone internal trabecular structure (Belinha et al., 2012b, 2015a). Additionally, this model has been applied in the study of dental implants (Belinha et al., 2015c; Duarte et al., 2016; Moreira et al., 2014b; Tavares et al., 2015).

In this way, it becomes very clear that several models describing bone remodeling caused by mechanical stimuli have been combined with distinct numerical methods. In this work, the remodeling algorithm chosen is based on Belinha's work (Belinha et al., 2012a) and it was combined with three numerical techniques, namely the FEM, the RPIM, and NNRPIM. Thus, using for the first time the RPIM in bone remodeling simulations and using the femur bone as the numerical example, the performance of these three methods is compared. Therefore, the following subsections focus on the formulation of these numerical methods.

17.2.1 The Finite Element Method

The FEM's approach involves discretizing the domain with a finite number of interconnected elements. This method is considered mesh-dependent because every element is connected, directly or indirectly, to every other element through common interfaces, constructing a mesh (Fig. 17.1A). Also, these elements can vary in size and type and can possess different properties, enabling the discretization of structures with mixed properties (Chao et al., 2002). Regarding the density of the mesh, a high number of elements increase significantly the computational cost of this technique. However, the accuracy of the results improves. In this work, triangular elements were used because of the simplicity of the expressions associated with this element. Thus, by using a simple formulation of the FEM, it is possible to do a fair comparison between this method, the RPIM, and the NNRPIM.

To determine the unknown variable, a set of piecewise-continuous functions is defined for each finite domain (Logan et al., 2007). Thus, the FEM general procedure requires to discretize the problem in a nodal mesh and its corresponding element mesh, identifying to which element each node belongs to. Afterward, an integration mesh is constructed, using the element grid and the Gauss−Legendre quadrature scheme. Then, it is possible to obtain the shape functions and its partial spatial derivatives. Classically, the shape functions can be obtained by using a polynomial basis functions defined in the Cartesian space or by means of an isoparametric element (which reduces significantly the computational cost of this particular task). Later, using the equivalent dimensional size of each integration point and the constructed shape functions, the integro-differential equations, governing the physical phenomenon under study, are used to create the system of equations, which can be used to solve the numerical problem in hands.

Because the FEM is extensively described in the literature (Logan et al., 2007), this section will not be as detailed as the meshless methods section.

17.2.2 Meshless Methods

Contrary to the FEM, the only information required for the meshless methods is the spatial location of each node discretizing the problem domain. In these types of methods, the nodal distribution does not form a mesh because no previous information is considered about the relation between each node.

When describing meshless methods, three concepts have to be analyzed: the nodal connectivity, the numerical integration scheme, and the shape functions. Therefore, briefly explaining, after discretization, the nodal connectivity is

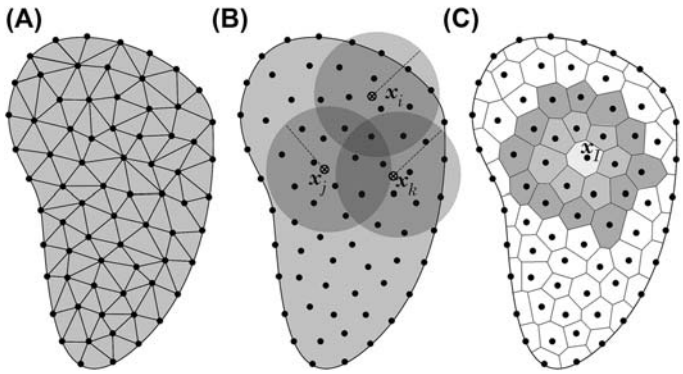

FIGURE 17.1 Imposition of the nodal connectivity using (A) the finite element method, (B) the radial point interpolation method, and (C) the natural neighbor radial point interpolation method.

This book belongs to Central Library BADJI Mokhtar-ANNABA UNIVERSITY Copyright Elsevier 2024

imposed by using either influence domains or Voronoï diagrams. Then, a background integration mesh is constructed and the interpolation functions of the unknown variable field functions are established. Thus, to fully comprehend the meshless methods used in this work, these three concepts will be separately analyzed for the RPIM and the NNRPIM.

17.2.2.1 Nodal Connectivity

In the RPIM, the nodal connectivity is obtained by the overlap of the influence domains of each node. Influence domains are determined performing a radial search. Therefore, for each node, the domain is composed by a certain number of nodes inside a certain area or volume. Many meshless methods (Atluri and Zhu, 1998; Liu et al., 1995; Wang and Liu, 2002a) use fixed size influence domains, but, for irregular nodal distributions, it can cause unbalanced connectivities. Therefore, to avoid this, the RPIM uses a fixed number of neighbor nodes instead. Thus, it used variable size influence domains, but with a constant number of nodes inside the domain, as illustrated by Fig. 17.1B.

In the NNRPIM, the nodal connectivity is obtained by constructing the Voronoï diagram. Therefore, using the natural neighbor concept (Sibson, 1981) and considering a set $\boldsymbol{N} = \{n_1, n_2,\ldots,n_N\}$ of N distinct nodes, the Voronoï diagram of $\boldsymbol{N}$ is the partition of the domain defined by $\boldsymbol{N}$ in subregions V_I, closed and convex. Each Voronoï cell V_I is the geometric place where all points in the interior of V_I are closer to the node n_I than to any other node n_J, being $n_J \in N(J \neq I)$. This way, the assemblage of the complete set of Voronoï cells $\boldsymbol{V} = \{V_1,V_2,\ldots,V_N\}$ define the Voronoï diagram. The following step is using the Voronoï diagram to determine the "influence cells" (Dinis et al., 2007), which can be of two different types: "first-degree influence cells" and "second-degree influence cells." In this work, it was used the "second-degree influence cell" concept. Therefore, to establish it, a node of interest, $\boldsymbol{x}_I$, starts by searching for its first natural neighbors nodes following the Natural Neighbor Voronoï construction, setting a preliminary influence cell (built by interest node $\boldsymbol{x}_I$, light-gray cell, and all natural neighbors of $\boldsymbol{x}_I$, gray cells), as represented in Fig. 17.1C. Then, based again on the Voronoï diagram, the natural neighbors of the first natural neighbors of $\boldsymbol{x}_I$ are added to the influence cell (dark-gray cells), allowing to obtain the influence cell shown in Fig. 17.1C.

17.2.2.2 Numerical Integration

To solve the integro-differential equation that governs the problem, it is necessary to use a numerical integration scheme. Therefore, regarding the RPIM, the solid domain is divided with integration cells, leading to an auxiliary grid. Then, in this background mesh, each grid cell is filled with integration points, following the Gauss−Legendre quadrature rule (Fig. 17.2).

Knowing the isoparametric coordinates of the integration points, $\{\xi_I, \eta_I\}$, the Cartesian coordinates of the quadrature points, $\{x_I, y_I\}$, are obtained using isoparametric interpolation functions, N_i, as follows:

$$\begin{aligned} x_I &= \sum_{i=1}^{m} N_i(\xi_I, \eta_I)\cdot x_i \\ y_I &= \sum_{i=1}^{m} N_i(\xi_I, \eta_I)\cdot y_i \end{aligned} \tag{17.1}$$

in which m is the number of nodes inside the grid cell and x_i and y_i are the Cartesian coordinates of the cells' nodes.

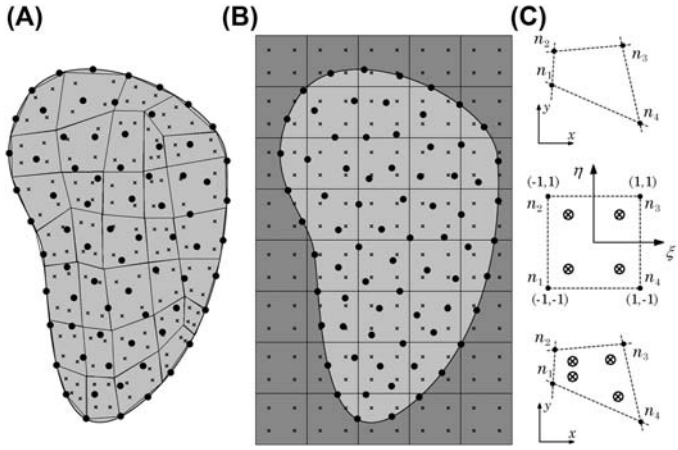

FIGURE 17.2 (A) Fitted Gaussian integration mesh, (B) nonfitted Gaussian integration mesh, and (C) transformation of the initial quadrilateral into an isoparametric square shape and application of the 2 × 2 quadrature point rule.

This book belongs to Central Library BADJI Mokhtar-ANNABA UNIVERSITY
Copyright Elsevier 2024

The interpolation functions, N_i, for quadrilateral and triangle grid cells can be found in Eqs. (17.2) and (17.3), respectively.

$$\begin{aligned} N_1(\xi,\eta) &= \frac{1}{4}(1-\xi)(1-\eta) \\ N_2(\xi,\eta) &= \frac{1}{4}(1-\xi)(1+\eta) \\ N_3(\xi,\eta) &= \frac{1}{4}(1+\xi)(1+\eta) \\ N_4(\xi,\eta) &= \frac{1}{4}(1+\xi)(1-\eta) \end{aligned} \tag{17.2}$$

$$\begin{aligned} N_1(\xi,\eta) &= 1-\xi-\eta \\ N_2(\xi,\eta) &= \eta \\ N_3(\xi,\eta) &= \xi \end{aligned} \tag{17.3}$$

Thus, to numerically approximate the integral, the function is evaluated at several sampling points. These points are chosen according to the Gauss's method that, for a given number of points, produces the best possible accurate result. Thus, besides the value of the function at each sampling point, the integration weight of the quadrature point, ω_i, is also required, as depicted by Eq. (17.4).

$$\int_{-1}^{1}\int_{-1}^{1} f(\xi,\eta)\, d\xi d\eta = \sum_{i=1}^{m}\sum_{j=1}^{n} \omega_i\omega_j f(\xi_i,\eta_i) \tag{17.4}$$

The integration weight of the quadrature point is obtained by multiplying the isoparametric weight of the quadrature point with the inverse of the determinant of the Jacobian matrix (Eq. 17.5) of the respective grid cell: $\omega(\boldsymbol{x}_I) = \omega_i\omega_j \det([J(\boldsymbol{x}_I)])$.

$$[J(\boldsymbol{x}_I)] = \begin{pmatrix} \frac{\partial x}{\partial \xi} & \frac{\partial x}{\partial \eta} \\ \frac{\partial y}{\partial \xi} & \frac{\partial y}{\partial \eta} \end{pmatrix} = \begin{bmatrix} \frac{dN_1}{dx} & \frac{dN_2}{dx} & \cdots & \frac{dN_m}{dx} \\ \frac{dN_1}{dy} & \frac{dN_2}{dy} & \cdots & \frac{dN_m}{dy} \end{bmatrix} \begin{bmatrix} x_1 & x_1 \\ x_2 & x_2 \\ \vdots & \vdots \\ x_m & x_m \end{bmatrix} \tag{17.5}$$

The NNRPIM numerical integration's approach assures its designation of a "truly" meshless method. This because, the integration scheme uses the nodal distribution to construct the integration mesh. Thus, the background mesh is completely dependent on the nodal mesh and it is built applying the Delaunay triangulation, which is the geometrical dual of the Voronoï diagram. Therefore, the background integration mesh is constructed by connecting the nodes whose Voronoï cells have common boundaries with, because a Delaunay edge exists between two nodes in the plane if and only if their Voronoï cells share a common edge. Therefore, with the Delaunay triangulation, the area of each Voronoï cell is subdivided in several subareas, with just two main steps. First, the intersection points, P_{Ii}, of the neighbor edges of the Voronoï cell, V_I, are settled. Then, the middle points, M_{Ii}, between n_I and its neighbor nodes are obtained, as Fig. 17.3 indicates. In this way, the Voronoï cells are divided in n quadrilateral subcells, S_{Ii}, n being the number of natural neighbors of node n_I.

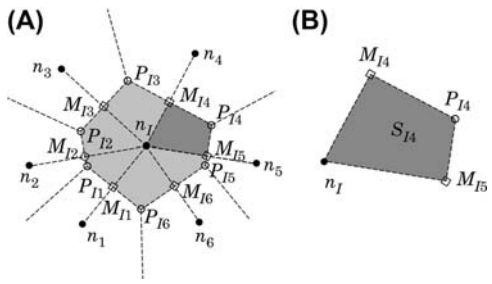

FIGURE 17.3 (A) Voronoï cell and the corresponding P_{Ii} intersection points and middle points M_{Ii}. (B) Respective generated quadrilaterals.

This book belongs to Central Library BADJI Mokhtar-ANNABA UNIVERSITY Copyright Elsevier 2024

It is important to notice that, because the set of Voronoï cells is a partition, without gaps, of the global domain, the set of subcells is also a partition, without gaps, of the global domain. Thus, these subcells can be used in several integration schemes such as the Gauss−Legendre numerical scheme. Therefore, the size of any Voronoï cell, V_I, can be determined using the size of the n subcells, S_{Ii},

$$A_{V_I} = \sum_{i=1}^{n} A_{S_{Ii}}, \ \forall A_{S_{Ii}} \geq 0 \tag{17.6}$$

being A_{V_I} the Voronoï cell area and $A_{S_{Ii}}$ the subcell area.

This work uses only one quadrature point in each subcell and second-degree influence cells because these parameters have proven to produce more accurate and stable results (Dinis et al., 2007).

17.2.2.3 Interpolation Functions

Both the RPIM and the NNRPIM use the radial point interpolation (Wang and Liu, 2002a) technique to construct the shape functions. Thus, both meshless methods use interpolation shape functions possessing the Kronecker delta property,

$$\varphi_i(x_j) = \delta_{ij} \tag{17.7}$$

where δ_{ij} is the Kronecker delta, $\delta_{ij} = 1$ if $i = j$ and $\delta_{ij} = 0$ if $i \neq j$. This property is considered an asset because it simplifies greatly the process of imposition of the boundary conditions.

The approximation function $u\ (\boldsymbol{x}_I)$, defined in the domain $\Omega \subset \mathbb{R}^2$, can be estimated to all values of nodes within the support domain of the point of interest $\boldsymbol{x}_I$ using an RBF, $R_i\ (\boldsymbol{x}_I)$, and a polynomial basis function, $p_j\ (\boldsymbol{x}_I)$.

$$u(\boldsymbol{x}_I) = \sum_{i=1}^{n} R_i(\boldsymbol{x}_I) \cdot a_i(\boldsymbol{x}_I) + \sum_{j=1}^{m} p_j(\boldsymbol{x}_I) \cdot b_j(\boldsymbol{x}_I) = \boldsymbol{R}(\boldsymbol{x}_I)^T \cdot \boldsymbol{a}(\boldsymbol{x}_I) + \boldsymbol{p}(\boldsymbol{x}_I)^T \cdot \boldsymbol{b}(\boldsymbol{x}_I) \tag{17.8}$$

where n is the number of nodes within the influence domain of the point of interest, $\boldsymbol{x}_I$, and m is the number of monomial of the polynomial basis functions. The coefficients a_i and b_j of $R_i(\boldsymbol{x}_I)$ and $p_j(\boldsymbol{x}_I)$, respectively, are represented as

$$\boldsymbol{a}^T = \{a_1, a_2, \ldots, a_n\} \tag{17.9}$$

$$\boldsymbol{b}^T = \{b_1, b_2, \ldots, b_m\} \tag{17.10}$$

The RBF is a function of distance r_{Ii} between the relevant node $\boldsymbol{x}_I$ and the neighbor node x_i, given by $r_{Ii} = |\boldsymbol{x}_i - \boldsymbol{x}_I|$. The RBF used in this work is the multiquadric RBF (Hardy, 1990), $R_i(\boldsymbol{x}_I) = R(r_{Ii}) = \left(r_{Ii}^2 + c^2\right)^p$, in which the shape parameter c takes a value close to zero, $c \cong 0$, and p close to one, $p \cong 1$ (Dinis et al., 2008, 2007). In the case of a two-dimensional problem, the polynomial basis function chosen from Pascal's triangle is expressed as

$$\boldsymbol{p}^T(\boldsymbol{x}_I) = \left[1, x, y, x^2, xy, y^2, \ldots\right] \tag{17.11}$$

To determine the coefficients a_i and b_j, the interpolation is enforced to pass through all n scattered nodal points within the influence domain. According to Eq. (17.8), there are $(n + m)$ unknowns. Thus, to guarantee a unique solution, m additional equations have to be added, which are the constraint conditions (Golberg et al., 1999) expressed in the following equation:

$$\sum_{i=1}^{n} p_j(\boldsymbol{x}_I) a_i = \boldsymbol{P}_m^T \boldsymbol{a} = 0, \quad j = 1, 2, \ldots, m \tag{17.12}$$

Combining Eqs. (17.8) and (17.12), the following equation system, in matrix form, can be established:

$$\widetilde{\boldsymbol{U}}_S = \begin{Bmatrix} \boldsymbol{u}_S \\ 0 \end{Bmatrix} = \begin{bmatrix} \boldsymbol{R} & \boldsymbol{p} \\ \boldsymbol{p}^T & 0 \end{bmatrix} \begin{Bmatrix} \boldsymbol{a} \\ \boldsymbol{b} \end{Bmatrix} = \boldsymbol{G}\boldsymbol{a}_0 \tag{17.13}$$

This book belongs to Central Library BADJI Mokhtar-ANNABA UNIVERSITY
Copyright Elsevier 2024

where $\widetilde{\boldsymbol{U}}_s = \{u_1\ u_2 \ldots u_n\ 0\ 0 \ldots 0\}$ is the vector of the nodal function values for the nodes on the influence domain. Because the moment matrix $\boldsymbol{R}$ is symmetric, the matrix $\boldsymbol{G}$ will also be symmetric. Solving Eq. (17.13), the unknowns can be obtained as

$$\boldsymbol{a}_0 = \begin{Bmatrix} \boldsymbol{a} \\ \boldsymbol{b} \end{Bmatrix} = \boldsymbol{G}^{-1} \begin{Bmatrix} \boldsymbol{u}_S \\ 0 \end{Bmatrix} \tag{17.14}$$

Substituting Eq. (17.14) into Eq. (17.8), it is now possible to define the interpolation function, $\boldsymbol{\Phi}(\boldsymbol{x}_I)$.

$$u(\boldsymbol{x}_I) = \{\boldsymbol{R}^T(\boldsymbol{x}_I), \boldsymbol{p}^T(\boldsymbol{x}_I)\}\, \boldsymbol{G}^{-1} \begin{Bmatrix} \boldsymbol{u}_S \\ 0 \end{Bmatrix} = \boldsymbol{\Phi}(\boldsymbol{x}_I) \begin{Bmatrix} \boldsymbol{u}_S \\ 0 \end{Bmatrix} \tag{17.15}$$

With this equation, it becomes clear that a certain field variable value for an interest point $\boldsymbol{x}_I$ is interpolated using the shape function values obtained at the nodes inside the influence domain of $\boldsymbol{x}_I$, being the interpolation function defined as $\boldsymbol{\Phi}(\boldsymbol{x}_I) = \{\varphi_1(\boldsymbol{x}_I), \varphi_2(\boldsymbol{x}_I), \ldots, \varphi_n(\boldsymbol{x}_I)\}$ for an interest point $\boldsymbol{x}_I$.

17.3 DISCRETE EQUATION SYSTEM

The strong-form system equations are the partial differential system equations governing the studied physic phenomenon. Using this formulation, the exact solution is always obtained. However, usually, this is an extremely difficult task in complex practical engineering problems.

Therefore, formulations based on weak forms are commonly used, allowing a discretized system of equations with a weaker consistency on the adopted approximation (or interpolation) functions. However, this formulation is able to produce stable algebraic system equations and highly accurate results (Belinha, 2014).

Thus, in this work, the discrete equation system is obtained using the Galerkin weak form, which is a variational method based on energy minimization.

Hence, considering a body described by the domain $\Omega \in \mathbb{R}^2$ and bounded by Γ, where $\Gamma \in \Omega$: $\Gamma_u \cup \Gamma_t = \Gamma \wedge \Gamma_u \cap \Gamma_t = \emptyset$, being Γ_u the essential boundary and Γ_t the natural boundary, the equilibrium equations governing the linear elastostatic problem are defined as

$$\begin{cases} \nabla \boldsymbol{\Lambda} + \boldsymbol{b} = 0 & \text{in } \Omega \\ \boldsymbol{\Lambda}\, \boldsymbol{n} = \bar{\boldsymbol{t}} & \text{on } \Gamma_t \\ \boldsymbol{u} = \bar{\boldsymbol{u}} & \text{on } \Gamma_u \end{cases} \tag{17.16}$$

in which ∇ is the divergence operator, $\boldsymbol{b}$ the body force per unit volume and $\boldsymbol{\Lambda}$ the Cauchy stress tensor, as defined previously. Additionally, in Eq. (17.16), $\boldsymbol{n}$ is the unit outward normal to Γ, $\bar{\boldsymbol{t}}$ the traction at the natural boundary Γ_t and $\bar{\boldsymbol{u}}$ is the prescribed displacement at the essential boundary Γ_u.

Using the Voigt notation and considering the Galerkin procedure in linear elasticity, the equilibrium equation in the variational form can be written. Therefore, the weak form for the discrete problem can be expressed as follows:

$$\delta \boldsymbol{L} = \int_\Omega \delta \boldsymbol{\varepsilon}^T \boldsymbol{\sigma}\, d\Omega - \int_\Omega \delta \boldsymbol{u}^T \boldsymbol{b}\, d\Omega - \int_{\Gamma_t} \delta \boldsymbol{u}^T \bar{\boldsymbol{t}}\, d\Gamma_t = 0 \tag{17.17}$$

The strain vector, $\boldsymbol{\varepsilon}$, can be defined by the combination of a differential operator and the displacement field, $\boldsymbol{u}$:

$$\boldsymbol{\varepsilon} = \boldsymbol{L}\boldsymbol{u} \tag{17.18}$$

where $\boldsymbol{L}$ is given by

$$\boldsymbol{L} = \begin{bmatrix} \dfrac{\partial}{\partial x} & 0 & \dfrac{\partial}{\partial y} \\ 0 & \dfrac{\partial}{\partial y} & \dfrac{\partial}{\partial x} \end{bmatrix}^T \tag{17.19}$$

Assuming the constitutive equation, known as Hooke's Law, the relation between stress and strain in the solid domain is given by

$$\boldsymbol{\sigma} = \boldsymbol{c}\boldsymbol{\varepsilon} \tag{17.20}$$

This book belongs to Central Library BADJI Mokhtar-ANNABA UNIVERSITY
Copyright Elsevier 2024

in which, $\boldsymbol{c}$ is the constitutive matrix, given by $\boldsymbol{c} = \boldsymbol{s}^{-1}$, being the matrix $\boldsymbol{s}$ the compliance elasticity matrix. For a general anisotropic material case and considering a plane stress formulation, matrix $\boldsymbol{s}$ is given by

$$\boldsymbol{s}_{\substack{plane\\stress}} = \begin{bmatrix} \frac{1}{E_{11}} & -\frac{\upsilon_{21}}{E_{22}} & 0 \\ -\frac{\upsilon_{12}}{E_{11}} & \frac{1}{E_{22}} & 0 \\ 0 & 0 & \frac{1}{G_{12}} \end{bmatrix} \tag{17.21}$$

while, when considering a plane strain formulation, matrix $\boldsymbol{s}$ is given by

$$\boldsymbol{s}_{\substack{plane\\strain}} = \begin{bmatrix} \frac{1-\nu_{31}\nu_{13}}{E_{11}} & -\frac{\upsilon_{12}+\nu_{31}\nu_{23}}{E_{22}} & 0 \\ -\frac{\upsilon_{12}+\nu_{32}\nu_{13}}{E_{11}} & \frac{1-\nu_{32}\nu_{23}}{E_{22}} & 0 \\ 0 & 0 & \frac{1}{G_{12}} \end{bmatrix} \tag{17.22}$$

being E_{ij} the elasticity modulus, ν_{ij} the material Poisson coefficient, and G_{ij} the distortion modulus in material directions i and j. Because, in this work, only linear elastic isotropic materials are considered, $E_{11} = E_{22}$ and $\nu_{ij} = 0.3\ \forall\ i, j \in \mathbb{N}$.

Obtaining the constitutive matrix $\boldsymbol{c}$, it is possible to align it with a new material referential $Ox'y'$ defined by the versors $\boldsymbol{i} = \left\{i'_x, i'_y\right\}$ and $\boldsymbol{j} = \left\{j'_x, j'_y\right\}$, using the following expression:

$$\boldsymbol{c}' = \boldsymbol{T}^{\boldsymbol{T}}\boldsymbol{c}\ \boldsymbol{T} \tag{17.23}$$

being $\boldsymbol{T}$ the transformation matrix given by

$$\boldsymbol{T} = \begin{bmatrix} \cos^2\alpha & \mathrm{sen}^2\alpha & -\sin 2\alpha \\ \mathrm{sen}^2\alpha & \cos^2\alpha & \sin 2\alpha \\ \sin\alpha\cdot\cos\alpha & -\sin\alpha\cdot\cos\alpha & \cos^2\alpha\cdot\mathrm{sen}^2\alpha \end{bmatrix} \tag{17.24}$$

where the angle α is the angle between the original material axis Ox and the new material axis Ox':$\alpha = \cos^{-1}(\boldsymbol{i}, \boldsymbol{i}')$.

Because, in this work, only 2D problems are analyzed assuming the plane strain or the plane stress deformation theory, each node $\boldsymbol{x}_i$ discretizing the problem domain possesses 2 degrees of freedom aligned with the referential axis: $\boldsymbol{u}_i = \{u_i, v_i\}$. Thus, according to Eq. (17.15), the virtual displacements, or the test functions, can be defined as

$$\delta\boldsymbol{u}(\boldsymbol{x}_I) = \delta\boldsymbol{u}_I = \boldsymbol{I}\begin{Bmatrix} \boldsymbol{\Phi}_I \\ \boldsymbol{\Phi}_I \end{Bmatrix}\delta\boldsymbol{u}_s = \begin{bmatrix} \varphi_1(\boldsymbol{x}_I) & 0 & \cdots & \varphi_n(\boldsymbol{x}_I) & 0 \\ 0 & \varphi_1(x_I) & \cdots & 0 & \varphi_n(\boldsymbol{x}_I) \end{bmatrix}\begin{Bmatrix} \delta u_1 \\ \delta v_1 \\ \vdots \\ \delta u_n \\ \delta v_n \end{Bmatrix} = \boldsymbol{H}_I\delta\boldsymbol{u}_s \tag{17.25}$$

Therefore, considering Eq. (17.25) and applying the Hooke's law, the first term of Eq. (17.17) can be simplified as

$$\begin{aligned} \int_\Omega \delta\boldsymbol{\varepsilon}^{\boldsymbol{T}}\boldsymbol{\sigma}\, d\Omega &= \int_\Omega (\delta\boldsymbol{L}\boldsymbol{u})^{\boldsymbol{T}}\boldsymbol{c}(\boldsymbol{L}\boldsymbol{u})\, d\Omega = \int_\Omega (\boldsymbol{L}\boldsymbol{H}_I\delta\boldsymbol{u}_s)^{\boldsymbol{T}}\boldsymbol{c}(\boldsymbol{L}\boldsymbol{H}_I\boldsymbol{u}_s)d\Omega = \int_\Omega \delta\boldsymbol{u}_s\boldsymbol{B}_I^{\boldsymbol{T}}\boldsymbol{c}\boldsymbol{B}_I\boldsymbol{u}_s d\Omega \\ &= \delta\boldsymbol{u}^{\boldsymbol{T}}\int_\Omega \boldsymbol{B}_I^{\boldsymbol{T}}\boldsymbol{c}\boldsymbol{B}_I\, d\Omega\boldsymbol{u} = \delta\boldsymbol{u}^{\boldsymbol{T}}\boldsymbol{K}\boldsymbol{u} \end{aligned} \tag{17.26}$$

This book belongs to Central Library BADJI Mokhtar-ANNABA UNIVERSITY
Copyright Elsevier 2024

in which the deformability matrix $\boldsymbol{B_I}$ for the n nodes constituting the element/influence domain/influence cell of interest point $\boldsymbol{x_I}$, can be defined as

$$B_i = \begin{bmatrix} \frac{\partial \varphi_1(\boldsymbol{x}_I)}{\partial x} & 0 & \frac{\partial \varphi_2(\boldsymbol{x}_I)}{\partial x} & 0 & \cdots & \frac{\partial \varphi_n(\boldsymbol{x}_I)}{\partial x} & 0 \\ 0 & \frac{\partial \varphi_1(\boldsymbol{x}_I)}{\partial y} & 0 & \frac{\partial \varphi_2(\boldsymbol{x}_I)}{\partial y} & \cdots & 0 & \frac{\partial \varphi_n(\boldsymbol{x}_I)}{\partial y} \\ \frac{\partial \varphi_1(\boldsymbol{x}_I)}{\partial y} & \frac{\partial \varphi_1(\boldsymbol{x}_I)}{\partial x} & \frac{\partial \varphi_2(\boldsymbol{x}_I)}{\partial y} & \frac{\partial \varphi_2(\boldsymbol{x}_I)}{\partial x} & \cdots & \frac{\partial \varphi_n(\boldsymbol{x}_I)}{\partial y} & \frac{\partial \varphi_n(\boldsymbol{x}_I)}{\partial x} \end{bmatrix} \tag{17.27}$$

The global stiffness matrix is expressed by $\boldsymbol{K}$ and the displacement field vector by $\boldsymbol{u}$. In an analogous way, the second and third terms of Eq. (17.17) can be also simplified, obtaining the following:

$$\int_{\Omega} \delta \boldsymbol{u}^T \boldsymbol{b}\, d\Omega = \int_{\Omega} (\boldsymbol{H_I} \delta \boldsymbol{u}_s)^T \boldsymbol{b}\, d\Omega = \delta \boldsymbol{u}^T \int_{\Omega} \boldsymbol{H}_I^T \boldsymbol{b}\, d\Omega = \delta \boldsymbol{u}^T \boldsymbol{f_b} \tag{17.28}$$

$$\int_{\boldsymbol{\Gamma}_t} \delta \boldsymbol{u}^T \bar{\boldsymbol{t}}\, d\Gamma_t = \int_{\boldsymbol{\Gamma}_t} (\boldsymbol{H_I} \delta \boldsymbol{u_S})^T \bar{\boldsymbol{t}} d\Gamma_t = \delta \boldsymbol{u}^T \int_{\boldsymbol{\Gamma}_t} \boldsymbol{H}_I^T \bar{\boldsymbol{t}} d\Gamma_t = \delta \boldsymbol{u}^T \boldsymbol{f_t} \tag{17.29}$$

being $\boldsymbol{f}_b$ the global body weight vector and $\boldsymbol{f}_t$ the global external forces vector.

Thus, equilibrium Eq. (17.17) becomes

$$\delta \boldsymbol{u}^T \boldsymbol{K} \boldsymbol{u} - \delta \boldsymbol{u}^T \boldsymbol{f_b} - \delta \boldsymbol{u}^T \boldsymbol{f}_t = 0 \Rightarrow \boldsymbol{K} \boldsymbol{u} = \boldsymbol{f_b} + \boldsymbol{f_t} \tag{17.30}$$

Therefore, considering the vector $\boldsymbol{f} = \boldsymbol{f}_b + \boldsymbol{f}_t$ as the sum vector of the applied forces, it is possible, using Eq. (17.30), to solve the linear equation system $\boldsymbol{u} = \boldsymbol{K}^{-1}\boldsymbol{f}$ and obtain the displacement field. Thenceforward, it is possible to determine numerous variable fields. The strain $\boldsymbol{\varepsilon}(\boldsymbol{x}_I)$, at the interest point $\boldsymbol{x}_I \in \Omega$, can be obtained using Eq. (17.18). Then, using the Hooke's law present in Eq. (17.20), the stress field, $\boldsymbol{\sigma}(\boldsymbol{x}_I)$, can also be calculated.

Considering both the strain and the stress fields, the SED field for an interest point $\boldsymbol{x}_I$ and a specific load case can be determined as follows:

$$U(\boldsymbol{x_I}) = \frac{1}{2} \int_{\Omega_I}^{a} \boldsymbol{\sigma}(\boldsymbol{x_I})^T \boldsymbol{\varepsilon}(\boldsymbol{x_I})\, d\Omega_I \tag{17.31}$$

The principal stresses $\sigma(\boldsymbol{x}_I)$ at the interest point $\boldsymbol{x}_I$ are obtained from the Cauchy stress tensor $\Lambda(\boldsymbol{x}_I)$ using the expression

$$det \left[\begin{bmatrix} \sigma_{xx}(\boldsymbol{x_I}) & \sigma_{xy}(\boldsymbol{x_I}) \\ \sigma_{xy}(\boldsymbol{x_I}) & \sigma_{yy}(\boldsymbol{x_I}) \end{bmatrix} - \sigma(x_I)_i \begin{bmatrix} 1 & 0 \\ 0 & 1 \end{bmatrix} \right) = 0 \tag{17.32}$$

and the principal directions $\boldsymbol{n}((\boldsymbol{x_I})_i) = \{n_x((\boldsymbol{x_I})_i), n_y((\boldsymbol{x_I})_i)\}^T$ are obtained with

$$\left[\begin{bmatrix} \sigma_{xx}(\boldsymbol{x}_I) & \sigma_{xy}(\boldsymbol{x}_I) \\ \sigma_{xy}(\boldsymbol{x}_I) & \sigma_{yy}(\boldsymbol{x}_I) \end{bmatrix} - \sigma(\boldsymbol{x}_I)_i \begin{bmatrix} 1 & 0 \\ 0 & 1 \end{bmatrix} \right) \begin{Bmatrix} n_x(\boldsymbol{x}_I)_i \\ n_y(\boldsymbol{x}_I)_i \end{Bmatrix} = 0 \tag{17.33}$$

The three principal stresses obtained can be used to determine the von Mises effective stress at each interest point $\boldsymbol{x}_I$ with the following expression:

$$\overline{\sigma}(\boldsymbol{x_I}) = \sqrt{\frac{1}{2}\left(\left(\sigma(\boldsymbol{x_I})_1 - \sigma(\boldsymbol{x_I})_2\right)^2 + \left(\sigma(\boldsymbol{x_I})_2 - \sigma(\boldsymbol{x_I})_3\right)^2 + \left(\sigma(\boldsymbol{x_I})_3 - \sigma(\boldsymbol{x_I})_1\right)^2 \right)} \tag{17.34}$$

17.4 MECHANOLOGIC MODEL

17.4.1 Phenomenological Law

As already mentioned, many mathematical models of bone remodeling have been created along time. Because of the development of numerical methods and the increasing knowledge about mechanical properties of bone tissue, these

This book belongs to Central Library BADJI Mokhtar-ANNABA UNIVERSITY
Copyright Elsevier 2024

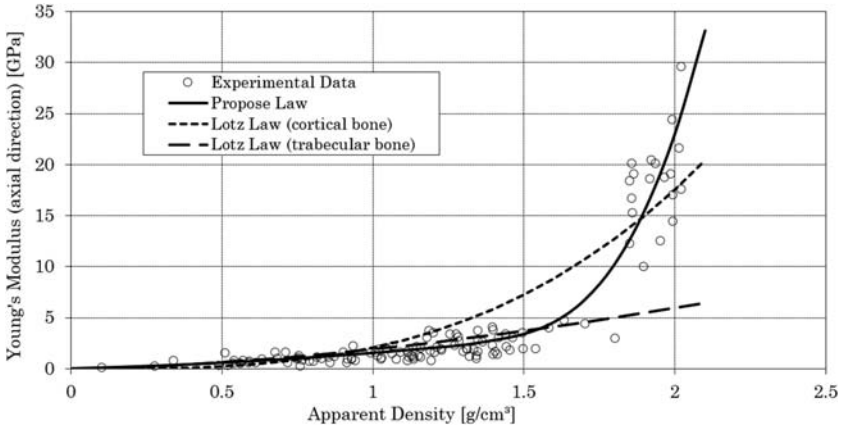

FIGURE 17.4 Correlation between apparent density and elasticity modulus.

models were capable to evolve (Belinha et al., 2015b). For this reason, early models assumed isotropic bone behavior (Wirtz et al., 2000). Later, based in experimental studies, these models considered the bone's orthotropic behavior.

One of the first models considering its orthotropic behavior was presented by Lotz et al. (1991). Then, since the Lotz's law, many other studies have tried to describe the mechanical behavior of bone tissue. Knowing that apparent density plays a crucial role in determining the mechanical properties of bone tissue, Zioupos' experimental work has proven to be very relevant (Zioupos et al., 2008) because it distinguished trabecular and cortical bone only based on apparent density measurements. In this work, it is proposed that the relation between the bone elasticity modulus and the medium apparent density is no longer the increasing monotonic function of Lotz but, instead, a function with a "boomerang"-like pattern (Fig. 17.4). This work reinforced the idea that apparent density is a salient property of bone.

However, Zioupos only analyzed the bone elasticity modulus in the axial direction (Belinha et al., 2012a). Thus, following Zioupos' work, Belinha (2014) proposed the mathematical curves for the elasticity modulus in the transversal direction and the ultimate compression stress in the axial and transversal directions, based on the values suggested by Lotz et al. (1991). In this way, using these curves, it is possible to predict the orthotropic mechanical behavior of bone tissue in respect to bone elasticity modulus and ultimate compression stress.

This work applies the Belinha's law, but only assumes an isotropic behavior. Moreover, instead of determining the apparent density accordingly to the ultimate compression stress, as proposed by Belinha, this work uses the von Mises effective stress, defined as $\overline{\sigma}(\boldsymbol{x}_I)$ for each interest point $\boldsymbol{x}_I$. Therefore, the mathematical curves that determine the elasticity modulus, E, and the von Mises effective stress, $\overline{\sigma}$, are presented in Eqs. (17.35)–(17.37) and the coefficients in Table 17.1.

$$E = \begin{cases} \sum_{j=0}^{3} a_j \cdot \rho^j & if \quad \rho \leq 1.3\ g/cm^3 \quad (17.35) \\ \sum_{j=0}^{3} b_j \cdot \rho^j & if \quad \rho > 1.3\ g/cm^3 \quad (17.36) \end{cases}$$

$$\overline{\sigma} = \sum_{j=0}^{3} c_j \cdot \rho^j \tag{17.37}$$

TABLE 17.1 Coefficients of Belinha's Law

Coefficient	$j = 0$	$j = 1$	$j = 2$	$j = 3$
a_j	0.000E + 00	7.216E + 02	8.059E + 02	0.000E + 00
b_j	−1.770E + 05	3.861E + 05	−2.798E + 05	6.836E + 04
c_j	0.000E + 00	0.000E + 00	2.680E + 01	2.035E + 01

This book belongs to Central Library BADJI Mokhtar-ANNABA UNIVERSITY
Copyright Elsevier 2024

The elasticity modulus and the von Mises effective stress are both expressed in MPa, whereas the apparent density, ρ, is in g/cm^3.

17.4.2 Remodeling Criterion

This work considers the remodeling algorithm presented by Belinha et al. (2012b), which is an adaptation for meshless methods of Carter's model (Carter et al., 1987). The remodeling model proposed uses a bone remodeling nonlinear equation, and it is adapted to work with the three numerical methods studied, namely the FEM, the RPIM, and the NNRPIM. This equation is a temporal−spatial functional, $\rho(x, t)$:$\mathbb{R}^{d+1} \mapsto \mathbb{R}$, discretized along a one-dimensional temporal line and a d-dimensional space. By presenting it as a differential equation and minimizing it with respect to time, this equation's expression is given by

$$\frac{\partial \rho(\boldsymbol{x}, t)}{\partial t} \cong \frac{\Delta \rho(\boldsymbol{x}, t)}{\Delta t} = \frac{(\rho_{model})_{t_{j+1}} - (\rho_{model})_{t_j}}{t_{j+1} - t_j} = 0 \tag{17.38}$$

In this algorithm, any problem being analyzed is discretized in space and time. Therefore, the d-dimensional spatial domain is assumed to be discretized in N nodes: $\boldsymbol{X} = \{\boldsymbol{x}_1, \boldsymbol{x}_2, \ldots, \boldsymbol{x}_n\} \in \boldsymbol{\Omega}$, leading to Q interest points: $\boldsymbol{Q} = \{\boldsymbol{x}_1, \boldsymbol{x}_2, \ldots, \boldsymbol{x}_Q\} \in \boldsymbol{\Omega}$, being $\boldsymbol{x}_i \in \mathbb{R}^d$ and $\boldsymbol{Q} \cap \boldsymbol{X} = \emptyset$. The temporal domain is discretized using iterative fictitious time steps $t_j \in \mathbb{R}$, with $j \in \mathbb{N}$.

Thus, the medium apparent density for the complete model domain is defined by $(\rho_{model})_{t_j}$ at a fictitious time t_j. Consequently, considering the same iterative step, the apparent density for the complete model domain, ρ_{model}, can be determined with

$$\rho_{model} = Q^{-1} \sum_{i=1}^{Q} \rho_i \tag{17.39}$$

being ρ_i the infinitesimal apparent density on interest point i defined by $\rho_I = g(\overline{\sigma}_I)$and given by Eq. (17.37).

However, the remodeling process does not occur at all interest points, $\boldsymbol{x}_I$. In fact, only the interest points presenting the SED values belonging to the interval indicated in Eq. (17.40) are identified and subjected to a density remodeling process, whereas all the other interest points maintain their previous density. The interval is given by

$$U(\boldsymbol{x}_I) \in [U_m, U_m + \alpha \cdot \Delta U[\cup] U_M - \beta \cdot \Delta U, U_M], \quad \forall\ U(\boldsymbol{x}_I) \in \mathbb{R} \tag{17.40}$$

being $U_m = \min(U)$, $U_M = \max(U)$, and $U = \mathrm{U}_M - U_m$. The parameters α and β define the growth rate and the decay rate of the apparent density, respectively, and vary according to the problem being analyzed. The third-order Eq (17.37) provides three different solutions, ρ_1, ρ_2, and ρ_3. Thus, if the interest points belong to the decay apparent density interval, the apparent density at interest point $\boldsymbol{x}_I$ is given by $\rho_I = \min(\rho_1, \rho_2, \rho_3)$. When the interest points belong to the increase apparent density interval, the apparent density at interest point $\boldsymbol{x}_I$ is given by $\rho_I = \max(\rho_1, \rho_2, \rho_3)$.

Lastly, the remodeling equilibrium is achieved when the following condition is met:

$$\frac{\Delta \rho}{\Delta t} = 0\mathrm{V}(\rho_{model})_{t_j} = \rho_{control} \tag{17.41}$$

17.4.3 Remodeling Procedure

The algorithm implemented in this work is schematized in Fig. 17.5. Initially, the algorithm starts with the preprocessing of the available medical images. Then, the problem domain is discretized with an unstructured nodal mesh $\boldsymbol{X} \in \boldsymbol{\Omega}$, and a background integration mesh is constructed, according to the numerical method selected by the user (the FEM, the RPIM, or the NNRPIM). Afterward, the initial material properties are allocated to the respective domain areas and the shape functions for each integration point $\boldsymbol{x}_I$ are constructed, $\varphi(\boldsymbol{x}_I)$, as previously explained. In addition, the essential and natural boundary conditions are imposed.

After this, to initiate the remodeling process, a preliminary elastostatic analysis of the problem is performed to determine the material orientation, by using the principal direction information at each integration point $\boldsymbol{x}_I$, by aligning the material constitutive matrix $\boldsymbol{c}$ with the principal direction $\boldsymbol{n}((\boldsymbol{x}_I)_1)$ of the corresponding maximum principal stress $\sigma(\boldsymbol{x}_I)_1$.

This book belongs to Central Library BADJI Mokhtar-ANNABA UNIVERSITY
Copyright Elsevier 2024

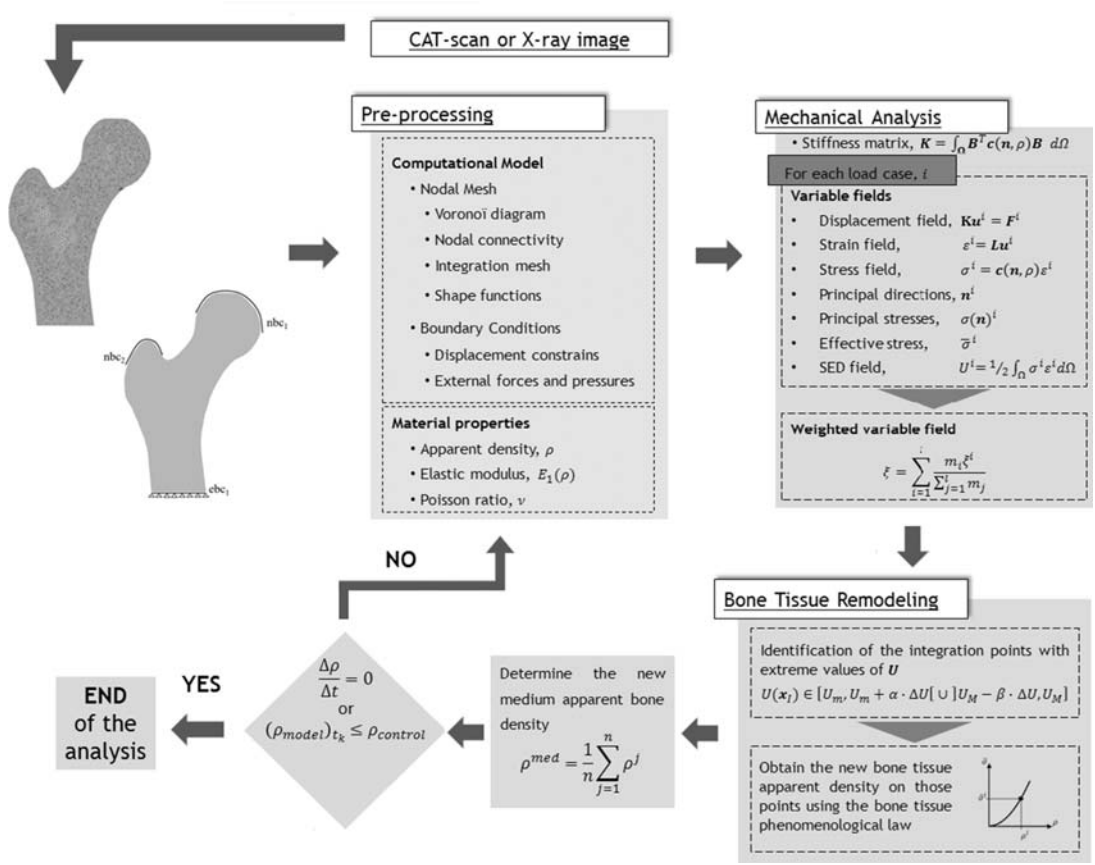

FIGURE 17.5 Proposed bone remodeling algorithm.

Only then, the iterative algorithm actually begins. Along the iterative process, a mechanical analysis is always performed at each time instant t_j. The local stiffness matrix, $\boldsymbol{K}_I$, at each integration point $\boldsymbol{x}_I$ is defined using the deformation matrix $\boldsymbol{B}_I$ and the constitutive material matrix $\boldsymbol{c}_I$. At the end of this process, all the local stiffness matrices $\boldsymbol{K}_I$ obtained are assembled, obtaining a global stiffness matrix, $\boldsymbol{K}$. Afterward, because the three numerical methods use the Galerkin weak form, the following equation system is obtained: $\boldsymbol{Ku} = \boldsymbol{f}$, being the unknown displacement field defined as $\boldsymbol{u}$ and the applied forces vector represented by $\boldsymbol{f}$. Having defined the displacement field, the strain, $\boldsymbol{\varepsilon}$, and the stress, $\boldsymbol{\sigma}$, fields are calculated as described previously. Then, the stress and strain fields can be used to determine the SED and the von Mises effective stress fields, as well as the principal stresses and directions. Because this algorithm allows to simultaneously consider various load cases $\boldsymbol{f}_j^k$, the process described up to this point is repeated for each load case. At the end, the variable fields obtained for each load case are weighted using the following expression:

$$\left\{\boldsymbol{u}_j, \boldsymbol{\varepsilon}_j, \boldsymbol{\sigma}_j, \boldsymbol{\sigma}(\boldsymbol{n})_j, \boldsymbol{n}_j, \overline{\boldsymbol{\sigma}}_j, \boldsymbol{U}_j\right\} = \sum_{k=1}^{l} \frac{m^{(k)}\left\{\boldsymbol{u}_j^{(k)}, \boldsymbol{\varepsilon}_j^{(k)}, \boldsymbol{\sigma}_j^{(k)}, \boldsymbol{\sigma}(\boldsymbol{n})_j^{(k)}, \boldsymbol{n}_j^{(k)}, \overline{\boldsymbol{\sigma}}_j^{(k)}, \boldsymbol{U}_j^{(k)}\right\}}{\sum_{s=1}^{l} m^{(s)}} \tag{17.42}$$

The variable fields weighted with Eq. (17.42) are the displacements, $\boldsymbol{u}_j^k$; the strains, $\boldsymbol{\varepsilon}_j^k$; the stresses, $\boldsymbol{\sigma}_j^k$; the principal stresses, $\boldsymbol{\sigma}(\boldsymbol{n})_j^k$; the principal directions, $\boldsymbol{n}_j^k$; the von Mises effective stresses, $\overline{\boldsymbol{\sigma}}_j^k$; and the SED, $\boldsymbol{U}_j^k$. As the expression indicates, the final weighted variable field of step j is obtained with the superposition of the number of relevant discrete load cases, l, weighted according to the corresponding number of load cycles, m.

Each mechanical analysis is followed by the bone tissue remodeling phase. Thus, the interest points belonging to the interval indicated in Eq. (17.40) are identified and subjected to a density remodeling process, whereas all the other interest points maintain the previous density.

Then, considering the weighted effective stress field, the interest points selected update their apparent density applying the phenomenological law. After establishing the new apparent density, the algorithm moves forward to the next iteration step.

This book belongs to Central Library BADJI Mokhtar-ANNABA UNIVERSITY
Copyright Elsevier 2024

Using the new apparent density field, the material properties are updated at each point of interest using again Eqs. (17.35) and (17.36). Afterward, the constitutive elasticity matrix, defined at each interest point, is rotated considering the principal directions obtained in the previous iteration step. This procedure permits to align iteratively the material properties with the actualized load path.

The process stops when the condition present in Eq. (17.41) is reached.

In conclusion, it is possible to state that the presented remodeling algorithm is a topology optimization-based model for bone adaptation because only a small fraction of bone material has its density updated each time. With this approach, the material's orientation is also continuously optimized.

17.4.4 Interpretation of the Results

The trabecular bone distribution for all numerical examples is represented using isomaps. Regarding the NNRPIM, this representation is accomplished using the subcells, represented in Fig. 17.3. For each of these subcells, it is possible to determine the volume porosity, $p(\boldsymbol{x}_J)$, at each integration point $\boldsymbol{x}_J$, using Eq. (17.43).

$$p(\boldsymbol{x}_J) = \frac{A_v}{A_j^{V_i}} \tag{17.43}$$

being A_v the area of the void in the subarea $A_j^{V_i}$ defined in Eq. (17.6).

Then, the local apparent density, $\rho(\boldsymbol{x}_J)$, can also be determined:

$$\rho(\boldsymbol{x}_J) = \rho_0(1 - p(\boldsymbol{x}_J)) \tag{17.44}$$

in which ρ_0 is the compact bone density, considered in this work as $\rho_0 = 2.1\ g/cm^3$. Thus, each integration point, $\boldsymbol{x}_J$, belonging to a certain Voronoï cell has a distinct local apparent density. Using Eq. (17.45), it is then possible to determine the local medium apparent density within each Voronoï cell V_i,

$$\rho(\boldsymbol{x}_i) = \frac{\sum_{J=1}^{k} \widehat{w}_J \cdot \rho(\boldsymbol{x}_J)}{\sum_{J=1}^{k} \widehat{w}_J} \tag{17.45}$$

where $\hat{w}_J$ is the integration weight of an integration point $\boldsymbol{x}_J$ belonging to the Voronoï cell V_i of the field node $\boldsymbol{x}_i$.

Now knowing the procedure, it becomes clear that the level of detail of the analysis can be enhanced by increasing the density of the nodal mesh discretizing the problem domain because it leads to smaller subdivisions. However, increasing the discretization level rises the computational cost of the analysis.

In regard to the FEM and the RPIM, this procedure is very similar because the local apparent density field is also obtained using Eq. (17.45). However, instead of using the Voronoï diagram, these methods employ the Gauss−Legendre quadrature scheme.

In this way, the results showing the evolution of the trabecular architecture are presented as gray tone isomaps, where the white color represents the maximum apparent density $\rho_0 = 2.1$ g/cm^3 and the dark-gray color represents the minimum apparent density $\rho_0 = 0.1$ g/cm^3 assumed in the analysis. The other gray tones in the middle represent transitional apparent densities, following a linear color grayscale gradient.

17.5 2D BONE PATCH ANALYSIS

17.5.1 Initial Conditions

In a first series of tests, the bone remodeling algorithm is applied to 2D bone micropatches, as the one presented in Fig. 17.6A. To validate the bone trabecular remodeling algorithm, a benchmark model is used. In this example, a compressive stress decreasing linearly from the top is applied and the nodal displacement is constrained in the x direction along the line $x = 0$ and on the axis' origin in both x and y directions. These natural and essential boundary conditions reveal a very specific trabecular morphology existent in long bones. In fact, trabecular bone, typically located at the proximal ends of long bones, has an arrangement relatively regular that reflects the direction of the principal mechanical stresses to which this kind of bone is being subjected. Fig. 17.6B and C display the boundary conditions and an available solution in literature for this benchmark example (Xinghua et al., 2002) obtained using the FEM. In all examples, a uniform apparent density distribution $\rho_{max} = 2.1$ g/cm^3 and Poisson ratio $\upsilon = 0.3$ are assumed, regardless of the material direction, assuming an isotropic behavior. The benchmark is analyzed using the numerical procedure described in previous sections,

This book belongs to Central Library BADJI Mokhtar-ANNABA UNIVERSITY Copyright Elsevier 2024

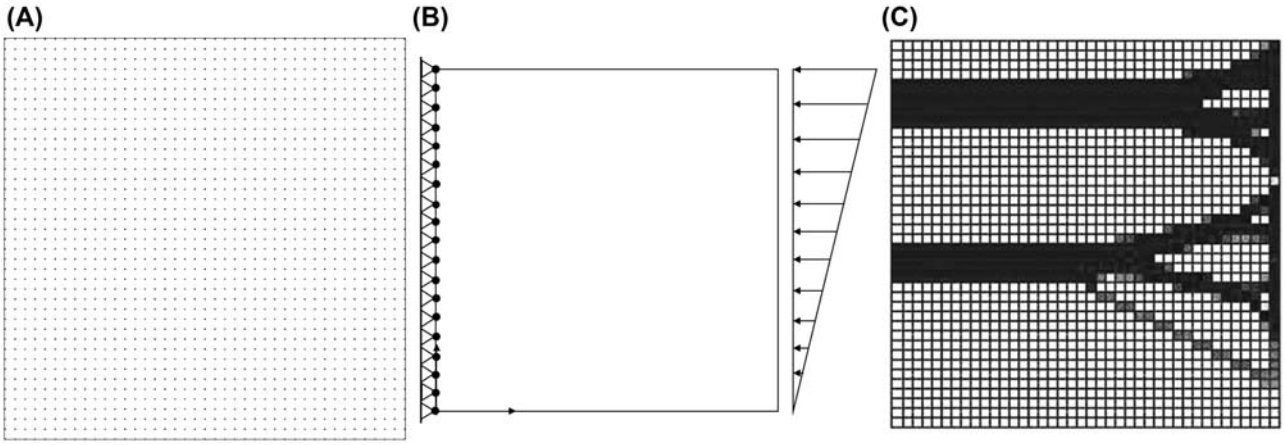

FIGURE 17.6 (A) Regular nodal distribution (1681 nodes). (B) Plate model geometry and essential and natural boundary conditions. (C) Benchmark example (Xinghua et al., 2002).

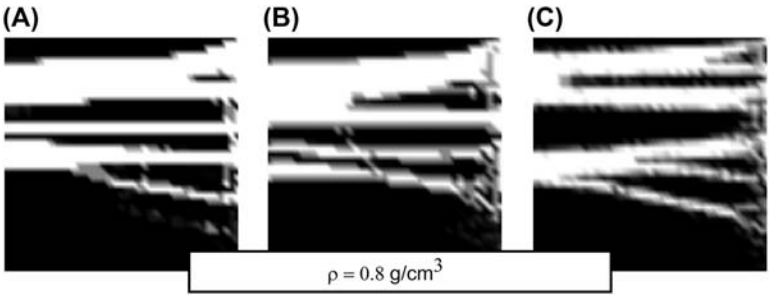

FIGURE 17.7 Trabecular morphology obtained with (A) the finite element method, (B) the radial point interpolation method, and (C) the natural neighbor radial point interpolation method.

using the FEM, the RPIM and the NNRPIM. The obtained results are shown and compared. The square patch is analyzed considering $\beta = 5\%$ and $\alpha = 0\%$.

17.5.2 Results and Discussion

The new bone remodeling algorithm has been applied successfully, as shown in Fig. 17.7. In all solutions, the topology is very similar to the one obtained earlier by Xinghua et al. (2002) and consistent with the physiological reality. These results prove that the remodeling algorithm is capable to describe bone's morphology adaptation to its mechanical environment. When comparing the different solutions, the NNRPIM's result presents a more gradual transition between bone and nonbone that is more similar to the real biological transition.

Because FEM is by far the most used method in problems of bone remodeling, the solution obtained using the FEM has been compared with each meshless solution. To validate the use of meshless methods, a comparison among them is performed by intersecting each pair of solutions. Fig. 17.8A displays the intersection of the FEM's and the RPIM's solutions, whereas Fig. 17.8B displays the intersection of the FEM's and the NNRPIM's solutions. The meshless solutions have also been compared and are represented by Fig. 17.8C.

In these figures, the white color indicates infinitesimal areas for which both compared techniques predict the formation of bone. The black color indicates infinitesimal areas for which both techniques predict contradictory results (for instances, one technique predicts the existence of bone while other techniques do not) or infinitesimal areas in which both methods predict the lack of bone tissue.

Because the exact location of the trabeculae differs from each method, the intersection does not lead to a perfect overlap of the solutions. Nevertheless, even with some missing parts, in every image, it is possible to detect that both compared techniques always predict the presence of two distinct trabeculae. Additionally, it is also possible to detect in each image, nonbone zones coherent for all methods. Thus, the use of meshless methods combined with this remodeling algorithm has been validated.

This book belongs to Central Library BADJI Mokhtar-ANNABA UNIVERSITY Copyright Elsevier 2024

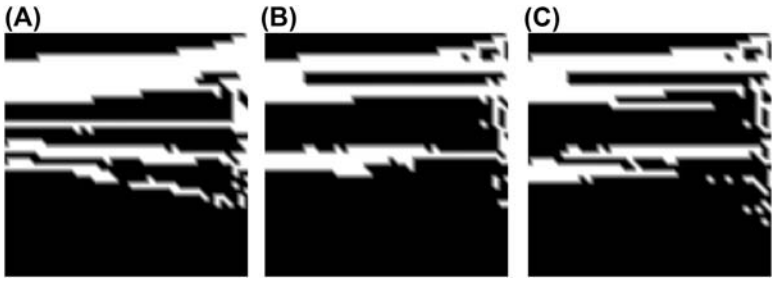

FIGURE 17.8 Intersection of each pair of solutions: (A) finite element method's (FEM's) and radial point interpolation method's (RPIM's) solutions, (B) FEM's and natural neighbor radial point interpolation method's (NNRPIM's) solutions, and (C) RPIM's and NNRPIM's solutions.

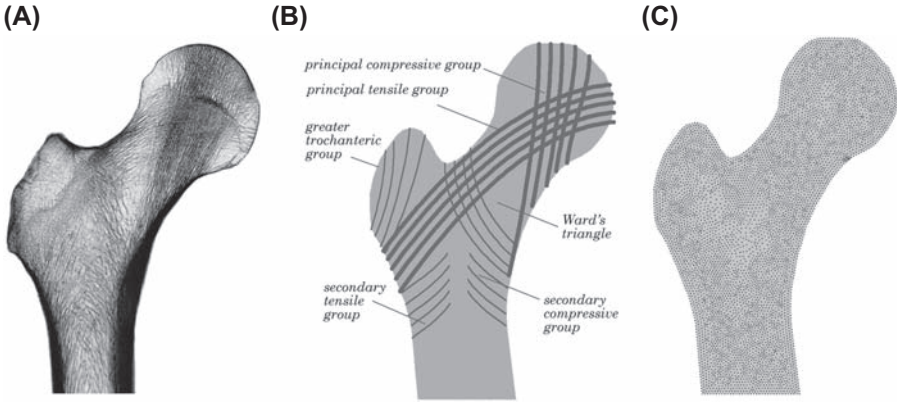

FIGURE 17.9 (A) Femoral X-ray plate. (B) Internal principal trabecular structures found in the femur bone. (C) Initial nodal distribution (5920 nodes).

17.6 2D FEMORAL ANALYSIS

The cross section of a femur is used to test the proposed algorithm. The use of the femur in these simulations is very advantageous because it is a very well-studied bone in biomechanics (Beaupré et al., 1990a,b; Doblaré and García-Aznar, 2002; Jacobs et al., 1997) and has a trabecular structure in the proximal portion relatively well oriented. Thus, using the femoral bone, the objective is to numerically obtain trabecular distributions resembling the real trabecular architecture observed in nature. Using X-ray images, such as the one depicted in Fig. 17.9A, it is possible to empirically obtain the principal compressive and tensile lines, as indicated in Fig. 17.9B, and to compare the obtained results.

17.6.1 Initial Conditions

To verify if the proposed model is able to reproduce the trabecular distribution featured in the femur, the geometry of a 2D proximal femur model is used, discretizing the domain with a nodal distribution, as represented in Fig. 17.9C. The 2D meshes are obtained from reconstructed computed tomography images.

The essential and natural boundary conditions for each test have been applied (Fig. 17.10). In this study, the three load cases proposed by Beaupré et al. (1990a,b) have been considered and adapted to the geometry of the model, decreasing in 10 degrees the angle of each load. Each one of these loads consists on one parabolic distributed load over the joint surface, nbc_1, and another parabolic distributed load on the trochanter, nbc_2, that represents the abductor muscle attachment. All degrees of freedom are constrained in the basis of the model, ebc_1.

This numerical example presents a uniform apparent density distribution $\rho_{max} = 2.1$ g/cm^3 and Poisson ratio $\upsilon = 0.3$, regardless of the material's direction. The bone tissue is assumed as isotropic, and the growth and decay rate of bone tissue are assumed as $\alpha = 0.0$ and $\beta = 0.01$.

Once again, the bone tissue remodeling algorithm described herein is combined with the FEM, the RPIM, and the NNRPIM, and the 2D discretized domain shown in Fig. 17.9C is analyzed. Firstly, each load case is considered separately, to understand the influence of each case. Then, to obtain a closer result to the real proximal femur X-ray plate (Fig. 17.9A),

This book belongs to Central Library BADJI Mokhtar-ANNABA UNIVERSITY Copyright Elsevier 2024

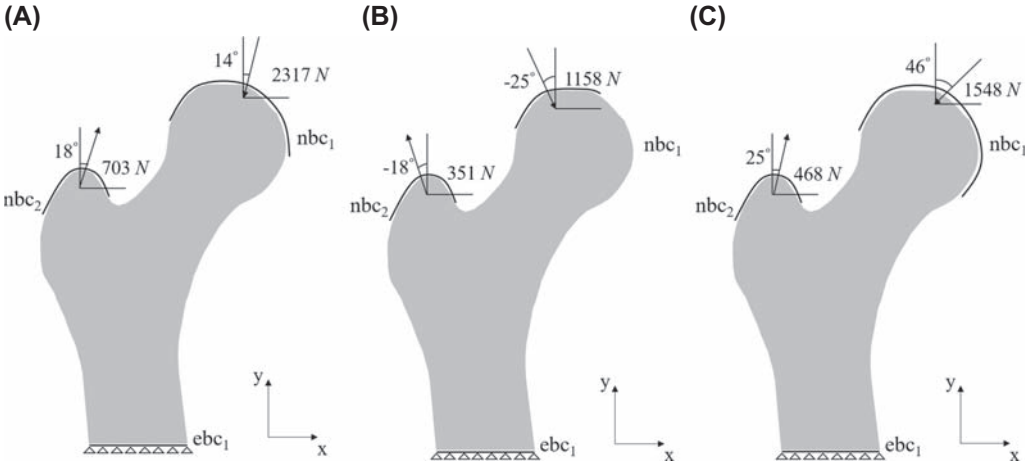

FIGURE 17.10 Loads and constraints of the various mechanical cases of the femur bone: (A) first mechanical case, (B) second mechanical case, and (C) third mechanical case.

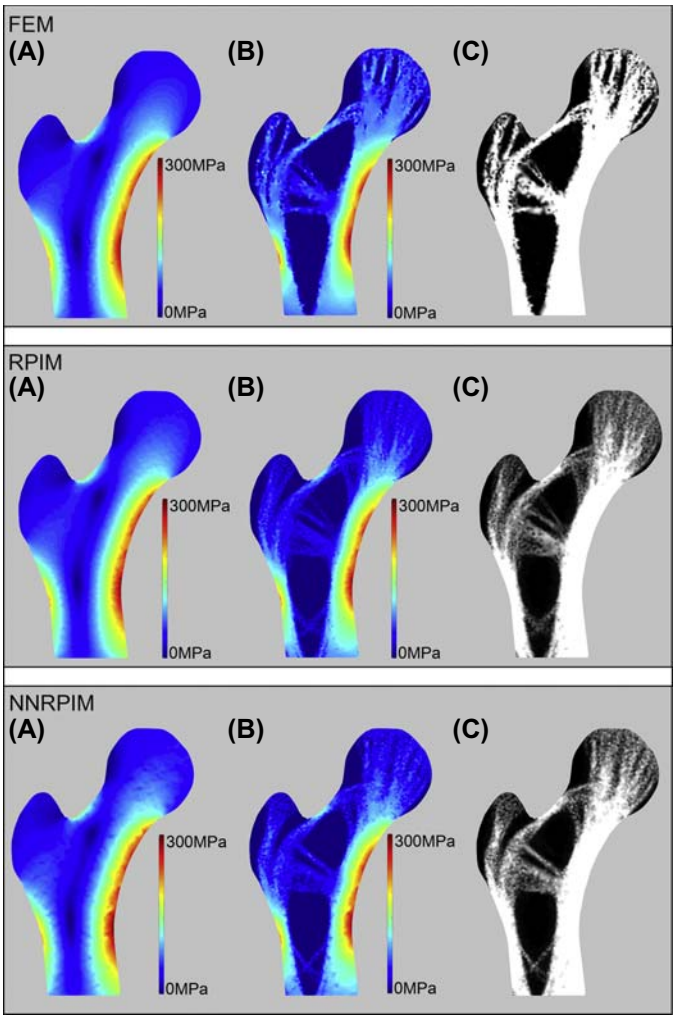

FIGURE 17.11 Combination of all mechanical cases for each numerical method: (A) Initial von Mises effective stress isomap, (B) final von Mises effective stress isomap, and (C) final obtained trabecular architecture. *FEM*, finite element method; *NNRPIM*, natural neighbor radial point interpolation method; *RPIM*, radial point interpolation method.

This book belongs to Central Library BADJI Mokhtar-ANNABA UNIVERSITY Copyright Elsevier 2024

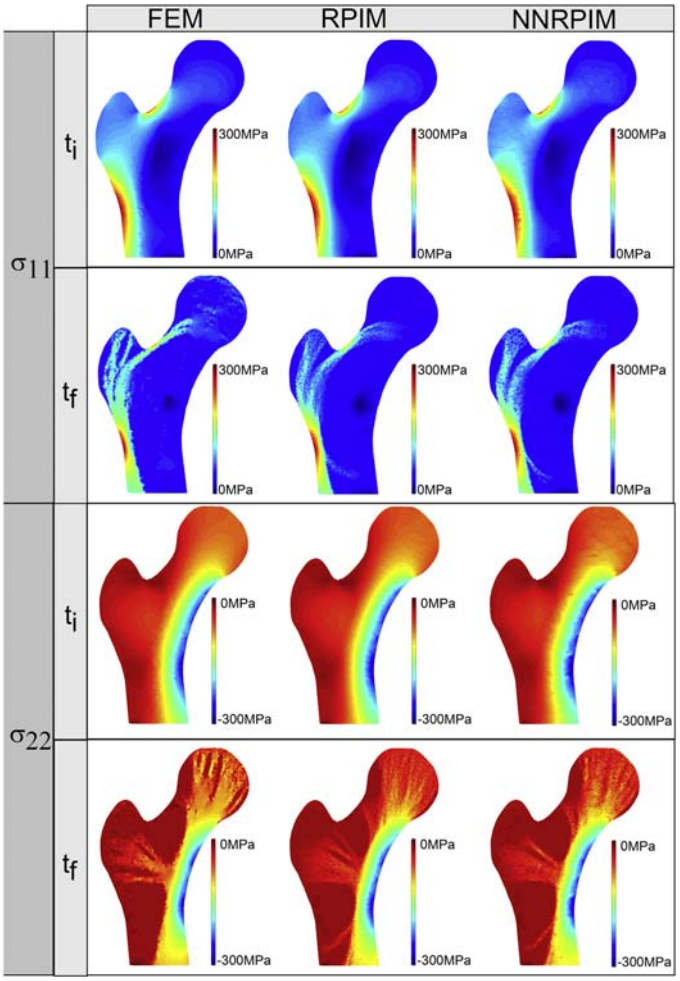

FIGURE 17.12 Principal stresses, σ_{11} and σ_{22}, isomaps for each numerical method (finite element method (FEM), radial point interpolation method (RPIM), and natural neighbor radial point interpolation method (NNRPIM)) at initial time step, t_i, and final time step, t_f.

all mechanical cases are applied simultaneously, assuming 6000 cycles per day for the first mechanical case and 2000 cycles per day for the second and third mechanical cases, as suggested in the literature (Beaupré et al., 1990a, 1990b).

17.6.2 Results and Discussion

Firstly, each one of the load cases has been independently analyzed. Only afterward, all mechanical cases have been simultaneously applied. The obtained results are shown in Figs. 17.11–17.13. In Fig. 17.11, for each numerical method, the von Mises effective stress isomap obtained for the first step of the iterative remodeling analysis, the final von Mises effective stress distribution obtained in the analysis, and the final trabecular architecture obtained in the analysis are presented. The final trabecular architecture is equivalent to a medium apparent density of 1.2 g/cm^3 for every numerical technique.

The simultaneous application of all mechanical cases results in a solution very close to the real proximal femur X-ray plate, being very perceptible the principal trabecular structures displayed in Fig. 17.9B. In all solutions, the presence of the principal compressive group, the principal tensile group, the greater trochanteric group, and the Ward's triangle were observed. Although not as distinct, the secondary trabecular structures can also be depicted but only in the meshless solutions.

Additionally, the principal stresses σ_{11} and σ_{22} have also been analyzed. In Fig. 17.12, for each numerical method, the principal stresses isomaps obtained for the first and the last steps of the iterative remodeling analysis are displayed. Observing the results, it is possible to conclude that isomap of σ_{11} reveals the trabeculae resultant from the tensile load

This book belongs to Central Library BADJI Mokhtar-ANNABA UNIVERSITY Copyright Elsevier 2024

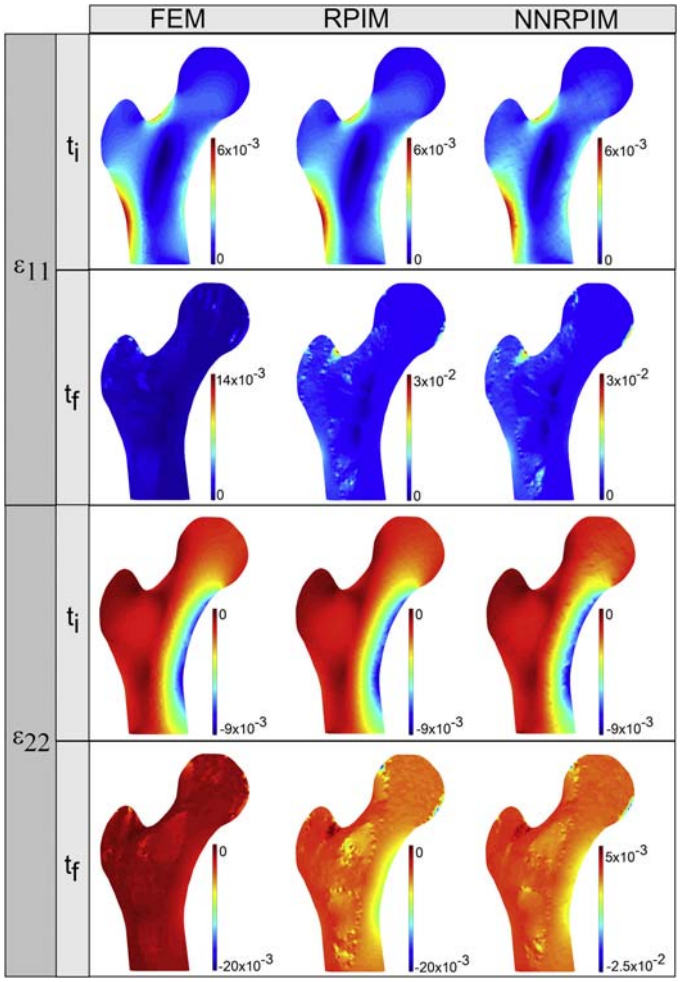

FIGURE 17.13 Principal strains, ε_{11} and ε_{22}, isomaps for each numerical method (finite element method (FEM), radial point interpolation method (RPIM), and natural neighbor radial point interpolation method (NNRPIM)) at initial time step, t_i, and final time step, t_f.

applied in the trochanter that corresponds to the abductor muscle attachment, whereas the isomap of σ_{22} allows the detection of the trabeculae resultant from the compressive load applied at the femur head.

In Fig. 17.13, the principal strains, ε_{11} and ε_{22}, isomaps again for the initial and final steps of the algorithm are depicted. As can be interpreted from the results, higher deformations occur in areas that undergo through bone resorption and lead to void zones in the end.

Regarding the numerical approaches, the remodeling algorithm is capable to reproduce the trabecular distribution observed in the femur bone for all numerical methods, producing coherent results between each other. Overall, it is visible that meshless results are considerably smoother, not having the crosshatch look typical of the FEM results. In addition, the FEM is the only method that cannot reproduce the secondary trabecular structures.

17.6.3 Conclusions

In this work, a new bone remodeling algorithm, based on Belinha's model, has been further developed and discussed. Results support the use of this algorithm to reproduce the trabecular distribution observed in real proximal femur. Additionally, the use of numerical meshless methods has been validated and the comparison among the three numerical methods allowed interesting observations. The meshless solutions are smoother and more accurate, being capable to reproduce some secondary trabecular structures that FEM cannot predict. Comparing the RPIM's and the NNRPIM's solutions, in the femoral analysis, results do not greatly differ. However, in the bone patch analysis, NNRPIM's solution is more accurate, presenting more gradual transitions. As future work, it is expected to integrate this model into a

This book belongs to Central Library BADJI Mokhtar-ANNABA UNIVERSITY Copyright Elsevier 2024

mechanobiological model, which will allow to test the interaction of bone cells, not only within mechanical environments but also within chemical and biological mediums.

ACKNOWLEDGMENTS

The authors truly acknowledge the funding provided by Ministério da Ciência, Tecnologia e Ensino Superior—Fundação para a Ciência e a Tecnologia (Portugal), under grant SFRH/BPD/111020/2015, and by project funding UID/EMS/50022/2013 (funding provided by the inter-institutional projects from LAETA). Additionally, the authors gratefully acknowledge the funding of Project NORTE-01-0145-FEDER-000022—SciTech—Science and Technology for Competitive and Sustainable Industries, cofinanced by Programa Operacional Regional do Norte (NORTE2020), through Fundo Europeu de Desenvolvimento Regional (FEDER).

REFERENCES

Atluri, S.N., Zhu, T., 1998. A new meshless local Petrov-Galerkin (MLPG) approach in computational mechanics. Computational Mechanics 22, 117−127.

Beaupré, G.S., Orr, T.E., Carter, D.R., 1990a. An approach for time-dependent bone modeling and remodeling. Theoretical development. Journal of Orthopaedic Research 8, 651−661.

Beaupré, G.S., Orr, T.E., Carter, D.R., 1990b. An approach for time-dependent bone modeling and remodeling-application: a preliminary remodeling simulation. Journal of Orthopaedic Research 8, 662−670.

Belinha, J., 2014. Meshless Methods in Biomechanics − Bone Tissue Remodelling Analysis. Springer International Publishing, Switzerland.

Belinha, J., Araújo, A.L., Ferreira, A.J.M., Dinis, L.M.J.S., Jorge, R.M.N., 2016a. The analysis of laminated plates using distinct advanced discretization meshless techniques. Composite Structures 143, 165−179.

Belinha, J., Azevedo, J.M.C., Dinis, L.M.J.S., Jorge, R.M.N., 2016b. The natural neighbor radial point interpolation method extended to the crack growth simulation. International Journal of Applied Mechanics 8, 1650006.

Belinha, J., Dinis, L.M.J.S., Jorge, R.M.N., 2013a. Composite laminated plate analysis using the natural radial element method. Composite Structures 103, 50−67.

Belinha, J., Dinis, L.M.J.S., Jorge, R.M.N., 2013b. Analysis of thick plates by the natural radial element method. International Journal of Mechanical Sciences 76, 33−48.

Belinha, J., Dinis, L.M.J.S., Jorge, R.M.N., 2013c. The natural radial element method. International Journal for Numerical Methods in Engineering 93, 1286−1313.

Belinha, J., Dinis, L.M.J.S., Jorge, R.M.N., 2014. The bone tissue remodelling analysis in dentistry using a meshless method. In: Proceedings of the III International Conference on Biodental Engineering. Taylor & Francis Group, Porto, pp. 213−220.

Belinha, J., Dinis, L.M.J.S., Jorge, R.M.N., 2015a. The analysis of the bone remodelling around femoral stems: a meshless approach. Mathematics and Computers in Simulation 121, 64−94.

Belinha, J., Dinis, L.M.J.S., Jorge, R.M.N., 2015b. The meshless methods in the bone tissue remodelling analysis. Procedia Engineering 110, 51−58.

Belinha, J., Dinis, L.M.J.S., Natal Jorge, R.M., 2015c. The mandible remodelling induced by dental implants: a meshless approach. Journal of Mechanics in Medicine and Biology 15, 1550059.

Belinha, J., Jorge, R.M.N., Dinis, L.M.J.S., 2012a. A meshless microscale bone tissue trabecular remodelling analysis considering a new anisotropic bone tissue material law. Computer Methods in Biomechanics and Biomedical Engineering 16, 1−15.

Belinha, J., Jorge, R.M.N., Dinis, L.M.J.S., 2012b. Bone tissue remodelling analysis considering a radial point interpolator meshless method. Engineering Analysis with Boundary Elements 36, 1660−1670.

Belytschko, T., Gu, L., Lu, Y.Y., 1994. Fracture and crack growth by element free Galerkin methods. Modelling and Simulation in Materials Science and Engineering 2, 519−534.

Carter, D.R., Fyhrie, D.P., Whalen, R.T., 1987. Trabecular bone density and loading history: regulation of connective tissue biology by mechanical energy. Journal of Biomechanics 20, 785−794.

Carter, D.R., Orr, T.E., Fyhrie, D.P., 1989. Relationships between loading history and femoral cancellous bone architecture. Journal of Biomechanics 22, 231−244.

Chao, T.Y., Chow, W.K., Kong, H., 2002. A review on the applications of finite element method to heat transfer and fluid flow. International Journal on Architectural Science 3, 1−19.

Compston, J.E., 2001. Sex steroids and bone. Physiological Reviews 81, 419−447.

Courant, R., 1943. Variational methods for the solution of problems of equilibrium and vibrations. Bulletin of the American Mathematical Society 49, 1−23.

Cowin, S.C., Hegedus, D.H., 1976. Bone remodeling I: theory of adaptive elasticity. Journal of Elasticity 6, 313−326.

Cowin, S.C., Nachlinger, R.R., 1978. Bone remodeling III: uniqueness and stability in adaptive elasticity theory. Journal of Elasticity 8, 285−295.

Cowin, S.C., Sadegh, A.M., Luo, G.M., 1992. An evolutionary Wolff's law for trabecular architecture. Journal of Biomechanical Engineering 114, 129−136.

Dinis, L.M.J.S., Jorge, R.M.N., Belinha, J., 2007. Analysis of 3D solids using the natural neighbour radial point interpolation method. Computer Methods in Applied Mechanics and Engineering 196, 2009−2028.

This book belongs to Central Library BADJI Mokhtar-ANNABA UNIVERSITY Copyright Elsevier 2024

Dinis, L.M.J.S., Jorge, R.M.N., Belinha, J., 2008. Analysis of plates and laminates using the natural neighbour radial point interpolation method. Engineering Analysis with Boundary Elements 32, 267–279.

Dinis, L.M.J.S., Jorge, R.M.N., Belinha, J., 2009a. The natural neighbour radial point interpolation method: dynamic applications. Engineering with Computers 26, 911–949.

Dinis, L.M.J.S., Jorge, R.M.N., Belinha, J., 2009b. Large deformation applications with the radial natural neighbours interpolators. Computer Modeling in Engineering and Sciences 44, 1–34.

Dinis, L.M.J.S., Jorge, R.M.N., Belinha, J., 2010a. An unconstrained third-order plate theory applied to functionally graded plates using a meshless method. Mechanics of Advanced Materials and Structures 17, 108–133.

Dinis, L.M.J.S., Jorge, R.M.N., Belinha, J., 2010b. Composite laminated plates: a 3D natural neighbor radial point interpolation method approach. Journal of Sandwich Structures and Materials 12, 119–138.

Dinis, L.M.J.S., Jorge, R.M.N., Belinha, J., 2010c. A 3D shell-like approach using a natural neighbour meshless method: isotropic and orthotropic thin structures. Composite Structures 92, 1132–1142.

Dinis, L.M.J.S., Jorge, R.M.N., Belinha, J., 2011a. A natural neighbour meshless method with a 3D shell-like approach in the dynamic analysis of thin 3D structures. Thin-Walled Structures 49, 185–196.

Dinis, L.M.J.S., Jorge, R.M.N., Belinha, J., 2011b. Static and dynamic analysis of laminated plates based on an unconstrained third order theory and using a radial point interpolator meshless method. Computer and Structures 89, 1771–1784.

Doblaré, M., García-Aznar, J.M., 2002. Anisotropic bone remodelling model based on a continuum damage-repair theory. Journal of Biomechanics 35, 1–17.

Doblaré, M., García-Aznar, J.M., 2010. Modelling living tissues: mechanical and mechanobiological aspects. In: Fitt, A.D., Norbury, J., Ockendon, H., Wilson, E. (Eds.), Progress in Industrial Mathematics at ECMI 2008. Springer, pp. 3–8.

Duarte, H.M.S., Andrade, J.R., Dinis, L.M.J.S., Jorge, R.M.N., Belinha, J., 2016. Numerical analysis of dental implants using a new advanced discretization technique. Mechanics of Advanced Materials and Structures 23, 467–479.

Golberg, M.A., Chen, C.S., Bowman, H., 1999. Some recent results and proposals for the use of radial basis functions in the BEM. Engineering Analysis with Boundary Elements 23, 285–296.

Gu, Y.T., Liu, G.R., 2001. A local point interpolation method for static and dynamic analysis of thin beams. Computer Methods in Applied Mechanics and Engineering 190, 5515–5528.

Hardy, R.L., 1990. Theory and applications of the multiquadric-biharmonic method 20 years of discovery 1968–1988. Computers and Mathematics with Applications 19, 163–208.

Heckbert, P.S., 1993. Introduction to finite element methods. In: Global Illumination Course Notes, SIGGRAPH 93. Anaheim, pp. 1–10.

Hegedus, D.H., Cowin, S.C., 1976. Bone remodeling II: small strain adaptive elasticity. Journal of Elasticity 6, 337–352.

Hofbauer, L.C., Kühne, C.A., Viereck, V., 2004. The OPG/RANKL/RANK system in metabolic bone diseases. Journal of Musculoskeletal and Neuronal Interactions 4, 268–275.

Hrennikoff, A., 1941. Solution of problems in elasticity by the frame work method. Journal of Applied Mechanics 8, 169–175.

Huiskes, R., Chao, E.Y., 1983. A survey of finite element analysis in orthopedic biomechanics: the first decade. Journal of Biomechanics 16, 385–409.

Huiskes, R., Hollister, S.J., 1993. From structure to process, from organ to cell: recent developments of FE-analysis in orthopaedic biomechanics. Journal of Biomechanical Engineering 115, 520–527.

Huiskes, R., Weinans, H., Grootenboer, H.J., Dalstra, M., Fudala, B., Slooff, T.J., 1987. Adaptive bone-remodeling theory applied to prosthetic-design analysis. Journal of Biomechanics 20, 1135–1150.

Jacobs, C.R., Simo, J.C., Beaupre, G.S., Carter, D.R., 1997. Adaptive bone remodeling incorporating simultaneous density and anisotropy considerations. Journal of Biomechanics 30, 603–613.

Krach, W., Rammerstorfer, F.G., Reiter, T.J., Zenz, P., 1995. In Vivo CT-based 3D-modelling of Human Bones with Respect to Inhomogeneity. American Society of Mechanical Engineers, Bioengineering Division (Publication) BED. ASME, pp. 57–58.

Lerner, U.H., 2006. Bone remodeling in post-menopausal osteoporosis. Journal of Dental Research 85, 584–595.

Liu, G.R., Gu, Y.T., 2001. A local radial point interpolation method (LRPIM) for free vibration analyses of 2-D solids. Journal of Sound and Vibration 246, 29–46.

Liu, G.R., Yan, L., Wang, J.G., Gu, Y.T., 2002. Point interpolation method based on local residual formulation using radial basis functions. Structural Engineering and Mechanics 14, 713–732.

Liu, G.R., Zhang, G.Y., Gu, Y.T., Wang, Y.Y., 2005. A meshfree radial point interpolation method (RPIM) for three-dimensional solids. Computational Mechanics 36, 421–430.

Liu, W.K., Jun, S., Zhang, Y.F., 1995. Reproducing kernel particle methods. International Journal for Numerical Methods in Fluids 20, 1081–1106.

Logan, D.L., Veitch, E., Carson, C., Burrell, K.R., Gould, V., Wagner, E., 2007. A First Course in the Finite Element Method, fourth ed. (Transport).

Lotz, J.C., Gerhart, T.N., Hayes, W.C., 1991. Mechanical properties of metaphyseal bone in the proximal femur. Journal of Biomechanics 24, 317–329.

McHenry, D., 1943. A lattice analogy for the solution of plane stress problems. Journal of the Institution of Civil Engineers 21, 59–82.

Moreira, S., Belinha, J., Dinis, L.M.J.S., Jorge, R.M.N., 2014a. Análise de vigas laminadas utilizando o natural neighbour radial point interpolation method. Revista Internacional de Métodos Numéricos para Cálculo y Diseño en Ingenieria 30, 108–120.

Moreira, S., Belinha, J., Dinis, L.M.J.S., Jorge, R.M.N., 2014b. A global numerical analysis of the "central incisor/local maxillary bone" system using a meshless method. Molecular and Cellular Biomechanics 11, 151–184.

Nayroles, B., Touzot, G., Villon, P., 1992. Generalizing the finite element method: diffuse approximation and diffuse elements. Computational Mechanics 10, 307–318.

This book belongs to Central Library BADJI Mokhtar-ANNABA UNIVERSITY Copyright Elsevier 2024

Pettermann, H.E., Reiter, T.J., Rammerstorfer, F.G., 1997. Computational simulation of internal bone remodeling. Archives of Computational Methods in Engineering 4, 295–323.

Reiter, T.J., Bohm, H.J., Krach, W., Pleschberger, M., Rammerstorfer, F.G., 1994. Some applications of the finite-element method in biomechanical stress analyses. International Journal of Computer Applications in Technology 7, 233–241.

Reiter, T.J., Rammerstorfer, F.G., Bohm, H.J., 1990. In: American Society of Mechanical Engineers, Bioengineering Division (Publication) BED (Ed.), Numerical Algorithm for the Simulation of Bone Remodeling. ASME, pp. 181–184.

Robling, A.G., Castillo, A.B., Turner, C.H., 2006. Biomechanical and molecular regulation of bone remodeling. Annual Review of Biomedical Engineering 8, 455–498.

Rossi, J.-M., Wendling-Mansuy, S., 2007. A topology optimization based model of bone adaptation. Computer Methods in Biomechanics and Biomedical Engineering 10, 419–427.

Sibson, R., 1981. A brief description of natural neighbour interpolation. In: Interpreting Multivariate Data. Wiley, Chichester, pp. 21–36.

Tavares, C.S.S., Belinha, J., Dinis, L.M.J.S., Jorge, R.M.N., 2015. The elasto-plastic response of the bone tissue due to the insertion of dental implants. Procedia Engineering 110, 37–44.

Wang, J.G., Liu, G.R., 2002a. A point interpolation meshless method based on radial basis functions. International Journal for Numerical Methods in Engineering 54, 1623–1648.

Wang, J.G., Liu, G.R., 2002b. On the optimal shape parameters of radial basis functions used for 2-D meshless methods. Computer Methods in Applied Mechanics and Engineering 191, 2611–2630.

Weinans, H., Huiskes, R., Grootenboer, H.J., 1992. The behavior of adaptive bone-remodeling simulation models. Journal of Biomechanics 25, 1425–1441.

Whalen, R.T., Carter, D.R., Steele, C.R., 1988. Influence of physical activity on the regulation of bone density. Journal of Biomechanics 21, 825–837.

Wirtz, D.C., Schiffers, N., Pandorf, T., Radermacher, K., Weichert, D., Forst, R., 2000. Critical evaluation of known bone material properties to realize anisotropic FE-simulation of the proximal femur. Journal of Biomechanics 33, 1325–1330.

Xinghua, Z., He, G., Dong, Z., Bingzhao, G., 2002. A study of the effect of non-linearities in the equation of bone remodeling. Journal of Biomechanics 35, 951–960.

Zienkiewicz, O.C., Taylor, R.L., Zhu, J.Z., 2013. Finite Element Method ;: Its Basis and Fundamentals, seventh ed. Butterworth-Heinemann, Oxford, UK.

Zioupos, P., Cook, R.B., Hutchinson, J.R., 2008. Some basic relationships between density values in cancellous and cortical bone. Journal of Biomechanics 41, 1961–1968.

This book belongs to Central Library BADJI Mokhtar-ANNABA UNIVERSITY

Copyright Elsevier 2024

This page intentionally left blank

This book belongs to Central Library BADJI Mokhtar-ANNABA UNIVERSITY

Copyright Elsevier 2024

Chapter 18

Strong- and Weak-Form Meshless Methods in Computational Biomechanics

G.C. Bourantas[1], G.R. Joldes[1,2], A. Wittek[1] and K. Miller[1,3]

[1]*The University of Western Australia, Perth, WA, Australia;* [2]*Murdoch University, Perth, WA, Australia;* [3]*Cardiff University, Cardiff, United Kingdom*

18.1 INTRODUCTION

Personalized treatment planning that takes into account individual characteristics of each patient is becoming a reality. Magnetic resonance (MRI) and computed tomography (CT) images acquired before surgery are now routinely used in planning of neurosurgery and other therapies. In recent years, computational biomechanics models that can predict organ deformations during surgery have been recognized as an emerging technology that can augment the image-based methods and further improve the accuracy of image-guided therapy. This requires patient-specific models that represent a given patient rather than generic models that focus on understanding of biomechanical phenomena in a human (or animal) organism. The transition from generic biomechanical models to the ones that represent an individual is one of the key challenges in modern biomechanics.

The success of this transition relies on our ability to create patient-specific (i.e., representing a given patient) biomechanical models from medical images in a manner and within a time frame compatible with a clinical workflow. This eliminates approaches that require large computational power, long calculations, and specialized knowledge of numerical methods of computational biomechanics to operate (as hospitals are unlikely to hire PhDs in computational mechanics).

At the moment, numerical simulations in biomechanics are dominated by mesh-based methods. Although they have been proven to be accurate and robust, especially in cases where a high-quality mesh (a mesh that resolves the underlying physics) is generated, their efficiency and accuracy drastically decreases when a low-quality mesh is used. Unfortunately, generation of a high-quality mesh remains a challenge and tends to involve a tedious and time-consuming process, especially for the irregular geometries such as the human body organs. Mesh generation is the bottleneck of the entire simulation. Although many automated 3D mesh generators are available, they exhibit important limitations in patient-specific biomechanical applications where hexahedral meshes, which do not exhibit volumetric locking for incompressible materials, such as soft tissues, are often the computational grid of choice, and the information about geometry of analyzed continuum (human body organs) needs to be obtained directly from pixelated images rather than computer-aided design data taken for granted in most engineering applications.

The drawbacks of the mesh-based methods in biomechanical applications can be eliminated by a numerical method that does not require a computational grid, in a form of a mesh of interconnected elements conforming to geometry of the analyzed continuum, and can facilitate generation of a computational grid/model directly from medical images. These requirements are satisfied by meshless methods (MMs) that utilize a cloud of points/nodes as a computational grid. The first collocation methods can be considered as the earliest developed MMs (Slater, 1934; Frazer et al., 1937; Lanczos, 1938). MMs can be considered as extensions of vortex methods, finite differences, and generalized finite difference (GFD) methods to irregular point clouds. Overall, there has been less research devoted to strong-form MMs. This may be partly because the strong-form MMs were believed to be less robust than the methods based on the weak form and research was concentrated on the finite element method (FEM) that used weak forms; it was then a natural step to weak-form MMs.

Numerical Methods and Advanced Simulation in Biomechanics and Biological Processes. https://doi.org/10.1016/B978-0-12-811718-7.00018-6
Copyright © 2018 Elsevier Ltd. All rights reserved.

This book belongs to Central Library BADJI Mokhtar-ANNABA UNIVERSITY

Copyright Elsevier 2024

From the early 1990s, there has been an increase in research devoted to weak-form MMs, and many new MMs have been developed. Examples are the diffuse element method (DEM) (Nayroles et al., 1992), the element-free Galerkin (EFG) method (Belytschko et al., 1994), the reproducing kernel particle method (RKPM) (Liu et al., 1995), the point interpolation methods (Liu and Gu, 2001a,b), and the meshless local Petrov−Galerkin (MLPG) method (Atluri and Zhu, 1998). Weak-form methods do not require a mesh for constructing the field variable approximations/interpolations. Shape functions and spatial derivatives are computed by using a set of arbitrary nodes, and there is no need for any kind of predefined information on node connectivity. On the other hand, a background mesh is necessary for integration to solve the governing equations. Adaptive analyses and simulations using MMs become very efficient and much easier to implement, even for problems that pose difficulties for the traditional FEM.

We will describe the application of MMs in patient-specific biomechanics, and we will discuss the strengths and shortcoming of MMs in their weak and strong formulations. This will address an important gap in the literature, as MMs relying on weak formulation have attracted so far more attention than the methods using a strong formulation.

18.2 MESHLESS INTERPOLATION SCHEMES

There are a handful of meshless approximating/interpolating methods. Among them we can find moving least squares (MLS) (Lancaster and Salkauskas, 1981), interpolating moving least squares (Netuzhylov and Zilian, 2009), radial basis functions (RBFs) (Fasshauer, 2007) in their local and global formulation, GFDs (Liszka and Orkisz, 1980), radial basis function−finite differences (Fornberg et al., 2013), and discretization corrected particle strength exchange (DC PSE) (Bourantas et al., 2016). Because of their interpolating properties and flexibility, facilitating operation for any kind of nodal distribution (in technical terms, the Vandermonde matrix involved in the shape functions computation is always invertible, with low condition number), MLS and RBF have been methods of choice in many applications.

In this section we will describe two newly developed meshless schemes that can be used in both weak and strong formulations: the modified moving least squares (MMLS) and the DC PSE method.

18.2.1 Modified Moving Least Squares

MMLS is a newly developed meshless approximation scheme (Joldes et al., 2015). Consider a set of N nodes scattered in the domain Ω and $\boldsymbol{x}_i$ the coordinates of node i. The function $u(\boldsymbol{x})$ around a point $\boldsymbol{x}$ is locally approximated by the function $u^h(\boldsymbol{x})$, which can be expressed as

$$u^h(\boldsymbol{x}) = \sum_{i=1}^{m} p_i(\boldsymbol{x}) a_i(\boldsymbol{x}) = \boldsymbol{p}^T(\boldsymbol{x})\boldsymbol{a}(\boldsymbol{x}), \tag{18.1}$$

where m is the number of terms in the basis, $\boldsymbol{p}(\boldsymbol{x})$ is a polynomial basis in the space coordinates that consists of monomials of the lowest order to ensure completeness (herein we consider a second order polynomial, thus $m = 6$ in 2D and $m = 10$ in 3D) and $a_i(\boldsymbol{x})$ are constants that, as indicated, are functions of the spatial coordinates $\boldsymbol{x}$. Because of the local nature of the approximation, the polynomial basis can be written as

$$\boldsymbol{p}^T(\boldsymbol{x}-\boldsymbol{x}_i) = \left[1, (x-x_i), (y-y_i), (x-x_i)^2, (x-x_i)(y-y_i), (y-y_i)^2\right], \tag{18.2}$$

in 2D and

$$\boldsymbol{p}^T(\boldsymbol{x}-\boldsymbol{x}_i) = \left[1, (x-x_i), (y-y_i), (z-z_i), (x-x_i)^2, (y-y_i)^2, (z-z_i)^2, (x-x_i)(y-y_i), (x-x_i)(y-y_i), (y-y_i)(z-z_i)\right] \tag{18.3}$$

in 3D.

The coefficients $a_i(\boldsymbol{x})$ are obtained by performing a weighted least square fit for the local approximation, which is obtained by minimizing the difference between the local approximation and the function. The fit of function $u(\boldsymbol{x})$ to the data values $u_1, u_2, \ldots, u_N$ can be evaluated by means of the error functional $\boldsymbol{J}(\boldsymbol{x})$ given as

$$\boldsymbol{J}^{MMLS}(\boldsymbol{x}) = \sum_{j=1}^{n}\left[\left(u^h(x_j)-u_j\right)^2 w(\|\boldsymbol{x}-\boldsymbol{x}_j\|)\right] + \mu_{x^2}a_{x^2}^2 + \mu_{xy}a_{xy}^2 + \mu_{y^2}a_{y^2}^2 \tag{18.4}$$

where

$$\boldsymbol{\mu} = \begin{bmatrix}\mu_{x^2} & \mu_{xy} & \mu_{y^2}\end{bmatrix} \tag{18.5}$$

This book belongs to Central Library BADJI Mokhtar-ANNABA UNIVERSITY
Copyright Elsevier 2024

is a vector of positive weights for the additional constraints and $w(||\boldsymbol{x}-\boldsymbol{x}_j||)$ is a weighting function with compact support. The weight function depends not only on data points $\boldsymbol{x}_j$; they are also functions of $\boldsymbol{x}$, the location in the spatial domain Ω where a fit is required. The weight functions have relatively large values for points $\boldsymbol{x}_j$ close to $\boldsymbol{x}$ and relatively small for the more distant points $\boldsymbol{x}_j$. The following choice of the weight function was used here

$$w(\|\boldsymbol{x}-\boldsymbol{x}_j\|) = w(d_j) = \begin{cases} e^{-\left(\frac{d_j}{a_0 h}\right)^2} & \text{inside support domain} \\ 0 & \text{outside support domain} \end{cases} \tag{18.6}$$

where $j = 1, 2, 3, \ldots, n$ are the nodes included in the support domain of node $\boldsymbol{x}_j$, $d_i = ||\boldsymbol{x}-\boldsymbol{x}_j||$ and a_0 is a prescribed constant, defined as a fraction of the radius of the support domain h. The value of a_0 has to be predefined, usually with the help of numerical experiments for the same class of problems where solutions already exist. A value between 0.2 and 0.3 gives satisfactory approximation of the field function. The value $a_0 = 0.2$ was used here, which was found to reproduce with excellent accuracy verified numerical solutions of benchmark problems. The choice of the additional constraints in the error functional ensures that when the classical MLS moment matrix is singular (multiple solutions), we obtain the solution having the coefficients for the higher order monomials in the bases equal to zero. By choosing the additional weights as small positive numbers we can ensure that the classical MLS solution is altered only very slightly when the moment matrix is not singular.

Eq. (18.4) can be rewritten in the form

$$\boldsymbol{J}^{MMLS} = (\boldsymbol{P}\boldsymbol{a}-\boldsymbol{u})^T\boldsymbol{W}(\boldsymbol{P}\boldsymbol{a}-\boldsymbol{u}) + \boldsymbol{a}^T\boldsymbol{H}\boldsymbol{a}, \tag{18.7}$$

where $\boldsymbol{H}$ is a matrix with all elements equal to zero except the last three diagonal entries, which are equal to $\boldsymbol{\mu}$:

$$\boldsymbol{H} = \begin{bmatrix} \boldsymbol{0}_{33} & \boldsymbol{0}_{33} \\ \boldsymbol{0}_{33} & diag(\boldsymbol{\mu}) \end{bmatrix} \tag{18.8}$$

and

$$\boldsymbol{u}^T = (u_1, u_2, \ldots, u_n) \tag{18.9}$$

$$\boldsymbol{P} = \begin{bmatrix} \boldsymbol{p}^T(\boldsymbol{x}_1) \\ \ldots \\ \boldsymbol{p}^T(\boldsymbol{x}_n) \end{bmatrix} \tag{18.10}$$

$$\boldsymbol{P}^T(\boldsymbol{x}_j) = (p_1(\boldsymbol{x}_j), \ldots, p_m(\boldsymbol{x}_j)) \tag{18.11}$$

$$\boldsymbol{W} = diag(w(\boldsymbol{x}-\boldsymbol{x}_1), \ldots, w(\boldsymbol{x}-\boldsymbol{x}_n)) \tag{18.12}$$

To compute the coefficients $\boldsymbol{a}(\boldsymbol{x})$, we minimize function $\boldsymbol{J}$ with respect of coefficients $\boldsymbol{a}(\boldsymbol{x})$

$$\frac{\partial \boldsymbol{J}^{MMLS}}{\partial \boldsymbol{a}} = [\boldsymbol{P}^T\boldsymbol{W}\boldsymbol{P}+\boldsymbol{H}]\boldsymbol{a}(\boldsymbol{x}) - \boldsymbol{P}^T\boldsymbol{W}\boldsymbol{u} = 0. \tag{18.13}$$

The modified moment matrix can be written as

$$\boldsymbol{M}^{MMLS} = \boldsymbol{P}^T\boldsymbol{W}\boldsymbol{P}+\boldsymbol{H} = \boldsymbol{M}+\boldsymbol{H}, \tag{18.14}$$

and

$$\boldsymbol{a}(\boldsymbol{x}) = (\boldsymbol{P}^T\boldsymbol{W}\boldsymbol{P}+\boldsymbol{H})^{-1}\boldsymbol{P}^T\boldsymbol{W}\boldsymbol{u}. \tag{18.15}$$

$$\boldsymbol{B}(\boldsymbol{x}) = \boldsymbol{P}^T\mathbf{W}(\boldsymbol{x}) = [w_1(\boldsymbol{x})\boldsymbol{p}(\boldsymbol{x}_1), w_2(\boldsymbol{x})\boldsymbol{p}(\boldsymbol{x}_2), \ldots, w_N(\boldsymbol{x})\boldsymbol{p}(\boldsymbol{x}_N)] \tag{18.16}$$

and therefore

$$\boldsymbol{a}(\boldsymbol{x}) = \boldsymbol{A}^{-1}(\boldsymbol{x})\boldsymbol{B}(\boldsymbol{x})\boldsymbol{u}. \tag{18.17}$$

Finally, the dependent variable $u^h(\boldsymbol{x})$ can then be expressed as

$$u^{MMLS}(\boldsymbol{x}) = \boldsymbol{P}^T(\boldsymbol{P}^T\boldsymbol{W}\boldsymbol{P}+\boldsymbol{H})^{-1}\boldsymbol{P}^T\boldsymbol{W}\boldsymbol{u} = \sum_{j=1}^{n}\Phi_j^{MMLS}(\boldsymbol{x})u_j, \tag{18.18}$$

This book belongs to Central Library BADJI Mokhtar-ANNABA UNIVERSITY
Copyright Elsevier 2024

with the new shape functions

$$\boldsymbol{\Phi}^{MMLS}(\boldsymbol{x}) = \left[\Phi_1^{MMLS}(\boldsymbol{x}) \quad \ldots \quad \Phi_n^{MMLS}(\boldsymbol{x})\right] = \boldsymbol{P}^T(\boldsymbol{P}^T\boldsymbol{W}\boldsymbol{P}+\boldsymbol{H})^{-1}\boldsymbol{P}^T\boldsymbol{W}. \tag{18.19}$$

The partial derivatives of the shape functions $\Phi_I(\boldsymbol{x})$ are obtained as

$$\Phi_{I,k}(x) = \sum_{j=1}^{m}\left[p_{j,k}\left(\boldsymbol{A}^{-1}\boldsymbol{B}\right)_{ji} + p_j\left(\boldsymbol{A}^{-1}\boldsymbol{B}_{,k} + \boldsymbol{A}_{,k}^{-1}\boldsymbol{B}\right)_{ji}\right], \tag{18.20}$$

with $(\ )_{,k}$ denotes differentiation with respect to k and, $\boldsymbol{A}_{,k}^{-1}$ represents the derivative of the inverse of matrix $\boldsymbol{A}$ given by

$$\boldsymbol{A}_{,\mathrm{k}}^{-1} = -\boldsymbol{A}^{-1}\boldsymbol{A}_{,k}\boldsymbol{A}^{-1}. \tag{18.21}$$

18.2.2 Discretization Corrected Particle Strength Exchange

We begin by considering a differential operator, of arbitrary order, for a sufficiently smooth field $f(\boldsymbol{x}) = f(x, y)$ at point $\boldsymbol{x}_p = (x_p, y_p)$ of a point set

$$\boldsymbol{D}^a f(\boldsymbol{x}_p) = \boldsymbol{D}^{m,n} f(\boldsymbol{x}_p) = \frac{\partial^{m+n}}{\partial x^m \partial y^n} f(x,y)\Big|_{x=x_p, y=y_p} \tag{18.22}$$

where m and n are integers that determine the order of the differential operator. The DC PSE operator for the spatial derivative $\boldsymbol{D}^{m,n} f(\boldsymbol{x}_p)$ is

$$\boldsymbol{Q}^{m,n} f(\boldsymbol{x}_p) = \frac{1}{\varepsilon(\boldsymbol{x}_p)^{m+n}} \sum_{\boldsymbol{x}_q \varepsilon \mathcal{N}(\boldsymbol{x}_p)} (f(\boldsymbol{x}_q) \pm f(\boldsymbol{x}_p))\eta\left(\frac{\boldsymbol{x}_p - \boldsymbol{x}_q}{\varepsilon(\boldsymbol{x}_p)}\right) \tag{18.23}$$

where $\varepsilon(\boldsymbol{x})$ is a spatially dependent scaling or resolution function, $\eta(\boldsymbol{x}, \varepsilon(\boldsymbol{x}))$ a kernel function, and $N(\boldsymbol{x}_p)$ is the set of points in the support domain of the kernel function. The sign in Eq. (18.23) is positive when $(m + n)$ is odd and negative when $(m + n)$ is even. We will construct the DC PSE operators so that as we decrease the average spacing between nodes, $h(\boldsymbol{x}_p) \to 0$, the operator converges to the spatial derivative $\boldsymbol{D}^{m,n} f(\boldsymbol{x}_p)$ with an asymptotic rate r

$$\boldsymbol{Q}^{m,n} f(\boldsymbol{x}_p) = \boldsymbol{D}^{m,n} f(\boldsymbol{x}_p) + O(h(\boldsymbol{x}_p)^r) \tag{18.24}$$

where it is convenient to explicitly define the component-wise average neighbor spacing as

$$h(x_p) = \frac{1}{N} \sum_{\boldsymbol{x}_q \in \mathcal{N}(\boldsymbol{x})} |x_p - x_q| + |y_p - y_q| \tag{18.25}$$

where N is the number of nodes in the support domain of $\boldsymbol{x}_p$. We need to find a kernel function $\eta(\boldsymbol{x})$ and a scaling relation $\varepsilon(\boldsymbol{x}_p)$ that satisfy Eq. (18.24). To achieve this, we replace the terms $f(\boldsymbol{x}_q)$ in Eq. (18.23) with their Taylor series expansions around the point $\boldsymbol{x}_\mathrm{p}$. This substitution gives

$$\boldsymbol{Q}^{m,n} f(\boldsymbol{x}_p) = \left.\sum_{i=0}^{\infty}\sum_{j=0}^{\infty} \frac{\varepsilon(\boldsymbol{x}_p)^{i+j-m-n}(-1)^{i+j}}{i!j!} \boldsymbol{D}^{i,j} f(\boldsymbol{x}_p) Z^{i,j}(\boldsymbol{x}_p)\right) \pm Z^{0,0}(\boldsymbol{x}_p)\varepsilon(\boldsymbol{x}_p)^{-m-n} f(\boldsymbol{x}_p) \tag{18.26}$$

where

$$Z^{(i,j)}(\boldsymbol{x}_p) = \sum_{\boldsymbol{x}_q \in \mathcal{N}(\boldsymbol{x})} \frac{(x_p - x_q)^i (y_p - y_q)^j}{\varepsilon(\boldsymbol{x}_p)^{i+j}} \eta\left(\frac{\boldsymbol{x}_p - \boldsymbol{x}_q}{\varepsilon(\boldsymbol{x}_p)}\right) \tag{18.27}$$

are the discrete moments of η. Now, if we restrict the scaling parameter $\varepsilon(\boldsymbol{x}_p)$ to converge at the same rate as the average spacing between points $h(\boldsymbol{x}_p)$, that is

$$\frac{h(\boldsymbol{x}_p)}{\varepsilon(\boldsymbol{x}_p)} \in O(1) \tag{18.28}$$

we find that the discrete moments $Z^{i,j}$ are $O(1)$ as $h(\boldsymbol{x}_p) \to 0$ and $\varepsilon(\boldsymbol{x}_p) \to 0$. Given Eq. (18.26), the convergence rate r of the DC PSE operator $\boldsymbol{Q}^{m,n}$ is determined by the coefficients of the terms $\varepsilon(\boldsymbol{x}_p)^{i+j-m-n}$ in Eq. (18.26). The coefficient of

This book belongs to Central Library BADJI Mokhtar-ANNABA UNIVERSITY
Copyright Elsevier 2024

$\varepsilon(\boldsymbol{x}_p)^{i+j-m-n}$ in Eq. (18.26) is required to be 1 when $i = m$ and $j = n$ and 0 when $i + j + m + n < r$. This results in the following set of conditions for the discrete moments:

$$Z^{i,j}(\boldsymbol{x}_p) = \begin{cases} i!j!(-1)^{i+j} & i = m, j = n \\ 0 & a_{min} < i + j < r + m + n \\ < \infty & \text{otherwise} \end{cases} \tag{18.29}$$

where α_{min} is 1 if $m + n$ is even and 0 if odd. This is due to the zeroth moment $Z^{0,0}$ canceling out for odd $i + j$. The choice of the factor $\varepsilon(\boldsymbol{x}_p)^{-m-n}$ in Eq. (18.23) acts as to simplify the expression of the moment conditions. For the kernel function $\eta(\boldsymbol{x})$ to be able to satisfy the l conditions given in Eq. (18.29) for arbitrary neighborhood node distributions, the operator must have l degrees of freedom. This leads to the requirement that the support $N(\boldsymbol{x})$ of the kernel function has to include at least l nodes. In this chapter, we use kernel functions of the form

$$\eta(\boldsymbol{x}) = \begin{cases} \sum_{i,j}^{i+j<r+m+n} a_{i,j} x^i y^i e^{-x^2-y^2} & \sqrt{x^2+y^2} < r_c \\ 0 & \text{otherwise} \end{cases}. \tag{18.30}$$

This is a monomial basis multiplied by an exponential window function, where r_c sets the kernel support and the $\alpha_{i,j}$ are scalars to be determined to satisfy the moment conditions in Eq. (18.29). The cutoff radius r_c should be set to include at least l collocation nodes in the support $N(\boldsymbol{x})$. In this chapter, r_c is set implicitly by using the l-1 nearest neighbors of each node (alternatively, adaptive methods can be used). If $\alpha_{min} = 1$, the $\alpha_{0,0}$ coefficient is a free parameter and can be used to increase the numerical robustness of solving the linear system of equations for the remaining $\alpha_{i,j}$.

To construct the operator $\boldsymbol{Q}^{m,n} f(\boldsymbol{x}_p)$ at node $\boldsymbol{x}_p$, the coefficients are found by solving a linear system of equations from Eqs. (18.26) and (18.27). With our choice of kernel function, we have

$$\boldsymbol{Q}^{m,n} f(\boldsymbol{x}_p) = \frac{1}{\varepsilon(\boldsymbol{x}_p)^{m+n}} \sum_{\boldsymbol{x}_q \in \mathcal{N}(\boldsymbol{x})} (f(\boldsymbol{x}_q) - f(\boldsymbol{x}_p)) \boldsymbol{p}\left(\frac{\boldsymbol{x}_p - \boldsymbol{x}_q}{\varepsilon(\boldsymbol{x}_p)}\right) \boldsymbol{a}^T(\boldsymbol{x}_p) e^{-\frac{(x_p-x_q)^2+(y_p-y_q)^2}{(\varepsilon(\boldsymbol{x}_p))^2}} \tag{18.31}$$

where $\boldsymbol{p}(\boldsymbol{x}) = \{p_1(\boldsymbol{x}), p_2(\boldsymbol{x}), \ldots, p_l(\boldsymbol{x})\}$ and $\boldsymbol{\alpha}(\boldsymbol{x})$ are vectors of the terms in the monomial basis and of their coefficients, respectively. Using this formulation, the operator system becomes trivial to solve. For example, if we set $r = 2$ and approximate the first spatial derivative in the x direction, $D^{1,0}$, we have $l = 6$ moment conditions and the monomial basis is $\boldsymbol{p}(x, y) = \{1, x, y, xy, x^2, y^2\}$. The linear system for the kernel coefficients then is

$$\boldsymbol{A}(\boldsymbol{x}_p)\boldsymbol{\alpha}^T(\boldsymbol{x}_p) = \boldsymbol{b} \tag{18.32}$$

where

$$\boldsymbol{A}(\boldsymbol{x}_p) = \boldsymbol{B}(\boldsymbol{x}_p)^T \boldsymbol{B}(\boldsymbol{x}_p) \in \mathbb{R}^{l \times l} \tag{18.33}$$

$$\boldsymbol{B}(\boldsymbol{x}_p) = \boldsymbol{E}(\boldsymbol{x}_p)^T \boldsymbol{V}(\boldsymbol{x}_p) \in \mathbb{R}^{k \times l} \tag{18.34}$$

$$\boldsymbol{b} = (-1)^{m+n} \boldsymbol{D}^{m,n} \boldsymbol{p}(\boldsymbol{x})\big|_{x=0} \in \mathbb{R}^{l \times 1} \tag{18.35}$$

The scalar number $k \geq l$ is the number of nodes in the support of the operator, l is the number of moment conditions to be satisfied, and $\boldsymbol{V}(\boldsymbol{x}_p)$ the Vandermonde matrix constructed from the monomial basis $\boldsymbol{p}(\boldsymbol{x}_p)$. $\boldsymbol{E}(\boldsymbol{x}_p)$ is a diagonal matrix containing the square roots of the values of the exponential window function at the neighboring nodes in the operator support. Furthermore, for node $\boldsymbol{x}_p$ we define $\{z_q(x_p)\}_{q=1}^{k} = (x_p - x_q)_{\boldsymbol{x}_q \in \mathcal{N}(\boldsymbol{x})}$ the set of vectors pointing to $\boldsymbol{x}_p$ from all neighboring nodes $\boldsymbol{x}_q$ in the support of $\boldsymbol{x}_p$. So then explicitly

$$\boldsymbol{V}(\boldsymbol{x}_p) = \begin{bmatrix} p_1\left(\frac{z_1(x_p)}{\varepsilon(x_p)}\right) & p_2\left(\frac{z_1(x_p)}{\varepsilon(x_p)}\right) & \cdots & p_l\left(\frac{z_1(x_p)}{\varepsilon(x_p)}\right) \\ p_1\left(\frac{z_2(x_p)}{\varepsilon(x_p)}\right) & p_2\left(\frac{z_2(x_p)}{\varepsilon(x_p)}\right) & \cdots & p_l\left(\frac{z_2(x_p)}{\varepsilon(x_p)}\right) \\ \vdots & \vdots & \ddots & \vdots \\ p_1\left(\frac{z_k(x_p)}{\varepsilon(x_p)}\right) & p_2\left(\frac{z_k(x_p)}{\varepsilon(x_p)}\right) & \cdots & p_m\left(\frac{z_k(x_p)}{\varepsilon(x_p)}\right) \end{bmatrix} \in \mathbb{R}^{k \times l} \tag{18.36}$$

This book belongs to Central Library BADJI Mokhtar-ANNABA UNIVERSITY
Copyright Elsevier 2024

$$\boldsymbol{E}(\boldsymbol{x}_p) = diag\left(\left\{e^{-\frac{|z_q(x_p)|^2}{2\varepsilon^2}}\right\}_{q=1}^{k}\right) \tag{18.37}$$

Once the matrix $\boldsymbol{A}(\boldsymbol{x}_p)$ is constructed at each node $\boldsymbol{x}_p$, the linear systems can be solved for the coefficients $\boldsymbol{\alpha}(\boldsymbol{x}_p)$ used in the DC PSE operators at each node as in Eq. (18.31). The matrix $\boldsymbol{A}(\boldsymbol{x}_p)$ only depends on the number of moment conditions l and the local distribution of nodes in $\boldsymbol{N}(\boldsymbol{x}_p)$. Therefore, if the system in Eq. (18.32) is solved using a decomposition (such as LU) of $\boldsymbol{A}(\boldsymbol{x}_p)$, this can be reused for multiple right-hand sides, i.e., for different differential operators (albeit with different convergence rates r). The matrix $\boldsymbol{A}$ has an analogue in MLS where it is often called moment matrix, and it contains information about the spatial distribution of the collocation nodes around the center point $\boldsymbol{x}_p$. The invertibility of $\boldsymbol{A}$ depends entirely on that of the Vandermonde matrix $\boldsymbol{V}$, due to $\boldsymbol{E}$ being a diagonal matrix with nonzero entries. The condition number of $\boldsymbol{A}$ depends on both $\boldsymbol{V}$ and $\boldsymbol{E}$ and determines the robustness of the numerical inversion.

Using the DC PSE method the spatial derivatives $\boldsymbol{D}^{\alpha} \equiv \boldsymbol{D}^{m,n}$ up to second order are given as

$$\boldsymbol{D}^{1,0} \equiv \frac{\partial}{\partial x}, \quad \boldsymbol{D}^{0,1} \equiv \frac{\partial}{\partial y} \tag{17.38}$$

And

$$\boldsymbol{D}^{1,1} \equiv \frac{\partial^2}{\partial x \partial y} = \frac{\partial^2}{\partial y \partial x}, \quad \boldsymbol{D}^{2,0} \equiv \frac{\partial^2}{\partial x^2}, \quad \boldsymbol{D}^{0,2} \equiv \frac{\partial^2}{\partial y^2} \tag{17.39}$$

18.3 WEIGHTED RESIDUAL METHOD

The weighted residual method is a general and powerful method for obtaining approximate numerical solutions for both ordinary differential equations and partial differential equations (PDEs). Many of the well-established numerical methods are based on the weighted residual method.

We consider a given spatial domain Ω and a PDE of the form

$$\mathcal{L}u(\boldsymbol{x}) = f(\boldsymbol{x}) \tag{18.40}$$

where $\mathcal{L}$ is a differential operator that when applied to the scalar function $u(\boldsymbol{x})$ produces the function $f(\boldsymbol{x})$. Additionally, boundary conditions are given as

$$\boldsymbol{G}u(\boldsymbol{x}) = h(\boldsymbol{x}) \tag{18.41}$$

To numerically solve the governing equations, the function $u(\boldsymbol{x})$ is approximated by a function $u^h(\boldsymbol{x})$ written as

$$u^h(\boldsymbol{x}) = \sum_{i=1}^{n} a_i \Phi_i(\boldsymbol{x}) = \boldsymbol{\Phi}\mathbf{a} \tag{18.42}$$

with $\Phi_i(\boldsymbol{x})$ being the *basis functions* or *trial functions*, a_i the unknown coefficients and, n the number of basis function used. By substituting Eq. (18.42) into Eqs. (18.40) and (18.41) we get

$$\mathcal{L}u^h(\boldsymbol{x}) \neq f(\boldsymbol{x}) \tag{18.43a}$$

$$\boldsymbol{G}u^h(\boldsymbol{x}) \neq h(\boldsymbol{x}) \tag{18.43b}$$

We can then obtain the following *residual* functions R_d and R_b, for the system of the governing equations, and the boundary conditions defined over the boundaries.

$$\boldsymbol{R_d} = \mathcal{L}u^h(\boldsymbol{x}) - f(\boldsymbol{x}) \tag{18.44a}$$

$$\boldsymbol{R_b} = \boldsymbol{G}u^h(\boldsymbol{x}) - h(\boldsymbol{x}) \tag{18.44b}$$

In case $u(\boldsymbol{x})$ is the exact solution of the governing equations, residuals R_d and R_b will be exactly zero. However, in the majority of the applications considered the exact solution cannot be obtained and, therefore, residuals R_d and R_b are not zero. We can force the residual to be zero in an average sense by setting weighted integrals of residuals to zero:

$$\int W_d R_d d\boldsymbol{x} + \int W_b R_b dS = 0 \tag{18.45}$$

This book belongs to Central Library BADJI Mokhtar-ANNABA UNIVERSITY
Copyright Elsevier 2024

where W_d and W_b are given weight functions for the residuals R_d and R_b, respectively. This is the formulation of the weighted residual method that is used in various numerical methods (e.g., FEM, finite volume method).

18.3.1 Collocation Method

In collocation methods we try to minimize the weighted residuals only at chosen points, distributed over the entire spatial domain (interior and boundary). The standard formulation for the collocation method can be obtained by using *Dirac delta function* $\delta(x - x_i)$ as the weight function in Eq. (18.45)

$$\begin{cases} W_d = \delta(x - x_i) \\ W_b = \delta(x - x_i) \end{cases} \tag{18.46}$$

For a field function $u(\boldsymbol{x})$, defined on a set of N points (nodes) $\boldsymbol{x}_i$ in the spatial domain Ω, we can write the approximation function $u^h(\boldsymbol{x})$ as

$$u_i \approx u_i^h = \sum_{I=1}^{N} \mathrm{g}_I I_{iI} \tag{18.47}$$

and in matrix notation

$$\boldsymbol{u}^h = \mathbf{gI} \tag{18.48}$$

where $\mathbf{g}$, $\mathbf{I}$ are the identity matrix. The derivatives of the unknown field function can be obtained in a straightforward manner by $D^a u_i^h(\boldsymbol{x}) = \sum_{I=1}^{N} D^a \mathrm{g}_I(\boldsymbol{x}) u_{iI}$, where $D^a u_i = \partial^{|a|} u_i \Big/ \partial x_1^{a_1} \quad \ldots \quad \partial x_d^{a_d}$, $|a| = \sum_{i=1}^{d} a_i$ is the differential operator.

In the collocation framework, derivatives are introduced into the governing equations and the residuals are enforced to be zero on the points set $(\boldsymbol{x}_i)_{i=1}^{N}$. Applying collocation to Eqs. (18.40) and (18.41) we obtain

$$\begin{aligned} \mathcal{L}(\mathbf{I}(\zeta_J))\mathbf{d} &= \mathbf{R}(\zeta_J) \quad \forall (\boldsymbol{x}_i) \in \Omega \\ \boldsymbol{G}(\mathbf{I}(\zeta_J))\mathbf{d} &= \mathbf{f}(\zeta_J) \quad \forall (\boldsymbol{x}_i) \in \partial\Omega \end{aligned} \tag{18.49}$$

18.3.2 Galerkin Method

In Galerkin method the trial functions used for the approximation of the field functions are also used as the weight functions

$$W_d = W_b = \boldsymbol{\Phi} \tag{18.50}$$

The Galerkin method has some advantages. The system matrix obtained by the Galerkin method is most of the times symmetric. Most important, Galerkin method has solid physical and mathematical foundations because in many cases it leads to the same formulations as those obtained using energy principles.

18.4 STRONG-FORM MESHLESS METHODS

We demonstrate the use of strong-form MMs by considering two representative test problems frequently encountered in biomechanics and bioengineering applications: blood flow in the ascending and descending aorta and microwaves tumor ablation. In both numerical examples examined, the nodal distributions were obtained directly from the raw image data. In the case of blood flow in the ascending and descending aorta, the image-based segmentation results in an stereo lithography (STL) file representing the surface, with the point cloud used being the pixelated image represented as a Cartesian grid embedded in the STL geometry.

18.4.1 Blood Flow in Aorta

To obtain the aorta geometry a patient underwent contrast-enhanced spiral CT (Siemens, Somatom Plus 4A). The examination protocol has been set to 120 kVp, 180 mAs, with administration of 140-mL nonionic iodinated contrast agent at 3.5 mL/s (time delay was set to 16 s). The scanning coverage was set to 26 cm with 2 mm/s table feed (total examination

This book belongs to Central Library BADJI Mokhtar-ANNABA UNIVERSITY Copyright Elsevier 2024

time was 130 s). A stack of raw DICOM files loaded into the 3D image processing software Analyze 6.0, and through an automated 3D reconstruction of the vessel lumen surface, has been obtained. Thresholding and seeded region growing techniques were applied to segment the renal arteries and the aorta. The triangulated surface was then exported in an STL format and imported in the CFD software. The interior domain (lumen) is represented by a uniform Cartesian grid embedded in the aorta geometry. The point cloud on the aorta boundaries and the Cartesian embedded grid form the nodal distribution used for the flow simulations.

The nondimensional Navier−Stokes equations for an incompressible Newtonian fluid (blood) can be written in terms of vorticity and velocity by taking the curl of the velocity−pressure linear momentum equations and the continuity equation, thus eliminating the pressure term from the formulation. Therefore, the governing equations in their velocity−vorticity formulation are summarized as

$$\frac{1}{Re}\nabla^2\boldsymbol{\omega} + \boldsymbol{\omega}\cdot\boldsymbol{\nabla}\boldsymbol{u} - \boldsymbol{u}\cdot\boldsymbol{\nabla}\boldsymbol{\omega} = 0 \tag{18.50a}$$

$$\boldsymbol{\nabla}\cdot\boldsymbol{u} = 0 \tag{18.50b}$$

$$\boldsymbol{\omega} = \boldsymbol{\nabla}\times\boldsymbol{u} \tag{18.50c}$$

For the boundary conditions, in the inlet a uniform profile is considered (plug flow) with inflow velocity $u = 0.1$ cm/s, whereas in the outlet a fully developed flow is applied ($\mathrm{d}u/\mathrm{d}x = 0$). In the remaining boundaries, no-slip boundary conditions are considered.

Fig. 18.1 shows the STL file of the aorta, the Cartesian embedded grid, and the streamlines computed by the meshless point collocation (MPC) scheme.

18.4.2 Tumor Ablation Simulation

The fully nonlinear extended Pennes bioheat equation (Eq. 18.51) is numerically solved using an MPC method. The MPC scheme shows that it can be safely used by considering both numerical and experimental data (Bourantas et al., 2014).

For the simulations, we consider nonuniform perfusion rate $\omega_b(T, \Omega)$ and accounting for blood flow direction. Additionally, the extended Pennes bioheat equation neglects certain physical phenomena that take place during thermal ablation, namely, water evaporation, and thermal tissue damage. Taking into account the above analysis, the extended bioheat equation becomes

$$\left(\rho(T)c(T) - \beta\frac{dw}{dt}\right)\frac{dT}{dt} = \nabla(k(T)\nabla T) + \omega_b(T,\Omega)\rho_b c_b(T_a - T) + Q_r + Q_m \tag{18.51}$$

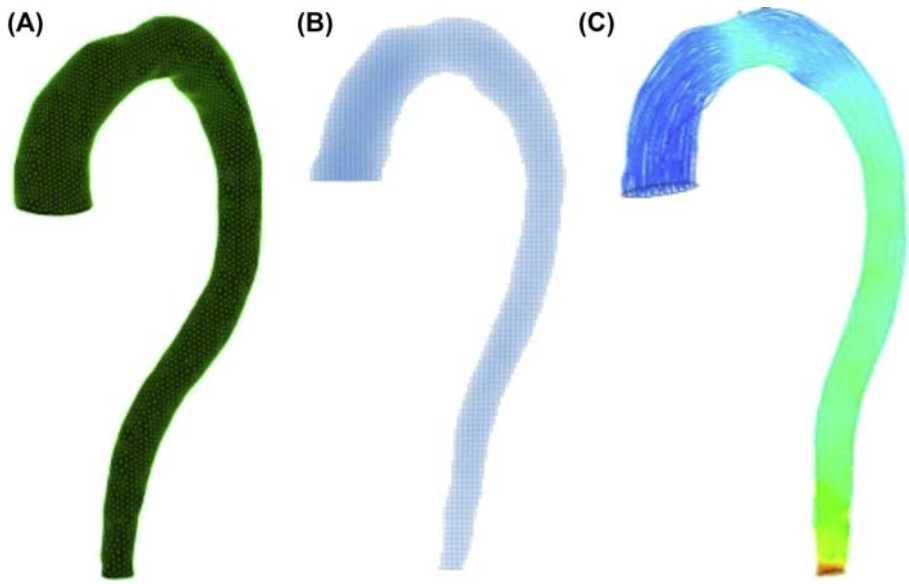

FIGURE 18.1 The collocation method uses an irregular nodal distribution on the boundaries and a Cartesian grid in the interior. (A) Triangulation of the surface of the aorta; (B) Cartesian embedded grid; and (C) streamlined obtained by solving the incompressible Navier−Stokes equations with the collocation method.

This book belongs to Central Library BADJI Mokhtar-ANNABA UNIVERSITY Copyright Elsevier 2024

where ρ is the density, β is the water latent heat constant, and c is the specific heat capacity. The thermal properties of both the tissue and the tumor are functions of temperature (T) and the water content (w). Using an empirical function for the dependence of the tissue water content on temperature to fit experimental data, one gets

$$w(T) = \begin{cases} 0.728 + 8.487e^{-2\left(\frac{T-123.286}{16.634}\right)^2}, & T \leq 103 \\ 0.024 + \dfrac{4.531}{1+e^{\left(\frac{T-30.173}{28.012}\right)^2}}, & T > 103 \end{cases} \tag{18.52}$$

Dynamic changes in blood perfusion rate with temperature and damage can be formulated as

$$\omega(T, \Omega) = \omega_{b_0} f_T f_u \tag{18.53}$$

where ω_{b_0} is the constitutive perfusion rate and $f_u = 1 - f_T$, with f_T a dimensionless function that accounts for vessel dilation at slightly elevated temperatures, which can be approximated as

$$f_T = \begin{cases} 4 + 0.6(T - 42) & 37°\text{C} \leq T < 42°\text{C} \\ 4 & T \geq 42°\text{C} \end{cases} \tag{18.54}$$

The extended bioheat equation is used to model the thermal distribution in the kidney, using a cubic geometry of length 0.02 m ranging from -0.01 m $\leq x, y, z \leq 0.01$ m and assuming adiabatic boundaries at all six faces.

A scenario of tumor ablation takes place using a heat source of finite volume located at the middle of the tumor with tumor radius 0.002 m. The symmetric geometry setup has been used to facilitate the imposition of the thermal boundary conditions, which can be described in two ways: the first is the Dirichlet boundary conditions, where the temperature far away from the source is constant, equal to that of the surrounding tissues (in most of the cases the temperature chosen is $T = 37°$C), and the second one is zero fluxes (meaning zero temperature gradients) at the boundaries, ensuring a dynamic equilibrium. In both cases, the length of the surrounding box has to be large enough compared with the dimensions of the tumor and, also, quite far from the source. The physical choice for this is to use a square box (symmetrical) instead of a rectangular one. Fig. 18.2 shows temperature isocontours at different time instances, locating the ablation region computed.

The meshless collocation method, which provides both accuracy and convergence for the harmonic operator, produces numerical results for the temperature distribution that are in very good agreement with analytical predictions or with the results of the flux continuity method for different benchmark problems.

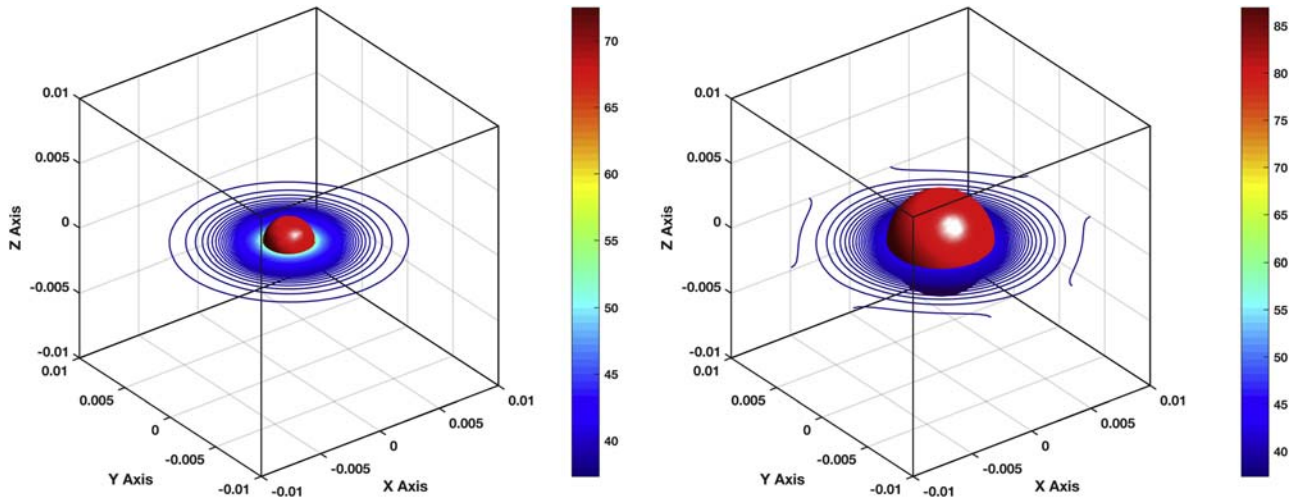

FIGURE 18.2 Temperature isocontour value ($T = 38°$C) plots at 600 s (left) and 1200 s (right) using the meshless point collocation method.

This book belongs to Central Library BADJI Mokhtar-ANNABA UNIVERSITY
Copyright Elsevier 2024

18.5 WEAK-FORM MESHLESS METHODS

Research on weak-form MMs significantly increased after the publication of the DEM, introduced in (Nayroles et al., 1992). The RKPM, presented by Liu et al. (1995), and the EFG method, presented by Belytschko et al. (1994), were the first weak-form MMs applied in solid mechanics. In contrast to EFG and RKPM methods, which use an intrinsic-type basis, other MMs were developed that use an extrinsic basis along with the partition of unity concept. This extrinsic basis was used in the *hp*-cloud method, presented in Liszka et al. (1996). In Melenk and Babuska (1996) the partition of unity FEM, similar to the *hp*-cloud method, has been presented, stressing out the similarities of meshless and FEMs. Recently, a class of MMs, based on local weighted residual weak form, have been developed. In this category, we can find the MLPG method presented by Atluri and Zhu (1998), the meshless local boundary integral equation method (Zhu et al., 1998), the local point interpolation method presented by Liu and Gu (2001a,b), and the radial point interpolation method (Wang and Liu, 2002). Despite their applicability, so far there are no reported results including full-scale calculations in biomechanical applications.

A numerical method applied in the field of biomechanics must produce dynamic results in real time. The meshless total Lagrangian explicit dynamics (MTLED) method (Horton et al., 2010; Miller et al., 2007) produces accurate results (less than 5% error compared with FEM), with increasing speed compared with the traditional mesh-based methods. The MTLED computes all variable in the initial configuration and integrates over a background grid that does not conform to the simulation geometry. Thus, it can be easily applied to complex geometries with complicated boundaries. Furthermore, the method can accept an almost arbitrary placement of nodes throughout the simulation geometry. Both the integration grid and the node placement for the algorithm can be created automatically for any geometry in an easy and straightforward procedure.

Numerical integration heavily affects the accuracy and the reproducibility of weak formulations. Weak MMs still have not established as a mainstream numerical method, mainly because of their difficulty in performing numerical integration (Joldes et al., 2015a, 2015b). EFG method offers noteworthy benefits compared with classical mesh-based numerical methods (such as making possible the simulation of very large deformations in elasticity, eliminating the need for the construction of a high-quality mesh). In MLPG, the integration domain is a fictitious domain that is defined and used only for the integration. The drawback is that the number of integration points needed to achieve accuracy similar to FEM is quite high compared with FEM. Additionally, in contrast to FEM, where there are very well-defined rules regarding numerical integration, performing numerical integration in MMs is more an art than to a science. In FEM there are well-defined integration rules; the integration cells are the elements used to discretize the spatial domain, and the number of Gauss points (integration points) are selected based on the required accuracy and the degree of the polynomial shape functions. In MMs, shape functions are nonpolynomial, having much larger support domain compared with FEM. Consequently, the error introduced is mainly due to the complicated shape functions and the mismatch between integration cells and the support domains.

18.5.1 Numerical Examples

Meshless weak formulations have been successfully applied in numerous biomechanical applications. They provide reliable and accurate results in problems where traditional numerical methods have poor accuracy or in some cases fail to deliver results.

Next, we briefly describe the problems of brain deformation and whole-body image registration (Li et al., 2015a, 2015b), where the weak-form MMs were successfully applied.

18.5.2 Brain Deformation

MMs can be effectively applied in cases where large deformation and rotation of soft tissue (e.g., brain) is considered. Accurate description and numerical modeling of large deformations has been a challenging problem in computational mechanics.

Because of the intensive research in the field, which is dominated by mesh-based numerical methods such as FEM, numerous researchers have successfully developed algorithms, based on finite element analysis, to handle large deformations. In fact, FEM can produce accurate numerical results, demonstrating a high level of precision that can be achieved in real-time simulations (e.g., surgical procedures) by using nonlinear (both geometric and material) biomechanical models. Despite their undoubtedly success, it is well recognized that FEM has certain inherent drawbacks: (1) time and labor costly mesh generation, (2) shear locking, (3) hourglass effects, (4) inaccurate derivative solutions, (5) massive mesh distortion under very large deformations, and (6) difficulty in handling problems of strain localization, crack

This book belongs to Central Library BADJI Mokhtar-ANNABA UNIVERSITY Copyright Elsevier 2024

propagation, and material penetration. The accuracy of the FE calculation relies entirely on the mesh quality; hence, it is desirable to use only good-quality mesh (with the best choice being the hexahedral mesh). Mesh generation is considered to be the bottleneck in the entire procedure of generating patient-specific models for real-time simulations.

The MTLED solution algorithm has been successfully applied (Miller et al., 2012; Zhang et al., 2012) in a comprehensive patient-specific surgical simulation. All anatomical components are represented by surfaces, generated by segmentation of the image raw data (Fig. 18.3). The parenchyma, tumor, and ventricle volumes were represented (filled) by a total of 31,753 nodes, having an average spacing of 3.5 mm. Representing this complex geometry by a point cloud is a straightforward and trivial procedure, whereas creating a good-quality finite element mesh, for the same geometry, is a tedious and time-consuming procedure that requires a lot of manual intervention (Miller et al., 2012). Integration across the volume is applied by using a regular Cartesian grid that consists of 53,672 integration points with 3 mm spacing between them (a background mesh, but this requires no manual work to create). A contact interface has been defined between the skull and the parenchyma surface, with nodes on the parenchyma surface not being able to penetrate the skull, but could slide without friction. The tumor and ventricle surfaces were tied (by shared nodes) to the internal surfaces of the parenchyma. The results obtained using the MTLED method are as useful and accurate as those obtained with the FE method. The contours in Fig. 18.4 show the good agreement between the results obtained by the MTLED and those using the FE method. Only in a few places are slightly different results seen and the differences are not larger than the voxel size of the intraoperative brain MRI.

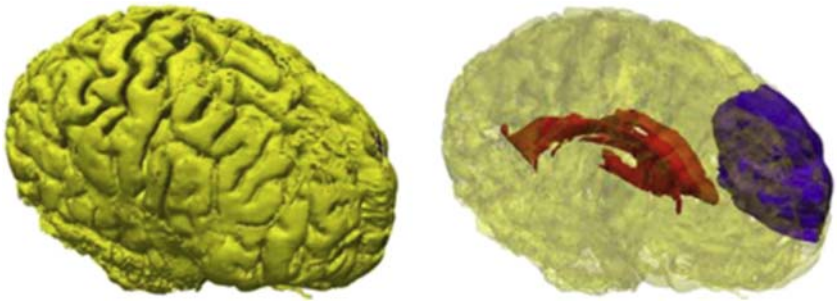

FIGURE 18.3 Definition and surface visualizations of the problem geometry; parenchyma (yellow (light gray in print versions)), tumor (blue (dark gray in print versions)), and ventricle (red (gray in print versions)).

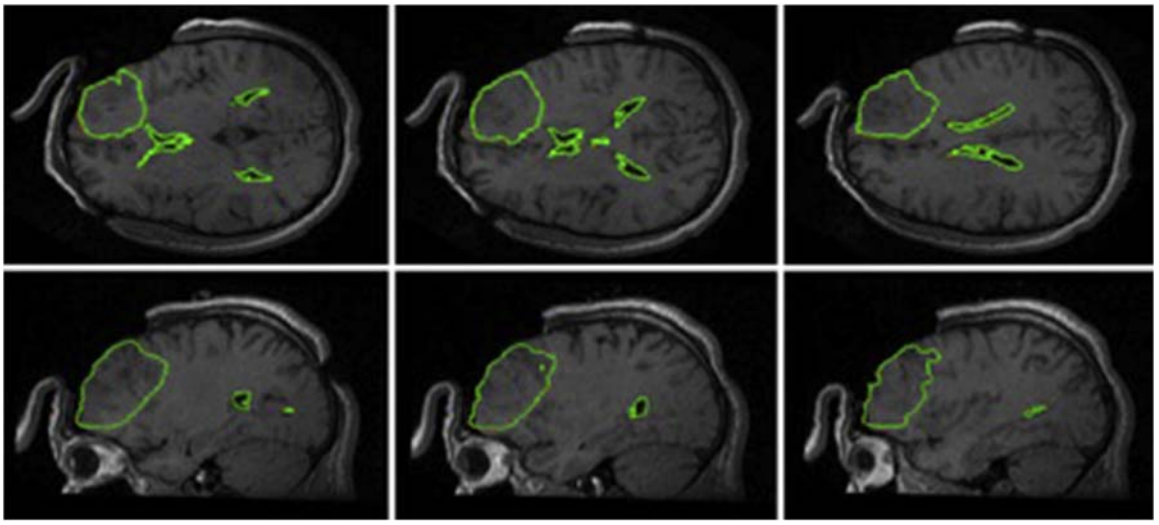

FIGURE 18.4 Intraoperative magnetic resonance images overlaid with contours (green lines (white in print versions)) of the deformed tumor and ventricle surfaces as generated by our meshless total Lagrangian explicit dynamics (MTLED)-based suite of algorithms. The three transverse sections (top row) and three sagittal sections (bottom row) were taken at 5 mm intervals. For reference, the red lines (light gray in print versions) represent the contours of the deformed ventricles and tumor computed by FEM, but these are almost entirely obscured by the very similar MTLED results.

This book belongs to Central Library BADJI Mokhtar-ANNABA UNIVERSITY Copyright Elsevier 2024

18.5.3 Whole-Body Image Registration

A general problem encountered in numerous biomechanical applications is the reliable (in terms of reproducibility) and accurate registration of source and target (medical) images. A quantitative comparison of images acquired at different times or in different modalities for a given patient is crucial for the analysis of disease progression and assessment of responses to therapies. Numerous registrations techniques have been developed and several (image processing based) registration algorithms have emerged. Despite the few successful attempts to improve the robustness of registration algorithms (Toews and Wells, 2013) and registration accuracy for selected body segments (for limited range of rigid body motion and soft organs/tissues deformation) (Stromqvist et al., 2009), the whole-body image registration (especially using CT images) still remains a largely unsolved problem (Li et al., 2008).

For whole-body registration involving large differences (deformations) between the source and target images, the biomechanical based methods, which account for the mechanical behavior of organs/tissues (Wittek et al., 2007; Hopp et al., 2013), provide a viable alternative to purely image-based methods. Registration algorithms based on biomechanical models rely on principles of mechanics to compute deformations that transform a source image to a target image. This ensures plausibility and robustness of the predicted deformations. Patient-specific biomechanical modeling has been successfully used in numerous studies for computing the brain deformations for neuroimage registration (Wittek et al., 2010). Quick and reliable generation of patient-specific computational models, automatic segmentation of radiographic images, and efficient solution methods are the main challenges that need to be addressed. Thus, the need to overcome these challenges when applying biomechanical modeling for medical image registration dictated the use of MMs.

The MTLED method has been used to compute the deformation of the source image to the target image configuration (Li et al., 2016), based on the patient-specific whole-body models. Three CT image data sets were used (Fig. 18.5), obtained from The Cancer Imaging Archive (https://public.cancerimagingarchive.net/ncia/login.jsf; Armato et al., 2008; Clark et al., 2013). Two image sets from each of the three data sets (Fig. 18.5) have been used; one considered as the source/moving image and another one as the target/fixed image. The complex geometry of the human body has been represented by a set of nodes (a trivial and straightforward exercise). Therefore, the torso volume was filled with nodes using an average spacing of 3.5 mm, which resulted in nodal distributions consisting of 78,573 nodes for Case I, 86,016 nodes for Case II, and 137,344 nodes for Case III. The tissue classification applied was based on the fuzzy C-means algorithm to assign the constitutive properties automatically at integration points of the computation grid (Zhang et al., 2013). This allows the development of the

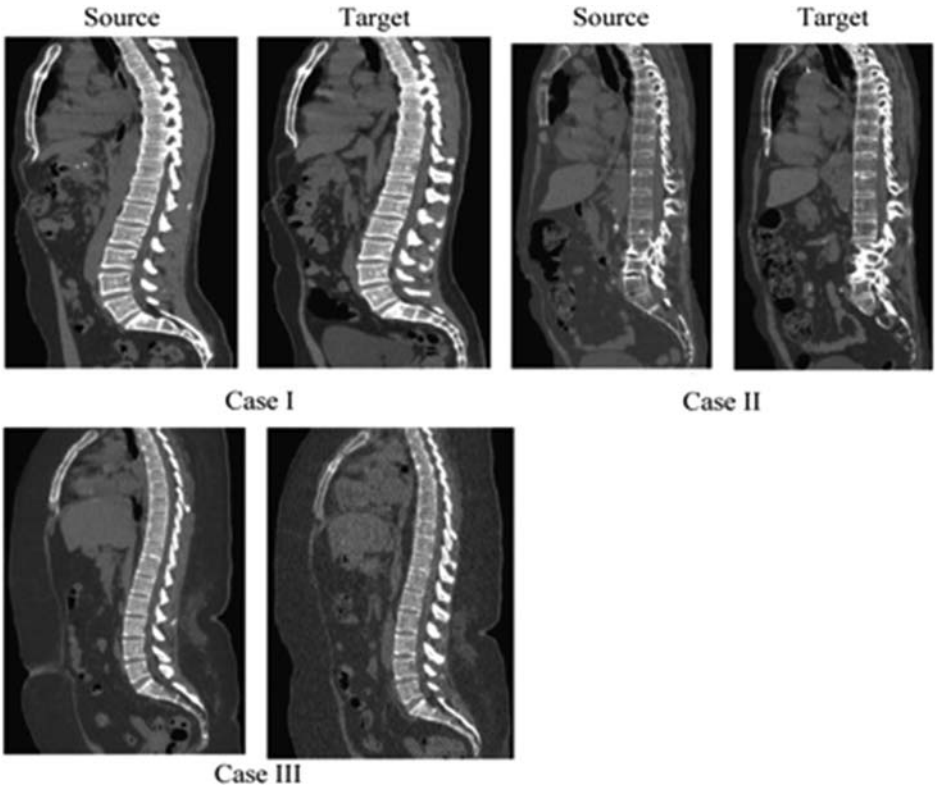

FIGURE 18.5 Sagittal sections of three whole-body computed tomography image data sets analyzed in Li et al. (2016). Copied from Li et al. (2016).

This book belongs to Central Library BADJI Mokhtar-ANNABA UNIVERSITY
Copyright Elsevier 2024

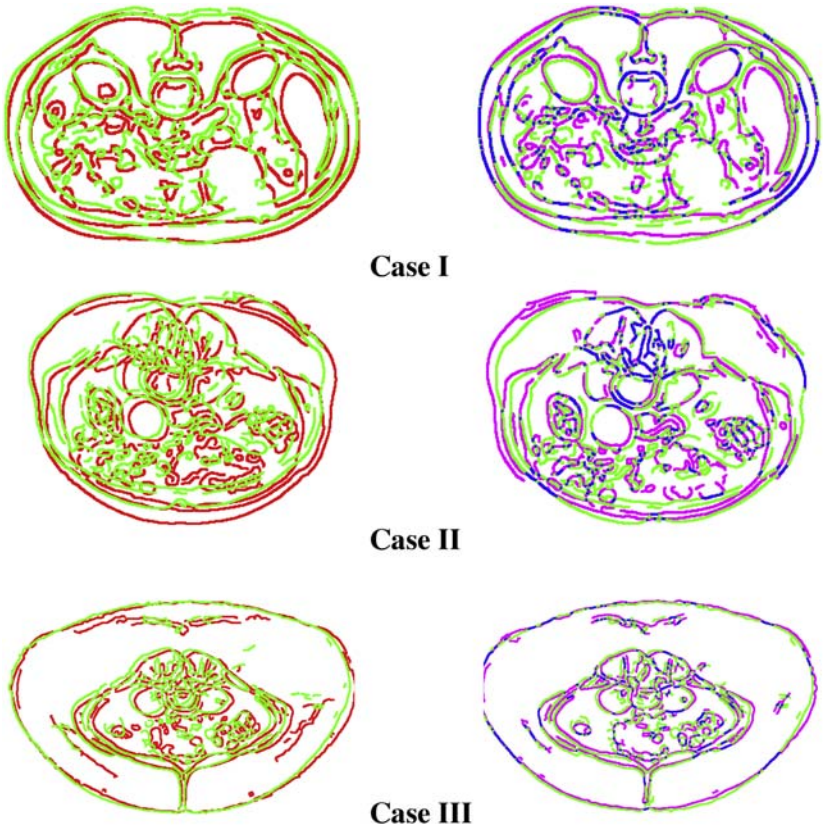

FIGURE 18.6 Qualitative evaluation of the registration accuracy for three computed tomography image data sets analyzed in Li et al. (2016) (transverse slices). Left column: comparison of the edges in the source and target images. Right column: comparison of the edges in the registered (i.e., deformed using the deformation computed by biomechanical models developed in this study) and target images. Edges in the source image are indicated by red color (light gray in print versions), edges in the target image by green, and edges in the registered image by pink. Good overlap (indicated by blue (dark gray in print versions) color, with some local misalignment) between the edges in registered and target images is evident. Copied from Li et al. (2016).

patient-specific biomechanical model in an automated manner. Based on the experimental evidence suggesting that soft tissues behave like hyperelastic materials, a neo-Hookean hyperelastic material model has been used. Computation of organ/tissue deformation for whole-body medical image registration is formulated as a "displacement−zero traction" problem of solid mechanics (Li et al., 2016). In this formulation, a biomechanical model is loaded by forced motion of the boundaries. Consequently, the computed deformations very weakly depend on the mechanical properties of the continuum (Li et al., 2016).

To validate the accuracy of the computed deformations, the contours/edges automatically detected using a Canny edge filter in the registered (i.e., source image deformed using the deformations predicted through the biomechanical model) and target images were visually compared in Li et al. (2016). The accuracy of the computations is typically assessed using various similarity measures to quantitatively compare the registered and target images. An edge-based Hausdorff distance metric on edges detected using a Canny filter. For over 99.5% of nodes, nodal displacements computed using models implemented using meshless (MTLED) and finite element (total Lagrangian explicit dynamics) models differed by less 1 mm (Fig. 18.6). As the resolutions of whole-body CT image data sets are $1.06 \times 1.06 \times 2.5$ (Case I), $0.8 \times 0.8 \times 2.5$ (Case II), and $0.98 \times 0.98 \times 2.5$ (Case III), this difference can be safely regarded as negligible.

18.6 CONCLUSIONS

Both strong and weak form MMs can be effectively applied in biomechanical applications. In contrast to mesh-based numerical methods, MMs are free of predefined information on the connectivity of the nodes and they can efficiently deal with cases concerning large deformations, often encountered in bioengineering applications, where FEM fails to solve accurately. Additionally, local refinement can be easily applied in a more straightforward manner than FEM and finite difference method.

This book belongs to Central Library BADJI Mokhtar-ANNABA UNIVERSITY Copyright Elsevier 2024

In real-world applications with increasing complexity, there is a strong necessity for accuracy and reduced computational cost. In some cases, we can sacrifice accuracy for the computational cost. FEM methods have dominated the field of biomechanics because they are easy to solve. When the mesh is constructed, the numerical solution can be easily obtained with high accuracy. On the other hand, when using MMs, it is straightforward to create the nodal distribution, but, up-to-date, there are no robust solvers able to efficiently solve the resulting sparse linear systems.

Concerning meshless collocation schemes, there is a continuous debate on their stability. It is mistakenly believed that the collocation methods are unstable, subjected to inaccuracies related to the distribution of the nodes and to the imposition of Neumann boundary conditions. This statement has no theoretical justification and, since collocation methods are a generalization of the FD method, there is no reason to be unstable. MLS methods, which are inherently unstable for local refinement (and for arbitrary positioning of the nodes), have motivated the debate on the instability of collocation methods. Newly developed interpolating schemes, such as Modified MLS and DC PSE, overcome this drawback and show a remarkable stability and reproducibility in a variety of applications. On the other hand, the accuracy of weak formulations such as EFG and MLPG depends on the integration scheme used. The latter is based on Gauss integration schemes, which are exact only for polynomial basis functions. The MTLED method is a stable, accurate, and reliable method based on a modified Galerkin method. It is explicit in nature, being well suited for parallel implementation.

MMs will find their place among the well-established numerical methods. Their inherent parallelization and accuracy makes them suitable for a variety of problems arising in science and engineering.

ACKNOWLEDGMENTS

This research was supported partially by the Australian Government through the Australian Research Council's Discovery Projects funding scheme (project DP160100714). The views expressed herein are those of the authors and are not necessarily those of the Australian Government or Australian Research Council. In addition, we wish to acknowledge the Raine Medical Research Foundation for funding G. R. Joldes through a Raine Priming Grant.

REFERENCES

Armato, S.G., McLennan, G., Meyer, C.R., Reeves, A.P., McNitt-Gray, M.F., Croft, B.Y., Clarke, L.P., 2008. The reference image database to evaluate response to therapy in lung cancer (rider) project: a resource for the development of change analysis software. Clinical Pharmacology and Therapeutics 84, 448−456.

Atluri, S.N., Zhu, T., 1998. A new meshless local Petrov-Galerkin (MLPG) approach in computational mechanics. Computational Mechanics 22, 117−127.

Belytschko, T., Lu, Y.Y., Gu, L., 1994. Element free Galerkin methods. International Journal for Numerical Methods in Engineering 37, 229−256.

Bourantas, G.C., Cheesman, B.L., Ramaswamy, R., Sbalzarini, I.F., 2016. Using DC PSE operator discretization in Eulerian meshless collocation methods improves their robustness in complex geometries. Computers and Fluids 136, 285−300.

Bourantas, G.C., Ghommem, M., Kagadis, G.C., Katsanos, K., Loukopoulos, V.C., Burganos, V.N., Nikiforidis, G.C., 2014. Real-time tumor ablation simulation based on the dynamic mode decomposition method. Medical Physics 41 (5), 053301.

Clark, K., Vendt, B., Smith, K., Freymann, J., Kirby, J., Koppel, P., Moore, S., Phillips, S., Maffitt, D., Pringle, M., 2013. The cancer imaging archive: maintaining and operating a public information repository. Journal of Digital Imaging 26, 1045−1057.

Fasshauer, G.E., 2007. Meshfree Approximation Methods with MATLAB. World Scientific.

Fornberg, B., Lehto, E., Powell, C., 2013. Stable calculation of Gaussian-based RBF-FD stencils. Computers and Mathematics with Applications 65, 627−637.

Frazer, R.A., Jones, W.P., Skan, S.W., 1937. Approximations to Functions and to the Solutions of Differential Equations. Great Britain Aero Counc. London. Rep. and Memo. No. 1799.

Hopp, T., Dietzel, M., Baltzer, P.A., Kreisel, P., Kaiser, W.A., Gemmeke, H., Ruiter, N.V., 2013. Automatic multimodal 2D/3D breast image registration using biomechanical FEM models and intensity-based optimization. Medical Image Analysis 17, 209−218.

Horton, A., Wittek, A., Joldes, G.R., Miller, K., 2010. A meshless total Lagrangian explicit dynamics algorithm for surgical simulation. International Journal for Numerical Methods in Biomedical Engineering 26, 977−998.

Joldes, G.R., Chowdhuty, H.A., Wittek, A., Doyle, B., Miller, K., 2015. Modified moving least squares with polynomial bases for scattered data approximation. Applied Mathematics and Computation 266, 893−902.

Joldes, G.R., Teakle, P., Wittek, A., Miller, K., 2015a. Adaptive quadrature in element-free Galerkin methods for solving structural problems. Engineering Computations 34 (3). http://dx.doi.org/10.1108/EC-01-2016-0017.

Joldes, G.R., Wittek, A., Miller, K., 2015b. Adaptive numerical integration in element-free Galerkin methods for elliptic boundary value problems. Engineering Analysis with Boundary Elements 51, 52−63.

Lancaster, P., Salkauskas, K., 1981. Surfaces generated by moving least squares method. Mathematics of Computation 37, 141−158.

Lanczos, C., 1938. Trigonometric interpolation of empirical and analytical functions. Journal of Mathematical Physics 17, 123−199.

This book belongs to Central Library BADJI Mokhtar-ANNABA UNIVERSITY

Copyright Elsevier 2024

Liszka, T., Orkisz, J., 1980. The finite difference method at arbitrary irregular grids and its application in applied mechanics. Computers and Structures 11, 83–95.

Liszka, T.J., Duarte, C.A.M., Tworzydlo, W.W., 1996. *hp*-meshless cloud method. Computer Methods in Applied Mechanics and Engineering 139, 263–288.

Liu, W.K., Jun, S., Li, S., Adee, J., Belytschko, T., 1995. Reproducing kernel particle methods for structural dynamics. International Journal for Numerical Methods in Engineering 38, 1655–1679.

Liu, G.R., Gu, Y.T., 2001a. A local radial point interpolation method (LR-PIM) for free vibration analyses of 2-D solids. Journal of Sound and Vibration 246 (1), 29–46.

Liu, G.R., Gu, Y.T., 2001b. A point interpolation method for two-dimensional solids. International Journal for Numerical Methods in Engineering 50, 937–951.

Li, X., Yankeelov, T.E., Peterson, T.E., Gore, J.C., Dawant, B.M., 2008. Automatic non-rigid registration of whole body CT mice images. Medical Physics 35, 1507–1520.

Li, M., Miller, K., Joldes, G.R., Doyle, B., Garlapati, R.R., Kikinis, R., Wittek, A., 2015a. Patient specific biomechanical model as whole-body CT image registration tool. Medical Image Analysis 22, 22–24.

Li, M., Wittek, A., Joldes, G.R., Miller, K., 2015b. Fuzzy tissue classification for nonlinear patient-specific biomechanical models for whole-body image registration. In: Joldes, G.R., Doyle, B., Wittek, A., Nielsen, P.M.F., Miller, K. (Eds.), Computational Biomechanics for Medicine: Imaging, Modeling and Computing. Munich, Germany.

Li, M., Miller, K., Joldes, G.R., Kikinis, R., Wittek, A., 2016. Biomechanical model for computing deformations for whole-body image registration: a meshless approach. International Journal for Numerical Methods in Biomedical Engineering e02771.

Melenk, J.M., Babuska, I., 1996. The partition of unity finite element method: basic theory and applications. Computer Methods in Applied Mechanics and Engineering 139, 289–314.

Miller, K., Joldes, G.R., Lance, D., Wittek, A., 2007. Total Lagrangian explicit dynamics finite element algorithm for computing soft tissue deformation. Communications in Numerical Methods in Engineering 23, 121–134.

Miller, K., Horton, A., Joldes, G.R., Wittek, A., 2012. Beyond finite elements: a comprehensive, patient-specific neurosurgical simulation utilizing a meshless method. Journal of Biomechanics 45, 2698–2701.

Nayroles, B., Touzot, G., Villon, P., 1992. Generalizing the finite element method: diffuse approximation and diffuse elements. Computational Mechanics 10, 307–318.

Netuzhylov, H., Zilian, A., 2009. Space-time meshfree collocation method: methodology and application to initial-boundary value problems. International Journal for Numerical Methods in Engineering 80, 355–380.

Slater, J.C., 1934. Electronic energy bands in metals. Physical Reviews 45, 794–801.

Stromqvist, B., Fritzell, P., Hagg, O., Jonsson, B., Surg, S.S., 2009. The Swedish Spine Register: development, design and utility. European Spine Journal 18, 294–304.

Toews, M., Wells, W.M., 2013. Efficient and robust model-to-image alignment using 3D scale-invariant features. Medical Image Analysis 17, 271–282.

Wang, J.G., Liu, G.R., 2002. A point interpolation meshless method based on radial basis functions. International Journal for Numerical Methods in Biomedical Engineering 54, 1623–1648.

Wittek, A., Miller, K., Kikinis, R., Warfield, S.K., 2007. Patient-specific model of brain deformation: application to medical image registration. Journal of Biomechanics 40, 919–929.

Wittek, A., Joldes, G., Couton, M., Warfield, S.K., Miller, K., 2010. Patient-specific non-linear finite element modelling for predicting soft organ deformation in real-time; Application to non-rigid neuroimage registration. Progress in Biophysics and Molecular Biology 103, 292–303.

Zhang, J.Y., Joldes, G.R., Wittek, A., Horton, A., Warfield, S.K., Miller, K., 2012. Neuroimage as a biomechanical model. Towards new computational biomechanics of the brain. In: Nielsen, P.M.F., Miller, K., Wittek, A. (Eds.), Computational Biomechanics for Medicine: Deformation and Flow. Springer, New York, pp. 19–28.

Zhang, J.Y., Joldes, G.R., Wittek, A., Miller, K., 2013. Patient-specific computational biomechanics of the brain without segmentation and meshing. International Journal for Numerical Methods in Biomedical Engineering 29, 293–308.

Zhu, T., Zhang, J.D., Atluri, S.N., 1998. A local boundary integral equation (LBIE) method in computational mechanics and meshless discretization approach. Computational Mechanics 21, 223–235.

This book belongs to Central Library BADJI Mokhtar-ANNABA UNIVERSITY Copyright Elsevier 2024

This page intentionally left blank

This book belongs to Central Library BADJI Mokhtar-ANNABA UNIVERSITY

Copyright Elsevier 2024

Chapter 19

The Finite Volume Particle Method: Toward a Meshless Technique for Biomedical Fluid Dynamics

N. Quinlan[1] and L. Lobovský[2]
[1]NUI Galway, Galway, Ireland; [2]University of West Bohemia, Plzeň, Czech Republic

19.1 INTRODUCTION

Very large structural deformations are characteristic of biomechanical fluid−structure interaction (FSI) systems. In heart valves, in particular, leaflet motion is on the order of the scale of the flow domain. Artery walls and red blood cells also undergo relatively large deformations. In this chapter we describe an emerging meshless method, which has the potential to solve some the problems of the difficulties of modeling fluid flow with large wall motion and coupled fluid−structure dynamics.

Our long-term goal is to develop a CFD method that can handle moving boundaries in a robust, general manner, with the potential for coupling to solid mechanics solvers for full FSI. Mechanical heart valves (MHVs) are considered as an initial target application. These present an extremely challenging case for computational fluid dynamics with large-scale wall motion, while presenting a relatively simple structural problem. MHVs are more durable than bioprosthetic valves, including transcatheter implants, but require lifelong anticoagulation treatment to manage the risk of thrombosis and thromboembolism due to nonphysiological materials and fluid dynamics. Because of their durability, they account for a significant proportion of valve replacements, particularly in younger patients. The fluid dynamics of prosthetic heart valves and MHVs in particular are reviewed comprehensively by several authors (Yoganathan et al., 2004, 2005; Kidane et al., 2009; Dasi et al., 2009). Although the first MHV was implanted in 1952, innovation on the basic concept continues. Notably, a recent clinical trial (Puskas et al., 2014) has shown that lower anticoagulation levels are appropriate for patients with the On-X bileaflet MHV, a device with modifications to geometry, kinematics, and materials with respect to the established designs (Chaudhary et al., 2016). This progress hints at potential for further optimization toward a non-thrombogenic MHV. In other mature mechanical technologies—in the aerospace industry, for example—computational simulation is a critical component of innovation and optimization. However, in the development of heart valve prostheses including MHVs, computational modeling is not yet routine.

There have been few highly resolved fully dynamic models of fluid dynamics around heart valves of any type. Dasi et al. (2017) recently noted that "the moving boundaries of the heart valve leaflets under complex flow conditions make [fluid-structure interaction simulation] an exceptionally difficult problem." Sotiropoulos and Borazjani (2009) identify two major classes of FSI methods for large structural deformations. In moving grid methods, the global mesh conforms to the moving boundaries and therefore must be continuously deformed and/or regenerated. In fixed grid methods, moving boundaries interact with a nonmoving (often Cartesian) background mesh through specially formulated boundary conditions such as Peskin's immersed boundary with a diffuse interface (Peskin, 1972) and sharp-interface immersed boundary methods (Vigmostad et al., 2010; Borazjani et al., 2008). Overset grids (Borazjani et al., 2013) and the lattice Boltzmann method (Krafczyk et al., 1998) have also been used with some success to model MHVs.

Numerical Methods and Advanced Simulation in Biomechanics and Biological Processes. https://doi.org/10.1016/B978-0-12-811718-7.00019-8
Copyright © 2018 Elsevier Ltd. All rights reserved.

This book belongs to Central Library BADJI Mokhtar-ANNABA UNIVERSITY
Copyright Elsevier 2024

All the above methods are essentially efforts to remedy the essential difficulties of modeling a moving wall on a mesh. Smoothed particle hydrodynamics (SPH) (Monaghan, 2012) is a meshless method, which has been widely adopted for fluid dynamics problems with moving interfaces. Shahriari et al. (2012) applied the technique to MHVs. The advantage of meshless methods such as SPH is that computational nodes move with local material velocity without any explicit connectivity. This avoids the difficulties of dealing with a moving interface on a stationary mesh.

In the present work we explore an alternative meshless approach, the finite volume particle method (FVPM) (Hietel et al., 2000; Nestor et al., 2009; Quinlan et al., 2014). This may be understood as a hybrid of SPH and the classical mesh-based finite volume method. It inherits the meshless character of SPH along with the conservation and consistency properties of finite volume methods. We will describe the basic method and the extensions required for practical application to cardiovascular flow. Detailed validation will be presented for a benchmark problem of flow coupled with rigid body motion, and a preliminary application to a 2D MHV model will be shown.

19.2 THE FINITE VOLUME PARTICLE METHOD

19.2.1 Smoothed Particle Hydrodynamics and the Finite Volume Particle Method

Perhaps the most widely used meshless method for fluid dynamics is SPH, created by Gingold and Monaghan (1977) and Lucy (1977) for astrophysical applications. The method was later adopted and developed for fluid mechanics (Shadloo et al., 2016; Monaghan, 2012) and other engineering applications.

In SPH, the material is discretized with computational points, called "particles," which move with Lagrangian velocity. They represent material packets of constant mass, governed by Newtonian mechanics, rather than molecules or any other physical particles. The governing partial differential equations are approximated with summations over neighboring particles. Detailed derivation of SPH is beyond the scope of this chapter, but the structure of the method can be illustrated with this common form of the SPH inviscid momentum equation:

$$\frac{\mathrm{d}\mathbf{u}_i}{\mathrm{d}t} = \sum_j \nabla W_{ij}(\mathbf{x}) \quad \frac{p_i}{\rho_i^2} + \frac{p_j}{\rho_j^2}\Bigg) m_j. \tag{19.1}$$

Here, ∇W_{ij} denotes the gradient of $W_i(\mathbf{x})$, the kernel function of particle i, evaluated at $\mathbf{x}_j$, the location of particle j. The index j ranges over all neighbor particles of i, p is pressure, ρ is density, and m is particle mass. Eq. (19.1) originates from a smoothing operation that approximates the discrete field with a continuous differentiable one, used to calculate the pressure gradient.

The kernel function $W_i(\mathbf{x})$ is usually smooth, bell shaped, and centered on the particle i, as shown in Fig. 19.1. Most often, the kernel is constructed such that $W_i(\mathbf{x}) = W(|\mathbf{x} - \mathbf{x_i}|, h)$, where $W(r, h)$ is a generic radially symmetric kernel function and h is the smoothing length. It is compactly supported such that it falls to zero at distance greater than $2h$ (by convention) from particle i. Because Eq. (19.1) is symmetric in i and j, the contribution of j to the momentum of i is equal and opposite to the contribution of i to j. Thus, momentum is conserved exactly.

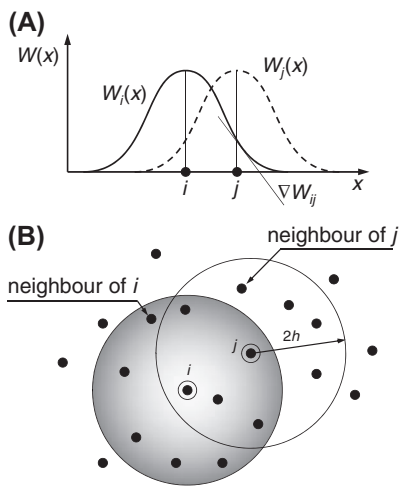

FIGURE 19.1 Schematic diagrams of the smoothed particle hydrodynamics kernel function in (A) one and (B) two dimensions.

This book belongs to Central Library BADJI Mokhtar-ANNABA UNIVERSITY
Copyright Elsevier 2024

However, the standard SPH formulation is not zero-order consistent. For example, in a uniform field with $p = p_0$ and $\rho = \rho_0$, with uniform particle mass m_0, the acceleration of particle i is computed as $2\frac{p_0}{\rho_0^2} m_0 \sum_j \nabla W_i(\mathbf{x})|_{\mathbf{x}=\mathbf{x}_j}$. This does not evaluate to zero for an arbitrary distribution of particles. More precisely, it has been shown that the SPH numerical approximation does not tend to the exact result as the particle size h tends to zero while the ratio of particle spacing to particle size $\Delta x/h$ is held constant (or the number of neighbors is held constant), although the error does tend to zero if $\Delta x/h$ is reduced sufficiently quickly while reducing and h (Quinlan et al., 2006).

Several authors have developed corrections to W and ∇W, which restore consistency of the zeroth order (i.e., exactly reproducing the values and gradients of a constant-valued field) or higher (Liu et al., 1995; Bonet and Lok, 1999; Dilts, 1999). However, the modified kernel must be computed locally for each particle, dependent on the positions of its neighbor particles. Thus, it cannot ensure an equal and opposite exchange between a pair of neighbors, and conservation is violated. In this approach it is impossible to preserve consistency of any order along with conservation.

A weakness of this theoretical criticism is that SPH particle distributions are not actually arbitrary. They are initialized systematically and evolve in a Lagrangian manner. It could be argued that consistency on an arbitrary static particle set is not necessary for convergence. The range of successful SPH applications (e.g, Shadloo et al., 2016) continues to grow in quality and quantity, regardless of theoretical concerns. Very recently, there has been progress toward a comprehensive formal proof of convergence (Zisis et al., 2016), but the question remains open. For comprehensive analysis and review of the state of the art in SPH, the reader is referred to Violeau (2012).

While development within the SPH formalism continues, FVPM can be understood as an alternative effort to retain both consistency and conservation in a particle framework. It was created by Hietel et al. (2000) and independently by Ismagilov (2006) as the smooth volume method. The basic formulation is

$$\frac{\mathrm{d}\mathbf{U}_i}{\mathrm{d}t} = \sum_j \beta_{ij} \cdot \mathbf{F}_{ij}, \tag{19.2}$$

where $\mathbf{U}$ is a vector of conserved quantities and $\mathbf{F}_{ij}$ is the flux exchanged between particles i and j. The vector $\boldsymbol{\beta}_{ij}$ is loosely analogous to ∇W_{ij} in SPH, which ascribes a strength and direction to the interaction between two particles. In fact it is more closely related to the intercell area in a finite volume mesh method, as discussed in the next section. It is defined by

$$\beta_{ij} = \int_\Omega \frac{W_i(\mathbf{x})\nabla W_j(\mathbf{x}) - W_j(\mathbf{x})\nabla W_i(\mathbf{x})}{\left(\sum_k W_k(\mathbf{x})\right)^2} \mathrm{d}\mathbf{x}, \tag{19.3}$$

where $W_i(\mathbf{x})$ is similar to the SPH kernel but is referred to as the volume weight function in the present work. The integrand of Eq. (19.3) is zero everywhere except regions in which both $W_i(\mathbf{x})$ and $W_j(\mathbf{x})$ are nonzero—that is, where the support volumes of i and j overlap. Particles with overlapping supports are considered neighbors, as illustrated in Fig. 19.2. The formulation (19.3) provides the desired properties of conservation, since $\beta_{ij} = -\beta_{ij}$ (ensuring interactions are equal and opposite), and zero-order consistency, since $\sum_j \beta_{ij} = 0$ (uniform flux results in zero rate of change).

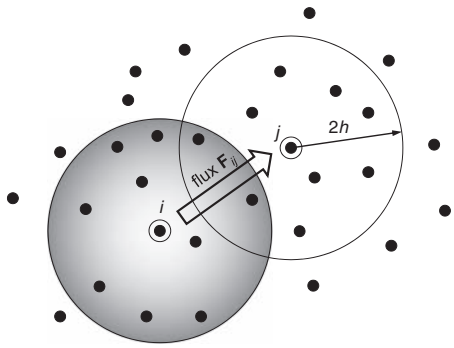

FIGURE 19.2 Schematic diagrams of finite volume particle method particle supports in two dimensions.

This book belongs to Central Library BADJI Mokhtar-ANNABA UNIVERSITY
Copyright Elsevier 2024

19.2.2 Finite Volume Particle Method as a Finite Volume Method

In this section, the systematic derivation of Eqs. (19.2) and (19.3) is outlined. Full details and further analysis are given by Hietel et al. (2000) and Junk (2003).

The approach follows the structure of a finite volume method. The equation system to be solved is written in conservation form as

$$\frac{\partial \mathbf{U}}{\partial t} + \nabla \cdot \mathbf{F}(\mathbf{U}) = 0, \tag{19.4}$$

where $\mathbf{U}$ is the vector of conserved variables and $\mathbf{F}$ is the flux function. As in SPH, a function $W_i(\mathbf{x},t)$ is now introduced that is nonzero only inside Ω_i, defined as the support of particle i. This is used to construct a test function:

$$\psi_i(\mathbf{x},t) = \frac{W_i(\mathbf{x},t)}{\sum_j W_j(\mathbf{x},t)}. \tag{19.5}$$

Eq. (19.4) is multiplied by ψ_i and integrated over space to yield

$$\frac{\mathrm{d}}{\mathrm{d}t}\int_\Omega \psi_i(\mathbf{x},t)\mathbf{U}\mathrm{d}\mathbf{x} - \int_\Omega \left(\nabla\psi_i(\mathbf{x},t)\cdot\mathbf{F}(\mathbf{U}) + \mathbf{U}\frac{\partial\psi_i}{\partial t}\right)\mathrm{d}\mathbf{x} + \int_{\partial\Omega}\psi_i(\mathbf{x},t)\mathbf{F}(\mathbf{U})\cdot\mathbf{n}\mathrm{d}S = 0. \tag{19.6}$$

Now the flux $\mathbf{F}(\mathbf{U})$ is approximated by an average value over the i–j overlap region, and $\mathbf{U}$ in the first integral is similarly replaced with an average $\mathbf{U}_i$ over Ω_i. After expansion of ψ_i and some manipulation, this leads to

$$\frac{\mathrm{d}}{\mathrm{d}t}(\mathbf{U}_i V_i) + \sum_j \beta_{ij}\cdot\mathscr{G}(\mathbf{U}_i,\mathbf{U}_j,\dot{\mathbf{x}}_i,\dot{\mathbf{x}}_j) + \beta_i^b\cdot\mathscr{G}_i^b = 0, \tag{19.7}$$

where $\mathscr{G}(\mathbf{U}_i,\mathbf{U}_j,\dot{\mathbf{x}}_i,\dot{\mathbf{x}}_j)$ is the numerical flux, a function of the states of particles i and j and the transport velocities $\dot{\mathbf{x}}$ of both particles (not necessarily equal to the fluid velocity). The boundary term is

$$\beta_i^b = \int_{\partial\Omega}\frac{W_i(\mathbf{x})}{\sum_j W_j(\mathbf{x})}\mathbf{n}\mathrm{d}S \tag{19.8}$$

and V_i is

$$V_i = \int_\Omega \psi_i(\mathbf{x},t)\mathrm{d}\mathbf{x}. \tag{19.9}$$

The only differences between Eq. (19.7) and the mesh-based finite volume method are $\sum_j \beta_{ij}$ and $\sum_j \beta_i^b$, which take the place of cell–cell and cell–boundary interface areas, respectively, in a mesh, and V_i, which is called the particle volume, by analogy. Junk (2003) has shown that the analogy is rigorous: β_{ij} has the properties required of cell face areas to ensure convergence of the classical mesh-based finite volume. Junk also showed that if $W_i(\mathbf{x}, t)$ is defined to be 1 inside polyhedral cell i and zero elsewhere, with the domain fully covered by such cells, β_{ij} reduces simply to the cell–cell interface area. The mesh-based finite volume method then emerges as a special case of FVPM.

The test function $\psi_i(\mathbf{x},t) = W_i(\mathbf{x},t)/\sum_j W_j(\mathbf{x},t)$ is a partition of unity. It can be interpreted as the fraction of a local volume element allocated to particle i. Because $\sum_i \psi_i = 1$, the total spatial volume is shared among all particles that cover each point. The normalizing function $\sum_j W_j(\mathbf{x},t)$ and ψ_i are plotted in Fig. 19.3 for a sample 1D particle distribution.

Thus, FVPM can be understood as a true finite volume method in which cells are allowed to overlap. Because they can overlap, they can also move in any desired manner, allowing Eulerian, Lagrangian, and arbitrary Lagrangian–Eulerian (ALE) schemes. It can accommodate many techniques developed in the finite volume literature, including any numerical flux function.

19.2.3 Computation of Interparticle Area

The calculation of $\boldsymbol{\beta}_{ij}$ proved to be a critical step in early development of FVPM. With W defined as smooth polynomials or piecewise polynomials, as shown in Fig. 19.3, the integral in Eq. (3) could be computed only by numerical quadrature. This

This book belongs to Central Library BADJI Mokhtar-ANNABA UNIVERSITY
Copyright Elsevier 2024

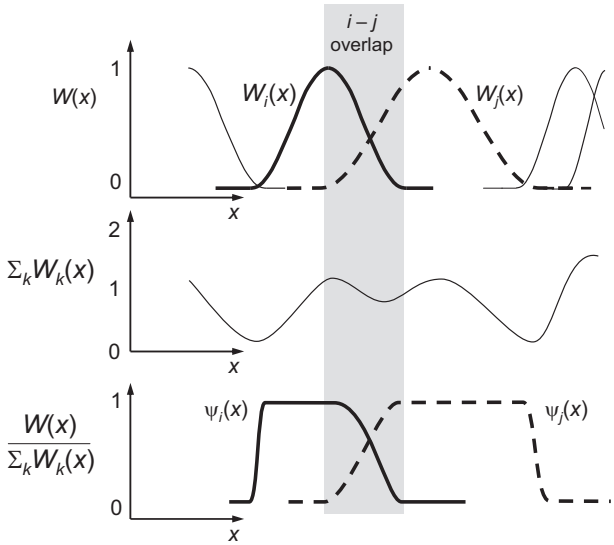

FIGURE 19.3 Smooth finite volume particle method volume weight functions in one dimension, with the resulting normalization functions and test functions. *Used with permission from Springer. From Quinlan, N.J., Nestor, R.M., 2011. Fast exact evaluation of particle interaction vectors in the finite volume particle method. In: Meshfree Methods for Partial Differential Equations V. Springer, pp. 219–234.*

typically requires 4^d to 8^d quadrature points (where d is the number of dimensions) in every particle pairwise overlap to achieve acceptable accuracy, and resulting approximate interparticle areas do not exactly satisfy the conservation and zero-order consistency properties. Correction techniques (Keck and Hietel, 2005; Teleaga, 2005) have been proposed to restore either of these properties, but not both simultaneously. Quadrature operations to compute $\boldsymbol{\beta}_{ij}$ and V_i can account for over 90% of computation time.

Quinlan et al. (Quinlan and Nestor, 2011; Quinlan et al., 2014) introduced top-hat weight functions in 2D, defined such that $W_i(\mathbf{x}) = 1$ inside particle i and 0 elsewhere. These and the resulting piecewise-constant test functions are shown in Fig. 19.4. Volume integrals of these functions reduce to integrals over particle support boundaries (because only there is $\nabla W \neq 0$). The integrals can be computed exactly and much more quickly than by quadrature, yielding a six- to eightfold

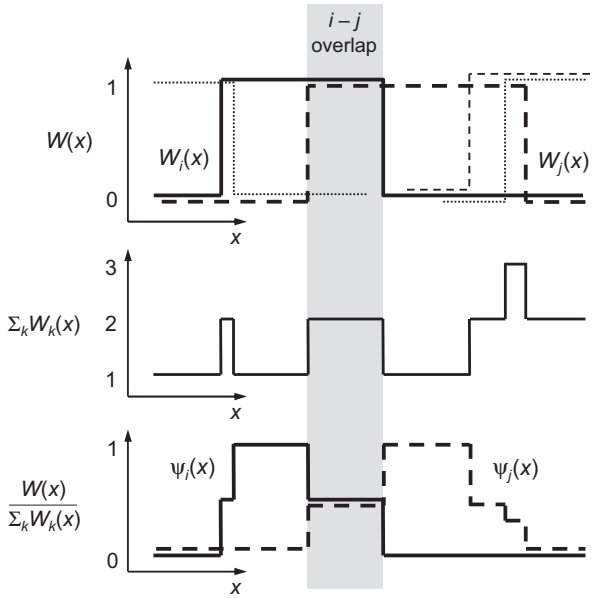

FIGURE 19.4 Top-hat finite volume particle method volume weight functions in one dimension, with the resulting normalization functions and test functions. *Used with permission from Springer. From Quinlan, N.J., Nestor, R.M., 2011. Fast exact evaluation of particle interaction vectors in the finite volume particle method. In: Meshfree Methods for Partial Differential Equations V. Springer, pp. 219–234.*

This book belongs to Central Library BADJI Mokhtar-ANNABA UNIVERSITY Copyright Elsevier 2024

reduction in total computation time. Convergence tests on a benchmark simulation show that, with this method, numerical error depends primarily on the particle size and only very weakly on the number of neighbors (Quinlan et al., 2014), as long as particles cover the domain without gaps. This enables simulations with relatively small numbers of neighbors, further reducing computational costs.

Kaland (2013) developed another exact method for exact calculation of interparticle area, using splines as weight functions. To date this method has not been implemented in multiple dimensions.

19.2.4 Extensions of the Basic Method

The capability to model viscous flow was introduced by Nestor et al. (2009), using first-order consistency-corrected SPH methods to determine velocity gradients, and hence viscous stress, at particle interfaces. In the same article, the MUSCL approach was introduced to enhance accuracy. Gradients are approximated at particle barycenters (again using SPH techniques) and used to extrapolate to particle interfaces. The Riemann problem between these extrapolated states is solved to determine the flux between the particles. In the examples presented in this chapter, the AUSM+-up approximate Riemann solver of Liou (2006) is used. Pressure projection techniques for incompressible flow have been implemented in FVPM by Keck and Hietel (2005) and Nestor et al. (2009). These are examples of the direct implementation of standard finite volume techniques in FVPM that has been validated for canonical laminar viscous flows such as the lid-driven cavity, Taylor−Green flow, and Rayleigh−Taylor instability at Reynolds numbers up to 1000 (Nestor et al., 2009; Quinlan et al., 2014).

19.3 INLET AND OUTLET BOUNDARY CONDITIONS IN FINITE VOLUME PARTICLE METHOD

The most common applications of SPH and related methods entail unbounded astrophysical domains and wall-bounded transient free-surface flows. Cardiovascular and other biomedical flow problems, however, involve long-duration pulsatile flows where the domain must be bounded by one or more inlets or outlets. In a particle method, particles must be introduced at or near an inlet in manner that is consistent with the discretization of the interior domain while prescribing the required analytical boundary condition. The motion of particles relative to the boundary introduces a layer of complexity, which is not present in a mesh-based method.

In Fig. 19.5, a particle is shown in the process of entering the domain through an inflow boundary. The particle is initialized in a position where it first interacts with the boundary. The particles effective support volume consists only of the segment of the particle's nominal volume (circle/sphere), which lies inside the domain (i.e., to the right of the boundary in Eq. 19.5). The calculation of particle volume according to Eq. (19.9) ensures that the portion of the particle outside the boundary does not contribute to volume. As the particle crosses the boundary, its volume increases smoothly until it lies fully inside the domain.

An appropriate boundary condition must be applied on the boundary segment that intersects with the particle. One approach is to prescribe velocity at an inflow boundary and determine pressure by extrapolation from the domain interior. Correspondingly, at an outflow boundary, pressure should be prescribed and velocity should be determined from the interior upstream. These pressure and velocity boundaries reflect acoustic waves, which may traverse the domain many times with little, if any, attenuation. In the context of a weakly compressible approximation to a nearly incompressible fluid such as blood, these waves are unphysical. Very long computational times may be required to dissipate these waves and reach a steady solution. In unsteady flow, they can overwhelm the underlying physical unsteadiness.

Instead, nonreflecting boundary conditions can be implemented by recasting the governing equations in terms of Riemann invariants, which are propagated along upstream and downstream-running waves (Moretti, 1969). In practice,

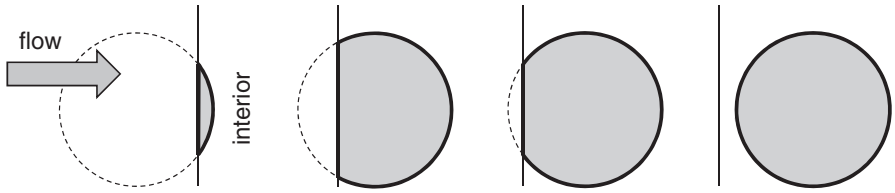

FIGURE 19.5 Schematic diagram of a finite volume particle method particle moving from left to right across an inflow boundary. The gray area is the active volume of the particle.

This book belongs to Central Library BADJI Mokhtar-ANNABA UNIVERSITY Copyright Elsevier 2024

however, it is difficult to implement characteristic-based boundary conditions rigorously because often the characteristic variables at boundaries are not known, or are dependent on the solution, for a physical problem under investigation. Giles proposed alternative boundary conditions based on a linearized set of governing equations, assuming a one-dimensional flow near boundaries, with small perturbations from a reference state. The pressure and velocity in the reference state are prescribed as part of the boundary condition and should approximate the known physical boundary conditions. Giles' approach was adapted for SPH by Lastiwka et al. (2009) and is extended to FVPM with minor modifications. At an inlet boundary, primitive variables (pressure and velocity) are determined by the interaction of Riemann invariants propagated from the particle barycenter to the boundary and from outside the domain to the boundary. The treatment is the same for inlet and outlet particles, except that inlet particles must be initialized with the reference inlet velocity and pressure. Outlet particles are simply deleted when they have no volume remaining inside the domain.

19.4 VALIDATION FOR FLOW COUPLED WITH RIGID BODY MOTION

The defining challenge of biomedical fluid dynamics is FSI with large-scale wall motion. This capability has been developed and validated in detail for flow about a cylinder with vortex-induced vibration. The simulation was described in detail by Nestor and Quinlan (2013) and is presented in outline in this section.

FVPM has been used to simulate two-dimensional flow at Reynolds number $Re_D = 100$ about a rigid cylinder that is elastically mounted with two translational degrees of freedom, as shown in Fig. 19.6. This problem has been extensively studied computationally (Williamson and Roshko, 1988; Govardhan and Williamson, 2000; Shiels et al., 2001; Singh and Mittal, 2005; Placzek et al., 2009) and experimentally (Anagnostopoulos and Bearman, 1992). Incompressible fluid approaches the cylinder at a uniform velocity. The cylinder may move parallel to the flow or transverse to it, but is restrained in both directions by linear elastic springs of equal stiffness. The cylinders rigid body dynamics are characterized by the dimensionless reduced velocity $U_r = U_\infty/(f_n d)$, where U_∞ is the freestream velocity, d is diameter, and f_n is the natural frequency, a function of spring stiffness and cylinder mass. At Reynolds number $Re_d = \rho U_\infty d/\mu$ higher than 45, the separated flow is unstable and results in alternate vortex shedding (the von Kármán street), which causes an oscillating transverse load. The interaction between vortex shedding and rigid body dynamics leads to complex behavior, particularly when the vortex-shedding frequency is close to the structural natural frequency.

FVPM is used for this problem in ALE mode, as shown in Fig. 19.7. Most particles are initially distributed on a Cartesian grid at a spacing of $\Delta x = d/5$. Near the cylinder, particles are spaced at $d/50$, to enable better resolution of high gradients near the surface. Particles near the cylinder move with the cylinder velocity to ensure that this fine resolution is retained. Outside this region, the particles are fully Eulerian (zero transport velocity). In an intermediate zone between the cylinder and the walls, the particle motion is determined by interpolation between the cylinder velocity and the zero background velocity. (In a mesh-based method, this would result in large element distortion.) This hybrid scheme ensures that a satisfactory particle distribution is retained at all times, particularly near the cylinder.

A sample instantaneous result is illustrated in Fig. 19.8. At the condition shown, the FVPM solution predicts the so-called C(2S) vortex-shedding mode in which vortices coalesce downstream of the cylinder (Williamson and Roshko, 1988). Operating conditions were varied by varying the structural natural frequency while holding the Reynolds number constant. Results are presented in Fig. 19.9, compared with results of Singh and Mittal (Peskin, 1972) from a finite

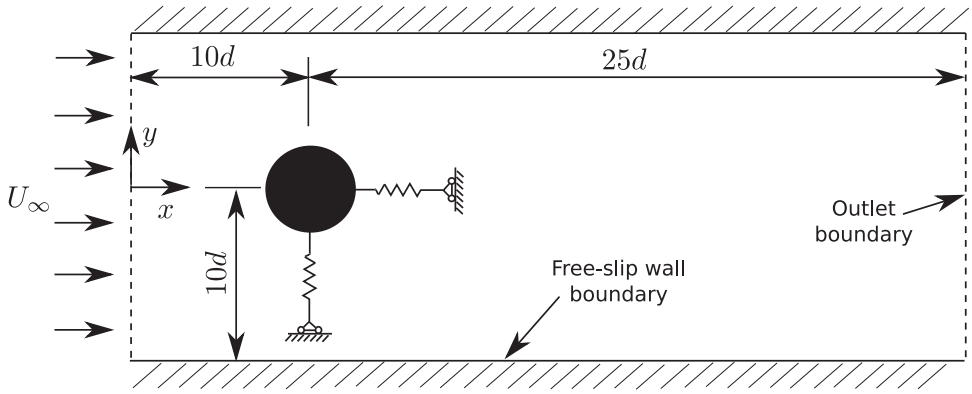

FIGURE 19.6 Configuration of the oscillating cylinder test. *Taken from Nestor, R.M., Quinlan, N.J., 2013. Application of the meshless finite volume particle method to flow-induced motion of a rigid body. Computers and Fluids 88, 386–399.*

This book belongs to Central Library BADJI Mokhtar-ANNABA UNIVERSITY Copyright Elsevier 2024

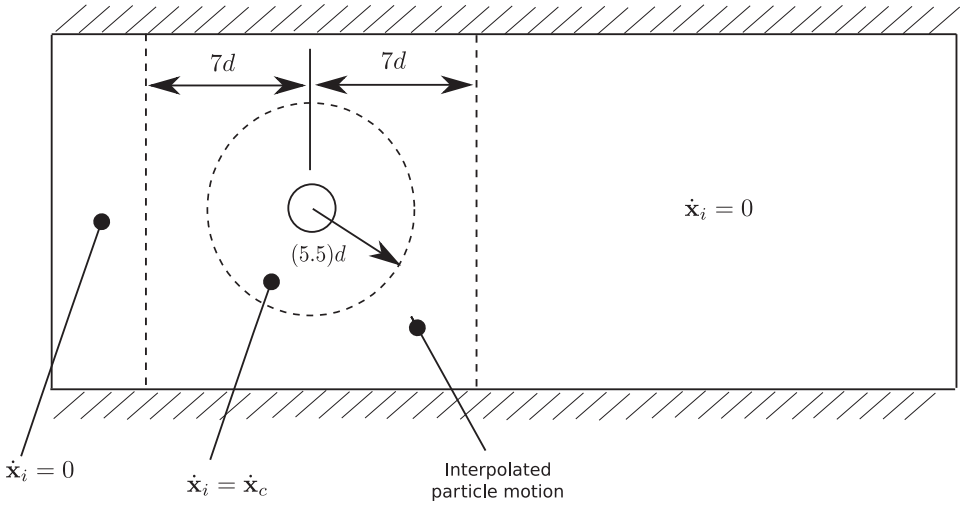

FIGURE 19.7 Application of particle motion schemes in the oscillating cylinder test. *Taken from Nestor, R.M., Quinlan, N.J., 2013. Application of the meshless finite volume particle method to flow-induced motion of a rigid body. Computers and Fluids 88, 386–399.*

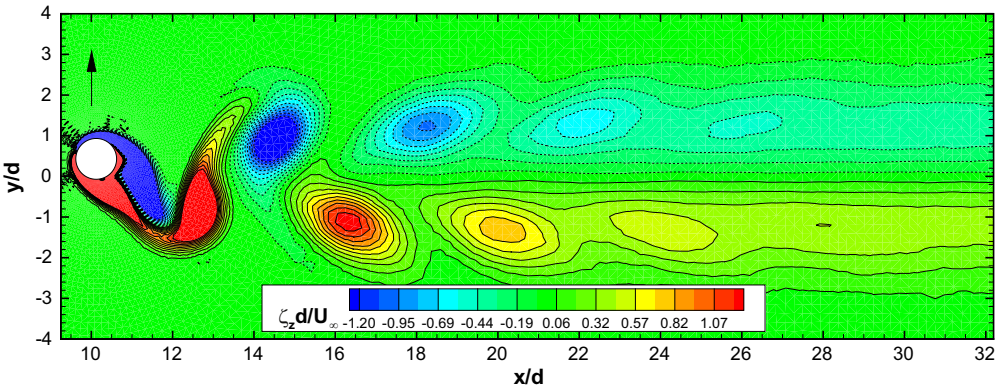

FIGURE 19.8 An instantaneous nondimensional vorticity field predicted by finite volume particle method for vortex-induced vibration of a circular cylinder at Reynolds number $Re_d = 100$, reduced velocity $U_r = 5.00$, and dimensionless time $t^* = 222$. The *arrow* indicates the instantaneous direction of the transverse cylinder motion. *Taken from Nestor, R.M., Quinlan, N.J., 2013. Application of the meshless finite volume particle method to flow-induced motion of a rigid body. Computers and Fluids 88, 386–399.*

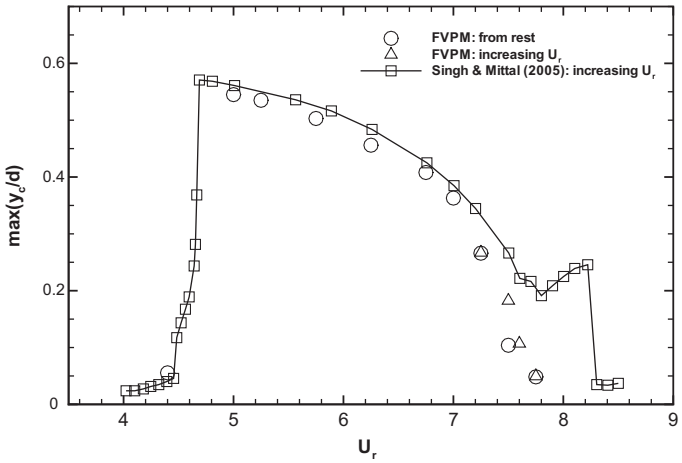

FIGURE 19.9 Variation of maximum nondimensional transverse cylinder displacement max(y_c)/d with the reduced velocity U_r for vortex-induced vibration of a circular cylinder at $Re_d = 100$. Comparison between finite volume particle method (FVPM) and the results of the finite element method of Singh and Mittal (2005). *Taken from Nestor, R.M., Quinlan, N.J., 2013. Application of the meshless finite volume particle method to flow-induced motion of a rigid body. Computers and Fluids 88, 386–399.*

This book belongs to Central Library BADJI Mokhtar-ANNABA UNIVERSITY Copyright Elsevier 2024

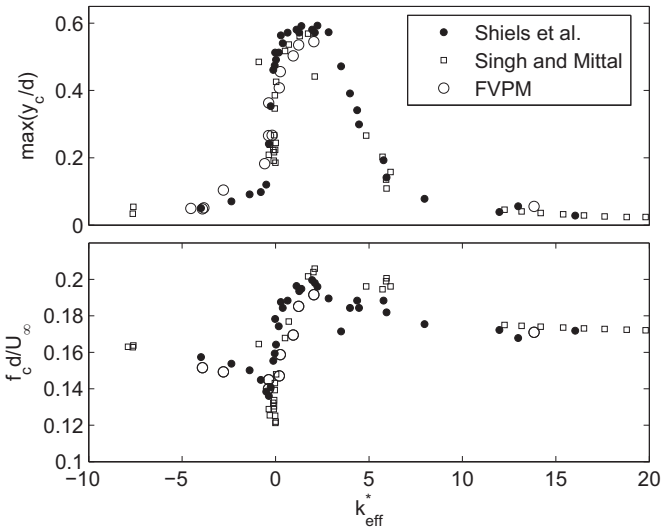

FIGURE 19.10 Variation of maximum nondimensional transverse cylinder displacement max(y_c)/d and nondimensional transverse cylinder vibration frequency $f_c d/U_\infty$ with the effective stiffness parameter k^*_{eff} of Shiels et al. (2001). Comparison between finite volume particle method (FVPM), the finite element method of Singh and Mittal (2005) and the highly resolved vortex method of Shiels et al. (2001). *Taken from Nestor, R.M., Quinlan, N.J., 2013. Application of the meshless finite volume particle method to flow-induced motion of a rigid body. Computers and Fluids 88, 386–399.*

element method with deforming mesh. Good agreement is evident in the predicted amplitude of oscillation over most of the range investigated. The results display high amplitudes for $4.5 \lesssim U_r \lesssim 7.8$. In this range, the vortex-shedding frequency for a fixed cylinder is close to the natural frequency of oscillation, and the vortex-shedding frequency "locks in" to the structural frequency, resulting in structural resonance. FVPM agrees with the literature on the onset of lock-in and the amplitudes of oscillation in the lock-in range and at lower frequency. To test for sensitivity to initial conditions, simulations were carried out both with gradually increasing U_r increasing from one test condition to another (labeled "increasing" in Fig. 19.9) and with simulations restarted for each condition ("from rest"). Results were nearly independent of the mode of start-up.

In Fig. 19.10, FVPM results are compared with the highly resolved vortex method calculations of by Shiels et al. (2001), as well as the results of Singh and Mittal. Data are presented in terms of the effective stiffness parameter of Shiels et al.

$$k_{eff} = \frac{k - 4\pi^2 m f_c^2}{\frac{1}{2}\rho U_\infty^2} = 8\pi^2 M^* \left(f_n^{*2} - f_c^{*2}\right), \tag{19.10}$$

which combines the structural inertia and stiffness in a single parameter. Here, $f_c^* = f_c d/U_\infty$, f_c is the cylinder oscillation frequency, and $f_n^* = f_n d/U_\infty = 1/U_r$. FVPM results agree closely with those of Shiels et al. (2001) for amplitude and frequency. In the region $-0.36 \lesssim k^*_{eff} \lesssim 0.01$ and $f_c^* \lesssim 0.13$, corresponding to $U_r \gtrsim 7.5$ in Fig. 19.9, FVPM agrees more closely with Shiels et al. than with Singh and Mittal.

19.5 APPLICATION TO SIMPLIFIED MECHANICAL HEART VALVE

In this section we present application of FVPM to simulate opening of a highly simplified MHV leaflet opening. Additional challenges of this test case, compared to the oscillating cylinder, are large rotational motion and the close proximity of the leaflet to other walls (when in or near its closed position). To deal with these cases, we introduce a new ALE particle motion scheme, described in Section 19.5.1.

19.5.1 Control of Particle Distribution Near Moving Bodies

The purposes of meshless methods are to free engineers and scientists from the difficult task of mesh generation and to reduce mesh sensitivity of solutions. In addition, in SPH and related methods, Lagrangian particle motion provides low dissipation and sharp resolution of interfaces. However, the physical velocity field does not necessarily distribute particles

This book belongs to Central Library BADJI Mokhtar-ANNABA UNIVERSITY Copyright Elsevier 2024

(the computational nodes) in a manner that is desirable from a numerical point of view. For example, with Lagrangian particles, we have observed failure of the simulation due to a loss of particle cover when one wall accelerates away from another. Available remedies for poor particle distribution include artificial pressure in SPH (Monaghan, 1999), ALE particle velocity correction in FVPM (Nestor et al., 2009), and the related particle shifting in SPH (Lind et al., 2012). These approaches enhance particle distribution, but require a degree of application-specific parameter tuning, and do not accommodate any nonuniform distribution of computational effort. Some control of particle distribution, based on expert human judgment, is desirable in challenging cases. The ALE meshless framework of FVPM enables some simple input to manage particle distribution, without requiring the connectivity of a mesh.

Here, a hybrid approach is proposed that combines local body-driven ALE motion with Lagrangian motion. Lagrangian particles are used throughout the domain. In addition, some particles are distributed on and near the body surface and follow the body motions. This approach ensures that there is always sufficient particle cover near the body, where poor particle distribution is most often observed, while the advantages of Lagrangian particle advection are retained in most of the domain.

To illustrate this technique, prescribed motion of a triangular body inside a square box is modeled. The body starts impulsively and moves upward at constant velocity until its apex touches the upper wall, when it stops instantaneously. The fluid is inviscid and weakly compressible, with speed of sound chosen for a Mach number of 0.05. When this flow is simulated in purely Lagrangian mode, the strong negative pressure in the body's wake leads to the formation of void regions, where there are gaps between particles, and numerical errors result. In the ALE approach adopted, the domain is initially populated with particles on a regular Cartesian grid at pitch of Δx_0. These particles move with Lagrangian velocity. A band around the body is filled with particles at a finer spacing of $\Delta x_0/3$, which move with the body's velocity. They interact in the usual way with each other and with the surrounding Lagrangian particles.

If a body approaches a wall or other boundary, the body-following particles may pass through the boundary. This is not necessarily a difficulty for FVPM. The particle support is truncated by the boundary, so only the portion of each particle's support inside the domain contributes to particle volume and interparticle area. The portion of the particle outside the domain does not participate in exchanges of mass and momentum. If a particle passes through the boundary completely, its volume should decrease to zero, at which point it has no effective part in the simulation. In practice, however, volume does not go exactly to zero because of time integration error. Also, particles become more susceptible to spatial discretization error as they pass through the wall because the ratio of effective surface area $\sum_j |\boldsymbol{\beta}_{ij}|$ to volume becomes large. To prevent these numerical problems, body-following particles are considered to have passed out of the domain when their volume falls below a small finite threshold. They are then frozen, rather than deleted, because they might later return to the domain, unlike outlet particles.

Images of the instantaneous particle distribution, particle volume and velocity fields are shown in Fig. 19.11. In Fig. 19.11A, the background Lagrangian particles (red) do not cover the wake region of the body. This highlights the value of the body-following (blue) particles. As illustrated in Fig. 19.11B, body-following particles fully outside the domain have volume equal to zero. Particles whose centers are outside the domain, but still close to the wall, have nonzero volume because part of their support lies inside the domain.

19.5.2 Mechanical Heart Valve

FVPM with body-following and Lagrangian particles has been used to model flow in opening of one leaflet of a simplified 2D symmetric bileaflet MHV. A schematic diagram of the model is shown in Fig. 19.12. Nonreflecting boundary conditions are applied at the inlet and outlet of the duct, as described in Section 19.3. A time-dependent reference velocity is prescribed at the boundaries, rising linearly from 5% to 100% of the final velocity, in an approximation to a physiological blood flow waveform. The leaflet is a rigid plate mounted on a frictionless hinge. In the initial (closed) position, there are small gaps between the leaflet and wall boundary (top boundary in Fig. 19.12) and the symmetry boundary below, simulating leakage gaps. The leaflet is free to move in rotation about the specified hinge center, and its motion is determined entirely by surface forces. It opens passively under the positive pressure gradient created by the inlet flow. The density of the solid is twice that of the fluid. Flow is approximated as inviscid and two dimensional. The Tait equation of state for a weakly compressible fluid is used with a maximum inlet Mach number of 0.082. Body-following particles are distributed around the leaflet and, elsewhere, particles are Lagrangian.

Samples of the computed velocity field are shown in Fig. 19.13. As the leaflet opens, it forms a divergent channel on its lower or downstream side. Lagrangian particles flowing beneath the opening leaflet must turn the convex corner to enter this passage. Although the computational particles are Lagrangian, they do not deform to fill space as physical fluid elements do. Each computational particle moves with a velocity that is representative of the average over its support region.

This book belongs to Central Library BADJI Mokhtar-ANNABA UNIVERSITY Copyright Elsevier 2024

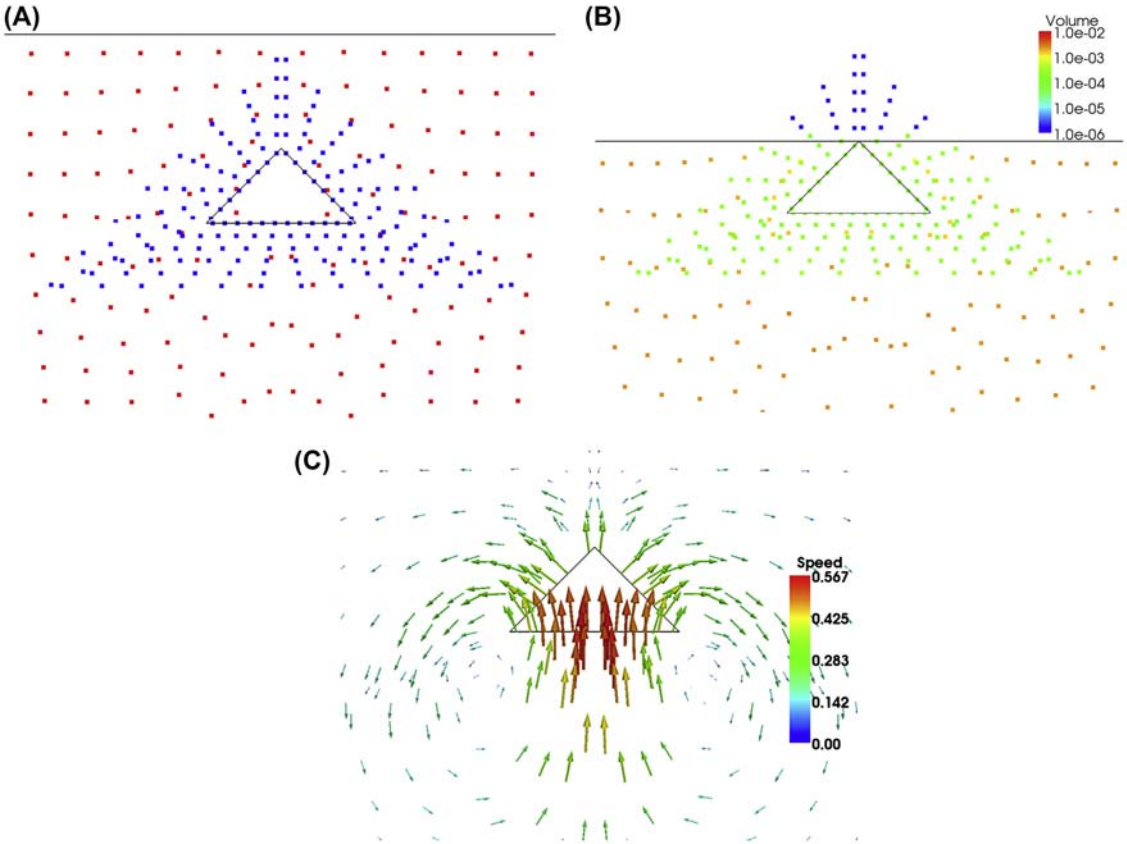

FIGURE 19.11 Flow around impulsively started triangular body. (A) Particle distribution after start-up, with body-following particles in blue (black in print versions) and Lagrangian particles in red (gray in print versions). (B) Particle volume after body impinges on wall. (C) Velocity distribution.

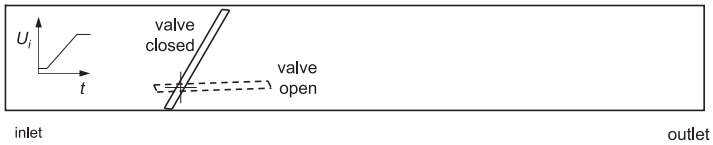

FIGURE 19.12 Schematic diagram of the idealized mechanical heart valve simulation.

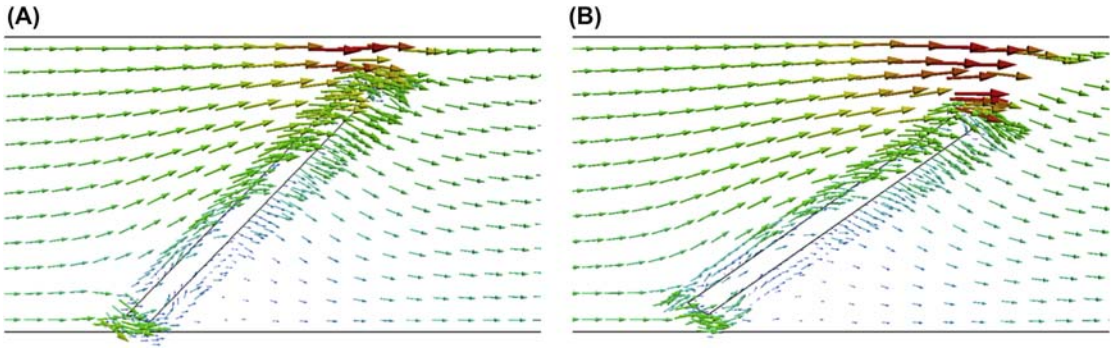

FIGURE 19.13 Computed instantaneous velocity fields in mechanical heart valve opening.

This book belongs to Central Library BADJI Mokhtar-ANNABA UNIVERSITY Copyright Elsevier 2024

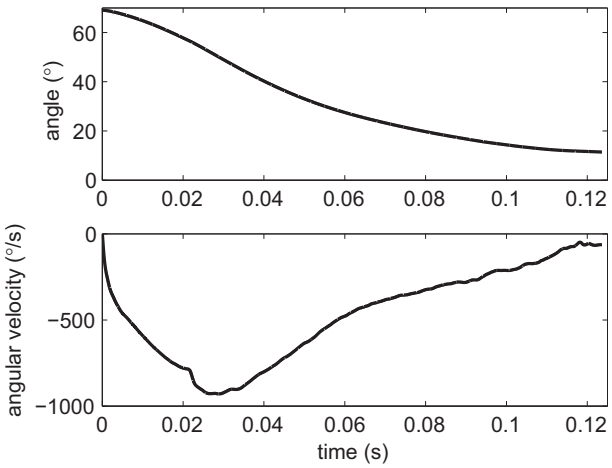

FIGURE 19.14 Computed angle and velocity of the leaflet during opening.

At the boundaries of the particle, discrepancies between the particle's bulk velocity and the true local velocity are manifested as fluxes due to nonzero velocity relative to the particle. In this case, gaps in particle cover are avoided by attaching body-following particles to the leaflet, to maintain adequate discretization of this region.

Leaflet kinematics is presented in Fig. 19.14. The opening time is approximately consistent with clinical and in vitro observations, but a quantitative comparison is not meaningful because of the idealizations inherent in this model. These results indicate that the method is capable of dealing with large wall motions.

19.6 CONCLUSIONS

In this chapter we have outlined the development of the FVPM that is essentially a finite volume method in which cells (particles) are free to overlap, and they require no connectivity. In other words, it is fully meshless, while retaining the properties that have made mesh-based finite volume methods so widely successful: exact conservation and a flexible framework that supports high-order discretizations and complex flow physics. In the literature, the method has been shown to be accurate for various 2D benchmark cases.

In principle, the meshless approach offers a solution to the problems of large wall motion, which are typical of biomedical applications. We have presented some progress toward practical applications to cardiovascular flow. Nonreflecting inlet and outlet boundaries have been implemented, which can allow particles to enter and exit a modeled vessel, while enforcing required boundary conditions and transmitting acoustic waves out of the domain freely. Large flow-induced motions of a dynamic rigid body have been implemented, and results have been validated for a benchmark problem. It has been found that pure Lagrangian particle motion is not ideal for flow around moving body, and an ALE scheme has been developed to maintain the particle distribution. These developments have been combined to simulate the opening of an idealized 2D MHV.

Simulations presented in this chapter have been two dimensional. Until recently, the obstacles to 3D FVPM have been the computational cost for quadrature-based method and the topological complexity of intersecting particle surfaces for exact integration of top-hat weight functions. However, Jahanbakhsh et al. have now developed algorithms for exact integration in 3D on cubic and spherical particles (Jahanbakhsh et al., 2016a,b) in acceptable computational time. This development opens the door to applications of FVPM to complex 3D biomedical fluid dynamics problems.

ACKNOWLEDGMENTS

This research has been supported by funding from the European Community's Seventh Framework Programme (FP7/2007−2013) under grant agreement 225967 "NextMuSE," the European Regional Development Fund (ERDF) project "NTIS—New Technologies for the Information Society" European Centre of Excellence CZ.1.05/1.1.00/02.0090, and Science Foundation Ireland through the CÚRAM Centre for Research in Medical Devices (grant number 13/RC/2073).

This book belongs to Central Library BADJI Mokhtar-ANNABA UNIVERSITY
Copyright Elsevier 2024

REFERENCES

Anagnostopoulos, P., Bearman, P., 1992. Response characteristics of a vortex-excited cylinder at low Reynolds numbers. Journal of Fluids and Structures 6, 39–50.

Bonet, J., Lok, T.-S.L., 1999. Variational and momentum preservation aspects of smooth particle hydrodynamic formulations. Computer Methods in Applied Mechanics and Engineering 180, 97–115.

Borazjani, I., Ge, L., Le, T., Sotiropoulos, F., April 2013. A parallel overset-curvilinear-immersed boundary framework for simulating complex 3d incompressible flows. Computers and Fluids 77, 76–96.

Borazjani, I., Ge, L., Sotiropoulos, F., August 2008. Curvilinear immersed boundary method for simulating fluid structure interaction with complex 3d rigid bodies. Journal of Computational Physics 227 (16), 7587–7620.

Chaudhary, R., Garg, J., Krishnamoorthy, P., Shah, N., Feldman, B.A., Martinez, M.W., Freudenberger, R., March 2016. The on-x valve. Cardiology in Review 1.

Dasi, L.P., Grande-Allen, J., Kunzelman, K., Kuhl, E., 2017. The pursuit of engineering the ideal heart valve replacement or repair: a special issue of the annals of biomedical engineering. Annals of Biomedical Engineering 45 (2), 307–309.

Dilts, G., 1999. Moving least-squares particle hydrodynamics I: consistency and stability. International Journal for Numerical Methods in Engineering 44, 1115–1155.

Gingold, R., Monaghan, J., 1977. Smoothed particle hydrodynamics: theory and application to non-spherical stars. Monthly Notices of the Royal Astronomical Society 181, 375–389.

Govardhan, R., Williamson, C., 2000. Modes of vortex formation and frequency response of a freely vibrating cylinder. Journal of Fluid Mechanics 420, 85–130.

Hietel, D., Steiner, K., Struckmeier, J., 2000. A finite volume particle method for compressible flows. Mathematical Models and Methods in Applied Science 10, 1363–1382.

Ismagilov, T., 2006. Smooth volume integral conservation law and method for problems in Lagrangian coordinates. Computational Mathematics and Mathematical Physics 46, 453–464.

Jahanbakhsh, E., Maertens, A., Quinlan, N., Vessaz, C., Avellan, F., 2016a. Exact finite volume particle method with spherical-support kernels. Computer Methods in Applied Mechanics and Engineering 317, 102–127.

Jahanbakhsh, E., Vessaz, C., Maertens, A., Avellan, F., 2016b. Development of a finite volume particle method for 3-D fluid flow simulations. Computer Methods in Applied Mechanics and Engineering 298, 80–107.

Junk, M., 2003. Do finite volume methods need a mesh? In: Griebel, M. (Ed.), Meshfree Methods for Partial Differential Equations. Springer, pp. 223–238.

Kaland, C., December 2013. The Finite Volume Particle Method : Recent Developments and Applications (Ph.D. thesis). Universität Hamburg.

Keck, R., Hietel, D., 2005. A projection technique for incompressible flow in the meshless finite volume particle method. Advances in Computational Mathematics 23, 143–169.

Kidane, A.G., Burriesci, G., Cornejo, P., Dooley, A., Sarkar, S., Bonhoeffer, P., Edirisinghe, M., Seifalian, A.M., January 2009. Current developments and future prospects for heart valve replacement therapy. Journal of Biomedical Materials Research Part B 88B (1), 290–303.

Krafczyk, M., Cerrolaza, M., Schulz, M., Rank, E., 1998. Analysis of 3d transient blood flow passing through an artificial aortic valve by lattice-Boltzmann methods. Journal of Biomechanics 31 (5), 453–462.

Dasi, L.P., Simon, H.A., Sucosky, P., Yoganathan, A.P., February 2009. Fluid mechanics of artificial heart valves. Clinical and Experimental Pharmacology and Physiology 36 (2), 225–237.

Lastiwka, M., Basa, M., Quinlan, N.J., 2009. Permeable and non-reflecting boundary conditions in SPH. International Journal for Numerical Methods in Fluids 61 (7), 709–724.

Lind, S.J., Xu, R., Stansby, P.K., Rogers, B.D., 2012. Incompressible smoothed particle hydrodynamics for free-surface flows: a generalised diffusion-based algorithm for stability and validations for impulsive flows and propagating waves. Journal of Computational Physics 231 (4), 1499–1523.

Liou, M.-S., 2006. A sequel to AUSM, part II: AUSM+-up for all speeds. Journal of Computational Physics 214, 137–170.

Liu, W., Jun, S., Zhang, Y., 1995. Reproducing kernel particle methods. International Journal for Numerical Methods in Fluids 20, 1081–1106.

Lucy, L., 1977. A numerical approach to testing the fission hypothesis. The Astronomical Journal 82, 1013–1924.

Monaghan, J.J., 1999. SPH without a tensile instability. Journal of Computational Physics 159, 290–311.

Monaghan, J.J., 2012. Smoothed particle hydrodynamics and its diverse applications. Annual Review of Fluid Mechanics 44 (1), 323–346.

Moretti, G., 1969. Importance of boundary conditions in the numerical treatment of hyperbolic equations. The Physics of Fluids 12 (12), II–13.

Nestor, R.M., Quinlan, N.J., 2013. Application of the meshless finite volume particle method to flow-induced motion of a rigid body. Computers and Fluids 88, 386–399.

Nestor, R., Basa, M., Lastiwka, M., Quinlan, N., 2009. Extension of the finite volume particle method to viscous flow. Journal of Computational Physics 228, 1733–1749.

Peskin, C.S., 1972. Flow patterns around heart valves: a numerical method. Journal of Computational Physics 10 (2), 252–271.

Placzek, A., Sigrist, J., Hamdouni, A., 2009. Numerical simulation of an oscillating cylinder in a cross-flow at low Reynolds number: forced and free oscillations. Computers and Fluids 38, 80–100.

Puskas, J., Gerdisch, M., Nichols, D., Quinn, R., Anderson, C., Rhenman, B., Fermin, L., McGrath, M., Kong, B., Hughes, C., Sethi, G., Wait, M., Martin, T., Graeve, A., April 2014. Reduced anticoagulation after mechanical aortic valve replacement: interim results from the prospective randomized on-x valve anticoagulation clinical trial randomized food and drug administration investigational device exemption trial. The Journal of Thoracic and Cardiovascular Surgery 147 (4), 1202–1211.e2.

This book belongs to Central Library BADJI Mokhtar-ANNABA UNIVERSITY Copyright Elsevier 2024

Quinlan, N.J., Nestor, R.M., 2011. Fast exact evaluation of particle interaction vectors in the finite volume particle method. In: Meshfree Methods for Partial Differential Equations V. Springer, pp. 219−234.

Quinlan, N., Lastiwka, M., Basa, M., 2006. Truncation error in mesh-free particle methods. International Journal for Numerical Methods in Engineering 66, 2064−2085.

Quinlan, N.J., Lobovskỳ, L., Nestor, R.M., 2014. Development of the meshless finite volume particle method with exact and efficient calculation of interparticle area. Computer Physics Communications 185 (6), 1554−1563.

Shadloo, M.S., Oger, G., Le Touzé, D., 2016. Smoothed particle hydrodynamics method for fluid flows, towards industrial applications: motivations, current state, and challenges. Computers and Fluids 136, 11−34.

Shahriari, S., Maleki, H., Hassan, I., Kadem, L., 2012. Evaluation of shear stress accumulation on blood components in normal and dysfunctional bileaflet mechanical heart valves using smoothed particle hydrodynamics. Journal of Biomechanics 45 (15), 2637−2644.

Shiels, D., Leonard, A., Roshko, A., January 2001. Flow-induced vibration of a circular cylinder at limiting structural parameters. Journal of Fluids and Structures 15 (1), 3−21.

Singh, S., Mittal, S., 2005. Vortex-induced oscillations at low Reynolds numbers: hysteresis and vortex-shedding modes. Journal of Fluids and Structures 20, 1085−1104.

Sotiropoulos, F., Borazjani, I., March 2009. A review of state-of-the-art numerical methods for simulating flow through mechanical heart valves. Medical and Biological Engineering and Computing 47 (3), 245−256.

Teleaga, D., 2005. A Finite Volume Particle Method for Conservation Laws (Ph.D. thesis). University of Kaiserslautern.

Vigmostad, S.C., Udaykumar, H.S., Lu, J., Chandran, K.B., 2010. Fluid-structure interaction methods in biological flows with special emphasis on heart valve dynamics. International Journal for Numerical Methods in Biomedical Engineering 26 (3−4), 435−470.

Violeau, D., 2012. Fluid Mechanics and the SPH Method. Oxford University Press, Oxford, UK.

Williamson, C., Roshko, A., 1988. Vortex formation in the wake of an oscillating cylinder. Journal of Fluids and Structures 2, 355−381.

Yoganathan, A.P., He, Z., Jones, C.S., 2004. Fluid mechanics of heart valves. Annual Review of Biomedical Engineering 6 (1), 331−362.

Yoganathan, A.P., Chandran, K.B., Sotiropoulos, F., December 2005. Flow in prosthetic heart valves: state-of-the-art and future directions. Annals of Biomedical Engineering 33 (12), 1689−1694.

Zisis, I., Evers, J.H.M., van der Linden, B., Duong, M.H., 2016. Recent results in the systematic derivation and convergence of sph. In: Hu, X. (Ed.), Proceedings of the 11th SPHERIC International Workshop.

This book belongs to Central Library BADJI Mokhtar-ANNABA UNIVERSITY

Copyright Elsevier 2024

Part VI

Lattice Boltzmann Methods

This book belongs to Central Library BADJI Mokhtar-ANNABA UNIVERSITY

Copyright Elsevier 2024

This page intentionally left blank

This book belongs to Central Library BADJI Mokhtar-ANNABA UNIVERSITY

Copyright Elsevier 2024

Chapter 20

Multicomponent Lattice Boltzmann Models for Biological Applications

A. Montessori[1], I. Halliday[2], M. Lauricella[3], S.V. Lishchuk[2], G. Pontrelli[3], T.J. Spencer[2] and S. Succi[3,4]
[1]University of Rome "Roma Tre", Rome, Italy; [2]Sheffield Hallam University, United Kingdom; [3]Istituto per le Applicazioni del Calcolo - CNR, Roma, Italy; [4]Harvard University, Cambridge, MA, United States

20.1 INTRODUCTION

In the last decade lattice Boltzmann (LB) methods have met with a huge success within the computational physics community because of their capability to simulate a very wide range of fluid dynamics phenomena and beyond. The LB models for fluid dynamics were first developed to cure some shortcomings of the lattice gas automata, such as the spurious invariants and the statistical noise, while preserving the local nature of the collisional and the linearity of the streaming operator along propagation characteristics. Since then, a great deal of effort has been devoted to the development of LB models capable of simulating complex flows across a wide range of scales of motion (Succi, 2015). In particular, LB models for nonideal fluids have seen a major boost in connection with the simulation of complex states of flowing matter, such as multiphase and multicomponent flows. The three basic LB multiphase methods are the color-fluid model (developed by Gunstensen et al., 1991.), the interparticle-potential model of Shan and Chen (1993), and the free-energy model (Swift et al., 1995). Here, we briefly outline the recent developments of each approach. The color-fluid model, proposed by Rothman and Keller (1988) and further developed by Grunau et al. (1993), is based on a two-component LB model, $f_{\alpha,i}(\mathbf{x}, t)$ and $f_{\beta,i}(\mathbf{x}, t)$, representing two different interacting fluids. The surface tension is encoded via a perturbation step namely, a modification of the original LB collision operator, while phase separation is maintained through a segregation step by forcing particles to regions of the same color. In the pseudopotential model (Shan and Chen, 1993) the interactions between fluid components are modeled through a modification of the collision operator by using an equilibrium velocity that includes an interactive force, which mimics an effective particle−particle potential at a mesoscopic level. This force guarantees phase separation and introduces surface tension effects. This model has been applied recently with considerable success (Montessori et al., 2015, Falcucci et al., 2013, Dollet et al., 2015). Moreover, it has been extended to include different van der Waals (vdW)−like equations of state by properly defining a suitable generalized functional form of the pseudopotential (Yuan and Schaefer, 2006, Qin, 2006). A multirange interaction model has been proposed to control the surface tension independently of the equation of state (Sbragaglia et al., 2007). The same can be done by modifying the attractive and repulsive terms of a vdW-like equation of state (Montessori et al., 2015). The free-energy model employs a free-energy function to include surface tension effects in a thermodynamically consistent manner (Orlandini et al., 1995). In addition to the methods outlined above, other promising methods based on a combination of the LB equation with explicit interface-tracking schemes are under development. One approach uses Peskin's (2002) distribution function for the interface force used in the immersed boundary (IB) method (Lallemand et al., 2007). More recently, interface tracking using the volume of fluid approach has been reported with promising results (Körner et al., 2005). In the following the pseudopotential approach for multiphase and multicomponent flows and the modified color-gradient method will be described in full detail, with a special emphasis on their prospective biological applications.

Numerical Methods and Advanced Simulation in Biomechanics and Biological Processes. https://doi.org/10.1016/B978-0-12-811718-7.00020-4
Copyright © 2018 Elsevier Ltd. All rights reserved.

This book belongs to Central Library BADJI Mokhtar-ANNABA UNIVERSITY
Copyright Elsevier 2024

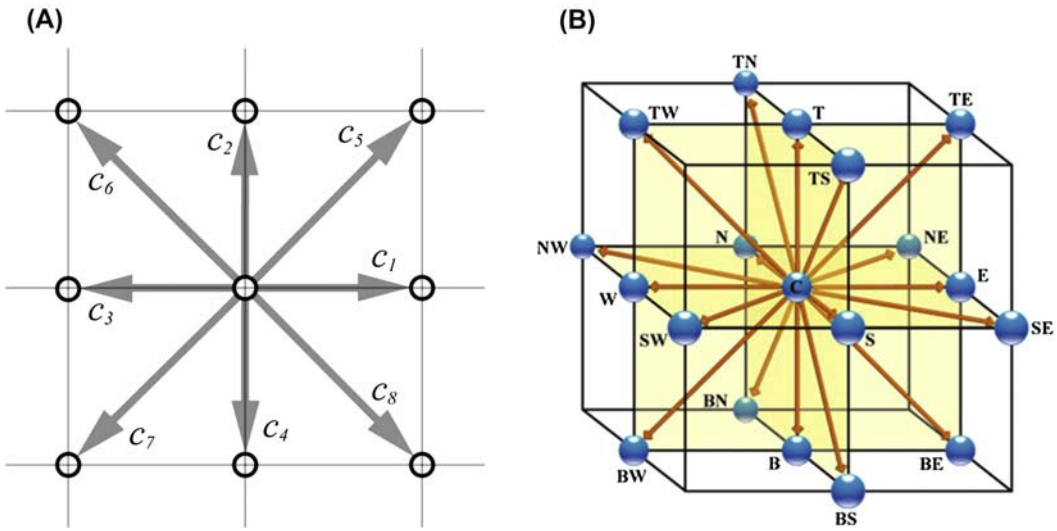

FIGURE 20.1 Sketch of the 9-speed two-dimensional (D2Q9) (A) and 19-speed three-dimensional lattices (D3Q19) (B).

20.2 THE LATTICE BOLTZMANN EQUATION

The LB equation with forcing terms reads as follows:

$$f_i(\mathbf{x}+\mathbf{c}_i\Delta t, t+\Delta t) - f_i(\mathbf{x}, t) \;=\; -\omega\Delta t[f_i - f_i^{eq}(\rho, \mathbf{u}+\mathbf{F}/\omega\rho)] \tag{20.1}$$

where $f_i(\mathbf{x},\ t) \equiv f(\mathbf{x},\ \mathbf{v}=\mathbf{c}_i,\ t)$ is the discrete distribution function providing the probability of finding a particle at lattice site $\mathbf{x}$ at time t with discrete velocity $\mathbf{c}_i$, being i the lattice direction (Qian et al., 1992; Succi, 2001) (Fig. 20.1). In Eq. (20.1), ω is the relaxation parameter and $\mathbf{F}$ is a shift force.

Eq. (20.1) describes the evolution of the discrete single-particle distribution function in terms of *streaming* (left-hand side) and *collision*, in the form of a relaxation toward a local equilibrium (first term at right-hand side). The local equilibria are computed as second-order expansion in the local Mach number, $\mathrm{Ma} = u/c_s$, $\boldsymbol{u}$ being the macroscopic flow velocity and $c_s \;=\; \sqrt{1/3}$ the lattice speed of sound:

$$f_i^{eq}(\mathbf{x}, t) \;=\; w_i\rho \quad 1 + \frac{\mathbf{u}\cdot\mathbf{c}_i}{c_s^2} + \frac{(\mathbf{u}\cdot\mathbf{c}_i)^2}{2c_s^4} - \frac{\mathbf{u}\cdot\mathbf{u}}{2c_s^2}\Bigg) \tag{20.2}$$

where w_i are weights of the discrete equilibrium distribution functions and

$$\rho(\mathbf{x}, t) \;=\; \sum_i f_i(\mathbf{x}, t), \quad \mathbf{u}(\mathbf{x}, t) \;=\; \frac{\sum_i f_i(\mathbf{x}, t)\mathbf{c}_i}{\rho(\mathbf{x}, t)} \tag{20.3}$$

the fluid density and the flow velocity, respectively. The second term at the right-hand side of Eq. (20.1) accounts for the effect of external/internal forces acting on the fluid molecules, such as gravity or, as we are going to describe in the following, a pseudomolecular interactive force that mimics an effective particle−particle potential at a mesoscopic level that promotes phase separation and introduces surface tension effects in a simple and efficient way (Shan and Chen, 1993).

20.3 THE PSEUDOPOTENTIAL APPROACH FOR MULTIPHASE AND MULTICOMPONENT FLOWS

In the Shan−Chen (SC) pseudopotential scheme, the nonideal force in Eq. (20.1) takes the form (Shan and Chen, 1993):

$$\mathbf{F}(\mathbf{x}, t) \;=\; -G\psi(\rho(\mathbf{x}, t))\Delta t \sum_i \lambda_i \mathbf{c}_i \psi(\rho(\mathbf{x}+\mathbf{c}_i\Delta t, t)) \tag{20.4}$$

This book belongs to Central Library BADJI Mokhtar-ANNABA UNIVERSITY
Copyright Elsevier 2024

where G is the strength of nonideal interactions, λ_i are the coefficients for the nth isotropic lattice, and the *generalized density* $\psi(\rho)$ contributes the excess pressure in the nonideal equation of state:

$$p = \rho c_s^2 + \frac{G}{2}\psi^2(\rho). \tag{20.5}$$

In the SC model, one has

$$\psi(\rho) = 1 - e^{-\rho} \tag{20.6}$$

which gives a critical pressure $p_c = (ln2 - 1/2)/3 \sim 0.063$ and a critical coupling $G_c = -4$. We recall that negative G's code for attraction, the only interaction in the SC model. Note that in the ideal gas limit $\rho \to 0$, the SC equation of state delivers $p = \rho c_s^2$, with a fixed sound speed $c_s^2 = 1/3$.

20.3.1 Discretization of the Nonideal Forcing Term on Higher-Order Lattices

Such spurious currents represent a serious tap to the numerical simulation of multiphase flows at substantial density ratios because their magnitude is directly related to the ratio between the densities of the coexisting phases. In pseudopotential multiphase models, spurious currents basically arise as a result of the lack of symmetry of the underlying lattice (Shan, 2006; Sbragaglia et al., 2007).

Improving the order of isotropy of the stencil employed to compute density gradient in SC-like models (see Fig. 20.2) may help in reducing the magnitude of such peripheral currents. Thus, a few additional comments on the implementation of pseudopotential forces on higher-order lattices are in order. By expanding the right-hand side of Eq. (20.4) in Taylor series, we obtain

$$\sum_i \lambda_i \psi(\mathbf{x} + \mathbf{c}_i \Delta t, t)\mathbf{c}_i = \nabla\psi \cdot E^{(2)} + \frac{1}{3!}\nabla^{(3)}\psi \cdot E^{(4)} + \frac{1}{5!}\nabla^{(5)}\psi \cdot E^{(6)} + \cdots \tag{20.7}$$

where the generic nth-order lattice tensor is defined as follows (Wolfram, 1986):

$$E^{(n)} = \sum_i \lambda_i c_{i\alpha_1} \cdots c_{i\alpha_n} \tag{20.8}$$

and the subscript α_j stands for the generic Cartesian component x, y, z. The quality of the left-hand side of Eq. (20.7) as an approximation of its continuum counterpart is strictly dictated by the degree of isotropy of the corresponding tensors $E^{(n)}$ (Shan, 2006). The main parameters of the higher-order lattices (Fig. 20.2) employed in (Montessori et al., 2015) are reported in Table 20.1.

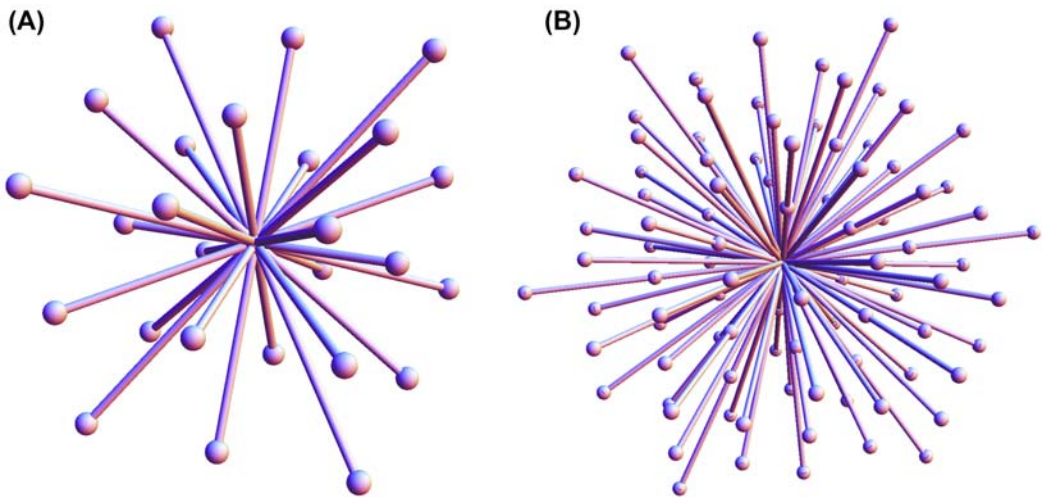

FIGURE 20.2 The set of discrete velocities for the fourth-order 27-speed (A) and of the eighth-order 93-speed lattices (B).

This book belongs to Central Library BADJI Mokhtar-ANNABA UNIVERSITY Copyright Elsevier 2024

TABLE 20.1 Coefficients of the Isotropic $E^{(4)}$ (D3Q27F27) and $E^{(8)}$ (*D3Q27F93*) (See the Text for the Notation) Lattices in 3D Pseudopotential Models.

Energy Shell	$E^{(4)}$	$E^{(8)}$	Degeneracy
$\lambda(1)$	16/216	448/15120	6
$\lambda(2)$	4/216	240/15120	12
$\lambda(3)$	1/216	96/15120	8
$\lambda(4)$		50/15120	6
$\lambda(5)$		16/15120	24
$\lambda(6)$		8/15120	24
$\lambda(8)$		1/15120	12

The numbers in brackets refer to the energy $E = \sum_{j=x,y,z} c_{i\alpha_j}^2$ of the corresponding shell, the index i spanning the full set of discrete speeds. The degeneracy indicates the number of discrete speeds in the given energy shell

20.3.2 Nonideal Equations of State in Pseudopotentials Approach

The pseudopotential approach was recently improved to incorporate more realistic vdW equations of state. Montessori et al. (2015) developed a higher-order pseudopotential approach augmented with the Carnahan−Starling (CS) equation of state, which reads as follows (Carnahan and Starling, 1969):

$$p = \rho v_T^2 \frac{1+\gamma+\gamma^2-\gamma^3}{(1-\gamma)^3} - a\rho^2 \tag{20.9}$$

where $v_T = \sqrt{k_B T/m}$ is the thermal speed, $\gamma \equiv b\rho/4$, and a, b are the standard vdW parameters associated with the strength of long-range attraction and short-range repulsion. The fluid critical temperature and pressure, T_c and p_c, respectively, are controlled by a and b, according to the relation:

$$T_c = 0.3773a/b, \quad p_c = 0.0707a/b^2 \tag{20.10}$$

where the gas constant has been set to $R = 1$. Based on Eq. (20.5), the CS generalized density is computed as

$$\psi(\rho) = \sqrt{2\frac{p/c_s^2 - \rho}{G}}. \tag{20.11}$$

where G ensures the positivity of the term under the square root (Yuan and Schaefer, 2006). As compared to the standard vdW, the CS Eq. (20.9) is characterized by a steepening of the repulsive interactions in the hard-core region, which results in higher vapor/liquid density ratios at sufficiently high densities. We also note that the presence of a tunable thermal speed v_T in Eq. (20.9), instead of the fixed sound speed c_s in the SC equation of state. By lowering the absolute temperature T at a given value of the reduced temperature T/T_c, it is therefore possible to implement weaker gradients on the vapor phase, compared with the SC case. This feature is crucial for the stability of the vapor−liquid interface in the CS simulations (Colosqui et al., 2012).

20.3.3 Pseudopotential Approach for Interacting Multicomponent Fluids

We start from a kinetic LB equation for a multicomponent fluid with M species (Montessori et al., 2016) whose evolution equation is

$$f_{ni}(\mathbf{x}+c_i\Delta t, t+\Delta t) - f_{ni}(\mathbf{x},t) = -\omega_n \Delta t[f_{ni} - f_{ni}^{eq}(\rho_n, u + F_n/\omega_n\rho_n)] \tag{20.12}$$

where $f_{ni}(\mathbf{x}, t)$ (resp. ω_n) generalizes $f_i(\mathbf{x}, t)$ (resp. ω) for the species n=1, 2,…,M (cf., Eq. 20.1). To be noted that the equilibrium for the species n is a function of the local species density:

$$\rho_n(\mathbf{x},t) = \sum_i f_{ni}(\mathbf{x},t) \tag{20.13}$$

This book belongs to Central Library BADJI Mokhtar-ANNABA UNIVERSITY
Copyright Elsevier 2024

and the common, or barycentral, velocity is defined as

$$\mathbf{u}(\mathbf{x},t) = \frac{\sum_n \omega_n \sum_i f_{ni}(\mathbf{x},t)\mathbf{c}_i}{\sum_n \omega_n \rho_n(\mathbf{x},t)} \tag{20.14}$$

This common velocity receives a shift from the force $\mathbf{F}_n$ acting on the species n (Benzi et al., 2009). This force may be an external one or it could also be due to intermolecular potential interactions. In its first form the pseudopotential force within each species consisted of a purely repulsive action between the M species. Benzi et al. (2009) extended this formulation to model more complex states of fluid matter, such as foams and glassy states. In their work, they develop a model that is able to simulate a disjoining pressure, at a mesoscopic level, which can act as a foam stabilizer. To do so, the pseudopotential force within each species consists of an attractive (a) component acting only on the first Brillouin region (belt, for simplicity), and a repulsive (r) one acting on both belts, whereas the force between species (X) is short ranged and repulsive:

$$\mathbf{F}_n(\mathbf{x},t) = \mathbf{F}_n^a(\mathbf{x},t) + \mathbf{F}_n^r(\mathbf{x},t) + \mathbf{F}_n^X(\mathbf{x},t) \tag{20.15}$$

where

$$\mathbf{F}_n^a(\mathbf{x},t) = -G_n^a \psi_s(\mathbf{x},t) \sum_{i\in belt1} \lambda_i \psi_n(\mathbf{x}_i,t)\mathbf{c}_i \tag{20.16}$$

$$\mathbf{F}_n^r(\mathbf{x},t) = -G_n^r \psi_s(\mathbf{x},t) \sum_{i\in belt1\cup belt2} \lambda_i \psi_n(\mathbf{x}_i,t)\mathbf{c}_i \tag{20.17}$$

$$\mathbf{F}_n^X(\mathbf{x},t) = -\frac{\rho_s(\mathbf{x},t)}{\rho_{0n}^2} \sum_{s'\neq s} \sum_{i\in belt1} G_{nn'} \lambda_i \rho_{n'}(\mathbf{x}_i,t)\mathbf{c}_i \tag{20.18}$$

In the above, the sets $belt1$ and $belt2$ refer to the first and second Brillouin zones in the lattice (Benzi et al., 2009). Apart from a normalization factor, these correspond to the values given in (Sbragaglia et al., 2007). In addition, $G_{nn'} = G_{n'n}$, $n' = n$, is the cross-coupling between species, ρ_{0n} is a reference density, and, finally, $\mathbf{x}_i = \mathbf{x} + \mathbf{c}_i\Delta t$ are the displacements along the $\mathbf{c}_i$.

20.4 BIOFLUIDIC APPLICATIONS

The above methods have met with increasing popularity for the simulation of a broad variety of microfluidic flows, as we are going to detail in the sequel.

20.4.1 Droplet Dynamics With Applications to Biomicrofluidics

Recent advances in bio- and nanotechnologies have led to the development of novel microsystems for bioparticle separation and analysis. Microsystems are already revolutionizing the way we do science and have led to the development of a number of ultrasensitive bioanalytical devices capable of analyzing complex biological samples. These devices have application in a number of diverse areas, such as pollution monitoring, clinical diagnostics, drug discovery, and biohazard detection. A deeper understanding of the dynamics governing fluids at the microliter to picoliter scale is pivotal to gain a full knowledge of the physics governing such strikingly interesting phenomena and to help engineers in the design process. In this regard, computational fluid dynamics is a powerful tool, which can be effectively used to reduce the number of prototypes needed to develop a diagnostic device and provide deeper insight into the underlying mechanics of fluid systems. LB models, due to their inherent programming simplicity and scalability on multicore architectures, represent a hot bed for such applications. Recently, higher-order pseudopotential approaches augmented with vdW-like equations of state have been employed to simulate droplet off-axis collisions (Montessori et al., 2015), as reported in Fig. 20.3. In the fluid dynamic regime associated with the nondimensional parameters considered (see Montessori et al., 2015), the droplets are expected to (Qian and Law, 1997)

1. merge, as they get close to each other;
2. stretch and form a ligament, due to their initial momentum along opposite (parallel) directions;
3. break up the ligament, with a so-called end-pinching mechanism, due to their speed and momentum;
4. separate again, at a small deflection angle, due to the large impact parameter, with the formation of multiple satellite droplets.

This book belongs to Central Library BADJI Mokhtar-ANNABA UNIVERSITY Copyright Elsevier 2024

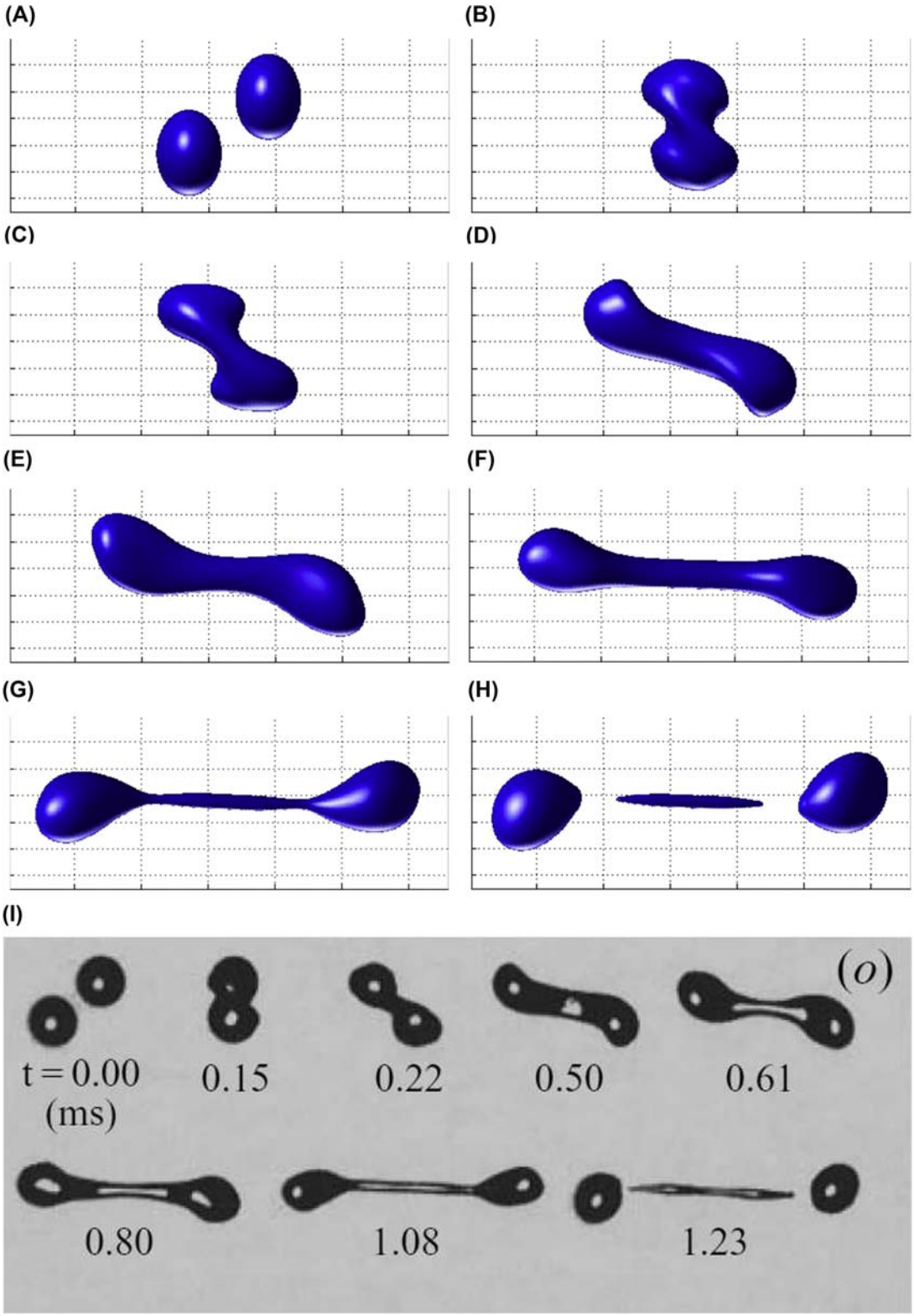

FIGURE 20.3 Off-axis collision between two droplets. The droplets are impulsively started with a horizontal speed $U/2 = \mp 0.09$ toward the opposite side of the computational domain. The Weber and Reynolds number of the simulation are We $\simeq$ 60.8 and Re $\simeq$ 313.7 and the density ratio is about 1:1000. The relaxation time is set to 0.62. The impact parameter is equal to 0.68 and the radius of the two droplets is set to 30 lattice points. The results are compared with those obtained by Qian and Law (1997). As one can see the evolution of the phenomenon is well captured by the numerical simulation. Indeed, as shown by the experiment, for this set of Reynolds and Weber, a kissinglike impact is performed after which a ligament appears that stretches and breaks up after an end-pinching mechanism. (A–H) Snapshots of the numerical simulation of the off-axis droplet impact. (I) Experimental results (Qian and Law, 1997). *Courtesy Montessori, A., Falcucci, G., La Rocca, M., Ansumali, S., Succi, S., 2015. Three-dimensional lattice pseudo-potentials for multiphase flow simulations at high density ratios. Journal of Statistical Physics 161 (6), 1404–1419.*

This book belongs to Central Library BADJI Mokhtar-ANNABA UNIVERSITY
Copyright Elsevier 2024

This is precisely the sequence of events emerging from the simulation, as reported in Fig. 20.3. It is to be noted that a water−air-like system is here considered, i.e., the density ratio between the light and heavy fluid is $\simeq 1000$. Notwithstanding the large density ratio, the density contours appear very neat, with no sign of numerical debris at any stage of this complex evolution, including the "critical" stages of merging and rupture. Moreover the evolution of the collision process is visually compared with the experiments carried out by Qian and Law. The results are in good agreement, at least qualitatively. Indeed the kissinglike merging process and the consequent ligament stretching followed by the end-pinching mechanism are well captured by the simulation.

Recently, Gupta and Sbragaglia (2014) investigated the effects of viscoelasticity on droplet dynamics and breakup in microfluidic in a T-junction geometry by means of a pseudopotentials multicomponent LB models coupled to a FENE-P (finitely extensible nonlinear elastic Peterlin) model (Gupta and Sbragaglia, 2014), employed to simulate the constitutive equations for finite extensible nonlinear elastic dumbbells.

It is worth noting that T-junction-like devices are currently employed in medical diagnostics, i.e., for chemical (enzymatic and nonenzymatic) reactions and cell analysis. In addition, droplet digital polymerase chain reaction represents a promising way to diagnose and manage cancer, avoiding expensive and invasive traditional biopsies and enabling frequent analysis of the tumor's molecular profile. Thus, the understanding of the fluid dynamics processes in these devices becomes fundamental for the designer to create and control tiny droplets with great precision, for example maintaining a consistent droplet size and frequency of droplet generation. Snapshot of the simulations for different values of the finite extensibility parameter of the FENE-P equation is reported in Fig. 20.4.

Kamali and Van den Akker (2013) also applied an SC-like approach to investigate the behavior of micron-sized droplets in complex geometries. Making use of the pseudopotential LB method, they simulated 2D dispersed gas−liquid flow through an inclined microchannel with two bends with applications in biological and biochemical processes. Dollet et al. (2015) employed a pseudopotential multicomponent approach with long-range repulsion for soft-glassy systems modeling to simulate the plastic rearrangement of emulsion in a quasi two-dimensional Hele-Shaw cell (Fig. 20.5). For the first time they highlighted a link between the localization lengthscale of the velocity profiles and that of plastic events across the channel, confirming the relevance of cooperativity for foams. These results confirm the capability of LB models to deal with extremely complex and physically rich fluid phenomena.

20.5 MODIFIED COLOR-GRADIENT METHOD

The dynamics of fluid−fluid boundaries are difficult to study because these interfaces are usually deformable and their shapes are not known a priori, being evolving in response to flow stresses.

Another classic method to model multicomponent fluids and multiphase flows in the continuum approximation dates back to Gunstensen et al. (1991). In it the phases are conveniently denoted by different colors, and interparticle interactions, responsible for phase separations, are modeled by a local color gradient, which is taken to give rise to an IB force (Peskin, 2002).

20.5.1 Two Immiscible Fluids

Let us consider two fluid distributions initially, which simultaneously occupy lattice link i, at position $\mathbf{x}$ and time t to be described by distribution functions, $f_{ri}(\mathbf{x}, t)$ and $f_{bi}(\mathbf{x}, t)$ (of course with $f_i(\mathbf{x},t) = f_{ri}(\mathbf{x}, t) + f_{bi}(\mathbf{x}, t)$). The nodal density of the red and blue fluid and their total density and momentum are defined as follows:

$$\rho_k = \sum_i f_{ki},\ \rho_k \boldsymbol{u_k} = \sum_i \mathbf{c}_i f_{ki} \quad k = r, b$$

$$\rho = \rho_r + \rho_b,\ \rho \boldsymbol{u} = \rho_r \boldsymbol{u_r}, + \rho_b \boldsymbol{u_b}$$

In addition to the LB collision step, which operates on the distribution function f_i, there is an extra body-forcing or source term (which gives rise to a body force at the continuum scale) and a recoloring step in the model (Latva-Kokko and Rothman, 2005). In this step, the color at a node is redistributed to the kinetic-scale, postcollision distribution function $f_i^\dagger$ and then propagated as:

$$f_{ri}(\mathbf{x} + \mathbf{c}_i \Delta t, t + \Delta t) = \frac{\rho_r(\mathbf{x})}{\rho(\mathbf{x})} f_i^\dagger(\mathbf{x}, t) + \beta w_i \frac{\rho_r(\mathbf{x})\rho_b(\mathbf{x})}{\rho(\mathbf{x})} \mathbf{c}_i \cdot \widehat{\boldsymbol{n}}, \tag{20.19}$$

$$f_{bi}(\mathbf{x} + \mathbf{c}_i \Delta t, t + \Delta t) = \frac{\rho_b(\mathbf{x})}{\rho(\mathbf{x})} f_i^\dagger(\mathbf{x}, t) - \beta w_i \frac{\rho_r(\mathbf{x})\rho_b(\mathbf{x})}{\rho(\mathbf{x})} \mathbf{c}_i \cdot \widehat{\boldsymbol{n}}.$$

This book belongs to Central Library BADJI Mokhtar-ANNABA UNIVERSITY
Copyright Elsevier 2024

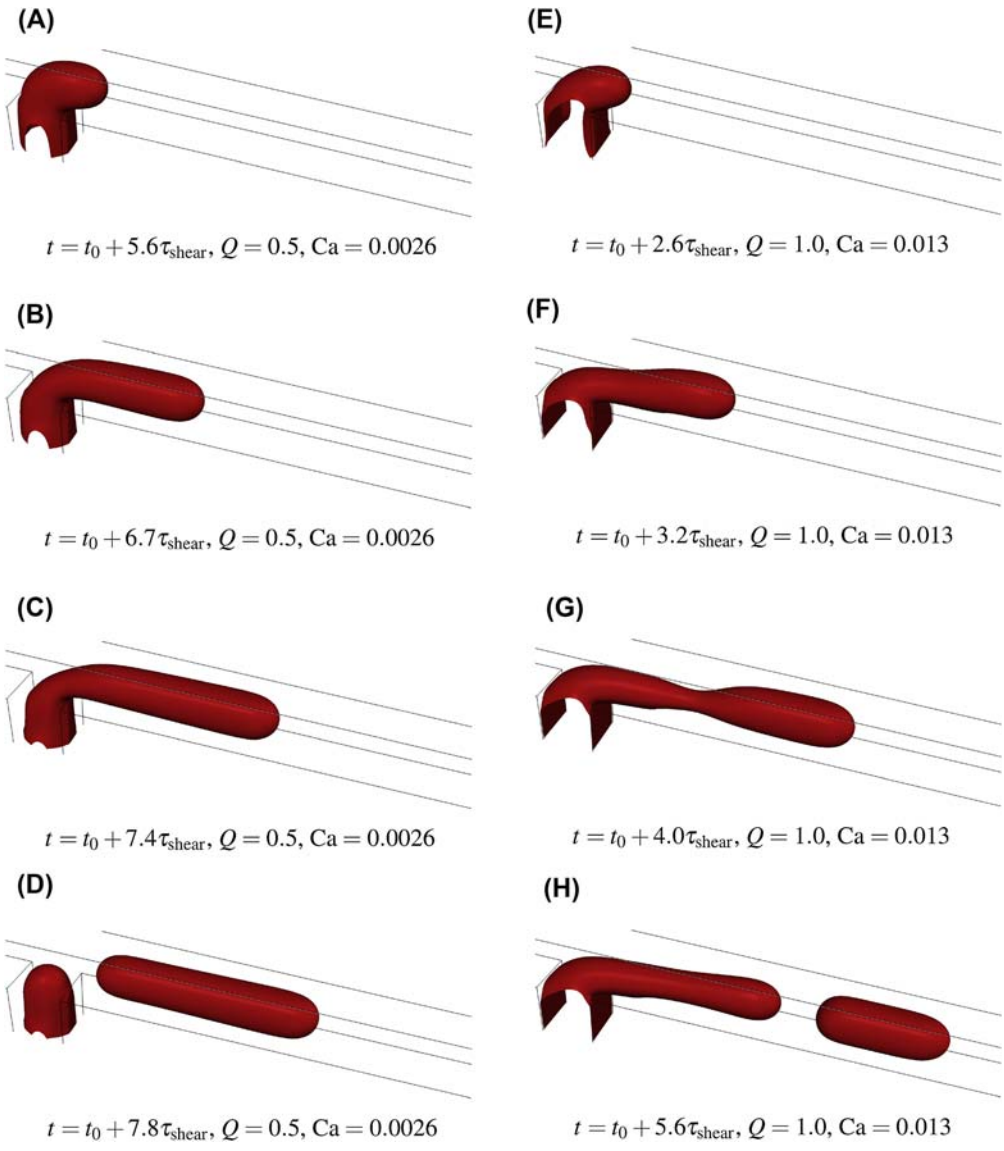

FIGURE 20.4 Droplet formation in T-junction geometries. Panels (A−D) illustrate the squeezing regime at Ca = 0.0026: the fluid thread enters and obstructs the main channel and breakup is mainly driven by the pressure buildup upstream of the emerging thread. Both the dynamics of breakup and the scaling of the sizes of droplets are influenced weakly by viscous forces. Panels (E−H) show typical features of the dripping regime at Ca = 0.013: the breakup process starts to be influenced by the shear forces, although the thread still occupies a significant portion of the main channel. This results in smaller droplets formed downstream of the T-junction. *Courtesy Gupta, A., Sbragaglia, M., 2016. A lattice Boltzmann study of the effects of viscoelasticity on droplet formation in microfluidic cross-junctions. The European Physical Journal E 39 (1), 1−15.*

Clearly, the above rule represents a balance between dispersion of color (first term) and its preferential redirection to a lattice region dominated by like color. The latter process is controlled by the segregation parameter β, discussed shortly. As a consequence of using the rule in Eq. (20.19), together with an appropriate IB force, a drop of red fluid will spontaneously form from an initially uniform mixture of red and blue fluid. In Eq. (20.19) the continuum scale interface normal $\hat{\boldsymbol{n}}$ is determined as follows. The local phase field is (Halliday et al., 2007)

$$\rho^N(\mathbf{x}, t) = \frac{\rho_r(\mathbf{x}, t) - \rho_b(\mathbf{x}, t)}{\rho_r(\mathbf{x}, t) + \rho_b(\mathbf{x}, t)}. \tag{20.20}$$

Surfaces of constant ρ^N value define the shape of the interfacial region with the surface $\rho^N = 0$ its center. Regions of the lattice characterized by $\rho^N = \pm 1$ are considered to contain pure, bulk fluids. Interfacial fluid occupies regions where $|\rho^N| < 1$.

This book belongs to Central Library BADJI Mokhtar-ANNABA UNIVERSITY Copyright Elsevier 2024

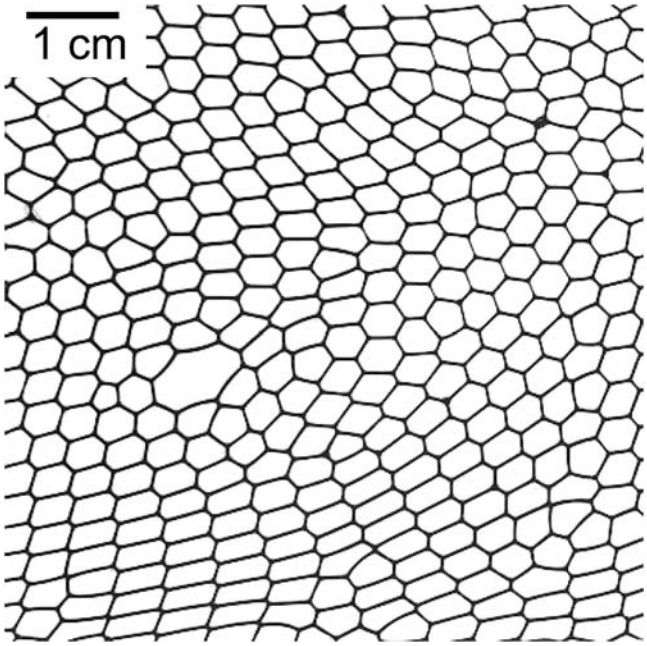

FIGURE 20.5 A snapshot of the bubbles in the foam flowing from left to right. *Courtesy Dollet, B., Scagliarini, A., Sbragaglia, M., 2015. Two-dimensional plastic flow of foams and emulsions in a channel: experiments and lattice Boltzmann simulations. Journal of Fluid Mechanics 766, 556–589.*

Throughout the narrow but distributed interfacial region, the local interface normal is determined using numerical gradients as

$$\widehat{\boldsymbol{n}} = -\frac{\nabla\rho^N}{|\nabla\rho^N|}. \tag{20.21}$$

For a red drop in a blue fluid, the interface normal unit vector, $\widehat{\boldsymbol{n}}$ points away from the enclosed red fluid. Local interfacial curvature is obtained from the surface gradient of $\widehat{\boldsymbol{n}} = \left(\widehat{n}_x, \widehat{n}_y\right)$, which, in 2D, is (Lishchuk et al., 2003)

$$\kappa \equiv \widehat{n}_x\widehat{n}_y\left(\frac{\partial\widehat{n}_y}{\partial x} + \frac{\partial\widehat{n}_x}{\partial y}\right) - \widehat{n}_y^2\frac{\partial\widehat{n}_x}{\partial x} - \widehat{n}_x^2\frac{\partial\widehat{n}_y}{\partial y}. \tag{20.22}$$

All the derivatives in Eqs. (20.21) and (20.22) may be computed to third-order accuracy if an appropriate stencil is used for the standard D2Q9 lattice (Halliday et al., 2013):

$$\frac{\partial f}{\partial x_\alpha} = \frac{1}{c_s^2}\sum_{i\neq 0} w_i f(\mathbf{x} + \boldsymbol{c}_i\Delta t)c_{i\alpha} + O\left(\boldsymbol{c}_i^4\right) \tag{20.23}$$

Eq. (20.19) can be analyzed and shown to generate a kinematically consistent interface profile (Halliday et al., 2007). For example, for a flat interface $\widehat{\boldsymbol{n}} = \widehat{\boldsymbol{e}}_x$ centered initially on x = 0, embedded within a fluid in uniform motion $\mathbf{u} = u_0\widehat{\boldsymbol{e}}_x$, one can show that the phase field is described by

$$\rho^N(\mathrm{x}, t) = \tan h\left(\beta(\mathrm{x} - u_0 t)\right), \tag{20.24}$$

which represents color kinematics appropriate to the continuum scale and immiscible components.

20.5.2 Many Mutually Immiscible Fluids

In fact, the segregation rule in Eq. (20.19) may be generalized straightforwardly to describe $M \gg 2$ mutually immiscible fluid components (Spencer et al., 2011) (see Section 20.3.3), each now identified by a subscript $n = 0,\ldots,M-1$ (with fluid $n = 0$ usually taken to be the background fluid):

$$f_{ni}(\mathbf{x} + \mathbf{c}_i\Delta t, t + \Delta t) = \frac{\rho_n(\mathbf{x})}{\rho(\mathbf{x})}f_i^\dagger(\mathbf{x}, t) + w_i\sum_{m=0}^{M-1}\beta_{nm}\frac{\rho_n(\mathbf{x})\rho_m(\mathbf{x})}{\rho(\mathbf{x})}\mathbf{c}_i\cdot\widehat{\boldsymbol{n}}_{nm}, \tag{20.25}$$

This book belongs to Central Library BADJI Mokhtar-ANNABA UNIVERSITY
Copyright Elsevier 2024

where the colored densities are defined as follows:

$$\rho_n = \sum_i f_{ni}, \quad \rho = \sum_{n=0}^{M-1} \rho_n \tag{20.26}$$

and a set of phase fields and associated gradients define the interfacial normals:

$$\rho_{nm}^N(\mathbf{x}, t) = \frac{\rho_n(\mathbf{x}, t) - \rho_m(\mathbf{x}, t)}{\rho_n(\mathbf{x}, t) + \rho_m(\mathbf{x}, t)}, \quad \widehat{\boldsymbol{n}}_{nm} = -\frac{\nabla \rho_{nm}^N}{\left|\nabla \rho_{nm}^N\right|}. \tag{20.27}$$

Note that it follows from the definition of the phase field that

$$\widehat{\boldsymbol{n}}_{nm} = -\widehat{\boldsymbol{n}}_{mn},$$

which means that color mass is conserved in Eq. (20.25). Now, if one makes additional assumptions regarding the absolute number of different fluids, which can be present at any lattice node, memory and execution speed scale only weakly with M, allowing for practical simulation of many, mutually immiscible drops or, indeed, vesicles (Dupin et al., 2004).

We defer further discussion of the application of this method to cellular-scale blood flow until we have accounted for the method by which the dynamics of a biological membrane may be encapsulated within multicomponent LB simulation.

20.6 MODELING MEMBRANES AS FLUID–FLUID INTERFACES

Correct interfacial kinematics arise from the segregation step previously considered: specifically, a kinematic property of mutual impenetrability emerges from the postcollision color segregation rules of the previous section. What we must now consider is the associated physical dynamics.

Generally, a spatially variable IB force distribution is applied to interfacial fluid (i.e., to regions of the lattice with $|\rho^N| < 1$) to recover target dynamic boundary conditions. A simple example is provided by the continuum scale force distribution $\mathbf{F} = \frac{1}{2}\sigma\kappa\nabla\rho^N$, which generates a Laplace pressure step of magnitude $\sigma\kappa$ between the separated bulk fluids (Lishchuk et al., 2003), along with a no-traction condition on tangential stress.

In this section, we consider a more complex class of interfaces such as closed membranes, which are defined as deformable boundaries separating two immiscible bulk fluids, each having conserved cross-sectional area. The enclosed liquid and membrane together form a vesicle. Unlike other interfacial problems where the area between the phases may increase or decrease, in the vesicle the total membrane or interface area is preserved, there being no mass exchange between the bilayer and the surrounding bulk fluid. However, like purely liquid–liquid boundaries, membranes can be regarded as an unsteady interface responsive to flow stresses between the segregated fluids.

On the foundation of the color-gradient model set out above, we have developed a Lishchuk-type force able to produce appropriate continuum scale membrane boundary conditions. Simulations that contain such a membrane achieve, e.g., a correct vesicle conformation by deforming and mediating appropriate physical stresses between the interior and exterior fluids. The detailed structure of a biological membrane's cytoskeleton and lipid bilayer is invisible at the continuum scale, so we adapt the approach of Kaoui et al. (2008) and postulate that interfacial fluid possesses properties representative of the membrane mechanics namely (1) preferred local curvature, (2) bending rigidity, (3) adjusted compressibility properties, (4) interfacial tension, and (5) conserved global length of the interfacial fluid. A representative force distribution derives from the variational derivative of an expression for overall membrane free energy incorporating effects (1)–(5) (Halliday et al., 2013). This force distribution is a normally directed, weighted fluid body force density acting only in the boundary region between the two fluids, i.e., on interfacial fluid:

$$\mathbf{F} = \frac{1}{2}\nabla\rho^N\left[\kappa\left(\sigma - \alpha\left(1 - \frac{l}{l_0}\right)\right) - \frac{b}{2}\kappa\left(\kappa^2 - \kappa_0^2\right) - b\frac{\partial^2\kappa}{\partial s^2}\right]. \tag{20.28}$$

In the above, s denotes distance measured along the direction of the membrane, $\frac{1}{2}\nabla\rho^N$ is a weight (Lishchuk et al., 2003), $\kappa(\kappa_0)$ the (preferred) interfacial curvature, α the interfacial compressibility, σ an interfacial tension further discussed below, $l(l_0)$ the (reference) length of the interface, and b its bending rigidity. Length l is maintained close to l_0 by allowing its value to modulate an effective interfacial tension $\sigma - \alpha\left(1 - \frac{l}{l_0}\right)$. That is, using that force density in Eq. (20.28), it results in an equilibrium shape, which is consistent with a constant enclosed volume, membrane cross-sectional area (length in 2D), membrane preferred curvature, and interfacial tension, which may nevertheless be deformed when external

This book belongs to Central Library BADJI Mokhtar-ANNABA UNIVERSITY
Copyright Elsevier 2024

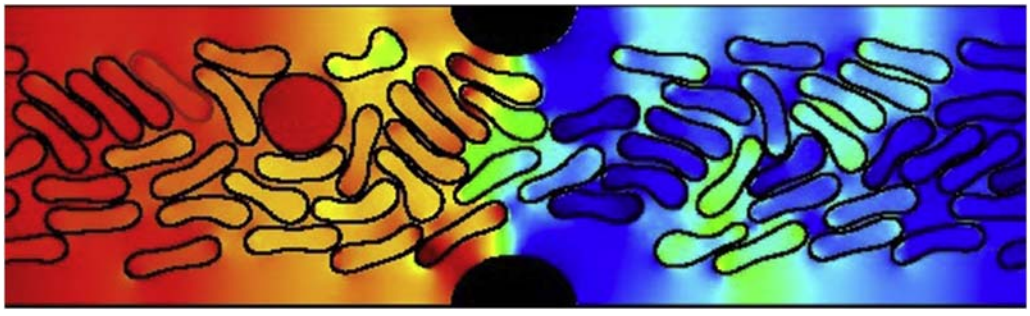

FIGURE 20.6 A snapshot of pressure driven flow of multiple vesicles in a channel with a constriction at $Re = 30$. Solid walls bound the domain, using the "link bounce-back method" (Succi, 2001). The pressure boundaries are implemented following Kim and Pitsch (2007). An exactly incompressible $D2Q9$ lattice Bhatnagar–Gross–Krook model was used with vesicles' properties as follows, all expressed in lattice units: bending rigidity $b = 0.55$, surface tension $\sigma = 0.008$, membrane compressibility $\alpha = 0.15$, all fluids' segregation parameters $\beta_{nm} = 0.67$, $\forall n$, m, and the membrane preferred curvature $\kappa_0 = 0$. For the almost-circular (low deflation) vesicle preferred length $l_0 = 254$ and its initial lattice area was 5153. For the 58 deflated vesicles, preferred length was $l_0 = 224$ and their initial area was 2706. The velocity field has been initialized at rest, $\mathbf{u} = 0$ and the snapshot of the flow configuration was taken at time step $t = 4444800$. The overall simulation lattice is of size 999×297.

traction is applied, as the embedding fluid flows. Note that the constraint of constant vesicle volume is automatic as long as the enclosed fluid is incompressible and the parameterization of the membrane is direct. By selecting appropriate parameters, the deflation and deformability of vesicles may be readily adjusted (Halliday et al., 2013).

It is necessary briefly to consider how a spatially variable body force may be applied in LB simulation. The membrane force in Eq. (20.28) is applied as an external force density to what is effectively a single lattice fluid described by kinetic-scale distribution function $f_i = f_{ri} + f_{bi}$. Doolen et al. (1998) and Guo et al. (2002) generalized the lattice Bhatnagar–Gross–Krook model, originally devised by Qian et al. (1992), to describe lattice fluid subject to a known, spatially variable external force density, $\mathbf{F}$. Collision and forcing of the distribution function expressed in Eq. (20.1) may be straightforwardly reexpressed as

$$f_i^{\dagger} = f_i^{(0)}(\rho, \rho\mathbf{u}) + (1-\omega) f_i^{(1)}(\nabla\rho, \ldots \partial_x u_y \ldots, \mathbf{F}) + F_i(\omega, \mathbf{F}, \mathbf{u}), \tag{20.29}$$

where, recall, the dagger superscript indicates a postcollision, prepropagation quantity, and $f_i^{(0)}(\rho, \mathbf{u})$ denotes the equilibrium distribution function (Succi, 2001), and the source term, F_i, is

$$F_i = w_i\left(1 - \frac{\omega}{2}\right)\left(\frac{\mathbf{c}_i - \mathbf{u}}{c_s^2} + \frac{(\mathbf{c}_i \cdot \mathbf{u})(\mathbf{c}_i)}{c_s^4}\right) \cdot \mathbf{F}, \tag{20.30}$$

where all symbols have their usual meaning. Importantly, in the presence of an external force $\mathbf{F}$, the value of the fluid velocity depends on that external force (Guo et al., 2002):

$$\mathbf{u} = \frac{1}{\rho}\sum_i f_i \mathbf{c}_i + \frac{1}{2\rho}\mathbf{F}. \tag{20.31}$$

We return to this matter shortly. In the method outlined so far, all the dynamics and kinematics of the multifluid system of plasma and vesicle(s) is embedded within (1) force distribution and (2) the fluids' phase field. The method requires no set of constrained Lagrangian points to indicate the location of any of its potentially many interfaces (Halliday et al., 2013), and it inherits all the advantages of computational scaling with the number of immiscible components (i.e., vesicles) outlined in Section 20.5.2. Hence, little additional expense is incurred as the number of simulated vesicles increases beyond $N = 5$, to produce data such as that in Fig. 20.6. In the system represented there, there are >50 vesicles at representative concentration $c = 0.42$, with a range of deflations. A pressure gradient is applied to the system (regions of low (high) relative pressure are rendered blue (red)) and all the vesicles advect, deform, and order in response to the flow generated by the pressure gradient and the physics of their membranes. Simulation details may be found in the figure caption.

Although the data of Fig. 20.6 represent an efficient numerical solution to a very complex flow containing many interacting vesicles at high volume fraction, each vesicle shape evolves with the global membrane length (only) conserved. Implicitly, the constraint of global length conservation allows for different rates of strain in different membrane (interfacial fluid) regions, which in turn allows a variation of its tangential velocity. Such motion is only acceptable for a liquid drop. Put another way, the physical effect of uniform tangential motion (*tank-treading motion*) in the vesicle membrane is not recovered.

This book belongs to Central Library BADJI Mokhtar-ANNABA UNIVERSITY Copyright Elsevier 2024

It was soon found that the method described so far must be enhanced if modalities associated with local incompressibility of membrane length elements are to be recovered from individual vesicles' fluid dynamics. We have recently introduced additional normal and tangential forces to encapsulate such effects. Enhanced dynamics is accomplished by adding to the body force density in expression (20.28) an additional contribution with a tangential component (Halliday et al., 2016):

$$\mathbf{F}' = \frac{1}{2}|\nabla\rho^N|\left(k\varepsilon\kappa\widehat{\boldsymbol{n}} + k\frac{\partial\varepsilon}{\partial s}\widehat{\boldsymbol{t}}\right), \tag{20.32}$$

where ε is a fictitious Hookean membrane strain and k its associated spring constant. The membrane strain field is computed from an explicit scheme solution of the equation:

$$\frac{\partial\varepsilon}{\partial t} = \frac{\partial u_t}{\partial s} - u_x\frac{\partial\varepsilon}{\partial x} - u_y\frac{\partial\varepsilon}{\partial y}, \tag{20.33}$$

where u_t is the local tangential velocity of the membrane. Upwinding is necessary to compute the derivatives in the right-hand side. Unfortunately, the solution ε of Eq. (20.33) is dependent on $\mathbf{u}$, which means that the correction force in Eq. (20.32) inherits a velocity dependence. Because $\mathbf{F}' = \mathbf{F}(\mathbf{u})$, Eqs. (20.31)−(20.33) must be solved by an iterative procedure (Halliday et al., 2016), to determine $\mathbf{u}$ and $\mathbf{F}'$.

Despite this elaborate procedure, the inclusion of $\mathbf{F}'$ introduces the tank-treading and tumbling behavior into the method, even for the quite deflated, biconcave shapes corresponding to red blood cells, at least in two dimensions, as we discuss this in the next section. In conclusion, notwithstanding the issue raised above, our approach dispenses entirely with the need explicitly to track the membrane, removes all need for computationally expensive and intricate interface tracking and remeshing, is completely Eulerian, and, not least, represents a two-way coupled vesicle membrane and flow within an LB framework.

20.7 FLUID-FILLED VESICLES IN A SHEAR FLOW

Vesicles are small structures consisting of an internal fluid enclosed by a lipid bilayer membrane, suspended in an external, aqueous solution. The physics of vesicles has attracted much theoretical and computational interest in recent decades. This is because of their ability to exhibit dynamical behaviors of relevance to living cells (such as red blood cells), the possibility of their exploitation as carriers of biomaterials (for example drugs), or their use in microencapsulation of active materials in drug delivery. Consequently, understanding the dynamical behavior of such deformable entities (shape, orientation, deformation, and migration), when the surrounding fluid is subject to shear, is an important issue worth investigating (Kaoui et al., 2009).

The physical properties of a vesicle membrane (surface tension, bending ratio, interfacial compressibility, etc.) originate at the molecular microscale, but, as we have shown above, they can be incorporated into a continuum-scale description by an effective hydrodynamic boundary condition based on an IB force distributions. In this section, the approach described previously is used to model one single suspended vesicle under shear flow, for a range of fluid viscosity contrasts (but no density contrast):

$$\Lambda = \frac{\eta_i}{\eta_e}$$

where η_i (η_e) is the shear viscosity of the internal (external) fluids and $\nu = \eta/\rho$ is the kinematic viscosity The data in Fig. 20.7 demonstrate our model's ability to recover a transition between tank-treading and tumbling. For a mild vesicle deflation 0.93, we denote the angular inclination with respect to the direction of undisturbed flow by θ (which is measured from the principal axes of the vesicle's inertia tensor). Where a steady inclination exists (identified in simulation $\frac{d\theta}{dt} \approx 0$) it is recorded. For $\Lambda > 2.5$ a steady inclination gives way to the unsteady, tumbling state. Again, refer to the figure caption for simulation data.

20.8 CONCLUSIONS

Summarizing, we have reviewed two major families of multicomponent LB models: pseudopotential methods and modified color-gradient methods. Both methods were originally intended to describe the dynamics of multicomponent and multiphase flows, such as droplets, foams, emulsions, and similar complex states of flowing matter. Lately, however, there has been a surge of interest in extending such models to the case of deformable bodies floating within a solvent fluid for problems of decided biological interest. The motivation is inherently computational, i.e., provide a fully Eulerian

This book belongs to Central Library BADJI Mokhtar-ANNABA UNIVERSITY
Copyright Elsevier 2024

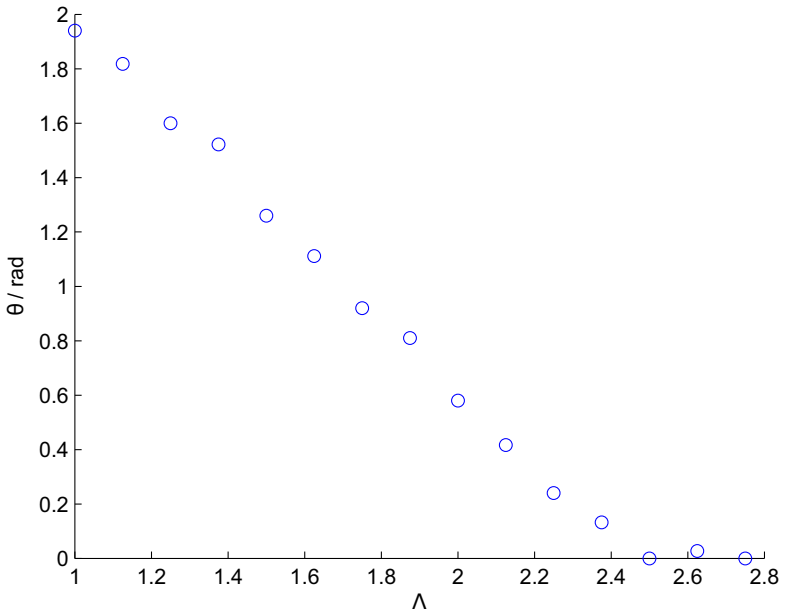

FIGURE 20.7 Data for a single vesicle with deflation 0.93 in a shear flow. The internal and external viscosities are in ratio Λ and the simulation was performed with lattice Bhatnagar–Gross–Krook with the external fluid parameterized by $\omega = 1$, $\nu = \frac{1}{6}$, $\beta = 0.67$. The angle θ denotes the steady inclination angle where it may be measured. For $\Lambda > 2.5$, $\theta \to 0$ tank-treading gives way to tumbling. The lattice dimensions were 131×105 lattice units.

alternative to mainstream Eulerian–Lagrangian techniques, whereby the fluid flow is typically solved by grid methods (including LB), whereas the motion of the deformable bodies is tracked by suitable off-grid particle methods. A realistic representation of the bodies may require a substantial amount of degrees of freedom, thereby considerably taxing the computational procedure, due to expensive interpolation/extrapolation procedures mapping the particles degrees of freedom to the grid and vice versa. In contrast, by letting the deformable interface dynamics emerge bottom-up from the specification of appropriate pseudopotentials and/or mesoscopic force fields incorporating the mechanical-elastic constraints, which characterized the body motion, the fully Eulerian approach would dispense from any fluid-particle coupling procedure. Albeit very appealing and potentially far reaching, the fully Eulerian approach still meets with a number of theoretical and computational challenges associated with the task of identifying the proper pseudopotentials and/or mesoscale forces and devises efficient procedures for their practical implementation on highly parallel computer platforms.

ACKNOWLEDGMENTS

This research has been funded from the European Research Council under the European Union's Seventh Framework Programme (FP/2007–2013)/ERC Grant Agreement n. 306357 (ERC Starting Grant "NANO-JETS").

REFERENCES

Benzi, R., Sbragaglia, M., Succi, S., Bernaschi, M., Chibbaro, S., 2009. Mesoscopic lattice Boltzmann modeling of soft-glassy systems: theory and simulations. The Journal of Chemical Physics 131 (10), 104903.

Carnahan, N.F., Starling, K.E., 1969. Equation of state for nonattracting rigid spheres. The Journal of Chemical Physics 51 (2), 635–636.

Colosqui, C.E., Falcucci, G., Ubertini, S., Succi, S., 2012. Mesoscopic simulation of non-ideal fluids with self-tuning of the equation of state. Soft Matter 8 (14), 3798–3809.

Dollet, B., Scagliarini, A., Sbragaglia, M., 2015. Two-dimensional plastic flow of foams and emulsions in a channel: experiments and lattice Boltzmann simulations. Journal of Fluid Mechanics 766, 556–589.

Doolen, G.D., He, X., Chen, S., 1998. A novel thermal model for the lattice Boltzmann method in incompressible limit. Journal of Computational Physics 146, 282–300.

Dupin, M.M., Spencer, T.J., Halliday, I., Care, C.M., 2004. A many-component lattice Boltzmann equation simulation for transport of deformable particles. Philosophical Transactions of the Royal Society of London A: Mathematical, Physical and Engineering Sciences 362, 1885–1914.

Falcucci, G., Jannelli, E., Ubertini, S., Succi, S., 2013. Direct numerical evidence of stress-induced cavitation. Journal of Fluid Mechanics 728, 362–375.

This book belongs to Central Library BADJI Mokhtar-ANNABA UNIVERSITY Copyright Elsevier 2024

Grunau, D., Chen, S., Eggert, K., 1989-1993. A lattice Boltzmann model for multiphase fluid flows. Physics of Fluids A: Fluid Dynamics 5 (10), 2557−2562.

Gunstensen, A.K., Rothman, D.H., Zaleski, S., Zanetti, G., 1991. Lattice Boltzmann model of immiscible fluids. Physical Review A 43 (8), 4320.

Guo, Z., Zheng, C., Shi, B., April 2002. Discrete lattice effects on the forcing term in the lattice Boltzmann method. Physical Review E 65, 046308.

Gupta, A., Sbragaglia, M., 2014. Deformation and breakup of viscoelastic droplets in confined shear flow. Physical Review E 90 (2), 023305.

Gupta, A., Sbragaglia, M., 2016. A lattice Boltzmann study of the effects of viscoelasticity on droplet formation in microfluidic cross-junctions. The European Physical Journal E 39 (1), 1−15.

Halliday, I., Hollis, A.P., Care, C.M., 2007. Lattice Boltzmann algorithm for continuum multicomponent flow. Physical Review E 76 (2), 026708.

Halliday, I., Lishchuk, S.V., Spencer, T.J., Pontrelli, G., Care, C.M., 2013. Multiple-component lattice Boltzmann equation for fluid-filled vesicles in flow. Physical Review E 87, 023307.

Halliday, I., Lishchuk, S.V., Spencer, T.J., Pontrelli, G., Evans, P.C., 2016. Local membrane length conservation in two-dimensional vesicle simulation using a multicomponent lattice Boltzmann equation method. Physical Review E 94, 023306.

Kamali, M.R., Van den Akker, H.E.A., 2013. Simulating gas-liquid flows by means of a pseudopotential lattice Boltzmann method. Industrial and Engineering Chemistry Research 52 (33), 11365−11377.

Kaoui, B., Ristow, G.H., Cantat, I., Misbah, C., Zimmermann, W., February 2008. Lateral migration of a two-dimensional vesicle in unbounded poiseuille flow. Physical Review E 77, 021903.

Kaoui, B., Biros, G., Misbah, C., October 2009. Why do red blood cells have asymmetric shapes even in a symmetric flow? Physical Review Letters 103, 188101.

Kim, S.H., Pitsch, H., 2007. A generalized periodic boundary condition for lattice Boltzmann method simulation of a pressure driven flow in a periodic geometry. Physics of Fluids 19 (10), 108101.

Körner, C., Thies, M., Hofmann, T., Thürey, N., Rüde, U., 2005. Lattice Boltzmann model for free surface flow for modeling foaming. Journal of Statistical Physics 121 (1−2), 179−196.

Lallemand, P., Luo, L.-S., Peng, Y., 2007. A lattice Boltzmann front-tracking method for interface dynamics with surface tension in two dimensions. Journal of Computational Physics 226 (2), 1367−1384.

Latva-Kokko, M., Rothman, D.H., 2005. Diffusion properties of gradient-based lattice Boltzmann models of immiscible fluids. Physical Review E 71 (5), 056702.

Lishchuk, S.V., Care, C.M., Halliday, I., 2003. Lattice Boltzmann algorithm for surface tension with greatly reduced microcurrents. Physical Review E 67, 036701.

Montessori, A., Falcucci, G., La Rocca, M., Ansumali, S., Succi, S., 2015. Three-dimensional lattice pseudo-potentials for multiphase flow simulations at high density ratios. Journal of Statistical Physics 161 (6), 1404−1419.

Montessori, A., Prestininzi, P., La Rocca, M., Falcucci, G., Succi, S., Kaxiras, E., 2016. Effects of Knudsen diffusivity on the effective reactivity of nanoporous catalyst media. Journal of Computational Science 17 (Part 2), 377−383.

Orlandini, E., Swift, M.R., Yeomans, J.M., 1995. A lattice Boltzmann model of binary-fluid mixtures. Europhysics Letters 32 (6), 463.

Peskin, C.S., 2002. The immersed boundary method. Acta Numerica 11, 479−517.

Qian, Y.H., d'Humieres, D., Lallemand, P., 1992. Lattice BGK models for Navier-Stokes equation. Europhysics Letters 17 (6), 479.

Qian, J., Law, C.K., 1997. Regimes of coalescence and separation in droplet collision. Journal of Fluid Mechanics 331, 59−80.

Qin, R.S., June 2006. Mesoscopic interparticle potentials in the lattice Boltzmann equation for multiphase fluids. Physical Review E 73, 066703. http://dx.doi.org/10.1103/PhysRevE.73.066703. URL: http://link.aps.org/doi/10.1103/PhysRevE.73.066703.

Rothman, D.H., Keller, J.M., 1988. Immiscible cellular-automaton fluids. Journal of Statistical Physics 52 (3−4), 1119−1127.

Swift, M.R., Osborn, W.R., Yeomans, J.M., 1995. Lattice Boltzmann simulation of nonideal fluids. Physical Review Letters 75 (5), 830.

Sbragaglia, M., Benzi, R., Biferale, L., Succi, S., Sugiyama, K., Toschi, F., 2007. Generalized lattice Boltzmann method with multirange pseudopotential. Physical Review E 75 (2), 026702.

Shan, X., 2006. Analysis and reduction of the spurious current in a class of multiphase lattice Boltzmann models. Physical Review E 73 (4), 047701.

Shan, X., Chen, H., 1993. Lattice Boltzmann model for simulating flows with multiple phases and components. Physical Review E 47 (3), 1815.

Spencer, T.J., Halliday, I., Care, C.M., 2011. A local lattice Boltzmann method for multiple immiscible fluids and dense suspensions of drops. Philosophical Transactions of the Royal Society of London A: Mathematical, Physical and Engineering Sciences 369 (1944), 2255−2263.

Succi, S., 2001. The Lattice Boltzmann Equation for Fluid Dynamics and Beyond. Oxford University Press.

Succi, S., 2015. Lattice Boltzmann 2038. Europhysics Letters 109 (5), 50001.

Wolfram, S., 1986. Cellular automaton fluids 1: basic theory. Journal of Statistical Physics 45 (3−4), 471−526.

Yuan, P., Schaefer, L., 2006. Equations of state in a lattice Boltzmann model. Physics of Fluids 18 (4), 042101.

This book belongs to Central Library BADJI Mokhtar-ANNABA UNIVERSITY

Copyright Elsevier 2024

Chapter 21

Lattice Boltzmann Models of Highly Viscous Fluids and Multicellular Self-Assembly

A. Cristea[1] and A. Neagu[2,3]

[1]Romanian Academy-Timisoara Division, Timisoara, Romania; [2]Victor Babes University of Medicine and Pharmacy Timisoara, Timisoara, Romania; [3]University of Missouri, Columbia, MO, United States

21.1 VISCOUS FLUIDS AND THE LATTICE BOLTZMANN METHOD

Complex fluids are multiphase and multicomponent systems of great interest for technological development. Numerical simulations enable us to study complex fluids, representing an alternative to expensive experiments. Nevertheless, building realistic models for multiphase/multicomponent fluids is difficult because of the complexity of the interactions between fluid particles.

Given the importance of the topic, a wealth of computational methods have been developed for modeling complex fluids at the mesoscopic length scale. One of the most widely used methods is based on lattice Boltzmann (LB) models. In 1872, Ludwig Boltzmann introduced his equation (Boltzmann, 1995; Harris, 1971; Huang, 1963), starting from the following hypotheses concerning the evolution of the single particle distribution function:

1. The only possible interparticle interactions are binary collisions.
2. The initial velocities of the particles involved in the collision are not correlated (hypothesis of the molecular chaos).
3. The external forces have no effect on the dynamics of local interactions.

Following these hypotheses, Boltzmann considered the collision operator $Q(f_1, f_2)$:

$$Q(f_1,f_2) = \int d\vec{v}_2 d\Omega |\vec{v}_1 - \vec{v}_2| \sigma(\Omega) \left[f_1' f_2' - f_1 f_2\right] \tag{21.1}$$

where $\sigma(\Omega)$ is the differential collision cross section for the two particle collision, which transform the velocities: $\{\vec{v}_1, \vec{v}_2\}$ (before collision) into $\left\{\vec{v}_1', \vec{v}_2'\right\}$ (after collision), and proposed an integrodifferential equation to describe fluid dynamics:

$$\left(\frac{\partial}{\partial t} + \vec{v}\frac{\partial}{\partial \vec{x}} + \vec{F}_{ext}\frac{\partial}{\partial \vec{v}}\right) f(\vec{x}, \vec{v}, t) = Q(f_1,f_2) \tag{21.2}$$

A major problem that appears when solving the Boltzmann equation is the complicated form of the collision term. In 1954, an ingenious way to simplify this term was proposed independently by Bhatnagar et al. (1954) and Welander (1954).

Numerical Methods and Advanced Simulation in Biomechanics and Biological Processes. https://doi.org/10.1016/B978-0-12-811718-7.00021-6
Copyright © 2018 Elsevier Ltd. All rights reserved.

This book belongs to Central Library BADJI Mokhtar-ANNABA UNIVERSITY

Copyright Elsevier 2024

This simplification, widely known as the *BGK approximation* (Harris, 1971; Succi, 2001; Wolf-Gladrow, 2000), is based on the operator $L(f)$, which replaces the Boltzmann collision operator $Q(f, f)$ and satisfies the following conditions:

1. $L(f)$ conserves the collision invariants $\psi \in \left\{\rho, \rho u_\alpha, \frac{1}{2}\rho u^2\right\}$, so we have:

$$\int L(f)\psi(v)d^3v = 0$$

2. The distribution function $f(\mathbf{x}, \mathbf{v}, t)$ relaxes to the Maxwell−Boltzmann equilibrium distribution function:

$$L(f) = -\frac{f(\mathbf{x}, \mathbf{v}, t) - f^{eq}(\mathbf{x}, \mathbf{v}, t)}{\tau} \tag{21.3}$$

The relaxation time τ is correlated with the mean time between two consecutive collisions of the particle. If we replace the collision operator in the Boltzmann Eq. (21.2) with the linearized collision term (Eq. 21.3), we get the following form of the evolution equation of the distribution function f:

$$\partial_t f + v_\beta \partial_\beta f + a_\beta \partial_\beta^v f = -\frac{1}{\tau}[f - f^{eq}] \tag{21.4}$$

(Here we used the notation $\partial_t = \partial/\partial t$, $\partial_\beta = \partial/\partial x_\beta$, $\partial_\beta^v = \partial/\partial v_\beta$, as well as the sum over the Greek indices representing the space coordinates runs from 1 to D for a model formulated in D-dimensional space.)

The independent variables $\mathbf{x}$ and $\mathbf{v}$ generate the phase space and belong to the continuum spectrum. The basic idea behind LB models is the *discretization of the phase space* (Chen et al., 1998; Rothman and Zaleski, 1997; Succi, 2001; Wolf-Gladrow, 2000). Accordingly, the distribution functions are defined only in the nodes of a *lattice* $\mathcal{L}$, which belongs to the D-dimensional space $D \in \{1, 2, 3\}$. The velocity space is reduced to a finite set of vectors $\{\mathbf{e}_i\}$, $i = 0, 1, \ldots \mathcal{N}$. After phase space discretization, the distribution function $f(\mathbf{x}, \mathbf{v}, t)$ is replaced by a finite set of $\mathcal{N}$ distribution functions $f_i \equiv f(\mathbf{x}, \mathbf{e}_i, t)$. The relaxation time τ is correlated with the mean time between two consecutive collisions of a particle. Thus, the Boltzmann equation is replaced by a system of $\mathcal{N}$ equations:

$$\partial_t f_i + \mathbf{e}_i \cdot \nabla f_i - \frac{1}{k_B T}\mathbf{F} \cdot [\mathbf{e}_i - \mathbf{u}] f_i^{eq} = -\frac{1}{\tau}[f_i - f_i^{eq}] \tag{21.5}$$

The equilibrium distribution functions, f_i^{eq}, are given by the well-known Maxwell−Boltzmann distribution:

$$f_i^{eq} = w_i \rho \left[1 + \frac{\mathbf{e}_i \cdot \mathbf{u}}{\chi c^2} + \frac{(\mathbf{e}_i \cdot \mathbf{u})^2}{2\chi^2 c^4} - \frac{\mathbf{u} \cdot \mathbf{u}}{2\chi c^2}\right] \tag{21.6}$$

The parameters w_i and χ are characteristics of the LB model (Qian et al., 1992). The Cartesian components of the vectors $\{\mathbf{e}_i\}$ satisfy the Gauss−Hermite quadrature to compute the hydrodynamic moments up to the fourth order (He and Luo, 1997a; Shan, 2006). The speed c is correlated with the thermal speed of the fluid particles (Luo, 2000):

$$c = \sqrt{\frac{k_B T}{\chi m}}. \tag{21.7}$$

Three distinct kinds of LB models have been proposed, which were continuously refined thereafter: the color gradient method of Gunstensen et al. (1991), the pseudopotential method of Shan and Chen (1993, 1994), and the Oxford free-energy model of Swift et al. (1995, 1996).

Gunstensen et al. (1991) developed the first multicomponent LB model. They proposed an extension where red and blue distribution functions, $f_i^{(r)}$ and $f_i^{(b)}$, represent two immiscible fluids. The color's model is written for each component:

$$f_i^c(\mathbf{x} + \mathbf{e_i}\delta t, t + \delta t) = f_i^c(\mathbf{x}, t) - \frac{1}{\tau^c}\left(f_i^c(\mathbf{x}, t) - f_i^{c(eq)}(\mathbf{x}, t)\right) + \left(\Omega_i^c\right)^{(2)} \tag{21.8}$$

This book belongs to Central Library BADJI Mokhtar-ANNABA UNIVERSITY
Copyright Elsevier 2024

where the local equilibrium distribution function depends on the local macroscopic variables of each component. The last part of the collision operator vanishes inside the bulk regions, but generates a surface tension in the mixed region. Phase segregation is achieved by a recoloring step, which adjusts the distribution, depending on the local color gradient. The mass of each phase and the total momentum are conserved at each node during collision.

In the pseudopotential model, the interaction force is given by the gradient of a repulsive potential:

$$\mathbf{F} = -G(\|\mathbf{e_i}\|)\psi(x)\sum_i \psi(\mathbf{x}+\mathbf{e_i})\mathbf{e_i} \tag{21.9}$$

$G(\mathbf{x}, \mathbf{x}')$ is the Green function and $\psi = \psi(\rho)$ is the "effective mass" (Shan and Chen, 1993; 1994).

The Oxford free-energy approach starts from the free energy functional:

$$\psi = \int d\vec{r}\left[\psi + \frac{\kappa}{2}(\nabla n)^2 + \frac{\kappa}{2}(\nabla\Delta n)^2\right] \tag{21.10}$$

where the parameter λ in the bulk free energy density

$$\psi = \frac{\lambda}{4}n^2\left[1-\frac{(\Delta n)^2}{n^2}\right] - Tn + \frac{T}{2}(n+\Delta n)\ln\left[\frac{n+\Delta n}{2}\right] + \frac{T}{2}(n-\Delta n)\ln\left[\frac{n-\Delta n}{2}\right], \tag{21.11}$$

controls the strength of the repulsive interaction between particles of different species; the constant κ controls the surface tension. In this model, the force was introduced in the expression of the equilibrium distribution functions. This model uses separate LB equations for the quantities $n = (n^0 + n^1)$ (the local particle density) and $\Delta n = (n^0 - n^1)$ (the order parameter) (Cristea and Sofonea, 2004; Swift et al., 1995, 1996).

For the general problem of multiphase viscous fluid flow, numerous studies have been carried out: Comparini and Mannucci (1998) solved theoretically a Bingham fluid (the simplest viscoplastic non-Newtonian fluid) in contact with a Newtonian fluid and Frigaard (2001) derived a series of nondimensional theoretical solutions for parallel multiphase Bingham flow. Bubble rising and droplet motion in a viscoplastic fluid, as well as formation and impact of viscous fluid droplets (Gross et al., 2012) were widely investigated. Coalescence of liquid droplets, once initiated, progresses due to surface tension. Assuming that the initial growth of the liquid bridge that connects the adjacent droplets is governed by the competition between surface tension σ and viscosity η, the characteristic velocity of the growth of the neck radius is given by the ratio $u_g = \sigma/\eta$. The Reynolds number $Re = \rho\sigma L/\eta^2$ is used to quantify the competition between these two types of forces. The domain $Re < 1$ defines the *viscous regime*, which is governed by the Stokes equations, in contrast to the *inertial regime*, characterized by $Re > 1$, which is described by the Euler equations.

The distribution function, f, in the LB equation can be expanded into a Chapman−Enskog series with respect to the Knudsen number ε (Succi, 2001; Wolf-Gladrow, 2000)

$$f \simeq f^{(0)} + \varepsilon f^{(1)} + \varepsilon^2 f^{(2)} + \ldots. \tag{21.12}$$

We can use two time scales, t_1 and t_2, and one length scale x_1 (Succi, 2001). The time and space derivative in the evolution equation are replaced with:

$$\partial_t = \varepsilon\partial_{t_1} + \varepsilon^2\partial_{t_2}, \;\; \partial_\beta = \varepsilon\partial_{\beta_1} \quad (\beta = 1,\ldots,D). \tag{21.13}$$

The expression of the kinematic viscosity, closely related to the relaxation parameter τ (Burgers, 1969; Grad, 1949; Sofonea and Sekerka, 2001, 2003), is of great importance because it states that the fluid behavior is independent of the discretization procedure used in LB models (Xie et al., 2016).

As noted by Yang and Boek (2013), the pseudopotential model is capable of simulating high-density ratio fluids (Yuan and Schaefer, 2006), but gives relatively low numerical stability and wide interfaces for multicomponent immiscible systems. Both the color gradient and free energy model are capable of simulating fluids with significant viscosity ratio and recover the analytical solutions of Poiseuille flow. We may conclude that the free energy and color gradient models seem appropriate to simulate the flow of binary fluids with high viscosity contrast and high numerical stability.

The numerical schemes used for solving the evolution equations introduce a supplementary term, the *spurious viscosity*. For the first order upwind scheme (see next section for details), the apparent value for the spurious viscosity is given by (Sofonea and Sekerka, 2003; Sofonea et al., 2004):

$$\eta_{ap_upwind} = \chi c^2(\tau + \psi) \tag{21.14}$$

This book belongs to Central Library BADJI Mokhtar-ANNABA UNIVERSITY
Copyright Elsevier 2024

where

$$\psi = \frac{\delta x}{c} \tag{21.15}$$

$\delta x = L/N$ is the lattice spacing ($L = 1$ is the system characteristic length) and c is the dimensionless velocity. To reduce the value of the numerical viscosity introduced by the upwind scheme, we should use $N \geq 10^4$ for $\tau \leq 10^{-3}$, which means a huge computational load, especially for 2D and 3D LB models.

For the flux limiter schemes, the value of the apparent viscosity is (Sofonea et al., 2004; Sofonea and Sekerka, 2005) as follows:

$$\eta_{ap_flux} = \chi c^2 \left[\tau + \frac{(\delta x)^2}{2cL} \right] \tag{21.16}$$

Because $\delta x < 1$, it can be seen that the value of the numerical viscosity is lower than in the upwind case, for the same values of δx and τ. Consequently, the use of flux limiter schemes leads to more realistic results, with smaller numerical errors. The following section discusses spurious velocities observed at interfaces and numerical schemes designed for reducing them.

Computer simulations of fluids require ample computational resources. A vast memory is needed for data storage and huge computing power is needed for data processing. An important feature of LB models is easy parallelization, which makes them attractive from the point of view of modern computational hardware, which evolves toward massive fine-grained parallelism. Computational performance is no longer increased by frequency scaling, but by parallelization and specialization. Usual CPUs have up to six cores, the cell processor is heterogeneous and graphics processing units (GPUs) are on the verge of becoming general purpose compute resources. On the software side, programming models for fine-grained parallelism are rapidly evolving.

The MPI (Message Passing Interface) standard (Gropp et al., 1999; Snir et al., 1999) defines the syntax and semantics of useful library functions for writing parallel computing codes. The message passing programming is explicit, with the user being responsible for process creation and data assignation to different processors. A major objective achieved by the MPI standard is the portability on a large class of parallel computing systems with different architectures. Portable, Extensible Toolkit for Scientific Computation (PETSc) (see the PETSc webpage in the list of references) is an ensemble of routines and functions developed at Argonne National Laboratory, Argonne, Illinois, for applications on parallel computing systems that support the MPI standard. PETSc contains parallel algorithms, routines, and functions for vector or matrix processing. These functions are designed to allow each processor to execute an independent job as well as to communicate with other processors, so that the user does not need to manage interprocessor communication or the load level on various processors. The main advantage of PETSc is portability: computer codes may be run on a large class of parallel computing systems with different architectures without user intervention. Computer clusters that include a large number of processors allow us to work on huge lattices while the run time decreases significantly.

The Compute Unified Device Architecture (CUDA) (Cheng et al., 2014; Ilvonen, 2012), released by NVIDIA, is the leading technology for general purpose GPU programming. It consists of hardware specifications, a specific programming model, and a programming environment. CUDA is a general-purpose parallel computing platform and programming model that leverages the parallel compute engine in NVIDIA GPUs to solve complex computational problems. Using CUDA, one can access the GPUs for computation, as has been traditionally done on CPUs. The CUDA platform is accessible through CUDA-accelerated libraries, compiler directives, application programming interfaces, and extensions to industry-standard programming languages, including C, C++, Fortran, and Python. The CUDA programming model relies on the concept of a kernel. A kernel is a function that is executed in concurrent threads on the GPU. A GPU consists in several streaming multiprocessors (SMs). Each SM contains scalar processors (SPs), an instruction unit, and a shared memory, concurrently accessible by the SPs through 16 memory banks. Two cached, read-only memories for constants and textures are also available. The device memory, usually named the global memory, is accessible by both the GPU and the CPU. Threads are grouped into blocks, which in turn form the execution grid. The execution grid's layout is specified at run time. A grid may have one or two dimensions. The blocks of threads within a grid must be identical and may have up to three dimensions. A thread is identified with respect to the grid using the two structures threadIdx and blockIdx. A block may only be executed on a single SM, which yields an upper bound of the number of threads within a block. Scheduling is carried out at the hardware level and may not be adjusted. It is still possible to place synchronization barriers, but their scope is limited to blocks. The only way to ensure global synchronization is to use a kernel for each step. The local variables of a kernel are stored in the registers. Their scope is limited to threads and they cannot be used for communication purposes. Data

This book belongs to Central Library BADJI Mokhtar-ANNABA UNIVERSITY
Copyright Elsevier 2024

exchanges between threads require the use of shared memory. The management of these exchanges is left to the programmer. It is worth noting that no protection mechanism is available; hence concurrent writes at the same memory location yield unpredictable results. The scope of the shared memory is limited to blocks. Communication between threads belonging to different blocks requires the use of the global memory.

LB simulation programs written under PETSc as well as under CUDA are widely used in the literature concerning various aspects of complex fluids and active matter (Mills et al., 2013).

21.2 NUMERICAL SCHEMES FOR REDUCING VELOCITIES AT INTERFACES

LB methods provide an alternative to computational fluid dynamics (Chen and Doolen, 1998; Rothman and Zaleski, 1997; Succi, 2001; Wolf-Gladrow, 2000). LB models are based on the physics at the mesoscopic scale, so that the macroscopic phenomena are recovered without solving the equations of continuous media mechanics. The time and space derivative operators, ∂_t and $\mathbf{e}_i \cdot \nabla$, in Boltzmann discretized Eq. (21.5), are applied to the distribution functions. To compute these operators on a discrete lattice $\mathcal{L}$, it is necessary to implement numerical schemes. The evolution of the distribution functions can be computed using the *forward time* (Euler) numerical scheme. For the term $\mathbf{e}_i \cdot \nabla f_i$ there is a wide choice of numerical schemes available in the literature (Cao et al., 1997; Gustafsson et al., 1995; Hirsch, 1988; LeVeque, 1992; Press et al., 1992; Sofonea and Sekerka, 2003, 2005; Sterling and Chen, 1996; Toro, 1999).

In an early multiphase LB model of a stationary bubble, a phenomenon known as *the spurious current* was discovered near the interface. The corresponding flow pattern had the same symmetry as the underlying lattice and the magnitude of the velocity scaled with the surface tension to viscosity ratio. Similar flow pattern was found in the subsequent LB model for nonideal gases and multiple components (Shan and Chen, 1993, 1994), although both the magnitude and the spatial extent of the spurious velocity were much reduced.

Subsequent studies revealed that spurious velocities only exist in the vicinity of an interface with nonzero curvature. Several attempts have been made to understand the origin of spurious velocities and to reduce their magnitude. Wagner (2003) assumed that the implementation of the additional LB equation for the total density and the momentum is the reason for the occurrence of the spurious velocities. In typical LB simulations, the dynamics of the distribution function is split into separate streaming and collision steps. Because of long-range interactions, momentum at each lattice site changes in the collision step. The overall momentum transfer is defined by the average of the momenta before and after the collision step. Once the proper interpretation is used, the velocity field vanishes completely in a flat stationary interface as required by the force balance law.

In the alternative multiphase LB model (Swift et al., 1995, 1996), the momentum is locally conserved on each lattice site and there is no momentum exchange. The spurious current has a different origin in this model. Therefore, with a given set of vectors, it is desirable to obtain the finite-difference gradient operator with the highest degree of isotropy. The spurious current in the nonideal gas LB model seems to be caused by insufficient isotropy in the density gradient calculation. Indeed, by adopting a finite difference gradient operator of sufficient isotropy, the spurious current can be made arbitrarily small (Shan, 2006).

The Oxford LB model for two-phase flow displayed the largest spurious velocity of $O(10^{-4})$ for a static circle droplet in quiescent gas at equilibrium state. This model, however, lacks Galilean invariance. Inamuro et al. (2000) improved the Oxford model by applying the asymptotic theory to satisfy Galilean invariance by incorporating a correction term in the equilibrium function, although no effort was made to remove the spurious velocity. A combination of intermolecular force terms in the potential form and an appropriate isotropic discretization of the derivatives in the intermolecular force terms were necessary to remove the spurious velocity (Lee and Fischer, 2006). The momentum conservation equation is actually sacrificed in this model (Pooley and Furtado, 2008). Starting from the model of Inamuro et al. (2000), using intermolecular force term derivatives and a fourth-order approximation scheme, the isotropy of the derivatives in the pressure tensor was improved, thereby reducing the spurious velocity (Seta and Okui, 2007). The Oxford model was extended by considering various equilibrium distributions, by computing the derivatives in an isotropic stencil, and by moving the gradient terms in the equilibrium distribution into the body force terms; as a result, spurious velocities were significantly reduced (Pooley and Furtado, 2008).

The remainder of this section provides an overview of several numerical schemes that target spurious velocities.

It was found that the spurious currents in a kinetic theory−based LB equation depend severely on the parity of the employed lattice. The spurious currents can be influenced by the discrete streaming operator, the force formulation, and the order of isotropy of the discrete gradient operator in the evaluation of the interaction force. Spurious currents seem to be related to the chequerboard effects of the LB equation (Guo et al., 2011). In the early models it was considered that the

This book belongs to Central Library BADJI Mokhtar-ANNABA UNIVERSITY
Copyright Elsevier 2024

phase interface may act like a boundary and excite the chequerboard invariants. The velocity oscillates between two constant values in each phase on the even lattice, which is a clear chequerboard pattern.

21.2.1 Finite Difference Schemes

Several methods have been proposed to suppress spurious invariants in LB models. For instance, a time-average method has been proposed to remove the staggered invariant (Ladd, 1994). On the other hand, Qian (1997) proposed a fractional propagation scheme to cancel the spurious invariants in both space and time. In this method, spatial averaging performed during time evolution successfully cancelled out chequerboard invariants. Another possibility is to use a Lax−Wendroff (LW) scheme to control the chequerboard effects on spurious currents (Guo et al., 2011). A finite difference scheme must guarantee particle number conservation and must minimize numerical errors while calculating physical quantities, such as diffusion coefficients, viscosity, or surface tension (Cao et al., 1997; Hirsch, 1988; Press et al., 1992; Sofonea and Sekerka, 2003, 2005).

For convenience, in this section we will use a simplified formulation of the LB equations:

$$\partial_t f_i + \mathbf{e}_i \cdot \nabla f_i = 0. \tag{21.17}$$

Because our numerical simulations were mainly done using the D2Q9 model (Qian et al., 1992), we will discuss numerical schemes for an LB model formulated on a square lattice. Nevertheless, they may be easily extended for other lattice types. The lattice spacing $|\delta r| = \delta x = \delta y$ is a simulation parameter. Space derivatives in the lattice node $\mathbf{r}$ (denoted by 0 in Fig. 21.1) may be computed using a centered finite difference scheme or an upwind scheme (Cao et al., 1997; Cristea and Sofonea, 2002a,b; Hirsch, 1988; Press et al., 1992).

We denote $f(\mathbf{r} + \delta\mathbf{r}_i)$ the value of the distribution function f in the lattice nodes i ($i = 1, 2, \ldots 8$), as shown in Fig. 21.1. The centered finite difference scheme used to compute the first order space derivatives of the function f in the node $\mathbf{r} = \mathbf{r}_0$ relies on the values of f in the adjacent nodes $\mathbf{r} + \delta\mathbf{r}_i$, $i = 1\ldots 4$:

$$\partial_x f(\mathbf{r}) = \frac{1}{2\delta\mathbf{r}}\left[f(\mathbf{r} + \delta\mathbf{r}) - f(\mathbf{r} - \delta\mathbf{r})\right] \tag{21.18}$$

For a vector $\mathbf{v}$, with components v_x and v_y ($\mathbf{v}$ could be any vector $\mathbf{e}_i$, $i = 1, 2, \ldots 8$), the upwind finite difference scheme used to compute the scalar product $\mathbf{v} \cdot \nabla f(\mathbf{r})$ is (Cao et al., 1997; Hirsch, 1988; Press et al., 1992) as follows:

$$v_x \partial_x f(\mathbf{r}) = \begin{cases} v_x[f(\mathbf{r}) - f(\mathbf{r} + \delta\mathbf{r}_3)]/\delta x & , \quad v_x \geq 0 \\ v_x[f(\mathbf{r} + \delta\mathbf{r}_1) - f(\mathbf{r})]/\delta x & , \quad v_x < 0 \end{cases} \tag{21.19}$$

Schemes based on Lagrange interpolation could be applied to compute the product $\mathbf{e}_5 \cdot \nabla f$ in node 0 (Fig. 21.1) using the values of the distribution function f in nodes 0, 3, 4, and 7 (Cao et al., 1997; Hirsch, 1988; Press et al., 1992). Using the general properties of the vectors $\mathbf{e}_i$ (He and Luo, 1997b; Rothman and Zaleski, 1997), one can build other finite difference schemes for the derivative operators ∇f and $\nabla^2 f$. After multiplication with the weight factors w_i, the gradient and the Laplace operator may be computed using a finite difference scheme (Press et al., 1992; Sofonea and Sekerka, 2003; Swift et al., 1995):

$$\nabla f_i(\mathbf{r}) = \frac{1}{\chi(\delta r)^2} \sum_{i=1}^{i=\mathcal{N}} w_i \delta\mathbf{r}_i f_i(\mathbf{r}_i + \delta\mathbf{r}_i) \tag{21.20}$$

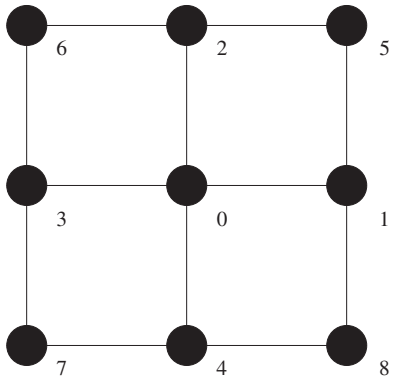

FIGURE 21.1 Neighbors of the node 0 in a square lattice.

This book belongs to Central Library BADJI Mokhtar-ANNABA UNIVERSITY
Copyright Elsevier 2024

$$\nabla^2 f_i(\mathbf{r}) = \frac{2}{\chi(\delta r)^2}\left[\sum_{i=1}^{i=\mathcal{N}} w_i f_i(\mathbf{r}_i + \mathbf{e}_i \delta r_i) - f_i(\mathbf{r}_i)\right] \tag{21.21}$$

These expressions use the values of the distribution functions in all neighbors of the lattice node 0, providing an alternative to the centered finite difference scheme, and have the advantage of using the information from all neighboring nodes to ensure smoothness.

21.2.2 Flux Limiter Schemes

The first-order upwind numerical scheme is widely used to compute the term $\mathbf{e}_i \cdot \nabla f_i$ in LB equations. According to the general approach to high-order *flux limiters* (Cristea and Sofonea, 2004; Gustafsson et al., 1995; LeVeque, 1992; Sofonea et al., 2004; Toro, 1999), the updating rule should be rewritten in a conservative form using two fluxes:

$$f_{i,j}^{n+1} = f_{i,j}^n - CFL\left[F_{i,j+1/2}^n - F_{i,j-1/2}^n\right] + \frac{\delta t}{k_B T}\mathbf{F}(\mathbf{r},t)\cdot[\mathbf{e}_i - \mathbf{u}(\mathbf{r},t)]f_i^{eq}(\mathbf{r},t) - \frac{\delta t}{\tau}[f_i(\mathbf{r},t) - f_i^{eq}(\mathbf{r},t)] \tag{21.22}$$

where $CFL = c\delta t/\delta s$ (δs is the lattice spacing) is the Courant−Friedrichs−Lewy number, and the fluxes $F_{i,j+1/2}^n$, $F_{i,j-1/2}^n$ are defined as follows:

$$F_{i,j+1/2}^n = f_{i,j}^n + \frac{1}{2}(1 - CFL)\left[f_{i,j+1}^n - f_{i,j}^n\right]\psi\left(\theta_{i,j}^n\right) \tag{21.23}$$

and

$$F_{i,j-1/2}^n = F_{i,(j-1)+1/2}^n = f_{i,j-1}^n + \frac{1}{2}(1 - CFL)\left[f_{i,j}^n - f_{i,j-1}^n\right]\psi\left(\theta_{i,j-1}^n\right) \tag{21.24}$$

The flux limiter $\psi\left(\theta_{i,j}^n\right)$ introduced in Eq. (21.23) is expressed as a function of the *smoothness*:

$$\theta_{i,j}^n = \frac{f_{i,j}^n - f_{i,j-1}^n}{f_{i,j+1}^n - f_{i,j}^n} \tag{21.25}$$

In particular, the Lax−Wendroff scheme is recovered for $\psi\left(\theta_{i,j}^n\right) = 1$, whereas the first-order *upwind* scheme is recovered as another particular case, when $\psi\left(\theta_{i,j}^n\right) = 0$.

A wide choice of flux limiters for hyperbolic partial differential equations is available in the literature (Gustafsson et al., 1995; LeVeque, 1992; Toro, 1999):

- Beam−Warming

$$\psi\left(\theta_{i,j}^n\right) = \theta_{i,j}^n \tag{21.26}$$

- Fromm

$$\psi\left(\theta_{i,j}^n\right) = \frac{1 + \theta_{i,j}^n}{2} \tag{21.27}$$

- LeVeque's MCD (monitorized central difference)

$$\psi\left(\theta_{i,j}^n\right) = \begin{cases} 0, & \theta_{i,j}^n \le 0 \\ 2\theta_{i,j}^n, & 0 \le \theta_{i,j}^n \le \frac{1}{3} \\ \frac{1 + \theta_{i,j}^n}{2}, & \frac{1}{3} \le \theta_{i,j}^n \le 3 \\ 2, & 3 \le \theta_{i,j}^n \end{cases} \tag{21.28}$$

This book belongs to Central Library BADJI Mokhtar-ANNABA UNIVERSITY
Copyright Elsevier 2024

21.2.3 Total Variation Diminishing Schemes

We will write the updating rule, using the two fluxes $F^n_{i+1/2}, F^n_{i-1/2}$ (Chen et al., 1998; Cristea, 2006; Teng et al., 2000):

$$f_i^{n+1} = f_i^n - \lambda\left[F^n_{i+1/2} - F^n_{i-1/2}\right] \tag{21.29}$$

where the numerical fluxes are given by Chen et al. (1998) and Teng et al. (2000)

$$F^n_{i+1/2} = \frac{1}{2}\left[cf_i^n + cf_{i+1}^n + g_i^n + g_{i+1}^n - Q\left(c + \gamma^n_{i+1/2}\right)\Delta^n_{i+1/2}\right]. \tag{21.30}$$

By definition, we have

$$g_i^n = M\left(g^n_{i+1/2}, g^n_{i-1/2}\right) \tag{21.31}$$

where

$$g^n_{i+1/2} = \frac{1}{2}\left(Q(c) - \lambda c^2\right)\Delta^n_{i+1/2} \tag{21.32}$$

The *minmod* function is defined as

$$M(x_1, x_2, \ldots, x_n) = \begin{cases} sign(x_1)min(\|x_1\|, \|x_2\|, \ldots \|x_n\|) & \text{if} \quad x_i \text{ has the same sign} \\ 0 & , \qquad \text{else} \end{cases} \tag{21.33}$$

The function $Q(x)$ eliminates the so-called entropy violation (Chen et al., 1998; Teng et al., 2000):

$$Q(x) = \begin{cases} \left(x^2/(4\varepsilon)\right) + \varepsilon, & \|x\| < 2\varepsilon \\ \|x\|, & \|x\| > 2\varepsilon \end{cases} \tag{21.34}$$

The γ function in Eq. (30) is given by

$$\gamma^n_{i+1/2} = \begin{cases} \left(g^n_{i+1} - g^n_i\right)\Big/\Delta^n_{i+1/2}, & \Delta^n_{i+1/2} \neq 0 \\ 0, & \Delta^n_{i+1/2} = 0 \end{cases} \tag{21.35}$$

and the $\Delta^n_{i+1/2}$ function is

$$\Delta^n_{i+1/2} = f^n_{i+1} - f^n_i. \tag{21.36}$$

Relying on the *artificial compression* technique (Chen et al., 1998; Teng et al., 2000) in the total variation diminishing (TVD) scheme, we introduce an antidiffusion term $A(f)$:

$$\frac{\partial f}{\partial t} + \frac{\partial}{\partial x}[cf + A(f)] = 0 \tag{21.37}$$

Then the numerical fluxes become:

$$F^n_{i+1/2} = \frac{1}{2}\left[cf_i^n + cf_{i+1}^n + g_i^n + g_{i+1}^n + A_i^n + A_{i+1}^n - Q\left(c + \gamma^n_{i+1/2} + \nu^{LM}_{i+1/2}\right)\Delta^n_{i+1/2}\right] \tag{21.38}$$

The function $\nu^{LM}_{i+1/2}$ is defined as

$$\nu^{LM}_{i+1/2} = \begin{cases} \left(A^n_{i+1} - A^n_i\right)\Big/\Delta^n_{i+1/2}, & \Delta^n_{i+1/2} \neq 0 \\ 0, & \Delta^n_{i+1/2} = 0 \end{cases} \tag{21.39}$$

whereas the function $g^n_{i+1/2}$ has the following form:

$$g^n_{i+1/2} = \frac{1}{2}\left(Q\left(c + \nu^{LM}_{i+1/2}\right) - \lambda\cdot\left(c + \nu^{LM}_{i+1/2}\right)^2\right)\Delta^n_{i+1/2} \tag{21.40}$$

This book belongs to Central Library BADJI Mokhtar-ANNABA UNIVERSITY

Copyright Elsevier 2024

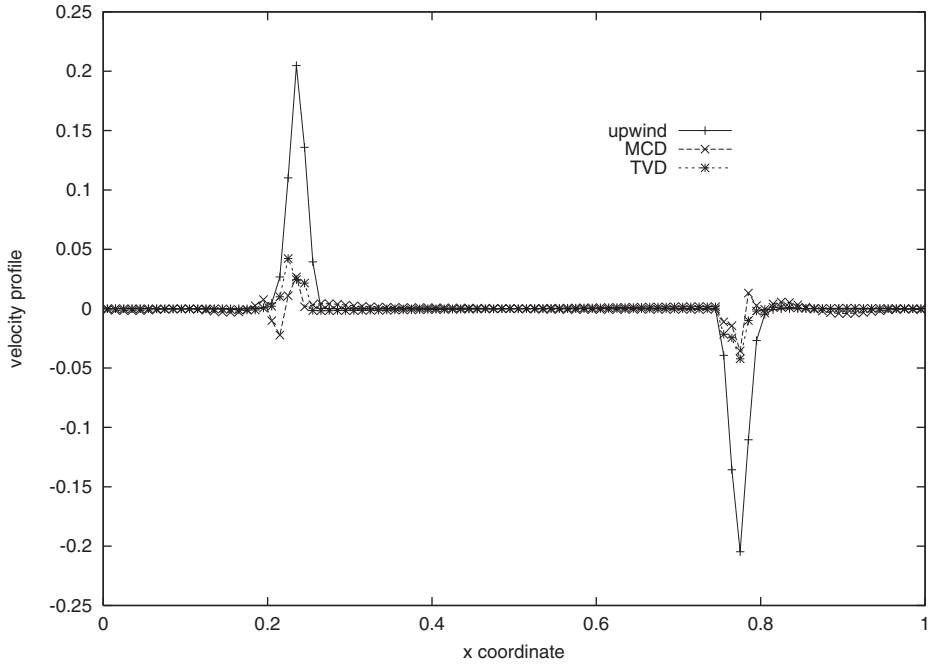

FIGURE 21.2 Velocity profiles recovered with the lattice Boltzmann model for plane interfaces. *MCD*, monitorized central difference; *TVD*, total variation diminishing.

To preserve the properties of the TVD schemes, the antidiffusion term can be defined as

$$A_i^n = sign\left(A_{i+1/2}^n\right)\cdot max\begin{cases} 0 \\ M\left(\eta A_{i-1/2}^n, A_{i+1/2}^n\right)\cdot sign\left(A_{i+1/2}^n\right) \\ M\left(A_{i-1/2}^n, \eta A_{i+1/2}^n\right)\cdot sign\left(A_{i+1/2}^n\right) \end{cases} \tag{21.41}$$

where

$$A_{i+1/2}^n = \frac{1}{2}\left(Q(c) - \lambda c^2\right)\left(\Delta_{i+1/2}^n - M\left(\Delta_{i-1/2}^n, \Delta_{i+1/2}^n, \Delta_{i+3/2}^n\right)\right) \tag{21.42}$$

The purpose of introducing the new parameter η is to keep the second order for A_i^n as in TVD scheme (Chen et al., 1998; Teng et al., 2000).

$$\eta = 2\left|\frac{\left|\Delta_{i+1/2}^n\right|^\beta - \left|\Delta_{i-1/2}^n\right|^\beta}{\left|\Delta_{i+1/2}^n\right|^\beta + \left|\Delta_{i-1/2}^n\right|^\beta}\right|, \quad \beta = 2.5 \tag{21.43}$$

The TVD with artificial compression scheme becomes equivalent to the TVD scheme when we choose $\eta \approx 0$ (Chen et al., 1998; Teng et al., 2000; Cristea, 2006).

The upwind scheme, being of first order, introduces larger numerical effects. The value of the spurious velocity is higher than in the flux limiters and TVD cases. To check the effect of high-order numerical schemes (MCD flux limiter scheme and TVD scheme) in the LB model, we plot the velocity profiles recovered with upwind versus flux limiters and TVD schemes (Fig. 21.2) because other flux limiters provide similar results (Cristea and Sofonea, 2004; Cristea, 2007; Sofonea et al., 2004). The spurious velocity, which appears in the interface region, is clearly related to the numerical errors introduced by the finite difference schemes (Cristea and Sofonea, 2002a, 2002b; 2003; Cristea, 2005, 2006; Cristea et al., 2006).

21.2.4 Surface Tension in the Force Term

The thickness of the phase interface has an important effect on the magnitude of the spurious currents. Increasing the thickness of the interface can reduce the spurious currents. Using multirange pseudopotentials, it is possible to change the

This book belongs to Central Library BADJI Mokhtar-ANNABA UNIVERSITY Copyright Elsevier 2024

interface width while keeping the surface tension and density ratio constant via rescaling the grid system. Hence, grid refinement is helpful for suppressing spurious currents. It was shown that doubling the grid resolution can reduce the amplitude of the spurious currents by nearly an order of magnitude (Sbragaglia et al., 2007). By increasing the width of the interface region, the surface tension decreases the density gradient. This increases the stability of the numerical simulation. This effect is noticeable even when using the upwind finite difference scheme (Cristea and Sofonea, 2002a,b). Adopting a proper scheme to incorporate the interaction terms into the pseudopotential model (Shan and Chen, 1993, 1994) helps to diminish the spurious currents, enhance the thermodynamic consistency, and unravel the coupling between viscosity and surface tension.

Typical equations of state (EOSs) are the van der Waals (vdW) EOS, Redlich–Kwong (RK) EOS, and the Peng–Robinson (PR) EOS. Several strategies have been proposed to incorporate different EOSs into the pseudopotential model (Cristea, 2007; Yuan and Schaefer, 2006).

For nonideal fluids subjected to no external force fields (such as gravity), one can use the following expression of the interparticle force (Cristea, 2006; Davis, 1996; Kondepudi and Prigogine, 1998; Martys et al., 1998):

$$\frac{F_\alpha}{m} = a_\alpha = -\frac{1}{\rho}\,\partial_\alpha(p_{nif} - p_i) \tag{21.44}$$

The dimensionless ideal gas pressure is

$$p_i = \chi c^2 \rho \tag{21.45}$$

The range of density ratios is very small and the spurious velocities are very high when the van der Waals EOS is introduced in the pseudopotential LB model (Yuan and Schaefer, 2006). Nevertheless, to safely conclude that the van der Waals EOS may be unsuitable for the LB models, a systematic investigation of various EOS becomes a necessity (Cristea, 2006, 2007) (Figs. 21.3 and 21.4):

van der Waals (vdW) EOS:

$$p_w = \frac{\rho T}{3-\rho} - \frac{3}{8}\rho^2$$

Redlich–Kwong (RK) EOS:

$$p_{rk} = \frac{\rho T}{3-\rho} - \frac{9}{8}\frac{\rho^2}{\sqrt{T}(3+\rho)}$$

Redlich–Kwong–Soave (RKS) EOS:

$$p_{rks} = \frac{\rho T}{3-\rho} - \frac{9}{8}\frac{\rho^2\left[1+(0.480+1.574\omega-0.176\omega^2)\left(1-\sqrt{T}\right)\right]^2}{3+\rho}, \quad \omega = 0.344$$

Peng–Robinson (PR) EOS:

$$p_{pr} = \frac{\rho T}{3-\rho} - \frac{27}{8}\frac{\rho^2\left[1+(0.37464+1.54226\omega-0.26992\omega^2)\left(1-\sqrt{T}\right)\right]^2}{9+6\rho-\rho^2}, \quad \omega = 0.344$$

When intermolecular forces are not neglected, the density gradient in the interfacial region leads to surface tension. In such cases, the equation of momentum conservation should be generalized by replacing the term $\partial_\alpha p$ (scalar pressure divergence) with the divergence of the pressure tensor $P_{\alpha\beta}$ (Cristea and Sofonea, 2003; Davis, 1996; Kondepudi and Prigogine, 1998; Swift et al., 1995):

$$\partial_t(\rho u_\alpha) + \partial_\beta(\rho u_\alpha u_\beta) = -\partial_\beta P_{\alpha\beta} + \nu\partial_\beta[\rho\partial_\alpha u_\beta + \rho\partial_\beta u_\alpha] + \rho a_\alpha \tag{21.46}$$

The widely used expression of the pressure tensor is (Kondepudi and Prigogine, 1998; Swift et al., 1995)

$$P_{\alpha\beta} = \delta_{\alpha\beta}\left[p_{nif} + \frac{3\kappa}{2}(\nabla\rho)^2 + 3\kappa\rho\nabla^2\rho\right] - 3\kappa(\partial_\alpha\rho)(\partial_\beta\rho) \tag{21.47}$$

Another pressure tensor form is described in Davis (1996):

$$P_{\alpha\beta} = \delta_{\alpha\beta}\left[p_{nif} - \frac{\kappa}{2}(\nabla\rho)^2 + \kappa\rho\nabla^2\rho\right] - \kappa(\partial_\alpha\rho)(\partial_\beta\rho) + 2\kappa\rho\partial_\alpha(\partial_\beta\rho) \tag{21.48}$$

This book belongs to Central Library BADJI Mokhtar-ANNABA UNIVERSITY
Copyright Elsevier 2024

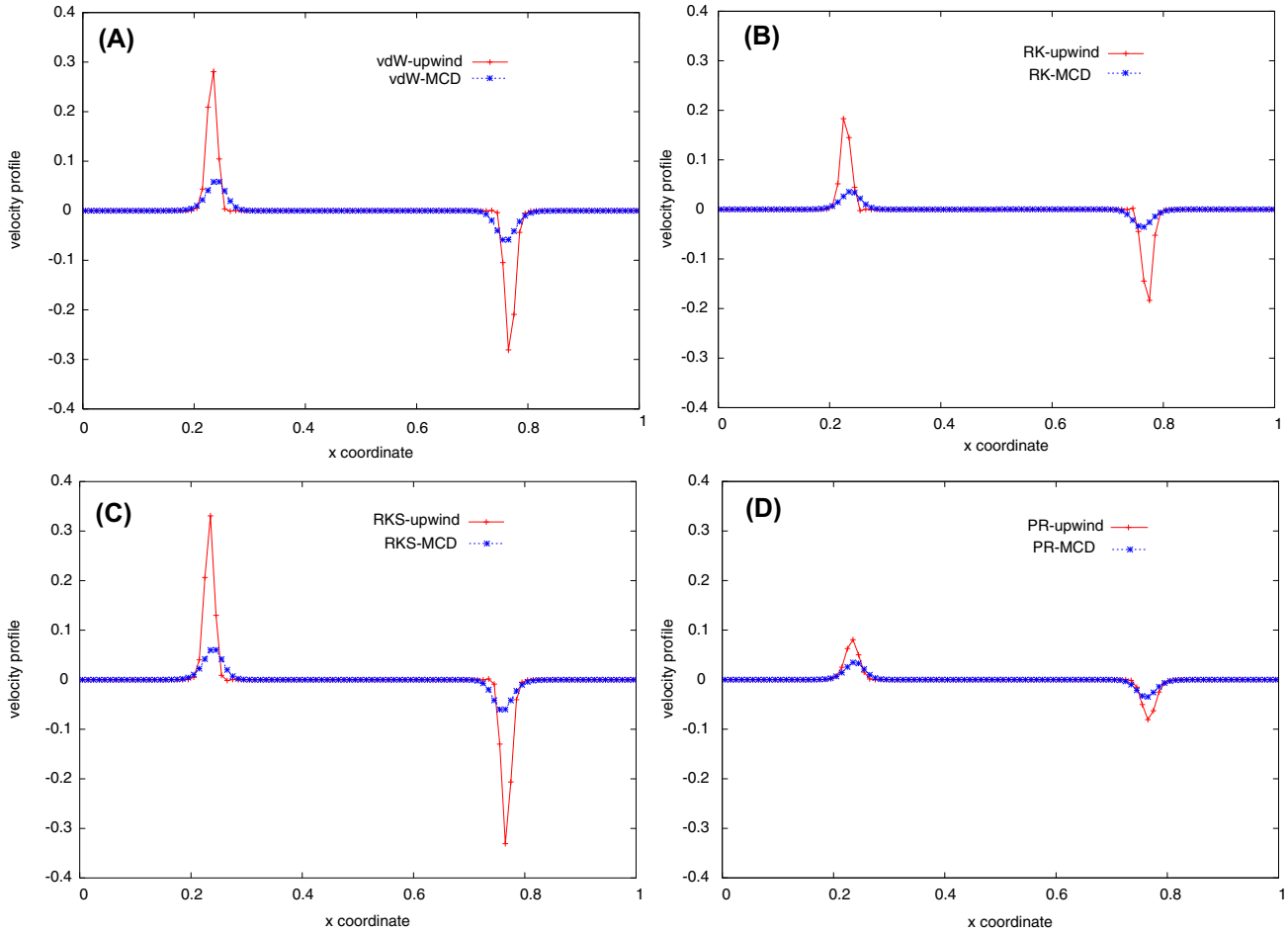

FIGURE 21.3 Local velocity profiles recovered with lattice Boltzmann model (upwind/monitorized central difference (MCD)) for various equations of state: (A) *van der Waals (vdW)*, (B) *Redlich–Kwong (RK)*, (C) *Redlich–Kwong–Soave (RKS)*, (D) *Peng–Robinson (PR)* in the absence of surface tension.

In the above expressions of the pressure tensor (Eqs. 21.47 and 21.48), the constant κ describes the influence of density variations on the surface tension. For a plane interface, the relation between the surface tension σ and the parameter κ (Davis, 1996) is given by ($n = \rho/m$):

$$\sigma = \kappa \int_{-\infty}^{+\infty} \left(\frac{\partial n}{\partial z}\right)^2 dz \tag{21.49}$$

To consider surface tension effects, the expression (21.44) of the force term must be modified. If we use the pressure tensor (Eq. 21.47), we have

$$\frac{F_\alpha}{m} = \frac{1}{\rho}\,\partial_\beta\left[-p_{nif} + p_{id} + \frac{3\kappa}{2}(\nabla\rho)^2 + 3\kappa\rho\nabla^2\rho\right] - \frac{1}{\rho}\,\partial_\beta[3\kappa(\partial_\alpha\rho)(\partial_\beta\rho)] \tag{21.50}$$

Alternatively, if we use the pressure tensor (Eq. 21.48), we get

$$\frac{F_\alpha}{m} = \frac{1}{\rho}\partial_\beta\left[-p_{nif} + p_i - \frac{\kappa}{2}(\nabla\rho)^2 + \kappa\rho\nabla^2\rho\right] - \frac{1}{\rho}\,\partial_\beta[\kappa(\partial_\alpha\rho)(\partial_\beta\rho) - 2\kappa\rho\partial_\alpha\partial_\beta\rho] \tag{21.51}$$

Both expressions (21.50) and (21.51) of the force term reduce to

$$\frac{\mathbf{F}}{m} = -\frac{1}{\rho}\nabla[-p_{nif} + p_i] + 3\kappa\nabla\left(\nabla^2\rho\right) \tag{21.52}$$

This book belongs to Central Library BADJI Mokhtar-ANNABA UNIVERSITY
Copyright Elsevier 2024

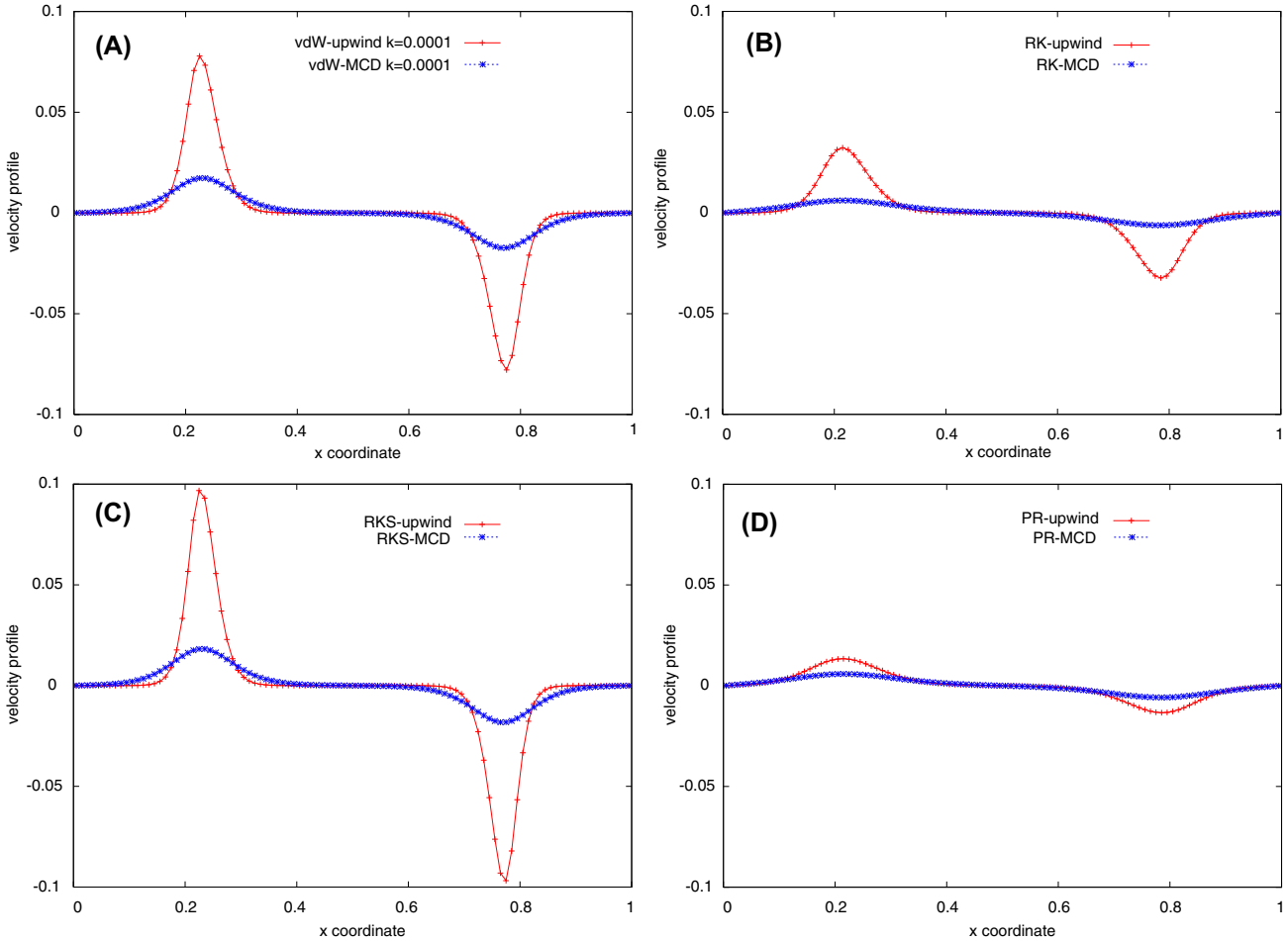

FIGURE 21.4 Local velocity profiles recovered with lattice Boltzmann model (upwind/monitorized central difference (MCD)) for various equations of state: (A) *van der Waals (vdW)*, (B) *Redlich–Kwong (RK)*, (C) *Redlich–Kwong–Soave (RKS)*, (D) *Peng–Robinson (PR)* with nonzero value of surface tension ($\kappa \neq 0$).

This expression of the force term includes both the phase separation term (Eq. 21.44), as well as a term accounting for the surface tension (Cristea and Sofonea, 2002b, 2003; Cristea, 2006; Cristea et al., 2006; Davis, 1996).

A nonvanished surface tension parameter ($\kappa \neq 0$) reduces spurious velocities because it stretches the width of the interface. Hence, the numerical stability is improved because the density gradient becomes smaller (Cristea and Sofonea, 2003; Cristea, 2005; Cristea et al., 2006; Sbragaglia et al., 2007).

Even in the case of the upwind scheme, for nonvanishing surface tension, the value of the spurious velocities are considerably smaller than the corresponding values recovered with zero surface tension (Cristea and Sofonea, 2003; Cristea, 2006, 2007; Cristea et al., 2006). The second-order finite difference flux limiters/TVD schemes together with the presence of surface tension may effectively reduce the spurious velocity observed at the interfaces (one can see differences between Figs. 21.2 and 21.5).

21.2.5 Corrections on the Force Term

Starting from the *real LB equations*, which account for the numerical effects induced by the numerical schemes (Sofonea and Sekerka, 2003), using the Chapman–Enskog expansion, we found an analytical expression of the spurious velocity (Cristea and Sofonea, 2003). The real LB equations were solved using the upwind scheme up to second order with respect to the lattice spacing δx:

$$\mathbf{e}_i \cdot \nabla f_i(\mathbf{x},t) - \psi e_{i\beta} e_{i\gamma} \partial_\beta \partial_\gamma f_i(\mathbf{x},t) = -\frac{1}{\tau}\left[f_i(\mathbf{x},t) - f_i^{eq}(\mathbf{x},t)\right] + \frac{1}{\chi c^2} f_i^{eq}\left[e_{i\beta} - u_\beta(\mathbf{x},t)\right] \cdot F_\beta(\mathbf{x},t) \quad (i = 0, 1, \ldots \mathcal{N}) \quad (21.53)$$

This book belongs to Central Library BADJI Mokhtar-ANNABA UNIVERSITY
Copyright Elsevier 2024

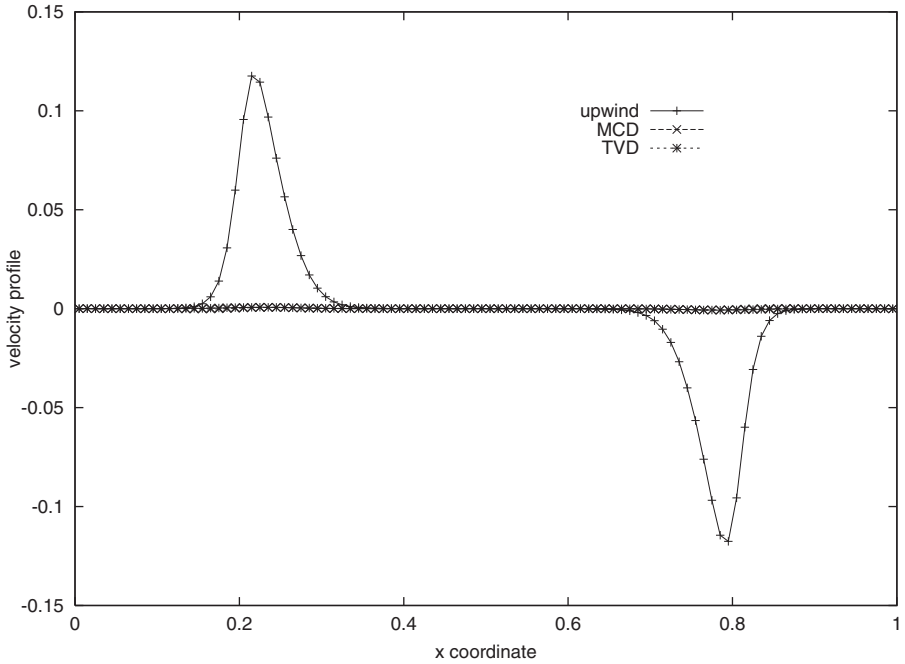

FIGURE 21.5 Velocity profiles recovered with the Lattice Boltzmann model for plane interfaces with surface tension ($\kappa \neq 0$). *MCD*, monitorized central difference; *TVD*, total variation diminishing.

where c is the dimensionless speed (Eq. 21.7) used in the LB models and $\psi = \delta x/c$ (Luo, 2000; Sofonea and Sekerka, 2003; Sofonea et al., 2004). For the stationary state, mass and momentum conservation equations are recovered from the real LB equations. From the mass conservation equation, we get the analytic expression of the spurious velocity, which appears in the interface region because of the presence of a density gradient (Cristea and Sofonea, 2003; Wagner, 2003):

$$u_\beta = \frac{\psi}{\rho}\partial_\gamma\left[\chi c^2 \rho \delta_{\beta\delta} + \rho u_\beta u_\gamma\right] \approx \frac{\psi \chi c^2}{\rho}\,\partial_\beta \rho \tag{21.54}$$

The values of the spurious velocity, computed using Eq. (21.54), are in excellent agreement with the ones found in LB simulations using the upwind scheme (Cristea and Sofonea, 2003). We introduce an additional force term in the evolution Eq. (21.53):

$$F^{\nu}_{i\beta} = \frac{\psi}{\rho}\left[-\partial_\beta(e_{i\gamma}A_\gamma) + (u_\gamma\partial_\beta + u_\beta\partial_\gamma)A_\gamma\right] \tag{21.55}$$

where

$$A_\gamma = \chi c^2 \partial_\gamma \rho + \partial_\delta(\rho u_\gamma u_\delta) \tag{21.56}$$

The LB Eq. (21.53) with the correction force term (Eq. 21.55) becomes

$$\mathbf{e}_i \cdot \nabla f_i(\mathbf{x},t) - \psi e_{i\beta} e_{i\gamma} \partial_\beta \partial_\gamma f_i(\mathbf{x},t) = -\frac{1}{\tau}\left[f_i(\mathbf{x},t) - f_i^{eq}(\mathbf{x},t)\right] + \frac{1}{\chi c^2} f_i^{eq}\left[e_{i\beta} - u_\beta(\mathbf{x},t)\right]\left[F_\beta + F^{\nu}_{i\beta}\right] \quad (i = 0, 1, \ldots \mathcal{N}) \tag{21.57}$$

The corrected force term cancels the spurious velocity term in the mass conservation equation.

Because the new force term does not modify the momentum conservation equations of the isothermal fluid, there is no need for Cartesian indices in Eq. (21.55):

$$F^{\nu}_i = -\frac{\psi}{\rho}(e_i - 2u)\left[\chi c^2 \nabla^2 \rho + \nabla^2(\rho u^2)\right] \tag{21.58}$$

This book belongs to Central Library BADJI Mokhtar-ANNABA UNIVERSITY Copyright Elsevier 2024

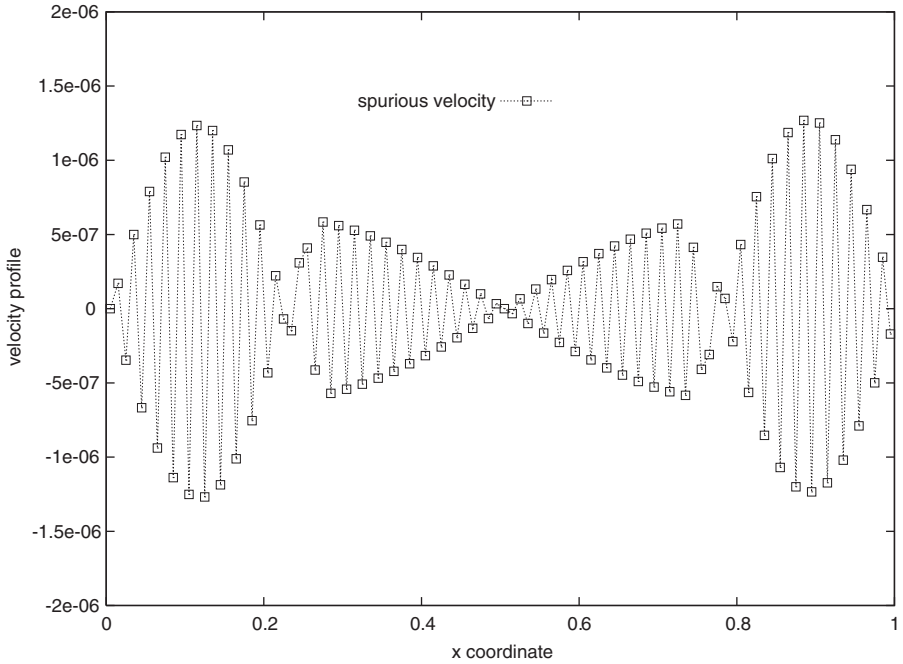

FIGURE 21.6 Local velocity profile recovered using the corrected force term (Eq. 21.55) in the absence of surface tension ($\kappa = 0$). *Reproduced from Cristea, A., Sofonea, V.V., 2003. Reduction of spurious velocity in finite difference lattice Boltzmann models for liquid − vapor systems. International Journal of Modern Physics C 14, 1251−1266 with permission from World Scientific (2003).*

Simulations done using the corrected force term (Eq. 21.55), using the computing rules described in Eqs. (21.20) and (21.21), lead to a remarkable result because we achieve also the reduction of the spurious surface tension, which stretches the interface region. As shown in Fig. 21.6, the spurious velocity is practically negligible. The local velocity profile still shows the wiggle phenomenon, but its amplitude is approximately 10.000 times lower than in the upwind case (Cristea and Sofonea, 2003).

21.3 SIMULATIONS OF MULTICELLULAR SELF-ASSEMBLY IN BIOPRINTED TISSUE CONSTRUCTS

Understanding multicellular self-assembly is important in developmental biology, tissue engineering (TE), and regenerative medicine. Tissue engineers seek to build multicellular constructs suitable to replace or repair damaged tissues of the human body (Griffith and Naughton, 2002). TE, a relatively young, interdisciplinary field of biomedical research, employs methods of developmental biology, cell biology, polymer chemistry, information technology, and engineering (Lanza et al., 2007). On the long term, TE has the potential of solving transplantable organ shortage by building functional organs; on the short term, the field thrives with building implantable tissue constructs, as well as model human tissues built for testing new drugs (Khademhosseini and Langer, 2016).

The vast variety of techniques developed by tissue engineers serve two strategies, known as top-down TE and bottom-up TE (Khademhosseini and Langer, 2007). In the top-down approach, cells are seeded on a biocompatible scaffold of suitable shape and microarchitecture. The scaffold serves as a substrate for anchorage-dependent cells, exposes cells to the cell culture medium, and confers mechanical strength to the construct (Langer and Vacanti, 1993). Ideally, the scaffold should degrade as cells divide and produce tissue-specific extracellular matrix (ECM)—a web of protein filaments bathed by interstitial fluid. In the bottom-up approach, microscopic building blocks are fabricated from cells and hydrogels, and the desired tissue is obtained via the self-assembly of these building blocks (Khademhosseini and Langer, 2007).

One approach to bottom-up TE is 3D tissue bioprinting. Depositing cells and supportive hydrogels layer by layer, the bioprinter (a cell-friendly 3D printer) enables precise positioning of a variety of cell types (Murphy and Atala, 2014). The bioink may consist of individual cells (Xu et al., 2005), multicellular spheroids (Jakab et al., 2008) or cylinders (Norotte et al., 2009), or cells dispersed uniformly in a hydrogel (Kolesky et al., 2016). In bioprinting, however, what you print is not what you get: cells take advantage of their motility to rearrange according to mechanisms known from developmental biology.

This book belongs to Central Library BADJI Mokhtar-ANNABA UNIVERSITY
Copyright Elsevier 2024

An important mechanism of spontaneous structure formation in multicellular systems, in the developing embryo as well as in a model tissue built in the laboratory, is the tendency of cells to establish strong interactions. To explain this tendency, Steinberg (1963) formulated the differential adhesion hypothesis (DAH), which states that adhesive cells rely on their motility to bring about the configuration of lowest energy of adhesion. DAH is supported by a wealth of experimental data, being considered a fundamental principle of developmental biology. Moreover, DAH was used to explain cellular rearrangements during wound healing and cancer progression (Steinberg, 2007).

Although most driving forces of cellular rearrangements are known, the complexity of a biological system composed of millions of cells makes it difficult to predict the evolution of a bioprinted system. Computational models needed for this task have been developed (Neagu, 2017; Robu et al., 2012; Semple et al., 2005).

Early models of postprinting structure formation were inspired by the cellular Potts model (Glazier and Graner, 1993). The system was represented on a lattice and movement was modeled by swapping neighbors; to simulate the system's evolution, the Metropolis Monte Carlo algorithm was used to minimize the adhesive energy as required by DAH (Neagu et al., 2005). These simulations predicted the observed shape changes of the bioprinted system, but did not tell how these changes occurred in time. To simulate time evolution, Sun and Wang employed another time-dependent algorithm, known as the kinetic Monte Carlo algorithm (Sun and Wang, 2013; Sun et al., 2014). Kosztin et al. (2012) developed an off-lattice, cellular particle dynamics (CPD) method, representing each cell as a collection of interacting volume elements (cellular particles). Thereby, they were able to track the movement and shape changes of individual cells within the evolving multicellular system. Moreover, CPD predicted the mechanical properties of the tissue construct. CPD simulations, however, are compute intensive: constructs composed of thousands of cells could be simulated on computer clusters of tens to hundreds of processors such that the simulation took less time than the real-time evolution of the corresponding experimental system.

A typical tissue construct is made of $10^6 - 10^9$ cells, whereas individual-based computer simulations are able to deal with up to 1 million cells. Nevertheless, the rapid increase in computer power combined with coarse graining might solve this problem in the near future. To deal with systems of realistic size, the authors developed an LB model of a multicellular cluster embedded in a biocompatible hydrogel (Cristea et al., 2011; Cristea and Neagu, 2016). Because LB simulations do not monitor each cell in part, they do not impose a limit on the number of cells in the simulated tissue construct.

Our D2Q9 LB model describes a system made of two components of different viscosities. Viewing multicellular clusters as highly viscous, incompressible fluids is in accord with DAH (Steinberg, 2007). Aggregates of adhesive cells fuse as liquid droplets do. Their fusion dynamics was used as a benchmark test of computer simulations of multicellular dynamics (Cristea et al., 2011; Flenner et al., 2008, 2012; Kosztin et al., 2012). Spheroids composed of a random mixture of two cell types sort out such that the more cohesive cell population occupies the central region of the aggregate, whereas the less cohesive cells occupy the periphery. As argued by Beysens et al. (2000) biological cell sorting evolves in close analogy with phase ordering in droplets composed of two immiscible fluids. Moreover, cell aggregates can be characterized by an effective tissue surface tension, which is measurable via parallel-plate compression experiments (Foty et al., 1994).

Treating the hydrogel as another viscous fluid phase is less justified. Nevertheless, the simulations of Cristea and Neagu (2016) were found in good agreement with experiments, presumably because cells are able to remodel the adjacent hydrogel. A specific family of enzymes, called matrix metalloproteases, enable cells to dismantle the ECM (Alberts et al., 2008). A gel that can be decomposed by cells does not hamper cellular rearrangements. In our LB model, the ability of cells to remodel the embedding gel is reflected by the viscosity of the gel phase.

Using our LB model, we simulated shape changes of multicellular systems composed of cell clusters surrounded by a biocompatible hydrogel. For example, simulations predicted the evolution of a system of contiguous, parallel cylinders made of millions of cells (Cristea and Neagu, 2016). Actually, the 2D LB simulations described the time course of the transversal cross section of a 3D system of multicellular cylinders that were much longer than their diameter. Such cylinders are currently used as bioinks (Norotte et al., 2009).

Two-dimensional LB simulations were able to predict the evolution of tubular tissue constructs obtained by printing contiguous cell cylinders (Fig. 21.7). The LB model was calibrated on the basis of experimental data (Norotte et al., 2009), establishing the real time that corresponds to one simulation time step: 5.184 s (Cristea and Neagu, 2016).

LB simulations revealed that a printing defect does not heal in time. In the context of tubular structures built by cell cylinder bioprinting, when imprecise positioning impeded the fusion of a pair of cylinders, subsequent evolution amplified the defect (Fig. 21.7B). Although it is unlikely to please experimentalists, this result is important because it indicates a time window for an attempt to repair the construct. According to Fig. 21.7B, on the fourth day after printing, the slit in the tube

This book belongs to Central Library BADJI Mokhtar-ANNABA UNIVERSITY Copyright Elsevier 2024

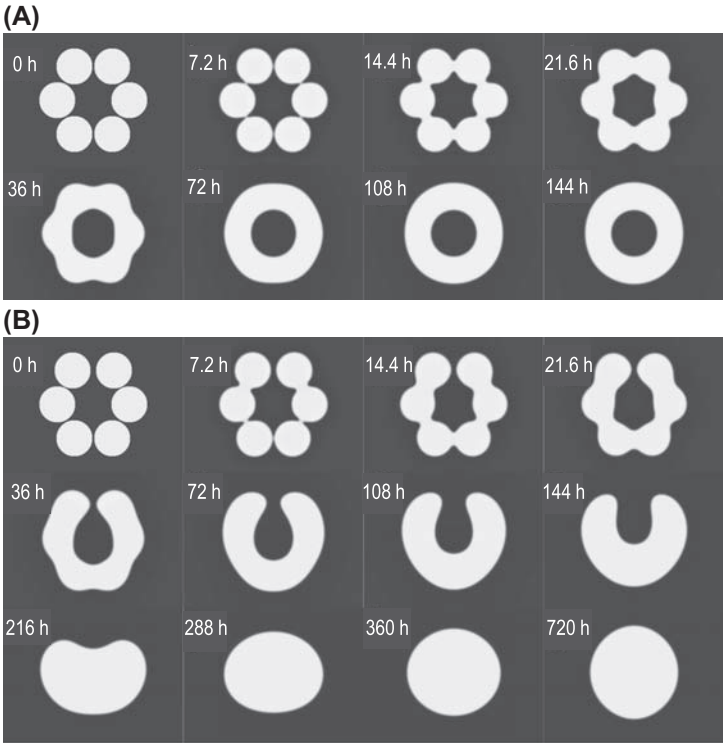

FIGURE 21.7 Fusion of cell cylinders printed in a hexagonal arrangement contiguously (A) and imprecisely (B). Shown are snapshots of a 2D lattice Boltzmann simulation of the evolution of the transversal cross-section of a 3D tubular structure built of multicellular cylinders. Snapshots are labeled by real time. According to the calibration (Cristea and Neagu, 2016), 5000 time steps of the simulation correspond to 7.2 h real time measured in the laboratory.

reaches the diameter of one building block. Provided that bioink is still available, the defect could be sealed by one cell cylinder printed along the slit by the end of the third day. If repair is not an option, at least one knows that the defective tube should be discarded, avoiding further experimental costs.

21.4 CONCLUSIONS

LB methods are suitable for simulating fluid dynamics at the mesoscopic scale. They proved successful in a wide variety of applications, including microfluidics and TE.

Although highly flexible and effective, LB methods may suffer from numerical instabilities due to spurious currents, which are hard to be distinguished from physical flow fields. Therefore, a considerable part of this chapter presented research that sought to discover the causes of spurious velocities and to devise methods to reduce them. In particular, it was shown that, in the presence of surface tension, second-order finite difference flux limiters and/or total variation diminishing schemes can effectively reduce the spurious velocities observed at interfaces.

Simulations of the dynamics of highly viscous fluids based on the LB method are feasible and useful in understanding in vitro morphogenesis. Despite their simplifying assumptions, LB simulations have clarified phenomena of interest in TE, such as postbioprinting evolution of tubular and planar tissue constructs.

Implemented under PETSc on computer clusters of tens of processors, or under CUDA on graphic blades, LB simulations are faster than trial-and-error experiments, and orders of magnitude cheaper.

The simulation programs developed so far for in silico studies of multicellular systems have several limitations: (1) they are 2D models, but 3D models are also feasible; (2) they describe only two components, although multicomponent models proposed in the literature might be adapted to deal with shape changes of living tissues; (3) they suffer from numerical instability when the viscosities of the components differ by more than one order of magnitude; (4) they do not account for cell proliferation, cell death, and synthesis of ECM proteins. If further research will overcome these limitations, the LB method will become a valuable tool for predicting the result of 3D tissue bioprinting.

This book belongs to Central Library BADJI Mokhtar-ANNABA UNIVERSITY Copyright Elsevier 2024

REFERENCES

Alberts, B., Johnson, A., Lewis, J., Raff, M., Roberts, K., Walter, P., 2008. The Molecular Biology of the Cell, fifth ed. Garland Science, New York (Chapter 19).

Beysens, D.A., Forgacs, G., Glazier, J.A., 2000. Cell sorting is analogous to phase ordering in fluids. Proceedings of the National Academy of Sciences 97, 9467−9471.

Bhatnagar, P.L., Gross, E.P., Krook, M., 1954. A model for collision processes in gases. I: small amplitude processes in charged and neutral one - component system. Physical Review 94, 511−525.

Boltzmann, L., 1995. Vorlesungen über Gastheorie (Lectures on Gas Theory), Dover.

Burgers, J.M., 1969. Flow Equations for Composite Gases. Academic Press, New York.

Cao, N., Chen, S., Jin, S., Martinez, D., 1997. Physical symmetry and lattice symmetry in the lattice Boltzmann method. Physical Review E 55, R21.

Chen, S., Doolen, G.D., 1998. Lattice Boltzmann method for fluid flows. Annual Review of Fluid Mechanics 30, 329−364.

Chen, Y., Teng, S., Shukuwa, T., Ohashi, H., 1998. Lattice Boltzmann simulation of two − phase fluid flows. International Journal of Modern Physics C 9, 1383−1391.

Cheng, J., Grossman, M., McKercher, T., 2014. Professional CUDA-C Programming. John Wiley and Sons, Inc.

Comparini, E., Mannucci, P., 1998. Flow of a Bingham fluid in contact with a Newtonian fluid. Journal of Mathematical Analysis and Applications 227, 359−381.

Cristea, A., 2005. High order numerical schemes for finite difference lattice Boltzmann models. In: International Conference "TAM 2005", Stuttgart, Germany, September 20−26 (Oral Presentation).

Cristea, A., 2006. Numerical effects in a finite difference lattice Boltzmann model for liquid − vapour system. International Journal of Modern Physics C 17, 1191−1201.

Cristea, A., 2007. Equations of state in a finite difference lattice Boltzmann model. In: ICMMES Conference 2007, July 16−20, Munich, Germany (Oral Presentation).

Cristea, A., Gonnella, G., Lamura, A., Sofonea, V., 2006. Finite-difference lattice Boltzmann model for liquid − vapor systems. Mathematics and Computers in Simulation 72, 113−116.

Cristea, A., Neagu, A., 2016. Shape changes of bioprinted tissue constructs simulated by the lattice Boltzmann method. Computers in Biology and Medicine 70, 80−87.

Cristea, A., Neagu, A., Sofonea, V., 2011. Lattice Boltzmann simulations of the time evolution of living multicellular systems. Biorheology 48, 185−197.

Cristea, A., Sofonea, V., 2002a. Lattice Boltzmann models for complex fluids. In: International aConference "Small Triangle Meeting in Physics", Snina, Kosice, Slovakia, October 8−10 (Invited Lecture).

Cristea, A., Sofonea, V., 2002b. Finite difference lattice Boltzmann model for liquid − vapour systems. Proceedings of the Romanian Academy, Series A 3, 87−90.

Cristea, A., Sofonea, V., 2003. Reduction of spurious velocity in finite difference lattice Boltzmann models for liquid − vapor systems. International Journal of Modern Physics C 14, 1251−1266.

Cristea, A., Sofonea, V., 2004. Two component lattice Boltzmann model with flux limiters. Central European Journal of Physics 2, 382−396.

Davis, H.T., 1996. Statistical Mechanics of Phases, Interfaces and Thin Films. VCH Publishers, Inc., New York.

Flenner, E., Janosi, L., Barz, B., Neagu, A., Forgacs, G., Kosztin, I., 2012. Kinetic Monte Carlo and cellular particle dynamics simulations of multicellular systems. Physical Review E 85, 031907.

Flenner, E., Marga, F., Neagu, A., Kosztin, I., Forgacs, G., 2008. Relating biophysical properties across scales. In: Schnell, S., Maini, P.K., Newman, S.A., Newman, T.J. (Eds.), Current Topics in Developmental Biology, Multiscale Modeling of Developmental Systems. Academic Press, pp. 461−483.

Foty, R.A., Forgacs, G., Pfleger, C.M., Steinberg, M.S., 1994. Liquid properties of embryonic tissues: measurement of interfacial tensions. Physical Review Letters 72, 2298−2301.

Frigaard, I.A., 2001. Super-stable parallel flows of multiple visco-plastic fluids. Journal of Non-Newtonian Fluid Mechanics 100, 49−75.

Glazier, J.A., Graner, F., 1993. Simulation of the differential adhesion driven rearrangement of biological cells. Physical Review E 47, 2128−2154.

Grad, H., 1949. On the kinetic theory of rarefied gases. Communications in Pure and Applied Mathemathics 2, 331−407.

Griffith, L.G., Naughton, G., 2002. Tissue engineering − current challenges and expanding opportunities. Science 295, 1009−1014.

Gropp, W., Lusk, E., Skjellum, A., 1999. Using MPI. MIT Press, Cambridge, Massachusetts.

Gross, M., Steinbach, I., Raabe, D., Varnik, F., 2012. Viscous Coalescence of Droplets − a Lattice Boltzmann Study. arXiv:1205.1436 [physics.flu-dyn].

Gunstensen, A.K., Rothman, D.H., Zaleski, S., Zanetti, G., 1991. Lattice Boltzmann model of immiscible fluids. Physical Review A 43, 4320−4327.

Guo, Z., Shi, B., Zheng, C., 2011. Chequerboard effects on spurious currents in the lattice Boltzmann equation for two-phase flows. Philosophical Transaction of the Royal Society A 369, 2283−2291.

Gustafsson, B., Kreiss, H.O., Oliger, J., 1995. Time Dependent Problems and Difference Methods. John Wiley and Sons, Inc., New York.

Harris, S., 1971. An Introduction to the Theory of the Boltzmann Equation. Holt, Reinehart and Winston Inc., New York.

He, X., Luo, L.S., 1997a. A priori derivation of the lattice Boltzmann equation. Physical Review E 55, R6333−R6336.

He, X., Luo, L.S., 1997b. Theory of the lattice Boltzmann method: from the Boltzmann equation to the lattice Boltzmann equation. Physical Review E 56, 6811−6817.

Hirsch, C., 1988. Numerical Computation of Internal and External Flows, Volume I: Fundamentals of Numerical Discretization. John Wiley and Sons, Chichester, New York.

This book belongs to Central Library BADJI Mokhtar-ANNABA UNIVERSITY Copyright Elsevier 2024

Huang, K., 1963. Statistical Mechanics. John Willey and Sons Inc., New York.

Ilvonen, S., 2012. Introduction to CUDA Programming, Course Notices. CSC IT Center for Science Ltd., Espoo, Finland. February 16–17.

Inamuro, T., Konishi, N., Ogino, F., 2000. A Galilean invariant model of the lattice Boltzmann method for multiphase fluid flows using free-energy approach. Computer Physics Communications 129, 32–45.

Jakab, K., Norotte, C., Damon, B., Marga, F., Neagu, A., Besch-Williford, C.L., Kachurin, A., Church, K.H., Park, H., Mironov, V., Markwald, R.R., Vunjak-Novakovic, G., Forgacs, G., 2008. Tissue engineering by self-assembly of cells printed into topologically defined structures. Tissue Engineering: Part A 14, 413–421.

Khademhosseini, A., Langer, R., 2007. Microengineered hydrogels for tissue engineering. Biomaterials 28, 5087–5092.

Khademhosseini, A., Langer, R., 2016. A decade of progress in tissue engineering. Nature Protocols 11, 1775–1781.

Kolesky, D.B., Homan, K.A., Skylar-Scott, M.A., Lewis, J.A., 2016. Three-dimensional bioprinting of thick vascularized tissues. Proceedings of National Academy of Science 113, 3179–3184.

Kondepudi, D., Prigogine, I., 1998. Modern Thermodynamics: From Heat Engines to Dissipative Structures. John Wiley and Sons, Chichester, New York.

Kosztin, I., Vunjak-Novakovic, G., Forgacs, G., 2012. *Colloquium*: modeling the dynamics of multicellular systems: application to tissue engineering. Reviews of Modern Physics 84, 1791–1805.

Ladd, A.J.C., 1994. Numerical simulations of particulate suspensions via a discretized Boltzmann equation. I. Theoretical foundation. Journal of Fluid Mechanics 271, 285–309.

Langer, R., Vacanti, J.P., 1993. Tissue engineering. Science 260, 920–926.

Lanza, R.P., Langer, R., Vacanti, J.P. (Eds.), 2007. Principles of Tissue Engineering, third ed. Elsevier Academic Press, Burlington.

Lee, T., Fischer, P.F., 2006. Eliminating parasitic currents in the lattice Boltzmann equation method for nonideal gases. Physical Review E 74, 046709.

LeVeque, R.J., 1992. Numerical Methods for Conservation Laws. Birkhäuser Verlag, Basel.

Luo, L.S., 2000. Theory of the lattice Boltzmann method: lattice Boltzmann models for nonideal gases. Physical Review E 62, 4982–4996.

Martys, N.S., Shan, X., Chen, H., 1998. Evaluation of the external force term in the discrete Boltzmann equation. Physical Review E 58, 6855–6857.

Mills, Z.G., Mao, W., Alexeev, A., 2013. Mesoscale modeling: solving complex flows in biology and biotechnology. Trends in Biotechnology 31 (7), 426–434.

Murphy, S.V., Atala, A., 2014. 3D bioprinting of tissues and organs. Nature Biotechnology 32, 773–785.

Neagu, A., 2017. Role of computer simulation to predict the outcome of 3D bioprinting. Journal of 3D Printing in Medicine 1, 103–121.

Neagu, A., Jakab, K., Jamison, R., Forgacs, G., 2005. Role of physical mechanisms in biological self-organization. Physical Review Letters 95, 178104.

Norotte, C., Marga, F., Niklason, L.E., Forgacs, G., 2009. Scaffold-free vascular tissue engineering using bioprinting. Biomaterials 30, 5910–5917.

PETSc web page: http://www.mcs.anl.gov/petsc/.

Pooley, C.M., Furtado, K., 2008. Eliminating spurious velocities in the free-energy lattice Boltzmann method. Physical Review E 77, 046702.

Press, W.H., Teukolsky, S.A., Vetterling, W.T., Flannery, B.P., 1992. Numerical Recipes in Fortran: The Art of Scientific Computing. Cambridge University Press, Cambridge.

Qian, Y.H., 1997. Fractional propagation and the elimination of staggered invariants in lattice- BGK models. International Journal of Modern Physics C 8, 753–761.

Qian, Y.H., d'Humières, D., Lallemand, P., 1992. Lattice BGK models for Navier-Stokes equation. Europhysics Letters 17, 479–484.

Robu, A., Aldea, R., Munteanu, O., Neagu, M., Stoicu-Tivadar, L., Neagu, A., 2012. Computer simulations of in vitro morphogenesis. BioSystems 109, 430–443.

Rothman, D.H., Zaleski, S., 1997. Lattice – Gas Cellular Automata, Simple Models of Complex Hydrodynamics. Cambridge University Press, Cambridge.

Sbragaglia, M., Benzi, R., Biferale, L., Succi, S., Sugiyama, K., Toschi, F., 2007. Generalized lattice Boltzmann method with multirange pseudopotential. Physical Review E 2, 026702.

Semple, J.L., Woolridge, N., Lumsden, C.J., 2005. In vitro, in vivo, in silico: computational systems in tissue engineering and regenerative medicine. Tissue Engineering 11, 341–356.

Seta, T., Okui, K., 2007. Effects of truncation error of derivative approximation for two-phase lattice Boltzmann method. Journal of Fluid Science and Technology 2, 139–151.

Shan, X., 2006. Analysis and reduction of the spurious current in a class of multiphase lattice Boltzmann models. Physical Review E 73, 047701.

Shan, X., Chen, H., 1993. Lattice Boltzmann model for simulating flows with multiple phases and components. Physical Review E 47, 1815–1819.

Shan, X., Chen, H., 1994. Simulation of nonideal gases and liquid-gas phase transitions by the lattice Boltzmann equation. Physical Review E 49, 2941–2948.

Snir, M., Otto, S., Huss-Lederman, S., Walker, D., Dongarra, J., 1999. MPI – The Complete Reference. MIT Press, Cambridge, Massachusetts.

Sofonea, V., Lamura, A., Gonella, G., Cristea, A., 2004. Finite difference lattice Boltzmann model with flux limiters for liquid – vapor systems. Physical Review E 70, 046702.

Sofonea, V., Sekerka, R.F., 2001. BGK models for diffusion in isothermal binary fluid systems. Physica A: Statistical Mechanics and its Applications 299, 494–520.

Sofonea, V., Sekerka, R.F., 2003. Viscosity of finite difference lattice Boltzmann models. Journal of Computational Physics 184, 422–434.

Sofonea, V., Sekerka, R.F., 2005. Diffusivity of two-component isothermal finite difference lattice Boltzmann models. International Journal of Modern Physics C 16, 1075–1090.

This book belongs to Central Library BADJI Mokhtar-ANNABA UNIVERSITY

Copyright Elsevier 2024

Steinberg, M.S., 1963. Reconstruction of tissues by dissociated cells. Some morphogenetic tissue movements and the sorting out of embryonic cells may have a common explanation. Science 141, 401–408.

Steinberg, M.S., 2007. Differential adhesion in morphogenesis: a modern view. Current Opinion in Genetics and Development 17, 281–286.

Sterling, J.D., Chen, S., 1996. Stability analysis of lattice Boltzmann methods. Journal of Computational Physics 123, 196–206.

Succi, S., 2001. The Lattice Boltzmann Equation for Fluid Dynamics and Beyond. Oxford University Press, Oxford.

Sun, Y., Wang, Q., 2013. Modeling and simulations of multicellular aggregate self-assembly in biofabrication using kinetic Monte Carlo methods. Soft Matter 9, 2172–2186.

Sun, Y., Yang, X., Wang, Q., 2014. In-silico analysis on biofabricating vascular networks using kinetic Monte Carlo simulations. Biofabrication 6, 015008.

Swift, M.R., Orlandini, E., Osborn, W.R., Yeomans, J.M., 1996. Lattice Boltzmann simulations of liquid – gas and binary fluid systems. Physical Review E 54, 5041–5052.

Swift, M.R., Osborn, W.R., Yeomans, J.M., 1995. Lattice Boltzmann simulation of non-ideal fluids. Physical Review Letters 75, 830–833.

Teng, S., Chen, Y., Ohashi, H., 2000. Lattice Boltzmann simulation of multiphase flows through the total variation diminishing with artificial compression scheme. International Journal of Heat and Fluid Flow 21, 112–121.

Toro, E.F., 1999. Riemann Solvers and Numerical Methods for Fluid Dynamics, second ed. Springer Verlag, Berlin.

Wagner, A.J.C., 2003. The origin of spurious velocities in lattice Boltzmann. International Journal of Modern Physics B 17, 193–196.

Welander, P., 1954. On the temperature jump in a rarefied gas. Arkiv för Fysik 7, 507–553.

Wolf-Gladrow, D.A., 2000. Lattice Gas Cellular Automata and Lattice Boltzmann Models. Springer Verlag, Berlin.

Xie, C., Zhang, J., Bertola, V., Wang, M., 2016. Lattice Boltzmann modeling for multiphase viscoplastic fluid flow. Journal of Non-Newtonian Fluid Mechanics 234, 118–128.

Xu, T., Jin, J., Gregory, C., Hickman, J.J., Boland, T., 2005. Inkjet printing of viable mammalian cells. Biomaterials 26, 93–99.

Yang, J., Boek, E.S., 2013. A comparison study of multi-component lattice Boltzmann models for flow in porous media applications. Computers and Mathematics with Applications 65, 882–890.

Yuan, P., Schaefer, L., 2006. Equations of state in a lattice Boltzmann model. Physics of Fluids 4, 042101.

This book belongs to Central Library BADJI Mokhtar-ANNABA UNIVERSITY

Copyright Elsevier 2024

This page intentionally left blank

This book belongs to Central Library BADJI Mokhtar-ANNABA UNIVERSITY

Copyright Elsevier 2024

Chapter 22

The Lattice Boltzmann Modeling: Solving Complex Flows Including Biological Cells

Z. Hashemi
Islamic Azad University, Bushehr, Iran

22.1 INTRODUCTION

Blood is a vital fluid that made up of two portions: a liquid part called plasma that is about 91.5% water and 8.5% solutes (Tortora and Derrickson, 2008) and a nonliquid part (formed elements) consisting of red blood cells (RBCs), white blood cells (WBCs), and platelets. Blood is circulated through the vascular system by the heart and delivers oxygen and nutrients to organs and sweeps away metabolic wastes. The nature of blood flow in the vascular system is sensitive to the vessel diameter. In thick vessels with diameters larger than 200 μm, the blood flow can be accurately modeled as a homogeneous fluid. However, in smaller vessels, such as arterioles, venules, and especially capillaries (4−10 μm), the blood flow has to be treated as a suspension of formed elements in a background fluid (plasma).

Generally, 55% of whole blood is occupied by plasma, lower than 1% by WBCs and platelets, and 45% by RBCs. In fact, in 1 mm^3 blood, there are 5,000,000 RBCs, 5000−8000 WBCs, and 300,000 platelets; that is, WBCs and platelets occupy less than 1/600 and 1/800 of cellular volume, respectively. Therefore, RBCs, also known as erythrocytes, are the most abundant elements in blood plasma.

RBCs are nucleus-free capsules consisting of an incompressible Newtonian viscous liquid enclosed by a highly deformable viscoelastic membrane, which makes RBC to deform and pass through microcapillaries with diameters as small as 3 μm.

Because RBCs are the essential constituents and the most abundant cells in the blood, their mechanical properties, such as deformability and shape, are among the most important factors in determination of whole blood hydrodynamic properties. In a number of human diseases, such as cancer, diabetes, malaria, sickle-cell anemia, and hereditary spherocytosis, the mechanical, physical, and/or geometrical properties of RBCs are varied; hence, the dynamic behavior of blood flow is significantly influenced. Knowing the effect of interfacial mechanical properties on flow-induced deformation of cells would lead to better understanding of disease progression mechanisms and developing innovative clinical therapies for such blood diseases.

The experimental studies in the field of dynamic behavior of RBCs (Chivukula et al., 2014; Forsyth et al., 2010; Kubota et al., 1996; Tomaiuolo et al., 2011; Tomaiuolo and Guido, 2011; Tsukada et al., 2001) are limited because of different challenges and difficulties, such as blood coagulation and the quality of blood filtering materials. In the past years, to reduce the risks and costs of experimental studies, many researchers have been relying on computer models. Significant efforts have been made to provide efficient computational strategies for modeling the motion and deformation of RBCs in the blood flow. From a computational standpoint, this problem can be considered as a complex moving boundary problem in which the boundaries are deformable. Many factors are involved in these complexities: the biconcave geometry of RBC, solving the Eulerian description of fluid flow associated the Lagrangian description of membrane, cell−cell, and fluid−cell interactions, and flow-induced deformation of RBC. One should note that because of the large deformations of RBC, linear elasticity theory, which is valid for small deformations, cannot be applied.

Computational challenges for modeling a real three-dimensional RBC have conducted researchers to develop two-dimensional models (Doddi and Bagchi, 2009; Li and Sarkar, 2008; Shi et al., 2012; Sui et al., 2008a). In these

Numerical Methods and Advanced Simulation in Biomechanics and Biological Processes. https://doi.org/10.1016/B978-0-12-811718-7.00022-8
Copyright © 2018 Elsevier Ltd. All rights reserved.

This book belongs to Central Library BADJI Mokhtar-ANNABA UNIVERSITY
Copyright Elsevier 2024

models, the membrane of RBC is simply considered as an elastic ring and discretized into a set of line elements; therefore the surface tension can be easily computed from the strains of these line elements. It should be noted that the discretization of a real three-dimensional interface would lead to plane elements and the approach for computing the tensions is not as easy as that of line elements. Reviewing the literature and comparing the 2D results with available experimental data indicates that, although the two-dimensional studies can predict some common features of flow-induced deformation of RBC, in this field, the two-dimensional approach is an improper simplification and cannot completely describe the physical/mechanical properties of a real membrane.

Significant development of computer power and computational methods in the last few decades had made it possible to study three-dimensional time-dependent flow-induced deformation of capsules extensively (Cordasco and Bagchi, 2014, 2016; Lac et al., 2004; Pozrikidis, 1995; Ramanujan and Pozrikidis, 1998; Shi et al., 2013a,b; Yazdani and Bagchi, 2011, 2013; Yazdani et al., 2011; Zhou and Pozrikidis, 1995). A comprehensive review of these progresses can be found in Barthès-Biesel (2011, 2016) and Freund (2014) in which different numerical strategies were presented along with their limitations and advantages.

In early three-dimensional numerical studies, to remove the difficulties derived from complex geometry and membrane mechanics, RBCs have been modeled as rigid/deformable spherical or ellipsoidal particles using different techniques such as boundary element method (BEM) (Kraus et al., 1996; Pozrikidis, 1995), immersed boundary method (IBM) (Barthes-Biesel et al., 2002; Diaz et al., 2000; Ramanujan and Pozrikidis, 1998), lattice Boltzmann method (LBM) (Eggleton and Popel, 1998; Hashemi et al., 2013, 2014a,b, 2015; Lac et al., 2004; Shi and Lim, 2007; Shi et al., 2013b), and some other methods (Lac et al., 2007; Zhang et al., 2008).

There are limited studies on the description of dynamic behavior of RBC as a deformable liquid capsule with biconcave discoid unstressed shape.

To study the dynamic behavior of an RBC in the plasma flow, a reliable and convenient computational tool is required, capable of predicting the complex physical phenomena tacking place in a fluid-membrane system. Therefore, a combined computational frame that can handle simulation of the plasma motion, the deformation and motion of RBC membrane, and fluid-membrane interaction is essential.

Because of the importance of the problem, in this chapter, a combined numerical strategy based on the LBM is presented in detail. The combined method composed of the LBM for the fluid flow simulation, the finite element method (FEM) for the membrane dynamics, and the IBM for the fluid-membrane interactions is fully described here and employed to model dynamic behavior of RBC in three dimensions. Using this approach, the transient deformation and motion of RBC in simple shear flow (Hashemi et al., 2015; Krüger et al., 2011, 2013; Lac et al., 2004; Sui et al., 2008b, 2010a,b) and microcapillary/microchannel flow (Hashemi and Rahnama, 2016; Hashemi et al., 2016; Krüger et al., 2014) has been studied, and the ability, as well as the limitations of this technique, to predict dynamic behavior of RBC has been verified.

22.2 LATTICE BOLTZMANN METHOD

22.2.1 General Concepts

In fluid-membrane systems, such as suspended RBCs in plasma flow, simulation of background fluid with high accuracy is of great importance. This is attributed to the fact that the hydrodynamic interactions between the plasma and the membrane of RBCs cause flow-induced deformation of RBCs. A powerful computational tool for simulating the fluid mechanics is the LBM, which was developed in 1880s based on the statistical mechanics. In contrast to conventional and macroscopic approaches in computational fluid dynamic (CFD) such as finite volume method (FVM) and finite difference method, and also microscopic approaches such as molecular dynamic, the LBM can be classified as a mesoscopic approach. This technique is a particle-based kinetic method in which the macroscopic quantities of the fluid flow are obtained by modeling the behavior of the fictitious fluid particles. Unlike traditional CFD techniques in which the Navier−Stokes equations are solved directly, the LBM is based on following the fictitious particles of fluid using the Boltzmann equation. It should be noted that the Navier−Stokes equations can be derived from the Boltzmann equation by using the Chapman−Enskog expansion.

Several comparisons between the LBM and the conventional CFD methods, such as finite difference (Ginzbourg and Adler, 1994; Noble et al., 1996; Sankaranarayanan et al., 2003; Zou and He, 1997), finite element (Chen et al., 1992; Geller et al., 2006; Kandhai et al., 1999; Martinez et al., 1994), and FVMs, have been done to verify the accuracy, performance, and the advantages of this method over the traditional ones. The results showed that LBM is a powerful competitor of conventional CFD approaches. Although the advantages and disadvantages of each method are case dependent, it was proved that LBM is faster and more efficient, especially in the field of multiphase flow (Hou et al., 1997; Huang et al., 2011; Kuzmin and Mohamad, 2010; Reis and Phillips, 2007) and problems involving complex geometries.

This book belongs to Central Library BADJI Mokhtar-ANNABA UNIVERSITY Copyright Elsevier 2024

In comparison with the other numerical methods, the LBM has several important features that make it an efficient and useful tool for modeling the fluid flow. The main features are summarized as follows (Shan and Chen, 1993; Yu et al., 2003): (1) The convection operator is linear in phase space (in contrast to Navier−Stokes solvers which is nonlinear). (2) The lattice Boltzmann (LB) equation is explicit in form. (3) It is not needed to solve a Poisson equation for the pressure. It can be easily computed by the equation of state. (4) Through the Chapman−Enskog expansion (Wolf-Gladrow, 2000), the incompressible Navier−Stokes equations can be derived from the lattice Boltzmann equation at the limit of low Mach number. (5) There are no systems of linear or nonlinear equations in the solution procedure because LBM treats with physical properties at the microscopic level. (6) The transferred information is local in space and time, so parallelization in LBM is much more suitable. (7) For microscale fluid flow problems and those involving complex geometries, LBM is much easier to implement.

These substantial features make the LBM an alternative tool for simulating the fluid flow in complex problems.

22.2.2 Mathematical Formulation

Based on the statistical physics, the Boltzmann equation introduced by Ludwig Boltzmann in 1872 with the external force term G can be read as

$$\frac{\partial f}{\partial t} + \xi \cdot \frac{\partial f}{\partial x} + G \cdot \frac{\partial f}{\partial \xi} = \Omega(f) \tag{22.1}$$

The f function is the particle distribution function that describes the collective behavior of fluid particles. The left-hand side of this equation shows the particle motion with microscopic velocity ξ at x position, whereas the right-hand side models the collision and particle−particle interactions. The discretization of this equation in velocity space, time, and space, and also substitution of the collision term with single relaxation time (SRT) (τ) Bhatnagar, Gross, Krook (BGK) model (Bhatnagar et al., 1954), results in the lattice Boltzmann equation, which can be written as follows:

$$f_\alpha(x + e_\alpha \Delta t, t + \Delta t) - f_\alpha(x,t) = -\frac{1}{\tau}\left(f_\alpha - f_\alpha^{eq}\right) \tag{22.2}$$

The main idea in the LBM is to divide the fluid domain into a simple, regular, Cartesian grid with high symmetry, called lattice. Each lattice consists of some links that show the probability of fluid particle motion on that direction. For two- and three-dimensional lattices, the most common structures for discretization of the velocity phase space are D_2Q_9 and D_3Q_{19} models, in which, according to Fig. 22.1, fluid particles can move with different velocities on 9 and 19 directions α, respectively. The zeroth direction ($\alpha = 0$) is accounted for stationary fluid particles that remain in the node.

The discrete velocity vectors for D_3Q_{19} model, which is used here, are expressed as

$$e_\alpha = \begin{cases} (0,0,0) & \alpha = 0 \\ (\pm1,0,0)c, (0,\pm1,0)c, (0,0,\pm1)c & \alpha = 1\sim6 \\ (\pm1,\pm1,0)c, (0,\pm1,\pm1)c, (\pm1,0,\pm1)c & \alpha = 7\sim18 \end{cases} \tag{22.3}$$

in which, c is the lattice speed and can be determined by the ratio of lattice spacing and time step, $\Delta x/\Delta t$.

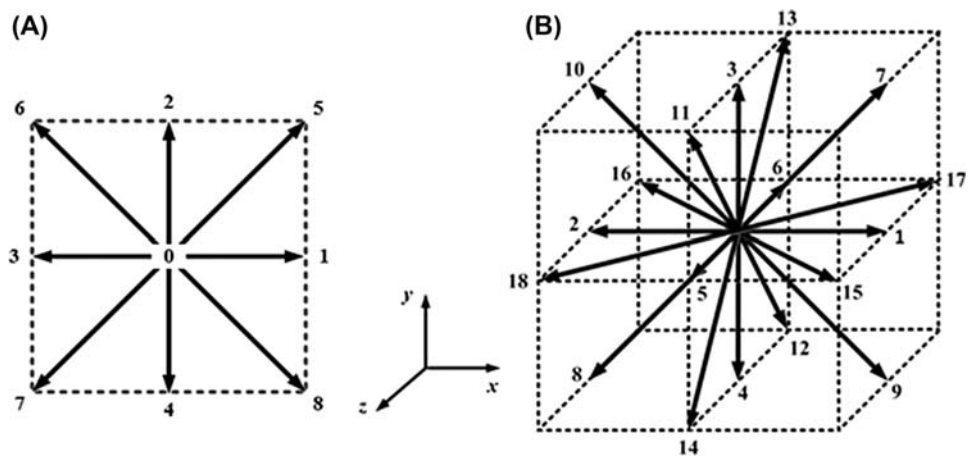

FIGURE 22.1 The most commonly used lattice models in (A) 2D: D_2Q_9 and (B) 3D: D_3Q_{19}.

This book belongs to Central Library BADJI Mokhtar-ANNABA UNIVERSITY Copyright Elsevier 2024

In Eq. (22.2), f^{eq} is the equilibrium distribution function. For D_3Q_{19} model, the component of this function can be calculated with

$$f_\alpha^{eq} = \omega_\alpha \rho \left[1 + \frac{3\,\boldsymbol{e}_\alpha \cdot \boldsymbol{u}}{c^2} + \frac{9(\boldsymbol{e}_\alpha \cdot \boldsymbol{u})^2}{2\,c^4} - \frac{3(\boldsymbol{u} \cdot \boldsymbol{u})}{2\,c^2}\right] \quad for \;\; \alpha = 0 \sim 18 \tag{22.4}$$

in which, ρ is the fluid density, u is the macroscopic fluid velocity, and ω_α are weighting factors that, for D_3Q_{19} model, are

$$\begin{cases} \omega_\alpha = 1/3 & \alpha = 0 \\ \omega_\alpha = 1/18 & \alpha = 1 \sim 6 \\ \omega_\alpha = 1/36 & \alpha = 7 \sim 18 \end{cases} \tag{22.5}$$

As mentioned before, in the LBM the macroscopic quantities of the fluid flow, such as density and velocity, can be obtained easily from the particle distribution functions,

$$\rho = \sum_\alpha f_\alpha \tag{22.6}$$

$$\rho \vec{u} = \sum_\alpha \vec{e}_\alpha f_\alpha \tag{22.7}$$

In the LBM, the kinematic viscosity υ is a function of the relaxation time and can be determined by

$$\upsilon = (\tau - 0.5) c_s^2 \Delta t \tag{22.8}$$

In this equation, c_s is the lattice speed of sound and is equal to $c_s^2 = c^2/3$. It should be noted that the relaxation time τ has to be greater than 0.5 to enforce the positive viscosity for fluid and guarantee the stability of solution.

One of the important feature of the LBM is that a Poisson equation for the pressure is not involved in solution procedure and it can be easily calculated by the equation of state as follows:

$$p = \rho c_s^2 \tag{22.9}$$

22.2.3 Numerical Implementation

The lattice Boltzmann equation, which is described in Eq. (22.2), can be numerically solved in two steps: collision step and streaming step.

In the collision step, the interactions between different fluid particles are modeled and the new distribution functions f_α^* are computed according to the distribution functions of the previous time step,

$$f_\alpha^*(x, t + \Delta t) = f_\alpha(x, t) - \frac{1}{\tau}\left(f_\alpha - f_\alpha^{eq}\right) \tag{22.10}$$

Actually, this step models the right-hand side of Eq. (22.2) and only includes the variables related to each node x, so it can be regarded as a local operator. This feature is very valuable and useful for parallelization process.

In the streaming step, the fluid particles streams to the neighboring cell according to their velocities in the original cell:

$$f_\alpha(x + e_\alpha \Delta t, t + \Delta t) = f_\alpha^*(x, t) \tag{22.11}$$

In this step, there is no mathematical calculation and just the information transfers between neighboring nodes.

These mentioned features of LBM, as well as its explicit form in time, regular grids, easy implementation, and parallelization (Han et al., 2007), make it as a popular and powerful technique with high efficiency.

To simulate the fluid flow in the lattice Boltzmann framework, first, the fluid domain has to be discretized into uniform and regular grids (lattices). The equilibrium distribution functions are computed according to Eq. (22.4), and the distribution functions f_α are initially set equal to these distribution functions. After that, the collision and streaming steps, Eqs. (22.10) and (22.11), are applied and the boundary conditions (BCs) are enforced. Finally, the macroscopic quantities of fluid flow can be obtained by using Eqs. (22.6) and (22.7).

This book belongs to Central Library BADJI Mokhtar-ANNABA UNIVERSITY
Copyright Elsevier 2024

22.2.4 Boundary Conditions

For different fluid mechanic cases, there are different kinds of BCs, which can be classified as Dirichlet (or first-type) BC, Neumann (or second-type) BC, and Robin (or third-type) BC. In the case of Navier−Stokes solvers, the BCs are expressed in the frame of macroscopic variables, such as pressure or velocity. However, in the LBM, the governing equations are based on the particle distribution functions. Therefore, the macroscopic BCs have to be transformed to the mesoscopic level and formulated for particle distribution functions.

In the streaming step of LBM, the distribution functions can be determined on all grid nodes, except those located on boundary nodes. Fig. 22.2 schematically depicts the distribution functions on boundary nodes for a three-dimensional channel in the $x-y$ plane. As shown in this figure for boundary nodes, some of the distribution functions move out of the computational domain (solid arrows) and some of them point in, from outside to the fluid domain (dashed arrows). Because there are no grid nodes out of the domain, the distribution functions that come in the boundary nodes cannot be determined. According to Fig. 22.2 the solid arrows are the known distribution functions and the dashed arrows are the unknown distribution functions on different sides of the channel. A constraint, called BC, can resolve the problem.

One of the simplest and the most convenient BC in the hydrodynamic problems is the periodic BC. In this condition the walls are eliminated and a small part of an infinite system, having a periodically repeating nature, is considered. In LBM, the missing boundary values at each side of the computational domain are substituted by transferring the known distribution functions from the opposite side of the domain.

In situations where the Knudsen number is small and the continuum theory is valid, the no-slip BC for solid walls has to be applied. The most widely used rule for enforcement the no-slip condition in LBM is the bounce-back rule (Kutay et al., 2006), which dictates that $f_{-i}(x,t+\Delta t) = f_i(x,t_+)$. $-i$ shows the opposite direction of i.

To implement the no-slip BC on solid boundary nodes, the model proposed by Zou and He (1997) can be applied. This method is based on the bounce back of nonequilibrium distribution functions and replaces the unknown distribution functions with their known opposite functions. More details about this model can be found in Zou and He (1997). For instance, the resulted formulations for inlet and top boundaries are presented through Eqs. (22.12)−(22.24), and the other unknown distribution functions on other sides of the channel can be determined by the same strategy.

22.2.4.1 Inlet Boundary (x = *0*)

To implement the velocity BC at the inlet plane of the channel, it is assumed that the component of velocity vector in x, y, and z directions are: $u = u_{in}$, $v_{in} = 0$, and $w_{in} = 0$. Extending the Zou and He model for three-dimensional cases, the density and missing distribution functions at the inlet boundary nodes can be determined as follows. These formulations are

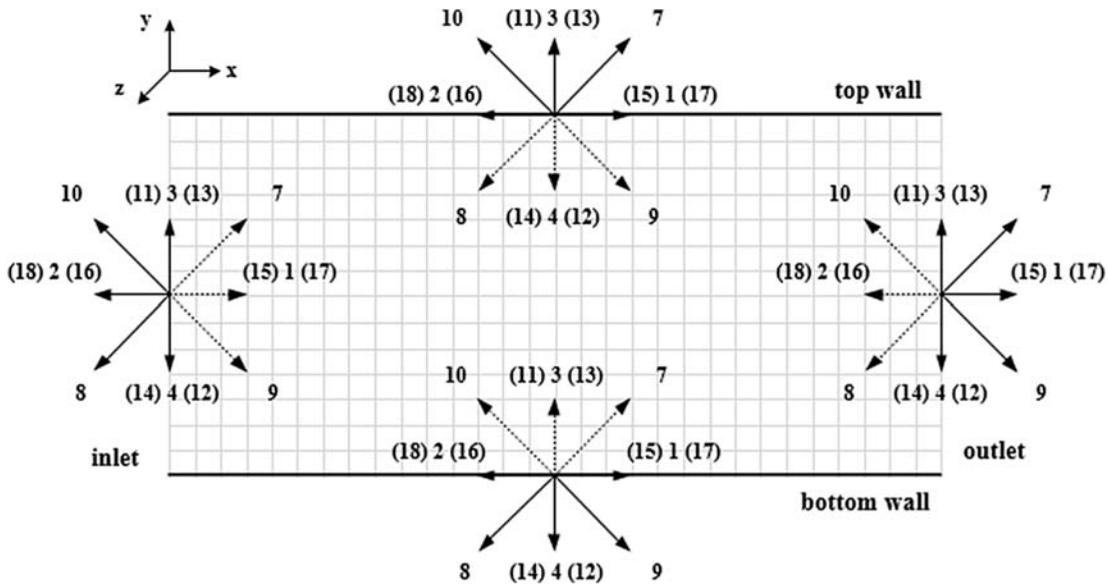

FIGURE 22.2 A schematic description of known (*solid arrows*) and unknown (*dashed arrows*) distribution functions in $x-y$ plane of a three-dimensional channel.

This book belongs to Central Library BADJI Mokhtar-ANNABA UNIVERSITY
Copyright Elsevier 2024

based on the bounce back rule for nonequilibrium part of those distribution functions that are perpendicular to the boundary (Hashemi, 2015).

$$\rho = \frac{1}{1-u_{in}}[f_0+f_3+f_4+f_5+f_6+f_{11}+f_{12}+f_{13}+f_{14}+2(f_2+f_8+f_{10}+f_{16}+f_{18})] \tag{22.12}$$

and,

$$f_1 = f_2 + \frac{1}{3}\rho u_{in} \tag{22.13}$$

$$f_7 = f_8 + \frac{1}{2}(f_4 - f_3 + f_{12} - f_{11} + f_{14} - f_{13}) + \frac{1}{6}\rho u_{in} + \frac{1}{2}\rho v_{in} \tag{22.14}$$

$$f_9 = f_{10} - \frac{1}{2}(f_4 - f_3 + f_{12} - f_{11} + f_{14} - f_{13}) + \frac{1}{6}\rho u_{in} - \frac{1}{2}\rho v_{in} \tag{22.15}$$

$$f_{15} = f_{16} + \frac{1}{6}\rho u_{in} + \frac{1}{6}\rho w_{in} \tag{22.16}$$

$$f_{17} = f_{18} + \frac{1}{6}\rho u_{in} - \frac{1}{6}\rho w_{in} \tag{22.17}$$

If the pressure is known at the inlet plane of the channel, the inlet velocity can be computed as

$$u = \frac{\rho_{in}-1}{\rho_{in}}[f_0+f_3+f_4+f_5+f_6+f_{11}+f_{12}+f_{13}+f_{14}+2(f_2+f_8+f_{10}+f_{16}+f_{18})] \tag{22.18}$$

22.2.4.2 Top Boundary (y = H)

Knowing that $u = u_x$, $v = 0$, and $w = 0$ on the top plane, we have (Hashemi, 2015)

$$\rho = f_0+f_3+f_4+f_5+f_6+f_{11}+f_{12}+f_{13}+f_{14}+2(f_2+f_8+f_{10}+f_{16}+f_{18}) \tag{22.19}$$

and

$$f_4 = f_3 \tag{22.20}$$

$$f_8 = f_7 - \frac{1}{2}(f_2 - f_1 + f_{16} - f_{15} + f_{18} - f_{17}) - \frac{1}{2}\rho u_x \tag{22.21}$$

$$f_9 = f_{10} + \frac{1}{2}(f_2 - f_1 + f_{16} - f_{15} + f_{18} - f_{17}) + \frac{1}{2}\rho u_x \tag{22.22}$$

$$f_{12} = f_{11} \tag{22.23}$$

$$f_{14} = f_{13} \tag{22.24}$$

22.3 IMMERSED BOUNDARY METHOD

22.3.1 General Concepts

To model the hydrodynamic interactions between plasma and RBC membrane, the IBM can be applied. This method was first proposed by Peskin (1972) to simulate blood flow in human heart. As shown schematically in Fig. 22.3, the basic idea is to employ two sets of independent grids that are not necessarily conform: a fixed Eulerian grid for the fluid flow and a moving Lagrangian grid for the immersed membrane. The information transfer between two meshes is carried on using a simple interpolation rule, i.e., Dirac delta distribution function. In the IBM, the presence of an immersed structure is introduced to the fluid flow via a source term in the fluid governing equations. The local forces on Lagrangian nodes of the membrane, which can be computed from membrane mechanics, are distributed to their neighboring Eulerian nodes by the Dirac delta function, and then the governing equations with an external force term are solved over the entire computational domain. The new velocity of Lagrangian nodes are interpolated from the fluid nodes, and thus the no-slip BC on membrane is imposed.

This book belongs to Central Library BADJI Mokhtar-ANNABA UNIVERSITY
Copyright Elsevier 2024

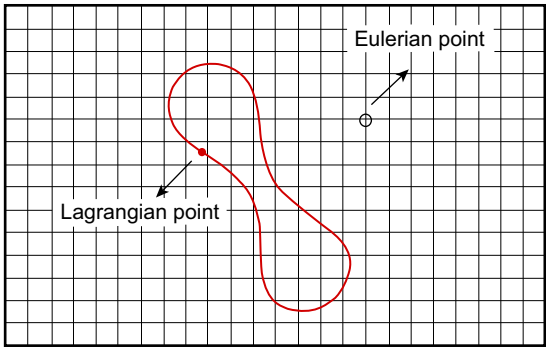

FIGURE 22.3 The immersed boundary method: two sets of independent grids in a two-dimensional domain: fluid Eulerian and membrane Lagrangian points.

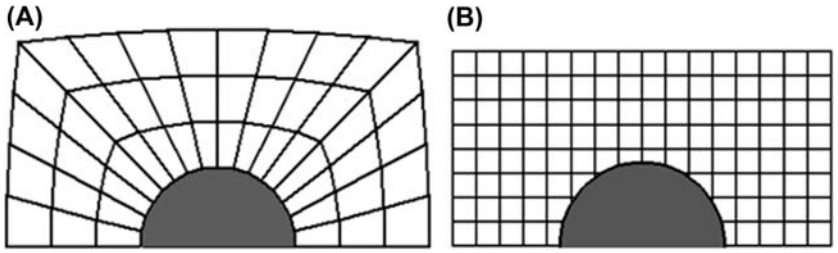

FIGURE 22.4 (A) Body-fitted and (B) non-body-fitted meshes around an immersed object.

The IBM has been gained attention by many motives. Some of them are listed as follows (Hashemi et al., 2017):

- The IBM is in the category of non-body-fitted methods, in which the computational grid is not needed to be conformed to the real physical boundary. It uses a stationary structured or unstructured computational grid and the frequent remeshing procedure is not required. This intrinsic feature of IBM eliminates the difficulty and time-consuming nature of remeshing process and makes it an efficient tool for modeling complex structures, such as RBCs.
- In comparison with the body-fitted method, such as arbitrary Lagrangian−Eulerian method (Hu, 1996; Hu et al., 1992) and deforming-spatial-domain/space-time method (Tezduyar et al., 1992a,b), the grid generation process in IBM is completely different. In the former methods, first the geometry is specified and then a structured/unstructured conformal mesh is generated, Fig. 22.4A. However, in IBM a simple nonconformal mesh is used, Fig. 22.4B, and the effect of immersed membrane is implemented in the solution process. It should be noted that computations for dynamic changes of immersed objects in the solution process is much simpler.
- Another advantage is that there is no user-defined parameters in IBM that have to be determined by flow conditions.
- It is easy to implement and can be simply coupled to a flow solver, such as NS or LB solvers, via an external force term.

Because of these interesting advantages, the IBM has been widely used to simulate different kinds of problems and has been emerged as a powerful method for modeling immersed structures with arbitrary shapes (Vahidkhah and Abdollahi, 2012).

22.3.2 Mathematical Formulation

The mathematical formulation of IBM was first presented by Peskin (1972). Consider the fluid domain Ω with Eulerian coordinates $\boldsymbol{x}$, in which an elastic boundary Γ with Lagrangian coordinates $\boldsymbol{s}$ is immersed. As mentioned in Section 22.4, the local Lagrangian forces $\boldsymbol{F}(\boldsymbol{s},t)$ due to flow-induced deformation can be computed by membrane mechanics. To obtain the total forces at the nearest fluid nodes $\boldsymbol{f}(\boldsymbol{x},t)$, an integration of $\boldsymbol{f}$ in the $\boldsymbol{s}$ coordinates can be performed, in which the local forces are transformed to their equivalent Eulerian forces,

$$\boldsymbol{f}(\boldsymbol{x},t) = \int_{\Gamma} \boldsymbol{F}(\boldsymbol{s},t)\delta(x - \boldsymbol{X}(\boldsymbol{s},t))ds \tag{22.25}$$

This book belongs to Central Library BADJI Mokhtar-ANNABA UNIVERSITY
Copyright Elsevier 2024

where δ is the Dirac delta function in three dimensions and $\boldsymbol{X}(\boldsymbol{s},t)$ is the position vector in Lagrangian system. This force density is added to the fluid governing equations to introduce the presence of the immersed membrane and model the fluid−membrane interactions.

In the IBM, to impose the no-slip BC at the surface of the membrane, the velocity of membrane nodes and fluid nodes has to be equal, i.e.,

$$\boldsymbol{U}(\boldsymbol{s},t) = \boldsymbol{u}(X(s,t),t) \tag{22.26}$$

in which $\boldsymbol{u}(\boldsymbol{x},t)$ is the velocity of Eulerian fluid node, and $\boldsymbol{U}(\boldsymbol{s},t)$ shows the velocity of Lagrangian nodes on immersed membrane as

$$\boldsymbol{U}(\boldsymbol{s},t) = \frac{\partial X(s,t)}{\partial t} \tag{22.27}$$

and can be determined by an interpolation from the velocities of Eulerian nodes:

$$\boldsymbol{U}(\boldsymbol{s},t) = \int_{\Omega} \boldsymbol{u}(\boldsymbol{x},t)\delta(x - \boldsymbol{X}(\boldsymbol{s},t))dx \tag{22.28}$$

The same Dirac delta function δ has to be applied for the force distribution Eq. (22.25) and the velocity interpolation Eq. (22.28).

22.3.3 Numerical Implementation

The equations of the previous subsection have to be discretized to simulate numerically the hydrodynamic interactions between fluid and membrane.

In three dimensions, the Dirac delta function δ can be discretized as

$$\delta(x - \boldsymbol{X}(\boldsymbol{s},t)) = \delta(x - \boldsymbol{X}(\boldsymbol{s},t))\delta(y - Y(s,t))\delta(z - Z(s,t)) \tag{22.29}$$

It is important to find a suitable discretized delta function in such a way that the momentum and angular momentum are conserved (Peskin, 2002). The following equations show the most common discretized delta functions that cover 2, 3, and 4 lattice nodes along each axis, respectively (Krüger et al., 2011).

$$\delta(r) = \begin{cases} 1 - |r| & |r| \le 1 \\ 0 & \text{otherwise} \end{cases} \tag{22.30}$$

$$\delta(r) = \begin{cases} \frac{1}{3}\left(1 + \sqrt{1 - 3r^2}\right) & |r| \le \frac{1}{2} \\ \frac{1}{6}\left(5 - 3|r| - \sqrt{-2 + 6|r| - 3r^2}\right) & \frac{1}{2} \le |r| \le \frac{3}{2} \\ 0 & \text{otherwise} \end{cases} \tag{22.31}$$

$$\delta(r) = \begin{cases} \frac{1}{8}\left(3 - 2|r| + \sqrt{1 + 4|r| - 4r^2}\right) & |r| \le 1 \\ \frac{1}{8}\left(5 - 2|r| - \sqrt{-7 + 12|r| - 4r^2}\right) & 1 \le |r| \le 2 \\ 0 & \text{otherwise} \end{cases} \tag{22.32}$$

A delta function with smaller coverage offers some advantages such as reducing the computational time at each time step, truly capturing the physical phenomena, and providing smaller numerical thickness for membrane that is of great importance in simulation of a large number of elastic membranes (Krüger et al., 2011). However, it should be noted that it introduces stronger fluctuations and an accelerated degradation that may arise in the computational mesh (Krüger et al., 2011).

This book belongs to Central Library BADJI Mokhtar-ANNABA UNIVERSITY
Copyright Elsevier 2024

Knowing the suitable delta function and the local Lagrangian forces (Section 22.4.4), one can discretize Eq. (22.25) to obtain the Eulerian forces on fluid node $\boldsymbol{x}$,

$$f(x) = \sum_{s\in\Gamma} F(s)\delta(x - X(s)) \tag{22.33}$$

The fluid governing equations, in which Eulerian forces are added as a source term, are solved to update the macroscopic quantities of fluid such as velocity $\boldsymbol{u}(\boldsymbol{x},t)$. Using the same delta function observed in Eq. (22.33), the discretized form of Eq. (22.28) can be obtained as

$$U(s) = \sum_{x\in\Omega} u(x)\delta(x - X(s)) \tag{22.34}$$

that means the velocity of each Lagrangian node can be determined by an interpolation between the velocities of its neighboring fluid nodes.

The no-slip BC dictates that

$$\frac{\partial X(s,t)}{\partial t} = \boldsymbol{u}(\boldsymbol{X}(\boldsymbol{s},t),t) \tag{22.35}$$

that means that the membrane has to be moved with the same velocity as the fluid around it. This motion causes some deformations in the membrane. Using an explicit Euler method for the time discretization, the new positions of the membrane nodes can be obtained as follow:

$$\boldsymbol{X}(\boldsymbol{s},t+\Delta t) = \boldsymbol{X}(\boldsymbol{s},t) + \boldsymbol{U}(\boldsymbol{s},t)\Delta t \tag{22.36}$$

22.3.4 Immersed Boundary−Lattice Boltzmann Method

The LBM is an Eulerian scheme that uses uniform Cartesian meshes. Therefore, it can be a good candidate to be combined with the IBM and solve flow field for it. Keeping the advantages of both methods simultaneously, this combination leads to an efficient and powerful computational tool for simulating the hydrodynamic interactions in fluid−membrane systems with arbitrary shapes. Because the equations in the solution process are locally solved, the computer parallelization is easier. This feature greatly facilitates the simulation of dense suspension of elastic membranes in fluid flow.

In fluid−membrane systems, when a membrane moves in the fluid, a force term that varies with time and space acts on fluid flow. Therefore, the LB equation, shown in Eq. (22.2), has to be modified to capture the effect of this force:

$$f_\alpha(x + e_\alpha\Delta t, t + \Delta t) - f_\alpha(x,t) = -\frac{1}{\tau}\left[f_\alpha(x,t) - f_\alpha^{eq}(x,t)\right] + \Delta t F_\alpha \tag{22.37}$$

To add a source term into LB equation, different schemes have been proposed. Mohamad and Kuzmin (2010) compared the most widely used schemes and stated that the method proposed by Luo (1993) is simpler and gives more accurate results. According to this comparison, the suggested method of Luo is used here:

$$F_\alpha = -3\omega_\alpha \rho e_\alpha \cdot f/c^2 \tag{22.38}$$

It should be noted that this force term has to be added into the collision term. In the Eq. (22.38), f is the external force at Eulerian nodes that can be computed by Eq. (22.33), via IBM.

22.4 MEMBRANE MECHANICS

22.4.1 General Concepts

Passing through the microcapillaries, having sizes as small as blood cells, RBCs undergo large deformations and show complex dynamic behaviors, especially in three-dimensional cases. In this situation, the relations between the stress and strain tensors are no longer linear, and hence, the simple linear elasticity theory, which is limited to small deformations, is not valid.

To model the dynamic behavior of RBC in the plasma flow, and calculate the elastic forces on RBC membrane due to flow-induced deformation, the finite element formulation that was proposed by Charrier et al. (1989) and Shrivastava and Tang (1993) can be applied. This scheme is capable to model large deformations of membranes of arbitrary shapes. For this

This book belongs to Central Library BADJI Mokhtar-ANNABA UNIVERSITY
Copyright Elsevier 2024

purpose, first the surface of the membrane has to be discretized into unstructured triangular elements, and then the finite element formulation along with a suitable constitutive law is applied to model RBC deformation and compute elastic forces on membrane nodes. These two steps are described in more details in the following subsections.

22.4.2 Membrane Discretization

In the FEM, the first step is to construct flat triangular elements on the surface of RBC. This can be done using a hollow sphere, which is discretized into triangular elements. The elements on the surface of the sphere can be mapped onto the surface of RBC by a proper mapping function.

In the FEM, accurate modeling of the membrane deformation implies using a highly refined homogeneous and isotropic mesh structure on the surface of the unstressed membrane. Because of the symmetry of Platonic solids, these regular polyhedrons turn out to be good choices for the starting point in the triangulation process. Among the Platonic solids, the regular icosahedron seems to be the best approximation for a sphere, and its surface area to volume ratio is closest that of a sphere of the same size. Therefore, a regular icosahedron is used here to start the triangulation process. Ramanujan and Pozrikidis (1998) performed a similar approach starting from a regular octahedron.

A regular icosahedron, Fig. 22.5A, is a convex polyhedron with 20 equilateral triangles as faces, 30 edges, and 12 vertices. For any closed surface, which is consisting of triangles, the number of faces N_f can be obtained by $N_f = 2N_n - 4$, in which N_n shows the number of vertices (Krüger et al., 2011). At the beginning of the triangulation process, each face is subdivided into four triangular elements by creating new vertices at the middle of each edge, Fig. 22.5B. These 80 triangles and 42 vertices are then projected radially onto the surface of a sphere, Fig. 22.5C. This process is repeated n times to obtain the desired resolution and increase the number of faces to $N_f = 4^n N_{0f}$, in which $N_{0f} = 20$ for an icosahedron. For example, after repeating the process two times, a sphere with 162 nodes and 320 elements is created (Fig. 22.5D); after three times a sphere with 642 nodes and 1280 elements (Fig. 22.5E); and after four times a sphere with 2562 nodes and 5120 elements (Fig. 22.5F).

In human blood, the shape of a healthy adult RBC is a biconcave disk with a flattened center. To discretize the membrane of an unstressed RBC into triangular elements, a proper mapping function from the surface of a sphere to the surface of RBC can be used. The analytical form of this function is (Doddi and Bagchi, 2009; Evans and Fung, 1972; Fung, 2013)

$$x = R_0 x', y = 0.5R_0\sqrt{1-r^2}\left(C_0 + C_2 r^2 + C_4 r^4\right), z = R_0 z' \tag{22.39}$$

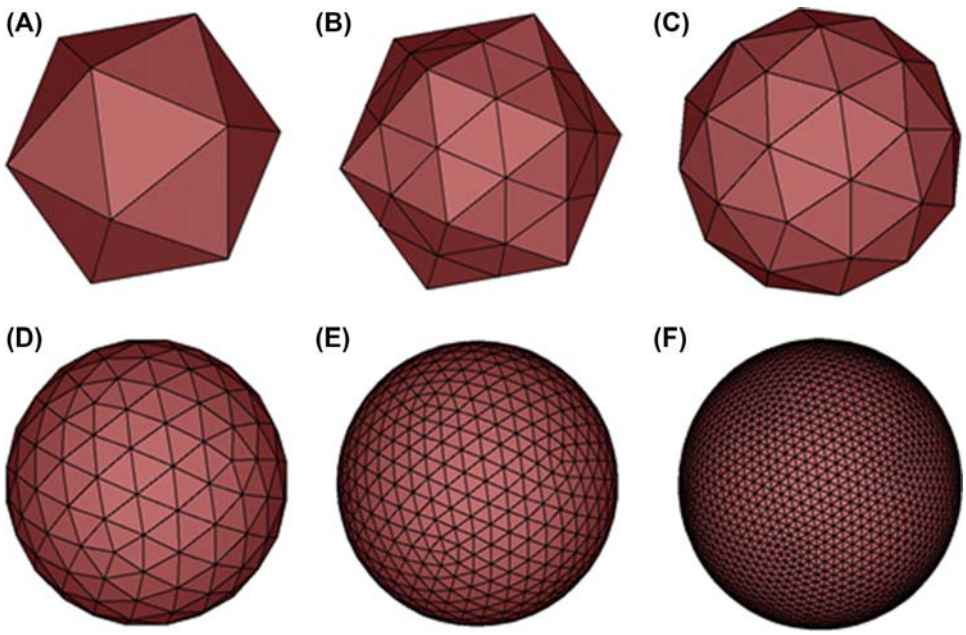

FIGURE 22.5 Generating triangular elements on the surface of a sphere: (A) a regular icosahedron, (B) creating new vertices at the middle of each edge, (C) projecting the vertices radially onto the surface of a sphere, (D) a sphere with 162 nodes and 320 elements, (E) a sphere with 642 nodes and 1280 elements, and (F) a sphere with 2562 nodes and 5120 elements.

This book belongs to Central Library BADJI Mokhtar-ANNABA UNIVERSITY Copyright Elsevier 2024

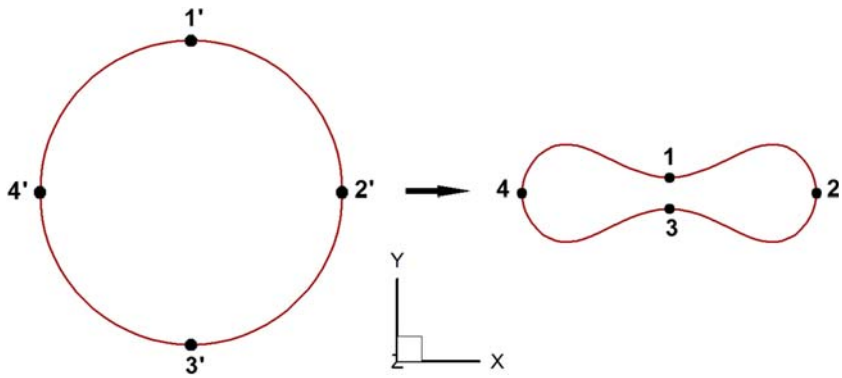

FIGURE 22.6 A two-dimensional view of mapping process: each node on the surface of the sphere is mapped to a specific node on the surface of red blood cells.

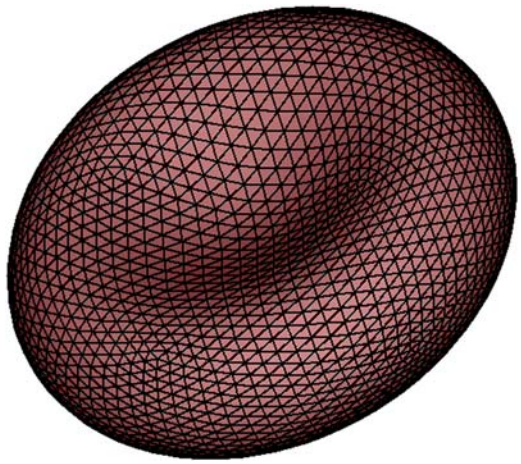

FIGURE 22.7 A triangulated red blood cell with 2562 nodes and 5120 elements.

where

$$r^2 = x'^2 + z'^2 \tag{22.40}$$

and x, y, z are the coordinates of the RBC surface, and x', y', z' are the coordinates of a unit sphere. The term R_0 is an adjusting factor to preserve the volume, and C_i ($i = 0, 2, 4$) are coefficients equal to $C_0/R_0 = 0.207$, $C_2/R_0 = 2.003$, and $C_4/R_0 = -1.123$.

As shown in Fig. 22.6, the above mapping function can project each node on the surface of the sphere to a specific node on the surface of RBC. Fig. 22.7 depicts a triangulated RBC that is mapped from a sphere with 2562 nodes and 5120 elements (Fig. 22.5F).

22.4.3 Constitutive Law

As mentioned earlier, the dynamic behavior of RBC in the plasma flow does not lie in the linear elasticity theory. A materially nonlinear theory is needed for biological cells, where the strain cannot be considered small. A nonlinear constitutive law is necessary to describe the realistic behavior of the membrane and relation between the stress and strain.

Different kinds of constitutive laws have been applied to capture the dynamic behavior of capsules in the fluid flow. The simplest equation is the neo-Hookean (NH) law in which the membrane is modeled as a volume-incompressible isotropic material. The strain energy function of this law is

$$W^{NH} = \frac{E_s}{6}\left(\lambda_1^2 + \lambda_2^2 - 3 + \frac{1}{\lambda_1^2\lambda_2^2}\right) \tag{22.41}$$

This book belongs to Central Library BADJI Mokhtar-ANNABA UNIVERSITY Copyright Elsevier 2024

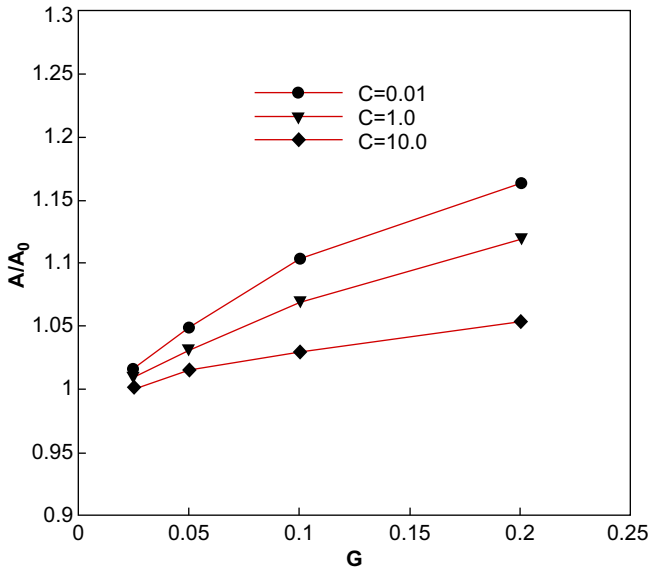

FIGURE 22.8 Effect of different values of the C coefficient in SK law on area change of a spherical capsule in simple shear flow at different dimensionless shear rates.

E_s is the surface shear elasticity modulus, and λ_1 and λ_2 are the principal strains or, in other words, the eigenvalues of the deformation tensor. Another version of NH model is called zero-thickness shell formulation (Ramanujan and Pozrikidis, 1998):

$$W^{ZT} = \frac{E_s}{6}\left(\lambda_1^2 + \lambda_2^2 - 2 - \log\left(\lambda_1^2\lambda_2^2\right) + \frac{1}{2}\log^2\left(\lambda_1^2\lambda_2^2\right)\right) \tag{22.42}$$

RBCs show stronger resistance to area change. Skalak et al. (1973) introduced a constitutive model, denoted by SK, to describe the lipid bilayer structure surrounding the RBC and model the elastic behavior of that. This model has the strain energy density as follows:

$$W^{SK} = \frac{E_s}{12}\left[\left(\lambda_1^4 + \lambda_2^4 - 2\lambda_1^2 - 2\lambda_2^2 + 2\right) + C\left(\lambda_1^2\lambda_2^2 - 1\right)^2\right] \tag{22.43}$$

The SK model contains an additional coefficient C, which represents the energy penalty for area change. $C \gg 1$ indicates the area-incompressibility approximation. It should be noted that higher values of this parameter may lead to numerical instability. The effect of different values of C coefficient on area change is depicted in Fig. 22.8 for an initially spherical capsule in simple shear flow at different dimensionless shear rates $G = \mu\gamma R/E_s$. Here, μ is the dynamic viscosity of plasma, γ is the shear rate, and R is the capsule radius. When $C = 10$, the maximum area change is about 5%. Therefore, it seems that $C = 10$ is sufficient to ignore the area change and prevent numerical instability during the deformation.

22.4.4 Finite Element Method

The large deformation of RBC is modeled using the FEM developed by Charrier et al. (1989), as well as by Shrivastava and Tang (1993). According to the procedure described in Section 22.4.2, the surface of the thin membrane is replaced with a patchwork of small flat triangular elements. Obeying a homogeneous deformation, these elements remain flat even after large deformations. The load on each element is replaced by concentrated loads at its three nodes. In three-dimensional cases the deformed element does not locate in the same plane as the undeformed element. A better comparison between these two configurations can be made in a common plane, for example the plane of deformed element. Because it just implies a rigid body motion of the undeformed element, the nodal forces are not affected. Therefore, the problem is reduced to plane deformation of the triangular elements.

This book belongs to Central Library BADJI Mokhtar-ANNABA UNIVERSITY
Copyright Elsevier 2024

To compute the nodal displacements and the corresponding nodal forces, two local coordinates for deformed and undeformed elements as $\boldsymbol{x}^L$ and $\boldsymbol{X}^L$ are defined, respectively:

$$\boldsymbol{x}_i^L = 0, \boldsymbol{x}_j^L = \boldsymbol{q}(\boldsymbol{x}_j - \boldsymbol{x}_i), \boldsymbol{x}_k^L = \boldsymbol{q}(\boldsymbol{x}_k - \boldsymbol{x}_i) \tag{22.44}$$

$$\boldsymbol{X}_i^L = 0, \boldsymbol{X}_j^L = \boldsymbol{Q}(\boldsymbol{X}_j - \boldsymbol{X}_i), \boldsymbol{X}_k^L = \boldsymbol{Q}(\boldsymbol{X}_k - \boldsymbol{X}_i) \tag{22.45}$$

in which, $\boldsymbol{i}, \boldsymbol{j}, \boldsymbol{k}$ indicate three nodes of the element, and $\boldsymbol{q}$ and $\boldsymbol{Q}$ are transformation matrices defined as, $q_{ij} = e_i^L \cdot e_j$ and $Q_{ij} = E_i^L \cdot e_j \cdot \{e_i^L\}$ and $\{E_i^L\}$ are the unit vectors corresponding to the deformed and undeformed elements at node i, respectively, and $\{e_i\}$ is a triad of unit vectors attached to the global coordinate system.

Because of the homogeneous deformation, the components of displacement vector $\boldsymbol{U} = (u, v)$ vary linearly inside the element. By using the concept of shape function N, one can find displacements as follows:

$$\boldsymbol{U}_i = N_i U_i + N_j U_j + N_k U_k \tag{22.46}$$

The shape function interpolates the solution between the discrete values obtained at all three nodes of the element. Typically, low-order polynomials are used as shape functions. In this work, linear shape functions are applied for each node as follows:

$$N = ax^L + by^L + c \tag{22.47}$$

The unknown coefficients a, b, and c can be determined by the fact that $N_m(x_n, y_n) = \delta_{mn}$, in which δ_{mn} is the Kronecker delta function.

By computing the local nodal displacements, $\boldsymbol{U} = \boldsymbol{X}^{\boldsymbol{L}} - \boldsymbol{x}^{\boldsymbol{L}}$, shape functions and their derivatives with respect to x and y directions, one can obtain displacement gradients $\left(\frac{\partial u}{\partial x}, \frac{\partial u}{\partial y}\right)$ and $\left(\frac{\partial v}{\partial x}, \frac{\partial v}{\partial y}\right)$ for each element by differentiating Eq. (22.43).

Let $\boldsymbol{F}$ be the deformation gradient tensor that relates the differential position vectors between two neighboring material points before and after the deformation as $d\boldsymbol{X} = \boldsymbol{F}\, d\boldsymbol{x}$. By definition $\boldsymbol{G} = \boldsymbol{F}^T\boldsymbol{F}$ is a symmetric positive definite tensor that its components can be written as

$$\boldsymbol{G} = \begin{bmatrix} \left(1 + \frac{\partial u}{\partial x}\right)^2 + \left(\frac{\partial v}{\partial x}\right)^2 & \left(1 + \frac{\partial u}{\partial x}\right)\left(\frac{\partial u}{\partial y}\right) + \left(1 + \frac{\partial v}{\partial y}\right)\left(\frac{\partial v}{\partial x}\right) \\ \left(1 + \frac{\partial u}{\partial x}\right)\left(\frac{\partial u}{\partial y}\right) + \left(1 + \frac{\partial v}{\partial y}\right)\left(\frac{\partial v}{\partial x}\right) & \left(\frac{\partial u}{\partial y}\right)^2 + \left(1 + \frac{\partial v}{\partial y}\right)^2 \end{bmatrix} \tag{22.48}$$

For planar deformation, the in-plane principal stretch ratios λ_1 and λ_2 are the eigenvalues of the matrix $\boldsymbol{G}$. By using the principal of virtual work and choosing a suitable constitutive law, the nodal forces in local system are obtained:

$$\begin{aligned} F_{xi}^L &= V_e \frac{\partial W}{\partial \lambda_1} \frac{\partial \lambda_1}{\partial u_i^L} + V_e \frac{\partial W}{\partial \lambda_2} \frac{\partial \lambda_2}{\partial u_i^L} \\ F_{yi}^L &= V_e \frac{\partial W}{\partial \lambda_1} \frac{\partial \lambda_1}{\partial v_i^L} + V_e \frac{\partial W}{\partial \lambda_2} \frac{\partial \lambda_2}{\partial v_i^L} \end{aligned} \tag{22.49}$$

in which, V_e is the volume of the undeformed element. The global components of the nodal forces for each element can now be determined by transforming back to the global coordinate system as $\boldsymbol{F}_i = \boldsymbol{R}^T \boldsymbol{F}_i^L$. Because there are six elements around each node, the total elastic force at each node is calculated by summing the resulting force from each element:

$$F_x(s,t) = \sum_{m=1}^{6} (F_{xi})_m, F_y(s,t) = \sum_{m=1}^{6} (F_{yi})_m, F_z(s,t) = \sum_{m=1}^{6} (F_{zi})_m \tag{22.50}$$

These forces are exactly those Lagrangian forces needed in the IBM, Section 22.3.3.

22.4.5 Volume Correction

In numerical simulation based on the original IBM, when the Lagrangian forces are regularized on the membrane, the no-slip condition is not enforced completely, and hence the fluid motion across the surface of the membrane decreases and

This book belongs to Central Library BADJI Mokhtar-ANNABA UNIVERSITY Copyright Elsevier 2024

the fluid penetration is not eliminated. This is due to the fact that the resultant interpolated velocity from IBM is not generally divergence free, even at incompressible fluid limit. This problem causes undesirable variation in membrane volume. To resolve this problem, one way is to add a constraint to the motion of membrane node so that the volume remains constant at all times. The following modification can be applied to the nodal displacement at each time step to enforce the desired constraint:

$$k = -3\frac{V - V_0}{A}\boldsymbol{n} \tag{22.51}$$

in which V_0 is the volume of the undeformed membrane, A is the area of the membrane, and $\boldsymbol{n}$ is the outward unit normal to the surface.

In the present simulations, the maximum volume deviation is about 2%, which is small enough to be neglected, especially for small shear rates.

22.5 SOLUTION ALGORITHM

The solution algorithm for simulation of RBC motion and deformation in plasma flow is presented in this section. In general, the solution algorithm at each time step for the combined IB−LB−FE method includes the following steps:

1. At the beginning of each time step, the position of membrane nodes and macroscopic quantities of fluid are known. According to the nodal displacement, the Lagrangian elastic forces, $\boldsymbol{F}(\boldsymbol{s},t)$, can be determined using the FEM, Section 22.4.
2. Using the IBM, the Lagrangian forces are distributed to their neighboring Eulerian nodes, Eq. (22.33), and the source term $\boldsymbol{f}(\boldsymbol{x},t)$ is obtained.
3. The lattice Boltzmann equation with the source term is solved to update the distribution functions, and compute new macroscopic quantities of the fluid $\boldsymbol{u}(\boldsymbol{x},t+1)$ and $\rho(x,t+1)$, Eqs. (22.6) and (22.7).
4. The new velocities of membrane nodes $\boldsymbol{U}(\boldsymbol{s},t+1)$ are computed using the IBM, Eq. (22.34).
5. The new position of membrane nodes $\boldsymbol{X}(\boldsymbol{s},t+1)$ are computed using Eq. (22.36).
6. Return back to step 1 for the next time step.

Fig. 22.9 shows the flowchart of the FEM. As mentioned in Section 22.4.2, the first step is generating symmetric and homogeneous triangular elements on the surface of the membrane. Following the process described in Fig. 22.9, one can find the Lagrangian elastic forces at each membrane node.

22.6 APPLICATION OF THE COMBINED METHOD TO SUSPENDED BIOLOGICAL CELLS

The present numerical strategy can be applied to model flow-induced deformation of biological cells, such as RBC. In this section, it is tried to compare and verify the obtained results with the present combined method. To do this end, some simple test cases including the dynamic behavior of a spherical capsule and RBC in simple shear flow, RBC in a pressure-driven channel flow, and sedimentation of RBC in a column of plasma are modeled.

22.6.1 A Spherical Capsule in Simple Shear Flow

In the systems consisting of suspended biological cells, the main concerns are accurately evaluating elastic forces and predicting the flow-induced deformation of cell according to the fluid−membrane interactions. Because the biconcave geometry of RBC is complex, a simpler test case of a spherical capsule can be very useful to ensure accurate force computation and hydrodynamic interactions in three dimensions. The problem of dynamic behavior of a spherical capsule in a simple flow geometry, i.e., simple shear flow, has been widely studied using different numerical methods (Doddi and Bagchi, 2009; Eggleton and Popel, 1998; Lac et al., 2004; Li and Sarkar, 2008; Ramanujan and Pozrikidis, 1998). This problem can be regarded as the first and simplest step in modeling suspended biological cells because it can verify the force evaluation and fluid−membrane interaction procedures.

Consider an initially spherical capsule located at the middle of an unbounded shear flow, where the top and bottom boundaries move in the opposite directions. The computations are performed at dimensionless shear rate $G = \mu\gamma R/E_s = 0.1$, and relatively small Reynolds number $Re = \rho\gamma R^2/\mu = 0.025$, which corresponds to Stokes flow regime. Here, ρ and μ are the density and dynamic viscosity of plasma, respectively, γ is the shear rate, and R is the capsule radius.

This book belongs to Central Library BADJI Mokhtar-ANNABA UNIVERSITY
Copyright Elsevier 2024

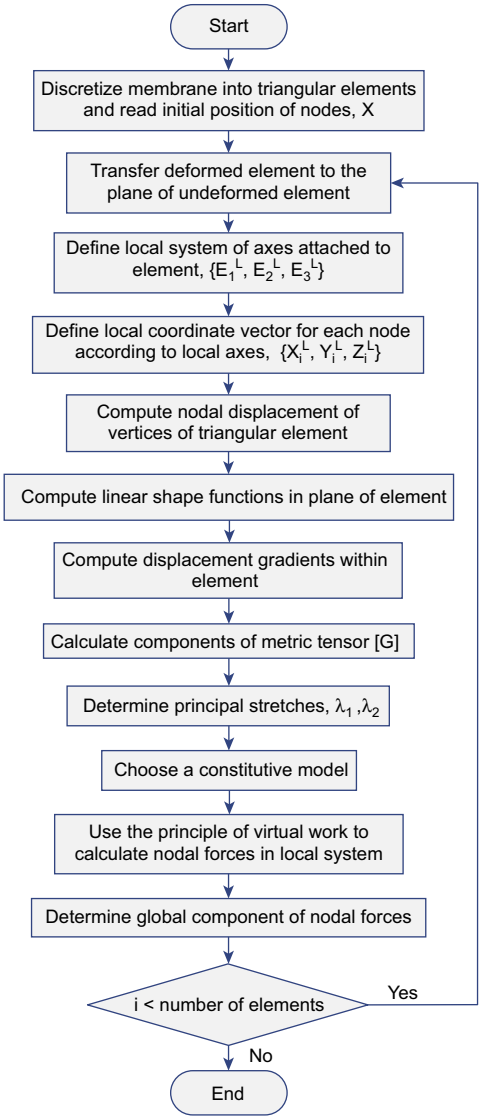

FIGURE 22.9 The solution algorithm of the finite element method for modeling red blood cell deformation (Hashemi, 2015).

When exposed to shear flow, the spherical capsule starts to deform gradually, until an ellipsoid-like shape is achieved. At this stage, the membrane is no longer deformed and experiences a tank treading motion: a continuous rotation of the membrane around its equilibrium shape. Figs. 22.10 and 22.11 depict clearly these phenomena and compare the obtained results with those obtained by BEM (Ramanujan and Pozrikidis, 1998). t^* is the dimensionless time defined as γt. A material point is shown in the capsule profiles to better represent the tank treading motion of the membrane in the last three figures. To illustrate the dynamic behavior of the capsule during the deformation, two parameters have been defined: the angle θ between the major axis of the membrane and the positive x direction, and Taylor deformation parameter D_{xy}, which can be formulated as (Hashemi et al., 2015)

$$D_{xy} = \frac{L_{\max} - L_{\min}}{L_{\max} + L_{\min}} \tag{22.52}$$

$L_{\max}$ and $L_{\min}$ are the largest and the smallest semiaxes of an ellipsoid with the same inertia tensor as the membrane.

This book belongs to Central Library BADJI Mokhtar-ANNABA UNIVERSITY Copyright Elsevier 2024

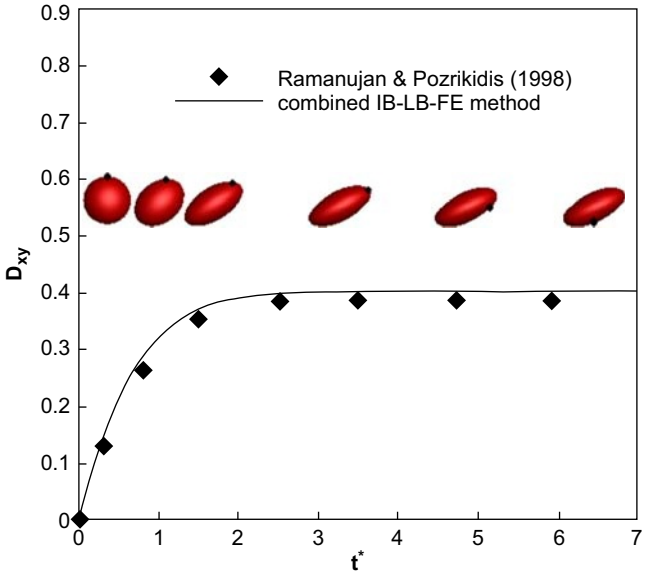

FIGURE 22.10 Transient evolution of deformation parameter and shape profiles for an initially spherical capsule under shear flow at Re = 0.025 and G = 0.1. *IB−LB−FE*, immersed boundary−lattice Boltzmann−finite element.

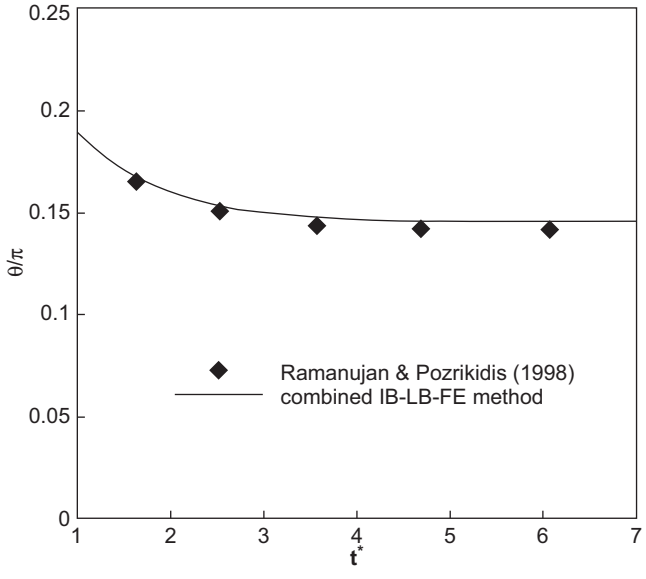

FIGURE 22.11 Transient evolution of inclination angle for an initially spherical capsule under shear flow at Re = 0.025 and G = 0.1. *IB−LB−FE*, immersed boundary−lattice Boltzmann−finite element.

Remarkably, the comparison between the present results and those obtained by BEM (Ramanujan and Pozrikidis, 1998) shows excellent agreement and confirms the validity of the combined IB−LB−FE method in computing elastic forces and modeling fluid−membrane interactions.

22.6.2 Red Blood Cell in Simple Shear Flow

The computations of the previous subsection are repeated here for an RBC with a realistic biconcave shape to verify the validity of the combined method for simulating complex structures in three dimensions. Consider a simple flow geometry consists of an unbounded shear flow at Stokes flow regime in which an RBC placed at the middle of the domain with initial

This book belongs to Central Library BADJI Mokhtar-ANNABA UNIVERSITY Copyright Elsevier 2024

TABLE 22.1 The Required Time for One Complete Iteration in Different Grid Resolutions

Membrane Grid Resolution	CPU Time
320 elements, 162 nodes	0.028
1280 elements, 642 nodes	0.032
5120 elements, 2562 nodes	0.04
20480 elements, 10242 nodes	0.08

inclination angle $\theta = \pi/4$ with the flow direction (Hashemi, 2015). Extensive grid studies have been performed to identify the sufficient grid resolutions for computational domain and RBC membrane. Finally, a membrane grid resolution with 5120 flat triangular elements connecting 2562 membrane nodes is chosen for the present computations. Table 22.1 summarizes the required time for one complete iteration at several membrane resolutions. It should be mentioned that the computations were carried out on a Core-i7/2.4 GHz processor.

Using the BEM, Ramanujan and Pozrikidis (1998) studied the transient deformation of a single RBC under shear flow. However, numerical instabilities due to grid degradation encountered in the computations and limited the reported results to initial transient period. It should be noted that BEM is valid only for creeping flow conditions.

Figs. 22.12 and 22.13 depict the comparison of the present transient deformation parameter, D_{xy}, and inclination angle, θ, with those of the BEM (Ramanujan and Pozrikidis, 1998). Close agreement between the predicted results from both methods reveals the accuracy of the combined computational method in modeling complex structures.

According to the experimental studies (Abkarian et al., 2007; Goldsmith and Marlow, 1972; Schmid-Schönbein and Wells, 1969), RBC may undergo two well-known modes of motion in simple shear flow. Tumbling motion is an unsteady rigid-body-like motion at small shear levels and swinging motion, defined as membrane rotation around a constant deformed geometry, occurred at high shear levels, and RBC undergoes periodic shape deformation and inclination angle. As shown in Figs. 22.14–22.16, the tumbling and swinging motions of an RBC at the dimensionless shear rates $G = 0.0005$, 0.87, and 1.5 can correctly be predicted by the combined IB–LB–FE method.

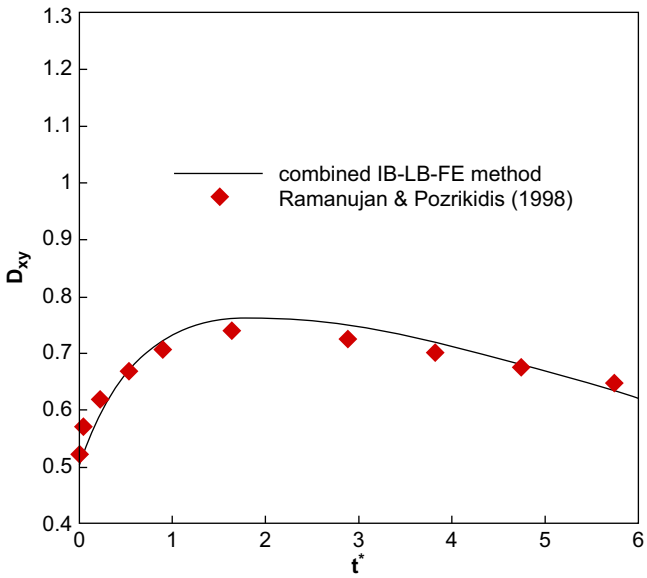

FIGURE 22.12 Transient evolution of deformation parameter for a red blood cell in shear flow at $G = 0.2$: comparison between the present method and the boundary element method. *IB–LB–FE*, immersed boundary–lattice Boltzmann–finite element.

This book belongs to Central Library BADJI Mokhtar-ANNABA UNIVERSITY
Copyright Elsevier 2024

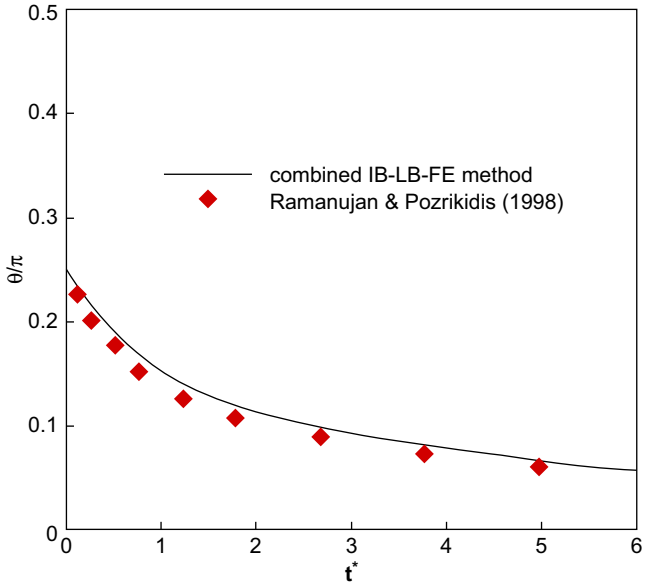

FIGURE 22.13 Transient evolution of inclination angle for a red blood cell in shear flow at G = 0.2: comparison between the present method and the boundary element method. *IB−LB−FE*, immersed boundary−lattice Boltzmann−finite element.

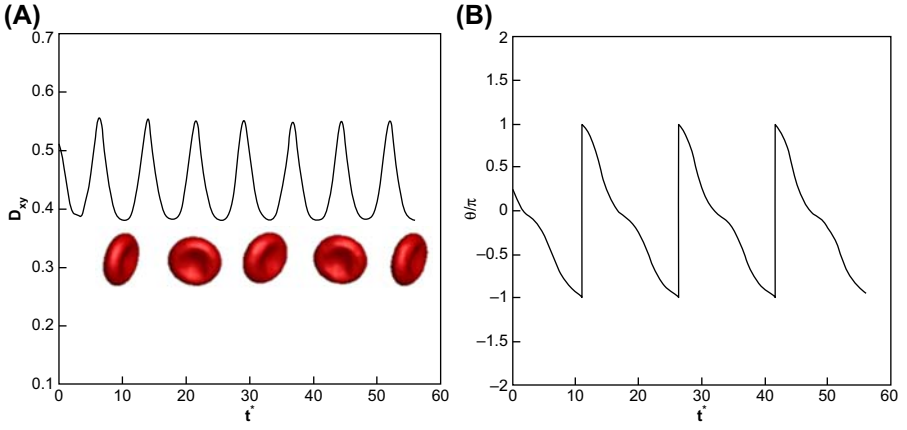

FIGURE 22.14 Transient evolution of (A) deformation parameter and shape profiles and (B) inclination angle for a red blood cell at tumbling motion, G = 0.0005.

22.6.3 Red Blood Cell in a Pressure-Driven Capillary Flow

Another challenge in modeling the dynamic behavior of RBC in the plasma flow is the free motion of RBC, hence a suitable coupling between the fluid phase and the membrane. To investigate this difficulty, the dynamic behavior of an RBC in the microcapillary flow is considered here. This problem was experimentally studied by Tsukada et al. (2001) at the steady-state condition. Assuming the same geometric parameters and the flow conditions (Hashemi and Rahnama, 2016) as those of experimental study of Tsukada et al. (2001), one can evaluate the ability of the combined IB−LB−FE method in modeling the freely motion and deformation of RBC in microcapillaries having sizes comparable with blood cells. To estimate the RBC deformation, according to Fig. 22.17, a deformation index DI, which is the ratio of the length to the diameter of RBC in the steady deformed configuration l/d, is defined.

This book belongs to Central Library BADJI Mokhtar-ANNABA UNIVERSITY
Copyright Elsevier 2024

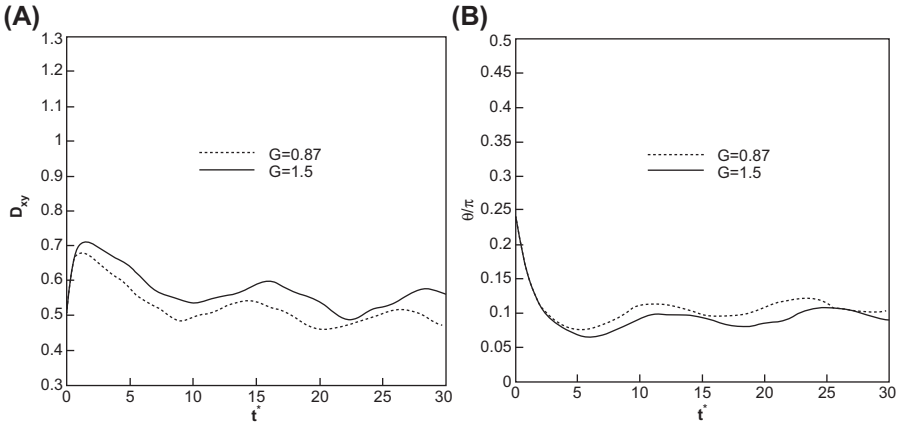

FIGURE 22.15 Transient evolution of (A) deformation parameter and (B) inclination angle for a red blood cell at swinging motion, G = 0.87 and 1.5.

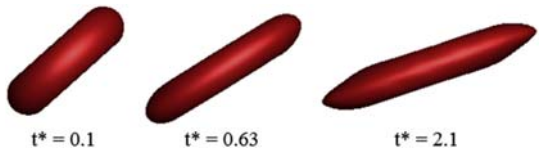

FIGURE 22.16 Shape profiles of red blood cell at $x-y$ plane in the swinging motion at different times and G = 0.87.

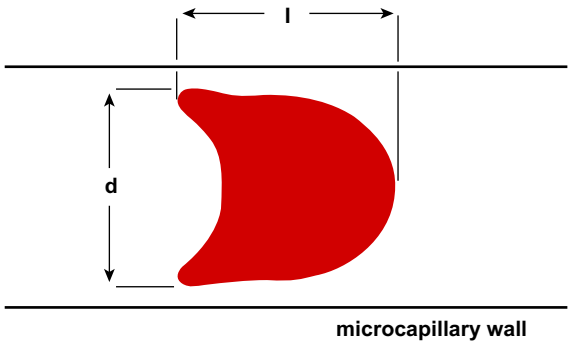

FIGURE 22.17 Definition of deformation index for a red blood cell at steady parachute configuration.

Based on the experimental observations in a pressure-driven microchannel flow, which can be regarded as a microcapillary flow, RBCs tend to deform into a parachute-like configuration at the steady-state condition. Fig. 22.18 depicts the variation of DI as a function of RBC velocity for an RBC located vertically and compares the present results with those of Tsukada et al. (2001). The steady parachute shapes of the RBC at different velocities are also included in this figure. The comparison shows the accuracy and ability of the combined IB−LB−FE method in simulation of deformation and motion of RBC in microcapillary flows.

22.7 LIMITATIONS OF THE COMBINED METHOD

22.7.1 Lattice Boltzmann Method

In general, the LBM requires two conditions: small Mach number Ma and small variations in density. That means that the model is suitable only for compressible flow in incompressible limit. Fortunately, in the field of suspended blood cells in the plasma flow, the lattice Mach number is below 0.1, and hence the flow is incompressible.

This book belongs to Central Library BADJI Mokhtar-ANNABA UNIVERSITY Copyright Elsevier 2024

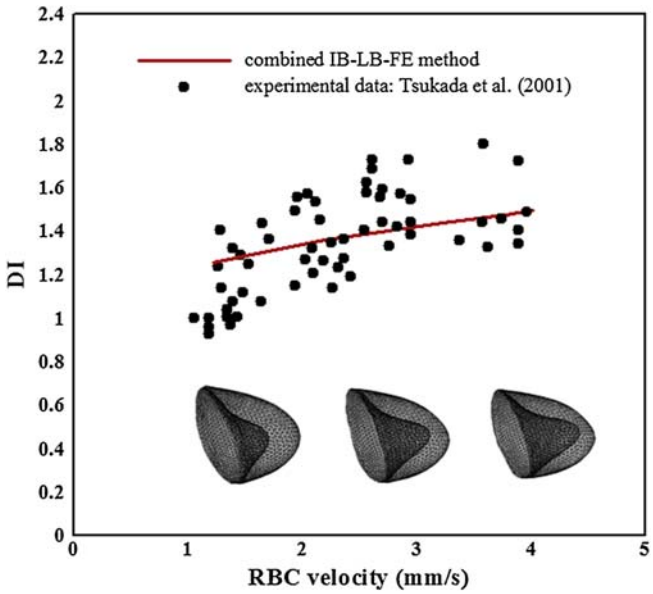

FIGURE 22.18 The deformation index as a function of red blood cell velocity: comparison between present results and those of Tsukada et al. (2001). *IB−LB−FE*, immersed boundary−lattice Boltzmann−finite element.

As previously mentioned, for most of the practical applications, the SRT BGK model has been widely applied for the collision term in Eq. (22.2). Although this approximation simplifies the complicated integral form of the collision term, it suffers from some physical limitations. For LB-based simulations at high Reynolds numbers, the collision frequency $1/\tau$ approaches to its upper bound ($1/\tau < 2$), and hence the stability problems may arise. At this range, the multirelaxation time (MRT) scheme (Higuera, 1989) is more stable than SRT (Aslan et al., 2014). It should be noted that in comparison with SRT, the computer code based on the MRT takes 15% more CPU time (Aslan et al., 2014).

In the present simulations, because the Reynolds number for the plasma flow is small, there is no stability problem related to collision frequency of LBM, and the CPU time can be saved by using the SRT scheme.

22.7.2 Immersed Boundary Method

The original IBM proposed by Peskin (1972) had a first-order accuracy in space. Until now, many modifications have been developed to improve the accuracy, and many benchmark problems have been studied to estimate the accuracy of IBM in different cases. A complete review of these efforts can be found in Hashemi et al. (2017).

When the IBM is used for modeling suspended solid structures, the main idea is considering the boundaries as deformable with high stiffness (Hashemi et al., 2017). In this case, instabilities may encounter in the solution at relatively large values of the stiffness constant. In addition, the required stiffness and damping constants are case dependent and sometimes put severe constraints on time step. In the combined IB−LB−FE method, the elastic force evaluation is performed using the FEM, and the IBM is just used to couple the fluid phase and the membrane. Therefore, there is no numerical problem related to the mentioned issue.

The IBM is based on a finite-width regularized Dirac delta function, so because of the distribution of boundary effects in the fluid domain, the accuracy of solution decreases. A delta function with smaller node coverage along each axis (Section 22.3.3) may cause stronger fluctuations and accelerated degradation in the computational mesh (Krüger et al., 2011).

When a suspended structure approaches the solid walls of the computational domain, there is not sufficient resolution in the gap between the solid walls and the membrane, so the interpolation process faces disruption. To resolve this problem, one can apply a higher mesh quality, introduce a lubrication force to move the structure away from the wall (Feng and Michaelides, 2004), or set a critical distance so that the gap between the membrane and the wall can never be lower than that (Bagchi, 2007).

As mentioned in Section 22.4.5, in the original form of IBM, the interpolated velocity is not divergence free. Therefore, the no-slip condition cannot be fulfilled completely, and the fluid penetration, which causes volume drift, is unavoidable. Until now many improvements have been developed to relax this drawback (Hashemi et al., 2017). At the present simulations, the volume correction at small shear rates is small.

This book belongs to Central Library BADJI Mokhtar-ANNABA UNIVERSITY
Copyright Elsevier 2024

Because the IBM is applied here to couple the fluid and the RBC membrane, the simulations are limited to the cases in which the viscosity of the interior fluid is the same to the exterior one. This restriction can be relaxed by replacing IBM with the front-tracking method (Lallemand et al., 2007; Unverdi and Tryggvason, 1992).

22.7.3 Finite Element Method

In the present FEM, the main assumption is that the membrane is a thin curved sheet in which no moment or transverse shear resistance exists, so the bending stiffness of membrane is neglected. However, for a flow-induced deformation of an RBC, which is a liquid-filled deformable capsule, the bending moments associated with transverse shear tension is as important as the in-plane stresses. A closer look at the RBC profiles in Fig. 22.14A reveals that RBC tends to buckle or fold slightly. Therefore, despite its small value, the method should be improved to include the bending stiffness to prevent developing wrinkles on the surface of the membrane and determine the steady configuration of the membrane.

Another limitation is related to mesh resolution of the membrane. In the present method, it is considered that the membrane is discretized into flat triangular elements which remain flat even after deformation. If the mesh resolution of the membrane is not adequate, the local curvature may develop in some places on the membrane and reduce the accuracy of the model for the force evaluation.

It should be noted that, in the case of the dense suspensions of RBCs in the plasma, the model has to be future improved to include cell−cell interactions and aggregation by adding appropriate repulsing forces.

22.8 DISCUSSION

A three-dimensional numerical strategy including the lattice Boltzmann, the immersed boundary, and the FEMs has been fully characterized and implemented to model the deformation and motion of a liquid-filled capsule enclosed by a deformable membrane in the fluid flow. This strategy has been applied here to simulate the dynamic behavior of suspended RBCs in the plasma flow. This combined method benefits from the advantages of all three methods simultaneously and presents an efficient and accurate computational tool for simulation of biological cells at low cost. Because of the intrinsic features of the LBM in the computer parallelization process, this method has a great capability in simulating the biological cells at high hematocrit to reduce high computational demand. The comparison of the obtained results from the combined method with the available numerical or experimental data confirms the accuracy and validity of the present method. To approach the more realistic situations, further developments and modifications are required to include bending moments, nonunit viscosity ratio, cell−cell interactions, and aggregation of RBCs at high hematocrit.

REFERENCES

Abkarian, M., Faivre, M., Viallat, A., 2007. Swinging of red blood cells under shear flow. Physical Review Letters 98 (18), 188302.

Aslan, E., Taymaz, I., Benim, A., 2014. Investigation of the lattice Boltzmann SRT and MRT stability for lid driven cavity flow. International Journal of Materials, Mechanics and Manufacturing 2 (4), 317−324.

Bagchi, P., 2007. Mesoscale simulation of blood flow in small vessels. Biophysical Journal 92 (6), 1858−1877.

Barthès-Biesel, D., 2011. Modelling the motion of capsules in flow. Current Opinion in Colloid and Interface Science 16 (1), 3−12.

Barthès-Biesel, D., 2016. Motion and deformation of elastic capsules and vesicles in flow. Annual Review of Fluid Mechanics 48, 25−52.

Barthes-Biesel, D., Diaz, A., Dhenin, E., 2002. Effect of constitutive laws for two-dimensional membranes on flow-induced capsule deformation. Journal of Fluid Mechanics 460, 211−222.

Bhatnagar, P.L., Gross, E.P., Krook, M., 1954. A model for collision processes in gases. I. Small amplitude processes in charged and neutral one-component systems. Physical Review 94 (3), 511.

Charrier, J., Shrivastava, S., Wu, R., 1989. Free and constrained inflation of elastic membranes in relation to thermoforming—non-axisymmetric problems. The Journal of Strain Analysis for Engineering Design 24 (2), 55−74.

Chen, S., Wang, Z., Shan, X., Doolen, G.D., 1992. Lattice Boltzmann computational fluid dynamics in three dimensions. Journal of Statistical Physics 68 (3−4), 379−400.

Chivukula, V., Mousel, J., Lu, J., Vigmostad, S., 2014. Micro-scale blood particulate dynamics using a non-uniform rational B-spline-based isogeometric analysis. International Journal for Numerical Methods in Biomedical Engineering 30 (12), 1437−1459.

Cordasco, D., Bagchi, P., 2014. Intermittency and synchronized motion of red blood cell dynamics in shear flow. Journal of Fluid Mechanics 759, 472−488.

Cordasco, D., Bagchi, P., 2016. Dynamics of red blood cells in oscillating shear flow. Journal of Fluid Mechanics 800, 484−516.

Diaz, A., Pelekasis, N., Barthes-Biesel, D., 2000. Transient response of a capsule subjected to varying flow conditions: effect of internal fluid viscosity and membrane elasticity. Physics of Fluids 12 (5), 948−957. 1994-present.

This book belongs to Central Library BADJI Mokhtar-ANNABA UNIVERSITY Copyright Elsevier 2024

Doddi, S.K., Bagchi, P., 2009. Three-dimensional computational modeling of multiple deformable cells flowing in microvessels. Physical Review E 79 (4), 046318.

Eggleton, C.D., Popel, A.S., 1998. Large deformation of red blood cell ghosts in a simple shear flow. Physics of Fluids 10 (8), 1834–1845. 1994-present.

Evans, E., Fung, Y.-C., 1972. Improved measurements of the erythrocyte geometry. Microvascular Research 4 (4), 335–347.

Feng, Z.-G., Michaelides, E.E., 2004. The immersed boundary-lattice Boltzmann method for solving fluid–particles interaction problems. Journal of Computational Physics 195 (2), 602–628.

Forsyth, A.M., Wan, J., Ristenpart, W.D., Stone, H.A., 2010. The dynamic behavior of chemically "stiffened" red blood cells in microchannel flows. Microvascular Research 80 (1), 37–43.

Freund, J.B., 2014. Numerical simulation of flowing blood cells. Annual Review of Fluid Mechanics 46, 67–95.

Fung, Y.-C., 2013. Biomechanics: Mechanical Properties of Living Tissues. Springer Science & Business Media, New York.

Geller, S., Krafczyk, M., Tölke, J., Turek, S., Hron, J., 2006. Benchmark computations based on lattice-Boltzmann, finite element and finite volume methods for laminar flows. Computers and Fluids 35 (8), 888–897.

Ginzbourg, I., Adler, P., 1994. Boundary flow condition analysis for the three-dimensional lattice Boltzmann model. Journal de Physique II 4 (2), 191–214.

Goldsmith, H., Marlow, J., 1972. Flow behaviour of erythrocytes. I. Rotation and deformation in dilute suspensions. Proceedings of the Royal Society of London B: Biological Sciences 182 (1068), 351–384.

Han, K., Feng, Y., Owen, D., 2007. Coupled lattice Boltzmann and discrete element modelling of fluid–particle interaction problems. Computers and Structures 85 (11), 1080–1088.

Hashemi, Z., 2015. Three Dimensional Analysis of a Red Blood Cell Motion in Blood Flow Using Lattice Boltzmann, Immersed Boundary and Finite Element Methods (Ph.D. dissertation (in Persian language)). Shahid Bahonar University of Kerman, Kerman, Iran.

Hashemi, Z., Abouali, O., Ahmadi, G., 2017. Direct numerical simulation of particle–fluid interactions: a review. Iranian Journal of Science and Technology, Transactions of Mechanical Engineering 41 (1), 71–89.

Hashemi, Z., Abouali, O., Kamali, R., 2013. Thermal three-dimensional lattice Boltzmann simulations of suspended solid particles in microchannels. International Journal of Heat and Mass Transfer 65, 235–243.

Hashemi, Z., Abouali, O., Kamali, R., 2014a. Three dimensional thermal lattice Boltzmann simulation of heating/cooling spheres falling in a Newtonian liquid. International Journal of Thermal Sciences 82, 23–33.

Hashemi, Z., Jafari, S., Rahnama, M., 2014b. Comparative study of momentum-exchange and smoothed profile methods in lattice Boltzmann method. Computers and Fluids 100, 65–71.

Hashemi, Z., Rahnama, M., 2016. Numerical simulation of transient dynamic behavior of healthy and hardened red blood cells in microcapillary flow. International Journal for Numerical Methods in Biomedical Engineering 32 (11).

Hashemi, Z., Rahnama, M., Jafari, S., 2015. Lattice Boltzmann simulation of three-dimensional capsule deformation in a shear flow with different membrane constitutive laws. Scientia Iranica. Transaction B, Mechanical Engineering 22 (5), 1877.

Hashemi, Z., Rahnama, M., Jafari, S., 2016. Lattice Boltzmann simulation of healthy and defective red blood cell settling in blood plasma. Journal of Biomechanical Engineering 138 (5), 051002.

Higuera, F., 1989. Boltzmann approach to lattice gas simulations. Europhysics Letters 9 (7), 663.

Hou, S., Shan, X., Zou, Q., Doolen, G.D., Soll, W.E., 1997. Evaluation of two lattice Boltzmann models for multiphase flows. Journal of Computational Physics 138 (2), 695–713.

Hu, H.H., 1996. Direct simulation of flows of solid-liquid mixtures. International Journal of Multiphase Flow 22 (2), 335–352.

Hu, H.H., Joseph, D.D., Crochet, M.J., 1992. Direct simulation of fluid particle motions. Theoretical and Computational Fluid Dynamics 3 (5), 285–306.

Huang, H., Wang, L., Lu, X.-Y., 2011. Evaluation of three lattice Boltzmann models for multiphase flows in porous media. Computers and Mathematics with Applications 61 (12), 3606–3617.

Kandhai, D., Vidal, D., Hoekstra, A., Hoefsloot, H., Iedema, P., Sloot, P., 1999. Lattice-Boltzmann and finite element simulations of fluid flow in a SMRX static mixer reactor. International Journal for Numerical Methods in Fluids 31 (6), 1019–1033.

Kraus, M., Wintz, W., Seifert, U., Lipowsky, R., 1996. Fluid vesicles in shear flow. Physical Review Letters 77 (17), 3685.

Krüger, T., Gross, M., Raabe, D., Varnik, F., 2013. Crossover from tumbling to tank-treading-like motion in dense simulated suspensions of red blood cells. Soft Matter 9 (37), 9008–9015.

Krüger, T., Holmes, D., Coveney, P.V., 2014. Deformability-based red blood cell separation in deterministic lateral displacement devices—a simulation study. Biomicrofluidics 8 (5), 054114.

Krüger, T., Varnik, F., Raabe, D., 2011. Efficient and accurate simulations of deformable particles immersed in a fluid using a combined immersed boundary lattice Boltzmann finite element method. Computers and Mathematics with Applications 61 (12), 3485–3505.

Kubota, K., Tamura, J., Shirakura, T., Kimura, M., Yamanaka, K., Isozaki, T., Nishio, I., 1996. The behaviour of red cells in narrow tubes in vitro as a model of the microcirculation. British Journal of Haematology 94 (2), 266–272.

Kutay, M.E., Aydilek, A.H., Masad, E., 2006. Laboratory validation of lattice Boltzmann method for modeling pore-scale flow in granular materials. Computers and Geotechnics 33 (8), 381–395.

Kuzmin, A., Mohamad, A., 2010. Multirange multi-relaxation time Shan–Chen model with extended equilibrium. Computers and Mathematics with Applications 59 (7), 2260–2270.

Lac, E., Barthes-Biesel, D., Pelekasis, N., Tsamopoulos, J., 2004. Spherical capsules in three-dimensional unbounded stokes flows: effect of the membrane constitutive law and onset of buckling. Journal of Fluid Mechanics 516, 303–334.

This book belongs to Central Library BADJI Mokhtar-ANNABA UNIVERSITY

Copyright Elsevier 2024

Lac, E., Morel, A., Barthes-Biesel, D., 2007. Hydrodynamic interaction between two identical capsules in simple shear flow. Journal of Fluid Mechanics 573, 149–169.

Lallemand, P., Luo, L.-S., Peng, Y., 2007. A lattice Boltzmann front-tracking method for interface dynamics with surface tension in two dimensions. Journal of Computational Physics 226 (2), 1367–1384.

Li, X., Sarkar, K., 2008. Front tracking simulation of deformation and buckling instability of a liquid capsule enclosed by an elastic membrane. Journal of Computational Physics 227 (10), 4998–5018.

Luo, L.-S., 1993. Lattice-Gas Automata and Lattice Boltzmann Equations for Two-Dimensional Hydrodynamics (Ph.D. dissertation). Georgia Institute of Technology, Georgia, USA.

Martinez, D.O., Matthaeus, W.H., Chen, S., Montgomery, D., 1994. Comparison of spectral method and lattice Boltzmann simulations of two-dimensional hydrodynamics. Physics of Fluids 6 (3), 1285–1298. 1994-present.

Mohamad, A., Kuzmin, A., 2010. A critical evaluation of force term in lattice Boltzmann method, natural convection problem. International Journal of Heat and Mass Transfer 53 (5), 990–996.

Noble, D.R., Georgiadis, J.G., Buckius, R.O., 1996. Comparison of accuracy and performance for lattice Boltzmann and finite difference simulations of steady viscous flow. International Journal for Numerical Methods in Fluids 23 (1), 1–18.

Peskin, C.S., 1972. Flow patterns around heart valves: a numerical method. Journal of Computational Physics 10 (2), 252–271.

Peskin, C.S., 2002. The immersed boundary method. Acta Numerica 11, 479–517.

Pozrikidis, C., 1995. Finite deformation of liquid capsules enclosed by elastic membranes in simple shear flow. Journal of Fluid Mechanics 297, 123–152.

Ramanujan, S., Pozrikidis, C., 1998. Deformation of liquid capsules enclosed by elastic membranes in simple shear flow: large deformations and the effect of fluid viscosities. Journal of Fluid Mechanics 361, 117–143.

Reis, T., Phillips, T.N., 2007. Lattice Boltzmann model for simulating immiscible two-phase flows. Journal of Physics A: Mathematical and Theoretical 40 (14), 4033.

Sankaranarayanan, K., Kevrekidis, I., Sundaresan, S., Lu, J., Tryggvason, G., 2003. A comparative study of lattice Boltzmann and front-tracking finite-difference methods for bubble simulations. International Journal of Multiphase Flow 29 (1), 109–116.

Schmid-Schönbein, H., Wells, R., 1969. Fluid drop-like transition of erythrocytes under shear. Science 165 (3890), 288–291.

Shan, X., Chen, H., 1993. Lattice Boltzmann model for simulating flows with multiple phases and components. Physical Review E 47 (3), 1815.

Shi, L., Pan, T.-W., Glowinski, R., 2012. Lateral migration and equilibrium shape and position of a single red blood cell in bounded poiseuille flows. Physical Review E 86 (5), 056308.

Shi, X., Lim, S.P., 2007. A LBM–DLM/FD method for 3D fluid–structure interactions. Journal of Computational Physics 226 (2), 2028–2043.

Shi, X., Lin, G., Zou, J., Fedosov, D.A., 2013a. A lattice Boltzmann fictitious domain method for modeling red blood cell deformation and multiple-cell hydrodynamic interactions in flow. International Journal for Numerical Methods in Fluids 72 (8), 895–911.

Shi, X., Wang, S., Zhang, S., 2013b. Numerical simulation of the transient shape of the red blood cell in microcapillary flow. Journal of Fluids and Structures 36, 174–183.

Shrivastava, S., Tang, J., 1993. Large deformation finite element analysis of non-linear viscoelastic membranes with reference to thermoforming. The Journal of Strain Analysis for Engineering Design 28 (1), 31–51.

Skalak, R., Tozeren, A., Zarda, R., Chien, S., 1973. Strain energy function of red blood cell membranes. Biophysical Journal 13 (3), 245.

Sui, Y., Chew, Y.-T., Roy, P., Low, H.-T., 2008a. A hybrid method to study flow-induced deformation of three-dimensional capsules. Journal of Computational Physics 227 (12), 6351–6371.

Sui, Y., Low, H., Chew, Y., Roy, P., 2008b. Tank-treading, swinging, and tumbling of liquid-filled elastic capsules in shear flow. Physical Review E 77 (1), 016310.

Sui, Y., Chen, X., Chew, Y., Roy, P., Low, H., 2010a. Numerical simulation of capsule deformation in simple shear flow. Computers and Fluids 39 (2), 242–250.

Sui, Y., Low, H., Chew, Y., Roy, P., 2010b. A front-tracking lattice Boltzmann method to study flow-induced deformation of three-dimensional capsules. Computers and Fluids 39 (3), 499–511.

Tezduyar, T., Behr, M., Liou, J., 1992a. A new strategy for finite element computations involving moving boundaries and interfaces—the deforming-spatial-domain/space-time procedure: I. The concept and the preliminary numerical tests. Computer Methods in Applied Mechanics and Engineering 94 (3), 339–351.

Tezduyar, T.E., Behr, M., Mittal, S., Liou, J., 1992b. A new strategy for finite element computations involving moving boundaries and interfaces—the deforming-spatial-domain/space-time procedure: II. Computation of free-surface flows, two-liquid flows, and flows with drifting cylinders. Computer Methods in Applied Mechanics and Engineering 94 (3), 353–371.

Tomaiuolo, G., Barra, M., Preziosi, V., Cassinese, A., Rotoli, B., Guido, S., 2011. Microfluidics analysis of red blood cell membrane viscoelasticity. Lab on a Chip 11 (3), 449–454.

Tomaiuolo, G., Guido, S., 2011. Start-up shape dynamics of red blood cells in microcapillary flow. Microvascular Research 82 (1), 35–41.

Tortora, G.J., Derrickson, B.H., 2008. Principles of Anatomy and Physiology. John Wiley & Sons.

Tsukada, K., Sekizuka, E., Oshio, C., Minamitani, H., 2001. Direct measurement of erythrocyte deformability in diabetes mellitus with a transparent microchannel capillary model and high-speed video camera system. Microvascular Research 61 (3), 231–239.

Unverdi, S.O., Tryggvason, G., 1992. A front-tracking method for viscous, incompressible, multi-fluid flows. Journal of Computational Physics 100 (1), 25–37.

Vahidkhah, K., Abdollahi, V., 2012. Numerical simulation of a flexible fiber deformation in a viscous flow by the immersed boundary-lattice Boltzmann method. Communications in Nonlinear Science and Numerical Simulation 17 (3), 1475–1484.

This book belongs to Central Library BADJI Mokhtar-ANNABA UNIVERSITY

Copyright Elsevier 2024

Wolf-Gladrow, D.A., 2000. Lattice-Gas Cellular Automata and Lattice Boltzmann Models: An Introduction. Springer Science & Business Media.

Yazdani, A., Bagchi, P., 2013. Influence of membrane viscosity on capsule dynamics in shear flow. Journal of Fluid Mechanics 718, 569−595.

Yazdani, A.Z., Bagchi, P., 2011. Phase diagram and breathing dynamics of a single red blood cell and a biconcave capsule in dilute shear flow. Physical Review E 84 (2), 026314.

Yazdani, A.Z., Kalluri, R.M., Bagchi, P., 2011. Tank-treading and tumbling frequencies of capsules and red blood cells. Physical Review E 83 (4), 046305.

Yu, D., Mei, R., Luo, L.-S., Shyy, W., 2003. Viscous flow computations with the method of lattice Boltzmann equation. Progress in Aerospace Sciences 39 (5), 329−367.

Zhang, J., Johnson, P.C., Popel, A.S., 2008. Red blood cell aggregation and dissociation in shear flows simulated by lattice Boltzmann method. Journal of Biomechanics 41 (1), 47−55.

Zhou, H., Pozrikidis, C., 1995. Deformation of liquid capsules with incompressible interfaces in simple shear flow. Journal of Fluid Mechanics 283, 175−200.

Zou, Q., He, X., 1997. On pressure and velocity boundary conditions for the lattice Boltzmann BGK model. Physics of Fluids 9 (6), 1591−1598. 1994-present.

This book belongs to Central Library BADJI Mokhtar-ANNABA UNIVERSITY

Copyright Elsevier 2024

Chapter 23

Lattice Boltzmann Methods for Bioengineering Applications

D.V. Papavassiliou[1], N.H. Pham[1], O.E. Kadri[2] and R.S. Voronov[2]
[1]*The University of Oklahoma, Norman, OK, United States;* [2]*University Heights Newark, Newark, NJ, United States*

23.1 INTRODUCTION

Recent advances in both experimental and computational technologies have led to the development and use of computational methods for understanding and predicting biophysical and biochemical phenomena at a wide multitude of scales. Modern imaging technologies have made the generation of patient-specific data rather commonplace. Detailed images of the vascular system, major organs (such as the heart and its valves), and anomalies in arteries (such as aneurysms, stenoses, genetic abnormalities) can be obtained. The resolution of the images is fine (Appel et al., 2013; Alam et al., 2016), to the point that one can generate digital geometries for simulating the flow of blood, the flow of air in the lungs, or the motion of food in the digestive system under very realistic conditions. In the meantime, advancement of numerical techniques and the availability of robust commercial software that can be used by scientists who are not necessarily experts in computational fluid dynamics (CFD) have allowed the study of biologically relevant flows at increasing rates. Considering further that computational power and speed has been increasing consistently over the past decades following Moore's law, it is no surprise that substantial advances in our knowledge and understanding of biological processes that depend critically on fluid dynamics have occurred. The expectations for the future are even brighter, and the promise for even more impressive advances leading to CFD applications with clinical relevance and routine use by physicians is very realistic.

The challenges to the simulation of fluid flow in biological systems are significant and push the boundaries of CFD capabilities. For example, to simulate blood flow accurately, one has to account for the rheology of blood (which behaves as a Newtonian fluid in large vessels and non-Newtonian in small vessels), to account for different phases in the blood (which is a fluid composed of plasma, red and white cells, and platelets) (Apostolidis and Beris, 2014), to account for the complicated geometry of blood vessels and for the biochemical interactions between the vessel walls and the blood, to determine the boundary conditions at the walls and at the inlet and outlet of the simulation domain, to account for flow regimes that range from creeping to turbulent flow, to account for the dynamic pressure field driving the flow, and to find solutions for simulating the flexible vessel walls. In fact, a whole class of numerical techniques known as fluid−structure interaction (FSI) methods has been developed to simulate the interactions between vessel walls and blood.

Among classical and new numerical techniques, the lattice Boltzmann method (LBM) stands out as a method that can address simulation difficulties due to the complexity of biological flows and as a technique that has recently found applications in a multitude of biological flow problems. It offers inherent advantages that other, typical numerical approaches do not. A main advantage of LBM over other methods is that it is a direct method for fluid flow simulations, in the sense that it uses first principles at the mesoscopic scale instead of modeling terms of the fluid flow governing equations. It is based on the solution of a discretized Boltzmann equation (Chen and Doolen, 1998; Succi, 2001; Sukop and Thorne, 2006; Aidun and Clausen, 2010; Lallemand and Luo, 2000), instead of solving the macroscopic equations for momentum or energy transfer. LBM techniques have been used in several application areas (e.g., turbulence (Cosgrove et al., 2003), multiphase flow (Swift et al., 1996; Ledesma-Aguilar et al., 2014), and complex fluid flow (Gabbanelli et al., 2005; Yoshino et al., 2007; Boyd et al., 2006)). In addition, the LBM method has gained in popularity among the scientific computing community because it is a method that can be parallelized easily on a supercomputer (Wang et al., 2005). For bioengineering applications, LBM is especially appropriate for simulating fluid flow in domains that are irregular, such

Numerical Methods and Advanced Simulation in Biomechanics and Biological Processes. https://doi.org/10.1016/B978-0-12-811718-7.00023-X
Copyright © 2018 Elsevier Ltd. All rights reserved.

This book belongs to Central Library BADJI Mokhtar-ANNABA UNIVERSITY
Copyright Elsevier 2024

as flow of blood through patient-specific vessels that can be obtained through medical imaging, or flow through domains that are porous (such as flow in lungs or in bone tissue). The reason is the use of structured grids with Cartesian coordinates, even in cases where the solid boundaries form a complicated geometry. In addition, LBM techniques have been coupled with other numerical techniques, such as FSI algorithms (Kolmakov et al., 2010; Buxton et al., 2005; Kwon, 2006) and lattice-spring methods (Buxton et al., 2001), and with particle methods (Voronov et al., 2010c; Pham and Papavassiliou, 2017) to simulate fluid−flexible wall interactions and mass transfer coupled with fluid flow problems.

Although LBM offers a multitude of advantages for biological flow simulations, as summarized above, it has not taken its place as a mainstream CFD approach, maybe because commercial CFD packages have not yet incorporated LBM algorithms. In this chapter, we review the LBM technique and present applications for simulations of in vitro flows in bioreactors combined with a review of particle techniques that can be used for mass transfer coupled to fluid flow simulations.

23.2 LATTICE BOLTZMANN METHOD ALGORITHM

23.2.1 Flow Simulation

The LBM is a link between microscopic flow phenomena and the macroscopic fluid flow behavior. A typical LBM algorithm applies a multispeed model consisting of either a two- or a three-dimensional multicomponent velocity. For example a 3D configuration is commonly denoted as (D3Qn), where n is the number of velocity mesh vectors, and a 2D configuration would be denoted as (D2Qn) (Chen and Doolen, 1998; Sukop and Thorne, 2006). The number of velocity lattice vectors for 3D simulations can be 15, 19, or 27. The main LBM features that set it apart from other numerical approaches are as follows (Chen and Doolen, 1998): (1) the nonlinear convection terms of the flow equations is handled in LBM by the combination of a linear streaming and a relaxation process; (2) LBM utilizes an equation of state to calculate the pressure whereas a Navier−Stokes solver solves the Poisson equation that often requires special numerical treatment; (3) calculation of macroscopic properties from the microscopic particle density functions is simple, because a minimal set of velocity vectors is used in LBM. The accuracy of LBM has also been found to be of second order, compared with finite difference discretization methods. Another advantage of LBM is that structured meshes can be used to mesh complex geometries rather than unstructured meshes that are typically used in conventional numerical approaches, such as finite volume or finite element methods. There is no need to generate a new numerical mesh for each new flow configuration with LBM, and the number of mesh points is not prohibitively large.

In 3D, a Cartesian mesh consisting of N_X, N_Y, and N_Z nodes in the x, y, and z directions, respectively is used. The grid points are assigned a binary value of being either in the fluid space or in the solid matrix space. The fluid on each fluid node is represented by a particle distribution function that can be used to compose the density, ρ, of the fluid as

$$\rho = \sum_{i=0}^{n} f_i \tag{23.1}$$

The n components f_i of the particle distribution function belong to one of three types, the rest position ($i = 0$), Class I ($i = 1,\ldots,6$), and Class II ($i = 7,\ldots,n-1$) components. Class I components are on the directions parallel to the Cartesian grid axes (see Fig. 23.1) and Class II components are in directions diagonal to the Cartesian axes.

At the beginning of the simulation, when the fluid velocity is zero, the density at a fluid node is distributed according to the weighting factors of the equilibrium particle distribution function among the three types of components (see Eq. 23.5).

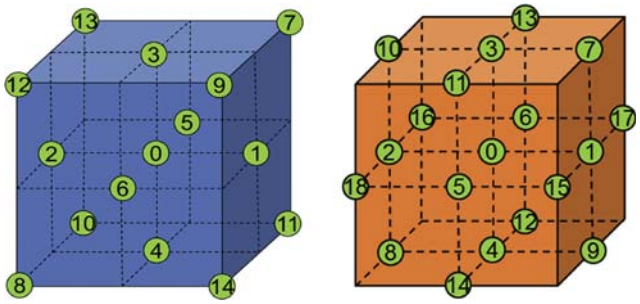

FIGURE 23.1 A typical D3Q15 (left) and D3Q19 (right) computational cell for lattice Boltzmann method simulations. The position 0 is the fluid particle rest position, whereas the node numbers shown on the figure designate the directions to which the particle probability function "streams" in each time step.

This book belongs to Central Library BADJI Mokhtar-ANNABA UNIVERSITY
Copyright Elsevier 2024

Periodic boundary conditions can be applied at the nonwall faces, in a typical fashion. The no-slip velocity boundary condition at the walls can be simulated by a bounce-back scheme (Wolfram, 1986; Lavallée et al., 1991) with Ziegler's suggestion (Ziegler, 1993) of shifting the wall boundary into the fluid by one-half mesh unit to achieve second-order accurate results (Sukop and Thorne, 2006).

The method is centered on the evolution of the particle distribution function that is calculated in space and time (McNamara and Zanetti, 1988) as follows:

$$\underbrace{f_i(\vec{x}+\vec{e}_i\Delta t, t+\Delta t) = f_i(\vec{x},t)}_{STREAMING} + \underbrace{\Omega_i(\vec{x},t)}_{COLLISION} \pm \underbrace{ff_i}_{FORCING} \tag{23.2}$$

where $\vec{x}$ is the position vector, t is time, Δt is the time step, $\vec{e}$ is the unit velocity vector along direction i, Ω is the collision operator, ff is the forcing factor, and the subscript "i" is the lattice direction index, as described earlier. The terms on the right-hand side of Eq. (23.2) correspond to the three steps of the LBM algorithm. First is the streaming step, when the fluid flows from one node location to another along direction i, then is the collision step and finally the forcing step, representing body forces on the fluid. At time t, during the streaming step the rest component f_0 remains at the center of the face-centered cubic lattice, while the six Class I components (f_i, $i = 1,\ldots,6$) move at time $t+\Delta t$ to new positions at the nearest neighboring nodes, and the Class II components ($f_i = 7,\ldots,n-1$) move along the diagonals toward corners of the cubic lattice. To restore any fluid that distributes in solid matrix nodes as a result of streaming, the bounce back boundary conditions are then applied. In the next algorithmic step, the fluid relaxes to equilibrium by applying collision rules. The collision operator has been an issue of intense research, and several collision models are available. The most common is the approximation according to Bhatnagar, Gross, and Krook, which is known as the BGK approximation (Bhatnagar et al., 1954; Koelman, 1991). The BGK collision operator is given as follows:

$$\Omega_i(\vec{x},t) = -\frac{1}{\tau}(f_i - f_i^{eq}) \tag{23.3}$$

The time τ appearing in Eq. (23.3) is the time scale that is characteristic of the relaxation of the local particle distribution function toward equilibrium. The relaxation time is the parameter that incorporates the kinematic viscosity of the fluid to the computations as

$$\nu = \frac{1}{3}\left(\tau - \frac{1}{2}\right) \tag{23.4}$$

The equilibrium particle distribution, f^{eq}, is given by (Succi, 2001)

$$f_i^{eq}(\vec{x}) = w_i\rho(\vec{x})\left[1 + 3\frac{\vec{e}_i\cdot\vec{U}}{c^2} + 9\frac{(\vec{e}_i\cdot\vec{U})^2}{c^4} - \frac{3}{2}\frac{\vec{U}^2}{c^2}\right] \tag{23.5}$$

where $c = \Delta x/\Delta t$ is the lattice speed, Δx is the lattice constant, w is a lattice specific weighing factor, ρ is local density, and U is the macroscopic velocity. For a D3Q15 discretization, the weighting factors are $w_0 = 2/9$, $w_{1-6} = 1/9$, and $w_{7-14} = 1/72$ (Qian et al., 1992). For a D3Q19 discretization, the weighting factors are $w_0 = 1/3$, $w_{1-6} = 1/18$, and $w_{7-18} = 1/36$. The choice of the weighting factors is such that the macroscopic Navier−Stokes equations can be recovered. More details about the derivation of the equilibrium functions can be found in LBM textbooks and reviews (Succi, 2001; Sukop and Thorne, 2006).

During the last step of the algorithm (the forcing step), body forces acting on the fluid, such as electromagnetic forces, can be applied as well as the pressure drop across the domain. Pressure drop is specified by adding the forcing factor, ff, to the components of the fluid particle distribution function that move in the positive streamwise direction and by subtracting it from those moving in the opposite direction. The fraction of the forcing factor applied to each component of the particle probability function can be determined, for example as described in Noble et al. (1995).

At the end of the computational steps, the density of the fluid can be calculated, as given in Eq. (23.1). The macroscopic velocity of the fluid at each computational mesh point is calculated from the conservation of momentum equation, which is as follows:

$$\rho\vec{U} = \sum_{i=0}^{n} f_i\vec{e}_i \tag{23.6}$$

by dividing Eq. (23.6) by Eq. (23.1). Simulations can be carried out at steady state, or they can be dynamic.

This book belongs to Central Library BADJI Mokhtar-ANNABA UNIVERSITY
Copyright Elsevier 2024

23.2.2 Two-Phase Flow

Eq. (23.2) can be extended to apply for flow simulation of two immiscible fluids as first proposed by Gunstensen et al. (1991). In their model, Eq. (23.2) is solved twice, once for a "red" and once for a "blue" distribution, $f_i^{(r)}$ and $f_i^{(b)}$, representing two different fluids with an addition of a second collision operator as follows (Chen and Doolen, 1998; Connington and Lee, 2012):

$$f_i^k(\vec{x} + \vec{e}_i \Delta t, t + \Delta t) = f_i^k(\vec{x}, t) - \frac{1}{\tau^k}\left(f_i^k - f_i^{k-eq}\right) + \left(\Omega_i^k\right)^2(\vec{x}, t) + ff_i^k \tag{23.7}$$

In this formulation, the superscript k denotes red or blue fluid. The correlation between τ and μ (Eq. 23.4) enables the choice of μ^k by picking the desired τ^k. Similarly to the single-phase flow LBM, the mass for each phase and the total momentum at each grid node must be conserved (Grunau et al., 1993). In Eq. (23.7), the second collision operator, $\left(\Omega_i^k\right)^2$, accounts for perturbation at the interfaces and for surface tension (Gunstensen et al., 1991; Grunau et al., 1993):

$$\left(\Omega_i^k\right)^2 = \frac{A^k}{2}|F|\left[\frac{(e_i \cdot F)^2}{|F|^2} - \frac{1}{2}\right] \tag{23.8}$$

where A^k is a free parameter, determining the surface tension, and F is the local color gradient, correlated to the density difference at the interfaces as

$$F(x) = \sum_i e_i[\rho^r(x + e_i) - \rho^b(x + e_i)] \tag{23.9}$$

Note that F is zero inside a single-phase region of the incompressible fluid and is nonzero at the interfaces, where the density difference occurs. Thus, the second collision operator only contributes at the interfaces and vanishes elsewhere. To achieve phase segregation, a recoloring step is performed, during which colored particles at the interfaces are redistributed to force them to move toward the fluid with the same color. Physically, the recoloring step maximized $-j \cdot F$, which is the work done by the color gradient against the local color momentum, $j = \sum_i \left(f_i^r - f_i^b\right) e_i$ (Chen and Doolen, 1998; Liu et al., 2012). It has been noted that the recoloring step causes lattice pinning and makes this method computationally inefficient because of calculations of local maxima (Chen and Doolen, 1998; Gupta and Kumar, 2010). More crucially, the introduction of the second collision operation is known to induce unphysical vortices near interfaces.

Despite its drawbacks, the Gunstensen et al. model has been continuously adopted for bioengineering simulations. Hussein et al. (2008) employed the model to compute distributions of shear stresses (SS) and pressure on the active layer of cartilage cells under a two-phase flow, consisting of nutrition supply (liquid component) and oxygen supply (gas component) inside a bioreactor. Simulation results show an asymmetric pattern of the pressure distributions across the top surface of the cartilage cells, whereas those of the SS distributions are symmetric. However, the model in its original form fails to model noncoalescing, nonevaporating colloidal suspension systems, such as blood. To broaden its applicability, a number of works have been done to either modify or replace the perturbation term, activated at the interfaces. For example, Halliday et al. (1998) added a concentration factor to the perturbation step, while Lishchuk et al. (2003) introduced a direct forcing term as an alternative for the perturbation term at the interfaces. Such works enable a great capacity of modeling multiparticle colloidal systems, especially large mesoscale blood flow, mainly consisting of dense, deformable red blood cells (RBCs) and Newtonian plasma.

23.2.3 Parallelization Approach

Computationally, LBM is very attractive because of its effective and inherently parallelizable numerical algorithm. Here we offer an example of a parallelization approach to single-phase flow simulation (Voronov, 2010). The algorithm can be parallelized with Message Passing Interface (MPI). Each MPI process works on a chunk of the problem (data parallelism), while keeping a "ghost" copy of its nearest neighbor's boundaries for implementation of the boundary conditions. Traditionally, in parallel implementations of the LBM method, the MPI computational domain is decomposed using one of two ways: "slice, box, and cube" partitioning scheme or "recursive bisection" techniques, although other approaches such as the "cell-based" methods have been proposed (Wang et al., 2005). We have implemented an algorithm that allows for the program to choose between the slice (1D), the box (2D), and the cube (3D) partitioning scheme depending on the problem dimensions, such that the load balance is optimized by this choice. For isotropic geometries, such as tissue engineering scaffolds that have isotropic porosity in all three dimensions throughout the whole computational domain, this method is expected to achieve sufficient load balance.

This book belongs to Central Library BADJI Mokhtar-ANNABA UNIVERSITY
Copyright Elsevier 2024

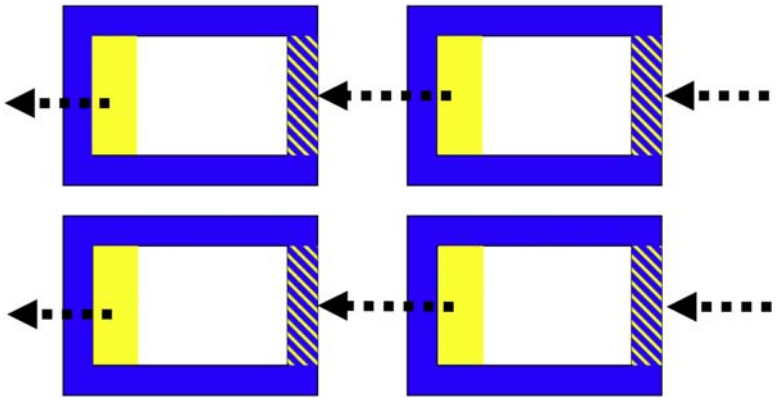

FIGURE 23.2 Example of Message Passing Interface (MPI) parallelization in 2D and four MPI processes. *Figure adapted from a dissertation by Voronov, R.S., 2010. Local Fluid Stress and Nutrient Transport Effects via Simulations of Perfusion through Bone Tissue Engineering Scaffolds (Doctor of Philosophy Ph.D. thesis). University of Oklahoma.*

Fig. 23.2 is an illustration of the "box" partitioning scheme as an example of MPI parallelization. Initially the problem is divided in four subdomains, each one to be solved by one of the four MPI processes. Each block in the figure represents the part of the 2D, XY domain assigned to each of the four MPI processes. The white part of the blocks indicates nodes of the computational mesh that are local and can be updated by the LBM calculation within the MPI process. The solid blue color (dark grey in print versions) indicated the part of the computational mesh that is on the boundary of each of the four subdomains—the values on these nodes cannot be updated without MPI communication between the subdomains. These are the "ghost" nodes that require information from their nearest neighbors, either on the horizontal or on the vertical direction. Yellow (light grey in print versions) and shaded colors show MPI communication taking place in the X direction (horizontal): shaded "ghost" cells are updated from right to left. The data for the computational mesh nodes that reside in the yellow area are passed to the subdomain neighbor to the left (as indicated by the black, *dashed arrows*). All the "ghost" nodes are then updated from left to right, such that all the blue "ghost" nodes become shades (i.e., updated with the most current values from the neighboring MPI process). After all the "ghost" nodes have been updated in the horizontal direction, the procedure is repeated in the vertical direction (up-down and down-up).

In Fig. 23.3 we plot the "speedup" of the LBM algorithm parallelized according to the strategy described here. Speedup refers to how much a parallel algorithm is faster than a corresponding nonparallel algorithm and is defined as

$$\text{Speedup}_P = \frac{\text{Non Parallel Execution Time}_1}{\text{Parallel Execution Time}_P} \text{ where } P \text{ is the number of processes} \tag{23.10}$$

Linear speedup occurs when the speedup increases linearly with the number of MPI processes, and when it occurs, we can conclude that the code is scalable. From Fig. 23.3 it is seen that the LBM code displays very good scalability at large

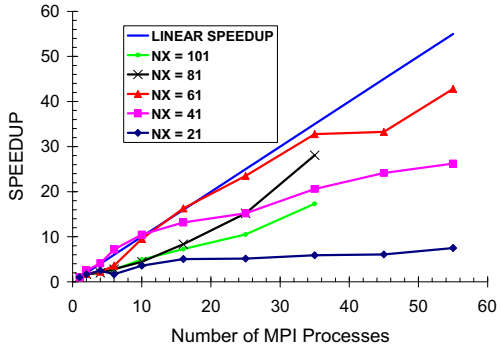

FIGURE 23.3 Speedup performance for lattice Boltzmann method code as a function of number of Message Passing Interface (MPI) processes for different simulation box sizes (NX is the number of nodes along one side of the cubic simulation domain), as measured on Lonestar supercomputer. The code was compiled with the Intel 9.1 compiler and -O3 -xT compiler optimization options. NX is the simulation box side size. *Figure adapted from a dissertation by Voronov, R.S., 2010. Local Fluid Stress and Nutrient Transport Effects via Simulations of Perfusion through Bone Tissue Engineering Scaffolds (Doctor of Philosophy Ph.D. thesis). University of Oklahoma.*

This book belongs to Central Library BADJI Mokhtar-ANNABA UNIVERSITY Copyright Elsevier 2024

problem sizes. This makes sense because the LBM algorithm is a memory-bound problem. Therefore, as the problem is broken up into smaller pieces along processes, the scalability improves. Of course as the number of processes becomes very large, it is expected that the communication time will dominate. However, for the number of processes tested in Fig. 23.3, this threshold was not reached. What this means is that the cost of parallelization is justified by the benefits that come from it, especially for large problem sizes. Fig. 23.4 is a typical flow chart for a single-phase flow LBM algorithm.

23.2.4 Mass and Heat Transport With Lagrangian Particle Tracking

In addition to flow simulation, biomechanical applications can involve the transport of substances and the transport of heat. For example, for the simulation of the behavior of a perfusion bioreactor for tissue growth, one needs to simulate not only the flow but also the transport of nutrients, oxygen, and the occurrence of chemical reactions. The problem becomes a multiphysics problem, where advection, diffusion, and (possibly) chemical reaction need to be simulated. However, the simulation of mass transfer with LBM is not as common as the simulation for flow.

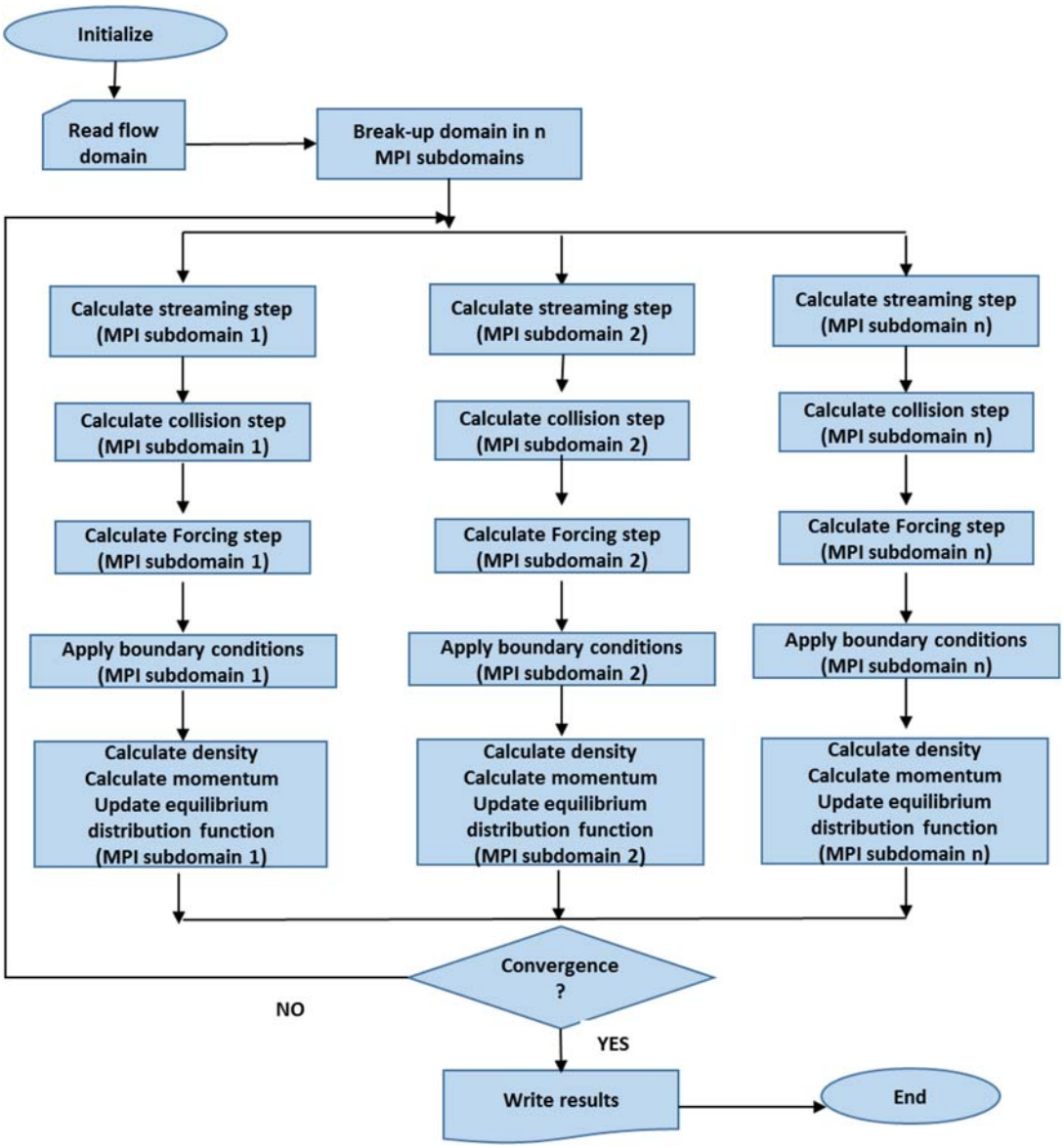

FIGURE 23.4 Flow chart for a typical lattice Boltzmann method algorithm for single-phase flow and Message Passing Interface (MPI).

This book belongs to Central Library BADJI Mokhtar-ANNABA UNIVERSITY
Copyright Elsevier 2024

Several methods exist for modeling scalar transport with LBM: for example a multicomponent LBM can be used, where the second component would represent a solute. For chemical reactions, where the reactions occur when the fluid interacts with the vessel walls, the LBM boundary conditions can be modified to account for the mass consumed by a heterogeneous reaction. The techniques for simulating heat or mass transfer with LBM are known as "thermal" LBM techniques (Chen and Doolen, 1998; Kang et al., 2007). They were initially developed for a narrow range of temperatures (Alexander et al., 1993; Shan, 1997). Later, models that introduced a separate internal energy distribution function to calculate the temperature field appeared in the literature (He et al., 1998; Tang et al., 2003). In general, thermal LBM models can be classified under two categories (see Jia et al., 2013; Liu et al., 2010): the multispeed methods and the passive scalar methods. Hybrid models have also been developed that can handle reaction−diffusion systems. Such models couple LBM-based algorithms to solvers for the discretized partial differential equations (Leemput et al., 2007).

A different approach is to simulate the transport of a scalar quantity with Lagrangian methods. Such techniques are known as Lagrangian scalar tracking (LST) techniques (Papavassiliou, 2006; Voronov et al., 2010c; Srinivasan and Papavassiliou, 2010), when a passive scalar (i.e., heat or mass dispersion that does not affect the flow field) is considered to be dispersed, or Lagrangian particle tracking (LPT) techniques when a particle representing mass is considered to be dispersed (Pham and Papavassiliou, 2017; Pham et al., 2014a) and the particle's presence might lead to modifications of the flow field. These techniques are based on the premise that one can place markers of heat or mass in the flow that move due to convection and diffusion. The presence of such markers at a location in the flow field is interpreted as temperature or concentration, depending on whether heat or mass transfer is considered. These markers are similar to fluid particles—they are larger than the molecular scale and the continuum assumption holds within them. Such techniques have been used in other situations (Verberg et al., 2006), for example dispersion in turbulent flow (Nguyen and Papavassiliou, 2016; Srinivasan and Papavassiliou, 2011, 2013; Mitrovic et al., 2004; Buaria et al., 2016; Bragg et al., 2016), for heat transfer calculations in nanocomposite materials (Duong et al., 2005, 2009b; Gong et al., 2014a), and for photothermal treatment of cancer cells (Duong et al., 2009a; Gong et al., 2014b). The equation of motion of a scalar marker in the flow field represents a convective step and a Brownian motion step, as follows:

$$\vec{X}_{t+\Delta t} = \vec{X}_t + \vec{U}_t \cdot \Delta t + \Delta \vec{X}_r \tag{23.11}$$

where $\vec{X}_t$ is the position of a marker at time t, Δt is the time step, $\vec{U}_t$ is the fluid velocity at location $\vec{X}_t$ at time t, and $\Delta \vec{X}_r$ is a random jump due to Brownian motion. Although a first-order forward difference scheme is employed in Eq. (23.7) for the convective motion step, one can employ any other higher order numerical scheme for the velocity integration.

The random motion due to molecular effects is calculated numerically by drawing a random number from a normal distribution that has a zero mean and a standard deviation that depends on the diffusivity of the scalar and the time step. This is based on Einstein's theory for Brownian motion. The standard deviation of the normally distributed motion in each one of the three Cartesian directions is given as

$$\sigma = \sqrt{2\Delta t D} \tag{23.12}$$

where D is the diffusivity of the scalar. The size of the Brownian random step is calculated for each space direction and for each marker after the convective step. As mentioned earlier, one can relate the presence of markers at a location in the flow field to concentration (Cermak, 1963; Hunt, 1985; Papavassiliou, 2002; Mitrovic and Papavassiliou, 2004). An advantage of this method is that a single flow field generated by the simulation of one flow realization can be used to simulate the scalar transport of a range of particles. This is achieved by changing the standard deviation of the Brownian motion to represent particles having a range of diffusivities (see Eq. 23.12), gaining in computational efficiency. Although the method converges as a half-order method (Succi, 2001), as expected by a particle method (Koumoutsakos, 2005), the efficiency of simulating multiple cases of particles with a single LBM flow simulation can overcome the delay in convergence. Furthermore, a second advantage of this method is that it can be used to simulate transport in a range of Schmidt numbers where thermal LBM cannot work. The Schmidt number is defined as $Sc = \nu/D$, where ν is the kinematic viscosity of the fluid. Thermal LBM techniques have inherent limitations to work for Sc on the order of 1, whereas the LST technique described herein can work for a very wide range of Sc. We have applied LST to cases of $0.1 \leq Sc \leq 50{,}000$. This is advantageous when the transport of oxygen in biological systems needs to be considered (for example, the Sc for oxygen diffusion in aqueous solutions is on the order of 382). The validation of the LST technique and guidelines for effective parallelization has been published elsewhere (Voronov et al., 2010c). It is worth noting here that the LST technique in conjunction with LBM have been implemented for cases of chemical reactions (Pham and Papavassiliou, 2017; Nguyen and Papavassiliou, 2008) and interactions of a diffusing substance with the vessel wall (Succi, 2001; Aidun and Clausen, 2010).

This book belongs to Central Library BADJI Mokhtar-ANNABA UNIVERSITY
Copyright Elsevier 2024

23.3 APPLICATION I—UNIVERSAL STRESS DISTRIBUTION AND CORRELATING FLOW FORCES TO SINGLE CELL BIOLOGY IN ENGINEERED BONE SCAFFOLD CULTURES

The use of scaffolds seeded with adult stem cells is often employed in tissue engineering applications to generate bone tissue for possible implantation. Seeding and culture can occur in a batch bioreactor or in a perfusion bioreactor. Based on observations about the growth of bone tissue inside the human body, it has been suggested that oscillatory flow of the culture media is beneficial to tissue growth (Tate et al., 1998; Burger and Klein-Nulend, 1999; Cowin, 1999). The flow of blood and the periodic application of stresses as a human moves and walks result in the development of a pressure gradient that creates fluid flow in the lacunocanalicular porous space of bones. This application of pressure and resulting stresses on the bone cells appears to stimulate the generation of bone matrix. The review of Allori et al. (2008) is quite informative for the details of the beneficial effects of mechanostimulation on the formation of bone. So far as tissue engineering applications, the use of a perfusion bioreactor to mimic the flow-induced stresses for bone tissue engineering can provide significant advantages for in vitro tissue growth (Sikavitsas et al., 2001, 2003; Holtorf et al., 2005). Because local shear forces on cells have been shown to promote osteoblastic differentiation, matrix deposition, and extracellular matrix mineralization, it would be very beneficial for the design of bioreactors to know a priori the level of stresses to be expected. One could not only design a bioreactor with controlled levels of stresses that optimize stem cell response but also avoid the case where excessive SS can result in the death of cells or their detachment from the scaffold and entrainment through the reactor (Porter et al., 2005; Cartmell et al., 2004; Alvarez-Barreto et al., 2007).

We used LBM to simulate the flow through different foamy poly-L-lactic acid (PLLA) scaffolds (Mikos et al., 1994) that were manufactured with different porosity and different pore-size distributions (Voronov et al., 2010a). The scaffold images were obtained with micro-computed tomography (μCT) techniques (see images on Fig. 23.5). After the calculation of the flow field in each of these scaffolds, the flow-induced stresses were calculated everywhere in the flow domain and on the fluid−solid interface. The stress distribution (seen on Fig. 23.6) was then constructed, and the average stresses were obtained as follows:

$$\overline{\tau}_B = (0.0851 \pm 0.0064)\left(\frac{\Delta P}{L}\right)^{0.503\pm0.015} U_s^{0.497\pm0.015} \text{ with an } R^2 = 0.997 \tag{23.13a}$$

$$\overline{\tau}_S = (0.096 \pm 0.003)\left(\frac{\Delta P}{L}\right)^{0.5} U_s^{0.5} \text{ with an } R^2 = 0.969 \tag{23.13b}$$

where $\overline{\tau}_B$ and $\overline{\tau}_S$ are the average bulk and surface stresses in Pa, respectively, $\Delta P/L$ is the pressure drop across a scaffold of length L in Pa/m, U_s is the superficial velocity of the fluid in m/s, and R^2 is the coefficient of determination for the equation fit. For high porosity (above 50%) the above equations work well. The utility of the two empirical equations above is now

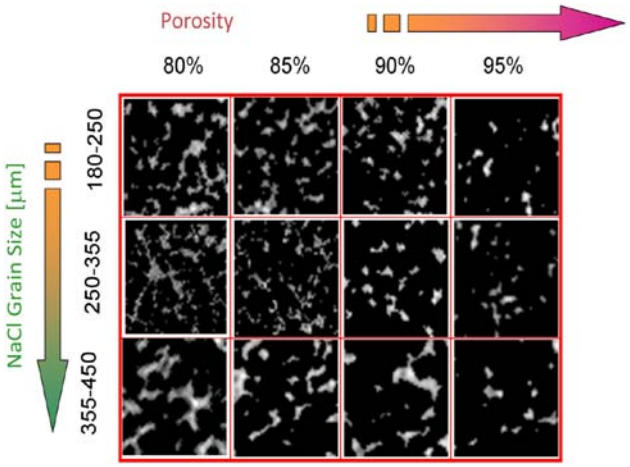

FIGURE 23.5 Images obtained with micro-computed tomography of poly-L-lactic acid (PLLA) scaffolds prepared by salt leeching (Hou et al., 2003). The grain size of the NaCl used in a mixture with the PLLA and was subsequently leached can be considered to represent the pore size. Grayscale intensity pixels represent the density of the scaffold material; black is space open to flow. Each image is a square with an edge equal to 2.142 mm, cut out from the middle of a scaffold. *Image reproduced from Voronov, R.S., VanGordon, S.B., Sikavitsas, V.I., Papavassiliou, D.V., 2010a. Computational modeling of flow-induced shear stresses within 3D salt-leached porous scaffolds imaged via micro-CT. Journal of Biomechanics 43(7), 1279−1286.*

This book belongs to Central Library BADJI Mokhtar-ANNABA UNIVERSITY
Copyright Elsevier 2024

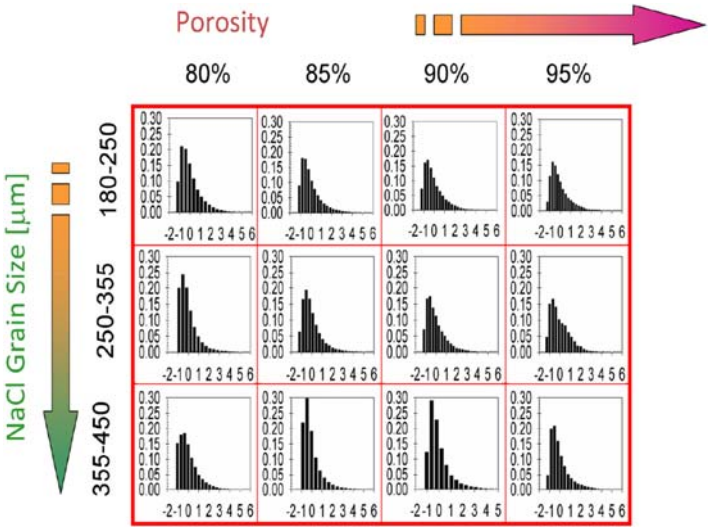

FIGURE 23.6 Comparison of histograms of surface stress distributions obtained from lattice Boltzmann method simulations for poly-L-lactic acid scaffolds that were prepared by salt leeching using various manufacturing parameters. Fig. 23.5 is a depiction of the scaffold structures at corresponding porosity and pore size distribution. The abscissa is the frequency of occurrence ranging from 0 to 0.3, and the ordinate is the normalized surface stress, as defined in Eq. (23.9), ranging from roughly −1 to 5. *The image is reproduced from Voronov, R.S., VanGordon, S.B., Sikavitsas, V.I., Papavassiliou, D.V., 2010a. Computational modeling of flow-induced shear stresses within 3D salt-leached porous scaffolds imaged via micro-CT. Journal of Biomechanics 43(7), 1279–1286.*

apparent. One can use them to estimate average values for the bulk stresses and for the flow-induced stresses on the solid–fluid interface within a scaffold—these would be the stresses that cells would be exposed on average during the culture period—as a function of two easily measured parameters: the superficial velocity and the pressure drop.

The LBM velocity field was used to obtain the flow-induced stress distributions following the Porter et al. scheme (2005). The fluid was assumed to be a Newtonian fluid and the stress tensor $\underline{\underline{\tau}}$ at each location in the flow field was found from the local velocity vector $\vec{U}$ as

$$\underline{\underline{\tau}} = \frac{1}{2}\mu\left(\nabla\vec{U} + \nabla\vec{U}^T\right) \tag{23.14}$$

where μ is the dynamic viscosity of the fluid. The flow-induced stresses were calculated as the largest eigenvalues of the stress tensor.

One can notice on Fig. (23.5) that the normalized distributions of the stresses are skewed to the right and the shape of the distributions looks to be similar. The stresses were normalized by subtracting the mean stress and dividing by the standard deviation, σ_τ, of the stress distribution, as follows:

$$\tau^* = \frac{(\tau - \overline{\tau})}{\sigma_\tau} \tag{23.15}$$

This is a dimensionless variable that is defined like the random variable for the standard normal distribution (in that case the mean is 0 and the standard deviation is 1). Further analysis and statistical testing of the LBM-obtained data lead to the realization that one, unique probability density function (pdf) can be used to describe the flow-induced stress distribution on the surface of a porous scaffold in a bioreactor (Voronov et al., 2010b). After testing 65 different pdf types, it was found that a single three-parameter gamma (gamma-3P) pdf exhibited the best statistical fit for all scaffolds tested. The gamma-3P pdf [usually designated as $\Gamma(\alpha, \gamma, \beta)$] is defined as

$$f(\tau_W^*) = \frac{(\tau_W^* - \gamma)^{\alpha-1}}{\beta^\alpha \Gamma(\alpha)} \exp\left[-(\tau_W^* - \gamma)/\beta\right] \tag{23.16}$$

where α is the shape parameter, β is the scale parameter, γ is the location parameter, and $\Gamma(\alpha)$ is a complete gamma function. In the case of $\gamma = 0$, the distribution becomes the standard gamma distribution $\Gamma(\alpha, 0, \beta)$, i.e., the two-parameter gamma distribution. The values of the parameters were found to be $\alpha = 2.91$, $\beta = 0.45$, and $\gamma = -1.43$. This finding indicated that one can predict analytically the stress distribution within highly porous scaffolds (porosity

This book belongs to Central Library BADJI Mokhtar-ANNABA UNIVERSITY
Copyright Elsevier 2024

above 80%) that are commonly used in bioreactors. The Γ(2.91, −1.43, 0.45) pdf fit within acceptable statistical accuracy data obtained by simulations and experiments by other investigators (Cioffi et al., 2008; Jia et al., 2009; Jungreuthmayer et al., 2008). The work of Jia et al. (2009) is of particular note because they used optical coherence tomography to measure the velocity within the porous scaffold. The three-point gamma distribution was found to describe the flow-induced wall stresses for structured scaffolds, such as those that can be manufactured with 3D printing techniques. Using CFD simulations based on finite volume techniques (not LBM), Pham et al. (2012) confirmed the ability of the Γ(2.91, −1.43, 0.45) pdf to fit the stress distribution in other scaffolds with lower porosity (as low as 50%). The distribution failed when the flow and the structural elements of the scaffold were oriented in the same direction—in that case the stress distribution was bimodal because there was one value of the SS on the sides of the scaffold elements (in the direction of the flow) and one value of stress for the normal stresses (as the fluid hits the scaffold elements that are perpendicular to the flow direction). Using LBM, as well as other CFD techniques, the calculation of the stress pdf is now common place in tissue engineering (Zermatten et al., 2014; Guyot et al., 2015; Campolo et al., 2013).

Regarding τ_B, the stress in the bulk space of tissue engineering porous scaffolds, the normalized stress distribution has been found to also follow a universal pdf (Pham et al., 2014b). A three-parameter log-normal distribution was found to be appropriate to describe the stress distribution in highly porous scaffold geometries. In this case, the appropriate distribution is log-normal(−2, 0.588, 0.4). The procedure to relate this distribution of a dimensionless stress to a distribution of dimensional stresses is described in detail in Pham et al. (2014b).

Most recently, we extended the image-based approach to scaffolds imaged using submicron resolution μCT and segmented using our "virtual histology" algorithm (Voronov et al., 2012). The latter allows telling apart cells, scaffold, soft tissue, and hard tissue without the use of any contrast agents. This opened the possibility for correlating the exact hydrodynamic environment established within the scaffold pores to patterns of tissue growth and cell behavior in complex media under flow (see Fig. 23.7) (Voronov et al., 2012).

23.4 APPLICATION II—DRUG AND AGONIST TRANSPORT WITHIN THROMBI IN VIVO

Achieving hemostasis following penetrating injuries is essential for the survival of organisms that possess a closed, high pressure circulatory system. However, pathological thrombosis and embolism can potentially lead to life-threatening

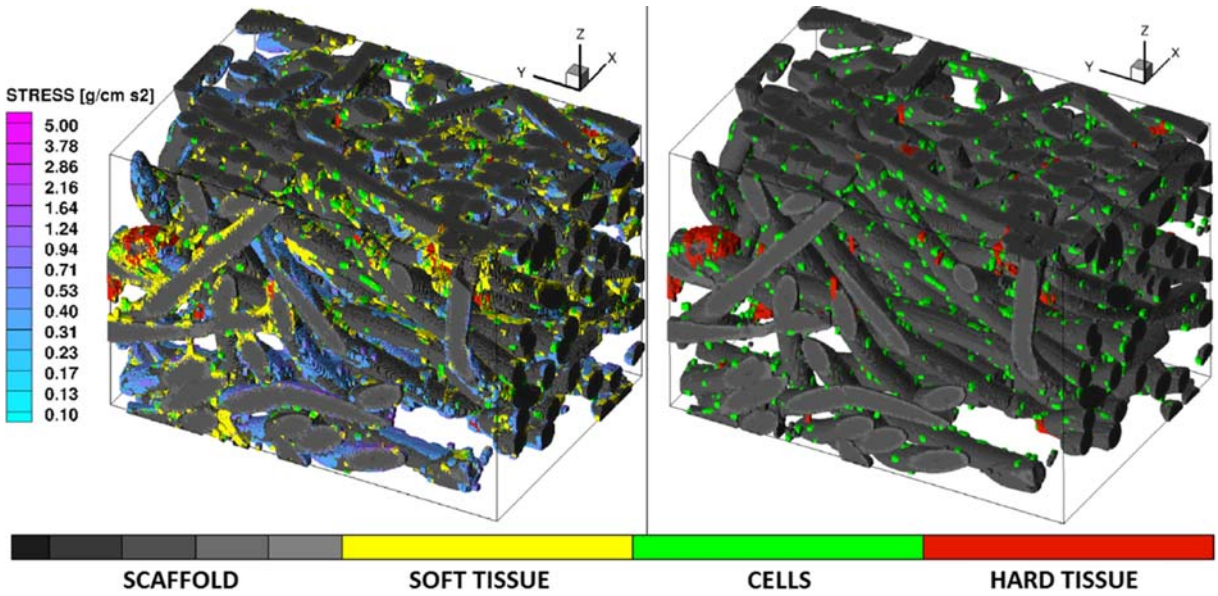

FIGURE 23.7 Scaffold modeled using lattice Boltzmann methods; Left: Calculated shear stresses (SS). Right: Soft tissue is subtracted using image processing. Images represent a 0.62 × 0.91 × 0.62 mm volume. In these images gray scale represents the poly-L-lactic acid fiber-mesh scaffold of 30 μm diameter, green (gray in print versions) color marks individual cells, yellow (white in print versions) is soft tissue, and red (dark gray in print versions) is calcification. The "cool" color map represents the fluid-induced surface SS for physiologically relevant stress levels of >0.1 g/cm s^2. *Image from Alam, T.A., Pham, Q.L., Sikavitsas, V.I., Papavassiliou, D.V., Shambaugh, R.L., Voronov, R.S., 2016. Image-based modeling: a novel tool for realistic simulations of artificial bone cultures. Technology 04(04), 229–233.*

This book belongs to Central Library BADJI Mokhtar-ANNABA UNIVERSITY
Copyright Elsevier 2024

complications when occurring in the heart (heart attack), brain (stroke), or lungs (DVT/PE). According to CDC, these kill ~1 million Americans every year, with diseases of the heart being the first leading cause of death in the United States and strokes the fourth. Conversely, deficiencies in the clotting mechanisms (hemophilia or due to drug interactions) result in bleeding risks that confront surgeons on a regular basis. Unfortunately, despite tremendous efforts by the medical research community (~$3 billion of annual expenditure on heart attack and brain stroke research), the problem, that essentially amounts to a clogged (or a leaky) "pipe," remains largely unsolved to this day. Therefore, insight into these processes would provide a greater understanding of thromboembolism and coagulopathy, as well as allow for better risk assessment and enhanced therapeutics.

Yet, a multitude of computational attempts (Xu et al., 2010, 2011, 2012; Sweet et al., 2011; Leiderman and Fogelson, 2011; Kamada et al., 2010; Basmadjian, 1990; Filipovic et al., 2008, 2007; Bedekar et al., 2005; Goodman et al., 2005) to model the thrombogenesis process have been unable to reproduce the heterogeneous thrombus architecture observed via advanced intravital microscopy (Stalker et al., 2013). The reason for this difficulty is the inherent complexity of the clot formation process: thrombogenesis is a combination of the coagulation cascade consisting of a multitude of chemical reactions coupled with intra- and intercell signaling, non-Newtonian fluid dynamics, and cell biomechanics. Therefore, instead of taking the conventional bottom-up approaches, we took the top-down route by imaging thrombi structures in vivo in mice and using their 3D reconstructions for the modeling (Voronov et al., 2013). Namely, we calculated the following: (1) the hydrodynamic environment experienced by the thrombi as they grow in the vasculature. This is important because platelet activation (an integral part of thrombogenesis) has been shown to be affected by the fluid-induced SS in the lumen (see Fig. 23.8, left); (2) thrombus permeability is a key parameter for drug delivery applications (see Fig. 23.8, center); and (3) mass transport of various-sized physiologically relevant molecules to/from the injury site beneath the thrombus (see Fig. 23.8, right), as this is the representative of antithrombotic drugs/platelet agonists traversing their way through the porous clot structure, respectively. (1) and (2) were solved via LBM, whereas (3) was calculated using LST.

Serendipitously, the LBM/LST results, like in Fig. 23.8 (right), offered a potential explanation for the existence of a compact "core" within the thrombus. Specifically, the models showed that the agonists emanating from the injury site are readily removed from the thrombus by the blood flow around it. Therefore, they have no chance to reach, and subsequently to "activate," the platelets on the periphery (in the region termed as the looser "shell" of the clot). Our study was the first of its kind because it reported values calculated based on realistic thrombi structures imaged in live animals.

23.5 DISCUSSION AND CONCLUSIONS

Recent advances in simulations and imaging of biological systems have resulted in the increasing use of LBMs as a tool of choice for the simulation of biological flows in complicated geometries. Reviews of the LBM have been offered in the literature (Chen and Doolen, 1998; Succi, 2001; Aidun and Clausen, 2010). Although other application areas have been the main drivers for the development of LBM, bioengineering applications are catching up because of both the advantages of

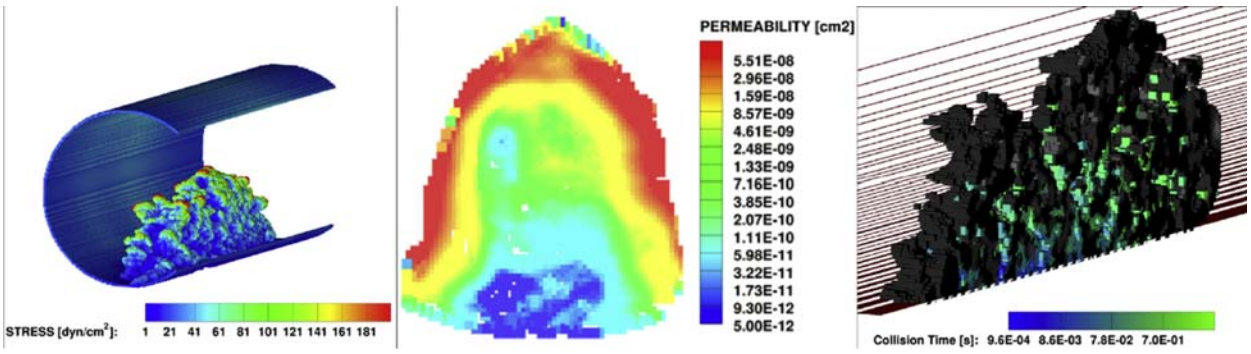

FIGURE 23.8 Left: Maximum viscous fluid surface stresses experiences by the thrombus within microvasculature calculated from lattice Boltzmann method (LBM). Center: Thrombus permeability calculated based on LBM results and averaged over the length of the thrombus in the flow direction (perpendicular to the image). Right: A map of average collision time for intrathrombus diffusive transport of adenosine diphosphate−sized tracers released from the injury site below the thrombus. Gray scale means that no collisions occurred at those particular locations. The simulation domain is cut into half along the flow direction to show the intrathrombus environment. The cut plane faces the reader, whereas the second half of the thrombus is omitted for clarity. *Images from Voronov, R.S., Stalker, T.J., Brass, L.F., Diamond, S.L., 2013. Simulation of intrathrombus fluid and solute transport using in vivo clot structures with single platelet resolution. Annals of Biomedical Engineering 41(6), 1297−1307.*

This book belongs to Central Library BADJI Mokhtar-ANNABA UNIVERSITY Copyright Elsevier 2024

LBM and the development of hybrid techniques that can connect LBM to other computational methodologies such as FSIs and LPT. Findings from our work have indicated that there are common probability functions that can describe analytically the distribution of stresses in tissue engineering bioreactors. Such understanding can be important for reactor design and for the directed manufacturing of tissue engineering scaffolds that can be used to seed stem cells in a way that optimizes the efficiency of cell differentiation and growth. In addition, it is important to explore the transient distribution of stresses, as cells grow and proliferate over time. The growth of the cell layer is expected to reduce the pore space of the cell-seeded scaffolds, leading to the increase of pore velocity and an increase of the values of the stresses. Such nonuniform layers can be generated by numerically seeding the cells on the surface of scaffold structures (Jungreuthmayer et al., 2009; McCoy et al., 2012). For simplicity, however, the assumption that there exists a uniform layer of cells covering the scaffold structures is also common (Lesman et al., 2010; Pham et al., 2012). Other bioengineering applications, such as the simulation of blood as a non-Newtonian fluid during the pulsatile cardiac cycle and through flexible vasculature, are good candidates for LBM computations. LBM can also be used for the simulation of thrombus formation (Voronov et al., 2013) and the simulation of flow effects and stresses that can lead to the lysis of RBCs and platelets.

ACKNOWLEDGMENTS

Parts of this work were supported by the National Science Foundation (NSF) under grant CBET-070081. Computations were carried out at the OU Supercomputing Center for Education & Research (OSCER) and at the Texas Advanced Computing Center under XSEDE allocation TG-CTS-090025.

REFERENCES

Aidun, C.K., Clausen, J.R., 2010. Lattice-Boltzmann method for complex flows. Annual Review of Fluid Mechanics 42 (1), 439–472.

Alam, T.A., Pham, Q.L., Sikavitsas, V.I., Papavassiliou, D.V., Shambaugh, R.L., Voronov, R.S., 2016. Image-based modeling: a novel tool for realistic simulations of artificial bone cultures. Technology 04 (04), 229–233.

Alexander, F.J., Chen, S., Sterling, J.D., 1993. Lattice Boltzmann thermohydrodynamics. Physical Review E 47 (4), R2249–R2252.

Allori, A.C., Sailon, A.M., Pan, J.H., Warren, S.M., 2008. Biological basis of bone formation, remodeling, and repair—part III: biomechanical forces. Tissue Engineering B: Reviews 14 (3), 285–293.

Alvarez-Barreto, J.F., Linehan, S.M., Shambaugh, R.L., Sikavitsas, V.I., 2007. Flow perfusion improves seeding of tissue engineering scaffolds with different architectures. Annals of Biomedical Engineering 35 (3), 429–442.

Apostolidis, A.J., Beris, A.N., 2014. Modeling of the blood rheology in steady-state shear flows. Journal of Rheology 58 (3), 607–633.

Appel, A.A., Anastasio, M.A., Larson, J.C., Brey, E.M., 2013. Imaging challenges in biomaterials and tissue engineering. Biomaterials 34 (28), 6615–6630.

Basmadjian, D., 1990. The effect of flow and mass transport in thrombogenesis. Annals of Biomedical Engineering 18 (6), 685–709.

Bedekar, A.S., Pant, K., Ventikos, Y., Sundaram, S., 2005. A computational model combining vascular biology and haemodynamics for thrombosis prediction in anatomically accurate cerebral aneurysms. Food and Bioproducts Processing 83 (C2), 118–126.

Bhatnagar, P.L., Gross, E.P., Krook, M., 1954. A model for collision processes in gases. I. Small amplitude processes in charged and neutral one-component systems. Physical Review 94 (3), 511–525.

Boyd, J., Buick, J., Green, S., 2006. A second-order accurate lattice Boltzmann non-Newtonian flow model. Journal of Physics A: Mathematical and General 39 (46), 14241.

Bragg, A.D., Ireland, P.J., Collins, L.R., 2016. Forward and backward in time dispersion of fluid and inertial particles in isotropic turbulence. Physics of Fluids 28 (1), 013305.

Buaria, D., Yeung, P.K., Sawford, B.L., 2016. A Lagrangian study of turbulent mixing: forward and backward dispersion of molecular trajectories in isotropic turbulence. Journal of Fluid Mechanics 799, 352–382.

Burger, E.H., Klein-Nulend, J., 1999. Mechanotransduction in bone—role of the lacuno-canalicular network. The FASEB Journal 13 (9001), 101–112.

Buxton, G.A., Care, C.M., Cleaver, D.J., 2001. A lattice spring model of heterogeneous materials with plasticity. Modelling and Simulation in Materials Science and Engineering 9 (6), 485.

Buxton, G.A., Verberg, R., Jasnow, D., Balazs, A.C., 2005. Newtonian fluid meets an elastic solid: coupling lattice Boltzmann and lattice-spring models. Physical Review E 71 (5), 056707.

Campolo, M., Curcio, F., Soldati, A., 2013. Minimal perfusion flow for osteogenic growth of mesenchymal stem cells on lattice scaffolds. AIChE Journal 59 (8), 3131–3144.

Cartmell, S.H., Porter, B.D., García, A.J., Guldberg, R.E., 2004. Effects of medium perfusion rate on cell-seeded three-dimensional bone constructs in vitro. Tissue Engineering 9 (6), 1197–1203.

Cermak, J.E., 1963. Lagrangian similarity hypothesis applied to diffusion in turbulent shear flow. Journal of Fluid Mechanics 15 (1), 49–64.

Chen, S., Doolen, G.D., 1998. Lattice Boltzmann method for fluid flows. Annual Review of Fluid Mechanics 30, 329–364.

Cioffi, M., Küffer, J., Ströbel, S., Dubini, G., Martin, I., Wendt, D., 2008. Computational evaluation of oxygen and shear stress distributions in 3D perfusion culture systems: macro-scale and micro-structured models. Journal of Biomechanics 41 (14), 2918–2925.

This book belongs to Central Library BADJI Mokhtar-ANNABA UNIVERSITY Copyright Elsevier 2024

Connington, K., Lee, T., 2012. A review of spurious currents in the lattice Boltzmann method for multiphase flows. Journal of Mechanical Science and Technology 26 (12), 3857–3863.

Cosgrove, J.A., Buick, J.M., Tonge, S.J., Munro, C.G., Greated, C.A., Campbell, D.M., 2003. Application of the lattice Boltzmann method to transition in oscillatory channel flow. Journal of Physics A: Mathematical and General 36 (10), 2609.

Cowin, S.C., 1999. Bone poroelasticity. Journal of Biomechanics 32 (3), 217–238.

Duong, H.M., Papavassiliou, D.V., Lee, L.L., Mullen, K.J., 2005. Random walks in nanotube composites: improved algorithms and the role of thermal boundary resistance. Applied Physics Letters 87 (1), 013101.

Duong, H.M., Papavassiliou, D.V., Mullen, K.J., Wardle, B.L., Maruyama, S., 2009a. A numerical study on the effective thermal conductivity of biological fluids containing single-walled carbon nanotubes. International Journal of Heat and Mass Transfer 52 (23–24), 5591–5597.

Duong, H.M., Yamamoto, N., Papavassiliou, D.V., Maruyama, S., Wardle, B.L., 2009b. Inter-carbon nanotube contact in thermal transport of controlled-morphology polymer nanocomposites. Nanotechnology 20 (15), 155702.

Filipovic, N., Kojic, M., Tsuda, A., 2007. A multiscale modeling of thrombosis using coupling of dissipative particle dynamics with continuum finite element method. International Journal of Artificial Organs 30 (8), 709.

Filipovic, N., Kojic, M., Tsuda, A., 2008. Modelling thrombosis using dissipative particle dynamics method. Philosophical Transactions of the Royal Society A-Mathematical Physical and Engineering Sciences 366 (1879), 3265–3279.

Gabbanelli, S., Drazer, G., Koplik, J., 2005. Lattice Boltzmann method for non-Newtonian (power-law) fluids. Physical Review E 72 (4), 046312.

Gong, F., Bui, K., Papavassiliou, D.V., Duong, H.M., 2014a. Thermal transport phenomena and limitations in heterogeneous polymer composites containing carbon nanotubes and inorganic nanoparticles. Carbon 78, 305–316.

Gong, F., Hongyan, Z., Papavassiliou, D.V., Bui, K., Lim, C., Duong, H.M., 2014b. Mesoscopic modeling of cancer photothermal therapy using single-walled carbon nanotubes and near infrared radiation: insights through an off-lattice Monte Carlo approach. Nanotechnology 25 (20), 205101.

Goodman, P.D., Barlow, E.T., Crapo, P.M., Mohammad, S.F., Solen, K.A., 2005. Computational model of device-induced thrombosis and thromboembolism. Annals of Biomedical Engineering 33 (6), 780–797.

Grunau, D., Chen, S., Eggert, K., 1993. A lattice Boltzmann model for multiphase fluid flows. Physics of Fluids A 5 (10), 2557–2562.

Gunstensen, A.K., Rothman, D.H., Zaleski, S., Zanetti, G., 1991. Lattice Boltzmann model of immiscible fluids. Physical Review A 43 (8), 4320–4327.

Gupta, A., Kumar, R., 2010. Effect of geometry on droplet formation in the squeezing regime in a microfluidic T-junction. Microfluidics and Nanofluidics 8 (6), 799–812.

Guyot, Y., Luyten, F.P., Schrooten, J., Papantoniou, I., Geris, L., 2015. A three-dimensional computational fluid dynamics model of shear stress distribution during neotissue growth in a perfusion bioreactor. Biotechnology and Bioengineering 112 (12), 2591–2600.

Halliday, I., Thompson, S.P., Care, C.M., 1998. Macroscopic surface tension in a lattice Bhatnagar-Gross-Krook model of two immiscible fluids. Physical Review E 57 (1), 514–523.

He, X., Chen, S., Doolen, G.D., 1998. A novel thermal model for the lattice Boltzmann method in incompressible limit. Journal of Computational Physics 146 (1), 282–300.

Holtorf, H.L., Jansen, J.A., Mikos, A.G., 2005. Flow perfusion culture induces the osteoblastic differentiation of marrow stromal cell-scaffold constructs in the absence of dexamethasone. Journal of Biomedical Materials Research, Part A 72A (3), 326–334.

Hou, Q., Grijpma, D.W., Feijen, J., 2003. Porous polymeric structures for tissue engineering prepared by a coagulation, compression moulding and salt leaching technique. Biomaterials 24 (11), 1937–1947.

Hunt, J.C.R., 1985. Turbulent diffusion from sources in complex flows. Annual Review of Fluid Mechanics 17 (1), 447–485.

Hussein, M.A., Esterl, S., Pörtner, R., Wiegandt, K., Becker, T., 2008. On the lattice Boltzmann method simulation of a two-phase flow bioreactor for artificially grown cartilage cells. Journal of Biomechanics 41 (16), 3455–3461.

Jia, X., McLaughlin, J.B., Derksen, J., Ahmadi, G., 2013. Simulation of a mannequin's thermal plume in a small room. Computers and Mathematics with Applications 65 (2), 287–295.

Jia, Y., Bagnaninchi, P.O., Yang, Y., Haj, A.E., Hinds, M.T., Kirkpatrick, S.J., Wang, R.K., 2009. Doppler optical coherence tomography imaging of local fluid flow and shear stress within microporous scaffolds. Journal of Biomedical Optics 14 (3), 034014.

Jungreuthmayer, C., Donahue, S.W., Jaasma, M.J., Al-Munajjed, A.A., Zanghellini, J., Kelly, D.J., O'Brien, F.J., 2008. A comparative study of shear stresses in collagen-glycosaminoglycan and calcium phosphate scaffolds in bone tissue-engineering bioreactors. Tissue Engineering Part A 15 (5), 1141–1149.

Jungreuthmayer, C., Jaasma, M.J., Al-Munajjed, A.A., Zanghellini, J., Kelly, D.J., O'Brien, F.J., 2009. Deformation simulation of cells seeded on a collagen-GAG scaffold in a flow perfusion bioreactor using a sequential 3D CFD-elastostatics model. Medical Engineering and Physics 31 (4), 420–427.

Kamada, H., Tsubota, K., Nakamura, M., Wada, S., Ishikawa, T., Yamaguchi, T., 2010. A three-dimensional particle simulation of the formation and collapse of a primary thrombus. International Journal for Numerical Methods in Biomedical Engineering 26 (3–4), 488–500.

Kang, Q., Lichtner, P.C., Zhang, D., 2007. An improved lattice Boltzmann model for multicomponent reactive transport in porous media at the pore scale. Water Resources Research 43 (12), W12S14.

Koelman, J.M.V.A., 1991. A simple lattice Boltzmann scheme for Navier-Stokes fluid flow. Europhysics Letters 15 (6), 603.

Kolmakov, G.V., Revanur, R., Tangirala, R., Emrick, T., Russell, T.P., Crosby, A.J., Balazs, A.C., 2010. Using nanoparticle-filled microcapsules for site-specific healing of damaged substrates: creating a "repair-and-go" system. ACS Nano 4 (2), 1115–1123.

Koumoutsakos, P., 2005. Multiscale flow simulations using particles. Annual Review of Fluid Mechanics 37 (1), 457–487.

Kwon, Y.W., 2006. Development of coupling technique for LBM and FEM for FSI application. Engineering Computations 23 (8), 860–875.

Lallemand, P., Luo, L.-S., 2000. Theory of the lattice Boltzmann method: dispersion, dissipation, isotropy, Galilean invariance, and stability. Physical Review E 61 (6), 6546–6562.

This book belongs to Central Library BADJI Mokhtar-ANNABA UNIVERSITY Copyright Elsevier 2024

Lavallée, P., Boon, J.P., Noullez, A., 1991. Boundaries in lattice gas flows. Physica D: Nonlinear Phenomena 47 (1), 233−240.

Ledesma-Aguilar, R., Vella, D., Yeomans, J.M., 2014. Lattice-Boltzmann simulations of droplet evaporation. Soft Matter 10 (41), 8267−8275.

Leemput, P.V., Vandekerckhove, C., Vanroose, W., Roose, D., 2007. Accuracy of hybrid lattice Boltzmann/finite difference schemes for reaction-diffusion systems. Multiscale Modeling and Simulation 6 (3), 838−857.

Leiderman, K., Fogelson, A.L., 2011. Grow with the flow: a spatial-temporal model of platelet deposition and blood coagulation under flow. Mathematical Medicine and Biology-A Journal of the IMA 28 (1), 47−84.

Lesman, A., Blinder, Y., Levenberg, S., 2010. Modeling of flow-induced shear stress applied on 3D cellular scaffolds: implications for vascular tissue engineering. Biotechnology and Bioengineering 105 (3), 645−654.

Lishchuk, S.V., Care, C.M., Halliday, I., 2003. Lattice Boltzmann algorithm for surface tension with greatly reduced microcurrents. Physical Review E 67 (3), 036701.

Liu, C.-H., Lin, K.-H., Mai, H.-C., Lin, C.-A., 2010. Thermal boundary conditions for thermal lattice Boltzmann simulations. Computers and Mathematics with Applications 59 (7), 2178−2193.

Liu, H., Valocchi, A.J., Kang, Q., 2012. Three-dimensional lattice Boltzmann model for immiscible two-phase flow simulations. Physical Review E 85 (4), 046309.

McCoy, R.J., Jungreuthmayer, C., O'Brien, F.J., 2012. Influence of flow rate and scaffold pore size on cell behavior during mechanical stimulation in a flow perfusion bioreactor. Biotechnology and Bioengineering 109 (6), 1583−1594.

McNamara, G.R., Zanetti, G., 1988. Use of the Boltzmann-equation to simulate lattice-gas automata. Physical Review Letters 61 (20), 2332−2335.

Mikos, A.G., Thorsen, A.J., Czerwonka, L.A., Bao, Y., Langer, R., Winslow, D.N., Vacanti, J.P., 1994. Preparation and characterization of poly(L-lactic acid) foams. Polymer 35 (5), 1068−1077.

Mitrovic, B.M., Le, P.M., Papavassiliou, D.V., 2004. On the Prandtl or Schmidt number dependence of the turbulent heat or mass transfer coefficient. Chemical Engineering Science 59 (3), 543−555.

Mitrovic, B.M., Papavassiliou, D.V., 2004. Effects of a first-order chemical reaction on turbulent mass transfer. International Journal of Heat and Mass Transfer 47 (1), 43−61.

Nguyen, K.T., Papavassiliou, D.V., 2008. Effects of a reacting channel wall on turbulent mass transfer. International Journal of Heat and Mass Transfer 51 (11−12), 2940−2949.

Nguyen, Q., Papavassiliou, D.V., 2016. A statistical model to predict streamwise turbulent dispersion from the wall at small times. Physics of Fluids 28 (12), 125103.

Noble, D.R., Chen, S., Georgiadis, J.G., Buckius, R.O., 1995. A consistent hydrodynamic boundary condition for the lattice Boltzmann method. Physics of Fluids 7 (1), 203−209.

Papavassiliou, D.V., 2002. Turbulent transport from continuous sources at the wall of a channel. International Journal of Heat and Mass Transfer 45 (17), 3571−3583.

Papavassiliou, D.V., 2006. Understanding macroscopic heat/mass transfer using meso- and macro-scale simulations. In: Gorban, A.N., Kevrekidis, I.G., Theodoropoulos, C., Kazantzis, N.K., Öttinger, H.C. (Eds.), Model Reduction and Coarse-Graining Approaches for Multiscale Phenomena. Springer, Berlin, Heidelberg.

Pham, N.H., Papavassiliou, D.V., 2017. Nanoparticle transport in heterogeneous porous media with particle tracking numerical methods. Computational Particle Mechanics 4 (1), 87−100.

Pham, N.H., Swatske, D.P., Harwell, J.H., Shiau, B.-J., Papavassiliou, D.V., 2014a. Transport of nanoparticles and kinetics in packed beds: a numerical approach with lattice Boltzmann simulations and particle tracking. International Journal of Heat and Mass Transfer 72, 319−328.

Pham, N.H., Voronov, R.S., Tummala, N.R., Papavassiliou, D.V., 2014b. Bulk stress distributions in the pore space of sphere-packed beds under Darcy flow conditions. Physical Review E 89 (3), 033016.

Pham, N.H., Voronov, R.S., VanGordon, S.B., Sikavitsas, V.I., Papavassiliou, D.V., 2012. Predicting the stress distribution within scaffolds with ordered architecture. Biorheology 49 (4), 235−247.

Porter, B., Zauel, R., Stockman, H., Guldberg, R., Fyhrie, D., 2005. 3-D computational modeling of media flow through scaffolds in a perfusion bioreactor. Journal of Biomechanics 38 (3), 543−549.

Qian, Y.H., D'Humières, D., Lallemand, P., 1992. Lattice BGK models for Navier-Stokes equation. Europhysics Letters 17 (6), 479−484.

Shan, X., 1997. Simulation of Rayleigh-Bénard convection using a lattice Boltzmann method. Physical Review E 55 (3), 2780−2788.

Sikavitsas, V.I., Bancroft, G.N., Holtorf, H.L., Jansen, J.A., Mikos, A.G., 2003. Mineralized matrix deposition by marrow stromal osteoblasts in 3D perfusion culture increases with increasing fluid shear forces. Proceedings of the National Academy of Sciences 100 (25), 14683−14688.

Sikavitsas, V.I., Temenoff, J.S., Mikos, A.G., 2001. Biomaterials and bone mechanotransduction. Biomaterials 22 (19), 2581−2593.

Srinivasan, C., Papavassiliou, D.V., 2010. Backwards and forwards dispersion of a scalar in turbulent wall flows. International Journal of Heat and Mass Transfer 53 (5−6), 1023−1035.

Srinivasan, C., Papavassiliou, D.V., 2011. Prediction of the turbulent Prandtl number in wall flows with Lagrangian simulations. Industrial and Engineering Chemistry Research 50 (15), 8881−8891.

Srinivasan, C., Papavassiliou, D.V., 2013. Heat transfer scaling close to the wall for turbulent channel flows. Applied Mechanics Reviews 65 (3), 031002−031002-20.

Stalker, T.J., Traxler, E.A., Wu, J., Wannemacher, K.M., Cermignano, S.L., Voronov, R., Diamond, S.L., Brass, L.F., 2013. Hierarchical organization in the hemostatic response and its relationship to the platelet-signaling network. Blood 121 (10), 1875−1885.

Succi, S., 2001. The Lattice Boltzmann Equation for Fluid Dynamic and beyond. Oxford University Press, New York.

This book belongs to Central Library BADJI Mokhtar-ANNABA UNIVERSITY

Copyright Elsevier 2024

Sukop, M.C., Thorne, D.T., 2006. Lattice Boltzmann Modeling: An Introduction for Geoscientists and Engineers. Springer, NewYork.

Sweet, C.R., Chatterjee, S., Xu, Z.L., Bisordi, K., Rosen, E.D., Alber, M., 2011. Modelling platelet-blood flow interaction using the subcellular element Langevin method. Journal of the Royal Society Interface 8 (65), 1760−1771.

Swift, M.R., Orlandini, E., Osborn, W.R., Yeomans, J.M., 1996. Lattice Boltzmann simulations of liquid-gas and binary fluid systems. Physical Review E 54 (5), 5041−5052.

Tang, G.H., Tao, W.Q., He, Y.L., 2003. Simulation of fluid flow and heat transfer in a plane channel using the lattice Boltzmann method. International Journal of Modern Physics B 17 (01n02), 183−187.

Tate, M.L.K., Knothe, U., Niederer, P., 1998. Experimental elucidation of mechanical load-induced fluid flow and its potential role in bone metabolism and functional adaptation. The American Journal of the Medical Sciences 316 (3), 189−195.

Verberg, R., Alexeev, A., Balazs, A.C., 2006. Modeling the release of nanoparticles from mobile microcapsules. The Journal of Chemical Physics 125 (22), 224712.

Voronov, R.S., 2010. Local Fluid Stress and Nutrient Transport Effects via Simulations of Perfusion through Bone Tissue Engineering Scaffolds (Doctor of Philosophy Ph.D. thesis). University of Oklahoma.

Voronov, R.S., Stalker, T.J., Brass, L.F., Diamond, S.L., 2013. Simulation of intrathrombus fluid and solute transport using in vivo clot structures with single platelet resolution. Annals of Biomedical Engineering 41 (6), 1297−1307.

Voronov, R.S., VanGordon, S.B., Shambaugh, R.L., Papavassiliou, D.V., Sikavitsas, V.I., 2012. 3D tissue-engineered construct analysis via conventional high-resolution microcomputed tomography without X-ray contrast. Tissue Engineering C: Methods 19 (5), 327−335.

Voronov, R.S., VanGordon, S.B., Sikavitsas, V.I., Papavassiliou, D.V., 2010a. Computational modeling of flow-induced shear stresses within 3D salt-leached porouss scaffolds imaged via micro-CT. Journal of Biomechanics 43 (7), 1279−1286.

Voronov, R.S., VanGordon, S.B., Sikavitsas, V.I., Papavassiliou, D.V., 2010b. Distribution of flow-induced stresses in highly porous media. Applied Physics Letters 97 (2), 024101.

Voronov, R.S., VanGordon, S.B., Sikavitsas, V.I., Papavassiliou, D.V., 2010c. Efficient Lagrangian scalar tracking method for reactive local mass transport simulation through porous media. International Journal for Numerical Methods in Fluids 67 (4), 501−517.

Wang, J., Zhang, X., Bengough, A.G., Crawford, J.W., 2005. Domain-decomposition method for parallel lattice Boltzmann simulation of incompressible flow in porous media. Physical Review E 72 (1), 016706.

Wolfram, S., 1986. Cellular automaton fluids 1: basic theory. Journal of Statistical Physics 45 (3), 471−526.

Xu, Z., Kamocka, M., Alber, M., Rosen, E.D., 2011. Computational approaches to studying thrombus development. Arteriosclerosis, Thrombosis, and Vascular Biology 31 (3), 500−505.

Xu, Z., Lioi, J., Mu, J., Kamocka, M.M., Liu, X., Chen, D.Z., Rosen, E.D., Alber, M., 2010. A multiscale model of venous thrombus formation with surface-mediated control of blood coagulation cascade. Biophysical Journal 98 (9), 1723−1732.

Xu, Z.L., Christley, S., Lioi, J., Kim, O., Harvey, C., Sun, W.Z., Rosen, E.D., Alber, M., 2012. Multiscale model of fibrin accumulation on the blood clot surface and platelet dynamics. Computational Methods in Cell Biology 110, 367−388.

Yoshino, M., Hotta, Y., Hirozane, T., Endo, M., 2007. A numerical method for incompressible non-Newtonian fluid flows based on the lattice Boltzmann method. Journal of Non-Newtonian Fluid Mechanics 147 (1−2), 69−78.

Zermatten, E., Vetsch, J.R., Ruffoni, D., Hofmann, S., Müller, R., Steinfeld, A., 2014. Micro-computed tomography based computational fluid dynamics for the determination of shear stresses in scaffolds within a perfusion bioreactor. Annals of Biomedical Engineering 42 (5), 1085−1094.

Ziegler, D.P., 1993. Boundary conditions for lattice Boltzmann simulations. Journal of Statistical Physics 71 (5), 1171−1177.

This book belongs to Central Library BADJI Mokhtar-ANNABA UNIVERSITY

Copyright Elsevier 2024

This page intentionally left blank

This book belongs to Central Library BADJI Mokhtar-ANNABA UNIVERSITY

Copyright Elsevier 2024

Index

'*Note*: Page numbers followed by "f" indicate figures, "t" indicate figures and "b" indicate boxes.'

A

ABAQUS, 30–31, 45, 191
ABMs. *See* Agent-based models (ABMs)
Activated receptor, 242
Active cell
  migration, 179
  motility, 179
"Adaptive elasticity" model, 303
ADC. *See* Apparent diffusion coefficient (ADC)
Adhesion forces, 258–259
Adipocytes, 173–174, 177–179, 183f
Adventitia, 290–291
AF. *See* Amniotic fluid (AF)
AFM. *See* Atomic force microscopy (AFM)
Agent
  abstract description, 271–272
  attribute variables, 287
  cells as, 240
  population, shape, and size, 286
Agent-based models (ABMs), 223, 239–240, 241f, 254, 271, 283–284, 286–290, 286f
  of artery wall, 286–290
  cells as agents, 240
  conjugate gradient, 253b
  environment, 240
  lattice models of multicellular systems, 223
    cellular automaton with one cell per lattice site, 224–233
    lattice-based models, 224
    LGCA models, 233
    with many lattice sites per cell, 233–235
  rules, 240
  in scaffold-free 3D bioprinting, 271–276
    abstract description of agent, 271–272
    generalized cellular Potts model, 272–276
    scales and emergence, 272
  of vascular tissue, 284–285
Agent-based numerical methods
  applications, 276–279
    cell sorting, 276–277
    chemotaxis, 278
    diffusion, 277–278
    hypoxia, 278–279
    spheroid fusion, 277
  models in 3D bioprinting, 270–271
  state of the art in 3D bioprinting, 269–270
ALE approach. *See* Arbitrary Lagrangian–Eulerian approach (ALE approach)
ALLDMD, 199
Amniotic fluid (AF), 126
Angiogenesis, 96, 171–172
Anisotropic/anisotropy
  of deformation process, 195
  fracture toughening mechanisms, 198
  growth, 21
  Hill's yield behavior, 193–194
  models, 21
  toughening mechanisms, 197–199
  volumetric growth, 20
Aorta
  aortic valve replacement, 217
  blood flow in, 331–332, 332f
Apparent diffusion coefficient (ADC), 64–65
Approximation function, 308
Arbitrary Lagrangian–Eulerian approach (ALE approach), 188, 344, 350, 397
  meshless framework, 349–350
Arteries, 415
Artery walls, 341
  ABMs of, 286–290
    agent attribute variables, 287
    agent population, shape, and size, 286
    creation of rules for agent-based models, 289–290
    inclusion of endothelial cells, 288–289
    periodic boundary conditions, 289
    proliferation of VSMC agents, 287–288
    seeding agents in spatial domain, 287
Articular cartilage, 37–38, 55, 65–66
  components, 37f
  experimental models, 51
  numerical implementation, 45
  numerical modeling, 38–45
    model formulation, 39–45
  proteoglycan macromolecule aggregation, 40f
  3D
    computational model for simulating, 51
    free swelling model for healthy cartilage parameters, 49t
  validation and experimental examples
    boundary conditions, 45
    computational process, 46f
    free swelling, 48–50
    initial conditions, 48
    model validation, 45
    parameters of simplified 3D model of cartilage, 46t–47t
    sample subjected to loading, 50
Artificial compression technique, 378
Artificial velocity, 211–212
Artificial viscosity, 208–209
Atherosclerosis, 95
Atomic force microscopy (AFM), 3–4
  AFM-based nanotests, 4
Automated algorithm, 10
Axial oscillating pressure gradient, 213–214

B

B-spline formulation, 160–161
Backward Euler method, 180
Bacterial cellulose hydrogel (BC hydrogel), 11–12
  microstructure of, 11–12
  prediction of axial modulus of nanofibers in, 11–14
    correlation of microstructure behavior and global response, 12
    generation of discontinuous finite element model, 13–14
    representative volume element, 14
  with random distribution of fibers, 12f
Balance equations, 59–60
Balloon angioplasty, calibration of rule set through simulation of, 297–298
Basis functions, 102, 106, 330
  Lagrangian, 45
  polynomial, 304–305, 308
BC hydrogel. *See* Bacterial cellulose hydrogel (BC hydrogel)
BCs. *See* Boundary conditions (BCs)
Belinha's law, 312, 312t
BEM. *See* Boundary element method (BEM)
Betti's reciprocity theorem, 152
BGK
  approximation, 371–372
  collision operator, 417
BIE method. *See* Boundary element equation method (BIE method)
Bileaflet mechanical heart valves (BMHVs), 217, 218f
Bingham fluid, 373
Bio-CAD modeling, 156, 158, 164
Biochemical factors modeling in odontoblasts differentiation, 88

This book belongs to Central Library BADJI Mokhtar-ANNABA UNIVERSITY
Copyright Elsevier 2024

Biodegradable scaffolds, 269
Bioengineering applications, LBM for
drug and agonist transport within thrombi in vivo, 424–425, 425f
flow simulation, 416–417
mass and heat transport with Lagrangian particle tracking, 420–421
parallelization approach, 418–420, 419f
two-phase flow, 418
universal stress distribution and correlating flow forces, 422–424
Biofluidic applications, 361–363
droplet dynamics with applications to biomicrofluidics, 361–363
Biological cells, 286
combined IB–LB–FE method application to suspended, 404–409
Biological growth, 17. *See also* Mechanobiological growth
initial state, 18–19
mechanical stimuli, 19
mechanobiological algorithm, 20–25
multiplicative decomposition of deformation gradient, 20f
Biological materials, 18
Biological models, 79–80, 223–224, 241
chemotaxis model, 80
glycolysis model, 80
Schnakenberg model, 79–80
Biomaterials, 3
Biomechanics
BEM in, 145–153
applications in fracture, 150–151
comparison of stress results in bone–implant application, 163
for elastostatic problems, 151–153
biomechanical based methods, 336
biomechanical model, 336–337
Biomedical
modeling issues in biomedical engineering applications, 158–163
processes, 171–172
sciences, 223
Biomicrofluidics, droplet dynamics with applications to, 361–363, 364f–365f
Bioprinted tissue construction, multicellular self-assembly simulations in, 384–386
Bioprinter, 384
Biphasic model
cartilage model, 66–68
corresponding permeability, 68
fluid and elastic solid contributions to stress, 66–67
viscoelasticity of solid constituents, 68
for soft tissues, 61–63
assumptions, 61
constitutive formulation, 62–63
entropy inequality, 62–63
kinematics, 62
volume fractions, 61
Blending operation, 161–162
blockIdx, 374–375
Blood, 391, 415
flow in aorta, 331–332, 332f
fluid mechanics, 284
BMHVs. *See* Bileaflet mechanical heart valves (BMHVs)
BMPs. *See* Bone morphogenetic proteins (BMPs)
Body-fitted method, 397
Boltzmann acceptance function, 273
Boltzmann equation, 270, 392–393
Bone
bone–implant application, 163
deformities in proximal femur in cerebral palsy, 30–31
healing, 146
cascade, 241
regeneration, 240–241
remodeling, 305
remodeling algorithm, 315–316
tissue remodeling algorithm, 317–319
2D bone patch analysis, 315–316
Bone cutting, numerical simulation of, 187
interpolation of gradient influence of neighboring particles, 189f
model challenges and requirement, 188–189
model formulation and implementation, 191–194
contact formulation, 192
material properties, 193–194, 193t
model geometry, 191
postyield stress–strain relationships, 194t
sensitivity analysis, 191
model results and analysis
anisotropic toughening mechanisms, 197–199
anisotropy of deformation process, 195
comparison of force and displacement diagrams, 195f
comparison of simulation results, 199f
effect of cutting force with penetration depth, 197f
distribution of equivalent plastic strain, 197f
distribution of equivalent stress, 196f
distribution of shear stress component, 196f
effect of energy evolution and plastic deformation, 199f
force–displacement characterization, 194–195
high-speed camera images, 198f
progressive damage effect, 196
SPH, 189–191
Bone morphogenetic proteins (BMPs), 87
BMP2, 88
Bottom-up TE, 384
Bounce-back rule, 395, 416–417
Boundary conditions (BCs), 394–396
implementation in SPH, 210–212
attraction and repulsion between wall and fluid particles, 211f
inflow/outflow boundary conditions, 212
no-slip boundary condition, 212f
periodic boundary conditions, 212
inlet boundary, 395–396
top boundary, 396
Boundary element (BE)
formulation, 146–147
modeling in biomedical engineering applications, 156–163
bad mesh generation, 163f
distorted lofting operation, 162f
FEM and BEM meshing issues, 156–158
mandible polygonal model, 162f
modeling issues in biomedical engineering applications, 158–163
3D discontinuous or semidiscontinuous elements, 157f
solution, 122–123, 128
Boundary element equation method (BIE method), 153
Boundary element method (BEM), 119–120, 123, 125, 145–153, 392, 407. *See also* Dual boundary element method (DBEM)
applications in fracture, 150–151
bioheat transfer model, 149
coefficient matrix, 150
comparison of stress results in bone–implant application, 163
crack modeling, 151f
discretization comparison with FEM, 149f
for elastostatic problems, 151–153
internal points distribution, 150f
Kelvin infinite domain, 153f
mesh density, 163f
model for acoustic responses, 148
Boundary integral methods in bioelectromagnetics, 119
exposure to high-frequency electromagnetic radiation
human brain exposure to plane wave, 136–140
human eye exposed to plane wave, 130–135
whole body exposure to plane wave, 141–142
governing equations of theoretical dosimetry, 120–121
Exposure to High-Frequency Fields, 120–121
Exposure to Low-Frequency Fields, 120
human head exposed to VDU electrostatic field, 121–125
boundary element solution, 122–123
computational examples, 123–125
pregnant woman/fetus exposure to low-frequency fields, 125–130
boundary element solution, 128
computational examples, 128–130
conductivity scenarios, 129t
Boundary nonlinearity, 293
Bovine cortical bone tissue, 193–194
Box partitioning scheme, 418
Brain
deformation, 334–335, 335f
human brain exposure to plane wave, 136–140

This book belongs to Central Library BADJI Mokhtar-ANNABA UNIVERSITY
Copyright Elsevier 2024

computational examples, 138–140
dosimetry, 137–138
peak and average SAR values, 140t
tissue growth, 21
Bridging effect, 197
Brittle damage pattern, 197
Brownian motion, 421
Brute-force algorithm, 287
for seeding agents in spatial domain for ABM, 287b
Bubnov–Galerkin scheme, 42–43

C

C-R direction. *See* Cutting in radial direction (C-R direction)
C(2S) vortex-shedding mode, 347–349
C3D8R particle, 191
CA. *See* Cellular automaton (CA)
CAD. *See* Computer-aided design (CAD)
CAE. *See* Computer-aided engineering (CAE)
Calibration of rule set through simulation of balloon angioplasty, 297–298
Capturing global/multiscale behavior, 279–280
Cardiocytes. *See* Heart cells
Cardiovascular flows, 213–214, 342
Carnahan–Starling equation (CS equation), 360
Cartesian directions, 421
Cartesian grid, 335
Cartesian mesh, 416
Cartesian needle array, 269–270
Cartilage
computational models, 38
as representative system, 65–72
Cathode ray tube (CRT), 121
Cauchy principal value integral, 154
Cauchy stresses, 63
tensor, 66
Cauchy–Green deformation tensor, 260–261
Cavity detection, 147
CBMs. *See* Center-based models (CBMs)
Cell_phenotype matrices, 240
Cell–cell
adhesion, 233
friction, 246
matrix interactions, 231
Cell–extracellular matrix (Cell–ECM)
adhesion, 233
interactions, 231
Cellular/cell
activity driven by intracellular processes, 242, 243f
as agents, 240
aggregates, 385
biological patterns, 272
cell-based modeling approach, 172
cell-based methods, 418
cell-free structure, 269
cell–substrate friction, 246
cell–substrate friction coefficient, 252
cycle, 226
cylinder bioprinting, 385
differentiation, 171
embryological processes, 87
growth, division, and death, 250–251, 259
interaction forces, 247–248
maturation and migration, 181
migration, 179, 228, 241, 242f, 245–246, 248–250, 259
numerical estimation of stochastic force term in Langevin equation, 249b
movement, 77, 228–229
phenotypes, 241
processes, 284
proliferation, 241
simulations at cellular level, 241
sorting, 270, 276–277
spheroids, 269–270
Cellular automaton (CA), 223, 270, 283–284
with many cells per lattice site, 231–232
models, 224
with one cell per lattice site, 224–233
cell movement and multiplicity of states, 228–229
cellular automaton with many cells per lattice site, 231–232
choice of lattice, 224
choice of new state, 229b
construction rules of irregular lattice, 225b
energy-dependent moves, 231
growth and division, 229–230
lattice gas cellular automaton, 231–232
lattice symmetry influence on growth figures, 230–231
lattice-based growth models, 225–226
numerical lattice model simulation, 231b
numerical simulation of master equation with fixed time step, 228b
pros and cons of Type B lattice growth models, 231–233
simulation results of growth simulations, 230f
time, 227–228
two exemplary configurations of cells on two-dimensional lattice, 229f
type A and type B numerical simulations differences, 232b
typical rules for lattice models of Type B, 225f
Cellular particle dynamics methods (CPD methods), 270–271, 385
Cellular particles (CPs), 270–271
Cellular Potts models (CPMs), 223, 233–235, 271, 272f, 285, 385. *See also* Generalized cellular Potts model
cell growth and division, 234
choice of lattice, 234
directed active cell movement, 235
energy functional, 233–234
pros and cons, 235
simulation of dynamics, 234–235
Center-based models (CBMs), 223, 245–254, 246f. *See also* Deformable cell models (DCMs)
cell growth, division, and death, 250–251
cell interaction forces, 247–248
cell migration and chemotaxis, 248–250
equation of motion, 246–247
extensions and solutions, 252
force-based agent-based modeling, 254
implementation, 252–254
measures for deformation, stress, and pressure, 251–252
Cerebral palsy, bone deformities in proximal femur in, 30–31
CFD. *See* Computational fluid dynamics (CFD)
CFL condition. *See* Courant–Friedrichs–Lewy condition (CFL condition)
Chapman–Enskog expansion, 382–383, 392
Chapman–Enskog series, 373
Chemical master equation. *See* Master equation
Chemical quantities, 179
Chemical signals, 174–175
Chemical stimuli, 174
Chemotaxis, 179, 235, 248–250, 259, 278
of cells, 95
model, 80
numerical estimation of stochastic force term in Langevin equation, 249b
Chip formation, 189
Closed membranes, 366
CMMs. *See* Constrained mixture models (CMMs)
Collagen, 285
fibers, 68
Collocation method, 331
Colloidal particle physics, 248
Color momentum, 418
Color-fluid model, 357
Color-gradient model, 366
Colors model, 372–373
Combined IB–LB–FE method
application to suspended biological cells, 404–409
RBC in pressure-driven capillary flow, 408–409, 410f
RBC in simple shear flow, 406–407
spherical capsule in simple shear flow, 404–406
limitations
FEM, 411
IBM, 410–411
LBM, 409–410
Complex automata (CxA), 284
Complex geometry, 336–337
Compression, 206–207
loads, 50
Computation of interparticle area, 344–346, 345f
Computational biomechanics, 325
mesh generation, 325
meshless interpolation schemes, 326–330
strong-form MMs, 331–333
weak-form MMs, 334–337
weighted residual method, 330–331

This book belongs to Central Library BADJI Mokhtar-ANNABA UNIVERSITY
Copyright Elsevier 2024

Computational fluid dynamics (CFD), 361, 392, 415
Computational models, 385
  in bioelectromagnetics, 119
  generation, 10–11
    PBCs, 11
    RVE, 10–11
Compute Unified Device Architecture (CUDA), 374–375
Computed tomography (CT), 18, 325, 336–337
Computer clusters, 374
Computer simulations of fluids, 374
Computer-aided design (CAD), 159
  surface tools, 161
  surface-based computational mesh model, 160f
Computer-aided engineering (CAE), 147
Concentration equation, 106–108
Conductivity scenarios, 129t
Conjugate gradient in agent-based models, 253b
Conservation
  of mass, 207
  of momentum, 207–209
Constant strain triangle, 292
Constitutive elasticity matrix, 315
Constitutive formulation, 61–63
Constitutive law, 401–402
Constitutive modeling approaches, 56
Constrained mixture models (CMMs), 283–284
Constrained node-based surfaces, 192
Contact detection, 252
Contact formulation, 192
Contact inhibition, 251
  of locomotion, 249–250
Contact resolution, 252
Continuity equation, 208
Continuous modeling approaches, 5
Continuum
  damage mechanics theory, 193–194
  domain, 204–205
  growth models, 283
  models, 261–262
Contour-based approach, 159
Contractile VSMCs, 287
Conventional CFD methods, 392
Convergence tests, 345–346
Copy attempts, 273
  Monte Carlo step of, 276b
Corneal surface, 131
Correction
  factor, 216–217
  on force term, 382–384
Coulomb friction law, 192
Coupled Eulerian–Lagrangian method, 188
Coupled finite element–agent-based models
  paradigms for agent-based models of vascular tissue, 284–285
  schemes and algorithms for implementation of agent-based models, 286–290
    coupling agent-based and finite element domains, 293–298
    finite element models, 290–293
Coupled mechanobiological models, 284
Coupling agent-based domain
  calibration of rule set through simulation of balloon angioplasty, 297–298
  coupled model overview, 293
  mapping deformed geometry, 294
  stress-driven rule set for vascular smooth muscle cell agents, 294–297
Courant–Friedrichs–Lewy condition (CFL condition), 210
  CFL number, 377
CPD methods. *See* Cellular particle dynamics methods (CPD methods)
CPMs. *See* Cellular Potts models (CPMs)
CPs. *See* Cellular particles (CPs)
Crack modeling, 154–155
Crank–Nicolson method, 41
Critical shear stress, 192
CRT. *See* Cathode ray tube (CRT)
CS equation. *See* Carnahan–Starling equation (CS equation)
CT. *See* Computed tomography (CT)
Cube partitioning scheme, 418
Cubic spline, 190
  kernel, 206
CUDA. *See* Compute Unified Device Architecture (CUDA)
Cumulative Gaussian distribution function, 287–288
Cutting in radial direction (C-R direction), 197
CxA. *See* Complex automata (CxA)
Cytokine production, 174–175
Cytokinesis process, 250

D

D2Q9 LB model. *See* 9-speed two-dimensional LB model (D2Q9 LB model)
D_3Q_{19} model. *See* 19-speed three-dimensional model (D_3Q_{19} model)
DAH. *See* Differential adhesion hypothesis (DAH)
Damage evolution process, 193–194
Damage mechanisms, 197
Data acquisition, 63–64
DBEM. *See* Dual boundary element method (DBEM)
DBIE. *See* Displacement boundary integral equation (DBIE)
DC PSE. *See* Discretization correction particle strength exchange (DC PSE)
Deformable cell models (DCMs), 223, 245, 254–261, 254f. *See also* Center-based models (CBMs)
  adhesion and repulsion forces, 258–259
  cell growth, division, and death, 259
  cell migration and chemotaxis, 259
  cell shape and cellular forces, 261
  equation of motion, 255
  implementation, 261
  internal forces between nodes, 255–258
  measures for deformation, stress, and pressure, 259–261
Deformation
  anisotropy of deformation process, 195
  mapping deformed geometry, 294
  measures for, 251–252, 259–261
Deformation index (DI), 408
Deforming-spatial-domain/space-time method, 397
Delaunay triangulation, 307
Delta function, 398
DEM. *See* Diffuse element method (DEM)
Density functional theory, 261
Dental morphogenesis, 78
Dentinal tubules
  DLX3 in heterogeneous location, 89–92
  morphogenesis, 87–89
  odontoblast pattern, 78f
  reaction–diffusion systems, 79–87
Device memory, 374–375
DG methods. *See* Discontinuous Galerkin methods (DG methods)
DGFEM. *See* Discontinuous Galerkin finite element method (DGFEM)
DI. *See* Deformation index (DI)
Differential adhesion hypothesis (DAH), 385
Differential equations, 285
Differentiation
  axis, 181
  model, 173–174, 174f
  of odontoblast, 78–79
    from papilla, 78
  phenomena, 172
  rate and stimuli, 175–177
Diffuse element method (DEM), 326
Diffusion, 277–278
  conditions for instability by, 81–82
  diffuse ductile damage pattern, 197
  tensor magnetic resonance imaging
    imaging experiment, 69
    implementation of data, 69
Diffusion tensor MRI (DT-MRI), 64–65
Diffusion–reaction equation, 99–102
Dirac delta function, 174–175, 190, 331
  distribution function, 396
Directed active cell movement, 235
Dirichlet boundary conditions (Dirichlet BC), 121, 333, 395
Discontinuous elements, 156
Discontinuous finite elements, 77–78
  model generation, 13–14
    fiber cross-links, 14
    network structure, 13
Discontinuous Galerkin finite element method (DGFEM), 77–78
Discontinuous Galerkin methods (DG methods), 96
  background on stem cell therapy, 97
  mathematical model, 97–98
  numerical method, 97, 99–109, 113–114
    extension to two spatial dimensions, 106–109
    numerical results, 110–113
    one-dimensional implementation, 99–106
    time integration algorithm, 110b
  snail trail model, 113

This book belongs to Central Library BADJI Mokhtar-ANNABA UNIVERSITY
Copyright Elsevier 2024

Discontinuous-based modeling, 5–9
alternative modeling approaches, 7–9
embedded fiber models, 6–7
fiber-deposition models, 7
fibrous network embedded in matrix, 6f
lattice models, 5–6
Discrete equation system, 309–311
Discretization correction particle strength exchange (DC PSE), 326, 328–330
Discretization of nonideal forcing term, 359, 359f, 362f
Displacement, 180
field, 179
Displacement boundary integral equation (DBIE), 151
Displacement integral equation, 152
Distribution functions, 395
DLX3, 87
in heterogeneous location of dentinal tubules, 89–92
biological processes, 90
mechanical forces, 92
numerical examples for heterogeneous domain, 91f
turing patterns, 91f
Donnan osmotic pressure, 66
Dosimetry, 137–138
Droplet digital polymerase chain reaction, 363
Droplet dynamics with applications to biomicrofluidics, 361–363, 364f–365f
DT-MRI. *See* Diffusion tensor MRI (DT-MRI)
Dual boundary element method (DBEM), 153. *See also* Boundary element method (BEM)
crack modeling, 154–155
discontinuous elements, 156
modeling strategy, 155, 156f
Dynamical behavior, 368
Dynamical systems, 77

E

Ear canals, 148
ECGI. *See* Electrocardiographic imaging (ECGI)
ECM. *See* Extracellular matrix (ECM)
ECs. *See* Endothelial cells (ECs)
Eden model, 225–226
EFG method. *See* Element-free Galerkin method (EFG method)
Eigen functions of rectangle, 83–84
Einstein's theory, 421
Elastic solid contributions to stress, 66–67
Elastin, 285
Elastography methods, 65
Elastostatic problems, BEM for, 151–153
Electrocardiographic imaging (ECGI), 157–158
Electromagnetic fields, 121
Electroneutrality condition, 40–41
Element deletion/removal, 188–189
Element selection, 292, 293f
Element-free Galerkin method (EFG method), 326, 334
ELF electric fields. *See* Extremely low-frequency electric fields (ELF electric fields)
Ellipsoidal approach, 252
Embedded fiber
approach, 6
models, 6–7
Emergence, 272
Empirical function, 332–333
Endochondral ossification, 19
Endogenous skeletal regeneration, 239
Endothelial cells (ECs), 286, 288
inclusion of, 288–289
pseudocode outlining algorithm, 289b
Energy
energy-based methods, 245
energy-dependent moves, 231
function, 233–234, 255
minimization, 270
ratio, 199
Enforcing incompressibility, 292
Engineering shear strain. *See* Octahedral shear strain
Enhanced dynamics, 368
Entropy
inequality, 61–63
violation, 378
EOSs. *See* Equations of state (EOSs)
Epoxy glue, 3–4
Equation of motion, 245–247
cartoon of center based model with cells, 247f
Equations of state (EOSs), 380
Equivalence theorem, 137
Erlang distribution, 227
Erythrocytes. *See* Red blood cells (RBCs)
Euler equations, 373
Euler scheme, 209–210, 253, 295–296, 375
Eulerian description
of motion, 59
of velocity, 59
Eulerian formulations, 188
Eulerian–Lagrangian interaction/contact, 188
Euler–Maruyama method, 179, 181
Experimental measurements, 3–4
Experimental models, 51
Exponential distribution, 171–172
Exposure
to high-frequency fields, 120–121
to low-frequency fields, 120
Extended bioheat equation, 333
"Extended Hertz model", 248
Extended Pennes bioheat equation, 332–333
Extension to two spatial dimensions, 106–109
concentration equation, 106–108
tips equation, 108–109
Extracellular matrix (ECM), 38, 240, 240f, 245–246, 269, 285, 384
Extremely low-frequency electric fields (ELF electric fields), 119

F

FA. *See* Fractional anisotropy (FA)
Faraday constant, 39–40
Fat tissue mass, 173
FCD. *See* Fixed charge density (FCD); Free charge density (FCD)
FDM. *See* Finite difference method (FDM)
FE. *See* Finite element (FE)
FEM. *See* Finite element method (FEM)
Femoral analysis, 2D, 317–321
FENE force. *See* Finitely extensible nonlinear elastic force (FENE force)
Fiber cross-links, 9–10, 9f, 14
Fiber reorientation, 13
Fiber-deposition models, 7
Fiber-reinforced example for soft tissues, 61–63
assumptions, 61
constitutive formulation, 62–63
entropy inequality, 62–63
kinematics, 62
volume fractions, 61
Fiber-to-fiber contact mechanisms, 7
Fibrous network(s), 5–8
BC fibrous network, 13
continuous models, 5
embedded in matrix, 6f
FE models, 4–5
3D complex microstructures, 7–8
types of cross-linking, 9f
Fick's law, 79
Filtering techniques, 180–181
Finite difference method (FDM), 77–78, 145, 392
Finite difference schemes, 376–377
Finite element (FE), 17, 77–78
analysis, 4–5, 25–26
domain, 293–298, 294f, 297f
calibration of rule set through simulation of balloon angioplasty, 297–298
interpreting finite element model results, 293
mapping deformed geometry, 294
stress-driven rule set for vascular smooth muscle cell agents, 294–297
formulation, 41
model, 284, 290–293
boundary nonlinearity, 293
element selection, 292
enforcing incompressibility, 292
geometric nonlinearity, 291
geometry, materials, and boundary conditions, 290–291, 290f, 291t
material nonlinearity, 291–292
of soft tissues, 55–56
simulations, 55–56, 70–71
solution
of bioheat transfer equation, 133–134
standard finite element discretization of Helmholtz equation, 134
Finite element method (FEM), 14, 37, 77–78, 85–87, 120, 123, 125, 145–148, 188, 304, 315–316, 325, 334–335, 392, 400, 402–403

This book belongs to Central Library BADJI Mokhtar-ANNABA UNIVERSITY
Copyright Elsevier 2024

Finite element method (FEM) (*Continued*)
comparison of stress results in bone–implant application, 163
discretization comparison with BEM, 149f
limitations of combined IB–LB–FE method, 411
mesh density, 163f
for partial differential equations, 179–180
Finite volume method (FVM), 392
Finite volume particle method (FVPM), 342, 347–350
application to simplified mechanical heart valve, 349–352
computation of interparticle area, 344–346
extensions of basic method, 346
FSI systems, 341
as FVM, 344
inlet and outlet boundary conditions in, 346–347
SPH, 342–343
validation for flow coupled with rigid body motion, 347–349
Finitely extensible nonlinear elastic force (FENE force), 257–258
First order upwind scheme, 373–374
First-order coupled system, 246
Fisher–KPP equation, 231
Fixed charge density (FCD), 40
Fixed grid methods, 341
Flexible cross-link, 9, 9f
Flow, 350
cardiovascular, 213–214, 342
multicomponent, 358–361
multiphase, 358–361
Poiseuille, 373
simulation, 416–417
simulation algorithm, 416–417
validation for flow coupled with rigid body motion, 347–349, 348f–349f
Womersley type, 213–214
Fluid
contributions to stress, 66–67
dynamic equations, 207
fluid-filled vesicles in shear flow, 368, 369f
fluid-membrane systems, 392
fluid–fluid interfaces, modeling membranes as, 366–368, 367f
fluid–solid coupling coefficient, 39–40
mechanics, 392
Fluid–structure interaction (FSI), 341, 415
Flux limiter schemes, 374, 377
"for" loops, 240
Force
corrections on, 382–384
force-based agent-based modeling, 254
force-based models, 245
force-biased algorithm, 8
force–displacement characterization, 194–195
surface tension in, 379–382
Formalism, 172
Forward Euler's method, 181
Forward time numerical scheme, 375
Fractional anisotropy (FA), 64–65
Fractional propagation scheme, 376
Fracture, BEM applications in, 150–151
Free charge density (FCD), 40–41
Free-energy model, 357
Friction in parallel direction, 247
FSI. *See* Fluid–structure interaction (FSI)
Fundamental solution Laplace equation, 122–123
Fusion, 271
FVM. *See* Finite volume method (FVM)
FVPM. *See* Finite volume particle method (FVPM)

G

GAGs. *See* Glycosaminoglycans (GAGs)
Galerkin equations, 107
Galerkin's finite element method, 180
Galerkin–Bubnov procedure, 133
gamma-3P. *See* Three-parameter gamma (gamma-3P)
Gauss' theorem, 180
Gauss's method, 307
Gauss–Hermite quadrature, 372
Gaussian kernel, 206
Gauss–Legendre points, 104
Gauss–Legendre quadrature, 105, 108–111
rule, 306
Gelatin, 285
Generalized cellular Potts model. *See also* Cellular Potts models (CPMs)
Hamiltonian, 274–275
implementation, 275–276
mathematical formulation, 273
methods and models, 273–274
qualitative description, 272–273
Generalized density, 359
Generalized finite difference (GFD), 325
Generalized trapezoidal method, 42
Generic biomechanical models, 325
Genetic diseases, 90–91
Geomagic Studio by 3D System, 159
Geometric analysis, 191
Geometric nonlinearity, 291
GFD. *See* Generalized finite difference (GFD)
Giles' approach, 346–347
Gillespie algorithm, 227, 228b, 385
Glucose molecule synthesis, 80
Glycolysis model, 80
Glycosaminoglycans (GAGs), 38
Governing equations of theoretical dosimetry, 120–121
high-frequency fields, exposure to, 120–121
low-frequency fields, exposure to, 120
Gradual transition of stem cells, 174
Graphics processing unit (GPU), 114, 374
Green's theorem, 128
Growth, 17, 20
criterion, 28f
factor, 240
modulator, 23, 23f–24f
multiplier, 29f
original meshed biceps model, 29f
stimulus function, 22

H

Half-order method, 421
Halpin–Tsai equations, 5
Hamiltonian, 234, 273–275
Healing, 241–242
cascade, 239
Heart cells, 95–96
Heart valve, application to simplified mechanical, 349–352
Heat transport with Lagrangian particle tracking, 420–421
Heaviside function, 98
Helmholtz equation, 132
Helmholtz free-energy function, 61, 62–63
Helmholtz system, 148
Hemodynamic characteristics, 149
HF exposure. *See* High-frequency exposures (HF exposure)
HIFU. *See* High-intensity focused ultrasound (HIFU)
High-frequency electromagnetic radiation, exposure to
human brain exposure to plane wave, 136–140
human eye exposed to plane wave, 130–135
whole body exposure to plane wave, 141–142
High-frequency exposures (HF exposure), 119
HF fields, exposure to, 120–121
High-intensity focused ultrasound (HIFU), 148
Higher-order lattices, 359, 359f, 360t, 362f
Hill's anisotropic yield criterion, 193–194, 194t
Homogeneous interior, 255
Homogeneous lossy dielectric model, 136
Homogeneous materials, 11
Homogeneous Neumann condition, 80
Hooke's law, 151, 309–310
Hopping rate, 228–229, 231
Hourglassing, 292
Human brain exposure to plane wave, 136–140
computational examples, 138–140
dosimetry, 137–138
peak and average SAR values, 140t
Human diseases, 391
Human eye exposure to plane wave, 130–135
boundary element solution, 132–133
computational examples, 134–135
finite element solution of bioheat transfer equation, 133–134
Human head exposure to VDU electrostatic field, 121–125
boundary element solution, 122–123
computational examples, 123–125
Human skin deformation, 149
Hybrid model, 172, 261–263, 262f, 350
Hybrid SPH + FE models, 191, 191f
"Hybridized" CPM, 276

This book belongs to Central Library BADJI Mokhtar-ANNABA UNIVERSITY
Copyright Elsevier 2024

Hydrogels, 3, 10, 385
mechanical behavior of, 3
Hyperelastic models, 291–292
Hypertrophy, 173
Hypoxia, 278–279, 278f

I

IBM. *See* Immersed boundary method (IBM)
Identification number, 273
"If-then" statements, 240
IH. *See* Intimal hyperplasia (IH)
Image analysis programs, 18
Image-based approach, 424
Image-based data acquisition, 63–65
diffusion, 64–65
mapping strain and material properties, 65
morphology and geometry, 64
Image-driven constitutive models, 65–72
biphasic cartilage model, 66–68
integration of computational modeling and experimental data, 69–71
diffusion tensor magnetic resonance imaging experiment, 69
finite element simulations, 70–71
implementation of diffusion tensor magnetic resonance imaging data, 69
material, compositional, and structural parameters, 70, 70t
model tradeoffs and considerations, 71–72
tissue complexity captured via model complexity, 71
true cartilage structure, 66f
Imaginary particles, 212, 212f
IMEX method, 180
Immersed boundary method (IBM), 357, 392, 396–397, 397f
immersed boundary–LBM, 399
limitations of combined IB–LB–FE method, 410–411
mathematical formulation, 397–398
numerical implementation, 398–399
Immiscible fluids
mutually, 365–366
two, 363–365
Implantology problems, 147
Implicit Euler scheme, 209–210
In-stent restenosis, 285
Incompatible configuration, 20
Indentation test, 70
Index mapping, 275
Individual-based computer simulations, 385
Individual-based models (IBMs). *See* Agent-based models (ABMs)
Induced current density, 120, 129
Industry-standard programming languages, 374–375
Inertial regime, 373
Inflammation, 26, 285
Inflow/outflow boundary conditions, 212, 213f
Inlet boundary, 395–396
Inlet boundary conditions in finite volume particle method, 346–347, 346f–347f
Integral interpolant, 204–205
Interacting multicomponent fluids, pseudopotential approach for, 360–361
Interface node, 192
Interface tracking, 357
Internal forces between nodes, 255–258, 256f–257f
Interparticle area, computation of, 344–346
Interpolating kernel, 204–205
function, 206–207
Interpolation functions, 308–309, 312f, 312t
Intima, 290–291
Intimal hyperplasia (IH), 285
Intraagent interactions, 272
Intracellular pathway, 242
Intracellular processes, cellular activity driven by, 242
Intramembranous ossification, 19
Intravascular stents, 283
Inverse parameter estimation, 4–5, 12, 13f
Irregular lattice, construction rules of, 225b
Iso2Mesh, 161
Isotropic volumetric
growth, 20
models, 20–21

J

J-integral technique, 153–154
Johnson–Kendal–Roberts theory (JKR theory), 248
Joint morphogenesis, 28–30

K

Kelvin infinite domain, 152, 153f
Kelvin–Voigt element (KVE), 255
Kenzan method, 269–270
Kernel estimation, 189
Kernel function, 262, 329, 342
Kinematics, 59, 62
growth models, 25
Kinetic LB equation, 360–361
Kinetic Monte Carlo algorithm. *See* Gillespie algorithm
Kinetic Monte Carlo methods (KMC methods), 270–271, 277f
Knudsen number (ϵ), 373, 395
Kronecker delta, 99–100, 152, 177, 233
property, 304–305
KVE. *See* Kelvin–Voigt element (KVE)

L

Lagrangian basis functions, 180
Lagrangian formulations, 188
Lagrangian parameters, 233–234
Lagrangian particle motion, 349–350
Lagrangian particle tracking techniques (LPT techniques), 421
mass and heat transport with, 420–421
Lagrangian points, 367
Lagrangian scalar tracking techniques (LST techniques), 421
Langevin equation, numerical estimation of stochastic force term in, 249b
Laplace–Beltrami formula, 258
Lattice, 273, 393
free models, 223, 245
lattice-based growth models, 225–226
lattice-based models, 224
models, 5–6, 223
network system, 5–6
spacing, 232–233
symmetry influence on growth figures, 230–231
Lattice Boltzmann methods (LBM), 270, 357, 392–393, 415–416
algorithm
flow simulation, 416–417
mass and heat transport with Lagrangian particle tracking, 420–421
parallelization approach, 418–420, 419f
two-phase flow, 418
BC, 395–396
drug and agonist transport within thrombi in vivo, 424–425, 425f
LB equation, 358, 358f, 393
limitations of combined IB–LB–FE method, 409–410
mathematical formulation, 393–394
numerical implementation, 394
universal stress distribution and correlating flow forces, 422–424
Lattice Boltzmann models (LB models), 371
collision step, 363
combined IB–LB–FE method application to suspended biological cells, 404–409
limitations, 409–411
RBC in pressure-driven capillary flow, 408–409, 410f
RBC in simple shear flow, 406–407
spherical capsule in simple shear flow, 404–406
immersed boundary method, 396–399
membrane mechanics, 399–404
multicellular self-assembly simulations in bioprinted tissue construction, 384–386
numerical schemes for reducing velocities at interfaces, 375–384
simulation programs, 375
solution algorithm, 404, 405f
viscous fluids and, 371–375
Lattice gas cellular automaton models (LGCA models), 224, 231–233
Lax–Friedrich flux, 103
Lax–Wendroff scheme (LW scheme), 376
LB models. *See* Lattice Boltzmann models (LB models)
LBIE method. *See* Local boundary integral equation method (LBIE method)
LBM. *See* Lattice Boltzmann methods (LBM)
LDs. *See* Lipid droplets (LDs)
Leaflet, 350
Leapfrog scheme, 209–210
Least-squares problem, 180
Left ventricle, 203–204, 212

This book belongs to Central Library BADJI Mokhtar-ANNABA UNIVERSITY
Copyright Elsevier 2024

Legendre polynomials, 99, 105
with Gauss–Legendre quadrature, 103
Lennard-Jones force, 211
LF exposure. *See* Low-frequency exposures (LF exposure)
LGCA models. *See* Lattice gas cellular automaton models (LGCA models)
LI. *See* Linear interpolation (LI)
Linear basis functions, 181
Linear elastic fracture mechanics, 150
Linear elasticity theory, 391
Linear elements, 180
Linear interpolation (LI), 157–158, 181
Linear speedup, 419–420
Linear triangular element, 292f
Linked list method, 210
Lipid droplets (LDs), 173
Local boundary integral equation method (LBIE method), 147
Local DG method, 113–114
Local equilibria, 358
Lotz's law, 312
Low-frequency exposures (LF exposure), 119
LF fields, exposure to, 120
LPT techniques. *See* Lagrangian particle tracking techniques (LPT techniques)
LST techniques. *See* Lagrangian scalar tracking techniques (LST techniques)
LW scheme. *See* Lax–Wendroff scheme (LW scheme)

M

Macroscopic variables, 395
Magnetic resonance imaging (MRI), 18, 56, 119, 325
Markov chain Monte Carlo method, 234
Mass transport with Lagrangian particle tracking, 420–421
Master equation, 227, 231–232
classical multivariate, 231–232
event-based numerical simulation of, 228b
numerical simulation of, 228b
Master–slave contact algorithm, 192
Material anisotropic constants, 193–194
Material anisotropy, 18
Material nonlinearity, 291–292
Mathematical formulation, 273
Mathematical models, 77
Matrix metalloproteases, 385
Matrix metalloproteinases (MMPs), 285
Maturation space, 172–173
Maugis–Dugdale continuum theory, 259
Maxwell element (ME), 256
Maxwell–Boltzmann distribution, 372
MCD. *See* Monitorized central difference (MCD)
MCS. *See* Monte Carlo step (MCS)
ME. *See* Maxwell element (ME)
Mechanical analysis, 314
Mechanical drag, 179, 181
Mechanical heart valves (MHVs), 341, 350–352, 351f–352f
Mechanical stimuli, 17, 19, 22–23, 28, 31, 174–176
Mechanobiological algorithm, 17, 20–25, 28, 30–32
Mechanobiological growth, 17–19. *See also* Biological growth
computational models of, 17
examples of mechanobiological growth simulations, 25–32, 26t
adaptation of murine cortical bone, 31–32
bone deformities in proximal femur in cerebral palsy, 30–31
hypertrophic muscle growth, 26–28
joint morphogenesis, 28–30
numerical implementation of growth algorithm, 27f
Mechanobiology, vascular, 284
Mechanoelectrochemical model, 45
Mechanologic bone tissue remodeling analysis
discrete equation system, 309–311
mechanologic model, 311–315
numerical methods, 304–309, 305f
SED, 303
2D bone patch analysis, 315–316
2D femoral analysis, 317–321
Mechanologic model
interpretation of results, 315
phenomenological law, 311–313, 312f
remodeling criterion, 313
remodeling procedure, 313–315, 314f
Mechanotransduction, 254–255
Medical imaging, 55–56
Membrane discretization, 400–401, 400f
Membrane force, 367
Membrane mechanics, 399–400
constitutive law, 401–402
FEM, 402–403
membrane discretization, 400–401, 400f
volume correction, 403–404
Mesenchymal stem cells, 179
differentiation, 171
Mesh
distortion, 188
generation, 325, 349–350
mesh-based methods, 261–262, 325
mesh-free method, 261–262
velocity, 174–175
Meshless collocation method, 333
Meshless interpolation schemes, 326–330
DC PSE, 328–330
MMLS, 326–328
Meshless local Petrov–Galerkin method (MLPG method), 326, 334
Meshless method (MM), 145, 305–309, 325, 342, 349–350
interpolation functions, 308–309
nodal connectivity, 306
numerical integration, 306–308
strong-form, 331–333
weak-form, 334–337
Meshless point collocation scheme (MPC scheme), 332
Meshless total Lagrangian explicit dynamics method (MTLED method), 334–335
Mesoscopic approach, 392
Message Passing Interface (MPI), 374, 418
Method of moments
solution via, 141–142
Method of moments solution (MoM solution), 119–120
Metropolis algorithm, 234, 234b, 250, 255
Metropolis Monte Carlo algorithm, 385
MHVs. *See* Mechanical heart valves (MHVs)
Micro–computed tomography-based methods (Micro-CT-based methods), 7–8, 422–423
Microscopic approaches, 392
Microscopic biological systems, 246
Microsystems, 361
MIMICS commercial software, 18
Minimal standard effective energy functional of CPM, 233
Minmod function, 378
Mirror particles, 211–212
Mitosis phase, 250
Mixed linear-quadratic mesh BEM model, 163
MLPG method. *See* Meshless local Petrov–Galerkin method (MLPG method)
MLS. *See* Moving least squares (MLS)
MM. *See* Meshless method (MM)
MMLS. *See* Modified moving least squares (MMLS)
MMPs. *See* Matrix metalloproteinases (MMPs)
Model complexity, tissue complexity captured via, 71
Model formulation, 39–45
proteoglycan macromolecule aggregation, 40f
spatial discretization, 42–45
system of differential equation, 41
temporal discretization, 42
weak formulation, 41
Model reliability tests, 191
Modeling membranes as fluid–fluid interfaces, 366–368, 367f
Modified color-gradient method, 363–366
mutually immiscible fluids, 365–366
two immiscible fluids, 363–365
Modified moving least squares (MMLS), 326
Molecular dynamics, 251, 392
MoM solution. *See* Method of moments solution (MoM solution)
Monitorized central difference (MCD), 377
Monte Carlo dynamics, 250
Monte Carlo sampling, 235
Monte Carlo step (MCS), 274, 276f
copy attempts, 276b
Monte Carlo–based scheme, 8
Moore's law, 415
Morphogenesis
of dentinal tubules, 87–89
modeling biochemical factors in odontoblasts differentiation, 88

This book belongs to Central Library BADJI Mokhtar-ANNABA UNIVERSITY
Copyright Elsevier 2024

numerical implementation, 88
results, 88–89
mechanism, 78–79
Morphology, 30
Moving least squares (MLS), 326
MPC scheme. *See* Meshless point collocation scheme (MPC scheme)
MPI. *See* Message Passing Interface (MPI)
MRI. *See* Magnetic resonance imaging (MRI)
MRT scheme. *See* Multirelaxation time scheme (MRT scheme)
MTLED method. *See* Meshless total Lagrangian explicit dynamics method (MTLED method)
Multicellular self-assembly simulations in bioprinted tissue construction, 384–386
Multicomponent flows, 358–361
Multicomponent LB models
biofluidic applications, 361–363
color-fluid model, 357
fluid-filled vesicles in shear flow, 368
LB equation, 358
modeling membranes as fluid–fluid interfaces, 366–368
modified color-gradient method, 363–366
pseudopotential approach for multiphase and multicomponent flows, 358–361
Multiphase continuum model
biphasic, fiber-reinforced example for soft tissues, 61–63
building blocks of, 56–63
multiphase framework, 56–61
balance equations, 59–60
concept of volume fractions, 57–58
constitutive formulation, 61
entropy inequality, 61
kinematics, 59
Multiphase flows, 358–361
Multiplicity of states, 228–229
Multirange interaction model, 357
Multirange pseudopotentials, 379–380
Multirelaxation time scheme (MRT scheme), 410
Multiscale modeling, 4–11
continuous modeling approaches, 5
discontinuous-based modeling, 5–9
fiber cross-links, 9–10
generation of computational model, 10–11
Multiscale nature of process, 239
Multivariate master equation, 234
Murine cortical bone, adaptation of, 31–32
Murine cortical bone adaptation, 31–32
MUSCL approach, 346
Muscle adaptation, 21
Muscle hypertrophy, 26
Musculoskeletal models, 18–19, 30
Mutually immiscible fluids, 365–366
Myoblasts, 174–175, 177–178
Myocardial infarctions, 95, 97
Myocardiocytes, 97
Myocytes, 173–174, 177–179, 183f

N

Nanobending, 3–4
Nanofibers, 3–4
Nanotension, 3–4
Native cell surface receptor (R_{nat}), 242
Natural hydrogels, 269
Natural neighbor radial point interpolation method (NNRPIM), 304–307
Navier equations, 151
Navier–Cauchy formulation, 177–178
Navier–Stokes equations, 207, 392
Navier–Stokes solver, 395, 416
Neighboring particles, search of, 210
Neo-Hookean law (NH law), 401–402
Network structure, 13
Neumann BC, 395
Newtonian dynamics, 246
Newtonian plasma, 418
NH law. *See* Neo-Hookean law (NH law)
9-speed two-dimensional LB model (D2Q9 LB model), 385
19-speed three-dimensional model (D_3Q_{19} model), 393
NNRPIM. *See* Natural neighbor radial point interpolation method (NNRPIM)
Nodal connectivity, 305–306
Noise-reduced variant, 226
NonCondensing cell types, 277, 277f
Nondimensional Navier–Stokes equations, 332
Nonideal equations of state in pseudopotentials approach, 360
Nonlinear convection, 416
Nonreflecting boundary conditions, 346–347, 350
Normalized energy dissipation, 199
Numerical estimation of stochastic force term in Langevin equation, 249b
Numerical implementation, 45, 88
Numerical integration, 306–308, 306f–307f
Numerical method, 97, 99–109, 113–114, 179–181, 304–309, 305f
cell maturation and migration, 181
extension to two spatial dimensions, 106–109
FEM, 305
finite element method for partial differential equations, 179–180
meshless methods, 305–309
numerical results, 110–113
one-dimensional results, 110–111
two-dimensional results, 112–113
one-dimensional implementation, 99–106
time integration algorithm, 110b
ZZ-gradient recovery method, 180–181
Numerical modeling, 38–45
Numerical schemes, 373–374
for reducing velocities at interfaces, 375–384
corrections on force term, 382–384
finite difference schemes, 376–377
flux limiter schemes, 377
surface tension in force term, 379–382
total variation diminishing schemes, 378–379
Numerical simulations, 371
Numerical time integration, 209–210
NURBS formulation, 160–161
nVidia, 374–375

O

OA. *See* Osteoarthritis (OA)
Octahedral shear strain, 176–178, 180
ODEs. *See* Ordinary differential equations (ODEs)
Odontoblast pattern, 77–78, 78f
Odontoblasts differentiation, biochemical factors modeling in, 88
Off-lattice agent-based models
CBMs, 245–254
DCMs, 254–261
hybrid modeling, 261–263
Ohm's law, 120
One-dimensional chemotaxis–diffusion–reaction equation, 102
One-dimensional implementation, 99–106
diffusion–reaction equation, 99–102
tips equation, 102–104
vessel density, 104–106
Open nonempty square domain, 97
Open source software, 18
Ordinary differential equations (ODEs), 295, 296f, 296t
Ornstein–Uhlenbeck process, 249
Osteoarthritis (OA), 55
Osteocytes, 303
Outlet boundary conditions in finite volume particle method, 346–347, 346f–347f
Oxford free-energy approach, 373
Oxford LB model, 375

P

Parallelization approach, 418–420, 419f
ParFEAP program, 71
Partial Cauchy
solid stress tensor, 63
stress tensor, 60
Partial differential equations (PDE), 172, 179, 330, 342
finite element method for, 179–180
Particle distribution control near moving bodies, 349–350, 351f
Particle finite element–based framework
approximation of gradient of solution, 182f
influence of disuse on muscle/fat contents in humans, 172f
mathematical framework, 173–179
ternary cell system, 173–179
mesenchymal stem cells differentiation, 171
numerical method, 179–181
simulations, 182–184

This book belongs to Central Library BADJI Mokhtar-ANNABA UNIVERSITY

Copyright Elsevier 2024

Particle(s), 342
method, 346
movement, 209
node, 192
particle-based Stokes' equations, 263
volume, 344
Passive convection term, 179
Passive migration. *See* Mechanical drag
Patient-specific biomechanical modeling, 336
PBCs. *See* Periodic boundary conditions (PBCs)
PC3D particle, 191–192
PDE. *See* Partial differential equations (PDE)
pdf. *See* Probability density function (pdf)
Peaked waiting time distribution, 227
Peng–Robinson EOS (PR EOS), 380
Periodic boundary conditions (PBCs), 11, 212, 213f, 289
pseudocode outlining algorithm, 290b
Periodic volume (PV), 10
Permeability, 68
Persistent random walk model (PRW model), 248
Personalized treatment planning, 325
PETSc. *See* Portable, Extensible Toolkit for Scientific Computation (PETSc)
PGs. *See* Proteoglycans (PGs)
Phagocytose, 251
Phase segregation, 372–373
Phase-field methods, 270
PIM. *See* Point interpolation method (PIM)
Pin joint, 9, 9f
Planar deformation, 403
Plane wave
human brain exposure to, 136–140
human eye exposed to, 130–135
Plasma, 391
Plastic strain hardening, 193–194
Platonic solids, 400
PLLA. *See* Poly-L-lactic acid (PLLA)
Point interpolation method (PIM), 304–305
Poisson process, 227
Polarity vector (P), 249
Poly-L-lactic acid (PLLA), 422–423
Polymer chain-based models, 5
Polymer hydrogels, 269
Polynomial basis functions, 305
PolyWorks by InnovMetric, 159
Portable, Extensible Toolkit for Scientific Computation (PETSc), 374
PR EOS. *See* Peng–Robinson EOS (PR EOS)
(Pre)adipocytes, 174–175
Pregnant woman/fetus exposure to low-frequency fields, 125–130
boundary element solution, 128
computational examples, 128–130
conductivity scenarios, 129t
Pressure, 251–252, 259–261
drop, 417
gradient, 207–208
pressure-driven capillary flow, RBC in, 408–409
Probability density function (pdf), 423–424
Progressive damage effect, 196
Proteoglycans (PGs), 37
PRW model. *See* Persistent random walk model (PRW model)
Pseudopotential approach, 358–361
discretization of nonideal forcing term on higher-order lattices, 359
for interacting multicomponent fluids, 360–361
nonideal equations of state in, 360
Pseudopotential LB method, 363
Pseudopotential model, 357, 373
PV. *See* Periodic volume (PV)

Q

Quadratic interpolation (QI), 157–158
Qualitative description, 272–273
Quasiincompressible equation of state, 208
Quasilinear viscoelastic theory, 38
Quasistatic model, 18–19

R

Radial basis functions (RBFs), 308, 326
Radial point interpolation (RPI), 304
Radial point interpolation method (RPIM), 304–306, 315, 319f–320f
Raman spectroscopy, 4
RBCs. *See* Red blood cells (RBCs)
RBFs. *See* Radial basis functions (RBFs)
RE software. *See* Reverse Engineering software (RE software)
Reaction–diffusion systems
biological models, 79–80
chemotaxis model, 80
glycolysis model, 80
Schnakenberg model, 79–80
conditions for Turing instability, 80–84
equations, 77, 79, 87, 250
finite element method, 85–87
PDEs, 261
reaction–diffusion equation, 79
Real LB equations, 382–383
Realistic human body models, 119
"Recursive bisection" techniques, 418
Red blood cells (RBCs), 203–204, 341, 391, 418
deformation, 399–400, 408
in pressure-driven capillary flow, 408–409, 410f
in simple shear flow, 406–407
Redlich–Kwong EOS (RK EOS), 380
Redlich–Kwong–Soave EOS (RKS EOS), 380
Regeneration process, 240
Regenerative medicine, 171
Registration algorithms, 336
Regular icosahedron, 400, 400f
Relative error of mean value (REMV), 14
Relative standard deviation (RSD), 14
Remodeling
algorithm, 304, 315
criterion, 313
cycle, 303
procedure, 313–315
REMV. *See* Relative error of mean value (REMV)
Representative volume element (RVE), 10–11, 14
Reproducing kernel particle method (RKPM), 326
Repulsion forces, 258–259
"Repulsive" interaction phenomenon, 249–250
Residual functions, 330
Restenosis, 285
Reverse Engineering software (RE software), 159–161
Reynold's transport theorem, 180
Reynolds number (*Re*), 347, 373, 410
Richardson model, 226
Rigid boundary conditions, 210–212
RK EOS. *See* Redlich–Kwong EOS (RK EOS)
RK3-TVD, 102
RKPM. *See* Reproducing kernel particle method (RKPM)
RKS EOS. *See* Redlich–Kwong–Soave EOS (RKS EOS)
Robin BC, 395
Rotating joint, 9f, 10
Rotation matrix, 177
Routh–Hurwitz conditions, 82
RPI. *See* Radial point interpolation (RPI)
RPIM. *See* Radial point interpolation method (RPIM)
RSD. *See* Relative standard deviation (RSD)
Rubberlike materials, 5
"Rules", 239–240
RVE. *See* Representative volume element (RVE)

S

SAR distribution. *See* Specific absorption rate distribution (SAR distribution)
SC pseudopotential scheme. *See* Shan–Chen pseudopotential scheme (SC pseudopotential scheme)
SC-like approach, 363
Scaffold-based methods, 269
Scaffold-free
biofabrication, 270
methods, 269–270
3D bioprinting
agent-based models in, 271–276
relevance for, 280
Scalar processors (SPs), 374–375
Scale separation map (SSM), 284
Scales, 272
Schnakenberg model, 79–80
Second Piola–Kirchhoff effective stress tensor, 68
SED. *See* Strain energy density (SED)
Seeding agents in spatial domain, 287
brute-force algorithm in spatial domain, 287b
Segregation rule, 365–366

This book belongs to Central Library BADJI Mokhtar-ANNABA UNIVERSITY
Copyright Elsevier 2024

"Self-healing" capacity of heart, 95–96
Self-optimization, 303–304
Semidiscretized system, 42–44
Sensitivity analysis, 191
  contour plots of vertical displacement and energy ratio comparison, 192f
  hybrid SPH + FE models, 191f
  stress–strain response of elastoplastic material, 192f
Shan–Chen pseudopotential scheme (SC pseudopotential scheme), 358–359
Shape functions, 86, 305, 326, 334, 403
Shear flow, fluid-filled vesicles in, 368, 369f
Shear loading history downstream of BMHVs, 217
Shear locking, 292
Shear stresses (SS), 418
Shifted radial Green's functions, 178
SIEs. *See* Surface integral equations (SIEs)
SIFs. *See* Stress intensity factors (SIFs)
Sigmoid function, 295, 295f
Silico models, 283
Simple shear flow, RBCs in, 406–407
Simplified mechanical heart valve
  application to, 349–352
  control of particle distribution, 349–350
  mechanical heart valve, 350–352
Single cell biology, correlating flow forces to, 422–424, 422f
Single relaxation time (SRT), 393
Skeletal regeneration, 239, 241
  application to, 239–240
Skeletal tissue regeneration, 239, 241
  ABMs and application to skeletal regeneration, 239–240
  processes at different length and time scales, 241–242
    cellular activity driven by intracellular processes, 242
    emergent behavior at tissue scale, 241–242
    simulations at cellular level, 241
Slice partitioning scheme, 418
Smoothed particle hydrodynamics (SPH), 188, 203, 261–262, 342–343, 342f–343f
  advantages and disadvantages, 204t
  applications to unsteady cardiovascular flows, 213–215
  BMHVs, 217
  boundary conditions implementation in, 210–212
  classical, 207
  conservation of mass, 207
  conservation of momentum, 207–209
  initial state of moon-forming disk, 204f
  interpolation, 205f
    kernel function, 206–207
  mathematical formulation, 204–207
  Navier–Stokes equations, 207
  numerical features, 209–210
    imaginary cells, 211f
    linked list method, 210
    neighboring particles, search of, 210
    numerical time integration, 209–210
    particle movement, 209
    variable time step, 210
    XSPH variant, 209
  WSS, 216–217
Smoothing
  function, 190
  length, 204–205
Snail trail model, 98, 113
Soft tissues
  building blocks of multiphase continuum model, 56–63
  finite element modeling of, 55–56
  hallmarks of, 55
  image-based data acquisition, 63–65
  image-driven constitutive models, 65–72
  motions of solid and fluid particles within, 62f
  need for imaging data to drive models, 56
  true structure of, 61f
Solid constituents, viscoelasticity of, 68
Somigliana identity for displacements, 152
"Space-free" ABMs, 223
Sparse symmetric matrix, 247
Spatial ABMs, 223
Spatial discretization, 42–45
Spatial domain, 287. *See also* Seeding agents in spatial domain
Specific absorption rate distribution (SAR distribution), 119–121, 138, 139f–140f
SPH. *See* Smoothed particle hydrodynamics (SPH)
Spheroid(s), 270
  fusion, 277, 279
SPs. *See* Scalar processors (SPs)
Spurious current, 375–376, 379–380
Spurious viscosity, 373–374
Square lattice, 225b, 234
SRT. *See* Single relaxation time (SRT)
SRT BGK model, 410
SS. *See* Shear stresses (SS)
SSM. *See* Scale separation map (SSM)
Stalking endothelial cells, 98
State of the art in 3D bioprinting, 269–270
Stem cell therapy, 95–97
Stem cells, 171–174
Stiffness of nanofibers
  biomaterials, 3
  experimental measurements, 3–4
  inverse parameter estimation, 4
  multiscale modeling, 4–11
  prediction of axial modulus of nanofibers in, 11–14
Stiffness_ECM matrices, 240
Stochastic process, 273
Stochastic transition rule, 279
Stokes equations, 373
Stokes' second problem, 215
Strain energy density (SED), 303
Strain energy release rate, 198
Strain(s), 19, 43
Stratton–Chu formulation, 132
Streamline upwind Petrov–Galerkin methods (SUPG methods), 96, 99, 114
Stress, 19, 251–252, 259–261, 294–295
  and deformation, 252
  fluid and elastic solid contributions to, 66–67
  stress-driven rule set for vascular smooth muscle cell agents, 294–297
  tensor, 251–252
Stress intensity factors (SIFs), 150
Strong-form MMs, 331–333. *See also* Weak-form MMs
  blood flow in aorta, 331–332, 332f
  tumor ablation simulation, 332–333, 333f
Strong-form system equations, 309
Submicron resolution mCT, 424
SUPG methods. *See* Streamline upwind Petrov–Galerkin methods (SUPG methods)
Support domain, 190
Surface integral equations (SIEs), 119
Surface tension in force term, 379–382
Swelling, 51
Swinging motion, 407
Synthetic VSMCs, 287
System of differential equation, 41

T

T-junction-like devices, 363
Target site, 273
TDOS. *See* Tricho–dento–osseous syndrome (TDOS)
TE. *See* Tissue engineering (TE)
Temporal discretization, 42
Tensor Green's function, 141
Tensor volume integral equation, 141–142
Ternary cell system, 173–179
  cell geometry and evolution, 177
  cell migration, 179
  chemical signals, 174–175
  differentiation model, 173–174, 174f
  differentiation rate and stimuli, 175–177
  mechanical approach, 177–179
Theory of porous media (TPM), 56–57, 59–60
Thermal LBM, 421
Thermomechanical effects, 60
Third Metaphysical principle of Truesdell, 60
threadIdx, 374–375
Three-dimension (3D)
  computational model for simulating, 51
  finite element modeling approach, 191
Three-parameter gamma (gamma-3P), 423–424
3D bioprinting, 269
  agent-based models in scaffold-free 3D bioprinting, 271–276
  models in, 270–271
    CPD methods, 270–271
    KMC methods, 271
    LB methods, 270
  state of the art in, 269–270
    scaffold-based methods, 269
    scaffold-free methods, 269–270

This book belongs to Central Library BADJI Mokhtar-ANNABA UNIVERSITY
Copyright Elsevier 2024

3D configuration (D3Qn), 415
Thrombogenesis, 425
Thrombus permeability, 425
Time calibration, 279
Time integration algorithm, 110b, 181, 181b
"Time", 227–228
Tip-sprout system, 97
Tips equation, 102–104, 108–109
Tissue complexity captured via model complexity, 71
Tissue engineering (TE), 37, 384
Tissue histology, 21
Tissue scale, emergent behavior at, 241–242
Tooth structure formation, 78
Top boundary, 396
Top-down TE, 384
Total variation diminishing scheme (TVD scheme), 378–379
TPM. *See* Theory of porous media (TPM)
  Runge–Kutta method, 101–102, 109
  time integration scheme, 106
Trabecular bone distribution, 315
Transition rule, 273
Transverse shear tension, 411
Trial functions, 330
Tricho–dento–osseous syndrome (TDOS), 89–91
Triphasic mechanoelectrochemical theory, 38
Tumbling motion, 407
Tumor ablation simulation, 332–333, 333f
Turing, Alain, 77
Turing instability, 77
  conditions for, 80–84
    conditions for instability by diffusion, 81–82
    Eigen functions of rectangle, 83–84
    Wave number, 82–83, 84f–85f
Turing patterns, 84f, 85, 91f
TVD scheme. *See* Total variation diminishing scheme (TVD scheme)
Two immiscible fluids, 363–365
Two-dimension (2D)
  approach, 391–392
  bone patch analysis
    initial conditions, 315–316, 316f
    results and discussion, 316, 316f–317f
  computing tension in 2D nodal structure, 260b
  femoral analysis, 317–321, 317f
    initial conditions, 317–319, 318f
    results and discussion, 318f–320f, 319–320
  indentation tests, 70
  LB simulations, 385
  problems, 310
  proximal femur model, 317
Two-phase flow algorithm, 418
2D configuration (D2Qn), 416
Type A lattice growth models, 231–232
Type B cellular automaton, 229–230

U

Universal stress distribution, 422–424, 422f
Unsteady cardiovascular flows, SPH applications to, 213–215
  benchmark case, 213–215
  comparison between analytical and SPH simulations, 214f–215f
Unstructured lattice, 225b, 226f
Unzipping, 188–189
Upwinding, 368

V

Validation
  and experimental examples
    boundary conditions, 45
    computational process, 46f
    free swelling, 48–50
    initial conditions, 48
    model validation, 45
    parameters of simplified 3D model of cartilage, 46t–47t
    sample subjected to loading, 50
  for flow coupled with rigid body motion, 347–349, 348f–349f
van der Waals equation (vdW equation), 357
  EOS, 380
Vandermonde matrix, 326, 329–330
Variable smoothing length, 206–207
Variable time step, 210
Vascular adaptation, 284
Vascular endothelial growth factors (VEGF), 95–96
Vascular mechanobiology, 284
Vascular smooth muscle cells (VSMCs), 286, 290b
  proliferation, 287–288
    pseudocode outlining algorithm, 288b
  stress-driven rule set, 294–297
Vascular tissue, paradigms for agent-based models of, 284–285
VDU. *See* Video display unit (VDU)
vdW equation. *See* van der Waals equation (vdW equation)
Vector Wiener process, 179
Vectorial stochastic variable, 181
VEGF. *See* Vascular endothelial growth factors (VEGF)
Velocity, 360–361
  artificial, 211–212
  Eulerian descriptions of, 59
  mesh, 174–175
Verlet scheme, 209–210
Vertex models (VMs), 255
Vesicles in shear flow, fluid-filled, 368, 369f
Vessel density, 104–106
Video display unit (VDU), 119, 121
Virial stress, 251
"Virtual biofabrication", 280
"Virtual histology" algorithm, 424
Virtual objects, 280
Virtual reality simulation of surgery, 148
Virtual tissue engineering, 280
VirtualLeaf (VMs), 261
Viscoelasticity
  of solid constituents, 68
  viscoelastic monophasic models, 38
Viscoplastic non-Newtonian fluid, 373
Viscous fluids and LB method, 371–375
Viscous regime, 373
VMs. *See* Vertex models (VMs); VirtualLeaf (VMs)
Volume correction, 403–404
Volume fractions, 57–58, 61
Volume strain locking, 292
Volume weight function, 343
von Mises stress potential, 193–194
von Mises–Fisher distribution, 8
von Neumann–Richtmyer viscosity, 208
Voronoi border, 225b
Voronoï cells, 308
Voronoi lattice, 234
Voronoi rule, 225b
Voronoi tessellation, 224, 226f, 252
Voxel-based approach, 159, 159f
VSMCs. *See* Vascular smooth muscle cells (VSMCs)
VTK, open source software, 18

W

Wall shear stress (WSS), 216–217
  particle in fluid domain and on wall, 216f
  two-dimensional velocity magnitude, vorticity, and turbulent shear stresses, 217f
  values for correction coefficient, 216f
Wave number, 82–83, 84f–85f
WBCs. *See* White blood cells (WBCs)
Weak formulation, 41
Weak-form MMs, 334–337. *See also* Strong-form MMs
  brain deformation, 334–335
  numerical examples, 334
  whole-body image registration, 336–337
Weight function, 326–327
Weighted effective stress field, 314
Weighted residual method, 330–331
  collocation method, 331
  Galerkin method, 331
Weighting function. *See* Interpolating kernel function
Welded joint, 9f, 10
"While" loops, 240
White blood cells (WBCs), 391
Whole body
  exposed to plane wave, 141–142
  image registration, 336–337, 336f–337f
Wiggle phenomenon, 384
Womersley number, 213–214
Womersley type flow, 213–214
WSS. *See* Wall shear stress (WSS)

X

XSPH variant, 209

Y

Young's modulus, 4

Z

ZZ-gradient recovery method, 180–182
ZZ-patch
  recovery method, 180
  ZZ-patch-based scheme, 97

This book belongs to Central Library BADJI Mokhtar-ANNABA UNIVERSITY
Copyright Elsevier 2024

Numerical Methods and Advanced Simulation in Biomechanics and Biological Processes

Edited by Miguel Cerrolaza, Sandra J. Shefelbine and Diego Garzón-Alvarado

Numerical Methods and Advanced Simulation in Biomechanics and Biological Processes covers modeling methods that can be used to understand biological phenomenon. This book contains a wide range of modeling approaches including finite element methods, boundary integral methods, discrete and particle methods, agent-based methods, meshless and mesh-free methods, and Lattice Boltzmann methods.

Basic theory of the methods is presented along with examples of application of these methods to both biomechanical and biological questions. Advantages and limitations of modeling strategies are discussed, making this an ideal resource for researchers, students, and R&D professionals.

Key Features

- Volume compiled by leading editors in their respective areas of research, who have many years of experience in computational biomechanics
- Includes state-of-the-art contributions from world-renowned experts in their fields
- Provides a clear, concise, and comprehensive description of simulation methods
- Evaluates pros and cons of each method to help you decide which method is most applicable to solving specific problems

About the Editors

Miguel Cerrolaza is Senior Researcher at the International Center for Numerical Methods in Engineering (BarcelonaTech) and Associate Professor in the Polytechnic University of Catalonia. His research areas are computational biomechanics, bone remodeling, and boundary elements.

Sandra J. Shefelbine is an Associate Professor in the Department of Mechanical and Industrial Engineering and Department of Bioengineering at Northeastern University. Her research areas are multiscale bone biomechanics and mechanoadaptation of bone and joints.

Diego Garzón-Alvarado is Full Professor in the Department of Mechanics and Mechatronic Engineering at the National University of Colombia. His research areas are morphogenesis and endochondral ossification, computational biomechanics, boundary and finite elements.

BIOMEDICAL ENGINEERING

ISBN 978-0-12-811718-7

9 780128 117187

ELSEVIER

ACADEMIC PRESS

An imprint of Elsevier

elsevier.com/books-and-journals

This book belongs to Central Library BADJI Mokhtar-ANNABA UNIVERSITY

Copyright Elsevier 2024